Springer Atmospheric Sciences

John T. Sullivan · Thierry Leblanc · Sara Tucker · Belay Demoz · Edwin Eloranta · Chris Hostetler · Shoken Ishii · Lucia Mona · Fred Moshary · Alexandros Papayannis · Krishna Rupavatharam *Editors*

Proceedings of the 30th International Laser Radar Conference

Springer

Springer Atmospheric Sciences

The Springer Atmospheric Sciences series seeks to publish a broad portfolio of scientific books, aiming at researchers, students, and everyone interested in this interdisciplinary field. The series includes peer-reviewed monographs, edited volumes, textbooks, and conference proceedings. It covers the entire area of atmospheric sciences including, but not limited to, Meteorology, Climatology, Atmospheric Chemistry and Physics, Aeronomy, Planetary Science, and related subjects.

John T. Sullivan • Thierry Leblanc • Sara Tucker •
Belay Demoz • Edwin Eloranta • Chris Hostetler •
Shoken Ishii • Lucia Mona • Fred Moshary •
Alexandros Papayannis • Krishna Rupavatharam
Editors

Proceedings of the 30th International Laser Radar Conference

Springer

Editors

John T. Sullivan
NASA Goddard Space Flight Center
Greenbelt, MD, USA

Sara Tucker
Ball Aerospace & Technologies Corp.
Boulder, CO, USA

Edwin Eloranta
Department of Atmospheric and Oceanic Sciences
University of Wisconsin–Madison
Madison, WI, USA

Shoken Ishii
Department of Aeronautics and Astronautics
Tokyo Metropolitan University
Hino-shi, Tokyo, Japan

Fred Moshary
Department of Electrical Engineering
The City College of New York
New York, NY, USA

Krishna Rupavatharam
Montana State University
Bozeman, MT, USA

Thierry Leblanc
Jet Propulsion Laboratory, California Institute of Technology
Pasadena, CA, USA

Belay Demoz
Department of Physics
University of Maryland, Baltimore County
Baltimore, MD, USA

Chris Hostetler
NASA Langley Research Center
Hampton, VA, USA

Lucia Mona
Institute of Methodologies for Environmental Analysis, National Research Council of Italy (CNR)
Potenza, Italy

Alexandros Papayannis
School of Applied Mathematical and Physical Sciences
National Technical University of Athens
Athens, Greece

ISSN 2194-5217 ISSN 2194-5225 (electronic)
Springer Atmospheric Sciences
ISBN 978-3-031-37817-1 ISBN 978-3-031-37818-8 (eBook)
https://doi.org/10.1007/978-3-031-37818-8

© The Editor(s) (if applicable) and The Author(s), under exclusive license to Springer Nature Switzerland AG 2023
This work is subject to copyright. All rights are solely and exclusively licensed by the Publisher, whether the whole or part of the material is concerned, specifically the rights of translation, reprinting, reuse of illustrations, recitation, broadcasting, reproduction on microfilms or in any other physical way, and transmission or information storage and retrieval, electronic adaptation, computer software, or by similar or dissimilar methodology now known or hereafter developed.
The use of general descriptive names, registered names, trademarks, service marks, etc. in this publication does not imply, even in the absence of a specific statement, that such names are exempt from the relevant protective laws and regulations and therefore free for general use.
The publisher, the authors, and the editors are safe to assume that the advice and information in this book are believed to be true and accurate at the date of publication. Neither the publisher nor the authors or the editors give a warranty, expressed or implied, with respect to the material contained herein or for any errors or omissions that may have been made. The publisher remains neutral with regard to jurisdictional claims in published maps and institutional affiliations.

This Springer imprint is published by the registered company Springer Nature Switzerland AG
The registered company address is: Gewerbestrasse 11, 6330 Cham, Switzerland

Paper in this product is recyclable.

Preface

For over 50 years, the International Laser Radar Conference (ILRC) has gathered more than 350 scientists, engineers, scholars, faculty members and students to foster state-of-the-art knowledge and contribute to the understanding of Earth Systems by means of laser remote sensing. The 30th edition of the ILRC was not an exception and unveiled many outstanding new results and discoveries in atmospheric science and laser remote sensing technology. With growing environmental concerns to address, such as air quality deterioration, stratospheric ozone depletion, extreme weather events and a changing climate, the lidar technique has never been more critical than it is today to monitor, alert, and help solve the current and emerging problems of this century.

Starting in early 2020, the Covid-19 pandemic caused a major disruption to all aspects of our lives. It was inevitable that the conference had to postponed. Due to continued risks and complications posed by the pandemic, we elected to move the conference to a virtual format. This new format offered more opportunities to collaborate with more attendees and reached a wider audience than in normal years. The ILRC conference program included all contemporary ILRC themes, leveraging on both the past events' legacy and the latest advances in lidar technologies and scientific discoveries. ILRC also collaborated with CLRC to offer a joint hybrid session between the two conferences. To celebrate 50 years of lidar atmospheric observations since ILRC-1 took place, there was a special session consisting of review talks followed by a plenary discussion on anticipated future directions and undertakings. As has been the tradition for past events, our 30th edition was specifically formatted to encourage participation by young scientists, ensuring continuity in excellence in the rapidly evolving field, that is, laser remote sensing.

Greenbelt, MD, USA — John T. Sullivan
Pasadena, CA, USA — Thierry Leblanc
Boulder, CO, USA — Sara Tucker
Baltimore, MD, USA — Belay Demoz
Madison, WI, USA — Edwin Eloranta
Hampton, VA, USA — Chris Hostetler

Hino-shi, Tokyo, Japan — Shoken Ishii
Potenza, Italy — Lucia Mona
New York, NY, USA — Fred Moshary
Athens, Greece — Alexandros Papagiannis
Bozeman, MT, USA — Krishna Rupavatharam

Organization

Organizing Committee

Sullivan, John (co-chair)	*NASA Goddard Space Flight Center, Greenbelt, MD, United States*
Leblanc, Thierry (co-chair)	*NASA Jet Propulsion Laboratory, Pasadena, CA, United States*
McFadden, Susan	*NASA Earth Science Project Office, Mountain View, CA, United States*
Murphy, Caitlin	*NASA Earth Science Project Office, Mountain View, CA, United States*
Kim, Samuel	*NASA Earth Science Project Office, Mountain View, CA, United States*

Program Committee

Belay Demoz (co-chair)	*University of Maryland, Baltimore County, Baltimore, MD, USA*
Ed Eloranta (co-chair)	*University of Wisconsin, Madison, WI, USA*
Sara Tucker (co-chair)	*Ball Aerospace, Boulder, CO, USA*
Chris Hostetler	*NASA LaRC, Hampton, USA*
Shoken Ishii	*Tokyo Metropolitan University, Tokyo, Japan*
Lucia Mona	*CNR, Potenza, Italy*
Fred Moshary	*CCNY, New York, USA*
Alex Papayannis	*National Technical University, Athens, Greece*
Krishna Rupavatharam	*Montana State University, Bozeman, USA*
John Sullivan	*NASA GSFC, Greenbelt, USA*
Thierry Leblanc	*Jet Prolusion Laboratory, Pasadena, USA*

Reviewers

Alain Dabas	*Meteofrance, Toulouse, France*
Alain Miffre	*Université Lyon 2, Lyon, France*
Alex Papayannis	*National Technical University, Athens, Greece*
Amanda Makowiecki	*NOAA, Boulder, USA*
Amin Nehrir	*NASA, Hampton, USA*
Andreas Fix	*DLR, Köln, Germany*
Angela Benedetti	*ECMWF, Reading, UK*
Atsushi Shimizu	*NIES, Tsukuba, Japan*
Belay Demoz	*UMBC, Baltimore, USA*
Chris Hostetler	*NASA LaRC, Hampton, USA*
Dave Donovan	*KNMI, De Bilt, The Netherlands*
Davide Dionisi	*CNR, Rome, Italy*
Dengxin Hua	*Xi'an University of Technology, Xian, China*
Dimitris Balis	*National Technical University, Athens, Greece*
Dong Liu	*Zhejiang University, Zhejian, China*
Ed Eloranta	*UWisc, Madison, USA*
Fabien Gibert	*Ecole Polytechnique, Palaiseau, France*
Fernando Chouza	*Jet Propulsion Laboratory, Pasadena, USA*
Fred Moshary	*CCNY, New York, USA*
Gary Gimmestad	*Georgia Tech, Atlanta, USA*
Georgios Tzeremes	*National Technical University, Athens, Greece*
Hajime Okamoto	*Kyushu University, Kiushu, Japan*
Hannes Vogelmann	*KIT, Garmisch-Partenkirchen, Germany*
Hassan Bencherif	*Université de La Réunion, Saint-Denis, France*
Igor Ptashnik	*IAO, Tomsk, Russia*
James Campbell	*NRL, Washington DC, USA*
Jason Tackett	*NASA GSFC< Greenbelt, USA*
Jasper Lewis	*NASA GSFC< Greenbelt, USA*
Javier Fochesatto	*University of Alaska, Fairbanks*
Jintai Li	*University of Alaska, Fairbanks*
John Sullivan	*NASA GSFC, Greenbelt, USA*
John Yorks	*NASA GSFC, Greenbelt, USA*
Joseph Shaw	*Montana State University, Bozeman, USA*
Kevin Repasky	*Montana State University, Bozeman, USA*
Krishna Rupavatharam	*Montana State University, Bozeman, USA*
Lucia Mona	*CNR, Potenza, Italy*
Makoto Abo	*Tokyo Metropolitan University, Tokyo, Japan*
Martin Wirth	*DLR, Koln, Germany*
Masaharu Imaki	*Mitsubishi Electric, Kanagawa, Japan*

(continued)

Michael Rennie	*ECMWF, Reading, UK*
Oliver Reitebuch	*DLR, Oberpfaffenhofen-Wessling, Germany*
Pablo Ristori	*CITEDEF, Buenos Aires, Argentina*
Panos Kokkalis	*National Technical University, Athens, Greece*
Patrick Rairoux	*Université Lyon 1, Lyon, France*
Ronnie Engelmann	*Leibniz Institute for Tropospheric Research, Leipzig, Germany*
Rory Barton-Grimley	*NASA LaRC, Hampton, USA*
Sara Tucker	*Ball Aerospace, Boulder, USA*
Shoken Ishii	*Tokyo Metropolitan University, Tokyo, Japan*
Silke Gross	*DLR, Oberpfaffenhofen-Wessling, Germany*
Simone Lolli	*CNR, Rome, Italy*
Sunil Baidar	*NOAA CSL, Boulder, USA*
Thierry Leblanc	*NASA Jet Prolusion Laboratory, Pasadena, USA*
Tom McGee	*NASA GSFC, Greenbelt, USA*
Tomoaki Nishizaw	*NIES, Tsukuba, Japan*
Trent Berg	*Montana Photonics, Bozeman, USA*
Upendra Singh	*NASA LaRC, Hampton, USA*
Xiao Mei Lu	*NASA LaRC, Hampton, USA*
Xinzhao Chu	*University of Colorado, Boulder, USA*
Yoshitaka Jin	*NIES, Tsukuba, Japan*

Contents

Part I Emerging Lidar Techniques, Methodologies, and Discoveries

1 Rotational Raman Scattering Through Narrow-Band Interference Filters: Investigating Uncertainties Using a New Rayleigh Scattering Code Developed Within ACTRIS 3
N. Siomos, I. Binietoglou, M. Adam, U. Wandinger, M. Haarig, B. Gast, G. D'Amico, and V. Freudenthaler

2 Performance of Low-Cost, Diode-Based HSRL System with Simplified Optical Setup 11
Zachary Noel Buckholtz, Ilya Razenkov, Joseph Garcia, and Edwin Eloranta

3 Sensitivity Study on the Performance of the Single Calculus Chain Aerosol Layering Module 19
K. A. Voudouri, P. Fountoukidis, N. Siomos, C. Dema, D. Balis, and G. D'Amico

4 Particle Complex Refractive Index from $3\beta + 2\alpha$ HSRL/Raman Lidar Measurements: Conditions of Accurate Retrieval, Uncertainties, and Constraints Provided by Information About RH 25
Alexei Kolgotin, Detlef Müller, Igor Veselovskii, and Mikhail Korenskiy

5 Field Testing of a Diode-Laser-Based MicroPulse Differential Absorption Lidar System to Measure Atmospheric Thermodynamic Variables 33
Robert A. Stillwell, Scott M. Spuler, Matthew Hayman, Kevin Repasky, and Owen Cruikshank

6 Semiconductor Lidar for Quantitative Atmospheric Profiling 41
Scott M. Spuler, Robert A. Stillwell, Matthew Hayman, and Kevin Repasky

7 Atomic Barium Vapor Filter for Ultraviolet High-Spectral-Resolution Temperature LiDAR 49
Madison Hetlage and Christopher Limbach

8 Future Lidars for Cutting-Edge Sciences in Ionosphere-Thermosphere-Mesosphere-Stratosphere Physics and Space-Atmosphere Coupling 57
Xinzhao Chu and Guotao Yang

9 Polarization Lidar for Monitoring Dust Particle Orientation: First Measurements 65
Alexandra Tsekeri, Vassilis Amiridis, Spiros Metallinos, Alexandros Louridas, George Georgoussis, Nikolaos Siomos, Peristera Paschou, Thanasis Georgiou, and Ioannis Binietoglou

10 Dust Flow Distribution Measurement by Low Coherence Doppler Lidar 73
Kosuke Okubo, Nofel Lagrosas, and Tatsuo Shiina

11 A Multiwavelength LED Lidar for Near-Ground Atmospheric Monitoring 79
Alifu Xiafukaiti, Nofel Lagrosas, and Tatsuo Shiina

12 Development of Low-Cost High Spectral Resolution Lidar Using Compact Multimode Laser for Air Quality Measurement 85
Yoshitaka Jin and Makoto Aoki

13 Deep-Learning-Based Convective Boundary Layer Determination for Aerosol and Wind Profiles Observed by Wind LiDAR 91
Chih-Wen Su, Wei-Nai Chen, Wei-Yao Chang, and M. Roja Raman

14 LITES: Laboratory Investigations of Atmospheric Aerosol Composition by Raman-Scattering and Fluorescence Spectra 101
Boyan Tatarov and Detlef Müller

15 Performance Simulation of a Raman Lidar for the Retrieval of CO_2 Atmospheric Profiles 109
M. Di Paolantonio, P. Di Girolamo, D. Dionisi, M. Cacciani, A. Di Bernardino, T. Di Iorio, N. Franco, A. M. Iannarelli, G. L. Liberti, and D. Summa

16 All Fiber Free-Running Dual-Comb Ranging System 117
Fu Yang, Yanyu Lu, and Guibin Liu

17 gPCE Uncertainty Quantification Modeling of LiDAR for Bathymetric and Earth Science Applications 125
Alexandra K. Wise, Kevin W. Sacca, and Jeffrey P. Thayer

18 When Can Poisson Random Variables Be Approximated as Gaussian? 133
Matthew Hayman, Willem J. Marais, Hristo G. Chipilski, Robert A. Stillwell, and Scott M. Spuler

19 Enhancing the Performance of the MicroPulse DIAL Through Poisson Total Variation Signal Processing 141
Matthew Hayman, Willem J. Marais, Robert A. Stillwell, Joshua Carnes, and Scott M. Spuler

20 Development of MicroPulse Lidar Network (MPLNET) Level 3 Satellite Validation Products in Advance of the EarthCARE Mission 149
Jasper R. Lewis, James R. Campbell, Simone Lolli, Sebastian A. Stewart, Larry R. Belcher, Rob Koopman, Michaël Sicard, Erica Dolinar, Stephanie Rusli, Jason Tackett, and Ellsworth J. Welton

21 Three-Dimensional Point Cloud Classification Using Drone-Based Scanning LIDAR and Signal Diversity 157
Kevin W. Sacca, Alexandra K. Wise, and Jeffrey P. Thayer

22 Design and Validation of an Elastic Lidar Simulator for Testing Potential New Systems for Aerosol Typing 165
Rebecca Howe, Ioannis Binnietoglou, Anna Gialitaki, and Joshua Vande Hey

23 Performance of Pulsed Wind Lidar Based on Optical Hybrid 173
G. A. Petrov, N. A. Baranov, G. E. Romanova, and M. Yu Sachkov

24 Demonstrating Capabilities of Multiple-Beam Airborne Doppler Lidar Using a LES-Based Simulator 181
James Kasic, Philipp Gasch, Oliver Maas, and Zhien Wang

25 All-Solid State Iron Resonance Lidar for Measurement of Temperature and Winds in the Upper Mesosphere and Lower Thermosphere 189
R. Collins, J. Li, B. Wiliams, B. Kaifler, and D. Thorsen

26 Improved Remote Operation Capabilities for the NASA GSFC Tropospheric Ozone Lidar for Routine Ozone Profiling for Satellite Evaluation 197
T. H. Nguyen, J. T. Sullivan, and L. W. Twigg

27 A Wind, Temperature, H_2O, and CO_2 Scanning Lidar Mobile Observatory for a 3D Thermodynamic View of the Atmosphere 205
Fabien Gibert, Dimitri Edouart, Paul Monnier, Claire Cénac, Vincent Gauthier, and Henri Salvador

28 Low-Cost and Lightweight Hyperspectral Lidar for Mapping Vegetation Fluorescence 213
Hampus Månefjord, Lauro Müller, Jacobo Salvador, Anna Runemark, Carsten Kirkeby, and Mikkel Brydegaard

29 SO_2 Plumes Observation with LMOL: Theory, Modeling, and Validation 219
Guillaume Gronoff, Timothy Berkoff, William Carrion, Liqiao Lei, and Daniel Phoenix

30 Possible Use of Iodine Absorption/Fluorescence Cell in High-Spectral-Resolution Lidar 227
Nobuo Sugimoto, Yoshitaka Jin, and Tomoaki Nishizawa

Part II Atmospheric Clouds and Aerosol Properties

31 Ten Years of Interdisciplinary Lidar Applications at SCNU, Guangzhou 235
J. B. Chi, Z. Duan, J. W. Huang, Y. Li, Y. Y. Li, M. Lian, Y. Y. Lin, J. C. Lu, Y. T. Sun, J. L. Wang, X. Wang, Y. Yuan, Q. Zhang, G. Y. Zhao, S. M. Zhu, and S. Svanberg

32 Feasibility Studies of the Dual-Polarization Imaging Lidar Based on the Division-of-Focal-Plane Scheme for Atmospheric Remote Sensing 243
Zheng Kong, Jiheng Yu, and Liang Mei

33 An Algorithm to Retrieve Aerosol Optical Properties from ATLID and MSI Measurements 249
Tomoaki Nishizawa, Rei Kudo, Akiko Higurashi, Satoru Takakura, Eiji Oikawa, and Hajime Okamoto

34 Observation of Polar Stratospheric Clouds at Dome C, Antarctica. 257
Marcel Snels, Luca Di Liberto, Ilir Shuli, Francesco Colao, Andrea Scoccione, and Federico Serva

35 Laboratory Evaluation of the Lidar Particle Depolarization Ratio (PDR) of Sulfates, Soot, and Mineral Dust at 180.0° Lidar Backscattering Angle 265
D. Cholleton, P. Rairoux, and A. Miffre

36 Fresh Biomass Burning Aerosol Observed in Potenza with Multiwavelength Raman Lidar and Sun Photometer 273
Benedetto De Rosa, Lucia Mona, Aldo Amodeo, Nikolaos Papagiannopoulos, Michail Mytilinaios, Donato Summa, and Igor Veselovskii

37 Aerosol Studies with Spectrometric Fluorescence and Raman Lidar 279
Jens Reichardt, Felix Lauermann, and Oliver Behrendt

38 Continuous Observations of Aerosol-Weather Relationship from a Horizontal Lidar to Simulate Monitoring of Radioactive Dust in Fukushima, Japan 287
Nofel Lagrosas, Kosuke Okubo, Xiafukaiti Alifu, and Tatsuo Shiina

39 Statistical Simulation of Laser Pulse Propagation Through Cirrus-Cloudy Atmosphere 295
T. V. Russkova, V. A. Shishko, and A. V. Konoshonkin

40 Aerosol Spatial Distribution Observed by a Mobile Vehicle Lidar with Optics for Near-Range Detection 303
Masanori Yabuki, Kazuhiko Miura, Tatsuhiro Mori, Hiroshi Hayami, and Hiroaki Kuze

41 Cloud Base Height Correlation Between a Co-located Micro-Pulse LiDAR and a Lufft CHM15k Ceilometer 311
Victoria Pinnegar, Paul Christiaans, Joe Clarke, Alexander Haefele, E. J. Welton, and Robert J. Sica

42 Comparison of Local and Transregional Atmospheric Particles over the Urmia Lake in Northwest Iran, Using a Polarization Lidar Recordings 317
Salar Alizadeh, Ruhollah Moradhaseli, Hossein Panahifar, and Hamid R. Khalesifard

43 Properties of Polar Stratospheric Clouds over the European Arctic from Ground-Based Lidar 325
Christine Böckmann and Christoph Ritter

44 Two Decades Analysis of Cirrus Cloud Radiative Effects by LiDAR Observations in the Frame of NASA MPLNET LiDAR Network 333
Simone Lolli, Erica Dolinar, Jasper R. Lewis, James R. Campbell, Sebastian A. Stewart, Larry R. Belcher, and Ellsworth J. Welton

45 Temporal Variability of the Aerosol Properties Using a Cimel Sun/Lunar Photometer over Thessaloniki, Greece: Synergy with the Upgraded THELISYS Lidar System 339
K. Michailidis, K. A. Voudouri, N. Siomos, and D. Balis

46 Long-Term Changes of Optical Properties of Mineral Dust and Its Mixtures Derived from Raman Polarization Water Vapor Lidar in Central Europe 347
D. M. Szczepanik, W. Kumala, C. F. Olusegun, E. Tetoni, V. Amiridis, D. Nicolae, D. Althausen, and I. Stachlewska

47 Planetary Boundary Layer Height Measurements Using MicroPulse DIAL 355
Luke Colberg, Owen Cruikshank, Kevin S. Repasky, Scott M. Spuler, Robert A. Stillwell, and Matthew Hayman

Part III Atmospheric Temperature, Water Vapor, Wind, Turbulence, and Waves

48 Performance Modeling of a Diode Laser-Based Direct Detection Doppler Lidar 365
Kevin S. Repasky, Owen Cruikshank, and Luke Colberg

49 Observation of Water Vapor Profiles by Raman Lidar with 266-nm Laser in Tokyo 373
Yuichi Uchiho, Kazuto Matsuki, Eiji Takeuchi, Toshikazu Hasegawa, and Masanori Yabuki

50 A 355-nm Direct-Detection Doppler Wind Lidar for Vertical Atmospheric Motion 379
Shoken Ishii, Hideki Takenaka, Kodai Kishibuchi, Yoshitaka Jin, Tomoaki Nishizawa, Nobuo Sugimoto, Hironari Iwai, Makoto Aoki, Seiji Kawamura, and Hajime Okamoto

51 Aircraft Wake Vortex Recognition and Classification Based on Coherent Doppler Lidar and Convolutional Neural Networks ... 387
Xinyu Zhang, Songhua Wu, Xiaoying Liu, Hongwei Zhang, and Guangyao Dai

52 MicroPulse Differential Absorption LiDAR for Temperature Retrieval in the Lower Troposphere 395
Owen Cruikshank, Luke Colberg, Kevin S. Repasky, Robert A. Stillwell, and Scott M. Spuler

53 Long-Term Calibration of a Pure Rotational Raman LiDAR for Temperature Measurements Using Radiosondes and Solar Background 403
Vasura Jayaweera, Robert J. Sica, Alexander Haefele, and Giovanni Martucci

54 Powerful Raman LiDAR for Water Vapor in the Free Troposphere and Lower Stratosphere as well as Temperature in the Stratosphere and Mesosphere 411
Hannes Vogelmann, Thomas Trickl, Lisa Klanner, Katharina Höveler, and Matthias Perfhal

55 Observation of Rainfall Velocity and Raindrop Size Using Power Spectrum of Coherent Doppler Lidar 419
Xiaoying Liu, Songhua Wu, Guangyao Dai, Pei Chen, Rongzhong Li, and Jiaping Yin

56 Comparison of Lower Tropospheric Water Vapor Vertical Distribution Measured with Raman Lidar and DIAL and The Impact of Data Assimilation in Numerical Weather Prediction Model 427
Tetsu Sakai, Satoru Yoshida, Tomohiro Nagai, Yasutaka Ikuta, and Yoshinori Shoji

57 Temperature Variations in the Middle Atmosphere Studied with Rayleigh Lidar at Haikou (19.9°N, 110.3°E) 435
Yang Jie, Wang Yu-Ru, Chen Wei-Peng, Zhang Yu-Hao, Yang Guo-Tao, Li Fa-Quan, Cheng Xue-Wu, Wang Ying-Pin, and Gong Shao-Hua

58 Convective Boundary Layer Sensible and Latent Heat Flux Lidar Observations and Towards New Model Parametrisations 443
Fabien Gibert, Dimitri Edouart, Paul Monnier, Julie Collignan, Julio Lopez, and Claire Cénac

Part IV Atmospheric Boundary Layer Processes

59 Observation of Structure of Marine Atmospheric Boundary Layer by Ceilometer Over the Kuroshio Current 453
Toshiyuki Murayama and Fumiaki Kobashi

60 ABL Height Different Estimation by Lidar in the Frame of HyMeX SOP1 Campaign 461
D. Summa, P. Di Girolamo, N. Franco, G. D'Amico, B. De Rosa, and G. Vivone

61 Temporal Evolution of Wavelength and Orientation of Atmospheric Canopy Waves 469
Alejandro Espinoza-Ruiz, Julia E. Colombini, Emily K. Everton, Pierre Dérian, and Shane D. Mayor

62 Assessment of Planetary Boundary Layer Height Variations Over a Mountain Region in Western Himalayas 475
Jaswant Rathore, S. R. Radhakrishnan, Shishir Kumar Singh, Devesh Kumar Shukla, and Chhemendra Sharma

63 Analysis of Updraft Characteristics from an Airborne Micro-pulsed Doppler Lidar During FIREX-AQ 483
Edward J. Strobach, Alan Brewer, Brandi McCarty, and Amanda Makowiecki

64 Diurnal Variability of MLH and Ozone in NYC Urban and Coastal Area from an Integrated Observation During LISTOS 2018 491
Yonghua Wu, Amin Nehrir, Kaihui Zhao, Guillaume Gronoff, Jianping Huang, James E. Collins, Timothy A. Berkoff, Liqiao Lei, Dingdong Li, Margarita Kulko, Mark Arend, Barry Gross, and Fred Moshary

65 Boundary Layer Dynamics, Aerosol Composition, and Air Quality in the Urban Background of Stuttgart in Winter 499
Hengheng Zhang, Wei Huang, Xiaoli Shen, Ramakrishna Ramisetty, Thomas Leisner, and Harald Saathoff

Part V Greenhouse Gases, Tracers, and Transport in the Free Troposphere and Above

66 DIAL Ozone Measurement Capability Added to NASA's HSRL-2 Instrument Demonstrates Tropospheric Ozone Variability Over Houston Area 509
Marta Fenn, Johnathan Hair, Taylor Shingler, and Richard Ferrare

67 Trajectory Analysis of CO_2 Concentration Increase Events in the Nocturnal Atmospheric Boundary Layer Observed by the Differential Absorption Lidar 517
Makoto Abo, Chikao Nagasawa, and Yasukuni Shibata

68 Efficiency Assessment of Single-Cell Raman Gas Mixture for DIAL Ozone Lidar 523
M. Roja Raman and Wei-Nai Chen

69 A Compact Raman Lidar for Atmospheric CO_2 and Thermodynamic Profiling: The System CONCERNING 531
Paolo Di Girolamo, Davide Dionisi, Marco Cacciani, Annalisa Di Bernardino, Noemi Franco, Donato Summa, Marco Di Paolantonio, Anna Maria Iannarelli, and Tatiana Di Iorio

70 Characterization of Recent Aerosol Events Occurring in the Subtropical North Atlantic Region Using a CIMEL CE376 GPN Micro-LiDAR 539
Y. González Ramos, I. Popovici, A. Barreto, M. F. Sanchez-Barrero, L. Pronieswki, S. Victori, F. A. Almansa, R. Ramos, and E. Cuevas

71 Tropospheric Ozone Differential Absorption Lidar (DIAL) Development at New York City 547
Dingdong Li, Yonghua Wu, Thomas Legbandt, Mark Arend, Maggie Liang, and Fred Moshary

Part VI Measurements in the Stratosphere, Mesosphere and Thermosphere

72 Accounting for the Polarizing Effects Introduced from Nonideal Quarter-Wave Plates in Lidar Measurements of the Circular Depolarization Ratio 557
N. Siomos, P. Paschou, G. Georgoussis, G. Tsaknakis, V. Amiridis, and V. Freudenthaler

73 Investigating the Geometrical and Optical Properties of the Persistent Stratospheric Aerosol Layer Observed over Thessaloniki, Greece, During 2019 565
K. A. Voudouri, N. Siomos, K. Michailidis, M. E. Koukouli, G. Peletidou, and D. Balis

74 New Lidar Data Processing Techniques for Improving the Detection Range and Accuracy of Atmospheric Gravity Wave Measurements 573
Jackson R. Jandreau and Xinzhao Chu

75 Extending the Useful Range of Fluorescence LIDAR Data by Applying the Layered Binning Technique 581
Gary W. S. Sutliff and Xinzhao Chu

Part VII Measurement Techniques and Observations of Ocean Properties

76 Interaction Between Sea Wave and Surface Atmosphere by Shallow Angle LED Lidar 589
Tatsuo Shiina, Kosuke Okubo, Nofel Lagrosas, and Alifu Xiafukaiti

77 First Results of the COLOR (*C*DOM-Proxy Retrieval from ae*O*Lus *O*bse*R*vations) Project 597
D. Dionisi, S. Bucci, C. Cesarini, S. Colella, D. D'Alimonte, L. Di Ciolo, P. Di Girolamo, M. Di Paolantonio, N. Franco, G. Giuliano, G. Gostinicchi, T. Kajiyama, G. Liberti, E. Organelli, and R. Santoleri

78 Dual Wavelength Heterodyne LDA for Velocity and Size Distribution Measurements in Ocean Water Flows 605
Hongwei Zhang, Ziwang Li, Xiangcheng Chen, Jintao Liu, Kailin Zhang, Songhua Wu, Yan He, Weibiao Chen, and Junwu Tang

Part VIII Space-Borne Lidar Missions, Instruments and Science

79 Mitigation Strategy for the Impact of Low Energy Laser Pulses in CALIOP Calibration and Level 2 Retrievals 617
Jason Tackett, Robert Ryan, Mark Vaughan, Anne Garnier, Brian Getzewich, David Winker, and Charles Trepte

80 Introducing the Cloud Aerosol Lidar for Global Scale Observations of the Ocean-Land-Atmosphere System: CALIGOLA 625
Paolo Di Girolamo, Alberto Cosentino, Francesco Longo, Noemi Franco, Davide Dionisi, Donato Summa, Simone Lolli, Enrico Suetta, Alessandro Perna, and Simona Zoffoli

81 An Overview of the NASA Atmosphere Observing System Inclined Mission (AOS-I) and the Role of Backscatter Lidar 631
John E. Yorks, Scott Braun, Ed Nowottnick, Matt McGill, Courtney Schumacher, Jun Wang, Melanie Follette-Cook, James Campbell, and Michael Pavolonis

82 Proposal for the Space-Borne Integrated Path Differential Absorption (IPDA) Lidar for Lower Tropospheric Water Vapor Observations 639
Makoto Abo, Chikao Nagasawa, Yasukuni Shibata, Osamu Uchino, Tetsu Sakai, Takashi Shibata, and Masaki Katsumata

83 Assimilation of Aerosol Observations from the Future Spaceborne Lidar Onboard the AOS Mission into the MOCAGE Chemistry: Transport Model 645
Flavien Cornut, Laaziz El Amraoui, Juan Cuesta, Roseline Schmisser, Jérôme Blanc, and Béatrice Josse

84 Aerosol Optical Properties over Western Himalayas Region by Raman Lidar During the December 2019 Annular Solar Eclipse 653
Shishir Kumar Singh, S. R. Radhakrishnan, Rathore Jaswant, and Chhemendra Sharma

85 The Clio HSRL Instrument Concept for the NASA AOS Mission ... 659
Chris Hostetler, Stephen Hall, Salvatore Scola, John Smith, Richard Hare, Amin Nehrir, Shane Seaman, Anthony Notari, Richard Ferrare, Sharon Burton, Kathleen Powell, Tyler Thorsen, Mark Vaughan, David Winker, Johnathan Hair, Robert Holz, Willem Marais, and Edwin Eloranta

86 Overview and Status of the Methane Remote Sensing Lidar Mission: MERLIN 667
Sabrina G. Arnold, Gerhard Ehret, Matthias Alpers, Caroline Bès, Philippe Bousquet, Cyril Crevoisier, Andreas Fix, Bruno Millet, and Martin Wirth

87 A Simulation Capability Developed for NASA GSFC's Spaceborne Backscatter Lidars: Overview and Projected Performance for the Upcoming AOS Mission 675
Edward P. Nowottnick, John E. Yorks, Matthew J. McGill, Patrick A. Selmer, and Kenneth E. Christian

88 Aerosol Typing and Spaceborne Lidars: Potentials and Limitations 683
Athena Augusta Floutsi, Holger Baars, Moritz Haarig, and Ulla Wandinger

89 Correcting CALIOP Polarization Gain Ratios for Diurnal Variations 691
Mark Vaughan, Sharon D. Rodier, Zhaoyan Liu, Anne Garnier, Kam-Pui Lee, Brian Getzewich, and Shan Zeng

90 Performance Simulation of a Spaceborne Raman Lidar for ATLAS 699
Noemi Franco, Paolo Di Girolamo, Andreas Behrendt, Volker Wulfmeyer, Adolfo Comerón, Donato Summa, and David N. Whiteman

91 Column Optical Depth (COD) Derived from CALIOP Ocean Surface Returns 707
Robert Ryan, Mark A. Vaughan, Sharon D. Rodier, Brian J. Getzewich, and David M. Winker

92 Assessing Aeolus Aerosol Observational Capabilities for Data Assimilation in Air Quality and NWP Models 715
E. Proestakis, A. Benedetti, A. Dabas, V. Amiridis, E. Marinou, P. Paschou, A. Georgiou, A. Gkikas, A. Kampouri, A. Gialitaki, A. Tsekeri, W. McLean, and L. Steele

93 High-Spectral-Resolution Lidars at the University of Wisconsin 723
Ilya Razenkov, Joseph Garcia, and Edwin Eloranta

94 ATLID Algorithms Applied to ALADIN 731
David P. Donovan, Gerd-Jan van Zadelhoff, Ping Wang, and Lev Labzovskii

Part IX Synergistic Use of Multiple Instruments and Techniques, Networks and Campaigns

95 Integrated Mobile System of Two-Wavelength Polarization Micro-pulse Lidar and Photometer for Aerosol Properties Retrievals: Comparisons with Reference Lidar 741
M. F. Sanchez Barrero, I. Popovici, P. Goloub, S. Victori, L. Proniewski, Q. Hu, T. Podvin, B. Holben, D. Giles, and A. LaRosa

96 Regional Changes in the Dominant Aerosol Type Over Europe During the ACTRIS COVID-19 Campaign 749
K. A. Voudouri, D. Nicolae, L. Mona, G. D'Amico, N. Papagiannopoulos, E. Marinou, A. Kampouri, J. Vasilescu, C. Talianu, I. Stachlewska, R. Fortuna, M. Sicard, A. Rodriguez, S. Romano, M. R. Perrone, A. Floutsi, X. Shang, N. Siomos, A. Gialitaki, A. Tsekeri, D. Balis, and V. Amiridis

97 The Role of Dry Layers and Cold Pools in the Activation of Mesoscale Convective Systems: A Characterization Study Based on the Combined Use of Raman Lidar and DIAL Measurements and MESO-NH Model Simulations 757
Paolo Di Girolamo, Marie-Noelle Bouin, Cyrille Flamant, Donato Summa, Benedetto De Rosa, and Noemi Franco

98 Advances in Characterizing Pollution Transport with Ground-Based and Airborne Profilers: Case Studies Within Houston, TX 765
John Sullivan, Johnathan Hair, Taylor Shingler, Richard Ferrare, Marta Fenn, Timothy Berkoff, Guillaume Gronoff, Maurice Roots, Trong Nyugen, Laurence Twigg, James Flynn, Travis Griggs, Paul Walter, Thomas Hanisco, Alexander Kotsakis, Ellsworth J. Welton, and Laura Judd

99 First Results of Inverted Aerosol Properties Through GRASP Algorithm, Using Polarized Data from the Multiwavelength Sun-Sky-Lunar Photometer in Barcelona, Spain 773
D. C. F. S. Oliveira, A. Rodriguéz-Gomez, A. Comerón, C. Muñoz-Porcar, O. Dubovik, A. Lopatin, M. E. Herrera, and M. Sicard

100 Radiative Budget in the Lower Tropical Stratosphere from the Combination of Balloon-Borne Lidar and Radiometric Measurements 781
François Ravetta, Thomas Lesigne, Vincent Mariage, Jérôme Bureau, Alain Hauchecorne, and Jacques Pelon

101 Spatial Distribution Analysis of the TROPOMI Aerosol Layer Height: A Pixel-by-Pixel Comparison to EARLINET and CALIOP Observations 787
K. Michaildis, M.-E. Koukouli, D. S. Balis, M. de Graaf, and J. P. Veefkind

102 First Results from the Aeolus Reference Lidar eVe During the Tropical Campaign JATAC at Cabo Verde 795
P. Paschou, N. Siomos, E. Marinou, H. Baars, A. Gkikas, G. Georgoussis, D. Althausen, R. Engelmann, J. von Bismarck, T. Fehr, and V. Amiridis

103 Analysis of a Mid-Atlantic Ozone Episode Using TOLNet and Pandora 803
Maurice Roots, Sergio Diaz, John T. Sullivan, Ruben Delgado, and Belay Demoz

104 A Difference of the Depolarization Ratio Detected at Locally Generated Dust and Transported Asian Dust Over Japan with AD-Net 811
Atsushi Shimizu, Tomoaki Nishizawa, Yoshitaka Jin, and Nobuo Sugimoto

105 Identification of Mixed-Phase Clouds Using Combined CALIPSO Lidar and Imaging Infrared Radiometer Observations 817
Anne Garnier, Jacques Pelon, David Winker, Melody Avery, Mark Vaughan, and Yongxiang Hu

106 Huntsville Mobile RO_3QET Launch 825
Shi Kuang, Mike Newchurch, Paula Tucker, Todd McKinney, Brendan Lee, Susan Alexander, and Casey Calamaio

Part X Model Validation and Assimilation Using Lidar Data

107 Retrieval of Aerosol Properties from Multiwavelength Raman Lidar Data Based on Maximum Likelihood Estimation 833
Yuyang Chang, Qiaoyun Hu, and Philippe Goloub

108 Polarimetric Multiple Scattering LiDAR Model Based on Poisson Distribution 841
Grégoire Tremblay and Gilles Roy

109 Assimilating Radar and Lidar Observations to Improve the Prediction of Bore Waves During the 2015 PECAN Field Campaign 849
Zhifeng Yang, David N. Whiteman, Xingchao Chen, Yunji Zhang, Belay Demoz, Jose D. Fuentes, Charles Ichoku, and Joseph L. Wilkins

Part XI Joint CLRC-ILRC Session: Past, Present and Future Synergy of Heterodyne and Direct Detection Lidar Applications

110 First Discovery of Regular Occurrence of Mid-Latitude Thermosphere-Ionosphere Na (TINa) Layers Observed with High-Sensitivity Na Doppler Lidar and New Data Processing Techniques over Boulder 861
Yingfei Chen and Xinzhao Chu

Part XII 50 Years of Lidar Observations: The Tip of the Laser Remote Sensing Iceberg?

111 Field-Widened Michelson Interferometer as the Spectral Discriminator in a 1064-nm HSRL 871
Zachary Noel Buckholtz, Ilya Razenkov, and Edwin Eloranta

112 Long-Term Monitoring of the Stratosphere by Lidars in the Network for the Detection of Atmospheric Composition Change 877
Wolfgang Steinbrecht, Thierry Leblanc, Sophie Godin-Beekmann, Sergey M. Khaykin, Alain Hauchecorne, Philippe Keckhut, Richard Querel, Daan P. J. Swart, and Thomas J. McGee

113 Stratospheric Aerosol: 45 Years of Lidar Measurements at Garmisch-Partenkirchen 885
Thomas Trickl, Hannes Vogelmann, Helmuth Giehl, Horst Jäger, and Matthias Perfahl

Part I
Emerging Lidar Techniques, Methodologies, and Discoveries

Chapter 1
Rotational Raman Scattering Through Narrow-Band Interference Filters: Investigating Uncertainties Using a New Rayleigh Scattering Code Developed Within ACTRIS

N. Siomos, I. Binietoglou, M. Adam, U. Wandinger, M. Haarig, B. Gast, G. D'Amico, and V. Freudenthaler

Abstract Accurate simulation of rotational Raman (RR) scattering from atmospheric molecules plays an important role in the design and data analysis of elastic, depolarization, extinction, and temperature lidar systems. As the intensity of RR scattering varies with temperature, the intensity of lidar signals is also temperature-dependent, an aspect exacerbated by the use of narrow-band interference filters (IFF) in lidar design. The strongly depolarizing RR lines lead to a shift in the detected molecular depolarization ratio with temperature. For the estimation of the systematic uncertainty of such measurements and its impact on the lidar products, it is important to be able to calculate the contribution of the Rayleigh scattering to the

N. Siomos (✉)
Meteorological Institute, Ludwig Maximilian Universität München (LMU),

Institute for Astronomy, Astrophysics, Space Applications and Remote Sensing, National Observatory of Athens (NOA-IAASARS), Athens, GreeceMunich, Germany
e-mail: nikolaos.siomos@lmu.de

I. Binietoglou
Institute for Astronomy, Astrophysics, Space Applications and Remote Sensing, National Observatory of Athens (NOA-IAASARS), Athens, Greece

M. Adam
National Institute of Research and Development for Optoelectronics (INOE), Magurele, Romania

U. Wandinger · M. Haarig · B. Gast
Leibniz Institute for Tropospheric Research (TROPOS), Leipzig, Germany

G. D'Amico
Consiglio Nazionale delle Ricerche, Istituto di Metodologie per l'Analisi Ambientale (CNR-IMAA), Potenza, Italy

V. Freudenthaler
Meteorological Institute, Ludwig Maximilian Universität München (LMU), Munich, Germany

© The Author(s), under exclusive license to Springer Nature Switzerland AG 2023

J. T. Sullivan et al. (eds.), *Proceedings of the 30th International Laser Radar Conference*, Springer Atmospheric Sciences,
https://doi.org/10.1007/978-3-031-37818-8_1

lidar signal intensities. Based on several codes existing in the ACTRIS (Aerosol, Clouds, and Trace Gases Research Infrastructure) community for the calculation of Raman lines, we developed a new, state-of-the-art version for a wide range of laser wavelengths and for the range of temperatures found in the atmosphere. It has been tested against the existing codes and is publicly available for use and further improvement. The code will be integrated into the ACTRIS lidar data analysis software single calculus chain (SCC). We used this new code for the estimation of possible errors due to the abovementioned experimental uncertainties and to estimate the overall error in the calculated molecular depolarization ratios.

Keywords Raman scattering · Interference filter · Depolarization ratio

1.1 Introduction

The scattering of electromagnetic radiation from air molecules is a major atmospheric scattering mechanism. In lidars, molecular backscattering computations are always necessary in order to separate the aerosol from the molecular contribution. It is also important to accurately determine the molecular linear depolarization ratio (MLDR) in depolarization lidar signals both for calibration purposes and for the calculation of the particle depolarization ratio. A small part of the molecular scattering is inelastic due to the RR scattering and occurs in discrete spectral lines aside the central elastic scattering wavelength with temperature-dependent cross-sections. Lidar systems typically utilize narrow-band IFFs for the suppression of the solar background. Rotational Raman lidars also rely on such filters to facilitate aerosol extinction measurements even during daytime. Due to the temperature-dependent nature of inelastic scattering, the transmission through an IFF can introduce temperature effects in the profiles of the particle depolarization ratio and the aerosol extinction coefficient. In this study we present ARC (algorithm for Raman Calculations), a new algorithm that has been developed within ACTRIS to provide accurate, state-of-the-art calculations of the filter-dependent molecular backscattering cross-section and depolarization ratio including these effects.

1.2 Presenting ARC: Algorithm for Raman Calculations

During its development, ARC has been compared with existing algorithms in the EARLINET community with a general agreement within the assumed numerical accuracy. Currently, only pure rotational Raman lines are considered. We plan to include a parameterization of the ro-vibrational lines in the future.

1.2.1 Isotropic Scattering of Light

Electromagnetic radiation is scattered by atmospheric gases mainly in a way that preserves both its original state of polarization and wavelength. This form of scattering is referred to as isotropic scattering (e.g., [1]). For single-atom gases as Ar, this is the only possible scattering mechanism. Even for air molecules such as N_2, O_2, and CO_2, this is also by far the most probable scattering process. The isotropic backscattering cross-section is calculated according to [1, 2] in ARC.

1.2.2 Anisotropic Scattering of Light

During scattering, molecules can be considered as electric dipoles. As such, there is a small probability that their vibration and rotation motions change the state of polarization of the scattered radiation. From a quantum mechanical point of view, this mechanism can be expressed as an excitation of the molecule from a specific rotational energy state in a virtual electronic energy level and instant reemission in a higher, lower, or even the original rotational state giving rise to the O (anti-Stokes), Q (part of the Cabannes line), and S (Stokes) pure rotational Raman branches, respectively. The corresponding wavelength shifts and the formulas for the cross-sections of each branch are provided by [2]. All constants required for the calculation of the wavelength shifts and the cross-sections can be found for N_2 and O_2 in [2] and for CO_2 in [3].

1.2.3 Backscattering Cross-Sections of the Rotational Raman Lines

The filtered backscatter cross-sections summed over all molecular components are presented below. The cross-section of each Raman branch σ_k and the isotropic cross-section σ_{iso} are calculated with Eqs. 1.1 and 1.2, respectively.

$$\sigma_k = \sum_i c_i \sum_J F\left(\lambda_{J,i}\right) \sigma_{k,J,i} \tag{1.1}$$

$$\sigma_{\text{iso}} = \sum_i c_i F\left(\lambda_o\right) \sigma_{\text{iso},i} \tag{1.2}$$

Here $\sigma_{k,J,i}$ is the anisotropic cross-section per rotational quantum number J, branch k (Q, S, or O), and gas i, while $\sigma_{\text{iso},i}$ is the isotropic cross-section per gas i. c_i is the molar fraction of each gas, F is the filter transmission function, $\lambda_{J,i}$ is the wavelength corresponding to a specific J, and λ_o is the wavelength of the incident

radiation. If no filter is applied, then $F(\lambda) = 1$. For the total (aka Rayleigh) cross-section, the isotropic part must be summed along with all three anisotropic parts (Eq. 1.3). For the Cabannes cross-section, the unshifted isotropic and the Q Raman branch parts are summed in Eq. 1.4.

$$\sigma_{\text{ray}} = \sigma_{\text{iso}} + \sum_k \sigma_k \tag{1.3}$$

$$\sigma_{\text{cab}} = \sigma_{\text{iso}} + \sigma_Q\left(\lambda_o\right) \tag{1.4}$$

1.2.4 Molecular Linear Depolarization Ratios

The Rayleigh depolarization ratios after transmission through a narrow-band IFF can be calculated as.

$$\delta_m\left(\lambda_o\right) = \frac{\frac{\delta_{\text{aniso}}}{1+\delta_{\text{aniso}}} \cdot \sum_k \sigma_k\left(\lambda_o\right)}{\sigma_{\text{iso}}\left(\lambda_o\right) + \frac{1}{1+\delta_{\text{aniso}}} \cdot \sum_k \sigma_k\left(\lambda_o\right)} \tag{1.5}$$

Here $\delta_{\text{aniso}} = 3/4$ is the linear depolarization ratio of the anisotropic part (e.g., [1]). The nominator and denominator of Eq. 1.5 correspond to the cross- and co-polar backscatter cross-sections, respectively. Only the anisotropic part σ_k can produce cross-polarized light. The isotropic part σ_{iso} is contributing only to the co-polar cross-section in the denominator along with the anisotropic co-polar part. For the calculation of the co- and cross-polar parts of a beam with known depolarization ratio, one can refer to [4]. The filter effect is included in the calculation of the cross-sections (Sect. 1.2.4).

1.3 Applications

1.3.1 Uncertainties Due to the Atmospheric Composition and Temperature

In this section, the effect of air composition on the molecular backscatter cross-section and depolarization ratios is examined. The US standard atmosphere model from 1976 is used in order to generate a vertical profile of realistic temperature and pressure values. In addition to algorithms that include only N_2 and O_2 in the calculation of the Raman lines (e.g., [1, 2]), ARC also includes the contributions of CO_2. Ar and H_2O molecules are included only in the calculation of the isotropic cross-section. H_2O should in principle also contribute to anisotropic scattering,

Table 1.1 The molar fractions of the four different atmospheric mixtures examined

Mixture	N_2	O_2	Ar	CO_2	H_2O
Basic	0.79	0.21	0	0	0
Dry	0.780796	0.209448	0.009339	0.000415	0
Moist	Dry composition scaled to the H_2O contribution with RH = 50%				
Saturated	Dry composition scaled to the H_2O contribution with RH = 100%				

but its anisotropic backscattering cross-section is much smaller than N_2, O_2, and CO_2, while its concentration in the atmosphere is also low. For these reasons and because its Raman spectrum is far more complicated than the other gases, the Raman contribution of H_2O is currently not supported. The absolute relative difference of the Rayleigh MLDR if H_2O is treated as an isotropic instead of an anisotropic gas is merely 0.05%, even for an unrealistically high H_2O molar fraction of 0.03. On the other hand, not including H_2O at all can lead to a non-negligible relative difference of up to 2%.

We assume four different air mixtures summarized in Table 1.1. The basic air mixture is often used in the literature (e.g., [1]). For dry air, Ar and CO_2 are included. The molar fraction of CO_2 corresponds to the 2021 global mean value. For the moist and saturated air mixtures, we reduce the dry air contributions with respect to the additional water vapor content for each altitude.

The Cabannes and Rayleigh MLDR profiles of a molecular atmosphere are presented in Fig. 1.1. By neglecting Ar and CO_2, the Rayleigh and Cabannes MLDR become both overestimated by about 0.5%. Using the dry air mixture and not including the water vapor effect at all lead to an overestimation of up to 1.3% for the lowest 3 km. The relative differences in the Rayleigh and Cabannes backscattering cross-sections between dry and saturated air (not shown here) are also rather low, in the order of 0.5%, in accordance with [2]. A temperature dependence following the USStd atmosphere can be seen in the Cabannes MLDR (Fig. 1.1). This happens because scattering in the Q branch is favored over the S and O branches for lower temperatures. As the temperature rises, the Q branch contribution approaches the classical limit of 0.25. The classical limit is often erroneously used in the literature when the electro-dynamic approach is applied instead of the line-by-line calculation, leading to an uncertainty of 0.5% (e.g., [1]).

1.3.2 Uncertainties in the MLDR Due to the Transmission Function of the IFF

To test the IFFs' effect on the MLDR, we assume three different filter functions: a Gaussian filter (GF) that is a common representation of an IFF, a square (SF), and a Lorentz filter (LF) as extreme cases of a multi- and a single-cavity filter, respectively (Fig. 1.2), all with a full-width-at-half-maximum (FWHM) bandwidth of 1 nm. It

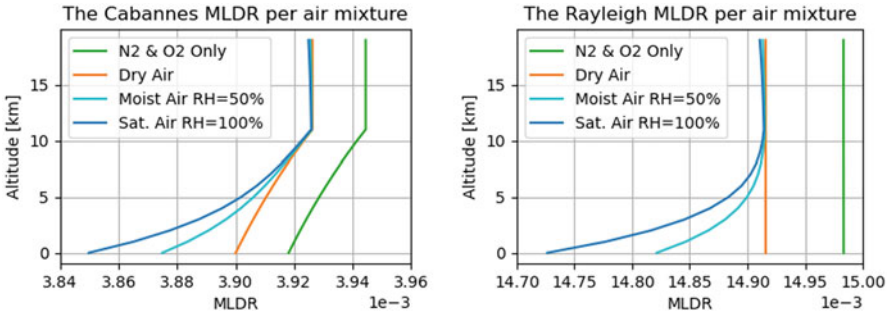


Fig. 1.1 The Cabannes (left) and Rayleigh (right) MLDR profiles of a US standard atmosphere are presented here for the four atmospheric mixtures of Table 1.1

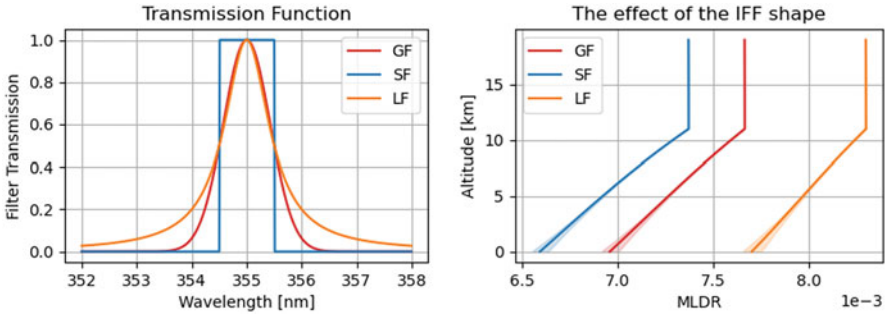


Fig. 1.2 (Left) Transmission of the filters. (Right) Measured MLDR of the USStd atmosphere with Moist air after transmission through each filter. The spread between the dry and saturated MLDR is shown as shadow

is obvious that a small bandwidth IFF reduces the measured MLDR significantly compared to Fig. 1.1, and the temperature effect between ground and 11 km is much stronger. Moreover, Fig. 1.2 illustrates that a steeper filter leads to lower MLDR because the anisotropic contribution from the O and S branches decreases.

To investigate the influence of the filters' manufacturing uncertainties, we vary the FWHM of each filter by ± 0.2 nm (Fig. 1.3, left) and shift the whole transmission functions by ± 0.2 nm (Fig. 1.3, right). The resulting relative uncertainty in the filtered MLDR due to the FWHM change can be as high as 16% of the original filtered MLDR. A filter shift of 0.2 nm either to the left or to the right increases the MLDR for the GF and the LF, because it lowers the transmission for the Cabannes line. This is not the case for the SF, but individual lines can be either fully included by the SF or entirely suppressed by even small shifts leading to increases or decreases in the filtered MLDR. The resulting relative uncertainty due to the central wavelength shift is smallest for the SF and can be up to 13% for the LF.

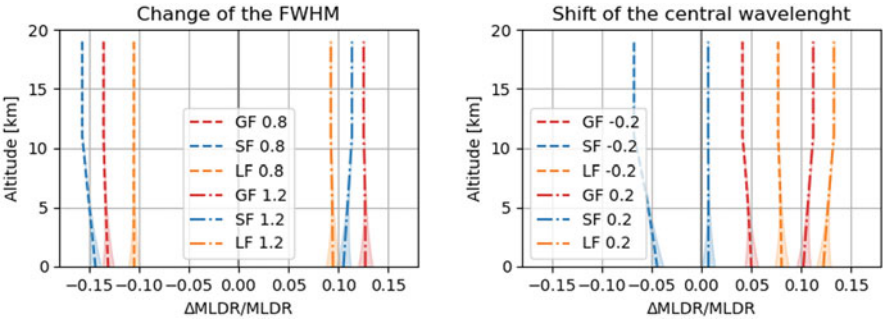


Fig. 1.3 Relative change of the measured MLDR due to change of the filter FWHM to 1.0 ± 0.2 nm (left) and with a center wavelength shift of ±0.2 nm with respect to the laser wavelength (right). The spread between the dry and saturated MLDR is shown as shadow

1.4 Summary

ARC is an ACTRIS activity to facilitate Raman line calculations for linear depolarization, rotational Raman, and temperature lidars. The general recommendation here is to include the isotropic scattering of water vapor for Rayleigh and Cabannes MLDR calculations. Temperature, pressure, and RH profiles should be ideally provided from radiosondes or model simulations. Alternatively, we propose to use a USStd atmosphere with a constant 50% RH. The application of different IFFs shows that characterizing their transmission functions is critical in order to accurately calculate the MLDR profile. Finally, ARC is publicly available in a git repository (https://gitlab.com/ioannis_binietoglou/lidar_molecular/), and its use is recommended from ACTRIS.

References

1. She, C.-Y.: Spectral structure of laser light scattering revisited: bandwidths of nonresonant scattering lidars. Appl. Opt. **40**(27), 4875–4884 (2001)
2. Adam, M.: Notes on Rayleigh scattering in lidar signals. Appl. Opt. **51**(12), 2135–2149 (2012)
3. Sioris, C.E., Evans, W.F.J.: Filling in of Fraunhofer and gas-absorption lines in sky spectra as caused by rotational Raman scattering. Appl. Opt. **38**, 2706–2713 (1999)
4. Eberhard, W.L.: Correct equations and common approximations for calculating Rayleigh scatter in pure gases and mixtures and evaluation of differences. Appl. Opt. **49**, 1116–1130 (2010)
5. Paschou, P., et al.: The eVe reference polarisation lidar system for the calibration and validation of the Aeolus L2A product. Atmos. Meas. Tech. **15**, 2299–2323 (2022)

Chapter 2
Performance of Low-Cost, Diode-Based HSRL System with Simplified Optical Setup

Zachary Noel Buckholtz, Ilya Razenkov, Joseph Garcia, and Edwin Eloranta

Abstract We present our prototype for a semiconductor-based high-spectral-resolution LiDAR (HSRL) system with a simplified optical setup. Traditionally, HSRL systems split the received signal into two channels: one channel measures the molecular backscatter, and the other channel measures both molecular and aerosol backscatters. An etalon or molecular vapor absorption line is used to separate out the narrow aerosol spectrum from the Doppler broadened molecular backscatter. By modulating our seed laser between the center of a rubidium absorption line and just off the absorption line, we are able to combine both HSRL channels into a single physical optical path.

Keywords High-spectral-resolution LiDAR · Aerosols · ground-based network

2.1 Introduction

Clouds and aerosols contribute the largest uncertainty in the modeling of climate change. Sustained measurements of the optical properties of clouds and aerosols in a widespread network with high vertical resolution are critical for reducing this uncertainty. The existing infrastructure capable of providing such measurements suffer from several drawbacks; micropulse LiDAR (MPL) uses unreliable prior assumptions and unstable algorithms. Satellite measurements, such as NASA's CALIPSO, have the same drawbacks as MPL and, while providing global coverage, do not provide continuous time series for a given location.

The high-spectral-resolution LiDAR (HSRL) and Raman LiDAR techniques can provide absolutely calibrated measurements of aerosol optical properties with high vertical resolution that do not rely on the assumptions and algorithms of other

Z. N. Buckholtz (✉) · I. Razenkov · J. Garcia · E. Eloranta
University of Wisconsin-Madison, Madison, WI, USA
e-mail: buckholtz@wisc.edu

© The Author(s), under exclusive license to Springer Nature Switzerland AG 2023

J. T. Sullivan et al. (eds.), *Proceedings of the 30th International Laser Radar Conference*, Springer Atmospheric Sciences,
https://doi.org/10.1007/978-3-031-37818-8_2

techniques. However, an important drawback of these systems is their high price tag. An additional drawback for Raman LiDAR is that these systems require high transmitted power making it difficult for them to be made eye safe for unattended operation.

In order to address these issues, researchers at the National Center for Atmospheric Research (NCAR) and Montana State University (MSU) have pioneered development of HSRL systems based on a semiconductor architecture [1, 2]. Numerous vendors now offer high-quality, off-the-shelf semiconductor laser diodes and amplifiers, providing a low-cost alternative to earlier laser technologies.

Here we present our approach to a low-cost, semiconductor-based HSRL system. While our system uses the same rubidium transition as the earlier NCAR system [1], we further simplify the optical setup by implementing the HSRL molecular and combined channels [3] in the same physical channel. This is done by modulating the seed laser's frequency between the center of the rubidium absorption line and just off of the line. The result is that the transmitted pulses alternate between measuring the molecular signals and combined signals.

2.2 Optical Setup

Our system is centered around the rubidium D2 line at 780 nm. The Rb D2 line provides a narrow and optically thick absorption feature, making it useful for the aerosol spectral discriminator. Additionally, the Rb D2 line is a common subject of research in Physics, resulting in widely available 780-nm semiconductor lasers, semiconductor optical amplifiers, and other optical components.

The transmitter of our system is shown in Fig. 2.1a. We use mainly fiber coupled components to make the design more modular. However, the seed laser, a distributed feedback (DFB) diode laser, is free space and passed through a free-space optical isolator. Once coupled into the fiber, the beam passes through a traveling wave amplifier (TWA) to boost the signal, a fiber optical switch (FOS) to reduce leakage between pulses, a fiber coupled isolator to reduce back reflections from the tapered amplifier, and finally the tapered amplifier (TPA). The TWA also aids in reducing leakage from the seed laser between pulses. The TPA is seeded with about 12 mW, and the peak power transmitted to the atmosphere is 1.75 W.

A key advantage of diode-based systems, besides cost and simplicity, is that the frequency of the transmitted pulses can easily be changed by adjusting the diode current or temperature. The seed controller in our system includes a voltage-controlled current source. We use this current source to modulate the diode's frequency between the center of the rubidium absorption line and just off of the absorption line. Since the online frequency is centered on the absorption feature, the narrow spectrum aerosol backscatter is absorbed giving the typical HSRL molecular signal. The offline frequency lets through the aerosol signal and much of the Cabannes–Brillouin backscatter giving the typical combined signal. The modulation then results in the transmitted pulses alternating between molecular and combined HSRL measurements. By using frequency to discriminate between HSRL channels,

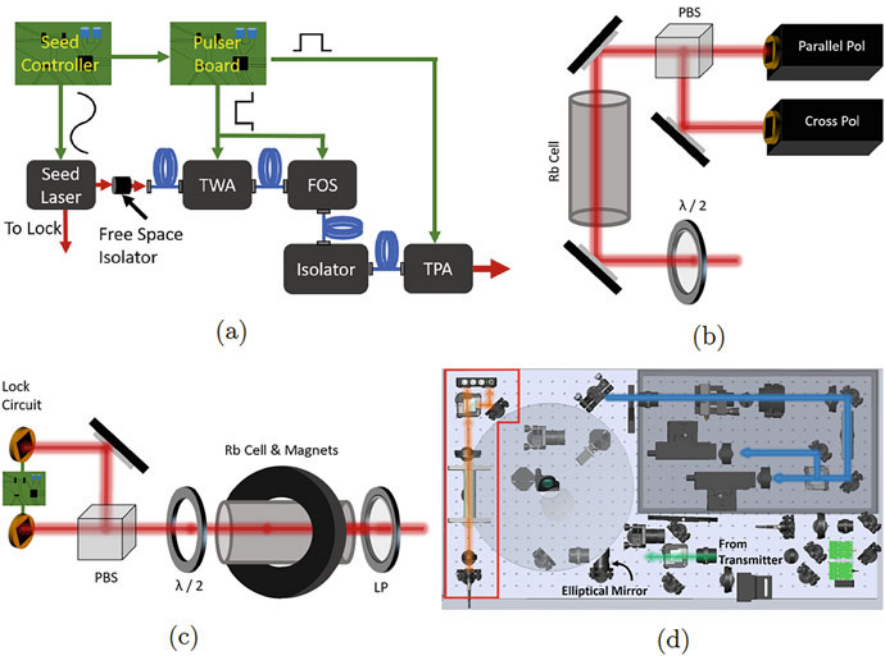


Fig. 2.1 Optical subsystems of the Rb HSRL. Figure 2.1a shows the mainly fiber coupled components of the transmitter. The seed controller circuit controls the seed laser modulation and pulse timing. The receiver and cross-pol channel are shown in Fig. 2.1b. The frequency locking setup is shown in Fig. 2.1c. The magnets (only one of two shown) produce the Zeeman splitting that the locking signal is based on. Figure 2.1d shows a to scale model of the Rb HSRL breadboard. The locking setup is outlined in red, the dark gray box with blue optical path is the receiver, and the transmitter is mainly on the bottom of the breadboard. The footprint of our Schmidt–Cassegrain telescope is represented by the large circle to the right of the locking setup. (**a**) Rb HSRL transmitter. (**b**) Rb HSRL receiver. (**c**) Rb HSRL locking system. (**d**) Rb HSRL to scale model

we can include both channels in the same optical path, reducing possible offsets between different physical channels and reducing the number of optical components needed.

The seed controller also controls the timing and lengths of the transmitted pulses by triggering a pulser board that gates the TWA, FOS, and TPA at the maxima and minima of each modulation cycle. The total pulse repetition rate we run at is 8 kHz with 4 kHz on the molecular frequency and 4 kHz on the combined frequency. The pulse lengths for each channel can be adjusted separately and can be set from 250 ns to 1000 ns.

Once out of the TPA, the beam is shaped and collimated with a cylindrical and spherical lens pair. After collimation, the beam is passed through a small off center hole in a mirror with an elliptical cross section. The purpose of this mirror is to separate the transmitted and received beams without losing depolarization signals.

Table 2.1 Specifications for Rb HSRL

Pulse lengths (ns)	≥250	Full overlap range (km)	3
Minimum time interval (s)	1.25	FOV (urad)	100
Peak transmitted power (W)	1.75	Modulation amplitude (GHz)	0.32
Maximum range (km)	12	C_{am}	1/300
Total pulse rep rate (kHz)	8	Lock accuracy (MHz)	±50

The offset for the hole is to avoid the secondary mirror's shadow. The transceiver telescope is a Schmidt–Cassegrain telescope.

The receiver, shown in Fig. 2.1b, includes a polarizing beam splitter and second detector for cross-polarization measurements, used in distinguishing liquid from ice particles. A rubidium vapor cell at a temperature of 35 °C with length 7.5 cm is in the beam path to act as the spectral discriminator. Preceding the optics shown in Fig. 2.1b is an afocal telescope with a magnification of 1/2 and a pinhole used to set the field of view (FOV) to 100 μrad (Table 2.1).

2.2.1 Locking

About 10% of the seed laser power is picked off for frequency locking. The locking setup is shown in Fig. 2.1c. The beam is passed through a second rubidium cell with two strong permanent magnets around it. The magnets produce a Zeeman split in the rubidium atoms where each of the split components absorbs a different polarization. The polarization of the beam transmitted through the Zeeman split rubidium atoms depends on the frequency of the beam. The beam transmitted through the Zeeman split rubidium is split by a polarizing beam splitter and detected by two photodiodes. The ratio of the signal from the two photodiodes is used to produce the locking signal and provides a steep slope to lock to. By taking the ratio, we can eliminate drifts in the incident power. The locking signal versus laser detuning is shown in Fig. 2.2b.

The rb HSRL system is contained in an insulated enclosure. The enclosure is controlled by 2 TECs and is in a room with the temperature controlled to within a few degrees. The locking circuit has some temperature dependence and is influenced by perturbations due to ambient room temperature fluctuations. These fluctuations cause the lock frequency to shift by ±50 MHz throughout the night.

2.3 Performance

An example of a calibration scan across the rubidium absorption cell can be found in Fig. 2.2a. Scans are performed by slowly changing the temperature of the laser diode. The laser diode is also undergoing the current modulation described above during the calibration scan. Thus, the scans are performed under operating

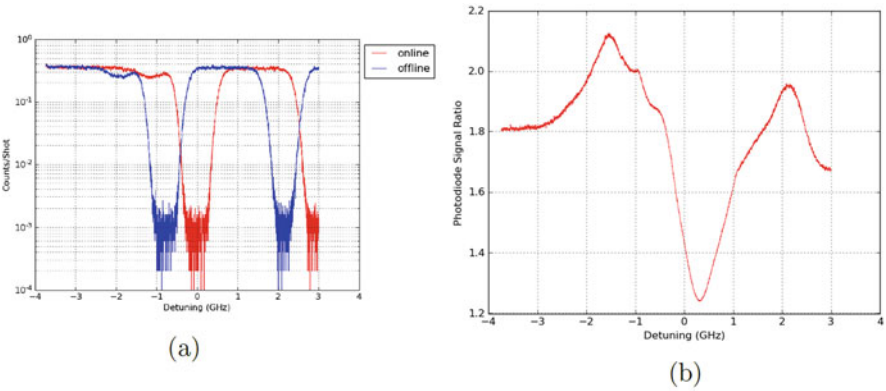


Fig. 2.2 The calibration and locking signals for the Rb HSRL. Figure 2.2a shows the transmission through the receiver's rubidium cell as the center frequency of the modulating laser frequency is swept across the absorption line. See text for details. Figure 2.2b shows the ratio of the two polarizations that are transmitted through the locking setup's Zeeman split rubidium cell. (**a**) Rb HSRL transmitter. (**b**) Rb HSRL receiver

conditions and allow us to see the relative frequency shift of between the molecular and combined channels. The red curve in Fig. 2.2a shows the transmission of pulses fired at the minimum of the laser current modulation. The blue curve is the transmission of shots fired when the laser current modulation is at a maximum. Non-scanning operating conditions correspond to when the red curve is at the center of the absorption feature and is acting as the molecular channel. The transmission shown in the blue curve when the red curve is tuned to this frequency is the transmission of the combined pulses. We can also use the data from Fig. 2.2a to calculate C_{am}, the amount of aerosol signal in the molecular channel. Typical values are around 1/300.

An example of data taken with our rubidium HSRL can be found in Fig. 2.3. These data were taken on the night of February 16, 2022. Solar background prevents us from taking data during the day. However, an etalon to reduce daytime background is part of a planned upgrade. Based on the aerosol backscatter coefficient and depolarization ratio, Fig. 2.3 shows cirrus clouds above 6 km, up to the system's maximum range of about 12 km, as well as other irregularly shaped aerosols below 4 km. The data in Fig. 2.3 were taken with 1000-ns molecular channel pulses and 500-ns combined channel pulses giving a vertical resolution of 75 m.

2.4 Conclusion

We have presented the results of a prototype HSRL system with a simplified optical setup. Our system is based on the 780-nm absorption line of rubidium as the spectral discriminator. Semiconductor laser diodes, amplifier, and optics are

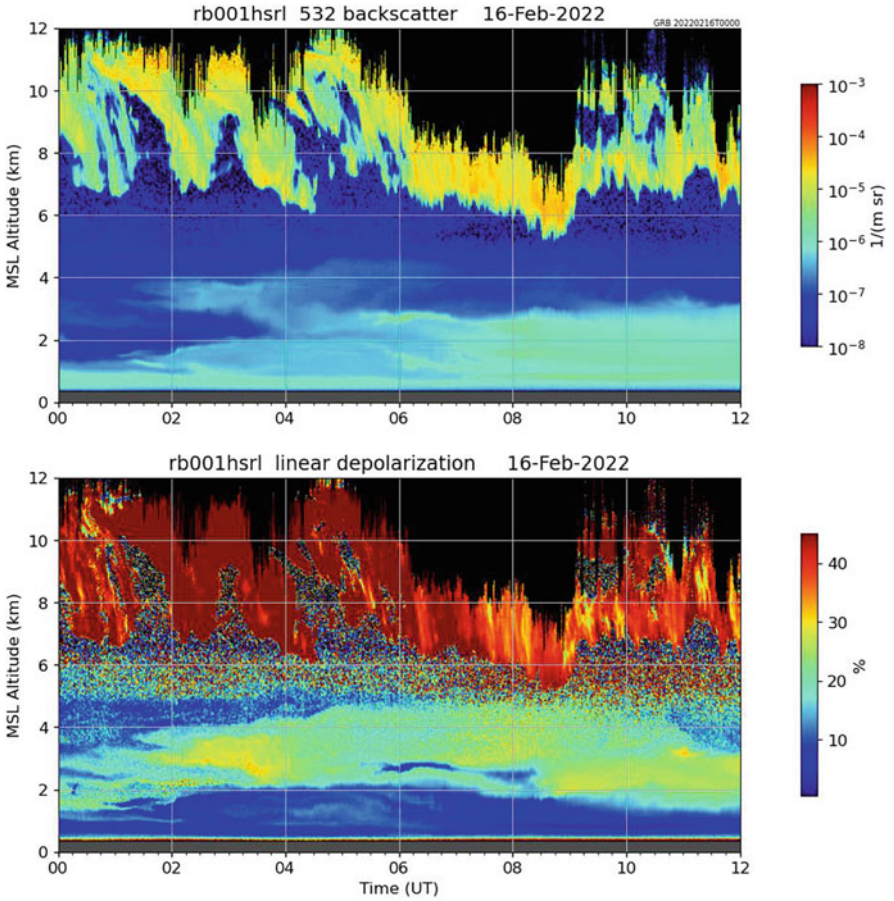


Fig. 2.3 Rb HSRL data from 16 Feb, 2022. The top plot shows the aerosol backscatter coefficient versus time and altitude. The bottom plot shows the depolarization ratio measured using the cross-pol channel

widely available at this wavelength. The result is that components are cheaper compared to non-semiconductor systems. The semiconductor-based architecture also allows us to easily modulate the seed laser's frequency between the center of the rubidium absorption line and just off of it. This modulation allows us to implement the molecular and combined HSRL channels in the same physical channel. These factors together have resulted in a low-cost HSRL system that is capable of measuring aerosol backscatter coefficients and depolarization ratios with a vertical resolution down to 37.5 m and a time resolution down to 1.25 seconds.

References

1. Hayman, M. Spuler, S.: Demonstration of a diode-laser-based high spectral resolution LiDAR (HSRL) for quantitative profiling of clouds and aerosols. Opt. Express **25**(24), A1096–A1110 (2017)
2. Spuler, S.M., Hayman, M., Stillwell, R.A., Carnes, J., Bernatsky, T., Repasky, K.S.: MicroPulse DIAL (MPD)—a diode-laser-based LiDAR architecture for quantitative atmospheric profiling. Atmos. Meas. Tech. **14** 4593–4616 (2021).
3. Eloranta, E.W.: Chapter 5: High spectral resolution LiDAR. In: Weitkamp, C. (ed.) LiDAR: Range-Resolved Optical Remote Sensing of the Atmosphere. Springer, New York (2005)

Chapter 3
Sensitivity Study on the Performance of the Single Calculus Chain Aerosol Layering Module

K. A. Voudouri, P. Fountoukidis, N. Siomos, C. Dema, D. Balis, and G. D'Amico

Abstract An assessment of the aerosol layering module (LTOOL), which has already been added to the European Aerosol Lidar Network's (EARLINET) Single Calculus Chain (SCC, https://scc.imaa.cnr.it) algorithm, is presented. Currently, the LTOOL module is applied to the EARLINET lidar data analyzer (ELDA) optical products and has been integrated in the SCC development web interface. The algorithm layering analysis utilizes the wavelet covariance transform method (WCT) for the layer boundary detection in order to extract the layers' geometrical features, i.e., the planetary boundary layer height and the lofted aerosol layers. LTOOL reproduces automatically the layers' geometrical properties (i.e., base, top, and center of mass), with a sufficient degree of temporal homogeneity. Sensitivity studies on the application of different dilation values are presented along with the stability of the intensive properties within the layer boundaries, derived from the lidar measurements of Thessaloniki's lidar station, which is part of EARLINET. The aim is to investigate the algorithms' accuracy in identifying persistent layers in various atmospheric conditions.

Keywords Single Calculus Chain · LTOOL module · Aerosol layers · Lidar

K. A. Voudouri (✉) · P. Fountoukidis · D. Balis
Laboratory of Atmospheric Physics, Aristotle University of Thessaloniki, Thessaloniki, Greece
e-mail: kavoudou@physics.auth.gr; pfountou@physics.auth.gr; balis@physics.auth.gr

N. Siomos
Meteorological Institute, Ludwig Maximilian Universität München, LMU, Munich, Germany
e-mail: Nikolaos.Siomos@physik.uni-muenchen.de

C. Dema · G. D'Amico
Consiglio Nazionale delle Ricerche, Istituto di Metodologie per l'Analisi Ambientale, (CNR-IMAA), Potenza, Italy
e-mail: claudio.dema@imaa.cnr.it; giuseppe.damico@imaa.cnr.it

© The Author(s), under exclusive license to Springer Nature Switzerland AG 2023

J. T. Sullivan et al. (eds.), *Proceedings of the 30th International Laser Radar Conference*, Springer Atmospheric Sciences,
https://doi.org/10.1007/978-3-031-37818-8_3

3.1 Methodology

The EARLINET SCC is a tool for the automatic analysis of lidar data [1, 2], providing high-quality aerosol properties (i.e., aerosol backscatter coefficient, aerosol extinction coefficient) at network level. It consists of basic lidar processing modules, while new ones are continuously developed and implemented in order to make the SCC a fully automatable tool [3]. An example of the planned implementation is the aerosol layering module, LTOOL, which can further contribute to the aerosol characterization and typing. The algorithm layering analysis utilizes the wavelet covariance transform (WCT) for the layer boundary detection in order to extract geometrical features, i.e., the planetary boundary layer height and the lofted aerosol layers [4]. The WCT is defined as follows:

$$W_f(a,b) = \left(\sum_{b}^{b+\frac{a}{2}} P(z) - \sum_{b-\frac{a}{2}}^{b} P(z) \right) \tag{3.1}$$

Where Δz is lidar's vertical resolution, α is the dilation which equals to $n\Delta z$, b is the translation parameter, and $P(z)$ is the lidar's products (i.e., aerosol backscatter and/or aerosol extinction coefficient profile).

Currently, the LTOOL module operates upon the EARLINET lidar data analyzer (ELDA) optical products. Local extrema of the WCT profiles indicate points of monotonic increase/decrease in the applied backscatter/extinction profiles, and as a result, at least one peak is included in the profiles within the layer boundaries. Masking threshold values that exclude undesired layers (i.e., low backscatter values) are applied. LTOOL returns the geometrical properties per identified layer, e.g., the center of the mass of the layer, the thickness of the layer, and the backscatter values in the base, peak, and top.

Sensitivity studies to investigate the algorithm's accuracy in identifying layers to Thessaloniki lidar dataset are presented below. Thessaloniki's lidar system (THELISYS) is operated and maintained by the Laboratory of Atmospheric Physics that is located in the Physics Department of the Aristotle University of Thessaloniki (40.5° N, 22.9° E; 50 m). THELISYS has been used for the detection of aerosol particles as a part of EARLINET [5] since 2000 and now as part of the Aerosols, Clouds, and Trace Gases Research InfraStructure (ACTRIS; https://www.actris.eu/).

3.2 Results

3.2.1 Sensitivity Study of the WCT Dilation Value

As the LTOOL module should automatically identify vertical regions of significant aerosol load where the aerosol composition is quite stable, the lidar signal from

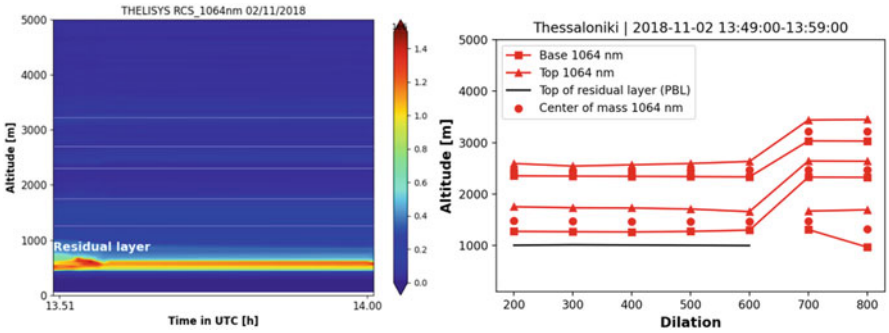


Fig. 3.1 Temporal variability of the range-corrected signal at 1064 nm (left) and the elevated layers geometrical properties variability, along with the different dilation values (right), for the case of Thessaloniki on 02 of November 2018 at 13:49–13:59 UTC

noisy structures should be discerned. Thus, a dilation parameter is applied in the WCT. However, the detection sensitivity of the inflection points decreases when choosing for layers far wider or sharper than the dilation value. Consequently, it is important to quantify the effect of this value in the retrieval of the layer boundaries under different aerosol conditions and check whether a fixed value is applicable or it will be let as a user-defined option in the SCC database. We conclude that for rather small values of the dilation, signal noise dominates while; a too large dilation may not permit the discrimination of thin aerosol layers. Thus, an optimum value should be defined, regarding the system's vertical resolution and the user's selected smoothing thresholds applied on the aerosol profiles. In order to test the algorithm's stability, a range of dilation values were tested (from 100 to 800 with step of 100) in a case study of Thessaloniki's measurement. Figure 3.1 presents the temporal variability of the range-corrected signal at 1064 nm at Thessaloniki station (left) and the variability of the elevated layers, the ones above the residual layer, on 2nd of November 2018 at 13:49–13:59 UTC.

The residual layer is identified at 1 km (for a dilation value between 200 and 600) and the variability of the geometrical depth of the first two elevated layers is discussed, in terms of the different dilation values applied. The identified first layer's base (1.2–1.8 km) is gradually increasing with the increased dilation value. For a dilation value above 700 (~94 m), this layer between 1.2 m and 1.8 m is defined as the second elevated layer, without the identification of the residual layer anymore available. Thus, when selecting a dilation value between 200 and 600, the discrimination between the residual layer and the first elevated layer is made. In Table 3.1, the number of identified layers at the 532 nm and 1064 nm channels is presented, along with the difference of the detected layers between the two wavelengths. A coarser dilation value (700–800) seems to lead in the same number of identified layers (for both wavelengths); however, the finer structures in the aerosol backscatter profiles at 1064 nm are no longer identified.

Table 3.1 The number of layers and difference between the identified layers –case study of Thessaloniki, November 02 , 2018

Dilation/λ	532 nm	1064 nm	Difference
200	5	9	4
300	4	8	4
400	4	7	3
500	4	6	2
600	3	5	2
700	3	3	0
800	3	3	0

3.2.2 Stability of the Intensive Properties Within the Layer Boundaries

Moreover, the stability of the intensive properties (i.e., lidar ratio – LR, backscatter-related Ångström exponent – BAE, extinction-related Ångström exponent – AE) within the layer boundaries is a metric that quantifies the algorithm's ability to detect aerosol layers with homogeneous composition. In what follows, we analyze the timeseries of Thessaloniki's lidar measurements (2013–2018), with a fixed dilation value of 400 (~55 m). The standard deviation of the intensive parameters within the layers is presented in Figs. 3.2 and 3.3. The BAE and AE standard deviation within the detected layer and within the whole profile is presented in Fig. 3.2, and the LR and AE standard deviation both within the identified layers and the whole profile are presented in Fig. 3.3.

LTOOL seems to perform well in detecting aerosol features when applying on the ELDA derived backscatter or extinction aerosol optical products. The standard deviation of the intensive properties within the identified layers is smaller than the one calculated on the whole profile, which includes both aerosol layers and aerosol-free regions.

3.3 Conclusions

In this study, we analyze the lidar timeseries of Thessaloniki's station to assess the aerosol layering module (LTOOL) that is planned to be implemented in the Single Calculus Chain (SCC). Currently, the LTOOL module is applied to the EARLINET lidar data analyzer (ELDA) optical products and has been integrated in the SCC development web interface. A sensitivity study of the dilation value is presented along with the stability of the intensive properties within the layer boundaries. In general, the LTOOL denotes a good performance in detecting aerosol features. In the future extensive comparison against layers detected by visual inspection is planned (and not a direct comparison with different layering techniques and approaches), and selected diurnal case studies from the EARLINET stations will be analyzed

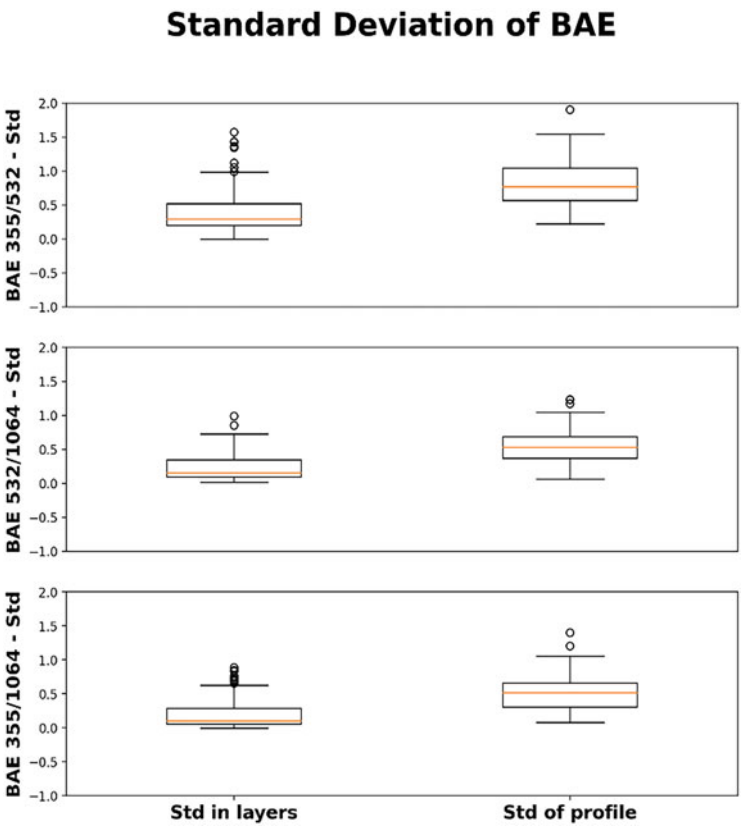


Fig. 3.2 Standard deviation of backscatter-related Ångström exponent (BAE) at 355/532 (up), 532/1064 (middle), and 355/1064 (down) both within the identified layers and the whole profile

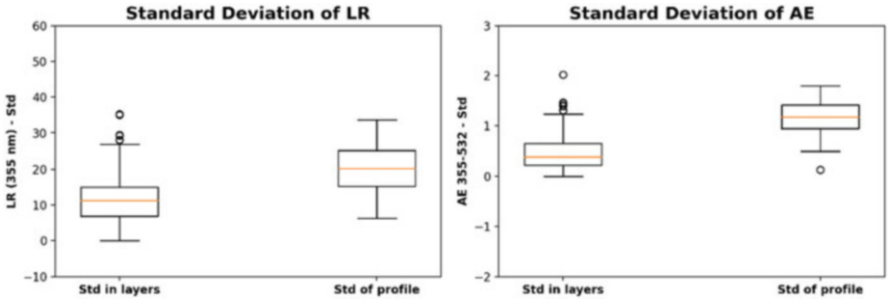


Fig. 3.3 Standard deviation of the lidar ratio at 355 nm (left) and the Ångström exponent 355–532 (right) both within the identified layers and the whole profile

in order to investigate the algorithms' accuracy in identifying persistent layers in diurnal measurements.

Acknowledgments KAV acknowledges support of this work by the project "PANhellenic infrastructure for Atmospheric Composition and climatE change" (MIS 5021516) which is implemented under the Action "Reinforcement of the Research and Innovation Infrastructure," funded by the Operational Programme "Competitiveness, Entrepreneurship and Innovation" (NSRF 2014-2020) and co-financed by Greece and the European Union (European Regional Development Fund).

References

1. D'Amico, G., Amodeo, A., Baars, H., Binietoglou, I., Freudenthaler, V., Mattis, I., Wandinger, U., Pappalardo, G.: EARLINET single calculus chain – overview on methodology and strategy. Atmos. Meas. Tech. **8**, 4891–4916 (2015)
2. Mattis, I., D'Amico, G., Baars, H., Amodeo, A., Madonna, F., Iarlori, M.: EARLINET single calculus chain – technical – part 2: calculation of optical products. Atmos. Meas. Tech. **9**, 3009–3029 (2016)
3. D'Amico, G., Mattis, I., Binietoglou, I., Baars, H., Mona, L., Amato, F., Kokkalis, P., Rodríguez-Gómez, A., Soupiona, O., Voudouri, K.-A.: Earlinet single calculus chain: new products overview. EPJ Web Conf. **176**, 09014 (2018)
4. Siomos, N., Balis, D.S., Voudouri, K.A., Giannakaki, E., Filioglou, M., Amiridis, V., Papayannis, A., Fragkos, K.: Are EARLINET and AERONET climatologies consistent? The case of Thessaloniki, Greece. Atmos. Chem. Phys. **18**, 11885–11903 (2018)
5. Pappalardo, G., Amodeo, A., Apituley, A., Comeron, A., Freudenthaler, V., Linné, H., Ansmann, A., Bösenberg, J., D'Amico, G., Mattis, I., Mona, L., Wandinger, U., Amiridis, V., Alados-Arboledas, L., Nicolae, D., Wiegner, M.: EARLINET: towards an advanced sustainable European aerosol lidar network. Atmos. Meas. Tech. **7**, 2389–2409 (2014). https://doi.org/10.5194/amt-7-2389-2014

Chapter 4
Particle Complex Refractive Index from 3β + 2α HSRL/Raman Lidar Measurements: Conditions of Accurate Retrieval, Uncertainties, and Constraints Provided by Information About RH

Alexei Kolgotin, Detlef Müller, Igor Veselovskii, and Mikhail Korenskiy

Abstract We developed a minimization procedure that can be used for the simultaneous and explicit retrieval of the spectrally and size-independent complex refractive index (CRI) and the corresponding monomodal particle size distribution from 3β + 2α HSRL/Raman lidar measurements. The 3β + 2α optical data are backscatter coefficients measured at 355, 532, and 1064 nm and extinction coefficients measured at 355 and 532 nm. Analysis of the results derived with the minimization procedure shows that the CRI can only be retrieved with preset accuracy if the input optical data are accurate to at least eight significant digits. The CRI cannot be estimated without introducing constraints, even if measurement uncertainties of the optical data are as low as 1–3%. We studied constraints provided by information about relative humidity (RH) and how far these constraints could allow us to restrict the retrieval uncertainties. To validate the results of the CRI retrieval, we analyzed a Raman lidar measurement of a smoke plume for which radiosonde and in situ data are available. The results derived with this novel approach were compared to our two-dimensional regularization algorithm and data taken with in situ instruments. We find good agreement of the results.

Keywords Lidar · Aerosol · Microphysical parameters · Algorithms

A. Kolgotin (✉) · I. Veselovskii · M. Korenskiy
A.M. Prokhorov General Physics Institute, Moscow, Russia
e-mail: kolgotin@pic.troitsk.ru

D. Müller
University of Hertfordshire, Hertfordshire, UK

© The Author(s), under exclusive license to Springer Nature Switzerland AG 2023

J. T. Sullivan et al. (eds.), *Proceedings of the 30th International Laser Radar Conference*, Springer Atmospheric Sciences,
https://doi.org/10.1007/978-3-031-37818-8_4

4.1 Introduction

In the past two decades, different types of methods were developed for the retrieval of atmospheric particle microphysical parameters (PMP) including the complex refractive index (CRI) from optical data taken with lidar [1]. The minimum number and type of optical data that are used for the most advanced algorithms are backscatter coefficients (β) measured at wavelengths $\lambda_1 = 355$, $\lambda_2 = 532$, and $\lambda_3 = 1064$ nm and extinction coefficients (α) measured at $\lambda_1 = 355$ and $\lambda_2 = 532$ nm. That set of data naturally requires the use of high-spectral-resolution lidar (HSRL) or Raman lidar [2, 3] as high-quality optical data, i.e., low measurement uncertainties are needed in order to derive microphysical properties of sufficient accuracy. One of the important features of the underlying retrieval method is the particle CRI. This parameter in general is not known. In the ideal case, it should be estimated simultaneously with the other PMPs of interest, i.e., effective radius (r_{eff}), and number (n), surface-area (s), and volume (v) concentrations. The uncertainty of the retrieved CRI usually leads to additional uncertainties of the retrieved PMPs. Therefore, even if the optical data have no measurement uncertainties, which of course is an unrealistic scenario, the methods currently employed do not allow for retrieving the PMPs with preset accuracy. The aim of this study is to develop the following:

(1) A reliable, mathematically sound minimization procedure, i.e., a method that allows us to simultaneously estimate the CRI and PMPs of monomodal particle size distribution (PSD) with preset accuracy and with a preset confidence level. In other words, the uncertainty of the retrieved data products should not become larger than what can be estimated by this minimization procedure.
(2) Constraints that can be used to restrict the CRI solution space on the basis of information about relative humidity (RH) in the case that optical data are erroneous and hence the applied retrieval methods cannot be used for distinguishing the true value.

In Sect. 4.2 we present the methodology. In Sect. 4.3 we carry out a numerical test with synthetic optical data. A case study is shown in Sect. 4.4. Section 4.5 summarizes our results.

4.2 Methodology

Optical particle properties $g(\lambda)$ measured with lidar, i.e., extinction $\alpha(\lambda)$ and backscatter $\beta(\lambda)$ coefficients at wavelength λ, are related to the unknown PSDs $f(r)$ via a Fredholm integral equation of the first kind:

$$\int_0^\infty K_g(\lambda, m, r)\, f(r) dr = g(\lambda) \quad g = \alpha, \beta \tag{4.1}$$

Here we consider only spherical particles. Therefore, the kernels of the integral equation $K_g(\lambda, m, r)$ are described by the theory of light scattering by spherical particles (Mie-scattering theory) of radius r and complex refractive index $m = m_R - im_I$ [4]. For naturally occurring particles, particle radius and CRI are approximately limited by the domains $r \in [0.01; 20]$ μm; $m_R \in [1.3;1.8]$; and $m_I \in [0; 0.1]$.

In this study the CRI is assumed to be spectrally and size independent. The CRI is unknown and therefore also needs to be identified aside from the PSD.

For the simultaneous retrieval of the CRI and the corresponding monomodal PSD, we modify the minimization procedure developed in our recent publication, where we show that m can be explicitly estimated from 3β + 2α lidar data if the $f(r)$ is known [5]. The modified procedure is intended for finding the minimum of the functional F_G:

$$F_G{}^2 = \frac{1}{4}\sum_{j=1}^{4} \rho_{G_j}^2(\mathbf{x}) \to \min_{\mathrm{x}} \tag{4.2}$$

The functional is expressed through the individual discrepancies:

$$\rho_{G_j}(\mathbf{x}) = \mid G_{\mathrm{inp},j} + G_j(\mathbf{x}) \mid / G_{\mathrm{inp},j} \quad j = 1, \ldots, 4 \tag{4.3}$$

where the parameters $G_{\mathrm{inp},j}$ denote the following ratios measured with lidar.

$$\left\{G_{\mathrm{inp},j}\right\} = \left\{\frac{\alpha(355)}{\alpha(532)}, \frac{\beta(355)}{\beta(532)}, \frac{\beta(532)}{\beta(1064)}, \frac{\alpha(355)}{\beta(355)}\right\} \tag{4.4}$$

The parameters $G_j(\mathbf{x})$ are determined similar to $G_{\mathrm{inp},j}$ but from the respective coefficients $g(\lambda,\mathbf{x})$ that are directly computed with the equations.

$$g(\lambda_l, \mathbf{x}) = \int_0^\infty K_g(\lambda_l, x_1 - ix_2, r)\, LN(x_3, x_4, r)\, dr \quad g = \alpha, \beta; l = 1, 2, 3 \tag{4.5}$$

In the latter equations, the vector $\mathbf{x}$ consists of elements x_j:

$$\mathbf{x} = \left\{x_j\right\} = \{m_R, m_I, \mu, \sigma\} \quad j = 1, \ldots, 4 \tag{4.6}$$

The function LN is described by a logarithmic-normal distribution with parameters μ and σ that stand for mean radius and standard deviation, i.e.,

$$\mathrm{LN}(\mu, \sigma, r) = \frac{1}{\sqrt{2\pi} r \ln\sigma} \exp\left[-\frac{(\ln r - \ln\mu)^2}{2(\ln\sigma)^2}\right] \tag{4.7}$$

Any kind of standard approach can be used for the implementation of the $F_g{}^2$-minimization procedure, for example, the method of cyclic descent [6]. It allows

us to find four optimal values for the CRI $m^{\text{opt}} = x_1{}^{\text{opt}} – i x_2{}^{\text{opt}}$ as well as for the parameters $\mu^{\text{opt}} = x_3{}^{\text{opt}}$ and $\sigma^{\text{opt}} = x_4{}^{\text{opt}}$ from four independent ratios (4.4) measured with lidar. We stress that the vector **x** contains a sufficient number of independent elements which thus permits for finding the approximation of any arbitrary monomodal PSD with $LN(\mu,\sigma,r)$.

Number concentration of the monomodal PSD approximated in such a way is a dependent parameter that is equal to the ratio of the input (measured) coefficient $g_{\text{inp}}(\lambda)$ to the directly calculated coefficient $g(\lambda,\mathbf{x})$. Therefore, four independent parameters $\{G_{\text{inp},j}\}$ can be used as input, which makes it possible from the theoretical point of view to retrieve four parameters $\{x_j\}$ that are unique and independent of each other. We can also use a more complicated aerosol model that describes, for example, a spectrally or size-dependent CRI or a bimodal PSD. In that model we obtain a vector **x** that contains more than four independent output parameters. In this case the mathematical task described by Eq. (4.1) becomes underdetermined for $3\beta + 2\alpha$ measurements (vector $\boldsymbol{G}_{\text{inp}}$) and may have an infinite number of solutions (vectors **x**).

4.3 Numerical Simulations

We carried out numerical simulations to test the minimization procedure. We considered a set of synthetic optical data $3\beta_{\text{inp}} + 2\alpha_{\text{inp}}$ directly computed with Eq. (4.1) at the input (true) CRI $m = 1.5ci0.001$ and a logarithmic-normal distribution (4.7) with mean radius $r_0 = 0.22$ μm, standard deviation $\sigma = 1.5$, and number concentration $n = 1$ cm^{-3}. This set of data is used as input for the minimization procedure and for different magnitudes of uncertainty 0%, 1%, and 15%.

Figure 4.1 shows the results obtained with the minimization procedure and the use of the three uncertainty levels. For each uncertainty value, we see a few local minima (one to three or more). Minima may cover seven orders of magnitude of discrepancy. All minima are distributed along a "canyon," which we denote a "CRI solution *trajectory*" [5].

The global minimum coincides with the true solution only in the first case (a). The discrepancy at the global minimum (4×10^{-7}) is significantly lower compared to discrepancies at all other minima that we find in the three cases (a–c). All elements of the vector $\mathbf{x}^{\text{opt}}$ of the global minimum coincide with the respective elements of the vector $\mathbf{x}^{\text{true}}$. In the other two cases (b) and (c), the global minimum does not coincide with the true solution.

Furthermore, we observe some smearing of the otherwise clearly located minima (see case (a)) for increasing uncertainty of the optical data. That means, whatever method of CRI retrieval we use, we will not be able to distinguish the different minima along the "canyon" which contains the global minimum (true solution), if we only use $3\beta + 2\alpha$ data. We need extra constraints that allow us to localize the true solution.

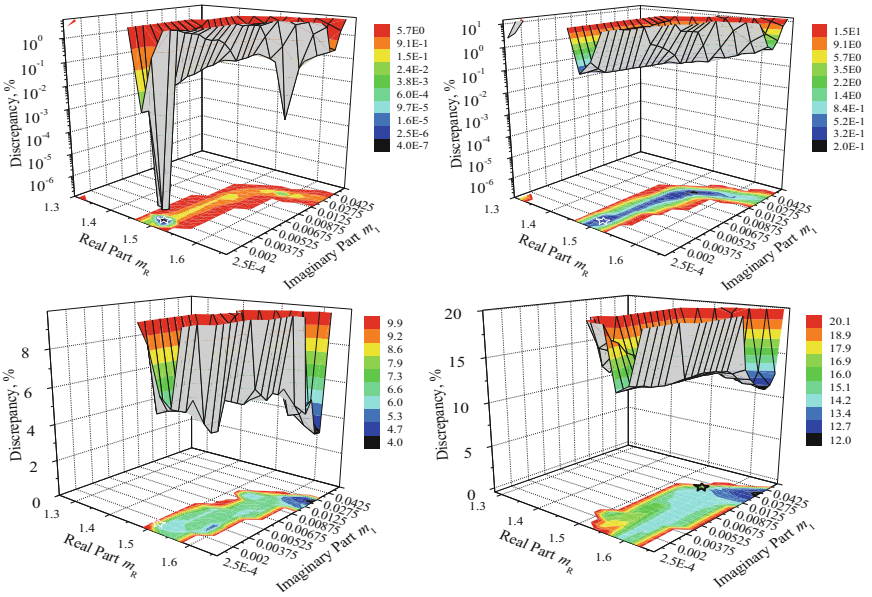


Fig. 4.1 Use of the minimization procedure in the numerical simulation for optical data uncertainties 0% (**a**), 1% (**b**), and 15% (**c**) and the case study from 22 July 2004 (data were taken from height level 3.8 km) (**d**). The stars in the (m_R, m_I)-plane show the true solution (white) and the result of the in situ observations (black), i.e., $m = 1.5 - i0.001$and $m \approx 1.55 - i0.02$ [2], respectively

We can estimate the PMPs along the CRI trajectory. Figure 4.2a shows the respective results for effective radius (red), surface-area (blue), and number (green) concentrations. The PMPs coincide with the respective true values (see grey vertical and horizontal lines) at $m^{\text{true}} = 1.5 - i0.001$. Besides this agreement, we see that increasing values of the real and imaginary parts of the CRI (x-axis) result in decreasing values of effective radius (red curve).

This interdependency resembles features of size growth of hygroscopic particles in which mean particle size and complex refractive index vary with ambient atmospheric relative humidity (RH). We collected some data in Table 4.1 for different aerosol types from the MERRA-2 model, which demonstrates these features [3]. In particular, the CRI for organic carbon (OC) shows a decrease from $m = 1.53 - i0.009$ to $1.35 - i0.001$ at $\lambda = 532$ nm and an increase of the growth factor from 1 to 2.5 for the case that RH increases from 0% to 100%. This strong resemblance of the pattern of interdependence triggered us to test if RH data can be of value in our search for the final solution space.

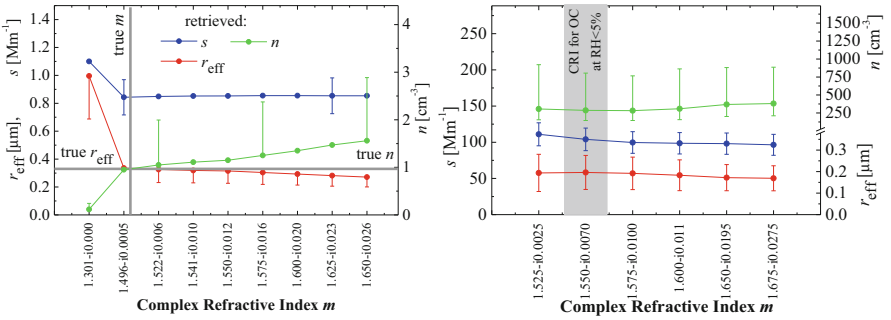


Fig. 4.2 Results of the retrieved parameters n (green), r_{eff} (red), and s (blue) versus CRI in the "canyon" shown in Fig. 4.1b for the numerical example (**a**) and in the "canyon" shown in Fig. 4.1d for the lidar measurement from 22 July 2004 at height 3.8 km (**b**) [2]. True CRI, effective radius, surface area, and number concentrations are $m^{\text{true}} = 1.5 - i0.001$ (grey vertical line), $r_{\text{eff}}{}^{\text{true}} = 0.33$ µm (grey horizontal line), $s^{\text{true}} = 0.85$ Mm^{-1} (not shown), and $n^{\text{true}} = 1$ cm^{-3} (grey horizontal line). The grey area describes the CRI of organic carbon (OC) on the condition that relative humidity is less than 5% (see Table 4.1)

Table 4.1 Aerosol types, respective CRI at 532 nm, and growth factors (GF) for some RH-intervals [3]

	RH < 5%		20% ≤ RH ≤ 25%		RH > 90%	
Aerosol types	GF	CRI	GF	CRI	GF	CRI
Organic carbon	1	1.53-*i*0.009	1.10	1.49-*i*0.007	2.5	1.35-*i*0.001
Black carbon	1	1.75-*i*0.44	1	1.75-*i*0.44	1.9	1.43-*i*0.100
Sea salt	1	1.50-*i*0.000	1.15	1.44-*i*0.000	2.5	1.35-*i*0.000
Sulfate	1	1.43-*i*0.000	1.18	1.40-*i*0.000	2.0	1.35-*i*0.000
Dust	1	1.53-*i*0.0026	1	1.53-*i*0.0026	1	1.53-*i*0.0026

4.4 Case Study

We carried out a validation test of the capabilities of the novel approach for the case of real measurement conditions. We investigated $3\beta + 2\alpha$ data obtained from lidar measurements of a smoke plume from 22 July 2004. We selected data at 3.8 km for which radiosonde and in situ data are available [2].

The results are shown in Figs. 4.1d and 4.2b. The solution space shows a wide spread of the PMPs along the CRI *trajectory* that extends on the (m_{R}, m_{I})-plane from $1.525 - i0.0025$ to $1.7 - i0.0425$. Number concentration ranges from 180 to 1000 cm^{-3} and effective radii from 0.3 to 0.1 µm (see green and blue curves in Fig. 4.2b, respectively).

We restrict the spread of the retrieved PMPs by constraining the range of values of the CRI by using information about relative humidity at 3.8 km. Relative humidity measured with radiosonde at 3.8 km is less than 5%. We select from Table 4.1 the CRI $m = 1.53 - i0.009$ for organic carbon at RH < 5% because for this aerosol type the value $m = 1.53 - i0.009$ is intermediate between $m = 1.525 - i0.0025$

and $m = 1.575 - i0.01$; see the x-axis of Fig. 4.2b. We use this value for the CRI in Fig. 4.2b. This value acts as constraint on the solution space of the CRI (see grey area). We see that all other CRIs in Table 4.1 do not coincide with the x-axis nodes at RH < 5%; see the "canyon" in Fig. 4.1d and the x-axis in Fig. 4.2b.

The results retrieved with this novel approach at $m \approx 1.55 - i0.007$ (see Figs. 4.1d and 4.2b) agree to results obtained with our two-dimensional regularization approach (not shown) and measured in situ (see star in Fig. 4.1d) [2].

4.5 Conclusion

We developed a minimization procedure for the simultaneous retrieval of spectrally and size-independent CRIs and monomodal PSDs from optical data $3\beta + 2\alpha$ taken with multiwavelength HSRL/Raman lidar. The minimization procedure allows us to estimate the PMPs including the CRI with any preset accuracy if the optical data are known to at least eight significant digits.

We show on the basis of a case study that measurement uncertainties of 1–3% of $3\beta + 2\alpha$ optical data result in a considerable spread of the CRI solution space. The retrieval uncertainty of the CRI can be described by a solution trajectory ("canyon") that crosses the complete (search) domain of the CRI (m_R, m_I)-plane from its lower-left corner to the top-right corner. The length and width of "canyon" are determined by the CRI domain and the measurement uncertainty of the input optical data, respectively. However, the true solution can be localized on the trajectory if we use information about RH. The results are validated by a case study from 22 July 2004 for which Raman lidar, radiosonde, and in situ data are available.

Acknowledgments We thank the Russian Science Foundation (project 21-17-00114) for support of this research.

References

1. Veselovskii, I., et al.: Inversion of multiwavelength Raman lidar data for retrieval of bimodal aerosol size distribution. Appl. Opt. **43**, 1180–1195 (2004)
2. Müller, D., et al.: Vertical profiles of microphysical particle properties derived from inversion with two-dimensional regularization of multiwavelength Raman lidar data: Experiment. Appl. Opt. **50**(14), 2069–2079 (2011)
3. Veselovskii, I., et al.: Characterization of smoke/dust episode over West Africa: Comparison of MERRA-2 modeling with multiwavelength Mie-Raman lidar observations. Atmos. Meas. Tech. **11**, 949–969 (2018)
4. Bohren, C.F., Huffman, D.R. (eds.): Absorption and Scattering of Light by Small Particles. Wiley, New York, NY, USA (1983)
5. Kolgotin, A. et al.: Perspectives of the explicit retrieval of the complex refractive index of aerosols from optical data taken with lidar. In: Proceedings of ILRC 27, July 2015, New York, PS-B5-17
6. Gill, P.E., et al.: Practical Optimization. Emerald Publishing (1982)

Chapter 5
Field Testing of a Diode-Laser-Based MicroPulse Differential Absorption Lidar System to Measure Atmospheric Thermodynamic Variables

Robert A. Stillwell, Scott M. Spuler, Matthew Hayman, Kevin Repasky, and Owen Cruikshank

Abstract Traditionally, quantitative lidar techniques like differential absorption lidar (DIAL) and high-spectral-resolution lidar (HSRL) utilize high-power-aperture product designs, which partially compensates for the need to take discrete derivatives of noisy data in post-processing (for number density for DIAL and extinction for HSRL) and provides for high-performance measurements, i.e., higher resolution, accuracy, or precision. Conversely, low-power-aperture product lidar designs are easier to make eye-safe, reliable, and cost-effective, which are important attributes for network development and field deployment. The atmospheric science community has expressed the need for high-quality, quantitative, robust, network deployable, and cost-effective sensors for a variety of applications such as improved numerical weather forecasting – in essence requiring the best of both worlds without the accompanying drawbacks. In response to this need, the National Center for Atmospheric Research and Montana State University have been developing the MicroPulse DIAL (MPD) architecture for thermodynamic profiling in the lower atmosphere. The MPD architecture takes advantage of the benefits of low-power, low-cost laser diodes, and fiber optics to achieve quantitative profiling leveraging narrowband filtering and efficient elastic scattering. A field-deployable MPD instrument capable of humidity, quantitative aerosol, and temperature profiling has recently been developed. This presentation will describe the current status of this thermodynamic profiler and the initial results from a recent field deployment. Emphasis will be given to the analysis of the temperature data including comparisons to co-located radiosondes to describe current performance.

R. A. Stillwell (✉) · S. M. Spuler · M. Hayman
National Center for Atmospheric Research, Earth Observing Lab, Boulder, CO, USA
e-mail: stillwel@ucar.edu

K. Repasky · O. Cruikshank
Electrical and Computer Engineering, Montana State University, Bozeman, MT, USA

© The Author(s), under exclusive license to Springer Nature Switzerland AG 2023

J. T. Sullivan et al. (eds.), *Proceedings of the 30th International Laser Radar Conference*, Springer Atmospheric Sciences,
https://doi.org/10.1007/978-3-031-37818-8_5

Keywords Water vapor · Temperature · Thermodynamics · DIAL · HSRL

5.1 Introduction

Water vapor (WV) number density and temperature, collectively referred to as thermodynamic variables, are critically important atmospheric state variables for the prediction of weather processes because many driving physical mechanisms of weather are direct functions of their spatiotemporal variability. As a result, the widespread measurement of atmospheric thermodynamic variables is integrally important to modern weather prediction. So great is the need for thermodynamic observations that radiosondes are launched in unison all over the world twice daily for ingestion into operational weather forecasting models, with more intensive observational campaigns targeting severe weather such as the use of dropsondes into hurricanes. This paradigm is well established and robust but is fundamentally limited in several key aspects, such as its resource-intensive nature and lack of continuous measurements. This has led several groups, leveraging both passive and active remote sensing techniques, to address some of the fundamental limitations.

Remote sensing techniques to measure thermodynamic variables include microwave radiometry, infrared spectrometry, Raman lidar, high-spectral-resolution lidar (HSRL), and differential absorption lidar (DIAL) [1, 2]. Microwave radiometers and infrared spectrometers can be used to measure temperature and WV, but the retrievals lack uniqueness and contain little information content, i.e., retrievals are very coarse in range. Raman lidar systems are conceptually simple and capable of measuring both WV and temperature in a range-resolved manner. However, Raman lidar systems require calibration from ancillary measurements; have a tendency to require high peak power lasers, which are an eye safety risk; and are difficult to make field-deployable with continuous observations. HSRL systems have shown promise to measure temperature, but have no WV sensitivity. DIAL systems have been shown to measure WV, and theoretical frameworks exist to measure temperature, but practical temperature measurements have remained elusive. In fact, the work of Theopold and Bösenburg to demonstrate DIAL temperature measurement [3, 4] is often cited as proof that DIAL systems can only practically measure temperature in highly restrictive circumstances. Therefore, there is no clear method useful for broad network deployment to perform continuous measurements of atmospheric thermodynamic variables.

DIAL systems are perhaps the easiest system type to imagine overcoming their current limitations as the limitations are technological in nature and not fundamental. DIAL measurements, leveraging oxygen absorption, are sensitive to temperature, WV number density, and lidar backscatter ratio [3, 4]. The partial pressure of WV in moist atmospheres modulates the number density of oxygen. Furthermore, the primary absorption lines available are narrow, with widths on the same order of magnitude at the scattered Rayleigh-Brillouin spectra. Therefore, scattered light by molecules and aerosols are absorbed slightly differently. As

a result of these sensitivities, to make accurate temperature measurements with oxygen DIAL, measurements of oxygen absorption, backscatter ratio, and WV are simultaneously needed. This implies three lidar systems. As a practical matter, engineering such a system was considered prohibitively complicated compared to other measurement methods, despite many clear advantages of DIAL measurements such as being independent of ancillary calibration.

With the advent of diode-laser-based (DLB) lidar systems, the complexity of developing a field-deployable DIAL lidar system capable of network deployment and continuous, long-term unattended operation has become tractable [5]. Diode lasers are robust and their low power nature allows for eye-safe operation. Furthermore, the low-cost, commercially available parts used to construct such DLB lidar systems facilitate the economic viability of network deployment. This presentation will discuss the efforts to develop and demonstrate such a system and specifically its field testing in the summer of 2021. The system – referred to as MicroPulse DIAL (MPD) – combines a WV DIAL with an O_2 DIAL which has an embedded potassium (K) HSRL. The system measures WV and backscatter ratio directly via the DIAL and HSRL techniques, respectively, and uses those variables as input into the retrieval for O_2 DIAL to measure temperature.

5.2 MicroPulse DIAL Hardware

The MPD system is shown as a block diagram in Fig. 5.1. Green components are used for O_2 DIAL and K HSRL, while the blue components are for WV DIAL. The quantitative lidar techniques used, DIAL and HSRL, do not require calibration from ancillary measurements. In general, such a system could require as many as five transmitted frequencies (WV online/offline, O_2 online/offline, and HSRL) with as many as four detectors (WV, O_2, and HSRL molecular/combined).

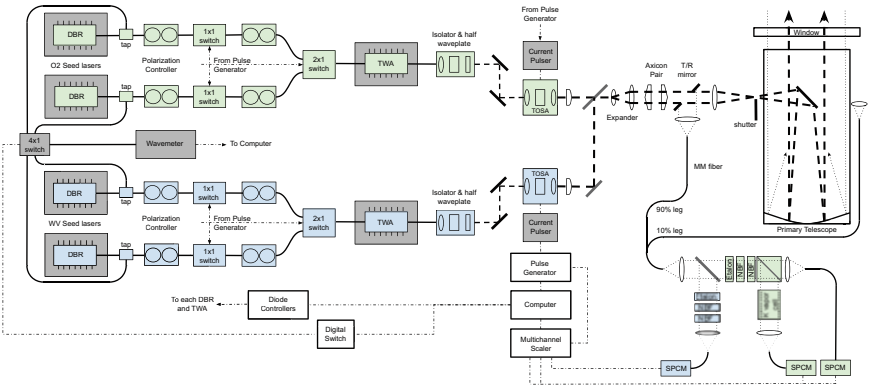


Fig. 5.1 Block diagram of the MPD capable of measuring WV and temperature

To allow practical implementation, a simplification is achieved by setting the O_2 offline wavelength at the potassium D1 line. This combines the O_2 offline and HSRL laser into one and removes the need for a dedicated O_2 detector. The benefits of this design include hardware simplicity, the ability to measure the HSRL geometric overlap function directly during data collection (the O_2 online laser is measured on the same path but lacks potassium absorption), and the fact that HSRL data is taken at the wavelength of interest, which removes the need to assume an Angstrom exponent. In summary, there are six photon-counting measurements: WV online/offline, O_2 online/offline-combined detector, and O_2 online/offline molecular detector. From those six measurements, four pieces of information may be gleaned directly: WV number density, backscatter ratio, HSRL geometric overlap function, and O_2 absorption. With this information, the temperature can be retrieved.

The first demonstration of this instrument was in 2019 [6]. The original demonstration instrument showed promise, but in practice, a number of instrument fragilities had to be addressed. Since then, a number of changes have been made including the implementation of a fiber-coupled seed laser system to replace free space diodes, the addition of fiber-coupled traveling-wave amplifiers, the addition of a wide field of view telescope to improve low-range overlap, automated receiver scanning ability to monitor optical stability, new receiver interference filters and etalons, and software updates for overall system stability [7]. These updates enabled a WV-only MPD system to successfully complete a 15-month continuous test and enabled long-term field testing of the full thermodynamic MPD instruments as well.

5.3 Field Testing

In the summer of 2021, NCAR deployed an MPD system to Fort Collins, CO, USA, from June 16 to August 20 in support of a test field campaign, referred to as Pre-PRECIP. Over that time period, the system operated continuously and in an unattended manner. A data sample from the first three weeks of the deployment is provided in Fig. 5.2. WV data is processed in two ways: the standard method as described by [7] and using an advanced processing technique referred to as PTV [8]. PTV provides similar data accuracy at low altitudes but extends the range of observations. The magenta line marks the top of the standard WV processing with PTV data shown above. Temperature data is processed as outlined in Table 2 of [6]. Surface temperature data is collected from a weather station mounted to the MPD instrument.

From June 20 to August 15, 2021, 42 radiosondes were launched that are used for comparison purposes. These sondes all targeted convective atmospheric conditions and were launched during the day (between 8 am and 3 pm local time), with 32 being from 11 am to 1 pm local time. This represents the most difficult comparison from a lidar perspective due to cloud and solar background conditions. These comparisons, shown in Fig. 5.3, indicate excellent agreement for WV measurements, with increased coverage resulting from PTV data processing. Temperature measurements

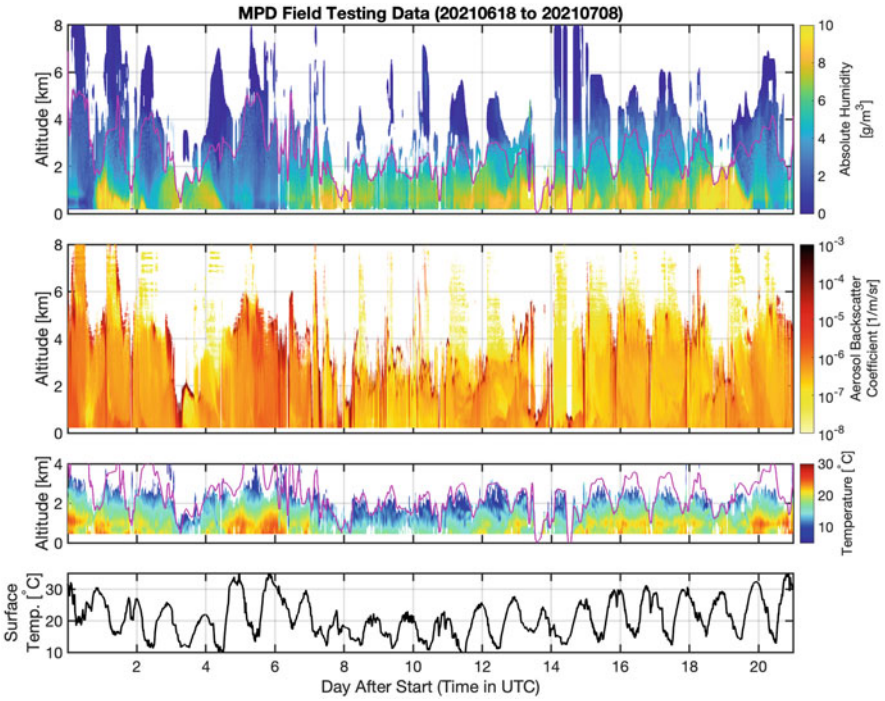


Fig. 5.2 MPD data from a 3-week period during the Pre-PRECIP deployment. The solid magenta line shows the highest altitude measured with standard WV processing and is used as a benchmark for the maximum altitude expected from temperature data. WV data above that line is retrieved using the PTV technique

also agree well with sondes, though have an approximately 1.5 °C warm bias. The source of this warm bias is under investigation but is suspected to be partially due to an incomplete spectroscopic model used for this preliminary data analysis. It should be noted that no ancillary data is required, or used, for the DIAL or HSRL data retrievals.

Temperature measurements with DIAL, shown in Fig. 5.2, show a number of key attributes. First, the atmospheric temperature clearly tracks with the temperature from the surface station even though the surface temperature is not used in the retrieval; an isothermal atmosphere was assumed as the retrieval starting position. Second, with the exception of strong cloud layers, the aerosol structure is not prominent in the temperature retrievals – demonstrating it is possible to overcome the primary issue identified by Theopold and Bösenberg which historically prohibited temperature retrievals. Finally, error analysis was performed using the bootstrapping method, outlined in [7]. The mask resulting from this error analysis method tracks the WV masking well, with the WV data having a slightly better range as the total bandpass of the receiver etalons is smaller, meaning less background light is present.

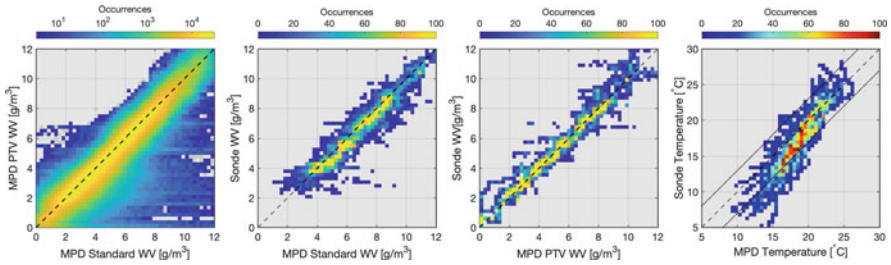


Fig. 5.3 Comparisons of MPD data products and radiosonde launches during Pre-PRECIP. MPD standard WV is processing as described in [7]. MPD PTV WV is processing as described in [8]. MPD temperature is processed as described in [6]

5.4 Summary

Atmospheric thermodynamic profiling is of great importance to the skill of weather prediction. As such, the development of a continuous, autonomous, network deployable sensor to provide such measurements is highly sought. MPD is one possible instrument architecture to provide these measurements leveraging DIAL and HSRL techniques to measure WV number density, backscatter ratio, and temperature. The initial demonstration of temperature measurements using O_2 DIAL, occurring over approximately 2 days presented in [6], showed both theoretical promise and yet technological fragility. This work leverages a number of hardware improvements to extend the measurement length and reliability. Measurements over more than 60 days including comparisons with 42 collocated radiosondes launches are used here to demonstrate a number of things. First, a three-in-one lidar system containing two DIAL systems and an HSRL is possible to develop and field deploy in a long-term measurement configuration. Second, adding extra temperature and HSRL measurements do not negatively impact current WV technological readiness. Finally, temperature measurements that do not require calibration are possible using DIAL when aerosol and WV structures are also measured, which is technologically possible primarily due to the development of diode-laser-based lidar systems.

Acknowledgments NCAR is sponsored by the National Science Foundation under Cooperative Agreement No. 1852977. Support from the National Science Foundation grant number 1624736 and 1930907 and the NOAA Office of Weather and Air Quality Research Programs, Next Generation of Mesoscale Weather Observing Platforms Award No. NA19OAR4590324 is gratefully acknowledged.

References

1. Foken, T. (ed.): Springer Handbook of Atmospheric Measurements. Springer Nature, Cham (2021)

2. Weitkamp, K. (ed.): Lidar. Range-Resolved Optical Remote Sensing of the Atmosphere. Springer, New York (2005)
3. Theopold, F.A., Bösenberg, J.: Differential absorption lidar measurements of atmospheric temperature profiles: Theory and experiment. J. Atmospheric Ocean. Technol. **10**(2), 165–179 (1993)
4. Bösenberg, J.: Ground-based differential absorption lidar for water-vapor and temperature profiling: Methodology. Appl. Opt. **37**(18), 3845–3860 (1998)
5. Spuler, S.M., et al.: Field-deployable diode-laser-based differential absorption lidar (DIAL) for profiling water vapor. Atmos. Meas. Tech. **8**(3), 1073–1087 (2015)
6. Stillwell, R.A., et al.: Demonstration of a combined differential absorption and high spectral resolution lidar for profiling atmospheric temperature. Opt. Express. **28**, 71–93 (2020)
7. Spuler, S.M., et al.: MicroPulse DIAL (MPD) – A diode-laser-based lidar architecture for quantitative atmospheric profiling. Atmos. Meas. Tech. **14**, 4593–4616 (2021)
8. Marais, W.J., Hayman, M.: Extending water vapor measurement capability of photon limited differential absorption lidars through simultaneous denoising and inversion. Atmos. Meas. Tech. Discuss. **15**, 5159–5180 (2022). https://doi.org/10.5194/amt-2021-352

Chapter 6
Semiconductor Lidar for Quantitative Atmospheric Profiling

Scott M. Spuler, Robert A. Stillwell, Matthew Hayman, and Kevin Repasky

Abstract It is well known that semiconductor lasers offer the important advantages of lower costs, smaller footprint, simplicity, and wider spectral coverage compared to solid-state lasers. However, despite many advances, the output power achievable from semiconductor lasers is still far from solid-state lasers and generally has restricted their use in atmospheric profiling to lidar that does not allow quantitative backscatter information (e.g., ceilometers). Over the past decade, we have been developing lidar architectures using semiconductor sources that provide quantitative observations needed to advance atmospheric science and weather forecasting. This chapter reviews some of the limitations and benefits of this flexible laser technology. We introduce a semiconductor lidar architecture, based on a pulsed overdriven tapered amplifier and traveling wave amplifier, the latter being leveraged as a multifunction switch. This design has been implemented and is being used for the measurement of water vapor, temperature, and calibrated aerosols via DIAL and HSRL techniques. Initial results from an intercomparison with a collocated instrument using our previous baseline architecture will be discussed.

Keywords Water vapor · Temperature · DIAL · HSRL

6.1 Introduction

Over the past decade, we have been developing lidar architectures using semiconductor sources that provide quantitative observations needed to advance atmospheric science and weather forecasting [1]. While semiconductor lasers offer important advantages compared to solid-state lasers, their limited output power can restrict

S. M. Spuler (✉) · R. A. Stillwell · M. Hayman
National Center for Atmospheric Research, Boulder, CO, USA
e-mail: spuler@ucar.edu

K. Repasky
Montana State University, Electrical and Computer Engineering, Bozeman, MT, USA

© The Author(s), under exclusive license to Springer Nature Switzerland AG 2023

J. T. Sullivan et al. (eds.), *Proceedings of the 30th International Laser Radar Conference*, Springer Atmospheric Sciences,
https://doi.org/10.1007/978-3-031-37818-8_6

their use in lidar atmospheric profiling. Semiconductor laser optical power output is limited by catastrophic optical mirror damage (COMD) [2, 3]. COMD primarily occurs from the semiconductor material absorbing a fraction of the laser energy resulting in localized heating at the facets. The advent of the tapered semiconductor optical amplifier – or simply "tapered amplifier" – allowed for a significant increase in laser power while also providing beam quality near the diffraction limit. These power amplification devices, covering the spectral range 650–1100 nm, are a key component in laser cooling and trapping experiments [4–7]. They typically have a ~4-μm-square waveguide input section which tapers to an output facet width of ~200 μm along the horizontal dimension. The tapered geometry allows the power density to be kept below the COMD while generating output powers of 1–3 W in continuous wave (cw) mode. Since COMD is essentially a thermal problem, in the pulsed regime, the tapered amplifier can be overdriven to obtain even higher peak powers at reduced duty cycles [8, 9].

Frequency agile lasers with spectrally narrow linewidth are required for many quantitative spectroscopy applications. This can be achieved by using tapered amplifiers in a master oscillator power amplifier (MOPA) configuration. The master oscillator – a spectrally narrow seed laser – is injected into the input facet of the device. It is amplified via the induced recombination in the inverted medium maintaining its spatial and spectral properties. When the tapered amplifier is operated near its saturation point (typically obtained with >10-mW-cw seed power), the stimulated emission from the gain medium is most efficient. Because of the small size on the input side of the device, it is very sensitive to both the alignment and power of the seed beam. A tapered amplifier will emit amplified spontaneous emission (ASE) from both facets with a broad spectral width of 20–30 nm when operated without optical input. The ASE is kept relatively low primarily due to the use of high-quality antireflection coatings at the facets (<0.01% reflectivity). Increasing the power of the seed beam decreases the contribution of ASE due to gain competition. The narrowband seed laser leads to a strong reduction in inversion over its spectral region which is filled by the charge carriers from other spectral regions. Thus there is less inversion for the spontaneous emission process. It is important to note that the spatial beam quality of broadband ASE is poor because the optical power inside the waveguide is far below the saturation power of the tapered region. Furthermore, it is multimode, so it has a different divergence than the amplified seed laser. These qualities allow for further suppression of the ASE if desired, by coupling the output of a tapered amplifier into a single-mode fiber with up to 60% coupling efficiency [10, 11].

6.2 Instrument Architecture

In our experience we have found that a tapered amplifier in a MOPA configuration can routinely yield peak power of >8 W when operated in pulsed mode with lifetimes of >30,000 h when operating at 0.5–0.7% duty cycles (e.g., 1 μs pulse duration

at 7 kHz). More importantly, the output of these semiconductor-based transmitters has suitable spectral properties for advanced quantitative lidar measurements such as differential absorption lidar (DIAL) and high spectral resolution lidar (HSRL), i.e., suitable frequency agility, narrow spectral linewidth, and high spectral purity. To be clear, these techniques are only achieved using longer than typical pulse length for lidar systems and careful receiver designs – using photon-counting receivers and suppressing the solar background with a narrow field-of-view and ultra-narrow optical filters. Still, atmospheric properties such as water vapor number density, calibrated aerosol backscatter coefficients, and temperature can be measured on spatial and temporal scales that are greatly needed by the atmospheric science and weather forecasting communities [1].

6.2.1 Recent Advances

Our more recent lidar architectures use a traveling wave amplifier to boost the seed laser power prior to the tapered amplifier. These single-stripe amplifiers contain essentially the same semiconductor architecture but without the taper (i.e., a waveguide with 3–5-μm input and output facets.) COMD typically limits these devices to <20–80 mW when operated in continuous wave mode although there are also maximum gain and maximum current specifications for these devices which must be considered. Like the tapered amplifier, when operated in pulsed mode (i.e., low-duty cycle), they can be driven to output peak powers above these levels. This is advantageous because, as previously mentioned, higher seed power results in improved suppression of the tapered amplifier ASE. Furthermore, when switched off, these devices have extinctions on the order of 40–50 dB. This means the traveling wave amplifier can be leveraged as a multifunction device (i.e., switch and amplifier), which both reduces cost and complexity while enhancing performance over traditional optoelectronic switching. Although a logical extension of previous semiconductor lidar architectures, pulsed current-overdriven traveling wave amplifiers are a unique addition to lidar architecture and provide higher isolation when switching between two seed lasers as needed for the DIAL technique.

A schematic of this new lidar transmitter design is shown in Fig. 6.1. It is an almost completely fiber-coupled design that is both stable and robust for continuous observations on time scales of tens of thousands of hours. The tapered amplifier is yet to be fiber-coupled as commercially available versions are optimized for cw applications. While the electrical pump level has a negligible impact on the coupling efficiency of the device, it does impact the output beam characteristics. Due to local thermal gradients, the index of refraction of the semiconductor gain medium changes slightly with the electrical pump current level [4]. The output from a tapered amplifier is highly divergent with an astigmatism that is a function of the index of refraction – which in turn is a function of carrier density and temperature. Therefore, the final location of the collimating optics, typically a fast aspheric lens

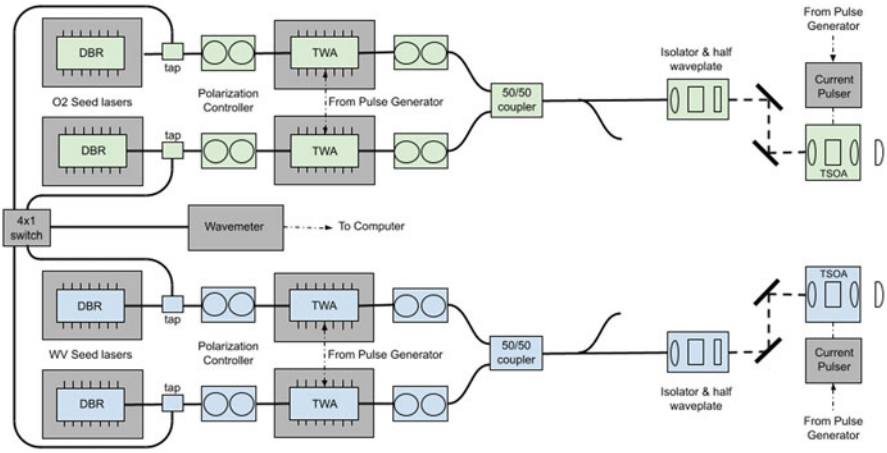


Fig. 6.1 Block diagram of a fiber-coupled lidar transmitter utilizing distributed Bragg reflector (DBR) seed lasers in a MOPA configuration with pulsed overdriven traveling wave amplifiers (TWA) as a multifunction device (switch and amplifier) and pulsed overdriven tapered semiconductor optical amplifiers (TSOA). Green-shaded components are for temperature profiling, and blue-shaded components are for water vapor DIAL (see Spuler et al. [1] for details of the receiver which are not shown in this figure)

and cylindrical lens, needs to be determined at the operating conditions to form a well-collimated beam.

For this pulsed current-overdriven traveling wave amplifier design, a 50/50 fiber coupler is used to combine the online and offline seed lasers within a single fiber which results in an approximate 50% reduction in the seed power available to the tapered amplifier. However, the improved output power from overdriving the traveling wave amplifier can be used to compensate for that loss. Additionally, the unused 50% power can be leveraged either for laser locking or status monitoring. The pulsed mode (0.8% duty cycle) traveling-wave amplifiers are operated to produce >40-mW equivalent cw power, and we have found them stable, operating continuously for over a year and counting. It may be possible to increase the output beyond these levels. However, we have found that 15–20 mW (equivalent cw power) supplied to the tapered amplifier is adequate to operate in a saturated gain mode, with suitable suppression of ASE and spectral purity.

6.3 Initial Test Results

Side-by-side testing between two thermodynamic profiling MicroPulse DIAL (MPD) units began in Dec 2021 from the NCAR Foothills Laboratory campus in Boulder, CO, USA. Both instruments provide water vapor, calibrated aerosol, and temperature profiles, with one unit in the Gen 5 configuration as discussed in

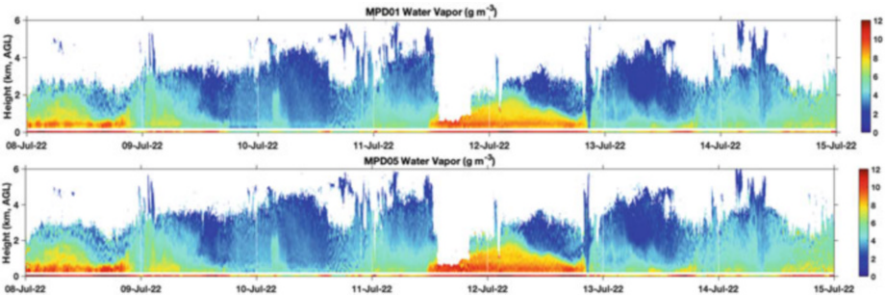


Fig. 6.2 Simple example comparison of water vapor, in g m^{-3}, measured with the new 4 kHz architecture (top, as MPD01) and the older Gen 5 system (on bottom, as MPD05)

Spuler et al. (2021) [1], and a second unit configured with the new pulsed seed architecture and the seed lasers (on/off) interleaved at 4 kHz (every second shot) instead of at 100 Hz. In general, the 2 units provide nearly identical measurements, but some differences at the lowest ranges still need to be examined more carefully. A simple example comparison of the water vapor measurement is shown in Fig. 6.2. At the time of this writing, we have 30 weeks of side-by-side data and the test is ongoing. During the test, we have investigated different hardware configurations such as tapered amplifiers, different pulse lengths, drive currents, etc. In the future, we hope to compare this dataset with the weekly GRUAN radiosonde launches from the Marshall field site (11 km away) and twice daily soundings from Denver International Airport (44 km away).

Construction of the second full thermodynamic MPD instrument helped to diagnose the source of a banding structure evident in the temperature data after we switched to using a 765-nm TOSA (following tests that had shown it to have slightly better spectral purity compared to a 780-nm TSOA). The 765-nm TSOA is shorter in length – 2.80 mm long – whereas the 830-nm and 780-nm TSOAs are 4.05 mm long. As a result, and likely due to the absorption coefficient of the chip as well, there is significantly less continuous-wave seed laser absorption when the tapered amplifier is switched off. This higher throughput level of continuous-wave laser light rises above the noise floor of the photon counters in the receiver. It is hypothesized that a type of Boltzmann population perturbation (i.e., Rabi oscillations in the two-level semiconductor system) occurs in the TSOA following the abrupt end of the drive pulse current. As a result the ground-state population and resulting absorption have a temporal fluctuation just after the pulse. With the continuous wave seed laser power leakage detectable by the photon counter, a fluctuating detector baseline results. This effect is not problematic in the regions where there is high SNR, but it does limit the technique to longer ranges. As a result, we reverted to using more highly absorbing 780-nm TSOA for the Gen 5 architecture and only using the 765-nm TSOA in the new pulsed seed laser architecture. These modifications have been tested and found to resolve the issue.

6.4 Summary

Lidar systems built with semiconductor lasers can capitalize on the advantage of lower cost, a smaller footprint, simplicity, and wider spectral coverage compared to solid-state lasers. When they are used in a MOPA configuration – utilizing current-overdriven tapered amplifiers – they can generate suitable output power for atmospheric profiling lidar and have suitable properties for advanced quantitative forms such as differential absorption lidar and high spectral resolution lidar. Therefore these types of semiconductor lidar architectures have the potential to advance atmospheric science and weather forecasting in ways that ceilometers or high-power solid-state lidar designs are not capable of providing. This chapter reviewed some of the limitations and benefits of this laser technology and introduced an updated atmospheric profiling lidar architecture. The design, using a traveling wave amplifier as a multifunction switch, is actively being used for the measurement of water vapor, temperature, and calibrated aerosols.

Acknowledgments NCAR is sponsored by the National Science Foundation. The authors would like to acknowledge the support of the National Science Foundation grant number 1624736 and the NOAA Office of Weather and Air Quality Research Programs, Next Generation of Mesoscale Weather Observing Platforms Award No. NA19OAR4590324.

References

1. Spuler, S.M., Hayman, M., Stillwell, R.A., Carnes, J., Bernatsky, T., Repasky, K.S.: MicroPulse DIAL (MPD) – a diode-laser-based lidar architecture for quantitative atmospheric profiling. Atmos. Meas. Tech. **14**, 4593–4616 (2021)
2. Gehrig, E., Hess, O.: Spatio – temporal dynamics of light amplification and amplified spontaneous emission in high-power tapered semiconductor laser amplifiers. IEEE J. Quantum Electron. **37**, 1345–1355 (2001)
3. Gehrig, E., Hess, O., Seibert, C., Woll, D., Wallenstein, R.: Amplification and wave mixing of induced and spontaneous emission in semiconductor laser amplifiers. Appl. Phys. B Lasers Opt. **76**, 285–288 (2003)
4. Kangara, J.C.B., Hachtel, A.J., Gillette, M.C., Barkeloo, J.T., Clements, E.R., Bali, S., Unks, B.E., Proite, N.A., Yavuz, D.D., Martin, P.J., Thorn, J.J., Steck, D.A.: Design and construction of cost-effective tapered amplifier systems for laser cooling and trapping experiments. Am. J. Phys. **82**, 805–817 (2014)
5. Nyman, R.A., Varoquaux, G., Villier, B., Sacchet, D., Moron, F., Le Coq, Y., Aspect, A., Bouyer, P.: Tapered-amplified antireflection-coated laser diodes for potassium and rubidium atomic-physics experiments. Rev. Sci. Instrum. **77**, 3 (2006)
6. Fuch, M.: Development of a High Power Stabilized Diode Laser System. University of Oregon, Thesis (2006)
7. Cole, R.: Construction and optimization of a tapered amplifier system for applications in ultracold plasma research. Colby College, Honors Thesis (2015)
8. Takase, K., Stockton, J.K., Kasevich, M.A.: High-power pulsed-current-mode operation of an overdriven tapered amplifier. Opt. Lett. **32**, 2617 (2007)
9. Nehrir, A.R., Repasky, K.S., Carlsten, J.L.: Eye-safe diode-laser-based Micropulse differential absorption lidar (DIAL) for water vapor profiling in the lower troposphere. J. Atmos. Ocean. Technol. **28**, 131–147 (2011)

10. Trubko, R., Gregoire, M.D., Holmgren, W.F., Cronin, A.D.: Potassium tune-out-wavelength measurement using atom interferometry and a multipass optical cavity. Phys. Rev. A. **95**, 052507 (2017)
11. Nicolai, F.V.: Design and construction of a fiber-coupled tapered amplifier system. University of Heidelberg, Thesis (2017)

Chapter 7
Atomic Barium Vapor Filter for Ultraviolet High-Spectral-Resolution Temperature LiDAR



Madison Hetlage and Christopher Limbach

Abstract A novel active vapor filtering approach functioning at the third harmonic of the commonly used Nd:YAG laser is introduced. The filter utilizes an excited state absorption feature in atomic barium vapor and is characterized by a unique, highly tunable, cusped, non-Maxwellian absorption curve. With adjustments to the pump intensity, frequency, and path length, the filter function width, depth, and central frequency can all be rapidly modified. A feasibility study for a temperature profiling high-spectral resolution LiDAR employing this notch filter is also presented.

Keywords Ultraviolet LiDAR · Barium vapor filter · High-spectral-resolution LiDAR · Actively pumped filters

7.1 Introduction

This chapter presents a novel vapor notch filter for use in high-spectral-resolution LiDAR (HSRL) systems. In a typical HSRL, vapor- or étalon-based, narrow-band filters are used to spectrally separate Rayleigh (molecular) and Mie (particle) return scattering signals. This technique has shown consistent success for the profiling of aerosol optical properties [3] and has been proposed for temperature measurements by taking advantage of the spectral temperature sensitivity of molecular scattering [8, 9]. While multiple vapor species have been suggested for HSRL measurements, including barium at 553.7 nm [1], rubidium at 780 nm [6, 9], cesium at 389 nm [9], potassium at 770 nm [8], the commercial accessibility, increased vapor pressure, and numerous absorption features near the commonly used Nd:YAG

M. Hetlage (✉)
Texas A&M University, College Station, TX, USA
e-mail: mhetlage@tamu.edu

C. Limbach
University of Michigan, Ann Arbor, MI, USA
e-mail: limbach@umich.edu

© The Author(s), under exclusive license to Springer Nature Switzerland AG 2023

J. T. Sullivan et al. (eds.), *Proceedings of the 30th International Laser Radar Conference*, Springer Atmospheric Sciences,
https://doi.org/10.1007/978-3-031-37818-8_7

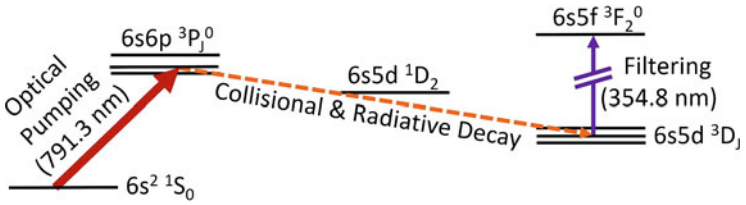


Fig. 7.1 Energy diagram of the low lying levels of barium. In the proposed filter, the red 791.3-nm line is used for optical pumping, while absorption from the purple $^3D_2$ level at 354.8 nm is used for filtering. Note: Figure adapted from [5]

second harmonic (532 nm) experienced by molecular iodine vapor make it the most popular choice [3]. However, iodine-based systems still suffer a variety of challenges, including weaker molecular scattering strength when compared to the ultraviolet, eye safety concerns, and high solar background. Near-ultraviolet operation alleviates these challenges without introducing the increased ozone absorption experienced below 300 nm. However, previously suggested filtering methods in this region are limited by uncommon required lasers, such as the XeCl excimer pumped dye laser utilized to reach the 389-nm transition in cesium vapor [9], and stabilization and alignment challenges, such as the étalon-based filtering approaches used at 355 nm [7]. Notably, vapor-based filters benefit from high acceptance angles and consistent absorption curves. Thus, this chapter aims to develop a vapor-based filter within this desired region (300–400 nm), which operates at a wavelength accessible by a commonly used laser (Nd:YAG third harmonic).

The proposed vapor filter functions by optically pumping a high-temperature barium vapor along the ground state (6s^2 $^1S_0$) $\rightarrow$ 6s6p $^3P_0^1$ transition with a continuous-wave infrared beam at 791 nm. From this upper level, the barium atoms rapidly collisionally and radiatively decay into the excited and metastable 6s5d $^3D_2$ electronic state, from which backscattered light at 354.8 nm can be absorbed along the 5s5d $^3D_2 \rightarrow$ 6s5f $^3F_2^0$ transition. This optical pumping scheme is presented visually in Fig. 7.1. A detailed theoretical and experimental study has been performed to characterize the light transmission of this filter and understand the complex kinetics involved in the optical pumping scheme. A subset of these results will be presented next in Sect. 7.2. Following this, in Sect. 7.3, an application of such a filter to a temperature HSRL will be explored.

7.2 Filter Characterization Measurements

Barium vapor was previously proposed for LiDAR filtering by Alvarez et al. along the ground state $\rightarrow$ 6s6p $^1P_1^0$ transition at 553.7 nm [1]. Despite the filter's significant Mie rejection ($\sim$30 dB) and easy alignment, the multiple engineering challenges present in barium (low vapor pressure, rapid oxidation) and the required

use of the less common tunable dye laser limited the feasibility of widespread filter adoption. As stated, the proposed filter benefits from the high-power, third-harmonic output of the robust, Nd:YAG laser. After several iterations, a unique vacuum-sealed filter design has been developed to overcome the listed engineering challenges. It incorporates multiple temperature-control measures, including a central heated and insulated region of barium capped by baffles and copper tubing water cooling, a PID temperature-control loop, and connections for vacuum and buffer gas lines. This design is able to reach temperatures above 850 K within the heated region and pressures below 0.01 Torr.

Absorption spectroscopy measurements have been conducted at several conditions to characterize this filter and the pumping scheme associated with it. The 354.8-nm absorption feature has been probed at varying pump intensities, frequencies, and path lengths. Some of the results of this chapter, which are discussed at length in [5], can be seen in Fig. 7.2. They demonstrate a highly tunable, non-Maxwellian, cusped absorption feature. Typical vapor filters are characterized by near-Maxwellian curves and are limited to thermal adjustments. The causes of this unique feature can be seen in absorption theory.

Light absorption through a medium is described by the Beer–Lambert Law, $I/I_0 = exp(-n\sigma l)$, where I is the light intensity, n is the absorber number density, σ is the absorption cross section, and l is the path length. The cross section is dependent on the vapor type and the absorption lineshape, a representation of the vapor's velocity distribution. When the pump intensity increases, a larger percentage of ground state barium atoms are "trapped" in the metastable $^3D_2$ level, thus increasing n and increasing absorption. Due to the narrow linewidth of the pump laser, only a select ground state velocity group is excited. Typically, collisions with other atoms or molecules would cause the excited atoms to thermalize. However, the cusped lineshape suggests that the excited atoms experience few velocity changing collisions prior to probing (or diffusion and quenching to the ground state), resulting in the persistence of the excited velocity, a trait most noticeable in the measurements with modified pump frequency. In the double-pass pump measurements, the increased path length of the pump beam results in increased number density in the $^3D_2$ level and thus follows the same trend as increasing pump intensity. Additionally, when the pump frequency is tuned off resonance ($\Delta\nu \neq 0$), two equal and opposite offset velocity groups are excited (one corresponding to each direction of light), resulting in the double peak feature seen here. While the measurements in Figs. 7.2a and b were taken at identical vapor filter conditions ($T \approx 742$ K, $p \approx 0.02$ Torr, $l = 25.4$ cm), the double-pass pump dataset (Fig. 7.2c) represents a shorter single-pass path length ($l = 15.2$ cm) but higher temperature ($T \approx 800$ K). Additionally, in Fig. 7.2b and 7.2c, the pump laser intensities are approximately 1.67 W/cm^2 and 1.35 W/cm^2, respectively. Despite the lowered pump intensity, the ~60 K temperature change results in a 7x increase in vapor number density, adding to the explanation of increased absorption.

Although significant progress has been made in the characterization of this filter, the current measurements lack the optical depth necessary for effective suppression of aerosol scattering. Despite this, the rapid tunability, ease of alignment when

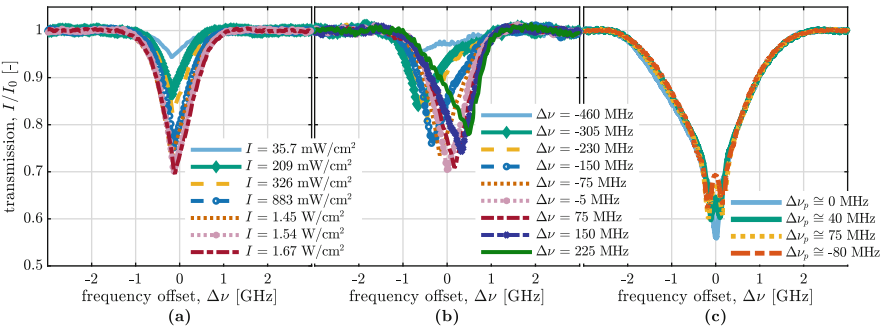


Fig. 7.2 5s5d $^3D_2 \rightarrow$ 6s5f $^3F_2^0$ absorption spectroscopy results for a single-pass pump beam with (**a**) varying pump intensities and (**b**) varying pump frequencies and a double-pass pump beam with (**c**) varying pump frequencies. Note: (**a**) and (**b**) were adapted from [5]

compared to etalons, and near-ultraviolet frequency are promising characteristics for several established diagnostic techniques from ground-based aerodynamic testing to remote sensing systems. A temperature LiDAR-specific application will now be discussed.

7.3 Temperature LiDAR Application

In a traditional temperature HSRL measurement, the elastic backscatter is sent through two notch filters at different temperatures. The ratio of the two transmissions is then used to eliminate the return dependence on the system parameters, atmospheric extinction, and the scatterer number density, resulting in an independent measurement of temperature. The rapid tunability of the barium filter presents an interesting case for this measurement as a single filter could oscillate between filter functions with each pulse, thus requiring only one filter and simplifying the detection chain. Multiple studies have been conducted to determine the optimal filter widths and properties for such a measurement [2, 6, 8]. A successful filter must primarily balance signal to noise (a function of filter transmission and scattering strength), temperature sensitivity, and aerosol extinction. A comparison of the barium filter to the commonly used iodine filter (532 nm) and a representative pure rotational Raman (RR) LiDAR (355 nm) is shown in Fig. 7.3. The right y-axis represents single-channel temperature sensitivity at 275 K and 0.75 atm. The full measurement temperature sensitivity is the difference between the two chosen single-channel sensitivities. Thus, a steep gradient in sensitivity is desired. The left y-axis shows the percent transmission of the RS (or RR) signal through the filter of interest (ϕ) multiplied by the relevant scattering differential cross section ($\delta\sigma/\delta\Omega$, normalized by the 532-nm molecular differential cross section). The intent of this combination is to represent a filter's signal to noise ratio (SNR). To create

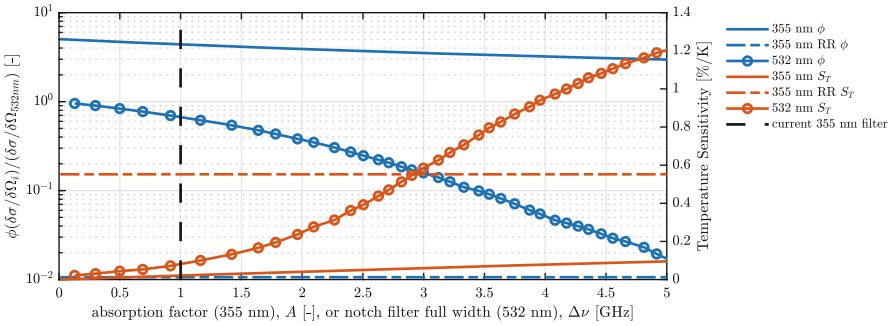


Fig. 7.3 Single-channel temperature sensitivity (right axis) and filter transmission × relative scattering strength (left axis) for an I_2 filter (532 nm), the proposed Ba filter (355 nm), and a RR LiDAR (355 nm) at 275 K and 0.75 atm. Current experimental Ba results correspond to A =1 and the black dashed line

a physically achievable comparison, the iodine filter parameters are plotted as a function of filter width; the barium filter parameters are plotted as a function of an absorption factor, A, where $I/I_0 = exp(-An\sigma l)$; and the RR LiDAR is assumed to have a constant filter width of 2 nm, centered at 353.0 nm with 10^6 suppression at the center wavelength. The Raman filter parameters were chosen to maximize Raman collection, while minimizing background elastic scattering, based on the analysis presented in [4]. While $A = 1$ represents the currently measured barium absorption feature, an absorption factor of 5 is assumed to be achievable through increases in vapor temperature and pump intensity. For this analysis, the zero-offset, double-pass pump measurements are used as the base barium filter function. At $A = 5, 95\%$ absorption is achieved. The proposed barium filter underperforms in temperature sensitivity (and sensitivity gradient) by nearly a factor of 10 from the iodine filter and 5 from the RR filter. However, the stronger backscattering coefficient and high Rayleigh scattering transmission due to the sharp cutoff—even at higher absorption factors, where Mie suppression is greater—result in a significant increase in SNR. To optimize sensitivity and transmission with the proposed filter, while still achieving sufficient aerosol absorption, these results suggest that an absorption factor greater than 5 would be necessary for the second filter function. An alternative option would be to use the RR signal as a reference for the filter as presented in [4].

Secondarily, it is important to consider factors such as filter function consistency, compatible laser availability and energy, safety, and overall design and alignment sensitivity. For example, the increase in maximum permissible exposure below 400 nm allows for higher transmitted power, when compared to the visible wavelengths. On the contrary, the lower temperature sensitivity creates more stringent requirements for filter stability. Using the $A = 5$ filter function, a change in barium vapor temperature of 1 K would result in a single-channel transmission change of ∼0.2%, which corresponds to a ∼2.3 K offset in measured temperature. The full measurement sensitivity using two filters would be even lower, further motivating increased absorption.

7.4 Conclusions

A novel vapor filtering approach utilizing an excited state in atomic barium vapor has been introduced. This filter, which functions at the third harmonic of the commonly used Nd:YAG laser, has undergone a detailed experimental characterization. The results demonstrate a steep, non-Maxwellian, cusped absorption curve, which can be rapidly tuned with changes to pump intensity, frequency, and path length. Despite the engineering challenges present, this filter has several implications for both in situ and remote sensing measurements. A sensitivity study of the filter demonstrates decreased temperature sensitivity when compared to the more commonly used I_2 HSRL and RR approaches but significantly increased SNR. More work is needed to stabilize the filter and achieve the absorption needed for an effective measurement. While outside the scope of this work, there are several other potential applications for this filter. The sharp peak and central frequency adjustment of the barium filter are attractive for wind velocity measurements. Additionally, by alternating the pump power, one can measure filtered and unfiltered results with the same detector. To fully demonstrate the effectiveness of this filter, a ground-based HSRL system is under development at Texas A&M University. Currently, the system is near functioning as a 355-nm backscatter LiDAR. However, the filter is in the process of being implemented into a controlled, table-top-filtered Rayleigh scattering temperature measurement, which will serve as a calibration for initial LiDAR testing.

Acknowledgments The work was supported by a NASA Space Technology Graduate Research Opportunity, Grant #80NSSC20K1190, and a NASA University Leadership Initiative award under Grant NNX17AJ96A.

References

1. Alvarez, R.J., Caldwell, L.M., Li, V.H., Krueger, D.A., She, C.Y.: High-spectral resolution LiDAR measurement of tropospheric backscatter ratio using barium atomic blocking filters. J. Atmos. Oceanic Technol. **7**, 876–881 (1990)
2. Hair, J.W., Caldwell, L.M., Krueger, D.A., She, C.Y.: High-spectral-resolution LiDAR with iodine-vapor filters: measurement of atmospheric-state and aerosol profiles. Appl. Opt. **40**(30), 5280–5294 (2001)
3. Hair, J.W., Hostetler, C.A., Cook, A.L., Harper, D.B., Ferrare, R.A., Mack, T.L., Welch, W., Izquierdo, L.R., Hovis, F.E.: Airborne high spectral resolution LiDAR for profiling aerosol optical properties. Appl. Opt. **47**(36), 6734–6753 (2008)
4. Hetlage, M., Limbach, C.: Combined Rayleigh and Raman airborne temperature LiDAR at 355 nm with a non-Maxwellian barium vapor filter. In: AIAA Scitech 2021 Forum, pp. 1–16. AIAA (2021)
5. Hetlage, M., Limbach, C.: Experimental and analytical evaluation of an active barium vapor notch filter functioning at 355 nm. Appl. Opt. **61**(15), 4591 (2022)
6. Miles, R.B., Yalin, A.P., Tang, Z., Zaidi, S.H., Forkey, J.N.: Flow field imaging through sharp-edged atomic and molecular 'notch' filters. Measur. Sci. Technol. **12**(4), 442–451 (2001)

7. Seaman, S.T., Cook, A.L., Scola, S.J., Hostetler, C.A., Miller, I., Welch, W.: Performance characterization of a pressure-tuned wide-angle Michelson interferometric spectral filter for high spectral resolution LiDAR. In: LiDAR Remote Sensing for Environmental Monitoring XV. vol. 9612, pp. 96120H1–96120H7. SPIE, San Diego (2015)
8. She, C.Y., Krueger, D.A., Yan, Z.A., Hu, X.: Atomic vapor filter revisited: a Cabannes scattering temperature/wind LiDAR at 770 nm. Opt. Exp. **29**(3), 4338–4362 (2021)
9. Shimizu, H., Noguchi, K., She, C.Y.: Atmospheric temperature measurement by a high spectral resolution LiDAR. Appl. Opt. **25**(9), 1460–1466 (1986)

Chapter 8
Future Lidars for Cutting-Edge Sciences in Ionosphere-Thermosphere-Mesosphere-Stratosphere Physics and Space-Atmosphere Coupling

Xinzhao Chu and Guotao Yang

Abstract In the last 15 years, the middle-upper-atmosphere lidar observations have evolved from narrow altitude ranges to the significantly extended altitude ranges of neutral profiling from near the ground up to ~200 km and of ion detection up to ~300 km. A latest development was the first detection of helium to ~700 km. These results demonstrate the huge potentials that lidars bring to the ionosphere-thermosphere-mesosphere-stratosphere (ITMS) physics research as well as to the plasma-neutral coupling studies in the near space environment. This chapter highlights several stunning discoveries made from lidar measurements, including the thermosphere-ionosphere metal (TIMt) layers, full coverage of gravity wave temporal spectrum, and multistep vertical coupling, to illustrate the significant progresses in atmosphere-space sciences. Then we focus on identifying future lidar technologies in enabling cutting-edge sciences in the ITMS physics and interactions between plasma space and neutral atmosphere.

Keywords Future lidars · Cutting-edge sciences · ITMS physics · Space-atmosphere interactions

X. Chu (✉)
Cooperative Institute of Research in Environmental Sciences & Department of Aerospace Engineering Sciences, University of Colorado Boulder, Boulder, CO, USA
e-mail: xinzhao.chu@colorado.edu

G. Yang
State Key Laboratory of Space Weather, National Space Science Center, Chinese Academy of Sciences, Beijing, China
e-mail: gtyang@nssc.ac.cn

© The Author(s), under exclusive license to Springer Nature Switzerland AG 2023

J. T. Sullivan et al. (eds.), *Proceedings of the 30th International Laser Radar Conference*, Springer Atmospheric Sciences,
https://doi.org/10.1007/978-3-031-37818-8_8

8.1 Introduction

Pushing lidar envelope is in demand for assisting and enabling human's explorations in this century. Hot topics include, but are not limited to, the life origin and sustainability, search for exoplanets that can potentially harbor life, understanding and forecasting space weather for the "technological-dependent" human society, understanding climate change and mitigating its negative impacts on humanity, and terrestrial weather forecasting and environmental monitoring. Among them, lidars are sought after to make important contributions to studies of space-atmosphere interactions that are a key factor in making a planet (such as the Earth) habitable and sustainable for life. In particular, lidars are expected to make unique measurements for plasma-neutral coupling that is crucial to space weather research. Moreover, lidar profiling will advance knowledge of atmospheric dynamical and thermal structures and their variability, which in turn contributes to the climate and space weather research and general circulation model development. Lidar can also lend support to environmental monitoring including air quality, weather forecast including water vapor, temperature, and wind measurements, and topographic mapping including glacier and seal level changes, etc. Advanced lidars will become one of the most powerful tools in explorations this century.

In this chapter, we focus on the lidar technologies that help advance cutting-edge sciences in the ionosphere-thermosphere-mesosphere-stratosphere (ITMS) physics and space-atmosphere interaction research. The future directions include, but are not limited to, the following six major aspects: (1) extending lidar measurement ranges of constituents, temperatures, and winds upward and well into the space-atmosphere interaction region, which demands extremely high detection sensitivities and signal-to-noise ratio (SNR); (2) detecting more species (e.g., various metal and meteoric species, atomic oxygen, helium, hydrogen, and important molecular species) with sufficient sensitivity, accuracy, and precision; (3) improving resolutions of lidar temperature and wind measurements in order to cover the complete temporal spectrum of atmospheric waves that play key roles in the transport of constituents, energy, and momentum throughout the Earth's atmosphere; (4) enhancing full diurnal capabilities of temperature and wind measurements in larger altitude ranges; (5) improving lidar automation for more data coverage and for long-term observations of climate change; and (6) innovating data processing and analysis techniques to release the full potentials of lidar data, including introducing artificial intelligence to lidars.

8.2 Stunning Science Discoveries Enabled by Lidars

The discovery of thermosphere-ionosphere metal layers made by lidar observations at McMurdo (77.84°S, 166.67°E), Antarctica in 2011 [1], and follow-up discoveries globally have extended lidar profiling upper limit from ~105 km to nearly 200 km.

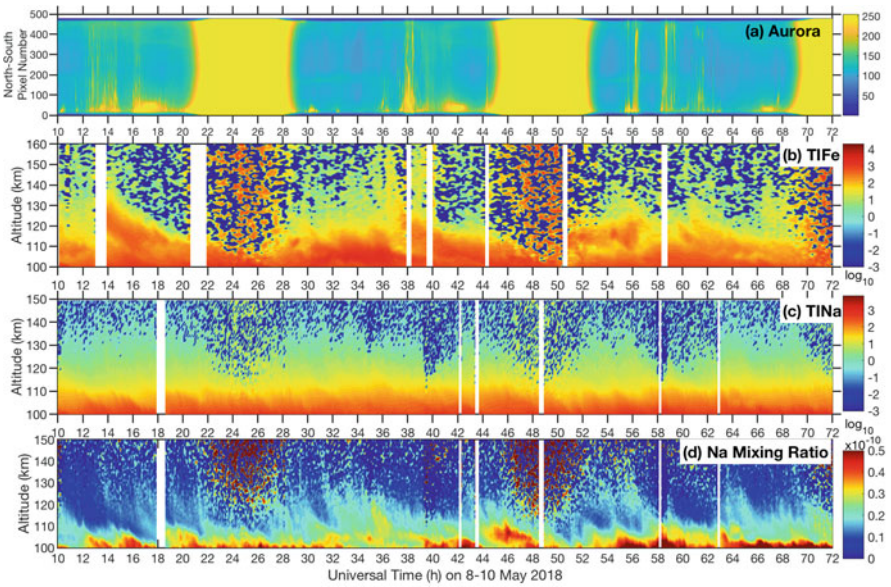


Fig. 8.1 (**a**) Aurora keogram observed by an all-sky-imager and (**b**) TIFe layers observed by an Fe lidar at McMurdo on May 8–10, 2018, revealing close correlation between the TIFe occurrence and aurora activity. (**c**) Diffuse TINa layers observed by a Na lidar on the same day are tenuous and persist long after the TIFe disappearance, revealing striking differences from TIFe. (**d**) Na mixing ratios show rich spectra of gravity waves. (This figure was adapted from Chu et al. [3])

Not only can these metal layers be used as tracers to profile neutral winds and temperatures in the fast transition E and F regions but also are the metal layers a unique natural laboratory enabling "experiments" of plasma-neutral coupling [2]. Figure 8.1 illustrates the rare simultaneous observations of TIMt layers in the Fe and Na species made with the Fe Boltzmann and Na Doppler lidars at McMurdo Station, which reveal stunning differences between TIFe and TINa as well as the one-to-one correspondence between TIFe and aurora activity at the edge of the polar cap and auroral oval [3].

Recent lidar observations at midlatitudes (Boulder and Beijing) have revealed stunning results – the regular occurrence of Na layers up to ~170 km [4] and the first detection of Ca^+ ions to ~300 km (see Fig. 8.2) [5].

These discoveries made with resonance-fluorescence lidars represent the major breakthroughs in extending the lidar detection range well into the thermosphere and the E–F regions of the ionosphere. Because it ablates meteoric materials, dissipates energetic particles from the sun, absorbs extreme solar radiations, regulates gaseous escape, and absorbs various waves coming from the Earth, the space-atmosphere interaction region (SAIR) is crucial to life survival on Earth. Resonance-fluorescence lidars like above with further improved capabilities will help advance the SAIR research.

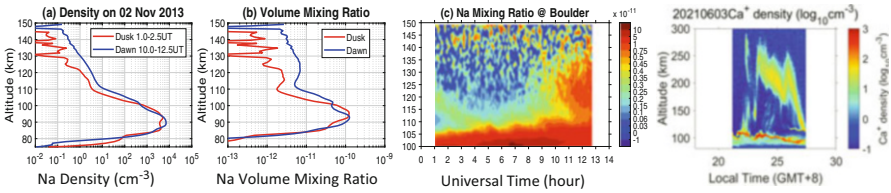


Fig. 8.2 Mid-latitude lidar observations of TIMt and TIMt^{+} layers at Boulder and Beijing. (**a–b**) Boulder dawn and dusk TINa layers plotted in number densities and volume mixing ratios. (**c**) Na mixing ratio contour for Nov 2, 2013 at Boulder. These three panels were adapted from Chu et al. [4]. (**d**) Lidar observations of Ca^{+} ion layers up to ~300 km at Beijing. Panel d was adapted from Jiao et al. [5]

The advanced lidar technologies have enabled the tracing of various atmospheric waves from near the ground to the thermosphere. In particular, lidar observations has begun to cover the full spectrum of gravity waves in the polar regions, enabling unprecedented studies of wave dynamics and their roles in the global transport of constituents, energy, and momentum over the Earth. An example is shown in Fig. 8.3, where vertical wind (W) and temperature (T) measurements with a Na Doppler lidar cover the complete temporal spectrum of gravity waves from ~5 min to inertial period of 12.3 h at McMurdo. The nearly 90° phase shift between w' and T' supports the polarization relation of high-frequency gravity waves with periods less than 20 min. The sensible heat and meteoric Na fluxes computed from such high-resolution and long-duration lidar data exhibit surprising results that the heat flux transitions from downward below 90 km to upward from 97–106 km, which contradicts conventional thinking but demonstrates the importance of the fully compressible solutions for polarization relations of primary and secondary gravity waves [6].

New lidar observations in the last decades have inspired the development of new theories on wave generation and coupling, and an example is the multistep vertical coupling of gravity waves from the surface to the upper thermosphere and ionosphere. This new theory states that momentum and energy are transferred from the lower atmosphere to the thermosphere-ionosphere via complex multistep vertical coupling processes involving the generation of primary, secondary, and tertiary gravity waves, possibly affecting the space weather research and forecast [7]. Lidar discovery of a new class of gravity waves, the persistent gravity waves in the McMurdo MLT (see Fig. 8.3), inspired the development of such multistep vertical coupling theories [8, 9]. Further improvement of lidar measurement ranges will help verify these theories on the tertiary gravity wave generation and propagation.

8.3 Future Lidar Directions and Key Lidar Technologies

With significant and ongoing advances in lasers, photonics, photo-detectors, optical fibers, telescopes, and data acquisition technologies, there are huge potentials to

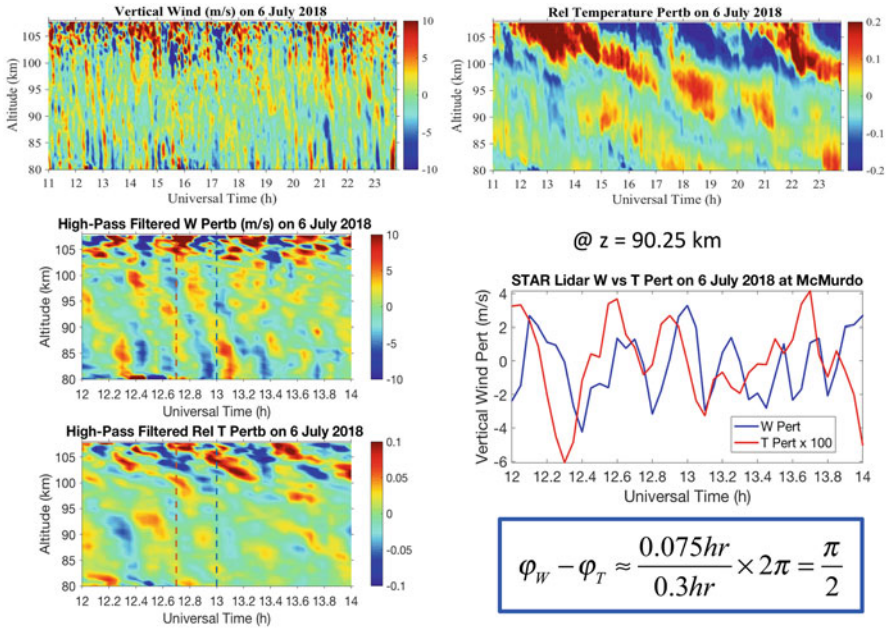


Fig. 8.3 High-resolution lidar observations of vertical wind and temperature in the mesosphere and lower thermosphere (MLT) above McMurdo, Antarctica, covering the full temporal spectrum of gravity waves. The time series of w' and T' demonstrate the phase shift of gravity waves

push lidar technologies to entirely new levels, which will contribute significantly to the ITMS physics and space-atmosphere sciences. Here we highlight emerging directions.

Detecting metal species, atomic oxygen (O), helium (He), and other atomic and molecular species and using them as tracers to extend the lidar measurements well into the thermosphere and ionosphere are the two major future directions of lidar technologies, which will help advance the studies of space-atmosphere interactions. In particular, simultaneous lidar observations of TIMt and $TIMt^{+}$, i.e., the neutral and ionic metal species, from ~70 km in the mesosphere to ~300 km and higher in the thermosphere and ionosphere, will most likely push cutting-edge sciences, especially in the plasma-neutral coupling areas. If they can be made with extremely high-detection sensitivities (from current 0.1 cm^{-3} to 0.01 cm^{-3} or better), then such high-sensitivity lidars with very large-altitude coverage likely produce signals with sufficient signal-to-noise ratio to enable profiling of temperatures and winds in SAIR and studies of vertical transport of constituents (including both neutrals and ions), energy, and momentum. For these purposes, the very large-aperture lidar concept like the "Observatory for Atmosphere-Space Interaction Studies (OASIS)" is a necessary path for future lidars. Furthermore, improving measurement resolutions, enhancing full diurnal capabilities, and improving lidar automation are another three potential directions for future lidars.

Key lidar technologies corresponding to these future directions lie in laser technologies, very-large receivers, high quantum-efficiency and high-sensitivity photo detectors, optical filters, and data retrieval and analysis techniques. In addition to further improve solid-state lasers such as pulsed alexandrite lasers, diode lasers, fiber lasers, and Nd-doped lasers as well as some suitable dye lasers, a promising type of lasers emerging on the market is injection-seeded optical parametric oscillator (OPO), which provides variety of tunable laser sources. However, robust methods must be implemented to lock the OPO laser frequencies accurately to the known spectroscopy features of the species being detected in order to measure temperatures and winds with sufficient accuracies. What was ignored for a very long time but now starts to gain attention is the innovative data processing and analysis techniques, such as the interleaved method proposed by Gardner and Chu [10] and demonstrated in the derivation of vertical fluxes by Chu et al. [6], which eliminates photon-noise-induced biases in the second-order parameters derived from lidar data. It is time to unlock the full potentials of existing and future lidar data with further advancement in sophisticated data handling. It is worth to consider artificial intelligence (AI) technologies as they evolve with time.

While spaceborne lidars offer huge potentials to cover the entire globe, let us be honest; they usually flow "matured" and thus old technologies. Ground-based lidars can use risky or less matured technologies that help push the envelope of lidar measurements, leading to new science discoveries, but they are usually not automated and need human intervention. Therefore, ground-based and spaceborne lidars complement each other, and both should be considered in the development of future lidars.

8.4 Conclusions

Many technologies are ready to be implemented into lidar systems, although quite some development of laser technologies is still needed. It is not realistic to accomplish all the directions mentioned above once, but it is wise to strategically plan the implementation with multiple steps. For example, pushing the detection range to higher and higher altitudes, lidars with powerful lasers and large telescope apertures are required, which may not be ready to be autonomous and full-diurnal coverage. However, such lidars will lead to new cutting-edge sciences in ITMS physics, providing fuel for and enabling discovery science. In the meantime, some moderate lidars can be developed into full-diurnal coverage and autonomous operations, which will help collections of large amount and long-term data, enabling studies such as long-term trend, solar cycles, and interplay of various dynamical and solar forcings. Strategic planning and development will significantly benefit lidar advancement and push cutting-edge sciences.

References

1. Chu, X., Yu, Z., et al.: Lidar observations of neutral Fe layers and fast gravity waves in the thermosphere (110–155 km) at McMurdo (77.8°S, 166.7°E), Antarctica. Geophys. Res. Lett. **38**(23) (2011). https://doi.org/10.1029/2011GL050016
2. Chu, X., Yu, Z.: Formation mechanisms of neutral Fe layers in the thermosphere at Antarctica studied with a thermosphere-ionosphere Fe/Fe^+ (TIFe) model. J. Geophys. Res. Space Phys. **122**, 6812–6848 (2017)
3. Chu, X., Nishimura, Y., et al.: First simultaneous lidar observations of thermosphere-ionosphere Fe and Na (TIFe and TINa) layers at McMurdo (77.84°S, 166.67°E), Antarctica with concurrent measurements of aurora activity, enhanced ionization layers, and converging electric field. Geophys. Res. Lett. **47**, e2020GL090181 (2020)
4. Chu, X., Chen, Y., et al.: Mid-latitude thermosphere-ionosphere Na (TINa) layers observed with high-sensitivity Na Doppler lidar over Boulder (40.13°N, 105.24°W). Geophys. Res. Lett. **48**, e2021GL093729 (2021)
5. Jiao, J., Chu, X., et al.: First lidar profiling of meteoric ca^+ ion transport from ~80 to 300 km in the midlatitude nighttime ionosphere. Geophys. Res. Lett. **49**, e2022GL100537 (2022)
6. Chu, X., Gardner, C.S., Li, X., Lin, Y.-T.: vertical transport of sensible heat and meteoric Na by the complete temporal spectrum of gravity waves in the MLT above McMurdo, Antarctica. J. Geophys. Res. Atmos. **127**, e2021JD035728 (2022)
7. Vadas, S.L., & Becker, E.: Numerical modeling of the generation of tertiary gravity waves in the mesosphere and thermosphere during strong mountain wave events over the Southern Andes. J. Geophys. Res. Space Physics. **124**, 7687–7718 (2019)
8. Chen, C., Chu, X., et al.: Lidar observations of persistent gravity waves with periods of 3–10 h in the Antarctic middle and upper atmosphere at McMurdo. J. Geophys. Res. Space Physics. **121**, 1483–1502 (2016)
9. Vadas, S.L., Zhao, J., Chu, X., & Becker, E.: The excitation of secondary gravity waves from local body forces: theory and observation. J. Geophys. Res. Atmos. **123**, 9296–9325 (2018)
10. Gardner, C.S., Chu, X.: Eliminating photon noise biases in the computation of second-order statistics of lidar temperature, wind, and species measurements. Appl. Opt. **59**, 8259–8271 (2020)

Chapter 9
Polarization Lidar for Monitoring Dust Particle Orientation: First Measurements

Alexandra Tsekeri, Vassilis Amiridis, Spiros Metallinos, Alexandros Louridas, George Georgoussis, Nikolaos Siomos, Peristera Paschou, Thanasis Georgiou, and Ioannis Binietoglou

Abstract Dust orientation is an ongoing investigation in recent years. Its potential proof will be a paradigm shift for dust remote sensing, invalidating the currently used simplifications of randomly oriented particles. Vertically resolved measurements of dust orientation can be acquired with a polarization lidar designed to target the off-diagonal elements of the backscatter matrix which are nonzero only when the particles are oriented. We constructed the "WALL-E" lidar system emitting linear and elliptical polarized light and detecting various states of polarization of the backscattered light. Herein we present measurements of oriented rain, ice, and dust or drizzle particles acquired in Athens, Greece, during the preparation of the system for the ESA Aeolus Cal/Val Campaign "ASKOS" at Cabo Verde (June 2022).

A. Tsekeri (✉) · V. Amiridis · S. Metallinos · T. Georgiou · I. Binietoglou
Institute for Astronomy, Astrophysics, Space Applications and Remote Sensing, National Observatory of Athens, Athens, Greece
e-mail: atsekeri@noa.gr

A. Louridas · G. Georgoussis
Raymetrics S.A., Athens, Greece

N. Siomos
Institute for Astronomy, Astrophysics, Space Applications and Remote Sensing, National Observatory of Athens, Athens, Greece

Fakultät für Physik, Meteorologisches Institut, Munich, Germany

Ludwig-Maximilians-Universität, Munich, Germany

P. Paschou
Institute for Astronomy, Astrophysics, Space Applications and Remote Sensing, National Observatory of Athens, Athens, Greece

Laboratory of Atmospheric Physics, Physics Department, Aristotle University of Thessalo-niki, Thessaloniki, Greece

© The Author(s), under exclusive license to Springer Nature Switzerland AG 2023

J. T. Sullivan et al. (eds.), *Proceedings of the 30th International Laser Radar Conference*, Springer Atmospheric Sciences,
https://doi.org/10.1007/978-3-031-37818-8_9

Keywords Lidar · Dust orientation · Rain orientation · Ice orientation

9.1 Introduction

Mineral dust is one of the most important aerosol types in terms of mass and optical depth and therefore significantly impacts radiation, while it also interacts with liquid or ice clouds modifying their optical properties and lifetimes. Electric fields in the atmos- phere may cause dust particle orientation, as indicated by ground-based astronomical polarimetry measurements during a Saharan dust episode recorded over Canary Islands [1] and a dust event at the island of Antikythera in Greece [2]. In order to investigate the possible orientation of dust particles in the atmosphere, and the related effects of this phenomenon, we constructed a new polarization lidar, nicknamed "WALL-E" [3]. The operating wavelength is at 1064 nm for better probing the dust coarse mode, and the system is capable of measuring at different zenith and azimuth viewing angles. The details of the design and calibration of the system are presented in Tsekeri et al. [3].

Herein we present the first measurements from the system, acquired in February and March 2022, in Athens, Greece, during the preparation for the ESA Aeolus Cal/Val Campaign "ASKOS" at Cabo Verde (June 2022).

9.2 WALL-E Lidar

WALL-E lidar is a two laser–two telescope–four detector lidar system that is able to detect the elliptically-polarized backscattered light from oriented particles in the atmosphere without using any moving parts for the emission or the detection of light. Its design targets the measurement of the off-diagonal elements of the backscatter matrix, which are non-zero only in case of oriented particles (e.g., [4]), or in case of bioaerosols (e.g., [5]). Instead of retrieving the individual off-diagonal elements of the backscatter matrix, WALL-E measures their combinations, providing direct measurements of dust orientation, in the form of flags of "yes" or "no" particle orientation.

The orientation flags are acquired from "laser A", emitting linearly polarized light at 45°. "Laser B", which is elliptically polarized, provides additional information for the particle orientation properties, as well as information on dust microphysics, e.g., an estimation of the particle size and refractive index. The retrieval of these properties is an ongoing work.

The orientation flags measured at the detection units after "telescope A" ($F_{\mathrm{LA_TA}}$) and "telescope B" ($F_{\mathrm{LA_TB}}$), are provided in Eqs. 9.1 and 9.2, respectively. The values of $F_{\mathrm{LA_TA}}$ and $F_{\mathrm{LA_TB}}$ are equal to 1 when the off-diagonal elements are

zero, indicating no particle orientation, and they are non-equal to 1 when the off-diagonal elements are non-zero, indicating particle orientation.

$$F_{\mathrm{LA_TA}} = \frac{1}{\eta_{\mathrm{TA}}} \frac{1 - f_{12} + f_{13} - f_{23} + g_{11}}{1 + f_{12} + f_{13} + f_{23} + g_{11}} \tag{9.1}$$

$$F_{\mathrm{LA_TB}} = \frac{1}{\eta_{\mathrm{TB}}} \frac{1 + f_{13} - f_{14} + f_{34} + g_{11}}{1 + f_{13} + f_{14} - f_{34} + g_{11}} \tag{9.2}$$

$^{\eta}{}_{\mathrm{TA}}$ and η_{TB} are the calibration factors of $F_{\mathrm{LA_TA}}$ and $F_{\mathrm{LA_TB}}$, respectively, $f_{ij} = \frac{F_{ij}}{F_{11}}$ are the off-diagonal elements of the backscatter Stokes phase matrix of the particles, divided by the first element F_{11}, and $g_{11} = \frac{G_{ij}}{F_{11}}$ is the first element of the backscatter Stokes phase matrix of the gas molecules, divided by F_{11}. The calibration factors The calibration factors η_{TA} and η_{TB} are derived from Eqs. 9.1 and 9.2, respectively, considering randomly oriented particles in the atmosphere.

9.3 First Measurements of Oriented Particles

Sections 3.1, 3.2 and 3.3 present cases for oriented rain, ice, and dust or drizzle particles. The oriented particles are detected using measurements of the orientation flag $F_{\mathrm{LA_TA}}$ (Eq. 9.1).

9.3.1 Oriented Rain Particles

The measurements of rain particles are performed to test the ability of WALL-E lidar to detect particles that are known to be oriented, as is the case for rain particles (e.g., [6]). The case presented here includes a cloud at ~1.2–4 km, and rain particles below the cloud (marked with the black box in Fig. 9.1).

The measurements were acquired with a viewing angle of 60° off-zenith. The choice of the viewing angle is done based on the assumption that dust particles are mostly vertically oriented in the atmosphere [1]; thus, we expect to see an orientation signal at angles far from the zenith. As shown from the orientation flag plot (Fig. 9.1, right), the cloud does not present any orientation ($F_{\mathrm{LA_TA}} = 1$), whereas the rain particles below the cloud are oriented ($F_{\mathrm{LA_TA}} \neq 1$ in the black box), as expected.

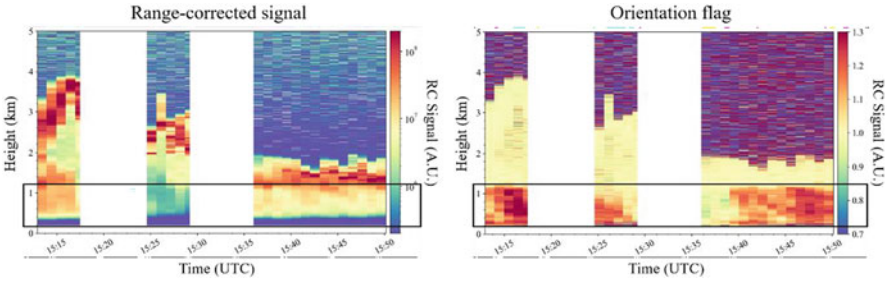


Fig. 9.1 WALL-E measurements of rain orientation. Left: range-corrected backscatter signal of laser A at 1064 nm, measured at the "transmitted" channel in the detection unit after telescope A. The black box marks the rain below a cloud at ~1.2–4 km. Right: orientation flag $F_{\mathrm{LA_TA}}$. Yellow color indicates no orientation for the cloud particles ($F_{\mathrm{LA_TA}} = 1$), whereas red or blue color indicate oriented rain particles ($F_{\mathrm{LA_TA}} \neq 1$). The measurements are acquired with a viewing angle of 60° off-zenith, at Athens, Greece, on 24 February 2022, at 15:13–15:51 UTC.

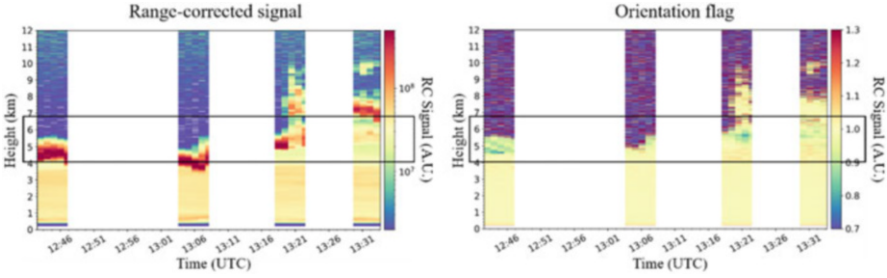


Fig. 9.2 WALL-E measurements of ice orientation. Left: range-corrected backscatter signal of laser A at 1064 nm, measured at the "transmitted" channel in the detection unit after telescope A. The black box marks the cloud formed at ~4–7 km on top of a dust layer mixed with pollution. Right: orientation flag $F_{\mathrm{LA_TA}}$. Yellow color indicates no orientation for the dust particles mixed with pollution ($F_{\mathrm{LA_TA}} = 1$), whereas blue color indicates oriented ice particles in the cloud on top of the dust layer ($F_{\mathrm{LA_TA}} \neq 1$). The measurements were acquired with a viewing angle of 53° off-zenith, at Athens, Greece, on 28 March 2022, at 12:43–13:34 UTC.

9.3.2 Oriented Ice Particles

Figure 9.2 shows oriented particles at heights ~4–7 km ($F_{\mathrm{LA_TA}} \neq 1$ in the black box), at the cloud formed on top of a dust layer mixed with pollution from the city of Athens. The presence of dust is derived from dust transport simulations in the area (not shown here). Figure 9.3 shows the temperature and relative humidity (RH) measurements from a radiosonde launched from the Athens international airport, at 12:00 UTC. These data indicate that the oriented particles at ~4–7 km are most probably ice particles, due to the low temperatures of −25 to −10 °C and high RH values of 70–100%.

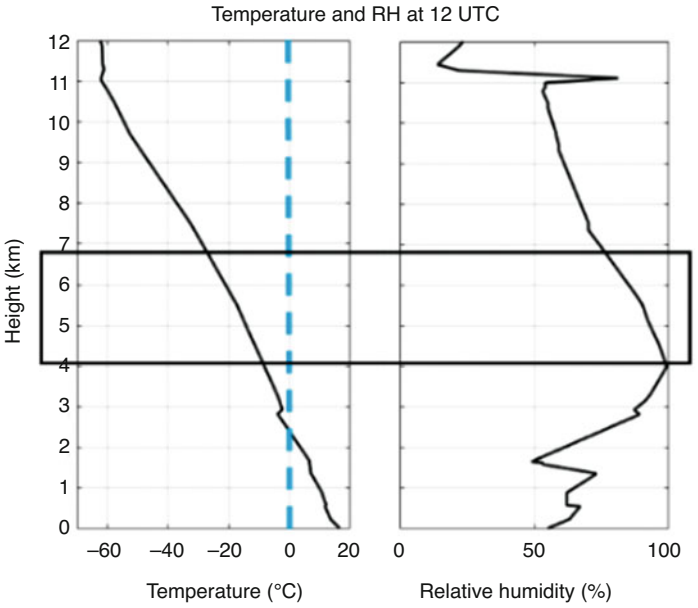


Fig. 9.3 Temperature profile (left) and RH profile (right), from radiosonde measurements launched from the Athens international airport, on 28 March 2022, at 12:00 UTC

9.3.3 Oriented Dust or Drizzle Particles

Figure 9.4 shows a feature containing oriented particles at ~1.5–2 km (black box in Fig. 9.4), below a cloud at ~2.2–2.5 km. The measurements were acquired with a viewing angle of 60° off-zenith. Figure 9.5 shows the temperature and relative humidity (RH) measurements from a radiosonde launched from the Athens international airport, at 12:00 UTC (3 h before the WALL-E measurements). The temperature (>0 °C) and RH (<70%) at ~1.5–2 km do not indicate the presence of ice particles at these heights (black box in Fig. 9.5). Due to the presence of the cloud above, at heights ~2.2–2.5 km, the orientation signal may be due to oriented drizzle particles.

Possible dust presence at the heights where the oriented particles are detected, is indicated from the concurrent PollyXT measurements at the PANGEA EARLINET station, at Antikythera, Greece (Fig. 9.6). The measured volume linear depolarization ratio (VLDR) at 532 nm, shows a depolarizing layer at ~1.5–2 km (black box in Fig. 9.6), which may be attributed to the presence of dust particles. The measurements at.

PANGEA station though, cannot be used to describe the atmospheric state at Athens, since the distance between Athens and Antikythera is ~250 km. Unfortu-

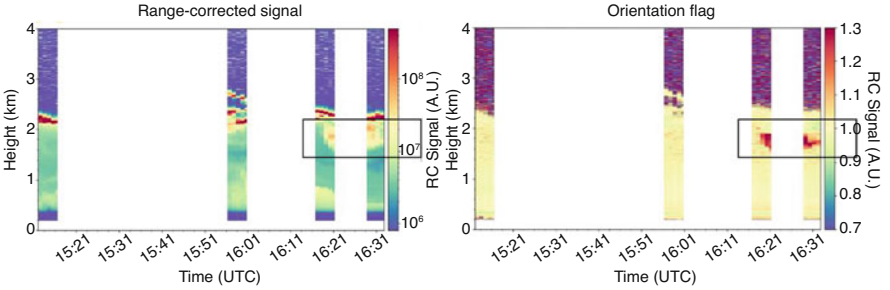


Fig. 9.4 WALL-E measurements of dust or drizzle orientation. Left: range-corrected backscatter signal of laser A at 1064 nm, measured at the "transmitted" channel in the detection unit after telescope A. Right: orientation flag $F_{\mathrm{LA_TA}}$. The black box marks a feature with oriented particles at ~1.5–2 km ($F_{\mathrm{LA_TA}} \neq 1$), below the cloud formed above, at ~2.2–2.5 km, where no orientation is detected ($F_{\mathrm{LA_TA}} = 1$). The measurements are acquired with a viewing angle of 60° off- zenith, at Athens, Greece, on 22 February 2022, at 15:13–16:33 UTC

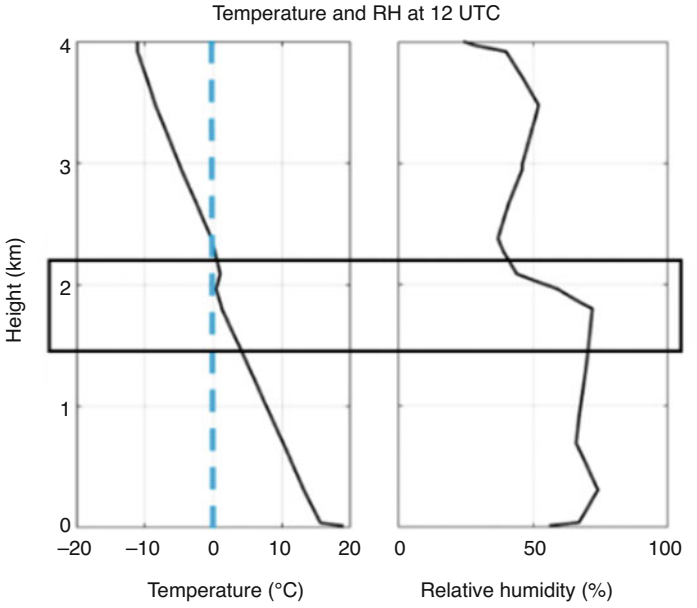


Fig. 9.5 Temperature profile (left) and RH profile (right), from radiosonde measurements launched from the Athens international airport, on 22 February 2022, at 12:00 UTC

nately, there are no concurrent VLDR measurements in Athens during this day, that would provide more convincing evidences for the presence of dust.

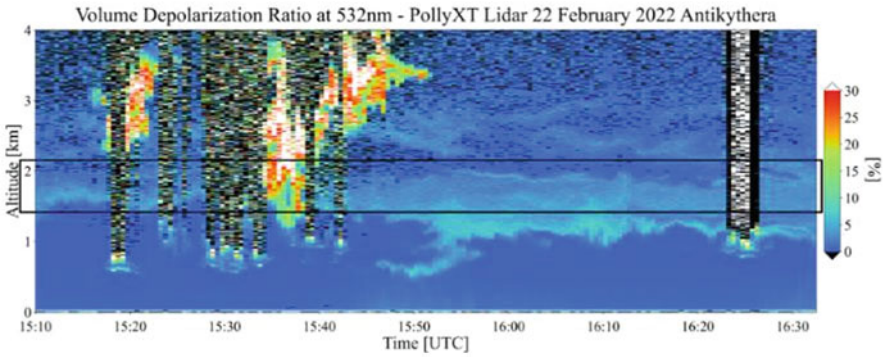


Fig. 9.6 VLDR measurements at 532 nm from PollyXT lidar, at the PANGEA EARLINET station, at Antikythera, Greece, on 22 February 2022, at 15:13–16:33 UTC. The black box indicates the heights at which we detect particle orientation with the WALL-E lidar in Athens

9.4 Summary and Future Steps

WALL-E lidar is designed to monitor possible dust particle orientation in the Earth's atmosphere. This work describes the first measurements of oriented particles acquired with the instrument. Specifically, detection of oriented rain, ice and drizzle or dust particles are presented and discussed. The next steps will include the dust measurements in Cabo Verde during the ESA Aeolus Cal/Val Campaign "ASKOS", on June 2022. The big suite of in-situ and remote sensing instruments participating in the ASKOS experiment will provide all necessary ancillary information needed to investigate in depth the orientation measurements of WALL-E and provide conclusive results for dust orientation in the atmosphere.

Acknowledgments The research leading to these results has received funding from the European Research Council under the European Community's Horizon 2020 research and innovation framework program/ERC grant agreement 725698 (D-TECT). We acknowledge PRACE for awarding us access to MareNostrum at Barcelona Super- computing Center (BSC), Spain. The work was supported by computational time granted from the National Infrastructures for Research and Technology S.A. (GRNET S.A.) in the National HPC facility – ARIS – under project ID pa170906-ADDAPAS, pr005038-REMOD, pr007032-RApID, pr009019-EXEED, and pr011016-DSA.

References

1. Ulanowski, Z., et al.: Alignment of atmospheric mineral dust due to electric field. Atmos. Chem. Phys. **7**, 6161–6173 (2007)
2. Daskalopoulou, V., et al.: Monitoring dust particle orientation with measurements of sun-light dichroic extinction, In: 15th International Conference on Meteorology, Climatology and Atmospheric Physics (COMECAP 2021) Proceedings, Zenodo, Conference paper (2021)

3. Tsekeri, A., et al.: Polarization lidar for detecting dust orientation: system design and Calibration. Atmos. Meas. Tech. **14**, 7453–7474 (2021)
4. Geier, M., Arienti, M.: Detection of preferential particle orientation in the atmosphere: Development of an alternative polarization lidar system. J. Quant. Spectrosc. Ra. **149**, 16–32 (2014)
5. Gassó, S., Knobelspiesse, K.D.: Circular polarization in atmospheric aerosols. Atmos. Chem. Phys. Discuss. **22**(20), 13581–13605 (2022)
6. Hayman, M., et al.: Polarization lidar operation for measuring backscatter phase matrices of oriented scatterers. Opt. Express. **20**, 29553–29567 (2012)

Chapter 10
Dust Flow Distribution Measurement by Low Coherence Doppler Lidar

Kosuke Okubo, Nofel Lagrosas, and Tatsuo Shiina

Abstract In this work, we propose a low coherence Doppler lidar (LCDL) to measure dust flow at near-surface atmosphere. To get dust flow information at near-surface atmosphere, it is necessary to measure it with high spatial and high temporal resolutions. Low coherence light source of $\Delta\lambda = 0.5$ pm can satisfy this high-resolution criterion of <1 m. In addition, by shortening the integration time to <5 ms, high-speed measurement can be performed on the small spatiotemporal scale of the lower atmosphere. A dust experiment is conducted to evaluate LCDL performance by shaking dust (wheat flour) off into a wind tunnel. The measurement speed of LCDL is compared with the speed of anemometer. At speeds from 0 to 5 m/s, they show good linear agreement. The distribution of dust flow is obtained with the Doppler shift frequency width of >1 MHz. We simulated the experiment condition to calculate it with a viscous resistance. The waveform obtained by the calculation has the same Doppler shift frequency width of >1 MHz with the experiment.

Keywords Doppler · Lidar · Dust · Low coherence · FFT

10.1 Introduction

Dust flows in the lower atmosphere are active. Dust dispersed at the ground surface is problematic for environmental conservation and human health, and it is important for elucidating the interaction between the surface atmosphere and the ground surface. To measure the movement of dust, it is necessary to measure remotely without disturbing the wind field. A Doppler lidar is effective for this purpose. Dust samplers are also available, but this method requires dust to be collected for a certain period of time and does not allow real-time monitoring of the dust flow. The Doppler lidar used at airports and other facilities is designed to measure the

K. Okubo (✉) · N. Lagrosas · T. Shiina
Chiba University, Chiba, Japan
e-mail: kobo0404the25th@chiba-u.jp; nofel@chiba-u.jp; shiina@faculty.chiba-u.jp

© The Author(s), under exclusive license to Springer Nature Switzerland AG 2023

J. T. Sullivan et al. (eds.), *Proceedings of the 30th International Laser Radar Conference*, Springer Atmospheric Sciences,
https://doi.org/10.1007/978-3-031-37818-8_10

wind field over vertical airspace and is used for long-time integration over a wide measurement range from 200 m to several kilometers. This is due to the fact that the atmospheric flow moves as a large mass at higher altitudes, resulting in larger spatial and temporal scales. On the other hand, the spatial and temporal scales of the lower atmosphere are small, and the dust flow in the lower atmosphere changes abruptly. High spatial resolution and high-speed measurements are required to capture the actual dust flows at the ground surface. Therefore, conventional Doppler lidars are not suitable for measuring dust flows.

In this study, a low coherence Doppler lidar (LCDL) is proposed. LCDL is a type of optical interferometer that uses a low-coherence light source to enable high spatial resolution measurements. The spatial scale of the lower atmosphere depends on the altitude. It is on the order of less than a few meters, and the coherence length is adapted to this order. The integration time is set to milliseconds to capture steep dust flows, too. The objectives of this study are the [1] development of the LCDL system, [2] laboratory-based dust measurements, and [3] validation of the dust speed distribution.

10.2 Low-Coherence Doppler Lidar

The light source of the LCDL system is a 975-nm distributed-feedback laser diode (DFB-LD) bulk element, which is a special product of Hamamatsu Photonics. The characteristic of this light source is that the coherence length can be controlled by the device temperature and the current. They are adjusted to 35 °C and 2A, respectively, and the linewidth of the light source is fixed as 0.5 pm. This line width allows a coherence length of about 1 m. The output power of this light source is approximately 1 W.

Table 10.1 summarizes the parameters of LCDL. Figure 10.1 shows its configuration. The system consists of five parts: transmitter optics, receiver optics, fiber optics, balance detection (BD) system, and signal processing system. In the transmitter optics, the light from the DFB-LD is divided into two parts by a

Table 10.1 Specifications of LCDL

Component	Qualification	Specification
Transmitter	Center wavelength	975 nm
	Laser power	0.7 W
	Coherence length	0.8 m
	Drive current, temperature	2A, 35 °C
Receiver	Diameter of aperture	0.061 m
	Light-receiving sensitivity of balanced detector (PD)	0.75A/W@$\lambda = 1.0\ \mu m$
	Sampling rate	250MSa/s
	Sampling time	5 ms

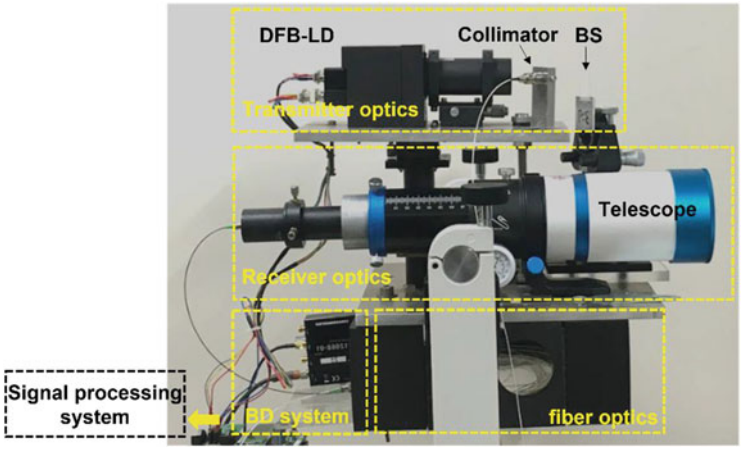


Fig. 10.1 LCDL configuration

beam splitter (BS): one part is trans- mitted toward the measurement path, and the other part is directed to the reference fiber by the collimator. The optical intensity introduced into the reference fiber is approximately 1 mW. The measurement area can be flexibly determined by changing the length of the reference fiber. In the receiver optics, backscattered light from the dust is focused by a refracting telescope and guided into the fiber coupler. In the fiber optics, the fiber coupler connecting the reference and receiving fibers has a coupling ratio of 50:50. Homodyne detection is performed with reference and receiving light. Movement of the dust particles imparts a Doppler shift on the backscattered photons, and the line-of-sight speed of the particles is calculated from that Doppler shift. Fast Fourier transforms (FFTs) of the homodyned signals is performed in the signal processing system to quantify the Doppler shift. The sampling rate is 250 MSa/s and the waveform acquisition time is 5 ms. The frequency resolution is set to 0.1 MHz by setting one frame of the acquired waveform to 10 μs, and it is integrated over 500 frames. This makes it possible to measure speed changes with the resolution of 0.05 m/s.

10.3 Laboratory-Based Dust Speed Measurement

Dust speed measurement is performed on a laboratory basis. In the experiment wind tunnel is used. It is 300 × 300 mm in height and width and 1300 mm in length. The wind tunnel is placed 6 m away from the LCDL. The dust is shaken off and diffused by a circulator. The dust used in the experiment is flour. Flour is easy to model dust speed because its physical properties are known, readily available, and easily diffused by wind. The wind direction from a circulator is headwind in the direction of the LCDL's line of sight. An anemometer is placed in the wind tunnel

and compared to the dust speed measured by the LCDL. Five trays are arranged at the interval of 250 mm in the wind tunnel. These trays collect the dust to determine the particle size distribution. Approximately 200 g of flour is shaken off per minute. The mode particle diameter of the flour is 6 μm.

10.4 Results and Discussion

Figure 10.2a, b show the simultaneous FFT signals of LCDL and wind speed of anemometer of flour measurement. The Doppler shift frequency of the central peak is 7.5 MHz, with a range of 6.0 ~ 7.6 MHz. This corresponds to a speed of 3.65 m/s for the central peak and a speed range of 2.93 ~ 3.70 m/s. The average speed of the anemometer measured at the same time is 3.39 m/s, and the speed range is 2.34 ~ 3.84 m/s. The speeds of the LCDL and the anemometer are in very good agreement. The LCDL and anemometer results agreed well over a range of wind

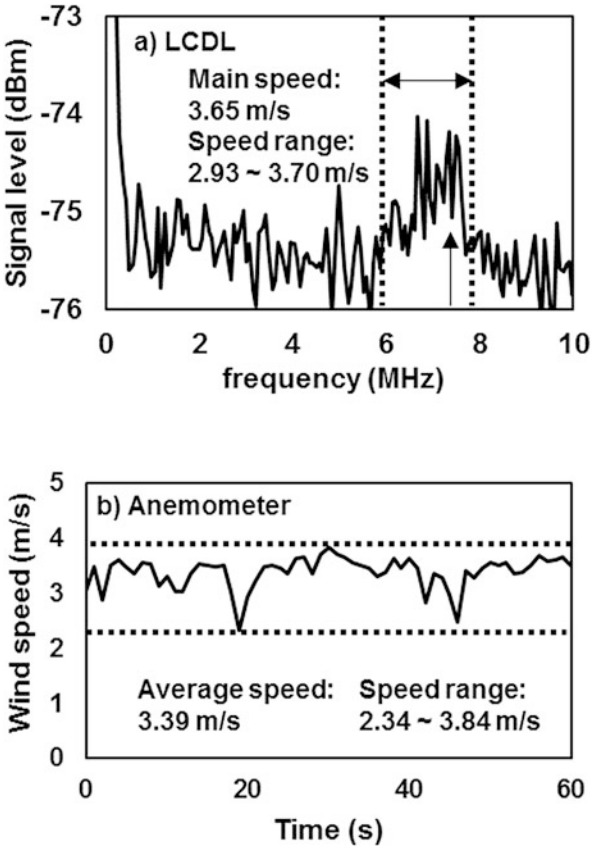


Fig. 10.2 Flour flow measurement results: (**a**) Doppler signal and (**b**) wind speed from anemometer

speeds from 0 to 5 m/s (correlation coefficient = 0.98). The waveform of Doppler shift frequency acquired by LCDL is wider by more than 1 MHz, and the peak position is not centered but shifted to the higher frequency side. This indicates that there is a distribution in the dust flow speed, with many dust particles having higher speeds. This distribution is related to the mass and size of the particles.

The speed distribution of dust particles is simulated. The amount of dust collected in the experiment decreases due to scattered distance, and this variation in the experiment reflects the distribution of the mass and size of the particles. In the simulation, fallen height of dust particle is 300 mm, and viscous resistance for air is assumed. The falling speed of the dust with viscous resistance is given by Eq. 10.1:

$$V_y(t) = \frac{mg}{k}\left(1 - \exp\left(\frac{-k}{m}t\right)\right) \tag{10.1}$$

where m is mass of dust particles; g is gravitational acceleration; and t is the time of trace. Air resistance coefficient k is set to 2.33×10^{-11} kg/m.

The particle size is converted from the mass to obtain the extinction coefficient Eq. [2].

$$\alpha = N\pi r^2 Q_{\text{ext}} \tag{10.2}$$

where N is the number of particles per unit volume, r is the mode radius, and Q_{ext} is the extinction coefficient.

As flour particle is sufficiently large, Q_{ext} can be assumed to be equal to 2. N is calculated from the collected amount of flour density of 600 kg/m^3. Based on the ex-tinction coefficient, the interference signal is simulated and FFT analysis is performed. Figure 10.3 shows simulation result of Doppler signal from the flour flow. In the simulation, the wind speed is set to 3.5 m/s. The range of Doppler shift frequencies obtained in the simulation is 5.7 ~ 7.5 MHz, and the velocity range is 2.78 ~ 3.65 m/s. The peak position of the Doppler shift frequency is 6.8 MHz, and

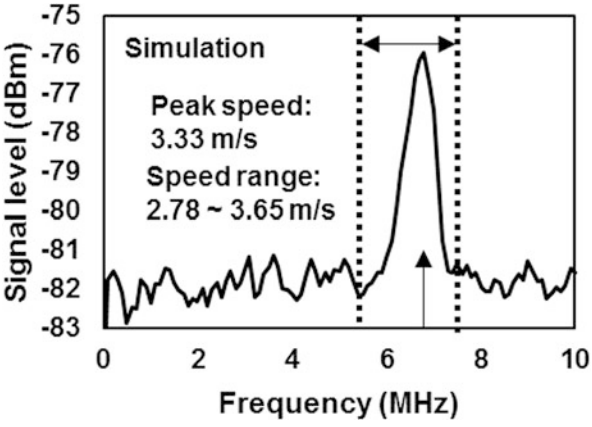


Fig. 10.3 Doppler signal simulation from flour

its speed is estimated as 3.33 m/s. The Doppler shift frequency range is wider than 1 MHz, which is equivalent to the lab experiment by LCDL, and the peak position is also shifted to the higher frequency side. The simulation result shows that the dust speed distribution is related to the mass and size of dust particles.

10.5 Conclusions

We have developed a low-coherence Doppler lidar to measure dust velocities in the lower atmosphere. It utilizes a special DFB-LD whose source linewidth can be controlled by the device temperature and current to obtain a coherence length of about 1 m. In laboratory-based dust flow experiment, the LCDL and the anemometer are simultaneously measured, and the measured speeds show very good agreement. The Doppler shift frequency width measured by LCDL is greater than 1 MHz. The simulated speed distribution in terms of mass and size of dust particles is also wide. It can be said that the Doppler shift frequency width of the LCDL provides the speed distribution of the dust in optical axis direction.

The next step is to measure different dust particles, such as actual sand dust, to distinguish the dust particles by the LCDL.

References

1. Johnson, W.B., Ludwig, F.L., Dabberdt, W.F., Allen, R.J.: An urban diffusion simulation model for carbon monoxide. J. Air Pollut. Control Assoc. **23**(6), 490–498 (1973)
2. Jiang, S., Sun, D., Han, Y., Han, F., Zhou, A., Zheng, J.: Performance of continuous-wave coherent Doppler Lidar for wind measurement. Curr. Opt. Photonics. **3**(5), 466–472 (2019)
3. Asai, K.: Coherent Lidar technique for measurement of atmospheric wind vector. Jpn. Soc. Infrared Sci. Technol. **3**(1), 40–49 (1993)
4. Diao, W., Zhang, X., Liu, J., Zhu, X., Liu, Y., Bi, D., Chen, W.: All fiber pulsed coherent lidar development for wind profiles measurements in boundary layers. Chin. Opt. Lett. **12**(7), 07280181–00728014 (2014)
5. Lingbing, B., Qiu, Z., Gao, H., Zhu, X., Liu, J.: All-fiber pulse coherent Doppler Lidar and its validations. Opt. Eng. **54**(12), 1231031–1231039 (2015)
6. Shiina, T.: Low coherence Doppler Lidar with high-power DFB-LD. In: Proceeding of 19th Coherent laser conference (2018)
7. Gordienko, V.M., Koryabin, A.V., Kravtsov, N.V., Firsov, V.V.: Wind Doppler Lidar with 1.5μm fiber laser. Laser Phys. Lett. **5**(5), 390–393 (2008)
8. Kameyama, S., Ando, T., Asaka, K., Hirano, Y.: All-fiber coherent Doppler Lidar system for wind sensing. In: Industrial Applications Laser Remote Sensing, pp. 115–142. Bentham Science, Sharjah (2012)

Chapter 11
A Multiwavelength LED Lidar for Near-Ground Atmospheric Monitoring

Alifu Xiafukaiti, Nofel Lagrosas, and Tatsuo Shiina

Abstract A multiwavelength lidar system with a light-emitting diode (LED)-based light source is designed and developed to continuously monitor near-surface atmosphere at nighttime. The LED light source does not require any heat dissipation system and can emit optical power for long periods with constant output. The LED light sources with wavelengths of 365, 450, 525, and 630 nm are used as lidar transmitters to detect hard target and atmospheric echoes. The pulse circuit for realizing the pulsed oscillation of the LED lights is applied by the avalanche breakdown of the transistor. These LED pulsed lights can be synchronized by serially concatenated to the circuit. The LED has a pulse width of around 17 ns, repetition frequency of over 250 kHz, and each peak power of up to 2 W. With these LED transmitter characteristics, the lidar system accomplishes monitoring the atmosphere's rapid activities in the near-range measurement. Initial near-surface observation results from 365 and 450 nm show that atmospheric echoes can be monitored in the range of 0–300 m at an accumulation time of a few tens of seconds at nighttime. Analysis of the backscattering light intensity with multiwavelengths from this LED lidar system produces a real-time extinction coefficient near the surface. This report discusses the design and practical test of the multiwavelength LED lidar.

Keywords LED · Multiwavelength lidar · Atmosphere

11.1 Introduction

Atmosphere monitoring near the surface is essential from the viewpoint of air pollution and radiation budget studies [1]. For the operation of a lidar system, the laser, as a transmitter, plays a vital role in the whole system [2]. Laser diodes and diode-pumped solid-state laser technology have evolved, making the lidar system

A. Xiafukaiti (✉) · N. Lagrosas · T. Shiina
Graduate School of Engineering, Chiba University, Chiba, Japan

© The Author(s), under exclusive license to Springer Nature Switzerland AG 2023

J. T. Sullivan et al. (eds.), *Proceedings of the 30th International Laser Radar Conference*, Springer Atmospheric Sciences,
https://doi.org/10.1007/978-3-031-37818-8_11

more compact [3, 4]. This miniaturization of the lidar system is suitable for portable measurements such as flux of aerosols and dust in urban areas, or motion of sea waves [5, 6]. However, conventional laser sources have a restriction for ground-based horizontal measurement when viewed from eye safety in urban areas. Also, it is vulnerable to static electricity, and it needs to stabilize electric power. Compared with a laser source, a light-emitting diode (LED)-based light source does not require any heat dissipation system and can emit optical power for long periods with constant output. Moreover, the broad band of LED source is not an issue when horizontally measuring the optical properties of aerosols (e.g., mixing of small and large particles, coating, etc.) near the ground A single-wavelength compact LED lidar was designed and developed [7]. This LED lidar system successfully observed the atmosphere echoes and hard targets in near-range measurement. However, a multiwavelength LED lidar is not yet developed, especially in the visible region. This work aims to develop a multiwavelength LED lidar to estimate the particle size distribution and Angstrom exponent of aerosols in the near-surface atmosphere. The objectives of this study are twofold: (1) to design and develop a multiple-wavelength LED lidar and (2) to evaluate hard target signals and atmospheric echoes using this developed LED lidar system. Analysis of the backscattering light intensities with multiwavelengths from this LED lidar system produces real-time extinction coefficients of aerosols near the surface.

11.2 Instruments and Methodology

This study utilizes a multiwavelength LED lidar operated at four wavelengths to monitor the near-ground atmosphere. Figure 11.1 and Table 11.1 show the schematic diagram and specifications of the multiwavelength LED lidar system, respectively.

The avalanche breakdown of the transistor is applied in the lidar pulse circuit to realize the pulsed oscillation of the LED lights. These LED lights around peak power of 2 W produce a pulse width of 17 ns and a repetition rate of 250 kHz. Due to the high repetition rate (250 kHz), signals below 600 m are received. Pulse wrapping appear over 600 m. The lens's focal length is 120 mm, and the LED beam is collimated at the divergence of 40 mrad with a beam size of 50 mmφ. PMTs is used for detectors in the photon-counting mode for both hard target and atmospheric observation. Interference filters with their bandwidths of 10 nm are placed in front of PMTs. A pinhole of 8 mmφ is used at the back of the telescope (153 mmφ), acting as the receiver's field of view (FOV) of 5 mrad. Here, the sensors are the photon-counting mode PMTs connected to a multichannel signal receiver (photon count recorder). The accumulation is about ten million times, and the time resolution of bin width is 5 ns (0.75 m). Currently, the LED lidar system can only be operated at nighttime due to high divergence LED beams with low power.

Total (aerosols and molecules) extinction coefficients are derived from the lidar data following the method used in our previous work [8]. Briefly, we determine the spatial distribution of the total extinction coefficient, $\alpha_{\text{total}}(R_C)$, by solving the lidar

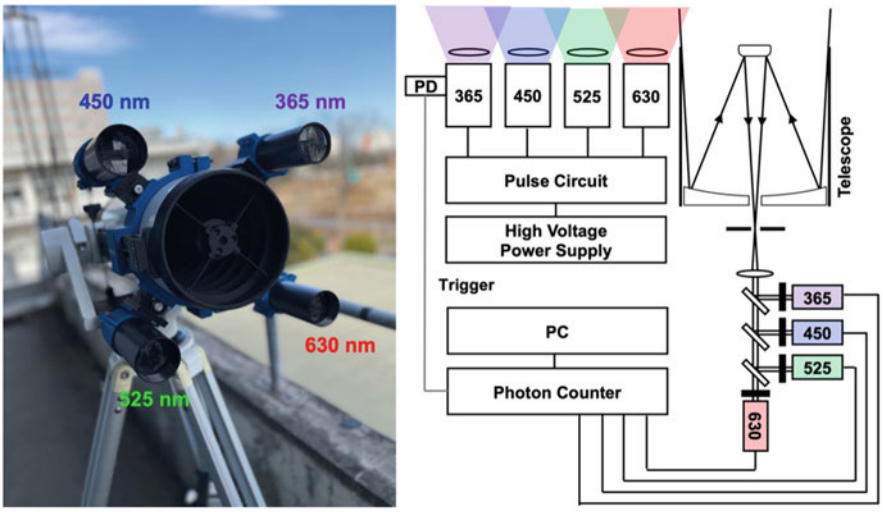


Fig. 11.1 Schematic diagram of the multiwavelength LED lidar system

Table 11.1 Specifications of the multiwavelength LED lidar system

LED light sources		
Transmitter	Wavelength	365, 450, 525, 630 nm
	Peak power (250 kHz)	2.1, 1.1, 0.4, 0.5 W
	Pulse width	~ 17 ns
	Beam divergence	~ 40 mrad
Receiver and detector	Telescope	Cassegrain type: 153 mmφ
	Filter CWL (FWHM)	365, 450, 525, 625 (10) nm
	Photomultiplier tube	Hamamatsu, H11901-110 × 4
Data acquisition	Photon count recorder (Trimatiz MSB-01)	
	Integration time	30 s
	Range resolution	0.75 m

equation using the Klett method [9]:

$$\alpha_{\text{total}}(R) = \frac{X(R)}{\frac{X(R_c)}{\alpha_{\text{total}}(R_c)} + 2\int_R^{R_c} X(R')\,dR'} \tag{11.1}$$

where $X(R) = P(R)R^2$ is the range-corrected signal (RCS) derived from the background-corrected and smoothened raw signal, $P(R)$. Here, compared with a laser lidar system, the raw signal, $P(R)$ needs to be calibrated due to large divergent of the LED compared to the FOV of the telescope. The overlap function can be calculated using the actual parameters of the transmitting and receiving optics system. The reference range (far range), R_C, and the value of $\alpha_{\text{total}}(R_C)$ are determined through the slope method [10]. R_C is defined as the maximum

range of the region in which, to a good approximation, the logarithm of RCS linearly decreases with the range. This situation occurs typically for the present configuration of the near-horizontal lidar observation [8]. Under this condition, we can assume $\partial(\ln(X(R))/\partial R \approx -2\alpha_{\text{total}}$ from the lidar equation itself (here α_{total} is range-independent). In this way, we can estimate the total extinction coefficient, $\alpha_{\text{total}}(R_{\text{C}})$, at R_{C}. Subsequently, this value of $\alpha_{\text{total}}(R_{\text{C}})$ is used in Eq. (11.1) to determine the spatial distribution of $\alpha_{\text{total}}(R)$.

11.3 Results and Discussion

Figure 11.2 shows the hard target measurements taken by the multiwavelength LED lidar at nighttime. A building is located around 40 m from the LED lidar system, and this building is applied as a hard target in this measurement. As a result, the higher peaks near 40 m appear as building echoes. Also, the atmospheric echoes in the 0–30 m range are captured and have smaller peaks than the peaks of building echoes. The hard target signal from 365 nm has the highest signal among the four wavelengths because it has the highest power output. It is confirmed that the order of the hard target signals depends of the LED's output power. It means that the receiver optics is adequate for multiwavelength detection purpose.

Figure 11.3 shows the temporal variations of the atmospheric measurements from 22:00, 5 May, to 04:30, 6 May 2022. The multiwavelength LED lidar system and a nephelometer are installed on the rooftop of the Academic Research Building, Chiba University (35.62°N, 140.1°E). The LED lidar is continuously operated in a fixed horizontal direction. The altitude of the lidar setup itself is approximately 60 m above sea level. In Fig. 11.3, the temporal variations of total extinction coefficients, $\alpha_{\text{total, 365 nm}}$ and $\alpha_{\text{total, 450 nm}}$ at the first overlap distance show similar temporal trends. Also, the value of $\alpha_{\text{total, 365 nm}}$ is higher than the value of $\alpha_{\text{total, 450 nm}}$ due to stronger scattering in the case of 365 nm wavelength. Moreover, the total extinction coefficients $\alpha_{\text{total, 450 nm}}$ from lidar measurement and scattering coefficient, $\alpha_{\text{sca, 450 nm}}$ from the nephelometer have the same average values. In Figs.

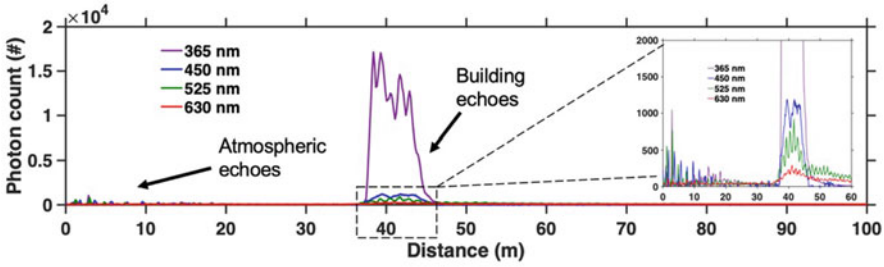


Fig. 11.2 Hard target observations using the multiwavelength LED lidar

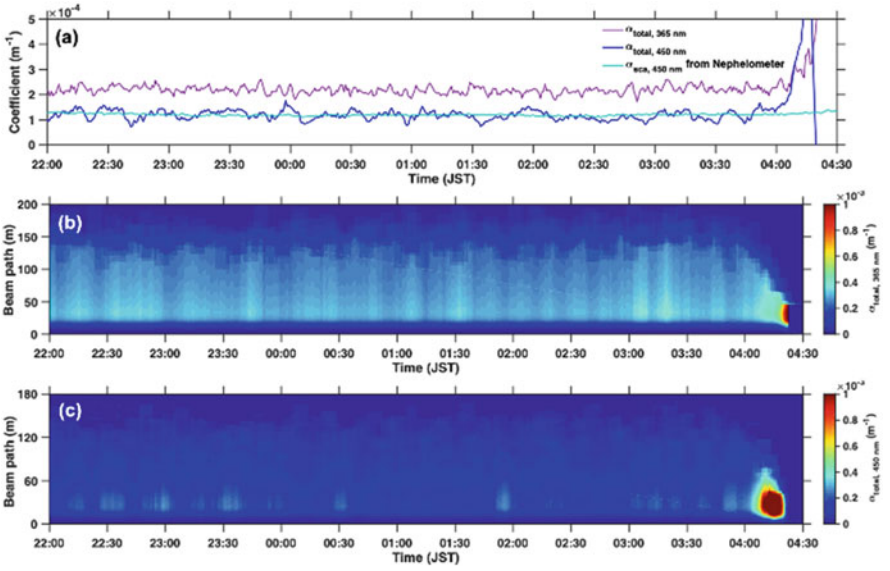


Fig. 11.3 Temporal variations of multiwavelength lidar measurements, and nephelometer observed for the period from 5 May to 6 May 2022: (**a**) total extinction coefficient from the LED lidar, scattering coefficient from the nephelometer; (**b**) 365-nm; and (**c**) 450-nm space-time indications of total extinction coefficient from the Klett analysis of the LED lidar data

11.3b and c, the changes of extinction coefficients for both wavelengths are not large due to clear sky conditions. According to the record of the weather monitor (Davis Vantage Pro2) operated at the same location, relative humidity changes only by 10% (from 80% to 90%), and this space-time indication of total extinction coefficient shows the stability of LED lidar measurement. In the case of daytime measurement (from 04:30 in Figs. 11.3b and c), LED lidar can't observe any backscattering signals, because the sun light is entered into the telescope. The measurement range gradually decreases from 04:00.

11.4 Conclusion

In this work, the multiwavelength LED lidar is designed and developed for near-ground atmospheric monitoring. The LED light source has a pulse width of around 17 ns, a repetition frequency of over 250 kHz, and each peak power of up to 2 W. The LED light sources with wavelengths of 365, 450, 525, and 630 nm successfully detect hard target at the same range. For the atmospheric measurements, extinction coefficient values from 365 and 450 nm are detected using Klett method and are consistent with values from the nephelometer data. For the next step, we will discuss the particle size distribution and Angstrom exponent of aerosols in the near-surface atmosphere with the multiwavelength observation data.

References

1. Seinfeld, J.H., Pandis, S.N.: Atmospheric Chemistry and Physics: From Air Pollution to Climate Change. Wiley, Hoboken (2016)
2. Weitkamp, C.: Lidar, Range-Resolved Optical Remote Sensing of the Atmosphere. Springer, New York (2005)
3. Takeuchi, N., Baba, H., Sakurai, K., Ueno, T.: Diode-laser random-modulation CW Lidar. Appl. Opt. **25**(1), 63–67 (1986)
4. Refaat, T.F., Singh, U.N., Petros, M., Yu, J., Singh, U.N.: Self-calibration and laser energy monitor validations for a double-pulsed 2-μm CO_2 integrated path differential absorption lidar application. Appl. Opt. **54**(24), 7240 (2015)
5. Shimizu, A., Sugimoto, N., Matsui, I., Arao, K., Uno, I., Murayama, T., Kagawa, N., Aoki, K., Uchiyama, A., Yamazaki, A.: Continuous observations of Asian dust and other aerosols by polarization lidar in China and Japan during ACE-Asia. J. Geophys. Res. **109**, D19S17 (2004)
6. Roshandel, S., Liu, W., Wang, C., Li, J.: 3D ocean water wave surface analysis on airborne LiDAR bathymetric point clouds. Remote Sens. **13**, 3918 (2021)
7. Shiina, T.: LED mini Lidar for atmospheric application. Sensors. **19**(3), 659 (2019)
8. Xiafukaiti, A., Lagrosas, N., Ong, P.M., Saitoh, N., Shiina, T., Kuze, H.: Comparison of aerosol properties derived from sampling and near-horizontal lidar measurements using Mie scattering theory. Appl. Opt. **59**(26), 8014–8022 (2020)
9. Klett, J.: Lidar inversion with variable backscatter extinction ratios. Appl. Opt. **24**(11), 1638–1643 (1985)
10. Kunz, G.J., Leeuw, G.: Inversion of lidar signals with the slope method. Appl. Opt. **32**(18), 3249–3256 (1993)

Chapter 12
Development of Low-Cost High Spectral Resolution Lidar Using Compact Multimode Laser for Air Quality Measurement

Yoshitaka Jin and Makoto Aoki

Abstract A low-cost high spectral resolution lidar (HSRL) was developed for aerosol profile measurement and to monitor air quality. A multi-longitudinal mode laser, which was widely used for aerosol lidars and lower cost compared to single-mode lasers, was used as the light source of HSRL. The multimode laser was designed to have the same mode spacing as the free spectral range of interferometer optimized for the HSRL measurement. As a result, the laser had a short cavity length and large mode spacing, but it had a narrow spectral width comparable to single-mode lasers. The interferometer was scanned over the range of one fringe, and the interference visibility containing aerosol backscatter information was obtained at each height through fitting analysis of the scan data. The interference visibility and fringe position were calibrated with the reference signals taken from the part of the transmitted laser. We successfully carried out continuous measurement of aerosol profiles during the daytime and nighttime. The performance of the new system was greater than a previous version, which employed a laser with a much longer cavity.

Keywords High spectral resolution lidar · Aerosols · Laser

12.1 Introduction

Quantitative measurement of aerosol profiles is essential to assess the effect of aerosols on the air quality. High spectral resolution lidar (HSRL) method is useful to measure aerosol extinction coefficient independently from aerosol backscatter with

Y. Jin (✉)
National Institute for Environmental Studies, Tsukuba, Japan
e-mail: jin.yoshitaka@nies.go.jp

M. Aoki
National Institute of Information and Communications Technology, Koganei, Japan
e-mail: maoki@nict.go.jp

© The Author(s), under exclusive license to Springer Nature Switzerland AG 2023

J. T. Sullivan et al. (eds.), *Proceedings of the 30th International Laser Radar Conference*, Springer Atmospheric Sciences,
https://doi.org/10.1007/978-3-031-37818-8_12

high sensitivity [1]. Low-cost and robust HSRL systems are required for spreading quantitative measurement of aerosols worldwide. A single-mode laser is typically used as the light source of HSRL because it is suitable for separating atmospheric scattering into Mie and Rayleigh components efficiently, but single-mode lasers are costly compared to multimode lasers widely used for aerosol lidars. Moreover, most of HSRLs need to tune laser wavelength to the spectral peak of high-resolution spectral filters, and such tuning system is sensitive to measurement environments (e.g., temperature).

Recently an HSRL using a multi-longitudinal, single-transverse mode laser was proposed [2]. In the proposed system, a scanning interferometer with the same mode spacing as the multimode laser was used for the spectral filter. By scanning the interferometer for the range of one fringe, interference visibility (or contrast), which contains aerosol backscatter information, was obtained at each height through fitting analysis of the scan data. The interference visibility and fringe position were calibrated with the reference signals taken from the part of the transmitted laser. Therefore, the system does not require feedback controls for the laser and interferometer. The proposed system was less expensive than the conventional HSRLs with single-mode lasers, but it was less efficient because a long interferometer was used to have the same mode spacing as the used commercial laser, which had a long optical cavity length (~60 cm).

In this study, we propose a low-cost HSRL system using a compact multimode laser, which is designed to increase the measurement efficiency compared to the previous study using a commercial multimode laser. The laser mode spacing is matched to the free spectral range (FSR) of the receiver interferometer optimized for HSRL measurement. As a result, the laser has a short cavity length and large mode spacing, but spectral width of the laser mode should be narrow comparable to single-mode lasers. To satisfy the above conditions, we develop a laser that comprises a master oscillator and a power amplifier. In this presentation, we present the configuration of the HSRL system and an evaluation of developed laser using a scanning interferometer. Examples of continuous aerosol measurement with the multimode HSRL are also shown.

12.2 Lidar System

Figure 12.1 shows a block diagram of HSRL using a multimode laser. A master oscillator power amplifier (MOPA) Nd:YAG laser with the second harmonic generation (532 nm wavelength) was used as the transmitter. The repetition rate was 100 Hz and laser pulse energy was 0.5 mJ at 532 nm. The laser after passing through a 6× beam expander had a 15-mm-diameter and 0.5-mrad beam divergence (full angle). Two types of telescopes were used in a biaxial configuration: a Schmidt-Cassegrain telescope with a 200 mm diameter for an HSRL receiver and a refracting telescope with a 50 mm diameter for near-range elastic lidar receivers. The HSRL receiver had a field of view (FOV) of 0.5 mrad. Backscattered light collected by the HSRL

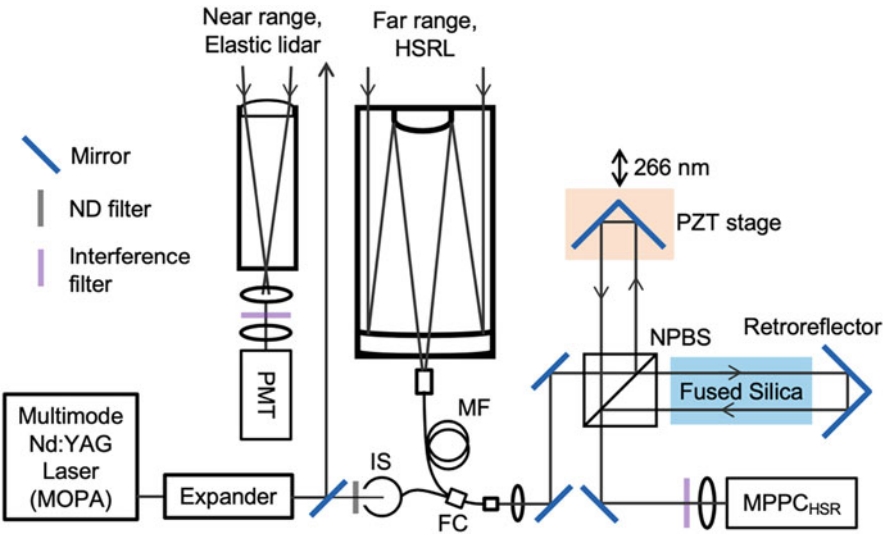


Fig. 12.1 Block diagram of high spectral resolution lidar using a multimode laser. IS, MF, FC, NPBS, MOPA, and MPPC are integrated sphere, multimode fiber, fiber coupler, non-polarizing beam splitter, master oscillator power amplifier, and multi-pixel photon counter, respectively

receiver was sent to a spectrometer using a multimode fiber. A mode scrambler was used for the fiber to homogenize the fiber output beam. A scanning Michelson interferometer was employed in the spectrometer as an HSR filter. The received light after the spectrometer was measured with a multi-pixel photon counter (MPPC) module (Hamamatsu C13366-3050GA). The measured signals were processed by a 160 MSPS A/D converter (AVALDATA ADO-1616-STD), and the digitized signals were recorded by a computer for every laser shot.

Atmospheric scattering stimulated by the multimode laser was spectrally filtered by a scanning interferometer. The optical path difference (OPD) of the interferometer was set to be 200 mm, and the FSR was consequently 1.5 GHz. The OPD was determined from the point of view of separation efficiency of Mie and Rayleigh scattering [3, 4]. To match mode spacing of the multimode laser with the interferometer FSR, the length of laser cavity was adjusted to the interferometer length. The laser cavity length was consequently approximately 100 mm, and therefore the master oscillator was compact. The laser spectrum could be resolved effectively using the interferometer. The interference visibility had the maximum value at the interferometer OPD of approximately 200 mm (Fig. 12.2). From the peak value of the interference visibility, the laser spectral width was estimated at approximately 60 MHz. Therefore, the multimode laser has optimized mode spacing and narrow spectral width for each mode, and it was suitable for HSRL.

The interferometer was scanned periodically over the range of a fringe. A retroreflector mounted on a piezo stage was continuously moved back and forth over a range of half wavelength (i.e., 266 nm). The scanning speed was set to 8.3 Hz,

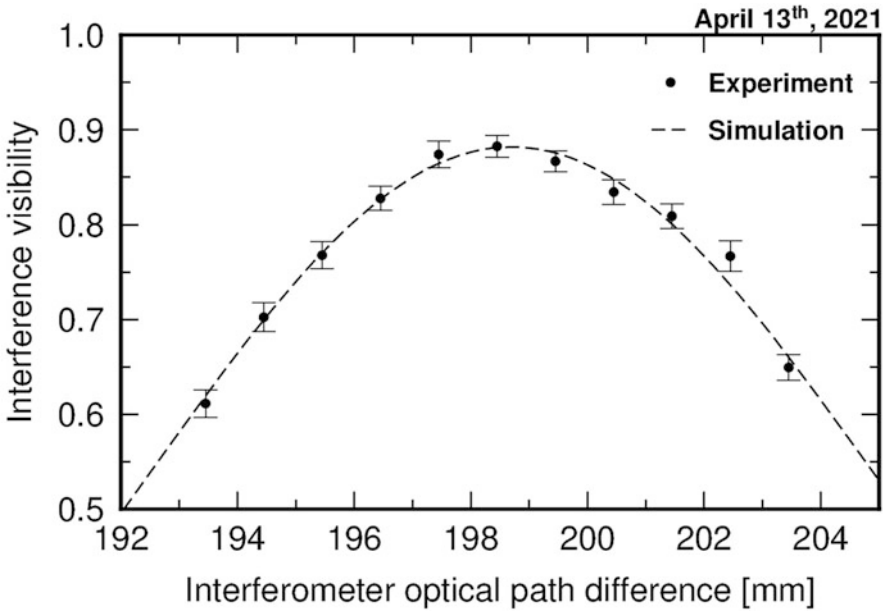


Fig. 12.2 Interference visibility versus interferometer optical path difference for the multimode laser. The simulated result is plotted by the dotted line. The error bar indicated the standard deviation of measurement

and 12-point data were obtained from the scan because the laser repetition rate was 100 Hz. The scanning speed was faster than the change in the laser wavelength, and we could fit a sinusoidal curve to the scan data. The phase of the scan curve could vary when the laser wavelength was shifted. To correct the phase shifts every scan, part of the transmitted laser was sent to the interferometer and used as the reference light. Part of the laser beam was collected by an integrating sphere and combined with the atmospheric scattering light by a fiber coupler with a 99:1 coupling ratio.

12.3 Aerosol Profile Measurement

Aerosol backscatter and extinction were retrieved from the HSRL scan signals. By fitting a sinusoidal curve to the scan signals, we obtained the interference visibility and the offset of the scan signals. The visibility and offset were averaged over 5 min to improve signal-to-noise ratio. Averaged visibility and offset were used to obtain the backscattering ratio. Aerosol backscatter was calculated from the backscattering ratio. By taking the ratio of offset signals (or Mie scattering signals) to backscattering ratio, Rayleigh scattering signals were obtained. Aerosol extinction was then retrieved by calculating the slope of Rayleigh scattering signals.

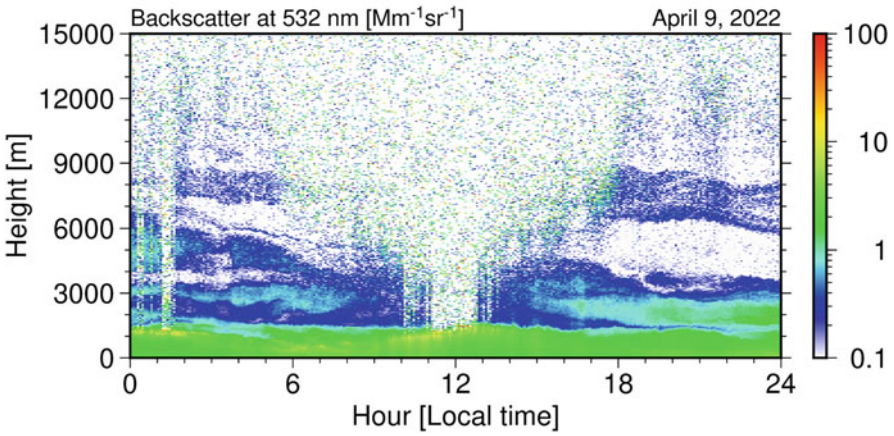


Fig. 12.3 Time-height indication of aerosol backscatter at 532 nm at Tsukuba, Japan, on April 9, 2022. The time and range resolutions are 5 min and 30 m, respectively. Averaged aerosol backscatter in the boundary layer was approximately 2.5 Mm^{-1} sr^{-1}

Figure 12.3 shows the 1-day continuous measurement of aerosol backscatter at Tsukuba, Japan, on April 9, 2022. Aerosol backscatter could be measured for dense aerosols in the boundary layer and thin aerosol layers in the free troposphere up to 10 km height. During the daytime, lidar signals at the upper atmosphere were noisy due to the low laser energy, but aerosols in the boundary layer could be adequately measured.

12.4 Conclusions

A simple and low-cost HSRL was developed using a multimode laser and a scanning interferometer. The multimode laser was designed to have the same spectral mode spacing as the interferometer FSR, which was optimized for HSRL measurement. Atmospheric Mie and Rayleigh scattering stimulated by the multimode laser were spectrally filtered using the scanning interferometer. The scan signals were used to obtain the interference visibility, which contains aerosol backscatter information. We successfully carried out continuous measurement of aerosol backscatter profiles using the HSRL. Quantitative measurement of aerosol profiles by the low-cost HSRL can be useful to investigate the effect of aerosols on the air quality.

The performance of the lidar was greater than a previous version, which employed a laser with a much longer cavity. Because the short-length interferometer optimized for the HSRL measurement was used, the interference visibility for the Mie scattering improved and the receiver FOV was wider, and therefore, the measurement efficiency was increased. Also, measurement stability improved because

the compact interferometer was used. We continue to study on the improvement of the multimode HSRL system for multispectral measurement using the single interferometer [4].

Acknowledgments This research was performed by the Environmental Research and Technology Development Fund (JPMEERF20205R01) of the Environmental Restoration and Conservation Agency provided by Ministry of the Environment of Japan.

References

1. Piironen, P., Eloranta, E.W.: Demonstration of a high-spectral-resolution lidar based on an iodine absorption filter. Opt. Lett. **19**, 234–236 (1994)
2. Jin, Y., Sugimoto, N., Ristori, P., Nishizawa, T., Otero, L., Quel, E.: Measurement method of high spectral resolution lidar with a multimode laser and a scanning Mach-Zehnder interferometer. Appl. Opt. **56**, 5990–5995 (2017)
3. Jin, Y., Nishizawa, T., Sugimoto, N., Ishii, S., Aoki, M., Sato, K., Okamoto, H.: Development of a 355-nm high-spectral-resolution lidar using a scanning Michelson interferometer for aerosol profile measurement. Opt. Express. **28**, 23209–23222 (2020)
4. Jin, Y., Nishizawa, T., Sugimoto, N., Takakura, S., Aoki, M., Ishii, S., Yamazaki, A., Kudo, R., Yumimoto, K., Sato, K., Okamoto, H.: Demonstration of aerosol profile measurement with a dual-wavelength high-spectral-resolution lidar using a scanning interferometer. Appl. Opt. **61**, 3523–3532 (2022)

Chapter 13
Deep-Learning-Based Convective Boundary Layer Determination for Aerosol and Wind Profiles Observed by Wind LiDAR

Chih-Wen Su, Wei-Nai Chen, Wei-Yao Chang, and M. Roja Raman

Abstract Modified stacked hourglass network is used to capture the height of convective boundary layer (CBLH) from radial wind speed and aerosol backscatter measured by a Doppler wind LiDAR. We collected a year's LiDAR data and generated over 30,000 maps for training. The results show that the data set of 4-directional wind speeds and aerosol backscatters (without vertical component), the mean absolute error (MAE) of the CBLH estimated by the proposed deep learning methods, is about 60 m. If only aerosol backscatter is used to train the model, the MAEs of CBLH are about 91 m and 86 m for daytime and nighttime measurements, respectively. This chapter shows the advantage of proposed deep learning method in better estimation of CBLH.

Keywords Doppler LiDAR · Deep learning · Convective boundary layer

13.1 Introduction

The planetary boundary layer (PBL) is a thin layer near the Earth's surface concentrating atmospheric aerosols and is directly influenced by the atmospheric processes. This layer typically responds to surface forcing mechanisms with a

C.-W. Su · W.-Y. Chang
Chung-Yuan Christian University, Taoyuan, Taiwan
e-mail: lucas@cycu.edu.tw

W.-N. Chen (✉)
Academia Sinica, Taipei, Taiwan
e-mail: wnchen@rcec.sinica.edu.tw

M. Roja Raman
Academia Sinica, Taipei, Taiwan
Satyabama Institute of Science and Technology, Chennai, India
e-mail: ramansvu@gmail.com

© The Author(s), under exclusive license to Springer Nature Switzerland AG 2023

J. T. Sullivan et al. (eds.), *Proceedings of the 30th International Laser Radar Conference*, Springer Atmospheric Sciences,
https://doi.org/10.1007/978-3-031-37818-8_13

timescale of about an hour or less [1]. The planetary boundary layer height (PBLH) can be considered as the height up to which the influence of the presence of the lower surface is detectable.

The convective boundary layer (CBL), in which the surface upward buoyance flux is positive, is an internal PBL structure that determines the atmospheric processes directly related to air pollution, including convective activity, aerosol distributions, and cloud/fog formation. As a result, PBLH/CBLH has been used as a key parameter in air quality models to determine turbulence mixing, vertical diffusion, convective transport, cloud/aerosol entrainment, and deposition of pollutants [2].

LiDAR is an active optical remote sensing instrument that can continuously monitor planetary boundary layer (PBL) with high spatial and temporal resolution. The conventional methods for identification of PBL pattern from LiDAR backscatter profiles in general require some criteria to be matched (see Emeis et al. [3] and references therein). However, that is difficult to have a criterion that can clearly identify a certain feature of convective boundary layer (CBL) in aerosol backscatter profile, especially when CBL is too shallow in the nighttime. To investigate the possibility to predict CBLH from aerosol backscatter profile, a deep learning model is used to build a non-supervised package to identify the CBLH from aerosol and wind products measured by coherent Doppler LiDAR (CDL).

The deep learning machine is trained by a convolutional neural network (NN) in a supervised way and be forced to learn how to retrieve CBL on real and non-ideal conditions in a fully automated and unsupervised manner. The stacked hourglass network [4] that we used in this chapter is a conv–deconv architecture typically applied to human pose estimation. Through successive downsampling and upsampling, the network can capture information at multiple scales to determine the precise location of the targets, such as the key points of human body.

One year of LiDAR data is collected in the central Taiwan, and over 30,000 maps are generated accordingly. The ground truth CBLH is determined from the vertical-velocity variance σ_w^2. In order to train the model, the observations are divided into two sets, radial wind speed and normalized backscatter (W_r+NBS) and NBS only. A set of 36, 72, 120, and 230 days data are randomly selected for the training to examine the minimum requirement for the training. The differences between ground truth and predicted CBLH are presented.

13.2 Methodology

13.2.1 Doppler LiDAR

A coherent Doppler LiDAR (CDL, WindPrint S-4000) was operated in Chung-Shan Medical Univ., Taichung in Central Taiwan, from Jan. 2018 to Jan. 2019 to provide horizontal and vertical wind profiles from 50 m up to 6 km altitude. This CDL is jointly developed by Ocean Univ. of China and Leice Transient Technology

Co., Ltd.The 5-directional (NESWV) radial wind speed measurements in off-zenith (60°) and zenith angles are recorded at every 4 seconds interval. However, to improve the signal detectability and for wind vector derivation, the profiles are averaged for 5-minute intervals, and the estimated wind speeds and signal-to-noise ratio (NBS) are stored in level 3 data that are used for this study.

The CBLH data set used to train the machine is determined from the variance of vertical speed measured by wind LiDAR (Berg et al., 2017, Huang et al. [5]) and was validated with co-launched radiosondes. The LiDAR profiles of radial wind speed and backscatter (NBS) are separated into 2D spatio-temporal maps at 15-minute intervals.

The vertical-velocity variance (σ_w^2) from the LiDAR is used to determine the CBL depth, for heights above the CDL's minimum range of 60 m. The profiles of σ_w^2 are calculated for every 15 mins and used to estimate the CBLH. The estimation of CBLH from σ_w^2 based on a threshold has been proved to be a suitable technique to find the CBLH present during the mid-day due to high solar insolation; however, caution is advised to use site-dependent threshold to find the optimum CBL height for a particular site [5]. Based on this, different threshold values are checked, and finally, a threshold of $0.035\,\mathrm{m^2 s^{-2}}$ is found suitable for our location and was validated with 31 co-launched radiosondes.

The CBLH can be easily determined from the σ_w^2 measured by CDL; however, that is difficult to have a criterion that can clearly identify a certain feature of CBL in aerosol backscatter power profile, especially when the CBL is too shallow in the nighttime. To investigate the possibility to derive CBLH from aerosol backscatter profile alone, the normalized backscatter obtained from the averaged backscatter power spectrum of CDL is used to train the deep learning model. For a given LOS, the backscatter power could be expressed as Eq. (13.1) [6]

$$P(r) = K E_0 \eta_h(z) \frac{1}{z^2} \beta(z) \exp(-2 \int_0^z \alpha(r) \mathrm{d}r), \tag{13.1}$$

where K and E_0 are system constant and pulse energy, η_h is heterodyne efficiency, $\beta(r)$ is the backscatter coefficient, and α is the extinction coefficient.

13.2.2 Deep Learning Model (Stacked Hourglass Network)

With the rise of convolutional neural networks in the past decade, object detection performance has been rapidly enhanced based on its rich feature representation. The hand-crafted features used in traditional machine learning are not sufficient for extracting semantic and scalable information from raw data. To precisely locate the height of CBL, we introduce a CNN-based method that can handle the similar localization problem in computer vision.

Stacked hourglass network is a state-of-the-art architecture for human pose estimation. To capture the joints of human body, image features are learned

by convolutional and pooling layers at multi-resolutions. The hourglass network combines features across different scales and outputs a set of heatmaps that predict the probability of a joint being at each pixel. A stacked hourglass network contains eight hourglass modules. The first hourglass module produces early predictions, and subsequent modules further improve the predictions.

To predict CBLH by the stacked hourglass network, the vertical profile of LiDAR data should be formatted as a 2D image. Since the ground truth of CBLH is determined every 15 minutes in our data set, the vertical profile is first sliced into 15-minute segments. For each segment, there are 184 LiDAR samples that can be periodically collected from south, east, west, and north. Each sample records the values of radial wind, NBS, and spectral intensity at 30-m intervals starting from a height of 60 m. As a result, each segment is encoded as an 184×192 RGB image. The values of radial wind speed, NBS (denoted as SNR in raw data), and spectral intensity are quantified to 256 levels as pixel values of the R, G, B channels, respectively. If only NBS is used to train the stacked hourglass network, the image will turn into to a monochromatic image. A RGB image encoded from CDL data, LiDAR range-corrected backscatter ($\mathrm{NBS} \times z^2$), and σ_w^2 are shown in Fig. 13.1.

Unlike the 2D localization of human joints, only the height of the CBL (i.e., the Y-coordinate position on the image) needs to be determined for each profile. Thus, we modified the loss function in the intermediate supervision step so that the loss function only considers the value of the y-coordinate. In fact, since the heatmap of each joint is isolated from those of the others, it is possible to locate the height of multiple layers at once. We have collected one year of CDL data and randomly selected 36 days, 72 days, 120 days, and 230 days from the whole data set as the ground truths for training. The flow chart of the training and localization process is shown in Fig. 13.2.

13.3 Results

The vertical profiles observed during 2018/12/30-2019/1/15 are selected to evaluate the performance of the deep learning model. The time–height evolution of the range-corrected backscatter signal (overlapping corrected) and the vertical-velocity variance measured during 1/12-1/13, 2019 is shown in Fig. 13.3 to demonstrate the performance of CBLH predicted by the deep learning model. The CBLH predicted from 72 days and 120 days W_r and NBS are composed in Fig. 13.3a and b, respectively. In elastic and Raman LiDAR systems, the atmospheric aerosols are used as tracers, and the PBLH is indicated by a gradient in the range-corrected LiDAR signal RCS [7–9]. Aerosol layer estimated by gradient method ($\partial \mathrm{RCB}/\partial z$) is shown for comparison. For training set of W_r+NBS, both sets of 72 days and 120 days are generally well-agreed with ground truths, but the time series of 120 days are more smoother than 72 days. Whereas for training sets using NBS only, the CBLH predicted from the set of 120 days is more consistent with ground truth than the CBLH predicted from the set of 72 days (Fig. 13.4).

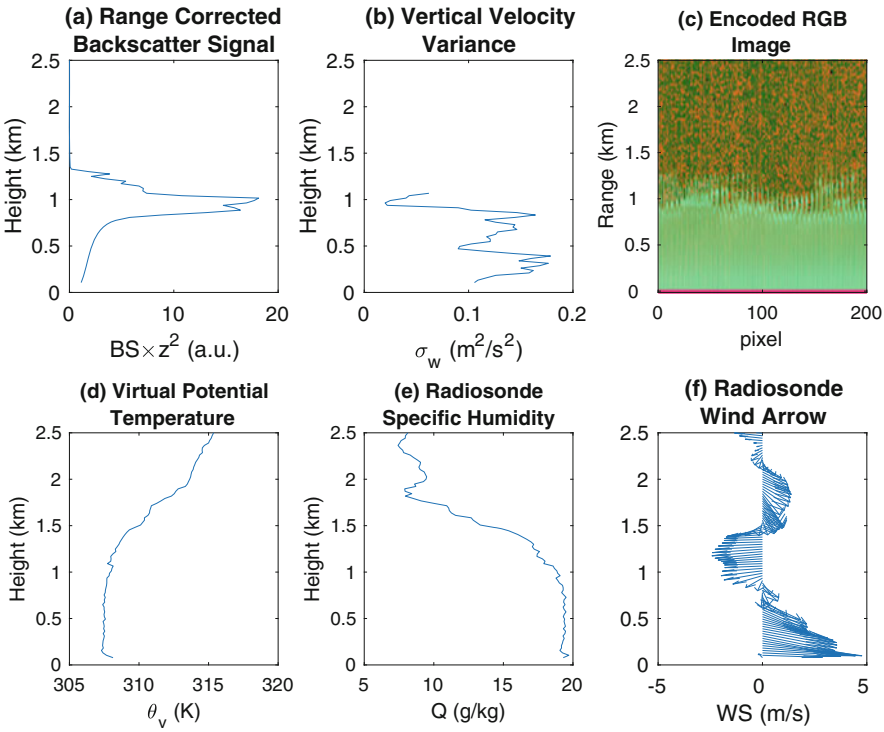


Fig. 13.1 (**a**) Range-corrected LiDAR backscatter, (**b**) vertical-velocity variance (σ_w), and (**c**) the image encoded from 15-minute vertical profiles (directional radial wind speed and NBS) segment observed on 2018/7/15 15:00L. (**d**–**f**) Virtual potential temperature, specific humidity, wind arrow measured by co-launched radiosonde

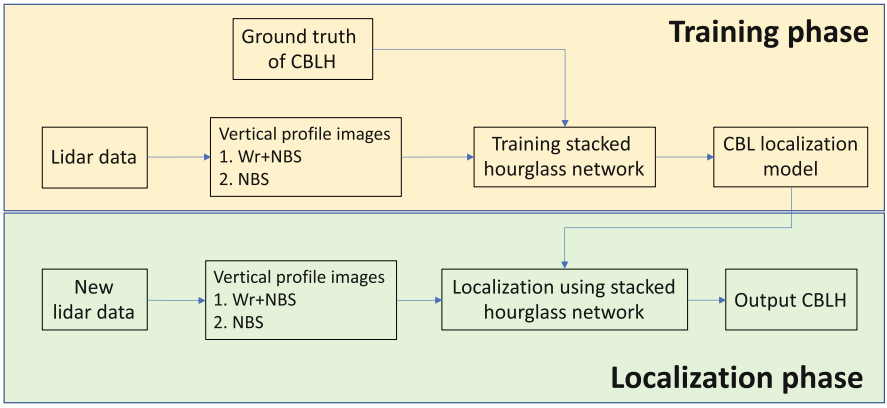


Fig. 13.2 The flow chart of the training and localization process

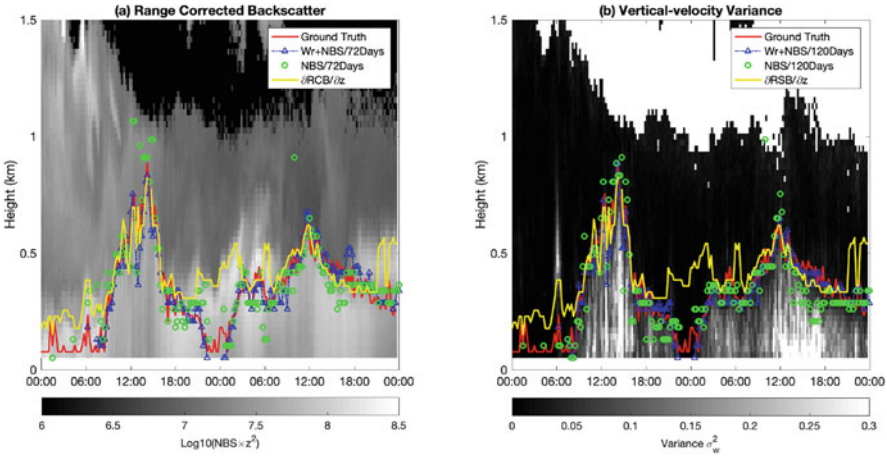


Fig. 13.3 (**a**) Range-corrected backscatter signal and (**b**) vertical-velocity variance measured during 1/12-1/13, 2019. The CBLH predicted from 72 days and 120 days W_r (blue △) and NBS (green ○) are composed in (**a**) and (**b**), respectively. Aerosol layer estimated by gradient method (∂RCB/∂z, yellow line) is shown for comparison

The time series of ground truths and the CBLH predicted by the modified stacked hourglass network that employ 36 days, 72 days, 120 days, and 230 days measurements (radial wind W_r+NBS) as the training base are shown in Fig. 13.5a. It can be noticed that the predicted CBLH generally well agrees with the ground truths. The mean absolute errors (MAEs) of the predicted CBLH are about 136 m, 75 m, 65 m, and 56 m for train bases 36 days, 72 days, 120 days, and 230 days, respectively. The analysis of frequency histogram (Fig. 13.5b) of the difference between predicted CBLH and ground truths shows that the error for more than 80% of predicted CBLH is within ±2 levels (52 m) except the 36 days training base. This result indicates the minimum requirement for the number of training base is about 72 days.

To investigate the possibility of using aerosol backscatter profile to obtain CBLH, 2D spatio-temporal monochromic images at 15-minute intervals generated from the normalized backscatter (NBS) measured by CDL are used as the training bases. A set of 36 days, 72 days, 120 days, and 230 days (the same days selected for W_r+NBS) 4-directional NBS are employed as the train bases. The MAEs for 36 days, 72 days, 120 days, and 230 days training bases are 147 m, 122 m, 104 m, and 89 m, respectively. The frequency histogram of the difference between predicted CBLH and ground truths is shown in Fig. 13.5b. As shown in Fig. 13.5b, the improvements of the accuracy of the predictions are not significant when training set is larger than 72 days, which is similar to W_r+NBS. And that can be noticed all training sets of NBS tend to overestimate than the ground truths. About 40% of predicted CBLH are underestimated and 50% are overestimated.

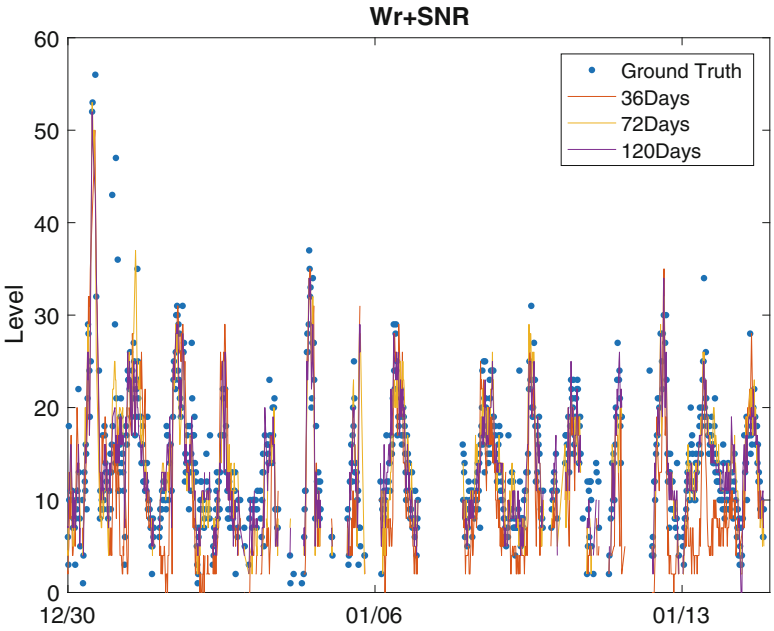


Fig. 13.4 (**a**) The time series (2018/12/30–2019/1/15) of CBLH predicted by stacked hourglass network using 36 days, 72 days, 120 days, and 230 days measurements (radial wind W_r+NBS) as the training base. (**b**) Frequency histogram of the difference between predicted CBLH and ground truths

The performances of the CBLH predictions based on training set of W_r+NBS and NBS are evaluated for daytime and nighttime, respectively (figures are not shown to save space). Figure 13.6b shows the frequency histogram of the errors for the predicted CBLH in daytime and nighttime. The predictions used here are based on 120 days training sets of W_r+NBS and NBS.

It can be noticed the differences between daytime and nighttime are not significant. Both W_r+NBS and NBS tend to 1 level (26 m) overestimated in the nighttime and 1 level underestimated in the daytime.

For the training set of W_r+NBS, about 47% of predicted daytime CBLH are underestimated and 41% are overestimated. And, about 45% of predicted nighttime CBLH are underestimated and 59% are overestimated. For the training set of NBS, about 46% of predicted daytime CBLH are underestimated and 44% are overestimated. And, about 32% of predicted nighttime CBLH are underestimated and 59% are overestimated.

The mean values of CBLH during the testing period are 433 m and 255 m in the daytime and the nighttime, respectively. The MAEs of predicted CBLH (120 days W_r+NBS) are about 62 m and 59 m for daytime and nighttime, respectively. The MAEs of predicted CBLH (120 days NBS) are about 101 m and 99 m for daytime and nighttime, respectively.

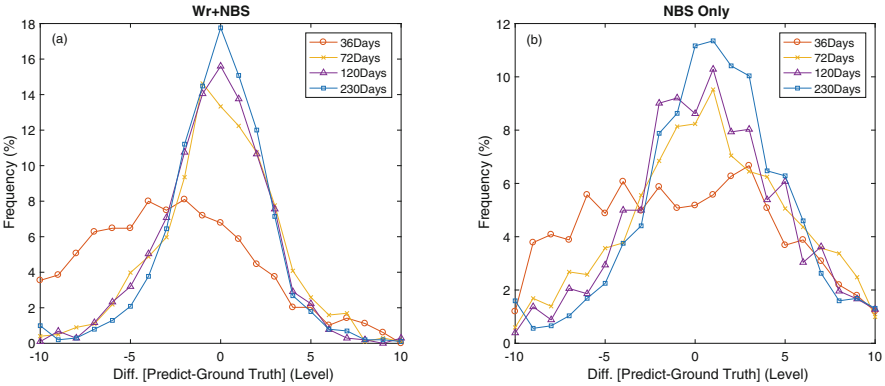


Fig. 13.5 (**a**) Frequency histogram of the difference between ground truths and CBLH predicted using 36, 72, 120, and 230 days W_r+NBS as train set. (**b**) Same as (**a**) but trained for data set of NBS only

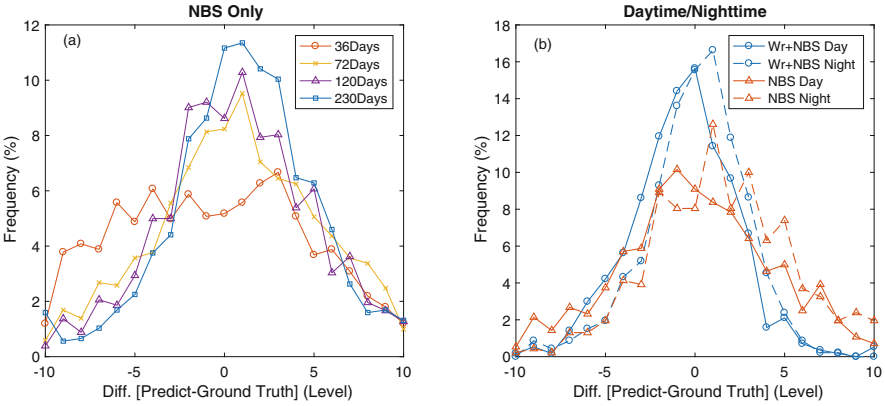


Fig. 13.6 (**a**) Same as Fig. 13.5b, the frequency histogram difference between predicted CBLH and ground truths using 36 days, 72 days, and 120 days radial NBS as training sets. (**b**) Frequency histogram of the difference between predicted daytime or nighttime CBLH (training set of 120 days) and ground truths

13.3.1 Conclusions

Unlike the conventional algorithms used to derive PBLH/CBLH from LiDAR backscatter profiles, our results show the deep-learning-based method can efficiently find the feature of CBLH from CDL products with MEA about 60∼120 m (depending on the size of training set) without any prior assumption, even if only backscatter is used as the training data set. Our results also indicate that it is possible to derive CBLH from backscatter profiles measured by Mie LiDARs.

Acknowledgments The authors would like to acknowledge the funding support from Academia Sinica, Taiwan. (AS-SS-107-03 and AS-SS-110-02).

References

1. Stull, R.B.: An Introduction to Boundary Layer Meteorology, vol. 13. Springer Netherlands, Dordrecht (1988). http://link.springer.com/10.1007/978-94-009-3027-8
2. Holtslag, A.A.M., Boville, B.A.: Local versus nonlocal boundary-layer diffusion in a global climate model. J. Clim. **6**(10), 1825–1842 (1993). https://doi.org/10.1175/1520-0442(1993)006%3C1825:LVNBLD%3E2.0.CO;2
3. Emeis, S., Schäfer, K.: Remote sensing methods to investigate boundary-layer structures relevant to air pollution in cities. Boundary-Layer Meteorol. **121**(2), 377–385 (2006)
4. Newell, A., Yang, K., Deng, J.: Stacked hourglass networks for human pose estimation. In: Leibe, B., Matas, J., Sebe, N., Welling, M. (eds.) Comput. Vis. – ECCV 2016, pp. 483–499. Springer, Cham (2016)
5. Huang, M., Gao, Z., Miao, S., Chen, F., LeMone, M.A., Li, J., Hu, F., Wang, L.: Estimate of boundary-layer depth over Beijing, China, using Doppler LiDAR data during SURF-2015. Boundary-Layer Meteorol. **162**(3), 503–522 (2017)
6. Dai, G., Wang, X.X., Sun, K., Wu, S., Song, X., Li, R., Yin, J., Wang, X.X.: Calibration and retrieval of aerosol optical properties measured with coherent Doppler LiDAR. J. Atmos. Ocean. Technol. **38**(5), 1035–1045 (2021)
7. Menut, L., Flamant, C., Pelon, J., Flamant, P.H.: Urban boundary-layer height determination from LiDAR measurements over the Paris area. Appl. Opt. **38**(6), 945 (1999)
8. Brooks, I.M.: Finding boundary layer top: application of a wavelet covariance transform to LiDAR backscatter profiles. J. Atmos. Ocean. Technol. **20**(8), 1092–1105 (2003). http://journals.ametsoc.org/doi/10.1175/1520-0426(2003)020%3C1092:FBLTAO%3E2.0.CO;2
9. Amiridis, V., Melas, D., Balis, D.S., Papayannis, A., Founda, D., Katragkou, E., Giannakaki, E., Mamouri, R.E., Gerasopoulos, E., Zerefos, C.: Aerosol LiDAR observations and model calculations of the Planetary Boundary Layer evolution over Greece, during the March 2006 Total Solar Eclipse. Atmos. Chem. Phys. **7**(24), 6181–6189 (2007). https://acp.copernicus.org/articles/7/6181/2007/

Chapter 14
LITES: Laboratory Investigations of Atmospheric Aerosol Composition by Raman-Scattering and Fluorescence Spectra



Boyan Tatarov and Detlef Müller

Abstract In regard to lidar applications, we will explore if the use of information on optical fingerprints (i.e., characteristic optical signals) allows for establishing vertically resolved identification of chemical components of atmospheric pollution. In this work we present hardware and experimental results of Raman and fluorescence spectra of a collection of different dust samples composed of quartz, hematite, kaolinite, barite, and calcite. We investigated these samples under laboratory conditions with two Raman microscopes.

Keywords Aerosol · Raman scattering · Fluorescence · Laser remote sensing

14.1 Introduction

Atmospheric aerosols such as mineral dust, bio-aerosols, and volcanic ash can be transported over thousands of kilometers away from their source regions. We currently focus on using optical signals (spectra) obtained with Raman/fluorescence microscope to collect "optical fingerprints" of aerosol samples, i.e., pure material and atmospheric samples collected from different source regions. This information can then be used in the context of lidar observations of pollution in the atmosphere, e.g., for improved characterization of optical and microphysical properties of aerosol pollution, which may lead to improvements of aerosol-typing schemes.

A Raman spectrum results from photons scattered by atmospheric particles at frequency f_R different from the frequency f of the incident photons. The frequency shift between incident and scattered photons (frequency difference) is described as Δf. The Raman spectrum is symmetrical around the frequency of the emitted

B. Tatarov (✉) · D. Müller
Department of Physics, Astronomy and Mathematics, School of Physics, Engineering and Computer Science, University of Hertfordshire, Hatfield, UK
e-mail: b.tatarov@herts.ac.uk

© The Author(s), under exclusive license to Springer Nature Switzerland AG 2023

J. T. Sullivan et al. (eds.), *Proceedings of the 30th International Laser Radar Conference*, Springer Atmospheric Sciences,
https://doi.org/10.1007/978-3-031-37818-8_14

photons, i.e., the Stokes Raman spectrum has maximum intensity (energy) at $f - \Delta f$. The anti-Stokes Raman spectrum has maximum intensity (energy) at $f + \Delta f$. Each molecule has a different Raman spectrum, which can be identified using Raman spectroscopy. By comparing the Raman spectrum of a sample to known Raman spectra of specific molecules, it is possible to determine types of molecules in the sample.

For a sample at room temperature the vibrational energy states of the sample will be predominantly at low energies. Thus, the individual anti-Stokes Raman peaks will have much lower intensity. The individual Stokes Raman scattering peaks can be preferred as reference data because of their greater intensity compared to anti-Stokes peaks. Anti-Stokes Raman, in contrast, may be preferred if fluorescence is interfering with the measurements [1].

In this case, a molecule absorbs the photon and is excited to a vibrational energy state. This molecule then emits some of the energy (that was gained in the absorption process) as a new photon. This new photon can have an energy that is different from the energy of the incident photon. In the case of fluorescence, the energy of incident photons is the determining factor, i.e., whether we observe fluorescence or not. The fluorescence spectra is measured in terms of intensity of re-emitted photons in dependence of frequency. As the light intensity of fluorescence is about one million times more intense than that of Raman scattering, fluorescence will often be a source of interference when measuring Raman scattering (spectra) [2].

In regard to the lidar that is part of our LITES (Lidar Innovations for Technologies and Environmental Sciences) facility at the University of Hertfordshire [3], we would like to use the information of optical fingerprints as a step toward establishing vertically resolved identification of chemical components of atmospheric pollution [4]. LITES combines a unique Lidar Spectroscopy Instrument (LiSsI) with in situ instruments such as Raman and fluorescence microscope, gas, and aerosol chambers.

We present experimental results of Raman and fluorescence spectra of a collection of different samples of atmospheric particles. These samples are well characterized in terms of their chemical composition. The samples include mineral dust (quartz, hematite, kaolinite, barite, calcite etc.) and bio-aerosols. Section 14.2 describes the methodology. We present results in Sect. 14.3. Section 14.4 summarizes our findings.

14.2 Equipment and Methods

We use two Raman/fluorescence microscopes. One microscope has been custom developed at the University of Hertfordshire (UH). The second microscope is a commercial Renishaw InVia Raman spectrometer.

The Raman/fluorescence microscope developed at UH comprises of the following elements. A LASOS DPSS laser that operates at 532 nm with power up to 150 mW. An Olympus BX51TRF-6 microscope that uses objective lenses

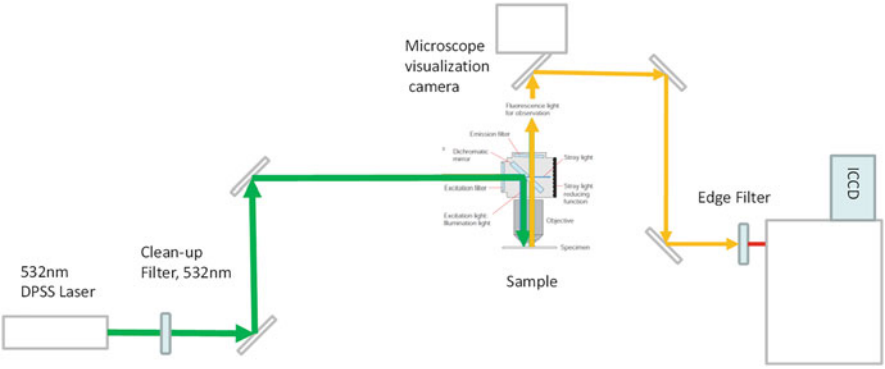


Fig. 14.1 Sketch of the Raman/fluorescence microscope custom developed at UH

with magnification factors ×5, ×10, ×20, ×50, and ×100. The setup includes a HORIBA 1250 M research spectrometer that can be used with four different gratings with groves (gr) of 2400 gr/mm, 1800 gr/mm, 1200 gr/mm, and 600 gr/mm. Signal detection is done by one of the following detectors: a PI-MAX4 ICCD camera, an ANDOR iXon3 EMCCD camera, a PMT, a Si single detector, and an InGaAs single detector. The spatial resolution of the microscopes depends on the objective lens. The resolution for individual objective is obtained by imaging of the "USAF Resolution Power Test Target 1951" [5]. We obtain a spatial resolution (of images) better than 1 μm with the x100 objective lens. The laser spot size is 2.2 μm on the focus point with the same objective. The spectral resolution depends on the type of the used grating, and the sizes of the entrance and exit slit, respectively. A spectral resolution better than 1 cm^{-1} can be achieved with the 2400 gr/mm grating and slit sizes of 10 μm (Fig. 14.1).

The second option for observations of Raman/fluorescence spectra is a Renishaw InVia instrument. In that case we use a wavelength of 785 nm. The maximum power of the pumping laser is 300 mW at wavelength of 785 nm. A Leica microscope is used for this instrument. The magnification factors of the objective lens are ×5, ×10, ×20, ×50, and ×100. The Renishaw InVia includes an inbuild spectrometer with one grating and an InGaAS CCD camera as detection unit.

Both microscopes are equipped with visualization cameras and software. The visualization cameras are used for the alignment of the samples on the focus point of the laser beam as well as for taking images of each sample.

Comparison of the results obtained with two different pumping wavelengths allows us to estimate the influence of fluorescence on the Raman spectra.

The procedure of acquiring a full spectrum of a sample includes the following:

(1) Calibration of the spectrometers and detectors. Initial calibration of the spectrometers is performed by using Hg and Ar calibration lamps which have well-known emission lines. For the fine calibration we use reference samples (Raman standards [6]) such as polystyrene, naphthalene, benzene, sulfur,

toluene, and acetamidophenol. The intensity calibration can be carried out with a deuterium-halogen lamp, which was radiometrically calibrated DH-2000, 220–1050.

(2) Blank slide characterization. The samples were placed on microscope slides for imaging. The slides are made of soda lime glass, and their dimensions are 76 × 26 × 1 mm. The microscope slides have their own Raman spectra. These spectra were recorded before making observations of any samples. In this way Raman peaks from the slide can be excluded from the Raman peaks generated by the mineral dust samples.

(3) Laser emission line characterization. The laser light source that was used for all measurements was a 532-nm diode-pumped solid-state laser. Software is used to vary the output power of the laser from 0 to 150 mW. Measurements of the light emitted by the laser showed two wavelengths, one at 532.2 nm and another one at 535.7 nm. To correct for this, we placed a 532.2-nm bandpass filter directly in front of the laser.

(4) Preparation of the sample on a microscope slide which is then mounted on the microscope.

(5) An image of the sample can be taken by the visualization cameras of the microscope.

(6) Spectra are acquired by signal detection, either with a PMT or an EMCCD or an ICCD.

(7) Data processing includes noise reduction, ambient light, and cosmic rays correction.

Figure 14.2 shows examples of Raman spectra of the polystyrene Raman standard (Aldrich #18, 243–5).

The Raman lines shifts in these in UH are in very good agreement with the reference spectra [6]. The agreement illustrates the very good performance of the two UH microscopes. The shifts of the lines are the same for both excitation wavelengths. However, the relative intensity if the lines is different. The intensity

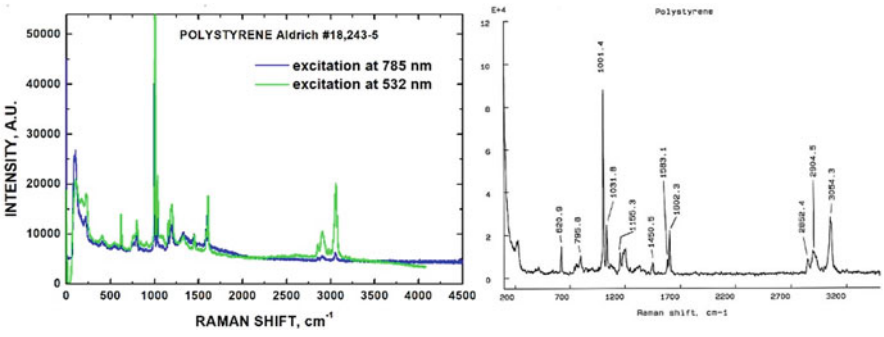


Fig. 14.2 Raman spectra of polystyrene Raman standard (Aldrich #18, 243–5). Left: spectra acquired from pumping wavelengths 532 nm (green) and 785 nm (blue). Right: Reference spectrum

of the lines in the spectrum acquired with laser-light pumping at 532 nm is higher than the intensity of the lines obtained with pumping at 785 nm. This effect can be clearly seen for the lines around 3000 cm^{-1}. The difference of the intensities has to be expected because of the Raman intensity depends with power-4 on the pumping wavelength.

14.3 Results and Discussion

The nitrogen backscatter and Raman scattering are very important for lidar applications. The scattering from nitrogen molecules can be used for the absolute calibration of lidar signal, as these signals allow us to infer the nitrogen molecules density.

Figure 14.3 shows the spectrum of the nitrogen vibration-rotation Raman spectra near 2330 cm^{-1} obtained by our UH custom-made microscope and 532-nm pumping wavelength. The signals were acquired with a PMT detector, an objective lens with x10 magnification, 30 mW power of the laser beam in the focus plane, and an acquisition time of 100 s per each point of spectrum. The intensity of the nitrogen vibration-rotation Raman peak can be used for reference or for calibration of the intensity of the Raman peaks of other dust samples.

Figure 14.4 presents experimental results of Raman and fluorescence spectra of corundum (Al_2O_3). The spectrum obtained with 532-nm pumping clearly shows Raman lines at shifts 386 cm^{-1}, 420 cm^{-1}, 432 cm^{-1}, 578 cm^{-1}, 645 cm^{-1}, and 752 cm^{-1}. The signal intensity continuously increases with increasing Raman shift (left to right in Fig. 14.4) which is caused by fluorescence. Corundum has an emission peak at 694.3 nm which is the exact wavelength of the Ruby laser. The

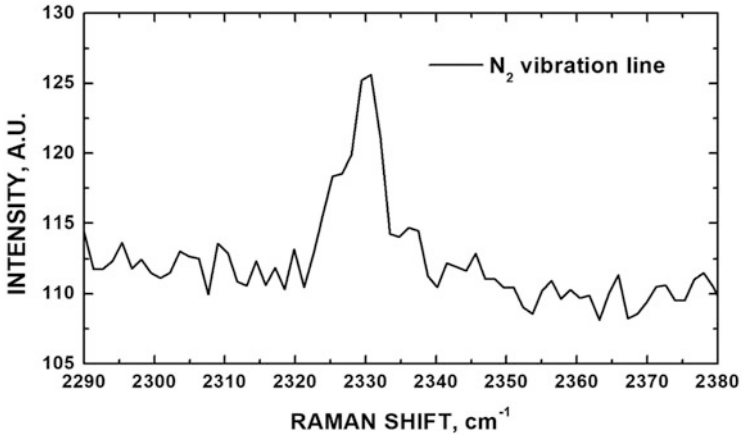


Fig. 14.3 Raman spectra of N_2 under ambient atmospheric conditions

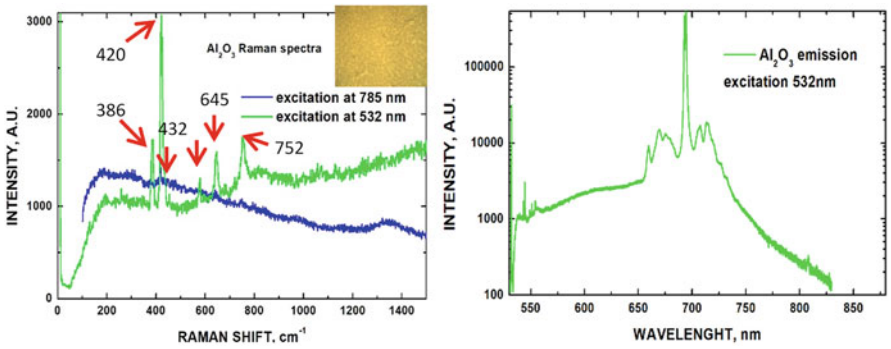


Fig. 14.4 Raman and fluorescence (emission) spectra of corundum (Al_2O_3). Left: spectra obtained with pumping wavelengths 532 nm (green) and 785 nm (blue). Also shown is a picture of the sample. Right: fluorescence/emission spectra for excitation at 532 nm

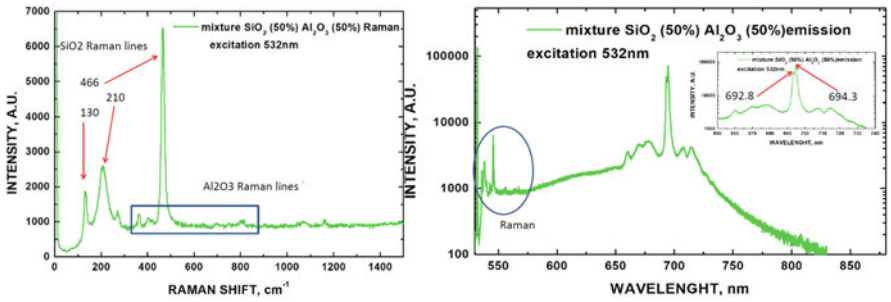


Fig. 14.5 Raman and fluorescence (emission) spectra of a mixture of SiO_2 (50%) + Al_2O_3 (50%). Left: Raman spectra obtained with pumping wavelength 532 nm (green). Right: fluorescence/emission spectra with excitation at 532 nm

intensity of this emission is approximately 400,000 times stronger than the emission by nitrogen which was observed in nearly the same conditions. The signal intensity shows the usefulness of this emission line for lidar/laser remote sensing, and for the detection of Al_2O_3 molecules in the atmosphere.

Figure 14.5 presents Raman and fluorescence spectra of a mixture of SiO_2 (50% by mass) and Al_2O_3 (50%). We see the typical quartz Raman lines at 210 cm^{-1} and 466 cm^{-1}, as well as the line at 130 cm^{-1}. We observe an emission peak at 694.3 nm (as in Fig. 14.4), which confirms that this line is suitable for remote sensing.

The results presented in Fig. 14.6 also clearly show the quartz Raman lines at 130 cm^{-1}, 210 cm^{-1}, and 466 cm^{-1}. The typical microcline ($KAlSi_3O_8$) lines at approximately 300 cm^{-1} and 800 cm^{-1}can also be seen in the spectra in Fig. 14.6.

Figure 14.7 shows the results of spectra of a sand sample. Sand is particularly important as it is the main component of dust. Figure 14.7 shows the Raman lines at 210 cm^{-1} and 466 cm^{-1} (associated to quartz) and a line at 1350 cm^{-1} embedded in strong fluorescence signals that peak a t 610 nm. The fluorescence at this wavelength

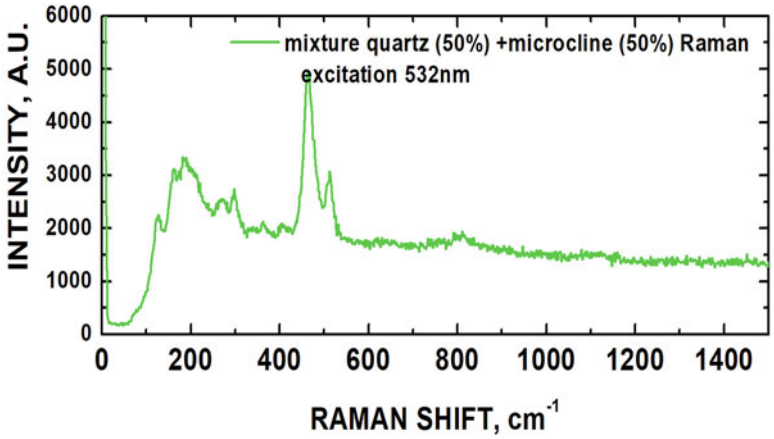


Fig. 14.6 Raman and fluorescence (emission) spectra of a mixture of SiO_2 (50%) + microcline ($KAlSi_3O_8$) (50%). with excitation at 532 nm

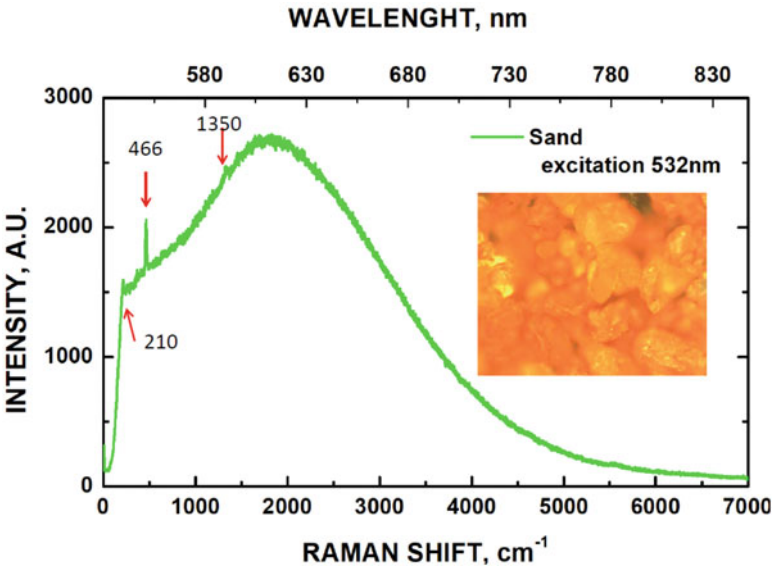


Fig. 14.7 Raman and fluorescence (emission) spectra of sand obtained with pumping wavelength 532 nm (green)

can significantly mask the nitrogen Raman signal at 607 nm (obtained from pumping at 532 nm). The results emphasize the need for taking into account the influence of fluorescence on signals obtained with traditional nitrogen Raman lidars.

14.4 Conclusions

In this work we present the first set of results obtained with Raman/fluorescence microscopy equipment operated at the University of Hertfordshire, UK. We also present experimental results of Raman and fluorescence spectra of different dust samples. Two Raman microscopes are used for this work. The results show what Raman and emission lines may be useful for lidar applications. Our results show that the influence of fluorescence must be taken into account in the analysis of data obtained with traditional nitrogen Raman lidar.

References

1. Smith, E., Dent, G.: Modern Raman Spectroscopy: A Practical Approach. Wiley, Hoboken (2002)
2. Schrader, B., Bougeard, D.: Infrared and Raman Spectroscopy: Methods and Applications. Wiley, Hoboken (1995)
3. Tatarov, B., Müller, D.: LITES: rotational Raman spectra of air molecules measured by high-resolution-spectroscopy lidar. Opt. Lett. **46**, 5173–5176 (2021)
4. Inaba and Kobayasi: Laser-Raman radar -laser-Raman scattering methods for remote detection and analysis of atmospheric pollution. Opto-Electronics. **4**, 101–123 (1972)
5. https://www.thorlabs.com/newgrouppage9.cfm?objectgroup_id=4338
6. Richard L.: McCreery. http://www.chem.ualberta.ca/~mccreery/ramanmaterials.html. Last accessed 15 May 2022

Chapter 15
Performance Simulation of a Raman Lidar for the Retrieval of CO_2 Atmospheric Profiles

M. Di Paolantonio, P. Di Girolamo, D. Dionisi, M. Cacciani, A. Di Bernardino, T. Di Iorio, N. Franco, A. M. Iannarelli, G. L. Liberti, and D. Summa

Abstract Within the frame of a project (CONCERNING) aimed at the development of a multichannel lidar for atmospheric monitoring, we investigated the current feasibility and the limits of a ground-based Raman lidar system dedicated to the measurement of CO_2 profiles. The performance of a state-of-the-art lidar system was investigated through a set of numerical simulations. The possibility of exploiting both CO_2 Raman lines of the $\nu 1{:}2\nu 2$ resonance is explored. An accurate evaluation and quantification of the contribution of the Raman O_2 lines on the signal and other (e.g., aerosol, absorbing gases) disturbance sources was carried out. The signal integration over the vertical and over time required to reach a useful signal-to-noise ratio both in daytime and nighttime needed for a quantitative analysis of carbon dioxide sources and sinks was evaluated. The above objectives were

M. Di Paolantonio (✉)
Università degli Studi della Basilicata, Potenza, Italy

ISMAR-CNR, Rome, Italy
e-mail: marco.dipaolantonio@artov.ismar.cnr.it

P. Di Girolamo · N. Franco
Università degli Studi della Basilicata, Potenza, Italy

D. Dionisi · G. L. Liberti
ISMAR-CNR, Rome, Italy

M. Cacciani · A. Di Bernardino
Università degli Studi di Roma, Rome, Italy

T. Di Iorio
ENEA, Rome, Italy

A. M. Iannarelli
Serco Italia SpA, Frascati, Rome, Italy

D. Summa
Università degli Studi della Basilicata, Potenza, Italy

IMAA-CNR, Tito Scalo, Potenza, Italy

© The Author(s), under exclusive license to Springer Nature Switzerland AG 2023

J. T. Sullivan et al. (eds.), *Proceedings of the 30th International Laser Radar Conference*, Springer Atmospheric Sciences,
https://doi.org/10.1007/978-3-031-37818-8_15

obtained developing an instrument simulator code consisting of a radiative transfer model able to simulate, in a spectrally resolved manner (0.0001 nm), all laser light interaction mechanisms with atmospheric constituents, a consistent background signal, and all the devices present in the considered Raman lidar experimental setup. The preliminary results indicate that the simulated lidar system, provided to have a low overlap height, could perform measurements on the low troposphere (<1 km) gradients (1–5 ppm) with sufficient precision both in daytime and nighttime with an integration time of 1–3 h and a vertical resolution of 75 m.

Keywords Raman lidar · CO_2 · Radiative transfer simulator

15.1 Introduction

The concentration of carbon dioxide (CO_2) in the atmosphere has reached values above 415 ppm, with an average annual growth rate of about 2.5 ppm; this is already having major effects on the Earth's climate, and a great deal of effort has been made over the years to predict future trends. Part of the emissions are absorbed by various natural sinks whose better quantification is necessary to accurately simulate possible future scenarios. In particular, uncertainty of land carbon sinks is the highest among all flux components, and accurate means to monitor land sinks are required [1–3].

While CO_2 has relatively uniform vertical distribution and therefore the total atmospheric content is well monitored with in situ as well as satellite measurements, the correct quantitative knowledge of source/sink processes, which occurs mostly close to surface, requires a vertically detailed sampling as well as subdiurnal temporal sampling. The Raman lidar technique has proved to be a valuable tool to provide profiles of a variety of geophysical variables of the atmosphere, with the advantage of providing a continuous monitoring of the sensed parameters, with high measurement accuracy and resolution and a high level of independence between measured variables. The roto-vibrational Raman lidar technique, traditionally used to measure water vapor mixing ratio profiles, has been explored in the past decades for the application in CO_2 profile measurements [4–7]. Despite the high potential, because of the low signal-to-noise ratio (SNR) characterizing CO_2 roto-vibrational Raman signals, the poor precision achieved by these measurements prevented an adequate diffusion of the technique. As new technological solutions for laser sources, spectral selection, and signal detection have been designed, new interest has arisen, and a new generation of lidar systems is now being developed for its exploitation.

The objective of this study is to investigate the current feasibility and the limits of a ground-based Raman lidar system dedicated to the measurement of CO_2 gradients in the lower troposphere. Therefore, the characteristics and performance of a state-of-the-art lidar system for the estimation of CO_2 atmospheric profiles were investigated through a set of numerical simulations.

In the frame of the project CONCERNING (COmpact RamaN lidar for Atmospheric CO_2 and ThERmodyNamic ProfilING), a Raman lidar will be developed capable to provide accurate and high-resolution measurements of the vertical profiles of CO_2, water vapor mixing ratio, temperature, and particle backscattering/extinction profiles.

In this study, the possibility of exploiting one or both Raman lines of the $\nu 1{:}2\nu 2$ resonance is investigated. As some roto-vibrational O_2 lines lie in the same spectral range and represent a potential source of contamination for the CO_2 measurements, an accurate evaluation and quantification of this and other (e.g., aerosol, absorbing gases) disturbance sources is being carried out. Thus, the optimal position and width of the filter for the measurement of the Raman backscattering from CO_2 was defined. The signal integration over the vertical and over time required to reach a useful signal-to-noise ratio both in daytime and nighttime needed for a quantitative analysis of carbon dioxide sources and sinks was evaluated. Finally, the capability to estimate variability of the CO_2 mixing ratio was assessed.

The above objectives were obtained developing an instrument simulator code consisting of a radiative transfer model able to simulate, in a spectrally resolved manner, all laser light interaction mechanisms with atmospheric constituents, a consistent background signal, and all the devices present in the considered Raman lidar experimental setup.

15.2 The Raman Lidar Simulator

The lidar simulator consists of numerical model calculating the various terms of the lidar equation [8]. The Raman backscattering term is calculated line-by-line for the different molecular species of the atmosphere. The O_2 and N2 backscattering single-line cross-sections were calculated according to [9]. The works of [10, 11], with the partition function estimated via a second-order fit of the values tabled in [12], were used to simulate the first four more intense CO_2 Raman lines (among which the Fermi doublet with $2\nu 2$ at 1285.4 cm^{-1} and $\nu 1$ at 1388.2 cm^{-1}). Pressure broadening (i.e., Lorentzian) was applied for a rough estimation of the impact of the tails of the O_2/N_2 broadened lines on the CO_2 measurements at low altitudes [8, 13]. A fixed value of 0.05 cm^{-1} HWHM was used for the Lorentzian broadening function. Molecular scattering was calculated as in [14], while the atmospheric profiles used were the AFGL atmospheric constituent profiles [15]. A fixed value of 415 ppm was used for the CO_2. Gas absorption was calculated for O_3, NO_2, and SO_2. Aerosol extinction was computed with a highly parametrized representation based on aerosol optical depth, angstrom exponent, and scale height. Background was calculated at 371.7 nm and 382.7 nm in single-scattering approximation for different solar zenithal angles and summed to the signal. The uncertainty is assumed as the square root of the signal/background.

The simulated lidar system has the following characteristics based on the components that will constitute the CONCERNING lidar:

- Monochromatic laser source at 354.74 nm, 0.1 J per laser impulse, 100 Hz.
- Optical transmission efficiency of 0.90.
- Receiving quantum efficiency of 0.43.
- Interference filter with peak transmission of 0.46 and a FWHM of 0.15 nm.
- Telescope radius of 0.25 m with a field of view (full angle) of 0.1 mrad.
- Lidar altitude of 0 m AMSL.
- Full overlap assumed for the whole atmosphere.

15.3 Results

First, the whole spectrum (350–410 nm) was simulated with a 0.0001-nm resolution in order to quantify the effect of the tails of the broadened O_2 and N_2 lines on the CO_2 measurements. Figure 15.1 shows the simulated spectrum (at 1013 hPa and 288 K) near the $2\nu 2$ and $\nu 1$ lines together with the transmittance of two filters centered at 371.69 nm (filter A) and 373.11 nm (filter B).

Preliminary calculations indicate that the broadened Rayleigh/Raman signal due to the tails, integrated over the filter A window, has an intensity comparable to the CO_2 signal. This should be an overestimation of the real expected Rayleigh and

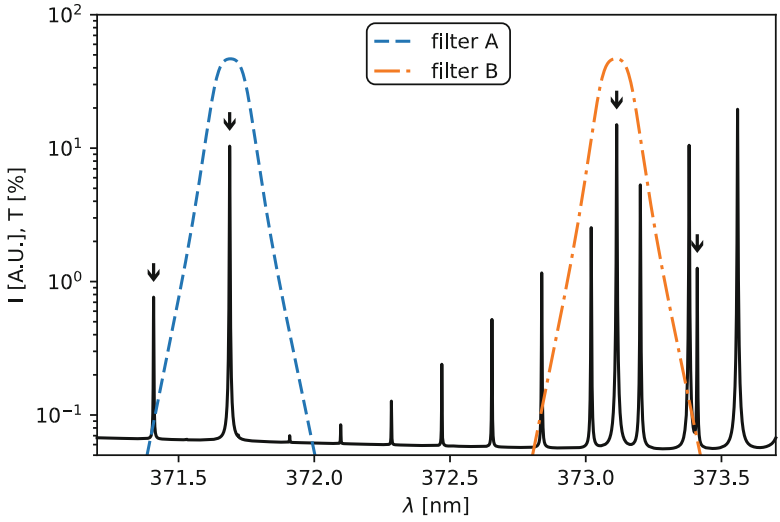


Fig. 15.1 Simulated Raman spectrum (solid line) and filter transmittance T for filter A (dashed line) and filter B (dash-dotted line). The CO_2 lines are indicated by the arrows; the remaining lines are O_2 roto-vibrational lines. The underlying background signal is the result of the broadening of all the calculated lines

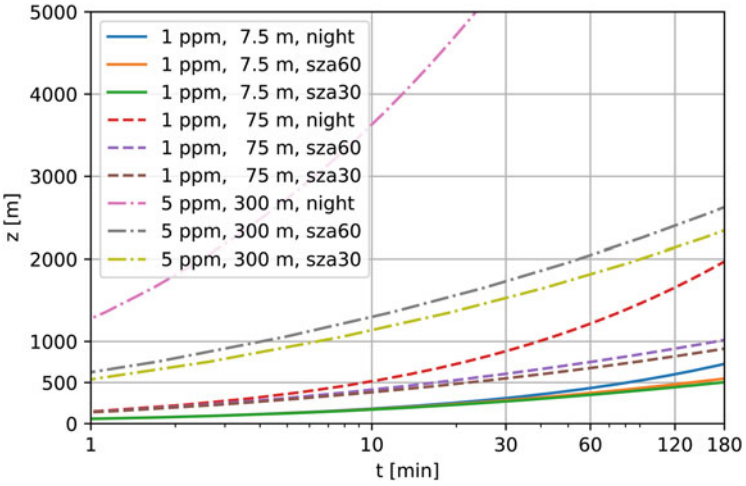


Fig. 15.2 Integration time t required to reach a given altitude z for different background conditions (night, SZA = 60°, SZA = 30°), vertical resolutions (7.5 m, 75 m, 300 m), and measurement precisions (1 ppm, 5 ppm)

Raman tail contribution, and the simulation should be performed with more accurate broadening coefficients. Furthermore, this component of the signal is expected to be negligible at higher altitudes where the Doppler broadening dominates. Nevertheless, due to the difficulty of modelling the broadened tails, in order to have accurate measurements at low altitudes, this contribution to the signal should be better investigated experimentally with measurements slightly below the $2\nu 2$ wavelength (e.g., with the same filter shifted in frequency with angle tuning or with a scanning spectrometer).

The second step was the evaluation of the impact of the unbroadened O_2 lines falling inside the filter transmission ranges. The simulation confirms the calculations done by [7], with less than 1 ppm systematic error due to the twenty-first O_2 roto-vibrational line contribution on the filter A signal. The O_2 contribution on filter B signal is instead in the order of 10%. Further narrowing of the interferential filters or an accurate estimation of the temperature dependency of the lines would be necessary to take advantage of the $\nu 1$ line. Line modeling paired with simultaneous temperature measurements should decrease the uncertainty on the filter B signal to less than 1 ppm/K.

As a third step, the temporal integration necessary to reach a sufficient SNR for filter A during nighttime and daytime was calculated. The results are plotted in Fig. 15.2. The results indicate that the simulated lidar system, provided to have a low overlap height, could perform measurements on the low troposphere gradients with sufficient precision both in daytime and nighttime with an integration time of 1–3 h.

15.4 Conclusions

Preliminary results confirm that a state-of-the-art Raman lidar system dedicated to the measurements of CO_2 profiles could perform measurements in the low troposphere with sufficient precision to estimate gradients due to carbon sources and sinks.

Both $2\nu 2$ and $\nu 1$ lines could be used and the signal contamination attributed to the O_2 Raman lines could be mitigated via line modeling. Further steps include a more accurate theoretical or experimental estimation of the signal contamination due to line broadening and the estimation of the uncertainty for different aerosol types and atmospheric profiles.

References

1. IPCC: Climate change 2021: the physical science basis. In: Contribution of Working Group I to the Sixth Assessment Report of the Intergovernmental Panel on Climate Change. Cambridge University Press, Cambridge (2021)
2. Han, G., Gong, W., Lin, H., Ma, X., Xiang, Z.: Study on influences of atmospheric factors on vertical CO_2 profile retrieving from ground-based DIAL at 1.6 μm. IEEE Trans. Geosci. Remote Sens. **53**, 3221–3234 (2015)
3. Qiu, R., Ge, H., Ma, X., Sha, Z., Tianqi, S., Xu, H., Zhang, M.: CO_2 concentration, a critical factor influencing the relationship between solar-induced chlorophyll fluorescence and gross primary productivity. Remote Sens. **12**, 1377 (2020)
4. Riebesell, M.: Raman Lidar for the remote sensing of the water vapor and carbon dioxide profile in the troposphere (in German) (1990)
5. Ansmann, A., Riebesell, M., Wandinger, U., Weitkamp, C., Voss, E., Lahmann, W., Michaelis, W.: Combined raman elastic-backscatter LIDAR for vertical profiling of moisture, aerosol extinction, backscatter, and LIDAR ratio. Appl. Phys. B Lasers Opt. **55**, 18–28 (1992)
6. Dionisi, D.: Development of a Raman Lidar for the measurement of atmospheric CO_2 concentration (2006)
7. Whiteman, D.N., Rush, K., Veselovskii, I., Cadirola, M., Comer, J., Potter, J.R., Tola, R.: Demonstration measurements of water vapor, cirrus clouds, and carbon dioxide using a high-performance Raman Lidar. J. Atmos. Ocean. Technol. **24**, 1377–1388 (2007)
8. Measures, R.M.: Laser Remote Sensing: Fundamentals and Applications. Wiley, New York (1984)
9. Weitkamp, C. (ed.): Lidar: Range-Resolved Optical Remote Sensing of the Atmosphere. Springer, New York (2005)
10. Tejeda, G., Maté, B., Montero, S.: Overtone Raman spectrum and molecular polarizability surface of CO_2. J. Chem. Phys. **103**, 568–576 (1995)
11. Lemus, R., Sánchez-Castellanos, M., Pérez-Bernal, F., Fernández, J.M., Carvajal, M.: Simulation of the Raman spectra of CO_2: Bridging the gap between algebraic models and experimental spectra. J. Chem. Phys. **141**, 054306 (2014)
12. Gray, L.D., Young, A.T.: Relative intensity calculations for carbon dioxide—IV: calculations of the partition function for isotopes of CO_2. J. Quant. Spectrosc. Radiat. Transf. **9**, 569–589 (1969)
13. She, C.Y., Friedman, J.S.: Atmospheric Lidar Fundamentals: Laser Light Scattering from Atoms and Linear Molecules. Cambridge University Press, Cambridge (2022)

14. Bodhaine, B.A., Wood, N.B., Dutton, E.G., Slusser, J.R.: On Rayleigh optical depth calculations. J. Atmos. Ocean. Technol. **16**, 8 (1999)
15. Anderson, G.P., Clough, S.A., Kneizys, F.X., Chetwynd, J.H., Shettle, E.P.: AFGL (Air Force Geophysical Laboratory) atmospheric constituent profiles (0. 120 km). Environmental research papers. Air Force Geophysics Lab, Hanscom AFB, MA (USA) (1986)

Chapter 16
All Fiber Free-Running Dual-Comb Ranging System

Fu Yang, Yanyu Lu, and Guibin Liu

Abstract Fast, real-time, and high-precision distance measurement is of great significance to satellite tracking, precision equipment manufacturing, gravitational wave detection, and many other fields. As a new measuring tool, optical frequency comb (OFC) has the characteristics of both wide spectral range and narrow linewidth of each comb. It can give full play to its advantages in the field of large-scale and high-precision absolute distance measurement. This chapter introduces an all fiber free-running dual-comb ranging (DCR) system without any mode locking equipments. In this system, the target distance can be adjusted by variable optical fiber delay line. During the signal processing, the peak position of the signal is accurately extracted by tracking the pulse repetition frequency (PRF) jitter of the optical combs and adaptive signal filtering. The PRF of optical frequency comb is about 180 MHz, and the PRF difference is about 1.8 kHz. The ranging accuracy of this dual-comb system can reach a distance precision of 16.2 microns, which can meet the need of high-precision range detection in many fields. The whole ranging system is connected with all fibers and does not need extra mode-locking equipment. The devices are all mature devices in 1550-nm communication band, which ensure the robust stability of the experiment system. The chapter provides a new way for high-precision distance measurement.

Keywords Range detection · Dual-comb · Range precision · Lidar

16.1 Background

Fast, real-time, and high-precision distance measurement is of great significance to satellite tracking precision equipment manufacturing, gravitational wave detection, and many other fields. The traditional ranging method uses the time-of-flight (TOF) method based on transmitting giant pulses. Its advantage is simple structure and

F. Yang (✉) · Y. Lu · G. Liu
Department of Applied Physics, Donghua University, Shanghai, China

© The Author(s), under exclusive license to Springer Nature Switzerland AG 2023

J. T. Sullivan et al. (eds.), *Proceedings of the 30th International Laser Radar Conference*, Springer Atmospheric Sciences,
https://doi.org/10.1007/978-3-031-37818-8_16

mature technology. But the laser peak power is too high so that the pulse PRF will be reduced during the long-range measurement. The distance measurement accuracy can reach only centimeter [1]. The accuracy of CW phase modulation ranging method is super high, and the precision can reach the order of nanometer, but the ambiguity range only reach the order of wavelength [2].

The advent of the OFC as a light source has provided a new choice for ranging and other metrology applications [3], which take into account both high-precision and large ambiguous range. Many ranging systems based on OFC have been proposed, such as TOF method based on optical cross-correlation technology [4]; synthetic wavelength interferometry [5] using different optical modes to generate harmonics of OFC repetition frequency; and dispersion interferometry involves calculating the phase slope of the frequency of the interference spectrum [6]. These methods based on single comb realize absolute distance measurement with certain accuracy, and the device is relatively simple. However, they do not make full use of all comb patterns because it is often difficult to distinguish adjacent comb lines with megahertz to gigahertz mode spacing. Therefore, these ranging methods based on single comb do not combine the advantages of high spectral range, fast pulse rate, and large ambiguity range of OFC [7].

The DCR system solves this problem by using two OFCs with slightly different repetition frequencies to realize multi-heterodyne spectrum and time-resolved interferograms (IGMs) based on comb lines [8]. In other words, the DCR system uses a large number of narrow spectral lines to measure the distance at the same time without any mechanical or electrical scanning devices. This concept has a unique combination of high spectral range coverage, fast measurement speed, and large ambiguity range. In order to obtain high range precision, the two combs are referenced back to an absolute frequency standard or CW lasers to improve the coherence [9–11], which increases the system complexity as well.

This chapter introduces an all-fiber free-running DCR system at 1550 nm with a repetition rate of about 180 MHz and PRF difference about 1.8 kHz. Through unique filtering methods, the high-precision distance information is extracted from the peak position of IGMs in time domain.

16.2 Principle

The DCR method uses two phase-locked optical combs with slight repetition frequency difference as signal light (SIG) and local oscillator light (LO), respectively. By means of asynchronous optical sampling (ASOPS), the multiheterodyne IGMs between the two optical combs is presented at radio frequency (RF) domain [12]. There is no need for any mechanical or electronic scanning device to manually adjust the optical path difference between SIG and LO to realize pulse alignment, which greatly simplifies the experimental system and ensures rapid measurement. The structural schematic diagram of DCR system is shown in Fig. 16.1.

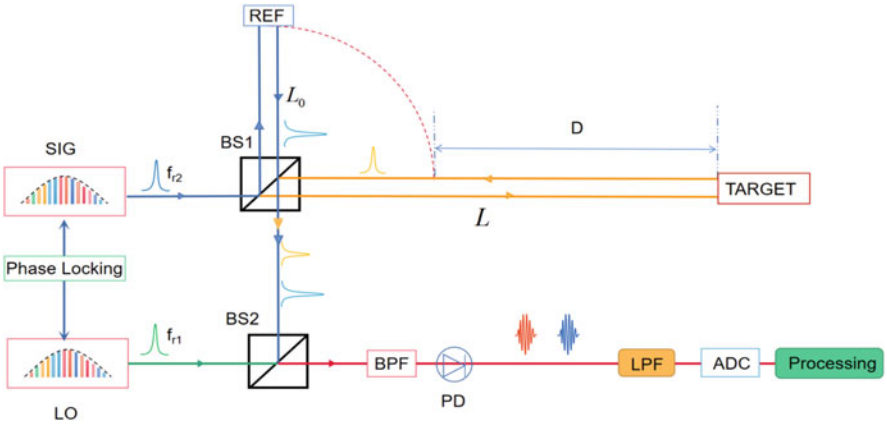


Fig. 16.1 The structural schematic diagram of DCR system

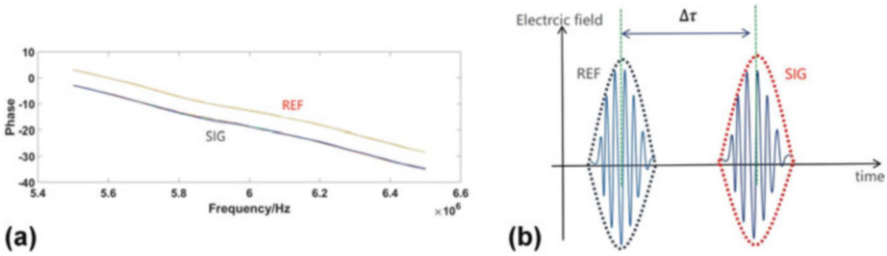


Fig. 16.2 (**a**) The principle of phase method. (**b**) The principle of peak extraction method

As shown in Fig. 16.1, due to the small difference in PRF between the two OFCs, LO laser can realize the optical sampling of two reflected signals (one from REF called REF signal, and the other is from the target called TARGET signal) through ASOPS. Therefore, two IGMs appear in the time domain as shown in Fig. 16.2. The period is IGMs is $T_{\text{update}} = 1/\Delta f_r$. The periodic difference between LO and SIG is $\Delta T_r \approx \Delta f_r / f_{r1}^2$. The optical path difference between REF SIG and TARGET SIG is considered as the target distance D. The BPF and LPF are used for avoiding confusing and aliasing, respectively. There are two ways to extract the target distance D. One is phase method and the other is peak extraction method. The phase method is executed by fast Fourier transform (FFT) of the IGMs to obtain the phase spectrum in the RF domain. Then the time delay $\Delta\tau$ is extracted by obtaining the unwrapped phase slope difference of the two IGMs as shown in Fig. 16.2a. The peak extraction method is to obtain the envelope of the interferograms, then locate the peak position of the envelope, and finally obtain the time delay $\Delta\tau$, as shown in Fig. 16.2b.

After time delay between interferograms $\Delta\tau$ is obtained, the target distance D can be calculated by Eq. 16.1

$$D = \frac{c\Delta\tau}{2n_g}\frac{\Delta f_r}{f_{r1}} \tag{16.1}$$

where c is the light speed in the vacuum and n_g is the group refractive index of the transmitting medium. From Eq. 16.1, the time interval and the target distance is scaled about $\Delta f_r/f_{r1}$ times (about 1e5 in the experiment), which means that the range precision is about 1e5 better than the traditional TOF method. That is why DCR method can make high-precision distance measurement possible.

16.3 Experiment Setup

The experiment diagram of all-fiber free-running DCR system is shown in the Fig. 16.3a, while Fig. 16.3b shows the real experiment system picture, Table 16.1 shows the parameters of the experimental system.

The system is all constructed by optical fibers. Two free-running OFC lasers are used as laser sources. Compared with Fig. 16.1, the path through fiber 2 is treated as REF path, and the path through fiber 1 is used as the target path. The PRF of both two OFCs is about 181 MHz, while the PRF difference is about 1.8 kHz, so the scaling factor is about 1e5. The variable delay line (VDL) is used to adjust the optical path difference for ranging experiment. A frequency meter is used to monitor real-pulse repetition rate of the two optical combs. A dense wavelength division multiplexing (DWDM) is used as the BPF in the experiment system. The analog-to-digital converter (ADC) converts the analog signal into digital signal, and the subsequent signal processing is carried out in the computer.

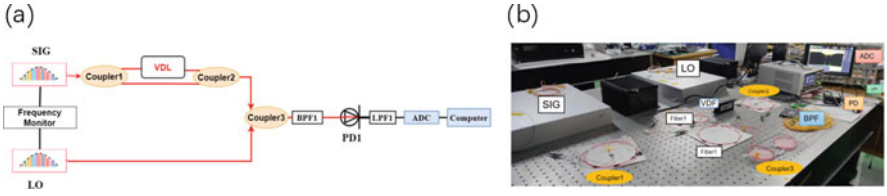


Fig. 16.3 (**a**) Experiment diagram of DCR system. (**b**) Real experiment system

Table 16.1 Parameters of the experimental system

Devices	Parameters	Devices	Parameters	Devices	Parameters
Comb1 (SIG)	PRF: 181.437 MHz Output: 20 mW 3 dB width: 51.7 nm	VDL	Distance resolution: 50 μm	BPF(DWDM)	Bandwidth:2 nm
Comb2 (LO)	PRF: 181.439 MHz Output: 20 mW 3 dB width: 107.6 nm	LPF	3 dB 80 MHz	Sampling rate	2 ~ 10G

16.4 Experiment Results

The IGMs of one RF period is shown in Fig. 16.4a. During the experiment, both peak extraction method and phase slope extraction method are tested. Because the optical comb is in a completely free running state, it is hard to distinguish the slope of the unwrapped phase spectrum. As a result, the phase method is not adopted in the following signal process. For the peak extraction method, two methods are used.

The first scheme is adaptive filtering. In fact, the effective RF bandwidth of the spectrum after filtered by DWDM is only about 2 MHz. However, the cut-off frequency of LPF is 80 MHz. A BPF is applied to the digital data to filter the effective signal, and then a relative cleaner IGMs in the time domain are got, as shown in Fig. 16.4b, which shows that the background noise is greatly reduced. Then the peak position can be located more accurately.

The second scheme is called fftfilt method, which is realized by "fftfilt" function of MATLAB, using the overlap-add method for FIR filtering based on FFT. This

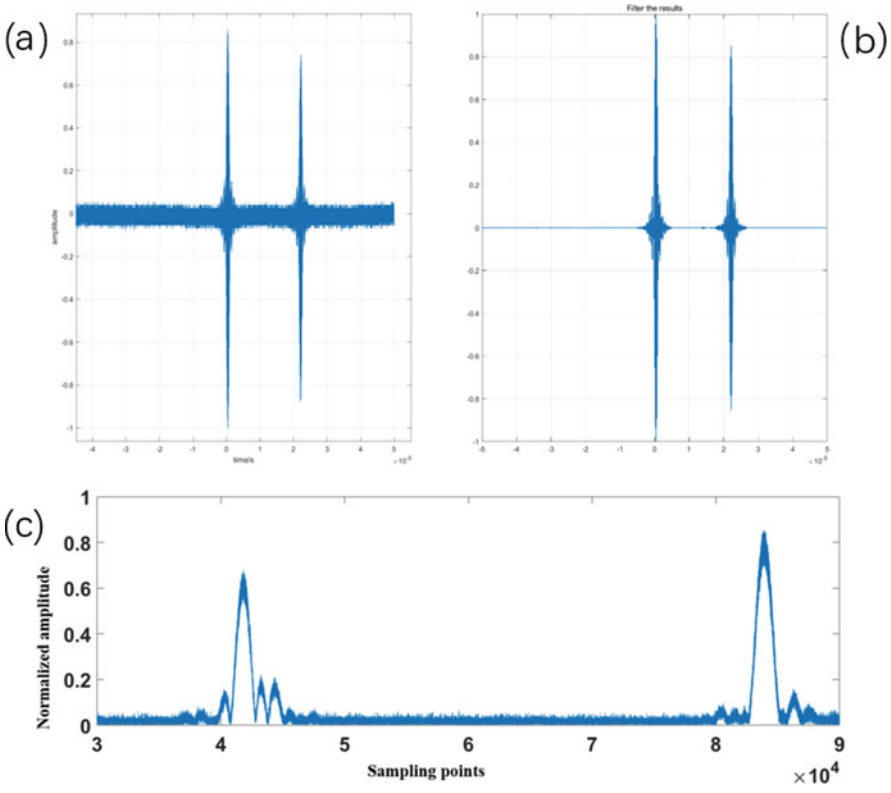


Fig. 16.4 (**a**) Original time domain signal. (**b**) Time domain signal after adaptive filtering. (**c**) Envelope of IGM window after Hilbert transform and fftfilt

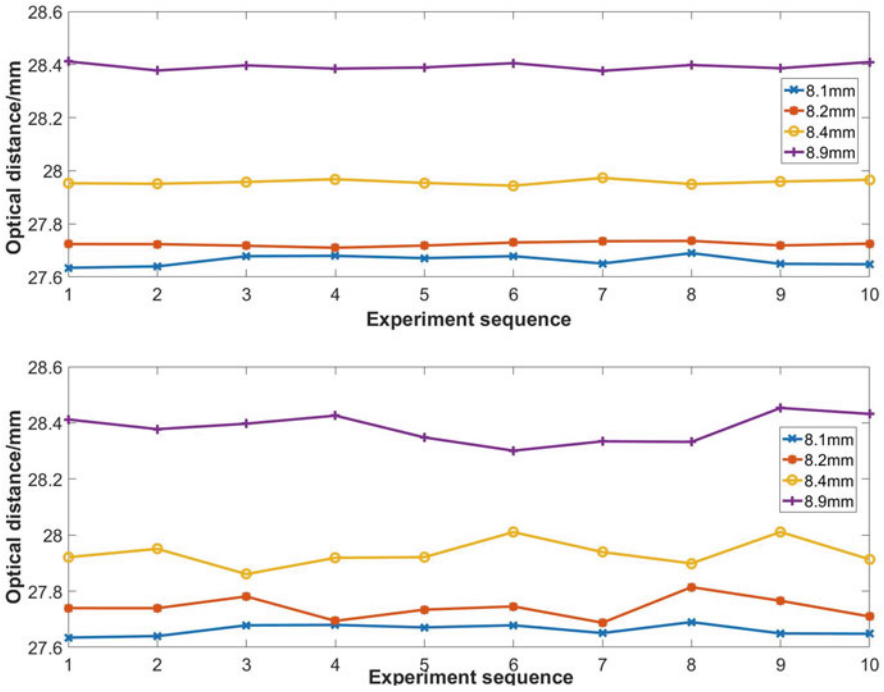


Fig. 16.5 (**a**) Adaptive filtering method 10 times measurement results; (**b**) fftfilt method 10 times measurement results

function can directly filter the time-domain signal without phase shift based on FFT, then the envelope of IGM can be executed by Hilbert transform. Finally, the envelope peak is executed from the envelope, and peak position can be located easily in a windowed IGM as shown in Fig. 16.4c.

Set the distance parameter of VDL to 8.1 mm, 8.2 mm, 8.4 mm, and 8.9 mm, respectively, and repeat the experiment for 10 times. Take the average distance as the measurement result, and the standard deviation (std) is treated as the measurement precision. By using the adaptive filter method, the measurement results are shown in the Fig. 16.5a, while the result obtained by the fftfilt method is shown in the Fig. 16.5b.

From Fig. 16.5 and Table 16.2, it can be seen that in both two methods, the measurement results increase with the VDL set values. The measurement precisions of the adaptive method are around 20 um, while around 50 um for the fftfilt method. The average target distance of the two methods are almost the same; the deviation is around 1%. A linear fit is conducted between the measurement average optical distance and VDL distance, as shown in Fig. 16.6.

It can be seen that the two process method agrees very well, and the slope of the fit line is about 0.93. In theory, the slope should be 1. The slope derivation is probably due to the manual error of VDL reading. The average results of multiple

Table 16.2 Measurement results of the two process methods

Filtering method	8.1 mm	8.2 mm	8.4 mm	8.9 mm
Adaptive (Ave mm/std. um)	27.65 mm/30 um	27.72 mm/8 um	27.95 mm/11 um	28.40 mm/14 um
Fftfilt (Ave mm/std. um)	27.65 mm/68 um	27.74 mm/39 um	27.94 mm/38 um	28.40 mm/47 um

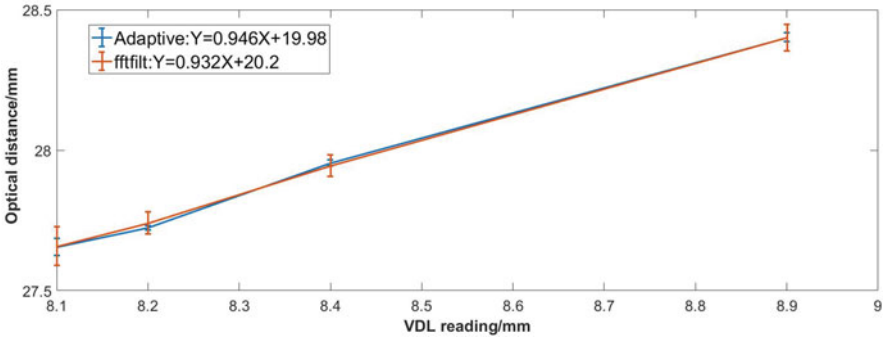


Fig. 16.6 Ranging results of different methods

groups of data are also shown in Fig. 16.6. From the linear fitting line in Fig. 16.6, the linearity between the ranging results and VDL readings is good, and the ranging results obtained by the two filtering methods are highly consistent. The standard deviation has been marked on the figure with error bars. The average standard deviation of adaptive filtering method is 16.2 μm, while the average standard deviation of fftfilt method is 48.5 μm. Although on the scale of micron, the measurement precision of the adaptive method is much smaller than the precision of fftfilt because of the noise corruption, which means the adaptive method have more advantages in noise reduction.

16.5 Conclusion

In conclusion, this chapter demonstrates an all-fiber free-running DCR system, which can realize a range precision about 16.2 um. The system has the advantages of high precision, fast measurement rate, large ambiguity range, simple system structure, and eye safe.

Acknowledgments The research is supported by No. 22ZR1402600 from the Shanghai Natural Science Foundation, Shanghai 2021 "Science and Technology Innovation Plan" Social Development Science and Technology Research Project(21DZ1205402). We also acknowledge the Key Laboratory of Space Laser Communication and Detection Technology of Shanghai Institute of Optics and Fine Mechanics, Chinese Academy of Science for offering the experiment platform.

References

1. Qin, P., Chen, W., Song, Y.J., et al.: Long range absolute distance measurement based on femtosecond laser balanced optical cross-correlation. Acta Phys. Sin. **61**(24), 240601
2. Yang, F., Shang, J., He, Y., Zhan, Y., Chen, W.: Advanced detection methods of spaceborne laser altimeter. In: Imaging and Applied Optics, Applied Industrial Optics: Spectroscopy, Imaging and Metrology, AIO, Seattle, JTu4A. 1 (2014)
3. Newbury, N.R.: Searching for applications with a fine-tooth comb. Nat. Photonics. **5**(4), 186–188 (2011)
4. Lee, J., Kim, Y.J., Lee, K., et al.: Time-of-flight measurement with femtosecond light pulses. Nat. Photonics. **4**(10), 716–720 (2010)
5. Liao, L., Yi, W.M., Yang, Z.H., et al.: Synthetic-wavelength based absolute distance measurement using heterodyne interferometry of a femtosecond laser. Acta Phys. Sin. **65**, 14 (2016)
6. Joo, K.N., Kim, S.W.: Absolute distance measurement by dispersive interferometry using a femtosecond pulse laser. Opt. Express. **14**(13), 5954 (2006)
7. Zhu, Z., Wu, G.: Dual-comb ranging. Engineering. **4**(6), 7 (2018)
8. Coddington, I., Swann, W.C., Nenadovic, L., et al.: Rapid and precise absolute distance measurements at long range. Nat. Photonics. **3**(6), 351–356
9. Wu, G., Qian, Z., Shen, L., et al.: Experimental optimization of the repetition rate difference in dual-comb ranging system. Appl. Phys. Express. **7**(10), 106602 (2014)
10. Wu, H., Zhao, T., Wang, Z., et al.: Long distance measurement up to 1.2 km by electro-optic dual-comb interferometry. Appl. Phys. Lett. **111**(25), 251901 (2017)
11. Zhao, X., Qu, X., Zhang, F., et al.: Absolute distance measurement by multi-heterodyne interferometry using an electro-optic triple comb. Opt. Lett. **43**(4), 807 (2018)
12. Shi, Y., Dingtong, H., Xue, R., Ziling, W., Dong, J., Tian, H., Wang, C., Wang, J., Minglie, H., Song, Y.: High speed time-of-flight displacement measurement based on dual-comb electronically controlled optical sampling. Opt. Express. **30**, 8391–8398 (2022)

Chapter 17
gPCE Uncertainty Quantification Modeling of LiDAR for Bathymetric and Earth Science Applications

Alexandra K. Wise, Kevin W. Sacca, and Jeffrey P. Thayer

Abstract Most LiDARs, though precise, are vulnerable to position and pointing errors, and while fidelity of location/pointing solutions can be extremely high, determination of uncertainty remains relatively basic. As a result, NASA's 2021 Surface Topography and Vegetation (STV) Incubation Study Report lists vertical, horizontal, and geolocation accuracy as an associated Science and Application Traceability Matrix product parameter for most identified Science and Application Knowledge Gaps (Surface Topography and Vegetation Incubation Study Team, 2021). Currently, standard uncertainty quantification (UQ) approaches are plagued by simplifying approximations, ignored covariances, as well as improperly modeled (often exclusively Gaussian) uncertainty sources. The presented generalized polynomial chaos expansion (gPCE)-based method has wide-ranging applicability to improve vertical, horizontal positioning and geolocation uncertainty estimates, for all STV disciplines, by more completely describing total aggregated uncertainties, from system level to geolocation, and intrinsically accounting for covariance between variables (without the need to manually construct a covariance matrix). gPCE also does not rely on many of the simplifying assumptions used in standard methods. Most importantly, it supports a number of additional (non-Gaussian) uncertainty sources and arbitrarily high orders of variable cross-moments. gPCE is presented here, for the bare Earth case, as a proof of concept.

Keywords Uncertainty quantification · Bathymetric LiDAR · TPU

Supported by NASA FINESST Award #80NSSC19K1351 and #80NSSC21K1597.

A. K. Wise (✉) · K. W. Sacca · J. P. Thayer
University of Colorado, Boulder, CO, USA
e-mail: alexandra.wise@colorado.edu

© The Author(s), under exclusive license to Springer Nature Switzerland AG 2023

J. T. Sullivan et al. (eds.), *Proceedings of the 30th International Laser Radar Conference*, Springer Atmospheric Sciences,
https://doi.org/10.1007/978-3-031-37818-8_17

17.1 Motivation

NASA's 2021 Surface Topography and Vegetation (STV) Incubation Study Report lists vertical, horizontal, and geolocation accuracies as associated Science and Application Traceability Matrix product parameters for most identified Science and Application Knowledge Gaps, highlighting one of the primary shortcomings of modern LiDARs [5]. Though the precision instrument location, pointing, and subsequent geolocation capabilities of modern LiDAR systems are very high, many systems are vulnerable to position and pointing errors, as even small deviations from the expected principal axis lead to projection errors on target [1–3]. Currently, uncertainty quantification (UQ) remains relatively basic or non-existent for most instruments. This is likely due to the difficulty posed by determining uncertainties and the dubious fidelity of common methods, such as total propagated uncertainty (TPU) and variations thereof. In fact, a known issue (since 2019) of the ICESat-2 Global Geolocated Photon data set (ATL03) has been the lack of dynamically calculated uncertainty estimates [4]. TPU methods, while computationally tractable, are often plagued by simplifying approximations and ignored covariances, potentially leading to under- or over-reporting of uncertainty estimates. Additionally, uncertainty sources are often exclusively modeled as Gaussian, inaccurately capturing some variable distributions, e.g., in the case of bathymetric LiDARs, wave spectral distributions are better described by Gamma distributions, which are supported under gPCE.

The presented research addresses specific knowledge gaps in LiDAR measurement uncertainty through a more complete description of total aggregated uncertainties, from system level to geolocation, by applying a generalized polynomial chaos expansion (gPCE)-based UQ approach. This method has wide-ranging applicability to improve vertical and horizontal positioning, and geolocation uncertainty estimates, for all STV disciplines. gPCE can do so, by accounting for a number of factors, including covariances between variables (without manually constructing a covariance matrix), by properly representing input variable uncertainty distributions, and by minimizing the number of required simplifying assumptions. This is done by constructing and analyzing a surrogate model of the LiDAR system and its components (including platform) and subsequently applying the results of the model to the data directly. In a sense, gPCE can be thought of as a combination of Monte Carlo (MC) and TPU methods, in which the LiDAR system is modeled over a range of possible inputs (as in MC methods), the results are analyzed and converted into a set of equations that can propagate uncertainties, and then these equations (as in TPU) are used to calculate individual uncertainties for each point in a point cloud. Point-wise positioning uncertainty determination using gPCE is less computationally expensive than Monte Carlo methods and more tractable for most dimensionalities of interest (roughly from 3 to 20+ input variables). gPCE also does not rely on simplifying assumptions used in typical TPU methods (most importantly, a number of non-Gaussian uncertainty sources and an arbitrarily high order of variable cross-moments can be represented). Finally, a key attribute of this

approach is that global sensitivity analysis (GSA), after obtaining gPCE coefficients, is trivial and nearly costless to compute. GSA of system configurations/uncertainty is a powerful tool to design and develop LiDAR systems with the measurement requirements integrated directly into the design solution, as well as in the efficient operation and management of pre-existing LiDAR systems. gPCE is presented here, for the bare-Earth use case as a proof of concept, with plans to expand to a bathymetric use case to demonstrate technique advantages due to complexities introduced by wave structure, roughness, entry angle, and water refractive index.

17.2 Generalized Polynomial Chaos Expansion

$$\hat{\vec{u}}(\vec{y}) = \sum_{i=0}^{P} c_{\vec{j}_i} \Psi_{\vec{j}_i}(\vec{y}) + \epsilon_{\hat{\vec{u}}}. \tag{17.1}$$

The generalized polynomial chaos expansion, shown in Eq. 17.1, can be thought of as analogous to the more familiar Fourier series expansion. It consists of a truncated infinite series of coefficients, $c_{\vec{j}_i}$, and orthogonal basis functions, $\Psi_{\vec{j}_i}$ (more accurately speaking, however, it is a Karhunen–Loève expansion, with error in the expansion $\epsilon_{\hat{\vec{u}}}$). The basis functions, as shown in Eq. 17.2, are the product of a number of Askey polynomial functions (of varying order) in a given variable (different Askey polynomials are chosen for different variable distributions).

$$\Psi_{\vec{j}_i}(\vec{y}) = \psi_{j_{i,1}}(y_1) \cdot \psi_{j_{i,2}}(y_2) \cdot \ldots \cdot \psi_{j_{i,d}}(y_d). \tag{17.2}$$

The ability to use multiple, and different, basis functions for different input variables, y_i, allows gPCE to avoid the assumption that all variables are Gaussian-distributed and is central to the convergence of the method. In this investigation, we make the choice to represent input variables in the form $y_i = x_i + \omega_i$, such that the deterministic and stochastic components of each input can be treated individually. This allows us to numerically integrate (computationally efficiently, thanks to gPCE's properties) over all stochastic components at particular deterministic components (data points), in order to find the error in a given measurement.

$$\underbrace{\begin{matrix}\vec{y}_1 \\ \vdots \\ \vec{y}_K\end{matrix}}_{\text{Input Samples}} \xrightarrow[\text{Simulations}]{\text{LiDAR System}} \underbrace{\begin{matrix}\vec{u}(\vec{y}_1) \\ \vdots \\ \vec{u}(\vec{y}_K)\end{matrix}}_{\text{Solution Samples}} \xrightarrow[\text{Invert to find } c_{\vec{j}_i}]{\text{Generate } \Psi_{\vec{j}_i}(\vec{y}_k),} \hat{\vec{u}}(\vec{y}) \xrightarrow[\text{LiDAR Data}]{\text{Apply to}} \hat{x}_{ph}, \sigma_{\hat{x}}, \ldots \tag{17.3}$$

Though it is possible to solve for $c_{\vec{j}_i}$, the expansion coefficients directly, this approach tends to be difficult due to the large number of terms in the expansion.

However, similar results can be had with other methods, such as inversion. In this investigation, the workflow shown in Eq. 17.3 is used: First, a large number of input samples are generated, then solution samples are calculated from these inputs (using the same algorithm as might be applied to real data), and finally, the basis functions are calculated at the input samples and the system is inverted to find the coefficients. Once the gPCE model is found, it (or a truncated version of it) can then be applied to the real LiDAR data, and the model can be used to calculate the quantities of interest, such as the "bounce-point" location, the error in that value, and other quantities of interest, at little computational cost.

17.3 Preliminary Topographic LiDAR gPCE Results

Results presented here were generated with the gPCE method introduced in the previous section, using the best analog for the ICESat-2 Photon Bounce-Point Geolocation Algorithm we could generate (and compared to actual ICESat-2 data), without direct access to either the ICESat-2 raw data or algorithm. Certain simplifications to this algorithm were made, e.g., atmospheric delay correction is not calculated, in order to advance this proof of concept. gPCE, like any error model, relies heavily on the completeness of the system and detector response description. Model fidelity, even in the face of algorithm simplifications, appears promising but requires further investigation beyond this proof of concept. ICESat-2 ATL02 and ATL03 data were used to inform the input variable ranges in order to generate input variable samples. Due to space constraints, this section contains only a brief overview of the most important results generated.

The gPCE technique, while still being actively developed and improved for use with LiDAR systems, yielded several results indicating the potential utility of the technique: Fig. 17.1 shows the relative significance of gPCE coefficients, generated by this technique, for the photon bounce-point location height component. Note the large difference between the most and least significant terms ($\approx$50 orders of magnitude). In fact, only approximately 40 terms of 4850 had a relative significance greater than 1 ppm, indicating that the gPC-expansion achieved satisfactory convergence, and that a further truncated expansion (with small terms removed) can still yield a high-fidelity solution (one potential significance truncation point is shown at the 100-ppt significance level).

A further significant result, shown in Fig. 17.2, is the ability of this technique to generate a high-fidelity assessment of input–output parameter relationships. Showing the same data points as Figs. 17.1, 17.2 has been changed to display the total order in any given input parameter via the color of each point, as one might be interested in for design purposes, and shows a few interesting results. Namely, that the roll, pitch, **and yaw** pointing angles (and their uncertainties) show a greater significance level than the spacecraft position (in Earth-centered inertial coordinates). The yaw pointing angle result, in particular, is a surprising one, given that the ICESat-2 instrument is a near-nadir pointing instrument, which intuitively

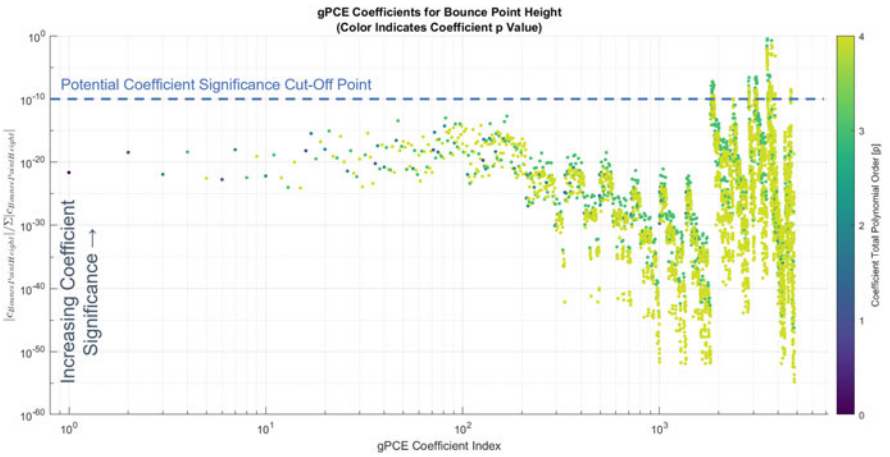


Fig. 17.1 gPCE coefficient significance for ICESat-2 Photon Bounce-Point Height (above WGS84), colors indicate coefficient polynomial order (violet = 0th to yellow = 4th order)

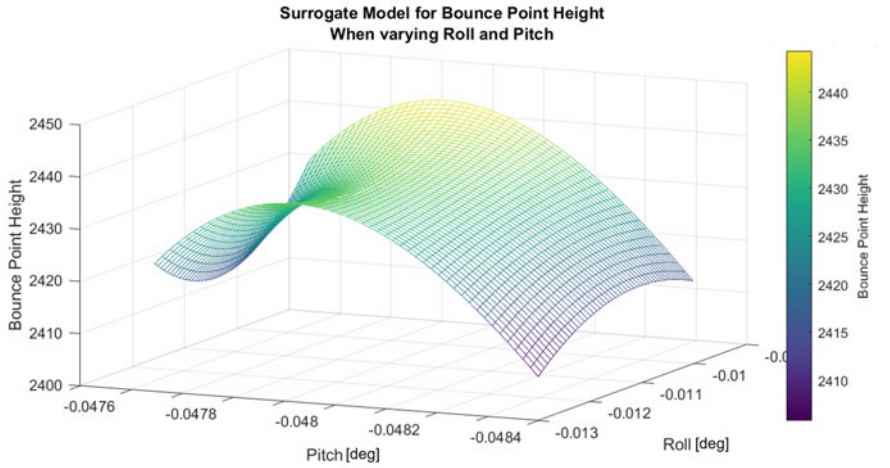


Fig. 17.2 gPCE coefficient relative significance for ICESat-2 photon bounce-point height (above WGS84), colors indicate coefficient polynomial order in a given variable (violet = constant in a given variable, yellow = 4th order in a given variable)

should not be significantly impacted by yaw errors; this result is likely due to the slight off-nadir components introduced by pitch and roll angles, which introduce a beam sweeping effect when the yaw angle is changed.

Figure 17.3 shows an important capability of the gPCE technique, namely that various relationships between variables can be individually investigated. The gPCE bounce-point height is evaluated at a particular set of input variables, which are all held constant, except for roll and pitch, which are allowed to vary. The resulting

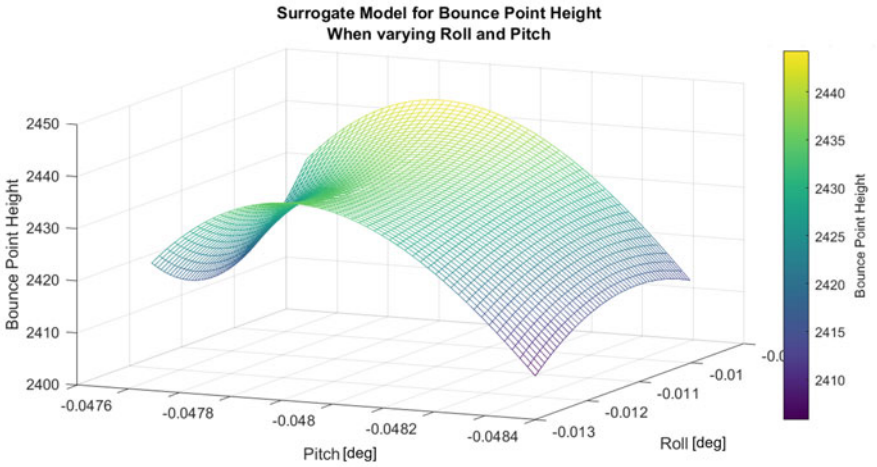


Fig. 17.3 gPCE model evaluated at a single data point with all variables held constant except roll and pitch, to show bounce-point height sensitivity to roll, pitch, and roll+pitch effects. (Roll, pitch ranges kept broad for illustrative purposes)

figure allows us to inspect visually the effect of the errors in each of these variables and how they are related; for example, near the center of the figure, a given set of roll and pitch will clearly result in a much smaller height error, than at any of the four corners of this figure. This result demonstrates the potential of the gPCE method to not only impact the design of new systems by revealing input–output relationships between variables (shown above), but also the potential to supplement or improve the data analysis pipelines for existing systems. Of additional interest is the fact that unlike the intuitive, bowl-shaped figure that may be expected when roll, pitch are varied (and ToF is held constant), the saddle shape shown in Fig. 17.3 more closely matches the physics of the ATLAS Photon Bounce-Point Geolocation Algorithm. Specifically, ICESat-2's velocity (and associated motion during the photon ToF) requires that the length of each leg of the round trip be allowed to vary independently, causing this effect.

17.4 Concluding Remarks

gPCE, with its ability to model covariances (as well as higher-order cross-moments), its reduced set of assumptions (over commonly used methods), and its ability to natively represent non-Gaussian error sources, shows promise to improve vertical, horizontal, and geolocation accuracy for a wide range of STV disciplines. Meanwhile, all of this is accomplished with a technique and code that is portable and extensible to a wide variety of systems, platforms, and LiDAR processes and

data products (e.g., bathymetric, atmospheric, topographical data, etc.) to enhance existing scientific returns and optimize future research.

Acknowledgments The authors would like to thank Professor Alireza Doostan, for his assistance in applying the gPCE Method to Air- and Spaceborne Topo-Bathymetric LiDAR Measurements, and the NASA FINESST Program for funding support via NASA FINESST Awards #80NSSC19K1351 and #80NSSC21K1597.

References

1. Bae, S., Helgeson, B., James, M., Magruder, L., Sipps, J., Luthcke, S., Thomas, T.: Performance of ICESat-2 precision pointing determination. Earth Space Sci. **8**(4), 1–8 (2021). https://doi.org/10.1029/2020EA001478
2. Luthcke, S.B., Thomas, T.C., Pennington, T.A., Rebold, T.W., Nicholas, J.B., Rowlands, D.D., Gardner, A.S., Bae, S.: ICESat-2 pointing calibration and geolocation performance. Earth Space Sci. **8**(3), 1–11 (2021). https://doi.org/10.1029/2020EA001494
3. Luthcke, S.B., Zelensky, N.P., Rowlands, D.D., Lemoine, F.G., Williams, T.A.: The 1-centimeter orbit: Jason-1 precision orbit determination using GPS, SLR, DORIS, and altimeter data. Mar. Geod. **26**(3–4), 399–421 (2003). https://doi.org/10.1080/714044529
4. Neumann, T.A., Brenner, A., Hancock, D., Robbins, J., Saba, J., Harbeck, K., Gibbons, A., Lee, J., Luthcke, S.B., Rebold, T., et al.: ICESat-2 ATL03 Known Issues. Tech. Rep. January 2021, NASA (2021). https://nsidc.org/sites/default/files/icesat2_atl03_known_issues_v004.pdf
5. Surface Topography and Vegetation Incubation Study Team: Observing Earth's Changing Surface Topography & Vegetation Structure. Tech. rep., NASA (2021)

Chapter 18
When Can Poisson Random Variables Be Approximated as Gaussian?

Matthew Hayman, Willem J. Marais, Hristo G. Chipilski, Robert A. Stillwell, and Scott M. Spuler

Abstract In photon counting LiDAR, photon detection is generally well described as a Poisson point process as long as photon arrival rates are sufficiently low to avoid significant nonlinear effects in the detection chain (e.g., deadtime). In general, it is straightforward to employ the Poisson-negative log-likelihood as a noise model in order to obtain a maximum likelihood estimate of photon counting LiDAR data. However, data assimilation methods employing Kalman filters (KF) and some processing methods such as optimal estimation method (OEM) were originally designed for observational data with Gaussian distributed noise, thus allowing for closed-form solutions. A common assumption when applying these methods to photon counting LiDAR data is that, by the central limit theorem, the Poisson distributed photon counts follow Gaussian distributions. While this approximation is technically correct at high photon counts (assuming linear detection), the accuracy trade-off of the approximation is not always clear and is likely to depend on the particular estimation problem. In this chapter, we investigate a few simple cases and suggest areas for further research.

Keywords Signal processing · Gases · LiDAR technology

18.1 Introduction

Photon counting is commonly employed in instruments requiring low light detection such as atmospheric LiDAR. One such instrument is the MicroPulse DIAL (MPD) that can perform retrievals of atmospheric constituents such as water vapor, backscatter ratio, and temperature while employing eye-safe (class M1) low-pulse

M. Hayman (✉) · H. G. Chipilski · R. A. Stillwell · S. M. Spuler
National Center for Atmospheric Research, Boulder, CO, USA
e-mail: mhayman@ucar.edu

W. J. Marais
Space Science Engineering Center, University of Wisconsin-Madison, Madison, WI, USA

© The Author(s), under exclusive license to Springer Nature Switzerland AG 2023

J. T. Sullivan et al. (eds.), *Proceedings of the 30th International Laser Radar Conference*, Springer Atmospheric Sciences,
https://doi.org/10.1007/978-3-031-37818-8_18

energy lasers. In addition, practical assessments for space-borne water vapor LiDAR have determined that photon counting would likely be required for such a mission.

Maximum likelihood estimation (MLE) is increasingly employed in an effort to improve LiDAR data products by more efficiently leveraging the information content, constraints, and uncertainties in LiDAR signals. However, unlike conventional methods, MLE requires knowledge of the LiDAR detection noise probability density function (PDF).

The PDF for photon counting within low photon flux regimes is known to be accurately described by a Poisson PDF

$$P(y;\alpha) = \frac{\alpha^y e^{-\alpha}}{y!}, \tag{18.1}$$

where y is the number of observed photon counts in an observation and α is the mean number of photon counts. The maximum likelihood estimate of α, given observation y photon counts, is that which minimizes the negative log-likelihood (NLL) of the noise PDF. From the definition in Eq. (18.1), we can define the NLL of a Poisson random variable as

$$\mathcal{L}(\alpha) = \sum_i \left[\alpha_i - y_i \ln \alpha_i\right], \tag{18.2}$$

where α is the mean of the Poisson PDF and either is the estimated variable or a function of the estimated variable. Note that in the definition of the NLL, the summation is included because we have expanded the estimation problem to consider multiple statistically independent observations and corresponding estimates.

While the noise model for photon counting LiDAR (within low photon flux regimes) is known to be accurately modeled by a Poisson PDF, this distribution presents a challenge to some processing approaches that are derived based on separability between signal and noise (e.g., the observation can be modeled $y = \mu + \epsilon$, where μ is the true mean signal and ϵ is noise generated by a random process). Poisson noise does not conform to this separability, because the noise is inherently signal dependent. However, if the noise can be approximated as Gaussian, separability might be reasonably approximated. Data assimilation techniques such as Kalman Filtering [1] and data processing techniques such as the Optimal Estimation Method (OEM) [2, 3] generally employ this assumption, and therefore, the validity of these approaches depends on the validity of this assumption.

18.2 Gaussian Approximation

The PDF of a Gaussian random variable is parameterized by the mean μ and variance σ^2 and given by

$$P(y;\mu,\sigma^2) = \frac{1}{\sqrt{2\pi\sigma^2}} \exp\left(-\frac{(y-\mu)^2}{2\sigma^2}\right). \tag{18.3}$$

The NLL of Gaussian observations is then given by

$$\mathcal{L}(\mu,\sigma^2) = \sum_i \left[\frac{1}{2}\ln(2\pi\sigma_i^2) + \frac{(y_i-\mu_i)^2}{2\sigma_i^2}\right]. \tag{18.4}$$

In this case, we do not assume knowledge of either of the parameters that define the Gaussian distribution. However, if we know the variance, the NLL collapses into a familiar form of weighted mean square error (where we omit constant terms because they are not relevant to optimization)

$$\mathcal{L}(\mu) = \sum_i \frac{(y_i-\mu_i)^2}{2\sigma_i^2}. \tag{18.5}$$

In approximating a Poisson random number as Gaussian, the mean and variance are both defined by the Poisson mean α. This means the variance and mean of the Gaussian are unknown and a strict interpretation of this approximation gives the following NLL based on Eq. (18.4)

$$\mathcal{L}(\alpha) = \sum_i \left[\frac{1}{2}\ln(2\pi\alpha_i) + \frac{(y_i-\alpha_i)^2}{2\alpha_i}\right]. \tag{18.6}$$

We will refer to this approximation as the "Gaussian Approximation."

While the variance of a Poisson random number is $\sigma^2 = \alpha$, it is commonly approximated by the photon counts themselves $\sigma^2 \approx y$. Though pervasive in the LiDAR community, such an approximation is not "strictly valid" [2]. The approximation does, however, allow the use of Eq. (18.5) to obtain a separable noise model with the following NLL:

$$\mathcal{L}(\alpha) = \sum_i \frac{(y_i-\alpha_i)^2}{2y_i}. \tag{18.7}$$

We will refer to this approximation as the "Separable Gaussian Approximation."

18.3 Simulations

In this chapter, we perform some simple simulations to assess the impact of approximating Poisson noise as Gaussian in estimation problems.

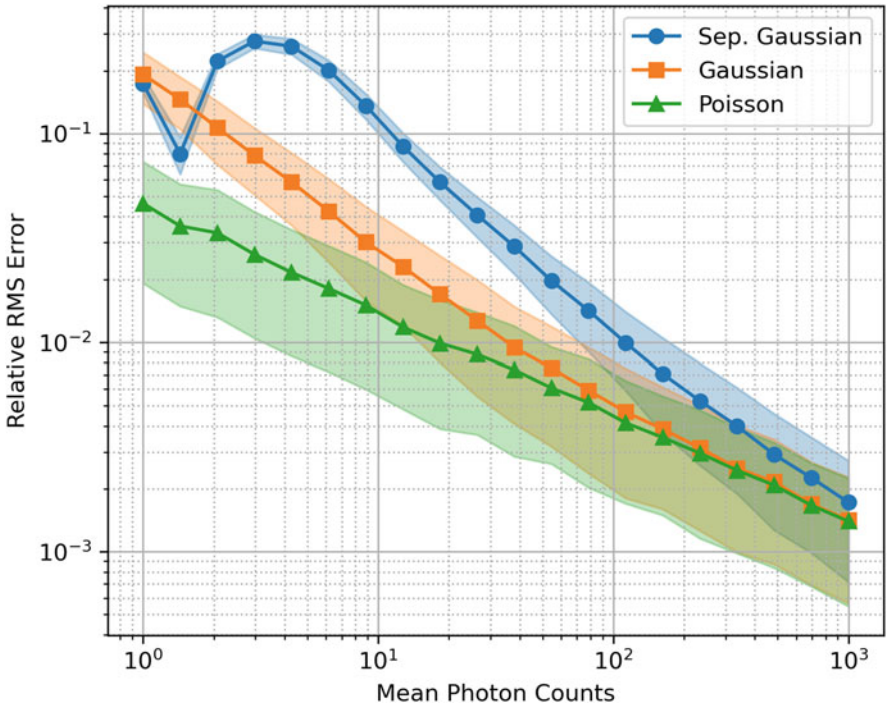


Fig. 18.1 Comparison of relative root mean square error for estimating α from 500 observations as a function of different values of α. The shaded regions indicate the standard deviation of those estimates (as obtained over 500 iterations). The label "Gaussian" refers to the approximation in Eq. (18.6) and "Sep. Gaussian" in Eq. (18.7)

In the first case, we observe 500 Poisson distributed samples parameterized by a constant mean α. We apply maximum likelihood estimation assuming each of the noise models estimate the true signal and repeat this 500 times to assess the accuracy and precision of each assumed noise model.

A summary of the mean relative errors and the standard deviations of each noise model is shown in Fig. 18.1. As expected, the errors resulting from the Gaussian approximations decrease as α increases. Above $\alpha = 100$ counts, the Gaussian approximation appears to be quite similar to the Poisson noise model, where both its statistical variation and mean estimate have largely converged. By contrast, while the mean of the separable Gaussian approximation is approaching the Poisson estimate at the highest photon counts ($\alpha = 1000$ counts), its statistical error still seems struggle to reflect the statistical errors in the Poisson estimates. It is important to note that because the separable Gaussian approximation fails to reflect actual uncertainties in the Poisson estimate, methods such as OEM do not categorically allow for complete inventory of the systematic uncertainties in a retrieval, as asserted in [3].

From this simple analysis, it is clear that the separable Gaussian approximation requires a very large number of photon counts before it can be treated as a valid approximation for Poisson noise. We should emphasize that this simple simulation represents the most optimistic retrieval, where nonlinear data products tend to be more sensitive to biases and errors in noise models.

In an effort to further evaluate the impact of assumed noise models on a LiDAR retrieval, we simulate an exponential decay signal and attempt to retrieve the amplitude and time constant from the noisy observations. Recovery of the time constant is similar to estimating optical depth from a LiDAR signal. The signal model is

$$f(t) = be^{at}, \tag{18.8}$$

where we want to estimate the amplitude b and the decay constant a. The simulation takes place in the time (t) domain over 0 to 1 ms at a 1 μs sample period. We evaluated amplitudes from 100 to 10,000 photon counts and the decay constant from 10^3 to 10^5 s^{-1}. We repeated each simulation case 500 times. The average relative errors of both estimated terms are reported in Fig. 18.2 for each noise model considered here.

As we might expect, the Poisson noise model performs best across all of the simulated cases considered here. Notably, at small decay constants, the Gaussian approximation performs relatively well. The separable Gaussian approximation appears to perform better than the Gaussian approximation in a band of decay constants between 10^4 s^{-1} and 3×10^4 s^{-1}; however, its error blows up for larger decay constants and shows more errors below. The significant sensitivity to the decay constant is probably the result of very low photon counts in the tails of the observation curve. When the exponential decays rapidly, a larger part of the observations is in the low photon count regime where we already showed in the previous simulations the approximations are the least accurate.

While generally the Gaussian approximation produces more reasonable results over a larger domain, the practical benefits of such an approximation are not clear since it does not enable a separable error model. One might just as easily use a Poisson noise model for estimation. However, evaluating the Gaussian approximation does serve to help separate the impact of assuming a Gaussian distribution versus the impact of assuming the variance can be approximated by the observed photon counts.

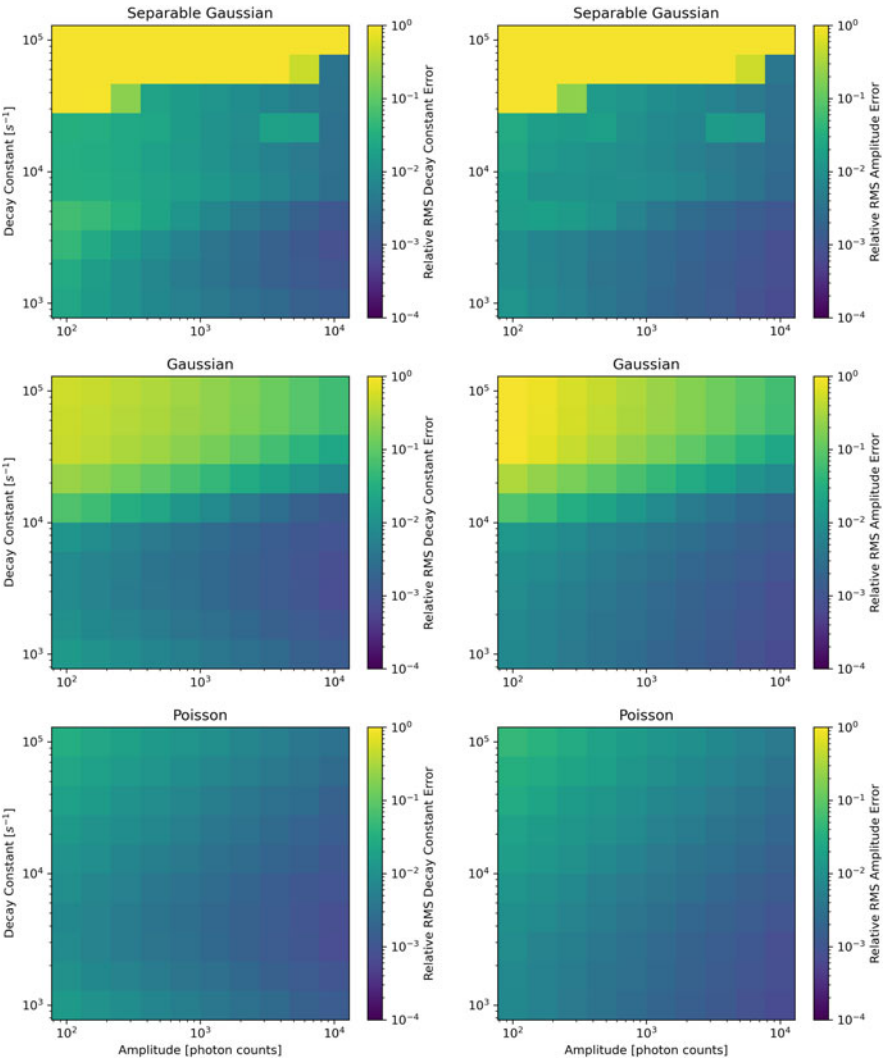


Fig. 18.2 Average relative root mean square error in estimates of exponential decay constant (left column) and amplitude (right column) when employing each noise model in the estimation process

18.4 Conclusion

This simulation effort highlights the need for more investigation into the errors imposed by approximations of Poisson noise. In particular, such approximations are generally not valid when performing analysis on photon-limited observations. This suggests that techniques that employ such approximations should not be applied to

high resolution processing, or regions of very low signal. In order to mitigate the errors in the approximations, assimilation and data processing routines either need to adapt to leverage a Poisson noise model or establish that errors imposed by the separable Gaussian approximation are below acceptable limits.

Acknowledgments This material is based upon work supported by NSF AGS–1930907 and the National Center for Atmospheric Research, which is a major facility sponsored by the National Science Foundation under Cooperative Agreement No. 1852977.

References

1. Kalman, R.E.: A new approach to linear filtering and prediction problems. Trans. ASME–J. Basic Eng. **82**, 35–45 (1960). https://doi.org/10.1115/1.3662552
2. Povey, A.C., et al.: Retrieval of aerosol backscatter, extinction, and LiDAR ratio from Raman LiDAR with optimal estimation. Atmos. Meas. Tech. **7**, 757–776 (2014). https://doi.org/10.5194/amt-7-757-2014
3. Sica, R.J., Haefele, A.: Retrieval of temperature from a multiple-channel Rayleigh-scatter LiDAR using an optimal estimation method. Appl. Opt. **54**(8), 1872–1889 (2015). https://doi.org/10.1364/AO.54.001872

Chapter 19
Enhancing the Performance of the MicroPulse DIAL Through Poisson Total Variation Signal Processing

Matthew Hayman, Willem J. Marais, Robert A. Stillwell, Joshua Carnes, and Scott M. Spuler

Abstract Poisson total variation (PTV) is a statistical signal processing technique that employs regularized maximum likelihood estimation with a known signal detection noise model to perform inversions on noisy observations. Here we describe current and possible application of PTV to estimate MicroPulse DIAL data products. We show results from development of water vapor DIAL processing where PTV has reduced errors in the retrieval and extended the instrument's useful range from 4–6 km up to 8 km. We describe the benefits of applying PTV to temperature estimation using oxygen DIAL. Finally, we highlight how this processing approach can be applied to different signal acquisition approaches by describing how the technique is used to process time-correlated single photon counting data.

Keywords Signal processing · Gases · Temperature · DIAL · HSRL · LiDAR technology

19.1 Introduction

Photon counting enables the capture of extremely weak optical signals. The technology is key to enabling micropulse LiDARs, where low-pulse-energy, high-repetition-rate lasers are employed to aggregate atmospheric observations over many laser shots. For example, such an operational paradigm is key for developing networks of unattended LiDAR, where eye safety limits and air traffic regulations can impose significant restrictions on transmitted laser intensity.

M. Hayman (✉) · R. A. Stillwell · J. Carnes · S. M. Spuler
National Center for Atmospheric Research, Boulder, CO, USA
e-mail: mhayman@ucar.edu

W. J. Marais
Space Science Engineering Center, University of Wisconsin-Madison, Madison, WI, USA

© The Author(s), under exclusive license to Springer Nature Switzerland AG 2023

J. T. Sullivan et al. (eds.), *Proceedings of the 30th International Laser Radar Conference*, Springer Atmospheric Sciences,
https://doi.org/10.1007/978-3-031-37818-8_19

While photon counting has been employed in LiDAR for decades, obtaining estimates of the atmospheric state that are both accurate and precise remains a challenge. To suppress noise, photon counting data must be averaged, but the appropriate averaging intervals are scene dependent. Even instances where averaging is optimized to the scene will tend to over average (resulting in biases) in some regions while under average in others (resulting in excessive noise).

Here we describe the application of a statistical signal processing technique that employs regularized maximum likelihood estimation to estimate LiDAR data products from photon-limited observations. By promoting correlated structure in the captured LiDAR signal, the algorithm effectively adapts averaging to the localized structure in the photon counting data and can deliver lower noise and lower bias observations than standard LiDAR processing techniques.

19.2 Poisson Total Variation

Poisson total variation (PTV) is numerical estimation technique for obtaining low-noise estimates of retrieved variables from noisy photon counting data. PTV approximates retrieved state variables as 2D piecewise constant functions and separates uncorrelated noise from spatially correlated image structure to obtain a denoised estimate of the data product. The technique is derived from approaches that have been successfully applied to medical imaging for nearly two decades [1]. The technique was first developed for LiDAR applications to estimate high-spectral-resolution LiDAR (HSRL) data products [2].

PTV estimates the retrieved variable x given a set of forward models $\{f_i(x)\}_{i=1}^{I}$ that map x onto the corresponding set of photon counting observations $\{y_i\}_{i=1}^{I}$. These forward models are physically derived and describe the instrument operation, relating the derived state variable to the actual observation. The algorithm obtains an estimate of the state variable through a minimization problem

$$\hat{x} = \underset{x}{\operatorname{argmin}} \left\{ \sum_{i=1}^{I} \mathcal{L}\left[f_i(x); y_i\right] + \lambda ||x||_{TV} \right\}. \tag{19.1}$$

The first term in Eq. (19.1) evaluates the quality of fit of the modeled observation with the actual observations. This evaluation is performed using the negative log-likelihood of the detector noise model derived from the observation probability distribution function (PDF). For Poisson distributed noise, the negative log-likelihood is

$$\mathcal{L}\left[f_i(x); y_i\right] = f_i(x) - y_i \ln f_i(x). \tag{19.2}$$

The second term in Eq. (19.1) enforces total variation regularization on $\hat{x}$ to limit the estimate's response to noise. Total variation is the sum of the absolute difference

between adjacent values of x such that for x with one dimension and J elements

$$||x||_{TV} = \sum_{j=1}^{J-1} |x_{j+1} - x_j|. \tag{19.3}$$

The coefficient λ is a constant that scales the total variation penalty. This scale term must typically be determined through holdout cross validation.

With the two terms in Eq. (19.1), the minimization process must find a value of x that balances between excessive variation and quality of fit. Note that because forward modeling is employed, instances of cross dependence in state variables or overconstrained retrievals are inherently managed in the minimization problem. There is never any need to merge different estimates of state variables.

19.3 DIAL Retrievals

The MicroPulse DIAL (MPD) is a thermodynamic profiling LiDAR with capability to measure water vapor (water vapor DIAL), backscatter ratio (HSRL), and temperature (oxygen DIAL) [3]. The instrument employs photon counting avalanche photodiode detectors and operates at a laser repetition rate of 8 kHz while staying below eye safety limits.

19.3.1 Water Vapor

The low-power architecture of the MPD results in low signal-to-noise at ranges typically above 4 km when employing our standard water vapor processing method [3]. We have now shown that by employing PTV, high altitude performance of the instrument can be enhanced [4]. For this effort, we found that PTV results were generally improved with an extra retrieval step, where water vapor was initially estimated at a coarse resolution that was made progressively finer. This coarse to fine approach is referred to as PTV-CF.

In a radiosonde comparison consisting of 130 sondes, PTV retrievals of water vapor typically have similar mean square error (MSE) with the standard retrieval below 2 km AGL. However, PTV provides significantly lower error above 2 km. This ability to suppress noise by adaptive averaging over correlated structure in the state variable has motivated us to increase the maximum processed altitude from 6 km to 8 km on the MPD instrument.

Figure 19.1 shows a comparison of absolute humidity retrieved using the standard method (described in [3]) and the PTV-CF along with a collocated sonde from

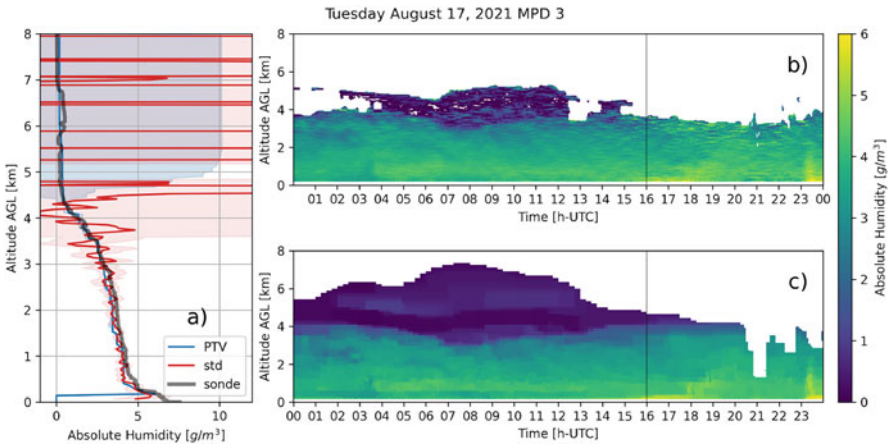


Fig. 19.1 A comparison between absolute humidity estimates from the MPD using standard processing (**b**) and PTV-CF (**c**). The gray vertical line indicates the time of the sonde launch used for comparison in (**a**). Prior to applying PTV-CF saturated photon rates are masked out, hence why (**b**) and (**c**) have different masks

the GRUAN network.[1] Both methods are masked when the estimated uncertainty exceeds 5 g/m^3.

A key finding in developing PTV for water vapor DIAL retrievals is that clouds and sometimes precipitation regions produce significant retrieval errors. Including these structures in the retrieval process results in nonsmooth validation curves and sometimes failure of the optimizer. At present, this is addressed by masking regions where count rates are high and structure is highly variable, resulting in slightly lower data availability at lower altitudes than the standard method. However, this issue suggests that where clouds and precipitation are present, there is an error in the LiDAR forward model, noise model or both, which is likely problematic, yet unquantified, for standard retrievals as well.

Our current hypothesis is that this error is the product of an inaccurate noise model when photon arrival rates are large and the scene under interrogation is highly dynamic. In those instances, the detection PDF is unlikely to be accurately described by a Poisson PDF, used to formulate Eq. (19.2), and standard detector deadtime correction formulas will fail.

[1] We thank Dale Hurst, Patrick Cullis, Emrys Hall, and Allen Jordan of the NOAA Global Monitoring Laboratory for providing this sounding data.

19.3.2 Temperature

Temperature DIAL leveraging oxygen absorption was attempted by Theopold and Bösenberg [5] who noted significant errors caused by aerosol gradients. Two decades later a solution was demonstrated leveraging the MPD architecture [6]. A challenge in this measurement is that the estimate of the oxygen absorption coefficient is affected by aerosol backscatter ratio and absolute humidity. To address this, the MPD leverages its existing water vapor DIAL channel along with a hybrid HSRL/O2-DIAL at 770 nm.

The standard technique for retrieving temperature relies on first processing the water vapor and HSRL channels and then using those data products as input for a perturbative estimate of the oxygen absorption that is subsequently used to retrieve temperature [7]. There are two challenges with this approach. First, noise from the absolute humidity and backscatter ratio estimates is ingested into the retrieval to compound with what is already a noise-prone estimate. Second, all three channels have interdependencies of varying amounts. Absolute humidity and backscatter ratio both use estimates of temperature in order to obtain their data products.

For these reasons, the prospect of applying a forward modeling approach such as PTV to the temperature estimation may offer important benefits. The entire MPD retrieval can be performed as a global estimation process, simultaneously obtaining temperature, absolute humidity, and backscatter ratio, ensuring consistency across all three retrievals while minimizing the effects of compounding noise.

19.4 TCSPC Processing

There is increasing interest in time-correlated single photon counting (TCSPC) or "time tagging" where data are not binned into histograms [8]. Instead, the individual photon arrival times are reported on a shot-by-shot basis. While the high-resolution nature of this approach is often touted as its primary benefit, many of the processing approaches eventually place the data in histograms. However, a noise model can be adapted for individual time tags [9] and therefore be used to process the scene using PTV. For example, the noise model for a non-homogeneous Poisson point process is given by

$$P(\{t_n = T_n\}_{n=1}^{N}, \rho(t)) = \exp\left(-\int_0^{\infty} \rho(\tau) d\tau\right) \prod_{n=1}^{N} \rho(t_n), \tag{19.4}$$

where $\rho(t)$ is the photon arrival rate parameterizing the PDF for observations of N time tags. This model can be further adapted to account for detector deadtime. In addition, the effect of a long laser pulse can be accounted for in forward modeling through a convolution operation with the known laser pulse duration. In this way, the effect of a long laser pulse can be deconvolved to recover sub-pulse length structure.

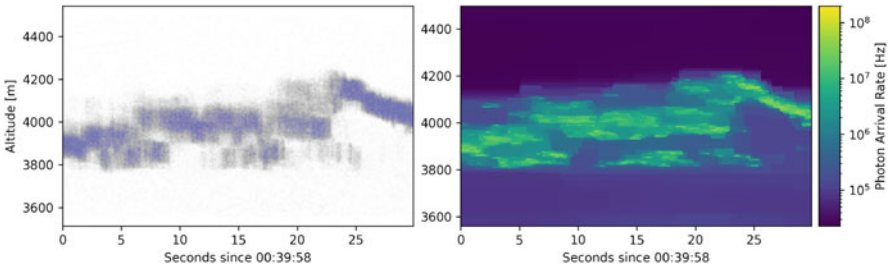


Fig. 19.2 Raw time tag data form MPD 1 on Aug. 18, 2021 where a cloud is present (left) and photon arrival rate (backscatter) estimated from the raw data using PTV (right)

An example of time tag data acquired on the MPD is shown on the left in Fig. 19.2. Those raw time tags were subsequently processed using PTV, while accounting for the 100-m laser pulse length, to obtain an estimate of the cloud structure on the right of the figure.

Note that this measurement is high resolution (the entire duration is 30 sec with 0.75 m range resolution). This highlights the level of structural variability when clouds are present and the potential biases caused by averaging over this structure. However, processing and storing large amounts of time tag data remain a challenge, and there is likely a need to reevaluate how photon counting acquisition systems compress data to make it manageable and transferable.

In summary, we have shown how PTV can enhance photon counting LiDAR by more efficiently leveraging information content in the signals. Examples of extending the range of WV profiles are shown, and the potential benefits to applying it to DIAL-based temperature retrievals were discussed. Furthermore, we showed how it enables the reconstruction of high-resolution vertical and spatial structures of clouds from a low-power long-pulse LiDAR when using time tagging. PTV can be adapted to a broad range of LiDAR sensors and methods.

Acknowledgments This material is based upon work supported by NSF AGS–1930907 and the National Center for Atmospheric Research, which is a major facility sponsored by the National Science Foundation under Cooperative Agreement No. 1852977.

References

1. Harmany, Z.T., et al.: This is SPIRAL-TAP: sparse poisson intensity reconstruction algorithms—theory and practice. IEEE Trans. Image Process. **21**(3), 1084–1096 (2012). https://doi.org/10.1109/TIP.2011.2168410
2. Marais, W.J., et al.: Approach to simultaneously denoise and invert backscatter and extinction from photon-limited atmospheric LiDAR observations. Appl. Opt. **55**(29), 8316–8334 (2016). https://doi.org/10.1364/AO.55.008316

3. Spuler, S.M., et al.: MicroPulse DIAL (MPD)—a diode-laser-based LiDAR architecture for quantitative atmospheric profiling. Atmos. Meas. Tech. **14**, 4593–4616 (2021). https://doi.org/10.5194/amt-14-4593-2021
4. Marais, W.J., Hayman, M.: Extending water vapor measurement capability of photon limited differential absorption LiDARs through simultaneous denoising and inversion. Atmos. Meas. Tech. Discuss. (2022). https://doi.org/10.5194/amt-2021-352
5. Theopold, F.A., Bösenberg, J.: Differential absorption LiDAR measurements of atmospheric temperature profiles: theory and experiment. J. Atmos. Ocean. Technol. **10**(2), 165–179 (1993). https://doi.org/10.1175/1520-0426(1993)010<0165:DALMOA>2.0.CO;2
6. Stillwell, R.A., et al.: Demonstration of a combined differential absorption and high spectral resolution LiDAR for profiling atmospheric temperature. Opt. Exp. **28**, 71–93 (2020). https://doi.org/10.1364/OE.379804
7. Repasky, K.S., et al.: Modeling the performance of a diode laser-based (DLB) micro-pulse differential absorption LiDAR (MPD) for temperature profiling in the lower troposphere. Opt. Exp. **27**(23), 33543–33563 (2019). https://doi.org/10.1364/OE.27.033543
8. Barton-Grimley, R.A., et al.: High resolution photon time-tagging LiDAR for atmospheric point cloud generation. Opt. Express **26**(20), 26030–26044 (2018). https://doi.org/10.1364/OE.26.026030
9. Rapp, J., et al.: Dead time compensation for high-flux ranging. IEEE Trans. Signal Process. **67**, 3471–3486 (2019). https://doi.org/10.1109/TSP.2019.2914891

Chapter 20
Development of MicroPulse Lidar Network (MPLNET) Level 3 Satellite Validation Products in Advance of the EarthCARE Mission

Jasper R. Lewis, James R. Campbell, Simone Lolli, Sebastian A. Stewart, Larry R. Belcher, Rob Koopman, Michaël Sicard, Erica Dolinar, Stephanie Rusli, Jason Tackett, and Ellsworth J. Welton

Abstract In this presentation, we aim to perform statistical comparisons of cloud, aerosol, and planetary boundary layer (PBL) properties derived from Level 3 (L3) MPLNET products to similar properties retrieved from the Cloud-Aerosol Lidar with Orthogonal Polarization (CALIOP) aboard CALIPSO as a precursor for

J. R. Lewis (✉)
University of Maryland Baltimore County, GESTAR II, Baltimore, MD, USA
e-mail: jasper.r.lewis@nasa.gov; jrlewis@umbc.edu

J. R. Campbell · E. Dolinar
Naval Research Laboratory, Monterey, CA, USA
e-mail: james.campbell@nrlmry.navy.mil; erica.dolinar.ctr@nrlmry.navy.mil

S. Lolli
Italian National Research Council (CNR), IMAA, Tito Scalo, PZ, Italy
e-mail: simone.lolli@cnr.it

S. A. Stewart · L. R. Belcher
Science Systems and Applications Inc., Greenbelt, MD, USA
e-mail: sebastian.a.stewart@nasa.gov; larry.r.belcher@nasa.gov

R. Koopman · S. Rusli
European Space Agency (ESA/ESTEC), Noordwijk, the Netherlands
e-mail: Rob.Koopman@esa.int; Stephanie.Rusli@esa.int

M. Sicard
Universitat Politècnica de Catalunya, Barcelona, Spain
e-mail: michael.sicard@upc.edu

J. Tackett
NASA Langley Research Center, Hampton, VA, USA
e-mail: jason.l.tackett@nasa.gov

E. J. Welton
NASA Goddard Space Flight Center, Greenbelt, MD, USA
e-mail: ellsworth.j.welton@nasa.gov

© The Author(s), under exclusive license to Springer Nature Switzerland AG 2023

J. T. Sullivan et al. (eds.), *Proceedings of the 30th International Laser Radar Conference*, Springer Atmospheric Sciences,
https://doi.org/10.1007/978-3-031-37818-8_20

retrievals from the Atmospheric Lidar (ATLID) instrument onboard the EarthCARE satellite. The L3 MPLNET products will be monthly diurnal statistical products for each site: hourly mean and median data arranged monthly. The MPLNET L3 products will be supplemented by the development of satellite-specific MPLNET validation products (e.g., L3-EC for EarthCARE or L3-CAL for CALIPSO). The satellite-specific products will utilize the same statistical analysis as developed for L3 but will be constrained to data acquired during satellite overpasses of MPLNET sites. Based on previous comparisons between ground-based and space-borne sensors, constraining observations to within a 200-km horizontal radius of the MPLNET site and ± 2-h time window of the closest satellite overpass is sufficient to make correlative measurements of both aerosols and clouds. Our CALIPSO-MPLNET analysis will be used to develop a standard operating procedure to be implemented during the EarthCARE mission.

Keywords MPLNET · EarthCARE · CALIPSO · Satellite validation

20.1 Introduction

20.1.1 Background

It is important to have highly accurate and quantitative data records of aerosol and cloud properties spanning several years and geographic regions. More specifically, there is a crucial need for vertical profiles of aerosol and cloud properties in order to improve the understanding of cloud-aerosol-radiation interactions and their parameterizations in climate and numerical weather prediction models. The Earth Clouds, Aerosols and Radiation Explorer (EarthCARE) mission, scheduled to launch late September to mid-October 2023, can potentially extend the rich data record begun by CloudSat and Cloud-Aerosol Lidar and Infrared Pathfinder Satellite Observations (CALIPSO) to multiple decades.

The stated EarthCARE validation plan recognizes the contributions long-term ground-based observation networks can provide. Specifically, the MicroPulse Lidar Network (MPLNET) and European Aerosol Research Lidar Network (EARLINET) are referenced as global or regional lidar networks that can be used to validate EarthCARE through statistical approaches.

20.1.2 MicroPulse Lidar Network (MPLNET)

The MPLNET (https://mplnet.gsfc.nasa.gov) is a federated network of MicroPulse Lidar (MPL) systems deployed worldwide in support of basic science [1]. Since beginning in 2000, MPLNET has operated using a standardized instrument and common suite of data processing algorithms with thorough uncertainty character-

Table 20.1 Comparison of MPL, ATLID, and CALIOP lidar characteristics

	MPL	ATLID	CALIOP
Method	Elastic backscatter lidar, polarized	HSRL, polarized	Elastic backscatter lidar, polarized, two wavelength
Wavelength	532 nm	355 nm	532 nm, 1064 nm
Telescope diameter	18 cm	62 cm	100 cm
Field of view	100 μrad	65 μrad	130 μrad
Vertical resolution	75 m	100 m, below 20 km	60 m, 8.2–20.2 km 30 m, below 8.2 km

ization, which makes for straightforward comparisons between sites. The MPL is a 532-nm elastic backscatter that provides unattended, continuous, day and night measurements, allowing observations of the full diurnal cycle. A summary of key MPL characteristics is provided in Table 20.1. Most MPLNET sites are collocated with the Aerosol Robotic Network (AERONET) [2], providing profile and column measurements of aerosols and clouds in tropical, mid-latitude, and polar climate regions.

A complete list of variables and metadata for current products can be found on the MPLNET Product Information page (https://mplnet.gsfc.nasa.gov/product-info). Following the modified Earth Observing Systems convention, data are publicly available at Level 1 (L1; near real time, no quality screening), Level 1.5 (L15; near real time, quality screened), and Level 2 (L2; upon request, not real time) product levels. The lidar signal data, normalized relative backscatter (NRB), are utilized in the processing of all other MPLNET products [3–9]. The aerosol (AER), cloud (CLD), and planetary boundary layer (PBL) products rely on the Goddard Earth Observing System, version 5 (GEOS-5), atmospheric general circulation model as an ancillary input while the AER and PBL products utilize L15 or L2 AERONET AOD.

Though there is history of using MPLNET data for satellite comparisons/validations [9–12], those studies utilized L2 data that were subsequently re-gridded and statistically analyzed to meet the needs of the various efforts. Similar studies using MPLNET data for model assessment have also been conducted, with the same issue of having to reanalyze L2 MPLNET data [7, 13, 14]. In advance of future satellite missions (e.g., EarthCARE and AtmOS), we aim to develop Level 3 (L3) MPLNET products to facilitate satellite-MPLNET validation and analysis (this will also benefit future modeling studies).

20.1.3 EarthCARE (Earth Clouds, Aerosols, and Radiation Explorer)

The EarthCARE satellite is expected launch in September to mid-October 2023. The EarthCARE satellite will fly in a sun-synchronous 97° inclination orbit at a

height of 393 km [15]. The mean equator local descending node crossing time is 1400 h with a 25-day repeat cycle. Of the four instruments onboard EarthCARE, the primary instrument considered for validation efforts using MPLNET is the Atmospheric Lidar (ATLID). ATLID characteristics are compared to the MPL in Table 20.1. Because ATLID is a high spectral resolution lidar (HSRL), the extinction and backscatter profiles can be determined without making assumptions about the extinction-to-backscatter ratio as required by the MPL and CALIOP systems. Compared to CALIOP, ATLID will measure ~25% more profiles within the ±60° latitude band, as a result of its lower flight altitude and effective pulse after averaging. Consequently, ATLID will achieve statistical representativity for a given geographic area (grid box) sooner than CALIOP, which is an advantage for ground-based validation efforts.

The remaining instruments onboard EarthCARE are the cloud profiling radar (CPR), multispectral imager (MSI), and broadband radiometer (BBR) [15, 16]. The CPR will provide detection of thin ice clouds and low-level stratus and stratocumulus. It will be the first atmospheric radar in space with Doppler velocity capabilities, allowing for observations of convective motions in clouds and hydrometeor fall velocities The MSI will take images of the Earth's atmosphere and surface in seven spectral bands (0.670, 0.865, 1.65, 2.21, 8.80, 10.80, and 12.00 mm), adding horizontal context to the ATLID and CPR vertical measurements, and providing additional information about aerosol and cloud properties. The BBR will measure TOA reflected solar and emitted thermal radiances using total wave (0.25–50 mm) and shortwave (0.25–4 mm) channels in three viewing directions. Data products will be processed for each individual EarthCARE instrument; however, the true value will be in the synergetic data products formed by using multiple sensors (Fig. 20.1).

As a precursor to the EarthCARE mission, MPLNET Level 3 satellite validation products are being developed using overpass times from the CALIOP instrument flown aboard the CALIPSO satellite [17]. Characteristics of CALIOP are also listed in Table 20.1. Comparisons of MPLNET and CALIOP will utilize the 5-km Level 2 merged layer product to identify aerosol and cloud layers and the Level 3 aerosol profile product for the extinction coefficient and aerosol optical depth (AOD) [18].

20.2 MPLNET Level 3 Products for Satellite Validation

Comparisons between ground-based and spaceborne lidars are difficult, because the satellite moves quickly over the stationary point-source of the ground-based lidar. In addition, CALIOP (and in the future, ATLID) is on a sun-synchronous low-earth orbit providing good spatial coverage, but poor temporal sampling. In contrast, ground sites in MPLNET provide poor spatial coverage globally, but continuous observations at 1-min data rate provide full diurnal sampling. Furthermore, low, attenuating clouds obstruct the view of high clouds from the surface that are easily

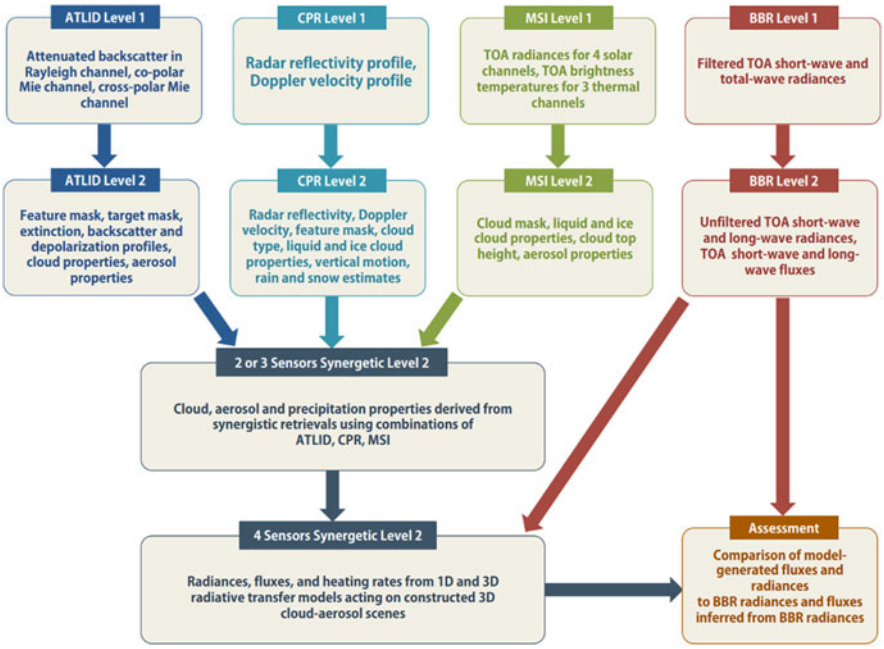


Fig. 20.1 Data products from individual and synergetic remote-sensing techniques to the achievement of EarthCARE mission objectives. (Adapted from Fig. 20.1 of Ref. [16])

observed from space. These two factors result in very different sampling volumes for ground-based and spaceborne measurements. Additionally, instrument sensitivities due to the characteristic shown in Table 20.1 further complicate direct comparisons between MPLNET and satellite-based lidars.

As a result, an aggregate collection of observations, where CALIOP or ATLID data are statistically compared to MPLNET data regionally (seasonally and globally), will be used for validation. The Level 3 (L3) MPLNET products will be monthly diurnal statistical products for each site derived from Level 2 NRB, CLD, AER, and PBL products. The MPLNET L3 products will be supplemented by development of satellite-specific MPLNET validation products (e.g., L3-EC for EarthCARE or L3-CAL for CALIPSO). The satellite-specific products will utilize the same statistical analysis as developed for L3 but will be constrained to data acquired during satellite overpasses of MPLNET sites (within 200 km and $\pm$ 2 h). Examples of the L3 and L3-CAL products using data from the Goddard Space Flight Center (GSFC) site are shown in Fig. 20.2.

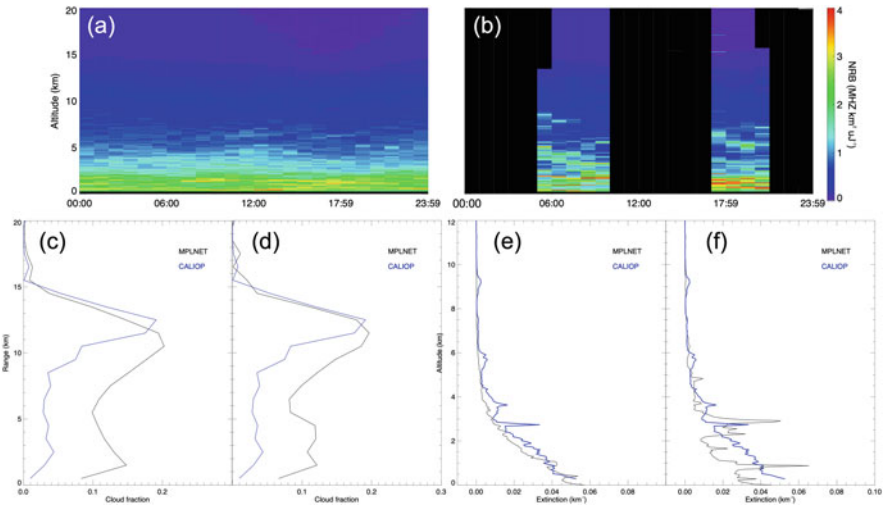


Fig. 20.2 Preliminary examples demonstrating (**a**) the L3 NRB lidar signal for the full set of MPLNET observations, (**b**) the L3-CAL NRB lidar signal constrained to CALIPSO overpasses, (**c**) nighttime L3 cloud fraction, (**d**) nighttime L3-CAL cloud fraction, (**e**) nighttime L3 aerosol extinction, and (**f**) nighttime L3-CAL aerosol extinction with comparisons to similar CALIOP observations. All data are from the GSFC site (2019–2021)

References

1. Welton, E.J., Campbell, J.R., Spinhirne, J.D., Scott, V.S.: Global monitoring of clouds and aerosols using a network of micro-pulse lidar systems. Proc. SPIE. **4153**, 151–158 (2001)
2. Holben, B.N., et al.: AERONET – a federated instrument network and data archive for aerosol characterization. Remote Sens. Environ. **66**, 1–16 (1998)
3. Campbell, J.R., Hlavka, D.L., Welton, E.J., Flynn, C.J., Turner, D.D., Spinhirne, J.D., Scott, V.S., Hwang, I.H.: Full-time, eye-safe cloud and aerosol lidar observation at atmosphere radiation measurement program sites: instrument and data processing. J. Atmos. Ocean. Technol. **19**, 431–442 (2002). https://doi.org/10.1175/1520-0426(2002)019,0431:FTESCA.2.0.CO;2
4. Welton, E.J., Campbell, J.R.: Micropulse lidar signals: uncertainty analysis. J. Atmos. Ocean. Technol. **19**, 2089–2094 (2002). https://doi.org/10.1175/1520-0426(2002)019,2089:MLSUA.2.0.CO;2
5. Welton, E.J., Voss, K.J., Quinn, P.K., Flatau, P.J., Markowicz, K., Campbell, J.R., Spinhirne, J.D., Gordon, H.R., Johnson, J.E.: Measurements of aerosol vertical profiles and optical properties during INDOEX 1999 using micropulse lidars. J. Geophys. Res. **107**, 8019 (2002). https://doi.org/10.1029/2000JD000038
6. Campbell, J.R., Welton, E.J., Spinhirne, J.D., Ji, Q., Tsay, S.-C., Piketh, S.J., Barenbrug, M., Holben, B.N.: Micropulse lidar observations of tropospheric aerosols over northeastern South Africa during the ARREX and SAFARI 2000 dry season experiments. J. Geophys. Res. **108**(D13), 8497 (2003). https://doi.org/10.1029/2002JD002563
7. Lewis, J.R., Welton, E.J., Molod, A.M., Joseph, E.: Improved boundary layer depth retrievals from MPLNET. J. Geophys. Res. Atmos. **118** (2013). https://doi.org/10.1002/jgrd.50570
8. Lewis, J.R., Campbell, J.R., Welton, E.J., Stewart, S.A., Haftings, P.C.: Overview of MPLNET version 3 cloud detection. J. Atmos. Ocean. Technol. **33**, 2113–2134 (2016). https://doi.org/10.1175/JTECH-D-15-0190.1

9. Lewis, J.R., Campbell, J.R., Stewart, S.A., Tan, I., Welton, E.J., Lolli, S.: Determining cloud thermodynamic phase from the polarized Micro Pulse Lidar. Atmos. Meas. Tech. **13**, 6901–6913 (2020). https://doi.org/10.5194/amt-13-6901-2020
10. Torres, O., Bhartia, P.K., Syniuk, A., Welton, E.J., Holben, B.: Total Ozone Mapping Spectrometer measurements of aerosol absorption from space: comparison to SAFARI 2000 ground-based observations. J. Geophys. Res. **110**, D10S18 (2005). https://doi.org/10.1029/2004JD004611
11. Liu, Y., Wang, Z., Wang, J., Ferrare, R.A., Newsom, R.K., Welton, E.J.: The effect of aerosol vertical profiles on satellite-estimated surface particle sulfate concentrations. Remote Sens. Environ. **115**, 508–513 (2011). https://doi.org/10.1016/j.rse.2010.09.019
12. Misra, A., Tripathi, S.N., Kaul, D.S., Welton, E.J.: Study of MPLNET-derived aerosol climatology over Kanpur, India, and validation of CALIPSO level 2 version 3 backscatter and extinction products. J. Ocean. Atmos. Tech. **29**, 1285–1294 (2012). https://doi.org/10.1175/JTECH-D-11-00162.1
13. Lolli, S., Welton, E.J., Benedetti, A., Jones, L., Suttie, M., Wang, S.-H.: MPLNET lidar data assimilation in the ECMWF MACC-II Aerosol system: evaluation of model performances at NCU lidar station. In: Proceedings of SPIE, 9246, Lidar Technologies, Techniques, and Measurements for Atmospheric Remote Sensing, X, p. 92460I (2014). https://doi.org/10.1117/12.2068201
14. Hegarty, J., Lewis, J.R., McGrath-Spangler, E., Henderson, J., Scarino, A.J., DeCola, P., Ferrare, R., Hicks, M., Adams-Selin, R.D., Welton, E.J.: Analysis of the planetary boundary layer height during DISCOVER-AQ Baltimore – Washington, DC with lidar and high-resolution WRF modeling. J. Appl. Meteorol. Climatol. **57**, 2679–2696 (2018). https://doi.org/10.1175/JAMC-D-18-0014.1
15. Illingworth, A.J., et al.: The EarthCARE satellite: the next step forward in global measurements of clouds, aerosols, precipitation, and radiation. Bull. Am. Meteorol. Soc. **96**, 1311–1332 (2015). https://doi.org/10.1175/BAMS-D-12-00227.1
16. Helière, A., Wallace, K., do Carmo, J.P., Eisinger, M., Wehr, T., Lefebvre, A.: EarthCARE instruments description. In: Koopma, R. (ed.) EC-TN-ESA-SYS-0891, Issue 1, 28pp. European Space Agency (2017)
17. Winker, D.M., et al.: The CALIPSO mission: a global 3D view of aerosols and clouds. Bull. Am. Meteorol. Soc. **91**, 1211–1229 (2010). https://doi.org/10.1175/2010BAMS3009.1
18. Tackett, J.L., Winker, D.M., Getzewich, B.J., Vaughan, M.A., Young, S.A., Kar, J.: CALIPSO lidar level 3 aerosol profile product: version 3 algorithm design. Atmos. Meas. Tech. **11**, 4129–4152 (2018). https://doi.org/10.5194/amt-11-4129-2018

Chapter 21
Three-Dimensional Point Cloud Classification Using Drone-Based Scanning LIDAR and Signal Diversity

Kevin W. Sacca, Alexandra K. Wise, and Jeffrey P. Thayer

Abstract Segmentation and classification methods for 3D lidar point clouds have been an important focus for years as machine learning (ML) methods and computational capabilities have improved exponentially. However, unsupervised 3D point cloud segmentation and classification remain challenging problems for surface topography, vegetation, and shallow water bathymetry applications. The amount of training data required in traditional ML methods can be prohibitively large to produce and label for these environments, which have an extremely diverse spectrum of conditions and objects. (National Aeronautics and Space Administration (NASA), Surface Topography and Vegetation Incubation Study Team White Paper, NASA Earth Science Decadal Survey, 2020). Water turbidity can severely attenuate laser power through absorption and scattering, reducing both the maximum depth penetration and the density of points on the subsurface. Even in shallow waters, lidar bathymetry is highly susceptible to turbidity hindering target detection and identification applications. Contrast and discernibility between points in lidar point clouds can be enhanced by incorporating lidar signal diversity using intensity, polarizability, or spectral response. These additional contextual data, based on physical properties of objects and media, can improve segmentation and classification efforts, especially when point clouds are sparse. Through drone-based scanning lidar measurements, an unsupervised classification scheme is demonstrated using derived data products, based on observed physical properties, that supplement 3D geometric analysis with additional point-descriptors for grouping points and assigning descriptive classification labels. For very large point clouds, pre-classified point cloud data products using lidar signal diversity would augment existing classification schemes and improve target recognition and identification efficiency.

Keywords Drone-based lidar bathymetry · Unsupervised classification

K. W. Sacca (✉) · A. K. Wise · J. P. Thayer
University of Colorado Boulder, Boulder, CO, USA
e-mail: Kevin.Sacca@Colorado.edu

© The Author(s), under exclusive license to Springer Nature Switzerland AG 2023

J. T. Sullivan et al. (eds.), *Proceedings of the 30th International Laser Radar Conference*, Springer Atmospheric Sciences,
https://doi.org/10.1007/978-3-031-37818-8_21

21.1 Background and Motivation

Three-dimensional lidar for geoscience applications is deployed in many different modalities to map surface topography, vegetation phenology, and bathymetry [1]. The ubiquity of accessible drone platforms and the commercialization of consumer lidar instrumentation has made drones a viable alternative to traditional aircraft platforms for lidar deployments. Drone-based platforms enable rapid, local-area coverage and inherently afford higher spatial resolution capability by operating at lower altitudes and slower speeds [2]. Lidar mapping from drone platforms enables greater resolvability for an expanded set of features that can be identified through geometric analysis and segmentation using point cloud statistics. Figure 21.1 shows a terrestrial region sampled by a drone-based, scanning, topographic/bathymetric lidar developed by LiteWave Technologies, Inc.

The range-colored, 3D point cloud in Fig. 21.1 will use additional attributes of polarization and point density in Sect. 21.2 to dissect the objects in the scene. Bathymetric observations and detections will be explored in future analysis, but an effort to employ bathymetric calibration targets for 3D imaging and object identification is described in Sect. 21.3.

21.2 Lidar Signal Diversity

Lidar signal diversity can be treated similarly in implementation to what is commonly called data fusion, as a combination of different data products where



Fig. 21.1 (*Left*) Color image captured by a drone-based camera of a small survey area. (*Right*) Nadir-looking view of the 3D point cloud collected by a drone-based scanning lidar instrument, colorized by relative height. (Data collected in collaboration with LiteWave Technologies, Inc.)

the final product contains more contextual information to describe and differentiate measurements. The difference is that derived data products serve as extensions to the original data, not as solitary derivative products. Polarization and point density attributes are used to demonstrate their applicability to improve contrast and discernibility of objects.

21.2.1 Point Density and Polarization

Lidar instruments measure the round-trip time of flight (TOF) of a laser pulse for ranging; however, some instruments are also sensitive to the polarization state of the received pulse return, which can be leveraged in point cloud analysis to discern neighboring points.

The 3D coordinates of a point measurement and their relative proximity to others within the point cloud can be used to generate a point density-based, i.e., pseudo-intensity data product, in which dense regions in the point cloud would indicate higher detectability. Point density has been demonstrated to be a valuable factor for traditional ML segmentation and classification methods in complex urban and terrestrial vegetation applications to discern between several large-scale classes of materials [3–6].

Drone-based scanning lidar platforms often revisit areas of interest for repeated measurements, resulting in very dense point clouds from different viewing angles that are most useful in geometric-based point cloud analysis. However, multiple passes over an area will also create irregular bias in point density distribution. This artificial bias detracts from the physical property-based contrast which is useful to discern objects. Therefore, a normalized point density is used instead, computed using data from individual flyovers with multiple flyovers subsequently averaged to avoid artificial biases.

The polarization state of a return signal can be a powerful point-descriptor measurement that describes a unique aspect of the target-pulse interaction. Scattering often imparts a change to an incident polarization state and can improve contrast between neighboring points (see Fig. 21.2). Retardance and depolarization of incident signals are physical scattering attributes of materials that can be leveraged by polarization-sensitive lidar systems for additional context in object detection and identification.

Demonstrated in Fig. 21.2, the contrast of void regions in the cross-polar data and the relative regularity of the co-polar data will distinguish areas by their respective co- to cross-polar ratios. The ratio of cross-polar to co-polar signal intensity is indicative of a target's polarizability properties, or how a material distributes the incident polarization state of a scattered signal. Point clouds with densities above 300 points/m^2 are common for this instrument and produce reliable depolarization ratio statistics for classification. Many materials have known polarizability characteristics, which will allow polarization-sensitive lidar to leverage that additional contextual information for object detection and identification.

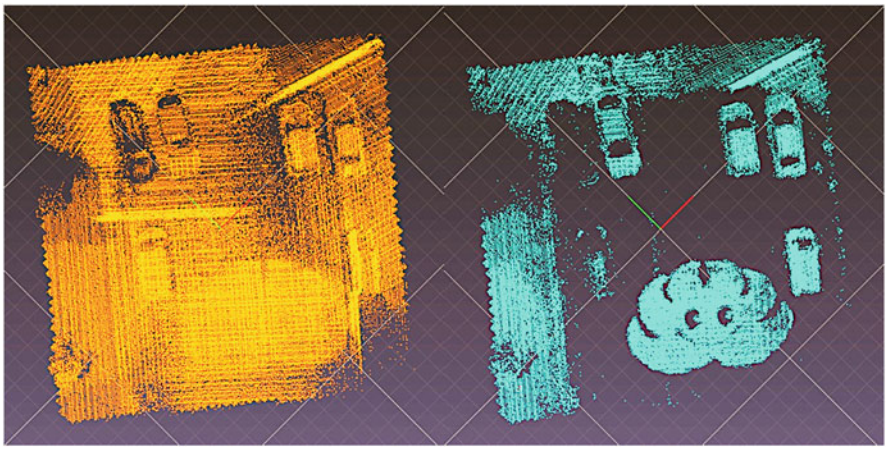


Fig. 21.2 (*Left*) Nadir-looking view of only the co-polar lidar measurements, uniformly colorized. (*Right*) The same nadir-looking view of only the cross-polar lidar measurements, uniformly colorized. Note the cross-polar void regions that contrasts the abundance of co-polar points

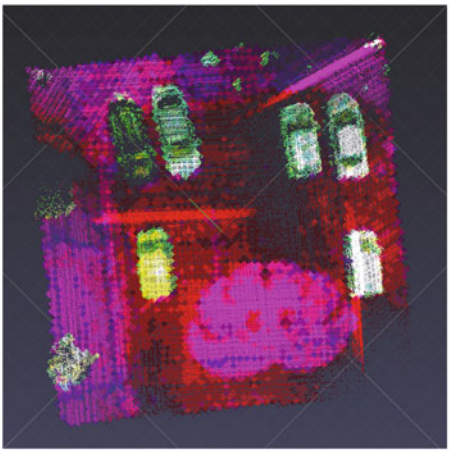
21.2.2 Physical Attribute Classification

A physical property-based classification scheme that assigns descriptive classes to each point is determined by combining the derived point density data products with separate, orthogonal polarization channels. Point density in co- and cross-polar channels were autonomously quartiled into four relative density classes of equal size using their respective histograms, and vertical height variance was regionally thresholded into 2 classes to generate 32 total endmember classes that describe each point (Fig. 21.3).

Visually, the primary features from the scene can be identified, but more importantly, the composition of classes making up the vehicles, grass, pavement, and paint is consistent throughout. There are also nonphysical classifications but fortunately do not represent many points in the scene. The utility of a physical attribute-based classification scheme is the addition of contextual information for discerning lidar data without hardware modifications; therefore, this method can be applied to existing lidar data.

21.3 Bathymetric Applications

Lidar point density has been demonstrated to be a powerful point-descriptor for terrestrial objects; however the bathymetric point density on the subsurface bottom decreases substantially as a function of depth. Therefore, the overall dynamic range of point densities decreases and varies for different bathymetric areas. One



Class ID	Co-Pol	Cross-Pol	Height	Count	Color
0	low co-density	low cross-density	low	0	
1	low co-density	low-mid cross-density	low	6	
2	low co-density	mid-high cross-density	low	0	
3	low co-density	high cross-density	low	0	
4	low-mid co-density	low cross-density	low	12486	
5	low-mid co-density	low-mid cross-density	low	3003	
6	low-mid co-density	mid-high cross-density	low	3217	
7	low-mid co-density	high cross-density	low	148	
8	mid-high co-density	low cross-density	low	24746	
9	mid-high co-density	low-mid cross-density	low	6089	
10	mid-high co-density	mid-high cross-density	low	22063	
11	mid-high co-density	high cross-density	low	6083	
12	high co-density	low cross-density	low	28112	
13	high co-density	low-mid cross-density	low	6523	
14	high co-density	mid-high cross-density	low	24293	
15	high co-density	high cross-density	low	56059	
16	low co-density	low cross-density	high	0	
17	low co-density	low-mid cross-density	high	3	
18	low co-density	mid-high cross-density	high	4	
19	low co-density	high cross-density	high	0	
20	low-mid co-density	low cross-density	high	795	
21	low-mid co-density	low-mid cross-density	high	1372	
22	low-mid co-density	mid-high cross-density	high	1311	
23	low-mid co-density	high cross-density	high	41	
24	mid-high co-density	low cross-density	high	1268	
25	mid-high co-density	low-mid cross-density	high	1331	
26	mid-high co-density	mid-high cross-density	high	4944	
27	mid-high co-density	high cross-density	high	1450	
28	high co-density	low cross-density	high	2210	
29	high co-density	low-mid cross-density	high	1587	
30	high co-density	mid-high cross-density	high	3569	
31	high co-density	high cross-density	high	15764	

Fig. 21.3 (*Left*) Nadir-looking view of the classified point cloud, colorized by physical property-based class assignment. (*Right*) Table of classification labels and their physical property descriptors. This example only uses three descriptors to classify the point cloud for ease of display as each descriptor represents a single color channel in RGB space for colorization (blue = cross-density, red = co-density, green = height)



Fig. 21.4 (*Left*) Image of CCR used as submerged point reflector target. (*Right*) Point cloud of three CCR targets with different polarization responses, colorized by detected polarization state (red = co-polar, blue = cross-polar). From left to right, an uncoated total-internal reflection CCR, a silver-coated specular CCR, and an identical silver CCR with a polarization-retarding filter

method to compensate for attenuation by water would be to model scale values and apply them as gain factors to the observed point density estimates. This will be an iterative approach using in situ calibration targets with turbidity and bottom substrate estimates.

Traditional calibration targets for bathymetry, such as Lambertian reflectors or Secchi disks, are challenged by high attenuation and weak, hemispherically distributed backscatter. Corner-cube retroreflectors (CCRs) are ideal targets for monostatic lidar systems, acting as point reflectors that specularly reflect pulses back to the transmitter (Fig. 21.4). CCR targets can be used as submerged fiducial markers for bathymetric point cloud registration but could also be used in calibration to estimate intensity loss from turbidity as a function of depth. Point reflectors for monostatic lidar can be described as targets that will backscatter for detection

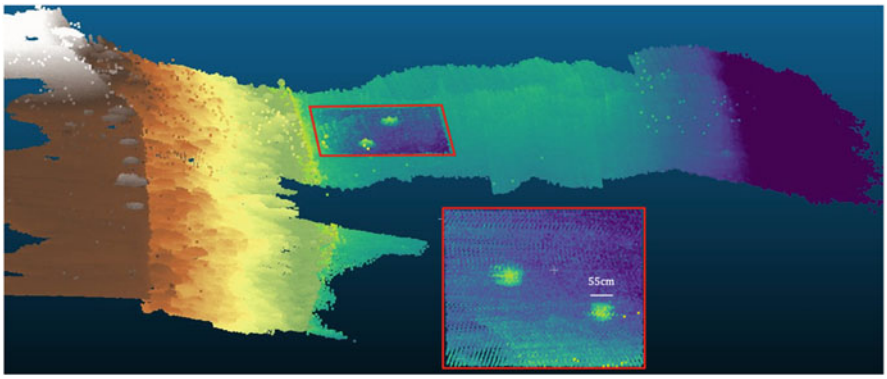


Fig. 21.5 Point cloud of a shallow water coastline with the water surface removed and a rectangular region highlighted to contrast the signal response by two submerged CCR targets from the bathymetric bottom, colorized by height. The targets sit approximately 50 cm below the water surface and 50 cm above the bottom. (Data collected in collaboration with LiteWave Technologies, Inc.)

whenever the target lies within the laser beam spot. Therefore, the response by a point reflector can easily be modeled for scanning lidar and used in point density-based analysis for calibration of water attenuation similar to the empirical line method (ELM).

ELM is a commonly used remote sensing image-correction technique to compensate for the dynamic range loss due to atmospheric attenuation using a gain factor [7]. Attenuation of lidar pulses results in fewer measurements, unlike the reduced intensity in imagery. Therefore, a gain factor to compensate for water column loss can instead be applied to derived data products like point density. While the loss of measurements is a limiting factor unique to lidar, the application of gain factors to bathymetric point density products stretches the effective dynamic range and improves contrast and discernibility between points, which is useful when point clouds are sparse. Planned future experiments and subsequent publications will specifically address the feasibility and suitable environmental conditions for ELM-derived gain factors for bathymetric data products.

Upcoming drone-based bathymetric lidar field campaigns conducted in partnership between CU Boulder and LiteWave Technologies, Inc. will have deployed known submerged reference targets and use the described signal diversity analysis to discern and classify features to improve unsupervised target identification applications (Fig. 21.5).

Acknowledgments The authors and this research are supported by two NASA FINESST grants, #80NSSC21K1597 and #80NSSC19K1351. The authors would also like to acknowledge and thank LiteWave Technologies, Inc. for supporting data collection with their drone-based lidar instrument system through a collaboration with the Active Remote SENsing Lab (ARSENL) at CU Boulder.

References

1. National Aeronautics and Space Administration (NASA), Surface Topography and Vegetation Incubation Study Team White Paper, NASA Earth Science Decadal Survey (2020)
2. Gisler, A., Thayer, J.P., Anderson, C., Crowley, G.: The First UAV-Borne Scanning Topographic and Bathymetric Lidar System for Mapping Coastal Regions. AGU Fall Meeting Abstracts, 2018, EP52D-33 (2018)
3. Brodu, N., Lague, D.: 3D terrestrial lidar data classification of complex natural scenes using a multi-scale dimensionality criterion: applications in geomorphology. ISPRS J. Photogramm. Remote Sens. **68**(C), 121–134 (2012)
4. Kim, A.M., Olsen, R.C., Kruse, F.A.: Methods for LiDAR point cloud classification using local neighborhood statistics. In: Proceeding of SPIE 8731, Laser Radar Technology and Applications XVIII, p. 873103 (2013)
5. Niemeyer, J., Rottensteiner, F., Soergel, U.: Conditional random fields for lidar point cloud classification in complex urban areas. ISPRS Ann. Photogramm. Remote Sens. Spat. Inf. Sci. **I-3**, 263–268 (2012)
6. Balsa-Barreiro, J., Lerma, J.L.: Empirical study of variation in lidar point density over different land covers. Int. J. Remote Sens. **35**(9), 3372–3383 (2014)
7. Smith, G.M., Milton, E.J.: The use of the empirical line method to calibrate remotely sensed data to reflectance. Int. J. Remote Sens. **20**(13), 2653–2662 (1999)

Chapter 22
Design and Validation of an Elastic Lidar Simulator for Testing Potential New Systems for Aerosol Typing



Rebecca Howe, Ioannis Binnietoglou, Anna Gialitaki, and Joshua Vande Hey

Abstract A novel lidar simulator based on first principles is presented. Here we describe our approach and initial results for simulating raw lidar signals and system SNR from system parameters and aerosol optical properties. We also include a validation method and sensitivity studies. The main motivation behind this work is to show how low-cost and physically small lidar systems would perform in various atmospheric conditions.

The simulator presented herein uses instrument component parameters and, based on known atmospheric scenarios, returns aerosol optical properties and signals. In particular, the simulator accounts for molecular effects, system overlap, different far boundary solutions, and the possibility of depolarization channels and is programmed to function at any UV- NIR wavelength. The simulator's performance is currently being validated against EARLINET and PollyNet datasets.

Keywords Aerosols · Lidar · SNR · Simulation · Validation

22.1 Introduction

Aerosols are small solid or liquid particles suspended into the Earth's atmosphere, originating from anthropogenic activities or natural sources. Aerosol exposure is associated with a range of adverse health effects including respiratory disease and

R. Howe (✉) · J. Vande Hey
University of Leicester, Leicester, UK
e-mail: rh394@le.ac.uk

I. Binnietoglou
INOE, Măgurele, Romania

A. Gialitaki
University of Leicester, Leicester, UK

Laboratory of Atmospheric Physics, Aristotle University of Thessaloniki, Thessaloniki, Greece

© The Author(s), under exclusive license to Springer Nature Switzerland AG 2023

J. T. Sullivan et al. (eds.), *Proceedings of the 30th International Laser Radar Conference*, Springer Atmospheric Sciences,
https://doi.org/10.1007/978-3-031-37818-8_22

cardiovascular disease, and 3.5 million premature deaths globally are attributable to exposure to ambient fine particulate matter (aerosols 2.5 μm and smaller) [1]. They also interact with radiation through scattering and absorption; they alter cloud properties, lifetimes, and Earth's surface albedo and, thus, indirectly affect the radiation equilibrium [2]. The aerosol field is subject to rapid temporal and spatial changes, hence the increased difficulty in quantifying their net effect on the planetary radiative budget and air quality.

Using lidar systems it is possible to characterize aerosol particles and derive their vertical distribution and concentration. Lidars can operate on the ground or on-board airborne and satellite platforms to provide coverage of the aerosol field at larger geographical scales. However, the sensors employed may face difficulties in providing highly localized data and are expensive to build and maintain.

Typically new lidar systems are based on existing systems as reference due to challenges in accurate forward modelling of system performance. The goal of this work is to improve our ability to understand realistic performance of novel low-cost lidar systems before building them through the development of a comprehensive simulation approach that takes into account the impact of each system component and parameter on the instrument performance under different atmospheric conditions.

22.2 Theory and Methodology

The simulator has been built entirely in Matlab R2020a as part of a PhD project at the University of Leicester, and is based on the Single Scattering Lidar Equation (SSLE) to simulate signals detected by a system and the Klett inversion for backscatter to validate the results [3]. The outputs of the simulator are tested against the output of the EARLINET single calculus chain (SCC), the simulation framework of which will not be discussed here but can be found in [4, 5].

22.2.1 The Single Scattering Lidar Equation

The SSLE is widely used as a way to calculate the signal received by a lidar system and can be used in situations where elastic returns from particles and molecules are assumed. It can be expressed in different ways; the form used here is shown in Eq. 22.1.

$$P(r) = P_0\, c\, \tau\, \eta\, A_0 \beta(r) \frac{O(r)}{2r^2}\, e^{-2\int_0^r \alpha(r)' dr'} \tag{22.1}$$

where $P(r)$ is the signal received from particle and molecular returns from a distance r, P_0 is the power of the laser in W, c is the speed of light in ms^{-1}, τ is the laser pulse width in s, η is the total efficiency of the lidar system, A_0 is the receiver area in m^2, $\beta(r)$ is the backscattering coefficient in $m^{-1}sr^{-1}$ at altitude r in m, $O(r)$ defines the overlap function, and $\alpha(r)$ is the extinction coefficient in m^{-1} at altitude r in m. The backscatter and extinction coefficients are a sum of their aerosol and molecular parts.

Aerosol backscatter coefficients are quite well characterized from lidar studies coupled with in situ measurements [6], so the retrieval of this parameter is useful in determination of aerosol type. By inputting a backscatter profile and using an estimate (for elastic systems) or measurement (Raman systems) of the lidar ratio (also known as the extinction-to-backscatter ratio) to calculate the extinction coefficient, the simulated signal detected by a system with a specific set of parameters can be calculated.

22.2.2 Simulator Framework

The framework of the simulator is built around the SSLE, and its results are validated against known profiles with a Klett inversion, the framework of which is shown in Fig. 22.1.

The backscatter coefficient profiles are taken from the EARLINET database and are used to estimate the extinction coefficient profiles when a retrieved profile is unavailable. The instrument parameters are variable depending on system components. The overlap function is represented by an "S" curve for when system overlap characterization is unavailable. The molecular backscatter and extinction profiles are calculated from radiosonde measurements or by using the United States Standard Atmosphere (USSA) when these measurements are unavailable. The signal-to-noise ratio (SNR) is calculated using the sky radiance equation and the instrument noise (Eq. 22.3). The form of the Klett inversion which is used for validation is shown in Eq. 22.4.

$$\beta_{\text{mol}} = \frac{8\pi^3\left(m^2-1\right)^2 N}{3N_S^2\lambda^4}\left(\frac{6+3\gamma}{6-7\gamma}\right)\left(\frac{P}{P_S}\right)\left(\frac{T_S}{T}\right) \tag{22.2}$$

Equation 22.2 shows the Rayleigh scattering equation [7], where m is the real refractive index, N is the molecular number density in m^{-3}, N_s is the molecular number density at standard pressure and temperature P_S and T_s, λ is the wavelength of emitted light, P and T are pressure and temperature, and γ is a depolarization factor, taken as 0.0279 here [7].

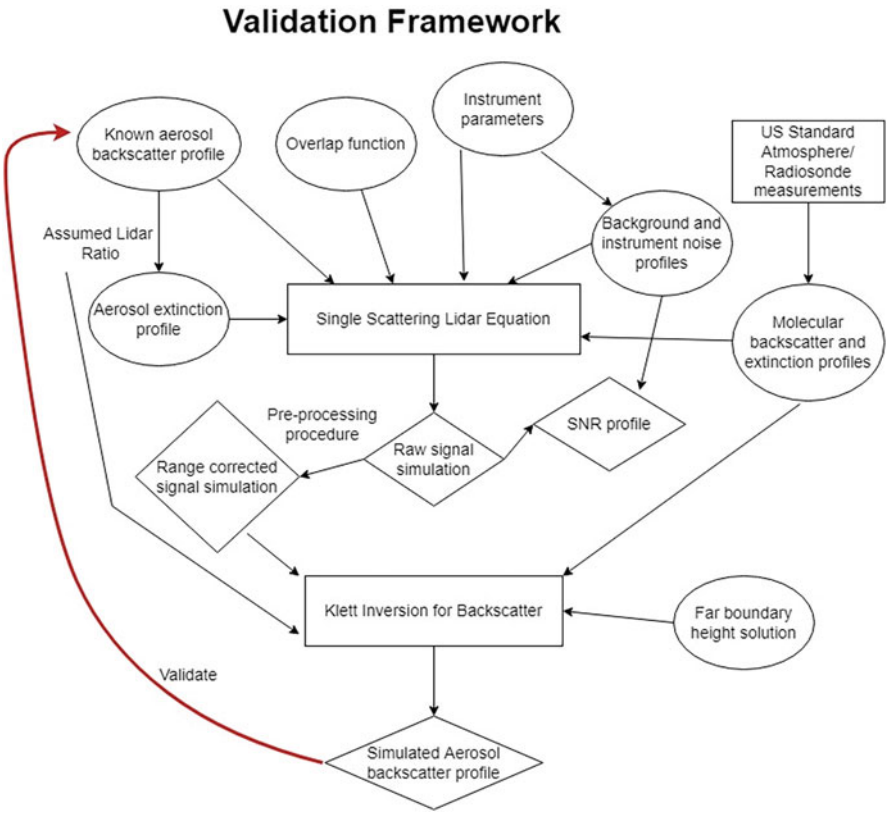


Fig. 22.1 Simulation framework for validation

$$\text{SNR} = \frac{P}{\sqrt{N_B + P}} \quad \text{where } N_B = f\,(\lambda)\;\Delta_{\lambda R}\,\pi\,\theta_H^2\;A_0 + NI \tag{22.3}$$

The SNR is calculated here from Poisson statistics using Eq. 22.3, where P is the received signal in counts, N_B is the total noise in W and then converted to counts, $f(\lambda)$ is the radiance of background light in $W/sr/nm/m^2$, $\Delta_{\lambda R}$ is the optical bandwidth of the filter in nm, θ_H is the half-angle field-of-view in $mrad$, A_0 is the area of the receiver in m^2, and N_I is the instrument noise converted to counts.

$$B_{\text{aer}}(r) + B_{\text{mol}}(r) = \frac{S(r)\exp\left\{-2\int_{r_0}^{r}\left[L_{\text{aer}}(r) - L_{\text{mol}}\right]\,\beta_{\text{mol}}(r)dr\right\}}{\frac{S(r_0)}{\beta_{\text{aer}}(r_0)+\beta_{\text{mol}}(r_0)} - 2\int_{r_0}^{r} L_{\text{aer}}(r)S(r)T\,(r, r_0)\,dr} \tag{22.4}$$

$$T\left(r, r_0\right) = \exp\left\{-2\int_{r_0}^{r}\left[L_{\text{aer}}\left(r'\right) - L_{\text{mol}}\right]\beta_{\text{mol}}\left(r'\right)dr'\right\}$$

The Klett backscatter inversion is shown in Eq. 22.4 where $S(r)$ is the range corrected signal, L_{aer} is the aerosol lidar ratio, L_{mol} is the molecular lidar ratio, r_0 is the far boundary height, and $T(r,r_0)$ is defined as the transmission term. By using an estimate of backscatter at a height r_0, the aerosol backscatter coefficient profile can be estimated using the signal simulated in Eq. 22.1 to validate this output.

22.3 Results and Discussion

22.3.1 Validation of the Simulator

The backscatter profiles retrieved by the EARLINET SCC were used to calculate extinction profiles by use of a lidar ratio assumption and used in the SSLE to output a range corrected signal simulation. To validate this output, the signal was used in a Klett inversion (Eq. 22.4), and the backscatter profiles were compared. Figure 22.2 shows the backscatter as calculated from the signal simulated by the single scattering lidar equation compared to the backscatter profile retrieved from the EARLINET pre-processors by way of the Klett inversion (Eq. 22.4).

22.3.2 Effect of Molecular Backscatter Profile Derivation

Figure 22.3 shows the effect of using a molecular profile derived from the USSA compared with one from local radiosonde measurements. It can be seen that the molecular profile affects the simulator more at lower altitudes.

22.3.3 SNR Dependency on System Parameters

Figure 22.4 shows the dependency of the SNR of the system on various parameters. Figure 22.5 illustrates how system component changes affect the SNR of a potential lidar system.

The SNR profiles shown in Figs. 22.4 and 22.5 are calculated from far-range receiver data and as such the overlap function has been set to unity for all altitudes. It can be seen that the SNR of the system is highly sensitive to small component changes; therefore, it is imperative that the appropriate hardware is chosen when designing and building a lidar system.

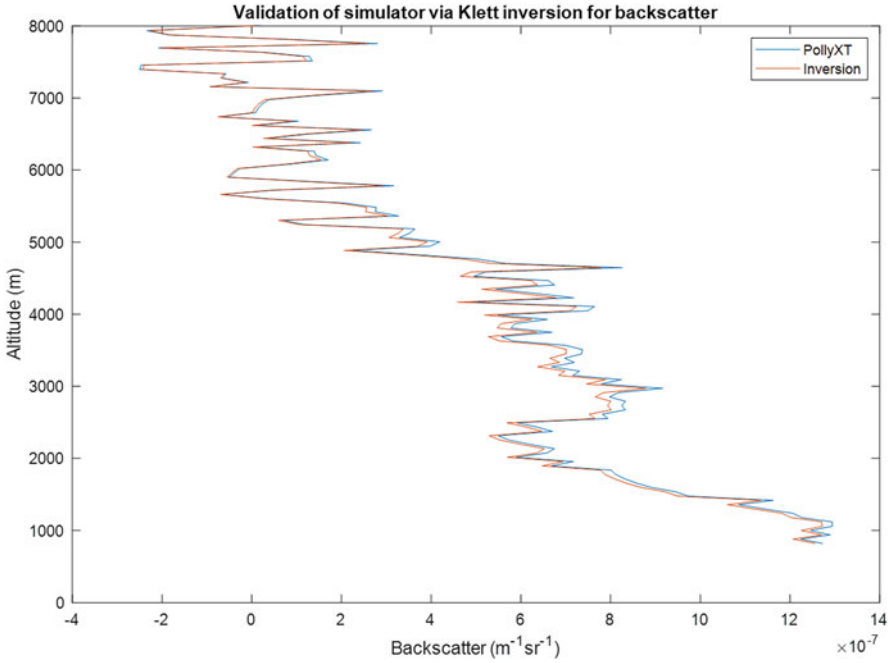


Fig. 22.2 Comparison of backscatter calculated from simulated signal and that retrieved from EARLINET pre-processors

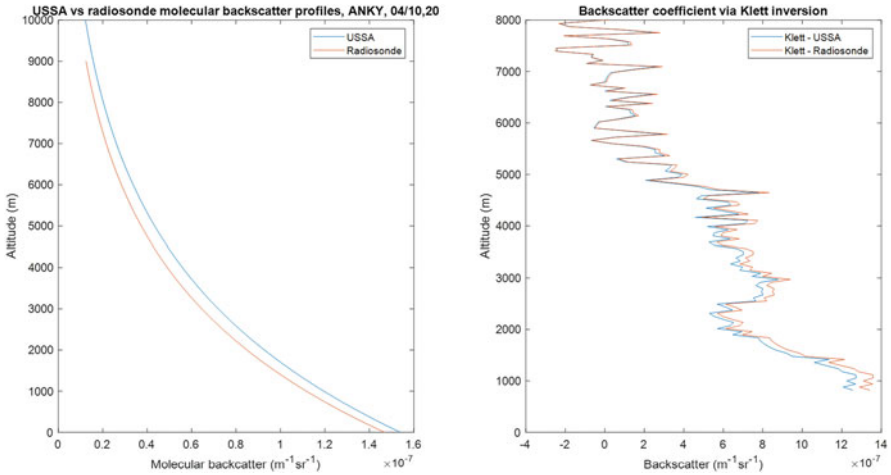


Fig. 22.3 The effect of differently derived molecular backscatter profiles on simulator output

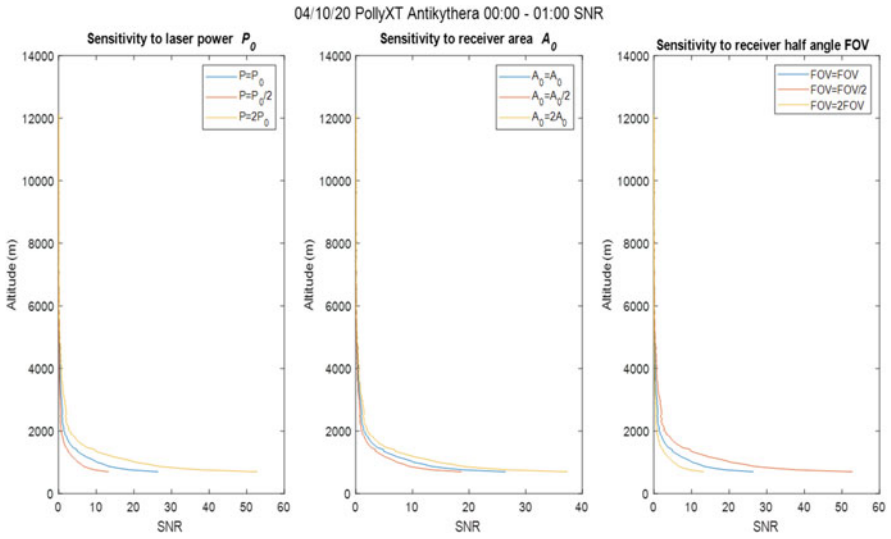


Fig. 22.4 SNR dependency on system variables, laser power P_0, telescope receiver area A_0, and receiver half angle field of view, *FOV*. Changes mainly impact the lowest 2 km of SNR simulations

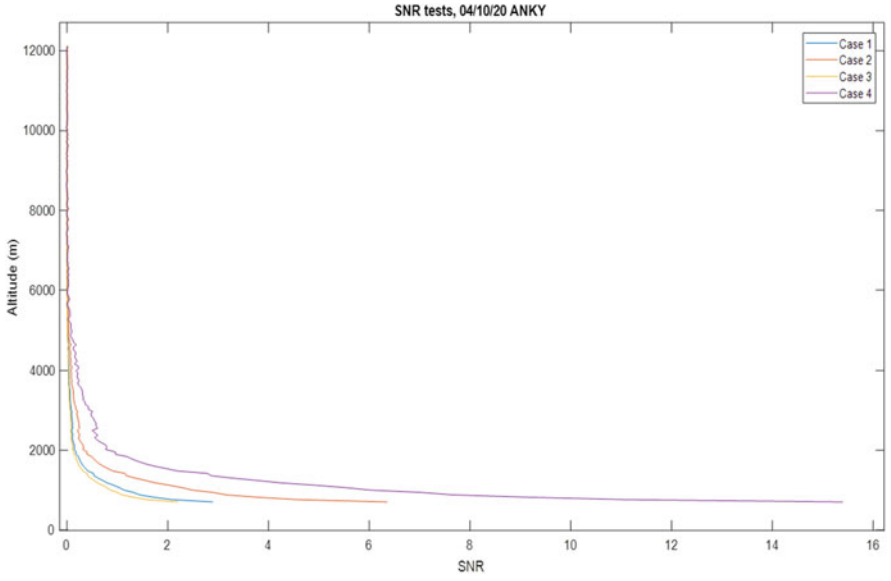


Fig. 22.5 Four cases to illustrate the SNR profile changes when multiple system parameters change in one run. Case 1: $P = 0.2\ W$, $\tau = 9\ ns$, $A_0 = 200\ mm$, $\Delta_{\lambda R} = 20\ nm$, $\theta_H = 0.73\ mrad$. Case 2: $P = 1\ W$, $\tau = 5\ ns$, $A_0 = 150\ mm$, $\Delta_{\lambda R} = 15\ nm$, $\theta_H = 0.8\ mrad$. Case 3: $P = 2.2\ W$, $\tau = 1\ ns$, $A_0 = 100\ mm$, $\Delta_{\lambda R} = 10\ nm$, $\theta_H = 0.83\ mrad$. Case 4: $P = 2.2\ W$, $\tau = 7\ ns$, $A_0 = 150\ mm$, $\Delta_{\lambda R} = 10\ nm$, $\theta_H = 0.83\ mrad$

22.4 Conclusions and Further Work

A simulator for outputting the expected received signal of a lidar system by way of the SSLE has been presented. The simulator has been validated by way of the Klett inversion for backscatter, and the dependencies of the SNR of the system has been investigated. An examination of the effects of the molecular backscatter profile derivations has been carried out. Work on this simulator will continue to be refined and expanded so that a wider array of system and atmospheric parameters can be accounted for so that the simulations can be as close to real conditions as possible. Validations will be carried out at every step to show that each integration is correctly applied.

Further work will also include the simulation of real hardware performance, and the effects of each variable will be further quantified to ensure the most accurate outputs. Cost, physical size, and specifications will all be considered in these simulations.

References

1. Vos, et al.: Global burden of 369 diseases and injuries in 204 countries and territories, 1990–2019: a systematic analysis for the Global Burden of Disease Study 2019. Lancet. **396**(10258), 1204–1222 (2019)
2. Bellouin, et al.: Bounding global aerosol radiative forcing of climate change. Rev. Geophys. **58**(1) (2020)
3. Klett, J.: Stable analytical inversion solution for processing lidar returns. Appl. Opt. **20**(2), 211 (1981)
4. D'Amico, G., Amodeo, A., Mattis, I., Freudenthaler, V., Pappalardo, G.: EARLINET single calculus chain – technical – part 1: pre-processing of raw lidar data. Atmos. Meas. Tech. **9**(2), 491–507 (2016)
5. Mattis, I., D'Amico, G., Baars, H., Amodeo, A., Madonna, F., Iarlori, M.: EARLINET single calculus chain – technical – part 2: calculation of optical products. Atmos. Meas. Tech. **9**(7), 3009–3029 (2016)
6. Schwiesow, R.L., Cupp, R.E., Derr, V.E., Barrett, E.W., Pueschel, R.F., Sinclair, P.C.: Aerosol backscatter coefficient profiles measured at 10.6 μm. J. Appl. Meteorol. (1962–1982). **20**(2), 184–194 (1981)
7. Kovalev, V., Eichinger, W.: Elastic Lidar. Wiley, Hoboken (2004)

Chapter 23
Performance of Pulsed Wind Lidar Based on Optical Hybrid

G. A. Petrov, N. A. Baranov, G. E. Romanova, and M. Yu Sachkov

Abstract A novel system of a pulsed IR coherent lidar for wind profile measurements is proposed. The characteristics of the lidar were analyzed from the point of view of its maximum detection range and signal-to-noise ratio (SNR). Two variations of the fiber scheme for Doppler lidar were considered: one of them uses an additional optical hybrid and the other system being the conventional scheme. As an optical hybrid operation is known to be based on the principle of splitting backscattered radiation into two parts, we use an additional amplifier in the scheme. The signal-to-noise balance is analyzed considering all the elements of the fiber optical part and the opto-electronic components. Besides, we discuss the signal character in both cases and the specific features of the signal processing both in the systems with an optical hybrid and without one.

Keywords Wind · Aerosols · Doppler lidar · Optical hybrid · Signal processing

23.1 Introduction

Nowadays lidars are applied, for ecological monitoring and wind measurement, as well as in airports, within ground-based measuring complexes, and in many other fields.

G. A. Petrov (✉)
St. Petersburg Electrotechnical University "LETI", St. Petersburg, Russia
e-mail: gapetrov@etu.ru

N. A. Baranov
Institution of Russian Academy of Sciences, Dorodnicyn Computing Centre, Moscow, Russia
e-mail: baranov@ccas.ru

G. E. Romanova · M. Y. Sachkov
ITMO University, St. Petersburg, Russia
e-mail: geromanova@itmo.ru; m.sachkov@itmo.ru

© The Author(s), under exclusive license to Springer Nature Switzerland AG 2023

J. T. Sullivan et al. (eds.), *Proceedings of the 30th International Laser Radar Conference*, Springer Atmospheric Sciences,
https://doi.org/10.1007/978-3-031-37818-8_23

To take advantage of the transparency of the atmosphere, and to eliminate radiation hazards for users, meteorological lidars use a wavelength of 1.55 microns, making it possible to detect an aerosol scattering signal, and hence, obtain information on wind flow speed. Pulsed wind lidars with this wavelength, as a rule, allow measurements at distances from 200 to 400 m to dozens of kilometers [1–3]. On the other hand, the range of a lidar instrument highly depends on the optical components and their operation within the device as well as on the specific signal processing algorithms.

Coherent Doppler lidars based on the heterodyne detection method have higher resistance to interference [1, 4] and, other conditions being equal, provide a greater range and higher reliability of receiving the reflected echo-signal compared to incoherent lidars.

Using an optical hybrid in a coherent Doppler wind lidar scheme improves its range characteristics: some previous research confirms this for a continuous lidar [5, 6]. However, as optical hybrid operation is based on splitting backscattered radiation into two parts, the working backscattered signal is lower. One possible way to mitigate this is using an additional amplifier to keep the adequate signal level and the SNR. We suggest a system with a fiber amplifier in the input path. Every element of the scheme adds its own noises into the signal-to-noise budget, so the detection range largely depends on the characteristics of the scheme. The chapter considers two variations of the scheme for a Doppler lidar: in one case, an optical hybrid is used, and the second system does not feature one and is designed using the conventional scheme. The properties of the two schemes are compared. The noise in the schemes from various sources is analyzed and simulated. Experiments conducted demonstrated the characteristics of a coherent pulsed wind lidar scheme using an optical hybrid.

The results demonstrate some features of signal processing and the performance achieved in both the system with an optical hybrid and without one.

23.2 Pulsed Wind Lidar System

The experimental setup includes the following elements (see Fig. 23.1):

- Laser source: a laser with circulator integrated
- PD: photodetector
- ADC: analog digital converter
- FPGA: field-programmable gate array
- PC: personal computer

The laser source, with the optical circulator integrated, forms laser pulses. We use a laser source with the following characteristics – see Table 23.1.

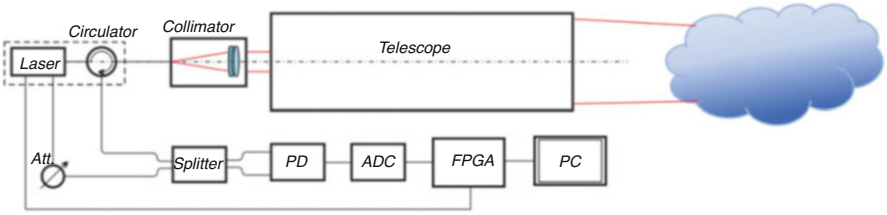


Fig. 23.1 Experimental setup scheme

Table 23.1 Laser source characteristics

	Parameter	Value
1	Energy per pulse	180 μJ
2	Pulse repetition frequency	10 kHz
3	Pulse duration	300 ns
4	Output frequency shift	160 MHz
5	Spectral linewidth	5 kHz

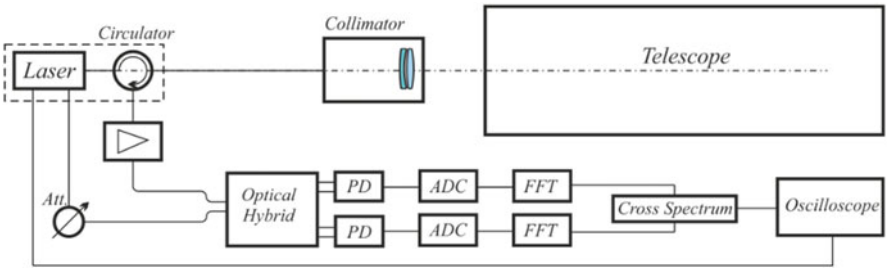


Fig. 23.2 System with an optical hybrid

Collimator optics is set on the fiber output end. After the collimator, the beam of rays proceeds to the telescope optics. The telescope forms an expanded beam with low residual divergence. A beam of rays, close to ideally parallel, is directed to the atmosphere, where it is scattered by aerosol particles. The backscattered light returns to the telescope and is transferred to the photodetector. This scheme was used as the basic one, to have the reference performance for a comparison with the other option.

The second setup introduces an optical hybrid in the fiber scheme; this scheme is presented in Fig. 23.2. In this scheme variation, two balanced photodetectors are installed at the output of the optical hybrid, the signals of which are processed together.

A fiber amplifier is set between circulator port 3 and the optical hybrid. Our experiments were conducted with the fiber optical scheme both with and without this active element. The main characteristics are presented in Table 23.2. The amplifier is a highly efficient InP/InGaAsP multiple quantum well (MQW) layer structure.

Table 23.2 Fiber amplifier characteristics

	Parameter	Value
1	Fiber to fiber gain	24 dB
2	Noise figure	8 dB
3	Gain ripple	1 dB

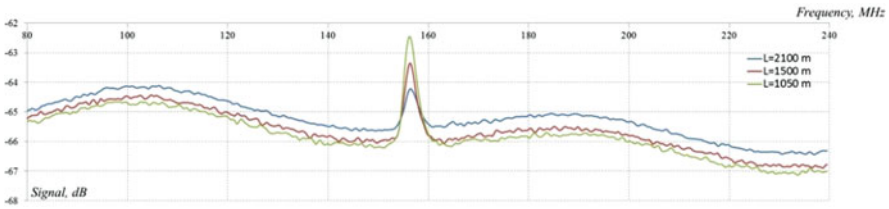


Fig. 23.3 Signals in the basic scheme for several distances

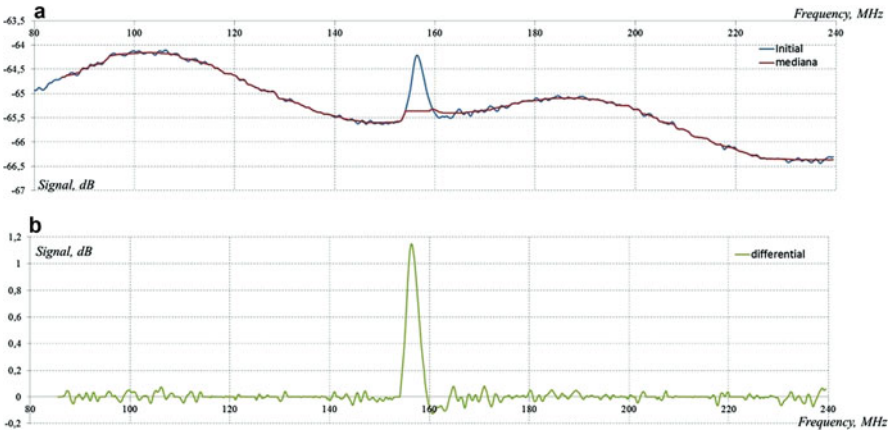


Fig. 23.4 Stages of signal processing in the basic scheme for the distance $L = 2100$ m. (**a**) initial signal and the shape of the signal after median filter, (**b**) resulting signal after processing

23.3 Signals and Their Processing

The signals detected by the basic scheme system are presented in Fig. 23.3.

The signals were registered in a series of experiments in the open atmosphere. The frequency 160 MHz corresponds to zero wind speed value. The signals were obtained by setting the time shift 17 mcsec relative to the laser pulse, which corresponds to the lidar operating range of 2100 m. The signals in the basic system were processed as follows:

1. A median filter was applied, and the averaging interval was chosen for the signal smoothing to be observed on the median graph (Fig. 23.4a, “mediana”).
2. The informative reference signal was found as the difference between the initial one and that obtained after applying the median filter (Fig. 23.4b, “differential”).

In the second scheme, the backscattered radiation reaches the optical hybrid. The two outputs of the optical hybrid are connected to a pair of balanced photodetectors.

The photodetectors receive the two mixed signals: $S_b + D$ and $S_{bs} + D$, where S_b is the reference signal without a phase shift and S_{bs} is the reference signal with the phase shift of one half wavelength. D is the backscattered signal.

The photodetector receives the mixture of signals, and there is interference causing light intensity alternation. The Doppler shift determines the frequency of the mixed signal that is transformed to a low-frequency envelope at the photodetector output [7]. Here, there are two electrical signals I and Q.

Determining wind speed becomes in fact the task of finding the Doppler shift frequency. The digitized and sampled signal proceeds the data processing circuit. First, the spectrum of the received signal is calculated. After that, the successively calculated spectra are summed up to increase the SNR.

The spectrum for signals is calculated according to the equations:

$$F_b = \mathrm{FFT}(I), \quad F_{bs} = \mathrm{FFT}(Q) \tag{23.1}$$

where FFT () is fast Fourier transform.

The calculation uses real and imaginary parts of the spectra. The signs of the calculated cross-spectra are uniquely determined by the sign of the frequency shift, i.e., wind direction. The cross-spectrum is calculated according to the equation:

$$C = \mathrm{Im}\,(F_b) \cdot \mathrm{Re}\,(F_{bs}) - \mathrm{Im}\,(F_{bs}) \cdot \mathrm{Re}\,(F_s) \tag{23.2}$$

The cross-spectrum C allows for amplitude summation of the two components. The main dependence of the sign of the cross-spectrum on the sign of the frequency shift is retained.

If we consider the SNR as the signal power divided by the standard deviation of the noise level, then SNR shows how much the Doppler peak is larger than the noise level. Thus, for the detector signals, including the signal I for the considered optical hybrid based scheme with two detectors, the SNR is as follows [5]:

$$\mathrm{SNR} = \frac{(S+N) - N}{\sigma_n(N)} = \sqrt{n}S/N \equiv \mathrm{SNR}_0 \tag{23.3}$$

The variance of the spectral estimate of the noise σ_n is calculated at a frequency range outside the Doppler peak. If we use both I and Q signal to calculate the reference signal, then the power will double, while the standard deviation of the noise increases only by $\sqrt{2}$. Thereby the SNR compared to the case of using only one of the two detectors will increase by the factor of $\sqrt{2}$.

For the cross-spectrum, we have the same SNR as for the case of the power spectra of I and Q taken together [5]. However, now the background spectrum is flat, and it is an advantage. The disadvantage is the fact that two separate computational modules are required for simultaneous calculation of the cross-spectra. The signal in the scheme with an optical hybrid is presented in Fig. 23.5. The effect of the SNR

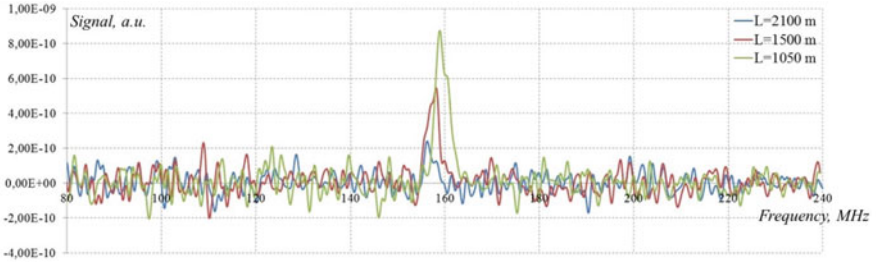


Fig. 23.5 Signal obtained in the scheme with an optical hybrid for the distances $L = 1050$ m, 1500 m, and 2100 m

increasing can be achieved with a large backscattered signal. The high backscattered signal can be obtained in, for example, short distances, high dust concentration, or other special conditions.

On the other hand, scanning for a long distance or in a clear atmosphere leads to changing the noise budget components. In the scheme based on an optical hybrid, the part of the noise caused by the detectors will increase, because there are two detectors, each of them adding noise to the total signal. Moreover, when we split the signal in this type of the scheme, the detectors work in more difficult conditions. To mitigate this, we amplified the signal in the optical path using a semiconductor fiber amplifier. The results of applying the fiber amplifier in the receiving part are as follows:

- For the relatively short distance (up to 5000 m), the SNR decreases because of the amplifier noise.
- For larger distances the amplifier improves SNR.

Hence, the main issue in the system is to find the optimal noise balance between all the elements of the scheme taking into consideration the scan conditions. The general result is that the fiber amplifier in the receiver part can provide more favorable working conditions for the detector.

23.4 Discussion and Conclusion

In our experiment we designed a system with an IQ detector to check the SNR. The optical hybrid allows getting a flat background spectrum and an optimal SNR throughout the scan range. Using a semiconductor fiber amplifier provides the maximum distance of scan compared to other schemes.

Based on this result, we expect that it would be possible to design a lidar scheme with an fiber optic switch. In this case there will be zero frequency shift after the modulator. Thus, the zero wind speed will correspond to zero frequency. In the IQ detection scheme, we can get the wind direction by cross-spectrum analysis.

The noise increase in low-frequency domain is expected to be leveled by another advantage of the scheme, namely, increasing SNR by $\sqrt{2}$.

This scheme will provide a cost-efficient pulsed Doppler lidar system because of significant reduction in the cost of the electronic part for the low-frequency signals. Actually, it will be necessary to have frequency range only 0–50 MHz instead of 110–210 MHz, which may require less sophisticated receivers, amplifiers, ADCs, and FPGA.

References

1. Liu, Z., Barlow, J.F., Chan, P.-W., Fung, J.C.H., Li, Y., Ren, C., Mak, H.W.L., Ng, E.: A review of progress and applications of pulsed Doppler wind LiDARs. Remote Sens. **11**, 2522 (2019)
2. Fujii, T., Fukuchi, T.: Laser Remote Sensing (Optical Science and Engineering), 912 pages. CRC Press (2019)
3. Liu, H., Yuan, L., Fan, C., Liu, F., Zhang, X., Zhu, X., Liu, J., Zhu, X., Chen, W.: Performance validation on an all-fiber 1.54-μm pulsed coherent Doppler lidar for wind-profile measurement. Opt. Eng. **59**(1), 014109 (2020)
4. Weitkamp, C.: Lidar: Range-Resolved Optical Remote Sensing of the Atmosphere, vol. 102. Springer Science & Business, New York (2006)
5. Pedersen, A.T., Abari, C.F., Mann, J., Mikkelsen, T.: Theoretical and experimental signal-to-noise ratio assessment in new direction sensing continuous-wave Doppler lidar. J. Phys. Conf. Ser. **524**, 012004 (2014)
6. Yang, J., Zhao, B., Liu, B.: Coherent pulse-compression Lidar based on 90-degree optical hybrid. Sensors. **19**, 4570 (2019)
7. Baranov, N.A., Petrov, G.A.: Data processing technique for the all-fiber wind profiler. In: Processing of SPIE 10429, Lidar Technologies, Techniques, and Measurements for Atmospheric Remote Sensing XIII, p. 104290G (2017)

Chapter 24
Demonstrating Capabilities of Multiple-Beam Airborne Doppler Lidar Using a LES-Based Simulator



James Kasic, Philipp Gasch, Oliver Maas, and Zhien Wang

Abstract Fine-scale wind measurements in the planetary boundary layer are required for understanding turbulence in complex terrain, flux of energy and aerosols, and severe weather events. The University of Colorado, Boulder (UCB), is developing an airborne Doppler lidar (ADL) system with five-fixed-direction beams to improve wind measurements in heterogeneous conditions. The five-fixed-beam system takes continuous radial wind velocity measurements at multiple angles including a dedicated nadir beam for high-resolution vertical measurements. Results of an ADL simulator, based on a large eddy simulation (LES) with 10 m vertical and horizontal resolutions, demonstrated that the five-beam system can reduce wind profile retrieval error due to turbulence by more than 40%, is less sensitive to restrictive design parameters, and can resolve planetary boundary layer 2D roll structures.

Keywords LIDAR · Boundary layer · Winds

24.1 Introduction

Improved planetary boundary layer (PBL) measurements are critical for advancing our understanding of PBL processes and for validating and improving weather, climate, and pollution models [1]. Ground-based Doppler lidars have provided many

J. Kasic (✉) · Z. Wang
Laboratory of Atmospheric and Space Science (LASP), University of Colorado Boulder (UCB), Boulder, CO, USA
e-mail: james.kasic@colorado.edu

P. Gasch
Karlsruhe Institute of Technology (KIT), Institute of Meteorology and Climate Research – Department of Troposphere Research (IMK-TRO, Karlsruhe, Germany

O. Maas
Leibniz University Hannover, Institute of Meteorology and Climatology, Hannover, Germany

© The Author(s), under exclusive license to Springer Nature Switzerland AG 2023

J. T. Sullivan et al. (eds.), *Proceedings of the 30th International Laser Radar Conference*, Springer Atmospheric Sciences,
https://doi.org/10.1007/978-3-031-37818-8_24

insights into PBL wind speed and turbulence, yet have limited spatial coverage [2]. Airborne Doppler lidar (ADL) adds the ability to quickly observe large regions of the atmosphere, while ground based systems sample a single region in space. ADL is also able to sample in regions where access is difficult on the ground and can change course to adapt to weather systems and PBL features as they evolve.

Existing ADL systems generally provide vertical and horizontal wind speeds by using a single scanning beam which moves through various viewing directions [3, 4]. The time needed for scanning limits the spatial resolution of measurements. Finer-scale wind measurements are required for understanding flow and turbulence in complex terrain, urban environments, and severe weather systems.

UCB is developing a five fixed-beam ADL system to improve wind measurement capabilities and to meet needs for PBL process studies. The fixed-beam setup allows for continuous radial wind velocity measurements at multiple azimuth angles while maintaining a dedicated nadir beam for high-resolution vertical wind measurements. The nadir beam can measure vertical velocities at a high spatial resolution, while measurements from the non-vertical beams can be used to estimate horizontal wind speeds. Here we demonstrate the potentials of the new ADL using LES-based simulation results.

24.2 ADL Simulator

An airborne Doppler lidar simulator (ADLS) has been developed at the Karlsruhe Institute of Technology (KIT) for the purpose of understanding the influence of ADL system setup on measurement error characteristics [3]. The ADLS gives insight into measurement errors since the true features of the simulated wind field are known exactly, allowing simulated ADL measurements to be compared to a known truth.

In a collaboration between UCB and KIT, the ADLS was updated to be able to simulate multiple-beam ADL system setups. The updated LES is used to demonstrate the improvements of the five-beam ADL design compared to traditional setups with a single scanning beam.

The ADLS mimics real-life measurement by moving a simulated aircraft through 3D wind fields generated by a parallelized LES model (PALM). The PALM has a 2.3 km high, 23 km long, and 17 km wide domain with 10 m resolutions in both the horizontal and vertical directions. Here, PALM simulates the turbulent PBL under five different average background wind speed cases: 0, 2, 5, 10, and 15 m/s. For each wind speed case, 56 statistically independent transects are simulated. Each transect represents a flight through a time-frozen LES. Along each transect, a variety of system setups are tested, varying the along-track averaging distance of simulated retrievals and scan elevation angles. A standard setup is chosen to have a 1300 m along-track averaging distance and use 60 degree scan elevation angle for non-vertical beams. Elevation angle is measured form the horizontal down. Details of

Table 24.1 Simulator settings

Parameters	System settings
Aircraft flight altitude	1100 m
Scan elevation angle	30°, 40°, 50°, 60°, 65°, 70°, 75°, 80°
Along-track averaging distance	325, 650, 975, 1300, 2600 m
Lidar measurement frequency	10 Hz
Height used for retrieval	0–800 m
Indicated air speed	65 ms^{-1}
Vertical averaging distance	60 m
Scan rotation speed	18° s^{-1}
Fixed-beam directions	Forward, right, backward, left, nadir
Background wind speed	0, 2, 5, 10, 15 ms^{-1}
LES time steps sampled	7
Transects flown per time step	8
Profiles retrieved per transect	6
Time separation between time steps	20 min

When multiple settings are listed for a single parameter, all listed settings were tested and the standard setting is underlined. Unless otherwise stated, results in this document use the standard setting

the ADLS parameters are shown in Table 24.1, with standard settings underlined. ADLS retrievals are computed using the airborne velocity azimuth display (AVAD) technique [5].

24.3 Results

24.3.1 Mean Wind Speed Retrieval Quality

The mean absolute error is expected to be significantly less for the fixed-beam setup because it has higher data density. The fixed-beam setup uses five beams that each take as many radial measurements as the single scanning beam, and with more data points in an averaging volume, the AVAD technique reaches a better fit, which is confirmed with simulation results in Fig. 24.1. While the scanning setup showed 0.75 ms^{-1} mean absolute error and 0.19 ms^{-1} bias, the fixed beam setup had only 0.44 ms^{-1} mean absolute error and 0.07 ms^{-1} bias. These error metrics depend on the characteristics of the atmosphere being measured, but the ADLS results show that the fixed-beam setup produced less retrieval error and bias than the scanning setup in the same atmosphere.

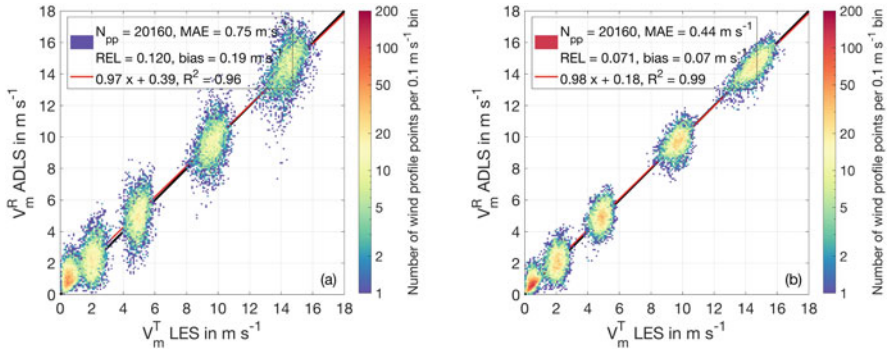


Fig. 24.1 Figure (**a**) shows results for the scanning system. Figure (**b**) shows results for the fixed-beam system

24.3.2 Dependence on Elevation Angle

The retrieval quality of ADL measurements is sensitive to the elevation angle used since this controls the projection of the horizontal wind on the non-vertical beams as well as the footprint of measurements. AVAD retrievals assume homogenous wind within the measurement volume (Fig. 24.2).

For both the fixed-beam and the scanning setups, the mean absolute error increases exponentially as elevation angle increases. With 60° elevation angles, the fixed-beam setup has 50% reduced error compared to the scanning setup, which increases to 70% reduced error with 70° angles. These results show that scanning systems have stricter design constraints on elevation angle than the multiple-fixed beam system. Steep elevation angles that would be untenable with a scanning system, due to increased retrieval error, can be considered when using the fixed-beam setup.

Longer along-track averaging distances reduce error in retrievals since more measurements can be included in the AVAD algorithm, but also provide lower resolution results. In many studies, it is advantageous to have reduced along-track averaging distance so that spatial differences along the flight track can be resolved.

Both system setups show increasing error for shorter along-track averaging distances. The fixed-beam system shows reduced error compared to the scanning system, and the difference is greater for shorter distances (Fig. 24.3).

24.4 Additional Capabilities of Multiple Beam System

While the fixed beam system can reduce retrieval errors in mean wind measurements using the AVAD technique, the presence of multiple beams opens up additional analysis options that are not possible for scanning systems. Figure 24.4 shows

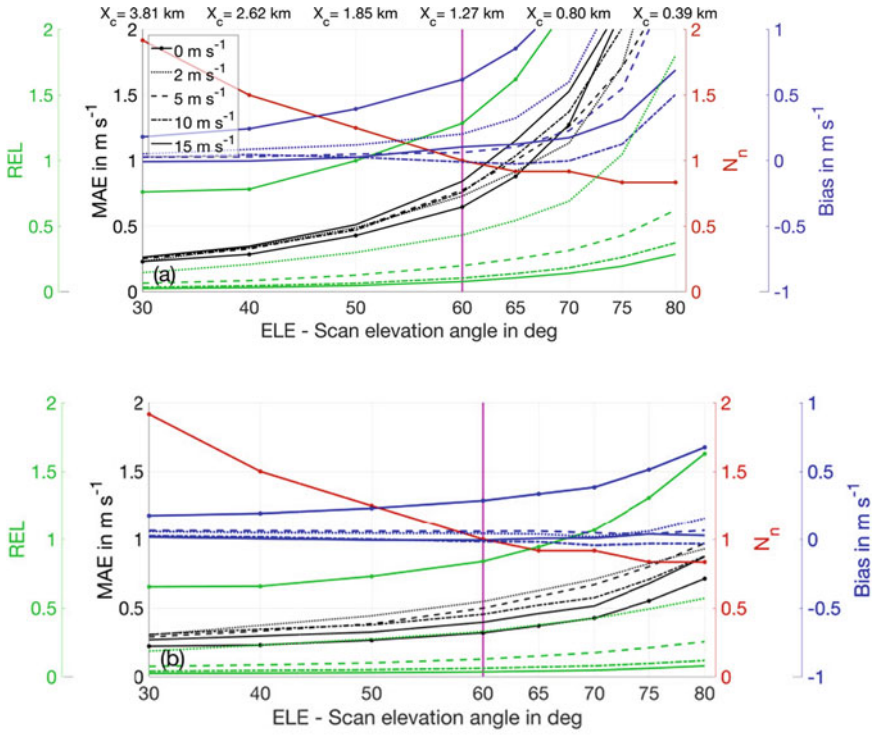


Fig. 24.2 The retrieval error of the scanning system (**a**) and the fixed beam setup (**b**) when using various elevations angles. Shown are the mean absolute error (black), the bias (blue), the relative error (green), and the normalized number of retrieval points (red). Different line styles represent different mean wind speed cases. The X_c value at the top of Fig. 24.2 represents the across-track measurement footprint distance. These results use an along-track averaging distance of 1300 m

fine-scale measurements in a turbulent boundary layer from the multiple beam system. The results were obtained using a least-squares fitting of the measured radial velocities to the 2-D wind vectors in the vertical and along-path plane. It is assumed the Taylor hypothesis is valid and that the forward, nadir, and backward beams are coplanar with the aircraft trajectory. The nadir beam provides high-resolution vertical wind measurements, and the combination of the forward and backward beams allows for good estimates of the along-track component of the wind. This sort of analysis could be valuable to understanding flow in complex terrain, such as mountain ranges, cities, or wind farms. Ongoing research at CU Boulder is exploring the new potentials of high-resolution wind imaging using multiple beam ADL.

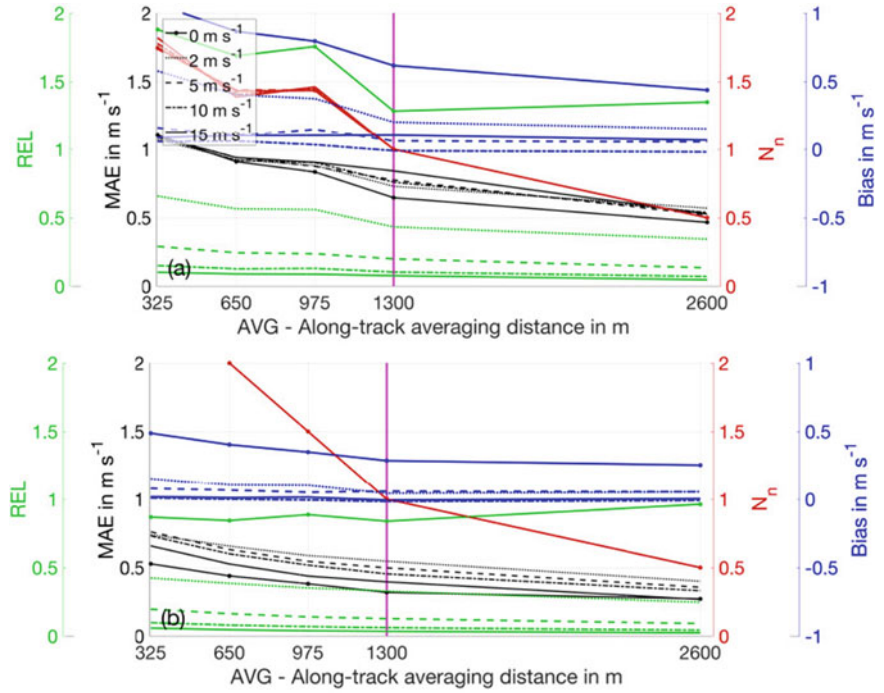


Fig. 24.3 The retrieval error of the scanning system (top) and the fixed-beam setup (bottom) when using various along-track averaging distances. Shown are the mean absolute error (black), the bias (blue), the relative error (green), and the normalized number of retrieval points (red). Different line styles represent different mean wind speed cases. These results use an elevation angle of 60°

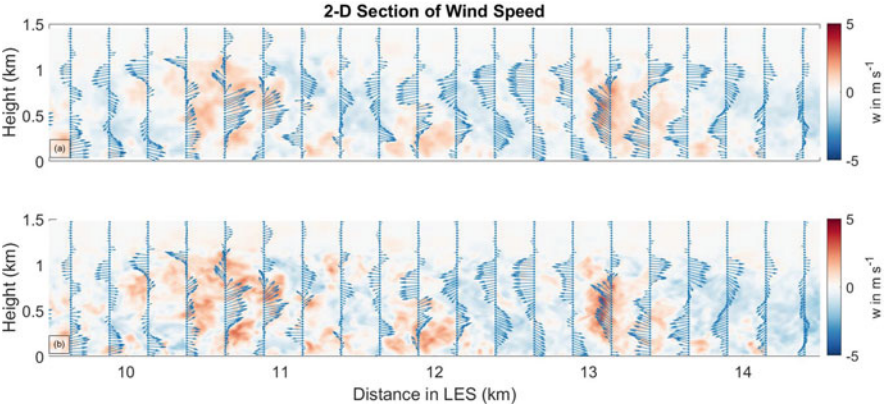


Fig. 24.4 2D wind retrievals shown as vectors representing the vertical plus the along-track wind speeds, with 0 ms^{-1} mean horizontal wind. The color image represents the magnitude of vertical wind. A segment of a transect is shown for both the ADLS retrieval (**a**) and the LES truth (**b**)

24.5 Conclusions

An LES-based ADL simulator is used to evaluate the potential of the new ADL system being developed, which uses multiple fixed beams instead of a single scanning beam. Simulating retrievals using the AVAD technique, the fixed beam system is shown to have significantly reduced retrieval errors compared to a scanning beam system. The comparison shows more than 40% reduced error in mean wind speed measurements. The ADLS also shows that the five-beam configuration has less sensitivity to steep viewing angles as well as short along-track averaging distances. The ADLS is shown to be a valuable tool for evaluating system designs and analysis strategies for the multiple-fixed-beam system in development. Simulation results show that the five-beam system can be expected to resolve 2D roll features, suggesting that UCB ADL system could be used to measure Turbulence Kinetic Energy (TKE) in difficult to sample areas such as cities or mountainous regions. Ongoing research at UCB is using ADLS to investigate the capabilities of in-development system for high-resolution wind speed and TKE measurements and how these can be applied to measurements over complex terrain.

References

1. Weissmann, M., Cardinali, C.: Impact of airborne Doppler lidar observations on ECMWF forecasts. Q. J. R. Meteorol. Soc. **133**(622), 107–116 (2007). https://doi.org/10.1002/qj.16
2. Liu, Z., et al.: A review of progress and applications of pulsed Doppler wind LiDARs. Remote Sens. **11**(21), 2522 (2019). https://doi.org/10.3390/rs11212522
3. Gasch, P., Wieser, A., Lundquist, J.K., Kalthoff, N.: An LES-based airborne Doppler lidar simulator and its application to wind profiling in inhomogeneous flow conditions. Atmos. Meas. Tech. **13**(3), 1609–1631 (2020). https://doi.org/10.5194/amt-13-1609-2020
4. Kavaya, M.J., et al.: The Doppler Aerosol Wind (DAWN) airborne, wind-profiling coherent-detection Lidar system: overview and preliminary flight results. J. Atmos. Ocean. Technol. **31**(4), 826–842 (2014). https://doi.org/10.1175/JTECH-D-12-00274.1
5. Leon, D., Vali, G.: Retrieval of three-dimensional particle velocity from airborne Doppler radar data. J. Atmos. Ocean. Technol. **15**(4), 860–870 (1998). https://doi.org/10.1175/1520-0426(1998)015<0860:ROTDPV>2.0.CO;2

Chapter 25
All-Solid State Iron Resonance Lidar for Measurement of Temperature and Winds in the Upper Mesosphere and Lower Thermosphere

R. Collins, J. Li, B. Wiliams, B. Kaifler, and D. Thorsen

Abstract The Arctic atmosphere and subauroral region are a natural laboratory for understanding plasma-neutral and dynamical coupling in the atmosphere and geospace. During geomagnetically active periods, the auroral electrojet and auroral precipitation are overhead at the High-Frequency Active Auroral Research Program (HAARP) facility in Gakona, Alaska (62°N, 145°W), and facilitate active experiments. Iron resonance lidar systems are uniquely suited for these active investigations as naturally occurring iron layers extend from the upper mesosphere to the middle thermosphere (~70–150 km). A novel lidar system has been demonstrated at the German Aerospace Center using an Nd:YAG laser that operated at a minor line at 1116 nm and was tripled to the iron resonance line at 372 nm. This prototype laser was fully solid-state without liquid dyes or flashlamps and with diode pumping. We are developing a lidar system based on that prototype system that can operate robustly at the remote location of HAARP. We will employ a diode-pumped Nd:YAG laser with second and third harmonic generations. The laser will be injection-seeded by a tunable diode laser allowing the laser to frequency scan the iron line. The laser pulse spectra will be recorded on a shot-by-shot basis using an etalon imaging system with a spectral reference. The lidar system is will operate at 372 nm, with a pulse repetition rate of 100 pps, a pulse energy of 30 mJ, and

R. Collins (✉) · J. Li · D. Thorsen
Geophysical Institute, University of Alaska Fairbanks, Fairbanks, AK, USA
e-mail: rlcollins@alaska.edu

B. Wiliams
GATS Inc., Boulder, CO, USA
e-mail: b.p.williams@gats-inc.com

B. Kaifler
Institute of Atmospheric Physics, German Aerospace Center, Oberpfaffenhofen-Wessling, BY, Germany
e-mail: bernd.kaifler@dlr.de

© The Author(s), under exclusive license to Springer Nature Switzerland AG 2023

J. T. Sullivan et al. (eds.), *Proceedings of the 30th International Laser Radar Conference*, Springer Atmospheric Sciences,
https://doi.org/10.1007/978-3-031-37818-8_25

a 0.9-m-diameter telescope. We present the system specifications and the expected performance of the system.

Keywords Resonance lidar · Solid state · Thermosphere

25.1 Introduction

25.1.1 Radar and Lidar Studies at HAARP

The HAARP (High-Frequency Active Auroral Research Program) facility in Gakona, Alaska (62°N, 145°W), has allowed controlled scientific investigation of the ionosphere for over 30 years [1]. However, the inability to measure neutral molecule properties has made it difficult to accurately interpret and model experimental data. In this paper we describe a resonance lidar that is intended to conduct coordinated observations with the established Ionospheric Research Instrument (IRI) at HAARP. The IRI can operate as both a radio frequency heater and a radio transmitter. A wind-temperature lidar at Gakona would support studies of the mesosphere, thermosphere, and ionosphere in the following areas: dusty space plasmas with lidar measurements of polar mesospheric clouds, and heater-radar measurements of polar mesospheric summer echoes; coupling of mesosphere and lower thermosphere with wind measurements through the D- and E-region; and generation of extremely low-frequency and very-low-frequency waves with measurements of neutral density and temperature.

25.1.2 Iron Resonance Lidar

Resonance lidar systems provide high-resolution temperature, wind, and metal density measurements in the upper mesosphere and lower thermosphere (~80–110 km) based on the occurrence of the meteoric metal layers at that altitude [2–4]. At altitudes below the metal layers, resonance lidar measures Rayleigh scatter that decreases with altitude and yields temperature measurements from 30 to 70 km [5, 6]. The stronger resonant scatter from metal atoms in the D- and lower E-region allows wind, temperature, and metal density measurements that are beyond the ability of current Rayleigh lidars. This combination of lidar techniques have yielded measurements of the atmospheric profile from the stratosphere to the thermosphere (~15–110 km) [7, 8].

Measurements with a high-sensitivity resonance lidar at McMurdo, Antarctica (78°S, 167°E), have revealed the extension of the neutral iron layer upward from the "traditional" altitudes of the MLT (~70 km–110 km) to an "extended" upper altitude of 170 km [5]. This extension has yielded measurements of temperature profiles in the E-region above 150 km. Lidar observations made during auroral activity (Kp ~ 6)

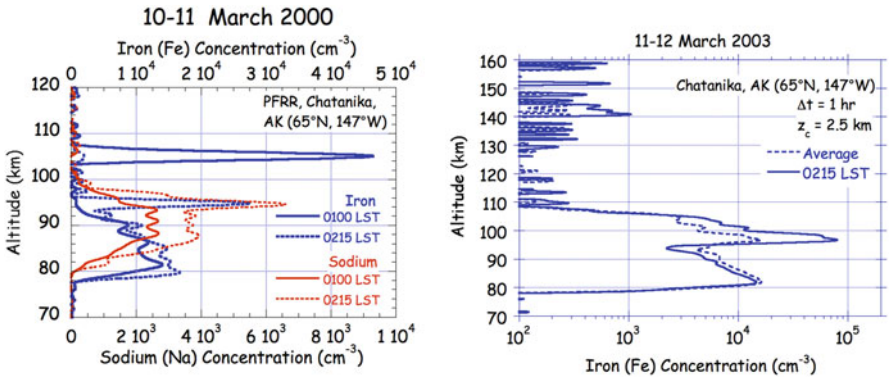


Fig. 25.1 Left: Lidar measurements showing coincidence of sporadic sodium and iron layers in the D-region (95 km) and presence of iron alone in the E-region (105 km). Right: Lidar measurements showing iron extending into the E-region (140 km and 150 km) above the traditional iron layer

documented the increase in neutral temperature associated with Joule heating during this geomagnetic storm. These extended neutral iron layers are observed commonly at McMurdo, with iron detected above 130 km over 25% of the time.

The more common appearance of iron than sodium is consistent with the higher abundance of iron in the thermosphere and faster electron-ion recombination rates for iron than sodium [9–12]. Observations of iron and sodium in Alaska with less sensitive broadband lidars confirm the Antarctic observations. Observations have shown that sporadic iron layers appear at altitudes above the traditional (or main) iron layer when sodium layers do not and that iron is present in the 140–150 km altitude range (Fig. 25.1). A contemporary iron resonance wind-temperature lidar is uniquely suited to investigating the polar ionosphere-thermosphere through the height of the E-region in the polar regions.

25.2 Iron Resonance Wind-Temperature Lidar

25.2.1 Spectroscopy of Nd:YAG

The spectroscopic and mechanical properties of neodymium-doped yttrium aluminum garnet (Nd:YAG: Nd^{3+}:$Y_3Al_5O_{12}$) make it an ideal laser material [11]. The $^4F_{3/2}$ Stark level manifold serves as the upper level for emission lines at 946 nm 1064 nm, 1112 nm, 1116 nm, 1123 nm, and 1319 nm (Fig. 25.2) [12]. The 1116-nm transition has upper and lower energy levels in the same manifolds as the familiar 1064-nm transition, but a stimulated emission cross-section that is an order of magnitude smaller than that of the 1064-nm line (~3×10^{-23} m^2).

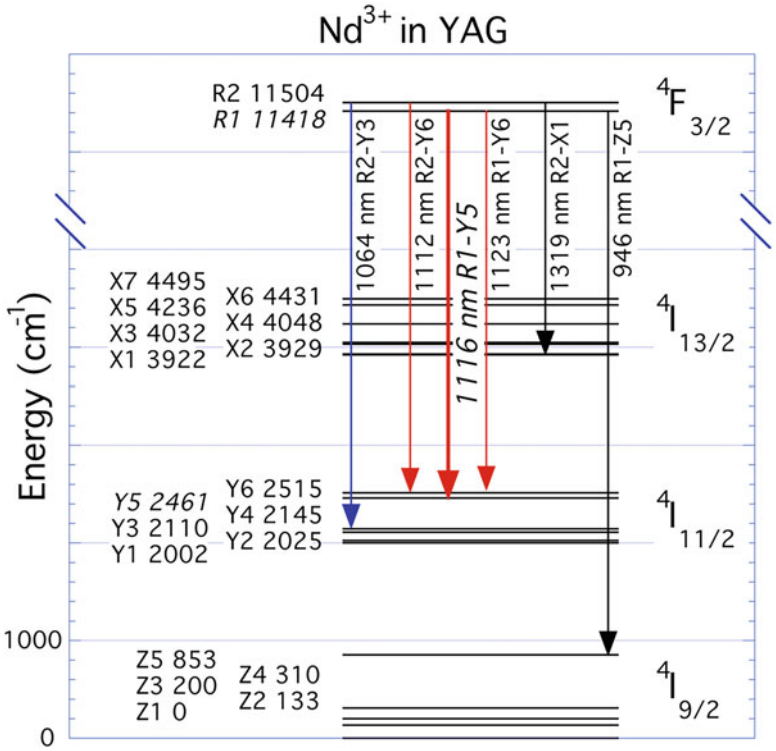


Fig. 25.2 Partial energy level diagram and transitions of Nd^{3+} in YAG

25.2.2 Prototype Nd:YAG-Based Iron Lidar

Serendipitously, the 1116-nm Nd:YAG line lies close to the tripled iron absorption line at 372 nm. A proof-of-principle iron resonance lidar system was demonstrated with a prototype laser optimized for operation at 1116 nm at 100 pps [13]. This prototype laser had a linear stable cavity with a cavity length of 80 cm incorporating an external cavity diode seed laser, diode pumping, and second harmonic and third harmonic generation (Fig. 25.3). The laser was designed to suppress lasing at 1064 nm while allowing lasing at 1116 nm. A thin-film polarizer was used to couple the seed laser into the laser cavity. The laser using a single-Nd:YAG rod with a twisted-mode technique to support single-mode operation. One of the end mirrors was mounted on a piezoelectric transducer to allow matching of the cavity length to the mode of the seed laser. The output coupling was implemented as a variable beam splitter using the combination of a half-wavelength plate and the thin-film polarizer. The cavity end mirrors were > 99.8% reflective at 1116 nm and < 5% and < 20% reflective at 1064 nm and 1319, respectively. The waveplates were antireflection (AR) coated at 1116 nm < 0.1%. A cavity etalon suppressed the

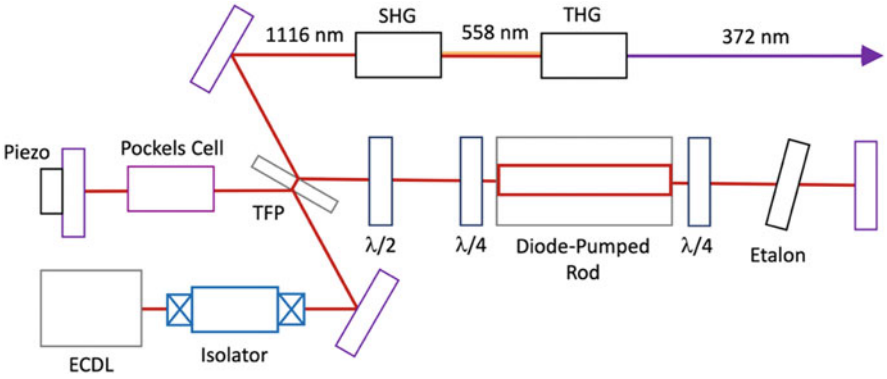


Fig. 25.3 Schematic of the laser system. *TFP* thin-film polarizer, *ECDL* external cavity diode, *SHG* second harmonic generator, *THG* third harmonic generator

1112-nm and 1123-nm lines. The second harmonic and third harmonic generation used Type I/II phase matching with a lithium triborate (LBO) crystals that were AR coated at 1116 nm (SHG, THG), 558 nm (SHG, THG), and 372 nm (THG). The laser linewidth at 372 nm was between 30 MHz and 79 MHz. The laser yielded an output power of 0.5 W at 372 nm. The prototype laser was incorporated into a lidar system and yielded observations of the mesospheric iron layer in November 2015. These first observations also demonstrated the ability to resolve the spectrum of the iron absorption line at sub-Doppler resolution based on the resonance lidar signal.

25.2.3 New Nd:YAG Lidar

Building on the prototype, we are designing a Nd:YAG laser operating at 1116 nm that employs a dual rod oscillator. A dual-rod architecture provides higher cavity gain and less thermal distortion than a single-rod design. The cavity may also adopt a U-shaped configuration. The U-shaped configuration would include turning mirrors that would be coated to provide further support of lasing at 1116 nm and suppression of 1064 nm. The U-shaped configuration would also support an increase in cavity length with longer laser and longer pulse length and decrease in peak pulse power. We will investigate the use of amplifier stages to increase the output optical power. The ramp-and-fire technique will be investigated to maintain single-frequency operation [14].

We estimate the performance capabilities of the lidar based on the expected signals and the associated photon noise [15]. The expected performance is tabulated in Table 25.1. For the daytime performance of the lidar, the receiver includes a double-etalon system with an effective bandwidth of 3 pm similar to established iron resonance temperature lidars [16].

Table 25.1 Nd:YAG-based iron resonance wind-temperature lidar

Transmitter	
Material	Nd:YAG
Wavelength	372 nm
Pulse energy	30 mJ
Repetition rate	100 pps
Linewidth	50 MHz
Receiver	
Telescope diameter	0.91 m
Resolution	
Temporal (night/day)	300 s/600 s
Range (night/day)	1000 m/2000 m
Measurement uncertainty	
Iron concentration (night/day)	0.6%/0.5%
Temperature (night/day)	2 K/5 K
Wind (night/day)	2 m/s/5 m/s

Acknowledgments The development of the new iron resonance wind temperature lidar is supported by the US National Science Foundation under grants 2048628 and 2048810.

References

1. Pedersen, T.: HAARP, the most powerful ionosphere heater on Earth. Phys. Today. **68**(12), 72–73 (2015)
2. Chu, X., Papen, G.C.: Resonance fluorescence lidar for measurements of the middle and upper atmosphere. In: Fujii, T.T., Fukuchi, T. (eds.) Laser Remote Sensing, pp. 179–432. Taylor and Francis, London (2005)
3. Gardner, C.S., Collins, R.L.: Lidar resonance. In: North, G.R.J., Pyle, J., Zhang, F. (eds.) Encyclopedia of the Atmospheric Sciences, pp. 305–308. Academic, Cambridge (2015)
4. Krueger, D.A., She, C.-Y., Yuan, T.: Retrieving mesopause temperature and line-of-sight wind from full-diurnal-cycle Na lidar observations. Appl. Opt. **54**(32), 9469–9489 (2015)
5. Chu, X., Yu, Z., Gardner, C.S., Chen, C., Fong, W.: Lidar observations of neutral Fe layers and fast gravity waves in the thermosphere (110–155 km) at McMurdo (77.8°S, 166.7°E) Antarctica. Geophys. Res. Lett. **38**(23), L23807 (2011)
6. Collins, R.L., Lehmacher, G.A., Larsen, M.F., Mizutani, K.: Estimates of vertical eddy diffusivity in the upper mesosphere in the presence of a mesospheric inversion layer. Ann. Geophys. **29**, 2019–2029 (2011)
7. Dou, X.K., Qiu, S.C., Xue, X.H., Chen, T.D., Ning, B.Q.: Sporadic and thermospheric enhanced sodium layers observed by a lidar chain over China. J. Geophys. Res. Space Phys. **118**(10), 6627–6643 (2013)
8. Kopp, M., Gerding, M., Höffner, J., Lübken, F.-J.: Tidal signatures in temperatures derived from daylight lidar soundings above Kühlungsborn (54°N, 12°E). J. Atmos. Sol. Terr. Phys. **127**, 35–50 (2015)
9. Chu, X., Yu, Z.: Formation mechanisms of neutral Fe layers in the thermosphere at Antarctica studied with a thermosphere-ionosphere Fe/Fe+ (TIFe) model. J. Geophys. Res. Space Phys. **122**(6), 6812–6848 (2017)

10. Chu, X., Nishimura, Y., Xu, Z., Yu, Z., Plane, J.M.C., Gardner, C.S., Ogawa, Y.: First simultaneous lidar observations of thermosphere- ionosphere Fe and Na (TIFe and TINa) layers at McMurdo (77.84°S, 166.67°E), Antarctica with concurrent measurements of aurora activity, enhanced ionization layers, and converging electric field. Geophys. Res. Lett. **47**(20), 1–10 (2020)
11. Koechner, W.: Solid State Laser Engineering, 6th edn, p. 747. Springer, New York (2006)
12. Singh, S., Smith, R.G., van Uitert, L.G.: Stimulated-emission cross section and fluorescent efficiency of Nd^{3+} in yttrium aluminum garnet at room temperature. Phys. Rev. B. **10**(6), 2566–2572 (1974)
13. Kaifler, B., Büdenbender, C., Mahnke, P., Damm, M., Sauder, D., Kaifler, N., Rapp, M.: Demonstration of an iron fluorescence lidar operating at 372 nm wavelength using a newly-developed Nd:YAG laser. Opt. Lett. **42**(15), 2858–2861 (2017)
14. Henderson, S.W., Yuen, E.H., Fry, E.: S.: fast resonance-detection technique for single-frequency operation of injection-seeded Nd:YAG lasers. Opt. Lett. **11**(11), 715–717 (1986)
15. Gardner, C.S.: Performance capabilities of middle-atmosphere temperature lidars: comparison of Na, Fe, K, Ca, Ca+, and Rayleigh systems. Appl. Opt. **43**(25), 4941–4956 (2004)
16. Chu, X., Pan, W., Papen, G.C., Gardner, C.S., Gelbwachs, J.A.: Fe Boltzmann temperature lidar: design, error analysis, and initial results at the North and South Poles. Appl. Opt. **41**(21), 4400–4410 (2002)

Chapter 26
Improved Remote Operation Capabilities for the NASA GSFC Tropospheric Ozone Lidar for Routine Ozone Profiling for Satellite Evaluation



T. H. Nguyen, J. T. Sullivan, and L. W. Twigg

Abstract To observe tropospheric ozone more effectively, the National Aeronautics and Space Administration (NASA) Goddard Space Flight Center Tropospheric Ozone Differential Absorption Lidar (GSFC TROPOZ DIAL) has been developed and validated within the Tropospheric Ozone Lidar Network (TOLNet). Efforts had been made to transform the system for remote observations that can accurately provide and archive continuous information about the vertical variability of ozone without constant supervision.

In this work, we describe major hardware and software upgrades implemented within the GSFC TROPOZ DIAL. These upgrades include full automation to the lidar system and controls of various sub-systems to characterize the overall health of the lidar system as well as useful weather data around the system's housing. Further improvements were made which led to real-time datalogging and daily archiving for internal system data files and crucial information to the NASA TOLnet cloud network. These feats were achieved with two main Python graphical user interface (GUI) programs as well as other smaller specialized programs which provide a consolidation of data from various weather detectors into coherent graphs, equipped with new file saving and back up mechanics. They also act as control centers for the system's electrical components during remote operation. The purpose of these changes was to allow unattended and scientifically rigorous observations to be collected during deployments. Selected observations produced with the newly updated system are shown to illustrate the final ozone profiles and various metrics provided by the automation software.

T. H. Nguyen (✉) · L. W. Twigg
Science Systems and Applications Inc., Lanham, MD, USA
e-mail: trong.h.nguyen@nasa.gov; laurence.w.twigg@nasa.gov

J. T. Sullivan
Atmospheric Chemistry and Dynamics Branch, NASA Goddard Space Flight Center, Greenbelt, MD, USA
e-mail: john.t.sullivan@nasa.gov

© The Author(s), under exclusive license to Springer Nature Switzerland AG 2023

J. T. Sullivan et al. (eds.), *Proceedings of the 30th International Laser Radar Conference*, Springer Atmospheric Sciences,
https://doi.org/10.1007/978-3-031-37818-8_26

Keywords Lidar

26.1 Introduction

As part of the efforts to measure tropospheric ozone level, the National Aeronautics and Space Administration (NASA) Goddard Space Flight Center Tropospheric Ozone Differential Absorption Lidar (GSFC TROPOZ DIAL) was developed and deployed in various missions in the United States and around the globe. Depending on the location where high concentration exists, ozone has different effects on human health and global warming. While acting as an effective greenhouse gas in the upper troposphere and lower stratosphere [1], high concentration of ground level ozone can cause serious harm to the human health [2]. It has also been shown that ozone can cause yield lost in different crops (USDA, 2011). Thus, the goal for the TROPOZ is to collect vertical tropospheric ozone within their respective urban regions. These profiles are recorded and analyzed from a series of measurements that can span across many days. The GSFC TROPOZ DIAL is one of many instruments currently taking measurements in the ground based Troposheric Ozone Lidar Network (TOLNet). The primary objective of the TOLNet group is to provide consistent, high-fidelity tropospheric ozone profiles, particularly the changing ozone dynamics and laminate inside the PBL. These measurements are also studied by the Geostationary Coastal and Air Pollutions Events (GEO-CAPE) team to validate the new satellite which is set to launch in 2022.

The instrument was built with the intention of being deployable anywhere in the world, with the whole setup fitted inside a 13-m transportable trailer. The trailer is equipped with its own HVAC system as well as electrical and internet connections allowing for it to be self-sustainable in different environments. The exact details and setup of the original TROPOZ DIAL instrument are provided in the Sullivan et al. [3]. While the instrument has been collecting measurements across many science missions over the last decade, there are some drawbacks that could be improved upon. Lidar ozone measurement is a tedious task that can require a lot of time and man power to be done correctly. With the way that the system was set up, an operator was required to attend to the system at all times during the measurement, which could span a whole day. This takes up valuable time where data analysis could have been done. In addition to that, there was a lack of data management that resulted in additional wasted time.

Thus, major efforts have been made over the past 2 years to completely automate the system, allowing for remote operation. Several significant software and hardware changes were implemented on the legacy system. As a result, it is possible for the team to carry out measurements completely remotely and still have access to the system. A new file-saving system and hierarchy was also implemented, creating a more efficient and reliable system. Files are now automatically upload to the perspective storage sites the minute after data are collected.

26.2 Hardware Improvements

Since the legacy system contains many components which were not compatible with the automation efforts, major hardware upgrades were made to support the effort. Most of the hardware are connected to a central computer through either ethernet or USB. Figure 26.1 outlines how all the component of the new system are integrated and connected. The details of these upgrades are listed below.

26.2.1 Hatch

The old hatch's doors system is controlled through a manual control box with individual switches for each door. The control box acts as a relay system that determines whether to open or close a hatch's door. To automate this component, an Arduino was utilized along with a compatible relay module. The power supply was rerouted through the relay which is controlled by code implemented on the Arduino. The old control box was kept as a fail-safe in the event that the new parts fail.

26.2.2 Power Distribution Units

One of the most important aspects of the automation effort is the ability to turn different components on/off at will. This feature allows the users to have full control over the system, being able to start and stop the measurements process at

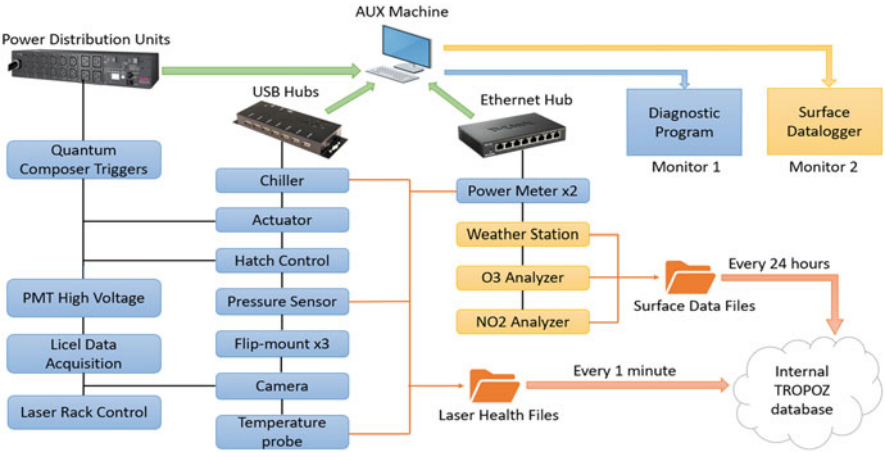


Fig. 26.1 Hardware diagram showing all connections and connections type to the AUX computer

will. Smart PDUs were integrated into the system to achieve this. The PDUs each have eight different outlets, individually powered and controlled through ethernet connections. The PDUs are powered independently, assuring that the components will still receive power even if the main computer is shut off.

26.2.3 Power Meters/Flip Mounts

Another component that received an upgrade are the power meter. New ethernet-connected power meters were acquired and integrated into the system to improve the accuracy of the reading. Along with the power meters, mirror flip mounts were also installed to allow the users to redirect the laser beam to different location during the measurements process. There are currently three different flip mounts and two new power meters that are being utilized to check the health of the laser.

26.2.4 Temperature Probes/Pressure Sensor

In order to monitor the health of the system remotely during an operation, new measurement sensors were built and installed in the system. The temperature probe monitors and displays humidity and temperature data in real time for the users. Another Arduino module was used to build an automate-compatible pressure sensor that shows the pressure of the Raman cell. Through these devices, the users are able to have an accurate view of the status of the lab at all time.

26.3 Automation Steps

The bulk of the software upgrade was focused on the automation effort and archival data, allowing for remote operations and (better) archival structure. The autonomous upgrade drastically shortens the amount of time the team needs to start and stop the system, while giving the team more time for analysis during a measurement as opposed to having to supervise the system. More time is also saved with the new archival system.

The complete system resides on three different computers. The dial acquisition machine (TROPOZ-DACQ) is responsible solely for the raw lidar files collected from the licel machine, which is currently being run of a LABview program. It's also tasked with controlling the laser unit through a web-based GUI. The analysis machine (TROPOZ-ANA) handles the real-time analysis of the raw licel files that were collected from the DACQ machine. The analysis includes a real-time curtain plot which is updated every 15 min along with other useful representations. The analysis software is run through LABview. The new automation system resides on

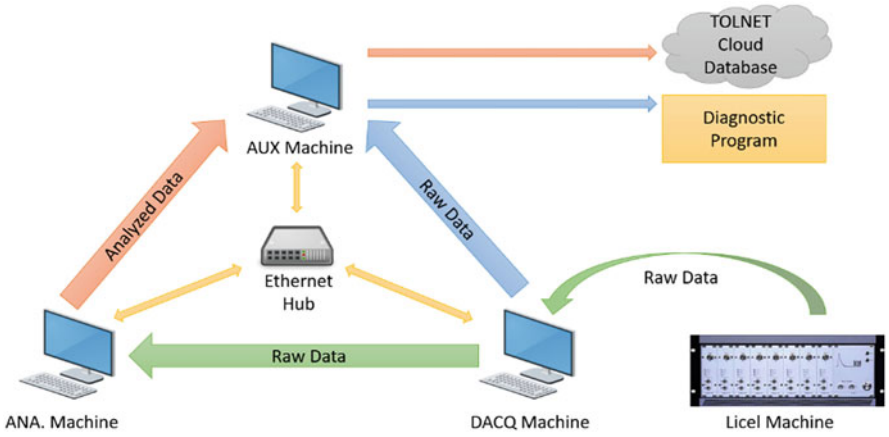


Fig. 26.2 Diagram showing how all three computers communicate with each other internally and externally

the auxiliary system (TROPOZ-AUX), which utilizes both the raw and analyzed files. All three computers are connected through ethernet connections for file transfers. Figure 26.2 shows the diagram of how the three machines interact with each other.

26.3.1 Diagnostic Program

The first main GUI is called the "Diagnostic Program." It is comprised of multiple mini modules which in turns control a hardware piece in the lab. The main objective of this GUI is to allow the user the ability to have a quick summary of what is happening in the lab while having the ability to change and control hardware that was once only manually accessible. Because of this, it is crucial for the start and stop operation; 90% of work is done here at startup and shutdown. The first module that is connected to the GUI is the chiller. The user has the ability to turn it on or off through here; once it is on, the temperature and pressure information are displayed. Other environment gauges are also connected to the GUI, such as a temperature probe with multiple sensors, displaying the lab's diagnostic information. A flip mount was installed to direct the beam to a power meter during initial startup; both hardware are displayed on the GUI. Data from live lidar measurement are pulled from the licel program, and different intensities' peaks are graphed, allowing the user to have a quick lance of the health of the laser.

One of the more important modules that the program has is the hatch module, which opens or closes the lab's hatch with a button as mentioned in Sect. 26.2. A camera is also installed pointing up at the hatch, allowing the team to have a view of the sky during measurements and making sure that the hatch is operating correctly.

An alignment module is installed, allowing the user to adjust the laser's beam during operation for the optimal position to obtain the most data. To do this, actuators are connected to the channel mirrors pointing up at the sky and the users can move them at different increments. Lastly, the GUI also contains all the controls for the PDUs, allowing the team to remotely supply or cut off power to any piece of hardware in the lab.

26.3.2 Surface Datalogger

The second main GUI is called the "Surface Datalogger." As opposed to the first GUI, where emphasis are placed on controlling hardware, this GUI's main purpose is to collected and displayed data from different analyzers. There are three acquisition devices that the software manages, a NO_2 analyzer, a O_3 analyzer, and a weather station. From these devices, eight different statistics are graphed in eight separate logs over the course of the day to show how they change. The data being collected are information about the environments around the trailer, i.e., surface ozone, temperature, wind-direction, etc. The plots are updated every minute, and at the end of the day, all the data and a final 24-h graph is produced and saved in a directory. An email alert system is also set up to let the team know whenever one of the three devices encounter a failure. Along with these two GUIs, there are mini specialty software that are used for other hardware, such as the spectrometer, rain sensor, laser rack, etc. Altogether, these software work in unison to make sure that the measurements run smoothly.

All of the diagnostic data as well as surface data are logged into separate files every day that are saved on the central computer for references and archival purposes. Currently, there are three files being saved and archived in real time from three different programs. It should be noted that the programs are run continuously during multiday operations; thus new files are created at midnight every night, while the files from the previous days are automatically uploaded to a secure internal server. The surface data and graph are additionally upload to the TOLNet servers.

26.4 Improved Data Collection

During the TRACER-AQ campaign, the newly automated system was able to continuously collect data for 120 h straight, which is a huge improvement from the previous record of 12 h. Figure 26.3 shows the curtain plot of one of the days where the system was collecting data continuously. It can be seen from the data that there is an interesting ozone features at 15:00 that is worth investigating. Because of the automation efforts, the team is able to have more and better data comparing to previous campaigns.

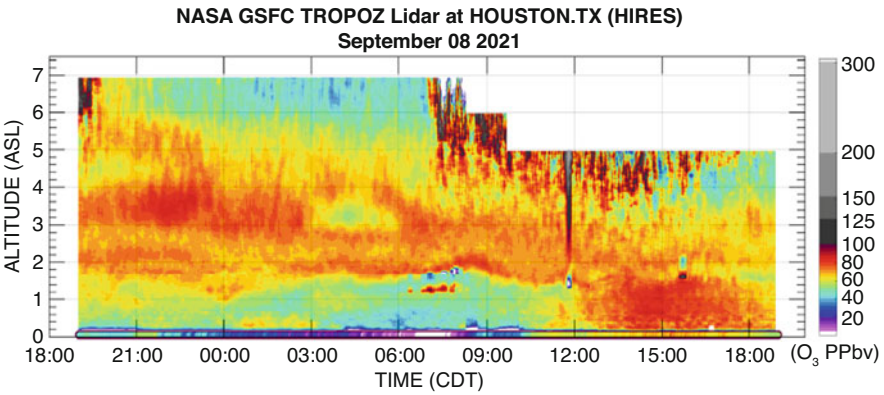


Fig. 26.3 Curtain plot from a successful run during the TRACER-AQ campaign

References

1. Fraser, P.J., Fung, I.J., Khalil, M.A.K., Manning, M., McCulloch, A., Mitra, A.P., Moore, B., Rodhe, H., Schimel, D., Siegenthaler, U., Skole, D., Stolarski, R.S.: Green House Gases: Sources and Sinks (1991)
2. Zhang, J., Wei, Y., Fang, Z.: Ozone Pollution: A Major Health Hazard Worldwide (2019)
3. Sullivan, J.T., McGee, T.J., Sumnicht, G.K., Twigg, L.W., Hoff, R.M.: A mobile differential absorption lidar to measure sub-hourly fluctuation of tropospheric ozone profiles in the Baltimore-Washington, D.C. region. Atmos. Meas. Tech. **7**, 3529–3548 (2014). https://doi.org/10.5194/amt-7-3529-2014

Chapter 27
A Wind, Temperature, H_2O, and CO_2 Scanning Lidar Mobile Observatory for a 3D Thermodynamic View of the Atmosphere



Fabien Gibert, Dimitri Edouart, Paul Monnier, Claire Cénac, Vincent Gauthier, and Henri Salvador

Abstract A ground-based mobile 3D lidar observatory has been developed for simultaneous measurements of wind speed, temperature, water vapor, and carbon dioxide absorption in the atmosphere. This chapter reports details of the instruments, assesses the current performances, and gives some examples of measurements for different geophysical applications.

Keywords Lidar observatory · 3D lidar · Scanning lidar · Doppler lidar · DIAL · Raman lidar · Coherent and direct detection

27.1 Introduction

The motivation of this work is to provide advanced observations of the main variables that characterize the land-atmosphere exchanges of momentum, temperature, water vapor, and carbon dioxide. The lidar mobile observatory is a prototype that hopefully will help to path the way to a future 3D thermodynamic view of the atmosphere that will match current and future Navier-Stokes equation simulation at different scales (large eddy simulation (LES), direct numerical simulation (DNS)) and will help our understanding of the carbon cycle in the context of global warming [1]. Multiple goals include (i) to address the representativeness of in situ measurements in heterogeneous landscape, especially for surface fluxes; (ii) to assess the relevance of Monin-Obukhov similarity theory (MOST) which links gradient and flux close to the surface; (iii) to address the issue of dissimilarity of scalar

F. Gibert (✉) · D. Edouart · P. Monnier · C. Cénac · V. Gauthier · H. Salvador
Laboratoire de Météorologie Dynamique (LMD/IPSL), École Polytechnique, Institut Polytechnique de Paris, Sorbonne Université, École normale supérieure, PSL Research University, CNRS, École des Ponts, Palaiseau, France
e-mail: gibert@lmd.polytechnique.fr

© The Author(s), under exclusive license to Springer Nature Switzerland AG 2023

J. T. Sullivan et al. (eds.), *Proceedings of the 30th International Laser Radar Conference*, Springer Atmospheric Sciences,
https://doi.org/10.1007/978-3-031-37818-8_27

transport such as heat and water vapor or CO_2 in inhomogeneous landscape; and (iv) to help to find advanced model parametrizations of land-surface- or boundary layer-free atmosphere exchanges and transport processes, for both convective and stable planetary boundary layers. To do so, new observations are needed that can provide, first, a 3D view of the atmosphere and second, that have turbulence-scale temporal and spatial resolutions in order to investigate flux-gradient relationships and estimate higher-order moments.

In this chapter, we present the main characteristics of the two lidars of this observatory, and we assess the performances in terms of precision and bias.

27.2 Instrumental Setup

27.2.1 3D Lidar Observatory

The mobile 3D lidar observatory consists in two containers with scanning lidars that operates in nonvisible UV and the NIR optical windows for eye safe reasons (Fig. 27.1). First, lidar is a temperature and water vapor Raman lidar at 355 nm (TERA), and second is a prototype DIAL and Doppler lidar at 2051 nm (COWI) for simultaneous wind speed and carbon dioxide (CO_2) absorption measurements. Lidar observations are completed by several in situ sensors to complete the dataset



Fig. 27.1 3-D lidar observatory in operation during the LIAISE field experiment, July 2021, Preixana, Spain

especially in the surface atmospheric layer. Two in situ flux stations with sonic anemometers and gas analyzers, one attached to the observatory and second deployed few kilometers apart, are especially used for turbulent-linked measurement references and to assess surface property heterogeneities.

27.2.2 TERA: Temperature and Water Vapor Raman Lidar

The main characteristics of TERA lidar are shown in Fig. 27.2. The lidar consists in a diode-pumped and seeded tripled Nd:YAG laser that provides 200-mJ pulses at 100 Hz at 354.8 nm (Merion-Lumibird SA) and a 50-cm-diameter telescope and associated scanning device (Fig. 27.2). The detection setup includes several interference filters in cascade: two for temperature rotational channels (RR1, 354.15 nm (0.3 nm bandwidth) and RR2, 353.3 nm (0.5 nm)) and one for H_2O

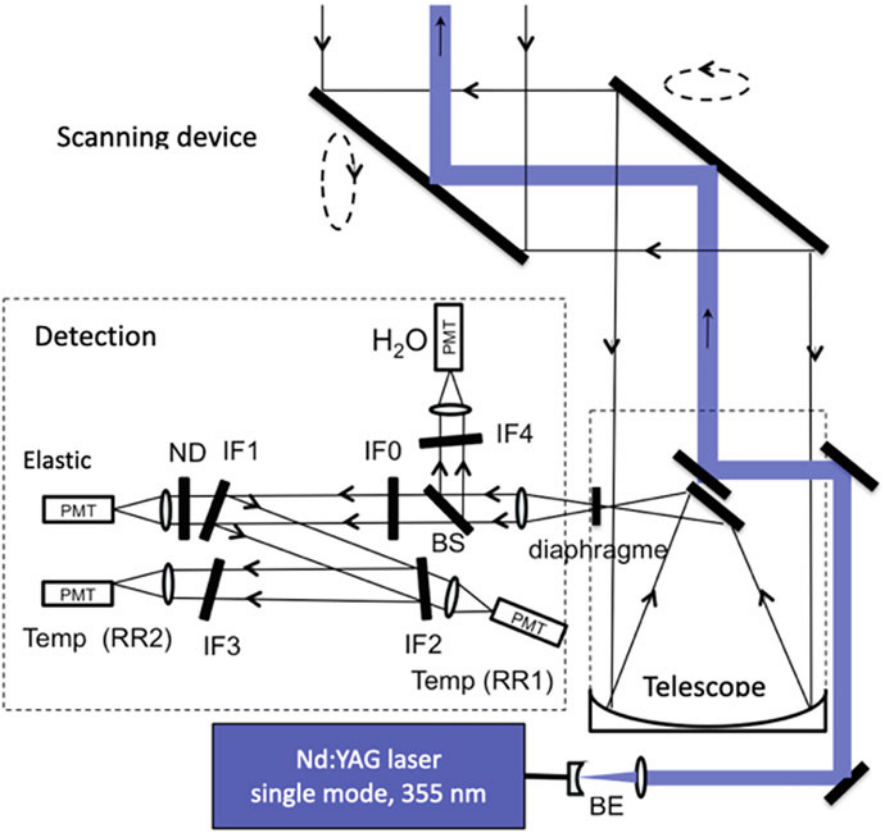


Fig. 27.2 TERA optical setup

vibrational Raman detection at 407.7 nm (0.3 nm) similar to the system that was developed in [2]. An elastic channel is used to monitor the structure of the atmosphere but also to calibrate the 3D axes of the scanning device with referenced hard targets. The detection and acquisition system use standard devices with PMTs and LICEL TR40-12-bit systems for simultaneous analogic and photon-counting detections. The power supply, including the cooling of the laser, is lower than 5 kW. The scanning device has been built in the lab and uses custom ellipsoidal gas fusion mirrors with an aluminum coating. TERA was specifically designed for high temporal and space resolution profiling of temperature and water vapor in the boundary layer for turbulence-linked measurements but longer averaging scales (1 h–200 m) enables to make measurement up to the stratosphere during the night.

27.2.3 COWI: CO_2 and Wind Lidar, Doppler, and DIAL

COWI lidar makes use of a thulium-fiber laser-pumped dual-wavelength seeded Ho:YLF MOPA emitter that provides 10-mJ pulses at 2 kHz [3].

The lidar has a coherent detection for wind speed measurement and a direct detection using a new HgCdTe APD and a 20-cm-diameter telescope for differential absorption measurement of CO_2 [4]. In the present configuration, two wavelengths are used to make DIAL measurements of CO_2 using the R30 absorption line at 2050.97 nm, but a third one may be added at 2050.53 nm to make simultaneous measurement of H_2O. Spectral purity is measured to be larger than 99.96%, and frequency stability (better than 150 kHz at 10 s) is achieved using a lab-made frequency reference system that relies on a CO_2-filled absorption cell, external frequency modulation, and Pound-Drever-Hall technique. Total power supply of the lidar is lower than 2 kW.

27.3 Measurements and Performances

27.3.1 3D Lidar Sensing

The main objectives of 3D lidar sensing are to provide tropospheric vertical profiles and to document at the same time the heterogeneity of surface layer properties that could explain these vertical profiles (Fig. 27.3).

In this way, the lidars are operated sequentially in three different modes: (i) vertical to get the troposphere characteristics, scalar profiles and moments, integral scales and fluxes using the eddy-covariance method; (ii) RHI (range-height indicator), low altitude vertical cross-section of the surface layer at a given azimuth angle to apply Monin-Obukhov similarity theory and estimate surface

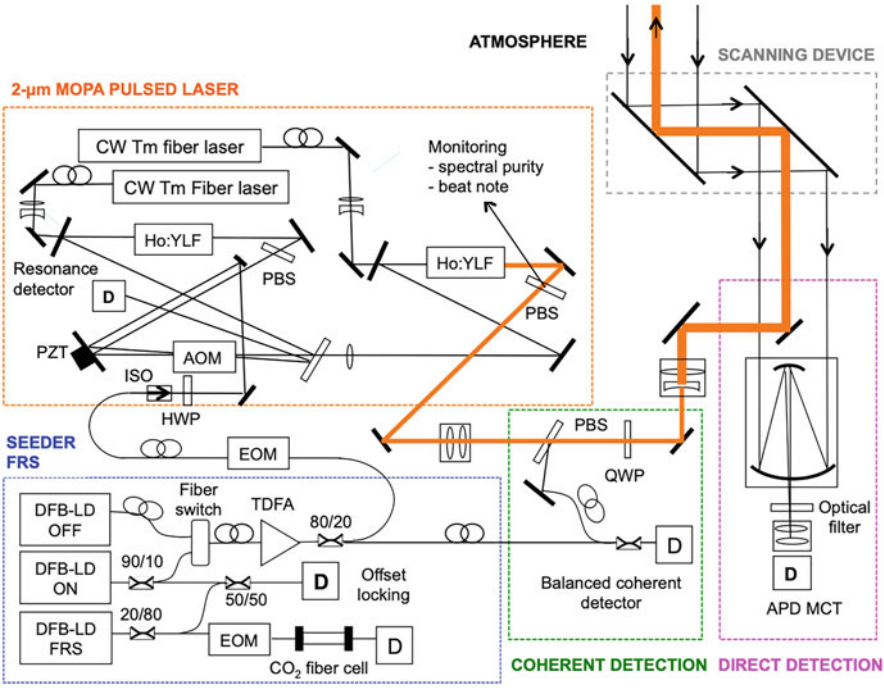


Fig. 27.3 COWI optical setup

fluxes heterogeneity; and (iii) PPI (plan polar indicator), low-altitude horizontal cross-section of the surface layer to measure scalar field heterogeneity.

27.3.2 Potential Temperature and Specific Humidity Gradients and Fluxes

One of the main objectives of this lidar observatory is to provide a continuous thermodynamic view of the convective boundary layer in order to improve model parametrizations of vertical transport. Correlation between radial wind speed and scalar profiles (temperature, H_2O, CO_2) requires co-located instruments, several altitude-referenced targets to calibrate scanning device elevation and azimuth angles, and synchronized data acquisition systems. Figure 27.4 shows an example of eddy-covariance sensible and latent heat fluxes calculated with time and space resolution of 30 min and 50 m. Instrumental and sampling errors are indicated. Mean potential temperature and specific humidity profiles are also displayed. Statistical errors are respectively lower than 0.5 K and 0.3 g/kg with time and space resolution of 2 min and 7.5 m in the first kilometer of the CBL. Comparison with radiosondes

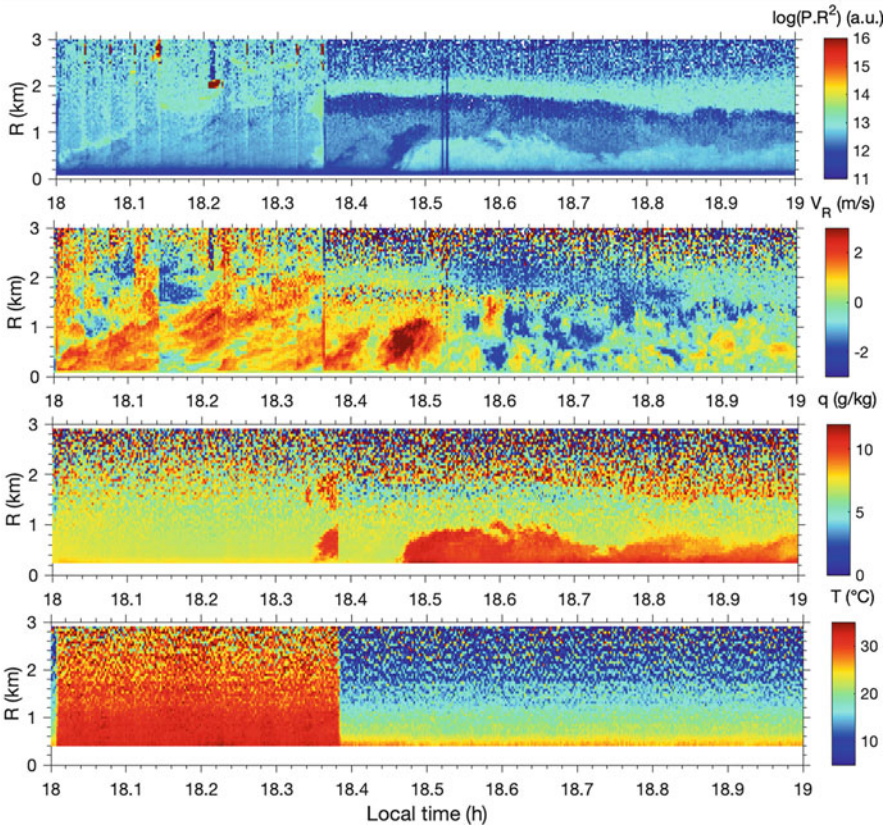


Fig. 27.4 Typical scanning lidar observations during one hour. Top to bottom: lidar reflectivity at 2 μm, radial wind speed, specific humidity, and temperature. Measurement starts with four 6° RHI, then a 30° PPI, again four 6° RHI, and vertical measurements for the rest of the hour. Time in range resolution are 8 s and 50 m, respectively

profiles show a bias for potential temperature profile for $z < 0.3$ km due to a different overlap function for the two lidar temperature channels (Fig. 27.5).

27.3.3 Some Insight in CO_2 DIAL Measurements

Simultaneous measurements of CO_2 with H_2O and temperature is of great interest to address the issue scalar diffusivity difference and scalar dissimilarity in the boundary layer. Up to now, such measurement is still difficult to achieve given the required precision and accuracy (<1%) especially when one wants to study turbulent exchanges. At least the CO_2 field heterogeneity may be investigated with a useful geophysical precision but still limited time and space resolution [5]. Figure 27.6

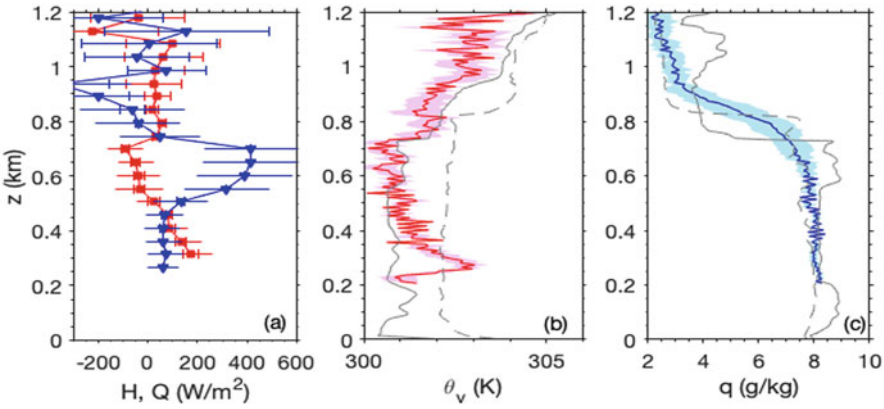


Fig. 27.5 (**a**) Lidar eddy covariance sensible heat (H) (red) and latent heat (Q) (bleu) flux profiles between 13.4 and 14 h calculated with native data resolution of 50 m and 8 s. Long cap error bars are for the instrumental error and no cap error bars for sampling error. (**b**) Virtual potential temperature profile and standard deviation. (**c**) Specific humidity profile and standard deviation. Time and space resolution are 2 min and 7.5 m. Radiosondes profiles are indicated at 13 h (solid grey line) and at 14 h (dashed grey line)

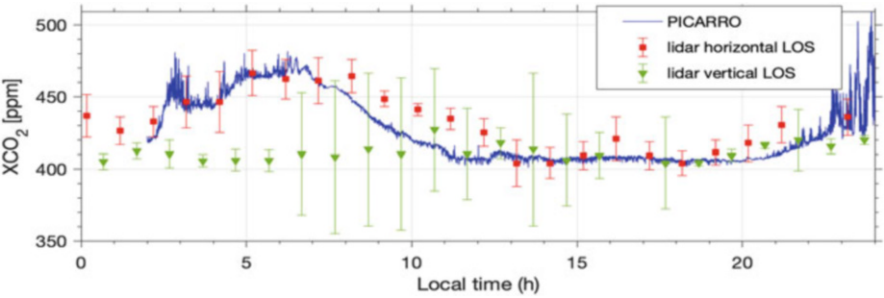


Fig. 27.6 CO2 coherent differential absorption lidar measurements with time and space resolution of 30 min and 500 m. PICARRO: in situ gas analyzer

shows an example of CO_2 diurnal cycle monitoring both in the surface layer and in the boundary-layer using the scanning ability of the COWI lidar. Measurements were made using the coherent detection. Unfortunately, the direct detection that uses the HgCdTe APD prototype detector has not been successful at this point [4]. A new detector made in the framework of the ongoing HOLDON H2020 [6] project is expected to give the necessary precision, space, and time resolution for serious CO_2 geophysical studies.

Acknowledgments This work is supported by the European Space Agency (ESA), the National Space Agency (CNES), the Directorate General of Armaments (DGA), the National Centre for Scientific Research (CNRS), and the Research National Agency (ANR).

References

1. Wulfmeyer, et al.: The GEWEX Land-Atmosphere Feedback Observatory (GLAFO). GEWEX Q. **30**(1), 6–11 (2020)
2. Radalch, et al.: Scanning rotational Raman lidar at 355 nm for the measurement of tropospheric temperature fields. Atmos. Chem. Phys. **8**, 159–169 (2008)
3. Gibert, et al.: 2-μm double-pulse single-frequency Tm:fiber laser pumped Ho:YLF laser for a space-borne CO2 lidar. Appl. Opt. **57**(36), 10370–10379 (2018)
4. Dumas, et al.: Evaluation of a HgCdTe e-APD based detector for 2 μm CO2 DIAL application. Appl. Opt. **56**(27), 7577–7585 (2017)
5. Gibert, et al.: 2-μm Ho emitter-based coherent DIAL for CO2 profiling in the atmosphere. Opt. Lett. **40**(13), 3093–3096 (2015)
6. HOLDON: HgCdTe APD optimisation for lidar detection of greenhouse gases, H2020 European commission project, (2018–2022)

Chapter 28
Low-Cost and Lightweight Hyperspectral Lidar for Mapping Vegetation Fluorescence

Hampus Månefjord, Lauro Müller, Jacobo Salvador, Anna Runemark, Carsten Kirkeby, and Mikkel Brydegaard

Abstract We have developed a hyperspectral Scheimpflug lidar for measuring vegetation fluorescence. The fluorescence spectra of leaves from several known Swedish trees were acquired remotely, and a three-dimensional point cloud was acquired from a forest edge with the hyperspectral lidar. The method can retrieve echoes, synchronized in time and space, from details in the vegetation structure across 70 effective bands from 400 to 800 nm. The fluorescence spectra were clustered using dimensionality reduction by spectral binning and singular value decomposition. Our instrument complements canopy lidar range statistics with fluorescence information for increased specificity.

Keywords Remote sensing · Scheimpflug lidar · Canopy profiling

H. Månefjord (✉) · L. Müller · J. Salvador
Department of Physics, Sölvegatan 14, Lund University, Lund, Sweden
e-mail: hampus.manefjord@forbrf.lth.se

A. Runemark
Department of Biology, Sölvegatan 35, Lund University, Lund, Sweden

C. Kirkeby
Department of Veterinary and Animal Sciences, Grønnegårdsv 8, Copenhagen University, Frederiksberg, Denmark

M. Brydegaard
Department of Physics, Sölvegatan 14, Lund University, Lund, Sweden

Department of Biology, Sölvegatan 35, Lund University, Lund, Sweden

Norsk Elektro Optikk A/S, Oslo, Norway

© The Author(s), under exclusive license to Springer Nature Switzerland AG 2023

J. T. Sullivan et al. (eds.), *Proceedings of the 30th International Laser Radar Conference*, Springer Atmospheric Sciences,
https://doi.org/10.1007/978-3-031-37818-8_28

28.1 Introduction

Vegetation profiling is a growing research field with a multitude of novel techniques for acquiring data for guiding sustainable management of our environment. Multi- and hyperspectral imaging of vegetation provides the presence and concentration of chlorophyll, species differentiation, vegetation moisture, nutrition, and health. Such data range from global coverage by space borne instruments to resolving individual plants from airplanes or branches and leaves from drones [1, 2]. However, the penetration depth of passive imaging is limited, and lidars can complement such imaging by resolving the height profiles of vegetation over the ground. This information improves the classification of tree species [3, 4]. In addition, while young, old, planted, and virgin forests can be composed of similar species, their height distributions widely differ. Therefore, vegetation lidar height distributions can be associated with the species richness of animals [5]. Recently, hyperspectral imaging and lidar measurements have also been complemented by assessing solar-induced fluorescence (SIF), reporting on plant growth, biomass production, and, thus, CO_2 uptake. This fluorescence imaging method can be accomplished during the daytime by resolving the narrow Fraunhofer lines in the atmospheres of our sun and Earth [6]. It is, however, limited to few spectral bands. We have developed active remote sensing concepts and designed a 3D-printed inelastic hyperspectral lidar for vegetation fluorescence to increase specificity while retaining a high spatial resolution and height distribution.

28.2 Instrumentation

We have developed a continuous wave fluorescence hyperspectral lidar [7] based on a violet 1 W 402-nm laser diode. The laser transect is imaged through a slit with a double Scheimpflug configuration and spectrally dispersed by a grating. The light is thus projected onto a 2D CMOS camera, resolving both range and photon energy. Stacking exposures of the acquisition camera provide an intensity data cube with the axes of range, wavelength, and time – thus constituting real-time hyperspectral full-waveform lidar echoes. The operation range was designed from 5 to 100 m, resolved by 70 effective spectral channels from 400 to 800 nm. The maximum framerate of the camera was 120 Hz, which was sufficient for our application. We employ a laser-modulated lock-in detection scheme whereby fluorescence signals can be retrieved during the daytime. For simplicity of assembly and to maintain a low cost, the instrument was partly constructed with 3D-printed parts. The bill of materials was ~US$ 6000, and the system weighs ~3 kg, excluding the tripod.

28.3 Experiment

Two experiments were conducted in August 2021 at the Stensoffa field station administrated by Lund University in southern Sweden. In the first case, the lidar was mounted on a tripod and directed toward a termination board 100 m away. The fluorescence signatures of 12 identified local tree species were scanned by manually walking with branches along the 100-m laser transect.

In the second experiment, the lidar was repositioned, viewing over a lake with a dense forest canopy along its shore. The motorized tripod was programmed to sweep the azimuth angle 45° and the elevation angle 30° to raster scan a portion of the forest edge with 30 ms exposures. The corresponding azimuth and elevation angles were coupled with each recorded lidar data file. The most prominent trees along the forest edge were identified visually, and their respective GPS coordinates were registered; see Fig. 28.1.

28.4 Data Processing and Results

The fluorescence of the 12 labeled species was normalized for the maximum fluorescence signal; see Fig. 28.2a. Two prominent peaks from chlorophyll photosystem I and II are observed at approximately 680 and 730 nm, respectively. Blue-green

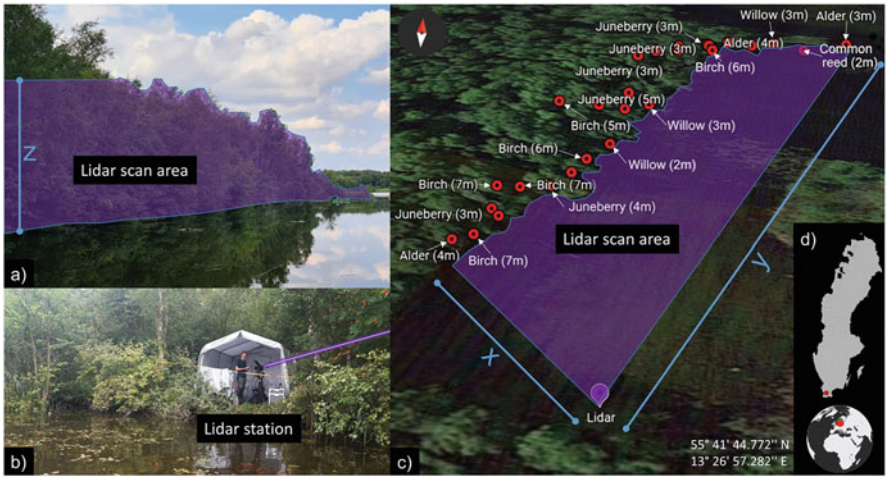


Fig. 28.1 The lidar scanned the forest edge along a lake shore. (**a**) The forest edge is displayed, indicating the z-direction. (**b**) The mounting location of the lidar is displayed together with a weather protection tent and the first author as the lidar operator. (**c**) A top view of the lidar scan area, indicating the x- and y-directions. The identified species and their estimated heights are noted. (**d**) The location of the measurement site

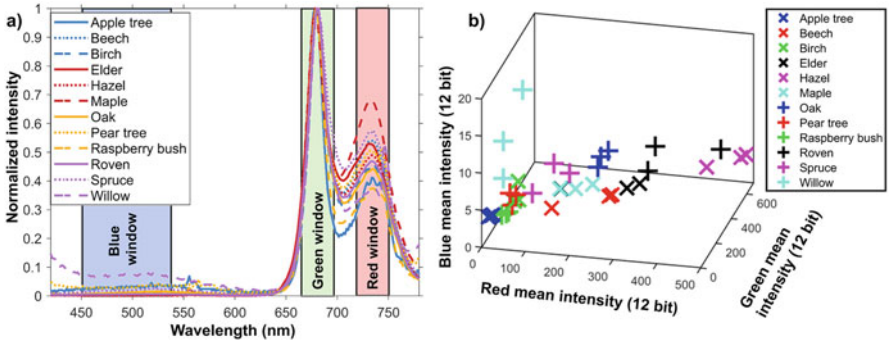


Fig. 28.2 (**a**) The mean of each species spectra acquired remotely. Three spectral windows are defined at wavelengths 440–520, 660–700, and 715–755 nm to cover the prominent fluorescence peaks. (**b**) The integrated intensity in the spectral windows of three measurements of each species

fluorescence from 450 to 550 is also observable for some tree species. Three spectral windows were defined accordingly. Integrating the intensity values over these spectral windows reduces the full-fluorescence signatures to three values. The integrated intensity of three measurements of each species was acquired at varying distances along the transect. Since these three intensity values are similar within the species, they could be used to determine which tree a specific spectrum likely originates from; see Fig. 28.2b.

Although such binning is helpful in, e.g., classification, noise reduction, and red, green, and blue (RGB) visualization purposes, a considerable amount of target information is lost by integrating the spectra into three bands. Therefore, dimensionality reduction with singular value decomposition (SVD) was explored; see Fig. 28.3. The significant number of eigenvalues of the ensemble of fluorescence spectra is five or seven, depending on the selected threshold; see Fig. 28.3a. The shape of the eigenvectors describing the spectral components is seen in Fig. 28.3b. The eigenvectors show details regarding the relative emission from the two chlorophyll emission peaks and regarding the short flank of photosystem I. Since this flank is located between the chlorophyll absorption at 660 nm and the photosystem I fluorescence, it implies that self-absorption displaces the flank toward longer wavelengths for high chloroplast concentrations. The scatterplot of the first three spectral components is visualized in Fig. 28.3c. Again, the spectra from the same species form small groups in the scatter plot. To investigate the similarity of species in more dimensions, we calculated the pairwise Euclidean distance between the first seven scores. These linkages were fed to unsupervised hierarchical clustering analysis (HCA). A dendrogram of the spectral distance is seen in Fig. 28.3d. To some extent, species could be grouped without any training.

Information reduced to three dimensions can be represented by a specific RGB color. Thus, the 3D spatial scanning spectra can be represented either by intensities in the spectral windows or by the scores of the first three eigenvectors. Applying both methods to the scan along the forest edge yielded three-dimensional point

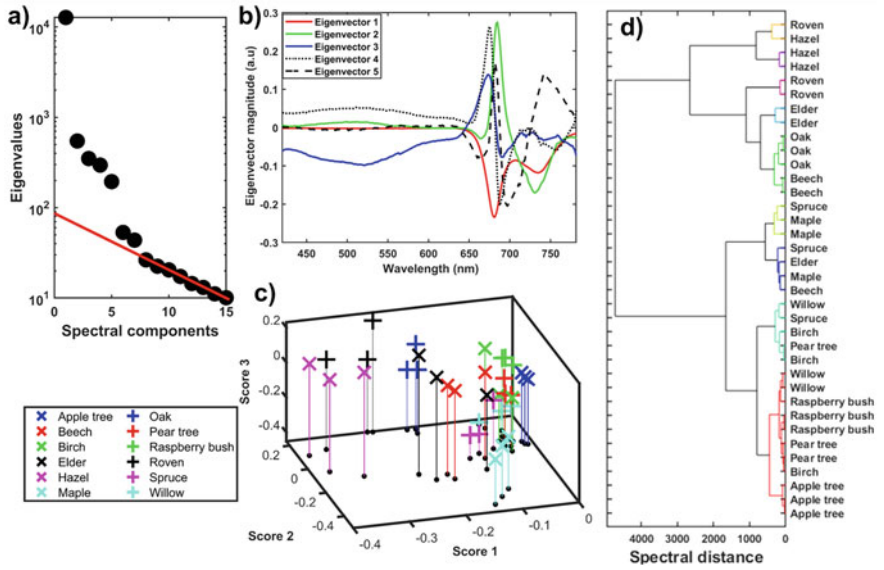


Fig. 28.3 The fluorescence data of three measurements of each species analyzed with singular value decomposition. (**a**) The significance of each eigenvector, and the red line indicates the noise level. (**b**) The spectral shape of the first five eigenvectors. (**c**) The first three scores of each measurement. (**d**) A hierarchical tree clustering the data based on spectral distance in seven dimensions

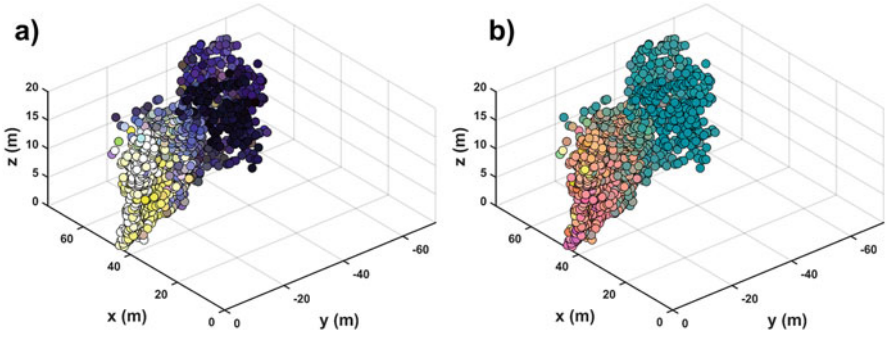


Fig. 28.4 3D raster scan of the vegetation along the forest edge with the fluorescence spectra represented by (**a**) spectral binning and (**b**) three first scores of the singular value decomposition. In both subfigures, the color values of the points were multiplied by the range squared to compensate for range attenuation. Thereafter, the values of the respective color channels were divided by the median of scores to represent an RGB color

clouds with spatial information along the axes and the fluorescence signature indicated by the RGB color of the points; see Fig. 28.4a, b.

28.5 Discussion, Summary, and Perspectives

A hyperspectral Scheimpflug lidar has been developed for measuring vegetation fluorescence. The lidar was evaluated by acquiring fluorescence spectra of leaves from 12 known Swedish trees at distances up to 100 m. Attempts of dimensionality reduction by spectral windows and SVD have been demonstrated. Unsupervised hierarchical clustering successfully grouped species. Vegetation point clouds with spectral information have been presented.

These results indicate that hyperspectral Scheimpflug lidar is a promising technique for remotely acquiring fluorescence spectra of vegetation. It also supports that fluorescence spectra from leaves can be used to gain contrast between species. Although measurements within one species are grouped close together, some species were mistaken by HCA in this study. In addition to the diversity of vegetation height profiles, spectral diversity could further enhance biodiversity assessment for both plants and animals. The fluorescence results of the 3D scan seen in Fig. 28.4 display contrast for both processing methods but were related to the labeled tree species, as shown in Fig. 28.1c within the scope of this study.

Future prospects include comparing night and daytime fluorescence (when light harvesting occurs). Early assessment shows it is feasible with the instrument in this study [7]. Besides providing grounds to compare fluorescence variations throughout the day, daytime measurements will also simplify the planning and execution of experiments. Other envisioned applications include mobile measurements with the lightweight lidar mounted on a drone flying over a forest canopy or on a rucksack for walking under a canopy. In these applications, a high-speed camera could be used to increase the spatial resolution of the scan.

Acknowledgments This project was supported by the Swedish Research Council.

References

1. Xue, J., Su, B.: Significant remote sensing vegetation indices: a review of developments and applications. J. Sens. **2017**, 1–17, 1353691 (2017). https://doi.org/10.1155/2017/1353691
2. Xie, Y., Sha, Z., Yu, M.: Remote sensing imagery in vegetation mapping: a review. J. Plant Ecol. **1**(1), 9–23 (2008)
3. Zhang, C.: Combining hyperspectral and LiDAR data for vegetation mapping in the Florida Everglades. Photogramm. Eng. Remote Sens. **80**(8), 733–743 (2014)
4. Bork, E.W., Su, J.G.: Integrating LIDAR data and multispectral imagery for enhanced classification of rangeland vegetation: a meta-analysis. Remote Sens. Environ. **111**(1), 11–24 (2007)
5. Zellweger, F., et al.: Remotely sensed forest structural complexity predicts multi species occurrence at the landscape scale. For. Ecol. Manag. **307**, 303–312 (2013)
6. Mohammed, G.H., et al.: Remote sensing of solar-induced chlorophyll fluorescence (SIF) in vegetation: 50 years of progress. Remote Sens. Environ. **231**, 111177 (2019)
7. Månefjord, H., et al.: 3D-printed fluorescence hyperspectral lidar for monitoring tagged insects. IEEE J. Sel. Top. Quantum Electron. **28**(5), 1–9 (2022)

Chapter 29
SO_2 Plumes Observation with LMOL: Theory, Modeling, and Validation



Guillaume Gronoff, Timothy Berkoff, William Carrion, Liqiao Lei, and Daniel Phoenix

Abstract LMOL, the NASA Langley Mobile Ozone LiDAR, is located near NASA's LaRC steam plant when not deployed in campaigns. The plant produces steam through the incineration of local trash, and its exhaust plume occasionally contains SO_2.

SO_2 is a known, regulated, pollutant that affects O_3 observations in the UV, as is the case with LMOL. In this chapter, we show how we modified LMOL to detect the plant SO_2 plumes and compute its density when the O_3 background is stable; we observed densities compatible with what is expected from the typical plume exhaust. The selection of laser lines so that an O_3 variation would not get confused with a SO_2 detection is explained in detail, and a model capable of simulating the LiDAR signal with (notably) O_3 and SO_2 absorption for the validation of the retrieval resolution and uncertainty is presented. Finally, the comparison between the modeled and observed performances of the system is shown: the maximum altitude, resolution, and error in the modeled signal and the observed signals are the same within reasonable margins.

This chapter demonstrates that LMOL is fully capable of working with SO_2. The next step being the addition of an additional laser channel, which is simplified by the tunable aspect of the LMOL laser, to address O_3 and SO_2 simultaneously, allowing the assessment of SO_2 when O_3 has variations.

Keywords LiDAR · SO_2 · Ozone · Air quality

G. Gronoff (✉) · W. Carrion · L. Lei · D. Phoenix
NASA Langley Research Center, Hampton, VA, USA

Science Systems and Application Inc., Hampton, VA, USA
e-mail: guillaume.p.gronoff@nasa.gov

T. Berkoff
NASA Langley Research Center, Hampton, VA, USA

© The Author(s), under exclusive license to Springer Nature Switzerland AG 2023

J. T. Sullivan et al. (eds.), *Proceedings of the 30th International Laser Radar Conference*, Springer Atmospheric Sciences,
https://doi.org/10.1007/978-3-031-37818-8_29

29.1 Introduction

29.1.1 LMOL

LMOL, the NASA Langley Mobile Ozone LiDAR, [3], is a tunable dial LiDAR: it is currently able to shoot at two wavelengths in the 285–292-nm range from a change in a software parameter (it is being developed for 4 wavelength operations). LMOL is part of the TOLNET network and has been used for several campaigns, notably dedicated to study the air quality [5–7]. Retrieving SO_2 with the LiDAR, in addition to O_3, would allow better understanding the local pollution sources.

29.1.2 The Hampton Steam Plant

The NASA/Hampton steam plant (https://hampton.gov/2255/HamptonNASA-steam-plant) is located North of NASA LaRC's location of LMOL (Fig. 29.1). It converts the local trash into steam through incineration, and the steam is used for local operations at NASA LaRC. The 2019 data give an estimated yearly ejection of the order of 50 tons of SO_2 after scrubbing by the different filtering systems [1, 2]. The stack, which rejects the exhaust at 75-m altitude high, is at a distance of 500 m from the location of LMOL from its 2019–2020 operations [6]. Solid-waste incinerators are known to reject NOx, CO, and SO_2 in large quantities [8, 9], as well as other pollutants in smaller quantities.

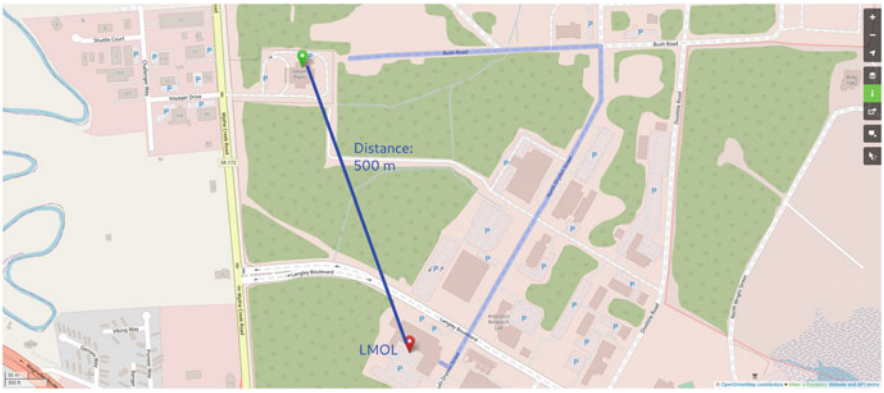


Fig. 29.1 The Hampton steam plant and its location relative to LMOL

29.2 Retrieval Theory

In the following, we will describe how we use the DIAL procedure to retrieve SO_2 with our LiDAR, and we explain the sensitivity approach.

In the DIAL procedure, the LiDAR signals—sent on two different wavelengths—are compared with each other; the differential absorption allows to retrieve the density of the absorbing species at each altitude bin. The highly absorbed wavelength is called the ONLINE, and the less absorbed one is the OFFLINE. In the wavelength range available, SO_2 and O_3 are major absorbers. If one uses the 286 and 292 wavelengths, SO_2 absorption is negligible compared to O_3's, which means that the LMOL operations in O_3 are easy. In addition, the difference in absorption is high (around 10^{-18} cm^2), which means that the sensitivity of the LiDAR is high. If $P.R^2$ is the returning power of the LiDAR in function of R, the range (and z the altitude), if we neglect the aerosol and the Rayleigh contribution, then we have the following equation:

$$\Delta\sigma_{SO_2} N_{SO_2} + \Delta\sigma_{O_3} N_{O_3} = \frac{1}{2}\frac{\partial}{\partial z}\left[ln\left(\frac{P_{\lambda_2}}{P_{\lambda_1}}\right)\right],$$

where $\Delta\sigma$ is the difference between the cross sections for the two wavelengths. If the SO_2 density was negligible, then λ_2 would be the offline wavelength (see Fig. 29.2). For retrieving the SO_2 density with 2 wavelengths from that equation, one should have stable O_3 background that could be subtracted and use a set of wavelengths optimized for the maximum SO_2 absorption (along with optimized laser power).

In the present study, we used the inverted wavelength technique: the ONLINE for SO_2 absorption would be the OFFLINE for the O_3 absorption and vice versa. This means that if the change in absorption is due to more O_3, the algorithm would detect a negative change of SO_2. In the case of the observation of point sources of SO_2, as it is the case here, this means that the system would give a negative value of SO_2 density, showing that the hypothesis of stable O_3 background is not met. (Said simply, $\Delta\sigma_{SO_2}$ and $\Delta\sigma_{O_3}$ have opposite signs.)

The use of the 288.34- and 288.99-nm wavelengths means that the change in O_3 density should be about -3 times the change in SO_2 density to get the same retried value (the system is more sensitive to SO_2), NO_2 is another gas that could affect the retrieval in the wavelength range considered; however, its small cross sections (an order of magnitude lower than the one of SO_2) that increase slowly with the wavelengths mean that it does not affect the retrieval in this case (the order of magnitude of SO_2 rejected by the plant is the same as NO_2 [2]). The small cross-section delta means that the sensitivity of SO_2 is smaller than the sensitivity in O_3 during the normal (286–292 nm) operations. Therefore, validation of the sensitivity with simulations is necessary (Fig. 29.3).

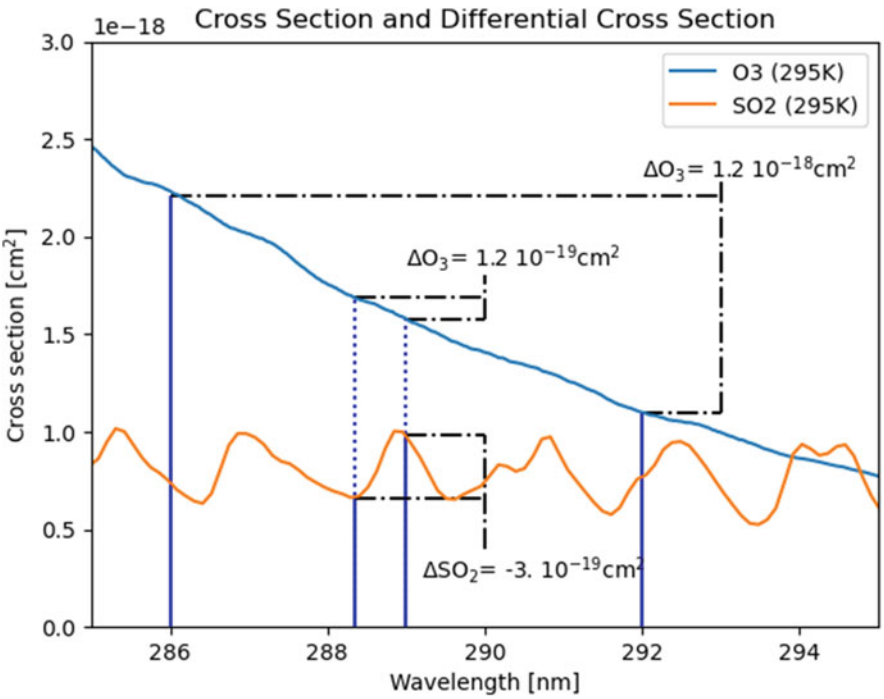


Fig. 29.2 The SO_2 and O_3 cross sections in the wavelength range available to LMOL. This figure shows how the wavelengths are selected

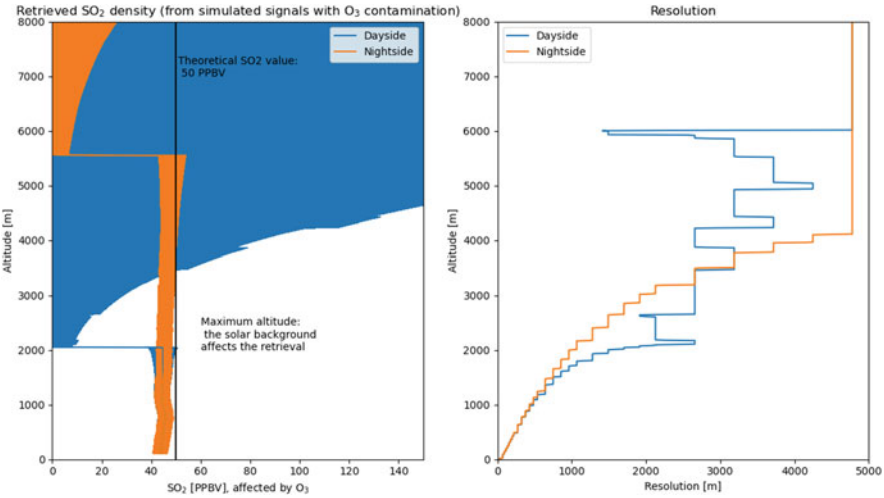


Fig. 29.3 Simulated retrieval of SO_2

29.3 Simulation

We used the LiDAR simulation of LibRadtran [4] to compute the return of LiDAR for LMOL for its O_3 and SO_2 operations. LMOL is composed of two main telescopes: the far field and the near field. These telescopes have different diameters and angular resolutions optimized for retrieving the data in the 100 m–2 km altitude for the near field and 1.5 km–10 km for the far field. Both of these channels were simulated with two wavelengths, using different values of O_3 and SO_2 background to compare the theory with the actual observations. A first comparison of the model with the observations was made for the standard O_3 data: the 296- and 292-nm wavelengths were simulated with a standard background of 100 PPBV of O_3. This allowed to discover a loss of sensitivity of a PMT in 2019: the difference in sensitivity of the system between the far field and the very near field was not consistent with the difference in the mirror diameters. Once the PMT was changed, the theory and experiment matched. The addition of a solar background in the model allowed to match the retrieved upper altitude in both model and experiment when performing O_3 retrievals. At this point, it was possible to simulate the SO_2 data and try to validate its retrieval. In addition, we added an optional O_3 background to verify how it affected the retrieved SO_2 (if it is stable, it gives a negative bias in the results that can be later corrected). The results for the far field and very near field for the SO_2 simulations are displayed in Fig. 29.4. It shows that the system can retrieve SO_2 with a correct vertical resolution for 5-minute averaging time. It is able to reach 2000 m altitude for the dayside and 5000 m in the nightside. Increasing the time averaging results in better vertical resolution (and higher maximum altitude in the nighttime; the dayside being limited by the solar background).

29.4 Observation

LMOL typically performs observations of O_3 from NASA LaRC. The nighttime usually presents very low values of O_3 at low altitude, of the order of 10/20 PPBV below 2000 m, stable during the night. These values are, however, sometime affected by "strange" noise below 200-m altitude. Using the 288-nm doublet optimized for SO_2 observations, we performed the retrieval of the night of 2020-02-18 to 2020-02-19. Around 03h UTC, the wind was blowing from the north at about 0.5 m/s, and values of the order of 80–100 PPBV on a vertical range of 50 m at around 250–300 m altitude. If we suppose that, at the location of LMOL, the plume of the power plant has a cross section of 2500 m^2 (i.e., a section of heigh/width near 50 m) with a speed of 0.5 m/s, then a 10 tons emission per year gives a SO_2 density of 90 PPBV, which is what we observe. This is very close to the 43 tons reported by the plant for 2019; considering the yearly variation of emissions (93 tons in 2017, 50 in 2018), it is possible that our simple estimation gave a good approximation of the total emission by the plant for that peculiar day. Better estimations would

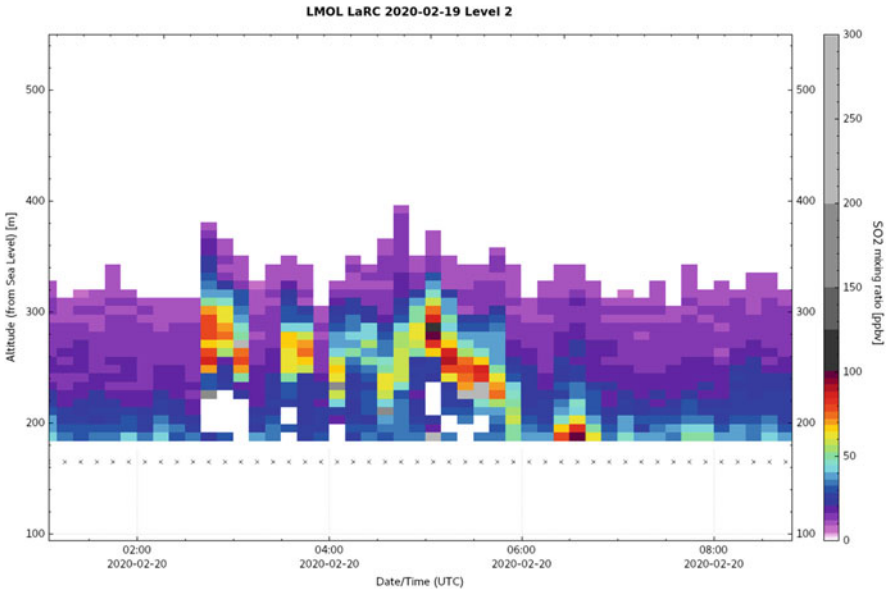


Fig. 29.4 Observed SO_2 plume from the Hampton Steam Plant

require a modeling of the plume and its chemistry as shown in [10]. This very simple comparison shows that we are observing the order of magnitude expected for the plant plume. However, we do not have the spatial resolution to observe the whole cross section of the plume, nor do we know the variations in time of the emitted SO_2. Better models of the plume and comparison with real-time sensors at the plant may allow a better appreciation of the capabilities of the LMOL in its SO_2 configuration. Overall, the system is able to observe SO_2 in a meaningful way for performing work relevant to local air quality/ the observation of point sources.

29.5 Future Work

The current work shows that the use of two wavelengths optimized for SO_2 retrieval allows LMOL to perform real-life observation of SO_2 plumes. The comparison of the observation with the expected values is excellent. However, these observations are limited by the O_3 background, which is expected to be stable for these observations. If one were to use 3 wavelengths, this limitation could be lifted. The following set of equations could be solved provided the 3 wavelengths are different (and the different determinant non-zero).

$$\Delta_1 \sigma_{SO_2} N_{SO_2} + \Delta_1 \sigma_{O_3} N_{O_3} = \frac{1}{2} \frac{\partial}{\partial z} \left[ln \left(\frac{P_{\lambda_2}}{P_{\lambda_1}} \right) \right] \tag{29.1}$$

$$\Delta_2 \sigma_{SO_2} N_{SO_2} + \Delta_2 \sigma_{O_3} N_{O_3} = \frac{1}{2} \frac{\partial}{\partial z} \left[ln \left(\frac{P_{\lambda_2}}{P_{\lambda_3}} \right) \right]. \tag{29.2}$$

To optimize the sensitivity (and reduce the data processing noise), a set of 2 wavelengths only sensitive to O_3 would allow to correct the O_3 background and the additional wavelength would maximize the sensitivity to SO_2 while minimizing the sensitivity to O_3. A 4-channel system was purchased for performing these studies. The laser system is currently being modified to produce these 4 wavelengths. In addition, a campaign named SOWLETS is in preparation to observe the SO_2 plume with LMOL along with SO_2 sonde measurements to validate the observations [11].

Acknowledgments LMOL, part of the TOLNET project, is funded by the NASA Tropospheric Composition Program, the Tropospheric Ozone LiDAR network (TOLNET), and Langley Internal Research and Development program (IRAD) for the development of the SO_2 capabilities.

References

1. Air Quality Reports | Virginia DEQ. https://www.deq.virginia.gov/air/air-quality-monitoring-assessments/air-quality-reports
2. Criteria emission pollutant reporting DEQ. https://www.deq.virginia.gov/home/showpublisheddocument/5428/637502721591700000
3. De Young, R., Carrion, W., Ganoe, R., Pliutau, D., Gronoff, G., Berkoff, T., Kuang, S.: Langley mobile ozone LiDAR: ozone and aerosol atmospheric profiling for air quality research. Appl. Opt. **56**(3), 721 (2017). https://doi.org/10.1364/AO.56.000721
4. Emde, C., Buras-Schnell, R., Kylling, A., Mayer, B., Gasteiger, J., Hamann, U., Kylling, J., Richter, B., Pause, C., Dowling, T., Bugliaro, L.: The libRadtran software package for radiative transfer calculations (version 2.0.1). Geosci. Model Dev. **9**(5), 1647–1672 (2016). https://doi.org/10.5194/gmd-9-1647-2016
5. Farris, B.M., Gronoff, G.P., Carrion, W., Knepp, T., Pippin, M., Berkoff, T.A.: Demonstration of an off-axis parabolic receiver for near-range retrieval of LiDAR ozone profiles. Atmos. Measur. Tech. **12**(1), 363–370 (2019). https://doi.org/10.5194/amt-12-363-2019
6. Gronoff, G., Berkoff, T., Knowland, K.E., Lei, L., Shook, M., Fabbri, B., Carrion, W., Langford, A.O.: Case study of stratospheric intrusion above Hampton, Virginia: LiDAR-observation and modeling analysis. Atmos. Environ. **259**, 118498 (2021). https://doi.org/10.1016/j.atmosenv.2021.118498
7. Gronoff, G., Robinson, J., Berkoff, T., Swap, R., Farris, B., Schroeder, J., Halliday, H.S., Knepp, T., Spinei, E., Carrion, W., Adcock, E.E., Johns, Z., Allen, D., Pippin, M.: A method for quantifying near range point source induced O_3 titration events using Co-located LiDAR and Pandora measurements. Atmos. Environ. **204**, 43–52 (2019). https://doi.org/10.1016/j.atmosenv.2019.01.052
8. Khallaf, M.: The impact of air pollution on health, economy, environment and agricultural sources. BoD–Books on Demand (2011)
9. Leckner, B., Lind, F.: Combustion of municipal solid waste in fluidized bed or on grate—a comparison. Waste Manag. **109**, 94–108 (2020). https://doi.org/10.1016/j.wasman.2020.04.050

10. Wissing, F., Wirtz, S., Scherer, V.: Simulating municipal solid waste incineration with a DEM/CFD method—influences of waste properties, grate and furnace design. Fuel **206**, 638–656 (2017). https://doi.org/10.1016/j.fuel.2017.06.037
11. Yoon, S., Kotsakis, A., Alvarez, S.L., Spychala, M.G., Klovenski, E., Walter, P., Morris, G., Corrales, E., Alan, A., Diaz, J.A., Flynn, J.H.: Development and testing of a novel sulfur dioxide sonde. Atmos. Measur. Tech. **15**(14), 4373–4384 (2022). https://doi.org/10.5194/amt-15-4373-2022

Chapter 30
Possible Use of Iodine Absorption/Fluorescence Cell in High-Spectral-Resolution Lidar

Nobuo Sugimoto, Yoshitaka Jin, and Tomoaki Nishizawa

Abstract The possibility of using fluorescence from the iodine-blocking filter in HSRL to detect the Mie scattering components in the backscattered signals was studied. An experiment was conducted with an HSRL using an iodine-blocking filter by adding a detector for measuring fluorescence from the iodine cell. Atmospheric backscattering signals were successfully measured, although the detection efficiency was limited by the low optical efficiency of collecting fluorescence from the iodine cell. In the atmospheric measurement, it was also shown that about half of Rayleigh scattering Cabannes line was also absorbed by the iodine cell. To improve the detection performance, a method using detector arrays surrounding the fluorescence cell was considered. The fluorescence excitation spectrum is dependent on the location of the fluorescence detectors, i.e., the penetration depth in the cell. Using this effect, it is possible to separate the Mie and Rayleigh components absorbed in the cell by measuring fluorescence intensity at multiple penetration depths.

Keywords Iodine-blocking filter · Fluorescence · High-spectral-resolution lidar

30.1 Introduction

Iodine absorption cell is often used as a blocking filter in the Rayleigh scattering receiver of high-spectral-resolution lidar (HSRL) at 532 nm to remove the Mie scattering component of the lidar backscattered signal. The light absorbed by the iodine cell is usually not used, but a part of the absorbed light is emitted as fluorescence. We experimentally studied the possibility of using the fluorescence to detect the Mie scattering signals. Although the sensitivity was limited by the low optical efficiency of collecting fluorescence from the iodine cell, we succeeded in measuring lidar backscattering profiles using the fluorescence [1]. Profiles of

N. Sugimoto (✉) · Y. Jin · T. Nishizawa
National Institute for Environmental Studies, Tsukuba, Ibaraki, Japan
e-mail: nsugimot@nies.go.jp

© The Author(s), under exclusive license to Springer Nature Switzerland AG 2023

J. T. Sullivan et al. (eds.), *Proceedings of the 30th International Laser Radar Conference*, Springer Atmospheric Sciences,
https://doi.org/10.1007/978-3-031-37818-8_30

aerosols and clouds were measured by the fluorescence channel up to an altitude of about 6 km. Analyzing the signals by comparing with those of the Rayleigh and total scattering channels, we confirmed that the fluorescence channel detects the Mie scattering component. The analysis also showed that about half of the Rayleigh scattering component was also absorbed by the iodine cell and detected in the fluorescence channel at the same time with the Mie scattering component, in our experimental conditions. The results were consistent with the previous studies on iodine blocking filter [2].

In this paper, we report on the study for improving the performance of the iodine fluorescence detector and discuss possible applications where this approach may have advantages.

30.2 Concept of the Iodine Fluorescence Detector

The concept of using fluorescence from the iodine-blocking filter in HSRL is illustrated in Fig. 30.1. In usual HSRL, the Rayleigh scattering signal transmitted through the iodine cell and the total backscattering signal are measured. In the experimental system, a detector was added to measure fluorescence from the iodine cell. This channel detects Mie scattering and the central part of Rayleigh scattering Cabannes line absorbed by the iodine cell, indicated by the circle in the left panel of Fig. 30.1.

Figure 30.2 shows the transmission and fluorescence excitation spectra of the iodine cell measured by directing the laser beam directly to the receiver and scanning the laser wavelength [1] around the absorption line 1111 (18788.4510 cm^{-1})

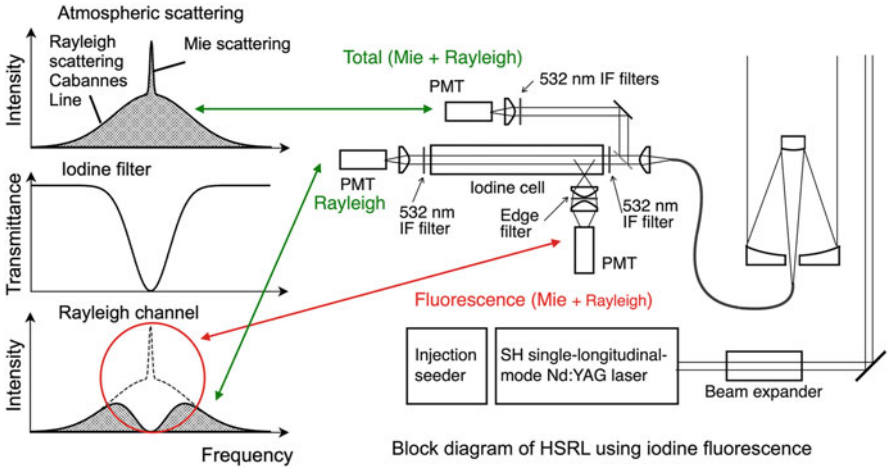


Fig. 30.1 Concept of HSRL using the fluorescence from the iodine-blocking filter

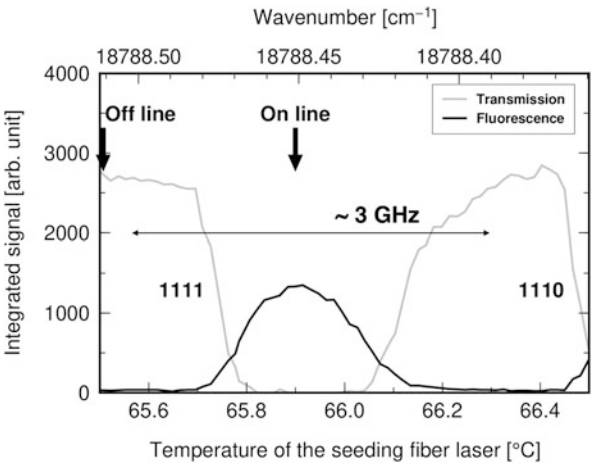


Fig. 30.2 Transmission and excitation spectra of the iodine cell [1]

[3] of iodine molecule (I_2). In the excitation spectrum measurement, the fluorescence decay signal was recorded and integrated to obtain fluorescence intensity. The temperature of the iodine cell was 22 °C, the iodine vapor pressure was 31.8 Pa, and the fluorescence lifetime (decay time) was ≈0.18 μs. The fluorescence quantum efficiency is expressed as τ_{obs}/τ_{rad}, where τ_{obs} is the observed decay time and τ_{rad} is the radiative lifetime, which is ≈2.3 μs [1]. The resulting fluorescence quantum efficiency was ≈0.08.

There is nonradiative relaxation process in the excited state ($B^3\Pi^+_{0u}$) of I_2 due to unimolecular predissociation [4], and the fluorescence lifetime extrapolated to zero pressure is ≈1.1 μs [5]. As a result, the maximum quantum efficiency at zero pressure is limited to ≈0.48. In the pressure range useful for absorption/fluorescence cell, the quantum efficiency is about 0.2 or smaller.

The overall efficiency as a detector is represented as the product of the fluorescence quantum efficiency and the efficiency of collecting fluorescence from the iodine cell. In the experimental system, fluorescence of iodine was measured only near the input window, and the optical efficiency was low (≈0.008). The fluorescence collecting efficiency, however, can be improved by using an integrating sphere or using arrays of detectors surrounding the iodine cell. In addition, the fluorescence decay time (≈1.1 μs at maximum) limits the temporal response as a detector, but the decay is a simple exponential function, and deconvolution methods may be applied.

30.3 Methods for Improving the Detector Performance

In our recent paper, we proposed a method using two iodine cells with different vapor pressure in series to optimize the fluorescence detection and the blocking filter characteristics, and we considered the use of an integrating sphere for

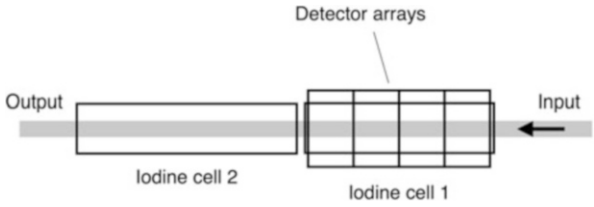


Fig. 30.3 Method using detector arrays surrounding iodine cell

fluorescence detection [1]. In this chapter, we consider an alternative method using detector arrays surrounding the fluorescence cell. The concept is illustrated in Fig. 30.3. Iodine cell 1 is for detecting fluorescence, and cell 2 is for optimizing the transmission characteristics as a blocking filter. Cell 1 is surrounded by detector arrays. In this figure, the detector arrays consist of four segments.

By the method using arrays of detectors, we may utilize the dependence of the excitation spectrum on the light penetration depth in the iodine cell. It is interesting to note in Fig. 30.2 that fluorescence, which is proportional to absorption, is not proportional to 1-transmission. The width of the transmission spectrum is much wider than that of the fluorescence excitation spectrum. The difference is because only the fluorescence from the part of the beam near the entrance of the cell was measured in the experiment.

A simple simulation for a Gaussian absorption line is shown in Fig. 30.4. Absorption spectrum, transmission spectrum to depth L, and excitation spectrum at depth L are shown in Fig. 30.4a–c, respectively. The depth L is defined so that the optical depth at the center of the absorption line is L. At the center of the absorption line, the fluorescence intensity decreases sharply with depth as seen in Fig. 30.4c, but it remains at the shoulder of the absorption line. If we integrate the fluorescence along the path up to depth L, we can confirm that integrated fluorescence is proportional to 1-transmission.

We then consider the depth dependence of the fluorescence intensity integrated with frequency for the Mie and Rayleigh backscattering signals. For simplicity, we assumed that both Mie and Rayleigh scattering have Gaussian spectrum, and the spectral width is 0.1 and 5 times the width of the absorption line, respectively. The results are shown in Fig. 30.5. The Mie scattering signal is absorbed sharply in the cell, and the fluorescence intensity decreases exponentially with penetration depth, but the Rayleigh scattering signal remains deeper in the cell. Using this difference, we can separate the Mie and Rayleigh scattering components absorbed in the cell by measuring the fluorescence intensity at multiple depths.

The absorption spectrum of iodine molecule is not simple Gaussian in reality. The spectral width is wider than the Doppler broadening determined by the molecular weight and temperature because of the hyperfine structure [6]. Also, there is an overlap of multiple absorption lines in some absorption lines. In principle, the narrower the spectral width, the better for both blocking filter and fluorescence detector. The line 1111 we used in our experiment due to a restriction in laser wavelength tuning was not an ideal choice, because two transitions overlap [3, 6]. We would use the lines 1110 or 1109 which have better characteristics in the future work.

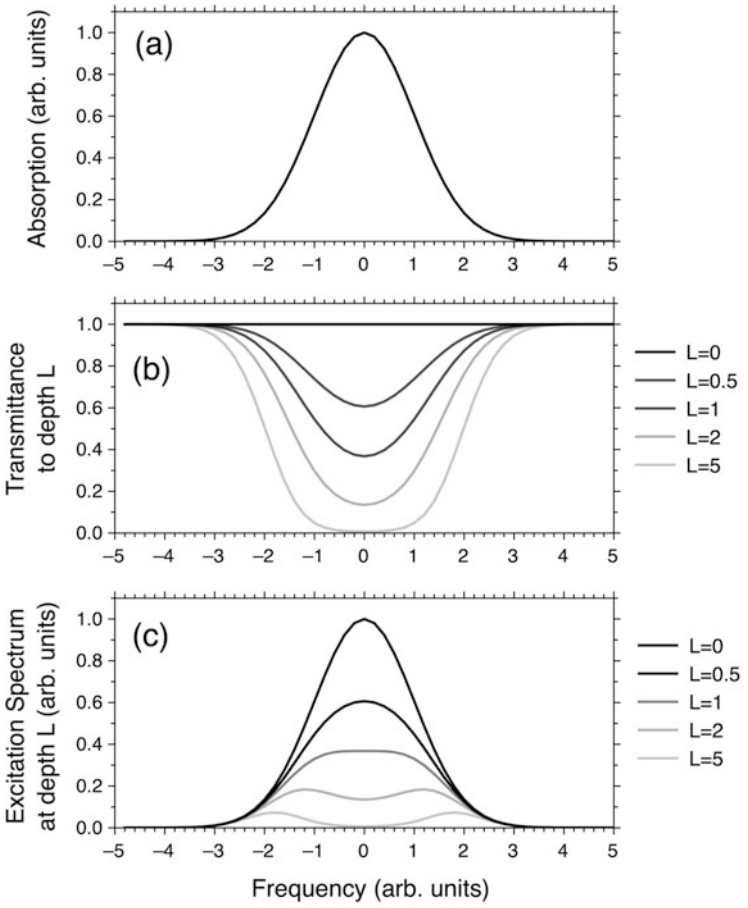


Fig. 30.4 A simulation showing the dependence of fluorescence excitation spectrum on the light penetration depth. (**a**) Absorption spectrum, (**b**) transmission spectrum to depth L, and (**c**) excitation spectrum at depth L

30.4 Conclusion

The method using fluorescence from the iodine cell may be useful, for example, for detecting very-low-density aerosols having very low Mie to Rayleigh scattering ratio, because the contrast between the Mie and Rayleigh signals is higher in the fluorescence detection channel compared with the total scattering channel. Also, the effect of solar background radiation can be reduced by a factor of $\approx 1/7$ [1], because the fluorescence channel is sensitive only to the wavelengths of iodine absorption lines.

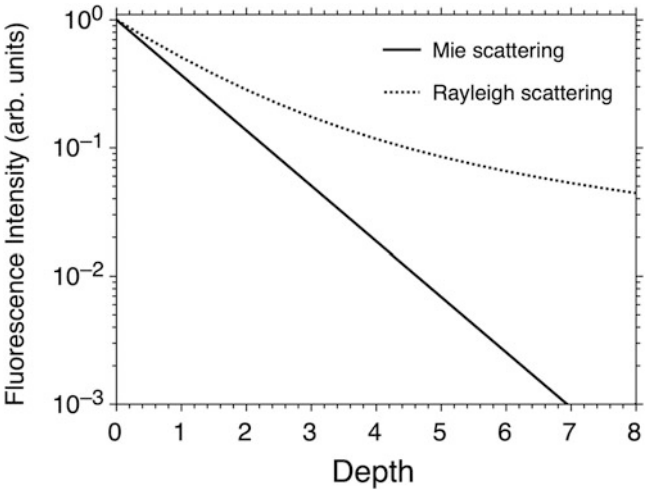


Fig. 30.5 Depth dependence of the fluorescence intensity integrated with frequency for the Mie and Rayleigh backscattering signals

The largest advantage of the iodine cell compared with the interferometric methods is that the spectral characteristics are not sensitive to the beam incident angle. Another advantage is invariance of the spectral characteristics. For example, even a multi-static HSRL having multiple wide field-of-view receivers can be easily constructed. The advantages of the fluorescence detection channel over the total scattering channel would be the higher contrast between the Mie and Rayleigh signals and the reduction of background radiation.

We are considering experimental studies using array detectors or a collecting mirror and a PMT for each segment illustrated in Fig. 30.3.

References

1. Sugimoto, N., Jin, Y., Nishizawa, T.: Possible use of fluorescence from iodine blocking filter in high-spectral-resolution lidar to detect Mie scattering signals. Appl. Opt. **60**(13), 3617–2622 (2021)
2. Zhang, Y., Liu, D., Shen, X., Bai, J., Liu, Q., Cheng, Z., Tang, P., Yang, L.: Design of iodine absorption cell for high-spectral-resolution lidar. Opt. Express. **25**, 15913–15926 (2017)
3. Gerstenkorn, S., Luc, P.: Atlas du spectre d'absorption de la molecule d'iode. Editions du Centre National de la Recherche Scientifique, Paris (1978)
4. Sakurai, K., Capelle, G., Broida, H.P.: Measurements of lifetimes and quenching cross sections of the $B^3\Pi^+_{0u}$ state of iodine using a tunable dye laser. Chem. Phys. **54**, 1220–1223 (1971)
5. Paisner, J.A., Wallenstein, R.: Rotational lifetimes and self-quenching cross sections in the $B^3\Pi^+_{0u}$ state of $^{127}I_2$. J. Chem. Phys. **61**, 4317–4320 (1974)
6. Forkey, J.N., Lempert, W.R., Miles, R.B.: Corrected and calibrated I_2 absorption model at frequency-doubled Nd:YAG laser wavelengths. Appl. Opt. **36**(27), 6729–6738 (1997)

Part II
Atmospheric Clouds and Aerosol Properties

Chapter 31
Ten Years of Interdisciplinary Lidar Applications at SCNU, Guangzhou



J. B. Chi, Z. Duan, J. W. Huang, Y. Li, Y. Y. Li, M. Lian, Y. Y. Lin, J. C. Lu, Y. T. Sun, J. L. Wang, X. Wang, Y. Yuan, Q. Zhang, G. Y. Zhao, S. M. Zhu, and S. Svanberg

Abstract A diversified and interdisciplinary lidar research program has been pursued during the recent 10 years at South China Normal University in Guangzhou, China. The activities include time-of-flight (TOF) lidar applications with pulsed lasers for differential absorption (DIAL), laser-induced fluorescence (LIF), and laser-induced break-down spectroscopy (LIBS) studies. Further, range-resolving (bi-static) lidars, based on Scheimpflug arrangements, have been employed. Mobile, drone-based, and hand-held systems were developed. Monitoring has been directed toward air pollutants, vegetation and crops, flying insects (agricultural pests and disease vectors), and water pollutants and fauna.

A mobile TOF lidar system was developed as a multipurpose platform for field work. A special adaption of the system is range-resolved monitoring of atomic mercury (absorbing around 254 nm) using the DIAL approach. A high-light was the mapping of mercury fumes from the underground burial chamber of the "Terracotta Army Emperor" Qin's mausoleum in Xi'an. Further, mercury in major cities as well as in a mining areas was studied. Remote LIF studies included corn and rice fields and concerned species characterization and fertilizer levels.

Two different compact LIF systems carried by a drone were developed for vegetation and water pollution studies, with typical flying heights of tens of m. The vegetation probing system and an underwater LIF monitoring system provide range-resolution combined with full-spectral recordings. Such systems could be complemented with compact hand-held instrumentation.

J. B. Chi · Z. Duan · J. W. Huang · Y. Li · Y. Y. Li · M. Lian · Y. Y. Lin · J. C. Lu · Y. T. Sun · J. L. Wang · X. Wang · Y. Yuan · Q. Zhang · G. Y. Zhao · S. M. Zhu
Applied Molecular Spectroscopy and Remote Sensing Group, South China Academy of Advanced Optoelectronics, South China Normal University, Guangzhou, China

S. Svanberg (✉)
Applied Molecular Spectroscopy and Remote Sensing Group, South China Academy of Advanced Optoelectronics, South China Normal University, Guangzhou, China

Department of Physics, Lund University, Lund, Sweden
e-mail: sune.svanberg@fysik.lth.se

© The Author(s), under exclusive license to Springer Nature Switzerland AG 2023

J. T. Sullivan et al. (eds.), *Proceedings of the 30th International Laser Radar Conference*, Springer Atmospheric Sciences,
https://doi.org/10.1007/978-3-031-37818-8_31

Scheimpflug CW lidar systems are powerful in monitoring flying insects. Characteristic information on reflectance, depolarization, and wing-beat frequencies can readily be obtained.

Keywords Differential absorption lidar · Elastic backscattering lidar · Fluorescence lidar

31.1 Introduction

During the recent 10 years, an interdisciplinary program of remote sensing based on lidar principles has been pursued at the South China Normal University in Guangzhou. The work draws on a long experience in the subject matter from Lund University, Sweden, and is also inspired by parallel activities in the related field of biophotonics [1].

We here provide an overview of the work, and start with well-known time-of-flight lidar measurements on atmospheric constituents but also laser-induced fluorescence (LIF) lidar studies on vegetation, as well as remote laser-induced break-down spectroscopy (LIBS) on metallic samples. Novel types of bi-static CW lidar systems based on the Scheimpflug principle were used in monitoring of aerial and aquatic fauna. Drone-based CW systems were employed for vegetation as well as water pollution studies. Finally, very compact handheld equipment was developed for short-range remote sensing, related to water quality measurements and fruit maturity assessment.

31.2 Pulsed Lidar Remote Sensing

As a base for field work, a mobile lidar system was constructed [2] with an Nd:YAG-pumped narrow-band dye laser as the transmitter and a 40-cm vertical Newtonian receiving telescope, the field of view of which was folded with a roof-top large mirror under full computer control. The system was optimized for monitoring of atomic mercury, a severe neurotoxic pollutant, but also a geophysical tracer gas. Mercury is special since it is the only air pollutant dominantly present in atomic form. Assessment of concentrations in major Chinese cities [3–6], in a mining area [7], and most prominently, in an archaeological investigation of mercury emission from the "Terracotta Army Emperor" Qin mausoleum in Xi'an (Fig. 31.1) [8] was pursued. Indeed, mercury fumes attributed to the underground coffin chamber of the never-opened tomb were observed, consistent with 2200-year-old chronicles on the burial arrangements.

Fluorescence from vegetation can be induced by frequency-tripled Nd:YAG radiation at 355 nm using a few cm diameter illumination spot on leaves at distances up to 120 m. We have studied signatures from maize and rice. In particular, species

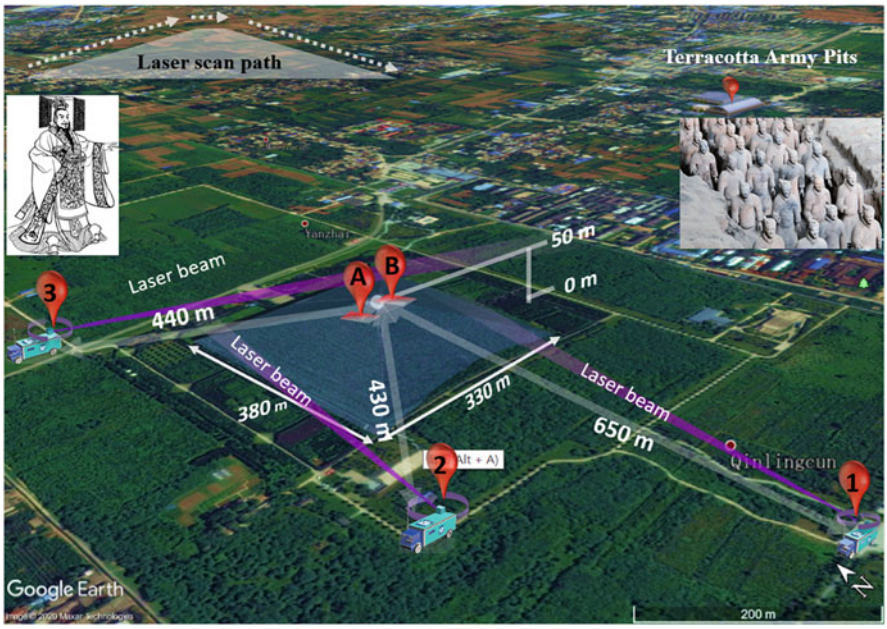


Fig. 31.1 Illustration of differential absorption lidar monitoring of atomic mercury emerging from the tomb of Emperor Qin, Xi'an. A halo of increased mercury concentration was observed over the upper parts of the tomb mound Ref. [8]. (Reproduced under the Creative Commons agreement)

and varieties can be separated using multivariate analysis of the spectral signatures, and the level of administrated fertilizers can be assessed [9–11]. Likewise, different types of Chinese marbles could be distinguished by the LIF lidar system based on large differences in spectral signatures [1]. By instead focusing the laser radiation to a high-intensity spot, LIBS spectra from metals could be recorded at distances up to 45 m [12].

31.3 CW Lidar Remote Sensing of Fauna

Recently, low-cost, short-baseline CW lidar systems based on the Scheimpflug principle were introduced [13] and have proven to be very useful, particularly in connection with ecological investigations of aerial and aquatic fauna [14]. By proper tilting of the detector array surface, sharp imaging can be achieved along the laser beam at close as well as at far range. Insects are of paramount interest because of their roles as pollinators, deadly disease vectors, and agricultural pests. Insect lidar monitoring on the Chinese scene is reported in [15–19]. Studies of diurnal variation in insect and predator number were done over rice fields, and in an orchard. Dark-field monitoring was also pursued using sunlight, or artificial illumination at

night [20]. Detailed laboratory insect characterization is discussed in [21]. Features studied include wing-beat frequencies (and contents of overtones), depolarization related to surface structure of the insect body, and differential reflection (color), which can be assessed by using more than a single laser wavelength. Combinations of parameters measured can help in species identification.

In the same way as CW lidar systems can be applied in the atmosphere over long distances with range resolution achieved based on triangulation, they can be implemented also in the underwater environment. Now ranges are limited to few meters due to the strong optical attenuation in water. Water-tank experiments on shrimps and fish reveal characteristic pleopod- and fin movement frequencies [22]. The system also has multispectral capability by imaging the laser beam at a 2D CMOS detector, displaying range in one direction and fluorescence spectrum in the other direction.

31.4 Drone-Based CW Fluorescence Lidar Studies

We have constructed two drone-based, light-weight fluorescence lidar systems. One system uses a 1.5-W 445-nm diode laser and a 2D detector to provide range and spectral resolution in fluorescence applications. The system weight was about 3 kg. It was used to map fluorescence from trees [23] from flying heights of typically 40 m. A second system, weighing 1.5 kg, combined a 1-W CW laser at 412 nm and a compact USB spectrometer to provide water pollution measurements as demonstrated over the Pearl River in Guangzhou. Since the drone can fly at a fixed altitude over the water surface (typically 10 m), there is no need for range-resolution capability [24].

31.5 Short-Range Active Remote Sensing

We also have constructed two short-range (few meters) in situ fluorescence measurement systems for water and agricultural applications. One hand-held system was aimed at water quality assessment and could easily characterize water bodies based on chlorophyll and dissolved organic matter (DOM) contents [25]. A further system, the size of a human palm, utilized a very compact (~cm) mini-spectrometer and was used for fruit maturity assessment in orchards [26]. Apart from fluorescence, reflectance (objective color) can also be used in such characterization [27]. Our remote-sensing studies of flying insects were also supported by the construction of two insect trap systems based on pheromone attraction, and where insects entering the system were detected by light shading or scattering employing LEDs [28], or image recording and processing [29]. Related to short-range/in situ measurement systems, it could be mentioned that we have also studied atomic mercury concen-

trations along major roads and also in certain buildings in Guangzhou, utilizing a LUMEX Zeeman modulation mercury monitor [30].

31.6 Enhanced Vision Through Scattering Modulation

Elastic or inelastic scattering is normally used beneficially in lidar applications, but scattering frequently also causes vision impairment. We have developed a simple method, where image blurring occurring due to detrimental close-range scattering can be reduced employing a spatial modulation technique [31].

We in this overview aim at illustrating how basic tools of lidar technology can be combined to address a large number of aspects of environmental and social importance.

Acknowledgments The authors gratefully acknowledge a very fruitful scientific collaboration with many colleagues, and strong support by professors Sailing He, Guofu Zhou, and Katarina Svanberg. Economic support was obtained from the Guangdong Province Innovation Research Team Program (201001D0104799318), the Science and Technology Program of Guangzhou (2019050001), and the Guangdong Provincial Key Laboratory of Optical Information Materials and Technology (2017B030301007).

References

1. Svanberg, S., Zhao, G.Y., Zhang, H., Huang, J., Lian, M., Li, T.Q., Zhu, S.M., Li, Y.Y., Duan, Z., Lin, H.Y., Svanberg, K.: Laser spectroscopy applied to environmental, ecological, food safety and biomedical research. Opt. Express. **24**, A515 (2016)
2. Zhao, G.Y., Lian, M., Li, Y.Y., Duan, Z., Zhu, S.M., Mei, L., Svanberg, S.: Mobile lidar system for environmental monitoring. Appl. Opt. **65**, 1506 (2017)
3. Mei, L., Zhao, G.Y., Svanberg, S.: Differential absorption lidar system employed for background atomic mercury vertical profiling in South China. Opt. Laser Eng. **55**, 128 (2013)
4. Zhao, G.Y., Wu, X.X., Lian, M., Svanberg, S.: Lidar monitoring of atmospheric atomic mercury and sulfur dioxide in Guangzhou, China. In: PIERS Proceedings, Guangzhou 2014, pp. 2711–2714
5. Lian, M., Zhao, G.Y., Duan, Z., Li, Y.Y., Svanberg, S., Hu, J.D.: Improvement of a mobile differential absorption lidar system and the first field measurement of atmospheric mercury. J. Optoelectron. Lasers. (in Chinese; accepted)
6. Duan, Z., Zhao, G.Y., Zhu, S.M., Lian, M., Li, Y.Y., Zhang, W.X., Svanberg, S.: Atmospheric mercury pollution in the Xi'an area, China. Atmos. **12**, 27 (2021)
7. Lian, M., Shang, L.H., Duan, Z., Zhao, G.Y., Li, Y.Y., Zhu, S.M., Qiu, G.L., Meng, B., Sommar, J., Feng, X.B., Svanberg, S.: Lidar mapping of atmospheric atomic mercury in the Wanshan area, China. Environ. Pollut. **240**, 353 (2018)
8. Zhao, G.Y., Zhang, W.X., Duan, Z., Lian, M., Hou, N.B., Li, Y.Y., Zhu, S.M., Svanberg, S.: Mercury as a geophysical tracer gas – emissions from the Emperor Qin tomb in Xi'an studied by laser radar. Sci. Rep. **10**, 10414 (2020)
9. Zhao, G.Y., Duan, Z., Ming, L., Li, Y.Y., Chen, R.P., Hu, J.D., Svanberg, S., Han, Y.L.: Reflectance and fluorescence characterization of maize species using laboratory measurements and lidar remote sensing. Appl. Opt. **55**, 5273 (2016)

10. Duan, Z., Peng, T., Zhu, S.M., Lian, M., Li, Y.Y., Fu, W., Xiong, J.B., Svanberg, S., Zhao, Q.Z., Hu, J.D., Zhao, G.Y.: Optical characterization of Chinese hybrid rice using laser-induced fluorescence techniques – laboratory and remote-sensing measurements. Appl. Opt. **53**, 3481 (2018)
11. Zhang, H., Duan, Z., Li, Y.Y., Zhao, G.Y., Zhu, S.M., Fu, W., Peng, T., Zhao, Q.Z., Svanberg, S., Hu, J.D.: Vis/NIR reflectance spectroscopy for hybrid rice variety identification and chlorophyll content evaluation for different nitrogen fertilizer levels. R. Soc. Open Sci. **6**, 191132 (2019)
12. Duan, Z., Li, Y., Wang, J.L., Hu, L.N., Zhao, G.Y., Svanberg, S.: Remote LIBS Measurements on Metals Using a Mobile Lidar System, in Asia Communications and Photonics Conference, Hangzhou. Optical Society (2018). https://doi.org/10.1109/ACP.2018.8596154
13. Brydegaard, M., Gebru, A., Svanberg, S.: Super resolution laser radar with blinking atmospheric particles – application to interacting flying insects. Prog. Electromagn. Res. **147**, 141 (2014)
14. Brydegaard, M., Svanberg, S.: Photonic monitoring of atmospheric and aquatic fauna. Lasers Photonics Rev. **12**, 1800135 (2018)
15. Zhu, S.M., Malmqvist, E., Li, W.S., Jansson, S., Li, Y.Y., Duan, Z., Svanberg, K., Feng, H.Q., Song, Z.W., Zhao, G.Y., Brydegaard, M., Svanberg, S.: Insect abundance over Chinese rice fields in relation to environmental parameters, studied with a polarization-sensitive CW near-IR lidar system. Appl. Phys. B Lasers Opt. **123**, 211 (2017)
16. Malmqvist, E., Jansson, S., Zhu, S.M., Li, W.S., Svanberg, K., Svanberg, S., Rydell, J., Song, Z.W., Bood, J., Brydegaard, M., Åkesson, S.: The bat-bird-bug battle: daily flight activity of insects and their predators over a rice field revealed by high resolution Scheimpflug lidar. R. Soc. Open Sci. **5**, 172303 (2018)
17. Song, Z.W., Zhang, B.X., Feng, H.Q., Zhu, S.M., Hu, L.N., Brydegaard, M., Li, Y.Y., Jansson, S., Svanberg, K., Zhao, G.Y., Bood, J., Svanberg, S., Li, D.S.: Application of lidar remote sensing of insects in agricultural entomology on the Chinese scene. J. Appl. Entomol. **144**, 161 (2020)
18. Lu, J.C., Li, Y., Yuan, Y., Zhu, S.M., Duan, Z., Zhao, G.Y., Svanberg, S.: Monitoring of Flying Insects using a Dual-Wavelength CW Lidar System, in Asia Communications and Photonics Conference 2019, p. M4A.4. Optical Society, Chengdu (2019)
19. Huang, J.W., Chi, J.B., Wu, Q.F., Svanberg, S., Li, D.S., Song, Z.W., Zhu, S.M.: Monitoring of Flying Horticulture Pest Insects Using a Bi-Static Lidar System, Asia Communication and Photonics Conference, Shanghai, p. T4A.270 (2021)
20. Zhu, S.M., Li, Y.Y., Gao, L.N., Li, T.Q., Zhao, G.Y., Svanberg, S., Lu, C.H., Hu, J.D., Huang, J.R., Feng, H.Q.: Optical remote detection of flying Chinese agricultural pest insects using dark-field reflectance measurements. Acta Sinica Entymologica. **59**, 1376 (2016)
21. Li, Y.Y., Zhang, H., Duan, Z., Lian, M., Zhao, G.Y., Sun, X.H., Hu, J.D., Gao, L.N., Feng, H.Q., Svanberg, S.: Optical characterization of agricultural pest insects: a methodological study in the spectral and time domains. Appl. Phys. B. **122**, 213 (2016)
22. Duan, Z., Yuan, Y., Lu, J.C., Wang, J.L., Li, Y., Svanberg, S., Zhao, G.Y.: Under-water spatially, spectrally, and temporally resolved optical monitoring of aquatic fauna. Opt. Express. **28**, 2600 (2020)
23. Wang, X., Duan, Z., Brydegaard, M., Svanberg, S., Zhao, G.Y.: Drone-based area scanning of vegetation fluorescence height profiles using a miniaturized hyperspectral lidar system. Appl. Phys. B Lasers Opt. **124**, 207 (2018)
24. Duan, Z., Ying Li, J.L., Wang, G.Y.Z., Svanberg, S.: Aquatic environment monitoring using a drone-based fluorosensor. Appl. Phys. B Lasers Opt. **125**, 108 (2019)
25. Lu, J.C., Yuan, Y., Duan, Z., Zhao, G.Y., Svanberg, S.: Short-range remote sensing of water quality by a handheld fluorosensor system. Appl. Opt. **59**, C1 (2020)
26. Zhang, Q., Sun, Y.T., Svanberg, S.: Compact fluorosensor for close-range remote-sensing characterization of fruits. SPIE. **12165**, 1216403 (2022)
27. Lin, X.B., Zhang, H., Hu, L.N., Zhao, G.Y., Svanberg, S., Svanberg, K.: Ripening of avocado fruits studied by spectroscopic techniques. J. Biophotonics. **13**, e202000076 (2020)

28. Wang, J.L., Zhu, S.M., Lin, Y.Y., Svanberg, S., Zhao, G.Y.: Mosquito counting system based on optical sensing. Appl. Phys. B. **126**, 28 (2020)
29. Sun, Y.T., Lin, Y.Y., Zhao, G.Y., Svanberg, S.: Identification of flying insects in the spatial, spectral, and time domains, with focus on mosquito imaging. Sensors. **21**, 3329 (2021)
30. Chen, G.P., Sun, Y.T., Zhang, Q., Duan, Z., Svanberg, S.: Atmospheric mercury concentrations in Guangzhou City, measured by spectroscopic techniques. Atmos. **13**, 1650 (2022)
31. Lin, Y.Y., Svanberg, S.: Foreground scattering elimination by inverse lock-in-like spatial modulation. Vision. **4**, 37 (2020)

Chapter 32
Feasibility Studies of the Dual-Polarization Imaging Lidar Based on the Division-of-Focal-Plane Scheme for Atmospheric Remote Sensing

Zheng Kong, Jiheng Yu, and Liang Mei

Abstract As a branch of atmospheric lidar, polarization lidar plays a significant role in characterizing the properties of cirrus clouds, classifying aerosol types, retrieving aerosol microphysical properties, etc. In this work, a dual-polarization imaging lidar technique, employing two continuous-wave laser diodes (458 nm and 808 nm) as light sources and two polarization cameras with a micro-polarizer array as detectors, has been proposed and demonstrated for all-day field measurements of atmospheric aerosols. Each polarization camera is able to capture a four-directional polarized image of the transmitted laser beam, from which four polarized atmospheric backscattering signals with 0°, 45°, 90°, and 135° polarization angles can be simultaneously measured. Thus, the linear volume depolarization ratio (LVDR) and the offset angles can be retrieved at wavelengths of 458 nm and 808 nm without employing additional optical components and sophisticated system adjustments. Atmospheric validation measurements on a near horizontal path have been carried out from February 18 to February 23, 2022 in Dalian, Northern China. The measurement results showed that the dual-polarization lidar technique opens up many possibilities for characterizing aerosol optical properties.

Keywords Dual-polarization · Imaging lidar · Atmospheric remote sensing · Polarization camera · Offset angle · Depolarization ratio

32.1 Introduction

Lidar, as an active remote sensing tool, has been widely employed in atmospheric aerosol sensing [1, 2]. As an important branch of the lidar families, polarization lidar

Z. Kong (✉) · J. Yu · L. Mei
School of Optoelectronic Engineering and Instrumentation Science, Dalian University of Technology, Dalian, China
e-mail: KongZheng@mail.dlut.edu.cn

© The Author(s), under exclusive license to Springer Nature Switzerland AG 2023

J. T. Sullivan et al. (eds.), *Proceedings of the 30th International Laser Radar Conference*, Springer Atmospheric Sciences,
https://doi.org/10.1007/978-3-031-37818-8_32

plays a significant role in characterizing the properties of cirrus clouds, classifying aerosol types [3–5]. Nowadays, dual- or multiple-wavelength aerosol polarization lidars [6–8] have been widely employed for investigating the aerosol microphysical properties and transportation [9, 10]. Recently, imaging lidar techniques have been developed for atmospheric pollution monitoring and aerosol polarization studies [11–17]. In this work, a dual-polarization imaging lidar technique based on the division-of-focal-plane scheme [18, 19], employing two continuous-wave laser diodes (458 nm and 808 nm) as light sources and two polarization cameras with a micro-polarizer array as detectors, has been proposed and demonstrated for all-day field measurements of atmospheric aerosols.

32.2 The Experimental Setup

The system schematic and picture of the dual polarization imaging lidar are shown in Fig. 32.1a, b. The transmitter mainly includes two high-power laser diodes, optical components (e.g., polarizer, beam splitter, collimation), and a system control unit. All optics and electronics are placed on an aluminum alloy base plate. A 458-nm laser diode with 4.75-W output power and an 808-nm laser diode with 5-W output power are used as the light sources. The fast axis of the 458-nm laser diode and

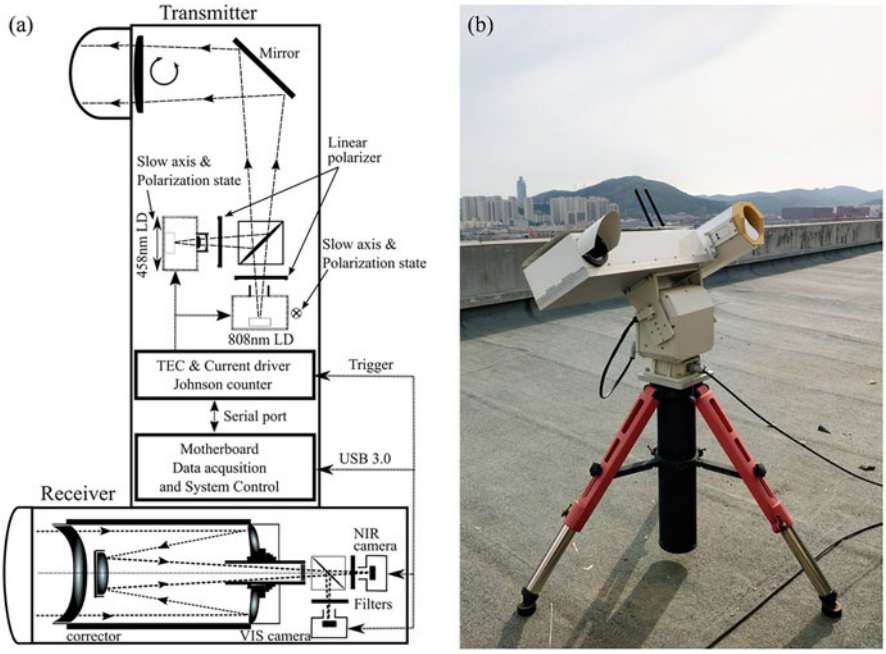


Fig. 32.1 (**a**) The architecture and (**b**) picture of the dual-polarization imaging lidar system

the slow axis of the 808-nm laser diode are placed perpendicular to the aluminum alloy base plate. Meanwhile, the polarization directions of the two laser beams are consistent with the slow axes of the laser diodes. As shown in Fig. 32.1, two linear polarizers at 458 nm and 808 nm are utilized to improve the degree of linear polarization (DoLP) of the transmitted laser beams. The transmission axis of the linear polarizer should be consistent with the polarization state of the emitted laser beam. The laser beams are coupled by a dichroic mirror placed with 45° tilted inside a cube, which are then folded by an elliptical mirror and transmitted into the atmosphere after collimated by a 76-mm achromatic lens ($f = 400$ mm, $\phi = 76$ mm).

The backscattering signals at 458 nm and 808 nm collected by the Maksutov-Cassegrain telescope are separated by a 45-degree tilted dichroic mirror and are then detected by two polarization cameras. A 458-nm interference filter with 2.3-nm full width at half maximum (FWHM) and an 808-nm interference filter with 3-nm FWHM are placed before the corresponding polarization cameras to suppress the sunlight background. The polarization camera, which integrates four-directional micro-polarizer elements (e.g., 0°, 45°, 90°, and 135°), captures a four-directional polarization image in a single shot. The laser beam image can then be decomposed into four polarization images with a size of 1224 (H) × 400 (V). Finally, the original lidar signals at four directional polarized channels can be obtained by vertically binning the pixel intensities for each polarization image.

In the present polarization imaging lidar, the linear volume depolarization ratio (LVDR, δ_v) and the offset angle (θ) can be retrieved through the Stokes-Mueller formalism, which are given by [19].

$$\begin{aligned}\tan 2\theta = & \frac{V_2 ER_{135^\circ}(ER_{45^\circ}+1)-ER_{45^\circ}(ER_{135^\circ}+1)}{V_2 ER_{135^\circ}(ER_{45^\circ}-1)+ER_{45^\circ}(ER_{135^\circ}-1)} \\ & \times \frac{ER_{0^\circ}(ER_{90^\circ}-1)+V_1 ER_{90^\circ}(ER_{0^\circ}-1)}{ER_{0^\circ}(ER_{90^\circ}+1)-V_1 ER_{90^\circ}(ER_{0^\circ}+1)}\end{aligned} \tag{32.1}$$

$$\delta_v = \frac{ER_{0^\circ}(V_1 ER_{90^\circ}-1)-ER_{90^\circ}(ER_{0^\circ}-V_1)\tan^2\theta}{ER_{90^\circ}(ER_{0^\circ}-V_1)+ER_{0^\circ}(1-V_1 ER_{90^\circ})\tan^2\theta} \tag{32.2}$$

Here ER_{0°, ER_{90°, ER_{45°, and ER_{135° are referred to as the extinction ratios at 0°, 90°, 45°, and 135° polarized channel, respectively. V_1 and V_2 are defined by $V_1 = (I_{90^\circ}\eta_{0^\circ})/(I_{0^\circ}\eta_{90^\circ})$ and $V_2 = (I_{135^\circ}\eta_{45^\circ})/(I_{45^\circ}\eta_{135^\circ})$, respectively. Here I_{0°, I_{90°, I_{45°, and I_{135° are the measured signal intensities at four polarized channels, respectively.

32.3 Atmospheric Aerosol Measurements

Atmospheric measurement was performed on a near horizontal path with an elevation angle of 3° from 18 February to 23 February 2022 in Dalian, Northern China. The backscattering signals with high SNR at nighttime were selected to

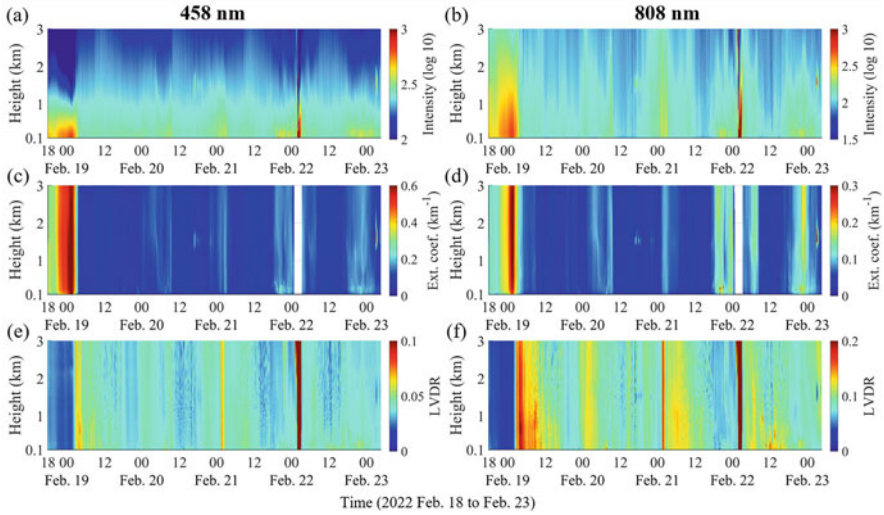


Fig. 32.2 (**a** and **b**) Time-space map of the 0°-polarized backscattering signal at 458 nm and 808 nm. (**c** and **d**) The time-space map of the extinction coefficient at 458 nm and 808 nm. (**e** and **f**) The time-space map of the LVDR at 458 nm and 808 nm

retrieve the offset angles at 458-nm and 808-nm based on the Stokes-Mueller formalism [20]. The offset angles in 5 consecutive days were −0.16° with a variation of 0.05° at 458 nm and 0.38° with a variation of 0.08° at 808 nm. The small variation of the offset angle caused a negligible error (<1%) [21].

The temporal-spatial map of the atmospheric backscattering signal, the aerosol extinction coefficient, and the LVDR at 458 nm and 808 nm are shown in Fig. 32.2. A slight haze occurred from 19:00 on February 18 to 2:00 on February 19, 2022. The PM10 particle concentrations increased from 45 to 75 $\mu g/cm^3$, and the relative humidity increased from 60% to 72%. The extinction coefficients increased from 0.31 to 0.69 km^{-1} at 458 nm and increased from 0.12 to 0.30 km^{-1} at 808 nm, which was consistent with the temporal variation of the PM10 concentration. Moreover, the LVDR decreased to 0.022 at 458 nm and 0.025 at 808 nm, indicating that spherical particles dominated in haze. At 3:00 on February 19, 2022, the PM10 concentration decreased to 29 $\mu g/cm^3$ with the arrival of the northwest wind. The extinction coefficients at 458 nm and 808 nm decreased to 0.13 km^{-1} and 0.11 km^{-1}, respectively, and the LVDR increased to 0.06 and 0.16, respectively. These phenomena showed that northwest winds blew away the local spherical haze particles. A flurry of light snow whirled down from the sky during 2:00 to 3:00 on February 22, 2022. The relative humidity increased sharply from 49% to 67%. The LVDR at 458 nm and 808 nm varied from 0.3 to 0.5, indicating irregular shapes of the snowflake. Moreover, the extinction coefficient was not retrieved during snowing due to the inhomogeneity of the atmosphere caused by the falling snowflakes. In summary, the promising measurement results indicated a great potential of utilizing the dual polarization lidar technique for all-day atmospheric polarization studies.

32.4 Conclusion

In this work, a dual-polarization imaging lidar technique, employing two continuous-wave laser diodes (458 nm and 808 nm) as light sources and two polarization cameras with a micro-polarizer array as detectors, has been proposed and demonstrated for all-day field measurements of atmospheric aerosols. Each polarization camera is able to capture a four-directional polarized image of the transmitted laser beam, from which four polarized atmospheric backscattering signals with 0°, 45°, 90°, and 135° polarization angles can be simultaneously measured. Thus, the LVDR and the offset angles can be retrieved in real time at wavelength of 458 nm and 808 nm without employing additional optical components and sophisticated system adjustments. Atmospheric measurements on a near horizontal path have been carried out from 18 February to 23 February 2022 in Dalian, Northern China. The measurement results showed that the dual-polarization lidar technique opens up many possibilities for characterizing aerosol optical properties.

References

1. Giannakaki, E., van Zyl, P.G., Muller, D., Balis, D., Komppula, M.: Optical and microphysical characterization of aerosol layers over South Africa by means of multi-wavelength depolarization and Raman lidar measurements. Atmos. Chem. Phys. **16**(13), 8109–8123 (2016)
2. Nishizawa, T., Sugimoto, N., Matsui, I., Shimizu, A., Hara, Y., Itsushi, U., Yasunaga, K., Kudo, R., Kim, S.W.: Ground-based network observation using Mie-Raman lidars and multi-wavelength Raman lidars and algorithm to retrieve distributions of aerosol components. J. Quant. Spectrosc. Radiat. Transf. **188**, 79–93 (2017)
3. Ansmann, A., Tesche, M., Althausen, D., Muller, D., Seifert, P., Freudenthaler, V., Heese, B., Wiegner, M., Pisani, G., Knippertz, P., Dubovik, O.: Influence of Saharan dust on cloud glaciation in southern Morocco during the Saharan Mineral Dust Experiment. J. Geophys. Res. Atmos. **113**(D4), 1–16 (2008)
4. Sassen, K., Zhu, J., Webley, P., Dean, K., Cobb, P.: Volcanic ash plume identification using polarization lidar: Augustine eruption, Alaska. Geophys. Res. Lett. **34**(8), 1–4 (2007)
5. Janicka, L., Stachlewska, I.S., Veselovskii, I., Baars, H.: Temporal variations in optical and microphysical properties of mineral dust and biomass burning aerosol derived from daytime Raman lidar observations over Warsaw, Poland. Atmos. Environ. **169**, 162–174 (2017)
6. Murayama, T., Müller, D., Wada, K., Shimizu, A., Sekiguchi, M., Tsukamoto, T.: Characterization of Asian dust and Siberian smoke with multi-wavelength Raman lidar over Tokyo, Japan in spring 2003. Geophys. Res. Lett. **31**(23), 1–5 (2004)
7. Sugimoto, N., Matsui, I., Shimizu, A., Uno, I., Asai, K., Endoh, T., Nakajima, T.: Observation of dust and anthropogenic aerosol plumes in the Northwest Pacific with a two-wavelength polarization lidar on board the research vessel Mirai. Geophys. Res. Lett. **29**(19), 1–4 (2002)
8. Groß, S., Freudenthaler, V., Schepanski, K., Toledano, C., Schafler, A., Ansmann, A., Weinzierl, B.: Optical properties of long-range transported Saharan dust over Barbados as measured by dual-wavelength depolarization Raman lidar measurements. Atmos. Chem. Phys. **15**(19), 11067–11080 (2015)

9. Burton, S.P., Hair, J.W., Kahnert, M., Ferrare, R.A., Hostetler, C.A., Cook, A.L., Harper, D.B., Berkoff, T.A., Seaman, S.T., Collins, J.E., Fenn, M.A., Rogers, R.R.: Observations of the spectral dependence of linear particle depolarization ratio of aerosols using NASA Langley airborne High Spectral Resolution Lidar. Atmos. Chem. Phys. **15**(23), 13453–13473 (2015)
10. Haarig, M., Ansmann, A., Althausen, D., Klepel, A., Groß, S., Freudenthaler, V., Toledano, C., Mamouri, R.-E., Farrell, D.A., Prescod, D.A., Marinou, E., Burton, S.P., Gasteiger, J., Engelmann, R., Baars, H.: Triple-wavelength depolarization-ratio profiling of Saharan dust over Barbados during SALTRACE in 2013 and 2014. Atmos. Chem. Phys. **17**, 10767 (2017)
11. Mei, L., Brydegaard, M.: Continuous-wave differential absorption lidar. Laser Photonics Rev. **9**(6), 629–636 (2015)
12. Mei, L., Brydegaard, M.: Atmospheric aerosol monitoring by an elastic Scheimpflug lidar system. Opt. Express. **23**(24), 1613–1628 (2015)
13. Mei, L., Guan, P., Yang, Y., Kong, Z.: Atmospheric extinction coefficient retrieval and validation for the single-band Mie-scattering Scheimpflug lidar technique. Opt. Express. **25**(16), A628–A638 (2017)
14. Mei, L., Kong, Z., Ma, T.: Dual-wavelength Mie-scattering Scheimpflug lidar system developed for the studies of the aerosol extinction coefficient and the Angstrom exponent. Opt. Express. **26**(24), 31942–31956 (2018)
15. Mei, L., Kong, Z., Guan, P.: Implementation of a violet Scheimpflug lidar system for atmospheric aerosol studies. Opt. Express. **26**(6), A260–A274 (2018)
16. Kong, Z., Ma, T., Chen, K., Gong, Z.F., Mei, L.: Three-wavelength polarization Scheimpflug lidar system developed for remote sensing of atmospheric aerosols. Appl. Opt. **58**(31), 8612–8621 (2019)
17. Kong, Z., Ma, T., Cheng, Y., Zhang, Z., Li, Y., Liu, K., Mei, L.: Feasibility investigation of a monostatic imaging lidar with a parallel-placed image sensor for atmospheric remote sensing. J. Quant. Spectrosc. Radiat. Transf. **254**, 107212 (2020)
18. Kong, Z., Ma, T., Cheng, Y., Fei, R., Zhang, Z., Li, Y., Mei, L.: A polarization-sensitive imaging lidar for atmospheric remote sensing. J. Quant. Spectrosc. Radiat. Transf. **271**, 107747 (2021)
19. Kong, Z., Ma, T., Zheng, K.X., Cheng, Y., Gong, Z.F., Hua, D.X., Mei, L.: Development of an all-day portable polarization lidar system based on the division-of-focal-plane scheme for atmospheric polarization measurements. Opt. Express. **29**(23), 38512–38526 (2021)
20. Kong, Z., Yin, Z., Cheng, Y., Li, Y., Zhang, Z., Mei, L.: Modeling and evaluation of the systematic errors for the polarization-sensitive imaging lidar technique. Remote Sens. (Basel). **12**(20), 3309 (2020)
21. Bravo-Aranda, J.A., Belegante, L., Freudenthaler, V., Alados-Arboledas, L., Nicolae, D., Granados-Munoz, M.J., Guerrero-Rascado, J.L., Amodeo, A., D'Amico, G., Engelmann, R., Pappalardo, G., Kokkalis, P., Mamouri, R., Papayannis, A., Navas-Guzman, F., Olmo, F.J., Wandinger, U., Amato, F., Haeffelin, M.: Assessment of lidar depolarization uncertainty by means of a polarimetric lidar simulator. Atmos. Meas. Tech. **9**(10), 4935–4953 (2016)

Chapter 33
An Algorithm to Retrieve Aerosol Optical Properties from ATLID and MSI Measurements

Tomoaki Nishizawa, Rei Kudo, Akiko Higurashi, Satoru Takakura, Eiji Oikawa, and Hajime Okamoto

Abstract We develop an algorithm to retrieve aerosol optical properties using data of 355-nm high spectral resolution lidar (HSRL) with depolarization measurement function "ATLID" onboard EarthCARE satellite. The ATLID has three channel data of Mie copolar, Mie crosspolar, and Rayleigh attenuated backscatter coefficients at 355 nm. Using the three channel data, the developed algorithm estimates (1) extinction coefficient (α), backscatter coefficient (β), and depolarization ratio (δ) of particles (aerosols and clouds) without assuming a particle lidar ratio (S); (2) identifies molecule-rich, aerosol-rich, or cloud-rich slab layers; (3) classifies aerosol type (e.g., dust and maritime) using the derived β, S, and δ by a threshold method; (4) retrieve planetary boundary layer height using the feature mask products (i.e., (2)); and (5) estimate extinction coefficients for several main aerosol components in the atmosphere (e.g., dust, sea salt, carbonaceous, and water-soluble aerosols) using difference in depolarization and light absorption properties of the aerosol components from the retrieved α, β, and δ. Furthermore, we develop an aerosol retrieval algorithm using both the ATLID and multi-spectral imager "MSI" onboard EarthCARE. This algorithm retrieves vertically mean mode-radii for dust and fine-mode aerosols as well as the extinction coefficients for the four aerosol components using the three channels of the ATLID and radiances at 670 nm and 865 nm of MSI.

T. Nishizawa (✉) · A. Higurashi
National Institute for Environmental Studies, Tsukuba, Japan
e-mail: nisizawa@nies.go.jp; hakiko@nies.go.jp

R. Kudo
Meteorological Research Institute, Tsukuba, Japan
e-mail: reikudo@mri-jma.go.jp

S. Takakura
University of Colorado, Boulder, CO, USA
e-mail: satoru.takakura-1@colorado.edu

E. Oikawa · H. Okamoto
Kyushu University, Kasuga, Japan
e-mail: oikawa_eiji@riam.kyushu-u.ac.jp; okamoto@riam.kyushu-u.ac.jp

© The Author(s), under exclusive license to Springer Nature Switzerland AG 2023

J. T. Sullivan et al. (eds.), *Proceedings of the 30th International Laser Radar Conference*, Springer Atmospheric Sciences,
https://doi.org/10.1007/978-3-031-37818-8_33

These products above are planned to be distributed by JAXA, Japan. We develop the aerosol component retrieval algorithm based on our developed algorithm for the Mie scattering lidar CALIOP onboard CALIPSO satellite.

Keywords Aerosol · EarthCARE · Algorithm

33.1 Introduction

Global measurements of the vertical distribution of the optical properties of atmospheric particles (aerosols and clouds) are important for assessing the climate impact of atmospheric particles via atmospheric radiative processes. For example, it has been reported that the presence of strongly light-absorbing aerosols (e.g., black carbon) above or below the cloud layer is influential enough to change the positive or negative radiative forcing at the top of the atmosphere [1]. The CALIPSO satellite is equipped with a dual-wavelength (532 nm, 1064 nm) polarized Mie scattering lidar, CALIOP, which has been measuring aerosol and cloud vertical distributions since its launch in 2006. Its role will be succeeded by the EarthCARE satellite (Earth Clouds, Aerosols and Radiation Explorer), which will carry the ATLID lidar. EarthCARE is a Japan-Europe collaboration between JAXA, NICT, and ESA [2] for the purpose of comprehensive global observations of clouds, aerosols, and atmospheric radiation. The EarthCARE satellite is equipped with a 95-GHz cloud profiling radar (CPR), a multi-wavelength spectral imager (MSI) with seven channels in the visible to infrared wavelength range, a broadband radiometer (BBR) to measure shortwave and longwave radiation, and a 355-nm polarized HSRL (ATLID). The MSI will be used to measure the horizontal distribution of clouds and aerosols, and the CPR and ATLID will be used to measure the vertical distribution of clouds and aerosols in three dimensions. Atmospheric radiation fluxes will also be simultaneously measured by BBR.

Unlike CALIOP, ATLID measures backscattered light by atmospheric particles (Mie signal) and backscattered light by atmospheric molecules (Rayleigh signal) separately. The most significant feature of ATLID is that it can independently extract the altitude distribution of the extinction coefficient (α_p) and backscatter coefficient (β_p) of atmospheric particles by analyzing these two signals. ATLID also measures polarization, resulting in a total of three channels of signals: a component parallel to the laser polarization (Copol component), a component perpendicular to the laser polarization (Crosspol component), and the Rayleigh signal at a wavelength of 355 nm. Signal calibration are performed on these measured signals and attenuated backscatter coefficients are published.

Measurements with multichannel lidars such as ATLID allow simultaneous retrieval of various optical and microphysical properties of atmospheric particles. For example, algorithms have been developed to estimate the particle size distribution and refractive index of all aerosols using α_p and β_p at two wavelengths (355 nm and 532 nm) extracted by the Raman lidar. In addition, the extinction

coefficients of several major aerosol species in the atmosphere (e.g., black carbon and mineral dust) have been estimated using α_p and β_p at 532-nm wavelength measured by HSRL and Raman lidar, and particle depolarization ratio (δ_p) and the total backscatter signal (Mie signal + Rayleigh signal) at a wavelength of 1064 nm have also been developed [3]. It has been reported that aerosols with strong light absorption properties (e.g., black carbon) affect cloud formation, atmospheric circulation, and water circulation in large-scale fields. Therefore, it is necessary to understand not only the optical and microphysical properties of all aerosols but also those of individual aerosol species.

The EarthCARE mission generates Level 1 (L1) products, which are calibrated signals, and Level 2 (L2) products, which are geophysical quantities related to clouds, aerosols, etc. estimated from the L1 products. The L1 products are generated by each sensor development organization (JAXA and NICT for CPR and ESA for others), and the L2 products are generated by JAXA and ESA using different algorithms. Therefore, the development of algorithms to estimate the optical properties of atmospheric particles using Copol component of Mie signal ($\beta_{\mathrm{Mie,co}}$), crosspol component of Mie signal ($\beta_{\mathrm{Mie,cr}}$), and Rayleigh signal (β_{Ray}) is underway with the support of JAXA and other organizations. In addition to the estimation algorithm using only the ATLID data (ATLID stand-alone algorithm), we are also developing a combined algorithm that also uses MSI (ATLID combined algorithm). In this combined algorithm, the radiance at 670 nm (R670) and 865 nm (R870), which are the L1 products of MSI, are used. In this paper, we present an overview of the ATLID stand-alone and combined algorithms under development and the products generated by these algorithms, showing examples of their application to simulation data and other satellite observation data.

33.2 Product

Table 33.1 lists the products generated by the ATLID stand-alone and combined algorithms. The algorithm identifies which component of atmospheric molecules, aerosols, or cloud particles is predominant at each altitude and outputs the identifier (feature mask product). It also estimates the optical properties of atmospheric particles at a wavelength of 355 nm (α_p, β_p, δ_p, and the lidar ratio S_p) at each altitude. Whether the derived optical properties of atmospheric particles are those of aerosols or clouds is determined according to the feature mask product (aerosol optical properties or cloud optical properties). Aerosol type (e.g., mineral dust type, marine aerosol type, etc.) and cloud particle type (water droplets or ice crystals) are also identified at each altitude (target mask), and atmospheric boundary layer altitude is also estimated (atmospheric boundary layer altitude). The above five products are treated as JAXA standard products (products that are always generated and whose accuracy is guaranteed). Similar products are also generated by ESA, although the estimation method is different.

Table 33.1 Products generated by the ATLID stand-alone and combined algorithms[*a]

Product name	Primary parameters	Resolution	
		Horizontal (km)	Vertical (km)
Feature mask product	Feature mask	1*/1/0.2	0.1
Target mask product	Target mask	1*/1	0.1
Aerosol product	α_p, β_p, δ_p, S_p	1*	0.1
Cloud products	α_p, β_p, δ_p, S_p	1*/1	0.1
Boundary layer height	PBL height	1*/1	–
Aerosol component	α_p (Water-soluble)	1*	0.1
	α_p (Dust)	1*	0.1
	α_p (Sea salt)	1*	0.1
	α_p (Black carbon)	1*	0.1
Aerosol component	α_p (Water-soluble)	1*	0.1
	α_p (Dust)	1*	0.1
	α_p (Sea salt)	1*	0.1
	α_p (Black carbon)	1*	0.1
	R_m (Water-soluble)	1*	0.1
	R_m (Dust)	1*	0.1

[*a]The term 1* indicates 1 km horizontal resolution running-averaged in 10-km horizontal range

In addition, the ATLID stand-alone algorithm estimates the extinction coefficients at 355 nm for the major aerosols in the atmosphere: water-soluble particles (WS: mixture of sulfate, nitrate, and organic aerosols), black carbon (BC), mineral dust (DS), and sea salt particles (SS) (aerosol component product). This product is treated as a JAXA research product (a product recommended to be generated to enhance the scientific value of the EarthCARE mission) and is one of the unique products not generated by ESA. The ATLID-MSI synergy algorithm generates one type of research product. Here, the mode radii of fine particles ($R_{m,f}$) and coarse particles ($R_{m,c}$) are estimated along with the extinction coefficients (WS, DS, SS, BC) of the above four aerosols at a wavelength of 355 nm. This product will be an advanced version of the ATLID stand-alone products.

33.3 Algorithm

33.3.1 Feature Mask

Figure 33.1 shows the analysis flow. We develop a feature mask scheme for the ATLID considering the previous studies [4, 5]. We use the β_{mie} ($=\beta_{\text{Mie,co}} + \beta_{\text{Mie,cr}}$) and β_{ray} as the diagnostic parameter ($P_{r,\text{mie}}$ and $P_{r,\text{ray}}$, respectively). Theoretically, only molecules exist when $P_{r,\text{mie}}$ is zero and $P_{r,\text{ray}}$ exceeds zero, and particles exist

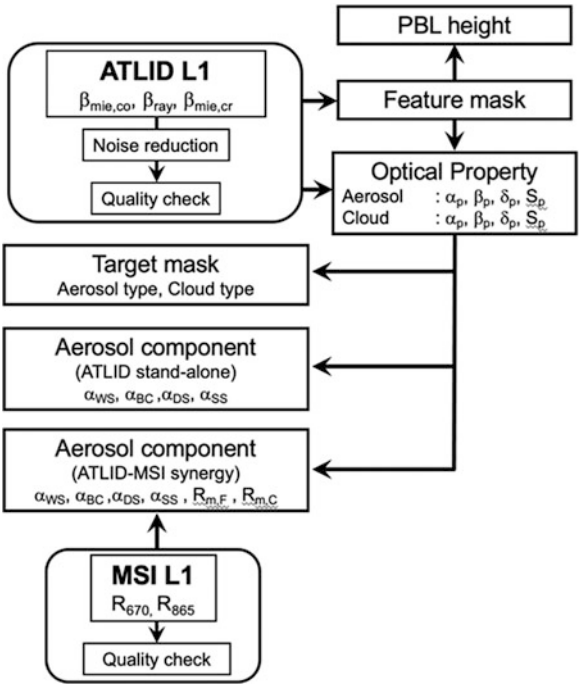


Fig. 33.1 Analysis flow of the algorithms

when $P_{r,\mathrm{mie}}$ exceeds zero. $P_{r,\mathrm{mie}}$ is generally greater for clouds than for aerosols. Thus, the algorithm provides flags in the slab-layer using the following criteria:

$$\text{Clear-sky (few aerosol)} : \text{when } P_{r,\mathrm{mie}} = 0 \text{ and } P_{r,\mathrm{ray}} > 0$$

$$\text{Aerosol} : \text{when } P_{\mathrm{th,cloud}} > P_{r,\mathrm{mie}} > 0 \text{ and } P_{r,\mathrm{ray}} > 0$$

$$\text{Cloud} : \text{when } P_r > P_{\mathrm{th,cloud}} \text{ and } P_{r,\mathrm{ray}} > 0$$

Here, $P_{\mathrm{th,cloud}}$ is a threshold value. Signal noise should be considered for the above method. Thus, the criteria are improved as follows:

$$\text{Clear-sky (few aerosol)} : \text{when } P_{\mathrm{th,Mie\text{-}noise}} > P_r \text{ and } P_{r,\mathrm{ray}} > P_{\mathrm{th,Ray\text{-}noise}}$$

$$\text{Aerosol} : \text{when } P_{\mathrm{th,cloud}} + P_{\mathrm{th,Mie\text{-}noise}} > P_{r,\mathrm{mie}} > P_{\mathrm{th,Mie\text{-}noise}} \text{ and } P_{r,\mathrm{ray}} > P_{\mathrm{th,Ray\text{-}noise}}$$

$$\text{Cloud} : \text{when } P_r > P_{\mathrm{th,cloud}} + P_{\mathrm{th,Mie\text{-}noise}} \text{ and } P_{r,\mathrm{ray}} > P_{\mathrm{th,Ray\text{-}noise}}$$

Here, $P_{\text{th,Mie-noise}}$ and $P_{\text{th,Ray-noise}}$ are computed from the signal-to-noise ratios of the measured data. The threshold $P_{\text{th,cloud}}$ is based on the cloud mask scheme which was studies based on satellite and ship-borne lidar data[10,11] and is given as follows:

$$P_{\text{th,cloud}} = 0.5\beta_{c,\text{th}} \exp(-2\tau_m) \{1 - \tanh(z - z_c)\} \tag{33.1}$$

τ_m is the molecular optical thickness up to the altitude (z) from the ATLID, given by $z_c = 5000$ m and $\beta_{c,\text{th}} = 10^{-5.25}$ [/m/sr].

It also identifies the followings as other features:

$$\text{Noisy : when } P_{r,\text{ray}} < P_{\text{th,Ray-noise}}$$

$$\text{Surface : } P_{r,\text{mie}} + P_{r,\text{ray}} > P_{\text{th,surf}}$$

$P_{\text{th,surface}}$ will be determined empirically based on the actual ATLID observed signals. In this surface identification, existing surface altitude data is used as refence data to reduce misclassification of clouds and dense aerosol layers. The layer that identified as "Noisy" under the optically thick particle layer is classified as a fully attenuated layer. The "Noisy" layer below the surface is classified as sub-surface.

33.3.2 Particle Optical Properties

α_p, β_p, and δ_p can be directly derived using the L1 data of $\beta_{\text{mie,co}}$, $\beta_{\text{mie,cr}}$, and β_{ray} using a conventional method. L1 data with a sufficient signal-to-noise ratio (SN ratio) are needed to derive the L2 parameters with sufficient precision. Thus, it is essential to average and/or smooth the measured signals to improve the SN ratio. As another approach, the MAP method (maximum a posteriori method) is being developed as a more robust estimation method for signal noise. The cost function F used in the MAP method is as follows.

$$F(x) = \{Y(x) - Y_{\text{obs}}\}^T W^{-1} \{Y(x) - Y_{\text{obs}}\} + Y_e(x)^T W_e^{-1} Y_e(x) \tag{33.2}$$

The vector x is an estimate. The vector Y_{obs} is the measured value; the vector $Y(x)$ is the calculated value. The vector Y_e is a function that enforces smoothness for the altitude distribution of each estimate. The matrix W (W_e) is a diagonal matrix and is weighted according to the measurement accuracy (forced smoothness). The cost function is minimized by the Gauss-Newton method, which is a combination of the line search method [6]. The details of this method and analysis results can be found in Nishizawa et al. [7].

33.3.3 Aerosol Types

Aerosol types and their optical models determined by cluster analysis of aerosol optical properties estimated from AERONET data were used in CALIOP data analysis [8], and this method is known well to be useful. Thus, we conducted cluster analysis of aerosol optical properties estimated from AERONET data and determine the aerosol optical properties at 355 nm. Here, we adopt Fuzzy-c means and NMF (nonnegative matrix factorization) methods to conduct cluster analysis. Four aerosol types (dust, dust+smoke, smoke, and urban) were selected by cluster analysis, and the particle size distribution and refractive index were modeled for each aerosol type. Following the AERONET product, a log-normal distribution consisting of two modes, fine-particle and coarse-particle modes, was assumed for the particle size distribution, and their mode radii and standard deviations were modeled. Using the modeled particle size distribution and refractive index, theoretical calculations were performed to derive the δ_p and S_p. In this theoretical calculation, smoke and urban particles are assumed to be spherical, and dust and dust+smoke particles are assumed to be spheroidal The marine type aerosol was also modeled by cluster analysis using AERONET island observation data in the open ocean (particle shape was assumed to be spherical). We are improving the modeled aerosol characteristics to improve the consistency with the lidar observations.

33.3.4 Planetary Boundary Layer

The PBL height has been derived from Mie scattering lidar measurements using various methods [9]. They used the gradient of the attenuated backscatter coefficient at 1064 nm and detected the top of the PBL. This method assumes that aerosol density is high in the PBL and rapidly decreases at the top of the PBL. Thus, as an analogy of their methods, the developed algorithm retrieves the PBL height.

33.4 Summary

An algorithm to generate EarthCARE L2 aerosol and cloud products using ATLID and MSI data is under development. These algorithms reduce the uncertainty of the products by taking advantage of the characteristics of ATLID, which is HSRL that enables independent extraction of dissipation and backscattering coefficients and create unique products such as black carbon vertical distributions that are indispensable for climate impact assessment. These ATLID air particle products also play a role as successors to the CALIOP products and are responsible for the creation of long-term global products with vertical distribution information, which is essential for the assessment of long-term changes in atmospheric particles.

To reduce the uncertainty and improve the retrieval uncertainty of the algorithms, we are improving the threshold values used in the feature mask, the optical model for each aerosol type, the optical model for each aerosol species used in the aerosol species estimation, and the numerical solution method.

Acknowledgments This research is supported by Grant-in-Aid for Scientific Research (KAKENHI) (project numbers: JP18KK0289, JP17H06139, JPS17H04477, JP15H01728, JP15H02808, JP25220101) and by JAXA funded research.

References

1. Takemura, T., et al.: Aerosol distributions and radiative forcing over the Asian Pacific region simulated by Spectral Radiation-Transport Model for Aerosol Species (SPRINTARS). J. Geophys. Res. **108**(D23), 8659 (2003)
2. Illingworth, A.J., et al.: The EarthCARE satellite: the next step forward in global measurements of clouds, aerosols, precipitation, and radiation. Bull. Am. Meteorol. Soc. **96**, 1311–1332 (2015)
3. Nishizawa, T., et al.: Ground-based network observation using Mie-Raman lidars and multi-wavelength Raman lidars and algorithm to retrieve distributions of aerosol components. J. Quant. Spectrosc. Radiat. Transf. **188**, 79–93 (2017)
4. Hagihara, Y., et al.: Development of a combined CloudSat-CALIPSO cloud mask to show global cloud distribution. J. Geophys. Res. **115**, D00H33 (2010)
5. Okamoto, H., et al.: Vertical cloud properties in the tropical western Pacific Ocean: validation of the CCSR/NIES/FRCGC GCM by shipborne radar and lidar. J. Geophys. Res. **113**, D24213 (2008)
6. Kudo, R., et al.: Vertical profiles of aerosol optical properties and the solar heating rate estimated by combining sky radiometer and lidar measurements. Atmos. Meas. Tech. **9**, 3223–3243 (2016)
7. Nishizawa, et al.: Aerosol and cloud retrieval algorithms using EarthCARE Satellite-Borne Lidar Data. J. Remote Sens. Soc. Jpn. **39**, 215–224 (2019) (in Japanese)
8. Omar, A.H., et al.: The CALIPSO automated aerosol classification and lidar ratio selection algorithm. J. Atmos. Ocean. Technol. **26**, 1994–2014 (2009)
9. Sugimoto, N., et al.: Continuous observations of aerosol profiles with a two-wavelength polarization lidar in Guangzhou in PRD2006. J. Appl. Meteorol. Climatol. **48**, 1822–1830 (2009)

Chapter 34
Observation of Polar Stratospheric Clouds at Dome C, Antarctica.

Marcel Snels, Luca Di Liberto, Ilir Shuli, Francesco Colao, Andrea Scoccione, and Federico Serva

Abstract The LiDAR observatory at Dome C, Antarctica, has been active since 2014. Its main goal is the observation of polar stratospheric clouds during the Antarctic winter, from early May until the end of September. Polar stratospheric clouds typically occur at altitudes between 12 and 26 km, when the stratospheric temperature is low enough to form liquid STS (Supercooled Ternary Solutions), solid NAT (Nitric Acid Trihydrate), and ice crystals. These aerosols reflect part of the light emitted by the LiDAR, and its backscattered fraction as well as its polarization can be measured. The recorded optical signals can then be used to distinguish the various aerosols composing the polar stratospheric clouds (PSCs). PSCs are important for the catalytic destruction of ozone and for the removal of nitric acid and water vapor from the stratosphere.

The Dome C LiDAR observatory is one of the few Antarctic stations accredited as a main station of the NDACC (Network for the Detection of Atmospheric Composition Change). The LiDAR can be remotely controlled and operates several times per day during the austral winter. Recently, a tropospheric channel has been added for the observation of cirrus clouds.

Supported by PNRA.

M. Snels (✉) · L. Di Liberto · I. Shuli
CNR-Institute of Atmospheric Sciences and Climate, Roma, Italy
e-mail: m.snels@isac.cnr.it; l.diliberto@isac.cnr.it; i.shuli@isac.cnr.it

F. Colao
ENEA, Frascati, Italy
e-mail: francesco.colao@enea.it

A. Scoccione
Aeronautica Militare, Pratica di Mare, Roma, Italy
e-mail: andrea.scoccione@aeronautica.difesa.it

F. Serva
Agenzia Spaziale Italiana (ASI); European Space Agency (ESA)Φ-lab, Roma, Italy
e-mail: federico.serva@asi.it

© The Author(s), under exclusive license to Springer Nature Switzerland AG 2023

J. T. Sullivan et al. (eds.), *Proceedings of the 30th International Laser Radar Conference*, Springer Atmospheric Sciences,
https://doi.org/10.1007/978-3-031-37818-8_34

Keywords Polar stratospheric clouds · LiDAR · Ozone

34.1 LiDAR Observations of Polar Stratospheric Clouds (PSCs) in Antarctica

PSCs have been observed since 1989 in Antarctica mainly by using ground-based LiDARs. The longest time records are held by the McMurdo station (1989–2010) and Dumont D'Urville (1989–1998, 2006–present). Most research stations are located on the coast or on the Antarctic peninsula (McMurdo, Dumont D'Urville, Davis, Syowa, Belgrano II, Rothera, and others), while very few are located on the plateau, most notably South Pole and Concordia station (Fig. 34.1).

The polar vortex is often symmetric with respect to the South Pole, but a displacement versus the Antarctica peninsula can be observed by the end of August. This implies that since PSCs are formed at cold temperatures (typically below 195 K), stations lying well within the vortex would be most indicated for observing PSCs. Indeed, a recent study [4] identifies Concordia station as the best location for observing PSCs. This study does not include the South Pole station, because it is based on observations by CALIPSO, whose orbit covers the globe from 82°

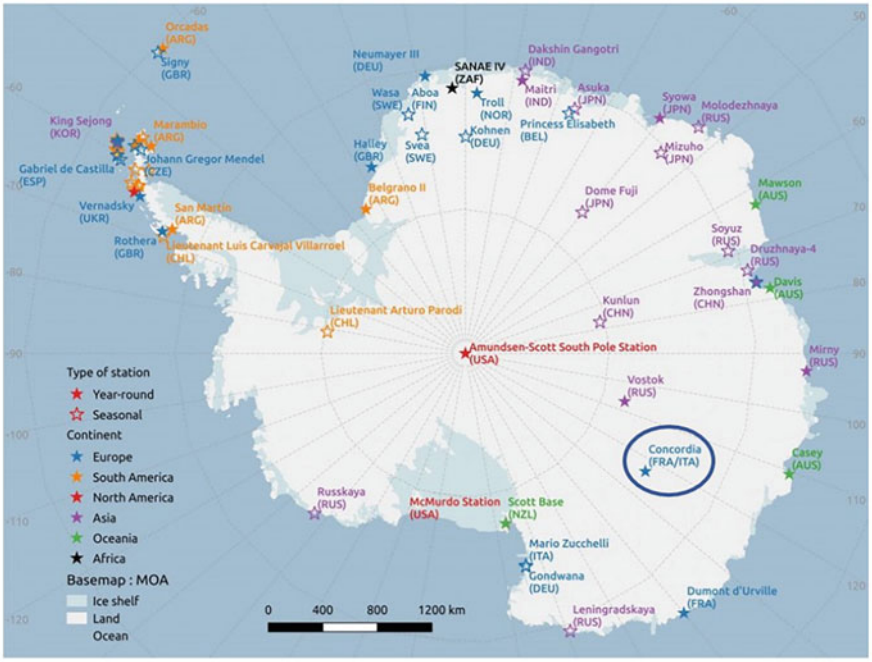


Fig. 34.1 The map shows the main research stations in Antarctica

South to 82° North. Since June 2006, the space-borne LiDAR CALIOP on the CALIPSO satellite has been observing polar stratospheric clouds, by using a laser emitting at 532 nm. Ground-based and space-borne LiDARs are complementary as they produce different kinds of information. Ground-based measurements allow process studies and long-term observations at specific locations, while satellite observations cover a large part of the globe but have long revisiting times for specific locations. For example, there are about 10 CALIPSO overpasses per month with a footprint within 50 km from Dome C (20–25 within 150 km). Ground-based LiDAR stations can provide a calibration for satellite missions and have, in principle, longer lifetimes than satellite missions (although the CALIPSO satellite has exceeded by far its nominal mission lifetime). The main disadvantage of ground-based observations is that they are limited to the location of the observatory. However, the situation at Concordia station is peculiar, since there are no important orographic features and being on a plateau the air mass in the area above the station is rather homogeneous in temperature and composition even at large distances. This makes Concordia station representative for a large area (the central plateau of Antarctica), while most other LiDAR observatories (Dumont D'Urville, Belgrano II, Davis, Rothera), being close to the coast or on the Antarctic peninsula, do not have this advantage.

34.2 PSC Classification

Polar stratospheric clouds are known to be composed of different aerosols, or mixtures of aerosols, with different chemical composition and morphology. The LiDAR measures two optical parameters, the backscatter ratio R and the perpendicular backscatter coefficient (β_{perp}), or an equivalent parameter, such as the volume or aerosol depolarization. An algorithm is used to detect PSCs and to classify the detected PSCs based on the values of the optical parameters measured. This procedure is illustrated in the figure below. If R or β_{perp} exceeds a threshold value, we detect a PSC. These thresholds have been determined from the noise of the detector and the statistical errors in the photon-counting process. All particles that have a β_{perp} below the threshold are considered spherical particles (liquid particles) since they produce a negligible depolarization, while all others are solid particles that are classified according to their R and β_{perp} values. This procedure closely follows the V2 algorithm used to classify the CALIOP PSC special data products, to allow for a meaningful comparison between datasets from ground-based and space-borne instruments (see Fig. 34.2 and [2, 3]).

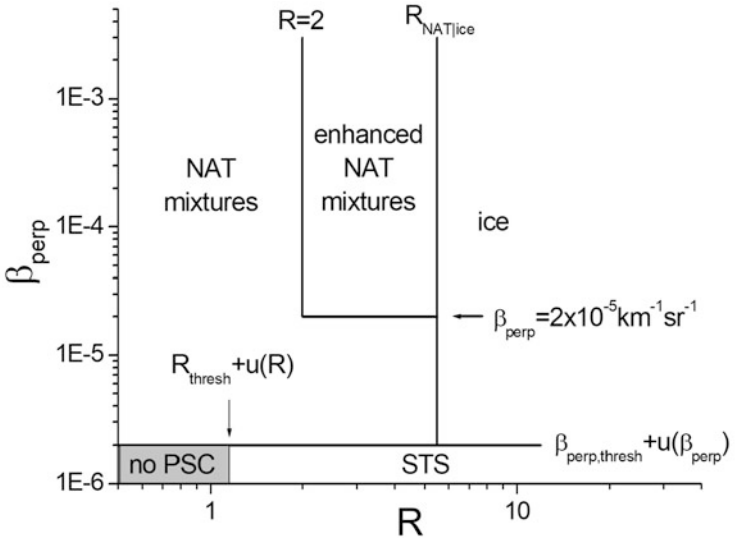


Fig. 34.2 The figure shows the detection and classification criteria of the V2 CALIOP algorithm. The classification of PSC particles, as STS, NAT mixtures, enhanced NAT mixtures, and ice requires that threshold conditions for R and/or $\beta_{\perp}$ are satisfied. Please note that the thresholds are dynamic thresholds, except for the threshold on R that separates NAT mixtures from enhanced NAT mixtures. The figure has been adapted from [3]

34.3 Comparison of Ground-Based LiDAR Data with CALIOP Data

Since ground-based and space-borne LiDARs provide complementary data, both datasets will be used to provide information about PSC occurrence on a short (seasonal) and long (>10 years) time scale, their formation and their dependence on temperature, the presence of cirrus clouds, etcetera. A simultaneous analysis of both data requires that we compare nearly coincident measurements to check that both instruments produce compatible data. We have selected LiDAR data from Concordia station that are quasi-coincident (within 15 minutes) with CALIOP data acquired during near overpasses (having a footprint within 150 km of Concordia station). A typical result is shown in Fig. 34.3. The figure shows the different PSC classes, as defined in [2] for all cases where both LiDARs detected a PSC. The PSC detection of both LiDARs shows a good agreement, being around 80%, meaning that both LiDARs observe (or do not observe) a PSC in 80% of all quasi-coincident observations. It can also be noted that they classify the PSC in the same way in most cases.

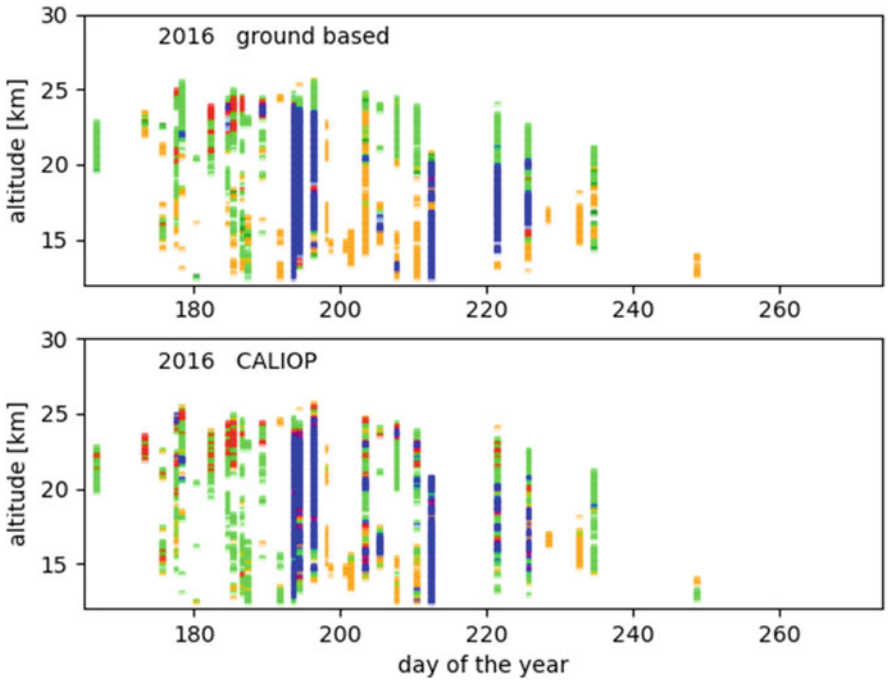


Fig. 34.3 Quasi-coincident observations where PSCs were observed by both LiDARs for 2016 above Dome C. Upper panel: Ground-based LiDAR. Lower panel: CALIOP above Dome C. The different colors indicate PSCs of different compositions; green = NAT mixtures, yellow = STS, red = enhanced NAT mixtures, blue = ice

When we consider all observations made close to Concordia station in a full PSC season, we can observe that the data are really complementary (see Fig. 34.4). This figure shows ground-based and CALIOP observations from June to September close to Concordia station. The black contour encloses the area where the local temperature is below the formation temperature of NAT PSCs. It can be seen that PSCs gradually descent toward the end of the season and that PSCs are rarely observed when the local temperature is above T_{NAT}. It should be noted that the formation temperatures for STS and ice PSCs are lower than that for the formation of NAT and that NAT can "survive" for a short time above T_{NAT} before evaporating. The circles in Fig. 34.4 indicate that measurements have been made but no PSCs were detected. Ground-state data are missing from the 2th to the 7th of August (day 214–219), due to instrumental problems.

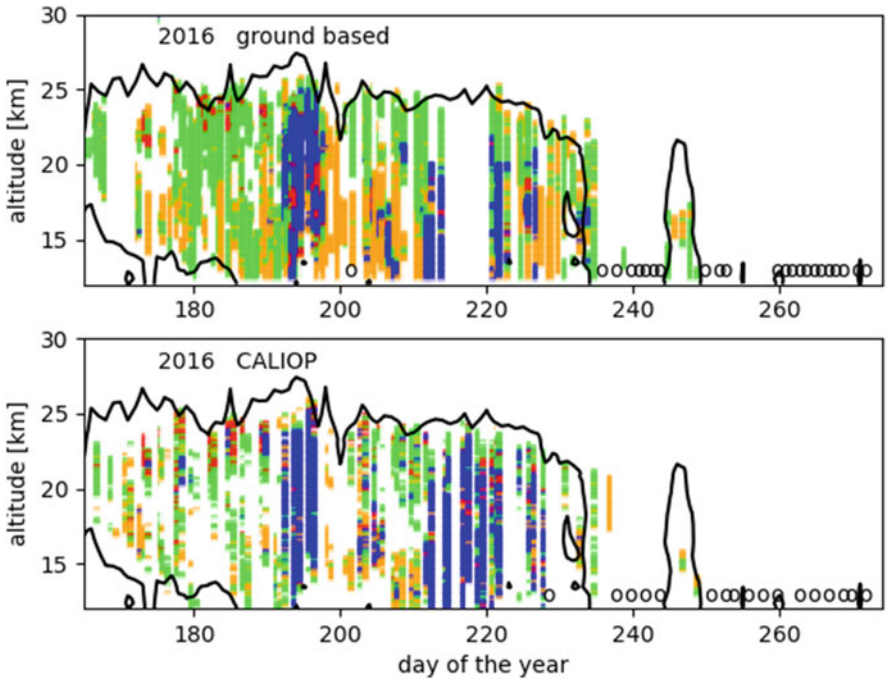


Fig. 34.4 All PSC observations for 2016 above Dome C. Upper panel: Ground-based LiDAR. Lower panels: CALIOP above Dome C. The different colors indicate classified PSCs; green = NAT mixtures, yellow = STS, red = enhanced NAT mixtures, blue = ice. The circles indicate measured profiles without PSCs. The black contour indicates the area with a temperature below T_{NAT}

The 2021 ozone hole season was one of the longest ever recorded, lasting up to late December, and was in some respect similar to the 2020 case [1]. While slow ozone recovery is reducing the overall size of the ozone hole, as well as its magnitude and the area covered, the last two seasons were notable for the very low ozone concentration values (minima below 100 DU). In particular, the polar vortex wind speed was significantly larger than average in 2021, reaching near-record intensity in several cases between September and December. Interactions between dynamical conditions and PSC occurrence are therefore important in determining interannual variations in the ozone hole evolution. We show in Fig. 34.5 the preliminary analysis of the PSCs observed during 2021. It is remarkable how many ice PSCs have been observed throughout the winter. This confirms the exceptional 2021 vortex.

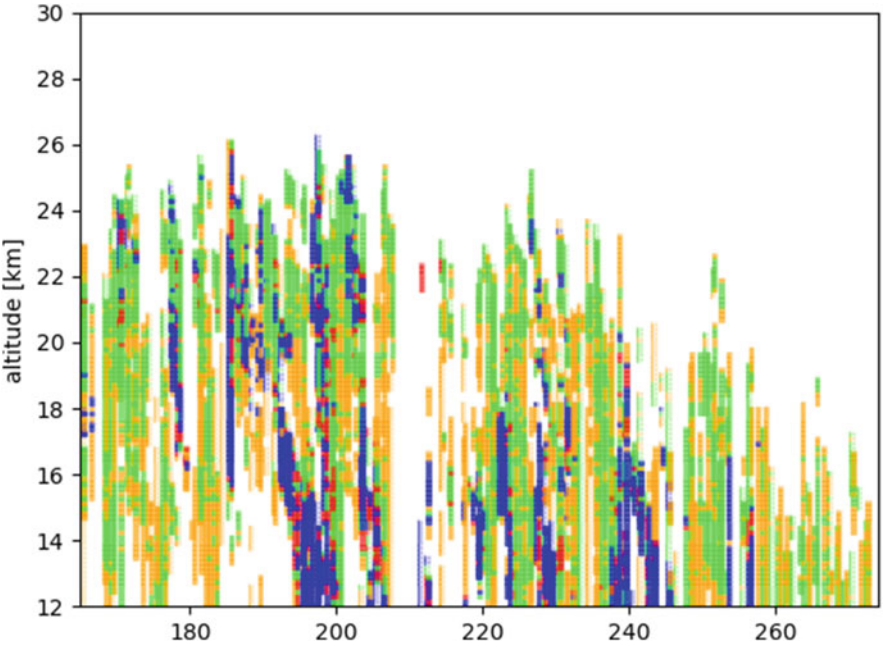


Fig. 34.5 All PSC observations for 2021 above Dome C. The different colors indicate classified PSCs; green = NAT mixtures, yellow = STS, red = enhanced NAT mixtures, blue = ice

Acknowledgments The authors acknowledge the financial support by PNRA in the framework of the projects 2009/B.08 and OSS-12. We also acknowledge the support of the ISSI-PSC initiative project. Logistical and winter-time technical support was provided by the Piano Nazionale della Ricerca in Antartide (PNRA). The authors thank Igor Petenko, Giampietro Casasanta, Simonetta Montaguti, Alfonso Ferrone, Filippo Cali Quaglia, Meganne Christian, Alberto Salvati, Rodolfo Canestrari, and Angelo Galeandro for performing the ground-based LiDAR measurements at Dome C during the winter and Maurizio Viterbini for his valuable technical support.

References

1. Klekociuk, A.R., Tully, M.B., Krummel, P.B., Henderson, S.I., Smale, D., Querel, R., Nichol, S., Alexander, S.P., Fraser, P.J., Nedoluha, G.: The Antarctic ozone hole during 2020. J. South. Hemisph. Earth Syst. Sci. **72**, 19–37. https://doi.org/https://doi.org/10.1071/ES21015
2. Pitts, M.C., Poole, L.R., Gonzalez, R.: Polar stratospheric cloud climatology based on CALIPSO spaceborne LiDAR measurements from 2006–2017. Atmos. Chem. Phys. **2018**, 10881–10913 (2018). https://doi.org/10.5194/acp-18-10881-2018
3. Snels, M., Colao, F., Cairo, F., Shuli, I., Scoccione, A., De Muro, M., Pitts, M., Poole, L., Di Liberto, L.: Quasi-coincident observations of polar stratospheric clouds by ground-based LiDAR and CALIOP at Concordia (Dome C, Antarctica) from 2014 to 2018. Atmos. Chem. Phys. **21**(3), 2165–2178 (2021). https://doi.org/10.5194/acp-21-2165-2021
4. Tesche, M., Achtert, P., Pitts, M.C.: On the best locations for ground-based polar stratospheric cloud (PSC) observations. Atmos. Chem. Phys. **21**(1), 505–516 (2021). https://doi.org/10.5194/acp-21-505-2021

Chapter 35
Laboratory Evaluation of the Lidar Particle Depolarization Ratio (PDR) of Sulfates, Soot, and Mineral Dust at 180.0° Lidar Backscattering Angle

D. Cholleton, P. Rairoux, and A. Miffre

Abstract In polarization lidar field experiments, the particles depolarization ratio (PDR) is key for accurate retrievals of particles backscattering vertical profiles specific to nonspherical particles, such as mineral dust. Precise values of the intrinsic depolarization of mineral dust are however difficult to obtain, due to the complexity of mineral dust in size, shape, and complex refractive index, which prevents from analytical solutions to the Maxwell's equations. In this contribution, a new approach is proposed, based on a laboratory experiment, to provide accurate evaluations of the lidar PDR of mineral dust and soot particles in laboratory (Miffre et al., J Quant Spectrosc Radiat Transf 169:79–90, 2016). This laboratory aerosol Pi-polarimeter takes benefit from the scattering matrix formalism to provide accurate evaluations of the lidar PDR in laboratory in the exact lidar backscattering direction of 180.0°, which is a world first (Miffre et al., J Quant Spectrosc Radiat Transf 169:79–90, 2016). After detailing the principle of the Pi-polarimeter, case studies are considered to reveal the intrinsic PDR of several mineral dust samples differing in size and mineralogy, allowing for the first time to our knowledge, to experimentally investigate the dependence of the lidar PDR with size and complex refractive index. The case study of soot particles (lidar PDR in the 10% range) is also studied (Paulien et al., J Quant Spectrosc Radiat Transf 260:107451, 2021), together with that of core-shell organic sulfates (Dubois et al., Phys Chem Chem Phys 23:5927–5935, 2021). We believe these laboratory findings, which provide accurate evaluations of lidar PDR at 180.0° lidar angle, may be used by the lidar community to interpret the complexity and the wealth of polarization lidar signals, which are every day worldwide acquired.

Keywords Particles depolarization ratio · Laboratory · Mineral dust · Soot

D. Cholleton · P. Rairoux · A. Miffre (✉)
University of Lyon, Université Claude Bernard Lyon 1, CNRS, Institut Lumière Matière, Villeurbanne, France
e-mail: alain.miffre@univ-lyon1.fr

© The Author(s), under exclusive license to Springer Nature Switzerland AG 2023

J. T. Sullivan et al. (eds.), *Proceedings of the 30th International Laser Radar Conference*, Springer Atmospheric Sciences,
https://doi.org/10.1007/978-3-031-37818-8_35

35.1 Introduction

Mineral dust and soot particles are highly important constituents of the atmosphere with multitude of impacts. For instance, mineral dust contributes to the Earth's radiative budget but also to the global carbon cycle by fertilizing nutrient-poor ecosystems. In the atmosphere, such aerosols are often mixed with other types of aerosols and to face such a complexity, lidar partitioning algorithms have been developed such as the $1\beta + 1\delta$ algorithm [4], used to discern the mineral dust contribution in two-component particles external mixtures. Such lidar-based aerosol retrievals however remain under-constrained since the number of input measurements is small compared to the large number of parameters describing the particles microphysics. Hence, such partitioning algorithms always depend on prior knowledge regarding some input parameters such as the lidar particles' depolarization ratio (PDR). As explained in light scattering textbooks [5], the lidar PDR, which quantifies the particles deviation from isotropy, actually depends on the particles size, shape, and complex refractive index. Light scattering numerical simulations have then been developed, assuming different particles shape such as the T-matrix mathematical spheroidal model applied for example to retrieve vertical profiles of microphysical properties for mineral dust during the SAMUM field campaign [6]. Likewise, the discrete-dipole-approximation (DDA) can be applied to lidar using stereograms, as we published [7]. Nevertheless, such numerical simulations rely on simplifying assumptions that should be carefully checked, and for that, laboratory measurements of the lidar PDR are coveted. Likewise, the lidar PDR retrieval proposed in [8] relies on a predefined value of the backscattering Angstrom exponent, and this assumption must be carefully checked for this methodology to hold. Laboratory experiments at lidar exact backscattering angle are then looked-for to provide accurate evaluations of the lidar PDR of a given aerosol, ideally at several wavelengths, to better constrain the lidar inversions. Existing laboratory light scattering experimental setups however operate at near backscattering angles only ($<180.0°$), which prevent them from accurate evaluations of the lidar PDR since at such angles, the PDR depends on F_{11} and F_{22} but also on F_{12}, and moreover F_{11} and F_{22} may differ from their value at exact backscattering angle, depending on the considered aerosol size, shape, and complex refractive index. As a result, addressing this specific lidar backward scattering direction is key for precise lidar PDR retrievals.

In this context, the goal of this contribution is to present a unique laboratory Pi-polarimeter for aerosols aimed at precisely evaluating the lidar PDR of several aerosols (mineral dust, soot) in the specific lidar exact backward scattering direction of 180.0°, which is a world first [1]. Please note that the laboratory evaluation of pollen lidar PDR is provided in a dedicated contribution. The principle of the laboratory aerosol Pi-polarimeter is presented in Sect. 35.2, together with the methodology to retrieve the lidar PDR. Section 35.3 is dedicated to mineral dust particles depolarization. There, the dependence of the lidar PDR with size and mineralogy is for the first time to our knowledge investigated at 180.0° lidar angle

in a laboratory experiment. The depolarization ratio of freshly emitted soot and light backscattering by organic sulfates is then measured in laboratory in Sect. 35.4. The contribution ends with a conclusion and proposes outlooks.

35.2 The Laboratory Aerosol Pi-Polarimeter [1]

The laboratory aerosol Pi-polarimeter is schemed in Fig. 35.1. As in lidar applications, it relies on a ns-pulsed laser source, and special care has been taken to cover the lidar exact backscattering direction with accuracy: $\theta = (180.0 \pm 0.2)°$ after a precise optical alignment with a precision of 1 mm out of 10 m. The laboratory aerosol Pi-polarimeter is actually composed of two identical polarimeters, one per wavelength, to evaluate the lidar PDR of a given aerosol at 355- and 532-nm wavelength simultaneously. Special care has been taken to ensure that polarization and wavelength cross-talks be negligible in the Pi-polarimeter. Moreover, to gain in accuracy in the lidar PDR-retrieval, the polarization state of the backscattered radiation is analyzed for a set of incident polarization states, obtained by modulating the incident polarization state with a quarter-wave plate (*QWP*). Interestingly, the Pi-polarimeter can be described in the framework of the scattering matrix formalism [5]. Hence, by accounting for the successive Mueller matrices encountered by the laser pulse, and after a few calculations, the detected backscattered intensity can be expressed as a function of the rotation angle ψ of the QWP:

$$I_\lambda(\psi) = I_{\lambda,0} \times [a_\lambda - b_\lambda \cos(4\psi)] \tag{35.1}$$

where $I_{\lambda,0}$ accounts for the laser power density and the distance to the aerosol sample. As the coefficients a_λ and b_λ are equal to $a_\lambda = F_{11,\lambda} + F_{22,\lambda}$ and

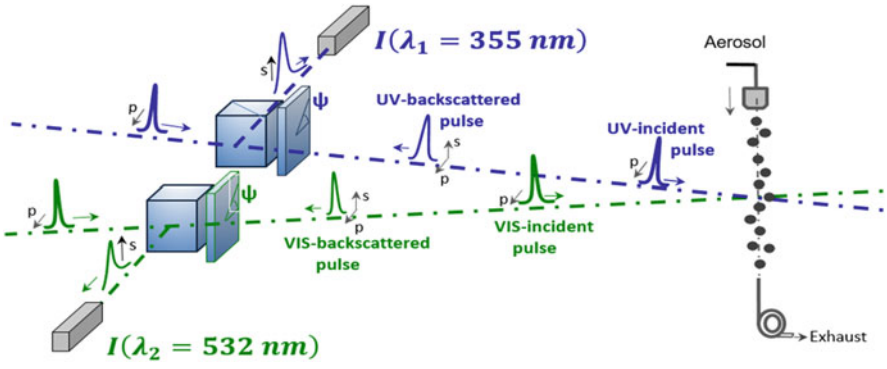


Fig. 35.1 Scheme of the aerosols laboratory π-polarimeter operating at lidar exact backscattering angle of $(180.0 \pm 0.2)°$ allowing accurate retrievals of the lidar *PDR* of an aerosol at 355- and 532-nm wavelength simultaneously Ref. [1]

$b_\lambda = 3F_{22,\lambda} - F_{11,\lambda}$, the ratio $F_{22,\lambda}/F_{11,\lambda}$ only depends on the ratio b_λ/a_λ. The latter ratio can interestingly be precisely evaluated by recording the variations of $I_\lambda(\psi)$, then adjusting these variations with Eq. (35.1) to retrieve $I_{\lambda,0}b_\lambda$ and $I_{\lambda,0}a_\lambda$,then b_λ/a_λ. As a result, the lidar PDR is obtained by noting that $\mathrm{PDR}_\lambda = (1 - b_\lambda/a_\lambda)/2$. The aerosol Pi-polarimeter was validated on spherical sulfate particles which follow the Mie theory: indeed, $F_{22,\lambda}/F_{11,\lambda}$ was found equal to unity, leading to zero particles depolarization.

35.3 Laboratory Evaluation of Mineral Dust Lidar PDR [1, 9]

Light backscattering by mineral dust is clearly much more complex than that of spherical sulfate particles for light backscattering is weaker for nonspherical particles. We could however adjust our experimental data points with Eq. (35.1) to reveal precise spectral and polarimetric fingerprints of the considered mineral dust samples. Mineral dust being a complex mixture of various chemical oxides, the mineral dust lidar PDR was measured for different particles sizes and mineralogy presented in Table 35.1 [9]. Silica (resp. hematite) has been considered as a main chemical component (a light absorbent) present in mineral dust. Also, Arizona and Asian dust were considered as natural mixtures containing these silica and iron oxides. In short, Arizona is rather silica rich, while Asian dust is rather hematite rich. From Table 35.1, we see that the well-known depolarization of 30% generally attributed to mineral dust is indeed retrieved for silica. The hematite depolarization ratio is however lower, mainly because it is a light absorbent. This leads to a reduction in the Asian dust depolarization ratio, which is hematite rich. Likewise, Arizona dust, which is silica rich, exhibits a higher depolarization ratio.

Table 35.1 Laboratory measurement of the ratio $F_{22,\lambda}/F_{11,\lambda}$ of scattering matrix elements and corresponding lidar PDR for silica, hematite, and Arizona and Asian dust, at exact backscattering angle ($\theta = \pi$), evaluated from the laboratory π-polarimeter

		Finer *SD*		Coarser *SD*	
Mineralogy	λ (*nm*)	$F_{22,\lambda}/F_{11,\lambda}$	PDR_λ (%)	$F_{22,\lambda}/F_{11,\lambda}$	PDR_λ (%)
Silica	355	0.622 ± 0.014	*23.3 ± 0.9*	0.506 ± 0.011	*32.8 ± 1.0*
	532	0.751 ± 0.016	*14.2 ± 0.9*	0.618 ± 0.016	*23.6 ± 1.1*
Hematite	355	0.805 ± 0.050	*10.8 ± 2.5*	0.823 ± 0.015	*9.7 ± 0.7*
	532	0.652 ± 0.055	*21.1 ± 3.5*	0.715 ± 0.019	*16.6 ± 1.1*
Arizona dust	355	0.514 ± 0.007	*32.1 ± 0.6*	0.489 ± 0.012	*34.3 ± 1.0*
	532	0.512 ± 0.012	*32.3 ± 1.0*	0.464 ± 0.012	*36.6 ± 1.1*
Asian dust	355	0.603 ± 0.009	*24.7 ± 0.6*	0.603 ± 0.011	*24.8 ± 0.8*
	532	0.622 ± 0.009	*23.3 ± 0.7*	0.558 ± 0.011	*28.4 ± 0.8*

The two size distributions (*SD*) were obtained by adding/removing a cyclone to the generated aerosol

Finally, the size distribution may somewhat modulate this feature. However, at specific backscattering angle, the dust lidar PDR appears to be strongly modulated by particles inhomogeneity. Structural differences then exist in the lidar PDR at backscattering angle. More laboratory work is planned to investigate further these issues.

35.4 Laboratory Evaluation of Soot Particle Lidar PDR [2, 3]

By applying the same methodology to freshly emitted soot particles, we could reveal the lidar PDR of such fractal aggregates and their spectral dependence at 355- and 532-nm wavelength. The fractal nature of these soot was confirmed with TEM images. Our laboratory findings [2] are the following: (11.7 ± 2.3) % for the lidar PDR of freshly-emitted soot at 355-nm and (8.7 ± 2.1) % at 532-nm wavelength. The precision of our laboratory experiment allowed us to discuss on the validity of existing light scattering numerical simulations in cooperation with ONERA (Office National d'Etudes et de Recherches Aérospatiales) who applied the superposition T-matrix method: an overall better agreement between our laboratory findings and their numerical simulation was found at both wavelengths for a polydisperse monomer model.

A complementary aspect is the contribution of soot particles to warm the Earth's climate, while sulfate particles, due to their backscattering property, are known to cool the Earth's climate. In the presence of certain organics, sulfate particles can however give an organic core-shell sulfate structure as recently identified by chemical colleagues [3]. Using the sensitivity and accuracy of our laboratory's Pi-polarimeter, we could reveal the existence of a net decrease in the backscattered light intensity from inorganic to such organic sulfates [3]. Since the particle shape remained spherical during the acquisitions (the Pi-polarimeter retrievals proved that), and as we spent time during the acquisitions to keep the size distribution constant, the observed decrease in backscattered light intensity can only be due to variations in the complex refractive index [3], whereas such chemistry is known to give a core-shell structure. For the involved chemistry is that of isoprene, the most abundant hydrocarbon emitted into the atmosphere, and also that of secondary organic aerosols, the observed decrease may play an important role in the direct radiative forcing of sulfates in the presence of organics, and thus in the impact of these aerosols on climate.

35.5 Conclusion and Outlooks

To conclude, this contribution proposed a unique laboratory approach to reveal the intrinsic lidar particles depolarization ratio (PDR) of several aerosols such as mineral dust or soot particles for the first time in the lidar exact backward

scattering direction of 180.0° in laboratory. Special care has been taken to precisely align the Pi-polarimeter to cover the lidar backscattering angle with accuracy ($\theta = (180.0 \pm 0.2)°$) and to minimize any wavelength and polarization cross-talks [1]. As a result, this controlled-laboratory experiment allows revealing spectral and polarimetric fingerprints of aerosols presenting a determined size, shape, and complex refractive index. Corresponding publications are here given for mineral dust [1, 9], soot [2], and organic sulfates [3]. These laboratory findings are important in a context where no light scattering numerical simulation can provide accurate evaluations of the lidar PDR since such particles are complex-shaped particles as for mineral dust, which exhibits highly irregular shapes, or for fractal soot aggregates. A striking result is that the lidar PDR of mineral dust is strongly modulated by the particles inhomogeneity. Also, when hematite is present, the lidar PDR clearly decreases. Please note that the laboratory evaluation of pollen lidar PDR is provided in a dedicated contribution [10]. The outlooks of this laboratory are numerous, and the very first step is to extend our approach to other different samples differing in size, shape, and mineralogy. Hence, lidar groups interested in investigating the lidar PDR of other aerosol samples are very welcome to provide such samples: our laboratory Pi-polarimeter is indeed open for cooperation. We indeed believe that this laboratory work may provide new insights to help interpret the complexity and wealth of polarization lidar signals, which are every day worldwide acquired.

References

1. Miffre, A., Mehri, T., Francis, M., Rairoux, P.: UV–VIS depolarization from Arizona Test Dust particles at exact backscattering angle. J. Quant. Spectrosc. Radiat. Transf. **169**, 79–90 (2016)
2. Paulien, L., Ceolato, R., Fossard, F., Rairoux, P., Miffre, A.: (UV, VIS) laboratory evaluation of the lidar depolarization ratio of freshly emitted soot aggregates from pool fire in ambient air at exact backscattering angle. J. Quant. Spectrosc. Radiat. Transf. **260**, 107451 (2021)
3. Dubois, C., Cholleton, D., Gemayel, R., Chen, Y., Surratt, J.D., George, C., Rairoux, P., Miffre, A., Riva, M.: Decrease in sulfate aerosol light backscattering by reactive uptake of isoprene epoxydiols. Phys. Chem. Chem. Phys. **23**, 5927–5935 (2021)
4. Tesche, M., Ansmann, A., Müller, D., Althausen, D., Engelmann, R., Freudenthaler, V., Groß, S.: Vertically resolved separation of dust and smoke over Cape Verde using multiwavelength Raman and polarization lidars during Saharan Mineral Dust Experiment 2008. J. Geophys. Res. **114** (2009)
5. Mishchenko, M.I., Travis, L., Lacis, A.: Scattering, Absorption, and Emission of Light by Small Particles. Cambridge University Press, Cambridge (2002)
6. Müller, D., Veselovskii, I., Kolgotin, A., Tesche, M., Ansmann, A., Dubovik, O.: Vertical profiles of pure dust and mixed smoke–dust plumes inferred from inversion of multiwavelength Raman/polarization lidar data and comparison to AERONET retrievals and in situ observations. Appl. Opt. **52**, 3178 (2013)
7. Mehri, T., Kemppinen, O., David, G., Lindqvist, H., Tyynelä, J., Nousiainen, T., Rairoux, P., Miffre, A.: Investigating the size, shape and surface roughness dependence of polarization lidars with light-scattering computations on real mineral dust particles: application to dust particles' external mixtures and dust mass concentration retrievals. Atmos. Res. **203**, 44–61 (2018)

8. Shang, X., et al.: Optical characterization of pure pollen types using a multi-wavelength Raman polarization lidar. Atmos. Chem. Phys. **20**, 15323–15339 (2020)
9. Miffre, A., Cholleton, D., Rairoux, P.: Investigating the size and refractive index dependence of the lidar PDR of pure dust with a laboratory polarimeter at 180.0° exact backscattering angle. Atmos. Meas. Tech. Submitted (2022)
10. Cholleton, D., Rairoux, P., Miffre, A.: Laboratory evaluation of the (355, 532) nm particle depolarization ratio of pure pollen at 180.0° lidar backscattering angle. Remote Sens. **14**(15), 3767 (2022)

Chapter 36
Fresh Biomass Burning Aerosol Observed in Potenza with Multiwavelength Raman Lidar and Sun Photometer

Benedetto De Rosa, Lucia Mona, Aldo Amodeo, Nikolaos Papagiannopoulos, Michail Mytilinaios, Donato Summa, and Igor Veselovskii

Abstract On 14 August 2021, the Lidar Raman MUSA and the CIMEL CE-318 sun photometer (operating at CIAO atmospheric observatory of CNR-IMAA in Potenza, Italy) observed an extremely fresh smoke plume. The forest fire started at 16:00 UTC, and the biomass burning plume, occurred at 1 km from CIAO, was transported over the CNR IMAA. The Lidar measurements have been carried out from 22:27 to 02:16 UTC. In the time interval from 22:27 to 23:19 UTC; measurements reveal a biomass burning layer below 2.7 km. The particle depolarization at 532 nm is 0.025, and Lidar ratios at 355 and 532 nm are, respectively, 40 and 38 sr. For all wavelengths, the mean value of Ångström exponent is 1.5. The value of surface concentration is 410 $\mu m^2 cm^{-3}$, the volume concentration is 21 μm^3 cm^{-3}, and the number density is 2300 cm^{-3}. The size distribution is bi-modal with a peak at 0.13 μm in the accumulation mode. The effective radius has a mean value of about 0.15 μm. Single-scattering albedo is approximately 0.96 at all wavelengths. Finally, the real part of the refractive index is 1.58, and the imaginary one is 0.006, indicating low absorption probably due to a negligible presence of black carbon. The measurements of the CIMEL 318 sun photometer at 05:34 UTC confirm the analysis of MUSA despite the lower concentration of the smoke plume at that time. The values of single scattering albedo at 440 nm are around 0.95, very similar to those observed with lidar.

Keywords Aerosol · Fresh biomass burning

B. De Rosa (✉) · L. Mona · A. Amodeo · N. Papagiannopoulos · M. Mytilinaios · D. Summa
Consiglio Nazionale delle Ricerche – Istituto di Metodologie per l'Analisi Ambientale CNR-IMAA, Potenza, Italy
e-mail: benedetto.derosa@imaa.cnr.it

I. Veselovskii
Physics Instrumentation Center of General Physics Institute, Moscow, Russia

© The Author(s), under exclusive license to Springer Nature Switzerland AG 2023

J. T. Sullivan et al. (eds.), *Proceedings of the 30th International Laser Radar Conference*, Springer Atmospheric Sciences,
https://doi.org/10.1007/978-3-031-37818-8_36

36.1 Introduction

In the summer of 2021, the dry and warm climate caused a high number of local fires. Regional climate and radiation are modified by biomass burning aerosols product by these fires. The Mediterranean basin is considered a wildfire hotspot, so in the coming years this scenario could get worse. Despite their importance, the literature of very fresh fire smokes (<24 h) is very poor.

Radiometers and satellite [1] are often used to characterize optical properties of smoke plumes. However, these techniques cannot characterize accurately the high variability of the vertical structure of smoke aerosol. Aircraft sampling could be used to investigate isolated layers. However aircraft regular measurements are too expensive. Lidar Raman systems with their high temporal and vertical resolutions have demonstrated, in the past decade, a strong capability to study fire smoke plumes [2, 3]. Important information about biomass burning parameters, such as particle depolarization, lidar ratio, and Ångström exponent, have been provided by lidar measurements performed within the European Aerosol Research Lidar Network (EARLINET, www.earlinet.org), which is part of ACTRIS infrastructure (www.actris.eu) [2, 4].

Generally, the small and spherical smoke particles are characterized by low depolarization, high Ångström exponents, and large lidar ratios values [2]. In particular, lidar ratio values for fresh smoke are generally lower compared to aged smoke [2]. Moreover, lidar measurements allow obtaining microphysical aerosol parameters through inversion algorithms [5].

The CIMEL CE-318 sun photometer has been used to improve the interpretation of the lidar results.

This chapter shows for the first time, to our knowledge, a characterization of vertical resolved optical and microphysical properties for a plume formed few minutes before the measurements. This provides the scientific community with a new insight for studying recurrent, distributed, and numerous forest fire events.

36.2 Instruments

Measurements reported in this paper have been collected at the CNR-IMAA Atmospheric Observatory (CIAO) [6]. CIAO is a key observatory for ACTRIS, the European Research Infrastructure for the aerosol, clouds, and trace gases investigation. CNR-IMAA is leading the node of the ACTRIS Data Center for the aerosol remote sensing (ARS) and is the Italian node the ACTRIS Center for the aerosol remote sensing (CARS). CIAO is also equipped with the instrumentation for being an ACTRIS National Facility for the aerosol remote sensing. In the frame of EARLINET (European Aerosol Research Lidar Network), the lidar MUSA of the CNR-IMAA is one of the reference lidar systems.

The lidar system is able to provide measurements of vertical profiles of aerosol extinction at 355 and 532 nm; aerosol backscatter at 355, 532, and 1064 nm; lidar ratio at 355 and 532 nm; particle and volume depolarization at 532 nm; and Ångström exponents at 355–532, 532–1064, and 355–1064 nm. These values are strictly related to the shape, size, and chemical composition of the aerosol [7].

The CIMEL CE-318 sun photometer is operational at CIAO in the frame of AERONET. The instrument provides measurements of aerosol columnar properties. It is a sun-and-sky radiometer, fully automatic that measures sky radiance and direct solar irradiance at different wavelengths. The products are columnar measurements of aerosol optical depth (AOD) at 340, 380, 440, 500, 675, 870, 1020, and 1640 nm, water vapor, single scattering albedo (SSA), size distribution, refractive index, absorption optical depth, extinction optical depth, and asymmetry factor.

The synergy of passive and active remote sensing techniques, such as Raman Lidar and sun photometer, provides the opportunity to improve the characterization of atmospheric aerosol.

36.3 Case of Study of 14 August 2021

On 14 August 2021, an oak forest of about 30 hectares at 1 km from the CIAO atmospheric observatory caught fire. The fire started at 16:00 UTC and went out at 23:00 UTC. The MUSA measurements started at 22:27 UTC, 6 h after the outbreak of the burning. The distance between MUSA and the fire was about 1 km. The quick look of the range-corrected lidar signal measured at 1064 nm (Fig. 36.1) shows the presence of a dense biomass burning layer at the beginning of the time series, when the fire was still active. After 23:30 UTC, the concentration decreases considerably. However, until the end of the lidar measurement, it was possible to observe a residual layer under 2 km. Indeed, in presence of local fires, the pyro-convection is not reached, and the fire plume remains confined inside the planetary boundary layer (PBL). Within the PBL region, the smoke remains mixed nearby the emission source. Furthermore, in the PBL region the lifetime of the plume is short due to dry and wet deposition. Indeed, after 00:52 UTC, the map shows an intense layer near the surface level.

36.3.1 Measurements

Figure 36.2 reports the vertical profiles of the particle backscatter coefficient (β); particle extinction coefficient (α); lidar ratio (LR); Ångström exponents (AEβ) at 355–532, 355–1064, and 532–1064 nm; particle linear depolarization ratio (PLDR); and volumelinear depolarization ratio (VLDP) at 532 nm obtained starting from lidar measurements averaged from the 22:37 to 23:19 UTC. Data have been

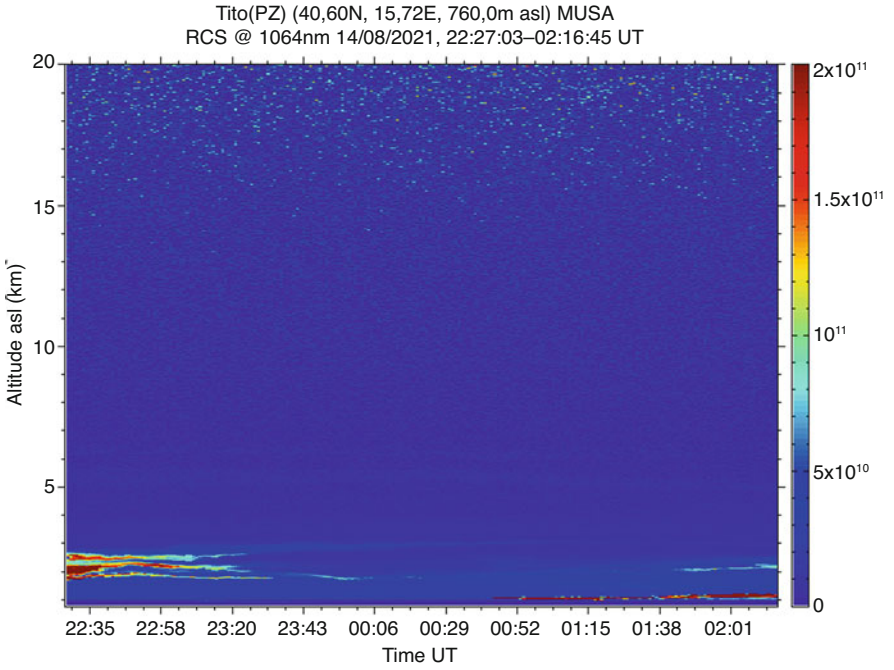


Fig. 36.1 Temporal evolution of the 1064-nm range-corrected lidar signal obtained with the MUSA lidar system on 14 August 2021 from 22:27 to 02:16 UTC

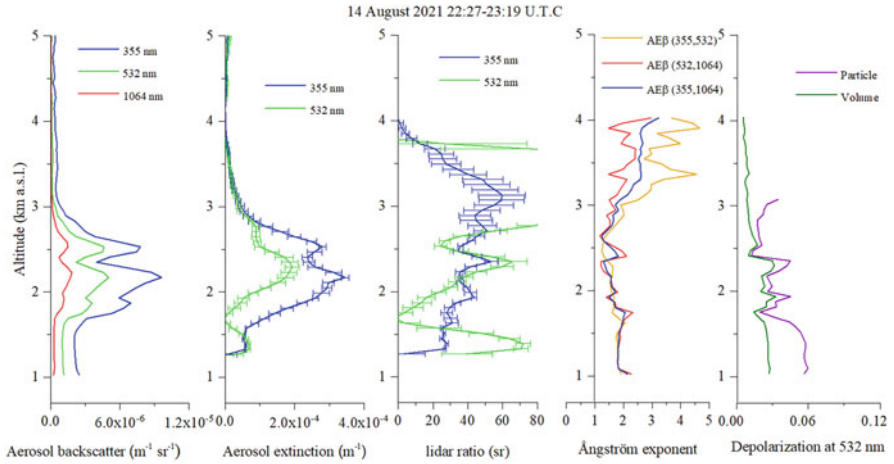


Fig. 36.2 Vertical profiles of optical parameters measured in Potenza on 14 August 2021 from 22:27 to 23:19 UTC, obtained with the multiwavelength Raman lidar MUSA

processed through the single calculus chain (SCC), the centralized processing tool developed within EARLINET/ACTRIS network [8].

β- and α-profiles show that in this time interval, the aerosol concentration is maximum, while low PLDR (less than 5%) and VLDP (less than 4%) indicate the presence of mostly spherical particles. The attenuation of the smoke layer is about 58% of the total; AOD at 532 nm obtained by the integration of the extinction coefficient over the biomass burning layer is 0.153, whereas the total AOD at the same wavelength is 0.261. The mean values of LR at 355 and 532 nm are, respectively, 40 and 38 sr and are indicative for low particle absorption. The values are similar to those found in previous studies for fires where the black carbon component is minimal [9]. The ratio of lidar ratio (RLR), that is, the ratio of LR 532 to LR 355, has values lower than 1. Values of RLR < 1 are indicative for fresh fire particles, while values of RLR > 1 are typical indicative for aged biomass burning aerosol [10]. The AEβ are approximately 1.5 at all wavelengths, indicative of small particles in the accumulation mode.

Aerosol microphysical properties have been retrieved through the lidar inversion method of Veselovskii et al. [5]. A time interval from 22:27 to 23:19 UTC and a range of altitude from 2170 to 2710 m, asl have been selected. In this layer, the smoke is particularly optically thick. The values of number concentration (N), surface concentration (S), and volume concentration (V) are 2300 cm^{-3}, 410 μm^2 cm^{-3}, and 21 μm^3 cm^{-3}, respectively. The mean effective radius in the smoke layer is 0.15 μm. Previous studies [9] report values between 0.12 μm (fresh smoke) and 0.21 μm (aged smoke). Recently, values from 0.19 to 0.44 μm have been measured for aged biomass burning aerosol layers [8], while for fresh smoke (1–3 days) [6], values from 0.13 to 0.15 μm have been obtained. However, none of the cases found in the literature reports young smokes like the ones observed in this study. The retrieved refractive index (m) is 1.58-i 0.006: the value of imaginary part of 0.006 and single scattering albedo (SSA) of 0.969 at 355 nm, 0.967 at 532 nm, and 0.953 at 1064 nm are indicative for low absorption aerosols and an almost lack of the black carbon component. As already mentioned, low black carbon values are often associated with smoldering undergrowth. Furthermore, the volume size distribution is bimodal; therefore the larger particles, even if present in lower concentrations, produce an increase in the overall scattering capability.

Sun photometer measurements started at 05:34 UTC, 3 h after the end of lidar measurements. The size distribution is bimodal, and it is clear how, following coagulation processes, the concentration of the fine fraction decreases. At 440 nm, SSA values are always around 0.95 and are similar to the values reported in literature for smoldering forest fires observed with sun photometer [10]. Moreover, as already observed in other studies of biomass burning [11], also here, single-scattering albedo decreases as the wavelength increases.

References

1. Kaufman, Y.J., Koren, I., Remer, L.A., Rosenfeld, D., Rudich, Y.: The effect of smoke, dust, and pollution aerosol on shallow cloud development over the Atlantic Ocean. PNAS. **102**(32), 11207–11212 (2015). https://doi.org/10.1073/pnas.0505191102
2. Amiridis, V., Balis, D.S., Giannakaki, E., Stohl, A., Kazadzis, S., Koukouli, M.E., Zanis, P.: Optical characteristics of biomass burning aerosols over Southeastern Europe determined from UV-Raman lidar measurements. Atmos. Chem. Phys. **9**, 2431–2440 (2009). https://doi.org/10.5194/acp-9-2431-2009
3. Veselovskii, I., Whiteman, D.N., Korenskiy, M., Suvorina, A., Kolgotin, A., Lyapustin, A., Wang, Y., Chin, M., Bian, H., Kucsera, T.L., Pérez-Ramírez, D., Holben, B.: Characterization of forest fire smoke event near Washington, DC in summer 2013 with multi-wavelength lidar. Atmos. Chem. Phys. **15**, 1647–1660 (2015). https://doi.org/10.5194/acp-15-1647-2015
4. Nicolae, D., Nemuc, A., Müller, D., Talianu, C., Vasilescu, J., Belegante, L., Kolgotin, A.: Characterization of fresh and aged biomass burning events using multiwavelength Raman lidar and mass spectrometry. J. Geophys. Res. **118**, 2956–2965 (2013). https://doi.org/10.1002/jgrd.50324
5. Veselovskii, I., Kolgotin, A., Griaznov, V., Müller, D., Wandinger, U., Whiteman, D.N.: Inversion with regularization for the retrieval of tropospheric aerosol parameters from multiwavelength lidar sounding. Appl. Opt. **41**, 3685–3699 (2002)
6. Madonna, F., Amato, F., Vande Hey, J., Pappalardo, G.: Ceilometer aerosol profiling versus Raman lidar in the frame of the INTERACT campaign of ACTRIS. Atmos. Meas. Tech. **8**(5), 2207–2223 (2015)
7. Müller, D., Ansmann, A., Mattis, I., Tesche, M., Wandinger, U., Althausen, D., Pisani, G.: Aerosol-type-dependent lidar ratios observed with Raman lidar. J. Geophys. Res.-Atmos. **112**, 2156–2202 (2007a)
8. D'Amico, G., Amodeo, A., Mattis, I., Freudenthaler, V., Pappalardo, G.: EARLINET Single Calculus Chain–technical–part 1: pre-processing of raw lidar data. Atmos. Meas. Tech. **9**(2), 491–507 (2016)
9. Reid, J.S., Hobbs, P.V.: Physical and optical properties of smoke from individual biomass fires in Brazil. J. Geophys. Res. **103**, 32013–32031 (1998). https://doi.org/10.1029/98JD00159
10. Eck, T.F., Holban, B.N., Reid, J.S., Sinyuk, A., Hyer, E.J., O'Neill, N.T., Shaw, G.E., Vande Castle, J.R., Chapin, F.S., Dubovik, O., Smirnov, A., Vermote, E., Schafer, J.S., Giles, D., Slutsker, I., Sorokine, M., Newcomb, W.W.: Optical properties of boreal region biomass burning aerosols in Central Alaska and seasonal variation of aerosol optical depth at an Arctic coastal site. J. Geophys. Res. **114**, D11201 (2009). https://doi.org/10.1029/2008JD010870
11. Reid, J.S., Eck, T.F., Christopher, S.A., Koppmann, R., Dubovik, O., Eleuterio, D.P., Holben, B.N., Reid, E.A., Zhang, J.: A review of biomass burning emissions: part III. Intensive optical properties of biomass burning particles. Atmos. Chem. Phys. **5**, 827–849 (2005). https://doi.org/10.5194/acp-5-827-2005

Chapter 37
Aerosol Studies with Spectrometric Fluorescence and Raman Lidar



Jens Reichardt, Felix Lauermann, and Oliver Behrendt

Abstract RAMSES (Raman lidar for atmospheric moisture sensing) is the operational spectrometric fluorescence and water Raman lidar of the German Meteorological Service at its Lindenberg site, Germany. With its three spectrometers covering the ultraviolet-A and visible wavelength range, it is optimally equipped to study the inelastic properties of aerosols. During its routine operation in 2020 and 2021, RAMSES collected a vast data set of atmospheric aerosol measurements covering distinct events such as wildfires, volcanic eruptions, Saharan dust outbreaks, and domestic biomass burning. In this contribution, results are presented for aerosols advected from Canadian and Russian wildfires. The associated fluorescence spectra exhibit a pronounced maximum in the visible light range and high fluorescence capacity. The center wavelength of the fluorescence maximum may shift, depending on a number of factors of which source region, atmospheric residence time, and trajectory history seem to be the most important. Correlation between aerosol elastic and inelastic optical properties can be high but is strongly case-dependent. To exploit the full information content of aerosol fluorescence, spectral measurements prove to be paramount, measurements with a discrete receiver channel are insufficient.

Keywords Spectrometric lidar · Aerosol fluorescence · Wildfires

37.1 Introduction

Aerosols are widely monitored with lidars, which are often sophisticated instruments such as multiwavelength Raman lidars. However, the focus of the obser-

J. Reichardt (✉) · F. Lauermann · O. Behrendt
Richard-Aßmann-Observatorium, Lindenberg, Germany
e-mail: jens.reichardt@dwd.de; felix.lauermann@dwd.de; oliver.behrendt@dwd.de

© The Author(s), under exclusive license to Springer Nature Switzerland AG 2023

J. T. Sullivan et al. (eds.), *Proceedings of the 30th International Laser Radar Conference*, Springer Atmospheric Sciences,
https://doi.org/10.1007/978-3-031-37818-8_37

vations is still mostly on the elastic optical properties of the aerosols although it has been demonstrated that measurements of their inelastic optical properties offer additional useful information [1]. Especially in the case of fluorescence, lidars that are equipped with spectrometers rather than only discrete detection channels allow investigations of aerosol type and cloud interaction never performed before [2, 3].

The spectrometric fluorescence and water Raman lidar RAMSES [4–6] is optimally equipped to study the inelastic properties of aerosols. During its routine operation in 2020 and 2021, RAMSES collected a vast spectrometric data set of aerosols originating from very different sources. This contribution can only provide a small insight into this treasure trove of data because of the complexity of the matter. First, it describes in broad detail certain aspects of the data analysis. Second, the efforts are outlined which are undertaken to determine the source regions of the aerosols measured with RAMSES. Finally, some measurement examples are presented. Here, emphasis is put on the aerosol-specific shape of the fluorescence spectrum and its relation to the elastic optical aerosol properties and the atmospheric environment. Interaction of aerosol and clouds is not discussed.

37.2 Instrument and Methods

RAMSES is equipped with three spectrometers, the water spectrometer predominantly used for measurements of water in all of its three phases but also ultraviolet-A (UVA) fluorescence [5, 6], an UVA-to-visible (VIS) spectrometer for water-vapor and fluorescence measurements [7] and a fluorescence spectrometer working in the visible light spectrum [3]. In this contribution, only data are presented that were obtained with the latter two instruments, hereinafter referred to as UVA and VIS spectrometer, respectively. The spectrum measurements are calibrated absolutely. In a first step, the detector channels of each spectrometer are calibrated relative to one another by means of calibrated light-emitting diodes (UVA spectrometer, 380–460 nm spectral range) or by cloud-free daylight measurements and radiative-transfer calculations (VIS spectrometer, 430–750 nm effective spectral range). Then the UVA spectrometer is absolutely calibrated using the water-vapor technique developed for the water spectrometer [5], and finally the VIS spectrometer as well by fitting the VIS fluorescence spectrum to the UVA fluorescence spectrum in the overlapping spectral range (430–460 nm).

Measurements of water content [6] and water-vapor mixing ratio are more affected by aerosol fluorescence the drier the atmosphere, the stronger the interfering fluorescence signal, and the wider the detector bandwidth. To account for this systematic error in the water-vapor measurements with the UVA spectrometer (detector bandwidth of ~2.6 nm around the Q branch of the gaseous water Raman spectrum), fluorescence backscatter coefficients to the left and right of the vapor Raman spectrum are averaged and subtracted from the contaminated Q branch Raman signal before further processing.

To study the origin of the air masses, we performed a trajectory analysis using the Hybrid Single-Particle Lagrangian Integrated Trajectory (HYSPLIT) model in ensemble mode. Additionally, we included fire data from the Moderate Resolution Imaging Spectroradiometer (MODIS) in the analysis, using NASA's Fire Information for Resource Management System (FIRMS), as well as daily global UV aerosol index data from the Suomi National Polar-Orbiting Partnership (NPP) Ozone Mapping and Profiling Suite (OMPS). The individual trajectories in the ensemble were compared to the location of active fires and the global propagation of aerosol layers to find the most probable source of the aerosol particles detected by RAMSES.

37.3 Measurement Examples

Figure 37.1 illustrates the RAMSES night measurement on 9–10 August 2021. Prominent features are the cirrus clouds and two biomass-burning aerosol (BBA) layers; the higher layer around 10.5 km (partly overlapping with the upper ranges of the clouds, thus suggesting aerosol-mediated particle formation) and the lower layer between 3.5 and 6.0 km. The wavelength of the maximum of the fluorescence spectrum increases with height. This is often observed for aerosols originating from wildfires, so it appears to be a common characteristic. Noticeable is the sudden increase in center wavelength around 4.5 km in the lower BBA layer, which hints at the existence of distinct aerosol filaments within the broader layer.

Figure 37.2 examines the relation between the elastic optical and the fluorescence properties of the lower BBA layer at 0 UTC 10 August 2021. According to the profiles, the layer splits over the mixing range between 4.5 and 5.0 km into a bottom filament and a top filament, having distinctly different characteristics each: While the bottom filament features higher particle backscatter coefficients, mean spectral backscatter coefficients and ratios of center-wavelength to 605-nm fluorescence backscatter coefficients, the top filament exhibits elevated particle depolarization and lidar ratios, a longer wavelength of the fluorescence maximum, and higher fluorescence capacities. Even though relative humidity (RH) is significantly higher in the bottom than in the top BBA filament (45–65% vs. 10–30%), it does not reach values high enough to expect notable water uptake by the aerosol particles from the gas phase. Within the filaments, there is also no indication that the BBA properties react to changes in RH, so it might be concluded that at least in this measurement case RH does not affect the elastic and inelastic optical aerosol properties. The detailed back-trajectory analyses suggest that the two filaments indeed have different source regions: While wildfires in Northern Canada are likely the source of BBA in the bottom filament, the particles in the top filament originated from fires in Siberia instead.

Finally, the fluorescence spectra are discussed for selected heights in Fig. 37.3. Different representations are shown to allow for competing interpretations of the spectrum dynamics. If normalized to the maximum of the fluorescence

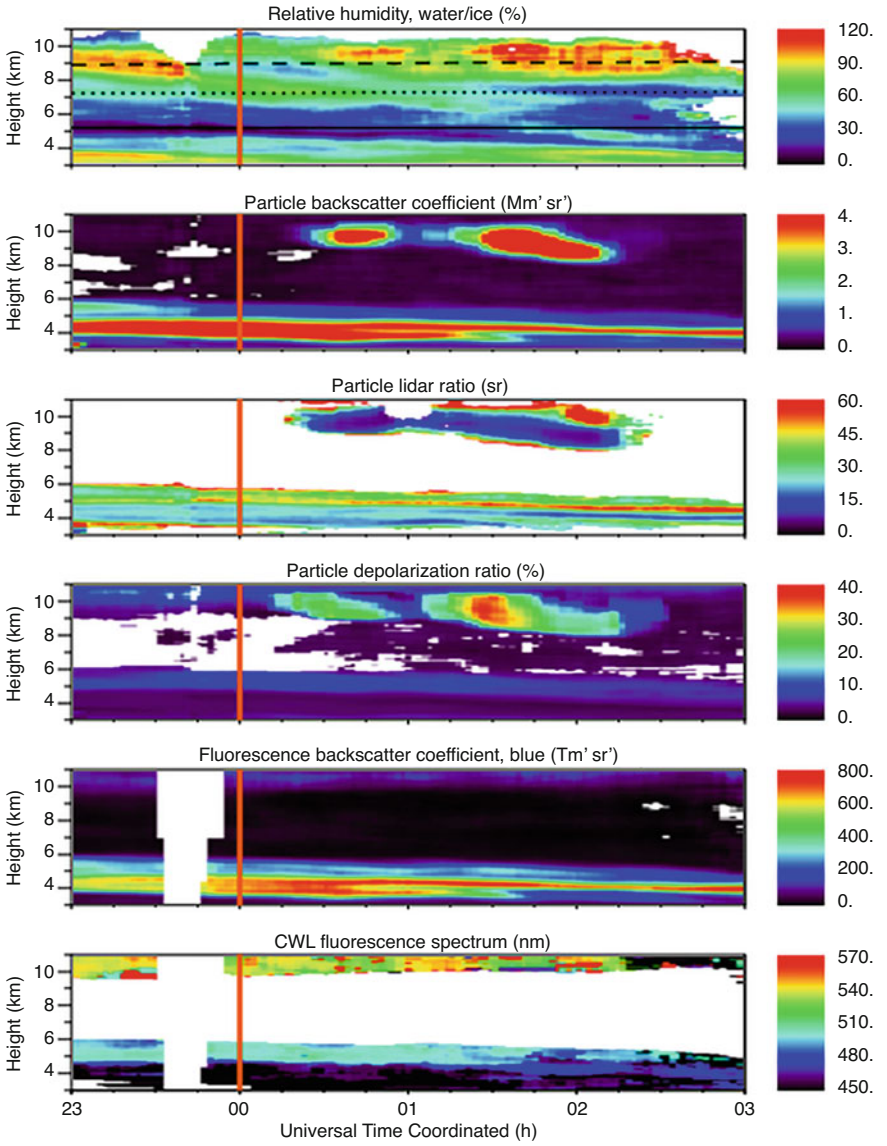


Fig. 37.1 Temporal evolution of (top to bottom) relative humidity (isotherms at −15 °C, −30 °C, and −45 °C indicated by black lines), particle backscatter coefficient, particle lidar ratio (not corrected for multiple scattering), particle depolarization ratio, fluorescence backscatter coefficient (spectrum integrated from 455 to 535 nm), and the wavelength of the maximum of the fluorescence spectrum as measured with RAMSES in the night of 9–10 Aug 2021. The measurement at 0 UTC (time marked by vertical orange line) is depicted in more detail in Figs. 37.2 and 37.3, respectively. For each profile, 1200 s of lidar data are integrated, the calculation step width is 120 s. The resolution of the raw data is 60 m; signal profiles are smoothed with a sliding-average length increasing with height

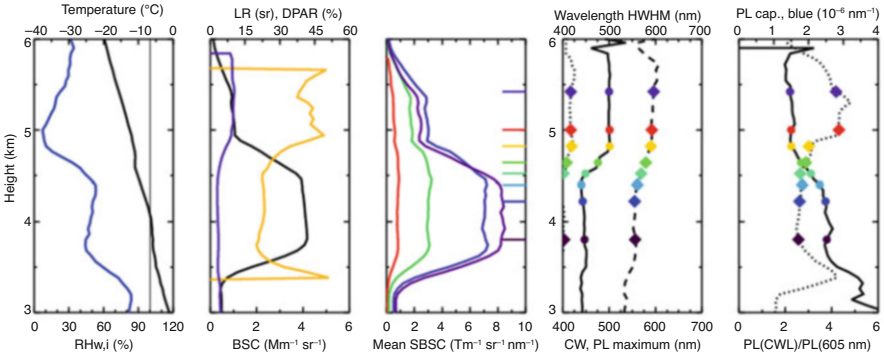


Fig. 37.2 Measurement of the lower BBA layer at 0 UTC 10 Aug 2021. (From left to right) Profiles of relative humidity with respect to water or ice (RHw, i (blue), saturation level indicated by vertical thin black line) and temperature (black); particle backscatter coefficient (BSC (black)), particle lidar ratio (LR (golden)), and particle depolarization ratio (DPAR (purple)); mean spectral fluorescence backscatter coefficients (SBSC) for the spectral bands ranging from 430 to 450 nm (purple), 455 to 535 nm (blue), 545 to 625 nm (green), and 630 to 710 nm (red); wavelength of the maximum of the fluorescence spectrum (CWL (solid)), and wavelength of the spectrum half width (HWHM) on the blue shoulder (dotted) and on the red shoulder (dashed); and ratio of CWL to 605-nm fluorescence backscatter coefficients (solid) and blue-band fluorescence capacity (PL cap. (dotted)). Colored symbols and horizontal lines indicate altitudes for which the fluorescence spectra are presented in Fig. 37.3

spectrum, one can clearly discern a shift of the whole spectra to longer wavelengths. Alternatively, if the spectra are normalized to the wavelength range between 560 and 660 nm (empirically it was found that this spectral region is relatively invariable if fluorescence intensity is taken into account), one observes a decay of the blue shoulder of the fluorescence spectrum. Independent of the representation chosen, however, fluorescence spectra in both filaments are independent of RH and temperature, which suggests that these state variables have no impact on fluorescence quantum yield and color center distribution in this case.

In summary, the RAMSES measurement on 9–10 August 2021 reveals a high correlation between elastic optical and fluorescence properties. As analysis of the RAMSES data set shows, this is rather the exception than the rule, because in most aerosol measurements the correlation is poor to nonexistent. So, elastic optical parameters cannot serve as proxies to infer the fluorescence properties and vice versa. Both are independent vectors that span the information space of aerosols, and spectral fluorescence measurements are needed to fully exploit its content.

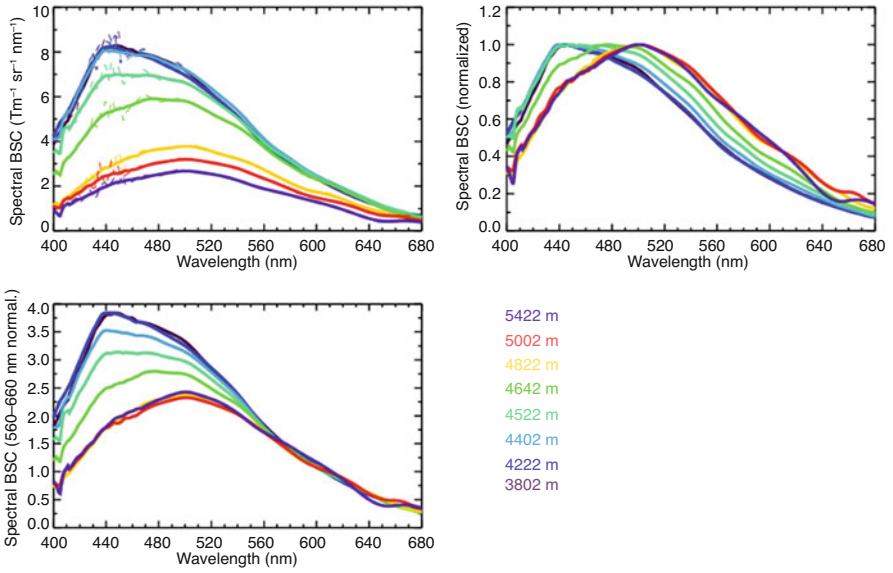


Fig. 37.3 Fluorescence spectra as measured at 0 UTC 10 Aug 2021. Different visualizations are chosen to highlight spectrum variability: As measured (top, left), normalized to the maximum of the fluorescence spectrum (top, right), and normalized to the wavelength range between 560 and 660 nm (bottom, left). Selected heights (color-coded) are indicated (see also Fig. 37.2). Data from the UVA spectrometer and the VIS spectrometer have been combined and smoothed with a sliding-average length of 5 spectrometer bins. The unsmoothed spectral measurements are shown for comparison (thin dashed curves; top, left)

Acknowledgments The authors acknowledge the NOAA Air Resources Laboratory (ARL) for the provision of the HYSPLIT transport and dispersion model and READY website (https://www.ready.noaa.gov), the Goddard Earth Sciences Data and Information Services Center for the provision of the OMPS-NPP data, and the use of fire data from NASA's FIRMS (https://earthdata.nasa.gov/firms), part of NASA's Earth Observing System Data and Information System (EOSDIS).

References

1. Müller, D., Mattis, I., Tatarov, B., Noh, Y.M., Shin, D.H., Shin, S.K., Lee, K.H., Kim, Y.J., Sugimoto, N.: Mineral quartz concentration measurements of mixed mineral dust/urban haze pollution plumes over Korea with multiwavelength aerosol Raman-quartz lidar. Geophys. Res. Lett. **37**, L20810 (2010)
2. Sugimoto, N., Huang, Z., Nishizawa, T., Matsui, I., Tatarov, B.: Fluorescence from atmospheric aerosols observed with a multi-channel lidar spectrometer. Opt. Express. **20**(19), 20800–20807 (2012)
3. Reichardt, J., Leinweber, R., Schwebe, A.: Fluorescing aerosols and clouds: Investigations of co-existence. EPJ Web Conf. **176**, 05010 (2018). https://doi.org/10.1051/epjconf/201817605010
4. Reichardt, J., Wandinger, U., Klein, V., Mattis, I., Hilber, B., Begbie, R.: RAMSES: German Meteorological Service autonomous Raman lidar for water vapor, temperature, aerosol, and cloud measurements. Appl. Opt. **51**(34), 8111–8131 (2012)
5. Reichardt, J.: Cloud and aerosol spectroscopy with Raman lidar. J. Atmos. Oceanic Technol. **31**(9), 1946–1963 (2014)

6. Reichardt, J., Knist, C., Kouremeti, N., Kitchin, W., Plakhotnik, T.: Accurate absolute measurements of liquid water content (LWC) and ice water content (IWC) of clouds and precipitation with spectrometric water Raman lidar. J. Atmos. Oceanic Technol. **39**(2), 163–180 (2022)
7. Reichardt, J., Stäudle, J., Begbie, R., Hilber, B., Stein, B., Kouremeti, N., Gröbner, J.: Spectral characterization of the new UV fluorescence spectrometer of RAMSES, the German Meteorological Service's Raman lidar for moisture sensing. In: Proceedings of the First European Lidar Conference, Thessaloniki, Greece, ELC (2018)

Chapter 38
Continuous Observations of Aerosol-Weather Relationship from a Horizontal Lidar to Simulate Monitoring of Radioactive Dust in Fukushima, Japan

Nofel Lagrosas, Kosuke Okubo, Xiafukaiti Alifu, and Tatsuo Shiina

Abstract Local transport of radioactive dust can put the environment and nearby people at risk. A plan to continuously monitor radioactive dust using synchronized measurements from horizontally pointing lidar and other instruments (e.g., weather monitor, dust sampler, particle counters) in uninhabited areas in Fukushima, Japan, is being considered. Data from continuous observations near a radioactive area can elucidate the effects of weather on the optical properties of aerosols. They can also provide information on how radioactive dust is transported when used in transport models. A pre-deployment continuous observations using a horizontal lidar and weather sensors were made on August and 21 December 2021. Results show that extinction coefficients are relatively higher (~4 $\times$ 10^{-3} m^{-1}) in August compared to the values observed in December (~2.5 $\times$ 10^{-3} m^{-1}). Diurnal effects on aerosol optical properties are highly observed in the depolarization ratio values. High depolarization ratios are observed during the daytime. A higher depolarization ratio (~0.12) is also measured in winter, and this can be attributed to changes in aerosol type due to changes in wind direction.

Keywords Horizontal lidar · Depolarization ratio · Near-ground aerosols · Aerosol-weather relationship · Aerosols

N. Lagrosas (✉) · K. Okubo · X. Alifu · T. Shiina
Chiba University, Chiba, Japan
e-mail: nofel@chiba-u.jp; kobo0404the25th@chiba-u.jp; xapkat_alip@chiba-u.jp; shiina@faculty.chiba-u.jp

© The Author(s), under exclusive license to Springer Nature Switzerland AG 2023

J. T. Sullivan et al. (eds.), *Proceedings of the 30th International Laser Radar Conference*, Springer Atmospheric Sciences,
https://doi.org/10.1007/978-3-031-37818-8_38

38.1 Introduction

Continuous exposure to radioactive aerosols can risk human health, especially when inhaled. Previous work has shown that inhaled radioactive aerosols under a dust concentration of 1×10^{-4} gm^{-3} have an effective dose received in 20 years of 5.6 μS [1]. The transport and effect of radioactivity from radioactive aerosols in the human body have been recently modeled [2]. The modeling results explain the impact of inhaled radioactive aerosols on human organs.

Radioactivity level in Fukushima, Japan, brought about as the combined result of the earthquake, tsunami, and nuclear accident in 2011, has decreased over the years [3]. However, continuous monitoring is needed to assess daily radioactivity level. Previously combined lidar and sampling measurements of radioactive dust have shown that aerosols with sizes less than 20 μm carry the most radioactivity (2×10^{-8} $Bqcm^{-3}$) even though this is lower than the safe limit of 10×10^{-5} $Bqcm^{-3}$ [4]. This information indicates that smaller aerosols, which are more likely to be inhaled, can risk human health under constant exposure.

Lidar can be used for detecting near-ground aerosols. Continuous measurement can explain the interaction between aerosol optical and local weather properties. In this work, a horizontal lidar with polarization measurements is continuously operated in August and December 2021 for pre-deployment assessment to check the lidar's performance and gather data used to compare with weather parameters. This work has the following objectives (1) to present the optical properties of aerosols obtained from the horizontal lidar measurements, (2) to quantify the relationship between near-ground aerosol optical and local weather parameters, and (3) to quantify the optical properties of near-ground aerosols obtained in summer (August) and winter (December) in Chiba, Japan.

38.2 Horizontal Lidar and Weather Instruments

The pre-deployment assessment of the horizontal lidar is on the nineth floor (68 m above sea level) of the engineering building at Chiba University (35.6278° N, 140.1031° E). The lidar is continuously operated from 12–31 August to 01–31 December 2021. The lidar is horizontally oriented in the west-northwest direction. The specification of the lidar system is shown in Table 38.1.

The horizontal lidar uses a diode-pumped solid-state (DPSS) laser with a 349-nm wavelength, pulse energy of 120 μJ (max), and is operated at 1 kHz. The transmitted beam has a P polarization, and the receiver receives both P and S polarization signals. The high-frequency specification of the laser permits the acquisition of data every 1 s. Thus, the horizontal lidar system can capture minute temporal changes in the optical properties of aerosols.

Table 38.1 Specifications of the horizontal lidar

Transmitter	
Laser model	Spectra-Physics Explorer One
Wavelength	349 nm
Pulse energy	120 μJ
Repetition frequency	1 kHz
Pulse duration	>3 ns
Transmitted polarization	P
Receiver	
Telescope diameter	10 cm
Interference filter (CWL)	349 nm
Interference filter (FWHM)	0.6 nm
PMT	Hamamatsu H11901-110
Received polarization	P and S
Maximum range	700 m

A weather monitor (Davis Vantage Pro 2) is placed in the same location as the horizontal lidar. The weather monitor gathers local weather parameters (temperature, relative humidity (RH), wind speed, wind direction, etc.) and records these parameters every 5 min.

38.3 Methodology

The data obtained from the continuous operation of the horizontal lidar is processed for extinction coefficient and depolarization ratio. The extinction coefficient in the horizontal distance between 100 and 300 m is calculated using the slope method [5]. The extinction coefficient shown in the results comes from a linear fit that has a high correlation coefficient ($r^2 > 0.9$).

The depolarization ratio (δ) is calculated as the ratio of the S and P signals, i.e.,

$$\delta = k\frac{S}{P} \tag{38.1}$$

where k is the depolarization calibration constant used to calibrate the S and P signals [6]. In this work, the calibration constant is obtained by carefully rotating the PMTs for the P and S signals so that each PMT is measuring signals at 0° and 90°. The signals are then compared, and the depolarization calibration constant is calculated.

A 5-min averaging is applied to the extinction coefficient and depolarization ratio so that these optical parameters can be compared to the weather parameters obtained every 5 min.

38.4 Results and Discussion

The horizontal path of the lidar implies that the laser encounters roughly the same air density along its path as compared with a slant or vertically pointing lidar. This design generates a high extinction coefficient. When observations are done near the ground, a high depolarization ratio is also expected, and this can be attributed to the dust from the ground. Continuous operation of the horizontal lidar has shown different distributions of extinction coefficients obtained in August and December 2021 (Fig. 38.1a). Extinction coefficients in December show lower values than those in August. The peaks of the extinction coefficient distribution in August and December are 0.0042 m^{-1} and 0.0025 m^{-1}, respectively. This result suggests that, near the ground, different aerosols are dominant each month, producing this distinguishable difference. In Chiba, the prevailing wind direction during the summer months is from the south and southwest, Tokyo Bay's location, which can bring in marine-type aerosols and humid air [7]. In winter, the dominant wind direction is from the north. The winter wind carries more land-based aerosols that are chemically different from summer. The wind from Tokyo Bay has more moisture, which can condense on the surface of aerosols changing the morphology close to a spherical shape [8, 9]. August's depolarization ratio (Fig. 38.1b) shows two distributions with peaks at 0.06 and 0.14. The lower (left side) and higher (right side) depolarization ratios occur at nighttime and daytime, respectively, which can be attributed to the diurnal effect of RH (described in the next section) on the aerosols. In December, the depolarization ratios show one distribution peaking at 0.13 (Fig. 38.1b) because of the low RH condition.

38.4.1 Relationship of Extinction Coefficient and Depolarization Ratio with Weather Data

Mean aerosol extinction coefficients observed in August tend to increase less with wind speed than in December observations. The standard variation of the

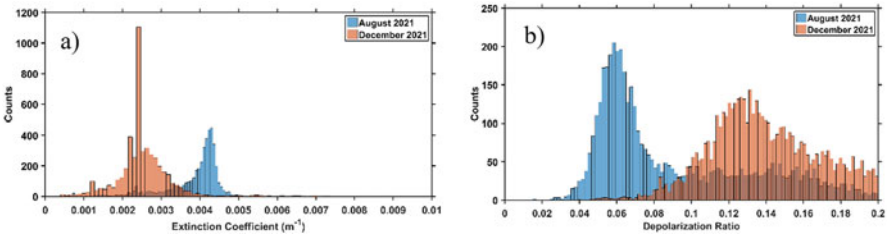


Fig. 38.1 August (blue) and December (orange) 2021 histogram of the (**a**) extinction coefficient and (**b**) depolarization ratio of near-ground aerosols

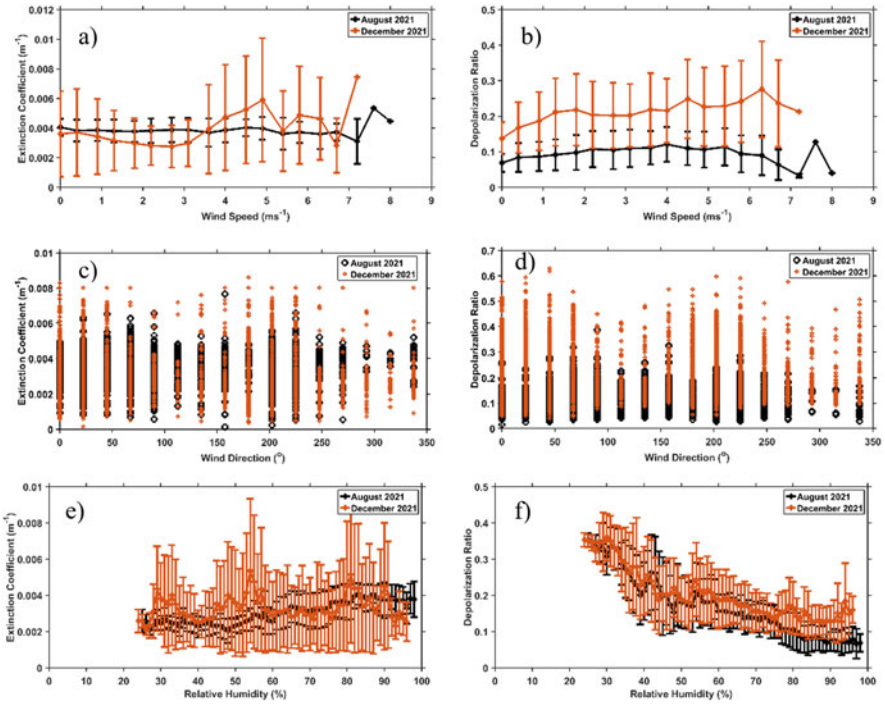


Fig. 38.2 Relationship between (**a**) extinction coefficient and wind speed, (**b**) depolarization ratio and wind speed, (**c**) extinction coefficient and wind direction, (**d**) depolarization ratio with wind direction, (**e**) extinction coefficient with RH, and (**f**) depolarization with RH during August and December 2021 observations

extinction coefficients is also lower in August (Fig. 38.2a). This result implies that when observations are made in Fukushima, the land-based aerosols indicate more radioactive aerosols in the air as wind speed increases. When compared with wind speed, depolarization ratio observations corroborate these results. In December, the mean depolarization ratios are generally higher than in August (Fig. 38.2b). This result indicates that the dry air in December can bring in dry and nonspherical aerosols as the wind speed increases. This result also implies that when continuous observations are implemented in Fukushima, an increased number of radioactive aerosols can be detected when the wind is dominantly from the land, the source of radioactive aerosols. However, in the case of August, a decrease in the mean depolarization ratio is observed as wind speed increases. This result implies that strong winds drive more spherical aerosols in August due to the condensation of water vapor on the surface of aerosols. Under such conditions, in Fukushima, coated radioactive aerosols can show a low depolarization ratio when the dominant wind direction is from the sea.

The measured extinction coefficients and depolarization ratio vary with each wind direction (Fig. 38.2c, d). From the observations in Chiba, the variation of

extinction coefficients and depolarization ratio is smaller when the wind is coming from the northwest direction. The variations of extinction coefficients with wind speed are relatively comparable in both months. However, the variation of the depolarization ratios is higher in December, indicating different aerosol types in both months.

The mean extinction coefficients and depolarization ratios show increasing and decreasing behaviors with RH (Fig. 38.2e, f). The response of the extinction coefficients with RH does not show a sharp increase as RH approaches 100% (Fig. 38.2e). The extinction coefficients observed in December are highly variable with RH, indicating that the detected aerosols are optically different from those observed in August due to a different dominant wind direction.

The mean depolarization ratios of the aerosols observed in both months show a decreasing trend with RH (Fig. 38.2f). The decrease in the mean depolarization ratio in August and December is relatively the same from RH = 20% to 60%. The difference in the trend is evident when RH > 60%. The average depolarization ratio in December shows a slightly higher value by 0.02–0.1 compared to August. Most studies have shown that deliquescence of aerosols occurs when RH > 50% [8]. These observations in Chiba indicate that the aerosols observed in August are mainly marine-type since the winds are coming from Tokyo Bay. A similar situation can be inferred when observations are done in Fukushima.

38.5 Conclusion

A horizontal lidar is continuously operated in Chiba to observe near-ground aerosols as a pre-deployment observation before observations of radioactive aerosols are implemented in Fukushima. The results obtained in August and December 2021 provide insights into the relationships between the optical properties of aerosols and local weather parameters that can be applied to future observations in Fukushima. The observations in December show a higher variation of extinction coefficient and depolarization with wind speed, wind direction, and RH trends than the August measurements. This study suggests that the relationship between aerosols and local weather can be further quantified when extended continuous operations are carried out.

References

1. Hanfi, M., Yarmoshenko, I., Zhukovsky, M.: Assessment of radiation dose from inhalation of outdoor dust containing natural radionuclides. Radiat. Prot. Dosimetry. **196**(3–4), 184–189 (2021)
2. Talaat, K., Xi, J., Baldez, P.: Hecht, A: Radiation dosimetry of inhaled radioactive aerosols: CFPD and MCNP transport simulations of radionuclides in the lung. Sci. Rep. **9**, 17450 (2019)

3. Fukushima Prefecture Radioactivity Measurement Map Homepage., http://fukushima-radioactivity.jp/pc/. Last accessed 2022/04/08
4. Shiina, T. Peng, Z., Okada, T., Sugita, Y., Yokozawa, T., Shinozaki, T.: Distribution estimation of radioactivity concentration by compact polarization lidar in Fukushima. In: Proceedings of SPIE 10791, Lidar Technologies, and Measurements for Atmospheric Remote Sensing XIV, Berlin, Germany, 107910C (2018)
5. Kunz, G., Leeuw, G.: Inversion of lidar signal with slope method. Appl. Opt. **32**, 3249–3256 (1993)
6. Xu, X., Xie, J., Li, Y., Miao, S., Fan, S.: Measurement report: Vehicle-based multi-lidar observational study of the effect of meteorological elements on the three-dimensional distribution of particles in the western Guangdong-Hong Kong-Macao Greater Bay area. Atmos. Chem. Phys. **22**, 139–153 (2022)
7. Fukagawa, S., Kuze, H., Bagtasa, G., Naito, S., Yabuki, M., Takamura, T., Takeuchi, N.: Characterization of seasonal variation of tropospheric aerosols in Chiba, Japan. Atmos. Environ. **40**(12), 2160–2168 (2006)
8. Tang, M., Chan, C., Li, Y., Su, H., Ma, Q., Wu, Z., Zhang, G., Wnag, Z., Ge, M., Hu, M., He, H., Wang, X.: A review of experimental techniques for aerosol hygroscopicity studies. Atmos. Chem. Phys. **19**, 12631–12686 (2019)
9. Lagrosas, N., Bagtasa, G., Manago, N., Hiroaki, K.: Influence of ambient relative humidity on seasonal trends of scattering enhancement factor for aerosols in Chiba, Japan. Aerosol Air. Qual. Res. **19**, 1856–1871 (2019)

Chapter 39
Statistical Simulation of Laser Pulse Propagation Through Cirrus-Cloudy Atmosphere

T. V. Russkova, V. A. Shishko, and A. V. Konoshonkin

Abstract The work proposes the original algorithm of the Monte Carlo method for simulating the propagation of laser pulses in the atmosphere taking into account high order scattering. The results of studying the features of pulse transfer and the formation of echo signals during remote sensing of a cloudy atmosphere are discussed. As clouds, cirrus cloudiness represented by a continuous homogeneous layer is considered. The capabilities of the original software developed for modeling lidar echo signals are briefly described.

Keywords Laser pulses · Cirrus clouds · Monte Carlo method

39.1 Introduction

39.1.1 The Current State of Problem-Solving

Light detection and ranging (LiDaR) systems have existed in the atmospheric science community for over 50 years. A variety of lidar technologies have been developed to provide atmospheric and surface properties during this period to support advancements in digital models of terrain, cryospheric discovery, hydrology, atmospheric science, and oceanography [1, 2]. Aerosol-cloud interaction is one of the primary sources of uncertainties in future climate predictions. Both single-lidar and multi-lidar measurements are needed under different aerosol and cloud conditions over multiple locations. For cloud studies, multiple scattering is still a challenging issue. Multiple scattering contains cloud microphysical and optical information and its further exploring together with lidar depolarization measurements could increase lidar capabilities to observe optically thick clouds.

T. V. Russkova (✉) · V. A. Shishko · A. V. Konoshonkin
V.E. Zuev Institute of Atmospheric Optics, Tomsk, Russian Federation
e-mail: btv@iao.ru

© The Author(s), under exclusive license to Springer Nature Switzerland AG 2023

J. T. Sullivan et al. (eds.), *Proceedings of the 30th International Laser Radar Conference*, Springer Atmospheric Sciences,
https://doi.org/10.1007/978-3-031-37818-8_39

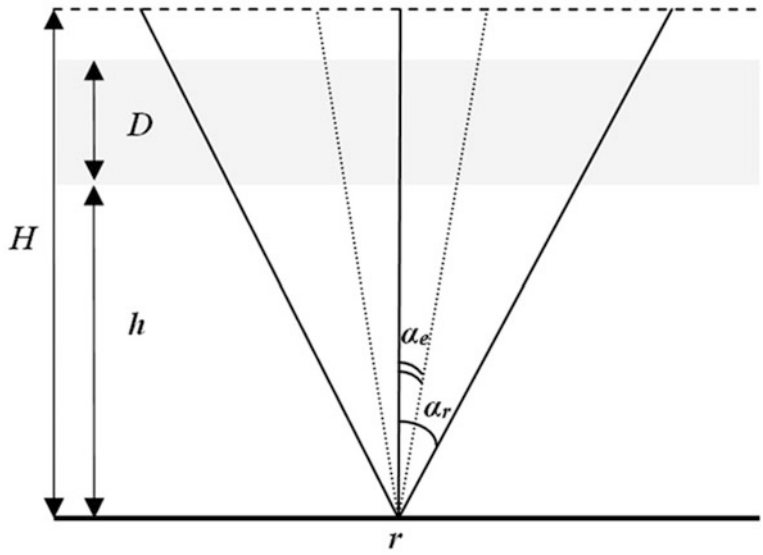


Fig. 39.1 The lidar setup and model atmosphere geometry

One of the most attractive capabilities of the laser sounding is its ability to continuously detect cloud properties. Multiple scattering effects play a large role in the sampling of optically thick clouds such as cumulus but are, in some ways, just as important when examining cirrus clouds of various optical depths.

The purpose of this research is to (a) describe a Monte Carlo model used for simulating echo signals, (b) investigate features unique to considered lidar system such as multiple scattering effects, and (c) provide generalized model returns from cirrus clouds.

39.1.2 Statement of the Problem

Assume that the following information is specified (Fig. 39.1). An optically isotropic scattering aerosol-molecular media is concentrated in a horizontal plane-parallel H-height layer. A low boundary of cloud is located at a height of h, and the cloud layer has a depth of D. The optical properties of aerosols, molecules, and cloud are described by an extinction coefficient σ, a single scattering albedo q, and a scattering phase function $g(\mu)$, where μ is the cosine between directions of the beam of light before and after scattering.

The emitter of the lidar is placed at the point $r = (0,0,0)$. The beam of light propagates from the emitter in the direction $\tilde{r} - r$, where $\tilde{r}$ is a point on the emitter semi-axis. Its energy is uniformly distributed with respect to the solid angle of the

emitter field of view with a given semi-aperture α_e. A laser pulse begins at the point $t = 0$ in time.

The receiver of the lidar with a semi-aperture α_r and emitter are collocated at the point r. The receiver is a circle perpendicular with radius R_r, its sensitivity being independent of the direction of the incoming light.

The objective is to compute the time dependence of a signal detected by the lidar receiver, or densities of the lidar return signal with respect to the time scale and with respect to the "photon path length" (which is equal to the time multiplied by the velocity of light).

39.2 The Monte Carlo Model

39.2.1 General Description

Monte Carlo modeling is used extensively in various scientific fields, including solar radiative transfer. It is an effective statistical approach to radiative transfer problems and has been used to model electromagnetic energy's interaction with the atmosphere. The approach is based on the probability of specific events occurring whose outcomes are represented by probability density functions.

A numerical algorithm was developed based on a single local estimator and Monte Carlo simulation of photon trajectories to compute multiple scattered monostatic lidar return signals. The trajectories of photons were simulated according to a well-known scheme [3].

Once a photon leaves the transmitter, a scattering site along the photon path must be selected. The length of each photon path segment within the cloud is randomly drawn from an exponential distribution such that the probability of the segment length l ($l > 0$) is

$$p(l) = \sigma\,(r(l)) \cdot e^{-\tau(l)}, \tag{39.1}$$

where τ is the total optical depth along the photon path to each scattering event. At the end of each path segment, the photon is scattered in a random direction, with a probability density function determined by $g(\mu)$. To make the model computationally more efficient, a weighting scheme is introduced. Photon trajectories are followed until they have traveled to a distance beyond the angular field of the receiver. The complexity of the problem is that the probability of a photon hitting the receiver is extremely small. Therefore, Monte Carlo simulation is a time-consuming process, and the estimate of the return signal is noisy in some cases. A special technique of dependent splitting of trajectories with respect to the first scattering was implemented to calculate the echo signal [3].

The signal is accumulated in time bins according to the total time of flight of the detected photons. The sum over all scattering events for all transmitted photons

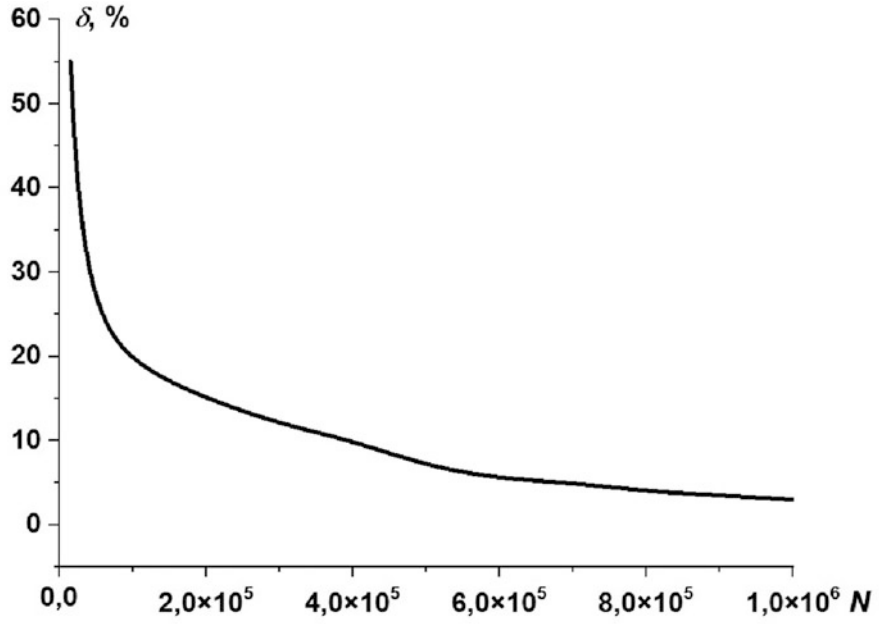


Fig. 39.2 Relative error as a function of number of photons per set for 1-km-thick homogeneous cirrus cloud composed of hexagonal crystals located 8 km above the lidar

represents the lidar signal. The results of computations are temporal return signals of the lidar (total and for different scattering orders). The square root of the variance is estimated for the total return signal.

39.2.2 Statistical Convergence

Simulation output was tested to ensure statistical convergence. Results were obtained by modeling a homogeneous 1-km-thick cirrus cloud composed of randomly oriented hexagonal ice crystals with an extinction coefficient of 0.4 km^{-1} located 8 km above the lidar at the wavelength of 0.532 μm in a standard atmosphere [4]. Figure 39.2 shows the relative errors δ, %, as a function of number of photons N per set.

These errors increase as the number of Rayleigh, aerosol, and cloud scatterers. It should be noted that the processing of significant number of photons is a time-consuming operation, but it is required in order to reduce the standard errors to statistically acceptable level.

39.3 Results

39.3.1 Effects of Multiple Scattering

A number of studies have been carried out to examine the effects of multiple scattering on the return signal. It was shown that the contribution from higher orders of scattering was highly dependent on receiver field of view [5]. D. Winker and L. Poole [6] estimated multiple scattering effects for both ground-based and space-borne lidars. They concluded that multiple scattering plays a much greater role for space-borne than for ground-based lidars, due mainly to the larger diameter of the receiver footprint on a cloud for the space-based systems.

The described model was used to investigate the importance of multiple scattering in the monostatic lidar. Model input variables included a pulse wavelength of 0.532 μm, cloud single scattering albedo of unity, and cloud optical depth (COD) of 0.5. Cirrus cloud properties are taken from B. Baum, P. Yang P. et al. [7]: the scattering phase function is calculated for randomly oriented hexagonal ice crystals with a moderate surface roughness. A vertically pointing lidar is assumed. The receiver fields of view set to 0.1, 1, and 10 mrad.

Figure 39.3 show results of model runs using different semi-apertures of receiver. The curves in the figure represent the ratio γ of return from multiple to single scattering.

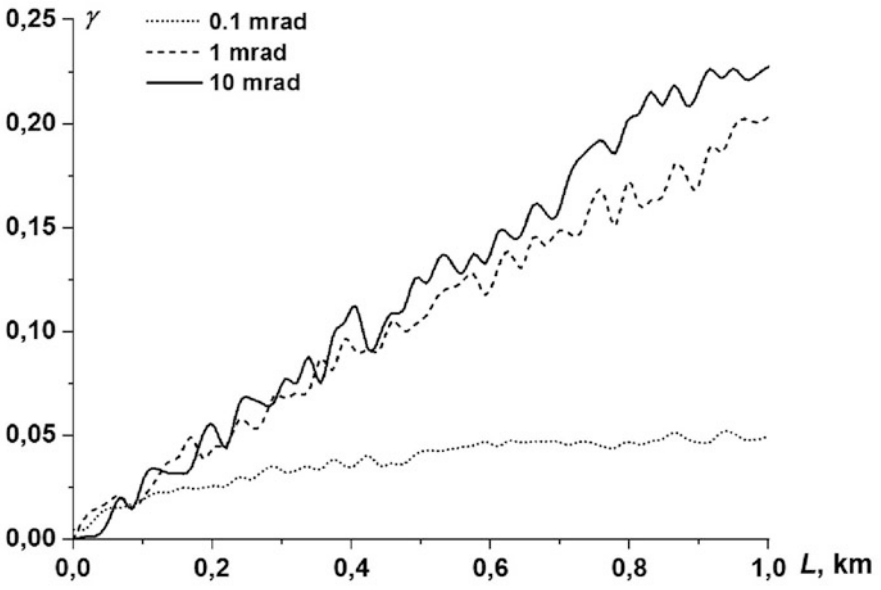


Fig. 39.3 Ratio of multiple to single scattering contribution for lidar return in cirrus-cloudy atmosphere, calculated for different values of semi-aperture of the receiver, and plotted vs. penetration depth L, km

As seen from the figure, the impact of multiple scattering increases farther into the depth of the cloud, but for semi-aperture equal to 0.1 mrad, the contribution of multiple scattering to lidar return remains comparatively small: higher-orders contribute about 5% of the total signal. The situation is changing after increasing the field of view of receiver. For semi-apertures equal to 1 and 10 mrad, the sum of the orders greater than one contributes as much as 20% and 23% of the total return to the receiver correspondingly.

39.3.2 Echo Signal in Cirrus-Cloudy Atmosphere

Using the developed model, simulations of lidar return from cirrus clouds in the atmosphere were conducted. These numerical experiments are presented to demonstrate the algorithm's ability to detect optically thin cirrus clouds. The input parameters are the same as in previous tests, but the calculations were carried out for different values of COD – 0.5 and 1.

Figure 39.4 shows a comparison of the smoothed return fluxes F (arb. units) from a cloudless atmosphere and model clouds placed in a standard background atmosphere.

In the sub-cloud region, returns are nearly identical, while in the cloud layer, there is a difference between echo signals from "clear" and cloudy atmospheres. Above the cloud, returns from background atmosphere with the cloud present are less than those from a cloudless atmosphere. This difference is the result of an increased extinction by scattering in the cloud: both the lidar pulse incident upon and the backscattered energy from the above-cloud layer suffer extinction by the cloud. It should be noted, that the difference of returns in the cloud layer is proportional to the volume extinction coefficient and the optical depth of the cloud as a consequence.

39.4 Conclusion

The proposed algorithm for simulation of the propagation of laser pulses in the atmosphere taking into account high order scattering demonstrates acceptable performance. Using the developed algorithm, the simulations of echo signal transfer for a vertically pointing lidar were performed. The ratio of multiple to single scattering contribution for lidar return in cirrus-cloudy atmosphere, calculated for different values of semi-aperture of the receiver, was obtained.

It was shown that the impact of multiple scattering increases the farther into the depth of the cloud, but for small values of semi-aperture, the contribution of multiple scattering to lidar return remains comparatively low. The situation is changing after increasing the field of view of receiver. For semi-apertures equal to 1 and 10 mrad, the sum of the orders greater than one contributes as much as 20% and 23% of the

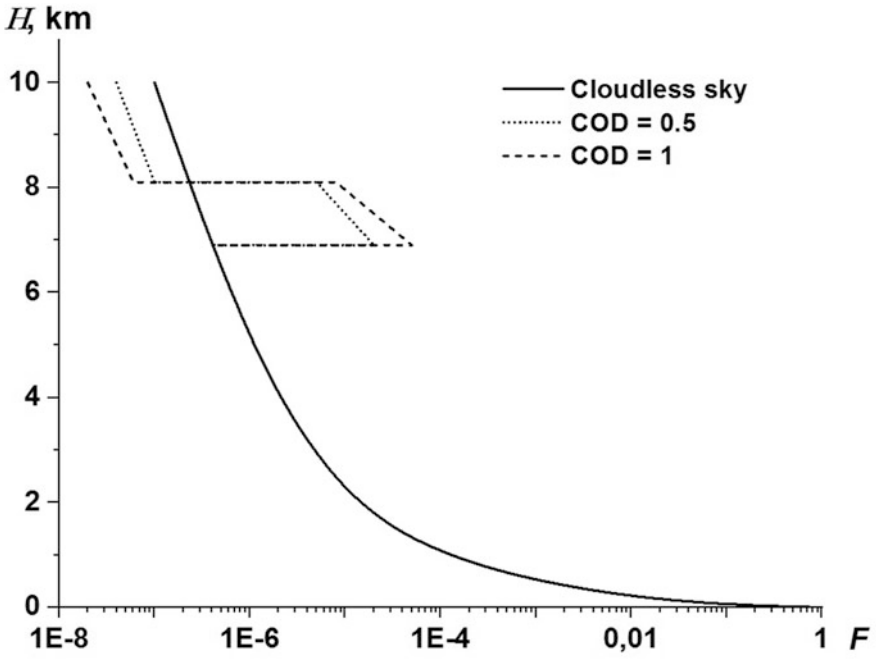


Fig. 39.4 Smoothed return signal for cloudless atmosphere and in the presence of a homogeneous cirrus cloud with optical depth 0.5 and 1

total return to the receiver correspondingly. The difference of returns in the cloud layer is proportional to the volume extinction coefficient and the optical depth of the cloud as a consequence.

The obtained results are in good agreement with the data, presented in the literature. The next step for improving the algorithm will be to take into account the polarization of emitted laser energy.

This work is supported by the Russian Science Foundation under grant No. 22-27-00719, https://rscf.ru/project/22-27-00719/.

References

1. Weitkamp, C.: Lidar: Range-Resolved Optical Remote Sensing of the Atmosphere. Springer Series in Optical Sciences 102 (2005)
2. Kashani, A., Olsen, M., Parrish, C., Wilson, N.: A review of lidar radiometric processing: from AD HOC intensity correction to rigorous radiometric calibration. Sensors. **15**, 28099 (2015)
3. Marchuk, G.I., Mikhailov, G.A., Nazaraliev, M.A.: Monte Carlo Methods in Atmospheric Optics. Springer Series in Optical Sciences 12 (1980)
4. Elterman L.: UV, visible and IR attenuation for altitudes to 50 km. Technical report AFGL-68-0153

5. Bruscaglioni, P., Ismaelli, A., Zaccanti, G.: Monte-Carlo calculations of lidar returns: procedures and results. Appl. Phys. B. **60**, 325–329 (1995)
6. Winker, D.M., Poole, L.R.: Monte-Carlo calculations of cloud returns for ground-based and space-based Lidars. Appl. Phys. B. **60**, 341–344 (1995)
7. Baum, B.A., Heymsfield, A.J., Yang, P., Bedka, S.T.: Bulk scattering models for the remote sensing of ice clouds. Part 1: microphysical data and models. J. Appl. Meteor. **44**(12), 1885–1895 (2005)

Chapter 40
Aerosol Spatial Distribution Observed by a Mobile Vehicle Lidar with Optics for Near-Range Detection



Masanori Yabuki, Kazuhiko Miura, Tatsuhiro Mori, Hiroshi Hayami, and Hiroaki Kuze

Abstract We describe a mobile vehicle lidar that enables near-range observations to achieve continuous monitoring of atmospheric aerosols with high spatiotemporal resolutions. The lidar employed a short-pulse laser of 355-nm wavelength. After passing the beam expander, the outgoing laser energy satisfied the eye-safety requirements, and the laser suspended the emission when detecting an overpass structure in the vehicle's travel direction. The near-range observation was implemented by slanting a part of the receiving optical axis by placing several wedge prisms in front of the receiver telescope. Normally, lidar observations were made in the vertical direction while driving the vehicle at speeds slower than 50 km/h. Two additional mirrors installed above the car's sunroof changed the directions of the laser beam and telescope field-of-view to achieve horizontal observation, if necessary. We demonstrated the capability of the proposed lidar system in detecting

M. Yabuki (✉)
Research Institute for Sustainable Humanosphere, Kyoto University, Kyoto, Japan
e-mail: yabuki@rish.kyoto-u.ac.jp

K. Miura
Department of Physics, Faculty of Science, Tokyo University of Science, Shinjuku-ku, Tokyo, Japan
e-mail: miura@rs.tus.ac.jp

Laboratory for Environmental Research at Mount Fuji, Shinjuku-ku, Tokyo, Japan

T. Mori
Department of Applied Chemistry, Faculty of Science and Technology, Keio University, Yokohama, Kanagawa, Japan
e-mail: tatsuhiro.mori@keio.jp

H. Hayami
Global Center for Science and Engineering, Waseda University, Shinjuku-ku, Tokyo, Japan
e-mail: hhayami@aoni.waseda.jp

H. Kuze
Center for Environmental Remote Sensing, Chiba University, Chiba, Japan
e-mail: hkuze@faculty.chiba-u.jp

© The Author(s), under exclusive license to Springer Nature Switzerland AG 2023

J. T. Sullivan et al. (eds.), *Proceedings of the 30th International Laser Radar Conference*, Springer Atmospheric Sciences,
https://doi.org/10.1007/978-3-031-37818-8_40

near-surface aerosol along a travel path of 25 km in the Tokyo Bay area, with an altitude range coverage between 7 and 650 m. Higher boundary layer heights with more significant aerosol loading were found in inland areas than over the coastal streets. Also, we observed aerosols over a rice paddy field of 600 m × 600 m by employing the horizontal observation mode.

Keywords Mobile vehicle lidar · Aerosol spatial distribution · Laser safety

40.1 Introduction

Monitoring the local behavior of atmospheric constituents in urban areas is indispensable for assessing and understanding changes in air quality. Atmospheric pollutants along streets with high-rise buildings exhibit inhomogeneous spatial distributions. In agriculture and forestry, horizontal and high-range-resolution studies of aerosol distributions are desirable for monitoring bioaerosols such as pollens. A vehicle for on-road mobile measurements provides a platform suitable for ground-based, in situ remote sensing. An on-road mobile lidar was applied to vertical PM10 distribution observations around Paris [1]. Similar profiling of aerosol optical properties, including the extinction-to-backscatter ratio and depolarization ratio, was conducted from Paris to Siberia [2]. Popovici et al. [3, 4] developed a compact mobile aerosol monitoring system (MAMS) equipped with a micropulse lidar, a sun photometer, and in situ instruments such as an aerosol spectrometer for mapping aerosol properties at a fine spatial scale: they demonstrated the system's capability in northern France and the North China Plain. These previous studies focused mainly on aerosol properties within and above the atmospheric boundary layer.

Knowledge of localized air quality within street canyons is important in urban areas with high-rise buildings that alter wind and pollutant transport. Detailed numerical simulations of air pollutants considering complex city block structures have been reported [5]. The purpose of the present study is to construct and demonstrate a mobile lidar for profiling optical properties of near-surface aerosols along the street canyon while maintaining the safety condition of the laser beam. The system is also applied to investigating horizontal distributions of bioaerosols over a rice paddy field with a high range resolution.

40.2 Methodology

40.2.1 System Setup of a Mobile Vehicle Lidar

Figure 40.1 shows the schematic diagram of the mobile vehicle lidar in a car with a sunroof. We employed the third harmonic output (355 nm) of an Nd:YAG laser with 42-μJ pulse energy at a repetition frequency of 1 kHz and a pulse width

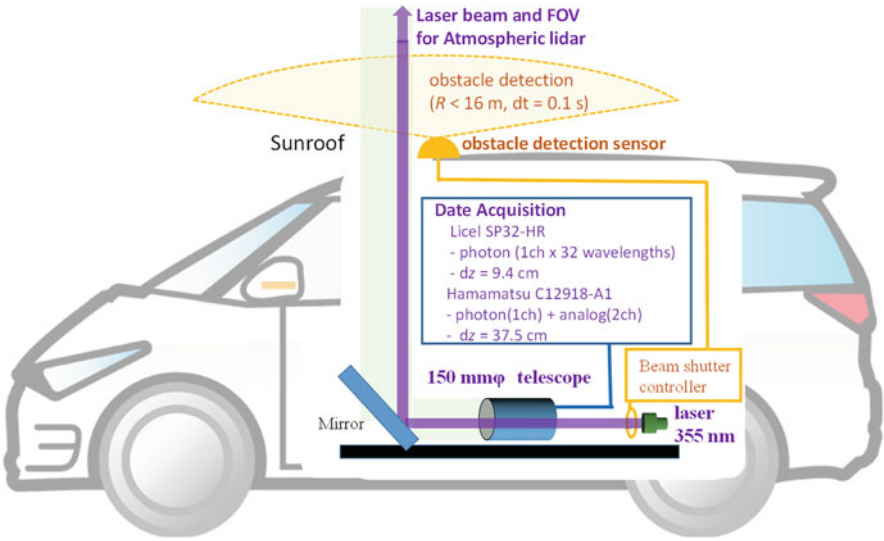


Fig. 40.1 Schematic diagram of a mobile vehicle lidar in the car with a sunroof

of <1.3 ns. After passing through the beam expander, the outgoing laser energy satisfied the eye-safety requirements. Furthermore, a 360° obstacle detection sensor and a mechanical beam shutter suspended laser emission when detecting an overpass structure such as a pedestrian deck in the vehicle's travel direction. A Newtonian-type telescope with a primary mirror diameter of 150 mm was used as an optical receiver. For near-range observation, we developed wedge prism optics similar to the laser-based air data system for aircraft control proposed by Fraczek et al. [6]. The near-measurable range after overlap correction was 7 m for the system using four wedge prisms.

The backscattered radiation was recorded in two ways. One method used photomultiplier tubes and a transient recorder (Hamamatsu C12918-A1) to acquire two analog and one photon-counting channel with a range resolution of 0.375 m. This channel was used for Mie scatter observations. The second method used a multispectral detector (Licel SP32-HR) for spectral observations such as Raman scattering and fluorescence. This study discusses the Mie-scattering component. The horizontal observation component was composed of two mirrors installed in the car and above the sunroof to change the directions of the laser beam and telescope field-of-view. An optical particle counter (OPC, Rion KC52) was equipped at the top of the vehicle to simultaneously observe the number concentrations of particles with diameters greater than 0.3, 0.5, 1.0, 2.0, and 5.0 μm.

40.2.2 Data Analysis

The extinction profiles were calculated by the Klett-Fernald method [7, 8] using the extinction-to-backscatter ratio of 50 sr. We integrated signals for 0.1–1.0 s according to the maximum observation range. The range resolutions for the vertical observation were 0.375 m and 1.875 m for ranges of 7–100 m and >100 m, respectively. The overlap functions of the lidar channels were estimated using horizontal profiles presumably homogeneous along the line of sight. We compared the retrieved extinction coefficients from the lidar and OPC measurements to evaluate the overlap correction.

The retrieval method of the extinction coefficients from the OPC number distribution and Mie scattering theory was based on the assumption of a complex refractive index and the shape of the number distribution for particle sizes outside the measurement range [9]. In the case of our experiment conducted at the observatory surrounded by a forest, we employed a complex refractive index of 1.43-0*i*, assuming the solid sulfate aerosols for the ultraviolet-visible wavelength range [10]. The coefficient of determination (R^2) of the extinction coefficients between the lidar and OPC was 0.68 and 0.54 at the range of 100 m and 10 m, respectively. The OPC-derived extinction coefficient was used as a reference for the initial value of the Klett-Fernald method when the initial value could not be assumed to be aerosol-free. Elevation corrections for road undulations (due to up and down slopes) were performed at each point using GPS data.

40.3 Results

40.3.1 Vertical Observation in Urban Areas

We tested the practical applicability of the proposed lidar for aerosol detection in the Tokyo Bay area. The driving speed was less than 50 km/h. We set a course with a total mileage of approximately 25 km that extended around the local road from the bay to inland areas. Most roads, except for a part of the Bay areas, were located in a high-rise community, satisfying the conditions of street canyons. Figure 40.2 shows the aerosol extinction coefficient distributions for an altitude range of 7–650 m observed along a travel path during 6:27–7:55 JST on July 3, 2020. Higher boundary layer heights with more significant aerosol loading were observed from the bay to inland areas. The heights of the layer trapping pollutants at low altitudes were approximately 300–400 m inland and 5 km for the bay areas.

The temporal change of aerosol profiles for a near-surface altitude range of 7–100 m is shown in Fig. 40.3 for two consecutive observations during (a) 5:00–6:20 JST and (b) 6:27–7:55 JST on July 3, 2020. Before the onset of morning traffic (Fig. 40.3a), a low aerosol-loading layer was observed at altitudes lower than 30–40 m in the high-rise community (inland area). In Fig. 40.3b, it is seen that the multilayered

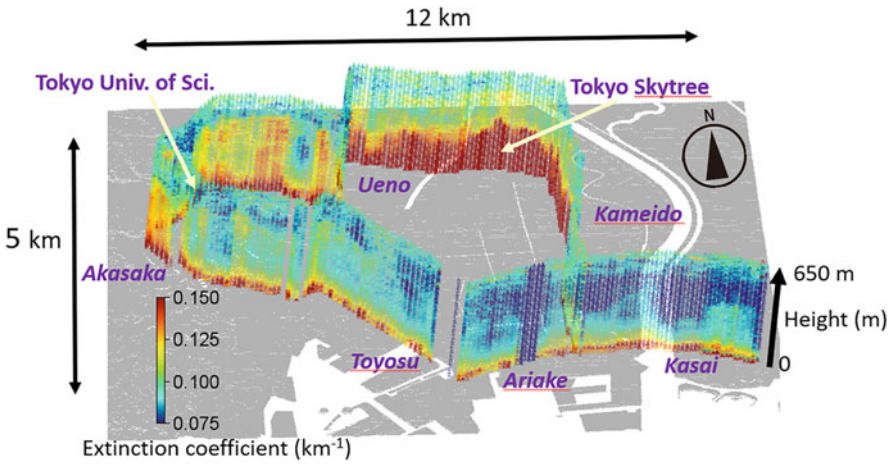


Fig. 40.2 Aerosol extinction coefficient at $\lambda = 355$ nm along with a travel path around Tokyo Bay area with an altitude range between 7 and 650 m at 6:27–7:55 JST on July 3, 2020

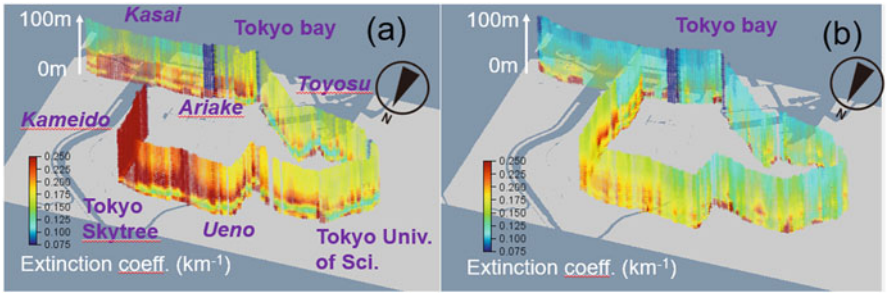


Fig. 40.3 The same as Fig.40.1, but an altitude range between 7 and 100 m during (**a**) 5:00-6:20 JST and (**b**) 6:27-7:55 JST on July 3, 2020

structure near the surface did not become apparent due to the progression of the convective mixing along with the increase in traffic.

40.3.2 Horizontal Observation Over Farmland

Horizontal observations were performed over a rice field area of approximately 600 m × 600 m (Iga, Mie) in August 2021. The driving speed of the mobile lidar was 30–40 km/h. Figure 40.4a shows the aerosol number concentrations with a diameter larger than 0.5 μm observed by the OPC at an altitude of 1.5 m along the travel path. Local differences in aerosol concentrations were observed even under such a low aerosol-loading condition. Figure 40.4b presents the aerosol extinction

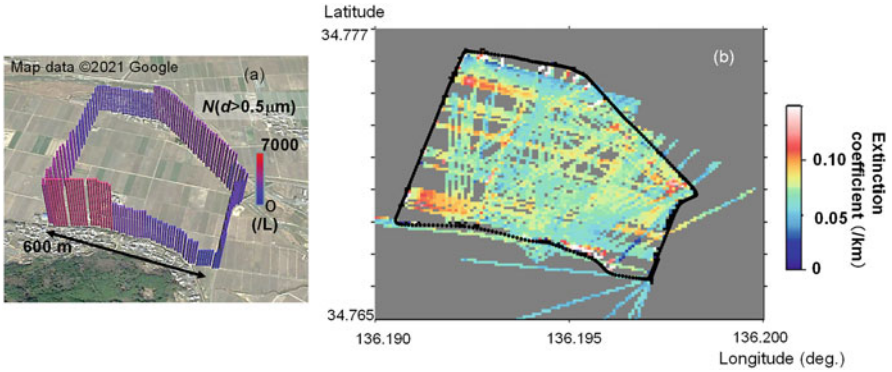


Fig. 40.4 (**a**) Number concentration distributions of aerosols with diameters larger than 0.5 μm along the travel path and (**b**) aerosol extinction coefficient at $\lambda = 355$ nm over a farmland area observed during 14:49–14:55 JST on August 22, 2021

coefficient observed by the mobile vehicle lidar over the farmland. The lidar measurement was suspended when obstacles (utility poles and trees) were detected in the observation area in the vehicle's travel direction since the detection sensor could not distinguish people from other objects. In the areas where the bank along the road was being mowed (e.g., lower-left of Fig. 40.4), the extinction coefficients and number concentrations of aerosols were relatively large. In the roadside area, the spatial pattern of the lidar-derived extinction coefficients was mostly consistent with that of the OPC number concentrations over the road.

40.4 Summary

We constructed a mobile vehicle lidar that performs on-road remote sensing to achieve continuous monitoring of atmospheric aerosols with high spatiotemporal resolutions. The system enables near-range observations while maintaining the safety condition of the laser beam. We have demonstrated lidar capability in observing inhomogeneous aerosol spatial distributions within street canyons in the Tokyo Bay area. Also, horizontal aerosol distribution has been monitored over an agricultural field, yielding a consistent result with the simultaneous data from the OPC onboard the same platform.

Acknowledgments Part of this study was supported by JSPS KAKENHI grants 26709042, 19H04238, and 20K21844. We thank Prof. S. Saito, Shinshu University, for discussing about the techniques and application of mobile vehicle lidar.

References

1. Raut, J.-C., Chazette, P.: Assessment of vertically-resolved PM10 from mobile lidar observations. Atmos. Chem. Phys. **9**, 8617–8638 (2009)
2. Dieudonné, E., Chazette, P., Marnas, F., Totems, J., Shang, X.: Lidar profiling of aerosol optical properties from Paris to Lake Baikal (Siberia). Atmos. Chem. Phys. **15**, 5007–5026 (2015)
3. Popovici, I.E., Goloub, P., Podvin, T., Blarel, L., Loisil, R., Unga, F., Mortier, A., Deroo, C., Victori, S., Ducos, F., Torres, B., Delegove, C., Choël, M., Pujol-Söhne, N., Pietras, C.: Description and applications of a mobile system performing on-road aerosol remote sensing and in situ measurements. Atmos. Meas. Tech. **11**, 4671–4691 (2018)
4. Popovici, I.E., Deng, Z., Goloub, P., Xia, X., Chen, H., Blarel, L., Podvin, T., Hao, Y., Chen, H., Torres, B., Victori, S., Fan, X.: Mobile on-road measurements of aerosol optical properties during MOABAI campaign in the North China Plain. Atmosphere. **13**, 21 (2021)
5. Kurppa, M., Hellsten, A., Auvinen, M., Raasch, S., Vesala, T., Järvi, L.: Ventilation and air quality in city blocks using large-eddy simulation—urban planning perspective. Atmosphere. **9**, 65 (2018)
6. Fraczek, M., Behrendt, A., Schmitt, N.: Laser-based air data system for aircraft control using Raman and elastic backscatter for the measurement of temperature, density, pressure, moisture, and particle backscatter coefficient. Appl. Opt. **51**(2), 148–166 (2021)
7. Klett, J.D.: Stable analytical inversion solution for processing lidar returns. Appl. Opt. **20**, 211–220 (1981)
8. Fernald, F.G.: Analysis of atmospheric lidar observations: some comments. Appl. Opt. **23**, 5 (1984)
9. Yabuki, M., Shiobara, M., Kobayashi, H., Hayashi, N., Hara, K., Osada, K., Kuze, H., Takeuchi, N.: Optical properties of aerosols in the marine boundary layer during a cruise from Tokyo, Japan to Fremantle, Australia. J. Meteorol. Soc. Jpn. **81**, 151–162 (2003)
10. Hess, M., Koepke, P., Schult, I.: Optical properties of aerosols and clouds: the software package OPAC. Bull. Am. Met. Soc. **79**, 831–844 (1998)

Chapter 41
Cloud Base Height Correlation Between a Co-located Micro-Pulse LiDAR and a Lufft CHM15k Ceilometer

Victoria Pinnegar, Paul Christiaans, Joe Clarke, Alexander Haefele, E. J. Welton, and Robert J. Sica

Abstract Several large-scale networks using automated ceilometers and LiDARs now exist. Some networks, such as MPLNET, have developed algorithms that can be applied uniformly across all instruments. However, cross-network tools are not so readily available such as those used for cloud base height comparison. The London (CDN) node of the CANadian Micro-pulse LiDAR Network (MPLCAN) hosts both a miniHD MPL (MPLNET) and Lufft 15k ceilometer (European E-PROFILE network). Each has its own algorithm to estimate cloud base height. The MPL algorithm was developed by the NASA Langley MPLNET team, and the ceilometer has the manufacturers provided Sky Condition Algorithm. The cloud base should be in principle the same for these co-located instruments. Using the MPLNET vs. Lufft measurements for the first year of operation, the monthly correlation coefficient, R, varies between 0.45 and 0.97. This difference between instruments is mostly accounted for by a poor comparison below 1 km due to aerosols, precipitation, and overlap uncertainties. Applying a gradient-based algorithm (GBD) onto the measurements improves the worst comparison to greater than $R = 0.9$. However, this GBD algorithm has low accuracy with decreased signal to noise. Thus, we can

Supported by the Canadian Foundation for Innovation and the National Scientific and Engineering Research Council.

V. Pinnegar (✉) · P. Christiaans · J. Clarke · R. J. Sica
Department of Physics and Astronomy, University of Western Ontario, London, ON, Canada
e-mail: vpinnega@uwo.ca

A. Haefele
Federal Office of Meteorology and Climatology MeteoSwiss, Payerne, Switzerland
e-mail: Alexander.Haefele@meteoswiss.ch

E. J. Welton
Goddard Space Flight Center, NASA, Greenbelt, MD, USA
e-mail: ellsworth.j.welton@nasa.gov

© The Author(s), under exclusive license to Springer Nature Switzerland AG 2023

J. T. Sullivan et al. (eds.), *Proceedings of the 30th International Laser Radar Conference*, Springer Atmospheric Sciences,
https://doi.org/10.1007/978-3-031-37818-8_41

utilize this tool to help verify the overall agreement of measurements between these 2 instruments, and it offers a tool for standard processes of the 2 instruments.

Keywords Cloud detection · Micro-pulse LiDAR · Ceilometer

41.1 Introduction

Cloud detection is an important tool for modern atmospheric remote sensing. Cloud detection measurements help to improve models of air mass movement and help to improve estimates of the energy budget, as clouds account for nearly 50% of the outgoing energy in the atmosphere's global radiation balance [1]. A current and future need of remote sensing networks is to produce global datasets for large-scale modeling, tracking, and accurate real-time analysis. A new member to these world-wide networks is MPLCAN (https://www.uwo.ca/sci/mplcan/). MPLCAN is a network of co-located mini-Micro-Pulse LiDARs (MPLs), CIMELs, and PurpleAir air-quality sensors. The MPLs have the ability to detect clouds, aerosols, and the planetary boundary layer, as well as to differentiate between water and ice in clouds via polarization measurements. These elastic LiDARs operate at 532 nm. MPLCAN's MPLs are part of NASA's MPLNET, the CIMELs are part of AEROCAN/AERONET, and for the London site, a ceilometer is part of the European Meteorological Network's E-PROFILE chain. The London ceilometer, which operates at 1064 nm, is situated 12 m from the MPL and points a few degrees off axis away from the MPL, ensuring no cross-talk between the systems.

41.2 Methodology

The London (Canada) micro-pulse LiDAR (MPL), a node in the MPLCAN network, has acquired approximately 18 months of usable data with few outages. There is also a co-located Lufft CHM15k ceilometer. Both instruments measure cloud base heights using their individual cloud base detection algorithms. The MPL runs the Version 3 Cloud detection produced by MPLNET (V3) [2]. The Lufft Ceilometer utilizes the manufacturer's Sky Condition Algorithm (SCA). The total cloud coverage reported by both of the instruments is shown in Table 41.1. The ceilometer reports a higher amount of cloud coverage, mostly within the first 3 km, with a similar number of detected clouds above the altitude of 3 km. The MPL reports more detections than the ceilometer above 9 km, due to the better SNR. The difference in reported first layers below 3 km may be caused by overlap uncertainties and low-lying aerosol layers. Applying the MPLNET's aerosol mask values to the ceilometer does mask out a significant amount of the lowest altitude clouds, indicating several false detections. High clouds can be resolved by increasing the

Table 41.1 Spring 2021 Cloud Coverage using only first layer

Altitude (km)	Ceilometer	MPL
"Clear Sky"	32%	39%
0–2	38%	26%
2–6	22%	22%
6–10	7%	10%
10<	1%	3%

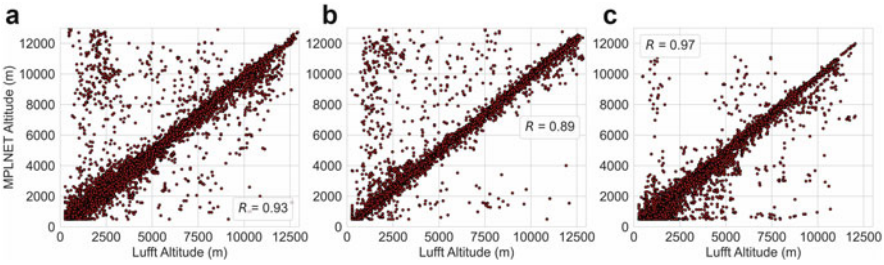


Fig. 41.1 From left to right is the equinox, summer and winter measurements of the first cloud layer's height. The MPLNET Versions 3 cloud detection sees the first layer at a higher altitude compared to the Lufft

time averages. For the ceilometer, this increase comes at the cost of decreased time resolution.

41.2.1 Comparison of the Instrument-Specific Cloud-Base Detection Algorithms

To evaluate the similarity of the simultaneous detection, the measurements where both instruments detected a cloud during the same temporal bin were grouped. The MPLNET and the Lufft values were put through a regression analysis using single-layer simultaneous detections. Figure 41.1 shows the comparison. As seen in the total cloud coverage, the ceilometer measures lower layers concentrated between 0 and 3 km during times when the MPL sees cirrus clouds and only aerosols below 3 km. The best R value is in Fig. 41.1a, the autumnal/vernal equinox (March, April, May, September, October, and November) group. Figure 41.1b represents the summer months of June, July, and August. It has a lower R value of 0.89, but also has far fewer data points than expected. On hot summer days, the humidity within the MPL enclosure would often rise to inoperable values, causing condensation to form on the enclosure window. The Winter group (Fig. 41.1c) represents December 2021 plus January and February 2022. The agreement is at its highest, with $R = 0.97$. During the months of December and January, their individual regressions showed values of 0.95. During all the winter months, the high comparison is due to the low aerosol environment.

41.2.2 The Gradient-Based Detection (GBD) Algorithm

A cloud-base algorithm has been written specifically for the London LiDARs to allow a standard comparison, with the hope it would eliminate biased hardware and unify the outputs. The CHM 15k has a lower signal-to-noise ratio in comparison to the MPL. The algorithm needed a generalized form to apply to both instruments. The resultant algorithm is based on MPLNET's Version 2 cloud detection (V2; [2]). The two main components are the gradient and threshold, determined in the following manner from the attenuated backscatter ratio. The derivative with respect to altitude is taken on the attenuated backscatter ratio

$$R(z) = \frac{\beta(z)T^2(z)}{\beta_{mol}(z)T^2_{mol}(z)}, \tag{41.1}$$

which is zero in clear air. The altitude gradient must have an increase across a minimum of 60 m and pass a threshold calculated as the range average of the backscatter profile ($\overline{\beta}$) multiplied by an empirical value C (set to 3.5 for this study). An additional test was added to allow the algorithm to minimize loss in continuous layers. Given a positive cloud detection in the previous profile and a negative detection in the current one, the surrounding kilometer of the previous cloud is rechecked for a positive gradient and threshold equal to half of $C\overline{\beta}$.

V3 and V2 switch out of gradient based at higher heights, which is accounted for but much less effective in GBCD. There is also a loss in high-altitude cloud detection not dissimilar to V2 as reported by Huang et al. [3]. Figure 41.2 shows a R value above 0.9 for both a) and b), although agreement is again highest in the winter. When further compared to the Lufft measurements, as Fig. 41.3 shows the R values increase for all cases. The R values are shown in Table 41.2.

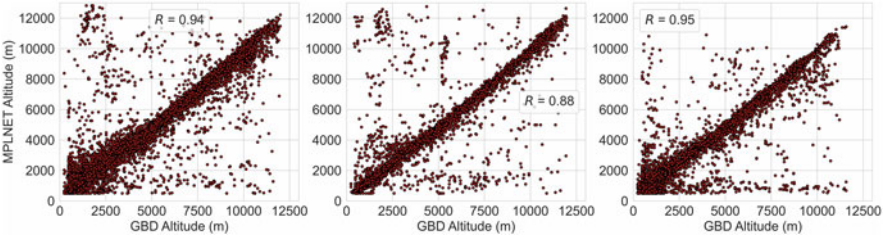


Fig. 41.2 Left to right is the Equinox, Summer, and Winter measurements with GBD applied to MPL measurements. The overall comparison between the GBD and V3 shows a high similarity, which should indicate high statistical similarity to V3 under 10 km

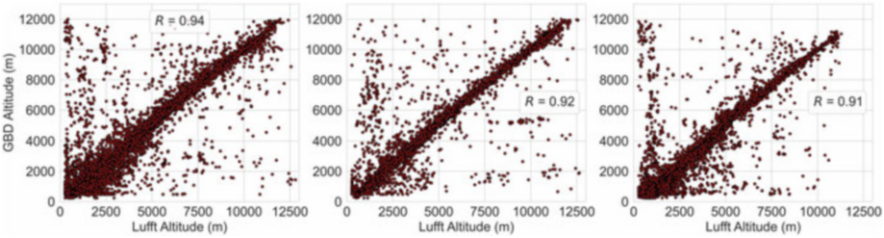


Fig. 41.3 Left to right is the Equinox, Summer, and Winter with GBD applied to MPL measurements vs. the Lufft product. Higher R values indicating higher similarity

Table 41.2 Regression coefficients for the 3 comparisons described in Figs. 41.1, 41.2, and 41.3

Comparison	Spring	Summer	Autumn	Winter
MPL V3 vs. Ceil	0.91	0.89	0.93	0.97
MPL-GBD vs. MPL	0.92	0.88	0.93	0.95
MPL-GBD vs. Ceil	0.95	0.92	0.94	0.91

41.3 Summary and Conclusions

Due to the algorithm's low effectiveness when the SNR is low, it is most useful on low-lying clouds but misses detections with the cirrus clouds. We implemented a low signal-to-noise detection for cirrus clouds, but the effectiveness is much less than that of the instruments algorithms and must be improved upon. Additionally, defining the minimum scattering depth of an aerosol with a cloud-masked objective threshold should allow for the detection of strong scattering aerosols and smoke layers. This tool can also be used to supplement the cloud products produced by each individual instrument in this network. It will be particularly useful when comparing measurements directly between instruments is important.

Due to the high initial comparison, MPLNET and E-PROFILE can be reliably compared using our GBD. The overall application of GBD onto MPL measurements improved the comparison to the Lufft ceilometer and could be reliably used, at least at this representative mid-latitude site. Our next steps will include additional error testing and signal-to-noise improvements to improve detections of high-altitude cirrus clouds, particularly with the ceilometer. We will also study more individual cases with high variance in cloud base heights due to high aerosol loading or precipitation. Both instruments cloud bases may be compared directly during these periods but must be checked manually for the effect of precipitation and high aerosol loading.

Acknowledgments Thanks to our MPLCAN partners for their contributions to this work. We acknowledge our instruments operate on the traditional lands of the Anishinaabek, Haudenosaunee, Lūnaapéewak and Chonnonton Nations, on lands connected with the London Township and Sombra Treaties of 1796 and the Dish with One Spoon Covenant Wampum.

References

1. Peixoto, J., Oort, A.: Physics of Climate, 1st edn. American Institute of Physics, College Park (1992)
2. Lewis, J., Campbell, J., Welton, E., Stewart, S., Haftings, P.: Overview of MPLNET version 3 cloud detection. J. Atmos. Oceanic Technol. **33**, 2113–2134 (2016)
3. Huang, J., Hsu N., Tsay S.-C., Jeong M.-J., Holben B.N., Berkoff, T.A., Welton, E.J.: 2011: Susceptibility of aerosol optical thickness retrievals to thin cirrus contamination during the BASE-ASIA campaign. J. Geophys. Res. **116**, D08214 (2011). https://doi.org/10.1029/2010JD014910

Chapter 42
Comparison of Local and Transregional Atmospheric Particles over the Urmia Lake in Northwest Iran, Using a Polarization Lidar Recordings

Salar Alizadeh, Ruhollah Moradhaseli, Hossein Panahifar, and Hamid R. Khalesifard

Abstract We have installed a scanning two-channel (532 nm) polarization lidar at the southwest coast of the hypersaline Urmia Lake since September 2018. Our measurements show dust layers are frequently transported to the region from sources like; Sahara, Mesopotamia, and Arabian Peninsula. Particles that are appearing at altitudes less than 2 km, have PDR < 25%, and mostly have local origins. From June to October, these lower altitudes atmospheric aerosols mostly are rising either from the dried lake bed or its coastal area. During cold months, atmospheric thermal inversion considerably increases the concentration of anthropogenic particles at altitudes less than 1 km AGL. Such particles possess PDR < 10%. We haven't been able to detect dust or salt-dust particles that are originated from the lake bed and transported to altitudes above 3 km AGL.

Keywords Urmia Lake · Polarization lidar · Dust · Salt dust

42.1 Introduction

The Urmia Lake, a hypersaline lake, is in northwest of Iran. The lake is facing a serious drying scenario. Even though the lake has been recovered a bit during recent years, but still its surface is below the ecological level. The dried lake bed and its coastal area are covered with salt crusts, dust, and mixtures of salt and dust which we call the latter the salt-dust particles [1]. Therefore, such areas have the

S. Alizadeh · H. Panahifar · H. R. Khalesifard (✉)
Physics Department, and Research Center for Climate Change and Global Warming, Institute for Advanced Studies in Basic Sciences, Zanjan, Iran
e-mail: khalesi@iasbs.ac.ir

R. Moradhaseli
Physics Department, Faculty of Science, Zanjan Brach, Islamic Azad University, Zanjan, Iran

© The Author(s), under exclusive license to Springer Nature Switzerland AG 2023

J. T. Sullivan et al. (eds.), *Proceedings of the 30th International Laser Radar Conference*, Springer Atmospheric Sciences,
https://doi.org/10.1007/978-3-031-37818-8_42

potential to become active sources of mineral particles and impact the neighboring and even distant lands to the lake. On the other hand, the Urmia Lake region, like other areas in the west and northwest of Iran, is considerably under the influence of dust sources in Mesopotamia, the Arabian Peninsula, and even North Africa [1–4]. It should be mentioned that more than 7 million inhabitants are living in the catchment area of the lake, and a considerable number of industries of different sizes are also active in this region. Therefore, urban-industrial particles also very frequently contaminate the atmosphere. To distinguish between different types of atmospheric particles that can be found in the atmosphere of this region, we have installed a polarization lidar at the southwest coast of the lake since 2018 [5]. In this paper, after introducing the lidar and measurements, we will discuss some recorded cases of different types of atmospheric particles including anthropogenic particles, dust and salt-dust from local sources, and transregional dust layers. An overview of all observed cases during the campaign will come after, and finally, the work is concluded in the last section.

42.2 Data Set and Measurements

The IASBS scanning polarization lidar (ISPL) has been installed at the southwest coast of the Urmia Lake (37.3438 N, 45.2947 E, 1282 m AMSL) since September 2018, but in this work, we are reporting just measurements from July 2020 to March 2022 where the lidar was in operation for 65 days. The transmitter of ISPL is a frequency-doubled Nd:YAG laser (150/100 mJ/pulse at 1064/532 nm, 10 ns pulse duration), and it has just two cross-polarized receiving channels at 532 nm. Details of the ISPL's structure appeared in our previous work [5]. Even though the lidar can work both in azimuthal and zenith directions, here we are reporting measurements just in the zenith direction. To retrieve the particle backscatter coefficient (β) from the lidar data, the well-known Klett method [6] has been used, and the particle depolarization ratio (PDR) has been calculated based on the work by Tesche, M. et al. [7].

MODIS AODs at 550 nm from Giovanni Deep Blue and radiosonde data from Tabriz airport are other complementary data that have been used in this work. Also, the NOAA HYSPLIT model has been used to track back the detected layers of atmospheric particles.

42.3 Results and Discussions

In this section, we are presenting three sample cases of detected layers of atmospheric particles. The first two cases represent particles originating from the local sources in, i.e., urban industrial pollution and salt-dust particles. The next case corresponds to transport of dust layers from Mesopotamia to the Urmia Lake

region. The last part of this section is an overview of all recorded events during the campaign.

42.3.1 Case Studies

Case I: Local Particles, 8–9 January 2022
Figure 42.1a is the range corrected time-height series of the ISPL parallel channel at 532 nm from 17:20 UTC, 8 January 2022 to 07:20 UTC, 9 January 2022. The figure shows a dense layer of particulate matter extended from the surface up to ~1 km above the ground level (AGL). The recorded data for the time period specified by two red dashed lines in Fig. 42.1a is used to retrieve the β, and PDR. Fig. 42.1b depicts the obtained profiles of β (blue line) and PDR (red line). Their corresponding error values are shaded areas around the lines. Figure 42.1a shows a very dense layer of atmospheric particles in the planetary boundary layer (PBL). Figure 42.1b has more details of this layer. Just at the vicinity of the surface, β is ~5.5×10^{-5} $km^{-1}sr^{-1}$ but is decreasing with the altitude, and another layer appears at ~400 m AGL. At the vicinity of the surface, PDR is ~12%, but for the layer at ~400 m AGL, it decreases to ~8%. The β-profile shows another layer at ~900 m AGL where its PDR is ~15%. The potential temperature (θ) profile in Fig. 42.1c (12:00 UTC, 8 and 9 January 2022, Tabriz Airport) shows a very stable atmosphere below 500 m AGL on 8 January, but this is not the case for the next day. The lidar time-height series in Fig. 42.1a also shows how the boundary layer raised to altitudes above 600 m AGL on 9 January. Since the lidar station is just at the coast of the lake, we expect the increase of PDR just at the vicinity of the surface is due to existence of some wet salt or salt-dust particles but the dens layer at ~400 m AGL should be a concentration of the urban-industrial pollution in a stable atmosphere. It is expected that the aerosol layer at ~900 m AGL that has higher values of PDR again had been originated from the lake bed. It should be mentioned that the obtained PDR values close to the surface and for the layer at ~900 m are in agreement with previously reported values of PDR for wet and dry salt particles [8], and CALIPSO recordings over the Urmia Lake [1, 9].

Case II: Local Particles, 19–20 August 2020
Figure 42.2a shows the parallel channel time-height series of range corrected lidar signal at 532 nm from 15:30 UTC, 19 August to 11:50 UTC, 20 August 2020. Referring to Fig. 42.2a, it can be found that a thick atmospheric aerosol layer is extended from the surface up to ~3 km AGL. Figure 42.2b depicts, for the part of the time series that is between two dashed red lines in Fig. 42.2a, β is almost constant up to ~2.0 km AGL, but PDR is ~25% close to the surface then decreases to a local minimum of ~18% at 1.35 km AGL where β is maximum. The PDR has a local maximum of ~19% at an altitude of ~1.8 km AGL. β and PDR have other local maxima ~2.7 km AGL, where PDR is ~14%. Fig. 42.2c depicts 48-h HYSPLIT backward trajectories ending at the lidar station. It clearly shows, particle

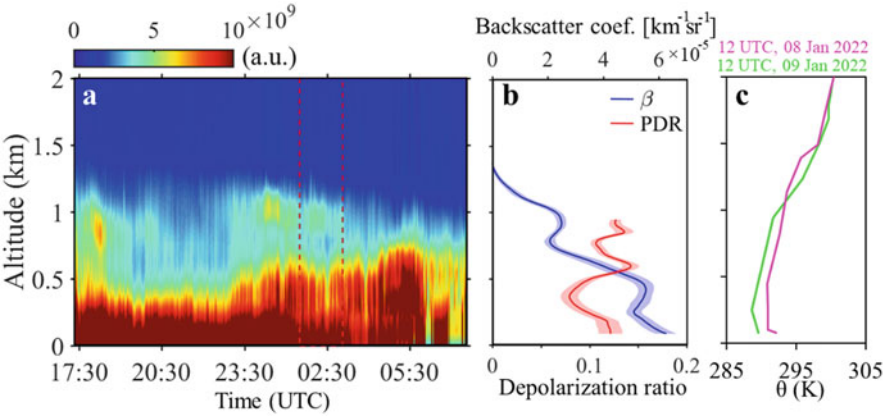


Fig. 42.1 (**a**) Parallel channel time-height series of range corrected lidar 8–9 January 2022. (**b**) β (blue) and PDR (red) profiles derived from lidar signals between two dashed red lines on (a), shaded areas are corresponding errors (**c**) potential temperature vertical profile at 12:00 UTC, 8 and 9 January 2022, Tabriz airport radiosonde. Altitudes are measured from the ground level

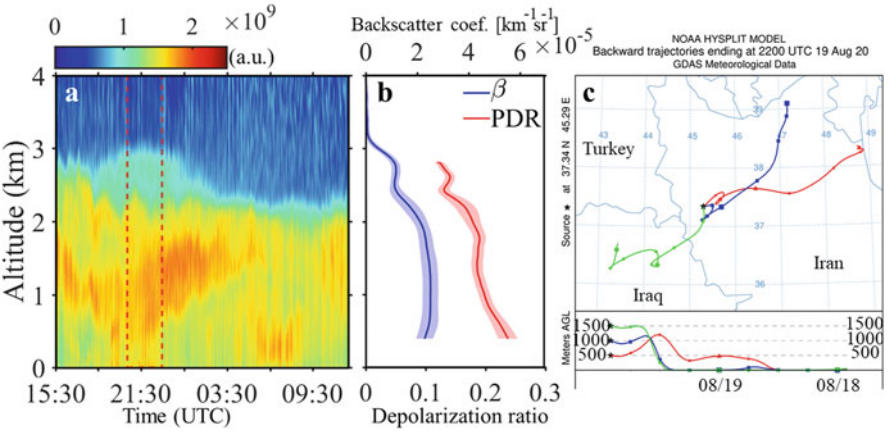


Fig. 42.2 (**a**) Parallel channel time-height series of range corrected lidar signal, 19–20 August 2020. (**b**) β (blue) and PDR (red) profiles derived from lidar signals between two red dashed lines on time-height series in (**a**), shaded areas are corresponding errors. (**c**) 48-h HYSPLIT backward trajectories ending at the lidar station at 22:00 UTC on 19 August 2020. Altitudes are measured from the ground level

layers in Fig. 42.2a have local origins. PDR values in Fig. 42.2b indicate, near the surface some pure dust particles should exist but at higher altitudes, there should be a mixture of dust, salt, and salt-dust particles.

Case III: Transregional Dust Layers, 22 and 23 July 2021

Figure 42.3a, b depicts two dust layers originated from the north of the Mesopotamian region (Fig. 42.3c). The Aqua-MODIS AOD at 550 nm over the

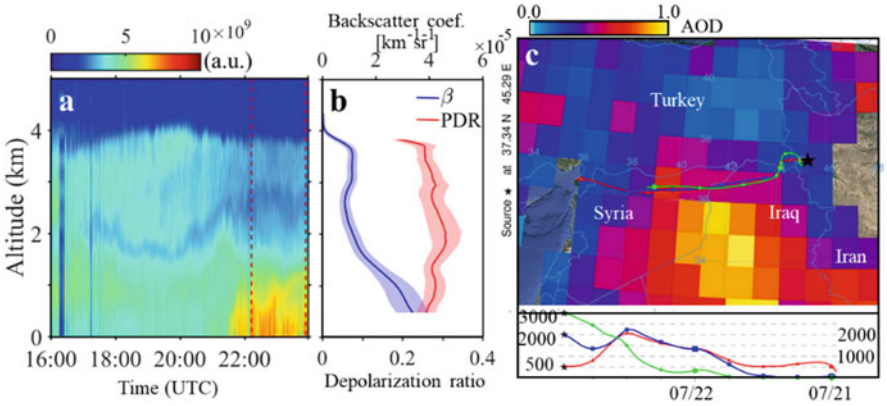


Fig. 42.3 (**a**) Parallel channel time-height series of range corrected lidar signal, 22–23 July 2021. (**b**) β (blue) and PDR (red) profiles derived from lidar signals between two red dashed lines on time-height series. (**c**) 48-h HYSPLIT backward trajectories ending at ISPL on 23:00 UTC 22 July 2021 overlaid on Aqua-MODIS daily deep blue AOD at 550 nm on 21 July 2021. Altitudes are measured from the ground level

region on 21 July 2021 is shown in Fig. 42.3c. The first layer is extended from the surface up to ~2.5 km AGL, and the altitude of the higher one is ~3 km AGL (Fig. 42.3a).

The retrieved PDR values for these layers vary from ~25% to 30%, where lower values are for that part of the lower layer that is closer to the surface even if it has higher β-values (Fig. 42.3b). It seems that when salt and salt-dust particles that have lower PDR values are mixed with pure dust, the PDR of the mixture is decreasing.

42.3.2 Overall Behavior of Atmospheric Particles

Table 42.1 is an overview of all recorded events from 13 July 2020 to 8 March 2022. It should be mentioned that the reported PDR values are averaged over all layers originated from a specific source. It is noticeable that from all the recorded events, 60% of them are from the sources inside the Urmia Lake catchment area and the rest 40% are from distant sources. When the particles are raising from the lake bed or its coastal area, the PDR is ~14–22%. However, in vicinity of the surface, for some cases like case II (Fig. 42.2), the PDR is getting close to that of pure dust [10]. From 39 events originated from local sources, only 5 (12%) of them correspond to anthropogenic particles. Table 42.1 shows the Mesopotamian region is the most influential distant source over the Urmia Lake and the Arabian Peninsula the least.

Table 42.1 An overview of all recorded events by the ISPL from 13 July 2020 to 8 March 2022

Source		Particle type	PDR averaged	Layer height (m)	Events frequency	
					(Days)	(%)
Local	Summer	Salt-dust	0.18 ± 0.04	1900 ± 600	18	28
	Winter	Anthropogenic	0.11 ± 0.01	500 ± 250	5	7
		Salt-dust	0.17 ± 0.02	800 ± 350	16	25
Distant	Mesopotamia	Dust	0.23 ± 0.05	2500 ± 850	20	31
	Africa	Dust	0.24 ± 0.04	4200 ± 1800	5	7
	Arabian Peninsula	Dust	0.23 ± 0.03	900 ± 200	1	2
Total					65	100

42.4 Conclusions

For the first time, we are reporting a comparison of atmospheric particles in the vicinity of the Urmia Lake in Northwest Iran using their particle depolarization ratio (PDR) retrieved from the recordings of a polarization lidar, ISPL. During a 21-month measurement campaign, we have recorded 65 days where different types of particles (salt, salt-dust, dust, anthropogenic) were contaminated the atmosphere. It is found that salt and salt-dust particles are the most dominant pollutant in this region (52% of all events). But distant sources also very frequently influence the region. Between them, the Mesopotamian region is the most influential one (31% of all events), but we even detected dust layers that had originated from North Africa and the Arabian Peninsula. We didn't find any case where the raised particles from the lake bed got transported to altitudes above 3 km AGL. In the other words, based on these measurements, most probably the Urmia Lake as a source of salt and salt-dust particles can't influence regions outside its catchment area.

Acknowledgments This work has been supported by Urmia Lake Restoration Program (ULRP) under grant No. 96100201 and Science and Technology Department of Iran Presidential office under grant No. 808504000. Authors are grateful to the NOAA Air Resources Laboratory (ARL) for the provision of the HYSPLIT transport model and to the NASA Langley Research Center Atmospheric Science Data Center for provision of the MODIS (https://giovanni.gsfc.nasa.gov/) data. We are very much thankful to the University of Wyoming Weather Center for providing the radiosonde data. Special thanks to the Department of Environment of Iran, Urmia, for hosting our lidar station during the campaign.

References

1. Ghomashi, F., Khalesifard, H.R.: Investigation and characterization of atmospheric aerosols over the Urmia lake using the satellite data and synoptic recordings. Atmos. Pollut. Res. **11**(11), 2076–2086 (2020)
2. Masoumi, A., et al.: Retrieval of aerosol optical and physical properties from ground-based measurements for Zanjan, a city in Northwest Iran. Atmos. Res. **120**, 343–355 (2013)

3. Panahifar, H., Khalesifard, H.R.: Observation of long-range dust transport from mesopotamia and Arabian peninsula toward Tehran, Iran. In: E3S Web of Conferences. 2019. EDP Sciences
4. Panahifar, H., Moradhaseli, R., Khalesifard, H.R.: Monitoring atmospheric particulate matters using vertically resolved measurements of a polarization lidar, in-situ recordings and satellite data over Tehran, Iran. Sci. Rep. **10**(1), 1–15 (2020)
5. Khalesifard, H.R., et al. Monitoring atmospheric aerosols over the urmia lake by CALIPSO and a ground based depolarized lidar. In: EPJ Web of Conferences. 2020. EDP Sciences
6. Klett, J.D.: Lidar inversion with variable backscatter/extinction ratios. Appl. Opt. **24**(11), 1638–1643 (1985)
7. Tesche, M., et al.: Vertically resolved separation of dust and smoke over Cape Verde using multiwavelength Raman and polarization lidars during Saharan Mineral Dust Experiment 2008. J. Geophys. Res. Atmos. **114**(D13) (2009)
8. Haarig, M., et al.: Dry versus wet marine particle optical properties: RH dependence of depolarization ratio, backscatter, and extinction from multiwavelength lidar measurements during SALTRACE. Atmos. Chem. Phys. **17**(23), 14199 (2017)
9. Ghomashi, F., Khalesifard, H.R.: CALIPSO recordings and categorization of atmospheric aerosols over the Urmia Lake. In: E3S Web of Conferences. 2019. EDP Sciences
10. Burton, S., et al.: Aerosol classification using airborne High Spectral Resolution Lidar measurements–methodology and examples. Atmos. Meas. Tech. **5**(1), 73–98 (2012)

Chapter 43
Properties of Polar Stratospheric Clouds over the European Arctic from Ground-Based Lidar

Christine Böckmann and Christoph Ritter

Abstract In this work, we present case studies from PSC cases observed over the European Arctic in the winter 2021/22 which consisted of spherical particles. Due to the possibility to apply clear sky conditions above and below the PSCs, it was possible to estimate the lidar ratio (LR355 = 20–25sr; LR532 = 55–60sr) for two PSC cases. Also, the uncertainties of the retrieved backscatter and extinction coefficients were estimated. Using these optical coefficients as an input for the inversion of microphysical properties, we derived mono-modal volume distributions with an effective radius around 0.35 μm and a refractive index of about 1.54 + i * 0.02. We repeated each inversion 10 times with different error realizations from the optical input data to confirm that the inverted results are stable concerning the volume distribution function, effective radius, and refractive index. Finally, also the single scattering albedo has been calculated, which is around 0.9 at 532 nm and lower (around 0.82) in the UV.

Keywords Polar stratospheric clouds · Variable lidar ratio · Inversion of lidar data

43.1 Introduction

Polar Stratospheric Clouds (PSCs) are a special type of cloud that forms below 195 K in the Polar winter mid-stratosphere. While in the Antarctic PSCs occur each winter, the occurrence of PSC in the Arctic region is more variable. However,

C. Böckmann
Universität Potsdam, Potsdam, Germany

Alfred Wegener Institut, Potsdam, Germany
e-mail: bockmann@uni-potsdam.de

C. Ritter (✉)
Alfred Wegener Institut, Potsdam, Germany
e-mail: christoph.ritter@awi.de

© The Author(s), under exclusive license to Springer Nature Switzerland AG 2023

J. T. Sullivan et al. (eds.), *Proceedings of the 30th International Laser Radar Conference*, Springer Atmospheric Sciences,
https://doi.org/10.1007/978-3-031-37818-8_43

climate change may lead to a colder polar stratosphere and, hence, an increased PSC occurrence in the future [1]. As PSCs provide the surface for ozone destruction, monitoring of their occurrence is an important topic.

Unlike tropospheric clouds, which are liquid water or ice, these PSCs can be ice, solid nitric acid trihydrate (NAT) crystals, supercooled liquid ternary (sulfuric acid/nitric acid/water) solution (STS) droplets, or combinations of these [2].

Most recent analyses of satellite PSC observations have assumed that NAT particles are nearly spherical. However, some infrared observations of large NAT particles can only be reconciled by assuming the particles have needle or disc-like shapes. Measurements of NAT particle shape would lead to more realistic calculations of NAT optical properties and improve the future characterization of PSC composition [2, 3].

As the derivation of particle extinction by Raman lidar is challenging due to the height of PSCs (typically above 20 km), it may be interesting to constrain lidar ratio and particle extinction by a backscatter lidar.

43.2 Observations

The date of this work has been recorded over Ny-Ålesund (78.9 N, 11.9 E), a research village on Svalbard archipelago in the European Arctic. The Alfred Wegener Institute operates a "$3\beta + 2\alpha + 2\delta$" Raman lidar at this site. Some of the main specifications of the system are a spectra 290/50 Nd:YAG with 50 Hz and 200 mJ per pulse and color, a 70-cm telescope with about 2 mrad fov, Licel electronics, operating both in analog and photocounting, as well as Hamamatsu PMT. Only for the 1064-nm branch, a Licel APD is used. This lidar is used for tropo- and stratospheric research. More information on the system is given in Hoffmann [4].

PSCs have been recorded in the winter 2021/22 from 14 December onward (the last observation without PSC was performed on 9 December 2021). Already from mid to end December, the thickest PSCs with BSR_532 nm >5 or a backscatter coefficient at 532 nm >3 * 10^{-7} sr^{-1} m^{-1} have been measured; see Fig. 43.1. Contrary, the PSCs recorded in Jan and Feb 2022 were mostly weaker (BSR < 3) and appeared more broken, like Ci clouds.

In Ny-Ålesund a daily Vaisala RS-41 radiosonde is launched at around 11 UT. At about UT 12 on 24 December, the sonde crossed the approximate height in which the PSC was visible in the lidar. However, due to the drift of the radiosonde, the profiles of lidar and sonde (Fig. 43.1, right) must not show precisely the same conditions. Nevertheless, temperatures clearly below 190 K have been recorded by the sonde. The same radiosonde recorded a high relative humidity of 39% over water (78% over ice) in 24-km altitude at the upper edge of the PSC, respectively.

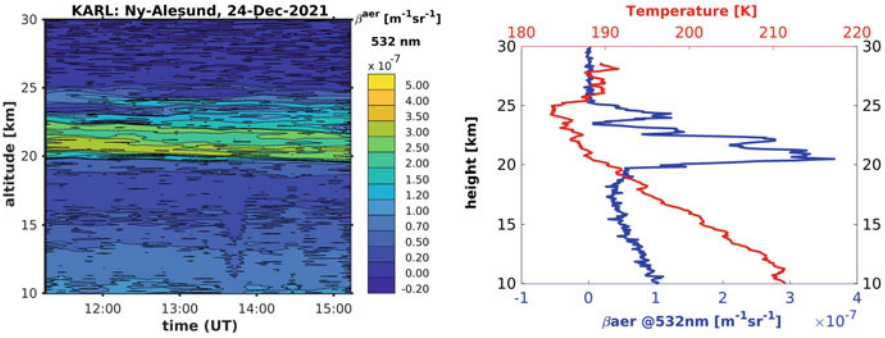


Fig. 43.1 Left: Contour plot of a PSC on 24 December 2021. Right: A local RS-41 radiosonde and contemporary lidar backscatter (UT 12 on 24 December 2021)

43.3 Evaluation of the Lidar Data

The lidar data of this work has been evaluated according to Klett [5] with a resolution of 7.5 m and 11 min. No smoothing of the lidar signals was applied. As a boundary condition the clear sky approximation was chosen above the PSC by assuming:

<BSR_532 nm> = 1.05 in 27–30 km altitude with an Ångström exponent of backscatter of −1.2

The choice of the Ångström exponent was taken from typical sun photometer observations at the site [6].

It is well known that the Klett solution (if extinction by particles cannot be neglected) depends on an a priori chosen lidar ratio (LR). When integrating from the altitude of the boundary conditions toward the instrument, a too-high/too-low chosen LR leads to a too-low/too-high backscatter below the layer with extinction. This concept has already been used by many researchers, e.g., [7], to determine the LR of cirrus clouds. The impact of the LR on the solution is shown in Fig. 43.2.

In this work we calculated the Klett solution with an average LR = 40sr (for 355 nm and 532 nm) for the whole stratosphere, with the exception of the PSC layer. For the PSC, different LR from 15sr to 90sr in steps of 5sr were used. We selected the final solution by that LR which minimized:

| min (BSR_below_PSC) – BSR_Fit |

where BSR_Fit is the abovementioned boundary condition and BSR_below_PSC all BSR values in all altitudes below the PSC. Hence, this approach required at least one height interval of clear air in the lidar profile.

This method works well for 355 and 532 nm; however, at 1064 the extinction of the PSC was negligible; hence the backscatter at 1064 in the Klett algorithm hardly depends on the assumed LR. Therefore, the 1064-nm channel was simply evaluated

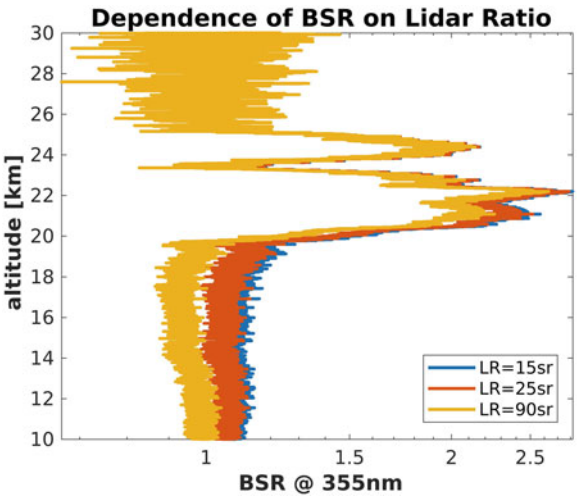


Fig. 43.2 Impact of the LR on the solution in the Klett approach. Too high/low LR provides too low/high backscatter below the PSC

by assuming an average lidar ratio of 45sr, and no aerosol extinction can be given for this wavelength.

We found significantly lower LR at 355 nm (20–25sr) compared to 532 nm (55sr < LR < 60sr) for two cases that were analyzed in detail (14 December and 24 December). We derived the aerosol extinction by the product of aerosol backscatter and LR without using the Raman channels of the lidar. Due to the higher LR at 532 nm, the extinction in both colors, and hence the insecurity for the determination of the LR in the Klett algorithm was comparable and around 5sr. Being able to estimate the LR, the uncertainty of the backscatter is mainly due to the assumed boundary condition. Five percent error of the aerosol backscatter was estimated.

Finally, the depolarization in both 355 and 532 nm was below 2%, indicating spherical particles in the PSC. Hence the inversion of the particle microphysics can be done by assuming Mie theory.

A second PSC with similar properties was observed on 14 December in 21–26-km altitude at T < 188 K (not shown for brevity).

43.4 Inversion of Microphysical Properties

For the microphysical property retrieval, we use the software which is described in detail in [8, 9] since the depolarization in both channels 355 and 532 nm was below 2%. The inversion of the particle volume size distribution (PVSD) is done by an iterative regularization technique [10].

We investigated two days 14 and 24 December 2021. We found similar results in particular a monomodal PVSD; see Fig. 43.3 (right, red curve). The second quite small raising is an artificially mathematical oszillation as usual in the inversion

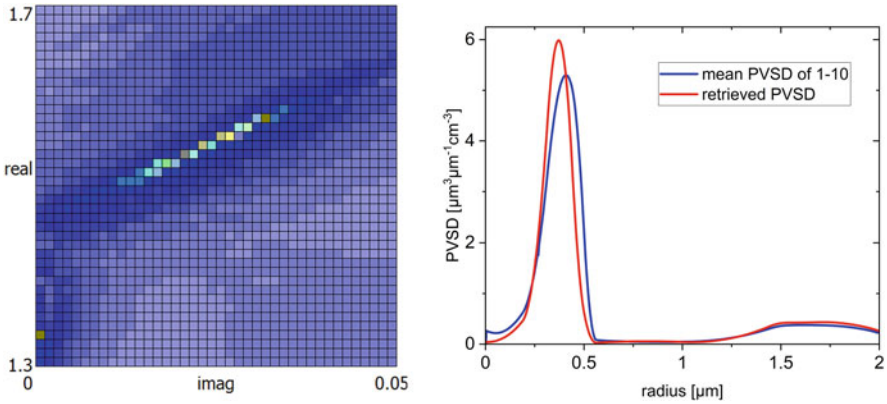


Fig. 43.3 Retrieved distribution of the refractive index (left) and the particle volume size distribution (right) for the PSC on 24 December 2021

process of an ill-posed problem. It is well known that the complex refractive index (CRI) is not uniquely invertible from only five lidar data coefficients. But for both days, surprisingly we found a very thin diagonal pattern between real and imaginary part of the refractive index; see Fig. 43.3 (left). Such distribution is normally a sign of stable inversion result [10].

We will report here on the second day. We made an experiment to learn how uncertainties in the optical properties affect the microphysical property retrieval. This was done by inversion of the retrieved extinction and backscatter coefficients from the lidar first. Subsequently we repeated the inversion 10 times for different realizations of the uncertainties in the extinction and backscatter coefficients estimated in the previous section. The results of the 10 cases are summarized in Table 43.1.

The inspection of Table 43.1 shows that the retrieved parameters from the inversion are surprisingly robust for changes in the input lidar data. Only if the extinction at 355 nm is lower than expected and at the same time the extinction at 532 nm is higher than expected (experiment Nos. 3, 7, and 9), a low refractive index (real part below 1.5, imaginary part below 1e-2) was found. This correlates with higher single scattering albedos. As for our example, the lidar ratio at 355 nm is significantly lower than that for 532 nm; we rate these realizations of noise, which would lead to extremely low extinction in this color (Nos. 3, 7, and 9) slightly less likely.

Using the 10 PVSDs from our experiment, we determined the mean PVSD; see Fig. 43.3 (right, blue line). As one can see the blue curve is nearly in agreement with the red one. This needs detailed future investigations.

The retrieved effective radius is 0.39 (mean value 0.35) µm; the total surface area and volume concentration is 10.43 (12.75) ($\mu m^2 cm^{-3}$) and 1.35 (1.39) ($\mu m^3 cm^{-3}$), respectively. The CRI is 1.549 + i * 0.0246 (1.531 + i * 0.0183) which is in a quite good agreement with findings in [11, 12].

Table 43.1 Error propagation from optical to microphysical parameters for the PSC on 24 December 2021

Experiment	Description	real(RI)	imag(RI)	r_eff	v_t	s_t	SSA355	SSA532
	Retrieved solution	1.549	2.46E-02	3.901E-01	1.35	1.043E+01	7.603E-01	8,645E-01
1	α355: too highα532: too high	1.536	2.20E-02	3.222E-01	1.39	1.311E+01	8.061E-01	8,832E-01
2	α355: too lowα532: too low	1.548	2.20E-02	4.261E-01	1.24	8.734E+00	7.620E-01	8.754E-01
3	α355: too lowα532: too high	1.461	6.84E-03	3.759E-01	1.78	1.618E+01	8.917E-01	9.467E-01
4	α355: too highα532: too low	1.574	2.05E-02	2.850E-01	1.13	1.196E+01	8.473E-01	8.913E-01
5	All β too low	1.540	2.28E-02	3.780E-01	1.31	1.062E+01	7.766E-01	8.759E-01
6	All β too high	1.541	2.12E-02	3.665E-01	1.32	1.090E+01	7.882E-01	8.825E-01
7	All β too lowα355: too lowα532: too high	1.457	7.42E-03	2.787E-01	1.80	2.383E+01	8.798E-01	9.470E-01
8	All β too lowα355: too highα532: too low	1.583	2.32E-02	2.807E-01	1.12	1.204E+01	8.320E-01	8.810E-01
9	All β too highα355: too lowα532: too high	1.498	1.59E-02	4.690E-01	1.76	1.127E+01	7.900E-01	8.990E-01
10	All β too highα355: too highα532: too low	1.549	1.42E-02	3.021E-01	1.12	1.121E+01	8.892E-01	9.231E-01
	Mean	1.531	1.83E-02	3.522E-01	1.39	1.275E+01	8.203E-01	8.972E-01
	Standard deviation	0.04	6.30E-03	6.350E-02	0.265	4.120E+00	5.030E-02	2.883E-02

43.5 Conclusions

PSCs were frequently observed in the winter 2021/22 in the European Arctic; the highest backscatter already occurred in December 2021 with BSR ≥ 5 at 532 m.

Clear sky conditions above and below PSC cases allowed us to estimate the LR and, hence the extinction from the elastic channels. We found LR355 < LR532.

We estimated the insecurities of the backscatter and extinction coefficients to run multiple inversions of the microphysical particle properties.

Stable results which did not critically depend on errors in the lidar input data have been found. Most likely the PSC cases consisted of spherical particles with a one-modal distribution around r_eff = 0.35 μm. Note that our inversion code is not limited to a one-modal distribution (see Fig. 43.3) and also [13]. The single scattering albedo at 532 nm was about 0.9 (and lower at 355 nm), and the refraction index was approximately 1.54 + i* 0.02.

References

1. von der Gathen, P., Kivi, R., Wohltmann, I., Salawitch, R.J., Rex, M.: Climate change favours large seasonal loss of Arctic ozone. Nat. Commun. **12**, 3886 (2021). https://doi.org/10.1038/s41467-021-24089-6
2. Poole, L.R.: New insights into polar stratospheric clouds. Eos. **102** (2021). https://doi.org/10.1029/2021EO215001. Published on 18 October 2021.
3. Tritscher, I., Pitts, M.C., Poole, L.R., Alexander, S.P., Cairo, F., Chipperfield, M.P., et al.: Polar stratospheric clouds: satellite observations, processes, and role in ozone depletion. Rev. Geophys. **59**, e2020RG000702 (2021). https://doi.org/10.1029/2020RG000702
4. Hoffmann, A.: Comparative aerosol studies based on multi-wavelength Raman LIDAR at Ny-Ålesund, Spitsbergen. PhD thesis, Univ. Potsdam (2011). https://epic.awi.de/id/eprint/24524/
5. Klett, J.D.: Lidar inversion with variable backscatter/extinction ratios. Appl. Opt. **24/11** (1985). https://opg.optica.org/ao/abstract.cfm?uri=ao-24-11-1638
6. Graßl, S., Ritter, C.: Properties of arctic aerosol based on sun photometer long-term measurements in Ny-Ålesund, Svalbard. Remote Sens. **11**, 1362 (2019). https://doi.org/10.3390/rs11111362
7. Nakoudi, K., Stachlewska, I.S., Ritter, C.: An extended lidar-based cirrus cloud retrieval scheme: first application over an Arctic site. Opt. Express **29/6** (2021). https://opg.optica.org/oe/fulltext.cfm?uri=oe-29-6-8553&id=448923
8. Müller, D., Böckmann, C., Kolgotin, A., Schneidenbach, L., Chemyakin, E., Rosemann, J., Znak, P., Romanov, A.: Microphysical particle properties derived from inversion algorithms developed in the framework of EARLINET. Atmos. Meas. Tech. **9**, 5007–5035 (2016). https://doi.org/10.5194/amt-9-5007-2016
9. Samaras, S., Nicolae, D., Böckmann, C., Vasilescu, J., Binietoglou, I., Labzovskii, L., Toanca, F., Papayannis, A.: Using Raman-lidar-based regularized microphysical retrievals and Aerosol Mass Spectrometer measurements for the characterization of biomass burning aerosols. J. Comput. Phys. **299**, 156–174 (2015). https://doi.org/10.1016/j.jcp.2015.06.045
10. Böckmann, C., Kirsche, A.: Iterative regularization method for lidar remote sensing. Comput. Phys. Commun. **174**, 607–615 (2006)
11. Sedona, R., Hoffmann, L., Spang, R., Cavallaro, G., Griessbach, S., Höpfner, M., Book, M., Riedel, M.: Exploration of machine learning methods for the classification of infrared limb

spectra of polar stratospheric clouds. Atmos. Meas. Tech. **13**, 3661–3682 (2020)
12. Scarchilli, C., Adriani, A., Cairo, F., Di Donfrancesco, G., Buontempo, C., Snels, M., Moriconi, M.L., Deshler, T., Larsen, N., Luo, B., Mauersberger, K., Ovarlez, J., Rosen, J., Schreiner, J.: Determination of polar stratospheric cloud particle refractive indices by use of in situ optical measurements and T-matrix calculations. Appl. Opt. **44**(16) (2005)
13. Ritter, C.A., Burgos, M., Böckmann, C., et al.: Microphysical properties and radiative impact of an intense biomass burning aerosol event measured over Ny-Ålesund, Spitsbergen in July 2015. Tellus B Chem. Phys. Meteorol. **70**(1), 1–23 (2018). https://doi.org/10.1080/16000889.2018.1539618

Chapter 44
Two Decades Analysis of Cirrus Cloud Radiative Effects by LiDAR Observations in the Frame of NASA MPLNET LiDAR Network

Simone Lolli, Erica Dolinar, Jasper R. Lewis, James R. Campbell, Sebastian A. Stewart, Larry R. Belcher, and Ellsworth J. Welton

Abstract Assessing the cirrus cloud radiative effect is crucial to establish their feedback on the Earth-atmosphere system. For this reason, cirrus clouds are of paramount importance in climate. Moreover, these tiny ice clouds are the most common cloud gene, continuously covering 30% of the Earth's surface, peaking to 70% in the tropical and equatorial regions. The same authors, in three different recent studies, assessed the yearly cirrus cloud radiative effects characteristics for other NASA MPLNET permanent observational sites, deployed at different latitudes, e.g., Goddard Space Flight Center, Singapore, and Fairbanks Alaska. The analysis put in evidence that the cirrus cloud can be both cooling and warming agents of the Earth-atmosphere system during the daytime, depending on their latitude. The cirrus clouds are warming agents in equatorial/tropical regions because of the higher averaged solar zenith angle and become neutral at mid-latitudes. At

S. Lolli (✉)
CNR-IMAA, Tito Scalo, Potenza, Italy

SSAI, Lanham, MD, USA
e-mail: simone.lolli@cnr.it; simone.lolli@imaa.cnr.it

E. Dolinar
Naval Research Laboratory, Monterey, CA, USA

J. R. Lewis
GESTAR, Baltimore, MD, USA

NASA GSFC, Greenbelt, MD, USA

J. R. Campbell
GESTAR, Baltimore, MD, USA

S. A. Stewart · L. R. Belcher
SSAI, Lanham, MD, USA

E. J. Welton
NASA GSFC, Greenbelt, MD, USA

© The Author(s), under exclusive license to Springer Nature Switzerland AG 2023

J. T. Sullivan et al. (eds.), *Proceedings of the 30th International Laser Radar Conference*, Springer Atmospheric Sciences,
https://doi.org/10.1007/978-3-031-37818-8_44

polar latitudes, cirrus clouds become cooling agents because of the lower solar zenith angle. In this analysis instead, of using the Fu–Liou–Gu radiative transfer model, we assess how the cirrus cloud radiative effects, at the both top of the atmosphere and surface, changed over twenty years. The analysis is extended also to evaluate also changes in cloud optical depth over the same period. This is unprecedented research, because to our knowledge, no other analysis has been carried out from ground-based measurement for such a long period. As a future perspective, the analysis will be repeated for the different observational sites of the MPLNET LiDAR network to evaluate cirrus cloud radiative effects on a global scale.

Keywords LiDAR · Cirrus clouds · Radiative transfer

44.1 Introduction

Cirrus clouds play a fundamental role in modulating the incoming and outgoing shortwave and longwave radiation. Their net relative effect is still not fully understood. Thanks to the NASA Micropulse LiDAR NETwork (MPLNET [1–6]), a network of LiDAR instruments deployed worldwide. LiDARs are active remote sensing instruments that started to develop after laser invention [7, 8] showing very high temporal and spatial resolution measurements. Those instruments were widely used in the last two decades to study both clouds, aerosols [9–12], and precipitation [13–15]. Thanks to its multi-decade database, it is possible to analyze unprecedented cirrus cloud observations, accounting for more than 20 years of MPLNET LiDAR measurements at Goddard Space Flight (GSFC) Center permanent observational site. Before this study, we assessed the radiative effect over one year at the top of the atmosphere (TOA) of cirrus clouds from other three different permanent MPLNET LiDAR network stations. The observational sites were located at the equator, at-mid-latitudes, and at polar latitudes. In this chapter, instead, we show results analyzing 20 years of cirrus cloud observations in terms of their radiative effects on the Earth-atmosphere system.

44.2 Methodology

MPLNET network LiDARs are commercially available instruments formerly produced by Sigma Space. The instruments are set with a temporal resolution of 1 minute and a spatial resolution of 75 m. (except in some cases when exceptional conditions are met and a higher spatial/temporal resolution is needed). The MPLNET cloud product [16] provides cirrus cloud extinction with the previously specified temporal and spatial resolutions. To account for the possible variability of cirrus clouds, the algorithm uses both 20sr and 30sr for the LiDAR ratio. Profiles that

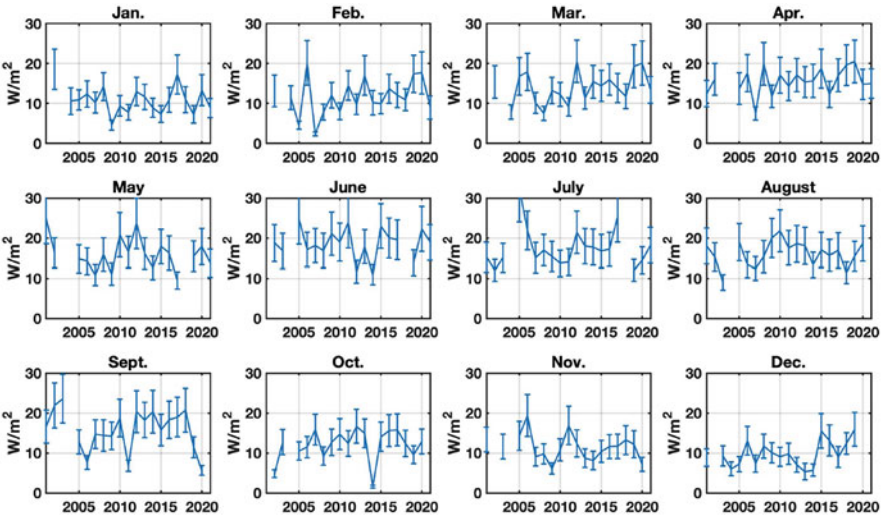


Fig. 44.1 Monthly atmospheric cirrus cloud radiative effect from 2001 to 2021 with relative accuracy. Feb, March, and April clearly show an upward trend. The other months no well-defined trend.

show multiple cloud layers are not considered. The vertically resolved cirrus cloud extinction profile is then converted into optical depth and used as input, among other meteorological variables, in the Fu–Liou–Gu (FLG) radiative transfer code. FLG output gives both the vertically resolved cloud radiative effect (CRE) and the heating rate with a vertical grid matching the LiDAR vertical resolution. The FLG radiative transfer model [17] considers also the effect of water vapor (available from the standard atmosphere atmospheric profile) and ozone present in the atmospheric column. Two simulations are performed: "pristine," where the cirrus clouds were excluded (totally clear conditions), and "total sky," where the cirrus clouds were included. For each run, the US1976 standard summer mid-latitude thermodynamics profile was used. The use of the standard atmosphere implies that the ozone water vapor profile was invariant year-to-year. We are aware that this is a limitation of the proposed methodology as the water vapor absorbs in the near-infrared and this could have an effect on the direct radiative forcing measurements.

44.3 Results

We evaluated the cirrus cloud radiative effects from 2001 to 2021 at NASA Goddard Space Flight Center, a permanent observational site of the MPLNET LiDAR network.

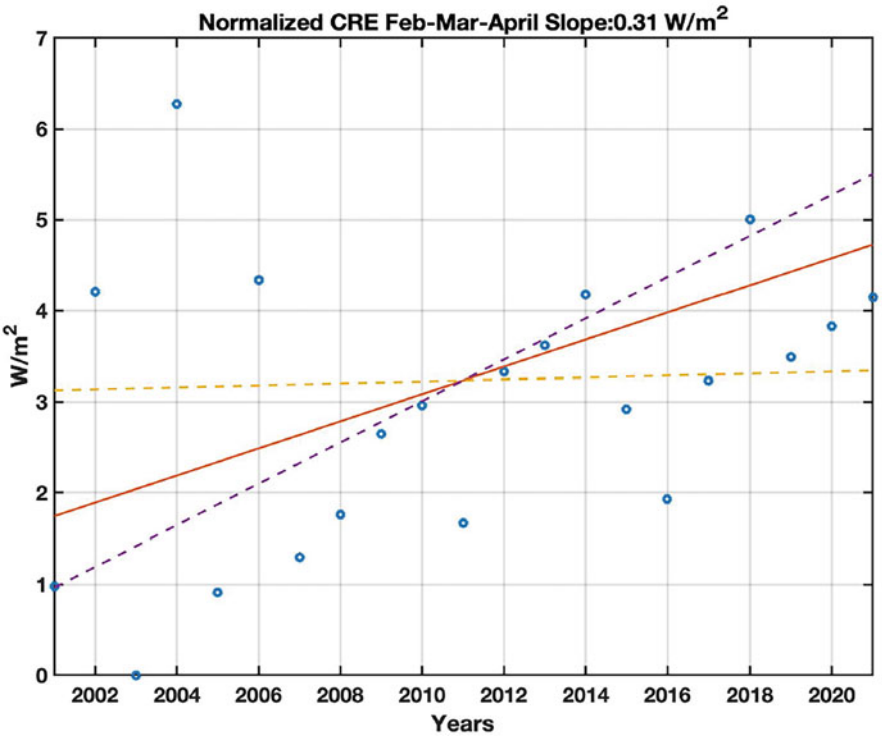


Fig. 44.2 February–March–April analysis shows a well-defined upward trend assessed by Theil–Sein statistics

We aggregated the computed cirrus cloud radiative effect on a month-by-month basis to assess any seasonal variability. To assess the net atmospheric radiative effect, we subtract from TOA CRE the surface CRE. Positive values mean warming of the system Earth-Atmosphere, and negative values a cooling. The results are shown in Fig. 44.1. At first glance, there is an upward trend over the 20 years for February, March, and April. For the other months, it is not so evident.

To check if the trend is statistically significant, we performed the Theil–Sein test with a tolerance of 5% on cirrus cloud observations aggregated during February, March, and April. We found that February and March show a positive trend over the two decades with a slope of 0.31 W/m^2 per year.

The future analysis will assess which factor, among surface albedo, cloud optical depth, and cloud base height, has a bigger impact on the increase of the cirrus cloud radiative effects during the last twenty years. Moreover, considering how much time the cirrus clouds are present in the atmosphere, it will be possible to assess how much those clouds heated the system Earth-atmosphere over the two decades (Fig. 44.2).

Acknowledgments The NASA Micro-Pulse LiDAR Network is supported by the NASA Earth Observing System (S. Platnick) and Radiation Sciences Program (H. Maring).

References

1. Welton, E.J., Campbell, J.R., Spinhirne, J.D., Scott III, V.S.: Global monitoring of clouds and aerosols using a network of micropulse LiDAR systems. In: LiDAR Remote Sensing for Industry and Environment Monitoring, vol. 4153, pp. 151–158. International Society for Optics and Photonics, Bellingham (2003)
2. Welton, E.J., Stewart, S.A., Lewis, J.R., Belcher, L.R., Campbell, J.R., Lolli, S.: Status of the NASA Micro Pulse LiDAR Network (MPLNET): overview of the network and future plans, new version 3 data products, and the polarized MPL. In: EPJ Web of Conferences, vol. 176, p. 09003. EDP Sciences, Les Ulis (2018)
3. Campbell, J.R., et al.: Full-time, eye-safe cloud and aerosol LiDAR observation at atmospheric radiation measurement program sites: Instruments and data processing. J. Atmos. Oceanic Technol. **19**(4), 431–442 (2002)
4. Lolli, S., Di Girolamo, P.: Principal component analysis approach to evaluate instrument performances in developing a cost-effective reliable instrument network for atmospheric measurements. J. Atmos. Oceanic Technol. **39**(2), 1642–1649 (2015)
5. Lolli, S.: Is the air too polluted for outdoor activities? Check by using your photovoltaic system as an air-quality monitoring device. Sensors **21**, 6342 (2021)
6. Lolli, S., Vivone, G., Lewis, J.R., Sicard, M., Welton, E.J., Campbell, J.R., Comerón, A., D'Adderio, L.P., Tokay, A., Giunta, A., Pappalardo, G.: Overview of the new version 3 NASA Micro-Pulse LiDAR Network (MPLNET) automatic precipitation detection algorithm. Remote Sens. **12**(1), 71 (2019)
7. Ciofini, M., Lapucci, A., Lolli, S.: Diffractive optical components for high power laser beam sampling. J. Opt. A Pure Appl. Opt. **5**(3), 186 (2003)
8. Lolli, S., Sauvage, L., Loaec, S., Lardier, M.: EZ LiDAR™: a new compact autonomous eye-safe scanning aerosol LiDAR for extinction measurements and PBL height detection. Validation of the performances against other instruments and intercomparison campaigns. Optica pura y aplicada **44**(1), 33–41 (2011)
9. Vivone, G., Arienzo, A., Bilal, M., Garzelli, A., Pappalardo, G., Lolli, S.: A dark target Kalman filter algorithm for aerosol property retrievals in urban environment using multispectral images. Urban Clim. **43**, 101135 (2022)
10. Landi, T.C., Bonasoni, P., Brunetti, M., Campbell, J.R., Marquis, J.W., Di Girolamo, P., Lolli, S.: Aerosol direct radiative effects under cloud-free conditions over highly-polluted areas in europe and mediterranean: a ten-years analysis (2007–2016). Remote Sens. **13**(15), 2933 (2021)
11. Lolli, S., Sauvage, L., Loaec, S., Lardier, M.: EZ LiDAR™: A new compact autonomous eye-safe scanning aerosol LiDAR for extinction measurements and PBL height detection. Validation of the performances against other instruments and intercomparison campaigns. Optica pura y aplicada **44**(1), 33–41 (2011)
12. Vivone, G., D'amico, G., Summa, D., Lolli, S., Amodeo, A., Bortoli, D., Pappalardo, G.: Atmospheric boundary layer height estimation from aerosol LiDAR: a new approach based on morphological image processing techniques. Atmos. Chem. Phys. **21**(6), 4249–4265 (2021)
13. Campbell, J.R., Dolinar, E.K., Lolli, S., Fochesatto, G.J., Gu, Y., Lewis, J.R., Marquis, J.W., McHardy, T.M., Ryglicki, D.R., Welton, E.J.: Cirrus cloud top-of-the-atmosphere net daytime forcing in the Alaskan subarctic from ground-based MPLNET monitoring. J. Appl. Meteorol. Climatol. **60**(1), 51–63 (2021)
14. Lolli, S., Di Girolamo, P., Demoz, B., Li, X., Welton, E.J.: Rain evaporation rate estimates from dual-wavelength LiDAR measurements and intercomparison against a model analytical solution. J. Atmos. Oceanic Technol. **34**(4), 829–839 (2017)

15. Zheng, Z., et al.: Diurnal variation of summer precipitation modulated by air pollution: observational evidences in the Beijing metropolitan area. Environ. Res. Lett. **15**(9), 094053 (2020)
16. Lewis, J.R., et al.: Determining cloud thermodynamic phase from the polarized Micro Pulse LiDAR. Atmos. Measure. Tech. **13**(12), 6901–6913 (2020)
17. Lolli, S., et al.: Monsoon season quantitative assessment of biomass burning clear-sky aerosol radiative effect at surface by ground-based LiDAR observations in Pulau Pinang, Malaysia in 2014. Remote Sens. **11**(22), 2660 (2019)

Chapter 45
Temporal Variability of the Aerosol Properties Using a Cimel Sun/Lunar Photometer over Thessaloniki, Greece: Synergy with the Upgraded THELISYS Lidar System

K. Michailidis, K. A. Voudouri, N. Siomos, and D. Balis

Abstract The main objective of this study is to assess the lidar-derived aerosol optical depth retrievals from the upgraded lidar system by comparing them with the new well-established sun-sky-lunar photometric measurements (CIMEL 318-T), located in the Laboratory of Atmospheric Physics (LAP), at Thessaloniki, Greece. The two instruments represent two individual networks, the European Lidar Aerosol Network (EARLINET) and the Aerosol Robotic Network (AERONET) following different measurement schedules. Thessaloniki lidar system (THELISYS; Raymetrics LR321-D400), part of the EARLINET, has been recently upgraded regarding its operational wavelengths and the detection configuration. Commissioning of the upgraded system operation started in October 2021. The new sun-lunar photometer (CE-318T) is capable to perform a complete cycle of diurnal photometric measurements at both day- and nighttime. The new improvements of this new device permit this new photometer version to extend the photometric information at nighttime using the moon as a light source. Quality-assured cases in cloudy-free conditions are selected to demonstrate the synergistic performance of the two instruments. Timeseries of the AOD measured by lidar and sun/lunar photometer provide a long-term aerosol monitoring for the investigation of the amount, sources, and atmospheric processes over Thessaloniki.

Keywords Lidar · THELISYS · EARLINET · AERONET · Direct sun-lunar photometry

K. Michailidis (✉) · K. A. Voudouri · D. Balis
Laboratory of Atmospheric Physics, Aristotle University of Thessaloniki, Thessaloniki, Greece
e-mail: komichai@auth.gr; kavoudou@physics.auth.gr; balis@auth.gr

N. Siomos
Meteorological Institute, Ludwig Maximilian Universitδt Mónchen, Munich, Germany
e-mail: Nikolaos.Siomos@physik.uni-muenchen.de

© The Author(s), under exclusive license to Springer Nature Switzerland AG 2023

J. T. Sullivan et al. (eds.), *Proceedings of the 30th International Laser Radar Conference*, Springer Atmospheric Sciences,
https://doi.org/10.1007/978-3-031-37818-8_45

45.1 Study Site and Instrumentation

Thessaloniki station – LAP (Laboratory of Atmospheric Physics), member of ACTRIS/EARLINET [1] – is a crossroads of long-range-transported pollution with complex nature, consisting of both natural and anthropogenic constituents [2]. LAP is located in the Physics Department of the Aristotle University of Thessaloniki, Greece (40.63°N, 22.96°E) at an elevation of 60 m. The background aerosol load is mostly characterized of urban, traffic-related particles, and marine aerosols. Among other atmospheric research instruments, the station operates a multispectral Raman/depolarization lidar system and a Cimel sun-lunar photometer (Fig. 45.1). Both instruments have been upgraded during 2021, in the frame of PANACEA, which is part of the Greek National Research Infrastructure for aerosol research, under the umbrella of the Euro-pean Strategy Forum on Research Infrastructures (ESFRI).



Fig. 45.1 Location of the Laboratory of Atmospheric Physics station in Thessaloniki (40.63°N, 22.96°E)

45.1.1 The Thessaloniki Lidar System (THELISYS)

Thessaloniki lidar system (THELISYS) is part of the multitype ground-based instruments that belong to the LAP and member station of EARLINET since 2000. THELISYS is a Raman and depolarization lidar with channels for elastic backscattering at 355, 532, and 1064 nm, and two channels for inelastic N2-Raman scattering at 387 and 607 nm. The linear depolarization ratio of particles (δ_p) is derived from two channels at 532 nm, separating co- and cross polarization. Knowledge of the particle lidar ratio (S_λ) and the particle linear depolarization ratio (δ_λ) for different aerosol types allows for aerosol typing and aerosol-type separation in lidar measurements. The optical design of THELISYS lidar allows the retrieval of aerosol profiles quite close to the ground, providing full overlap above 500 m depending on field stop adjustments and amplifier settings. The system was finally upgraded during June 2021 by Raymetrics S.A. In addition, a new Nd-YAG laser system (SpitLight 400, InnoLas, Germany) has been installed on March 2022, operating at 1064 nm, 532 nm and 355 nm with a repetition rate of 20 Hz. All the quality standards esablished within EARLINET stations have been followed, in order to assure that THELISYS is able to provide high-quality products. The internal checkup procedures including telecover test for the near-range Rayleigh fit for the far range and depolarization calibration test. Quality assurance (QA) tests [3] are important and performed at least once per month as well as after each major system upgrade and change in the system configuration.

45.1.2 CIMEL Sun/Lunar Photometer (AERONET)

A new sun-sky-lunar photometer (CE318-T) is operating at "Thessaloniki" AERONET (http://aeronet.gsfc.nasa.gov) site since June 2021. This type of instrument is able to perform daytime and nighttime photometric measurements using the sun and the moon as light source. Therefore, this new device permits a complete cycle of diurnal aerosol measurements valuable to enhance atmospheric monitoring to be extracted. The new sun-sky-lunar Cimel CE318-T photometer has been developed in order to perform both daytime and nighttime (lunar) measurements and providing additional and enhanced operational functionalities compared with the standard AERONET sun photometer, extensively described in [4]. Due to the low signal in the UV channels at night, AOD cannot be obtained, and therefore, UV information is restricted to the daylight period. The technical specifications of the instrument and AERONET data products are given in detail in [5].

45.2 Data and Methodology

AERONET sun-sky-lunar photometer measurements performed along almost 1 year (June 2021–April 2022) are analyzed in this study. AODs at 340 and 380 nm cannot be obtained at nighttime because of the low signal in the UV channels, and in the frame of this analysis, we use only AOD values at 440 nm. Results reported in this study are based on Level 1.5 day-data from the V3 Direct Sun Algorithm and Level 1.5 night-data from the V3 Direct Moon Algorithm. We are aware that some anomalies could be found in the "provisional" lunar data. For comparison reasons, since the CIMEL photometer doesn't operate in the same wavelengths as the lidar, we convert the integrated backscatter to AOD values. In order to calculate the AOD from the lidar observations, the Klett-Fernald (KF) method [6, 7] and the Raman method [8] were utilized for daytime and nighttime measurements, respectively. The Fernald method needs the assumption of a lidar ratio, which is dependent on aerosol types. During daytime, the KF inversion is applied and the backscatter coefficient profiles at 355, 532, and 1064 nm are calculated. To invert the elastic lidar equation, it is necessary to assume proper climatological values for the lidar ratio parameter. In this study a constant a priori climatological values of 60, 50, and 40sr for 355, 532, and 1064 nm were used, respectively. The Raman method can achieve better accuracy, because it does not need the critical assumption of lidar ratio. The lidar ratio values also indicate the prevalence of mixed aerosols over Thessaloniki, mainly of marine and anthropogenic origin [2]. For the calculation of the optical depth below the lower limit of the corrected profile, assumptions have been made that the value at the lowest height of the extinction profile is representative down to the surface. The lowermost trustworthy value of the extinction coefficient was assumed constant (height-independent) and also representative of the aerosol load in the overlap region.

45.3 Results

45.3.1 Case Study: 20 October 2021

An example of continuous measurements performed by the upgraded THELISYS lidar along with the CE318-T Sun/Sky/Lunar photometer at Thessaloniki station presented below for 20 October 2021. The aerosol optical properties are presented in order to demonstrate the systems performance. Increased backscatter and extinction values were observed on this day over Thessaloniki at an altitude range between 0.6 and 2.2 km a.s.l., which could be attributed to polluted continental particles and polluted dust. The extinction and backscatter coefficients at 355 and 532 were calculated using the Raman technique, and in the case of the FK method, an assumption of climatological LR values is considered. In Fig. 45.2 (left), we present the temporal evolution from 05:00 to 02:00 UTC on 20 October 2021 of the aerosol

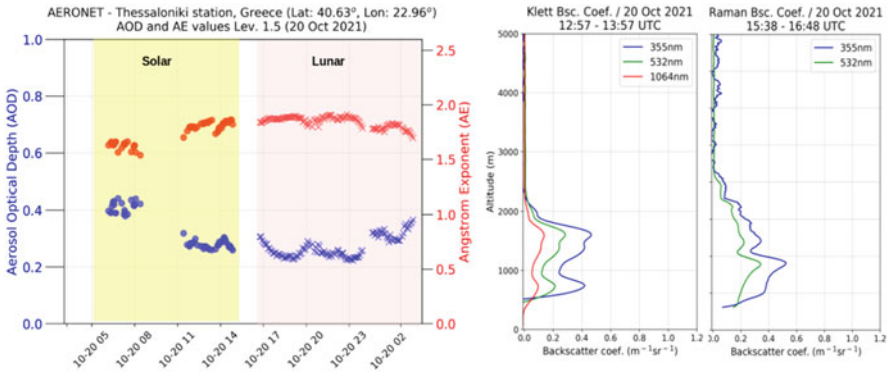


Fig. 45.2 (Left) Time evolutions of the aerosol optical depth (at 440) and the Angstrom exponent parameter (at 440–870 nm) derived by Cimel 318-T, on 20 October 2021. (Right) Aerosol backscatter coefficient profiles using KF and Raman method

optical depth and the Ångström exponent (AE) over Thessaloniki AERONET site. The results from the CE318-T are in a good agreement with a mean AOD at 440 nm of 0.327 ± 0.065 and 0.269 ± 0.0.36 and a mean AE at 440–870 nm of 1.74 ± 0.09 and 1.84 ± 0.05, respectively. Both results indicate the presence of fine mode particles. The AOD retrievals from KF and Raman procedures are found equal to 0.41 and 0.24, respectively. Figure 45.2 (right) depicts the mean aerosol backscatter profiles at 355, 532, and 1064 nm derived from THELISYS this day.

45.3.2 Variability of AERONET AOD and Comparison with THELISYS

Here we analyze the 1-year variability of the AOD at 440 nm during the study period from June 2021 to April 2022. Figure 45.3 presents the temporal evolution of the aerosol optical depth over Thessaloniki AERONET site for the study period. Figure 45.3 (right) presents the distribution of the AOD differences between solar/lunar measurements. The mean value of the AOD difference is found 0.005 (±0.091), which corresponds to the estimated AOD absolute uncertainty for AERONET field instruments.

Figure 45.3 shows the AOD at 440 nm for all the analyzed measurements, covering almost one year. The AOD obtained from direct sun and lunar values at 440 nm span the 0.04–0.98 and 0.03–0.76 range, respectively. As can be seen, AOD in Thessaloniki is usually low, with average AOD at 440 nm of 0.22 ± 0.12 for direct sun and 0.23 ± 0.14 for lunar, respectively, with occasional larger values related to Saharan dust intrusions. In addition, the mean AE440-870 is 1.49 ± 0.45 for direct sun and 1.55 ± 0.48 for lunar observations, indicating small aerosols produced

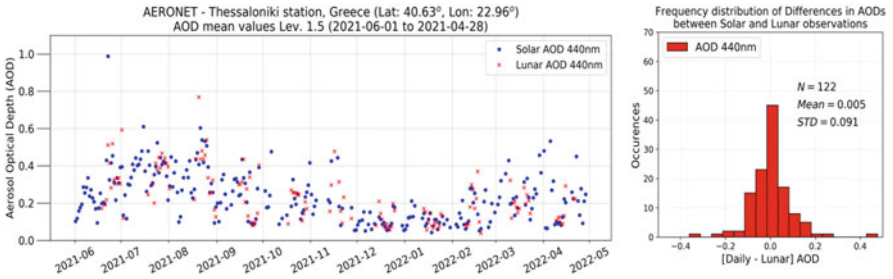


Fig. 45.3 (Left) Time evolution of the direct sun (blue) and lunar (red) instantaneous mean AODs at 440 nm for the study period. (Right) Direct sun and lunar AOD difference

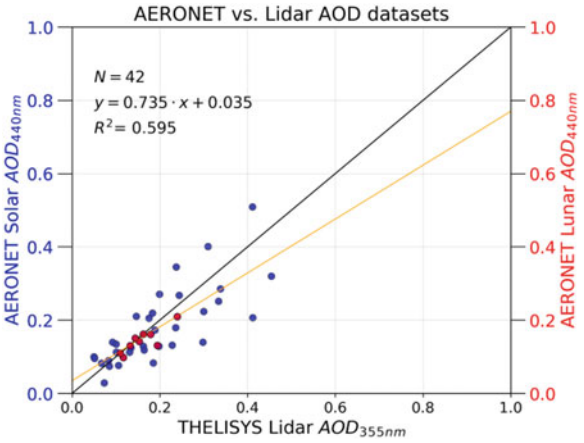


Fig. 45.4 Comparison of the AOD (440) obtained from the Lev. 1.5 AERONET solar and lunar data against AOD (at 340 nm) from lidar extinction profiles during the study period (42 cases)

mainly by urban pollution, with occasional reductions to 0.2 in coincidence with transport of Saharan dust to the site. Scatterplot of Fig. 45.4 shows the direct comparison of the optical depths values at 355 nm derived from the lidar against the closest in time AOD at 440 nm from CIMEL. A total of 42 common cases were analyzed and compared. A fair agreement is found, with a slope of 0.6 (best-fit straight line, yellow line).

To compare the two AOD datasets, we selected the time closest AOD values from AERONET to the lidar measurement time. The variability between the two datasets is caused by spatiotemporal-varying aerosol conditions and variations in the wavelength dependence of AOD at 355 and 440 and, therefore, in the aerosol size distribution. Lidar misalignment of the far-range sensing also causes some signal noise in the lidar data. Moreover, the lidar system is notable to probe the lower part (0–700 m) of the atmosphere, where an important fraction of aerosol particles is present. During days of high air pollution loads in the PBL, the difference between the lidar- and Cimel-derived AODs becomes significant.

45.4 Conclusions

In this paper, we compared the AOD measured by the upgraded lidar system and AERONET sun-lunar photometer in Thessaloniki for a selected study period between June 2021 and April 2022. A total of 42 common cases are compared. The results presented here constitute the first comparison of the AOD load derived by two upgraded CIMEL 318-T and lidar system at Thessaloniki station. In general, the AOD lidar retrievals show reasonable agreement (R2 = 0.6) with the data retrieved from CIMEL observations. Results on day-to-night-retrieved aerosol parameters from sun-lunar photometer are also presented and discussed. Further analysis of a more extended period is planned.

Acknowledgments We acknowledge support of this work by the project "PANhellenic infrastructure for Atmospheric Composition and climatE change" (MIS 5021516), which is implemented under the Action "Reinforcement of the Research and Innovation Infrastructure," funded by the Operational Programme "Competitiveness, Entrepreneurship and Innovation" (NSRF 2014-2020) and co-financed by Greece and the European Union (European Regional Development Fund).

References

1. Pappalardo, et al.: EARLINET: towards an advanced sustainable European aerosol lidar network. Atmos. Meas. Tech. **7**, 2389–2409 (2014)
2. Siomos, N., et al.: Are EARLINET and AERONET climatologies consistent? The case of Thessaloniki, Greece. Atmos. Chem. Phys. **18**, 11885–11903 (2018)
3. Freudenthaler, V. et al.: EARLINET lidar quality assurance tools, Atmos. Meas. Tech. Discuss. (2018). https://doi.org/10.5194/amt-2017-395, in review
4. Holben, B.N., et al.: AERONET–A federated instrument network and data archive for aerosol characterization. Remote Sens. Environ. **66**, 1–16 (1998)
5. Barreto, A., et al.: A new method for nocturnal aerosol measurements with a lunar photometer prototype. Atmos. Meas. Tech. **6**, 585–598 (2013)
6. Klett, J.D.: Stable analytical inversion solution for processing lidar returns. Appl. Opt. **20**, 211–220 (1981)
7. Fernald, F.G.: Analysis of atmospheric lidar observations: some comments. Appl. Opt. **23**, 652–653 (1984)
8. Ansmann, A., et al.: Combined Raman elastic-backscatter LIDAR for vertical profiling of moisture, aerosol extinction, backscatter, and LIDAR ratio. Appl. Phys. B. **55**, 18 (1992). https://doi.org/10.1007/BF00348608

Chapter 46
Long-Term Changes of Optical Properties of Mineral Dust and Its Mixtures Derived from Raman Polarization Water Vapor Lidar in Central Europe

D. M. Szczepanik, W. Kumala, C. F. Olusegun, E. Tetoni, V. Amiridis, D. Nicolae, D. Althausen, and I. Stachlewska

Abstract A comparative analysis of long-range inflows of desert dust and its mixtures over Central Poland, in particular optical properties, were obtained from lidar surveys. The mineral dust inflows over Warsaw were identified based on lidar measurements and three independent models (HYSPLIT, BSC-DREAM8b, and NAAPS), which resulted in preparing unique database of optical properties of mineral dust and its mixtures. This has a potential to be used for further studies of aerosol microphysical properties. Aerosol properties during inflows were also analyzed in relation to meteorological parameters and local climatic data revealing an increase in the number and duration of observed episodes of mineral dust

D. M. Szczepanik (✉) · W. Kumala · C. F. Olusegun · I. Stachlewska
Faculty of Physics, University of Warsaw (UW), Warsaw, Poland
e-mail: dominika.szczepanik@fuw.edu.pl; wojciech.kumala@fuw.edu.pl; christiana.olusegun@fuw.edu.pl; iwona.stachlewska@fuw.edu.pl

E. Tetoni
Institut für Physik der Atmosphäre, Deutsches Zentrum für Luft- und Raumfahrt (DLR), Oberpfaffenhofen, Germany
e-mail: eleni.tetoni@dlr.de

V. Amiridis
Institute for Astronomy, Astrophysics, Space Applications and Remote Sensing (IAASARS), National Observatory of Athens, Penteli, Greece
e-mail: vamoir@noa.gr

D. Nicolae
Research Institute for Analytical Instrumentation, National Institute for Research and Development of Optoelectronics Bucharest INOE 2000, Cluj-Napoca, Romania
e-mail: nnicol@inoe.ro

D. Althausen
Leibniz Institute for Tropospheric Research (TROPOS), Leipzig, Germany
e-mail: dietrich@tropos.de

© The Author(s), under exclusive license to Springer Nature Switzerland AG 2023

J. T. Sullivan et al. (eds.), *Proceedings of the 30th International Laser Radar Conference*, Springer Atmospheric Sciences,
https://doi.org/10.1007/978-3-031-37818-8_46

intrusions over Poland. Optical properties of mineral dust vary with the amount and type of admixtures of other aerosols.

Keywords Mineral dust · Aerosol · Lidar · Remote sensing · Depolarization

46.1 Introduction

Deserts are one of the major natural sources of the atmospheric aerosol system. Large amounts of the mineral dust lifted from a dry surface can be advected over long distances in the free troposphere. Therefore, it can be observed in different places over the globe, even very far from the source [1]. Desert dust influences climatic and environmental conditions in several ways. It can affect climate both directly and indirectly: first, by scattering and absorbing the incoming solar and outgoing terrestrial radiation fluxes [2], and second, by causing the changes in the cloud cover, acting as cloud condensation nuclei [3]. This indirect effect can influence the optical properties and lifetime of cloud and may reduce the precipitation as well, leading to the prolonged periods of droughts [4]. The primary source of mineral dust observed over Eastern and Southern Europe originates either from the Sahara or Middle East deserts.

Due to climate change, we observe more dynamical weather patterns like prolonged periods of droughts or heatwaves hitting all over the globe. Such changes may lead to questions like: do we observe any changes concerning the dust transport intensity and pathways? Can we improve dust prediction models? Are we able to warn the aviation of the possible occurrences of dust plumes which locally can reduce the visibility? Our study and similar ones may give a possibility to answer such questions.

46.2 Methodology

For this study, we took the data collected between July 2013 and December 2020 with the eight-channel next-generation Polly^{XT} lidar (details in [5]) at the Remote Sensing Laboratory (RS-Lab), Institute of Geophysics, Faculty of Physics, University of Warsaw. The data quick look plots, available via the PollyNET Website (http://polly.tropos.de), were explored to find the possible cases of mineral dust observation.

Typical fingerprints of the desert dust are high depolarization observed in the free troposphere and raised air temperatures observed during the inflow since the air masses originated from the subtropical area. The mineral dust inflows over Warsaw were identified manually, based not only on lidar and meteorological measurements but also on the three independent models: backward trajectory model - HYSPLIT; mineral dust prediction model - BSC-DREAM8b; and aerosol prediction model -

NAAPS. The HYSPLIT model [6] enables the estimation of a possible source of detected aerosol. It was used with the reanalysis meteorological data, calculating the trajectories of the air masses within the observed aerosol layer, lasting 120 h and ending in Warsaw. The BSC-DREAM8b model [7] predicts the life cycle of the eroded desert dust in the atmosphere providing maps of aerosol optical thickness caused by it (https://dust.aemet.es/products/daily-dust-products). Finally, the NAAPS model [8] enables determination of the possible presence of other aerosol types.

The measurements performed according to the recommendation of the EARLINET lidar network of the ACTRIS research infrastructure allowed the recovery of high-quality sets of profiles ($3\beta + 2\alpha + 2\delta$). Lidar data were analyzed both manually with Verlauf software [9] and semi-automatically with the Single Calculus Chain (SCC) web interface [10]. Both methods allowed for applying the classical Raman approach, which enables obtaining the particle backscattering (β at 1064, 532, and 355 nm) and extinction (α at 532 and 355 nm) coefficients profiles independently, with the only assumption of the Ångström exponent (AE = 1). The particle depolarization ratio profiles (δ at 532 and 355 nm) were obtained using the $\pm 45°$ calibration method. All profiles were calculated with a temporal resolution of 30, 45, or 60 min with 7.5 m vertical resolution and smoothed with a running mean of 49 and 101 range-bins for β- and α-related profiles, respectively. More detailed information on the methodology used can be found in Szczepanik et al. [11].

46.3 Results

During the discussed period (07/2013–12/2020), we described 20 independent mineral dust inflows. Analysis of the results presented in Fig. 46.1 reveals that the number of dust observations over Warsaw is getting higher from one to two episodes per year before 2017 to even six cases in 2019 (with June strewn with days with mineral dust presence in the free troposphere over Warsaw). The length of the observed dust inflow is getting longer starting from 2016 and reaching up to 36 h of mineral dust observations per event. What have to be stressed here, some periods might be underestimated with a number of mineral dust episodes, for example, autumn 2020, when the lidar was not operating for a month due to technical issues, while the prediction models (BSC-DREAM8b and NAAPS) were likely showing the Saharan dust presence over Central and Western Europe. Meteorological conditions, like temperatures significantly higher than the typical temperatures for autumn in Warsaw, make it more likely that we were missing some mineral dust occurrences.

For the identified cases of mineral dust observation in the free troposphere over Warsaw, we obtained 120 sets of profiles containing at least backscattering and particle depolarization coefficients. For all the cases, we selected three groups. One called MD for pure mineral dust occurrence when HYSPLIT backward trajectories suggested uniform inflow from desert regions, and the NAAPS model did not indicate any other aerosol type. Second, called MD+S for cases when the NAAPS

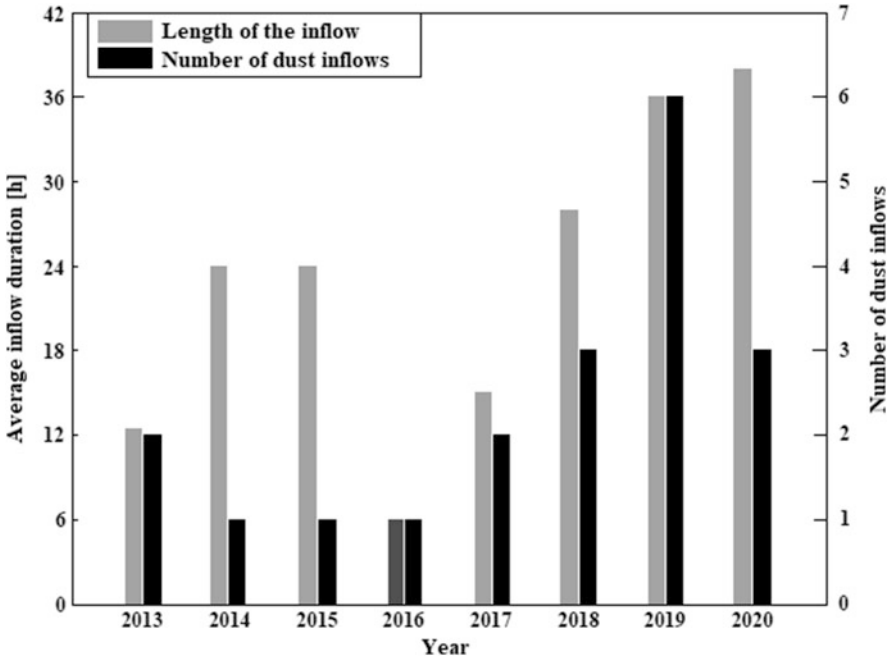


Fig. 46.1 Histogram showing the number of inflows and their average duration for the identified episodes of the desert dust inflow over Warsaw

Table 46.1 Average values of optical properties and layer height for pure desert dust (MD) and its mixtures with sulfates (MD+S) and with aerosol originating from biomass combustion (MD+BB) observed over Warsaw in 2013–2020

Parameter	MD	MD+S	MD+BB
β 355 nm [$Mm^{-1}sr^{-1}$]	1.60 ± 0.76	1.32 ± 0.92	3.16 ± 0.85
β 532 nm [$Mm^{-1}sr^{-1}$]	1.22 ± 0.50	0.93 ± 0.53	1.80 ± 0.80
β 1064 nm [$Mm^{-1}sr^{-1}$]	0.82 ± 0.49	0.45 ± 0.31	1.08 ± 0.57
α 355 nm [Mm^{-1}]	69 ± 29	78 ± 41	248 ± 73
α 532 nm [Mm^{-1}]	48 ± 16	49 ± 28	173 ± 85
δ 355 nm [%]	10.53 ± 3.86	6.77 ± 2.99	2.23 ± 0.83
δ 532 nm [%]	15.46 ± 5.49	10.79 ± 3.22	4.49 ± 2.16

model shows the possible presence of sulfates and dust. The last group – MD+BB – covers the profiles of the atmosphere when the air was transporting both mineral dust and biomass burning aerosol. Typical values of the optical properties of the aerosol are presented in Table 46.1.

As one can see, the presence of additional aerosol types affects the optical properties of mineral dust. An additive of the sulfates slightly lowers every discussed optical property given in Table 46.1. In the case of biomass burning admixture, α values are significantly higher than in two other groups, which might have been

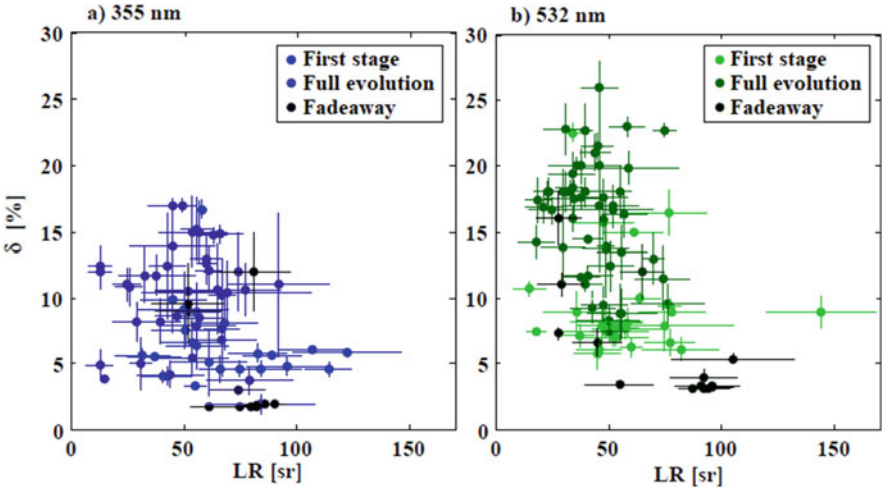


Fig. 46.2 Depiction of δ vs. LR for 355 nm (left panel) and 532 nm (right panel) depending on inflow development. The number of points is 120 for 532 nm and 83 for 355 nm

caused by the absorbing properties of biomass burning aerosol. The lowest values of the δ result from the shape of the biomass burning aerosol, which is more likely spherical than dust. The amount of the additive may also play a role here, but it is hard to estimate this. What can be interesting is that the δ values for clean mineral dust are lower than for the dust observed close to the source [1].

Last but not least, we tried to track the changes in the values of the δ and lidar ratio (LR) of the aerosol depending on the stage of the inflow evolution. The results of this analysis is depicted in Fig. 46.2. The highest values of the δ are observed during the full evolution of the dust inflow, while the lowest occur during the fadeaway phase. Another feature of this figure is a kind of grouping of the points — for the first stage and the full evolution of the inflow (more visible for 532 nm). Some outlying points stands for the cases of observation of mixture of dust with another aerosol.

46.4 Conclusions

The rising number of mineral dust inflows over Central and Eastern Europe with higher intensity of the inflow may be one of the evidences of the ongoing climate change impacts. The climate-dust feedback will probably play a more and more important role in this region of the globe. A higher amount of longer mineral dust inflow episodes may lead to prolonged periods of drought due to dust influence on cloud and precipitation formation.

The values of the δ for clean mineral dust are lower than for the dust observed close to the source which can suggest that long-range transport is lowering the number of coarse mineral dust grains arriving in Central Europe. It can be explained by the gravitational sedimentation of the largest particles. This may be also caused by the aerosol hydration, which strongly affects the shape of the grains.

The presence of the additive aerosol within observed mineral dust layers changes the observed optical properties of the mixture. It may cause lower values of delta when adding spherical-shape aerosol grains. Higher extinction and, as a result, LR may be caused by aerosol strongly absorbing light.

It is important to track the event evolution since the observed changes in the aerosol optical properties may give information about the intensity of the aerosol transport as well as the processes of the gravitational sedimentation. Observing such processes over one lidar station gives a chance to expand the study to different stations over the pathway of air masses movement to better understand the processes ongoing during the aerosol transport.

Acknowledgments The work was done within the European Commission grants: ACTRIS (no. 262254), ACTRIS-2 (no. 654109), and ACTRIS PPP (no. 739530). The work was developed in a scientific collaboration between the Faculty of Physics of the University of Warsaw (FUW) and the Leibniz Institute of Tropospheric Research (TROPOS) in the frame of the Polish Foundation of Science and Technology (GrantNo.519/FNITP/115/2010). The lidar signals within this paper were evaluated according to the Quality Assurance (QA) and Quality Control (QC) procedures of the ACTRIS-EARLINET Data Base. We thank Volker Freudenthaler at the MIM-LMU for evaluating the QA tests and Lucia Mona at the IMMA-CNR for running the QC procedures. Authors acknowledge the vital support from the IMAA CNR for the Single Calculus Chain provision and development.

We gratefully acknowledge the NOAA Air Resources Laboratory (ARL) for the provision of the HYSPLIT transport and dispersion model and/or READY website (https://www.ready.noaa.gov) used in this study, as well as the NAAPS model output obtained via NRL/Monterey Aerosol Page (https://www.nrlmry.navy.mil/), and the BSC-DREAM8b Barcelona Supercomputing Center which were used via webpage https://ess.bsc.es/bsc-dust-daily-forecast.

The research was funded by the project Preludium 19: Study of differences in optical and microphysical properties of local agricultural dust and long range transported desert dust. no: 2020/37/N/ST10/02682.

References

1. Mamori, R.E., Ansmann, A.: Fine and coarse dust separation with polarization lidar. Atmos. Meas. Tech. **7**, 3717–3735 (2014)
2. Granados-Muñoz, M.J.: Impact of mineral dust on shortwave and longwave radiation: evaluation of different vertically resolved parameterizations in 1-D radiative transfer computations. Atmos. Chem. Phys. **19**, 523–542 (2019)
3. Karydis, V.A.: On the effect of dust particles on global cloud condensation nuclei and cloud droplet number. J. Geophys. Res. **116**, D23204 (2011)
4. Schepanski, K.: Transport of mineral dust and its impact on climate. Geosciences. **8**, 151 (2018)

5. Engelmann, R.: The automated multiwavelength Raman polarization and water-vapor lidar PollyXT: the next generation. Atmos. Meas. Tech. **9**, 1767–1784 (2016)
6. Stein, A.F.: NOAA's HYSPLIT atmospheric transport and dispersion modeling system. Bull. Am. Meteorol. Soc. **96**(12), 2059–2077 (2015)
7. Basart, S.: Development and evaluation of the BSC-DREAM8b dust regional model over Northern Africa, the Mediterranean and the Middle East. Tellus B. **64**, 1–23 (2012)
8. Maciszewska, A.: A multiyear analysis of aerosol optical thickness over Europe and Central Poland using NAAPS model simulation. Acta Geophys. **58**(6), 1147–1163 (2010)
9. Baars, H.: An overview of the first decade of Polly NET: an emerging network of automated Raman-polarization lidars for continuous aerosol profiling. Atmos. Chem. Phys. **16**, 5111–5137 (2016)
10. Mattis, I.: EARLINET single calculus chain – technical – Part 2: calculation of optical products. Atmos. Meas. Tech. **9**, 3009–3029 (2016)
11. Szczepanik, D.M.: Properties of Saharan Dust versus Local Urban Dust – a case study. Earth Space Sci. **8**(12) (2021)

Chapter 47
Planetary Boundary Layer Height Measurements Using MicroPulse DIAL

Luke Colberg, Owen Cruikshank, Kevin S. Repasky, Scott M. Spuler, Robert A. Stillwell, and Matthew Hayman

Abstract The MicroPulse DIAL (MPD) is a diode-laser-based instrument for thermodynamic profiling in the lower troposphere. These instruments are eye-safe, low-cost, and can operate unattended, making them well-suited for network deployment. These instruments combine the differential absorption lidar and the high-spectral-resolution lidar techniques to provide range-resolved vertical profiles of atmospheric water vapor, temperature, and aerosol optical properties. As these instruments are deployed for field experiments, efforts are being made to add additional data products, such as the planetary boundary layer height (PBLH). This chapter describes a technique for using MPD-measured aerosol and water vapor profiles to locate the PBLH.

Keywords Planetary boundary layer height · High-spectral-resolution lidar · Differential absorption lidar

47.1 Introduction

The planetary boundary layer (PBL) is the lowest layer in the Earth's atmosphere that is affected by surface conditions on the time scale of minutes to an hour [1]. The planetary boundary layer height (PBLH) is the vertical extent of the PBL.

L. Colberg (✉) · O. Cruikshank
Montana State University, Electrical and Computer Engineering Department, Bozeman, MT, USA
e-mail: luke.colberg@student.montana.edu

K. S. Repasky
Montana State University, Electrical and Computer Engineering Department, Bozeman, MT, USA

National Center for Atmospheric Research, Earth Observing Laboratory, Boulder, CO, USA

S. M. Spuler · R. A. Stillwell · M. Hayman
National Center for Atmospheric Research, Earth Observing Laboratory, Boulder, CO, USA

© The Author(s), under exclusive license to Springer Nature Switzerland AG 2023

J. T. Sullivan et al. (eds.), *Proceedings of the 30th International Laser Radar Conference*, Springer Atmospheric Sciences,
https://doi.org/10.1007/978-3-031-37818-8_47

The PBLH strongly affects PBL processes such as turbulent mixing and convective transport. Additionally, the PBLH is a critical factor in the vertical mixing of surface pollutants. Therefore, the PBLH is an essential parameter in numerical weather forecasting and forecasting pollution events [2–4]. However, the PBLH is difficult to measure. The PBLH follows a diurnal cycle driven by the sensible heat flux of the Earth's surface, and it varies widely from day to day. Radiosondes from the global radiosonde network only provide two PBLH estimates per day, failing to capture the temporal variation and daily cycle in its entirety. Lidar instruments provide the opportunity to continuously monitor the PBLH, capturing the daily cycle and temporal variation.

Ground-based lidar can monitor the PBLH at a single location [5]. These observations can be used to inform forecasting models or evaluate the accuracy of model estimation of the PBLH. Currently, determining the PBLH from a lidar relies on vertical profiles of a passive tracer, like aerosol concentration. This technique assumes that the tracer concentration will decrease sharply in the transition zone between the PBL and the free troposphere. One method of locating this transition zone is the Haar wavelet covariance transformation (HWT) method [6]. The HWT method has been implemented in several forms to determine the PBLH from lidar profiles [7–9].

Researchers at Montana State University and the National Center for Atmospheric Research are developing MicroPulse DIAL (MPD) instruments. These instruments combine the differential absorption lidar (DIAL) and the high-spectral-resolution lidar (HSRL) techniques for thermodynamic and aerosol profiling in the lower troposphere. The MPD instruments use diode-laser-based technology and can provide eye-safe operation. A network of five MPD instruments for water vapor (WV) profiling is in operation. Two of these instruments additionally perform calibrated aerosol and temperature profiling. A sixth instrument can perform aerosol and temperature profiling without WV measurements. Efforts continue to improve the data products from these instruments. This chapter builds on the PBLH retrieval method that uses aerosol profiles measured by the HSRL presented in Colberg et al. [10]. The method is adapted to locate the PBLH using profiles retrieved by the WV-DIAL.

47.2 Instrumentation

Data for this chapter were collected using an MPD instrument containing a WV-DIAL for humidity profiling, an O_2-DIAL for temperature profiling, and an HSRL that uses a potassium absorption cell for aerosol profiling. Details regarding this MPD instrument are available in Stillwell et al. [11] and Spuler et al. [12]. The MPD was deployed to Fort Collins, CO (40.59 °N, 105.14 °W) in the summer of 2021. During this deployment, radiosondes (Vaisala RS41-SGP) were launched from a co-located radiosonde station. These radiosondes provide range-resolved atmospheric parameters, including temperature and relative humidity.

47.3 Methods

The PBLH retrieval algorithm uses the HWT of the aerosol backscatter coefficient (at 770 nm) in a series of successive steps to determine the daytime PBLH. The nocturnal PBLH is frequently beneath the minimum range of the MPD, so it was not determined consistently. The retrieval algorithm first identifies clouds in the lidar signal. It then uses a simple metric to locate the free troposphere. The HWT of the aerosol backscatter coefficient is used to locate the capping inversion and the bottom of residual layers, which are used in turn to set an upper limit for the PBLH retrieval algorithm. Finally, the HWT of the aerosol backscatter coefficient is used to locate the PBLH below the upper limit. The PBLH is set to the location of the lowest maxima in the HWT of the aerosol backscatter coefficient greater than a fixed threshold value, in this case, 0.05 [unitless]. In the presence of PBL clouds, the PBLH is set to the top of the cloud layer. Details regarding this algorithm can be found in Colberg et al. [10].

The HWT retrieval method was adapted to locate the PBLH using the WV mixing ratio profiles retrieved by the WV-DIAL. The vertical profile of the mixing ratio takes the place of the aerosol backscatter coefficient profile in this retrieval. The negative gradient at the PBLH in the mixing ratio profile tends to be less steep than the gradient in the aerosol backscatter coefficient profile. For this reason, different threshold values for locating each layer were used. The PBLH was set to the location of the lowest maxima in the HWT of the mixing ratio profile greater than 0.03 [unitless].

The PBLH was determined from radiosondes by locating a maximum potential temperature gradient in the lowest inversion layer. An inversion layer was defined as a layer where the potential temperature gradient was greater than 5 $\frac{K}{km}$.

47.4 HSRL PBLH Retrievals

The HSRL PBLH retrieval could consistently determine the daytime PBLH in clear-sky or thin-cloud conditions. The daytime PBLH determined by HSRL and by radiosonde is shown from June 29 to July 3, 2021, with the aerosol backscatter coefficient, β_{aer}, on a logarithmic scale in Fig. 47.1. Additionally, two radiosonde-measured potential temperature, θ, profiles are compared to aerosol backscatter coefficient profiles. The transition between the PBL and the free troposphere is the region of the steep increase in the potential temperature and steep decrease in the aerosol backscatter coefficient with an increase in range. Table 47.1 shows the PBLH values as determined by the HSRL and by a subset of radiosondes from June 30 to July 3. Close agreement is seen in clear-sky and thin-cloud conditions on June 30, July 2, and July 3. The PBLH values retrieved during heavy cloud-cover conditions and precipitation on July 1 have larger differences between the HSRL

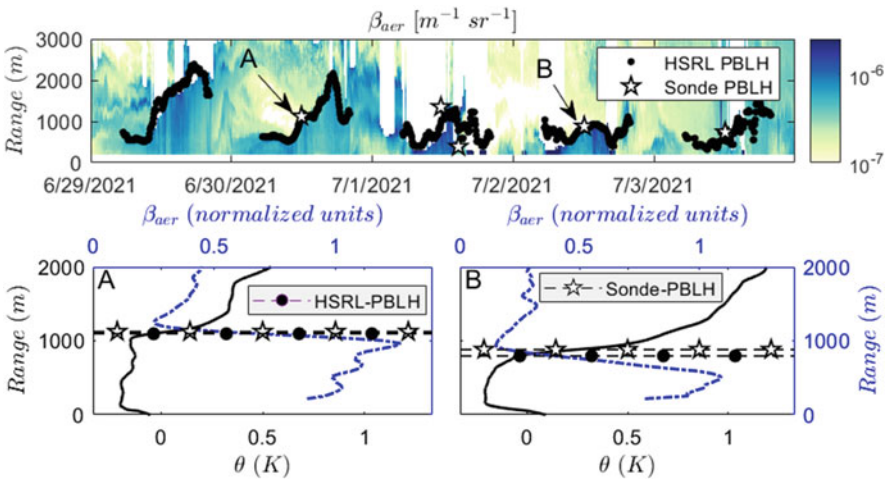


Fig. 47.1 Top: the daytime PBLH determined by the HSRL and sondes with the aerosol backscatter coefficient on a logarithmic scale. Bottom left: the potential temperature from sonde A and the aerosol backscatter coefficient from the HSRL are the black solid and blue dot-dashed lines, respectively. The PBLHs determined by the HSRL and sonde A were 1096 m and 1124 m, respectively. Bottom right: Same as bottom left for sonde B. The PBLHs determined by the HSRL and sonde B were 796 m and 881 m, respectively

Table 47.1 Comparison of PBLH values from the HSRL and radiosondes

Date	Launch time (MDT)	HSRL PBLH (m)	Sonde PBLH (m)
June 30, 2021	11:55	1096	1124
July 1, 2021	11:42	1133	1353
July 1, 2021	14:39	459	389
July 2, 2021	12:05	796	881
July 3, 2021	12:06	721	740

and the sonde PBLH values. Similar agreements were seen for the other radiosonde launches during this deployment.

47.5 WV-DIAL PBLH Retrievals

The WV-DIAL PBLH retrieval was less consistent than the HSRL PBLH retrieval. It worked best in conditions with a humid PBL and a steep gradient in the WV mixing ratio in the transition zone. The WV-DIAL PBLH retrieval frequently tracked lofted residual layers instead of the PBLH in dry conditions. A side-by-side comparison of the PBLH values from the HSRL and the WV-DIAL for a representative case can be seen in Fig. 47.2. The WV-DIAL tracked a residual layer in the morning, causing an overestimation of the PBLH. The WV-DIAL and the HSRL PBLH retrievals showed

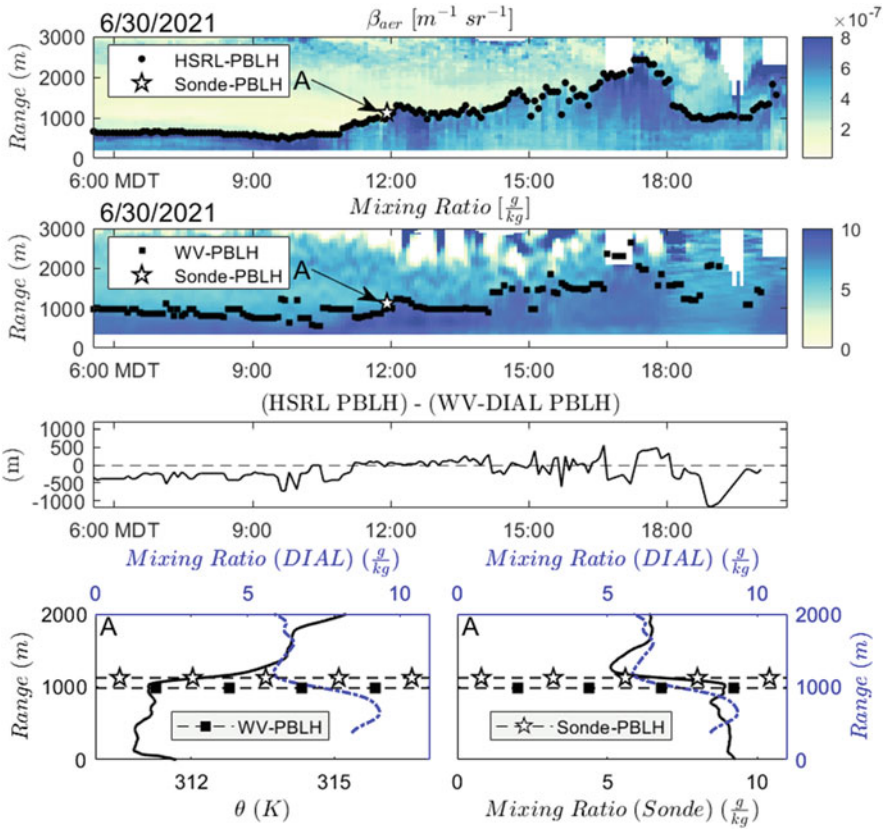


Fig. 47.2 Top: the daytime PBLH determined by the HSRL and sondes with the aerosol backscatter coefficient. Second from top: the PBLH determined by the WV-DIAL and sondes with the WV mixing ratio. Third from top: the PBLH from the HSRL minus the PBLH from the WV-DIAL. Bottom left: the potential temperature and mixing ratio from sonde A are the black solid and blue dot-dashed lines, respectively. The PBLH values determined by the WV-DIAL and the sonde are 984 m and 1124 m, respectively. Bottom right: the mixing ratio from sonde A and the mixing ratio from the WV-DIAL are the black solid and blue dot-dashed lines, respectively

close agreement during the middle of the day and then showed more significant differences in the evening transition period. Additionally, the potential temperature, θ, and mixing ratio profiles determined by a radiosonde are compared to the mixing ratio determined by the WV-DIAL in Fig. 47.2. The transition zone is the steep increase in potential temperature and the steep decrease in the mixing ratio with an increase in range. The WV gradients tend to be less steep than the aerosol backscatter coefficient gradients in the transition zone. The lower threshold needed to detect these smaller gradients does not entirely suppress noise, making WV-DIAL PBLH retrievals less reliable than HSRL PBLH retrievals. Also, the longer averaging times in the DIAL technique tend to smooth regions of change, further

complicating PBLH retrievals. Finally, the higher minimum range (∼450 m) in WV-DIAL retrievals made low-altitude PBLH retrievals more difficult for the WV-DIAL than for the HSRL (∼225 m).

47.6 Conclusion

PBLH retrievals were demonstrated using the aerosol and WV profiles from the HSRL and the WV-DIAL. The HSRL PBLH retrieval showed close agreement to radiosondes in clear-sky and thin-cloud conditions. The WV-DIAL PBLH retrieval worked best in conditions with a humid PBL but could not track the PBLH consistently. The WV mixing ratio was not as good of a passive tracer for the PBLH as the aerosol backscatter coefficient. The smaller gradients were more difficult to detect. Additionally, the longer averaging times and higher minimum range in the WV-DIAL retrieval of the mixing ratio complicated PBLH retrievals. However, these are preliminary results, and efforts will continue to improve the robustness of the PBLH retrieval using the aerosol and WV profiling capabilities of the MPD instruments. Future work will seek to leverage temperature profiles from the O_2-DIAL to retrieve the PBLH using potential temperature methods, such as the theta gradient or the parcel method, which are widely used for locating the PBLH using radiosondes.

Acknowledgments The National Science Foundation supported this research through grant #1917851.

References

1. Stull, R.B.: An Introduction to Boundary Layer Meteorology, vol. 13. Springer Science and Business Media, Dordrecht (1988)
2. Hu, X.M., et al.: Evaluation of three planetary boundary layer schemes in the WRF model. J. Appl. Meteor. Climatol. **49**(9), 1831–1844 (2010)
3. Cohen A.E., et al.: A review of planetary boundary layer parameterization schemes and their sensitivity in simulating Southeastern U.S. cold season severe weather environments. Weather Forecasting **30**(3), 591–612 (2015)
4. Su, T., et al.: Relationships between the planetary boundary layer height and surface pollutants derived from lidar observations over China: regional pattern and influencing factors. Atmos. Chem. Phys. **18**(21), 15921–15935 (2018)
5. Boers, R., et al.: lidar observations of mixed layer dynamics: tests of parameterized entrainment models of mixed layer growth rate. J. Appl. Meteor. Climatol. **23**(2), 247–266 (1984)
6. Gamage N., Hagelberg, C.: Detection and analysis of microfronts and associated coherent events using localized transforms. J. Atmos. Sci. **50**(5), 750–756 (1993)
7. Cohn, S.A., Angevine, W.M.: Boundary layer height and entrainment zone thickness measured by lidars and wind-profiling radars. J. Appl. Meteor. Climatol. **28**(1), 1233–1247 (2000)
8. Brooks, I.M.: Finding boundary layer top: application of a wavelet covariance transform to lidar backscatter profiles. J. Atmos. Oceanic Technol. **20**(8), 1092–1105 (2003)

9. Baars, H., et al.: Continuous monitoring of the boundary-layer top with lidar. Atmos. Chem. Phys. **8**(23), 7281–7296 (2008)
10. Colberg L., et al.: Planetary boundary layer height retrieval from a diode-laser-based high spectral resolution lidar. J. Appl. Remote Sens. **16**(2), 024507 (2022)
11. Stillwell, R.A., et al.: Demonstration of a combined differential absorption and high spectral resolution lidar for profiling atmospheric temperature. Opt. Express **28**(1), 71–93 (2020)
12. Spuler, S.M., et al.: MicroPulse DIAL (MPD) – a diode-laser-based lidar architecture for quantitative atmospheric profiling. Atmos. Meas. Tech. **14**(6), 4593–4616 (2021)

Part III
Atmospheric Temperature, Water Vapor, Wind, Turbulence, and Waves

Chapter 48
Performance Modeling of a Diode Laser-Based Direct Detection Doppler Lidar



Kevin S. Repasky, Owen Cruikshank, and Luke Colberg

Abstract Researchers at Montana State University (MSU) and the National Center for Atmospheric Research (NCAR) are developing diode laser-based (DLB) MicroPulse DIAL (MPD) instruments for thermodynamic profiling of the lower atmosphere. Current instruments include the capability of measuring humidity, temperature, aerosol profiles, and boundary layer structure to address the needs expressed by the science community for cost-effective networkable ground-based thermodynamic profiling instruments. In this paper, the efficacy of adding the capability of vertical wind profiling using the DLB MPD architecture is discussed. A design for a dual-edge direct detection Doppler wind lidar channel is presented with a retrieval method that utilizes an ancillary measurement of the aerosol backscatter ratio. Performance modeling results indicate that an error in the retrieved wind velocity measurement of 0.56 m/s can be achieved with a 150-m range resolution and a 5-min averaging time. These results indicate that vertical wind profiling capability can successfully be added to the MPD thermodynamic profiling instruments.

Keywords Doppler wind lidar · MicroPulse DIAL · thermodynamic profiling

48.1 Introduction

Thermodynamic profiling of the lower atmosphere, including humidity profiles, temperature profiles, boundary layer structure, and wind profiles, is an important parameter that helps define the state of the atmosphere. The ability to perform real-time thermodynamic profiling using ground-based remote sensing instruments that captures both the time evolution and coarse spatial resolution through network

K. S. Repasky (✉) · O. Cruikshank · L. Colberg
ECE Department, Montana State University, Bozeman, MT, USA
e-mail: repasky@montana.edu; cruikshank@student.montana.edu; luke.colberg@student.montana.edu

© The Author(s), under exclusive license to Springer Nature Switzerland AG 2023

J. T. Sullivan et al. (eds.), *Proceedings of the 30th International Laser Radar Conference*, Springer Atmospheric Sciences,
https://doi.org/10.1007/978-3-031-37818-8_48

deployment has been identified as a high-priority measurement needed by the atmospheric science and weather forecasting research communities [1–5].

A collaborative research program at Montana State University (MSU) and the National Center for Atmospheric Research (NCAR) is working to address the observational needs through the development of cost-effective diode laser-based (DLB) MicroPulse DIAL (MPD) instruments that can provide real-time thermodynamic profiling with instruments capable of long-term autonomous operations in a networkable deployment. Currently, a network of five MPDs for humidity profiling is operational [6, 7], three MPD instruments can provide high spectral resolution lidar (HSRL) measurements for aerosol profiling [8] and boundary layer structure [9], and three instruments can provide temperature profiling [10, 11].

The DLB MPD instrument architecture utilizes commercial diode lasers, semiconductor optical amplifiers, single-photon counting modules (SPCMs), and commercial optical components. These optical components allow MPD instrument development in the 700 nm–1 μm spectral region making possible the development of multiple measurement techniques.

A design for an MPD instrument capable of measuring vertical wind profiles is presented, along with a summary of the performance modeling indicating the overall instrument capability. The proposed instrument utilized a direct detection dual-edge configuration to allow the measurement of the Doppler-shifted return signal. The retrieval technique relies on an ancillary measurement of the backscatter ratio, the ratio of the total backscatter to the molecular backscatter, based on the HSRL measurement technique [8]. This ancillary HSRL measurement allows for the spectral distribution of the scattered light to be accounted for in the measured return signal.

This chapter is organized as follows. A brief description of the proposed direct detection Doppler wind lidar channel is presented in Sect. 48.2. An overview of the retrieval method is discussed in Sect. 48.3. A summary of the performance modeling is presented in Sect. 48.4. Finally, some brief concluding remarks are presented in Sect. 48.5.

48.2 Instrument Overview

A schematic of the direct detection Doppler wind lidar channel that will be added to the existing MPD profiling instruments with existing HRSL capabilities is shown in Fig. 48.1. The output from a fiber-coupled distributed Bragg reflector (DBR) laser operating at 780 nm is incident on a fiber tap with 10% of the light directed to a second fiber tap. One output from this second tap is directed to a wavemeter that provides a coarse frequency stabilization to within 50 MHz of a set wavelength. The second output from this fiber tap is used to direct light to a rubidium vapor cell for frequency locking to within 0.50 MHz utilizing a Pound-Drever-Hall locking technique [12]. The remaining 90% of the light from the first fiber tap is then coupled into a tapered semiconductor optical amplifier (TSOA) to produce a pulse

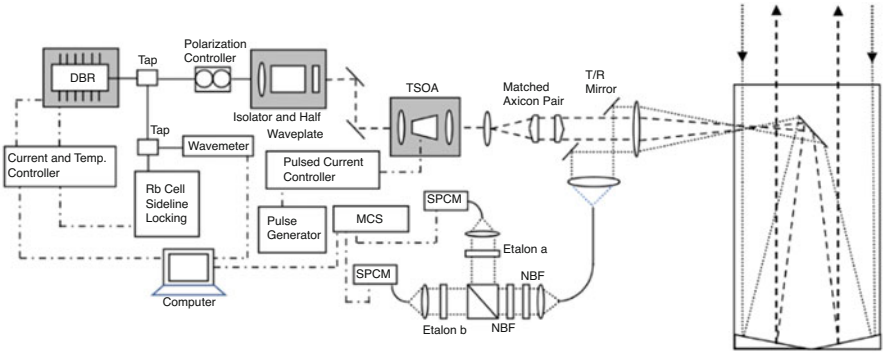


Fig. 48.1 Schematic of the proposed DLB direct detection Doppler wind lidar instrument. Dashed lines indicate optical paths, solid lines indicate fiber optical cables, and dot-dashed lines represent electrical cables

train of 1-μs pulse duration, a 5-μJ pulse energy, and a pulse repetition rate up to 10 kHz. The output from the TSOA is collimated, and a matched axicon pair is used to produce an annular beam that is coupled into the inner half of a 40-cm diameter Newtonian telescope.

Light collected by the outer half of the telescope is reflected from the T/R mirror and fiber-coupled into a 105-μm diameter multimode fiber. The output from this fiber is expanded, collimated, and passed through two narrowband filters with a 0.75-nm bandwidth. A beam-splitting cube directs 50% of the collected light through a etalon and is then fiber-coupled into an SPCM. The remaining 50% of the light is directed by the beam-splitting cube through etalon b and is then fiber-coupled with the output of the fiber connected to an SPCM. Light reflected from the etalons is not used. The two SPCMs are monitored using a multichannel scaler (MCS) that integrates return signals in user-defined range bins over a user-defined time period.

The resonant frequency of each etalon is offset from the laser transmitter operating frequency to provide a dual-edge detection discriminator that allows an estimate of the Doppler shift of the scattered light that can be used to infer radial wind velocity. The etalon bandwidth of 5 pm, the free spectral range of 100 pm, and the etalon offset of 1.9 GHz were chosen to provide the lowest error in the retrieved wind velocity [13].

48.3 Wind Velocity Retrieval

The retrieval of the wind velocity is achieved using a differential measurement of the return signals that pass through etalon a, $N_a(r)$, and etalon b, $N_b(r)$. This differential measurement takes on the form

$$M(r) = \frac{N_a(r) - N_b(r)}{N_a(r) + N_b(r)} \tag{48.1}$$

The return signal, $N_x(r)$, can be calculated using

$$N_x(r, f) = N_0 \frac{c\tau}{2} \frac{A_0}{r^2} \beta_m(r) T_{atm}^2(r) O(r) \varepsilon_x \left[(B(r) - 1) \delta(f_0 + \Delta f - f) + g(r, f_0 + \Delta f, f) \right] T_{e,x}(f) \tag{48.2}$$

where x can take on the value of a or b depending on which etalon the signal passed through in the receiver. In Eq. (48.2), N_0 is the number of outgoing photons, c is the speed of light, τ is the pulse duration, A_0 is the effective area of the optical receiver, $\beta_m(r)$ is the molecular backscatter, $T_{atm}(r)$ is the atmospheric transmission, $O(r)$ is the overlap function, ε_x is the receiver efficiency, $B(r)$ is the backscatter ratio, f_0 is the laser transmitter operating frequency, $\Delta f = \frac{2v_r f_0}{c}$ is the Doppler frequency shift with v_r representing the radial wind velocity, $g(r,f)$ is the Doppler broadened lineshape associated with the molecular scattering, and $T_{e,x}(f)$ is the etalon transmission. Using Eq. (48.1) and Eq. (48.2), $M(r)$ can be written

$$M(r) = \frac{\begin{array}{c}(B(r) - 1)\left(\varepsilon_a T_{e,a}(f = f_0 + \Delta f) - \varepsilon_b T_{e,b}(f = f_0 + \Delta f)\right) \\ + \int g(r, f_0 + \Delta f, f)\left(\varepsilon_a T_{e,a}(f) - \varepsilon_b T_{e,b}(f)\right) df\end{array}}{\begin{array}{c}(B(r) - 1)\left(\varepsilon_a T_{e,a}(f = f_0 + \Delta f) + \varepsilon_b T_{e,b}(f = f_0 + \Delta f)\right) \\ + \int g(r, f_0 + \Delta f, f)\left(\varepsilon_a T_{e,a}(f) + \varepsilon_b T_{e,b}(f)\right) df\end{array}}. \tag{48.3}$$

The wind velocity can be retrieved in the following manner. Theoretical values of $M(r)$ can be calculated as a function of wind velocity and range using the measured backscatter ratio, $B(r)$, provided by an ancillary HSRL measurement and a simple modeled atmosphere. At each range, the wind velocity that minimizes the difference between $M(r)$ calculated using the return signals in the two arms of the receiver in Eq. (48.1) and from $M(r)$ calculated from Eq. (48.3) as a function of wind velocity and an atmospheric model is assigned as the retrieved wind velocity.

48.4 Performance Estimates

The first major source of error considered in the performance model is the Poisson noise associated with the photon counting nature of the MPD instruments. A plot of the retrieved wind velocity as a function of range is shown in Fig. 48.2. A range resolution of 150 m and an averaging time of five minutes were used for

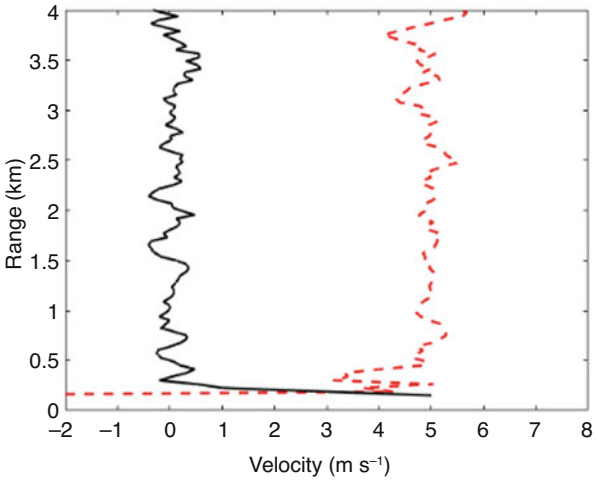


Fig. 48.2 A plot of a single modeled retrieved wind velocity as a function of range. The black solid (red dashed) line represents a 0-m/s (5-m/s) wind velocity used in the atmospheric model

these calculations. The black solid (red dashed) line indicates a 0-m/s (5-m/s) wind velocity used in the model. The error associated with the Poisson noise in the wind velocity retrieval was estimated as follows. Twenty-five retrievals were completed using a modeled atmosphere with a 1-m/s wind velocity. The wind velocity was calculated every 37.5 m. The error in the retrieved velocity was calculated between 0.5 and 4 km, and a statistical analysis was completed, indicating a mean value of 0.989 m/s and a standard deviation of 0.33 m/s.

Two other major sources of error must be considered, the laser transmitter frequency stability and the etalon frequency stability. The effects of the laser stability on the retrieved radial velocity can be estimated by taking the derivative of the Doppler shift with respect to the radial velocity resulting in the expression $df/d\upsilon_r = 2f_0/c$. For a laser transmitter with a frequency stability of 0.5 MHz, the estimated error in the retrieved velocity is 0.20 m/s. The error in the retrieved velocity resulting from the etalon stability was estimated by considering the effect of thermal expansion on the resonant frequency of the etalons. For a temperature stability of 5 mK, the estimated shift in the resonant frequency of the etalon is 1 MHz. Shifting the etalon transmission spectrum for each etalon in the retrieval program by 1 MHz results in an error of 0.40 m/s in the retrieved wind velocity. The total error in the retrieved radial velocity can be estimated by adding the individual errors in quadrature since each error is independent, resulting in an estimated error in the retrieved radial velocity of 0.56 m/s.

48.5 Conclusions

A design for a dual-edge direct detection Doppler wind lidar for vertical wind profiling was presented based on the successful MPD architecture. Using the existing capability of the MPD instruments to measure the aerosol backscatter ratio and the proposed instrument design, a retrieval method was briefly outlined. Finally, the performance modeling indicates that vertical wind profiles can be measured with a range of 4 km, a range resolution of 150 m, and an accuracy of 0.56 m/s. Future work will focus on incorporating the direct detection Doppler wind lidar channel described in Fig. 48.1 with the existing thermodynamic profiler network under development by MSU and NCAR.

Acknowledgments The work was supported by the National Science Foundation through grant #1917851.

References

1. National Research Council: Observing Weather and Climate from the Ground Up: A Nationwide Network of Networks, 250 pp. National Academies Press (2009). https://doi.org/10.17226/12540
2. National Research Council: When Weather Matters: Science and Services to Meet Critical Societal Needs, 198 pp. National Academies Press (2010). https://doi.org/10.17226/12888
3. National Academies of Sciences, Engineering, and Medicine: The Future of Atmospheric Boundary Layer Observing, Understanding, and Modeling: Proceedings of a Workshop, 58 pp. National Academies Press (2018). https://doi.org/10.17226/25138
4. Wulfmeyer, V., et al.: A review of the remote sensing of lower tropospheric thermodynamic profiles and its indispensable role for the understanding and the simulation of water and energy cycles. Rev. Geophys. **53**(3), 819–895 (2015). https://doi.org/10.1002/2014RG000476
5. Bell, T.M., Greene, B.R., Klein, P.M., Carney, M., Chilson, P.B.: Confronting the boundary layer data gap: evaluating new and existing methodologies of probing the lower atmosphere. Atmos. Meas. Tech. **13**(7), 3855–3872 (2020). https://doi.org/10.5194/amt-13-3855-2020
6. Spuler, S.M., Repasky, K.S., Morley, B., Moen, D., Hayman, M., Nehrir, A.R.: Field-deployable diode-laser-based differential absorption lidar (DIAL) for profiling water vapor. Atmos. Meas. Tech. **8**(3), 1073–1087 (2015). https://doi.org/10.5194/amt-8-1073-2015
7. Spuler, S.M., Hayman, M., Stillwell, R.A., Carnes, J., Bernatsky, T., Repasky, K.S.: MicroPulse DIAL (MPD) – a diode-laser-based lidar architecture for quantitative atmospheric profiling. Atmos. Meas. Tech. **14**(6), 4593–4616 (2021). https://doi.org/10.5194/amt-14-4593-2021
8. Hayman, M., Spuler, S.: Demonstration of a diode-laser-based high spectral resolution lidar (HSRL) for quantitative profiling of clouds and aerosols. Opt. Express. **25**(24), A1096–A1110 (2017). https://doi.org/10.1364/OE.25.0A1096
9. Colberg, L., Cruikshank, O., Repasky, K.S.: Planetary boundary layer height retrieval from a diode-laser-based high spectral resolution lidar. J. Appl. Remote Sens. **16**(2), 024507 (2022). https://doi.org/10.1117/1.JRS.16.024507
10. Repasky, K.S., Bunn, C.E., Hayman, M., Stillwell, R.A., Spuler, S.M.: Modeling the performance of a diode laser-based (DLB) micro-pulse differential absorption lidar (MPD) for temperature profiling in the lower troposphere. Opt. Express. **27**(23), 33543–33563 (2019). https://doi.org/10.1364/OE.27.033543

11. Stillwell, R.A., Spuler, S.M., Hayman, M., Repasky, K.S., Bunn, C.E.: Demonstration of a combined differential absorption and high spectral resolution lidar for profiling atmospheric temperature. Opt. Express. **28**(1), 71–93 (2020). https://doi.org/10.1364/OE.379804
12. Drever, R.W., Hall, J.L., Kowalski, F.V., Hough, J., Ford, G.M., Munley, A.J., Ward, H.: Laser phase and frequency stabilization using an optical resonator. Appl. Phys. B: Lasers Opt. **31**, 97–105 (1983). https://doi.org/10.1007/BF00702605
13. Repasky, K.S., Cruikshank, O., Colberg, L.: Performance modeling of a diode-laser-based direct-detection doppler lidar for vertical wind profiling. J. Atmos. Oceanic Technol. **39**(11), 1655–1668 (2022). https://doi.org/10.1175/JTECH-D-22-0001.1

Chapter 49
Observation of Water Vapor Profiles by Raman Lidar with 266-nm Laser in Tokyo

Yuichi Uchiho, Kazuto Matsuki, Eiji Takeuchi, Toshikazu Hasegawa, and Masanori Yabuki

Abstract Water vapor is an important parameter in understanding extreme weather events, and a Raman lidar is a useful technique to measure distribution of water vapor at high spatiotemporal resolution. We have been developing a Raman lidar with a 266-nm laser due to low solar background radiation below a wavelength of 300 nm by ozone absorption and demonstrated the results of continuous water vapor profiles throughout a year at an observatory surrounded by forest. In this study, we report the observation results of water vapor with the Raman lidar in an urban area, Tokyo, to evaluate the impact of the surface ozone.

Keywords Raman lidar · water vapor · 266 nm

49.1 Introduction

Water vapor plays a significant role in atmospheric processes, and its distribution is related to clouds and rainfall. Therefore, water vapor is a key parameter in understanding localized extreme weather events such as torrential rains and floods. Information on the distribution of water vapor at high spatiotemporal resolution is beneficial for improving the accuracy of weather forecasts. A Raman lidar is a useful technique to capture such information. While most Raman lidars have been studied with a 355-nm laser as an excitation source, a Raman lidar with a 266-nm laser with a grating polychromator has been reported by several groups [1, 2]. Solar radiation in the wavelength range below 300 nm can be reduced to a much

Y. Uchiho (✉) · K. Matsuki · E. Takeuchi · T. Hasegawa
EKO Instruments Co., Ltd, Shibuya-ku, Tokyo, Japan
e-mail: uchiho@eko.co.jp

M. Yabuki
Research Institute for Sustainable Humanosphere, Kyoto University, Uji, Kyoto, Japan
e-mail: yabuki@rish.kyoto-u.ac.jp

© The Author(s), under exclusive license to Springer Nature Switzerland AG 2023

J. T. Sullivan et al. (eds.), *Proceedings of the 30th International Laser Radar Conference*, Springer Atmospheric Sciences,
https://doi.org/10.1007/978-3-031-37818-8_49

lower level because of absorption by the ozone layer in the stratosphere. This allows for the measurement of water vapor with low background noise even during the daytime. We developed a Raman lidar employing a 266-nm laser and an interference filter-based polychromator. In 2018, our system demonstrated the ability to acquire continuous water vapor profiles at an observatory surrounded by forest throughout a year [3]. In this study, we conducted an observation of water vapor in an urban city area, Tokyo, during the summer of 2020 to evaluate the impact of the surface ozone on the measurement performance, as the surface ozone tended to increase in urban areas in summer.

49.2 Methodology

49.2.1 Raman Lidar System

The optical system of the Raman lidar is illustrated in Fig. 49.1. The fourth harmonic output (266 nm) of an Nd:YAG laser was used as an excitation source with a repetition rate of 10 Hz and a pulse width of 7 ns. The laser was operated at a pulse energy of 50 mJ. The beam divergence of the laser was <1 mrad in full angle, and the laser light was irradiated into the atmosphere after passing through the beam expander (×3). A custom-made Cassegrain telescope with a primary mirror diameter of 200 mm was used as an optical receiver. Dichroic beam splitters and the interference filters separated the backscattered light into three vibrational Raman scattering light: oxygen (277.5 nm), nitrogen (283.6 nm), and water vapor (294.6 nm). A photomultiplier tube (PMT; R9880U, Hamamatsu, Japan) was used

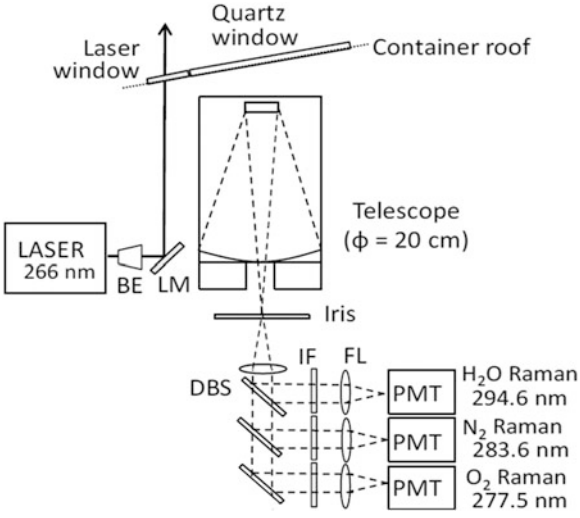


Fig. 49.1 Schematic setup of Raman lidar. *BE* beam expander, *LM* laser mirror, *FL* focusing lens, *DBS* dichroic beam splitter, *IF* interference filter, *PMT* photomultiplier tube

for detecting each backscattered light. The output signals from the PMTs were recorded and accumulated in both the analog and photon counting modes using a transient recorder (TR 20-16bit, Licel, Germany). The lidar system was encased in a temperature-controlled container with two separate quartz windows: one for transmitting the outgoing laser light and the other for the scattered light from the atmosphere.

49.2.2 Retrieval of Water Vapor Profiles

The water vapor mixing ratio (WVMR) m at range R was obtained from the Raman backscatter signals of water vapor P_{H_2O}, nitrogen P_{N_2}, and oxygen P_{O_2} as follows:

$$m(R) = K \frac{P_{H_2O}(R)}{P_{N_2}(R)} \times \left[\frac{P_{O_2}(R)}{P_{N_2}(R)} \right]^{\gamma}, \tag{49.1}$$

where K is the calibration constant and γ is the correction factor for ozone absorption [1]. The calibration constant was derived by comparing the water vapor mixing ratio of the Raman lidar and a radiosonde (LMS6, Lockheed Martin, USA). The Raman signals were accumulated over 15 min and the range resolution was 75–150 m.

49.3 Results and Discussions

The Raman lidar was placed on the rooftop of the building of the EKO Instruments, Tokyo, Japan (35°40′N, 139°40′E, 50 m a.s.l.) from July 26 to August 30, 2020. The building was located near a highway, and the traffic was consistently heavy. Figure 49.2 shows the typical WVMR profiles of the Raman lidar and a radiosonde. Both WVMR profiles agreed well from 200–1500 m during the daytime and nighttime. The variation in the calibration constants was 3.7% for eight times radiosonde observations.

The time-height series of the WVMR profiles and the time series of the surface ozone concentrations are shown in Fig. 49.3. The WVMR data were adopted when the statistical error of the WVMR was $\leq$20%. We used the surface ozone data of the ambient air quality monitoring stations (AAQMS) provided by the website of the Ministry of the Environment [4]. The distance between the Raman lidar measurement site and the AAQMS was approximately 2.5 km. The averaged ozone concentration was 30 ppb during this period, and the maximum ozone concentration was 199 ppb at 14:00 on August 15. Figure 49.4 shows the relationship between the surface oxidant (ozone) concentration and the maximum measurable altitude. It is noted that the maximum measurable altitudes included cases where they were

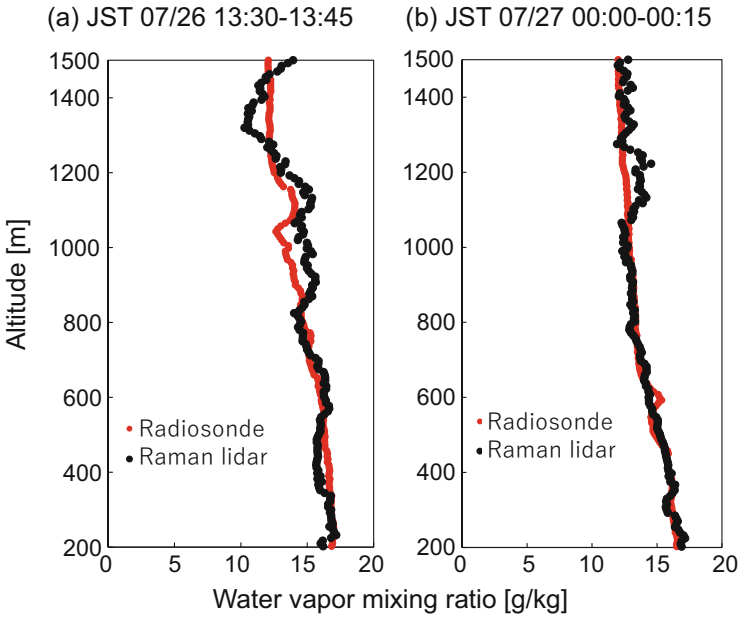


Fig. 49.2 Vertical water vapor mixing ratio profiles obtained by Raman lidar and radiosonde in (**a**) daytime (July 26, 13:30) and (**b**) nighttime (July 27, 00:00)

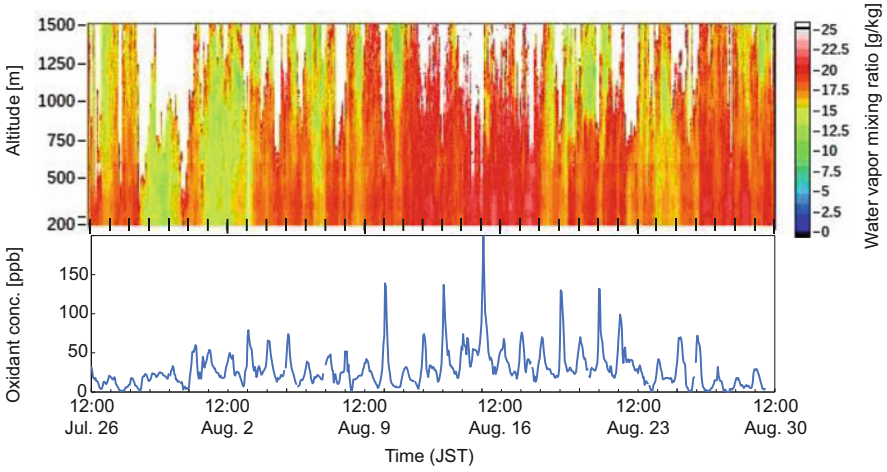


Fig. 49.3 (Upper panel) Time-height series of water vapor mixing ratio from July 26 to August 30 in 2020 and (bottom panel) time series of oxidant (ozone) concentration

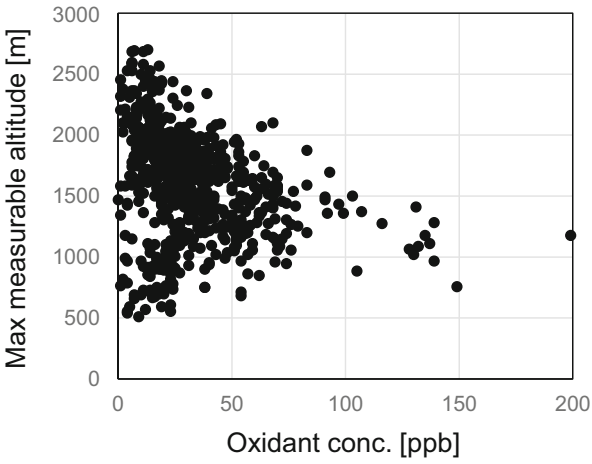


Fig. 49.4 Scatter plot for surface oxidant (ozone) concentration and maximum measurable altitude for all available data from July 26 to August 30 in 2020

limited by cloud. A weak negative correlation was observed ($r = -0.30$). The results indicated that a significant increase in the surface ozone concentration decreased the measurable altitude of the Raman lidar with a 266-nm laser because the surface ozone absorbs both the incident light and the Raman scattered light. Therefore, one may need to consider the drop in measurable altitude when observing at times and locations of high surface ozone concentrations.

49.4 Conclusions

We observed water vapor mixing ratio (WVMR) profiles in an urban city, Tokyo, using the Raman lidar that employs a 266-nm laser and an interference filter-based polychromator. The WVMR profiles from the radiosonde and the Raman lidars agreed well up to approximately 1500 m both during the daytime and nighttime. The variations in the calibration constants were small, indicating the Raman lidar worked reliably. Results of continuous measurement also supported the reliability of the Raman lidar, although the maximum measurable altitude was reduced under high surface-ozone concentration conditions.

References

1. Renaut, D., Pourny, J.C., Capitini, R.: Daytime Raman-lidar measurements of water vapor. Opt. Lett. **5**(6), 233–235 (1980)
2. Lazzarotto, B., Frioud, M., Larchevêque, G., Mitev, V., Quaglia, P., Simeonov, V., Thompson, A., Van Den Bergh, H., Calpini, B.: Ozone and water-vapor measurements by Raman lidar in the planetary boundary layer: error sources and field measurements. Appl. Opt. **40**(18), 2985–2997 (2001)

3. Yabuki, M., Kawano, Y., Tottori, Y., Tsukamoto, M., Takeuchi, E., Tsuda, T.: A Raman lidar with a deep ultraviolet laser for continuous water vapor profiling in the atmospheric boundary layer. In: EPJ Web of Conferences, vol. 237, p. 03001. EDP Sciences (2020)
4. Ministry of Environment website (Japanese). https://soramame.env.go.jp/. Last accessed 19 Apr 2022

Chapter 50
A 355-nm Direct-Detection Doppler Wind Lidar for Vertical Atmospheric Motion

Shoken Ishii, Hideki Takenaka, Kodai Kishibuchi, Yoshitaka Jin, Tomoaki Nishizawa, Nobuo Sugimoto, Hironari Iwai, Makoto Aoki, Seiji Kawamura, and Hajime Okamoto

Abstract We developed a simple 355-nm direct-detection Doppler wind lidar (DWL) for atmospheric motion study. The 355-nm direct-detection DWL uses the double-edge technique for a receiver with Fabry-Perot etalon interferometer and a wedge prism to form a double-edge filter. Preliminary experimental line-of-sight (LOS) wind measurements were made to investigate wind measurement performance of the 355-nm direct-detection DWL on July 22, 2021. Although the observational range limit depends on its telescope area and atmospheric conditions, the 355-nm direct-detection DWL for three different accumulation times (10 min, 15 min, 30 min) could make wind measurement with random error of less 1 m/s at altitudes of 1.8, 2.1, and 2.7 km, respectively. In this chapter, we describe development and preliminary experimental result of the 0.355-μm direct-detection DWL.

Keywords Doppler wind lidar · 355 nm · Direct-detection · vertical motion

S. Ishii (✉) · H. Takenaka · K. Kishibuchi
Tokyo Metropolitan University, Hino, Tokyo, Japan
e-mail: sishii@tmu.ac.jp; takenaka.hideki@tmu.ac.jp; kishibuchi-kodai@ed.tmu.ac.jp

Y. Jin · T. Nishizawa · N. Sugimoto
National Institute for Environmental Studies, Tsukuba, Ibaraki, Japan
e-mail: jin.yoshitaka@nies.go.jp; nisizawa@nies.go.jp; nsugimot@nies.go.jp

H. Iwai · M. Aoki · S. Kawamura
National Institute of Information and Communications Technology, Koganei, Tokyo, Japan
e-mail: iwai@nict.go.jp; maoki@nict.go.jp; s-kawamura@nict.go.jp

H. Okamoto
Kyushu University, Kasuga, Fukuoka, Japan
e-mail: okamoto@riam.kyushu-u.ac.jp

© The Author(s), under exclusive license to Springer Nature Switzerland AG 2023

J. T. Sullivan et al. (eds.), *Proceedings of the 30th International Laser Radar Conference*, Springer Atmospheric Sciences,
https://doi.org/10.1007/978-3-031-37818-8_50

50.1 Introduction

The physical characteristics of clouds are closely related to the Earth's radiation and water balances. Observations by the Earth's observation satellites provide us with information on global distributions of clouds and aerosols, which make remarkable improvements in the evaluation of the Earth's radiation balance and water balance. Potential uncertainties in cloud cover and microphysical characteristics of aerosols and clouds [1] are shown in the observational studies using satellite observation data. These satellite observations show that there is a large difference in the reproducibility of physical characteristics of clouds between the results of different climate change prediction models [2, 3]. Atmospheric vertical motion in clouds and parameterization of mass flux based on the type of cloud and precipitation particles cause changes in the vertical distribution of cloud water content and ice water content in general circulating models (GCMs) [4, 5]. It is important to understand the interaction between vertical flow and mass flux [6]. It is essential to establish a well-equipped synergetic observable remote sensing site that can comprehensively evaluate the vertical flow, parameterization of cumulus convection, and aerosol-cloud interaction. To evaluate the atmospheric vertical motion, synergetic observations with Doppler wind lidar (DWL) to measure the background atmospheric flow and/or falling speed of aerosols and clouds are useful approaches. We have developed a simple 355-nm direct-detection DWL to measure the line-of-sight (LOS) wind speed of the background atmosphere from atmospheric molecule return signals with and without aerosols and clouds. This paper describes the new DWL and preliminary experimental results on vertical LOS wind speed measurements.

50.2 Lidar Instrument

A direct-detection DWL has the advantage that wind measurement can be made any aerosol conditions because it uses the light backscattered by molecules (Rayleigh scattering). The feature is one of the characteristics of the direct-detection DWL. The Tokyo Metropolitan University, National Institute for Environmental Studies, National Institute of Information and Communications Technology (NICT) (Koganei, Tokyo), and Kyushu University developed a simple 355-nm direct-detection DWL with a double-edge technique. The developed direct-detection DWL is installed at the NICT. Figure 50.1 and Table 50.1 show a block diagram and specifications of the direct-detection DWL. The direct-detection DWL uses a single-frequency flash-lump-pumped Q-switched Nd:YAG laser (Continuum: Surelite I), a 50-mm diameter 0.4-m focal-length refractive telescope with, a wedge prism at an angular deviation of 0.2°, a Fabry-Perot etalon, a lens, a knife-edge right-angle prism mirror, two interference filters, and two photomultiplier tubes (Hamamatsu: R9880U-113). The single-frequency flash lump-pumped Q-switched

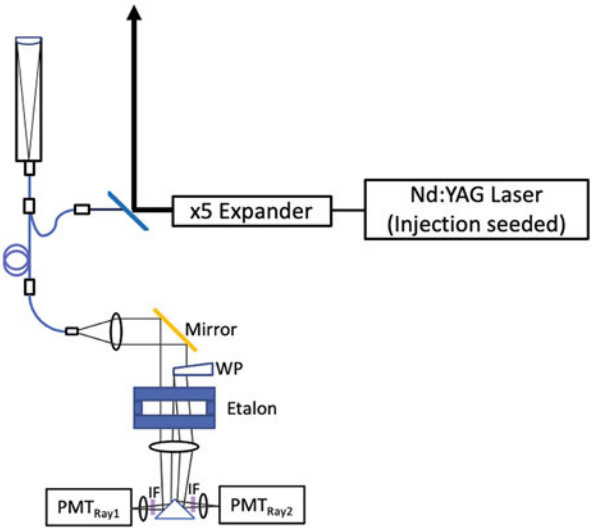


Fig. 50.1 Block diagram of a new and simple direct-detection Doppler wind lidar

Nd:YAG operating at a wavelength of 0.355 ∝m can emit an output energy of 100 mJ with a pulse width of 10 ns (FWHM) at a pulse repetition frequency of 10 Hz. The wavelength of backscattered light is Doppler-shifted from that of the incident laser light by the moving molecules and aerosols. The backscattered light is collected by the refractive telescope. The backscattered light from the multi-mode fiber with a numerical aperture of 0.12 and a core diameter of 100 μm is collimated by a lens with a focal length of 0.1 m. The 25-mm-diameter backscattered light with the divergence of 1 mrad passes through the relay optics, and it is split into two paths using the wedge prism. The divergence of the backscattered light beam is set to be equal to the full-angle divergence of the light beam in a Fabry-Perot étalon. Each split light beam passes through the Fabry-Perot étalon (which functions as an edge filter) and is focused on each detector.

The number of photons $N_{s,i=1,2}$ detected at each detector for the LOS wind speed of v_{LOS} (m/s) is given as Eq. (50.1),

$$N_{s,i=1,2}(r, \nu, \Delta\nu) = \frac{E_{\mathrm{T}} \cdot \mathrm{Freq} \cdot \Delta t}{h\nu_L} \cdot T_{\mathrm{o}} \cdot O_{\mathrm{A}}(r) \cdot Q_{\mathrm{e}} \cdot \frac{A_T}{r^2} \cdot \Delta r \cdot T_{\mathrm{A}}^2 \cdot \left[\int_{-\infty}^{\infty} \left\{ \beta_{\mathrm{M}}(r) \cdot T_{F,i}(\nu) \cdot G_L * G_{\mathrm{M}}(\nu, \Delta\nu) + \beta_{\mathrm{A}}(r) \cdot T_{F,i}(\nu) \cdot G_{\mathrm{L}} * L_{\mathrm{A}}(\nu, \Delta\nu) \right\} d\nu \right]. \tag{50.1}$$

where E_{T} is the transmitted laser energy, Freq is the pulse repetition frequency, Δt is the inte- gration time, ν_{L} is the laser frequency, A_{T} is the telescope area, T_{o} is the optical efficiency of the system without etalon transmission, $O_{\mathrm{A}}(r)$ is an overlap function, Q_{e} is the quantum efficiency of the detector, Δr is the range bin, r is the distance to the target atmosphere, T_{A} is the atmospheric transmission,

Table 50.1 Specifications for a simple direct-detection Doppler wind lidar

Transmitter	
Laser	Injection seeded, Q-switched Nd:YAG laser
Wavelength	354.8 nm
Pulse repetition frequency	10 Hz
Energy	100 mJ
Beam divergence	0.1 mrad
Receiver	
Telescope	Refractive type
Diameter	50 mm
Focal length	400 mm
FOV	0.25 mrad
Interferometer	
Interferometer type	Fabry-Pérot etalon
Etalon type	Air space
Etalon plate spacing	12.5 mm
Rayleigh filter spacing between CH1 and CH2	5.2 GHz
Detector and signal processing	
Detector	Photomultiplier tube
Data acquisition	40 MHz counting rate (Licel PR40)
Temporal resolution	50 ns correspond to 7.5 m range gate

$T_{F,i=1,2}(\nu)$ is the transmission at a frequency of ν for an edge filter centered at ν_{L}, β_{m} and β_{a} are the molecule and aerosol backscattering coefficients, G_{L} and G_{m} are Gaussian line-broadening functions for the laser-line spectrum and the Rayleigh-Brillouin spectrum, L_{a} is a Lorentzian function for the aerosol-line spectrum, $\Delta\nu$ is the Doppler-shifted frequency, the asterisk denotes a convolution operation, and h is Planck's constant. The photon noise is the dominant noise source. In the paper, we assume that the standard deviation of N_i is given by a Poisson distribution. $\mathrm{SNR}_{s,i=1,2}(r)$ is given as Eq. (2),

$$\mathrm{SNR}_{S,i}(r) = \frac{N_{s,i}\,(r, \nu, \Delta\nu)}{\sqrt{N_{s,i}\,(r, \nu, \Delta\nu)}}. \tag{50.2}$$

where $\mathrm{SNR}_{s,i=1,2}(r)$ is the SNR for each PMT. The LOS wind speed error σ_{LOS} is given by

$$\sigma_{\mathrm{LOS}} = \frac{c}{\frac{2}{\nu}\left(\frac{1}{N_1(r,\nu,0)}\frac{d}{d\nu}N_{s,1}\,(r, \nu, 0) + \frac{-1}{N_2(r,\nu,0)}\frac{d}{d\nu}N_{s,2}\,(r, \nu, 0)\right)}\sqrt{\frac{1}{\mathrm{SNR}_{s,1}^2} + \frac{1}{\mathrm{SNR}_{s,2}^2}}. \tag{50.3}$$

50.3 Results

The LOS wind measurement performance of the direct-detection DWL was investigated to demonstrate the system capabilities for remote measurement of wind speed in the atmospheric boundary layer and lower free troposphere. Experimental vertical LOS wind measurements were made on at 7 UT on July 22, 2022. Figure 50.2a–c show examples of profile of LOS wind speed measured by the direct-detection DWL for three different accumulation times: (a) 10 min, (b) 15 min, and (c) 30 min. The thick gray line shows the profile of LOS wind speed measured by the coherent DWL installed at the NICT [7]. The coherent DWL can make a LOS wind speed with bias of 0.02 m/s and random error of <0.10 m/s in the atmospheric boundary layer airmass where aerosols are rich [8]. The direct-detection DWL can make wind measurement at an altitude of 1.8, 2.1, and 2.7 km with an LOS wind speed error of 1 m/s for three different accumulation times, respectively. Although the range limit depends on the telescope area and atmospheric conditions, in the preliminary wind measurement, the LOS wind speed error of the direct-detection DWL wind measurement derived from the atmospheric return for a 15-min accumulation time at altitudes of up to 3.5 km was <2 m/s. The vertical wind profile observed by the direct-detection DWL was consistent with those by the CDWL within the measurement error bars. There were limited available paired data points available at altitudes of 1–2 km. Further statistical investigations will be required for the assessment of the wind measurement performance of the direct-detection DWL.

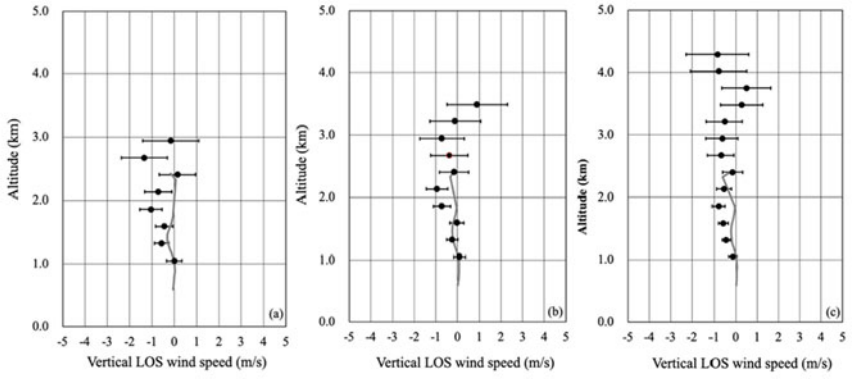


Fig. 50.2 Measured profile of LOS wind speed measured at 7 UT on July 22, 2021, for various accumulation time: (**a**) 10 min, (**b**) 15 min, (**c**) 30 min. Closed circles with error show vertical LOS wind speeds measured by the direct-detection DWL. Thick line shows profile vertical LOS wind speed measured by the CDWL (gray)

50.4 Summary

In this chapter, we developed a simple 355-nm direct-detection DWL to measure the LOS wind speed of the background atmosphere from atmospheric molecule return signals with and without aerosols and clouds. The developed 355-nm direct-detection DWL uses the double-edge technique for a receiver with Fabry-Perot etalon interferometer, and it uses a wedge prism to form a double-edge filter. Preliminary experimental LOS wind measurements were made to investigate wind measurement performance of the 355-nm direct-detection DWL on July 22, 2021. We found that the observational altitudes for the three accumulation times of 10, 15, and 30 minutes were 1.8, 2.1, and 2.7 km, respectively. The vertical profiles of the LOS wind speed measured by the developed 355-nm direct-detection DWL were compared with those obtained from the coherent DWL and were consistent with those from the coherent DWL within the margin of measurement error. There are several limitations to the proposed direct-detection DWL, such as the stability of the optical alignment to prevent the deterioration of wind measurement performance owing to optical misalignment, limited observational range, and spatiotemporal resolution and the current algorithm used to derive the LOS wind speed. The wind measurement with higher temporal resolution is needed for the understanding of the vertical atmospheric motion in clouds because clouds are highly turbulent objects. A laser operating at high pulse repetition frequency and a telescope with a large diameter are required for the improvement of the LOS wind measurement. The direct-detection and coherent DWLs are used for the LOS wind measurements for the background atmosphere and for the atmosphere around and inside clouds, respectively. The combination of direct-detection and coherent DWLs could provide useful information on the vertical atmospheric motion around and inside clouds. We will improve the systematic performance and the current algorithm and contribute to the scientific goals of the Earth Clouds Aerosol and Radiation Explorer (EarthCARE) satellite.

References

1. Cesana, G., Chepfer, H., Winker, D., Getzewich, B., Cai, X., Jourdan, O., Mioche, G., Okamoto, H., Hagihara, Y., Noel, V., Reverdy, M.: Using in situ airborne measurements to evaluate three cloud phase products derived from CALIPSO. J. Geophys. Res. **121**(10), 5788–5808 (2016)
2. Waliser, D.E., Li, J.-L.F., Woods, C.P., Austin, R.T., Bacmeister, J., Chern, J., Del Genio, A., Jiang, J.H., Kuang, Z., Meng, H., Minnis, P., Platnick, S., Rossow, W.B., Stephens, G.L., Sun-Mack, S., Tao, W., Tompkins, A.M., Vane, D.G., Walker, C., Wu, D.: Cloud ice: a climate model challenge with signs and expectations of progress. J. Geophys. Res. **114**(D8), D00A21 (2009)
3. Li, J.-F., Waliser, D., Woods, C., Teixeira, J., Bacmeister, J., Chern, J., Shen, B.-W., Tompkins, A., Tao, W.-K., Köhler, M.: Comparisons of satellites liquid water estimates with ECMWF and GMAO analyses, 20th century IPCC AR4 climate simulations, and GCM simulations. Geophys. Res. Lett. **35**(19), L19710 (2008)

4. Donner, L.J.: A cumulus parameterization including mass fluxes, vertical momentum dynamics, and mesoscale effects. J. Atmos. Sci. **50**(6), 889–906 (1993)
5. Lin, Y., Donner, L.J., Colle, B.A.: Parameterization of riming intensity and its impact on ice fall speed using ARM data. Mon. Weather Rev.**139**(3), 1036–1047 (2011)
6. Del Genio, A.D., Wu, J., Wolf, A.B., Chen, Y.H., Yao, M.-S., Kim, D.: Constraints on cumulus parameterization from simulations of observed MJO events. J. Climate. **28**(16), 6419–6442 (2015)
7. Ishii, S., Mizutani, K., Fukuoka, H., Ishikawa, T., Baron, P., Iwai, H., Aoki, T., Itabe, T., Sato, A., Asai, K.: Coherent 2 μm differential absorption and wind lidar with conductively cooled laser and two-axis scanning device. Appl. Opt. **49**(10), 1809–1817 (2010)
8. Iwai, H., Ishii, S., Oda, R., Mizutani, K., Sekizawa, S., Murayama, Y.: Performance and Technique of coherent 2-μm differential absorption and wind lidar for wind Measurement. J. Atmos. Oceanic Technol. **30**(3), 429–449 (2013)

Chapter 51
Aircraft Wake Vortex Recognition and Classification Based on Coherent Doppler Lidar and Convolutional Neural Networks

Xinyu Zhang, Songhua Wu, Xiaoying Liu, Hongwei Zhang, and Guangyao Dai

Abstract Aircraft wake vortices are serious threats to aviation safety and limit airport capacity greatly. The pulsed coherent Doppler lidar (PCDL) has been widely used in the observation of aircraft wake vortex due to its advantages of high spatial-temporal resolution and high precision. However, the post-processing algorithm cannot meet the needs of real-time detection of wake vortices at airports due to the long-time consumption. This chapter focuses on the development of a real-time wake vortex monitoring system which will significantly improve the detection efficiency of the wake vortex and the introduction of a quick image recognition method to identify the wake vortex based on convolutional neural network (CNN)

X. Zhang · X. Liu · G. Dai
College of Marine Technology, Faculty of Information Science and Engineering, Ocean University of China, Qingdao, China
e-mail: zhangxinyu@stu.ouc.edu.cn; lxy6302@stu.ouc.edu.cn; daiguangyao@ouc.edu.cn

S. Wu (✉)
College of Marine Technology, Faculty of Information Science and Engineering, Ocean University of China, Qingdao, China

Institute for Advanced Ocean Study, Ocean University of China, Qingdao, China

Laboratory for Regional Oceanography and Numerical Modeling, Pilot National Laboratory for Marine Science and Technology (Qingdao), Qingdao, China
e-mail: wush@ouc.edu.cn

H. Zhang
College of Marine Technology, Faculty of Information Science and Engineering, Ocean University of China, Qingdao, China

Laboratory for Regional Oceanography and Numerical Modeling, Pilot National Laboratory for Marine Science and Technology (Qingdao), Qingdao, China

Key Laboratory of Space Laser Communication and Detection Technology, Shanghai Institute of Optics and Fine Mechanics, Chinese Academy of Sciences, Shanghai, China
e-mail: zhanghongwei8944@ouc.edu.cn

© The Author(s), under exclusive license to Springer Nature Switzerland AG 2023

J. T. Sullivan et al. (eds.), *Proceedings of the 30th International Laser Radar Conference*, Springer Atmospheric Sciences,
https://doi.org/10.1007/978-3-031-37818-8_51

models. In this method, a large amount of wake vortices generated by multiple aircrafts in different weather conditions are collected to build the radial velocity and spectrum width (RV-SW) data sets and to be trained using the CNN models, including the target recognition model and the image classification model. The speed and accuracy of recognition and classification could be improved significantly especially when atmospheric turbulence or other interferences exist. The results show that deep learning models can significantly improve the recognition and classification efficiency of aircraft wake vortices. This method is expected to be applied to the development of a real-time wake vortex monitoring system and further compress the existing wake vortex spacing criteria, which has broad application prospects in the field of airport aviation security assurance.

Keywords Aircraft wake vortex · Coherent Doppler lidar · Convolutional neural network

51.1 Introduction

Aircraft wake vortex is a pair of vortex structures, generated by the lift force exerted on the wings of aircraft, producing potential hazards to the following aircraft. During the landing and take-off phases, the aircraft is close to the ground, so it is difficult to recover quickly once involved in the wake vortex area, causing serious damage [1]. For safety concerns, the regulations based on conservative separation have been used in most airports, of which the capacities are seriously limited consequently. Facing the problems of safety and capacity, there has been a quantity of researches on reducing the minimum separation between two adjacent aircrafts reasonably [2]. As one of the means stipulated by the International Civil Aviation Organization to detect wake vortices, the coherent Doppler lidar has been widely used in wake vortex observations in quite a few airports, covering the aspects of wake vortex decay process, wake vortex evolution under different circumstances, and so on [3, 4]. In recent years, convolutional neural network (CNN) has been used widely, especially in the field of image recognition and classification, providing a new method for the identification of wake vortices and the calculation of circulations.

51.2 Experiments and Data

A pulsed coherent Doppler lidar (PCDL) has been configured at the Qingdao Liuting International Airport (QLIA) to investigate the characteristics of aircraft wake vortex evolution during November 2019 and June 2020. The PCDL was configured at the southeast of the Runway 17/35, approximately 400 m vertically from the Runway 35, as Fig. 51.1 a shows, in which the pentacle represents the location of



Fig. 51.1 A sketch map (**a**) and the lidar location and scanning mode (**b**) of wake vortex observation experiments at QLIA

the lidar and the dots represent two observation positions, about 400 m and 1 km away from the lidar, respectively. Figure 51.1b shows the scanning strategy of the PCDL under different wind directions. The PCDL was operated to observe the wake vortices with range-height-indicator (RHI) scanning strategy. The azimuth angle was set to 260° under south wind to detect the wake vortices generated in Runway 35, while the azimuth was fixed at 320–340° under north wind to scan Runway 17.

51.3 Methodology

The main data process flow chart of aircraft wake vortex (WV) recognition and classification is illustrated in Fig. 51.2, which includes four parts: Data Pre-processing module, WV Recognition module, Feature Extraction module, and WV Classification module.

The Data Pre-processing module aims to build the RV-SW data set for the object detection model. The WV algorithm is used to obtain radial velocity (RV) and spectrum width (SW) images, forming the RV-SW data set according to circulation from the raw data, which will be further illustrated in Sect. 51.3.1.

The WV Recognition module identifies the possible positions of wake vortices while WV Classification module divides the WV region data set into different categories, which will be further introduced in Sect. 51.3.2.

The Feature Extraction module is used to build the WV region data set for the image classification model. The disturbances of the non-WV region will be removed according to the coordinates of wake vortices obtained from the WV Recognition module.

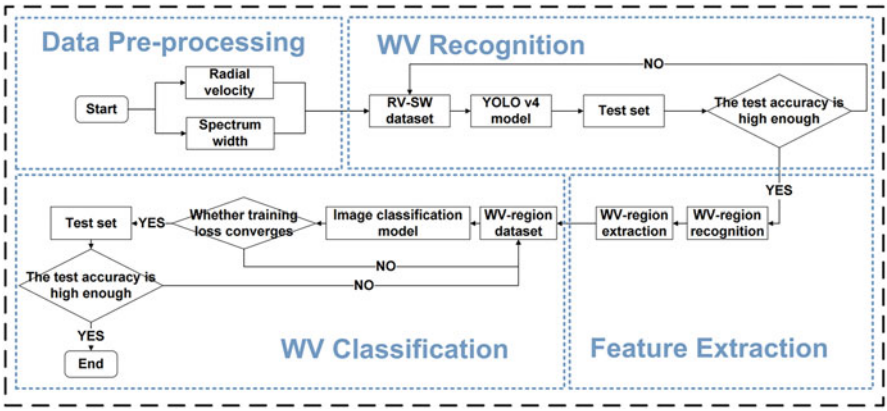


Fig. 51.2 Flow chart of the main methodology of aircraft wake vortex recognition and classification

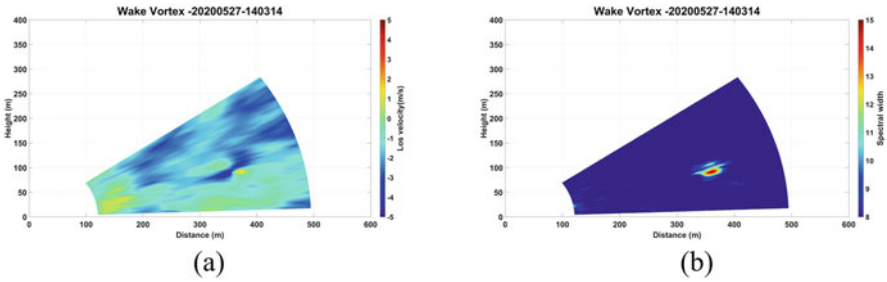


Fig. 51.3 Radial velocity (**a**) and spectrum width (**b**) of wake vortex

51.3.1 Establishment of Data Set

Wake vortices can be recognized from the ambient wind field by the special eddy character. The radial velocity forms a crossover structure in the RHI scans where the wake vortex exits, according to which it can be distinguished from the background wind field, shown in Fig. 51.3a. Meanwhile, the existence of wake vortex will also cause a broadening in the spectrum. The FFT data of a certain range bin and pitch angle has three intersection points with a selected threshold, representing three velocities [3], while the difference between the maximum velocity and the minimum velocity is calculated as the spectrum width in this chapter as Fig. 51.3b shows.

The radial velocity and spectrum width can be integrated to retrieve the positions of vortex cores and thus to calculate the circulation and other parameters. Due to the influence of turbulence and other air flow disturbances, it is difficult to analyze the characteristics of wake vortex by utilizing single radial velocity or single spectrum width information. In this chapter, the radial velocity images and spectrum width images were stacked to build the WV data set. RV-SW images were divided into

strong WV, weak WV, and disturbance according to both circulation value and evolution of wake vortices.

51.3.2 Convolutional Neural Network Models

You Only Look Once (YOLO) network is a viral and widely used one-stage object detection algorithm. YOLO model has become the most frequently used object detection machine learning model, which has been further studied, and the subsequent versions such as YOLO v2, YOLO v3, YOLO v4, and YOLO v5 have been studied and used widely [5]. In this chapter, the YOLO v4 model is used to detect the characteristics of RV-SW images.

YOLO v4 consists of three parts: backbone (CSP Darknet53), neck (SPP and PAN), and head (YOLOv3). The Cross Stage Partial Network (CSPNet) is added to enhance learning ability and reduce computational bottlenecks and costs [6]. The Spatial Pyramid Pooling (SPP) can solve the problem of fixed-size constraint, and the Path Aggregation Network (PANet) can boost the flow of information.

VGGNet was firstly introduced in 2015 for its small convolution filters to increase the depth of the network and expand receptive fields. Mostly the number of weight layers of VGGNet is 11–19; the VGG-16 is used most widely [7]. In this chapter, WV classification model is established by employing a VGG-like network much smaller than VGG-16.

The WV classification model consists of the convolution layer, batch normalization layer, and ReLU layer. The convolution filters are set to be 3×3, and the window of max-pooling is 2×2. The softmax layer classifies the WV region images into strong WV, weak WV, and disturbance.

51.4 Results and Discussion

Figure 51.4 shows the loss curves of the CNN models. The loss function can be used to measure the quality of the model prediction and show the difference between the predicted results and the actual data. The training loss and validation loss of YOLO v4 are shown in Fig. 51.4a, while the losses of WV classification model can be seen in Fig. 51.4b. Both loss functions converge during training processes. The convergence speed of the training curve is faster at the beginning and then gradually slows down with the increase of epochs. The training of YOLO v4 and WV classification model reaches saturation at 15 and 250 epochs, respectively. After training, a test set with 210 images including three categories of strong WV, weak WV, and disturbance was used to test the accuracy of the models.

The accuracy of test results of the trained YOLO v4 model reaches 95.57%; the error mostly lies in missed detection. The intensity and characteristics of wake vortex decrease with evolution, especially when the atmospheric turbulence is

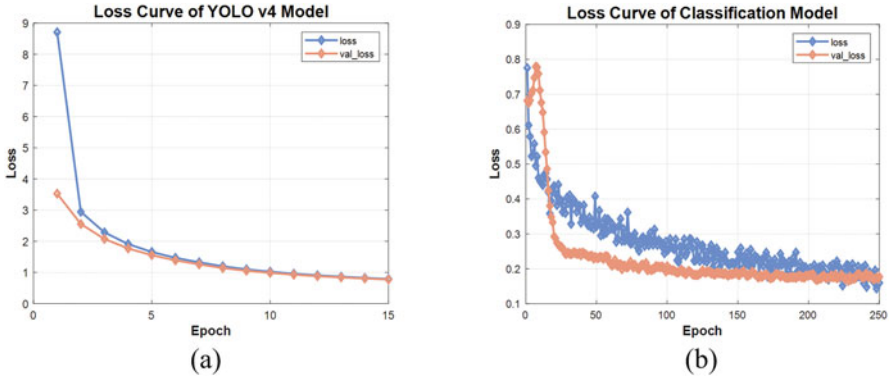


Fig. 51.4 Loss curves of YOLO v4 model (**a**) and WV classification model (**b**)

strong, causing the trained model cannot effectively identify the wake vortex in this period. The strong turbulence may cause mistakenly detection either, since the broadening of spectrum width occurs in the regions of both wake vortex and turbulence.

As for WV classification model, the accuracy of test results reaches 92.26%, in which the test accuracy of the disturbance category is the highest. The test accuracy of weak WV is lower than the other classes, especially when it is affected by the turbulence and unstable atmospheric background wind field. Since the characteristics of strong and weak wake vortices are quite similar, most of the classification errors of the trained classification model focus on identifying strong WV as weak WV or mistaking the latter as the former.

The results indicate that the CNN models can be utilized for the wake vortex recognition and classification effectively based on PCDL data in different wake vortex evolution phases and atmospheric conditions. The future work is to expand the data set and explore how to improve the accuracy of WV recognition and classification models under different background wind fields including stronger turbulence conditions, as well as how to perform more refined intensity classification.

51.5 Conclusion

In this chapter, a series of observation experiments were conducted at QLIA for more than half a year to obtain wake vortex data using the PCDL system under different weather conditions. The data set was established by stacking RV and SW images. In order to improve the model accuracy and avoid turbulence interference, two CNN models including the YOLO v4 model and the WV classification model were built to recognize the possible position of wake vortices and to divide them into three categories. The test accuracy reaches 95.57% and 92.26%, respectively.

The models can significantly improve the recognition and classification efficiency of aircraft wake vortices and provide real-time classifications of wake vortex intensity. It can be considered to expand the data set with more diverse WV scans and further study models of more refined WV classification. The work described in this chapter would have wide application value in the aviation meteorology field.

References

1. Wu, S., Zhai, X., Liu, B.: Aircraft wake vortex and turbulence measurement under near-ground effect using coherent Doppler lidar. Opt. Express. **27**(2), 1142–1163 (2019)
2. Gerz, T., Holzäpfel, F., Bryant, W., Köpp, F., Frech, M., Tafferner, A., Winckelmans, G.: Research towards a wake-vortex advisory system for optimal aircraft spacing. C. R. Phys. **6**(4–5), 501–523 (2005)
3. Köpp, F., Rahm, S., Smalikho, I.: Characterization of aircraft wake vortices by 2-μm pulsed Doppler lidar. J. Atmos. Ocean. Technol. **21**(2), 194–206 (2004)
4. Liu, X., Zhang, X., Zhai, X., Zhang, H., Liu, B., Wu, S.: Observation of aircraft wake vortex evolution under crosswind conditions by pulsed coherent Doppler lidar. Atmos. **12**(1), 49 (2020)
5. Sultana, F., Sufian, A., Dutta, P.: A review of object detection models based on convolutional neural network. In: Intelligent Computing: Image Processing Based Applications, pp. 1–16. Springer Singapore (2020)
6. He, K., Zhang, X., Ren, S., Sun, J.: Spatial pyramid pooling in deep convolutional networks for visual recognition. IEEE Trans. Pattern Anal. Mach. Intell. **37**(9), 1904–1916 (2015)
7. Simonyan, K., Zisserman, A.: Very deep convolutional networks for large-scale image recognition. arXiv preprint arXiv:1409.1556. (2014)

Chapter 52
MicroPulse Differential Absorption LiDAR for Temperature Retrieval in the Lower Troposphere

Owen Cruikshank, Luke Colberg, Kevin S. Repasky, Robert A. Stillwell, and Scott M. Spuler

Abstract A collaborative research effort by Montana State University and the National Center for Atmospheric Research has led to the development of a MicroPulse DIAL (MPD) instruments for water vapor profiling, aerosol profiling, boundary layer structure, and temperature profiling of the lower troposphere. The MPD instruments utilize a diode-laser-based instrument architecture, have demonstrated long-term autonomous network operation, and have the potential to address the needs of the science community for networkable ground-based thermodynamic profilers that can provide data in near real time. In this chapter, the recent improvements to the temperature retrieval using the MPD instruments are discussed and initial results from the improved temperature retrieval algorithm are presented.

Keywords DIAL · Temperature · HSRL

52.1 Introduction

The planetary boundary layer (PBL) is the lowest part of the atmosphere and is affected by interactions with the Earth's surface. The PBL typically experiences a diurnal cycle driven by the incoming solar radiation, and the water vapor, temperature, and wind fields as well as the aerosol distribution vary in time and space. The ability to measure these thermodynamic variables is important for understanding of atmospheric dynamics and climate processes and is recognized as a needed measurement capability [1].

O. Cruikshank (✉) · L. Colberg · K. S. Repasky
Montana State University, Bozeman, MT, USA
e-mail: owen.cruikshank@student.montana.edu

R. A. Stillwell · S. M. Spuler
National Center for Atmospheric Research, Boulder, CO, USA

© The Author(s), under exclusive license to Springer Nature Switzerland AG 2023

J. T. Sullivan et al. (eds.), *Proceedings of the 30th International Laser Radar Conference*, Springer Atmospheric Sciences,
https://doi.org/10.1007/978-3-031-37818-8_52

Researchers at Montana State University (MSU) and the National Center for Atmospheric Research (NCAR) are collaborating on the development of MicroPulse Differential Absorption LiDAR (DIAL), or MPD, instruments for thermodynamic profiling of the lower troposphere [2]. These MPD instruments utilize diode-laser-based instrument architecture that are cost-effective and eye-safe and have demonstrated long-term autonomous networkable operations. Currently, a network of five MPD instruments for water vapor profiling has been developed. Aerosol profiling using the high-spectral-resolution LiDAR (HSRL) technique has also been demonstrated, and more recently, a planetary boundary layer height retrieval has been developed that can retrieve the boundary layer structure [3]. Additionally, an MPD instrument operating near 770 nm has been developed for measuring the absorption due to a temperature-sensitive oxygen (O_2) absorption feature. From the retrieved O_2 absorption profile, a temperature profile can be inferred.

This chapter will discuss the recent advances to the temperature retrieval algorithm and present initial data that utilize the updated temperature retrieval algorithm.

52.2 Temperature Retrieval

The goal of the O_2 DIAL measurement is the retrieval of the temperature-sensitive on-line absorption coefficient used to retrieve the temperature profile. The measurement of the return signals at the on-line ($N_1(R)$) and off-line ($N_2(R)$) wavelengths coupled with the ancillary HSRL measurement does not allow for a closed-form solution to the DIAL equation. An approximate solution can be found for the on-line absorption coefficient by using a perturbative solution where the absorption coefficient, $\alpha(R)$, can be written $\alpha(R) = \alpha_0(R) + \Delta\alpha(R)$, where $\alpha_0(R)$ is a zeroth-order term and $\Delta\alpha(R)$ is a correction. The zeroth-order term, $\alpha_0(R)$, can be found using [4]

$$\frac{ln\left[\frac{N_1(R_2)N_2(R_1)}{N_1(R_1)N_2(R_2)}\right]}{\Delta R} = -2\alpha_0(R), \tag{52.1}$$

where $\Delta R = c\tau/2$ is the range bin size, c is the speed of light, and τ is the pulse duration. Using the results from this zeroth-order equation and the HSRL measurement, the first-order correction, $\Delta\alpha(R)$, can be found to first order as

$$\Delta\alpha(R) = \frac{1}{2}\left(G_1(R) - \alpha_0(R)W(R)\right), \tag{52.2}$$

where $W(R)$ can be written as

$$W(R) = \frac{\int g(\nu - \nu_1, R)E(\nu - \nu_0)\left[f(\nu, R) - 1\right]T_M(\nu, R)d\nu}{\int g(\nu - \nu_1, R)E(\nu - \nu_0)T_M(\nu, R)d\nu}, \tag{52.3}$$

where $E(\nu - \nu_0)$ is the normalized etalon transmission function used in the receiver, $f(\nu, R)$ is the molecular absorption lineshape, $T_M(\nu, R) = exp\left(-\int_0^R \alpha_0(R')dR'\right)$ is the one way molecular absorption transmission and uses the zeroth-order term $\alpha_0(R')$, and $g(\nu - \nu_1, R) = \frac{\beta_A(R)}{\beta(R)}\delta(\nu - \nu_1) + \frac{\beta_M(R)}{\beta(R)}l(\nu - \nu_1, R)$ is the effective lineshape of the backscattered signal near the on-line frequency ν_1 with $\beta(R)$, $\beta_A(R)$, and $\beta_M(R)$ the total, aerosol, and molecular backscatter, and $l(\nu - \nu_1, R)$ the Doppler broadened lineshape. The term $G_1(R)$ can be written as

$$G_1(R) = \frac{\int \frac{dg(\nu-\nu_1,R)}{dR} E(\nu - \nu_0)T_M(\nu, R)d\nu}{\int g(\nu - nu_1)E(\nu - \nu_0)T_M(\nu, R)d\nu}. \tag{52.4}$$

Once the O_2 absorption coefficient is determined, the temperature profile can be inferred. The temperature retrieval requires an initial guess at the temperature profile, T_i, to seed the retrieval (typically, the initial guess uses the surface temperature and a lapse rate of 6.5 K/km). Using the retrieved absorption coefficient and the initial guess at the temperature, an updated temperature profile, T_{i+1}, is estimated. This updated temperature profile is then used as the new seed temperature profile and, again using the retrieved O_2 absorption coefficient, an updated temperature profile is estimated. This iterative process is repeated until the updated temperature profile matches the seed temperature profile. In contrast to Repasky et al. [4], a second absorption line is added to the iterative process where $\alpha(R) = \alpha_a(R) + \alpha_b(R)$ and subscripts a and b indicate the two absorption lines. The updated temperature profile can be calculated as follows:

$$T_{i+1}(R) = T_i(R) + \Delta T_i(R) = T_i(R) + \frac{\alpha_{O_2}(R) - C_{1a}(R)C_{2a}(R)g_a(\nu, R) - C_{1b}(R)C_{2b}(R)g_b(\nu, R)q_{O_2}(1 - q_{wv}(R))}{C_{1a}(R)C_{2a}(R)C_{3a}(R)g_a(\nu, R)C_{1b}(R)C_{2b}(R)C_{3b}(R)g_b(\nu, R)q_{O_2}(1 - q_{wv}(R))}, \tag{52.5}$$

where $\alpha_{O_2}(R)$ is the retrieved absorption, $q_{wv}(R)$ is the water vapor mixing ratio, and

$$C_{1x}(R) = \frac{S_x(T_0)T_0P_i(R)exp\left(\frac{\epsilon_x}{kT_0}\right)}{k}, \tag{52.6}$$

$$C_{2x}(R) = T_i(R)^{-2}exp\left(\frac{-\epsilon_x}{kT_i(R)}\right), \tag{52.7}$$

$$C_{3x}(R) = \frac{-2}{T_i(R)} + \frac{\epsilon_x}{kT_i^2(R)}, \tag{52.8}$$

where $S(T_0)$ is the line strength at the temperature T_0 and ϵ is the ground-state energy. The two absorption lines use separate $S(T_0)$, $g(\nu, R)$, and ϵ substituted into

Eqs. 52.5–52.8. Also in contrast to Repasky et al. $P_i(R) = P_s \left(\frac{T_{si}}{T_{si+L_i R}} \right)^{g_0 M / \bar{R} L_i}$ is used as a pressure model based on a fitted lapse rate L_i, where g_0 is the acceleration due to gravity, M is the molar mass of air, and $\bar{R}$ is the universal gas constant.

52.3 Results

A plot of the absorption as a function of range is shown in Fig. 52.1. The blue line indicates the zeroth-order absorption and is the result of standard DIAL retrieval. The red line is the retrieved absorption profile based on the perturbative retrieval described above. The orange line represents the absorption profile resulting from data collected from a collocated radiosonde launch. For data presented here, pulse rep rate is 7 kHz integrated to a grid of 1 min and averaged over 30 min. A 1 µs pulse sampled at 250 ns for a range resolution of 37.5 m is used and is averaged over 300 m. To achieve a better estimate of temperature, more averaging may be required, especially above 3 km.

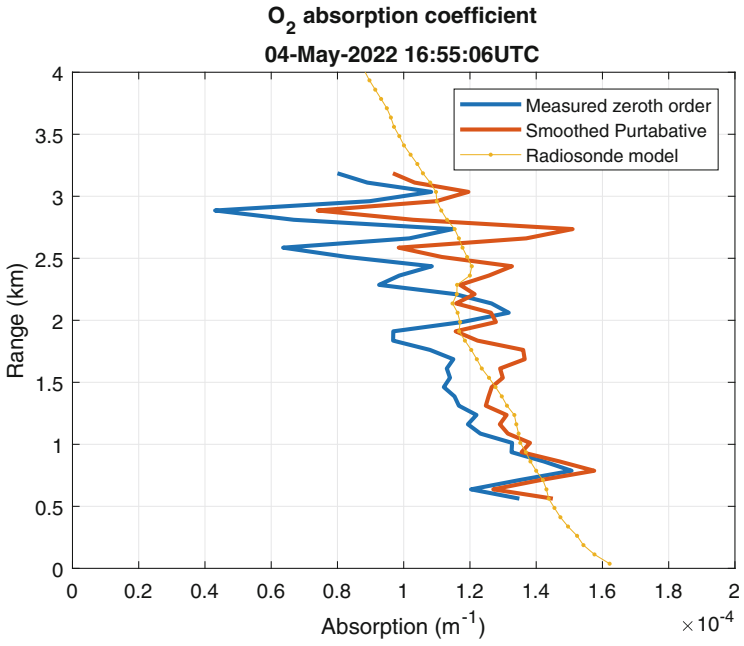


Fig. 52.1 Retrieved profiles from the MPD at MSU. Left: backscatter ratio (total backscatter over molecular backscatter). Right: in blue is the absorption coefficient without the perturbative correction. In red is the absorption coefficient with the perturbative correction. The dot-dashed line represents a model of absorption coefficient based on radiosonde measurements for comparison

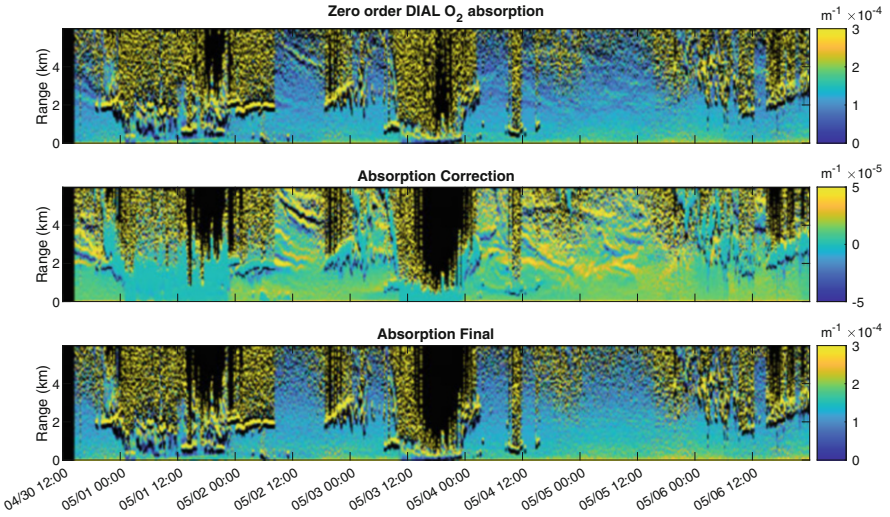


Fig. 52.2 Top: zero-order O_2 absorption from standard DIAL equation. Middle: absorption correction based on the perturbative process. Corrections based on aerosol layers are clearly visible. Bottom: final corrected O_2 absorption. Errors from aerosol layers visible in the top plot are almost fully corrected in the bottom plot. The color scale in the center plot is on a different scale than the other two

A plot of the absorption as a function of range and time is shown in Fig. 52.2. The upper plot shows the zeroth-order retrieved absorption based on the Eq. 52.1 above. This result is equivalent to the standard DIAL retrieval. The middle plot shows the perturbative correction to the absorption coefficient and shows corrections in areas of high backscatter gradients as well as areas of predominantly molecular scattering. The perturbative correction can range up to approximately 10% of the zeroth-order value, causing errors in retrieved temperature in excess of 20–30 °C. The bottom plot shows the total absorption profile. Correction in high-aerosol layers and in inversion layers is visible.

A plot of the temperature as a function of range and time is shown in Fig. 52.3. A data mask for clouds results in gaps in the retrieved temperature seen in the left-hand side of the plot. The dashed vertical lines indicate the launch of radiosondes used for comparison.

A plot of the retrieved temperature profile as a function of time is shown as the left-hand plot in Fig. 52.4. The blue line indicates the retrieved temperature using the absorption profile retrieved using the standard DIAL equation, while the red line indicates the temperature profile retrieved using the absorption profile based on the perturbative retrieval. The orange line indicates the temperature profile measured using the collocated radiosonde. The right-hand plot in Fig. 52.4 shows the temperature difference between the retrieved temperature profile and the temperature profile measured by the radiosonde.

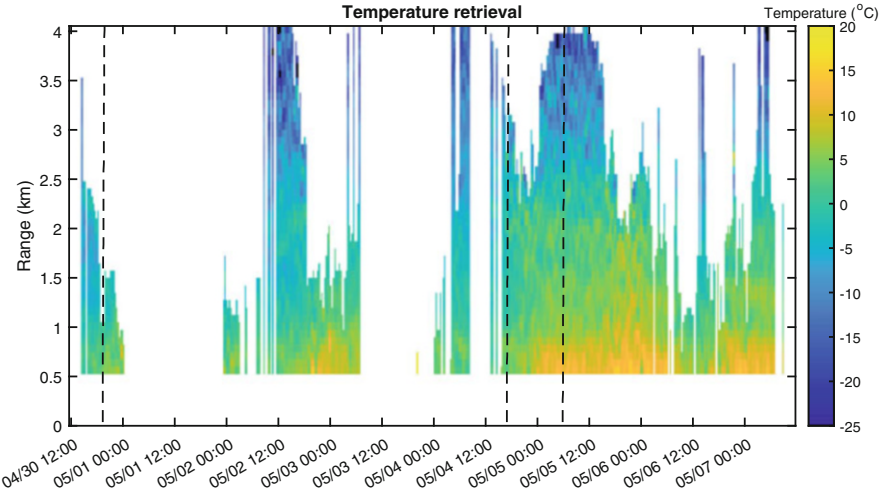


Fig. 52.3 Temperature retrieval from the MSU MPD system in April and May 2022. Areas in white are masked based on signal-to-noise ratio, clouds, and data availability. Vertical dashed lines show radiosonde launches

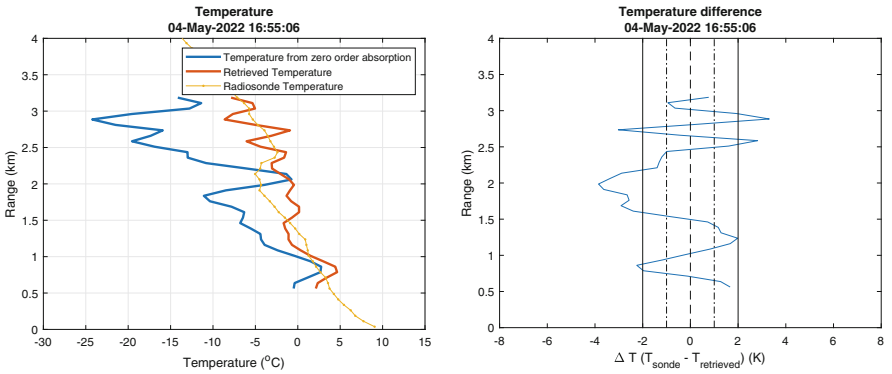


Fig. 52.4 Left: retrieved temperature profile from the MPD at MSU. In blue is the temperature profile without the perturbative absorption correction. In red is the temperature retrieval with the perturbative correction. The dot-dashed line represents the radiosonde temperature measurement for comparison. Right: temperature difference between retrieved temperature and the radiosonde measurement. Vertical lines at 0, 1, and 2 °C for reference

52.4 Summary

Thermodynamic profiles based on the MPD instruments are being developed by MSU and NCAR. These instruments are cost-effective and have demonstrated long-term autonomous networkable operation. Recently, temperature profiling capabilities have been demonstrated, and ongoing research efforts are aimed at improving

the temperature retrieval. Recent improvements to the temperature retrieval program include addition of a second absorption line and an improved pressure model. Work on collecting a long-term data set for validation of the temperature retrieval from the MPD instruments using collocated radiosondes is currently in progress.

Acknowledgments This material is based upon work supported by the Observations Program within NOAA/OAR Office of Weather and Air Quality under Award No. NA19OAR4590323 and NA19OAR4590324. This work was supported by the National Science Foundation grant number 1917851.

References

1. Wulfmeyer, V., Hardesty, R.M., Turner, D.D., Behrendt, A., Cadeddu, M.P., Di Girolamo, P., Schlüssel, P., Van Baelen, J., Zus, F.: A review of the remote sensing of lower tropospheric thermodynamic profiles and its indispensable role for the understanding and the simulation of water and energy cycles. Rev. Geophys. **53**(3), 819–895 (2015). https://doi.org/10.1002/2014RG000476
2. Spuler, S.M., Hayman, M., Stillwell, R.A., Carnes, J., Bernatsky, T., Repasky, K.S.: MicroPulse DIAL (MPD) – a diode-laser-based LiDAR architecture for quantitative atmospheric profiling. Atmos. Meas. Tech. **14**(6), 4593–4616 (2021)
3. Colberg, L., Cruikshank, O., Repasky, K.S.: Planetary boundary layer height retrieval from a diode-laser-based high spectral resolution LiDAR. J. Appl. Remote Sens. **16**(02), 024507 (2022). https://doi.org/10.1117/1.JRS.16.024507
4. Repasky, K.S., Bunn, C.E., Hayman, M., Stillwell, R.A., Spuler, S.M.: Modeling the performance of a diode laser-based (DLB) micro-pulse differential absorption LiDAR (MPD) for temperature profiling in the lower troposphere. Opt. Exp. **27**(23), 33543 (2019)

Chapter 53
Long-Term Calibration of a Pure Rotational Raman LiDAR for Temperature Measurements Using Radiosondes and Solar Background

Vasura Jayaweera, Robert J. Sica, Alexander Haefele, and Giovanni Martucci

Abstract Raman LiDARs are an important tool for measuring the water vapor content and temperature of the troposphere. We present a technique to calibrate temperature measurements from a rotational Raman LiDAR using solar background (internal method), as opposed to requiring a radiosonde measurement (external method) for each calibration. The method is tested using measurements from the Raman LiDAR for Meteorological Observations (RALMO), located at the Swiss Meteorological Services (MeteoSwiss) facility in Payerne, Switzerland. For an accurate temperature or relative humidity trend analysis, minimizing the uncertainties of the LiDAR measurements is vital. The calibration factor used for the temperature measurements is one of the major components contributing to the uncertainty budget of the temperatures. Our goal was to first establish a temperature calibration time series based on the external method using Vaisala RS92 radiosonde measurements certified by the Global Climate Observing System (GCOS) Reference Upper-Air Network (GRUAN). Next, we produced a temperature calibration time series based on the background method. Then, we compared and merged the two calibration data sets to produce a more accurate temperature calibration time series. Finally, we used the calibration constants obtained from the background and the external methods to compare nine RALMO temperature profiles

V. Jayaweera (✉) · R. J. Sica
Department of Physics and Astronomy, Western University, London, ON, Canada
e-mail: yjayawee@uwo.ca; sica@uwo.ca

A. Haefele
Department of Physics and Astronomy, Western University, London, ON, Canada

MeteoSwiss, Payerne, Switzerland
e-mail: ahaefel@uwo.ca; Alexader.Haefele@meteoswiss.ch

G. Martucci
MeteoSwiss, Payerne, Switzerland
e-mail: Giovanni.Martucci@meteoswiss.ch

© The Author(s), under exclusive license to Springer Nature Switzerland AG 2023

J. T. Sullivan et al. (eds.), *Proceedings of the 30th International Laser Radar Conference*, Springer Atmospheric Sciences,
https://doi.org/10.1007/978-3-031-37818-8_53

from the end of 2011 to the end of 2014. The maximum temperature difference, mean bias, and standard deviation of temperature obtained through external vs. background methods are 0.27 K, 0.013 K, and 0.035 K, respectively. While the maximum temperature difference (1 night) was larger for the comparison set used in this study, the mean bias and standard deviation were less than the traditional method applied to RALMO.

Keyword LiDAR

53.1 Introduction

Water vapor is the dominant greenhouse gas in our atmosphere. Its concentration is significantly controlled by surface temperature. The increase in the concentration of water vapor is also considered to be the cause of positive climate feedback leading to increases of temperatures [1, 2]. The primary goal of our project is to investigate the climatology and the trends of relative humidity in the Upper Troposphere and Lower Stratosphere (UTLS) region using simultaneous Raman LiDAR measurements of water vapor and temperature. Accurate relative humidity retrievals are vital for a trend analysis task, and therefore, the validity of the calculated trends is heavily dependent on minimizing the uncertainties associated with these measurements. One of the significant factors contributing to the uncertainty budget of Raman LiDAR measurements is the calibration constants associated with the temperature measurements. Therefore, to minimize these uncertainties, it is vital to refine and improve the calibration methods used. Mahagammulla Gamage et al. [3] have presented a methodology accounting for the full complexity of the Raman LiDAR equation as opposed to using an empirical calibration function. However, the accuracy of this external method still depends on the accuracy and the number of the reference radiosondes used. Hicks-Jalali et al. [4] have also presented an internal calibration technique called the background calibration method, which uses the solar background to determine the calibration constant associated with water vapor mixing ratios. This method is advantageous over the external method since it can compute the entire calibration times series based on one radiosonde measurement, thus reducing the uncertainty contributions from the reference instrument. Our work aims to apply this background calibration method to temperature and to render the variation of the temperature calibration time series independent of radiosonde measurements. We will compare and merge the calibration time series obtained through the external and internal methods to produce a more accurate temperature calibration series that will be helpful for our future trend analysis tasks.

53.2 Measurements and Methodology

53.2.1 Raman LiDAR for Meteorological Observations (RALMO)

To test our technique, we used Raman LiDAR measurements obtained by the Raman LiDAR for Meteorological Observations (RALMO), located at the Swiss Meteorological Services' (MeteoSwiss') Payerne facility (46°48′ N, 6°56′ E, 492 m a.s.l) in Switzerland. It was built by the Swiss Federal Institute of Technology, Lausanne (École Polytechnique Fédérale de Lausanne) and has been operating continuously since 2007. The instrument uses a narrow field-of-view LiDAR receiver and a frequency-tripled Nd:YAG Q-switched laser with an energy of 300–400 mJ at 355 nm, enabling daytime measurements. See for a detailed explanation of the system [5].

RALMOs Pure Rotational Raman (PRR) polychromator separates PRR spectral lines and isolates Rayleigh and Mie lines (Cabannes line). The PRR spectrum of diatomic molecules such as N_2 and O_2 consists of approximately regularly spaced lines distributed on either side of the exciting wavelength in Stokes and anti-Stokes branches. The intensity of the PRR spectra is temperature-dependent, and by analyzing the intensity of an individual or a set of adjacent lines, one can retrieve vertical profiles of the temperature throughout the troposphere and lower stratosphere [6]. Martucci et al. [7] have validated RALMO measurements against two reference operational radiosounding systems (ORSs) co-located with RALMO. Their study shows that RALMO measurements meet the OSCAR (Observing Systems Capability Analysis and Review Tool) breakthrough uncertainty requirements of 1 K for high-resolution numerical weather prediction (NWP). The RALMO water vapor polychromator separates the rotational–vibrational spectral lines of water vapor and nitrogen molecules. Using these measurements, a relative vertical profile of the water vapor mixing ratio can be obtained, which can be made in absolute units via an external calibration.

53.3 Calibration of Temperature Measurements

53.3.1 External Calibration for Temperature

Raman LiDARs make relative measurements of water vapor and temperature. Thus, a calibration is required to convert these relative profiles into physical units. Following [3], we can define an external calibration constant, (CC_{ext}), as follows:

$$CC_{ext} = \frac{C_{JH}}{C_{JL}}, \tag{53.1}$$

where C_{JH} and C_{JL} are the LiDAR constants for the high-quantum-number (JH) and low-quantum-number (JL) digital channels of RALMO, respectively. By using the Raman LiDAR equation for the back-scattered PRR signal in combination with Eq. 53.1, we can obtain

$$CC_{ext} = \frac{\frac{N_{JH}-B_{JH}}{N_{JL}-B_{JL}}}{\frac{\sigma_{JH}}{\sigma_{JL}}}, \tag{53.2}$$

where N_{JH} and N_{JL} are the raw signal for the JH and JL digital channels, B_{JH} and B_{JL} the background photon counts for the JH and JL digital channels, and σ_{JH} and σ_{JL} the differential cross sections for the JH and JL digital channels. Mahagammulla Gamage et al. [3] used this calibration technique along with an optimal estimation method to determine temperature and the uncertainty budget of the random and systematic uncertainties.

53.3.2 Internal Calibration for Temperature: The Solar Background Method

Even though external calibration methods are the most preferred calibration techniques, they require access to an external reference instrument. The most common external references are balloon-borne radiosondes. However, radiosonde calibration can be affected by the balloon's flight path, which depending on conditions can drift horizontally and enter a different air mass than that sampled by the LiDAR. Such drifts in radiosonde measurements will significantly affect the accuracy of the calibration time series.

To improve and extend the external calibration method, [8] presented an internal calibration method that uses the solar background to compute the change in calibration constant as a function of time. Their technique requires only one reference radiosonde measurement to compute the entire calibration times series, thus significantly reducing the uncertainties associated with the reference instrument. We used a similar technique to calculate the solar background ratio of the JH and JL digital channels over time to obtain a relative calibration time series $r_{solar}(t)$,

$$r_{solar}(t) = \frac{B_{JH}^{solar}}{B_{JL}^{solar}}, \tag{53.3}$$

where B_{JH}^{solar} and B_{JL}^{solar} are the solar backgrounds (for RALMO the signal above 55 km) measured by the JH and JL digital channels. The above function is normalized using an external calibration and solar measurement at time t_0 to obtain the background calibration constant (CC_{BCM}) as follows:

$$CC_{BCM}(t) = CC_{ext}(t_0)\frac{r_{solar}(t)}{r_{solar}(t_0)}. \tag{53.4}$$

Here $CC_{ext}(t_0)$ and $r_{solar}(t_0)$ can be calculated using any point in the time series.

53.4 Results

Figure 53.1 shows a comparison between the temperature calibration time series obtained by the external method and the background calibration method. The time series was computed for a selected number of dates spanning from the end of 2011 to the end of 2014, during which MeteoSwiss in Payerne, Switzerland, has been launching Vaisala RS92 sondes to obtain GRUAN-certified profiles of temperature and humidity. For the external method, reference radiosondes launched at midnight were used to compute the calibration time series. As for the background calibration technique, the ratio between the solar background retrievals (30 min integration) at a time corresponding to 70° solar zenith angle from JH and JL digital channels above 55 km was considered to produce the calibration time series. The t_0 calibration was chosen on 2014.07.18.

To understand the meaning of the differences in the calibration values found with each method, each calibration constant was used to compute a nightly averaged temperature profile. The difference in temperature between each set of profiles was then computed (Fig. 53.2). By definition, the temperature differences for the internal

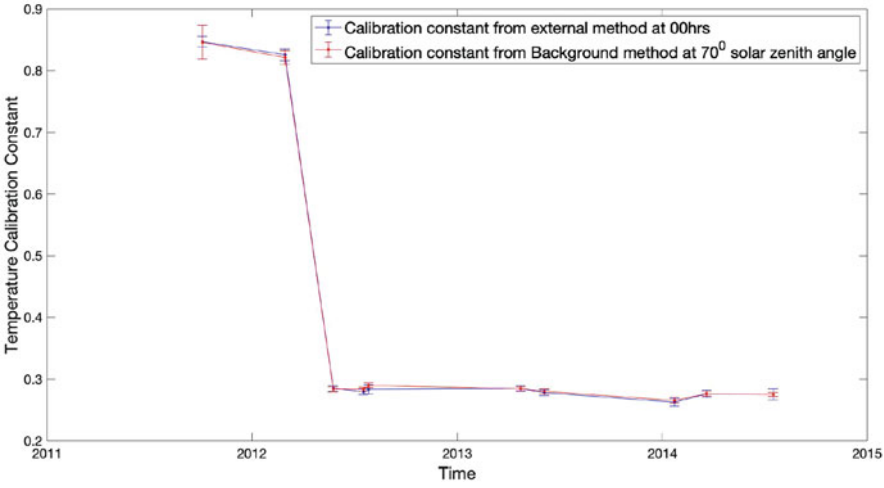


Fig. 53.1 Comparison between the two temperature calibration time series obtained by the external method and the background calibration method for 10 radiosonde external calibrations. The t_0 calibration is at 2014-07-18, the last point in the time series

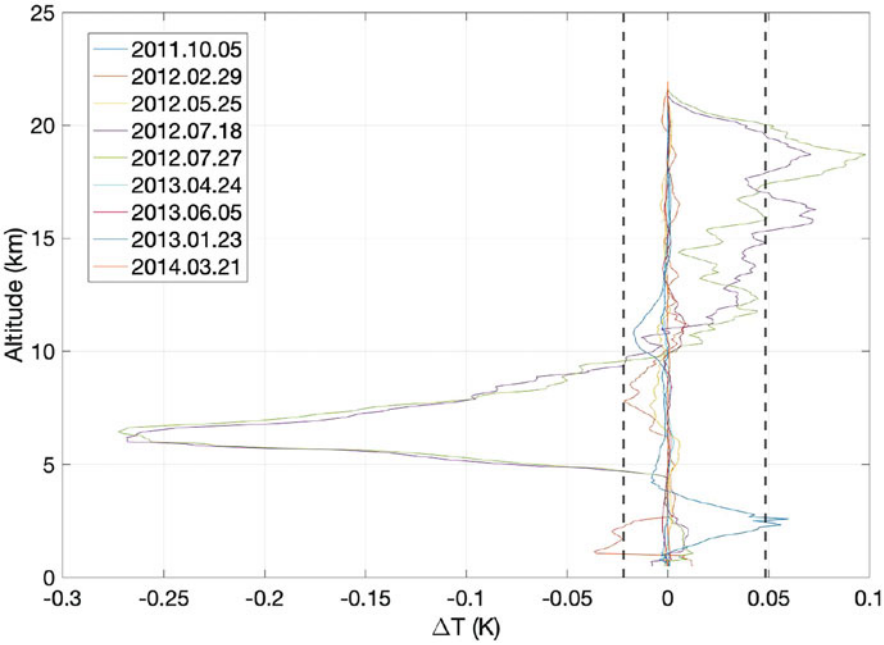


Fig. 53.2 The temperature profile difference between the external and background methods for the dates in the calibration time series. The mean temperature difference was obtained as 0.013 K. The dashed lines show the standard deviation about the mean, that is 0.013 ± 0.035 K

and external points at t_0 are identical. The other 9 profiles show the differences between the temperature profiles obtained from the external and background methods are less than 0.3 K, with a maximum difference of 0.27 K. The mean of the 9 profiles is 0.013 K with a standard deviation of 0.035 K.

53.4.1 Conclusions

The agreement between the external and internal calibration methods to the 2σ level is about 0.07 K, with a bias of 0.013 K. This comparison suggests that we will be able to use the background calibration technique as an alternative to external calibrations to determine our relative humidity climatology. The solar background calibration method will enable us to produce an entire calibration time series based on one external reference instrument measurement. It will help us minimize the effects of drifts, both in the radiosonde measurements and in the LiDAR detector system, thus significantly reducing the uncertainty contributions of the radiosonde calibration on the final temperature profiles.

References

1. Dessler, A., Schoeberl, M., Wang, T., Davis, S., Rosenlof, K.: Stratospheric water vapor feedback. Proc. Natl. Acad. Sci. **110**, 18 087–18 091 (2013)
2. Held, I.M., Soden, B.J.: Water vapor feedback and global warming. Ann. Rev. Energy Environ. **25**, 441–475 (2000)
3. Mahagammulla Gamage, S., Sica, R.J., Martucci, G., Haefele, A.: Retrieval of temperature from a multiple channel pure rotational Raman backscatter LiDAR using an optimal estimation method. Atmos. Meas. Tech. **12**, 5801–5816 (2019)
4. Hicks-Jalali, S., Sica, R.J., Martucci, G., Maillard Barras, E., Voirin, J., Haefele, A.: A Raman LiDAR tropospheric water vapour climatology and height-resolved trend analysis over Payerne, Switzerland. Atmos. Chem. Phys. **20**, 9619–9640 (2020)
5. Dinoev, T., Simeonov, V., Arshinov, Y., Bobrovnikov, S., Ristori, P., Calpini, B., Parlange, M., Bergh, H.: Raman LiDAR for meteorological observations, RALMO–Part 1: instrument description. Atmos. Meas. Tech. **6**, 1329–1346 (2013)
6. Dinoev, T., Simeonov, V., Calpini, B., Parlange, M.: Monitoring of Eyjafjallajökull ash layer evolution over Payerne Switzerland with a Raman LiDAR. In: Proc. TECO (2010)
7. Martucci, G., Navas-Guzmán, F., Renaud, L., Romanens, G., Gamage, S.M., Hervo, M., Jeannet, P., Haefele, A.: Validation of pure rotational Raman temperature data from the Raman LiDAR for Meteorological Observations (RALMO) at Payerne. Atmos. Meas. Tech. **14**, 1333–1353 (2021)
8. Sherlock, V., Hauchecorne, A., Lenoble, J.: Methodology for the independent calibration of Raman backscatter water-vapor LiDAR systems. Appl. Opt. **38**, 5816–5837 (1999)

Chapter 54
Powerful Raman LiDAR for Water Vapor in the Free Troposphere and Lower Stratosphere as well as Temperature in the Stratosphere and Mesosphere



Hannes Vogelmann, Thomas Trickl, Lisa Klanner, Katharina Höveler, and Matthias Perfahl

Abstract A high-power Raman LiDAR system has been installed at the mountain research station Schneefernerhaus (UFS, Garmisch-Partenkirchen, Germany) at 2675 m a.s.l. on Mt. Zugspitze. An industrial XeCl laser (350 W, 308 nm) was modified for linearly polarized narrowband single-line operation at an average power of up to 180 W. Together with a receiving telescope with a diameter of 1.5 m, this allows for a sounding range of up to 25 km for water vapor within a measurement time of just 1 h, at an uncertainty level of the mixing ratio in the stratosphere of 1 to 4 ppm. The LiDAR was successfully validated with a balloon-borne cryogenic frost-point hygrometer. In addition, 1-h temperature profiles are retrieved to altitudes beyond 80 km that agree well with temperature profiles from radiosondes, NCEP, and satellites, as well as mesospheric OH fluorescence data. Routine temperature measurements under remote control have been started.

Keywords High power · Raman LiDAR · Water vapor · Temperature

54.1 Introduction

Water vapor in the upper troposphere and lower stratosphere (UTLS) controls the thermal infrared radiation emitted from the Earth and its atmosphere into space [1–3]. In a warmer climate, more water evaporates from the sea surface. This increase could be counteracted by cloud formation and precipitation. Also, vertical exchange processes could become more significant in a warmer climate [4, 5]. Quite interestingly, measured water vapor trends in the troposphere have indicated a

H. Vogelmann (✉) · T. Trickl · L. Klanner · K. Höveler · M. Perfhal
Karlsruhe Institute of Technology, IMK-IFU Campus Alpin, Garmisch-Partenkirchen, Germany
e-mail: vogelmann@kit.edu

© The Author(s), under exclusive license to Springer Nature Switzerland AG 2023

J. T. Sullivan et al. (eds.), *Proceedings of the 30th International Laser Radar Conference*, Springer Atmospheric Sciences,
https://doi.org/10.1007/978-3-031-37818-8_54

humidity decrease at most altitudes [6–8]. This contradicts the expectations from climate modeling. These results suggest that the optimization of high-accuracy, range-resolved vertical sounding instrumentation for water vapor covering the entire free troposphere and the lower stratosphere is highly important [9]. There is some instrumental deficit between 10 and 20 km for vertically resolved measurements. LiDAR-based measurements have the potential of good temporal and vertical resolutions and are, therefore, attractive for resolving the transport-related variability of water vapor. However, the use of LiDAR systems for water vapor implies a major challenge due to the strong decrease of both the backscatter signal and the water-vapor concentration with altitude. The very small stratospheric mixing ratio of water vapor is only 4 to 5 ppm [10]. Despite the problems related to the extreme signal dynamics, the NDACC (Network for the Detection of Atmospheric Composition Change) LiDAR working group has strongly advocated to develop powerful ground-based water-vapor LiDAR systems with UTLS capability, with focus on the Raman LiDAR technique. Several Raman LiDAR systems have already reached a reasonable stratospheric performance [11–13]. However, vertical ranges up to more than 20 km a.s.l. require averaging over many hours. It is obvious that an order-of-magnitude increase in Raman backscatter signal is needed to overcome these issues. At the Karlsruhe Institute of Technology (KIT IMK-IFU), a high-power Raman LiDAR has been built that extends the range of water-vapor profiling with the existing differential-absorption LiDAR (DIAL) [14] into the lower stratosphere during nighttime, with a data acquisition time of just 1 h [15]. The system is operated side by side with the DIAL at the Schneefernerhaus mountain station (UFS) on Mt. Zugspitze at an altitude of 2675 m, which offers the possibility of direct and accurate calibration of the Raman LiDAR. The DIAL has been thoroughly validated and is free of bias at an uncertainty level of 1% of average concentrations or less up to about 7 km [16, 17]. Both systems probe the same atmospheric volume and can be very reliably compared in this part of the operating range of the DIAL. The large system allows us to make temperature measurements up to the mesosphere based on an established approach for inverting the Rayleigh backscatter signal for 355 nm [18]. In this way, not only the primary greenhouse gas, but also the most important climate parameter is provided.

54.2 System Description

The UFS Raman LiDAR system and some results were recently described in detail by Klanner et al. [15]. Here, we just give a brief overview of the most important design properties. The laser system is a 350-W XeCl laser (1 J, 350 Hz) from Coherent (formerly Lambda Physik), modified for single-line operation with linear polarization. In this configuration, up to 180 W has been achieved, ten times the power of existing stratospheric Raman LiDAR systems. Due to thermal issues of some of the optical components caused by residual absorption, the power after hours of operation is somewhat lower. We expect a much better performance

from loss-free intracavity components that are meanwhile available. In addition, a considerable increase in power can be expected from shortening the laser cavity in order to obtain more round trips. For the temperature measurements, we meanwhile use an injection-seeded frequency-tripled Nd:YAG laser (Continuum, Powerlite 8020 Precision) with 160 mJ at 355 nm. The limiting factor here is the low repetition rate of 20 Hz.

The receiver consists of a primary mirror with 1.5 m diameter and a focal length of 5 m and a six-channel polychromator. These channels are Rayleigh backscatter at 308 nm and 355 nm, rotational Raman return at two wavelengths near 308 nm, and ro-vibrational Raman returns from both nitrogen and water vapor at 332 nm and 347 nm, respectively. The polychromator consists of relay-imaging modules and efficiently suppresses the strong Rayleigh return in the Raman channels. The data evaluation yields water-vapor mixing ratios retrieved from the nitrogen and water-vapor signals and the temperature based on inverting the 355-nm return. The H_2O procedure includes now an extinction correction that improved the tropospheric performance by a few percent. The temperature procedure first evaluates the atmospheric density in a Klett-type approach and then the temperature by integration. The recent improvements are further discussed in Sect. 54.3.

54.3 Results for Water Vapor and Temperature

Between 2015 and February 2019, many test measurements were made. A few examples are described by Klanner et al. [15]. Here, we show the revised retrievals for a validation campaign on February 5–7, 2019. This campaign benefitted from several balloon ascents with cryogenic frost-point hygrometers (CFH) carried out at IMK-IFU (Garmisch-Partenkirchen, 730 m a.s.l., 9 km to the north–east from UFS) by a team from the Forschungszentrum Jülich (Germany). Figures 54.1 and 54.2 show one result from late February 5, one of the two cases during this night with perfect temporal overlap of LiDAR and CFH sonde. The revised algorithm yielded reasonable mixing ratios for the LiDAR up to 25 km a.s.l. The humidity step at 12.8 km is widened in the LiDAR results due to the long averaging time of 1 h. The sonde rose almost vertically within the troposphere, a unique situation for a comparison. However, there is a discrepancy between the two instruments in the range 3.7 km to 5.7 km. This is explained by the onset strongly layered stratospheric air entering our area starting on that evening, as also seen in our ozone soundings. One has to consider not only the pronounced spatial inhomogeneity of this air mass, but also the long averaging time of the LiDAR under these conditions. Again, our measurements underline the necessity of using the DIAL as the calibration source that ensures probing the same volume. A new laser is under development [20]. The measurements are limited not only by the laser power. First, the background could not be reduced to less than 2–3 counts per hour and bin (no dark counts). The reason for this background has not been identified. Second, broadband spectral filtering the H_2O return, to cover all three rotational branches and to avoid the transmission

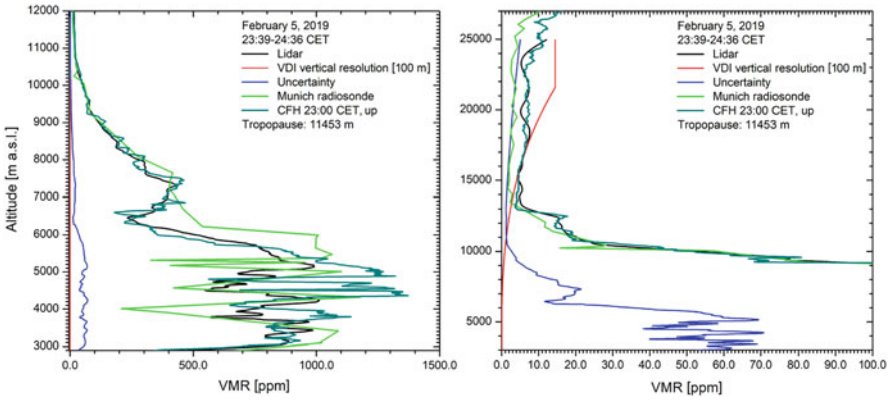


Fig. 54.1 Left: Volume mixing ratios (VMR) from measurements around midnight between February 5 and 6, 2019: LiDAR (black), CFH (dark blue), and Munich radiosonde (1:00 CET = 0:00 UTC, green). Right: Zoomed section where the red curve represents the vertical resolution interval as defined by VDI [19], maximizing at 1.45 km. For the uncertainty curve (blue), see [9]

loss of the narrowband filter, would yield a three times higher signal. In summary, modifications could yield at least six times more signal. The results suggest that we are almost ready for routine measurements. Routine operations will start after the laser upgrading and the revival of the H_2O DIAL. Meanwhile, routine temperature measurements have started under remote control. First retrievals for 2021 verify the range up to more than 80 km found in the case study of Ref. [15]. Here we show an example from October 21, 2021 (Fig. 54.2). We introduced two improvements, most importantly an aerosol correction. The aerosol backscatter coefficients are taken from our routine measurements within NDACC [21] and converted from 532 nm to 355 nm. This resulted in a positive temperature bias of about 3 K at 20 km under the conditions of October 2021. This bias is canceled by applying a tiny exponential correction of the analog raw signal [15, 19] that turned out not to be fully negligible. The agreement with the temperature from the Munich radiosonde and NCEP (National Centers for Environmental Predictions) analyses is impressive, which fully justifies our technical approach not relying just on photon counting. The performance of the LiDAR above 70 km must be improved in order to fulfill the objective of routine comparisons with the mesospheric temperature retrievals from OH fluorescence measurements at UFS [22]. Diode-laser-pumped Nd:YAG lasers with reasonable pulse energy are now available with repetition rates of 300 Hz and more. For the retrieval in the mesosphere, an option is to use these data obtained as reference temperatures for the LiDAR retrieval (see example in [15]).

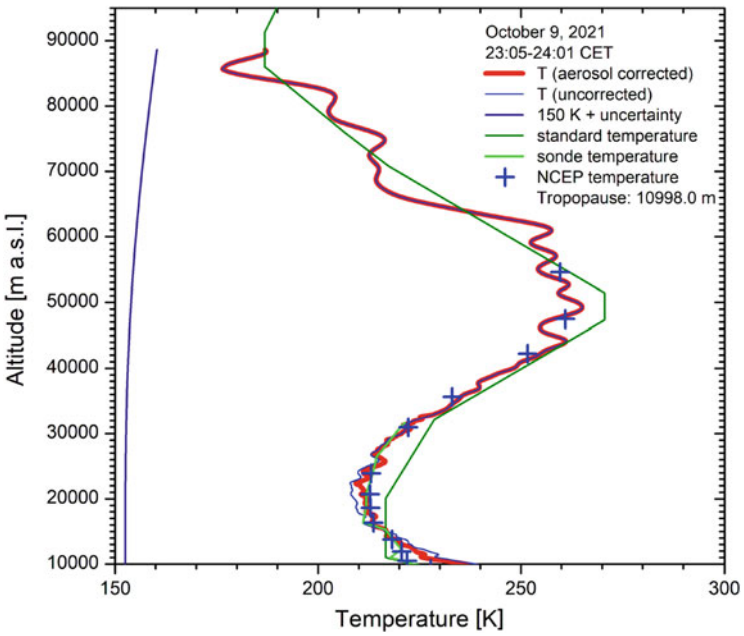


Fig. 54.2 Temperature profiles on October 9, 2021: LiDAR (red: with aerosol correction; blue: without aerosol correction), Munich radiosonde (light green), NCEP (blue crosses), U.S. Standard Atmosphere (green)

54.4 Conclusions

Water-vapor profiling up to the lower stratosphere (25 km) with a Raman LiDAR within only one hour and a reasonable vertical resolution (≈1 km) connotes a significant progress in Raman LiDAR technology. This was achieved by scaling up the laser power (180 W) and by using a very large receiver telescope (1.5 m). The latter is also the key to temperature profiling up 90 km in the same integration time. Further steps of improvement will be routine operation, remote control of the system, and operational data evaluation.

References

1. Kiehl, J.T., Trenberth, K.E.: Earth's annual global mean energy budget. B. Am. Meteorol. Soc. **78**, 197–208 (1997)
2. Lacis, A.A., Hansen, J.E., Russell, G.L., Oinas, V., Jonas, J.: The role of long-lived greenhouse gases as principal LW control knob that governs the global surface temperature for past and future climate change. Tellus Ser. B Chem. Phys. Meteorol. B **65**, 19734 (2013)

3. Schmidt, G.A., Ruedy, R.A., Miller, R.L., Lacis, A.A.: Attribution of the present-day total greenhouse effect. J. Geophys. Res. **115**(D20), D20106 (2010)
4. Trickl, T., Feldmann, H., Kanter, H.J., Scheel, H.E., Sprenger, M., Stohl, A., Wernli, H.: Forecasted deep stratospheric intrusions over central Europe: case studies and climatologies. Atmos. Chem. Phys. **10**(2), 499–524 (2010). http://www.atmos-chem-phys.net/10/499/2010/
5. Trickl, T., Vogelmann, H., Ries, L., Sprenger, M.: Very high stratospheric influence observed in the free troposphere over the Northern Alps – just a local phenomenon? Atmos. Chem. Phys. **20**(1), 243–266 (2020). https://acp.copernicus.org/articles/20/243/2020/
6. Paltridge, G., Arking, A., Pook, M.: Trends in middle- and upper-level tropospheric humidity from NCEP reanalysis data. Theor. Appl. Climatol. **98**(3–4), 351–359 (2009)
7. Solomon, S., Rosenlof, K.H., Portmann, R.W., Daniel, J.S., Davis, S.M., Sanford, T.J., Plattner, G.K.: Contributions of stratospheric water vapor to decadal changes in the rate of global warming. Science **237**(5970), 1219–1223 (2010)
8. Hegglin, M.I., Plummer, D.A., Shepherd, T.G., Scinocca, J.F., Anderson, J., Froidevaux, L., Funke, B., Hurst, D., Rozanov, A., Urban, J., von Clarmann, T., Walker, K.A., Wang, H.J., Tegtmeier, S., Weigel, K.: Vertical structure of stratospheric water vapour trends derived from merged satellite data. Nat. Geosci. **7**(10), 768–776 (2014)
9. Kämpfer, N. (ed.): Monitoring Atmospheric Water Vapour – Ground-Based Remote Sensing and In-situ Methods. Springer, Berlin (2013)
10. Hurst, D.F., Oltmans, S.J., VöMel, H., Rosenlof, K.H., Davis, S.M., Ray, E.A., Hall, E.G., Jordan, A.F.: Stratospheric water vapor trends over Boulder, Colorado: Analysis of the 30 year Boulder record. J. Geophys. Res. (Atmos.) **116**(D2), D02306 (2011)
11. Whiteman, D.N., Rush, K., Rabenhorst, S., Welch, W., Cadirola, M., McIntire, G., Russo, F., Adam, M., Venable, D., Connell, R., Veselovskii, I., Forno, R., Mielke, B., Stein, B., Leblanc, T., McDermid, S., Vömel, H.: Airborne and ground-based measurements using a high-performance Raman LiDAR. J. Atmos. Oceanic Technol. **27**(11), 1781–1801 (2010)
12. Leblanc, T., McDermid, I.S., Walsh, T.D.: Ground-based water vapor Raman LiDAR measurements up to the upper troposphere and lower stratosphere for long-term monitoring. Atmos. Meas. Tech. **5**(1), 17–36 (2012)
13. Vérèmes, H., Payen, G., Keckhut, P., Duflot, V., Baray, J.L., Cammas, J.P., Evan, S., Posny, F., Körner, S., Bosser, P.: Validation of the water vapor profiles of the Raman LiDAR at the Maïdo observatory (Reunion Island) calibrated with global navigation satellite system integrated water vapor. Atmosphere **10**(11), 713 (2019)
14. Vogelmann, H., Trickl, T.: Wide range sounding of free tropospheric water vapor with a differential absorption LiDAR (DIAL) at a high altitude station. Appl. Opt. **47**(12), 2116–2132 (2008)
15. Klanner, L., Höveler, K., Khordakova, D., Perfahl, M., Rolf, C., Trickl, T., Vogelmann, H.: A powerful LiDAR system capable of 1 h measurements of water vapour in the troposphere and the lower stratosphere as well as the temperature in the upper stratosphere and mesosphere. Atmos. Meas. Tech. **14**(1), 531–555 (2021). https://amt.copernicus.org/articles/14/531/2021/
16. Vogelmann, H., Sussmann, R., Trickl, T., Borsdorff, T.: Intercomparison of atmospheric water vapor soundings from the differential absorption LiDAR (DIAL) and the solar FTIR system on Mt. Zugspitze. Atmos. Meas. Tech. **4**(5), 835–841 (2011). http://www.atmos-meas-tech.net/4/835/2011/
17. Trickl, T., Vogelmann, H., Fix, A., Schäfler, A., Wirth, M., Calpini, B., Levrat, G., Romanens, G., Apituley, A., Wilson, K.M., Begbie, R., Reichardt, J., Vömel, H., Sprenger, M.: How stratospheric are deep stratospheric intrusions? LUAMI 2008. Atmos. Chem. Phys. **16**(14), 8791–8815 (2016). http://www.atmos-chem-phys.net/16/8791/2016/
18. Hauchecorne, A., Chanin, M.L.: Density and temperature profiles obtained by LiDAR between 35 and 70 km. Geophys. Res. Lett. **7**(8), 565–568 (1980)
19. Trickl, T., Giehl, H., Neidl, F., Perfahl, M., Vogelmann, H.: Three decades of tropospheric ozone LiDAR development at Garmisch-Partenkirchen, Germany. Atmos. Meas. Tech. **13**(11), 6357–6390 (2020). https://amt.copernicus.org/articles/13/6357/2020/

20. Vogelmann, H., Speidel, J., Perfahl, M., Trickl, T.: Transverse-pumping approach for a powerful single-mode Ti:sapphire laser for near infrared LiDAR applications. Appl. Opt. **61**(29), 8553–8562 (2022). http://opg.optica.org/ao/abstract.cfm?URI=ao-61-29-8553
21. Trickl, T., Vogelmann, H., Giehl, H., Jäger, H., Perfahl, M.: Stratospheric aerosol – 45 years of LiDAR measurements at Garmisch-Partenkirchen. In: The 30th International Laser Radar Conference (ILRC 30) (2022). This volume
22. Schmidt, C., Höppner, K., Bittner, M.: A ground-based spectrometer equipped with an InGaAs array for routine observations of OH(3-1) rotational temperatures in the mesopause region. J. Atmos. Sol. Terr. Phys. **102**, 125–139 (2013)

Chapter 55
Observation of Rainfall Velocity and Raindrop Size Using Power Spectrum of Coherent Doppler Lidar

Xiaoying Liu, Songhua Wu, Guangyao Dai, Pei Chen, Rongzhong Li, and Jiaping Yin

Abstract Precipitation plays an important role in meteorology, hydrology, and the coupling of water, energy, and biogeochemical cycles in the Earth system. Lidar can be utilized as a valuable remote sensing instrument to detect rain because of its high temporal and spatial resolutions. This paper introduces the observation of rainfall velocity and raindrop size by analyzing the power spectrum of coherent Doppler lidar taking vertical staring mode. The rain measurement campaign was conducted at the Laoshan campus of Ocean University of China. A ground-based coherent Doppler lidar and a Parsivel^2 disdrometer deployed on the top of the building with a height of 12 m are used for comparative measurements. The rain and wind power spectrum can be identified simultaneously by using a two-component Gaussian model. The spectrum width of lidar during the rain events is wider than that on

X. Liu (✉) · G. Dai · P. Chen
College of Marine Technology, Faculty of Information Science and Engineering, Ocean University of China, Qingdao, China

S. Wu
College of Marine Technology, Faculty of Information Science and Engineering, Ocean University of China, Qingdao, China

Institute for Advanced Ocean Study, Ocean University of China, Qingdao, China
e-mail: wush@ouc.edu.cn

Laboratory for Regional Oceanography and Numerical Modeling, Pilot National Laboratory for Marine Science and Technology (Qingdao), Qingdao, China
e-mail: wush@ouc.edu.cn

R. Li
College of Marine Technology, Faculty of Information Science and Engineering, Ocean University of China, Qingdao, China

Qingdao Leice Transient Technology Co., Ltd., Qingdao, China
e-mail: lirongzhong@leice-lidar.com; yinjiaping@leice-lidar.com

J. Yin
Qingdao Leice Transient Technology Co., Ltd., Qingdao, China
e-mail: lirongzhong@leice-lidar.com; yinjiaping@leice-lidar.com

© The Author(s), under exclusive license to Springer Nature Switzerland AG 2023

J. T. Sullivan et al. (eds.), *Proceedings of the 30th International Laser Radar Conference*, Springer Atmospheric Sciences,
https://doi.org/10.1007/978-3-031-37818-8_55

a clear day. Unlike the disdrometer, the lidar provides the rainfall velocity profiles at different heights. This chapter also investigates the raindrop size distribution from the lidar spectrum. Furthermore, the comparison of rainfall velocity distribution between lidar and disdrometer is presented in this chapter as well.

Keywords Coherent Doppler lidar · Rainfall velocity · Raindrop size distribution

55.1 Introduction

Precipitation becomes an important parameter in many fields, such as meteorology [1, 2], hydrology [3], and the coupling of water, energy, and biogeochemical cycles in the Earth system [4]. Rain observation helps to forecast extreme weather events, avoid potential flight accidents under rainy conditions, and reduce the leading-edge erosion of wind turbine blades. Rain parameters can be measured by various instruments, including in situ and remote sensing techniques. For in situ techniques, disdrometers become the most common and cost-effective instrument [5], such as the Joss-Waldvogel disdrometer (JWD), laser precipitation monitor (LPM), and particle size and velocity (Parsivel). The disadvantage of disdrometers is that they only measure raindrops at a certain point. Regarding remote sensing techniques, radars, which can provide rain profiles, are the popular instruments in rain observation. However, radars are limited to detecting rain in the lower atmospheric boundary layer due to the errors induced by ground clutters [5].

In recent years, coherent Doppler lidar (CDL) has been used for rain study as a new precipitation detection instrument. It provides the profiles of rain parameters from near the ground with high temporal and spatial resolutions. During rain events, lidar has been proved to measure simultaneously wind and rain by power spectrum analysis [6]. The direct rain parameter measured by CDL is rainfall velocity. The two-peak power spectrum of wind lidar is first reported in the literature using a vertically pointing CDL [7]. The two-component Gaussian model is proposed to identify the rain and aerosol spectra based on the double-peak power spectrum [5]. Moreover, raindrop size distribution (DSD) can be estimated from the lidar spectrum using vertical stare mode [5, 6].

This chapter investigates rain identification and rainfall velocity retrieval using coherent Doppler lidar. Raindrop size distribution is estimated by lidar measurement data. In addition, the comparison results of DSD between lidar and disdrometer are provided in this chapter as well.

55.2 Experiments

The rain measurement campaign was conducted at the Laoshan campus of Ocean University of China. A ground-based coherent Doppler lidar, Wind3D 6000, is

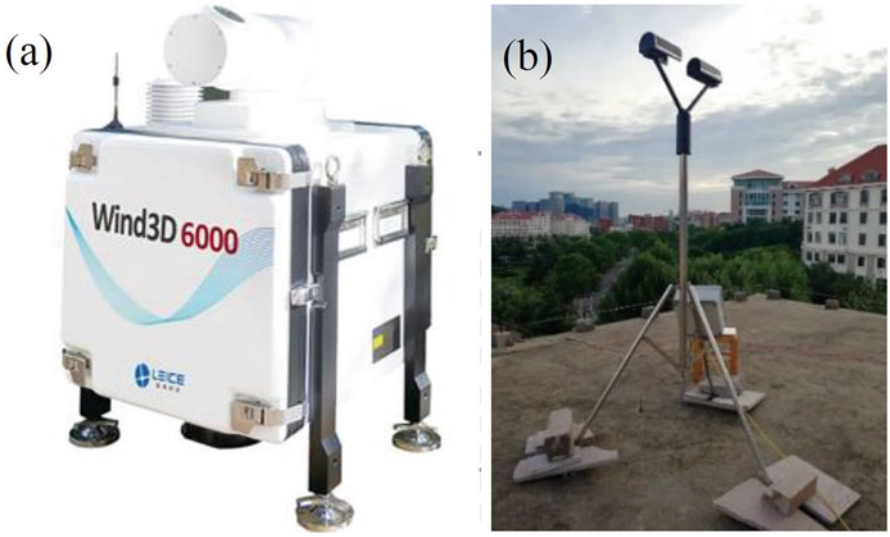


Fig. 55.1 The measurement instruments. (**a**) Wind3D 6000 lidar system. (**b**) Parsivel^2 disdrometer

applied to observe rain in this study, as shown in Fig. 55.1a. Additionally, a Parsivel^2 disdrometer was deployed on the top of the building with a height of 12 m, as shown in Fig. 55.1b. The horizontal distance between lidar and disdrometer is around 25 m.

The wind velocity measured by the Wind3D 6000 has been verified to have a good agreement with that observed by cup anemometers in our previous study [8]. Table 55.1 lists the main technical specifications of Wind3D 6000 scanning wind lidar for the data set analysis. In this study, the CDL operates with a range gate resolution of 30 m and a temporal resolution of 1 s. A total of 1024 points including the number of zero padding of 768 was used for FFT with a rectangular window. The CDL adopts the pulse shots of 10,000 with each pulse duration of 200 ns. The spectral width of a hard target is 3.52 MHz. Parsivel^2 measures raindrops at a laser wavelength of 650 nm with a time resolution of 1 min, 32 diameter classes, and 32 velocity diameter classes.

55.3 Results

55.3.1 Lidar Power Spectrum Analysis During Rain Events

On a clear day, the motion of aerosol particle produces a narrow band in the lidar power spectrum at different heights due to the Doppler effect, as shown in Fig. 55.2a. The lidar power spectrum at a certain height (such as 90 m as shown in Fig. 55.2d) has a single peak. During rain events, as shown in Fig. 55.2b, falling raindrops also

Table 55.1 Technical specifications of Wind3D 6000 scanning wind lidar

Parameter	Specification
Wavelength	1.55 μm
Pulse repetition frequency	10 kHz
Sampling frequency	1 GHz
Pulse duration	200 ns
Pulse energy	150 μJ
Measurement range	45–6000 m
Range gate resolution	15–60 m
Intermediate frequency	49.39 MHz
FFT length N	1024
Zero padding number	768
Data update rate	1–10 Hz

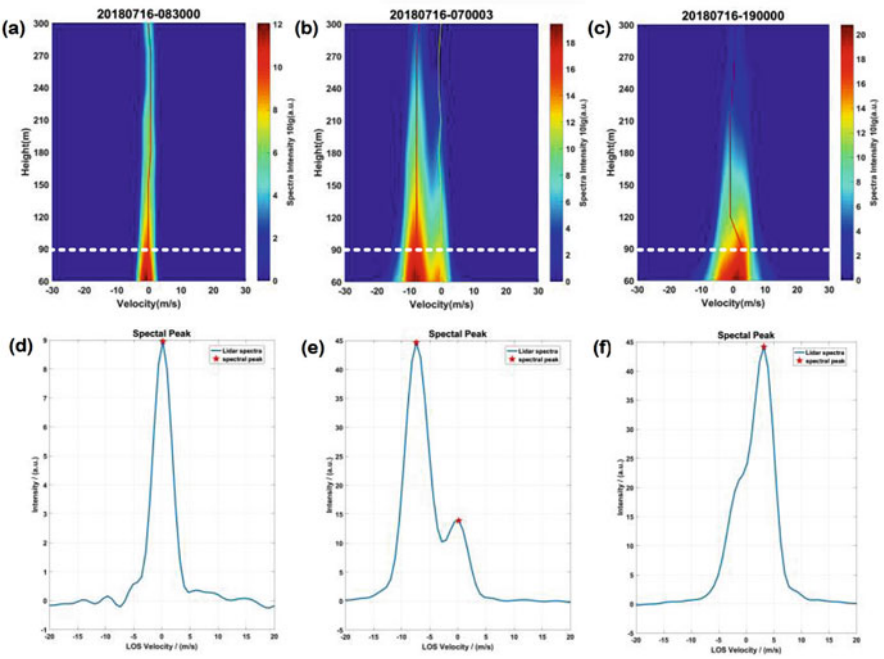


Fig. 55.2 Lidar power spectra under different weather conditions. (**a**) Single narrow spectral band on a clear day at different heights, (**b**) two spectral bands on a rainy day at different *heights*, (**c**) *single broadening spectral band on a rainy day at different heights*, (**d**) *single peak of the* spectrum on a clear day at 90 m, (**e**) obvious double peaks of the spectrum on a rainy day at 90 m, and (**f**) hidden double peaks of the spectrum on a rainy day at 90 m

introduce the Doppler shift to the power spectrum with the broadening band. Figure 55.2e shows the lidar power spectrum with obvious double peaks at the height of 90 m. In this case, the spectrum is the superposition of the backscattering signal from aerosol particles and raindrops at various velocities. Different from the cases

in Fig. 55.2a, b, the spectrum with a broadening band only has a single peak, as illustrated in Fig. 55.2c, f. It is called the hidden peak spectrum in this chapter. The velocities of aerosols and raindrops in the hidden peak spectrum are closer than those in the obvious double peak spectrum because of the different rain conditions.

55.3.2 Rain Identification

Disdrometer recorded three rain events on August 23, 2021, as illustrated in Fig. 55.3. In this rain detection experiment, CDL also detected these rain events by taking vertical stare mode. Rain power spectra caused by the motion of falling raindrops are observed by CDL. The rain power spectrum and aerosol power spectrum can be fitted using a two-component Gaussian model [5]. The negative sign of the radial velocity, in this chapter, indicates that particles are moving in the direction close to the lidar. Therefore, the left spectral model represents the rainfall velocity spectrum (green lines in Fig. 55.4) because of the falling raindrops along vertical lidar beams. The red dash line in Fig. 55.4 represents the vertical wind velocity fluctuating around 0 m/s.

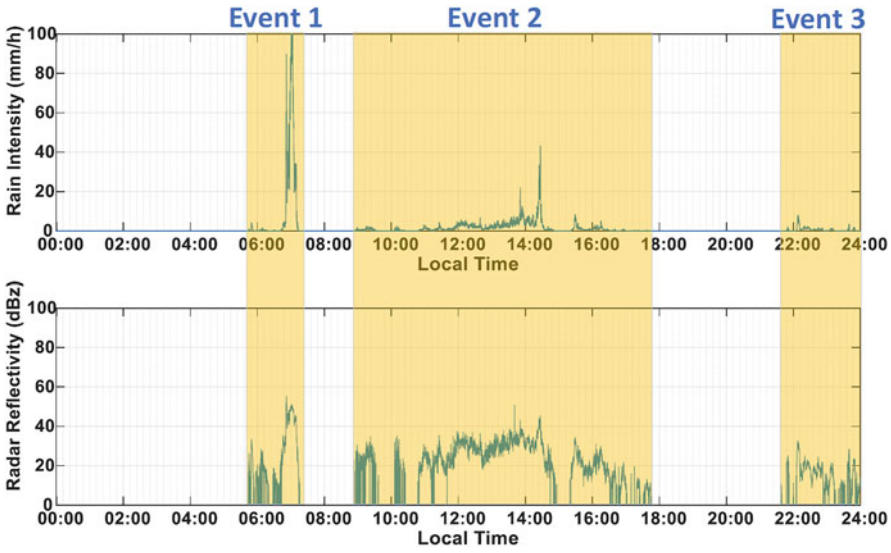


Fig. 55.3 Rain events measured by disdrometer on August 23, 2021

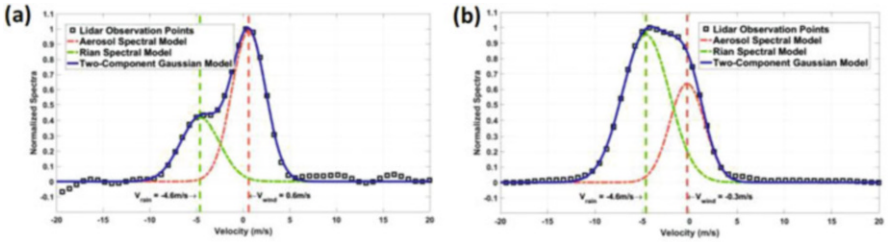


Fig. 55.4 Rain identification using a two-component Gaussian model

55.3.3 Estimation of Raindrop Size Distribution

The nonparametric method [5] is adopted to estimate the raindrop size distribution in this work. The rain power spectrum $S_{\text{rain}}(v)$ measured by lidar can be expressed in Eq. (55.1), where the parameter C is the calibration factor, $N(D)$ is the raindrop size distribution, σ_{bk} is the backscattering cross section which can be calculated using backscattering efficiency Q_{bk} in Eq. (55.2), D is the equivalent spherical diameter, and v is the terminal rainfall velocity. dD/dv is calculated by the empirical equation, as shown in Eq. (55.3):

$$S_{\text{rain}}(v) = CN(D)\sigma_{bk}(D)dD/dv \tag{55.1}$$

$$\sigma_{bk}(D) = \left[\pi D^2 Q_{bk}(D)\right]/4 \tag{55.2}$$

$$v(D) = 9.65 - 10.3 \quad \exp(-0.6D) \tag{55.3}$$

Figure 55.5a shows the backscattering efficiency of raindrop particles. For the spherical raindrops with diameters ranging from 0.1 to 1 mm, the MiePlot model is used to simulate the Q_{bk}. Differently, the backscattering efficiency of nonspherical rain particles is estimated by the vectorial complex ray model (VCRM) at the diameter range from 1 to 8 mm. The blue circles in Fig. 55.5b represent the 1-min raindrop size distribution calculated from lidar. The observed 1-min DSD from Parsivel^2 disdrometer is given in red asterisks under the rain intensity of 3.27 mm/h obtained from disdrometer. Lidar and Parsivel^2 disdrometer have similar raindrop size distribution around the diameter of 1–3 mm. Within the diameter of 1 mm, the difference of DSD between lidar and Parsivel^2 may be caused by the effect of vertical wind velocity, turbulence, and window function [9, 10]. The rain intensity calculated by Eq. (55.4) [11] from lidar is 3.44 mm/h, which is a little bit larger than that from disdrometer due to the difference of DSD within the diameter of 1 mm.

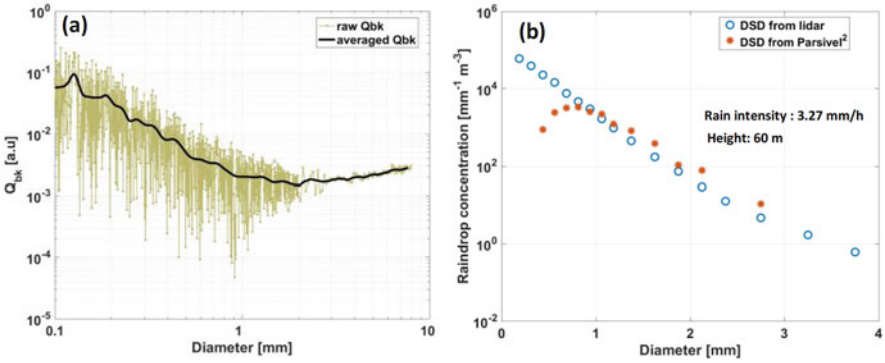


Fig. 55.5 Estimation of raindrop size distribution. (**a**) Backscattering efficiency of a raindrop; (**b**) raindrop size distribution observed from lidar and disdrometer at 12:10 on August 23, 2021

$$R = 6\pi * 10^{-4} \int_0^{D_{\max}} D^3 v(D) N(D) dD \tag{55.4}$$

55.4 Conclusions and Discussions

The rain observation campaign was carried out at the Laoshan campus of Ocean University of China during rain events. A ground-based wind lidar and Parssivel^2 disdrometer were applied to measure rain parameters. The motions of aerosol particles and raindrops bring the Doppler effect into the lidar power spectrum during rain events, producing the obvious double peaks or hidden double peaks in the lidar power spectrum. The weighted rainfall velocity and vertical wind velocity are obtained simultaneously using a two-component Gaussian model. Moreover, the raindrop size distribution is calculated by taking the nonparametric method. The comparison results of DSD between lidar and disdrometer are also provided in this chapter. In the future, more data will be collected for comparison and further analysis. We will remove the effect of vertical wind velocity, turbulence, and window function on the estimation of DSD.

Acknowledgments This research is supported by the National Natural Science Foundation of China (No. 61975191, No. 42106182) and the National Key Research and Development Program of China (2019YFC1408002).

References

1. Hasager, C., Vejen, F., Bech, J.I., Skrzypiński, W.R., Tilg, A.M., Nielsen, M.: Assessment of the rain and wind climate with focus on wind turbine blade leading edge erosion rate and expected lifetime in Danish Seas. Renew. Energy. **149**, 91–102 (2020)
2. Cao, Y., Wu, Z., Xu, Z.: Effects of rainfall on aircraft aerodynamics. Prog. Aerosp. Sci. **71**, 85–127 (2014)
3. Berne, A., Delrieu, G., Creutin, J.-D., Obled, C.: Temporal and spatial resolution of rainfall measurements required for urban hydrology. J. Hydrol. **299**(3–4), 166–179 (2004)
4. Hou, A.Y., Kakar, R.K., Neeck, S., Azarbarzin, A.A., Kummerow, C.D., Kojima, M., Oki, R., Nakamura, K., Iguchi, T.: The global precipitation measurement mission. Bull. Am. Meteorol. Soc. **95**(5), 701–722 (2014)
5. Aoki, M., Iwai, H., Nakagawa, K., Ishii, S., Mizutani, K.: Measurements of rainfall velocity and raindrop size distribution using coherent Doppler lidar. J. Atmos. Ocean. Technol. **33**(9), 1949–1966 (2016)
6. Wei, T., Xia, H., Hu, J., Wang, C., Shangguan, M., Wang, L., Jia, M., Dou, X.: Simultaneous wind and rainfall detection by power spectrum analysis using a VAD scanning coherent Doppler lidar. Opt. Express. **27**(22), 31235 (2019)
7. Lottman, B.T., Frehlich, R.G., Hannon, S.M., Henderson, S.W.: Evaluation of vertical winds near and inside a cloud deck using coherent Doppler lidar. J. Atmos. Ocean. Technol. **18**(8), 1377–1386 (2001)
8. Wu, S., Sun, K., Dai, G., Wang, X., Liu, X., Liu, B., Song, X., Reitebuch, O., Li, R., Yin, J., Wang, X.: Inter-comparison of wind measurements in the atmospheric boundary layer and the lower troposphere with Aeolus and a ground-based coherent Doppler lidar network over China. Atmos. Meas. Tech. **15**(1), 131–148 (2022)
9. Wakasugi, K., Mizutani, A., Matsuo, M., Fukao, S., Kato, S.: A direct method for deriving drop-size distribution and vertical air velocities from VHF Doppler radar spectra. J. Atmos. Ocean. Technol. **3**(4), 623–629 (1986)
10. Kobayashi, T., Adachi, A.: Retrieval of arbitrarily shaped raindrop size distributions from wind profiler measurements. J. Atmos. Ocean. Technol. **22**(4), 433–442 (2005)
11. Zhang, G.: Weather Radar Polarimetry. CRC Press (2016)

Chapter 56
Comparison of Lower Tropospheric Water Vapor Vertical Distribution Measured with Raman Lidar and DIAL and The Impact of Data Assimilation in Numerical Weather Prediction Model

Tetsu Sakai, Satoru Yoshida, Tomohiro Nagai, Yasutaka Ikuta, and Yoshinori Shoji

Abstract To evaluate the performance of water vapor lidars for measuring the vertical distribution in the lower troposphere and its potential utility for numerical weather prediction, the vertical distributions of water vapor mixing ratio (w) were measured with a Raman lidar developed by the Meteorological Research Institute (MRI-RL) and a differential absorption lidar that is being developed by Vaisala (Vaisala-DIAL) at Tsukuba, Japan, during the summer of 2020. The measured values were compared with those obtained with collocated radiosondes. The MRI-RL-derived w values mostly agreed within 1 g/kg with those obtained with the radiosonde between altitudes of 0.2 and 3 km and were 0.2–0.5 g/kg higher than them at 0.1 km. The Vaisala-DIAL-derived w values were 0.6–0.7 g/kg lower than those obtained with the radiosonde below 0.5 km and 1–2 g/kg higher than them above 1 km.

We assimilated the lidar-derived w in the initial condition of the mesoscale model (MSM) developed by the Japan Meteorological Agency using a four-dimensional variational (4D-Var) method to study the impact of the lidar data on the water vapor field predicted by the model. The results of the assimilation showed that w values predicted by MSM got closer to the radiosonde-derived values by assimilating MRI-RL and Vaisala-DIAL data. The correction by assimilating MRI-RL data was slightly better than the Vaisala-DIAL data. Our results showed that (1) assimilating the lidar water vapor data in the model can improve the predicted water vapor field and (2) the data with smaller bias and RMSD have a better impact on the prediction of water vapor field.

T. Sakai (✉) · S. Yoshida · T. Nagai · Y. Ikuta · Y. Shoji
Meteorological Research Institute, Tsukuba, Ibaraki, Japan
e-mail: tetsu@mri-jma.go.jp

© The Author(s), under exclusive license to Springer Nature Switzerland AG 2023

J. T. Sullivan et al. (eds.), *Proceedings of the 30th International Laser Radar Conference*, Springer Atmospheric Sciences,
https://doi.org/10.1007/978-3-031-37818-8_56

Keywords Water vapor · Raman lidar · DIAL · Data assimilation · Numerical weather prediction

56.1 Introduction

Water vapor in the lower troposphere plays important roles in convection initiation and precipitation development because it forms cloud and precipitation and creates energy of convection by releasing latent heat at the time of condensation.

In the last 50 years, the occurrence frequency of localized heavy rainfall capable of causing extensive damage has been increasing in Japan [1]. For early prediction of heavy rainfall, a numerical weather prediction (NWP) model is employed along with conventional meteorological observation data. However, the lead time (period of time between the issuance of a forecast and the occurrence of the rainfall) and accuracy of the prediction are limited, in part, because of the coarse temporal and spatial resolutions of water vapor distribution observations by radiosonde, ground-based Global Navigation Satellite System (GNSS) and microwave radiometer, and satellites. Water vapor lidar is a candidate that complements those observations because it measures the vertical water vapor distribution continuously with a high temporal and spatial resolution. The Meteorological Research Institute (MRI) has been studying the potential of water vapor lidar for the lower tropospheric water vapor monitoring system for NWP. This paper reports result of (1) validation of Raman lidar developed by MRI (MRI-RL) and differential absorption lidar being developed by Vaisala (Vaisala-DIAL) by comparison with the collocated radiosonde measurements and (2) impact of the lidar-derived water vapor measurements on the initial condition of the mesoscale model by using a data assimilation technique.

56.2 MRI Raman Lidar (MRI-RL) and Vaisala-DIAL

56.2.1 MRI-RL

The characteristics of the MRI-RL are given in Table 56.1. It employs a Nd:YAG laser operating at 355 nm with a pulse energy of ~250 mJ and a repetition rate of 30 Hz. The beam diameter is expanded fivefold to a diameter of ~5 cm by a beam expander, and the beam is emitted vertically into the atmosphere. The light backscattered by atmospheric gases and particles is collected by a Cassegrain telescope with a diameter of 40 cm that is co-axially aligned with the transmitted laser beam. The received light is separated into three spectral components, Raman water vapor (407.5 nm), nitrogen (386.7 nm), and elastic (355 nm) backscatter light and is detected by photomultiplier tubes (PMTs). The signals are acquired with a transient recorder operating in photon counting mode. The data quantity obtained

Table 56.1 Characteristics of the MRI-RL and Vaisala-DIAL used in this study

Instruments	MRI-RL	Vaisala-DIAL
Transmitter		
Laser wavelength	355 nm	911 nm (ON) and 910.6 nm (OFF)
Pulse energy	~250 mJ/pulse	9 μJ/pulse
Pulse repetition	30 Hz	10 kHz
Receiver		
Diameter	40 cm	15 cm and 28 cm
Interference filter bandwidth	0.3 nm	2.4 nm
Detector	PMT	APD
Detection type	Photon counting	Analog
Data quantities	Water vapor mixing ratio and aerosol backscatter	
Vertical resolution	75 m (<1 km) or 150 m (>1 km)	10–500 m (increase with height)
Temporal resolution	20 min	20 min

from the signals are the vertical distribution of the water vapor mixing ratio (w) and the aerosol backscattering ratio. The measurement uncertainties are estimated from the photon counts by assuming Poisson statistics and the uncertainty of the calibration coefficient. The detail of the lidar system, data analysis procedure, and uncertainty estimation are provided in [2].

56.2.2 Vaisala-DIAL

The prototype Vaisala-DIAL has been developing by Vaisala since 2017. It has been updating the hardware and software to improve the measurement accuracy and performance (private communication with Vaisala, 2021). The details on the system are provided in [3]. It is a compact, low-power remote sensing system that uses semiconductor laser sources at wavelengths around 911 nm (Table 56.1). The system includes two vertically pointing measurement units with single-lens telescopes with a diameter of 15 cm and 28 cm, one optimized for the near range and the other for the far range. The receivers use avalanche photodiode (APD) detectors in analog mode. The receivers are located coaxially with the transmitters. The measurement algorithms use auxiliary information about molecular absorption, as well as ground level pressure, temperature, and humidity. The reported data quantity is the water vapor mixing ratio and the range-corrected backscatter signal every 1 min with an averaging interval of 20 min. The measurement uncertainty is obtained from the standard deviation of the 2-min data over the 20-min averaging period.

56.3 Results of the Measurements and Comparison with Radiosonde

To characterize the performance of the instruments, measurements for validation were made on 65 days, from 1 September to 5 November 2020, over Tsukuba, Japan (36.06° N, 140.12° E). The distance between the two lidars was 6 m. We validated the water vapor mixing ratio obtained with the lidars by comparing them with collocated and coincident radiosonde (Vaisala RS41-SG). The radiosondes were launched twice daily (8:30 and 20:30 LST) from an Aerological Observatory located 80 m northeast of the lidars. For comparison, the vertical resolution of the all the data is adjusted to that of the MRI-RL, that is, 75 m below an altitude of 1 km and 150 m above that. For quality control of the lidar-derived w values, we used the data points with an MRI-RL measurement uncertainty of less than 30% that were estimated from the photon count assuming the Poisson statistics. In addition to this, we rejected the data with a vertical gradient of w larger than 5 g/kg/75 m to remove spurious noise spikes and high photon counts in Raman water vapor signals. For the data points with a Vaisala-DIAL measurement, we use the data points below the maximum resolved height determined from the statistics of the 5-s signal ratio over the 20-min averaging period.

Figure 56.1 shows the altitude-time cross sections of w obtained with the Vaisala-DIAL and MRI-RL as well as the vertical distributions obtained with the lidars and radiosonde at 8:30 LST and 20:30 LST on 8 September 2020. We can see in Fig. 56.1 that the altitude range of Vaisala-DIAL measurement is from near the surface to 1.0–1.5 km day and night, while MRI-RL measurement is from 0.1 km to over 2.5 km in night and less than 1 km in day because of the low signal-to-noise ratio (SNR) in strong sunlight.

The vertical distributions of w (right panels of Fig. 56.1) show that the w values obtained with Vaisala-DIAL were 1–2 g/kg lower than those obtained with the radiosonde below 0.5 km and higher than them above 1 km. The w obtained with MRI-RL were closer to the radiosonde data than Vaisala-DIAL data.

Figure 56.2 shows the vertical distribution of difference in w between the lidars and the radiosonde for the period from 2 September to 4 November in 2020. The difference of MRI-RL-derived w values from the radiosonde-derived values were on average within 0.5 g/kg between 0.2 and 3 km in altitude. However, they were 0.2–0.5 g/kg higher than those obtained with the radiosonde at an altitude of 0.1 km, possibly because of the inaccurate correction of the overlap between the laser beam and receiver's field of view at that altitude and spatial non-uniformity of detectors. The Vaisala-DIAL-derived w values were 0.6–0.7 g/kg lower than those obtained with the radiosonde below 0.5 km and more than 1–2 g/kg higher above 1 km. According to the manufacturer, the probable reasons for that were problems in the algorithm of the software computing w from the lidar signal and the parameter setting of the hardware and software. These problems are now being corrected by the manufacture.

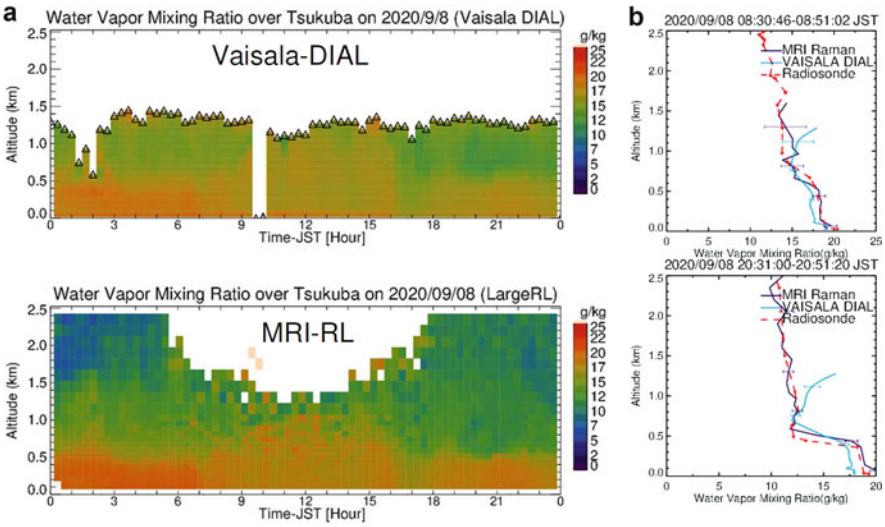


Fig. 56.1 (Left) Altitude-time cross sections (left) of water vapor mixing ratios obtained with the (**a**) Vaisala-DIAL and (**b**) MRI-RL on 8 September 2020. The triangles in Fig. 56.1a are the maximum resolved height that produces an acceptable measurement result provided by the manufacturer that were determined from the statistics of the 5-s signal ratio over the 20-min averaging period. (Right) Vertical distributions of water vapor mixing ratio obtained with Vaisala-DIAL (solid cyan), MRI-RL (solid black), and radiosonde (dashed red) at 8:30 LST (top) and 20:30 LST on 8 September 2020

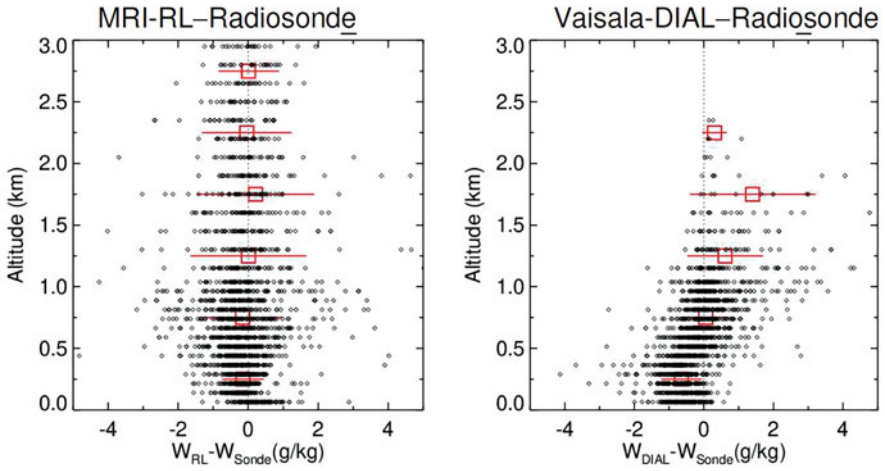


Fig. 56.2 Vertical distribution of difference in *w* obtained with lidars (MRI-RL in left and Vaisala-DIAL in right) from radiosonde for the period from 2 September to 4 November in 2020. Squares represent the mean error, and red bars represent the 1-sigma standard deviation in the error at 0.5 km intervals

56.4 Data Assimilation Experiment of Lidar Data in the Mesoscale Model

In order to study impact of the lidar data on the water vapor field predicted by the numerical weather prediction model, we assimilated the lidar-derived *w* in the initial condition of the non-hydrostatic mesoscale model (MSM) developed by JMA [4] by means of a four-dimensional variational (4D-Var) method [5]. The horizontal resolution of the MSM is 5 km, and the vertical resolution varies from 20 m at surface to 640 m at 21 km in height. The integral time step of the numerical simulation is 33.3 s. The initial condition is provided from JMA mesoscale analysis (MA), and the lateral boundary condition is provided by JMA global scale model (GSM) in which operational observations with radiosonde, buoys, surface-based instruments, satellites, radar, GNSS, and wind profilers are ingested.

We assimilated the lidar data in the MSM for the period from 3 September to 3 October 2020. The lidar data were quality controlled as described in Sect. 56.2 and assimilated every hour on the hour in the model. The observational errors were given by the measurement uncertainties estimated from the lidar signal as described in Sect. 56.2.

Figure 56.3 shows the histogram of difference of *w* forecasted by MSM assimilating the lidar data and that without assimilating the lidar data from radiosonde observation at the grid point of the model closest to the observation site. The forecast time is at the time of radiosonde measurements (9 LST and 21 LST) from 6 LST and 18 LST. The altitude range of the comparison is between 0.1 and 2 km. We can see in Fig. 56.3 that the mean difference (MD) and root mean square difference (RMSD) of *w* forecasted by assimilating the lidar data were closer to zero than those without assimilating the lidar data. The correction by assimilating MRI-RL data was slightly better than Vaisala-DIAL data. Table 56.2 summarizes the result of data assimilation. The values of MD and RMSD of *w* predicted by MSM and the

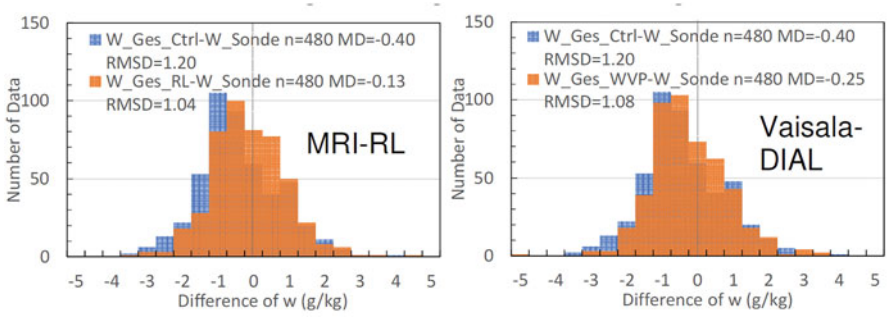


Fig. 56.3 Histograms of difference of *w* forecasted by MSM assimilating the lidar data (orange) and without assimilating the lidar data (blue) from radiosonde observation for the period from 3 September to 3 October in 2020. Left and right panels show the results for MRI-RL and Vaisala-DIAL, respectively

Table 56.2 Summary of data assimilation experiment of lidar water vapor measurements

Difference from radiosonde	Without assimilation	Assimilating MRI-RL data	Assimilating Vaisala-DIAL data
Mean difference (g/kg)	−0.40	−0.13	−0.25
RMSD (g/kg)	1.20	1.04	1.08

radiosonde-derived values were −0.13 g/kg and 1.04 g/kg by assimilating MRI-RL data and −0.25 g/kg and 1.08 g/kg by assimilating Vaisala-DIAL data, whereas they were −0.4 g/kg and 1.2 g/kg without assimilating the lidar data. Possible reasons for the difference of the magnitude of corrections between two lidar data were the differences in bias and RMSD of the two lidar data. These results showed that (1) assimilating the lidar water vapor data in the mesoscale model can correct the predicted water vapor field and (2) the measured data with smaller bias and RMSD have a better impact on the prediction of water vapor field.

Acknowledgments This study was partly supported by JSPS KAKENHI Grant Number 19H01983.

References

1. Japan Meteorological Agency homepage: https://www.data.jma.go.jp/cpdinfo/extreme/extreme_p.html. Last accessed 1 May 2022
2. Sakai, T., Nagai, T., Nakazato, M., Matsumura, T., Orikasa, N., Shoji, Y.: Comparisons of Raman lidar measurements of tropospheric water vapor profiles with radiosondes, hygrometers on meteorological observation tower, and GPS at Tsukuba, Japan. J. Atmos. Ocean. Technol. **24**, 1407–1423 (2007)
3. Newsom, R.K., Turner, D.D., Lehtinen, R., Münkel, C., Kallio, J., Roininen, R.: Evaluation of a compact broadband differential absorption lidar for routine water vapor profiling in the atmospheric boundary layer. J. Atmos. Ocean. Technol. **37**, 47–65 (2020)
4. Japan Meteorological Agency: Local analysis. Outline of the Operational numerical weather prediction at the Japan Meteorological Agency, 40–43 (2019)
5. Ikuta, Y., Fujita, T., Ota, Y., Honda, Y.: Variational data assimilation system for operational regional models at Japan meteorological agency. J. Meteor. Soc. Japan. **99**, 1563–1592 (2021)

Chapter 57
Temperature Variations in the Middle Atmosphere Studied with Rayleigh Lidar at Haikou (19.9°N, 110.3°E)

Yang Jie, Wang Yu-Ru, Chen Wei-Peng, Zhang Yu-Hao, Yang Guo-Tao, Li Fa-Quan, Cheng Xue-Wu, Wang Ying-Pin, and Gong Shao-Hua

Abstract Based on the long-term observations of Hainan lidar (19.9°N, 110.3°E) during 2010–2020, temperature variation characteristics in the middle atmosphere (32–64 km) are investigated by analyzing the Rayleigh backscattering data. The stratopause over Haikou was in the altitude range of 42–51 km, with a maximum temperature of ~262 K. After an annual plus semiannual and seasonal fit was applied to lidar observation results, it is found that temperature variation in the stratosphere exhibited a prominent annual oscillation tendency while temperature variations in the stratopause and the lower mesosphere were dominated by annual and semiannual oscillations. Interannual variation of stratopause temperature is compared to the change of solar activity, and it is revealed that stratopause temperature had a good response to the index change of solar radiation while the solar radiation flux F10.7 varied significantly. However, when the solar activity became calm, there was no correlation in the variation tendency between them. These observation results could be significant to the comprehensive understanding of global climate change.

Y. Jie · W. Yu-Ru · C. Wei-Peng · Z. Yu-Hao · W. Ying-Pin
College of Physics & Electronic Engineering, Hainan Normal University, Haikou, China

Y. Guo-Tao
State Key Laboratory of Space Weather, National Space Science Center, Chinese Academy of Sciences, Beijing, China
e-mail: gtyang@swl.ac.cn; shhgong@hainnu.edu.cn

L. Fa-Quan · C. Xue-Wu
Innovation Academy for Precision Measurement Science and Technology, Chinese Academy of Sciences, Wuhan, China
e-mail: lifaquan@wipm.ac.cn; lidar@apm.ac.cn

G. Shao-Hua (✉)
College of Physics & Electronic Engineering, Hainan Normal University, Haikou, China

State Key Laboratory of Space Weather, National Space Science Center, Chinese Academy of Sciences, Beijing, China
e-mail: gtyang@swl.ac.cn; shhgong@hainnu.edu.cn

© The Author(s), under exclusive license to Springer Nature Switzerland AG 2023

J. T. Sullivan et al. (eds.), *Proceedings of the 30th International Laser Radar Conference*, Springer Atmospheric Sciences,
https://doi.org/10.1007/978-3-031-37818-8_57

Keywords Lidar · Temperature in the middle atmosphere · Solar radio flux F10.7

57.1 Introduction

In the middle and upper atmosphere (20–110 km), there are full of complex physical and chemical dynamic processes, and they are the main mechanism of energy and momentum coupling between the lower and the upper atmospheres [1]. Temperature is an important parameter of atmosphere, and temperature variations are meaningful to human activities and global climate change [2].

Lidar is an effective instrument for temperature measurements in the middle atmosphere [3–5]. Over the past few decades, based on the long-term measurements of lidar, different temperature variation characteristics have been reported at different locations [6, 7]. Hainan Island is located in the South China Sea near the equator, and its climate is mainly influenced by the marine monsoon. In the global circulation system, the changes in atmospheric temperature in this region have a significant impact on China's terrestrial space environment and climate change. Based on the long-term observation of Hainan lidar (19.9°N, 110.3°E) during 2010–2020, the temperature variation characteristics in the middle atmosphere are investigated in this paper.

57.2 Instrumentation and Analysis Methodology

Hainan lidar (19.9°N, 110.3°E) was developed in 2010, and it was working with dual-wavelength (@532 nm and 589 nm) [8]. During 2010–2020, 6704.6 h of observation data were accumulated in 903 nights. By analyzing the Rayleigh scattering signal (@589 nm), temperature profiles (32–64 km) were calculated in the method described by Hauchecorne and Chanin [3]. According to the photon number profile detected by lidar, atmospheric density and temperature at the altitude z can be calculated with Eqs. (57.1)–(57.2):

$$\rho(z) = \frac{z^2 \left(N(z) - N_B\right)}{z_0^2 \left(N\left(z_0\right) - N_B\right)} \rho\left(z_0\right) \tag{57.1}$$

$$T(z) = \frac{\rho\left(z_0\right)}{\rho(z)} T\left(z_0\right) + \frac{M}{R} \int_z^{z_0} \frac{\rho\left(z'\right) g\left(z'\right)}{\rho(z)} d\left(z'\right) \tag{57.2}$$

where $\rho(z)$, $T(z)$, and $N(z)$ are, respectively, the atmospheric density, temperature, and number of echo photons received by lidar at altitude z. N_B, M, and R are the background noise, atmospheric molar mass, and thermodynamic constant, respectively. $\rho(z_0)$ and $T(z_0)$ are, respectively, the atmospheric density and temperature at the reference altitude z_0, and they are generally from the results of model or

satellite measurements. The spatial and temporal resolutions of lidar observation are, respectively, 90 m and 3 min, and the relative measurement error of temperature at different altitudes is less than 5%.

57.3 Results and Discussions

57.3.1 Annual, Semiannual, and Seasonal Variations of Temperature in the Middle Atmosphere

By averaging the observation results on the same date in different years, date-dependent temperature structure of the middle atmosphere (32–64 km) over Haikou (19.9°N, 110.3°E) is plotted in Fig. 57.1. It is found that the daily average temperature of the middle atmosphere varied periodically with the date, and the highest temperature (262 K) occurred at altitude range of 43–52 km in the spring. The altitudes with the highest average temperature in different date are marked with white crosses, as shown in Fig. 57.1; the altitude of stratopause over Haikou also changed periodically with the date. The stratopause is mainly located at the altitude range of 42–51 km, and the lowest and the highest altitudes occurred in March and August, respectively.

Since the variation of atmospheric temperature is mainly related to the periodical change of solar-terrestrial environment, lidar observation results at different altitudes are fitted with Eq. (57.3), and the corresponding components of annual, semiannual, and seasonal variations are shown in Fig. 57.2, respectively.

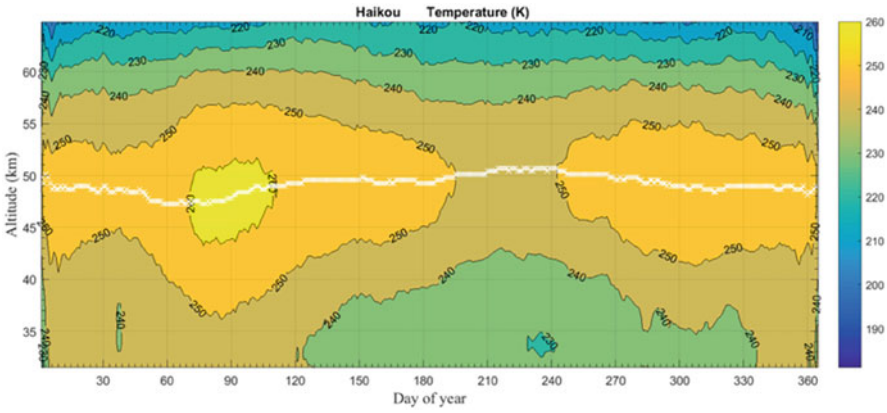


Fig. 57.1 Date-dependent temperature structure of the middle atmosphere (32–64 km) observed with lidar at Haikou (19.9°N, 110.3°E). The altitudes with the highest temperature in different dates are marked with white crosses

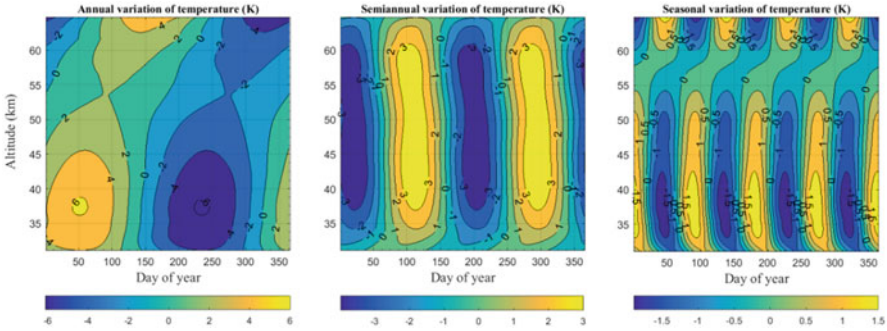


Fig. 57.2 Annual, semiannual, and seasonal variations of temperature in the middle atmosphere (32–64 km) over Haikou (19.9°N, 110.3°E)

$$\hat{x}\,(d)=A_0+A_1\cos\left[\frac{2\pi}{365}\,(d-d_1)\right]+A_2\cos\left[\frac{4\pi}{365}\,(d-d_2)\right]+A_3\cos\left[\frac{8\pi}{365}\,(d-d_3)\right] \tag{57.3}$$

where A_0 is the average temperature; A_1, A_2, and A_3 are respectively the annual, semiannual, and seasonal variation amplitudes; and d_1, d_2, and d_3 are their corresponding phases.

In the altitude range of 32–64 km, as shown in Fig. 57.2a, the annual variation amplitude of temperature first decreased gradually and then increased with the increase of altitude. The maximum amplitudes (~6.0 K) occurred around 37.5 km, and the positive and the negative maximum occurred in February and August, respectively. Especially, the annual variation amplitude around 53 km was the smallest, and it kept 0 in most months. Semiannual variation characteristic was obvious at all heights, as shown in Fig. 57.2b, and the maximum variation amplitude of temperature was ~3.8 K. The positive maxima occurred in spring (day 95–140) and autumn (days 270–320), and the negative maxima occurred in summer (days 85–220) and winter (days 1–40). In Fig. 57.2c, obvious seasonal variation characteristics were shown in the stratosphere (34–52 km), and the positive maxima of seasonal variation component occurred, respectively, around days 90, 180, 270, and 360. The negative maxima occurred, respectively, around days 40, 130, 220, and 320. However, the amplitude of seasonal variation was approximately 0 at altitudes 54–60 km. At altitudes ranged 60–64 km, amplitude of seasonal variation monochromatically increased with height, and the maximum was ~1.5 K. Meanwhile, contrasted to the seasonal variations in the altitude of 34–52 km, the seasonal variation of atmospheric temperature above 60 km lagged behind the latter about 46 days, meaning that the seasonal variation of atmospheric temperature in the lower mesosphere (above 60 km) was completely opposite to that in the stratosphere in phase variation.

To compare with other lidar observations at lower latitudes, similar variation characteristics of temperature in the middle atmosphere were reported. At Gadanki (13.5°N, 79.2°E), *Krishnaiah* et al. [9] reported that temperature variation in the middle atmosphere presented an obvious annual variation tendency. The stratopause locates at the altitude range 43–58 km, and its temperature varied in 255–270 K. At Sao Jose dos Campos (23.2°S, 45.8°W), *Batista* et al. [10] reported that the highest temperature in the middle atmosphere was ~265 K and temperature variation in the stratosphere showed an annual tendency. However, the temperature variation in the stratopause and the mesosphere mainly presented a semiannual oscillation. At Hawaii (19.5°N, 155.6°W), Leblanc et al. [7] reported that the stratopause (@47 km) temperature had a maximum of 266 K and temperature variations in 25–80 km were mainly dominated by semiannual oscillation.

57.3.2 Interannual Variation of Stratopause Temperature

After removing annual, semiannual, and seasonal variations, interannual variation of temperature in the middle atmosphere often presents obvious Quasi-Biennial oscillation (QBO), El Niño-Southern oscillation (ENSO), and an 11-year solar cycle [11, 12]. Especially, the long-term variations of atmospheric temperature in the middle and lower atmosphere are directly related to the change of solar activity due to the photochemical reactions of ozone layer. Therefore, the correlations between the variation tendencies of lidar-observed stratopause temperature and solar activity were analyzed in Fig. 57.3. Since solar radiation flux 10.7 is one important index of solar activity, it was plotted for comparison. In addition, the lidar-measured daily averages of stratopause temperature were depicted with blue circles, and they were the average values of lidar-measured temperature at altitudes of 47.5–50.5 km. Those lidar-measured stratopause temperatures are firstly filtered with low-pass filter, and then the dominant variation components in temperature variation were extracted with wavelet analysis method; finally the interannual variation of stratopause temperature was reconstructed with green solid line in Fig. 57.3 [13, 14].

The reconstructed curve in Fig. 57.3 shows that the temperature variation in the stratopause presented a periodical oscillation during 2010–2020, and the maxima occurred in January 2012, April 2015, and March 2019. The highest temperature (~267 K) occurred in April 2015, and the lowest temperature (~251 K) occurred in October 2010. To compare with the red curve in Fig. 57.3, during the solar radiation flux 10.7 enhancement period (December 2010–December 2014), an obvious increase of the stratopause temperature was also observed by lidar, and the highest temperature (267 K) occurred in April 2015. Meanwhile, during the time period of solar radiation flux decrease (January 2015–December 2016), constant decline of the stratopause temperature was detected by lidar, and the minimum temperature occurred in May 2017. Thus, the temperature variation in the stratopause had a good response to the change of solar activity, although the highest temperature lagged

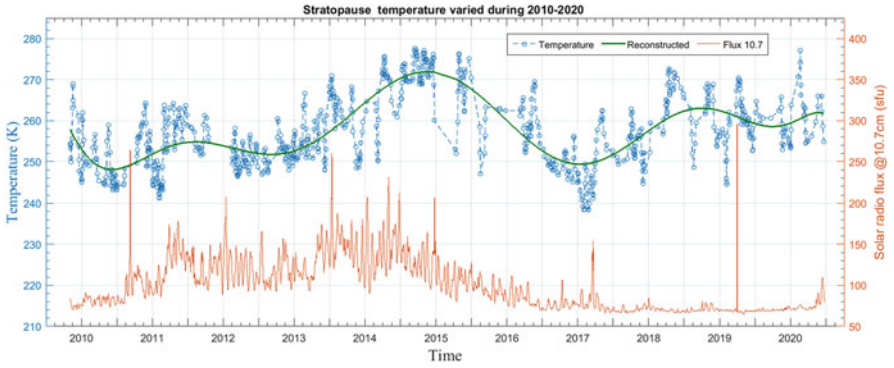


Fig. 57.3 Daily mean stratopause temperature over Haikou (19.9°N, 110.3°E) and the solar radio flux 10.7 during 2010–2020

behind the solar activity peak for several months. However, during the quiet period of solar activity (2018–2020), as shown in Fig. 57.3, no corresponding relationship can be found between the stratopause temperature variation and the solar radiation flux change. Therefore, it can be deduced that the long-term variations of stratopause temperature over Haikou had been directly affected by the change of solar activity, but it should be modulated by other mechanisms as well.

57.4 Conclusion

Based on the long-term observations of Hainan (19.9°N, 110.3°E) lidar during 2010–2020, the variation characteristics of temperature in the middle atmosphere (32–64 km) over Haikou were investigated. It was revealed that the temperature in the middle atmosphere over Haikou varied periodically with date and the stratopause was within the altitude range of 43–52 km, with a maximum temperature of 262 K. The temperature variation presented a prominent annual oscillation tendency in the stratosphere. At the altitudes of 52–60 km, temperature in the stratopause was mainly dominated by annual and semiannual variations, and the seasonal variation tendency were not obvious. Regarding the interannual variation of stratopause temperature, it had a good response to the obvious change of solar activity, although its oscillation tendency could be simultaneously modulated by other mechanisms. Since the temperature variations in lower latitude regions have significant influences on global circulation, these lidar observation results will be helpful to researches of climate changes in China.

References

1. Fritts, D.C., Alexander, M.J.: Gravity wave dynamics and effects in the middle atmosphere. Rev. Geophys. **41**(1), 1003 (2003)
2. Cohen, J., Screen, J.A., Furtado, J.C., et al.: Recent Arctic amplification and extreme mid-latitude weather. Nat. Geosci. **7**(9), 627–637 (2014)
3. Hauchecorne, A., Chanin, M.L.: Density and temperature profiles obtained by lidar between 35-km and 70-km. Geophys. Res. Lett. **7**, 565–568 (1980)
4. She, C.Y., Yu, J.R.: Simultaneous three-frequency Na lidar measurements of radial wind and temperature in the mesopause region. Geophys. Res. Lett. **21**, 1771–1774 (1994)
5. Alpers, M., Eixmann, R., Fricke-Begemann, C., Gerding, M., Ffner, J.H.: Temperature lidar measurements from 1 to 105 km altitude using resonance, Rayleigh, and rotational Raman scattering. Atmos. Chem. Phys. **4**(1), 793–800 (2004)
6. Argall, P.S., Sica, R.J.: A comparison of Rayleigh and sodium lidar temperature climatologies. Ann. Geophys. **25**(1), 27–35 (2007)
7. Leblanc, T., Mcdermid, I.S., Hauchecorne, A., Keckhut, P.: Evaluation of optimization of lidar temperature analysis algorithms using simulated data. J. Geophys. Res. Atmos. **103**(D6), 17191–17204 (1998)
8. Gong, S., Yang, G., Dou, X., Xu, J., Chen, C., et al.: Statistical study of atmospheric gravity waves in the mesopause region observed by a lidar chain in eastern China. J. Geophys. Res. Atmos. **97**, 7619–7634 (2015)
9. Krishnaiah, M., Raju, U.J.P., Kumar, Y.B., Raghunath, K., Kumar, V.S.: Lidar observations of middle atmosphere temperature variability over low latitude. Indian J. Radio Space Phys. **33**(1), 50–57 (2004)
10. Batista, P.P., Clemesha, B.R., Simonich, D.M.: A 14-year monthly climatology and trend in the 35–65 km altitude range from Rayleigh Lidar temperature measurements at a low latitude station. J. Atmos. Sol. Terr. Phys. **71**(13), 1456–1462 (2009)
11. Li, T., Mcdermid, I.S., Mcdermid, I.S.: Interannual variations of middle atmospheric temperature as measured by the JPL lidar at Mauna Loa Observatory, Hawaii (19.5°N, 155.6°W). J. Geophys. Res. Atmos. **113**(D14), 109 (2008)
12. Crooks, S.A., Gray, L.J.: Characterization of the 11-year solar signal using a multiple regression analysis of the ERA-40 dataset. J. Clim. **18**, 996–1015 (2005)
13. Gong, S., Yang, G., Xu, J., Liu, X., Li, Q.: Gravity wave propagation from the stratosphere into the mesosphere studied with lidar, meteor radar, and TIMED/SABER. Atmosphere. **10**(2), 81 (2019)
14. Torrence, C., Compo, G.P.: A practical guide to wavelet analysis. Bull. Am. Meteorol. Soc. **79**(1), 61–78 (1998)

Chapter 58
Convective Boundary Layer Sensible and Latent Heat Flux Lidar Observations and Towards New Model Parametrisations

Fabien Gibert, Dimitri Edouart, Paul Monnier, Julie Collignan, Julio Lopez, and Claire Cénac

Abstract Model parametrisations in the convective boundary layer are still at work especially in the interfacial layers with the surface and the free troposphere. This chapter reports simultaneous turbulence-scale lidar observations of wind speed, temperature, and specific humidity in the convective boundary layer in temperate and semiarid regions. The collected data are used to assess new parametrisations in particular in the entrainment layer.

Keywords Lidar observatory · 3D lidar · Scanning lidar · Doppler lidar · DIAL · Raman lidar · Coherent and direct detection

58.1 Introduction

The turbulent transport of heat, matter, and momentum in the convective boundary layer (CBL) is a key process to understand the 3D distribution of scalars in the atmosphere. Particularly critical are the surface and the entrainment layers that buffer the CBL, at the bottom with the soil and at the top with the free troposphere, respectively. If the surface layer exchanges are usually well documented by in situ observations and well understood following Monin-Obukhov similarity theory (MOST), the entrainment processes are still an unknown field both for observations and models. However, a robust parametrisation of entrainment fluxes is essential for transport models to link surface fluxes and tropospheric vertical profiles of scalars such as H_2O, CO_2, and CH_4 [1]. This is of particular importance for current

F. Gibert (✉) · D. Edouart · P. Monnier · J. Collignan · J. Lopez · C. Cénac
Laboratoire de Météorologie Dynamique (LMD/IPSL), École Polytechnique, Institut Polytechnique de Paris, Sorbonne Université, École normale supérieure, PSL Research University, CNRS, École des Ponts, Palaiseau, France
e-mail: gibert@lmd.polytechnique.fr

© The Author(s), under exclusive license to Springer Nature Switzerland AG 2023

J. T. Sullivan et al. (eds.), *Proceedings of the 30th International Laser Radar Conference*, Springer Atmospheric Sciences,
https://doi.org/10.1007/978-3-031-37818-8_58

and future space-borne GHGs missions like GOSAT, OCO, and MERLIN that try to estimate surface fluxes from column-integrated mixing ratio measurements [2]. To do so, new observations are needed that can provide, first, a 3D view of the atmosphere and, second, that have turbulence-scale temporal and spatial resolutions in order to investigate flux-gradient relationships and estimate higher-order moments [3]. The observations will also have to be made in different climate zones in order to study the robustness of advanced parametrisations.

In this chapter, we will present a preliminary analysis of the data from a 3D mobile lidar observatory that provides simultaneous measurements of radial wind speed, temperature, and specific humidity. Several scientific goals of this study include (i) to address the issue of dissimilarity of scalar transport such as heat and water vapor in different climate regions, (ii) to test model parametrisation of the interfacial layer especially for fluxes and scalar variances, and (iii) to assess the relevance of MOST which links gradient and flux close to the surface in heterogeneous landscape.

58.2 Instrumental Deployment

A new wind, temperature, H_2O, and CO_2 scanning lidar mobile observatory has been developed at the Laboratoire de Météorologie Dynamique, Ecole Polytechnique, France, during the last years. It is detailed in paper 017. Two different scanning lidars are involved: (1) a temperature and water vapor Raman lidar at 355 nm and (2) a prototype DIAL and Doppler lidar at 2051 nm with a coherent and direct detection for radial wind speed and CO2 absorption measurements. The mobile observatory was operated in a temperate region at SIRTA observatory, Palaiseau, France, and then in the semiarid area of Lleida, Spain, during the LIAISE experiment (land surface interactions with the atmosphere over the Iberian semiarid environment) in July 2021 (Fig. 58.1).

The LMD lidar measurements were completed by routine in situ instrumentation in the surface layer; pressure, temperature, and specific humidity; and wind speed and direction with colocated 30-m (SIRTA) and 50-m (LIAISE) tall tower. Daily (SIRTA) and hourly (LIAISE) soundings were also made which enables first to calibrate and validate LMD Raman lidar measurements and second to provide lidar-independent profiles for temperature, humidity and wind. Several eddy-covariance stations with sonic anemometers and gas analyzers were located close to lidar observatory at different height but also at few kilometres apart to provide turbulence-linked surface layer data like sensible and latent heat fluxes, friction and free-convection scaling velocities and Monin-Obukhov length. Other remote sensing instruments like radar UHF or Doppler lidar were also used to get continuous profiles of wind speed and shear.



Fig. 58.1 3D lidar observatory and other instrumentation used in this study during two field experiments in a temperate region at SIRTA observatory, France (left panels), and in a semiarid region with irrigated fields during LIAISE experiment, Spain (right panels). *EC* eddy-covariance station, *RS* radiosondes

58.3 Lidar Eddy-Covariance Flux

Lidar eddy-covariance measurements require the colocation of the two lidars used to provide vertical wind speed profiles for one part and temperature and specific humidity profiles on the other part. In addition, the two lidar scanning device azimuth and elevation angles are referenced using specified surface targets with known altitude with respect to lidar observatory. Even if the two lidar acquisition systems are synchronised, a cross-covariance of the data is used to correct for a potential lag time between the two time series (Fig. 58.2).

The maximum is an estimate of the turbulent flux as clearly seen in Fig. 58.2a. However, this maximum is sometimes not clearly seen for temperature, and in that case, we use the lag position given by water vapour. Eddy-covariance flux estimates using the integral of the co-spectrum are then not applicable here, like it is for in situ data [4]. Figure 58.2b, c show latent and sensible heat flux profiles monitored in the convective boundary layer (CBL) during LIASE experiment with the associated uncertainty that is accounted by both instrumental and sampling errors [5]. The native data used to make such calculations have a time and space resolution of 8 s

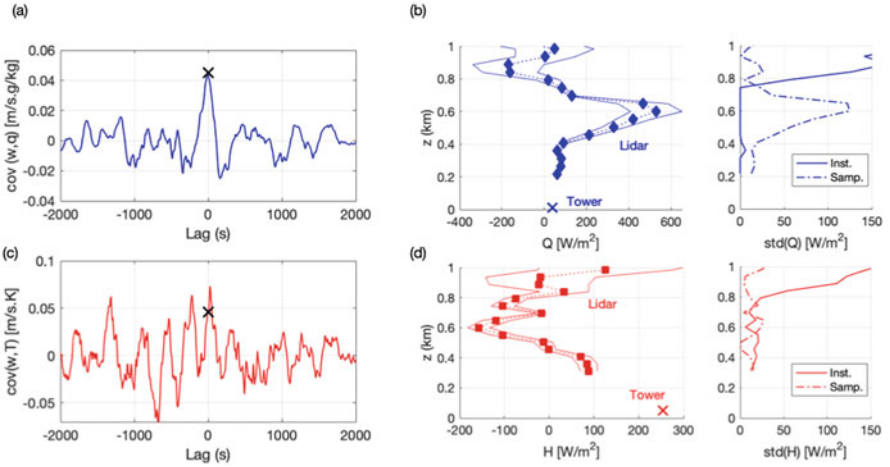


Fig. 58.2 (**a**) and (**c**) Cross-covariance between lidar vertical wind speed and specific humidity (**a**) and temperature (**c**) at a given height. (**b**) Latent heat flux profile and associated instrumental and sampling error. (**d**) Sensible heat flux profile and associated instrumental and sampling error. Time and space resolution are, respectively, 30 min and 50 m. Eddy-covariance in situ surface layer fluxes are indicated with an X

and 50 m, respectively, in order to respect integral scales of turbulence and avoid biases in flux estimates.

The flux profiles in Fig. 58.3 are actually typical profiles that can be measured in semiarid environment with surface large sensible and negligible latent heat fluxes [6]. Entrainment fluxes depend on surface properties as well as the strength of temperature inversion, the wind shear at the top of the CBL, and water vapour gradient at the interface with the free troposphere.

58.4 First Insight in Gradient and Flux Relationships in CBL Entrainment Layer

58.4.1 Theoretical Considerations

In a similar way of molecular diffusion, one expects that the flux through an interface is related to the mean gradient of the scalar. An eddy diffusivity coefficient K for each scalar, that is, virtual potential temperature and specific humidity in our case, may be defined as follows:

$$\overline{w'\theta_v'} = K_\theta \frac{\partial \theta_v}{\partial z}; \overline{w'q'} = K_q \frac{\partial q}{\partial z}$$

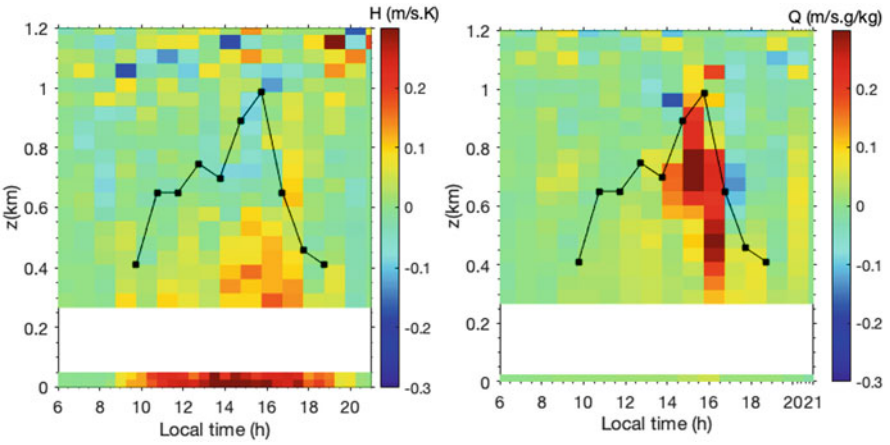


Fig. 58.3 Lidar eddy covariance sensible heat (H) and latent heat (Q) flux profiles. Black line is for the height of the convective boundary layer estimated with the minimum of sensible heat flux. Surface layer flux measurements from the 50-m tall tower are also indicated

Using a dimensional analysis and the *Buckingham Pi theorem*, which prescribes the optimal approach to determining a dependent variable in a physical problem, Obukov built in 1946 similarity laws that linked gradient and flux in the surface layer. The same approach was used by Sorbjan et al. [7, 8] for the entrainment layer. Identifying the main physical parameters at work in this layer, that is, surface heat flux, CBL height, interfacial gradient of temperature and specific humidity and wind shear, one may build a set of equations to link gradient and flux:

$$K_\theta(z_i) = \frac{w_*^2}{N_E} C_H f_H(Ri_E)\,;\; K_q(z_i) = \frac{w_*^2}{N_E} C_Q f_Q(Ri_E) \text{ with } f_{H,Q} = \frac{1 + c_{H,Q}/Ri_E}{\sqrt{1 + 1/Ri_E}}$$

where N_E is the Brunt-Väisälä frequency and Ri_E is the gradient Richardson number in the entrainment layer. We kept Sorbjan et al.'s notation with constants C_H and C_Q taking out of the f_H and f_Q functions.

58.4.2 *Assessment of Entrainment Flux Parametrisation with Observations*

A first assessment of scalar gradient and flux link in the interfacial layer was made using the dataset collected during LIAISE experiment. The main reason is that hourly radiosondes were made at the LMD lidar site during several days which enables to check lidar data and to have two independent dataset to calculate f_H and f_Q functions.

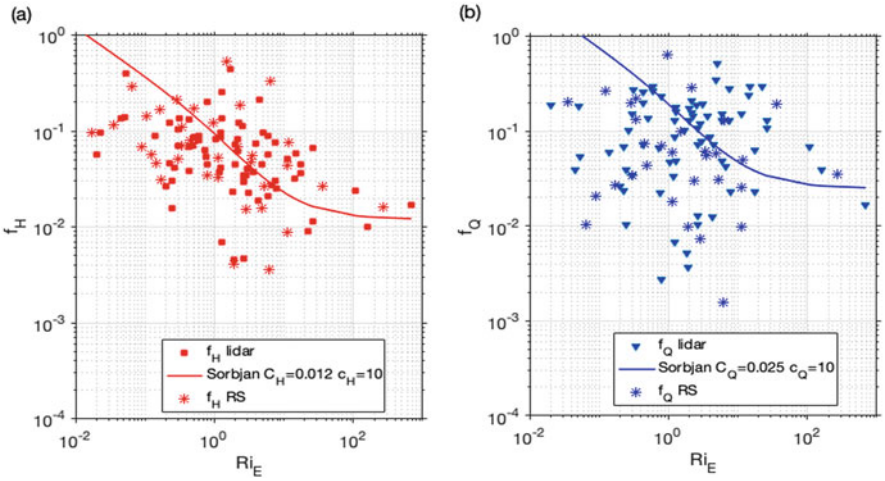


Fig. 58.4 Scaling fluxes in dependence of Ri_E using lidar (square) and radiosondes (stars) dataset

In the first dataset, we estimated the scalar gradient in the entrainment layer using Raman lidar measurements at high space resolution (7.5 m) and moderate time resolution (2 min). The reason is that 50 m is a too coarse resolution to capture the gradient in sharp inversion. The wind shear and then Richardson number was calculated using a second Doppler lidar and the radar UHF. In the second dataset, radiosondes were used to calculate scalar gradient, wind shear, Brunt-Väisälä frequency and Richardson number. In the two cases, we used eddy covariance lidar estimates of fluxes in the entrainment layer. Figure 58.4 shows the results for temperature and specific humidity. First comment is that C-constants suggested by Sorbjan et al. (that were found with large eddy simulations (LES) tests) can also match the observations. The evolution of the temperature data seems to follow the theoretical linear evolution (in log scale) for Richardson number larger than one but not for lower values (weak inversion, large wind shear). Second comment is that it seems that such parametrisation does not work for specific humidity despite a better data precision. Error bars for flux and gradient which are not shown here are not sufficient to explain the scatter of the data. Finally, the two datasets used here seem to give the same results which also shows that (i) lidar gradient and radar wind shear estimate uncertainties are not a relevant reason for parametrisation mismatch (ii) as described by Sorbjan et al. the parametrisations seem to be relevant for time-averaged profiles as well as punctual profiles.

Acknowledgements This work is supported by CNRS with the programme HyMeX and by the Agence Nationale de la Recherche with the project HILAISE. We also want to thank SIRTA observatory team and UKMO team during LIAISE experiment (Jeremy Price, Jenifer Brooke) who provides additional in situ and remote sensing data to LMD lidar observations.

References

1. Wulfmeyer, et al.: A review of the remote sensing of lower tropospheric thermodynamic profiles and its indispensable role for the understanding and simulation of water and energy cycles. Rev. Geophys. **53**, 819–895 (2015). https://doi.org/10.1002/2014RG000476
2. Ehret, et al.: MERLIN: a French-German space lidar mission dedicated to atmospheric methane. Remote Sens. **9**(10), 1052 (2017). https://doi.org/10.3390/rs9101052
3. Wulfmeyer, et al.: Determination of convective boundary layer entrainment fluxes, dissipation rates and the molecular destruction of variances: theoretical description and a strategy for its confirmation with a novel lidar system synergy. J. Atmos. Sci. **73**, 667–692 (2016). https://doi.org/10.1175/JAS-D-14-0392.1
4. Gibert, et al.: Can CO2 turbulent flux be measured by lidar? A preliminary study. J. Atmos. Ocean. Technol. **28**(3), 365–377 (2011)
5. Giez, et al.: Water vapor flux measurements from ground-based vertically pointed water vapor differential absorption and Doppler lidar. J. Atmos. Ocean. Technol. **16**, 237–250 (1999)
6. Canut, et al.: Observations and large-eddy simulations of entrainment in the sheared Sahelian boundary-layer. Bound.-Layer Meteorol. **142**, 79–101 (2012)
7. Sorbjan, Z.: Statistics of scalar fields in the atmospheric boundary-layer based on Lares-eddy simulations. Part 1: free convection. Bound.-Layer Meteorol. **116**, 467–486 (2005)
8. Sorbjan, Z.: Statistics of scalar fields in the atmospheric boundary-layer based on Lares-eddy simulations. Part 2: forced convection. Bound.-Layer Meteorol. **116**, 467–486 (2006)

Part IV
Atmospheric Boundary Layer Processes

Chapter 59
Observation of Structure of Marine Atmospheric Boundary Layer by Ceilometer Over the Kuroshio Current

Toshiyuki Murayama and Fumiaki Kobashi

Abstract Shipboard ceilometer observation was conducted during May 2021 on R/V Shinsei-maru in the southwest region of the middle of Japan to study the effects of the large meandering warm Kuroshio current on the atmosphere. Here we focus on the observations across the Kuroshio from the offshore to a colder sea inshore under clear sky condition. The atmospheric boundary (ABL) heights determined by the BL-View software coincide well with those obtained by the radiosonde observation. The height of the ABL over the Kuroshio varied at 500–800 m. At the transitional region between the Kuroshio and the cold sea inshore, spontaneous lifts of the ABL by 400 m were observed, which might be caused by the passage of the front of anticyclone over the Honshu island, Japan. Over the cold sea, a shallower ABL appeared, while the upper ABL was continuously observed at the same level as over the Kuroshio. The upper ABL is considered as the residual layer from the Kuroshio region. The lower ABL developed up to 300 m in the afternoon. Thus, highly temporal variation of the structure of the ABL was observed by the ceilometer associated with the BL-View analyses.

Keywords Ceilometer · Marine atmospheric boundary layer · Kuroshio

59.1 Introduction

In the Kuroshio and its extension region, the ocean releases a huge amount of heat to the atmosphere, influencing weather and climate over the Northern Hemisphere [e.g., 1]. We have employed ceilometers in research cruises for the observation of clouds and aerosols over the ocean, mainly the North Pacific near Japan, for the last

T. Murayama (✉) · F. Kobashi
Tokyo University of Marine Science and Technology, Koto, Tokyo, Japan
e-mail: tmuray0@kaiyodai.ac.jp; kobashi@kaiyodai.ac.jp

© The Author(s), under exclusive license to Springer Nature Switzerland AG 2023

J. T. Sullivan et al. (eds.), *Proceedings of the 30th International Laser Radar Conference*, Springer Atmospheric Sciences,
https://doi.org/10.1007/978-3-031-37818-8_59

decade. The data have been widely used for the study of the interaction between the atmosphere and ocean [e.g., 2, 3].

The height of marine atmospheric boundary layer (MABL) is also derived from the Vaisala BL-View in addition to the cloud base from the ceilometer observations. Because of continuous observation of the ceilometer, these ceilometer data would contribute to studies integrating the radiosonde and comprehensive surface and marine observations from the research vessel. In general, the lidar ceilometers are often used over the land at fixed sites for the study of the ABL for a long term [e.g., 4, 5]. However, the use of the ceilometer on the ship [e.g., 2, 3, 6] has been limited compared with the land use. Here we focus on the cruise across the Kuroshio front under fair weather condition.

59.2 Observations and Methodology

In May 24–31, 2021, the research cruise KS-21-9 of the R/V Shinsei-maru of the Japan Agency for Marine-Earth Science Technology (JAMSTEC) was conducted on the meandering Kuroshio (warm sea current flowing along the south of Japan) to examine the effects on the meteorology near the south coast of Japan. This study has been involved in "mid-latitude ocean-atmosphere interaction hotspots under the changing climate" of the Granted-in-Aid for Scientific Research on Innovative Areas, Minister of Education, Culture, Science and Technology [7].

The ship track is indicated in Fig. 59.1 with the radiosonde observation sites, S001 ~ S031, and the sea surface temperature (SST) obtained by the satellite [8]. We installed a Vaisala CL31 ceilometer with the shock absorber (Vaisala CT35022) on the upper deck, about 10 m MSL, which recorded the backscatter signal every 15 s up to 7.5 km m height with 10 m resolution. In this study, we applied the BL-View (Vaisala Boundary Layer View Software) to the raw data obtained during the cruise.

BL-View built-in automatic time and altitude averaging is as follows: Typical averaging time ranges from 14 min at night to 52 min under bright, cloudy sky conditions depending on the signal noise. Altitude averaging varies with the altitude and ranges from 80 m near the surface to 360 m above 1.5 km. Here we present the results from the BL-View with the algorithm of the gradient method [9]. The aerosol particles re-leased from the surface are capped by the temperature inversions, then the local minimum of the gradient of the backscatter profile gives the boundary layer heights (BLHs). The BL-View detects the BLH up to third.

Global positioning system (GPS) radiosonde observations were conducted with an iMS-100 radiosondes and an RD-08 AC receiver (Meisei Electric Co., Ltd) a total of 31 times along the ship route (Fig. 59.1). Radiosonde gives accurate profiles of the temperature, relative humidity (RH), and wind speed and direction with high vertical resolution (typically ~5 m). However, the number of the radiosonde is limited because of high operational costs and tasks. The vessel equipped many instruments to monitor the atmospheric and marine conditions.

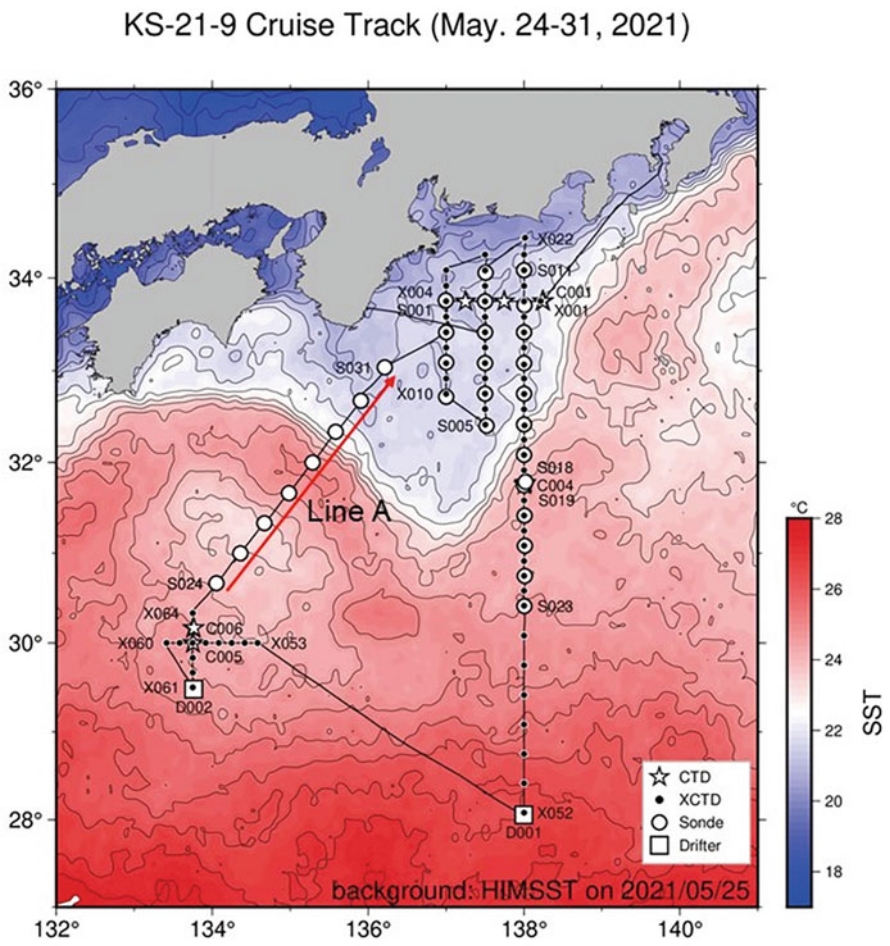


Fig. 59.1 Ship track and radiosonde launch site (circle) during the KS-21-9 cruise. The color contour indicates the SST on May 25, 2021 [8]. Line A shows the straight track across the Kuroshio front

A reasonable agreement of the MABL structure was obtained from the radiosonde and the ceilometer. We regard the lowest ABL height as the mixed layer height (MLH). Here we define the MLH from the radiosonde observation as the lowest level where the virtual potential temperature (T_v) increases by 1 °C from the surface [10]. An example of the comparison of the MLH derived from the radiosonde and ceilometer is shown in Fig. 59.2, which is the case of well-mixed ABL over the Kuroshio as indicated by a uniform T_v in the ML. The MLH well agree with the first BLH. Thus, the determined MLH from the radiosonde agrees with the lowest BLH found by the BL-View more than 70% during the cruise. In

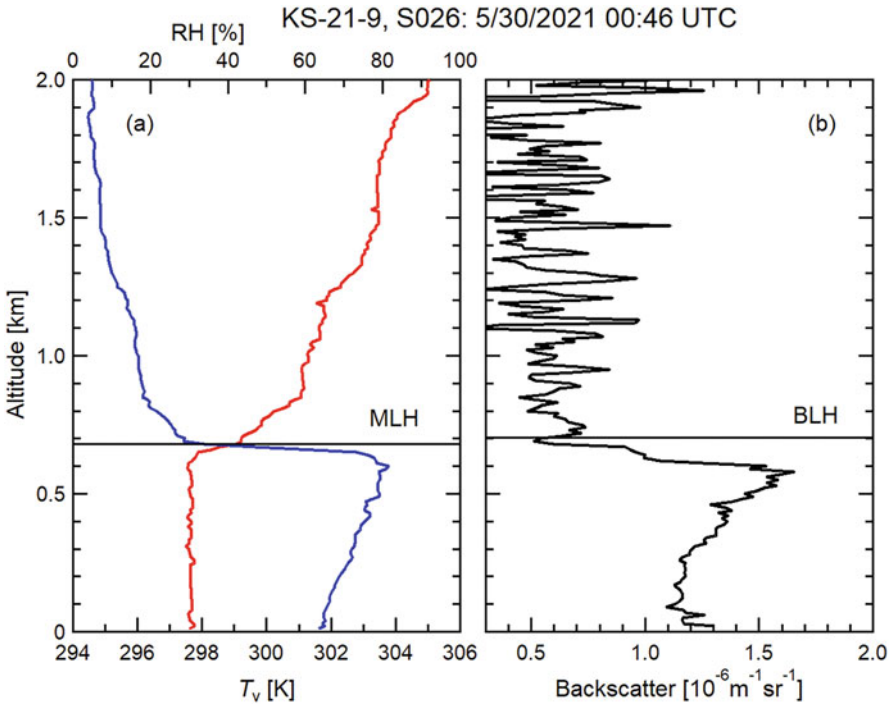


Fig. 59.2 Example of the deamination of the mixing layer height by the radiosonde S026 and the ceilometer: (**a**) Tv (red) and RH (blue) and (**b**) backscatter profile. The horizontal lines indicate the MLH and BLH at 00:46 UTC (LT = UTC-9) May 30, 2021

addition, the elevated second and third BLH often agree with the inversions over the MLH observed by the radiosonde.

The research vessel moved across the large meandering Kuroshio to northern inshore sea having colder SST. We present the observations along the line-A cruise shown in Fig. 59.1 hereafter. Seven radiosondes from S024 to S031 were launched every 30 min in latitude.

59.3 MABL Structure Over the Kuroshio

Figure 59.3 indicates the time-to-height cross section of the attenuated backscatter coefficients, the BLHs derived from the BL-View, the cloud base heights, and the MLH from radiosonde along the line A. Figure 59.4 shows the time series of the BLH, SST, surface air temperature (SAT), sensible and latent heat flux (Q_h, Q_e [W/m^2]), and wind speed U [m/s] and direction DIR [degrees]. SST-SAT (=S) is

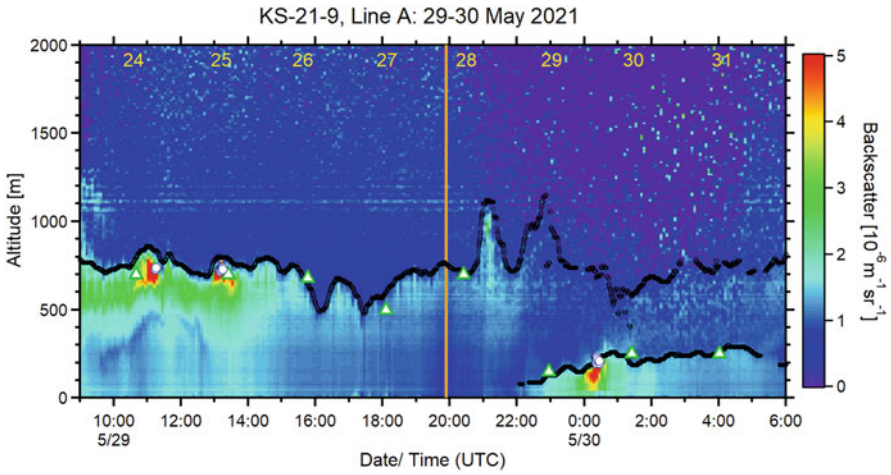


Fig. 59.3 Time to height plot of the attenuated backscatter on May 29–30, 2021 along the line A together with the BLHs (black circle). The white and blue circle indicates cloud bases. The white and green triangles show the MLH derived from the radiosondes (S024-S031; the numbers are indicated in orange at the top). The orange vertical line indicates the sunrise time

considered as a parameter of atmospheric stability [10]. Surface heat fluxes are calculated from surface meteorological data using the aerodynamical bulk method [11]. In the line A cruise, an interesting transitional phenomenon was observed across the Kuroshio from warm to the cold sea.

Over the Kuroshio, the BLH was as high as 500–800 m continuously associated with relatively high positive S and heat flux out of the ocean. Spontaneous lifts of the BLH from 700 to 1100 m happened twice during 20:30–23:30 UTC (LT = UTC-9) May 29, 2021. This remarkable jump of the BLH might be caused by following reasons: The accidental passage of the subsynoptic-scale anticyclone over the Honshu island, Japan (based on the surface weather analysis), brought a northern wind over the observation site, which is confirmed by a rapid change of the DIR (Fig. 59.4f). Then the SAT decreased ~0.5 h before the decrease of the SST as seen in Fig. 59.4b. These facts must have increased the heat flux and S 100 W/m^2 and 1.5 °C, respectively (Fig. 59.4c, d), which lifted the BLH instantaneously.

After the transition period, the colder air from the north and the low SST probably formed a shallow MLH. Thus, two BLHs were observed after 22:00 UTC. The upper second BLH as high as the MLH over the Kuroshio has been continuously existed, which is also confirmed also by the radiosonde. The origin of the second BLH must be a residual layer developed over the Kuroshio.

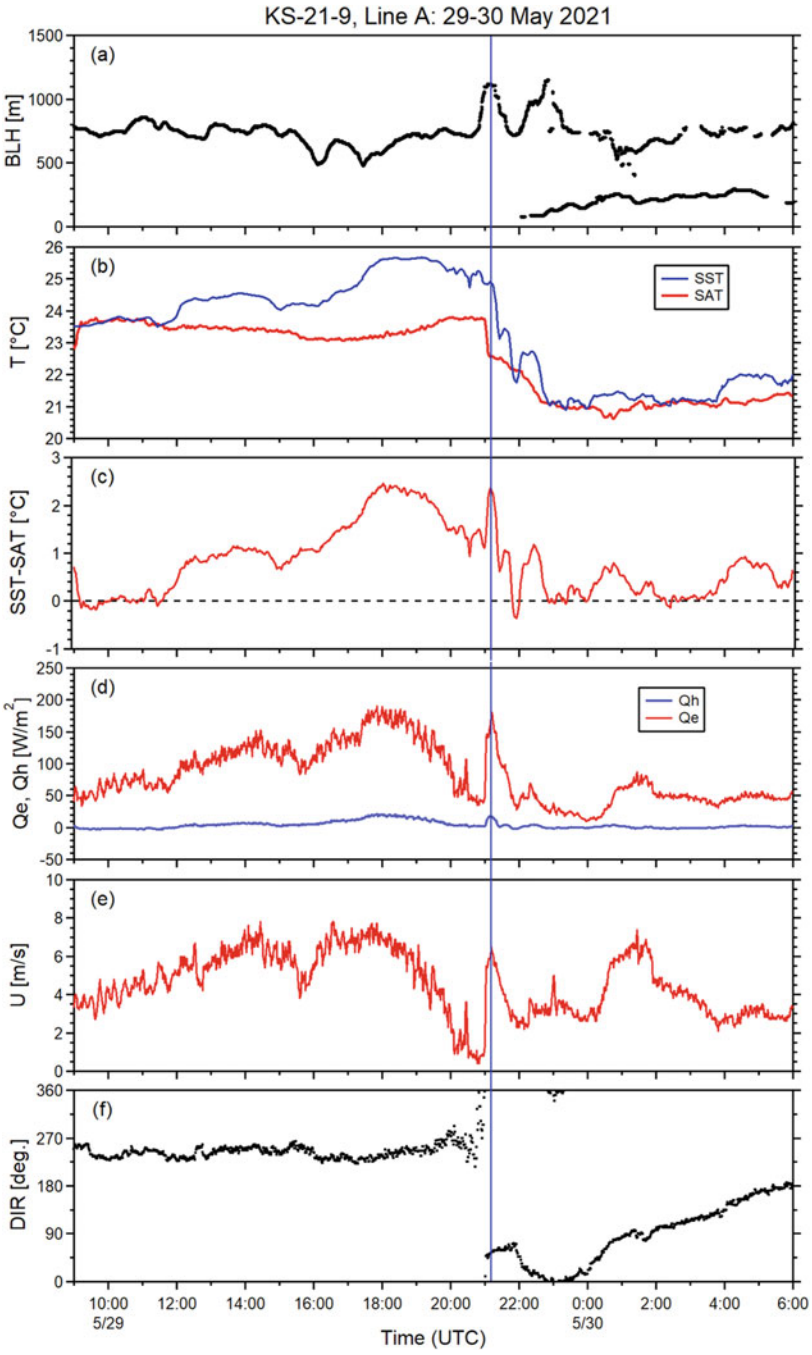


Fig. 59.4 From top to bottom, time series of the (**a**) BLH, (**b**) SST and SAT, (**c**) the difference SST-SAT, (**d**) sensible heat flux Q_h and latent heat flux Q_e, (**e**) wind speed U, and (**f**) wind direction DIR during line A of the cruise KS-21-9 on May 29–30, 2021. Vertical line indicated the time when the first peak of the BLH appeared

59.4 Summary

We have successfully conducted the ceilometer observation on R/V Shinsei-maru during the research cruise KS-21-9 in May 2021 over the Kuroshio. We applied the BL-View by importing the raw data. Along line A across the Kuroshio front, a highly variable structure of the ABL was observed.

Over the Kuroshio region, relatively high MLHs of 500–800 m were observed. At the Kuroshio front, sudden increases of the MLH (~400 m elevation from 700 to 1100 m) were detected. These extraordinary jumps of the MLH might be caused by the coupling of the marine and atmospheric meteorological conditions. Accidental passage of an anticyclone in the north brought the cold air over the warm sea. Then the surface heat flux increased instantaneously, which affected the MLH. In the cold sea apart from the front, a shallow ABL newly appeared. The continuous existing BLH about 700 m is considered as the residual layer developed over the Kuroshio. A highly temporal and drastic change of the MABL is successfully captured by the real-time continuous operation of the ceilometer. We will continue observation cruises combined with the ceilometer.

Acknowledgments We sincerely thank the captain and crews of R/V Shinsei-maru. This work was supported by a Grant-in-Aid for Scientific Research on Innovative.

Areas 6102 (KAKENHI Grant Nos. JP19H05699 and 19H05700) from JSPS of Japan.

References

1. Minobe, S., et al.: Influence of the Gulf Stream on the troposphere. Nature. **452**(13), 206–209 (2008). https://doi.org/10.1038/nature06690
2. Tanimoto, Y., et al.: Observations of marine atmospheric boundary layer transitions across the summer Kuroshio extension. J. Clim. **22**, 1360–1374 (2009). https://doi.org/10.1175/2008JCLI2420.1
3. Kawai, Y., et al.: In site evidence of low-level atmospheric responses to the Oyashio front in early spring. J. Metorol. Soc. Jpn. **97**(2), 423–438 (2019)
4. Knepp, T.N., et al.: Assessment of mixed-layer height estimation from single-wavelength ceilometer profiles. Atmos. Meas. Tech. **10**, 3963–3983 (2017)
5. Mues, A., et al.: Investigation of the mixed layer height derived from ceilometer measurements in the Kathmandu Valley and implications for local air quality. Atmos. Chem. Phys. **17**, 8157–8176 (2017)
6. Sempreviva, A.M., et al.: Observed development of the vertical structure of the marine boundary layer during LASIE experiment in the Ligurian Sea. Ann. Geophys. **28**, 17–25 (2010)
7. JAMSTEC HP: https://www.jamstec.go.jp/apl/hotspot2/overview_e.html
8. JMA Homepage: https://ds.data.jma.go.jp/gmd/goos/data/pub/JMA-product/him_sst_pac_T/Readme_him_sst_pac_T
9. Münkel, C., et al.: Retrieval of mixing height and dust concentration with lidar ceilometer. Bound.-Layer Metorol. **124**, 117–128 (2007)
10. Tokinaga, H., et al.: Atmospheric sounding over the winter Kuroshio extension: effect of surface stability on atmospheric boundary layer structure. Geophys. Res. Lett. **33**, L04703 (2006). https://doi.org/10.1029/2005GL025102
11. NOAA PMEL Homepage: https://www.pmel.noaa.gov/ocs/flux-documentation0

Chapter 60
ABL Height Different Estimation by Lidar in the Frame of HyMeX SOP1 Campaign

D. Summa, P. Di Girolamo, N. Franco, G. D'Amico, B. De Rosa, and G. Vivone

Abstract This work stems from the idea of improving the study and characterization of ABL at high resolution and in unstable weather conditions, characterized by strong turbulence and precipitation. A new approach based on the rotational temperature signals of a lidar system (BASIL) is used for the characterization of the ABL in the lower troposphere. The elastic signals at wavelength 532 nm and pure rotational Raman signals (strongly dependent on temperature variation) at 355 nm are considered. In particular, the case study considered to evaluate the ABL refers to observations made during HyMex campaign from 16th to 21th day of October 2012. The ABL heights retrieved by the new approach have been compared against the corresponding ones obtained by using other innovative methods such as a recently published algorithm based on morphological image processing techniques named MIPA as well as the ones retrieved by using more traditional methods based on gradients on temperature or water vapor profiles. For each methodology, a statistical analysis of the corresponding data is carried out.

Keywords PBL · Water vapor · Aerosol · Range-corrected signals · MIPA · Potential temperature · Lidar system

D. Summa (✉) · B. De Rosa
CNR-IMAA, Tito Scalo, Pz, Italy

School of Engineering, University of Basilicata, Potenza, Italy
e-mail: donato.summa@imaa.cnr.it

P. Di Girolamo · N. Franco
School of Engineering, University of Basilicata, Potenza, Italy
e-mail: donato.summa@imaa.cnr.it

G. D'Amico · G. Vivone
CNR-IMAA, Tito Scalo, Pz, Italy

© The Author(s), under exclusive license to Springer Nature Switzerland AG 2023

J. T. Sullivan et al. (eds.), *Proceedings of the 30th International Laser Radar Conference*, Springer Atmospheric Sciences,
https://doi.org/10.1007/978-3-031-37818-8_60

60.1 Introduction

The atmospheric boundary layer height (ABLH) is an important variable with a strong effect on a variety of fields such as weather forecasting and climate change modeling [1, 2]. Furthermore, the ABLH defines the atmospheric portion available for pollutant dispersion [2]. This height varies as a function of sea or land characteristics, atmospheric pattern, and solar heating. Moreover, the atmospheric boundary layer (ABL) is the region of the atmosphere directly in contact with the Earth's surface subjected to complex interactions between the land, the ocean, and the free troposphere. The time scale this region responds to surface forcing mechanisms is about 1 h. Our understanding of air quality and extreme event, for example, severe storms, is currently partial due to an incomplete knowledge of ABL processes. In the last years, different approaches have been proposed for detecting the ABLH and the aerosol layers within the ABL [1–3]. One approach is based on the determination of first (starting from the Earth's surface) the most significative gradient of the elastic lidar backscatter signal, assuming the atmospheric particles as ABL tracers [4]. In this study, we have used different approaches based on different algorithms and also on different sensors like lidar system, wind profiler, and radiosonding. Among the considered approaches, we have included also the algorithm MIPA developed in the frame of the European Aerosol Research Lidar Network (EARLINET). MIPA [5] is based on a fully image-based methodology (2-D): instead of analyzing the lidar observations profile by profile, the retrieval takes into account also the temporal dimension (at very high resolution). The lidar system Basil operated in Cevennes (CV) during the HyMex campaign 2012 in Montpellier (south of France). The selected period (16–21 October 2012) was mostly affected by orographic rain giving us the possibility to evaluate the performances of the considered ABLH retrievals under quite unstable atmospheric conditions. A key component of this program is its first field experiment, also called the special observation period (SOP1), dedicated to heavy precipitation and flash floods in northwestern Mediterranean [6].

More specifically, the selected measurement period is characterized by highly variable meteorological conditions, with aerosols and water layers (corresponding to different concentrations of vapor) at different altitudes. Such layers extend from the surface up to higher levels as it can be seen from the map obtained by the lidar system. Basil was operating in those days (see Fig. 60.1).

Different approaches for the ABLH estimation have been considered. In particular, we have applied MIPA algorithm on elastic high-resolution range-corrected lidar time series and a new approach to estimate the ABLH based on pure rotational Raman backscattered signals strongly linked to the temperature variation (the main driving force of the ABL in the atmosphere). Moreover, the values coming from these two techniques were compared with further techniques already present in the literature.

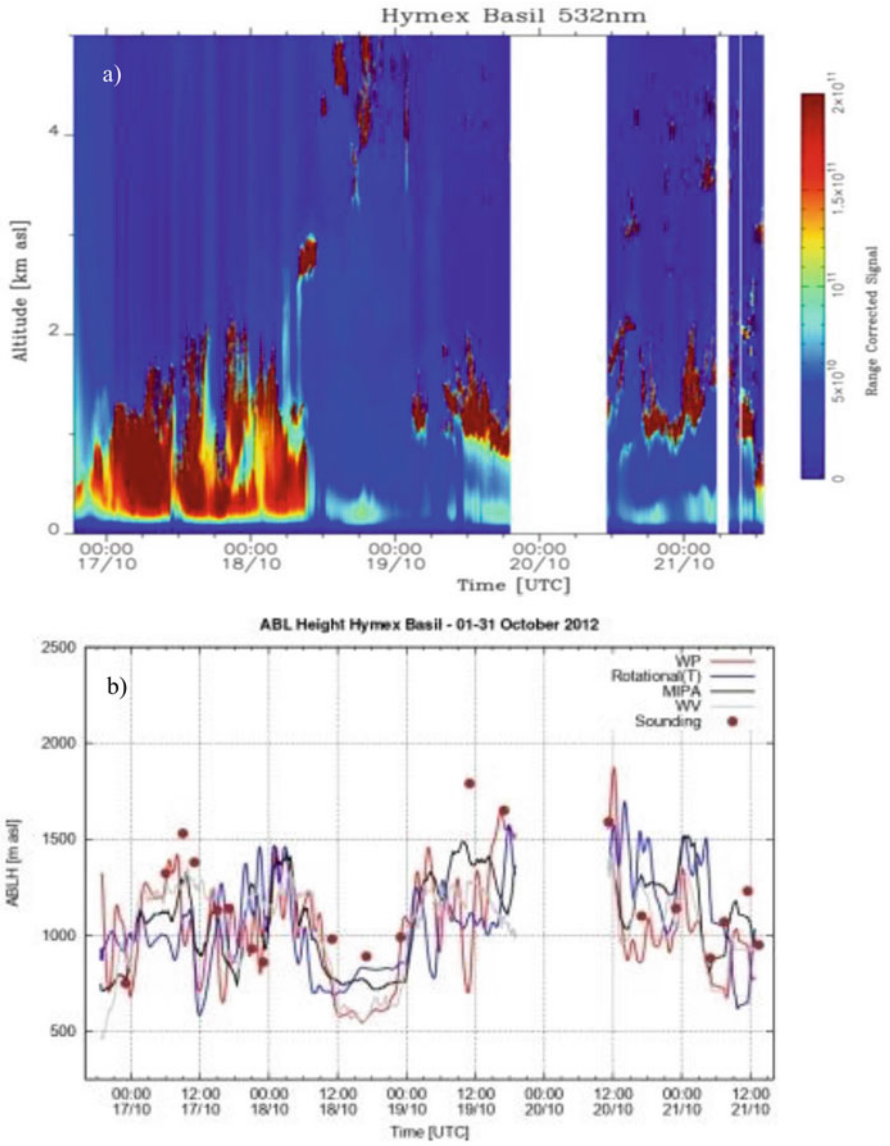


Fig. 60.1 RCS at wavelength 532 nm for the cases study 16–21 October 2012 panel (**a**) with the determination of ABL with different methods in panel (**b**) ABLH determination with different approaches. In particular we can see the ABL determination with different methods

60.2 Dataset and Method Description

BASIL system makes use of a Nd:YAG laser source, equipped with second and third harmonic generation crystals, capable to emit pulses at 1064, 532, and 355 nm. Laser pulses at these three wavelengths are simultaneously transmitted in the atmosphere along the zenith. The shortest of these wavelengths (355 nm) is used to stimulate vibrational and rotational Raman scattering from water vapor and nitrogen and oxygen molecules. These scattering processes, and the corresponding lidar echoes, are exploited to ultimately measure water vapor mixing ratio and temperature. The use of the 355 nm wavelength maximizes lidar performance, as in fact Raman scattering cross sections are proportional to the fourth negative power of the wavelength. For the specific operation of HyMeX-SOP1, the laser source was upgraded to generate a single pulse energy power at 355 nm of 500 mJ (corresponding to an average power of 10 W at a pulse repetition frequency of 20 Hz). The received is developed around a Newtonian telescope, with a primary mirror diameter of 0.45 m. Throughout the duration of HyMeX-SOP1, the University of Basilicata ground-based Raman lidar system (BASIL) was deployed in the Ceveninnes-Vivres site (Candillargues, Southern France, Lat: 43°37′ N, Long: 4° 4′ E, Elev: 1 m) and operated between 5 September and 5 November 2012, collecting more than 600 h of measurements, distributed over 51 measurement days and 19 intensive observation periods (IOPs).

The major feature of BASIL is represented by its capability to provide high-resolution and accurate measurements of atmospheric temperature and water vapor, both in daytime and nighttime, based on the application of the rotational and vibrational Raman lidar techniques in the UV.

The elastic range-corrected signals measured between 16 and 19 October 2012 by BASIL at 532 nm are plotted of 16–19 October to highlight the structures present in the observation period that goes from 16 to 19 October (Fig. 60.1a) from BASIL system at wavelength of 532 nm.

As the residual layer height corresponds to a higher altitude temperature inversion, the pure rotational Raman signals can potentially be used to infer both the mixed layer and the residual layer heights. In this respect, we need to recall that temperature measurements are performed by BASIL through the application of the rotational Raman lidar technique in the UV [7]. In particular, the rotational Raman backscattered signals from nitrogen and oxygen molecules within two narrow spectral regions that include rotational lines from these two species with opposite sensitivity to temperature changes have been used: rotational lines near to the laser wavelength λ_0, with lower values of the rotational quantum number J, increase in intensity with decreasing temperature, and rotational lines more distant from the laser wavelength, corresponding to higher values of J, increasing their intensity with increasing temperature.

The atmospheric temperature profile, $T(z)$, is obtained from the ratio of the signal with low quantum number J, $P_{\mathrm{LoJ}}(z)$, with the signal including high quantum number J, $P_{\mathrm{HiJ}}(z)$.

$$P_{\mathrm{RCS}}(z) = \frac{P_{\mathrm{HiJ}}\left(z\left[T\right]\right)}{P_{\mathrm{LoJ}}\left(z\left[T\right]\right)} \simeq \exp\left[T(z)\right] \tag{60.1}$$

These same rotational signals can be used to determine the ABL height [3]. Rotational lines fall within two narrow spectral bands in the proximity of the laser wavelength: one including lines characterized by low quantum rotational numbers, $P_{\mathrm{LoJ}}\ (z)$, and the other including lines characterized by high quantum rotational numbers, $P_{\mathrm{HiJ}}\ (z)$. We will consider the first minimum starting from the ground of the quantity (60.1) to detect ABLH. In the same way, we consider the first minimum of the water vapor vertical profile for the determination of the height of the ABL.

Morphological image processing approach (MIPA) framework used to detect the ABL when lidar data are involved. These latter can be represented as an image of range-corrected vertically resolved profiles acquired sequentially in time by RCS of lidar system.

MIPA consists of four main blocks: (i) a vertical spatial resolution adjustment step to reach a (target) working spatial resolution (around 30 m), (ii) a preprocessing based on mathematical morphology, (iii) an edge detector (i.e., the wavelet covariance transform (WCT) [5] in this work), and (iv) a post-processing relied upon both mathematical morphology and an object-based analysis to get the final result. It is worth to be remarked that MIPA is a blind approach and, thus, it does not exploit any prior information (Table 60.1).

60.3 Conclusion

Different methods were used for the determination of the ABLH for the dataset relating to the HyMex measurement during campaign in October 2012. The complex cases from 16 to 19 October were selected to study the planetary boundary layer using different methods ranging from more traditional to more innovative such as rotational signals and imaging methods.

The ABLH obtained from the radiosonde data based on the temperature gradient method have been used as a reference for the calculation [8, 9].

The final results, on the various techniques used for the study of the PBL, reported in terms of absolute and standard deviation (see Table 60.2 below), are comforting in particular; it is evident that the difference between the different methods in terms of error in the standard deviation is relatively low.

Table 60.1 The MIPA framework

Algorithm
Vertical spatial resolution adjustment of **I** by a factor R to get **I**D
Preprocess **I**D by low-pass filtering using half-gradients to get **I***pre*
Detection of the edges of **I***pre* using the WCT to get the edge map **E**
Post-process **E** using directional morphological filters and an object-based analysis to get **E***out*
The vertical spatial resolution adjustment block starts from a matrix
I: E ⊆ Z 2 → V ⊆ Z, which is the daily sequence of the attenuated backscatter profiles forming the columns of **I**. the down sampling with a factor R, which aims to reduce the bins' spatial resolution, is implemented by a low-pass filter (i.e., a moving-average filter) along each column of **I** plus decimation with a factor R. A low-pass filter based on half-gradients is used to preprocess $\mathbf{I}_{\mathrm{D}}$. A line structuring element in the horizontal direction (i.e., the time direction) is exploited, thus smoothing the lidar image along the horizontal axis (where the dynamic of the ABL is quite slow) reducing noise and preserving vertical edges. The result of the preprocessing of $\mathbf{I}_{\mathrm{D}}$ is denoted as $\mathbf{I}_{pre}$. Every edge detector can generally be exploited to extract a first estimation of the ABL starting from $\mathbf{I}_{pre}$ (e.g., the WCT, Canny's edge detector, or a gradient-based approach). In this work, we use the WCT to get a first estimation of the edge map, **E**. The edge map, **E**, is further analyzed by post-processing procedures. Furthermore, these results obtained by MIPA, pure rotational Raman signals, and water vapor time series were compared with the ABLH obtained by using more traditional sensors and methods such as wind profiler and radiosondes launched on site and used as a reference. Figure 60.1 Shows the evolution of the ABLH calculated for the different sensors and techniques described before and RCS at the length of 532 nm for the case study 16–21 October and the determination of ABL with different approaches.

Table 60.2 Table of statistical results of different approaches applies on the dataset

ABL method	Mean [m]	Standard deviation [m]	Standard error [m]
MIPA	207.57	127.5	29.25
Water vapor	238.61	144.12	33.25
Rotational	221.31	142.9	32.04
Wind profiler	235.68	161.39	36.33

Acknowledgments Wind profiler dataset were obtained from the HyMeX program, sponsored by Grants MISTRALS/HyMeX and ANR-11-BS56-0005 IODA-MED project (contact person: Said Frederique Laboratoire d'Aérologie, Université de Toulouse. CNRS 5560).

References

1. Melfi, S.H., Spinhirne, J.D., Chou, S.H., Palm, S.P.: Lidar observations of vertically organized convection in the planetary boundary layer over the ocean. J. Appl. Meteorol. Climatol. **24**(8), 806–821 (1985); Flamant, C., Pelon, J., Flamant, P.H., Durand, P.; Lidar determination of the entrainment zone thickness at the top of the unstable marine atmospheric boundary layer. Bound.-Layer Meteorol. **83**, 247–284 (1997). https://doi.org/10.1023/A:1000258318944
2. Di Girolamo, P., Ambrico, P.F., Amodeo, A., Boselli, A., Pappalardo, G., Spinelli, N.: Aerosol observations by lidar in the nocturnal boundary layer. Appl. Opt. **38**(21), 4585–4595 (1999)

3. Summa, D., Di Girolamo, P., Stelitano, D., Cacciani, M.: Characterization of the planetary boundary layer height and structure by Raman lidar: comparison of different approaches. Atmos. Meas. Tech. **6**(12), 3515–3525 (2013)
4. Russell, P.B., Uthe, E.E., Ludwig, F.L., Shaw, N.A.: A comparison of atmospheric structure as observed with monostatic acoustic sounder and lidar techniques. J. Geophys. Res. **79**(36), 5555–5566 (1974)
5. Vivone, G., D'Amico, G., Summa, D., Lolli, S., Amodeo, A., Bortoli, D., Pappalardo, G.: Atmospheric boundary layer height estimation from aerosol lidar: a new approach based on morphological image processing techniques. Atmos. Chem. Phys. **21**(6), 4249–4265 (2021)
6. Chazette, P., Flamant, C., Raut, J.C., Totemsa, J., Shanga, X.: Tropical moisture enriched storm tracks over the Mediterranean and their link with intense rainfall in the Cevennes-Vivara is area during HyMeX. Q. J. R. Meteorol. Soc. (2015). https://doi.org/10.1002/qj.2674
7. Menut, L., Flamant, C., Pelon, J., Flamant, P.H.: Urban boundary-layer height determination from lidar measurements over the Paris area. Appl. Opt. **38**(6), 945–954 (1999)
8. Madonna, F., Summa, D., Di Girolamo, P., Marra, F., Wang, Y., Rosoldi, M.: Assessment of trends and uncertainties in the atmospheric boundary layer height estimated using radio sounding observations over Europe. Atmosphere. **12**, 301 (2021). https://doi.org/10.3390/atmos12030301
9. Summa, D., Vivone, G., Franco, N., D'Amico, G., De Rosa, B., Di Girolamo, P.: Atmospheric Boundary Layer Height: Inter-Comparison of Different Estimation Approaches Using the Raman Lidar as Benchmark. Remote Sens. **15**, 1381 (2023). https://doi.org/10.3390/rs15051381, https://doi.org/10.1038/s41598-023-34715-6

Chapter 61
Temporal Evolution of Wavelength and Orientation of Atmospheric Canopy Waves

Alejandro Espinoza-Ruiz, Julia E. Colombini, Emily K. Everton, Pierre Dérian, and Shane D. Mayor

Abstract We describe an algorithm that can be applied to horizontally scanning atmospheric aerosol LiDAR data to determine canopy wave orientation and wavelength objectively. We applied it to over 1500 images of canopy waves from 53 episodes collected during the Canopy Horizontal Array Turbulence Study (CHATS) that took place in Dixon, California, in 2007. By doing so, we created time series of wavelength and wave crest orientation. Results from episode 25 from April 30 are presented.

Keywords Boundary layer processes · Image processing · Canopy waves · Gravity waves · Stable boundary layers · Elastic backscatter aerosol LiDARs

61.1 Introduction

Canopy waves are small-scale vertical oscillations of the stable atmospheric boundary layer that occur near the top of forest canopies due to the drag of the trees. An inflection point in the mean wind speed profile results in Kelvin–Helmholtz instability that excites the waves. If the waves increase in amplitude over time, they may break and generate turbulence that is an efficient transporter of heat, trace gases, and momentum. We are studying the temporal evolution of atmospheric canopy waves using scanning LiDAR data in an effort to better understand the factors that control the formation and dissipation of the waves or their transition to turbulence.

We applied an algorithm (created by P. Dérian) to horizontally scanning aerosol LiDAR images to objectively determine the wavelength and orientation of the wave

A. Espinoza-Ruiz (✉) · J. E. Colombini · E. K. Everton · S. D. Mayor
California State University Chico, Chico, CA, USA
e-mail: aespinozaruiz1@mail.csuchico.edu; sdmayor@csuchico.edu

P. Dérian
Independent Researcher, Nantes, France

© The Author(s), under exclusive license to Springer Nature Switzerland AG 2023

J. T. Sullivan et al. (eds.), *Proceedings of the 30th International Laser Radar Conference*, Springer Atmospheric Sciences,
https://doi.org/10.1007/978-3-031-37818-8_61

crests. We applied it to scans from the Raman-shifted Eye-safe Aerosol LiDAR (REAL) [1] from the Canopy Horizontal Array Turbulence Study (CHATS) that was conducted in Dixon, California [2]. The data set includes 53 episodes of canopy waves distributed over a three-month period [3]. Episodes ranged from a few minutes in duration to more than an hour in some cases. Therefore, the number of scans (or frames) in an episode ranged from 7 to 148. The frame update rate ranged from once every 10 to 30 seconds but was almost always constant during an episode. The algorithm determines a single salient wavelength and orientation angle of the waves from a square subset of pixels that is typically hundreds of meters wide in each dimension.

Mifsud et al. [4] demonstrated that the objectively determined wavelengths and orientations were very close to subjectively determined values. In that work, only one frame per episode was examined. We applied the algorithm to all frames of all episodes to determine the temporal evolution of wavelength and orientation. By applying the algorithm to all frames in an episode, we can efficiently monitor the wave characteristics over time. Unfortunately, due to the large amount of natural variability from case to case, we have yet to find a good way to display and summarize the time-series results of all 53 episodes. Therefore, in this chapter, we show just one of the 53 episodes.

Wavelength is the distance from one wave crest to the next. The orientation is the angle between the axis of the wave crests and north. For example, wave crests running from west to east have a 90° orientation. Wave crests running from the NW to the SE have a 135° orientation. In general, the orientation of the waves is perpendicular to the wind direction. In other words, the wave crests are *wind perpendicular* bands (in contrast to *wind parallel* features such as plumes).

61.2 Algorithm

The algorithm computes an autocorrelation function (ACF) for a rectangular subset of pixels in a horizontal LiDAR scan. The subset of pixels is called a region of interest (ROI) (Fig. 61.1, left) that must be manually set to avoid areas with hard-target returns and non-wave aerosol features such as dust plumes. The ACF (Fig. 61.1, right) reveals smooth bands of positive correlation each of which is spaced at intervals of wavelength and oriented the same as the salient wavelength and orientation in the image. To extract orientation and wavelength from the ACF, the pixels are averaged in narrow angular sectors (Fig. 61.2, left) and concentric rings (Fig. 61.3, left), respectively. These averages, as functions of angle and radius, contain local maxima that correspond to the orientation and wavelength (Fig. 61.2, right and Fig. 61.3, right). We apply this algorithm to each LiDAR scan in an episode to construct the time series of wavelength and orientation.

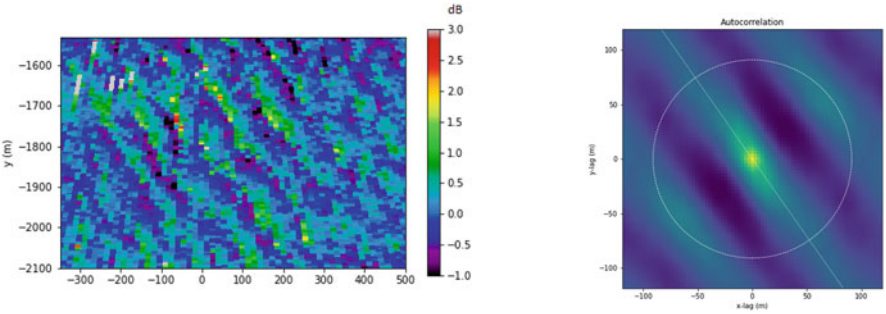


Fig. 61.1 Left panel: A subset of pixels from a full LiDAR scan featuring the canopy waves of interest. Right panel: The 2D autocorrelation function of the image in the left panel

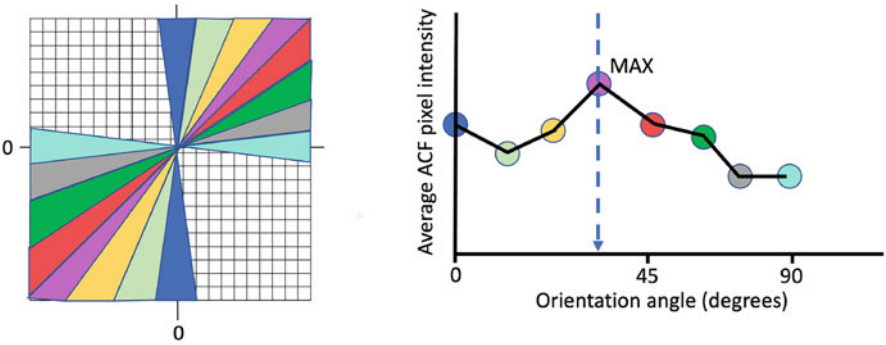


Fig. 61.2 Left panel: ACF pixels are averaged in narrow angular sectors to find the wave orientation. Right panel: The average of the sectors as a function of angle

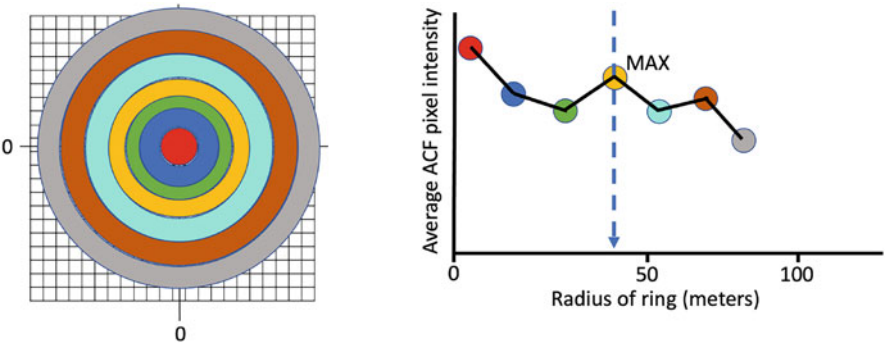


Fig. 61.3 Left panel: ACF pixels are averaged in circular rings to find the wavelength. Right panel: The average of the pixels in the rings as a function of radius

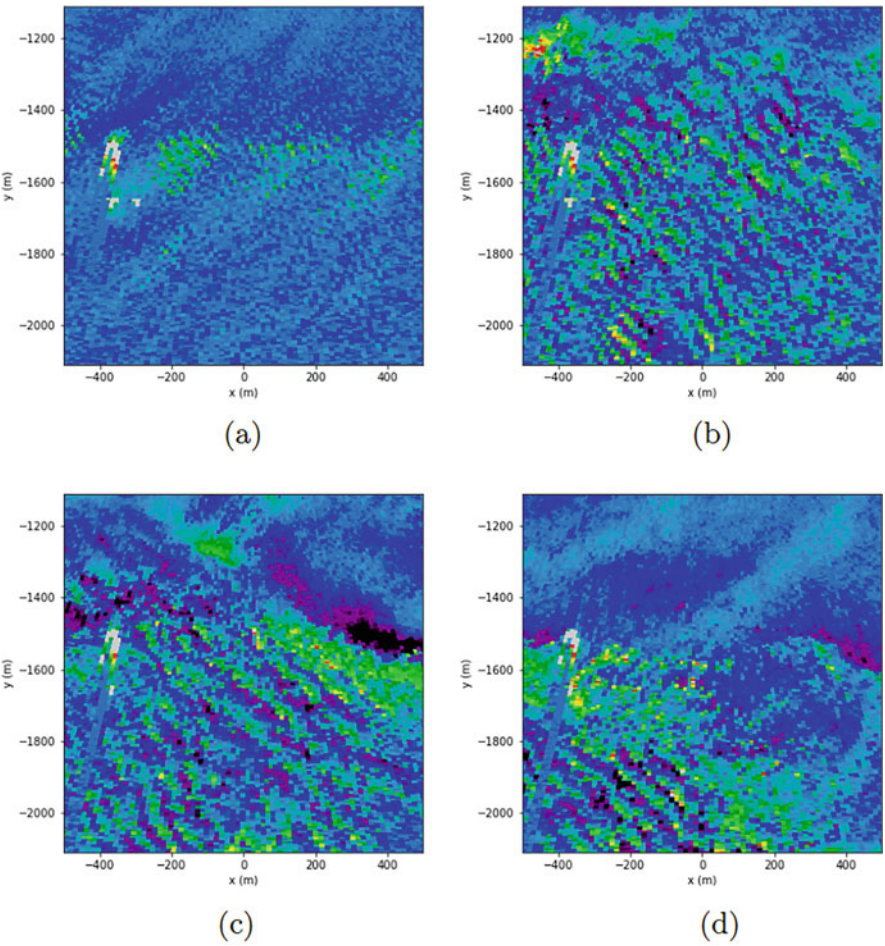


Fig. 61.4 A subset of 4 of 31 LiDAR images of the canopy waves in episode 25. Each area is 1 km × 1 km and centered on the location of the CHATS 30 m vertical tower. The green colors represent higher aerosol backscatter intensity. The LiDAR data have been high-pass median filtered in their native polar coordinate system. (**a**) Time: 12:36:26 UTC. (**b**) Time: 12:41:59 UTC. (**c**) Time: 12:48:33 UTC. (**d**) Time: 12:51:34 UTC

61.3 Results

We chose to show episode 25 (30 April 2007) because the wavelength changes significantly and steadily starting at 30 m and increasing to over 80 m in 11 minutes. (Note: The range of wavelengths over all 53 episodes ranges from about 30 m to 100 m.) After 12:47, the objectively determined wavelengths become erratic as the episode ends and the flow begins to reverse. In the beginning of this episode, the wind was from the SW. The erratic excursions in wavelength after 12:47 are

not likely to be wavelengths as the waves are losing coherence during that time. Figure 61.4 shows a subset of 4 of the 31 frames centered on the instrumented 30 m tower.

The first frame (12:36:26) reveals very fine-scale waves limited to a relatively small area. The second frame (12:41:59) shows that the waves have grown dramatically in terms of area extent and wavelength. The third frame (12:48:33) shows a band of aerosol advecting in from the NE that is associated a reversal in the flow and the end of the episode. The fourth frame (12:51:34) shows that the aerosol band has moved across the center of the images where the tower is located.

The algorithm successfully captures the increase in wavelength during this episode (see top panel in Fig. 61.5). The wave orientations (see bottom panel in Fig. 61.5) are fairly consistent (about 145°) over the first 10 minutes with the exception of one data point at 12:38. The orientations near the end of the episode change. We cannot detect rotation of the wave crests during the end of the episode, so the last 10 data points may not be meaningful. (Note, 90° at the last data point would be east–west orientation.)

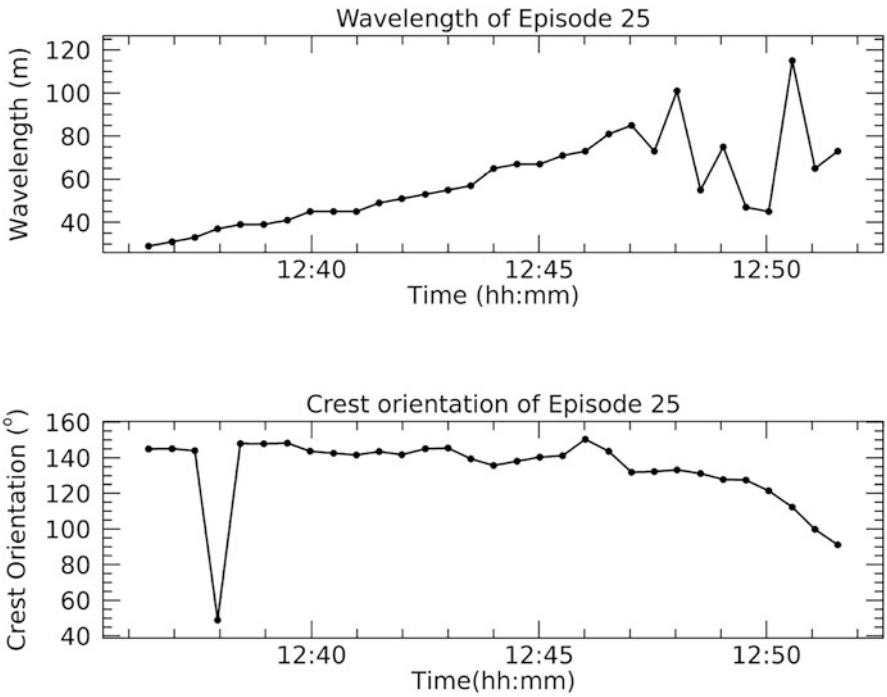


Fig. 61.5 Time series of wavelength (top) and orientation (bottom) for episode 25

61.4 Conclusions

Scanning aerosol LiDAR data can reveal important quantitative information on microscale wave structure and evolution. However, algorithms are necessary to extract that quantitative information. Here, we applied a new algorithm to extract wavelength and orientation from image sequences in order to produce time series.

We have learned that it is important to restrict the region of interest to avoid hard-target and non-wave aerosol features. The algorithm will only provide reliable results when a single-wave train is in the ROI. We have occasionally observed two wave trains with different wavelengths and orientations present simultaneously. In these cases, the algorithm can only lock onto one or the other, and it may hop back and forth erratically.

In the future, we plan to explore whether any consistent trends exist and whether the wavelength and orientation can be linked to other variables such as wind velocity and static stability as measured by in situ sensors on the tower. We also plan to objectively delineate the individual wave crests and their phase propagation velocity. Doing so will allow us to track all wave crests in the group and explore the temporal and spatial evolution of the waves in unprecedented detail.

Acknowledgments This material is based upon work supported by the National Science Foundation under Grant AGS 2054969. The first three coauthors are undergraduates majoring in environmental sciences at California State University Chico.

References

1. Mayor, S.D., Spuler, S.M., Morley, B.M., Loew, E.: Polarization LiDAR at 1.54-microns and observations of plumes from aerosol generators. Opt. Eng. **46**, 096201 (2007)
2. Patton, E.G., et al.: The Canopy Horizontal Array Turbulence Study (CHATS). Bull. Am. Meteorol. Soc. **92**, 593–611 (2011)
3. Mayor, S.D.: Observations of microscale internal gravity waves in very stable atmospheric boundary layers over an orchard canopy. Agric. For. Meteorol. **244–245**, 136–150 (2017)
4. Mifsud, K.E., Iqbal, M., Dérian, P., Mayor, S.D.: Objective determination of wavelength and orientation of atmospheric canopy waves. In: Fall Meeting of the American Geophysical Union, 16 December, New Orleans. Poster presentation A45C-1867 (2021)

Chapter 62
Assessment of Planetary Boundary Layer Height Variations Over a Mountain Region in Western Himalayas

Jaswant Rathore, S. R. Radhakrishnan, Shishir Kumar Singh, Devesh Kumar Shukla, and Chhemendra Sharma

Abstract We have investigated the evolution or growth of planetary boundary layer (PBL) height for the first time over a mountain topography at a Western Himalayan station Palampur (32.11° N, 76.54° E, 1347 m altitude amsl). For this, we have used ground-based Raman lidar measurements from June 2016 to May 2019 to determine the monthly and seasonal variations in PBL height using wavelet covariance transform (WCT) method. Results reveal that the PBL height was observed lower in the colder months of December and January with lowest in January having an average value of 524 ± 83 m and higher PBL heights were observed in the May and June. The seasonal PBL height was calculated as 631 ± 208 for winter (December, January, February, March), 1308 ± 595 for summer (April, May, June), 1413 ± 460 for monsoon (July, August, September), and 904 ± 190 for post monsoon (October, November). Although the highest monthly and seasonal PBL height was observed in the month of July and post monsoon season respectively, that can be due to the lesser number of observation days because of rain. The obtained PBL variations have also been studied with the meteorological conditions which includes ambient

J. Rathore
Environmental Sciences and Biomedical Metrology Division, CSIR-National Physical Laboratory, New Delhi, India

Academy of Scientific and Innovative Research (AcSIR), Ghaziabad, Uttar Pradesh, India

Centre for Atmospheric Sciences, Indian Institute of Technology Delhi, New Delhi, India
e-mail: jrathore@cas.iitd.ac.in

S. R. Radhakrishnan (✉) · S. K. Singh · C. Sharma
Environmental Sciences and Biomedical Metrology Division, CSIR-National Physical Laboratory, New Delhi, India

Academy of Scientific and Innovative Research (AcSIR), Ghaziabad, Uttar Pradesh, India
e-mail: rkrishnan@nplindia.org

D. K. shukla
Environmental Sciences and Biomedical Metrology Division, CSIR-National Physical Laboratory, New Delhi, India

© The Author(s), under exclusive license to Springer Nature Switzerland AG 2023

J. T. Sullivan et al. (eds.), *Proceedings of the 30th International Laser Radar Conference*, Springer Atmospheric Sciences,
https://doi.org/10.1007/978-3-031-37818-8_62

temperature, relative humidity (RH), wind velocity, and atmospheric pressure, and the results show that the PBL height was showing a strong positive correlation with correlation coefficient as 0.89 with average temperature and a strong negative correlation with atmospheric pressure ($r = -0.92$). However, the results suggested a weak positive ($r = 0.34$) and a weak negative correlation ($r = -0.18$) with relative humidity and wind speed, respectively.

Keywords Raman lidar · Western Himalayas · Planetary boundary layer height

62.1 Introduction

The PBL is an atmospheric layer which directly interacts with the Earth's surface. It plays a prominent role in the vertical mixing and pollutants' dispersion and has a large effect on local environmental conditions. The PBL measurements can be helpful to comprehend (i) cloud formation and convection [1], (ii) mixing processes of different tracers such as greenhouse gases (GHG), aerosols and other gases and pollutant's dispersion [2], (iii) enhancing predictions of storms and climate projections [3], (iv) generation of renewable energy [4], and (v) other interlinked phenomena that affect climate, weather, and air pollution [5]. The information on PBL height will also be critical for advancement in numerical models and improving parameterizations as all weather, climate, or air quality models require PBL data as an input parameter. Therefore, the study of PBL height evolution becomes extremely significant especially over complex mountain topography such as Western Himalayas.

Though several instruments and techniques exist to determine the PBL height, but over the years, lidar remote sensing has not only proven to provide the vertical structure of aerosols and clouds but also PBL height measurements in the atmosphere [6]. In this study, we have used ground-based Raman lidar observations over Palampur from June 2016 to May 2019 to study the monthly and seasonal variations in PBL height and their relationship with the meteorological conditions including air temperature, RH, air wind speed, and atmospheric pressure.

62.2 Study Site and Instrumentation

62.2.1 Study Site

The Raman lidar utilized in this work is installed in the atmospheric observatory of CSIR-National Physical Laboratory. This observatory is located (32.093° N and 76.543° E) at the campus of CSIR-Institute of Himalayan Bioresource Technology (IHBT), Palampur, India, in the southwest Himalayan region at a height of 1347 m (amsl). The map of the site is shown in Fig. 62.1. This location is 6 km far from

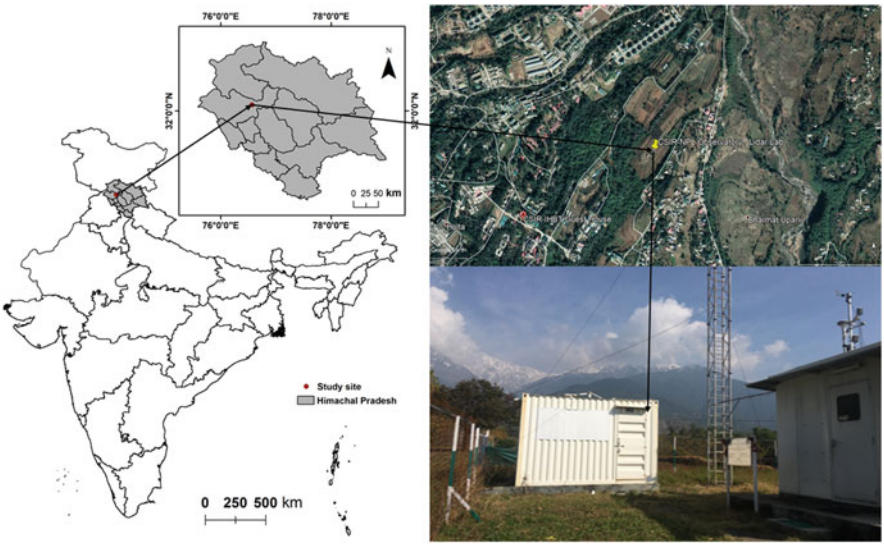


Fig. 62.1 Map of the study site with image of portacabin where lidar is installed

the main city Palampur, and it is bordered by forest areas and agricultural lands. This site experiences very less anthropogenic activities and that is why it can be considered as a background site.

62.2.2 Instrumentation

A Raman lidar system (model: LR111-D200) manufactured by Raymetrics, Greece, consisting of two depolarization channels at 355 nm, and a N2 Raman channel at 387 nm was used for this study. This lidar uses a pulsed Nd:YAG laser source having 32.8 mJ pulse energy and 20 Hz pulse repetition rate transmitting frequency tripled 355 nm pulses in the atmosphere. To receive the backscattered light, a 20 cm Cassegrainian telescope is used. The light is filtered and separated to co-polarized and cross-polarized components at 355 nm along with the Raman component at 387 nm using an optical unit. These light components are converted to electrical signals using three Hamamatsu PMTs, and their strength is acquired using Licel Transient Digitizer which records the signal in both analog and photon count (PC) mode. The Licel digitizer is equipped with a 20 MHz analog to digital converter (ADC) along fast photon counting system with 250 MHz counting capability. Some brief details of the installed Raman lidar are shown in Table 62.1 and detailed specifications of this system are mentioned in [7].

Table 62.1 Details of LR111-D200 Raman lidar

Parameter	Specifications
Laser	Nd:YAG (frequency tripled at 355 nm)
Energy of the pulse	32.8 mJ
Pulse repetition rate	20 Hz
Telescope	20 cm Cassegrainian
Data acquisition	Licel transient recorder (20 MHz, 12-bit, 7.5 m spatial resolution)
Detector	Three Hamamatsu PMTs

62.3 Methodology

To estimate the PBL height from backscattered lidar signal, the wavelet covariance transform (WCT) method proposed by [8] was used. The WCT method was chosen since it gets less affected to background noise and can be used in different meteorological conditions [6]. The WCT function $W_f(a, b)$ can be defined as

$$w_f(a,b) = \frac{1}{a}\int_{Z_{\min}}^{Z_{\max}} \mathrm{RCS}(z)h\left(\frac{z-b}{a}\right)dz \tag{62.1}$$

Here, RCS(z) is the range-corrected lidar signal, that is, $P(z)z^2$; a and b are the dilation and translation parameters. $z_{\min}$ and $z_{\max}$ are the lower and higher altitude limits in which WCT is applied and h is the Haar function which is defined in Eq. 62.2. The value of the height at which the first maximum of W_f occurs corresponds to the PBL height:

$$h\left(\frac{z-b}{a}\right) = \begin{cases} +1, b - {}^{a}\!/_{2} \le z \le b \\ -1, b \le z \le b + {}^{a}\!/_{2} \\ 0, \text{elsewhere} \end{cases} \tag{62.2}$$

62.4 Results and Discussions

The PBL height obtained from the range-corrected glued signal has been analyzed with the meteorological conditions (temperature, pressure, RH, and wind speed) between June 2016 and May 2019. Figure 62.2a displays the Box-Whisker plot of the monthly variations of the PBL height over Palampur from June 2016 to May 2019 with annual average of 1049 ± 553 m above ground level. The PBL height was observed lower in the colder months of December and January with lowest in the January having an average value of 524 ± 83 m, and the higher PBL heights were observed in the hot months of May and June. The seasonal PBL height was calculated as 631 ± 208 m for winter (December, January, February, March),

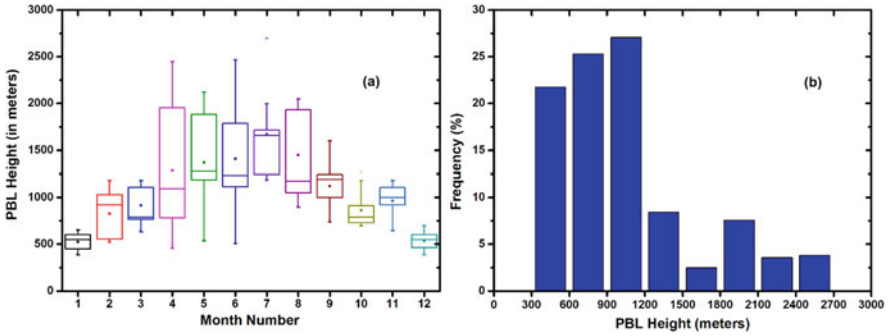


Fig. 62.2 (**a**) Box-Whisker plot of the monthly variation of the daily mean PBL height determined from glued signal for the period of June 2016–May 2019. The "*x*" indicates the minimum and maximum PBL height, and dot indicates the mean value for each month over the study period. (**b**) Shows the frequency distribution (%) of the daily mean PBL height from June 2016 to May 2019

1308 ± 595 m for summer (April, May, June), 1413 ± 460 m for monsoon (July, August, September), and 904 ± 190 m for post monsoon (October, November) during the study period [9]. Although the highest monthly and seasonal PBL height was observed in the month of July and post monsoon season, respectively, that can be due to the lesser number of measurement days because of rain. Figure 62.2b presents the percentage frequency distribution of the PBL height over Palampur from June 2016 to May 2019. The PBL height was ranging from 300 to 2700 m during the study period, and approximately 83% of the values were lying below 1500 m. The maximum frequency distribution (27%) was found from 900 to 1200 m and nearly 10% of the values were above 2000 m.

The diurnal variation of PBL height is plotted in Fig. 62.3, where we have taken the elastic channel data of 8 days for June 2016 and 5 days of November 2016. It was followed by finding the hourly average for each day and then averaging the hourly averaged values over the month along with the standard deviation. The diurnal variation shows that in June 2016, PBL height was ranging from 290 to 1800 m with mean as 738 ± 423 m. The diurnal variation for November 2016 ranges from 184 to 1116 m with mean value of 542 ± 273 m. For both the months, higher values were seen during afternoon and lower values during nighttime.

The monthly average of daily mean PBL was compared with the monthly average of meteorological parameters for the same period by determining correlations between the PBL height and the average temperature, average atmospheric pressure, average wind speed, and average relative humidity. The results of these comparisons are displayed in Fig. 62.4, and it can be seen that the PBL height was showing a strong positive correlation ($r = 0.89$) with the average temperature and a strong negative correlation with the atmospheric pressure ($r = -0.92$). However, the results showed a weak positive correlation ($r = 0.34$) with relative humidity and a weak negative correlation ($r = -0.18$) with wind speed. Overall, the monthly cycle of the PBL height was following the monthly cycle of the temperature and negatively

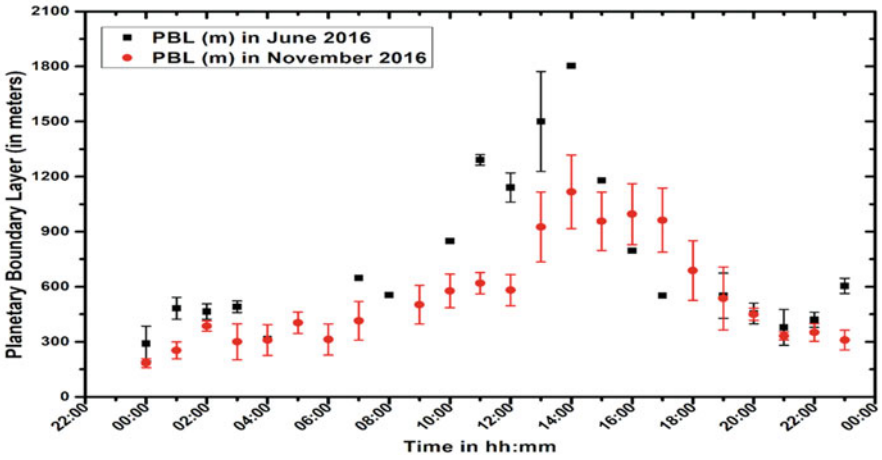


Fig. 62.3 Diurnal variation of PBL height over the study site during the study period

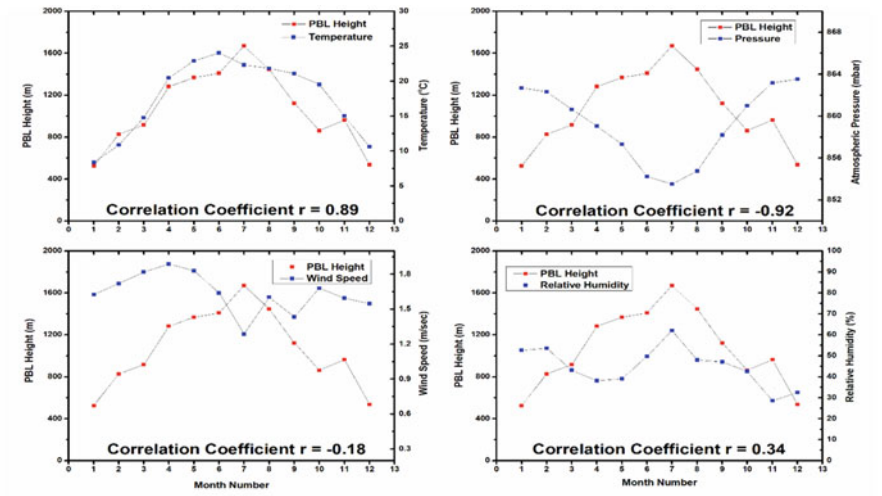


Fig. 62.4 Relationship of the annual average of the monthly averaged PBL height with the meteorological parameters (**a**) average temperature for the same time, (**b**) same time average atmospheric pressure, (**c**) average wind speed for the same time, and (**d**) average relative humidity for the same time of June 2016–May 2019

following the atmospheric pressure which is analogous to the findings of the [10] over the United States and Europe and [11] over China. Although some studies have shown the relationship between PBL height and RH [12], yet we could not found the relationship of RH with the PBL height.

62.5 Conclusions

This study reports the monthly and seasonal variations in PBL height over a mountain region at Palampur in Western Himalayas during June 2016–May 2019 using Raman lidar system. Results show that lowest PBL height was observed in January with average value of 524 ± 83 m and higher PBL heights were observed in May and June. The seasonal average values were obtained as 631 ± 208 m for winter, 1308 ± 595 for summer, 1413 ± 460 for monsoon, and 904 ± 190 for post monsoon. The correlation analysis of PBL height with meteorological parameters shows a strong positive correlation ($r = 0.89$) with average temperature and a strong negative correlation with atmospheric pressure ($r = -0.92$). However, the results showed a weak positive correlation ($r = 0.34$) with relative humidity and a weak negative correlation ($r = -0.18$) with wind speed.

References

1. Pal, S., et al.: 3-dimensional observations of atmospheric variables during the field campaign COPS. IOP Conf. Ser. Earth Environ. Sci. **1**, 012031 (2008)
2. Janssen, R.H.H.: Combined effects of surface conditions, boundary layer dynamics and chemistry on diurnal SOA evolution. Atmos. Chem. Phys. **12**(15), 6827–6843 (2012)
3. Cohen, A.E.: A review of planetary boundary layer parameterization schemes and their sensitivity in simulating Southeastern U.S. cold season severe weather environments. Weather Forecast. **30**(3), 591–612 (2015)
4. Stevens, R.J.A.M.: Using the coupled wake boundary layer model to evaluate the effect of turbulence intensity on wind farm performance. J. Phys. Conf. Ser. **625**, 012004 (2015)
5. Board on Atmospheric Sciences and Climate, Ocean Studies Board, Division on Earth and Life Studies, and National Academies of Sciences, Engineering, and Medicine: The Future of Atmospheric Boundary Layer Observing, Understanding, and Modeling: Proceedings of a Workshop, p. 25138. National Academies Press, Washington, DC (2018)
6. Baars, H.: Continuous monitoring of the boundary-layer top with lidar. Atmos. Chem. Phys. **8**(23), 7281–7296 (2008)
7. Jaswant, R.: Initial assessment of lidar signal and the first result of a Raman lidar installed at a high altitude station in India. Remote Sens. Appl.: Soc. Environ. **18**, 100309 (2020)
8. Granados-Muñoz, M.J.: Automatic determination of the planetary boundary layer height using lidar: one-year analysis over southeastern Spain: determination of the PBL height. J. Geophys. Res. Atmos. **117**(D18), D18208 (2012)
9. Nakoudi, K.: Planetary boundary layer height by means of lidar and numerical simulations over New Delhi, India. Atmos. Meas. Tech. **12**(5), 2595–2610 (2019)
10. Seidel, D.: Climatology of the planetary boundary layer over the continental United States and Europe: boundary layer climatology: U.S. and Europe. J. Geophys. Res. Atmos. **117**(D17) (2012). https://doi.org/10.1029/2012JD018143
11. Guo, J.: The climatology of planetary boundary layer height in China derived from radiosonde and reanalysis data. Atmos. Chem. Phys. **16**(20), 13309–13319 (2016)
12. Pal, S.: Forcing mechanisms governing diurnal, seasonal, and interannual variability in the boundary layer depths: five years of continuous lidar observations over a suburban site near Paris. J. Geophys. Res. Atmos. **120**(23) (2015). https://doi.org/10.1002/2015JD023268

Chapter 63
Analysis of Updraft Characteristics from an Airborne Micro-pulsed Doppler Lidar During FIREX-AQ



Edward J. Strobach, Alan Brewer, Brandi McCarty, and Amanda Makowiecki

Abstract The Fire Influence on Regional-to-Global-Environments Experiment – Air Quality (FIREX-AQ) – offered an opportunity to interrogate the dynamics of wildfire plumes with an airborne Doppler lidar system. A technique was developed to target updrafts embedded in wildfire plumes in order to analyze the complex interaction that developing updrafts have with the neighboring environment. The general characteristics of updrafts are described from the current sample size, and the fine structure details related to impacts of counter-rotating vortex (CRV) structures on developing updrafts are examined. The development of these techniques comes in a timely manner since the California Fire Dynamics Experiment (CalFiDE) is planned to target wildfires during late summer 2022. It is the goal of this study to improve upon scanning strategies to better target wildfire plumes in order to understand the governing dynamics that dictate their evolution.

Keywords Wildfires · Doppler lidar · Entrainment · Plume dynamics

63.1 Introduction

An increase in observational research related to wildfires has been conducted in recent years as a result of increased wildfire frequency in areas prone to their development. Research targeting plume development has been used to assess plume rise models [1]; to understand the vortical structure, energetics, and mixing

E. J. Strobach (✉) · B. McCarty · A. Makowiecki
Boulder/NOAA Chemical Sciences Laboratory, CIRES/University of Colorado, Boulder, CO, USA
e-mail: edward.strobach@noaa.gov; brandi.mccarty@noaa.gov; amanda.makowiecki@noaa.gov

A. Brewer
NOAA Chemical Sciences Laboratory, Boulder, CO, USA
e-mail: alan.brewer@noaa.gov

© The Author(s), under exclusive license to Springer Nature Switzerland AG 2023

J. T. Sullivan et al. (eds.), *Proceedings of the 30th International Laser Radar Conference*, Springer Atmospheric Sciences,
https://doi.org/10.1007/978-3-031-37818-8_63

properties of plumes [1, 2]; and to determine the role that the inflow/outflow characteristics have on plume dynamics [3]. While some studies have featured controlled burns, many other studies have used stationary and mobile remote sensing capability to target plumes in active wildfire areas.

The Fire Influence on Regional to Global Environments Experiment – Air Quality (FIREX-AQ) – measurement campaign in 2019 featured a multi-institutional effort to target different wildfires in the Contiguous United States (CONUS). Wind measurements from a micro-Joule class pulsed Doppler lidar mounted on a NOAA Twin Otter probed the dynamics associated with wildfire plumes during the 07/27/2019–08/12/2019 time period. Fire temperature measurements derived from a shortwave infrared camera were used to determine local hotspots in order to zoom in on plumes within the larger burn area. Relatively high spatial resolution provided detailed snapshots of plume structures within the wildfire perimeter that allowed the characterization of plume dynamics.

The remainder of the chapter is as follows. A background of the instrumentation that was used will be given. Following will be a discussion of results that includes general characteristics of updrafts identified, dynamical characteristics of updraft profiles, and the interaction of updrafts with the near-field environment. Last is a summary and a note on future work.

63.2 Instrumentation

63.2.1 Micro-Joule Class Pulsed Coherent Doppler Lidar

FIREX-AQ offered an opportunity to test the micro-Joule class pulsed coherent Doppler lidar, or DL, over different wildfire hotspots across the Pacific northwest with the NOAA Twin Otter. The DL samples aerosols embedded in the flow with a 1550 nm laser. The frequency of the scattered atmospheric return is compared to that of the local oscillator (LO) using heterodyne detection to measure the along-beam Doppler shift. The along-beam resolution is approximately 62 m and is determined by the pulse width of the laser. The DL has the capability of measuring out to 7200 m but was restricted by the fact that the DL was pointing downward toward the surface at a height below 3000 m.

During FIREX-AQ, the DL operated two scan modes: azimuthally scanning at a fixed 15-degree off nadir elevation angle – plan position indicator (PPI) – and the vertical stare. The horizontal winds and vertical velocity for the former scan mode are calculated using the velocity azimuth display (VAD) method. The scan rate is additionally restricted to rotate no more than 60 degrees/second to circumvent "beam sweeping contamination." The small elevation angle from nadir minimizes the impact of flow heterogeneities caused by an enlarged DL footprint. Since the volume of the cone is inverted – i.e., the DL beam originates from above – the widening of the cone is most prominent near the surface. In complex terrain, the

VAD method may suffer from flow heterogeneities which may decrease the accuracy of horizontal wind measurements near the surface.

For both scanning modes, the DL system had to be motion compensated to account for the Twin Otter cruising speed (~51 m/s) as well as any tilts relative to nadir that might be incorporated into the measurement. The orientation and speed of the aircraft were measured using a VectorNav 200 inertial navigation unit (INU). The INU output was used to calculate and remove the aircraft motion projected along the line of site of the Doppler measurements and to actively stabilize the pointing of the system during vertical stares. The relatively slow cruising speed of the Twin Otter and the high temporal resolution of the DL (10 Hz) allowed for increased horizontal resolution along the flight track less than 10 m. Further details can be found in Schroeder et al. [4].

63.2.2 NightFox Ham-Cam

The ham-cam is part of an airborne Fire Radiative Power measurement package that operated from the NOAA Twin Otter. It has a 25.5-degree field of view with a square aspect ratio. Each sensor has 64 × 64 pixels and produce images at a rate of 1 Hz. The short-wave infrared imaging capability at 1.6 microns allows the ham-cam to quantify thermal emissions from heat associated with wildfires. The fact that the ham-cam sensor can saturate leads to limitations in quantifying temperatures associated with extreme heat. Therefore, the ham-cam is used to determine areal coverage of wildfire hotspots instead of being a strict measure of fire temperature. Output from the ham-cam indicating the presence of a wildfire hotspot is used to determine updrafts induced by fire-driven convection.

63.3 Results

63.3.1 Isolating Updrafts in Wildfire Plumes

Combining the fire temperature output from the Ham-Cam and vertical wind measurements derived from the vertical stare of the DL allowed the determination of updrafts over wildfire source points. This was made possible by taking the ham-cam coverage output to determine whether the Twin Otter was approximately over a wildfire source point – see Fig. 63.1 which shows an example of fire temperature below enhanced vertical motion and range corrected intensity (RCI). Three available channels – left, center, and right – were used to evaluate whether a source point was identified. If one or more of the channels yielded a value of 1 (source point) as opposed to 0 (no source point), then that location was selected and used to determine whether there was positive vertical motion directly above the surface.

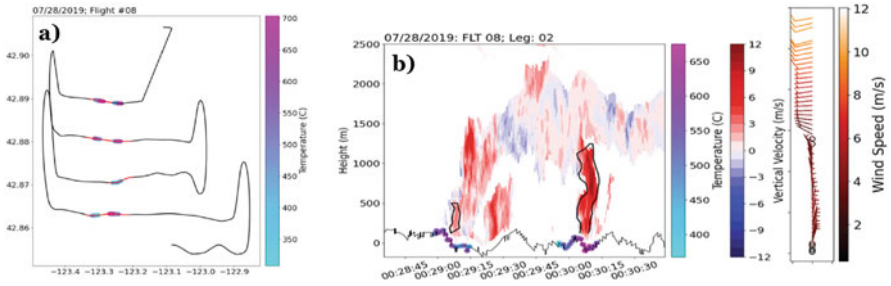


Fig. 63.1 Vertical velocity overlaid with fire temperature for the second leg (second from north in inset) of flight 8 during 00z. Overlaid are the outlined updrafts. Wind barbs during this time are averaged throughout the hour and shown to the right

The black outlines in Fig. 63.1 show two examples where updrafts along the flight track were identified. Images from each flight leg are subjectively analyzed to determine whether updrafts were approximately captured along the transect. Combining the flight track data (inset in Fig. 63.1) and horizontal wind vectors from VAD scans (wind barbs to the right in Fig. 63.1) provides some guidance when determining whether some portion of the isolated plume extends perpendicular to the flight track.

63.3.2 General Characteristics

Figure 63.2 shows a scatter plot of plume width v. plume depth. The markers are color-coded based on different types of analyses, where blue represents developing counter-rotating vortices (CRV) at the flanks of updrafts (7), green pertains to cases where updrafts exhibit rotationality (1), red are analyses where both CRVs and rotationality are present (2), and brown are cases where none of the above analyses could be done (4). The trend shows deeper updrafts lead to wider plumes and that the plume width is about half the plume depth. Although the correlation is relatively high (~0.91), the small sample size does not lead to statistical robustness, and it is quite possible that the algorithm's design, which is more tailored for upright plumes, is limited when it comes to a diversified selection sample. There is also a great possibility of examples that deviate from the findings in Fig. 63.2 that include wide and short plumes or tall and narrow plumes. It is difficult to say whether updrafts are more inclined to follow the behavior in Fig. 63.2 or if updrafts tend to be associated with examples that deviate from these findings.

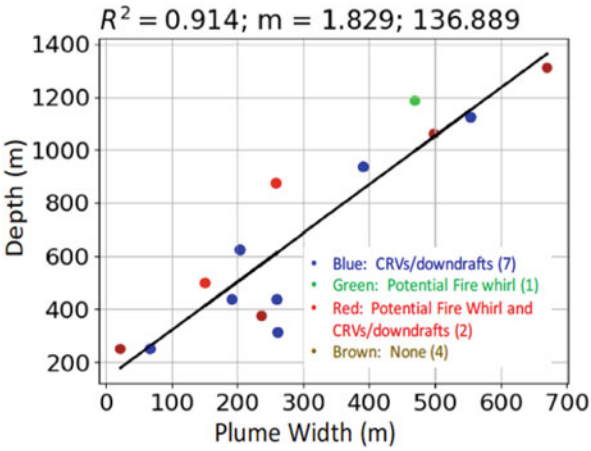


Fig. 63.2 Comparisons of estimated plume depth v. plume width from isolated updrafts identified during FIREX-AQ. Cases above are color-coded according to analysis

63.3.3 Counter-Rotating Vortex (CRV) Structures and Their Interaction with Updrafts

Figure 63.3a shows an example of an updraft that has been isolated by combining the DL and fire temperature data to isolate updrafts over wildfires. The scaled vertical velocity on the y-axis is done to vertically separate the vertical velocities so that the horizontal structure of vertical velocity can be viewed with respect to height. The upper-right portion of this plot shows a zoom-in of the curtain plot that depicts the outline of the updraft as well as the positive core vertical velocities and the negative vertical velocities outside the updraft.

The vertical velocity in Fig. 63.3a has a maximum peak velocity at about 400 m. The red vertical velocity profile in Fig. 63.3b represents the average vertical velocity across the updraft overlaid with the horizontal variability across its width; the weaker blue profile represents an updraft detected along the same transect. It can be seen that the horizontal variability is larger for the red profile and that the horizontal variability maximizes where the structure is most peaked, suggesting that variability is associated with the shape of the updraft core structure.

Figure 63.3c shows length scales derived for the left (blue) and right (green) sides of updraft defined by local minima in the downdraft velocity. The left side provides a complete record while the right side represents a partial record. Focusing on the left side, it is clear that the horizontal extent of the CRV decreases with height and that the maximum extent is approximately 140 m near the bottom. The downdraft profiles in Fig. 63.3d are averaged between the orange squares in Fig. 63.3a. The profile shape is parabolic and does not match the shape of the length scale profile. It's reasonable to assume that the CRV near the surface is deformed by its interaction with the terrain which could lead to the spread of momentum horizontally, thereby leading an increase in length scale near the surface. The downdraft minimum coincides with a height a little less than 300 m at 2.5 m/s,

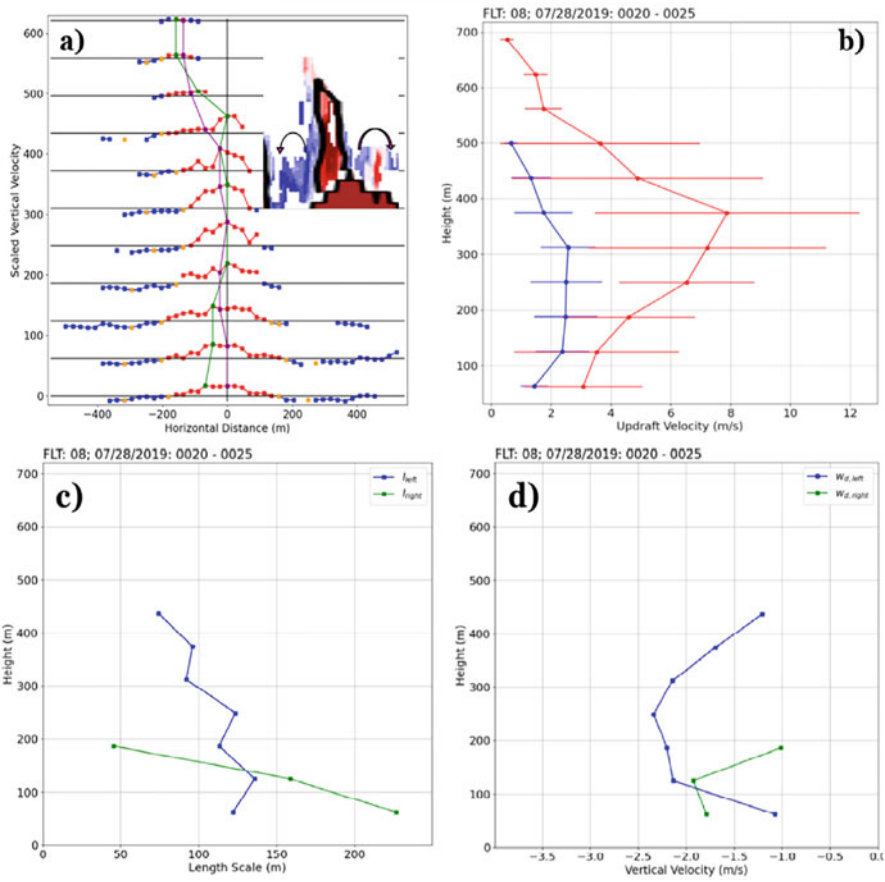


Fig. 63.3 (**a**) Scaled vertical velocity of red updraft profile in (**b**). Blue squares are outside of the updraft and fall below horizontal lines (negative velocities) while red squares are within updraft region. The orange squares represent the separation between the updraft interface and the most distant local downdraft minimum identified. The green and purple lines represent the location of the maximum wind and updraft center, respectively. At the inset of (**a**) is a zoom-in of a curtain plot of the same updraft. (**b**) represents profiles identified along the first flight leg of flight 8 starting at 00z, with the red profile representing the updraft of interest. Horizontal bars are overlaid on the average vertical velocity across the updraft width and represent horizontal variability of the updraft. Profiles of the (**c**) horizontal length scales of detected CRVs and (**d**) downdraft profiles are given for the left (blue) and right (green) sides of the updraft

which is considerably less than the maximum updraft strength of about 8 m/s. The momentum that is detrained out of the updraft likely minimizes the updraft strength potential below the core velocity.

63.4 Summary and Future Work

Results from this work show key dynamical processes that remain elusive when diagnosing the evolution of wildfire plumes. Here, we explored the general characteristics and the fine structure details of a particular cases. While the updrafts identified tended be wider for deeper plumes, we acknowledge the fact that the detection process is limited not only in sample size but also restricted more to upright plume structures. Part of future work will aim to expand the sample size and potentially look at options for targeting bent over plumes.

Isolating updrafts allowed the characterization of the updraft dynamics, and the interaction updrafts may have with the neighboring environment. CRVs deposit momentum away from the updraft but also act as mean of recirculating momentum at the updraft base. This leads to modifications in the updraft structure that are difficult to quantify. We examined the length scales of CRVs as well as downdraft structures in order to understand how drag-induced jet cores from updrafts lead to developing CRVs. Improvements in deriving length scales are currently underway, and it is a goal to apply this technique to an increased sample size in the future.

High-resolution large eddy simulations (LES) will provide some extra context when testing the methods disclosed. It is our aim to test these techniques against LES in preparation for the California Fire Dynamics Experiment (CalFiDE). Additionally, lessons learned from FIREX-AQ and the results enclosed should result in better scanning strategies which is currently underway.

References

1. Lareau, N.P., Clements, C.B.: The mean and turbulent properties of a wildfire convective plume. J. Appl. Meteorol. Climatol. **56**(8), 2289–2299 (2017)
2. Arreola Amaya, M., Clements, C.B.: Evolution of plume core structures and turbulence during a wildland fire experiment. Atmosphere. **11**(8), 842 (2020)
3. Charland, A.M., Clements, C.B.: Kinematic structure of a wildland fire plume observed by Doppler lidar. J. Geophys. Res. Atmos. **118**(8), 3200–3212 (2013)
4. Schroeder, P., Brewer, A.B., Choukulkar, A., Weickmann, A., Zucker, M., Holloway, M.W., Sandberg, S.: A compact, flexible, and robust micropulsed Doppler lidar. J. Atmos. Ocean. Technol. **37**(8), 1387–1402 (2020)

Chapter 64
Diurnal Variability of MLH and Ozone in NYC Urban and Coastal Area from an Integrated Observation During LISTOS 2018

Yonghua Wu, Amin Nehrir, Kaihui Zhao, Guillaume Gronoff, Jianping Huang, James E. Collins, Timothy A. Berkoff, Liqiao Lei, Dingdong Li, Margarita Kulko, Mark Arend, Barry Gross, and Fred Moshary

Abstract Mixing layer height (MLH) and land-sea breeze in the coastal area play an important role in ozone (O_3) dispersion and transport. This study presents the multiple-platform observations of MLH dynamics for a high O_3 event during Long Island Sound Tropospheric Ozone Study (LISTOS) in summer 2018. The diurnal evolution and spatial variability of MLH are observed from ground-based aerosol Lidar, Vaisala Ceilometer, Coherent Doppler Wind Lidar, and airborne lidar in New York City (NYC) urban and the coastal area in Long Island on August 28–29, 2018. The results indicate that the MLH growth in the morning shows a time lag of 1–2 h

Y. Wu (✉) · M. Kulko · M. Arend · B. Gross · F. Moshary
City College of New York, New York, NY, USA

NOAA Cooperative Science Center for Earth System Sciences and Remote Sensing Technologies, New York, NY, USA
e-mail: yhwu@ccny.cuny.edu

D. Li
City College of New York, New York, NY, USA

A. Nehrir
NASA Langley Research Center, Hampton, VA, USA

K. Zhao
Department of Atmospheric Sciences, Yunnan University, Kunming, China

G. Gronoff · J. E. Collins · L. Lei
NASA Langley Research Center, Hampton, VA, USA

Science Systems Applications, Inc. (SSAI), Hampton, VA, USA

T. A. Berkoff
NASA Langley Research Center, Hampton, VA, USA

J. Huang
NOAA/NCEP/EMC and Lynker, College Park, MD, USA

© The Author(s), under exclusive license to Springer Nature Switzerland AG 2023

J. T. Sullivan et al. (eds.), *Proceedings of the 30th International Laser Radar Conference*, Springer Atmospheric Sciences,
https://doi.org/10.1007/978-3-031-37818-8_64

in the coastal area versus that in the NYC urban area. The spatial gradient variation of MLH from the urban to the coastal area is demonstrated from the NASA High Altitude Lidar Observatory (HALO) airborne high spectral resolution lidar (HSRL) observations by showing lower values in the coastal and marine area. Meanwhile, the ground O_3 are consistently much higher at noon in the coastal sites than those in the NYC urban sites reaching the maximum value of 100–120 ppb in exceedance of the O_3 NAAQS, which is closely relevant to the urban pollutant transport, MLH dynamics, and sea breeze. The observation data are further used to assess the model product of PBLH and O_3 at the NYC urban and coastal sites.

Keywords Lidar · MLH · Ozone · Sea breeze

64.1 Introduction

Ozone (O_3) exceedances of the National Ambient Air Quality Standard (NAAQS, 70 ppb maximum daily 8-h average O_3-MD8AO) frequently occur during summer in New York City (NYC) and its downwind coastal area in the Connecticut and Long Island or Long Island Sound [1, 2]. Such high O_3 episodes are usually related to the complex interaction of urban emissions and pollutants, downwind transport, photochemical transformation, and land-sea breeze effects [2–4]. To address this issue and understand O_3 formation processes, the Long Island Sound Tropospheric Ozone Study (LISTOS) campaign was launched in the summer of 2018 [2]. This study presents the multiple platform observations of mixing layer height (MLH) dynamics for a high O_3 event during LISTOS 2018. We focus on the analysis of MLH dynamics and spatial variability from the different lidar observations in NYC urban and coastal area and demonstrate their potential effects on a high O_3 event in the coastal area. The model predict product of MLH and O_3 are preliminarily evaluated with the observation data.

64.2 Methodology and Observation

At the City College of New York (CCNY, 40.82° N, 73.949° W) site, the remote sensing and in situ instruments are deployed for air quality and meteorological monitoring, which includes a 3-wavelength Mie-Raman scattering lidar, ceilometer (Vaisala CL51 or Lufft CHM15K), coherent Doppler wind lidar (Leosphere Windcube 200S), Cimel sun/sky radiometer (AERONET-Aerosol Robotic Network), in situ samplers for O_3, NO_2 and aerosol size distribution, and a surface weather station. Meanwhile, there is a surface air quality station operated by the NYSDEC at the CCNY campus for $PM_{2.5}$, O_3, and CO measurements. In addition, we deployed the ceilometer (Vaisala CL31) and O_3 monitor (2B Tech model 202/205) at the North Shore of Long Island (Eatons Neck, 40.9541° N, 73.3985° W). We also made



Fig. 64.1 Ground site location used in this study

the boat measurements with CL-51 ceilometer and O_3-monitor for a few days in Long Island Sound. The MLHs are estimated with a wavelet transform analysis and quality assurance method with a 5–10 min average [5]. Therefore, ground O_3, MLH, low-altitude aerosol plumes, and cloud height can be simultaneously measured in the NYC urban and downwind coastal area in Long Island. Figure 64.1 shows the ground sites for the data used in this study.

During LISTOS 2018, the NASA High Altitude Lidar Observatory (HALO) airborne high spectral resolution lidar (HSRL) made airborne observations [6], and the MLHs from the urban to coastal and marine area are derived. In addition, the NASA LaRC Mobile Ozone Lidar (LMOL) was deployed at Sherwood Island State Park, Westport, CT (73.337° W, 41.118° N, 2.5-meter ASL, coastal CT) to measure O_3 vertical profile using a differential absorption principle at the UV wavelength pair of 287–292 nm [7].

As part of the NYS-Mesonet [8], coherent Doppler wind lidars (Leosphere WindCube 100 s) are deployed to measure wind profiles in Bronx (Lehman College, 40.872° N, 73. 894° W, 59.3 m ASL, 7.5 km to the NE of CCNY, urban) and Stony Brook (40.9196° N, 73.133° W, 55.1 m ASL) near the north shore of Long Island and other areas (see Fig. 64.1 for their location). The data are collected, quality-controlled, and archived. Information on air advection and vertical mixing in the planetary boundary layer (PBL) can be obtained from these observations. The variance of vertical velocity generally represents vertical mixing or turbulence intensity thereby indicating convective boundary layer height (CBLH) or MLH while stable boundary layer (SBL) height may be estimated from horizontal wind gradient with altitude in the coastal and marine area [9].

64.3 Result and Discussion

64.3.1 Diurnal and Spatial Variation of MLH in the NYC Urban and Coastal Area

Figure 64.2 gives the MLH diurnal variation and comparison in the NYC urban and coastal area on August 28–29, 2018. The MLHs are measured from the CCNY aerosol lidar in the NYC urban area and the ceilometer (CL-31) at Eatons Neck (coast), respectively. The CL-51 ceilometer was operated at CCNY on August 28 and then deployed to a boat measurement over water on August 29. In the urban area as shown in Fig. 64.2a, the MLH or PBLH is low (≤0.5 km) before 10:00 am and then gradually increases from 10:00 to 13:30. However, at the coastal area, the MLH growth (Fig. 64.2b) starts from 11:00 am and attains the maximum at 14:00–15:00. Figure 64.3 gives the comparisons of MLH and surface temperatures in the urban and coastal area. There is a time lag for the MLH increase in the morning in the coastal area versus the urban area. This is probably relevant to the land-water surface contrast that shows different temperature and sensible heating (Fig. 64.3b), which can affect thermal-dynamic process in the PBL.

Figure 64.4 shows the spatial variability of MLH from the NYC urban to the coastal and marine area from NASA airborne HALO-HSRL observations on August 28, 2018; the flight track and time are given in Fig. 64.4a. The MLHs are generally higher in the NYC urban area but lower in the coastal area. At 17:00–19:00 UTC (13:00–15:00 local time), the MLHs show a dramatic gradient variation from the NYC urban to the coastal and marine area with the value at 1.5 km in NYC urban but 0.7 km in the coastal and marine area. These results are consistent with the ground observations at CCNY and the coastal area in Long Island.

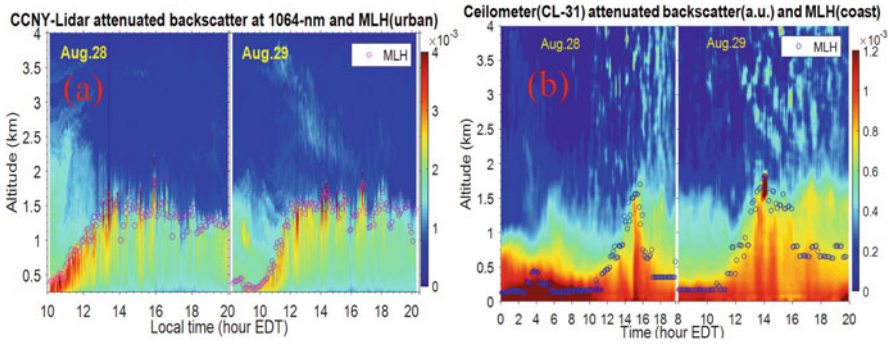


Fig. 64.2 (**a**, **b**) MLH evolution at the NYC urban (CCNY) and coastal area (Eatons Neck) in Long Island on August 28–29, 2018

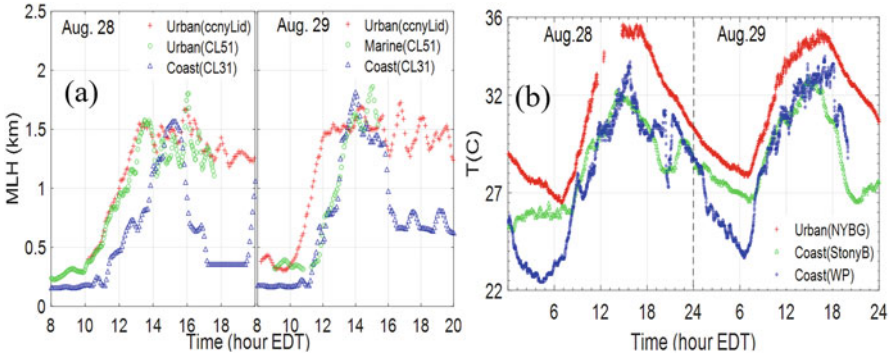


Fig. 64.3 (**a**, **b**) Comparison of MLH and surface temperature in the NYC urban/coastal area

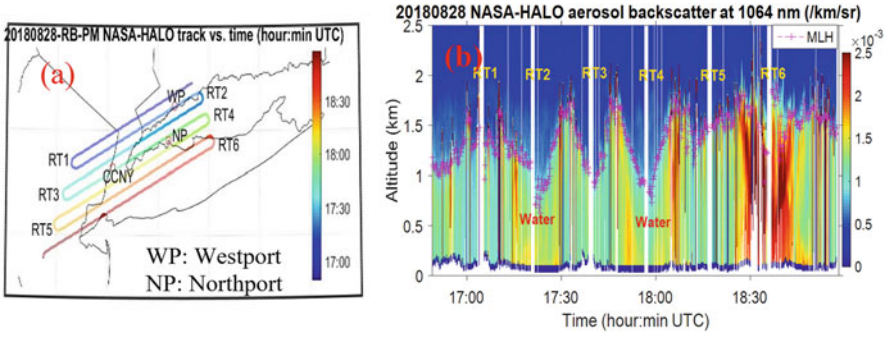


Fig. 64.4 (**a**, **b**) NASA-HALO flight track, time, and MLH in the afternoon of August 28, 2018. (*UTC-4* local time or EDT, RT_i Raster Turning, *WP* West Port, *NP* North Port)

64.3.2 Comparison of O_3 and MLH Diurnal Variation

Figure 64.5 shows the diurnal variation of ground O_3 and NO_2 in the NYC urban and coastal area in Long Island and Connecticut (CT) on August 28–29, 2018. At the coastal sites (EN, Eatons Neck; FP, Flax Pond; WP, West Port in CT), the ground O_3 are consistently much higher than those at the urban site (CCNY) at 13:00–17:00 EDT whereas the MLHs are generally lower than those in the urban area (Fig. 64.3a). Figure 64.5b gives the time-height distributions of O_3 at WP site measured by the NASA LaRC O_3 lidar; the results indicate consistent temporal variation with the ground observations and high O_3 in the PBL. As one of O_3 major precursors, the NO_2 at the coastal area (FP and WP) are much lower than those in the urban (CCNY) site (Fig. 64.5c). The air backward trajectories ending at 200-m altitude (Fig. 64.5d) at the coastal sites show coincident origin or transport from the NYC urban area but at different altitudes. In addition, the wind lidar observations indicate the prevailing southwest winds in the NYC urban area which means the downwind urban pollutant transport to the coastal area in CT and Long Island. But near the

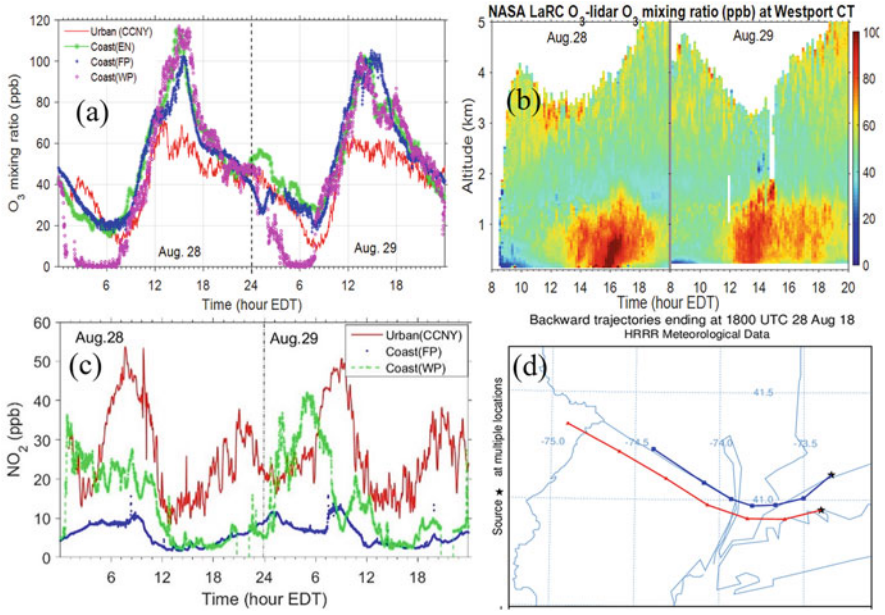


Fig. 64.5 (**a**, **b**) Diurnal variation of ground and vertical profile of O_3, (**c**) ground NO_2, and (**d**) air backward trajectories ending at 200-m altitude in the coastal area (sites: *EN* Eatons Neck, *FP* Flax Pond, *WP* Westport)

coastal Long Island, there are the prevailing northwest winds which may prevent the off-shore dispersion of O_3. Thus, high O_3 at the coastal area might be attributed to the urban transport, lower MLH, and sea-land breezes.

64.3.3 Model Product Validation for O_3 and PBLH

With the observation data, we made initial evaluation of NOAA operational NAM-CMAQ model forecast product of ground O_3 and PBL height (PBLH) on August 27–29, 2018. At the urban site (CCNY), the model products show good agreement with the observation. But at the coastal site (Riverhead), the comparisons in Fig. 64.6 indicate that there was a time delay for the maximum O_3 from the model product whereas the model PBLH growth in the morning starts earlier than those from the observations.

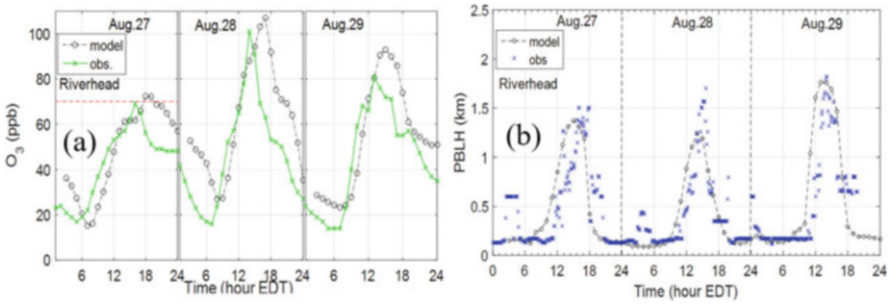


Fig. 64.6 (**a**–**b**) ground O_3 and PBLH comparison between the NAM-CMAQ model forecast and observation at the coastal site (Riverhead) during August 27–29, 2018

64.4 Conclusion

In summary, this study presents the diurnal evolution and spatial variability of MLH and O_3 and their comparisons in the NYC urban and downwind coastal areas. Higher O_3 attaining 100–120 ppb and exceeding the NAAQS are observed at the coastal area whereas the MLHs are lower in the coastal area. The MLHs attain 1.5 km altitude in the urban area but 0.7–0.8 km in the coastal and marine area at noon on August 28, 2018. The MLH growth also shows a time lag in the morning at the coastal area against the NYC urban area. In addition, the ground NO_2 are much lower in the coastal area than those in the urban area. Thus, high O_3 in the coastal area might be attributed to the urban transport, MLH dynamics, and sea breezes. The model forecast product generally shows similar variation of O_3 and PBLH with the observations except the timing shift for the maximum O_3 and PBLH growth at the coastal site; further analysis is expected for understanding such bias.

Acknowledgments This work is supported by the New York State Energy Research and Development Authority (grant no. 137482), NESCAUM (grant no. 2417), and the NOAA under the CESSRST agreement NA16SEC4810008. We appreciate the data from NYS-Mesonet/SUNY-Albany, NYSDEC, NOAA, and NASA. The statements contained within the presentation are not the opinions of the funding agencies nor of the US government but only reflect author's opinions.

References

1. Miller, P.J.: Retrospective and Future Analysis of Air Quality in and Downwind of New York City, DRAFT White Paper. Available at ww.nescaum.org/documents/listos (2017)
2. Karambelas, A.: LISTOS: Toward a Better Understanding of New York City's Ozone Pollution Problem (An Overview of the Long Island Sound Tropospheric Ozone Study). EM A&WMA (2020)
3. Wu, Y., et al.: Synergistic aircraft and ground observations of transported wildfire smoke and its impact on air quality in New York City during the summer 2018. Sci. Total Environ. **773**, 145030 (2021)

4. Han, Z.S., et al.: Observed sea breeze life cycle in and around NYC impacts on PBL and surface UHI and ozone patterns. Urban Clim. **42**, 101109 (2022)
5. Li, D., et al.: Correlation study of planetary-boundary-layer-height retrievals from CL51 and CHM15K ceilometers with application to PM2.5 dynamics in New York City. EPJ Web Conf. **237**, 03010 (2020)
6. Nehrir, A.R., et al.: Emerging technologies and synergies for airborne and space-based measurements of water vapor profiles. Surv. Geophys. **38**(6), 1445–1482 (2017)
7. Gronoff, G., et al.: A method for quantifying near range point source induced O3 titration events using co-located lidar and Pandora measurements. Atmos. Environ. **204**, 43–52 (2019)
8. Brotzge, J.A., et al.: A technical overview of the New York State Mesonet standard network. J. Atmos. Ocean. Techol. **37**(10), 1827–1845 (2020)
9. Tucker, S.C., et al.: Doppler lidar estimation of mixing height using turbulence, shear, and aerosol profiles. J. Atmos. Ocean. Technol. **26**, 673–688 (2009)

Chapter 65
Boundary Layer Dynamics, Aerosol Composition, and Air Quality in the Urban Background of Stuttgart in Winter

Hengheng Zhang, Wei Huang, Xiaoli Shen, Ramakrishna Ramisetty, Thomas Leisner, and Harald Saathoff

Abstract The spatial distribution and temporal variations of aerosols within the planetary boundary layer is of special interest for the city of Stuttgart, which is located in a basin. To characterize the evolution of boundary layer structure and its relation to surface-level aerosol concentrations, we collected comprehensive datasets from February 5 to March 5, 2018 in the urban background of downtown Stuttgart. The boundary layer height was determined from lidar and radiosonde measurements. Furthermore, aerosol particle number, size, chemical composition, and various trace gases were measured at 3.7 m above the ground level, by employing

H. Zhang (✉) · T. Leisner · H. Saathoff
Institute of Meteorology and Climate Research, Karlsruhe Institute of Technology, Eggenstein-Leopoldshafen, Germany
e-mail: hengheng.zhang@kit.edu

W. Huang
Institute of Meteorology and Climate Research, Karlsruhe Institute of Technology, Eggenstein-Leopoldshafen, Germany

Institute for Atmospheric and Earth System Research/Physics, Faculty of Science, University of Helsinki, Helsinki, Finland

X. Shen
Institute of Meteorology and Climate Research, Karlsruhe Institute of Technology, Eggenstein-Leopoldshafen, Germany

Department of Earth, Atmospheric, and Planetary Sciences, Purdue University, West Lafayette, IN, USA

R. Ramisetty
Institute of Meteorology and Climate Research, Karlsruhe Institute of Technology, Eggenstein-Leopoldshafen, Germany

TSI Instruments India Private Limited, Bangalore, India

© The Author(s), under exclusive license to Springer Nature Switzerland AG 2023

J. T. Sullivan et al. (eds.), *Proceedings of the 30th International Laser Radar Conference*, Springer Atmospheric Sciences,
https://doi.org/10.1007/978-3-031-37818-8_65

a mobile container equipped with various instruments including an aerosol mass spectrometer. The main novelty of our study is that our scanning lidar conducted zenith scanning measurements from 90° to 5°. These measurements allow us to investigate the evolution of details of the boundary layer structure and aerosol spatial distributions and furthermore to retrieve optical parameters of the aerosol near the ground level that can be compared with the *in situ* measurements. The boundary layer heights retrieved from lidar data show a good agreement with radiosonde data and ECMWF Reanalysis v5 (ERA5) data from different meteorological situations. As expected, the ground-level aerosol concentrations showed a negative correlation with boundary layer height. In addition, meteorological conditions like wind speed, temperature, solar radiation, and relative humidity affect not only the structure of the boundary layer but also the relationship between boundary layer heights and surface aerosol concentrations.

Keywords Boundary layer dynamics · Scanning aerosol lidar · Aerosol Composition

65.1 Introduction

Global and regional distributions of aerosol particles are of great concern to the public, partly because they are much more visible than gaseous pollution [1] and also because they have discernible adverse effects on human health [2]. The regional air quality is greatly affected by these distributions, which are related to the emissions of anthropogenic pollution, boundary layer structure, and the meteorological conditions. Many methods including remote sensing (e.g., lidar) and *in situ* aerosol characterization were used to investigate the boundary layer dynamics and its relationship with ground-level aerosols. The most obvious relationship is that the surface-level aerosol concentrations have a negative correlation with boundary layer heights [3]. Stuttgart is a big city and an important industrial center in southwest Germany with a population of more than 600,000 in a metropolitan area and 2.6 million inhabitants. It is situated in the steep valley of the Neckar river, in a "bowl" surrounded by a variety of hills, small mountains, and valleys. The complex topography can hinder the dispersion of air pollutants, and the location is characterized by low wind speeds and weak air circulation [4].

In this work, we collect a comprehensive datasets to study the structure of boundary layer and its relationship with aerosols at the ground level from February 5 to March 5, 2018 in the urban background of the downtown Stuttgart. One main object is to study the evolution of boundary layer especially during the night time and its relationship with aerosol concentrations at the ground level. Furthermore, this comprehensive dataset can help us validate different retrievals and quantify uncertainties of different methods. Our study therefore adds an important piece of information on air quality in Stuttgart by investigating the boundary layer dynamics, aerosol concentrations evolution, and optical proprieties of aerosols in this city.

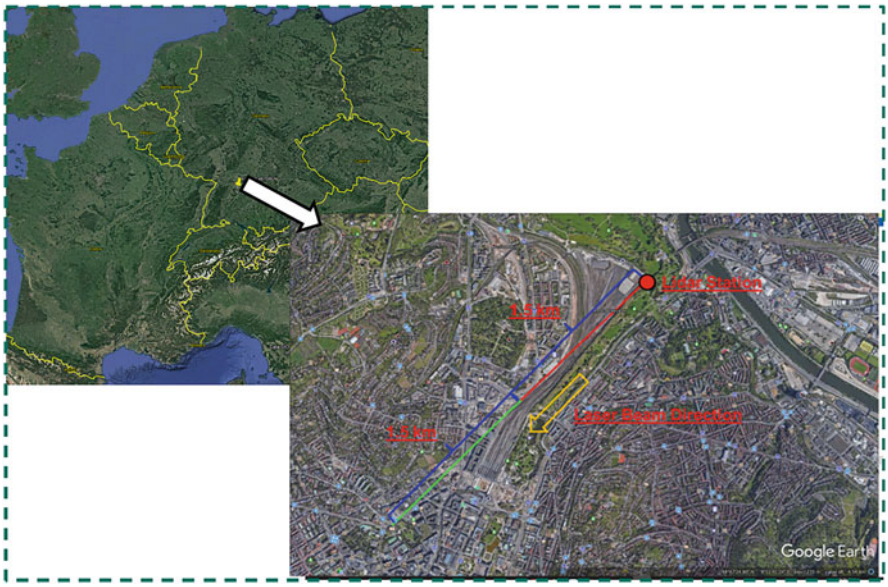


Fig. 65.1 The observation station and the laser beam direction of lidar during the field campaign in the city of Stuttgart

65.2 Method

The experiment was conducted from February 5 to March 5, 2018, in the urban background of the downtown Stuttgart. A measurement container was installed on a railway bridge in the Rosensteinpark (9.2024°E 48.7986°N, 247 m above the sea level), downtown of Stuttgart, as shown in Fig. 65.1. This container contained *in situ* instruments including High Resolution Time-of-Flight Aerosol Mass Spectrometer (HR-TOF-AMS), Aethalometer, Condensation Particle Counter (CPC), Optical Particle Counters (OPC), trace gas sensors and meteorological sensors, and a scanning lidar that was installed on the roof of the container. In addition, radiosondes were launched frequently by Deutscher Wetterdienst (DWD) that provided vertically resolved meteorological parameters.

65.3 Results and Discussion

Figure 65.2 shows the range corrected lidar signal (RCS) for the whole period as well as boundary layer heights retrieved from lidar during cloud-free period. Boundary layer derived from radiosonde and ERA5 are indicated as black star and gray dashed line, respectively. This figure shows that the retrieved boundary layer from lidar agrees well with those retrieved from radiosonde and ERA5. The

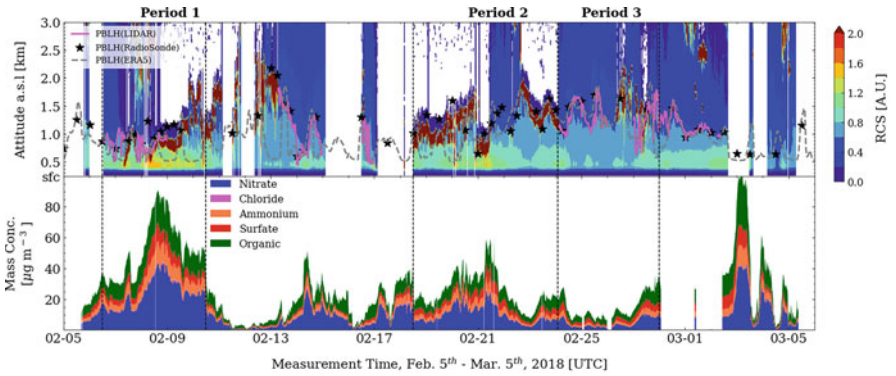


Fig. 65.2 Overview of range corrected lidar signal and boundary layer height derived from scanning aerosol lidar (pink line), Radiosonde (black start), and ERA5 dataset (gray dashed line) (upper panel) and the corresponding evolution of mass concentrations measured by HR-TOF-AMS (bottom panel)

evolution of aerosol composition measured by HR-TOF-AMS indicates dominant nitrate concentration during this time period (see Fig. 65.2). A detailed analysis of chemical composition in Stuttgart can be found in Huang et al. [5]. Three periods are selected according to aerosol mass concentrations and boundary layer heights measured in this experiments. Comparing to the other two periods (i.e., Periods 2 and 3), Period 1 has the highest aerosol concentrations and the lowest boundary layer heights, which reflected that the decreased boundary layer height will accumulate the aerosols while increased boundary layer height will dilute the aerosols at the ground level.

65.3.1 Ground-Level Aerosol Optical Properties Characterized by In Situ and Remote-Sensing Measurements

Quantitative analysis between *in situ* and lidar measurement can be studied by comparing extinction coefficients retrieved from lidar measurement and from Mie calculation based on size distribution measured by Fidas-OPC measurement. Figure 65.3 shows time series of extinction coefficients retrieved from aforementioned two methods. The extinction coefficients obtained from lidar were retrieved from slope retrieval method as well as Raman retrieval method, and these two methods show a good agreement with each other. Please note that the Raman channel of this lidar system only worked at night time. However, the extinction coefficient calculated from Mie is systematically lower than that from lidar measurement. The reason is that the aerosols had already lost the water before it was captured by Fidas-OPC. Hence, humidity correction is needed for Mie calculated extinction coefficient

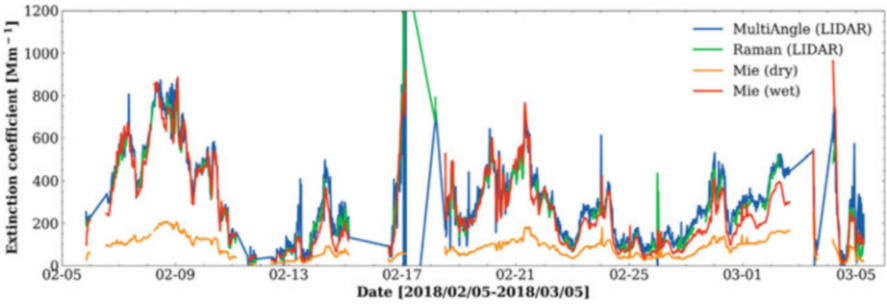


Fig. 65.3 Ground-level extinction coefficients retrieved from multi-angle retrieval method, Raman retrieval method, Mie calculation, and humidity-corrected Mie calculation from February 5 to March 5, 2018, in Stuttgart

so that it can be compared with that from lidar measurement. The correction is conducted based on Eq. 65.1 with κ_{sca} value being 1.0.

$$\frac{\sigma_w}{\sigma_d} = 1 + \kappa_{sca} \frac{RH}{100 - RH} \tag{65.1}$$

where σ_w and σ_d are wet and dry extinction coefficients, RH is relative humidity, and κ_{sca} is a parameter that fits this equation best. The humidity-corrected extinction is also shown in Fig. 65.3 and is well consistent with extinction coefficient from lidar measurement with the slope being 0.90 and Pearson correlation coefficient being 0.95. This good agreement among these methods reflects the high quality of the measurements as well as the retrieval algorithms.

65.3.2 Case Study on Evolution of Boundary Layer and Its Impact on Surface-Level Aerosol

In Fig. 65.2, the evolution of boundary layer and its impact on surface aerosol concentrations were illustrated for the whole period. In this section, we selected one case to investigate these processes in detail as shown in Fig. 65.4. Figure 65.4a shows the vertical extend backscatter coefficient, the evolution of boundary layer height (white line), and residue layer (white dashed line) as well as mixing layer height measured by radiosonde (yellow triangle). Time series of aerosol chemical composition measured by HR-TOF-AMS is shown in Fig. 65.4b, and black carbon concentration measured by AE51 is shown in Fig. 65.4c. Figure 65.4d shows time series of solar radiation measured by weather sensor. The vertical extend extinction coefficient in this figure reflects the evolution of vertical aerosol distribution for the ground level to 2 km, which indicated that most of aerosols stayed in boundary layer

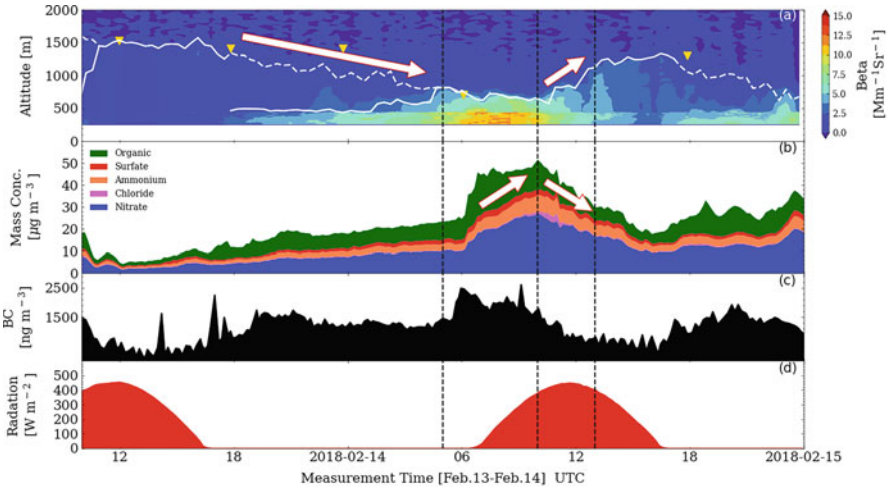


Fig. 65.4 Time series of backscatter coefficients from lidar measurements (contour plot), the boundary layer height retrieved lidar (black line), and DWD radiosonde (yellow triangle) (**a**), the aerosol mass concentrations measured by HR-TOF-AMS (**b**), black carbon concentration (**c**), and the global radiation measured by an meteorological sensor (WS700) (**d**) for case 1 from February 13 to February 14, 2018

and could not reach to free troposphere. We also found that the mixing layer heights measured by lidar and radiosondes show a good agreement for this case. This figure well illustrated a typical example of the evolution of boundary layer and its impact on surface aerosol concentrations.

65.4 Conclusions

The work presents our investigation on the structure of boundary layer and its relationship with the surface-level aerosols as well as physics properties of aerosols in the ground level by combining a scanning aerosol lidar, a mobile container, and radiosondes in the downtown of Stuttgart in the winter. The main advantage is that scanning lidar can get the boundary layer structure and vertical profiles of aerosols at low altitude (below 500 m). This altitude range is usually in the overlap region and cannot get validated measurement. This comprehensive dataset can help us better characterize the structure of boundary layer, chemical composition, concentration, and optical properties of the aerosols in detail in the downtown of Stuttgart.

Acknowledgments We acknowledge the support by the staff of the Institute of Meteorology and Climate Research and financial support by the project Modular Observation Solutions for Earth Systems (MOSES) of the Helmholtz Association (HGF).

References

1. Guo, J.P., Zhang, X.Y., Che, H.Z., Gong, S.L., An, X., Cao, C.X., Guang, J., Zhang, H., Wang, Y.Q., Zhang, X.C., Xue, M., Li, X.W.: Correlation between PM concentrations and aerosol optical depth in eastern China. Atmos. Environ. **43**(37), 5876–5886 (2009). https://doi.org/10.1016/j.atmosenv.2009.08.026, https://www.sciencedirect.com/science/article/pii/S1352231009007493
2. Li, J., Li, C., Zhao, C., Su, T.: Changes in surface aerosol extinction trends over China during 1980–2013 inferred from quality-controlled visibility data. Geophys. Res. Lett. **43**(16), 8713–8719 (2016). https://doi.org/10.1002/2016GL070201
3. Li, Z., Guo, J., Ding, A., Liao, H., Liu, J., Sun, Y., Wang, T., Xue, H., Zhang, H., Zhu, B.: Aerosol and boundary-layer interactions and impact on air quality. Natl. Sci. Rev. **4**(6), 810–833 (2017). https://doi.org/10.1093/nsr/nwx117, https://doi.org/10.1093/nsr/nwx117
4. Schwartz, J., Spix, C., Wichmann, H., Malin, E.: Air pollution and acute respiratory illness in five German communities. Environ. Res. **56**(1), 1–14 (1991). https://doi.org/10.1016/S0013-9351(05)80104-5, https://www.sciencedirect.com/science/article/pii/S0013935105801045
5. Huang, W., Saathoff, H., Shen, X., Ramisetty, R., Leisner, T., Mohr, C.: Seasonal characteristics of organic aerosol chemical composition and volatility in Stuttgart, Germany. Atmos. Chem. Phys. **19**(18), 11687–11700 (2019). https://doi.org/10.5194/acp-19-11687-2019, https://acp.copernicus.org/articles/19/11687/2019/

Part V
Greenhouse Gases, Tracers, and Transport in the Free Troposphere and Above

Chapter 66
DIAL Ozone Measurement Capability Added to NASA's HSRL-2 Instrument Demonstrates Tropospheric Ozone Variability Over Houston Area

Marta Fenn, Johnathan Hair, Taylor Shingler, and Richard Ferrare

Abstract NASA Langley Research Center (LaRC) fielded its second-generation multiwavelength high spectral resolution lidar (HSRL-2), which also includes wavelengths to enable ozone differential absorption lidar (DIAL) measurements, aboard the NASA Gulfstream-V (G-V) aircraft during September 2021. Flying at 9 km, the lidar provided nadir profiles of ozone and aerosol backscatter, extinction, and depolarization over the Houston metropolitan region, including Galveston Bay and the Houston Ship Channel. These observations were part of a larger air quality assessment of the region, TRACER-AQ (Tracking Aerosol Convection ExpeRiment – Air Quality), which is NASA mission conducted in collaboration with an effort led by the DOE (Department of Energy) and TRACER (Tracking Aerosol Convection Interactions ExpeRiment). Additional participants including from academia and TCEQ (Texas Commission on Environmental Quality) provided meteorological and atmospheric constituent measurements from ground sites, mobile laboratories, and from boats. Here we present a description of HSRL-2 measurement capabilities and examples of tropospheric ozone and aerosol measurements collected during TRACER-AQ. The flight tracks were overlapping raster patterns repeated three times throughout the day to measure the temporal and spatial variability in ozone and aerosols over the region. These measurements will help understand and evaluate space-based air quality observations from future satellite passive UV-VIS sensors such as the NASA TEMPO satellite.

Keywords Aerosols · Ozone

M. Fenn (✉)
SSAI, Hampton, VA, USA
e-mail: Marta.A.Fenn@nasa.gov

J. Hair · T. Shingler · R. Ferrare
NASA Langley Research Center, Hampton, VA, USA
e-mail: Johnathan.W.Hair@nasa.gov; Taylor.J.Shingler@nasa.gov; Richard.a.ferrare@nasa.gov

© The Author(s), under exclusive license to Springer Nature Switzerland AG 2023

J. T. Sullivan et al. (eds.), *Proceedings of the 30th International Laser Radar Conference*, Springer Atmospheric Sciences,
https://doi.org/10.1007/978-3-031-37818-8_66

66.1 Introduction

66.1.1 Rationale

Air quality experts now have a bird's eye view of the complex atmospheric composition of the Houston metropolitan region during late summer conditions, when the surface ozone concentration most frequently exceeds regulatory limits. TRACER-AQ [1] was the most recent of a series of air quality studies conducted by NASA and TCEQ to inform changes in regulations as well as assess their results along with changes in industry and meteorology. Anticipating data products from the TEMPO satellite, these observations can help develop strategies to use space-based observations.

66.1.2 Instrument Information

NASA Langley Research Center's HSRL-2 instrument can be configured to measure ozone profiles via the DIAL technique, in addition to the existing ability to measure profiles of aerosol backscatter and depolarization at three wavelengths (355, 532, and 1064 nm) and aerosol extinction via the HSRL technique at two wavelengths (355 and 532 nm). This ozone measurement capability was first demonstrated in flights aboard NASA's ER2 and UC-12 aircraft during 2015 and 2016 [2]. Figure 66.1 shows HSRL-2 deployed on the NASA G-V aircraft for TRACER-AQ.

66.1.3 Sampling Strategy

The HSRL-2 instrument provided a three-dimensional picture of the aerosol and ozone distributions from the surface up to about 8 km above the Houston metropolitan region (the source of urban emissions), as well as Galveston Bay and the Houston Ship Channel (the source of petrochemical industry emissions), while the G-V flew a raster pattern over the entire region (Fig. 66.2a). A fourth dimension, time, was addressed by repeating the entire 3-h raster three times during each flight (morning (beginning around 8:30 LT (local time)), midday (beginning around 11:30 LT), and afternoon (beginning around 14:30 LT)) to observe the changes in the ozone and aerosol distributions caused by boundary layer dynamics, the interaction of sea/bay breezes in this coastal environment, as well as synoptic weather events. The NASA G-V platform flew over 90 h during 11 flights from September 1 through September 27, 2021.

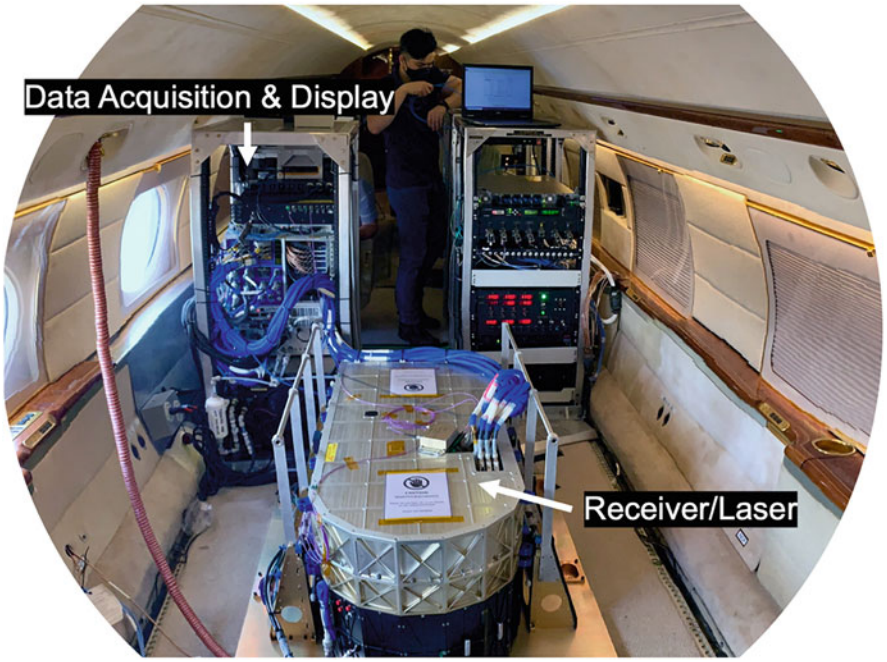


Fig. 66.1 HSRL-2 on board the NASA G-V during TRACER-AQ

66.2 Data Products

66.2.1 Ozone

Ozone mixing ratio profiles were measured using the HSRL-2 differential absorption lidar (DIAL) wavelengths of 290 nm (online) and 300 nm (offline) at 13 km horizontal and 300 m vertical resolution from 350 m to 5750 m above ground level (Fig. 66.2b). These curtains of ozone inform transport contributions to ground level ozone. Additional ozone products include average ozone mixing ratios in near-surface layers (0.35–0.5 km, 0.35–1 km, and 0.35–2 km) useful for comparison with ground-based monitoring stations (Fig. 66.3).

66.2.2 Aerosol Products

A suite of aerosol products retrieved at three wavelengths, 1064 nm, 532 nm, and 355 nm, were calculated beneath the aircraft along the flight track. These include particulate backscatter profiles and depolarization profiles at all three wavelengths at a horizontal resolution of about 2 km and a vertical resolution of 15 m, reported

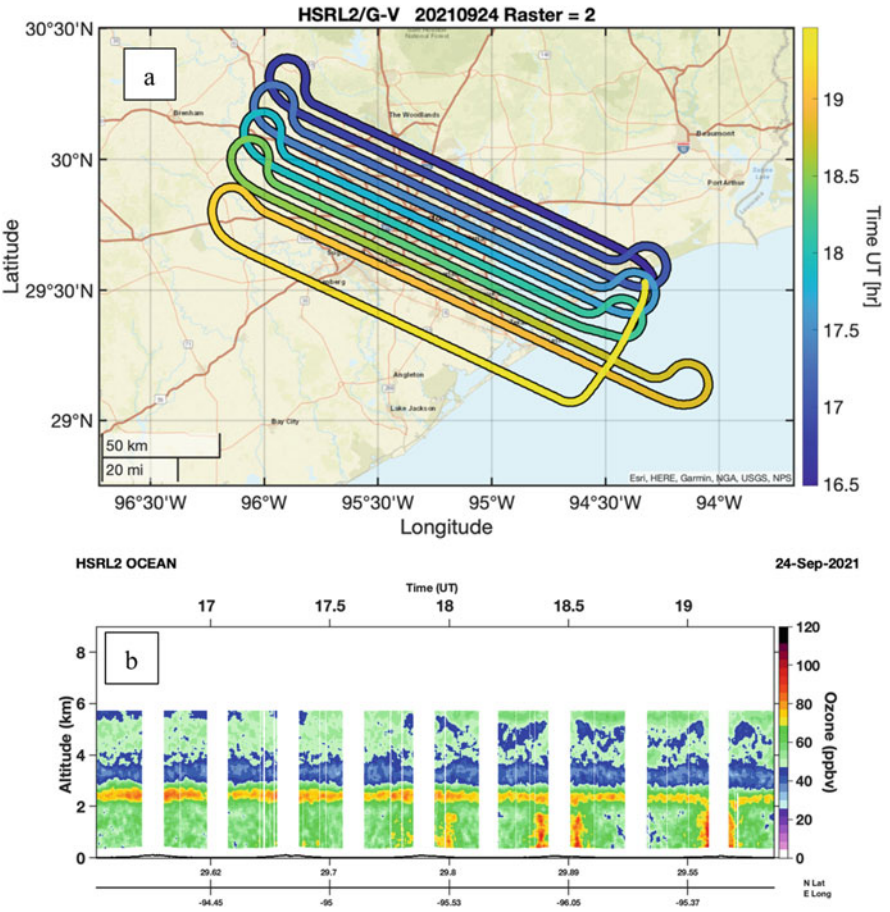


Fig. 66.2 (**a**) Typical flight track of the G-V aircraft with nadir viewing HSRL-2 on board. This pattern was flown up to three times per day at an altitude of 9 km. The color scale indicates that each pattern took approximately 3 h. (**b**) Ozone curtain collected from the mid-day raster (raster #2) on September 24, 2021

between 60 m above ground level to 8500 m, and aerosol extinction and aerosol extinction/backscatter ratio ("lidar ratio") profiles at 355 nm and 532 nm calculated at about 13 km horizontal and 300 m vertical resolution from 350 to 7300 m above ground level. Also provided are aerosol optical thickness profiles, aerosol backscatter Angström exponents (355–532 nm, 532–1064 nm), and an aerosol extinction Angström exponent (355–532 nm). A sample of selected data products is provided in Fig. 66.4, and instrument details are provided in [3, 4].

Additional aerosol products include average aerosol extinction within near-surface layers (0.3–0.5 km, 0.3–1 km, and 0.3–2 km) useful for comparison with ground-based monitoring stations (Fig. 66.5).

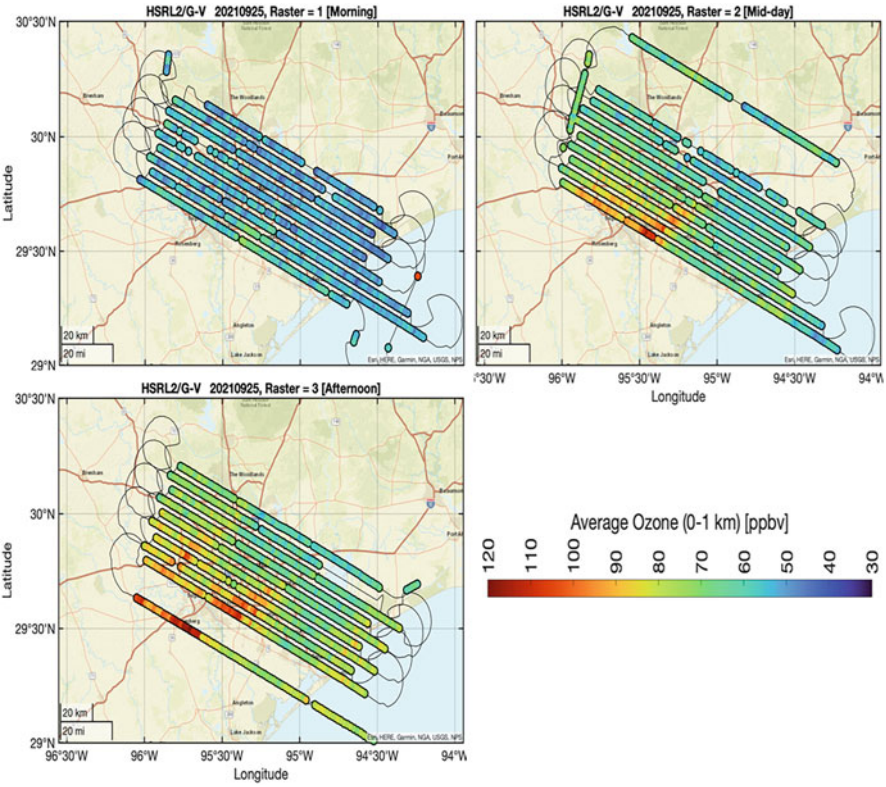


Fig. 66.3 Average ozone mixing ratios in the layer between 0.35 and 1 km measured during the (top left) morning, (top right) midday, and (bottom) afternoon at a higher horizontal resolution (2 km) on September 24, 2021

66.3 Aerosol Corrections for DIAL Ozone Measurements

The HSRL-2 wavelengths used for DIAL ozone retrievals (290 and 300 nm) are close enough together to reduce anomalous effects caused by differences in the scattering and extinction behavior of aerosols. However, sharp aerosol gradients benefit from additional correction. NASA's Airborne UV_DIAL system utilized a Bernoulli correction scheme that assumed constant aerosol backscatter and extinction Angström coefficients for the entire flight [5]. Since HSRL-2 measures aerosol backscatter and extinction profiles at 355 nm and 532 nm, the ozone retrieval uses these measurements to derive the aerosol Angström coefficients needed for such correction on a profile-by-profile basis, leading to improved accuracy in the derived ozone profiles. TRACER-AQ provided the opportunity for comparing HSRL-2 retrievals of ozone profiles with those from other instruments, such as ground-based

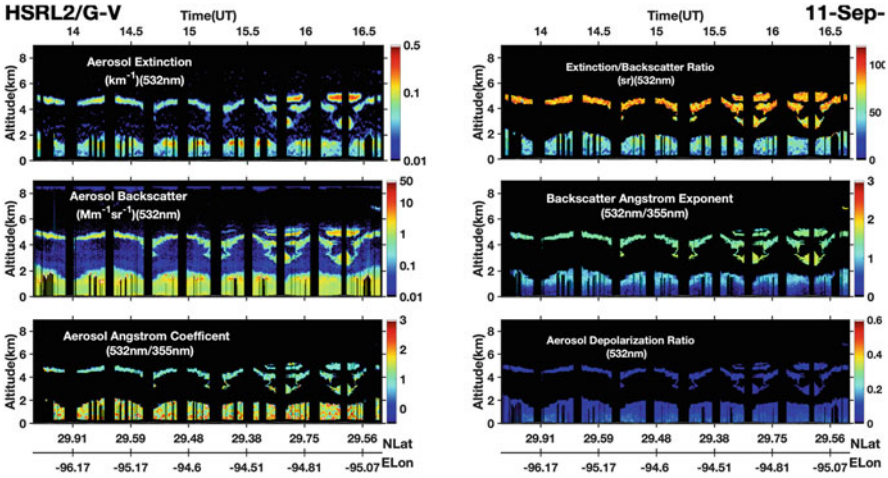


Fig. 66.4 Selected HSRL-2 aerosol products from September 11, 2021

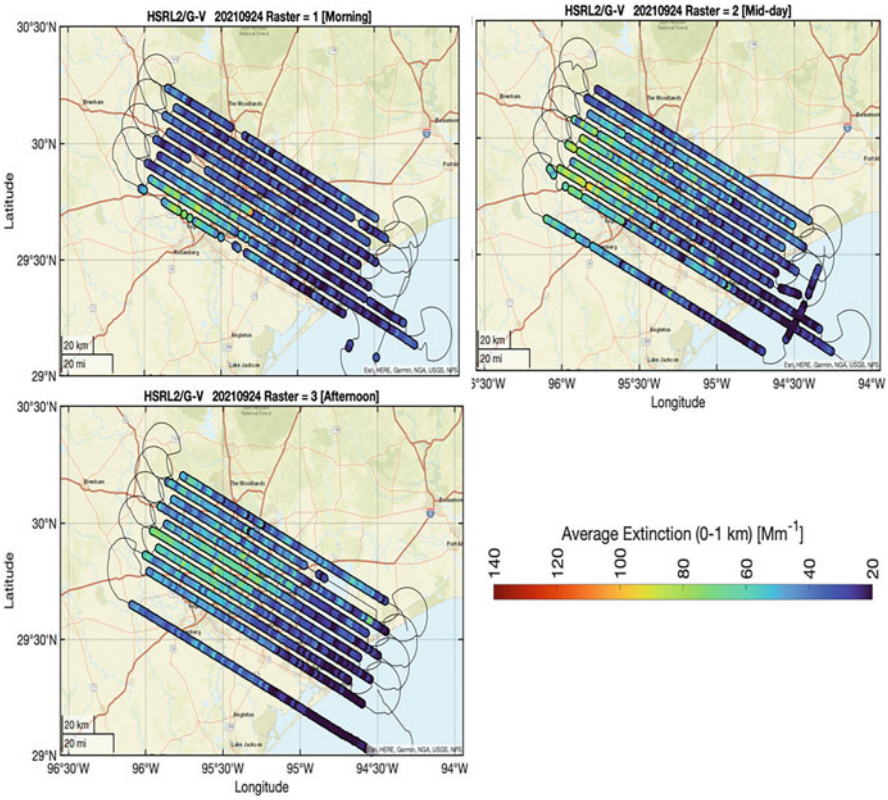


Fig. 66.5 Same as Fig. 66.3, except for average aerosol extinction

lidars and ozone sondes. Comparisons of the resulting aerosol-corrected ozone profiles with ozone measurements from these will be shown in the poster.

References

1. TRACER-AQ archive site https://www-air.larc.nasa.gov/cgi-bin/ArcView/traceraq.2021
2. Hair, J.W.: International Laser Radar Conference 28, Proceedings (2018)
3. Hair, J.W., Hostetler, C.A., Cook, A.L., Harper, D.B., Ferrare, R.A., Mack, T.L., Welch, W., Izquierdo, L.R., Hovis, F.E.: Airborne high spectral resolution lidar for profiling aerosol optical properties. Appl. Opt. **47**, 6734–6752 (2008)
4. Burton, S.P., Hostetler, C.A., Cook, A.L., Hair, J.W., Seaman, S.T., Scola, S., Harper, D.B., Smith, J.A., Fenn, M.A., Ferrare, R.A., Saide, P.E.: Calibration of a high spectral resolution lidar using a Michelson interferometer, with data examples from ORACLES. Appl. Opt. **57**(21), 6061–6075 (2018)
5. Browell, E.V., Ismail, S., Shipley, S.T.: Ultraviolet DIAL measurements of O_3 profiles in regions of spatially inhomogeneous aerosols. Appl. Opt. **24**(17), 2827–2836 (1985)

Chapter 67
Trajectory Analysis of CO_2 Concentration Increase Events in the Nocturnal Atmospheric Boundary Layer Observed by the Differential Absorption Lidar

Makoto Abo, Chikao Nagasawa, and Yasukuni Shibata

Abstract CO_2 is the primary greenhouse gas emitted through human activities. For the detailed analysis of forest carbon dynamics and CO_2 fluxes in urban areas, vertical CO_2 concentration profiles with high spatial and temporal resolution in the lower atmosphere have been conducted by a differential absorption lidar (DIAL). We have developed the range-resolved DIAL with the 1.6 μm wavelength for measurements of the vertical CO_2 concentration profiles. Several vertical profiles of CO_2 concentrations for nighttime and daytime from 0.45 to 2.5 km altitude with range resolution of 300 m and an integration time of 1 h have been measured. In order to estimate the extraction of information on the origin of the CO_2 masses, one-day back trajectories were calculated by using a three-dimensional (3D) atmospheric transport model.

Keywords DIAL · Boundary layer · CO_2

67.1 Introduction

Atmospheric gases, including carbon dioxide (CO_2), methane, ozone, chlorofluorocarbons, and water vapor, absorb some of the energy radiated by the Earth's surface and thereby retain and warm our planet. To predict the impact of global warming and develop appropriate policy responses, it is necessary to clarify the current status of these "greenhouse" gases. CO_2 measurements for vertical profiles in the troposphere have been limited due to limited observations by using campaign-style aircraft and the commercial airlines with limited spatial and temporal coverage.

M. Abo (✉) · C. Nagasawa · Y. Shibata
Tokyo Metropolitan University, Hino, Tokyo, Japan
e-mail: abo@tmu.ac.jp

© The Author(s), under exclusive license to Springer Nature Switzerland AG 2023

J. T. Sullivan et al. (eds.), *Proceedings of the 30th International Laser Radar Conference*, Springer Atmospheric Sciences,
https://doi.org/10.1007/978-3-031-37818-8_67

In addition to the ground-level CO_2 measurement network, vertical CO_2 profiles are also important parameters for the estimation of carbon budget and future global distribution. Inverse techniques using atmospheric transport models were developed to estimate CO_2 sources and sinks based on the observed data. The accurate vertical CO_2 profiles in the troposphere are highly desirable in the inverse techniques to improve quantification. Lidar instruments are thought to be one of the best methods for observing the vertical distribution of greenhouse gases.

We have developed the 1.6 μm range-resolved DIAL for measurements of the vertical CO_2 concentration profiles [1, 2]. Several vertical profiles of CO_2 concentrations for nighttime and daytime from 0.45 to 2.5 km altitude with a range resolution of 300 m and an integration time of 1 h have been measured. In order to extract information on the origin of the CO_2 masses, one-day back trajectories were calculated by using a three-dimensional (3D) atmospheric transport model.

67.2 CO_2-DIAL System

We have developed a ground-based direct detection 1.6 μm differential absorption lidar (DIAL) for measurements of vertical CO_2 profiles in the atmosphere. In the DIAL technique, laser pulses are transmitted at three wavelengths that the first wavelength λ_{on} is located on the peak of a CO_2 absorption spectrum, the second λ_{off} is located on the weak absorption, and the third λ_T is located between these two wavelengths. The difference in the returns between the λ_{on} and λ_{off} is used to calculate the CO_2 density profiles. In addition, to improve the accuracy of the CO_2 absorption coefficient, the vertical distribution of the temperature is measured at the same time using λ_{on} and λ_T. The measured air temperature profiles are used to improve the accuracy of the CO_2 mixing ratio. Figure 67.1 shows schematic diagram of the 3-wavelength 1.6 μm DIAL for measurements of CO_2 concentration and atmospheric temperature profiles, and Table 67.1 shows the DIAL specifications.

67.3 CO_2 Measurement and Trajectory Analysis

We have continuously observed the vertical distribution of CO_2 mixing ratio from the ground to an altitude of 5 km at Tokyo Metropolitan University (TMU) in the suburbs of Tokyo. From the observation results, it is observed that the CO_2 mixing ratio in the boundary layer during the daytime in fine weather regularly decreases due to photosynthesis but often increases at nighttime. The source of such an increase in CO_2 mixing ratios within the atmospheric boundary was unknown at nighttime (Fig. 67.2).

A simple trajectory simulation by the particle tracking method was performed using wind data from numerical weather prediction Meso-Scale Model interpolated to a spatial resolution of 1 km × 1 km, an altitude resolution of 105 m, and a time

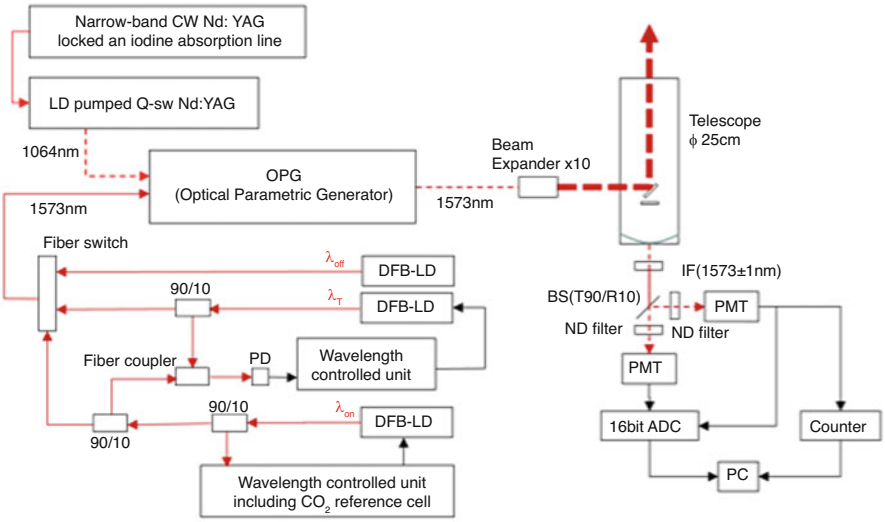


Fig. 67.1 Schematic diagram of the 3-wavelength 1.6 μm DIAL for measurements of CO_2 concentration and atmospheric temperature profiles

Table 67.1 Specifications of the 3-wavelength 1.6 μm DIAL

Wavelengths	1572.992 nm (λ_{on})1573.137 nm (λ_{off})1573.040 nm (λ_T)
Pulse energy	6 mJ
Repetition rates	400 Hz (Total)200 Hz (λ_{on}) and 100 Hz (λ_{off} and λ_T)
Vertical resolution	300 m
Time resolution	30 min
Telescope diameter	250 mm
Quantum efficiency	8%
Interference filter	1.0 nm (FWHM)

interval of 20 min. Figure 67.3 shows backward trajectory analysis at 10 altitudes, start of run at 3:00, December 8, 2020. Map area is 78km × 78km, × mark is the location of factory, and + mark is the lidar site. At an altitude of 500 or less, it can be seen that the air mass is coming from the north of the lidar site.

CO_2 emissions from factories around the observation point were estimated from public data, dispersed vertically and horizontally using the Gaussian plume model, and the increase in CO_2 concentration was calculated as a three-dimensional time series:

$$C(x, y, z) = \frac{Q}{2\pi U \sigma_y \sigma_z} e^{\left(-\frac{y^2}{2\sigma_y^2}\right)} e^{\left(-\frac{z^2}{2\sigma_z^2}\right)} \tag{67.1}$$

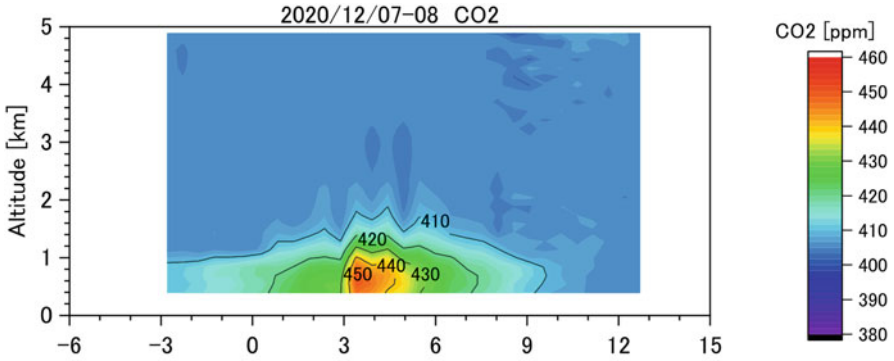


Fig. 67.2 Time-height cross section of CO_2 mixing ratio at the TMU lidar site (21:00, December 7; 13:00, December 8, 2020)

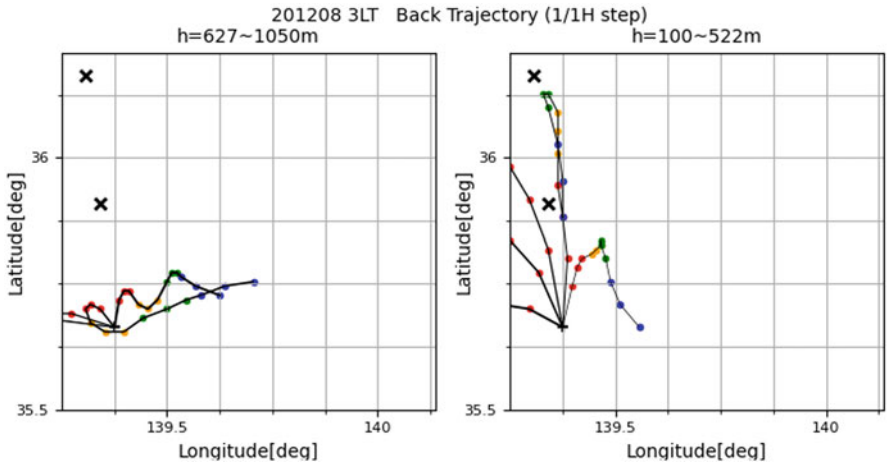


Fig. 67.3 Backward trajectory analysis at 10 altitudes, start of run at 3:00, December 8, 2020

where $C(x,y,z)$ is the mean concentration of diffusing substance at a point (x,y,z) [ppm/m^3]; x is downwind distance [m]; y is crosswind distance [m]; z is vertical distance above ground [m]; Q is mean concentration of diffusing substance at a point (x,y,z) [ppm/s]; σ_y and σ_z are lateral and vertical dispersion coefficient function, respectively, [m]; and u is mean wind velocity in downwind direction [m/s].

Figure 67.4 shows a result of local three-dimensional dispersion trajectory analysis at 10 altitudes, start of run at 3:00, December 8, 2020. Map area is 34 km × 78 km and • mark is lidar site. Two factories were set up as sources. CO_2 emissions estimated from public data of each factory are 4×10^7 [ppm/s]. At an altitude of 700 or less, it can be seen that the dispersed CO_2 had reached above the lidar site.

Figure 67.5 shows a time-height cross section of the increase in the CO_2 mixing ratio at the TMU lidar site calculated by three-dimensional dispersion trajectory analysis at 12 altitudes (21:00, December 7; 13:00, December 8, 2020). Compared

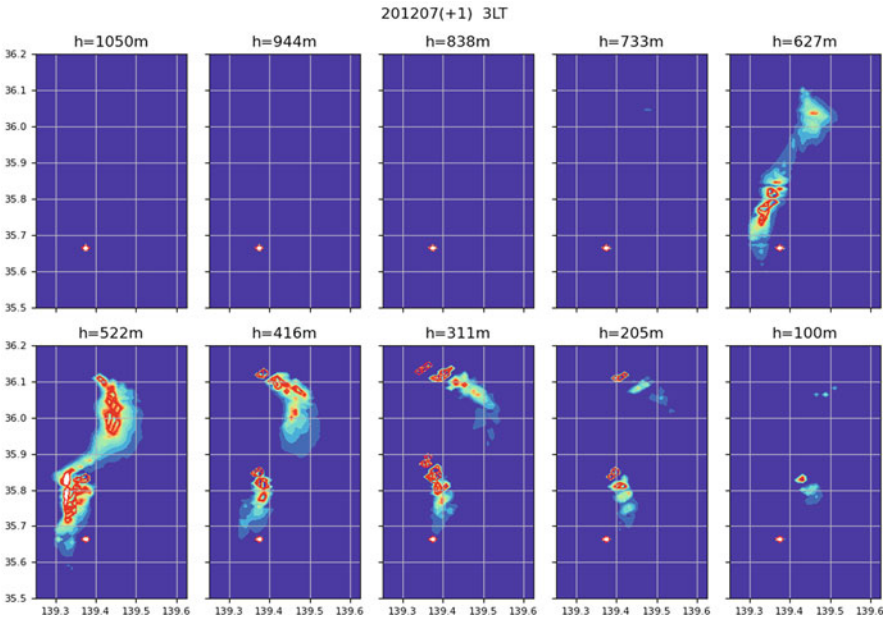


Fig. 67.4 Three-dimensional dispersion trajectory analysis at 10 altitudes, start of run at 3:00, December 8, 2020. Map area is 34 km × 78 km and • mark is lidar site. Two factories were set up as sources. It can be seen that the dispersed CO_2 had reached above the lidar site

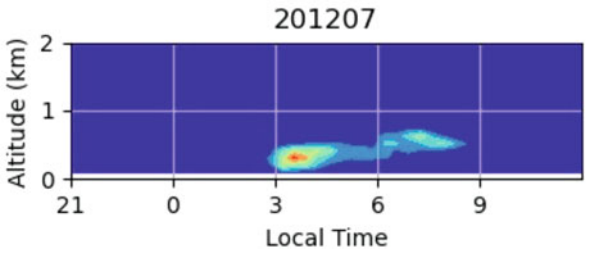


Fig. 67.5 Time-height cross section of the increase in the CO_2 mixing ratio at the TMU lidar site calculated by local three-dimensional dispersion trajectory analysis at 12 altitudes (21:00, December 7; 13:00, December 8, 2020)

with the observation results in Fig. 67.2, the increase in the CO_2 mixing ratio is in good agreement in both time and altitude.

67.4 Conclusion

Local three-dimensional dispersion analysis was used to reproduce the rapid increase in CO_2 mixing ratio in the lower layer at night. It is presumed that the source of this CO_2 is estimated to be a factory to the north of the observation site, and it is thought that high concentrations of CO_2 were transported to the lidar

site due to local wind convergence during the night. It has been shown that CO_2-DIAL is useful for identifying the source of CO_2 and monitoring the amount of CO_2 emissions.

References

1. Shibata, Y., Nagasawa, C., Abo, M.: Development of 1.6 μm DIAL using an OPG/OPA transmitter for measuring atmospheric CO_2 concentration profiles. Appl. Opt. **56**, 1194–1201 (2017)
2. Shibata, Y., Nagasawa, C., Abo, M., Inoue, M., Morino, I., Uchino, O.: Comparison of CO_2 vertical profiles in the lower troposphere between 1.6 μm differential absorption lidar and aircraft measurements over Tsukuba. Sensors. **18**, 4064 (2018)

Chapter 68
Efficiency Assessment of Single-Cell Raman Gas Mixture for DIAL Ozone Lidar

M. Roja Raman and Wei-Nai Chen

Abstract The conversion efficiency and flexibility of using single Raman cell with a mixture of high-pressure Raman active gases H_2 and CH_4 have been tested and reported in this chapter. Though the higher conversion efficiency could be achieved with independent gases, the pre-mixed gas combination could emit a coaxial beam of two wavelengths 288.4 nm and 299.1 nm with a total conversion efficiency of about 45% along with the residual 266 nm coaxial beam. However, a suitable gas mixing ratio needs to be selected to avoid carbon particle formation inside the cell which attenuates the laser energy. In the present case, a volume mixing ratio of 2:1 (H_2+CH_4) at a total cell pressure of 18 bar is found optimum for the generation of required wavelengths with almost equal energies. This configuration of generating coaxial beam of multiple SRSs with a single Raman cell greatly reduces the optical configuration and makes the DIAL system compact for mobile operations for ozone profiling.

Keywords Stimulated Raman Scattering · Raman cell · Mixture gases · Ozone

68.1 Introduction

Differential Absorption Lidar (DIAL) technique has been extensively used by various authors for the determination of the vertical profiles of atmospheric gases. Out of various gaseous species, ozone in the lower and upper atmosphere has been one of the major greenhouse gases being observed owing to its great influence on

M. R. Raman
Research Center for Environmental Changes, Academia Sinica, Taipei, Taiwan

Center for Remote sensing and Geoinformatics, Sathyabama Institute of Science and Technology, Chennai, India

W.-N. Chen (✉)
Research Center for Environmental Changes, Academia Sinica, Taipei, Taiwan
e-mail: wnchen@rcec.sinica.edu.tw

© The Author(s), under exclusive license to Springer Nature Switzerland AG 2023

J. T. Sullivan et al. (eds.), *Proceedings of the 30th International Laser Radar Conference*, Springer Atmospheric Sciences,
https://doi.org/10.1007/978-3-031-37818-8_68

the Earth's radiation budget as well as environmental impacts. Though several gas constituents are present in the real atmosphere, most of the gaseous species does not require vertical profiling due to their well-mixed chemical activity in the surface layers [1].

High-resolution profiling of ozone concentrations in the free troposphere requires suitable wavelengths in the ozone absorption UV band to be transmitted into the atmosphere. However, the selection of optimum wavelengths depends on various factors like the availability of the laser source emitting required wavelengths, maximum altitude of interest, laser attenuation in the day light when transmitted, and also the temperature conditions. Moreover, the aerosol back scattering and extinction coefficients in the second and third terms in the DIAL equation are highly dependent on the pair of wavelengths transmitted to the atmosphere. Thus, the most convenient spectral region for monitoring ozone in the troposphere with the differential absorption technique was found to be between 250 and 300 nm. Within this band, the optimal ozone measurement can be achieved when $\frac{\Delta\sigma_{O_3}}{\Delta\lambda}$ is maximized.

Stimulated Raman Scattering (SRS) in the Raman cell filled with high-pressure Raman active gases like Hydrogen (H_2), Deuterium (D_2), Methane (CH_4), Nitrogen (N_2), and Carbon Dioxide (CO_2) excited with intense UV laser has been widely used to generate the λ_{ON} and λ_{OFF} to estimate the profiles of Ozone concentrations in DIAL technique. Among these, the combination of CH_4 and H_2 is found best suitable to generate two spatially separated wave lengths of 288.4 nm and 299.1 nm, respectively. Several researchers used these two wavelengths to measure Ozone, as the former (strong O_3 absorption) has an absorption cross section nearly 3 times as large as the later (weak O_3 absorption), and both wavelengths can be generated reliably (and much more cost-effectively than dye or tunable cavity lasers) using SRS in high-pressure Raman cells [2]. This report explains the performance characteristics of the single Raman cell to produce the optimum energy conversion efficiency of 288.4 nm (CH_4) and 299.1 nm (H_2) with different mixing ratios under different total cell pressure and laser excitation energy.

68.2 SRS Technique

SRS is a coherent nonlinear optical mixing process that is mainly dependent on the laser spectral linewidth, the input laser intensity, and the interaction length of the Raman active medium [3]. SRS technique is used to generate the required frequency (wavelength) range above and below the range of laser pump frequency by passing through some nonlinear medium like H_2 or CH_4.

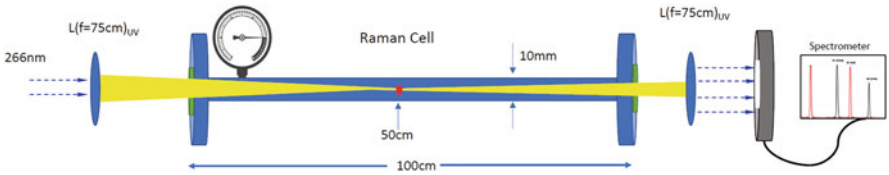


Fig. 68.1 Block diagram of the Raman cell setup used in this work

68.3 Experimental Setup

The block diagram of the Raman cell setup is shown in Fig. 68.1. This system utilizes a stable Nd:YAG laser (LOTIS TII LS-2138N) to generate the fourth harmonic laser beam of 266 nm at 100 Hz that is steered through the Raman cell filled with high-pressure Raman active gases to generate required ON and OFF wavelengths of laser output. This fourth harmonic of 266 nm laser beam diameter of ~5 mm with a beam divergence of <1.5 mrad and pulse duration of 10 ns is then steered to the Raman cell using two high reflectance UV grade 266 nm mirrors. Note that the optical path loss after reflection from two reflecting mirrors is about 10% of the input laser energy. Furthermore, a double convex lens of 75 cm focal length is placed in front of the cell to focus the laser beam at about 50 cm which is almost center of the length of Raman cell. This is done to achieve the maximum energy density required for SRS to happen with high-pressure gaseous mixture present in the cell and produce maximum conversion efficiency of required wavelengths. The addition of lens induced another 10% loss of laser energy resulting in a total loss of 20% of laser energy from the source to the entrance of the cell.

The Raman cell is a stainless steel hollow tube of about 100 cm length and an outer diameter of about 12 mm and inner diameter of 10 mm to facilitate the 5-mm diameter laser beam pass through the cell without hitting the inner walls. The outer edges of the cell are made such that high transmission UV grade optical windows can be fixed to seal the cell leak proof for high-pressure gas filling. A high-pressure gas valve is fixed at the cell inlet and end of the cell to control the gas inflow and outflow. A pressure gauge of 0–70 bar is fixed at the inlet position of the cell to monitor the total cell pressure. The SRS output from the cell is further collimated using another 75-cm focal length Plano convex lens and focused on to the spectrometer detector for further visualization and recording. The total setup is fixed on the optical bench for safety and stability.

68.4 Results and Discussion

In general, the SRS of Raman active medium excited with high energy laser generates higher order stokes lines in addition to the required wavelengths. Depending

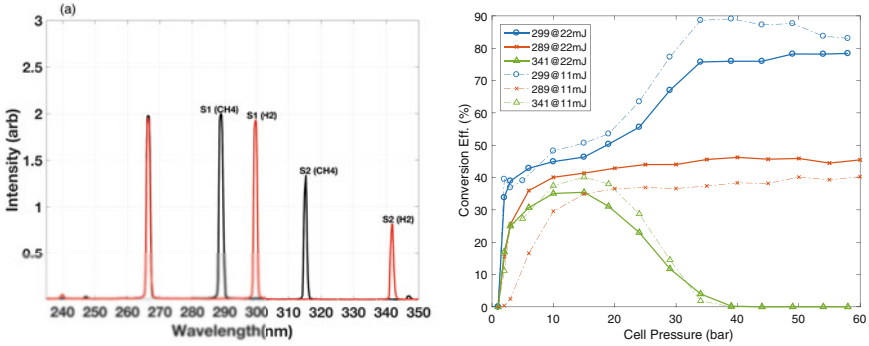


Fig. 68.2 (**a**) SRS spectrum of pure CH_4 and H_2 at 20 bar excited with 25-mJ quadrupled 266-nm laser. (**b**) Conversion efficiency of pure H_2 and CH_4 (lower CE of 299.1 nm in at low pressure is owing to high S2). Intensities of 314 nm are low, hence not shown

on our required wavelengths, other orders need to be suppressed to maximize the conversion efficiency of required wavelengths. The SRS spectrum of H_2 and CH_4 at 20 bar excited with 25 mJ laser beam is shown in Fig. 68.2a. Here, the second-order stokes of 314 nm (CH_4) and 342 nm (H_2) can be noticed along with the required first-order stokes 288.4 nm (CH_4) and 299.1 nm (H_2).

The conversion efficiency (η) of the Raman-shifted line is measured as the ratio of the intensity of the particular Raman-shifted line ($I_{\lambda S}$) to the sum of intensities of all lines in the output spectrum measured at the exit of the Raman cell.

$$\eta = \frac{I_{\lambda S}}{I_{266} + \sum_{S=1}^{n} I_{Sn}} \times 100\% \tag{68.1}$$

where I_{266} is the intensity of residual 266 nm line in the output spectrum, $S = 1, 2, 3 \ldots n$ is the order of stokes line, and I_{Sn} is the intensity of n-stoke line.

The conversion efficiency of independent gases H_2(299.1 nm) and CH_4 (288.4 nm) is estimated initially with variable pressure and laser energy and shown in Fig. 68.2b. It can be noticed that H_2 could exhibit SRS at a relatively low pressure of 3 bar compared to CH_4 which starts SRS at 9 bar. Furthermore, the maximum conversion efficiency of both gases is found lower at lower laser energy (11 mJ) compared to higher laser energy (22 mJ). Moreover, at lower energy (11 mJ), the intensity of second stokes remained unchanged with increasing pressure. With laser energy of 22 mJ, the efficiency of first stokes of H_2 becomes higher (40%) than second stokes at 20 bar, and however the total cell pressure of 45 bar is required to achieve maximum efficiency of first stokes (70%), while the second stokes is completely suppressed. Similarly, the maximum conversion efficiency (42%) of CH_4 first stokes is achieved at about 25 bar with nearly constant efficiency at higher pressures. It is interesting to see that the second stokes for CH_4 is not visible with higher (22 mJ) laser input. Though, higher conversion efficiency of independent H_2

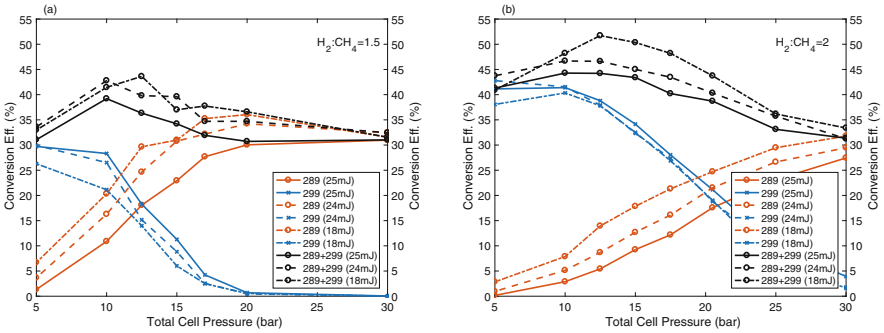


Fig. 68.3 The conversion efficiency of 299.1 nm (H_2) and 288.4 nm (CH_4) with mixing ratios of (**a**) R=1.5 and (**b**) R=2 under varying pressure and laser energy

and CH_4 gases can be achieved, but it is necessary to use two independent Raman cells to generate these two wave lengths that make the optical configuration of DIAL system complex.

Furthermore, the single-cell configuration is used to estimate the conversion efficiency of mixed gas H_2+CH_4 filled with varying pressure and laser energy. The conversion efficiency of 299.1 nm (H_2) and 288.4 nm (CH_4) with mixing ratio of 2 under varying pressure and energy is shown in Fig. 68.3b. It is to be noted here that, with all input laser energies (18 mJ, 24 mJ, and 25 mJ), the efficiency of 299.1 nm gradually decreases with increasing pressure while 288.4 nm gradually increases with pressure. At a certain pressure, the intensity(efficiency) of both wavelengths becomes nearly equal. It can be noted here that the pressure of nearly equal intensity (efficiency) decreases with decreasing laser energy, whereas the total conversion efficiency increases. Thus, with H_2:CH_4 mixing ratio of 2, the total conversion efficiency (288.4 + 299.1 nm) of 52% is achieved with 18-mJ input laser energy at 13 bar. However, the total conversion efficiency of 45% is achieved at 18 bar with 18-mJ input energy when the intensity of both first stokes lines is nearly equal. Furthermore, the efficiency with a mixing ratio of 1.5 is measured and shown in Fig. 68.3a. With this mixing ratio, the total conversion efficiency is found slightly less than the mixing ratio 2 with similar input energies and pressure. The maximum total conversion efficiency is found to be about 42% at 13 bar.

Similarly, the conversion efficiency of different mixing ratios with varying pressure and laser energy is estimated, and the consolidated picture is shown in Fig. 68.4. One can observe that higher cell pressure and higher laser input energy are required for higher H_2:CH_4 mixing ratios to achieve near equal intensities of two wavelengths. Furthermore, while comparing the total conversion efficiency achieved with each mixing ratio when two wave lengths are equal shows that the H_2:CH_4 mixing ratio of 2:1 with a total cell pressure of 18 bar and laser input energy of 18 mJ is found best suitable for the generation of two wavelengths with nearly equal intensity.

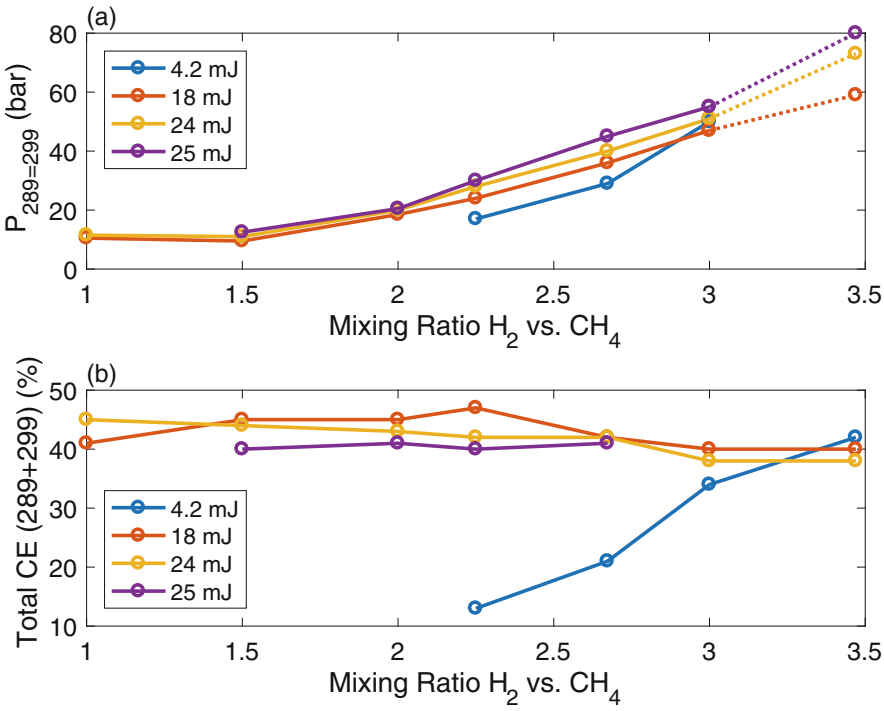


Fig. 68.4 (**a**) The total cell pressure vs. mixing ratio when the intensity of both wave lengths 288.4 nm and 299.1 nm becomes nearly equal. (**b**) The total conversion efficiency achieved with each mixing ratio when wavelengths are equal

68.5 Conclusion

A compact single Raman cell system has been set up to achieve the coaxial beam of SRS wavelengths CH_4 (288.4 nm) and H_2(299.1 nm) with the maximum possible conversion efficiency. The conversion efficiency of CH_4 and H_2 Raman shift intensities under different laser energies and the total cell pressure with individual gases and mixture of gases is observed. While the individual gases are used, with a laser energy of 25 mJ, the maximum conversion efficiency of first stokes of about 70% for H_2 and 42% for CH_4 can be achieved. The conversion efficiency of 288.4 nm and 299.1 nm with H_2: CH_4 mixing ratio of 1(50%:50%) at a total cell pressure of 21 bar could generate near equal intensities of ON and OFF wavelengths, and however the optical windows were damaged due to carbon formation inside the cell after few hours [4]. A detailed investigation on the carbon formation inside the cell is yet to be carried out.

Furthermore, several combinations were tested and found that the higher mixing ratios require higher total cell pressure to generate similar conversion efficiency at lower mixing ratios with lower cell pressure. However, it is found that the laser input

energy of higher than 4.2 mJ is required to get reasonable conversion efficiency. Altogether, a mixing ratio of 2:1 (H_2:CH_4) at 18 bar total cell pressure is found best suitable to generate 45% optimum energy conversion efficiency with an output energy of 14 mJ of wavelength pair 288.4 nm and 299.1 nm that can be used for DIAL ozone lidar profiling.

References

1. Trickl, T.: Tropospheric trace-gas measurements with the differential-absorption lidar technique. Recent Advances in Atmospheric Lidars **7**, 87–147 (2010)
2. Milton, M.J., Ancellet, G., Apituley, A., Bösenberg, J., Carnuth, W., Castagnoli, F., Trickl, T., Edner, H., Stefanutti, L., Schaberl, T., Sunesson, A., Weitkamp, C.: Raman-shifted laser sources suitable for differential-absorption lidar measurements of ozone in the troposphere. Appl. Phys. B Lasers Opt. **66**(1), 105–113 (1998)
3. Jones, R.R., Hooper, D.C., Zhang, L., Wolverson, D., Valev, V.K.: Raman techniques: fundamentals and frontiers. Nanoscale Res. Lett. **14**(1), 1–34 (2019)
4. Simeonov, V., Mitev, V., van den Bergh, H., Calpini, B.: Raman frequency shifting in a CH4:H2:Ar mixture pumped by the fourth harmonic of a Nd:YAG laser. Appl. Opt. **37**(30), 7112 (1998)

Chapter 69
A Compact Raman Lidar for Atmospheric CO_2 and Thermodynamic Profiling: The System CONCERNING

Paolo Di Girolamo, Davide Dionisi, Marco Cacciani, Annalisa Di Bernardino, Noemi Franco, Donato Summa, Marco Di Paolantonio, Anna Maria Iannarelli, and Tatiana Di Iorio

Abstract The research project CONCERNING was funded by the Italian Ministry of University and Scientific Research as part of the "Special Integrative Research Fund (FISR) 2019" Call. The project is aimed at the design and experimental development of an innovative Raman lidar system for measuring the vertical profiles of the two main greenhouse gases present in the atmosphere, that is CO_2 and water vapor, as well as temperature and multi-wavelength particle backscatter, extinction, fluorescence, and depolarization profiles. The capability to measure this suite of atmospheric compositional and thermodynamic properties represents an important observational potential for improving our understanding of feedback and coupling mechanisms of these two species with the biogeochemical cycles in the Earth system.

P. Di Girolamo (✉) · N. Franco · M. Di Paolantonio
Scuola di Ingegneria, Università della Basilicata, Potenza, Italia
e-mail: paolo.digirolamo@unibas.it

D. Dionisi
ISMAR-CNR, Roma, Italia
e-mail: davide.dionisi@artov.ismar.cnr.it

M. Cacciani · A. Di Bernardino
Dipartimento di Fisica, Università degli Studi di Roma Sapienza, Roma, Italia
e-mail: marco.cacciani@uniroma1.it

D. Summa
IMAA-CNR, Tito Scalo, Potenza, Italia
e-mail: donato.summa@imaa.cnr.it

A. M. Iannarelli
SERCO-ESA/ESRIN, Frascati, Italia

T. Di Iorio
ENEA Centro Ricerche Casaccia, Santa Maria di Galeria, Italia
e-mail: tatiana.diiorio@enea.it

© The Author(s), under exclusive license to Springer Nature Switzerland AG 2023

J. T. Sullivan et al. (eds.), *Proceedings of the 30th International Laser Radar Conference*, Springer Atmospheric Sciences,
https://doi.org/10.1007/978-3-031-37818-8_69

The low-weight compact ground-based system illustrated in this paper has been sized to accurately measure the abovementioned parameters with high time and space resolution to allow for the resolution of convection scales and turbulent processes. Such a system, exploiting both the rotational and vibrational Raman lidar techniques in the UV through cutting-edge technologies for spectral selection, optical signal detection, and data acquisition, is hosted in sealed and rugged container, equipped with fused-silica windows, and capable to operate in all weather conditions. The development of the prototype and the verification of its measurement capabilities, possibly assisted by specific measurement campaigns, will allow to demonstrate the enormous potential impact of a network of such systems.

Keywords Low-weight compact ground-based Raman and fluorescence lidar · CO_2 · Aerosol typing · Size and microphysical properties · Atmospheric thermodynamic properties

69.1 Introduction

Atmospheric CO_2 concentration has enormously increased in recent decades, from values close to 300 ppm in the 1950s to the current 415–420 ppm, with an annual increase rate of around 2 ppm. About half of the amount of CO_2 produced through the combustion of fossil fuels and other human activities is released into the atmosphere and accumulates there. The remaining half is absorbed by the oceans and the terrestrial biosphere [1]. An adequate quantitative assessment of the various components of the carbon cycle requires accurate measurements of the sink and source mechanisms and, ultimately, an accurate estimate of the gross primary production (or GPP).

To quantify the atmospheric CO_2 uptake by forests and its contribution to the carbon cycle, accurate measurements of CO_2 gradients between the forest floor and the top of the canopy are needed [2], as well as measurements of their temporal variations. This requires accurate, high vertical and horizontal resolution measurements of the CO_2 mixing ratio profiles. In defining the observational requirements for CO_2, it must be taken into account that its seasonal and annual mean profiles are determined by the combined effect of surface flows and atmospheric mixing. During the summer season in the Northern Hemisphere, atmospheric CO_2 concentrations are typically lower in the planetary boundary layer (PBL) and higher in the free troposphere, due to the prevalence of the effects of photosynthesis over those associated with industrial emissions [3]. On the contrary, during the winter season, the respiration of the animals and vegetation, the vegetation decay, and the use of fossil fuels determine the presence of higher CO_2 concentrations in the PBL and lower in the free troposphere. The amplitude gradients are comparable in the two seasons (of the order of 10 ppm). Additionally, as a result of forest capture, CO_2 gradients between the forest floor and the top of the canopy (at ~ 30 m) are between

75 and 100 ppm during the day and 10–50 ppm at night, in spring conditions when the development of the leaf area of the canopy is not yet completed.

The above considerations suggest the need for CO_2 mixing ratio vertical profile measurements with an accuracy of 2–5 ppm, with vertical resolutions of the order of 100–200 m (to be increased up to ~10 m in the surface layer) and with temporal resolutions of the order of 1 h.

Although the space and ground network for CO_2 monitoring instruments has regularly expanded over the past 50 years, it presently does not guarantee the necessary spatial and temporal resolution needed for a quantitatively reliable characterization of CO_2 sources and sinks and the atmospheric component of the carbon cycle. Additionally, presently operational space sensors provide CO_2 measurements above forest canopies, which do not allow to properly estimate the gross primary production.

For what concerns atmospheric thermodynamic properties, it has to be underlined that our current understanding of the Earth's hydrological and energy cycles shows important gaps on all spatial and temporal scales due to the unavailability of accurate measurements with high vertical and temporal resolution of atmospheric humidity and temperature profiles, especially in the lower troposphere. These measurements are fundamental to improve meteorological forecasts and analyses and are of primary importance for the study of land-atmosphere feedback mechanisms.

The measurement gaps illustrated above can be filled with the development and operation of roto-vibrational Raman lidar systems [4–9] with the capability to carry out profile measurements of atmospheric temperature, water vapor, and CO_2 mixing ratio simultaneously with high accuracy and precision, as well as with high vertical and temporal resolution. By exploiting the three wavelengths emitted by a Nd: YAG laser source in the UV, VIS, and nIR, the polarized and depolarized elastic lidar (Rayleigh-Mie) and Raman echoes from atmospheric constituents, the low-weight compact ground-based system developed in the frame of the research project CONCERNING will carry out vertical profile measurements of atmospheric temperature, water vapor, and CO_2 mixing ratio, the particle backscatter coefficient at 354.7, 532, and 1064 nm; the extinction coefficient at 354.7 and 532 nm; and the depolarization ratio at 354.7, 532, and 1064 nm. A specific channel will measure fluorescence from atmospheric particles to be used for the purpose of aerosol typing [10].

The system is presently under development. A simulation model was applied to simulate the expected performance of the Raman lidar. More specifically, an end-to-end lidar simulator was applied in the verification of the "instrumental concept" of the lidar system and in the definition of the technical specifications of the laser source, telescope, spectral selection devices, and detectors. The possible "trade-offs" between the optical power of the laser source and the telescope aperture were evaluated, and different values of the divergence of the laser beam and the field of view of the receiver were considered. The optical design includes a diode-pumped Nd:YAG "master oscillator-power amplifier" laser source configuration. The single pulse energy at 355 nm is 110 mJ and the frequency repetition is 100 Hz (UV radiant power of 11 W). The telescope, in Dobsonian configuration, has a primary mirror

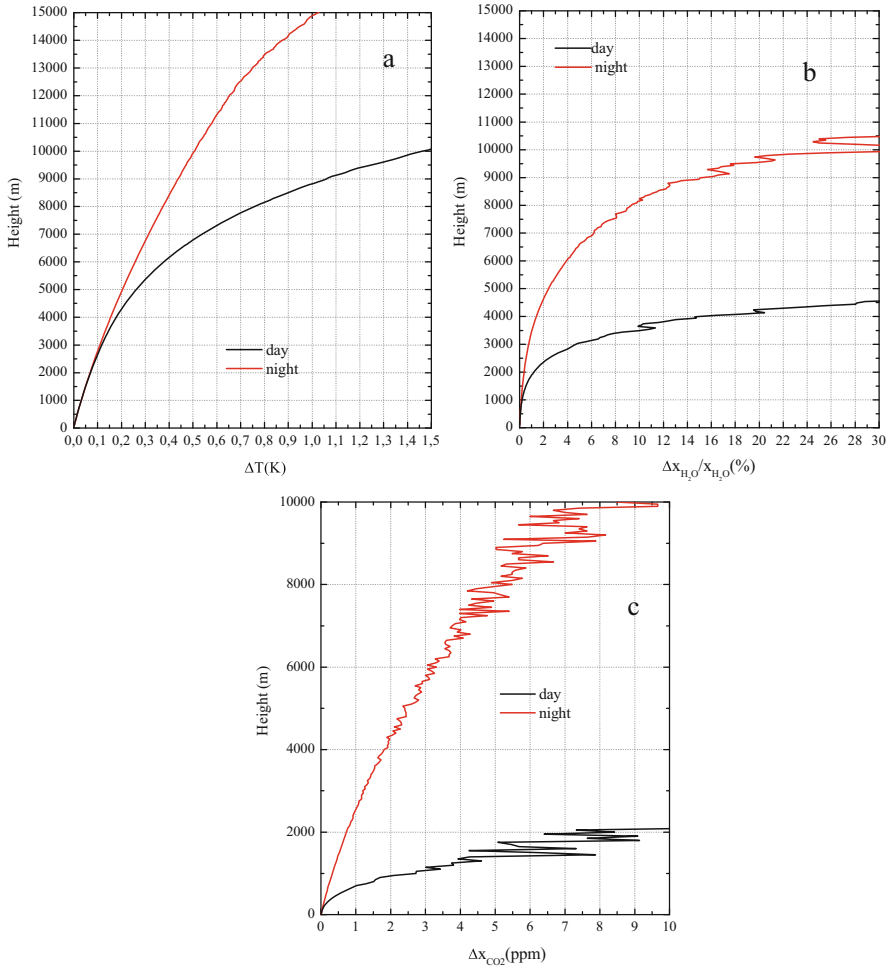


Fig. 69.1 Vertical profiles of the statistical uncertainty for (**a**) temperature [K], (**b**) water vapor mixing ratio of [%], and (**c**) of carbon dioxide [%]

with a diameter of 500 mm, a focal ratio equal to 3.6, therefore corresponding to a focal length of 1800 mm. The distance between the primary and secondary mirrors is about 1500 mm, with the secondary mirror having an elliptical shape inclined by 45° in order to allow the positioning of the telescope focus on a plane placed laterally outside the telescope tube. The following spectral specifications were considered fort the interference filters:

1. Filter for the Raman signal of water vapor (H_2O), central wavelength, 407.5 nm; bandwidth (FWHM), 0.3 nm; and peak transmission, 83%
2. Filter for the Raman signal of molecular nitrogen (N_2), central wavelength, 386.7 nm; bandwidth (FWHM), 0.3 nm; and peak transmission, 83%

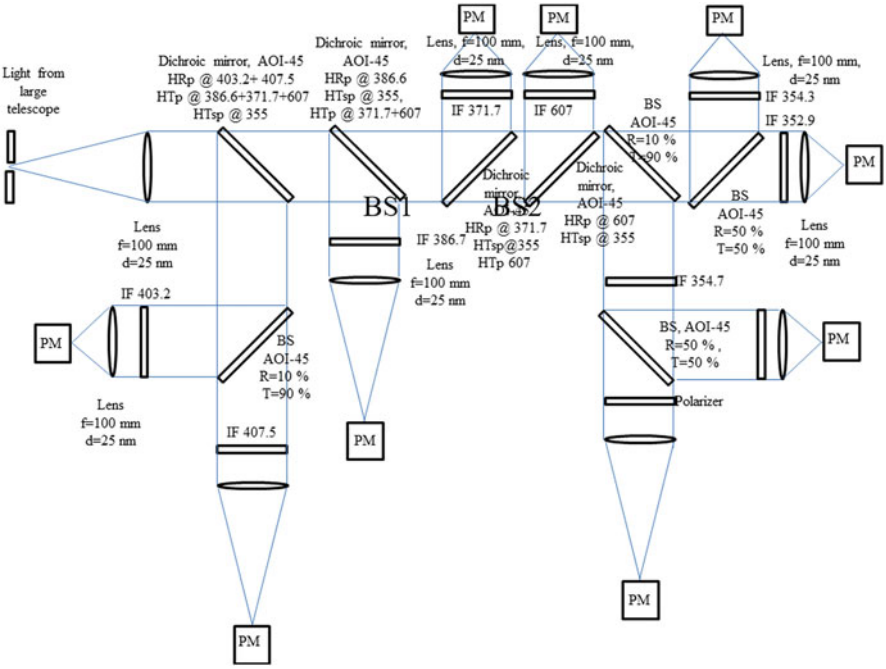


Fig. 69.2 Receiver optical layout

3. Filter for the Raman signal of CO_2, central wavelength, 371.71 nm; bandwidth (FWHM), 0.15 nm; and peak transmission, 60%
4. 354.7 nm elastic signal filter, bandwidth (FWHM), 0.5 nm, and peak transmission, 80%
5. Filters for N_2 and O_2 rotational Raman signals, bandwidth (FWHM), 0.3 nm (LoJ) and 0.5 (HiJ), and peak transmission, 80%

In the various measurement channels, detectors with quantum efficiency at 354.7 nm exceeding 40% and photon count samplers were considered.

Figure 69.1 illustrates the vertical profiles of the simulated statistical measurement uncertainty (precision), obtained by considering a temporal and vertical resolution of 1 min (3 h for CO_2) and 50 m, respectively, and two possible environmental noise conditions (day and night). The figure includes the results for the mid-latitude summer atmosphere model. The simulations show that the statistical uncertainty affecting nighttime atmospheric temperature measurements is smaller than 0.5 K up to an altitude of 10 km and smaller than 1 K up to 15 km, while the statistical uncertainty characterizing daytime measurements is less than 0.5 K up to 7 km and less than 1 K up to 9 km. Simulations also show that the statistical uncertainty affecting nighttime water vapor mixing ratio measurements is less than 6% up to 7 km and less than 20% up to 10 km, while the statistical uncertainty of daytime measurements is smaller than 10% up to 3.5 km and smaller than 30% up to 4.5 km.

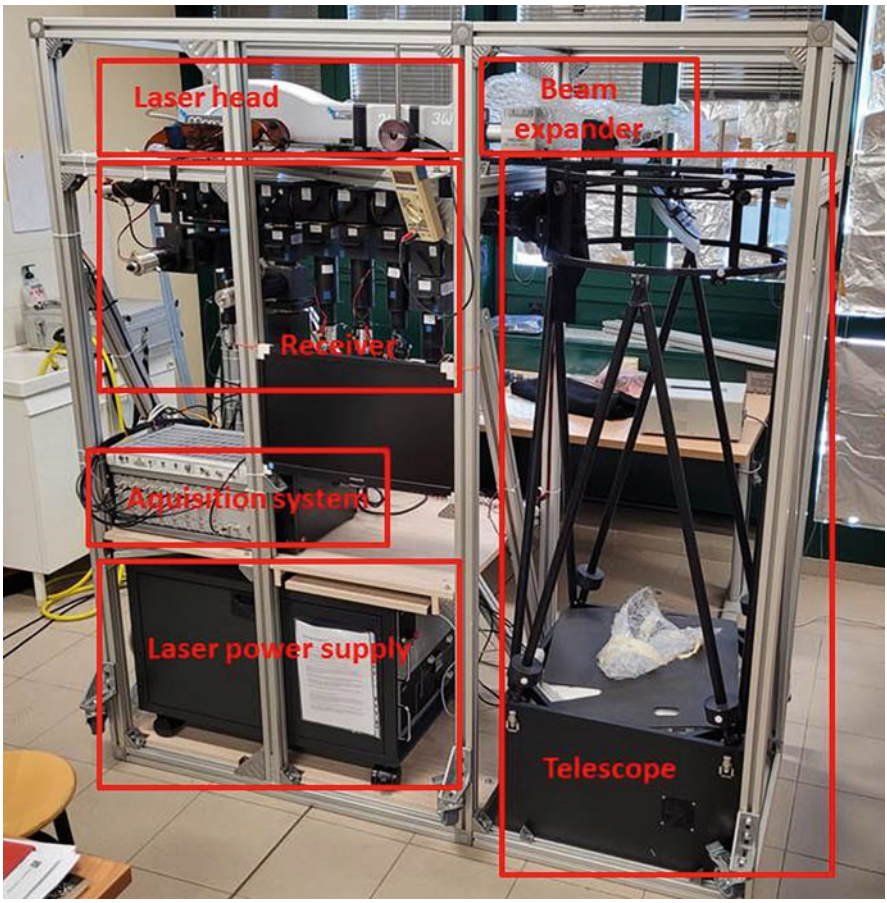


Fig. 69.3 Preliminary breadboard of the system

Figure 69.2 illustrates the optical layout for the lidar receiver. The preliminary breadboard of the system is shown in Fig. 69.3, which shows the instrumental frame including the telescope, the receiving channels, and the signal sampling system.

References

1. Le Quéré, C., et al.: The global carbon budget 1959–2011. Earth Syst. Sci. Data. **5**, 165–185 (2013)
2. Nabuurs, G.J., et al.: Forestry. In: Climate Change 2007: Mitigation. Contribution of Working Group III to the Fourth Assessment Report of the Intergovernmental Panel on Climate Change. Cambridge University Press, Cambridge/New York (2007)

3. Stephens, B.B., Gurney, K.R., Tans, P.P., Sweeney, C., Peters, W., Bruhwiler, L., Ciais, P., Ramonet, M., Bousquet, P., Nakazawa, T., Aoki, S., Machida, T., Inoue, G., Vinnichenko, N., Lloyd, J., Jordan, A., Heimann, M., Shibistova, O., Langenfelds, R.L., Steele, L.P., Francey, R.J., Denning, A.S.: Weak northern and strong tropical land carbon uptake from vertical profiles of atmospheric CO2. Science. **316**(5832), 1732–1735 (2007). https://doi.org/10.1126/science.1137004
4. Di Girolamo, P., Marchese, R., Whiteman, D.N., Demoz, B.B.: Rotational Raman Lidar measurements of atmospheric temperature in the UV. Geophys. Res. Lett. **31**, L01106 (2004). https://doi.org/10.1029/2003GL018342
5. Di Girolamo, P., Summa, D., Ferretti, R.: Multiparameter Raman lidar measurements for the characterization of a dry stratospheric intrusion event. J. Atmos. Ocean. Technol. **26**, 1742–1762 (2009). https://doi.org/10.1175/2009JTECHA1253.1
6. Di Girolamo, P., Summa, D., Lin, R.-F., Maestri, T., Rizzi, R., Masiello, G.: UV Raman Lidar measurements of relative humidity for the characterization of cirrus cloud microphysical properties. Atmos. Chem. Phys. **9**, 8799–8811. ISSN: 1680-7316 (2009). https://doi.org/10.5194/acp-9-8799-2009
7. Di Girolamo, P., Cacciani, M., Summa, D., Scoccione, A., De Rosa, B., Behrendt, A., Wulfmeyer, V.: Characterisation of boundary layer turbulent processes by the Raman lidar BASIL in the frame of HD(CP)2 Observational Prototype Experiment. Atmos. Chem. Phys. **17**, 745–767 (2017). https://doi.org/10.5194/acp-17-745-2017
8. Di Girolamo, P., Behrendt, A., Wulfmeyer, V.: Space-borne profiling of atmospheric thermodynamic variables with Raman lidar: performance simulations. Opt. Express. **26**(7), 8125–8161 (2018). https://doi.org/10.1364/OE.26.008125
9. De Rosa, B., Di Girolamo, P., Summa, D.: Temperature and water vapour measurements in the framework of the Network for the Detection of Atmospheric Composition Change (NDACC). Atmos. Meas. Tech. **13**, 405–427 (2020). https://doi.org/10.5194/amt-13-405-2020
10. Veselovskii, I., Hu, Q., Goloub, P., Podvin, T., Choël, M., Visez, N., Korenskiy, M.: Mie–Raman–fluorescence lidar observations of aerosols during pollen season in the north of France. Atmos. Meas. Tech. **14**, 4773–4786 (2021). https://doi.org/10.5194/amt-14-4773-2021

Chapter 70
Characterization of Recent Aerosol Events Occurring in the Subtropical North Atlantic Region Using a CIMEL CE376 GPN Micro-LiDAR

Y. González Ramos, I. Popovici, A. Barreto, M. F. Sanchez-Barrero, L. Pronieswki, S. Victori, F. A. Almansa, R. Ramos, and E. Cuevas

Abstract A CIMEL CE376 GPN micro-LiDAR was installed at the facilities of the Izaña Atmospheric Research Center (2368 m a.s.l., Tenerife, Canary Islands) in August 2021, and it operates in continuous mode since then. During this period, the pristine dust-free clean conditions that characterize this mountain-top site have been mainly disrupted by two-type aerosol events: the Saharan dust outbreaks that pass over the site on their way toward the Atlantic and the eruption of Cumbre Vieja Volcano (La Palma, Canary Islands) last fall (September 19, 2021). We show two study cases that provide a brief overview of aerosol properties under Saharan dust conditions and volcanic emissions using volume depolarization ratio (VDR), particle linear depolarization ratio (PLDR) at 532 nm, and lidar extinction coefficient products from the CE376 at 532 and 808 nm, as well as aerosol optical depth from AERONET photometers. We also performed a 20-day intercomparison between the CE376 and MPL-4B LiDAR from the NASA Micro-Pulse Lidar Network (MPLNET). The retrieved aerosol products show the good performance of the CE376 micro-LiDAR as a tool for the characterization of the vertical distribution of atmospheric aerosols.

Keywords Volume depolarization ratio · Extinction · Dust · Volcanic aerosols

Y. González Ramos (✉) · F. A. Almansa
CIMEL Electronique, Paris, France

Izaña Atmospheric Research Centre, S/C de Tenerife, Spain
e-mail: y-gonzalez@cimel.fr; f-almansa@cimel.fr

I. Popovici · M. F. Sanchez-Barrero · L. Pronieswki · S. Victori
CIMEL Electronique, Paris, France
e-mail: i-popovici@cimel.fr; m-sanchez@cimel.fr; l-pronieswki@cimel.fr; s-victori@cimel.fr

A. Barreto · R. Ramos · E.Cuevas
Izaña Atmospheric Research Centre, S/C de Tenerife, Spain
e-mail: abarretov@aemet.es; rramosl@aemet.es; ecuevasa@aemet.es

© The Author(s), under exclusive license to Springer Nature Switzerland AG 2023

J. T. Sullivan et al. (eds.), *Proceedings of the 30th International Laser Radar Conference*, Springer Atmospheric Sciences,
https://doi.org/10.1007/978-3-031-37818-8_70

70.1 Introduction

Understanding the distribution and properties of aerosol particles at regional and global scales will contribute reducing the uncertainties of models predicting future climate scenarios. Low-cost polarization LiDAR instruments are opening a new path for extending the aerosol measurements around the world. Here we present the performance of a low-cost and compact CE376 micro-pulse LiDAR for aerosol characterization at the remote site of the Izaña Atmospheric Research Centre.

The Izaña Observatory (Tenerife, Canary Islands), located at 2372 m a.s.l., is representative of the well-stratified subtropical North Atlantic lower troposphere. The pristine clean conditions that characterize the site are disrupted by the regional dust production and exportation from North Africa within the Saharan Air Layer (SAL), especially in summertime [1, 2]. Some sporadic events of long-range transport of pollutants from North America and Europe are also observed. This site also witnessed the eruption of the Cumbre Vieja volcano (La Palma, Canary Islands) last fall. The variety of aerosol events occurring during last summer and fall made Izaña a perfect laboratory to test the performance of new instruments for aerosol characterization.

70.2 Specifications of the CE376 and Ancillary Information

70.2.1 Specifications of the CE376

The CE376 micro-pulse LiDAR is an eye-safe compact elastic backscatter LiDAR, emitting and measuring at two wavelengths with a pulsed diode pumped solid-state laser in the visible (532 nm) and a pulsed laser diode emitting in the near infrared (808 nm). The 532 nm laser has a pulse energy of 7.8 μJ, a pulse width of 0.89 ns, and a pulse repetition rate of 4.6 kHz. The CE376 is a biaxial system with a small field of view for emission (50 μrad) and reception (120 μrad) at 532 nm. At 808 nm, the emission field of view is 230 μrad and 260 μrad in reception. With a range resolution of 15 m and 1-min integration time, the CE376 can detect the backscattered signal at distances from 8 km during daylight up to more than 20 km by night at 532 nm and provides depolarization at 532 nm for enhanced aerosol characterization.

The CE376 uses avalanche photodiode detectors (APD) in photon counting mode for all reception channels. The dead time of the channels varies between 23 and 28 ns. The range-corrected signal (RCS) is obtained after applying a series of additional corrections, such as background, dead-time and overlap to the raw signal. The CE376 installed at Izaña achieves a full overlap at 2.6 km a.g.l. in the 532 nm channel and at 1.9 km a.g.l. in the 808 nm. The incomplete lidar signal is corrected using the overlap function [3] determined using clean atmospheric conditions (Izaña, AOD of 0.02–0.03). Due to the effect of the overlap uncertainty

(~10%) [4] and the saturation of the detector in the near range, the information below 600 m is disregarded in this initial evaluation.

The polarized channels were calibrated using the ±45° method [5] on site. Using a reference height of approximately at 6–7 km (depending on the aerosol content of the layer in each particular case), we determine the extinction coefficient from the Klett-Fernald inverse integration method [6, 7]. We check the performances of the CE376 lidar by following the standard EARLINET procedures [8], namely, the Rayleigh fit (5–10% relative deviations from molecular) applied to a micro-LiDAR.

70.2.2 Ancillary Information

AOD and AE from AERONET. We use cloud-screened and quality-assured AERONET level 2.0 [9] column-integrated aerosol optical depth (AOD) and Ångstrom Exponent (AE) from the CE-318 sun photometer at Izaña site. The synegy between the CE376 and the sun photometer at Izaña station allows us to determine the extinction profile and the column-integrated extinction-to-backscatter ratio (or lidar ratio LR) [7]. *VDR from MPL-4B.* The micropulse lidar MPL-4B is an eye-safe elastic lidar operating at 532 nm with depolarization capability in continuous mode with a low pulse energy (5–6 μJ) laser and a repetition rate of 2.5 kHz. MPL is the standard lidar system with standardized data processing algorithms within the federated global NASA Micro-Pulse Lidar Network (MPLNET, https://mplnet.gsfc.nasa.gov) [4]. During August 2021, the CE376 and an MPL-4B were together measuring at Izaña site. The volume depolarization ratio (VDR) from MPL-4B level 1.5 (L15-NBR) was compared with the CE376 VDR product as part of the analysis of the performance of the CE376.

Meteorological profiles from radiosondes. Meteorological vertical profiles are provided by radiosondes launched by AEMET at the coastline of Güímar at 12:00 UTC (28.3° N, 16.4° W at 105 m a.s.l.), 11 km from Izaña.

Backtrajectories. The kinematic trajectory model FLEXTRA-ERA5 from the European Centre for Medium-Range Weather Forecasts (ECMWF) [11] ran at 120 h determined the origin of the different air masses arriving at Izaña.

70.3 Characterization of Dust and Volcanic Aerosol Properties Using the CE376

During August 2021, Izaña was frequently impacted by African dust transported west-ward within the Saharan Air Layer (SAL). In this period, not only the CE376 micro-pulse LiDAR but also an MPL-4B LiDAR from the Nasa Micro-Pulse Lidar Network (MPLNET) was measuring at the site. The two systems were located in the same mountain plateau at 2368 m. a.s.l. and distancing 223 m from each other.

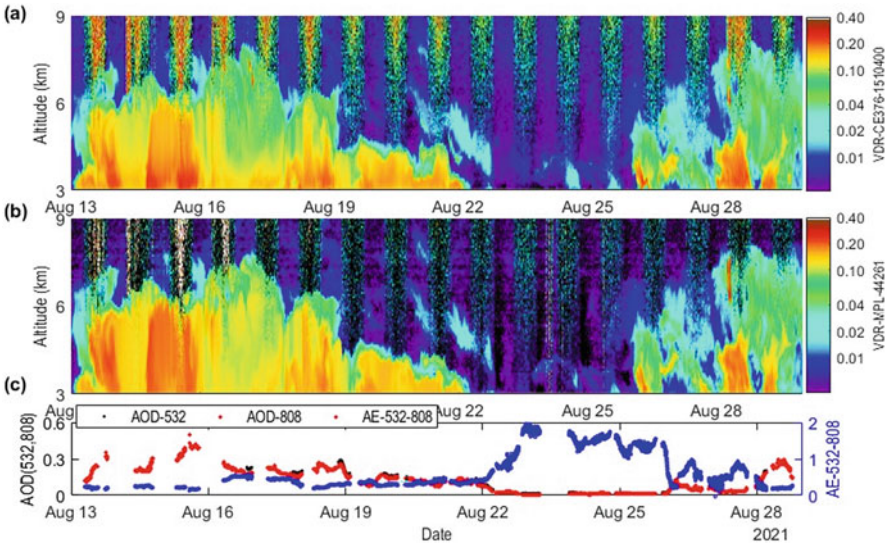


Fig. 70.1 Volume depolarization ratio (VDR) at 532 nm obtained with the (**a**) CE376–1510400, (**b**) the MPL-44261, and (**c**) AOD at 532 nm and 808 nm and AE at 532–808 nm computed from AERONET

Figure 70.1 shows the VDR profiles at 532 nm from CE376 and MPL instruments as well as the AOD and AE at 532 and 808 nm computed from AERONET for 13–29 August 2021. Between August 14 and 19, Izaña received the impact of the SAL. The layer was observed up to 8 km height [2, 10]. In this event, the AOD at 532 nm was 0.27 ± 0.06 and 0.24 ± 0.06 at 808 nm, AE for 532–808 was 0.3 ± 0.1, and VDR ranged between 0.04 and 0.2 in agreement with previous publications [5]. To compare the aerosol products of both systems, the CE376 VDR profiles were averaged to the 75 m vertical resolution of the MPL, and 10-min resolution was kept. A good general agreement is observed between the two instruments (see Fig. 70.1).

The first row of Fig. 70.2(1a–1d) shows the retrieved profiles on August 16, 2021, at 20:00 PM (15-min average). The range-corrected signal (RCS) at 532 and 808 nm follows the Rayleigh fit in the regions of the atmosphere where only molecular signal is expected (>8 km). The profiles show the impact of the SAL up to 7.5 km height. The profiles of extinction coefficients for both channels (between 0.05 and 0.04 km^{-1}, respectively, within the SAL) lead to LR of 53 sr at 532 nm and in the range of those previously observed in the free troposphere in this region [10]. The AE for 532–808 from the CE376 of 0.5, between 4 and 6 km, is in agreement with that given by the photometer. In addition, AOD at 532 nm of 0.22, and relative high depolarization (VDR ~ 0.1, PLDR ~ 0.23), shows the presence of relatively large particles within the layer and agrees with previous studies [5].

During August 25–26, backtrajectories (not shown for the sake of brevity), AE for 532–808 nm of 0.27 ± 0.06, AOD at 532 nm of 0.05 ± 0.03, and low

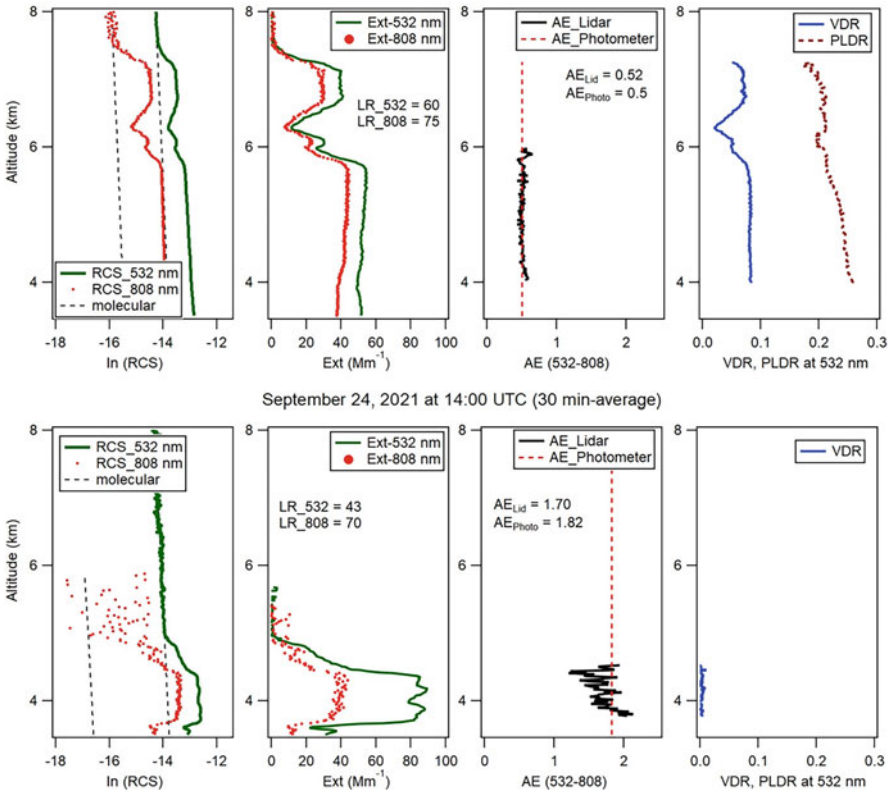


Fig. 70.2 Range-corrected signals (RCS) and extinction coefficients (Ext) at 532 and 808 nm, lidar AE at 532–808 nm, and volume depolarization ratio (VDR) and particle linear depolarization ratio (PLDR) for (1) August 16, 2021, at 20:00 UTC in the first row and (2) September 24, 2021, at 14:00 UTC

depolarization (VDR of 0.03 ± 0.01, see Fig. 70.1) indicate the arrival at Izaña of long-range transport of smaller particles associated with pollution from North America, followed by a new Saharan dust event on August 28.

During the first days of Cumbre Vieja eruption, clouds of SO2 travelling to Izaña were observed in the RGB satellite and detected by the instrumentation at Izaña station (September 23–24, 2021, figure not shown for the sake of brevity). The second row of Fig. 70.2(2a–2d) shows the retrieved 30 min-average profiles on September 24, 2021, at 14:00 PM. The RCS follows the Rayleigh fit in the absence of aerosols (>5 km). Small particles associated with SO2 emissions from the Cumbre Vieja were observed between 3.5 and 4.5 km height. These particles present extinction coefficients close to 0.08 km^{-1} at 532 nm and 0.04 km^{-1} at 808 nm (in average), LR of 43 sr at 532 nm, relatively high AE for 532–808 (1.70), AOD at 532 nm of 0.16, and low depolarization (VDR < 0.01), in agreement with previous studies [12].

70.4 Conclusions

We present the first results on aerosol characterization provided by the CIMEL CE376 GPN micro-LiDAR installed at Izaña site, specifically for two case scenarios where the station was impacted by the arrival of Saharan dust particles and volcanic emissions from the Cumbre Vieja volcano. The results on volume depolarization ratio at 532 nm, aerosol extinction at 532 and 808 nm, and AE for 532–808 nm retrieved profiles show the good performance of the micro-LiDAR CE376. These first aerosol products, together with future work focused on the 808 nm channel, will provide a better insight of the possibilities of this instrument for atmospheric aerosol characterization in remote sites.

Acknowledgments The work has been developed as part of the activities of the World Meteorological Organization (WMO) Commission for Instruments and Methods of Observations (CIMO) Izaña Testbed for Aerosols and Water Vapor Remote Sensing Instruments.

References

1. Cuevas, E., et al.: Izaña Atmospheric Research Center Activity Report 2015–2016, Tech. Rep. WMO/GAW No. 236, World Meteorological Organization & Izaña Atmospheric Research Center (AEMET). Available at https://library.wmo.int/doc_num.php?explnum_id=4139
2. Rodríguez, S., et al.: Transport of desert dust mixed with North African industrial pollutants in the subtropical Saharan Air Layer. Atmos. Chem. Phys. **11**, 6663–6685 (2011). https://doi.org/10.5194/acp-11-6663-2011
3. Kunz, G.J., de Leeuw, G.: Inversion of the lidar signals with the slope method. Appl. Opt. **32**(18), 3249–3256 (1993)
4. Welton, E.J., Campbell, J.R.: Micropulse lidar signals: uncertainty analysis. J. Atmos. Ocean. Technol. **19**(12), 2089–2094 (2002). https://doi.org/10.1175/1520-0426(2002)019<2089:MLSUA>2.0.CO;2
5. Freudenthaler, V., et al.: Depolarization ratio profiling at several wavelengths in pure Saharan dust during SAMUM 2006. Tellus Ser. B Chem. Phys. Meteorol. **61**(1), 165–179 (2009). https://doi.org/10.1111/j.1600-0889.2008.00396.x
6. Fernald, F., Herman, B., Reagan, J.: Determination of aerosol height distribution by lidar. J. Appl. Meteorol. **11**, 482–489 (1972)
7. Klett, J.D.: Lidar inversion with variable backscatter/extinction ratios. Appl. Opt. **24**, 1638–1643 (1985). https://doi.org/10.1364/AO.24.001638
8. Freudenthaler, V., Linné, H., Chaikovski, A., Rabus, D., Groß, S.: EARLINET lidar quality assurance tools. Atmos. Meas. Technol. Discuss. (2018). https://doi.org/10.5194/amt-2017-395
9. Giles, D.M., et al.: Advancements in the Aerosol Robotic Network (AERONET) Version 3 database – automated near-real-time quality control algorithm with improved cloud screening for Sun photometer aerosol optical depth (AOD) measurements. Atmos. Meas. Technol. **12**, 169–209 (2019). https://doi.org/10.5194/amt-12-169-2019
10. Barreto, A., et al.: Long-term characterisation of the vertical structure of the Saharan Air Layer over the Canary Islands using lidar and radiosonde profiles: implications for radiative and cloud processes over the subtropical Atlantic Ocean. Atmos. Chem. Phys. **22**, 739–763 (2022). https://doi.org/10.5194/acp-22-739-2022

11. Stohl, A., Seibert, P.: Accuracy of trajectories as determined from the conservation of meteorological tracers. Q. J. Roy. Meteorol. Soc. **125**, 1465–1584 (1998)
12. Prata, A.T., Young, S.A., Siems, S.T., Manton, M.J.: Lidar ratios of stratospheric volcanic ash and sulfate aerosols retrieved from CALIOP measurements. Atmos. Chem. Phys. **17**, 8599–8618 (2017). https://doi.org/10.5194/acp-17-8599-2017

Chapter 71
Tropospheric Ozone Differential Absorption Lidar (DIAL) Development at New York City

Dingdong Li, Yonghua Wu, Thomas Legbandt, Mark Arend, Maggie Liang, and Fred Moshary

Abstract Ozone (O_3) pollution episodes often occur on hot days in summer in the New York City (NYC) metropolitan area and its downwind coastal area due to large amounts of urban emissions, chemical productions, and meteorological and regional transport effects. To understand the formation process of high ozone, it is important to observe the ozone vertical distribution and its evolution. In this chapter, we reported an Ozone Differential Absorption Lidar (DIAL) developed at the City College New York (CCNY) and present the initial observations. The results show that the CCNY O_3-DIAL is able to retrieve O_3 concentration from 0.2 to 8.5 km altitude with 10-minute time resolution, depending on operation conditions. The O_3 retrievals from the near-range and far-range channels have good consistency at 0.9–1.8 km altitude. In addition, under favorable weather conditions, the O_3 retrievals at near-surface show a consistent temporal variation with the co-located in situ O_3 measurements. Our observation cases indicated the elevated O_3 concentration above the planetary boundary layer (PBL) which might be associated with the regional pollution transport such as the wildfire smoke plumes. The CCNY-Ozone DIAL will be installed in a trailer in the near future which allows mobile observation for the field campaign.

Keywords Ozone · Differential Absorption Lidar · Air pollution

D. Li (✉)
City College of New York, CUNY, New York, NY, USA
e-mail: dingdong.li280@gmail.com

Y. Wu · T. Legbandt · M. Arend · M. Liang · F. Moshary
City College of New York, CUNY, New York, NY, USA

NOAA Center for Earth System Sciences and Remote Sensing Technologies (CESSRST), New York, NY, USA

© The Author(s), under exclusive license to Springer Nature Switzerland AG 2023

J. T. Sullivan et al. (eds.), *Proceedings of the 30th International Laser Radar Conference*, Springer Atmospheric Sciences,
https://doi.org/10.1007/978-3-031-37818-8_71

71.1 Introduction

Over the past years, high ozone episodes with ozone concentration exceeding the 70 ppb National Ambient Air Quality Standard (NAAQS) have been reported over the New York City (NYC) metropolitan area and locations downwind, particularly during the summer. Emissions from transportation and other industrial activities in the urban area generate abundant ozone precursors, such as NO_x and VOC. High temperature, strong solar radiation, weak winds, and stable atmospheric boundary layer provide favorable conditions to drive the photochemical reactions that produce ozone. In addition, the subsidence of the ozone layer aloft from the regional transported smoke plumes can also increase the ambient ozone concentrations.

To better understand the ozone formation process and dynamics, it is important to obtain the vertical distribution of the ozone concentration. Currently, there are six ozone lidars in the Tropospheric Ozone Lidar NETwork (TOLNet) in North America, which provides high spatio-temporal resolution and high-fidelity ozone profile measurements within the troposphere (https://www-air.larc.nasa.gov/missions/TOLNet/). However, such ground-based ozone lidar had not yet been developed in the NYC metropolitan area. In this chapter, we present the characteristics of the CCNY-Ozone DIAL and its initial results.

71.2 System Description

The entire ozone DIAL system comprises one transmitter and two receiver channels, including the far-range and near-range channels and one data acquisition unit, as shown in Fig. 71.1. For the transmitter, a quadrupled Nd:YAG laser ((Quantel Q-Smart 450, 266 nm, 50 mJ at 20 Hz) pumped a CO_2-filled Raman cell (1-m long) and generates the "on" and "off" wavelength at 287.2 nm and 299.1 nm through the Stimulated Raman Scattering (SRS) principle [6, 8]. We varied the CO_2 pressure to maximize the output energy of 299.1 nm, which has the lowest energy as the third-Stokes line of SRS. Our measurements showed that at CO_2 pressure of 150 psi, the 299.1-nm beam has the maximum output energy. The energy conversion efficiencies for the three Stocks lines, namely 276.2 nm (S1), 287.2 nm (S2), and 299.1 nm (S3), were 31%, 28%, and 16.6%, respectively. The output beams from the Raman cell are collimated and directed to the atmosphere.

The receivers include a large Newtonian telescope (diameter 50.8 cm, F#3.5) for the far-range O_3 detection and a small telescope (diameter 5.08 cm, F#3) for the near-range O_3 detection. The current configuration of this ozone DIAL system shares the large telescope with a multi-wavelength Mie–Raman aerosol lidar. The dichroic mirror (DM1 in Fig. 71.1 AVR Optics) allows the light with wavelength shorter than 325 nm to be reflected into the ozone far-channel receiver optics, while the light with a longer wavelength passes through to the aerosol lidar receiver. For the near-range O_3 detection, an optical fiber is connected to the small telescope and

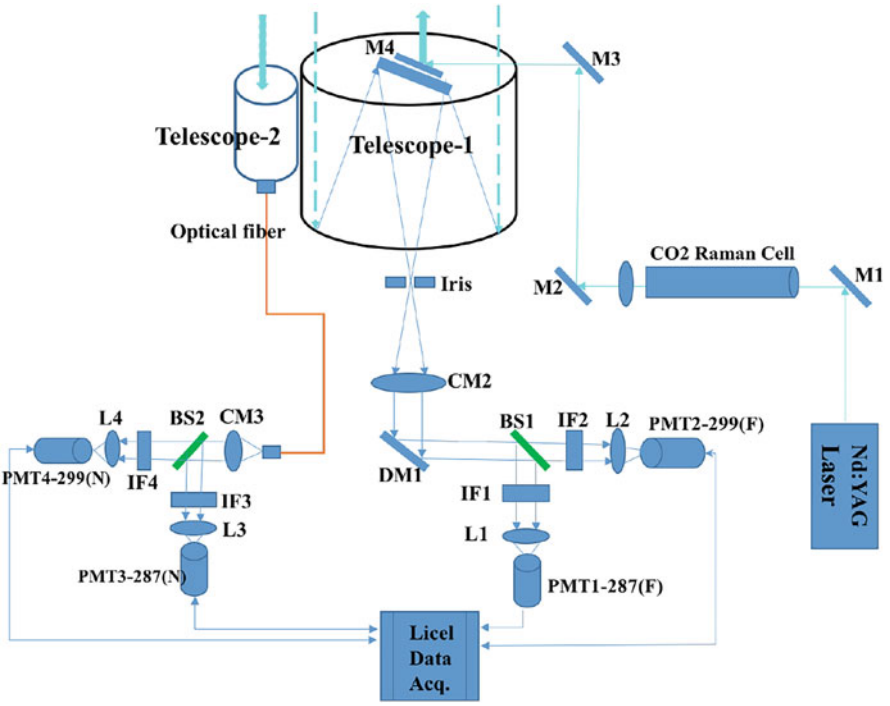


Fig. 71.1 Schematic diagram of CCNY O_3-DIAL system

guides the optical signals to the near-range receiver optics and detectors. All the four channels of signal detection use the same type of detectors (Hamamatsu R9880U-113) and the Licel transient recorders (TR40-16bit-3U, 40 MHz). The raw signals are collected with 1-min average (1200 laser shots) and 3.75 m range resolution, and each signal profile has 6000 bins, corresponding to 22.5 km.

71.3 Methodology

71.3.1 Ozone DIAL Equation

The ozone DIAL emits two wavelengths in the Hartley band region which have different ozone absorption characteristics [5]. The emitted wavelength with stronger absorption is referred to as "on" wavelength and the other weakly absorbed is "off" wavelength. By manipulating the lidar equations of the two wavelengths, we can obtain the ozone number density as follows [1]:

$$N_{O_3}(z) = \frac{1}{2\Delta\sigma_{O_3}}\left[\frac{d}{dz}\ln\left(\frac{P_{\text{on}}}{P_{\text{off}}}\right) - \frac{d}{dz}\ln\left(\frac{\beta_{\text{on}}}{\beta_{\text{off}}}\right)\right] - \frac{\Delta\alpha_{\text{mol}}}{\Delta\sigma_{O_3}} - \frac{\Delta\alpha_{\text{aer}}}{\Delta\sigma_{O_3}} - \frac{N_{\text{g}}\Delta\sigma_{\text{g}}}{\Delta\sigma_{O_3}}, \tag{71.1}$$

where $N_{O_3}(z)$ is the ozone number density at altitude z and $\Delta\sigma_{O_3}$ is the ozone differential absorption cross sections of "on" and "off" wavelength. $P(z)$ and $\beta(z)$ denote the lidar return signal and atmospheric backscatter coefficient at altitude z of either the "on" or "off" wavelengths. $\Delta\alpha_{\text{mol}}$, $\Delta\alpha_{\text{aer}}$, and $N_{\text{g}}\Delta\sigma_{\text{g}}$ are the extinction difference of molecules, aerosols, and other interfering gases such as sulfur dioxide (SO_2) and nitric oxide (NO_2).

71.3.2 Ozone Retrieval

Prior to ozone retrieval, the raw signals are averaged every 10 minutes. Then, we applied the dead-time correction to the photo-counting (PC) signals following the non-paralyzable model: $C_t = \frac{C_m}{1-C_m\tau_d}$, where C_t is the true count rate, C_m is the observed count rate, and τ_d is the system dead-time constant, which is about 3.7 ns for our system. Next, we subtracted the signal by its background, which is calculated by averaging the last 200 bins. After the background subtraction, the parallel analog and PC signals were glued together in the range where the ratios of analog and PC signals are constant. The analog–PC combined signal will subsequently go through the cloud-screening process. We used the gradient of the range-corrected signal profile to identify the cloud-base height (CBH), and the signals above the cloud base are excluded from retrieval. The signal profiles which are preprocessed as outlined above are used to retrieve the ozone number density based on Eq. (71.1). The derivatives of the signal ratios of both channel were calculated using the second-order Savitzky–Golay (SG) differentiation filter [7]. The window size of the SG filter corresponds to the vertical resolution and varies from 31 to 200 bins at the different altitude in order to reduce the statistical errors of O_3 retrieval due to the signal random noise [2, 3, 8, 9]. Afterward, the calculated O_3 number density profiles from the far- and near-channel were merged together in the range where they are consistent. Finally, we applied the molecular and aerosol corrections to the calculated ozone number density. The molecular extinction correction terms can be obtained using the radiosonde measurements or the standard atmosphere model [10]. The aerosol extinction and backscatter correction terms are retrieved from the collocated Lufft CHM15k ceilometer measurements. We chose measurements of the ceilometer instead of the aerosol lidar to retrieve the aerosol backscatter coefficients because the aerosol lidar data were not available at the study period, and we have demonstrated in another paper that the Lufft ceilometer can retrieve the aerosol backscatter coefficients above 0.2 km [4]. Since the SO_2 or NO_2 concentrations and differential absorption cross section at 287–299 nm are relatively low [2, 3, 9], the influence due to these interference gases is not corrected here.

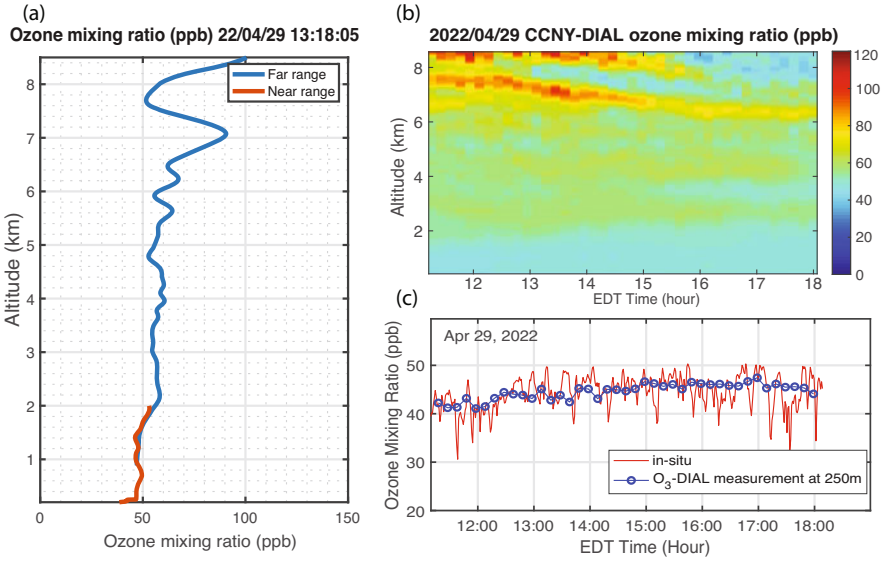


Fig. 71.2 CCNY-DIAL ozone mixing ratio retrieval on April 29, 2022. (**a**) Ozone mixing ratio profiles from the far- and near-channel at 2022 April 29th 13:18:05 (EDT). (**b**) Time–altitude curtain plot of the near–far range merged ozone mixing ratio from 11:00 to 18:00 (EDT). (**c**) The comparison of DIAL-measured ozone mixing ratio at 250 m and ground ozone measurements

71.4 Observation Results

Figure 71.2 is an example of the ozone mixing ratio retrieved from the CCNY-Ozone DIAL on April 29, 2022. In Fig. 71.2a, the blue and red lines represent the ozone mixing ratio profiles of the far- and near-channel at 13:18 (EDT), respectively. To avoid signal saturation at lower altitude, the gated PMT detectors turned on at about 855 m for the far-channel and 60 m for the near-channel. The ozone retrievals show good consistency between the two channels in the range of 0.9–1.8 km, indicating the viability of the Ozone DIAL system, as the two receivers are taking measurements independently. Figure 71.2b displays the merged ozone retrievals from these two channels. The ozone mixing ratios above 1.1 km come from the far-channel retrieval and the values below 0.9 km are taken from the near-channel retrieval, and the ozone mixing ratios between 0.9 and 1.1 km are calculated by the weighted average of the two ranges. From 11:00 to 16:00 EDT, elevated ozone concentration can be seen around 7.5 km and above 8.5 km. These high ozone layers may be due to the transportation of aerosol plumes from other regions or related to the dynamic mixing of stratosphere ozone into the troposphere. More meteorological information and further investigation are needed to confirm the source of the aloft high ozone layers. On the other hand, the ozone level within the PBL is relatively low and stable. Since the ozonesonde data is not available in NYC and surrounding regions, we compared the DIAL retrievals at 250 m with

the near-surface measurements of an ozone monitor (2B Technologies Model 202). As shown in Fig. 71.2c, throughout the entire observation period, the ozone mixing ratio from DIAL at 250 m altitude showed consistent temporal variation with the ozone mixing ratio from the surface ozone monitor, meaning that the ozone DIAL is able to retrieve the ozone mixing ratio near the ground level.

71.5 Conclusion

In this chapter, we demonstrated a newly built Ozone DIAL system at the City College of New York. The DIAL uses an Nd:YAG laser pumping a CO_2 Raman cell to generate the desired wavelengths at 287.1 nm and 299.2 nm. The receiver utilizes two telescopes that cover the near-range and far-range ozone measurement from near-surface to upper troposphere. We have made experimental observations and evaluated the O_3 retrievals with the in situ measurements. The results indicate consistent O_3 retrievals in the upper PBL between the far-range and near-range channels. Meanwhile, the O_3 results at near-surface ($\sim$0.2 km) show good agreement with the ground in situ measurements under favorable weather condition. Our observations show aloft O_3 layers in the free troposphere in NYC area, which might be associated with the regional transport from the wildfire smoke and/or the stratosphere–troposphere exchange. These initial results show that the CCNY-Ozone DIAL is able to provide reliable ozone profiles in the troposphere. Currently, we are continuing the system optimization and regular experiments. The DIAL system will be moved into a trailer which allows mobile observation for the field campaign and inter-comparison with other ozone vertical measurements.

Acknowledgments This research was in part funded by NESCAUM (grant # 2427) and the New York State Energy Research Development Authority (NYSERDA, grant # 137482). Maggie Liang is a NOAA CESSRST EPP MIS fellow supported under NOAA EPP MSI CESSRST award NA16SEC4810008. The information herein was not reviewed by the funding agencies and the opinions expressed in this report do not necessarily reflect those of the agencies but only reflect the authors' opinions.

References

1. Gimmestad, G.G.: Differential-absorption lidar for ozone and industrial emissions. In: Lidar: Range-Resolved Optical Remote Sensing of the Atmosphere, vol. 102, pp. 187–212. Springer, Berlin (2005)
2. Kuang, S., Newchurch, M.J., Burris, J., Liu, X.: Ground-based lidar for atmospheric boundary layer ozone measurements. Appl. Opt. **52**(15), 3557–3566 (2013)
3. Leblanc, T., Sica, R.J., Van Gijsel, J.A., Godin-Beekmann, S., Haefele, A., Trickl, T., Payen, G., Liberti, G.: Proposed standardized definitions for vertical resolution and uncertainty in the NDACC lidar ozone and temperature algorithms–part 2: Ozone dial uncertainty budget. Atmos. Meas. Tech. **9**(8), 4051–4078 (2016)

4. Li, D., Wu, Y., Gross, B., Moshary, F.: Capabilities of an automatic lidar ceilometer to retrieve aerosol characteristics within the planetary boundary layer. Remote Sens. **13**(18), 3626 (2021)
5. Malicet, J., Daumont, D., Charbonnier, J., Parisse, C., Chakir, A., Brion, J.: Ozone UV spectroscopy. II. absorption cross-sections and temperature dependence. J. Atmos. Chem. **21**(3), 263–273 (1995)
6. Nakazato, M., Nagai, T., Sakai, T., Hirose, Y.: Tropospheric ozone differential-absorption lidar using Stimulated Raman Scattering in carbon dioxide. Appl. Opt. **46**(12), 2269–2279 (2007)
7. Savitzky, A., Golay, M.J.: Smoothing and differentiation of data by simplified least squares procedures. Anal. Chem. **36**(8), 1627–1639 (1964)
8. Strawbridge, K.B., Travis, M.S., Firanski, B.J., Brook, J.R., Staebler, R., Leblanc, T.: A fully autonomous ozone, aerosol and nighttime water vapor lidar: a synergistic approach to profiling the atmosphere in the Canadian oil sands region. Atmos. Meas. Tech. **11**(12), 6735–6759 (2018)
9. Sullivan, J., McGee, T., Sumnicht, G., Twigg, L., Hoff, R.: A mobile differential absorption lidar to measure sub-hourly fluctuation of tropospheric ozone profiles in the Baltimore–Washington, dc region. Atmos. Meas. Tech. **7**(10), 3529–3548 (2014)
10. US Standard Atmosphere: National Oceanic and Atmospheric Administration (1976)

Part VI
Measurements in the Stratosphere, Mesosphere and Thermosphere

Chapter 72
Accounting for the Polarizing Effects Introduced from Nonideal Quarter-Wave Plates in Lidar Measurements of the Circular Depolarization Ratio

N. Siomos, P. Paschou, G. Georgoussis, G. Tsaknakis, V. Amiridis, and V. Freudenthaler

Abstract In this study, we present a methodology for the calculation of the retardation and rotation errors introduced from a nonideal quarter-wave plate (QWP). We performed laboratory measurements in a lidar ellipsometer (LEM) in Raymetrics S.A., Athens, and also on-field with the EVE (Enhancement and Validation of ESA products) lidar in order to test a high-energy Crystalline Quartz zero-order QWP at 355 nm from Altechna. We found an absolute retardation error of about 4.8° ± 0.6° and 4.9° ± 0.4° when we performed the test directly on EVE and using its two lasers A and B, respectively. It was possible to repeat the same test directly in the laboratory with an ellipsometer using a QWP produced in the same batch as the one installed in EVE. We measured a similar absolute retardation error of 4.7° ± 1.1°. Nonideal retardation in the QWP directly affects the calibration factor and the volume and particle circular depolarization profiles of EVE. Quantifying it is also important because if it is known, it can be corrected with the GHK method.

Keywords Quarter-wave plate · Depolarization lidar · Ellipsometry

N. Siomos (✉)
Meteorological Institute, Ludwig Maximilian Universität München, LMU, Munich, Germany
e-mail: nikolaos.siomos@lmu.de

P. Paschou · V. Amiridis
Institute for Astronomy, Astrophysics, Space Applications and Remote Sensing (IAASARS), National Observatory of Athens (NOA), Athens, Greece

G. Georgoussis · G. Tsaknakis
Raymetrics S.A., Athens, Greece
e-mail: support@raymetrics.com

V. Freudenthaler
Meteorological Institute, Ludwig Maximilian Universität München, LMU, Munich, Germany

© The Author(s), under exclusive license to Springer Nature Switzerland AG 2023

J. T. Sullivan et al. (eds.), *Proceedings of the 30th International Laser Radar Conference*, Springer Atmospheric Sciences,
https://doi.org/10.1007/978-3-031-37818-8_72

72.1 Introduction

Depolarization lidars excel in detecting nonspherical particles such as desert dust, volcanic ash, and cirrus ice crystals. While previous lidars usually rely on linearly polarized laser beams, recent advances show the usefulness of elliptical and/or circular polarization in the lidar profiling. Such measurements are only possible with the use of quarter-wave plates (QWP) in lidar systems. While linear polarizers (LP) and polarizing beamsplitter cubes (PBS) are broadly adopted and tested in the lidar community; this is not the case for the QWP. In this study, we present a methodology for measuring the retardation of a QWP directly in a lidar system. The test was repeated in the laboratory with an ellipsometer in order to verify the findings. The EVE (Enhancement and Validation of ESA products) lidar upon which the technique was applied is presented in brief in Sect. 72.2. The theoretical background of the technique is summarized in Sect. 72.3. Finally, the retrievals are discussed in Sect. 72.4.

72.2 The EVE Lidar

The EVE lidar system belongs to the European Space Agency (ESA). It is the product of collaboration among the National Observatory of Athens, the Ludwig-Maximilian University of Munich, and the Raymetrics S.A. company. The system operates at 355 nm. Two laser beams, one linearly polarized and one circularly polarized, are detected in parallel by two receivers with, one with a linear and the other with a circular analyzer, resulting in four different measurement setups. The system was designed as the ground truth for the lidar of the AEOLUS satellite and is described in detailed by [2].

While performing measurements with EVE, we noticed that the calibration factor of the circular analyzer (receiver 2) was different by approximately 10% when linearly polarized light at $-45°$, $0°$, and $45°$ was applied. The zero-order QWP from Altechna, which is installed before the PBS in receiver 2, was suspected to cause this effect. But a misalignment of the QWP by a few degrees alone cannot explain these differences, pointing toward a retardation error.

For the determination of the retardation, we use the linearly polarized beams from lasers A and B which are recorded by the circular analyzer of EVE in receiver 2 (setups A2 and B2 in [2]). In order to achieve this for laser B, the QWP installed, there was removed. Both setups are shown in Fig. 72.1.

Both linearly polarized laser beams are transmitted through the protective windows of EVE (M_E). The scattered radiation ($\boldsymbol{F}(a)$) from the atmosphere is collected by telescope 2 (T2). A manual rotator (MR) is installed after the collimating lens of the telescope. The circular analyzer consists of a QWP installed at $45°$ in front of a PBS. The only optics between the collimating lens and the QWP is a 355 nm bandpass interference filter (IFF). The protective windows were tested and found to

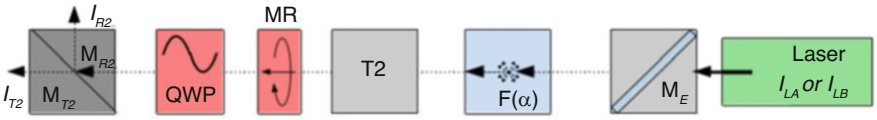


Fig. 72.1 Experimental setups of EVE. For details see in the text

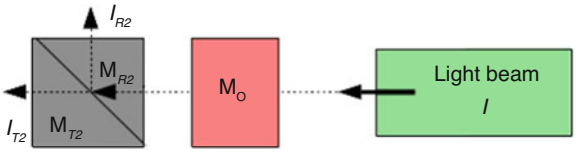


Fig. 72.2 A schematic of the system where the methodology presented here is to be applied

not produce any polarizing effects. The IFF, the telescope, and the collimator lens are not expected to produce any artifacts either.

72.3 Methodology

The inversion method is applicable to a system that contains the following parts (see also Fig. 72.2): a PBS as linear analyzer, two detectors after the PBS that collect the co- and cross-polar radiation, the optics (or array of optics) to be tested (M_O) placed in front of the PBS, and a beam $I(i,q,u,v)$ incident to the optic.

The global coordinate reference system is defined according to [1], with the x-axis parallel and the y-axis perpendicular to the plane of incidence of the PBS, and the z-axis in direction of the light propagation. The general solution for a totally unknown optics is described in Sect. 72.3.1. A special application for a nonideal QWP optic is presented in Sect. 72.3.2.

72.3.1 The General Case

Assuming the optical arrangement described above, the intensity measured by the detector S is given by Eq. 72.1:

$$\boldsymbol{I_S} = \eta_S \boldsymbol{M_{PBS}} \boldsymbol{M_O} \boldsymbol{I} \tag{72.1}$$

where S corresponds to either R or T for the reflected and transmitted channels, respectively. I_S is the measured Stokes vector of channel S, $\boldsymbol{I} = \boldsymbol{I}(i,q,u,v)$ is the Stokes vector of the light that is incident on the unknown optic, η_S is the opto-electronic gain of the S channel, and M_{PBS} and M_O are the Müller matrices of a

PBS and the unknown optic. Their mathematical expressions can be found in [1]. By using the Bra-Ket formalism for Müller matrices (see [1]), we get Eq. 72.2.

$$I_S = \eta_S T_S T_O \left[(1 + D_R m_{21})\, i + (m_{12} + D_R m_{22})\, q + (m_{13} + D_R m_{23})\, u + (m_{14} + D_R m_{24})\, v \right] \tag{72.2}$$

Here T_O and T_S are the transmissions of M_O and M_{PBS}, respectively. D_S is the diattenuation of the PBS per path S and $m_{i,j}$ are the matrix elements of $\boldsymbol{M_O}$. It is obvious here that only the two upper rows of $\boldsymbol{M_O}$ can affect the measured intensities I_R and I_T when a PBS is used as an analyzer. For the ratio of the measured signals I_R and I_T, one gets.

$$\frac{I_R}{I_T} = \frac{\eta_R T_R}{\eta_T T_T} \frac{(1 + D_R m_{21})\, i + (m_{12} + D_R m_{22})\, q + (m_{13} + D_R m_{23})\, u + (m_{14} + D_R m_{24})\, v}{(1 + D_T m_{21})\, i + (m_{12} + D_T m_{22})\, q + (m_{13} + D_T m_{23})\, u + (m_{14} + D_T m_{24})\, v} \tag{72.3}$$

Using

$$w = \frac{I_R - \eta\, I_T}{D_T I_R - \eta\, D_R I_T} \text{ with } \eta = \frac{\eta_R T_R}{\eta_T T_T} \tag{72.4}$$

with η being the calibration factor between the R and T channels, Eq. 72.3 becomes.

$$w\ \ q\ m_{12} + w\ u\ m_{13} + w\ v\ m_{14} + i\ m_{21} + q\ m_{22} + u\ m_{23} + v\ m_{24} = -wi \tag{72.5}$$

The factor w includes the measured intensities, η, and the diattenuation of the PBS for the R and T channels. If the PBS is "cleaned" [1], then $D_R = -1$ and $D_T = 1$. With multiple known states of polarization $I_n(i,q,u,v)$, one can measure different w_n ratios that include the effect introduced by the unknown optic. Consequently, the following system of linear equations can be formed with the elements of M_O as the unknowns:

$$\begin{pmatrix} w_1 q_1 & w_1 u_1 & w_1 v_1 & i_1 & q_1 & u_1 & v_1 \\ w_2 q_2 & w_2 u_2 & w_2 v_2 & i_2 & q_2 & u_2 & v_2 \\ \vdots & & & & \ddots & & \\ w_n q_n & w_n u_n & w_n v_n & i_n & q_n & u_n & v_n \end{pmatrix} \begin{pmatrix} m_{12} \\ m_{13} \\ m_{14} \\ m_{21} \\ m_{22} \\ m_{23} \\ m_{24} \end{pmatrix} = \begin{pmatrix} -w_1 i_1 \\ -w_2 i_2 \\ \vdots \\ -w_n i_n \end{pmatrix} \tag{72.6}$$

The system must be either determined or overdetermined in order to solve it. Consequently, at least 7 known states of polarization must be provided. These states

must produce a coefficient matrix $\boldsymbol{A}$ that is well conditioned with a rank = 7. Such a system can then be solved using the linear least squares method according to Eq. 72.7.

$$AX = B \Rightarrow X = \left(A^T A\right)^{-1} A^T B \tag{72.7}$$

72.3.2 Solving for a Nonideal QWP

Our target is to apply the inversion described in Sect. 72.3.1 in order to characterize the QWP mounted in the EVE detector. By setting $\boldsymbol{M}_O = \boldsymbol{M}_{\mathrm{QWP}}$ in Eq. (72.1) without diattenuation (i.e., all elements in Eq. (72.6) except m_{22}, m_{23}, and m_{24} are zero for a rotated retarder according to [1]), Eq. 72.7 can be further simplified to Eq. 72.8:

$$\begin{pmatrix} q_1 & u_1 \\ q_2 & u_2 \\ \vdots & \vdots \\ q_n & u_n \end{pmatrix} \begin{pmatrix} m_{22} \\ m_{23} \end{pmatrix} = \begin{pmatrix} -w_1 i_1 \\ -w_2 i_2 \\ \vdots \\ -w_n i_n \end{pmatrix} \tag{72.8}$$

Since no amount of circular polarized light exists in I_n, $v_n = 0$ always, excluding m_{24} from the system of equations. The mathematical expression of the nonideal QWP (rotated retarder) is provided in [2, Eq. S.10.12.1]. After calculating m_{22} and m_{23}, one can solve analytically for the retardation Δ_{O} and rotation φ of the QWP with Eq. 72.9 and Eq. 72.10, respectively:

$$\Delta_O = 2\,k\pi \pm \arccos\left(m_{22} + \frac{m_{23}^2}{1 - m_{22}}\right) \tag{72.9}$$

$$\varphi = \frac{k\pi}{2} + \frac{1}{2}\arctan\left(\frac{1 - m_{22}}{m_{23}}\right) \tag{72.10}$$

where $k = 0,1,2...$ For a non-ideal QWP, at least two known states of polarization of the incident Stokes vector must be provided to get a well-conditioned coefficient matrix $\boldsymbol{A}$ of rank = 2. It is also obvious that the technique might not produce reliable Δ_{O} and φ results for $m_{22} \to 1$ and $m_{23} \to 0$, which is the case for a QWP rotation angle $\to 0°$ or 90°. For this reason, we align the QWP at $\varphi = 45° + \varepsilon_{\mathrm{QWP}}$ for all the tests described in Sect. 72.4, where $\varepsilon_{\mathrm{QWP}}$ is a small rotation error that occurs in the alignment process.

72.4 Application and Results

The technique described in Sect. 72.3.2 can be directly applied to EVE for both lasers. For the calculations below, we always select atmospheric regions without aerosol identified through a Rayleigh fit test. A Monte Carlo error simulation has been applied for the calculation of all statistical uncertainties. For the calculation of w_n in Eq. 72.4, the calibration factor η of the receiver must be known. As long as a QWP is placed in front of a PBS, a $\Delta 90$ calibration before the QWP is not applicable. Therefore, the QWP was removed for the $\Delta 90$ calibration with the manual rotator of EVE (Fig. 2 and also [2]). The PBS of EVE is cleaned so that $D_R = -1$ and $D_T = 1$.

For the different states of polarization needed for Eq. 72.8, we use the manual rotator (MR). Because both the QWP and the PBS are mounted on the same platform, this is equivalent to rotating the polarization orientation of the incident Stokes vector I with respect to the reference system. We select the following three rotation angles $\theta_i = -45^\circ$, 0°, and $+45^\circ$. The index i here marks the states of polarization provided. It can be proven that the incident Stokes vector can be calculated by Eq. 72.11:

$$I_{i,j} = I_o \begin{pmatrix} 1 \\ ac_{2\varepsilon_{i,j}}\, p_j \\ -as_{2\varepsilon_{i,j}}\, p_j \\ 0 \end{pmatrix} \tag{72.11}$$

where j can be either A or B depending on the laser, a is the atmospheric polarization parameter for molecules in the aerosol-free region, p_j is the degree of polarization of the laser beam, and $\varepsilon_{i,j} = 90 + \alpha_j + \theta_i$ is the rotation of the laser polarization orientation including the rotation error α_j, the angle θ_i due of the MR, and the 90° rotation of the laser polarization orientation with respect to the PBS. I_o is the intensity of the beam that is canceled in the ratios of Eqs. (72.3) and (72.4).

The temperature dependence of a is included. The lasers were tested in the laboratory with a lidar ellipsometer (LEM), and only a negligible amount of circular polarization was found. An atmospheric Rayleigh measurement was performed without the QWP in order to determine the p_A and p_B values ($p_A = 0.9974 \pm 0.0002$, $p_B = 0.9698 \pm 0.0002$). The rotation errors α_A and α_B can be calculated from the $\Delta 90$ calibration [1] ($\alpha_A = 0.57 \pm 0.04$, $\alpha_B = 0.83 \pm 0.05$). Since all necessary parts of Eq. (72.11) are known, the MR is placed at the three angles θ_i and parallel measurements of the $I_{R,i,j}$ and $I_{T,i,j}$ channels are performed. We solve Eq. 72.7 for Δ_O and φ for each laser in molecular signal regions (Table 72.1).

The rotation angle φ is close to 45°, as expected. The retardation Δ_O deviates from the ideal value of 90° by approximately 5°. Similar values occur with both lasers. The LEM test in the laboratory was done with a QWP of the same batch, and similar values were found (Table 72.1). Unfortunately, it was not possible to perform the laboratory tests directly on the QWP of EVE because it is currently installed at

Table 72.1 Retrievals when using the EVE lasers and from the LEM measurements

	m_{22} (10^{-2})	m_{23} (10^{-2})	Δ_O (°)	φ (°)	ω (°)	ε_{QWP} (°)
Laser A	8.4 ± 1.1	1.3 ± 1.2	85.2 ± 0.6	44.7 ± 0.3	-4.8 ± 0.6	-0.3 ± 0.3
Laser B	8.6 ± 0.7	2.3 ± 0.9	85.1 ± 0.4	44.4 ± 0.2	-4.9 ± 0.4	-0.6 ± 0.2
LEM	8.2 ± 1.9	2.3 ± 2.0	85.3 ± 1.1	44.3 ± 0.6	-4.7 ± 1.1	-0.7 ± 0.6

Cape Verde in the framework of the ASKOS campaign, organized by the National Laboratory of Athens and the European Space Agency.

A retardation error of 5° is not negligible. It affects both the calibration factor of the receiver 2 of EVE and also the purity of the circularly polarized emission when placed in front of laser B. The actual calibration factor of receiver 2 can be determined by removing the QWP before the PBS which can be done for specific experiments but not operationally. However, even with the correct η, the volume circular depolarization ratio of EVE is affected by the QWP in front of the laser B. With the knowledge of the actual QWP retardation and rotation errors, it is possible to account for them in the GHK correction [1]. While this procedure is out of the scope of this study, it highlights the necessity of characterizing all lidar optics regarding their polarization behavior.

72.5 Summary

A zero-order QWP has been tested and its retardation was measured directly on field in the EVE lidar system. The QWP was found to introduce an absolute retardation error of about $5° \pm 1°$. Similar values occurred from tests with both lasers of EVE and also from measurements in the laboratory. If not accounted for, the non-ideal performance of the QWP affects the determination of the volume and particle circular depolarization ratio.

References

1. Freudenthaler, V.: About the effects of polarising optics on lidar signals and the $\Delta 90$ calibration. Atmos. Meas. Tech. **9**, 4181–4255 (2016)
2. Paschou, P., et al.: The eVe reference polarisation lidar system for the calibration and validation of the Aeolus L2A product. Atmos. Meas. Tech. **15**, 2299–2323 (2022)

Chapter 73
Investigating the Geometrical and Optical Properties of the Persistent Stratospheric Aerosol Layer Observed over Thessaloniki, Greece, During 2019

K. A. Voudouri, N. Siomos, K. Michailidis, M. E. Koukouli, G. Peletidou, and D. Balis

Abstract A persistent stratospheric layer first appeared during July 2019 above Thessaloniki, Greece (40.5°N, 22.9°E), initially at 12 km and during August 2019 even up to 20 km, with increased thickness and reduced attenuated backscatter levels. In this study, we analyze the geometrical and optical properties of this stratospheric layer, using both the ground-based multi-wavelength depolarization measurements performed with Thessaloniki's lidar system (THELISYS), which is part of the European Aerosol Research Lidar NETwork (EARLINET) and the spaceborne lidar CALIOP retrievals (Cloud–Aerosol Lidar with Orthogonal Polarization), onboard CALIPSO (Cloud-Aerosol Lidar and Infrared Pathfinder Satellite Observation). The origin of the plume is linked with the two major sources of stratospheric air pollution that were active in the summer of 2019, the Raikoke volcano eruption in the Kuril Islands and the intense forest fires at mid and high northern latitudes. Thus, in July, pure volcanic sulfate aerosol layers (particle linear depolarization ratio < 0.05) are mainly identified in the stratosphere, while in August, wildfire smoke is dominating. Temporal changes in the aerosol properties throughout the 2019 measuring period that signify changes in the composition of the long-lasting stratospheric plume over Thessaloniki are identified and discussed.

Keywords Stratospheric aerosol layer · Multi-wavelength depolarization Raman lidar measurements · Volcanic sulfate aerosol layer · Wildfire smoke · CALIPSO aerosol typing scheme

K. A. Voudouri (✉) · K. Michailidis · M. E. Koukouli · G. Peletidou · D. Balis
Laboratory of Atmospheric Physics, Aristotle University of Thessaloniki, Thessaloniki, Greece
e-mail: kavoudou@physics.auth.gr; komichai@physics.auth.gr; mariliza@auth.gr; gpeletid@auth.gr

N. Siomos
Meteorological Institute, Ludwig Maximilian Universitδt Mónchen, LMU, Munich, Germany
e-mail: nsiomos@physics.auth.gr

© The Author(s), under exclusive license to Springer Nature Switzerland AG 2023

J. T. Sullivan et al. (eds.), *Proceedings of the 30th International Laser Radar Conference*, Springer Atmospheric Sciences,
https://doi.org/10.1007/978-3-031-37818-8_73

73.1 Introduction

73.1.1 Possible Sources of the Stratospheric Layer

A persistent stratospheric layer first appeared during July 2019 above Thessaloniki, Greece, initially at 12 km and later on August 2019 even up to 20 km. In the summer of 2019, the Raikoke volcano in the Kuril Islands (48.3°N, 153.3°E) erupted on June 2, 2019, emitting ash and volcanic gases over the North Pacific [1]. Additionally, an intense wildfire activity at high northern latitudes (i.e., Alaska, Canada, Siberia) is reported during the summer and autumn of 2019. Especially intense, record-breaking wildfires in central and eastern Siberia took place, with the most intensive fire period from July 19 to August 14, 2019 [2]. Both types of events can create updrafts strong enough to penetrate the tropopause, and it is possible that both sources have contributed to the long-lasting observed aerosol plume over Thessaloniki almost till the end of 2019. The stratospheric layers first appeared on the ground-based measurements on June 11, 2019. On August 1, 2019, distinct layers were monitored in similar altitudes but with increased thickness and reduced attenuated backscatter levels. During September, the backscatter levels decreased even further while the layer thickness started growing. During October, the layer extended from 13 to 20 km.

73.1.2 Instrumentation and Dataset

The stratospheric features were monitored with THELISYS (THEssaloniki LIdar SYStem), the multi-wavelength lidar system for aerosol characterization designed and operated by the Laboratory of Atmospheric Physics in Aristotle University of Thessaloniki (LAP-AUTH). THELISYS is part of the European Aerosol Research Lidar NETwork (EARLINET) [3] since 2000 and currently is part of the Aerosols, Clouds, and Trace gases Research InfraStructure (ACTRIS; https://www.actris.eu/). It consists of three elastic channels at 355, 532, and 1064 nm, two nighttime-only Raman channels at 387 nm and 607 nm, and two depolarization channels at 532 nm (cross polarized and parallel polarized to the linearly polarized laser beam). The combined use of the analog and photon-counting mode allows for the retrieval of the aerosol optical properties from 800 m up to ~20 km above the ground. The main and basic aerosol optical properties, derivable from the lidar observations, are the particle backscatter coefficient profiles (355, 532, and 1.064 nm), the particle extinction coefficient profiles (355, 532 nm), the respective extinction-to-backscatter ratio (lidar ratio) at 355 and 532 nm, and the particle linear depolarization ratio (PLDR) at 532 nm [4, 5]. THELISYS aerosol products are publicly available at https://www.earlinet.org/.

Aerosol geometrical and optical properties were also available during the same period from satellite measurements, performed with the CALIOP lidar on

board the CALIPSO platform a dual-wavelength standard backscatter lidar with three measurement channels [6]. Its basic products are the attenuated backscatter coefficients at 532 and 1064 nm and the volume linear depolarization ratio and the particle linear depolarization ratio at 532 nm [7]. The individual backscatter coefficient profiles at 532 nm are aggregated at a vertical resolution of 60 m from −0.5 to 20.2 km and 180 m from 20.2 to 30.1 km. The following three datasets are used in this study: (i) the CALIPSO level 2 version 4 (v4) aerosol profile product (APro), (ii) the aerosol layer (Alay) product, and (iii) the vertical feature mask (VFM) product.

73.2 Results: Overview of the Stratospheric Layer

In Fig. 73.1, the evolution of the atmospheric features monitored by THELISYS can be seen during the July–October 2019 period. In total, 41 daytime and 17 nighttime measurements were performed during this period, with 12 CALIPSO overpasses in close proximity to Thessaloniki. The stratospheric layers first appeared on July 11, 2019, with low particle linear depolarization ratio. On July 31, 2019, all layers almost disappeared only to reappear the next day, on August 1, 2019 in similar altitudes but with increased thickness and reduced attenuated backscatter levels. In September, the backscatter levels decreased even further while the layer thickness started growing. In October, the layer can be seen to extend from 13 to 20 km.

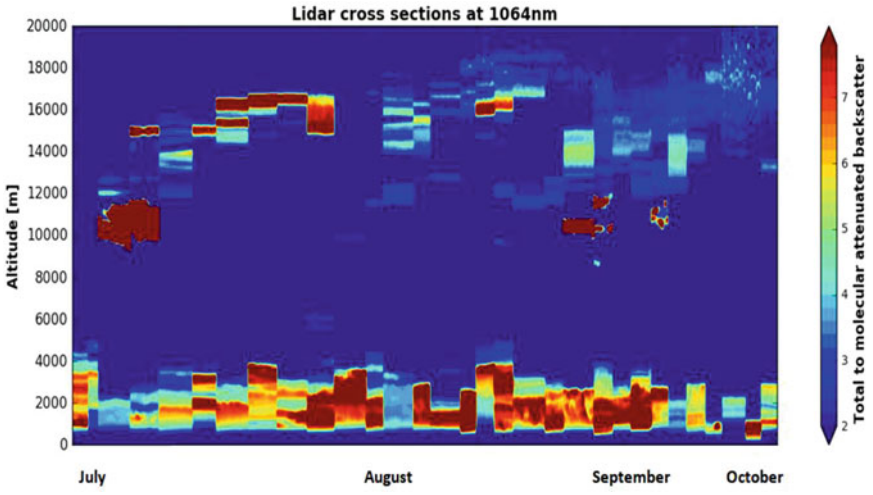


Fig. 73.1 Attenuated backscatter profiles at 1064 nm divided with the molecular profiles (normalized at 8 km) in the period between July 4, 2019 and October 21, 2019. Cases have been placed one next to the other for visualization purposes

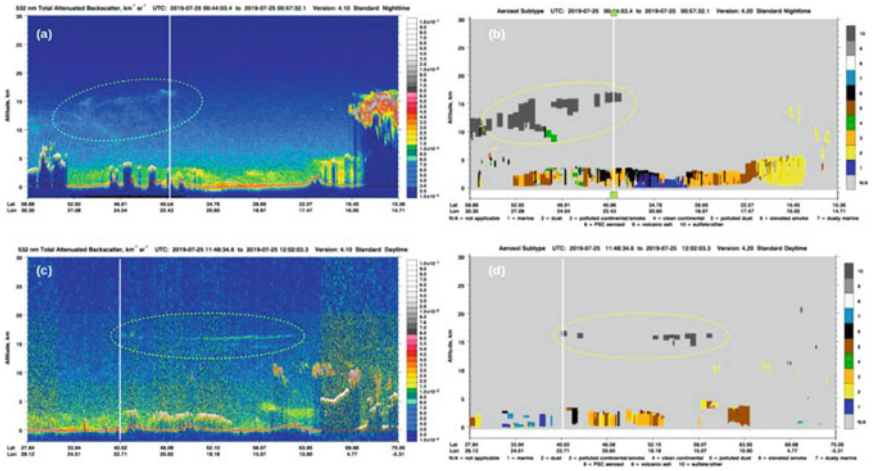


Fig. 73.2 (**a**, **c**) Attenuated backscatter coefficient at 532 nm and (**c**, **d**) atmospheric features subtyping for the CALIOP observations of aerosol and cloud layers along the flight track crossing the Greece, during day and night, CALIPSO overpasses close to Thessaloniki on July 25, 2019. The white vertical line denotes the closest track point location to Thessaloniki lidar station. Figures adapted from online figures on the CALIPSO website.

73.2.1 Geometrical and Optical Properties of the Volcanic Aerosol Layer in the Stratosphere on July 25, 2019

In Fig. 73.2, the CALIOP observations of July 25, 2019, are shown. The first overpass occurred at night (00:44:03–00:57:32 UTC) at 60.1 km distance from Thessaloniki, and the second overpass occurred during the day (11:48:34–12:02:03) at 50.3 km. Volcanic sulfate aerosol was the dominant aerosol component in the stratosphere over Thessaloniki. The attenuated backscatter coefficient shows aerosol structures between 12.5 and 17.5 km from 39 to 48°N during the nighttime overpass and between 15.6 and 16.9 km height from 40 to 43°N during the daytime overpass.

The CALIPSO aerosol typing scheme classified the layer as stratospheric aerosol layer and finally as aerosol sulfate type in Fig. 73.2b, d. These aerosol layers show low PLDR values at 532 nm (PLDR <0.075), suggesting the presence of spherical, liquid sulfuric acid-containing water droplets. The total attenuated backscatter values exhibit values of the order of 0.001–0.005 km^{-1} sr^{-1} and the mean aerosol optical depth (AOD) at 532 nm is found around 0.016.

CALIPSO aerosol vertical distributions generated by the volcanic layers are analyzed to investigate the aerosol layer boundaries. The aerosol presence and properties, including layer top and base, depolarization ratio, and AOD, are derived from the Version 4 CALIOP Level-2 5 km aerosol layer products (CAL_LID_L2_05kmALay-Standard-V4-21, NASA/LARC/SD/ASDC, 2018). Figure 73.3 shows the bottom and top altitude of the detected aerosol plumes

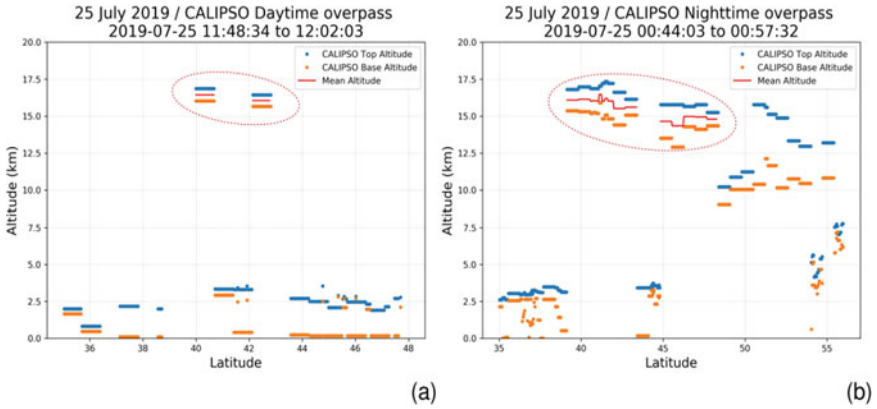


Fig. 73.3 Aerosol layer boundary retrievals (top, base, mean) from Level-2 aerosol layer product (CAL_LID_L2_05kmALay-Standard-V4–21), during the CALIPSO (**a**) daytime and (**b**) nighttime overpass. Red dashed ellipse indicates the aerosol layer plume classified as sulfate

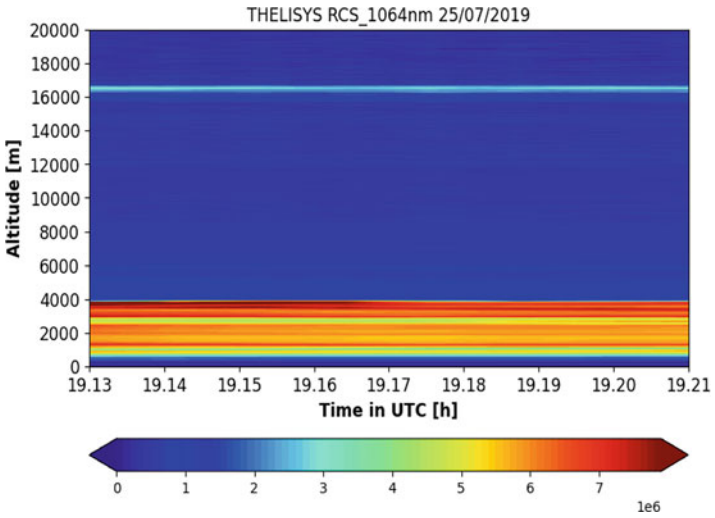


Fig. 73.4 Range-corrected signal at 1064 nm during the nighttime THELISYS measurement

where blue, orange, and red lines represent the base, top, and mean heights of the detected aerosol layers classified as sulfate by the CALIPSO algorithm scheme. Aerosol top heights of the vertically homogenous sulfate layers are found to range between 12.5 and 17.5 km.

The same aerosol plume can be seen in Fig. 73.4, which presents the 1064 nm range-corrected signal retrieved by THELISYS during 19:13 UTC to 19:21 UTC. The stratospheric layer, detected between 16.2 and 16.8 km, is persistent throughout the entire measurement period, exhibiting low depolarization values (PLDR lower

Table 73.1 Summary of the stratospheric geometrical and optical retrievals on July 25, 2019

Lidar observations	THELISYS	CALIPSO daytime overpass	CALIPSO nighttime overpass
Layer base height	16.2	16.04	15.4
Layer top height	16.8	16.44	16.68
PLDR	<0.05	<0.05	<0.05
AOD	0.0095 (1064 nm)	–	0.016 (532 nm)
Subtyping	–	Sulfates	Sulfates

than 0.05) and mean AOD at 1064 nm around 0.095. A summary of the geometrical and optical properties measured with THELISYS and CALIOP is given in Table 73.1. Both ground-based and satellite retrievals agree in terms of geometrical and optical metrics of the detected stratospheric plume over Thessaloniki.

73.3 Conclusion

Complex stratospheric aerosol conditions with simultaneously occurring volcanic and smoke layers took place in the late summer, autumn, and winter of 2019. A persistent stratospheric layer with variable geometric boundaries (from 12 up to 20 km) is monitored with a multi-wavelength depolarization Raman over Thessaloniki, Greece, starting from July 2019. The temporal evolution of the plume is further monitored by spaceborne lidar observations during the CALIPSO satellite overpasses close to Thessaloniki. We show that the CALIPSO aerosol typing identified the volcanic sulfate aerosol type on July 25, 2019 (before the Siberian smoke layer entered the stratosphere). In what follows, the microphysical properties are obtained using T-matrix simulations with refractive indexes and aspect ratios typical for biomass burning and volcanic (sulfate and/or ash) aerosols found in literature. The mixtures that best describe the optical properties of the long-lasting stratospheric plume over Thessaloniki are used as an indicator of whether the stratospheric layer is pure volcanic ash, pure aged smoke, or both.

Acknowledgments We acknowledge support of this work by the project "PANhellenic infrastructure for Atmospheric Composition and climatE change" (MIS 5021516) which is implemented under the Action "Reinforcement of the Research and Innovation Infrastructure," funded by the Operational Programme "Competitiveness, Entrepreneurship and Innovation" (NSRF 2014-2020) and co-financed by Greece and the European Union (European Regional Development Fund). The CALIPSO data used in this study were obtained from the NASA Langley Atmospheric Science Data Center 25 (https://eosweb.larc.nasa.gov/project/calipso/calipso_table).

References

1. Vaughan, G., Wareing, D., Ricketts, H.: Measurement report: Lidar measurements of stratospheric aerosol following the 2019 Raikoke and Ulawun volcanic eruptions. Atmos. Chem. Phys. **21**, 5597–5604 (2021). https://doi.org/10.5194/acp-21-5597-2021
2. Ohneiser, K., et al.: The unexpected smoke layer in the high Arctic winter stratosphere during mosaic 2019–2020. Atmos. Chem. Phys. **21**, 2021 (2021)
3. Pappalardo, G., et al.: EARLINET: towards an advanced sustainable European aerosol lidar network. Atmos. Meas. Tech. **7**, 2389–2409 (2014)
4. Siomos, N., et al.: Are EARLINET and AERONET climatologies consistent? The case of Thessaloniki, Greece. Atmos. Chem. Phys. **18**, 11885–11903 (2018)
5. Voudouri, K.A., et al.: Comparison of two automated aerosol typing methods and their application to an EARLINET station. Atmos. Chem. Phys. **19**, 10961–10980 (2019)
6. Winker, D.M., et al.: Overview of the CALIPSO mission and CALIOP data processing algorithms. J. Atmos. Ocean. Technol. **26**, 2310–2323 (2009)
7. Kim, M.H., et al.: The CALIPSO version 4 automated aerosol classification and Lidar ratio selection algorithm. Atmos. Meas. Tech. **11**, 6107–6135 (2018)

Chapter 74
New Lidar Data Processing Techniques for Improving the Detection Range and Accuracy of Atmospheric Gravity Wave Measurements

Jackson R. Jandreau and Xinzhao Chu

Abstract Lidar observations offer a valuable window into gravity waves due to their high temporal and spatial resolutions. However, second-order parameters of these waves calculated via lidar have an inherent bias. Over the years, a few methods have been developed to correct this. This study tests noise-variance subtraction, spectral proportion, and the interleaved method and compares their results using data and a forward model. Variance subtraction is found to only work on high SNR data, spectral proportion works with high- to mid-SNR data, and interleaved works on all data but requires more data to reliably use.

Keywords Atmospheric waves · Data processing techniques · Variance/flux

74.1 Introduction

Lidar observations pose one of the most feasible routes to introduce new, meaningful information into studies of atmospheric gravity waves (GW). The high-resolution and wide vertical coverage that lidar offers cannot be matched using other instruments. Ground-based radar and satellite measurements of these parameters are often either too sparse in coverage or low resolution to resolve much of the GW spectrum. As GW energy coupling is a developing area of study, lidar measurements of GW are necessary to develop new theories and keep these theories grounded in observations.

When studying atmospheric GWs, many dynamic factors rely on second-order parameters like variances, fluxes, and spectra. GW second-order parameters inherently contain a positive bias when calculated directly from lidar data. While mean-zero noise is typically eliminated when averaging first-order parameters, these

J. R. Jandreau (✉) · X. Chu
CIRES, University of Colorado Boulder, Boulder, CO, USA
e-mail: jackson.jandreau@colorado.edu; xinzhao.chu@colorado.edu

© The Author(s), under exclusive license to Springer Nature Switzerland AG 2023

J. T. Sullivan et al. (eds.), *Proceedings of the 30th International Laser Radar Conference*, Springer Atmospheric Sciences,
https://doi.org/10.1007/978-3-031-37818-8_74

second-order parameters are biased by it. This bias often obscures or even entirely prevents the interpretation of results, making it difficult to develop a full picture of GW activity. Over the years, techniques have been developed to compensate for or eliminate the bias, extending the lidar GW studies to higher altitudes and enabling observations to be made in much lower signal-to-noise ratio (SNR) environments.

Atmospheric variances and fluxes are valuable GW-related quantities upon which a lot of valuable research is being done. Variance, for example, is a quantity used in calculating GW potential energy density (E_{pm}) and is calculated from temperature or atmospheric density, represented here as r, by

$$\mathrm{Var}\left[r'_{\mathrm{Total}}(z)\right] = \overline{\left[r'_{\mathrm{Total}}(z,t)\right]^2} = \overline{(r'+\Delta r)^2} = \overline{(r')^2} + \overline{(\Delta r)^2} + \overline{2r'\Delta r}, \tag{74.1}$$

where r'_{Total} is the observed perturbation in the data, r' is perturbation due to atmospheric fluctuations, Δr is perturbation due to random noise in the signal (i.e., shot noise, instrumentation noise), and the overbar represents a sample time average over the observation. There are different approaches to calculating the perturbations, but all start by subtracting the time-mean background. Then, spectral filtering can be applied to tune the spectra of waves in the signal and remove residual background [1]. Eq. 74.1 shows that variance consists not only of the square of r' (the quantity of interest) but also on the cross-term between these two perturbations and the square of Δr. While the cross-term trends toward zero under sufficient averaging due to non-correlation, the noise-term will remain, constituting the previously discussed bias. The noise term is typically reduced when averaging first-order parameters, yet the square in the variance forces positivity in these terms leading to no cancellation upon averaging. It is this bias that obscures variance without the use of a correction method.

The three methods of bias removal explored here are called noise-variance subtraction, spectral proportion, and the interleaved method. The noise-variance subtraction method [2] calculates and subtracts the noise bias from Eq. 74.1. While it performs well under high SNR, low SNR can result in the correction being greater than the total variance, giving a physically meaningless negative variance. The spectral proportion method was developed [1] to prevent negative variance. This method uses a Monte Carlo simulation informed by the parameter error (δr) to estimate the proportion of r'_{Total} 's spectrum due to random noise. This proportion is used to scale down $\mathrm{Var}\left[r'_{\mathrm{Total}}\right]$, resulting in a near-biasless variance. Yet, forward modeling shows that this method can overestimate in low SNR due to algorithmic inconsistencies in finding the proportion. The interleaved method [3] is able to eliminate the bias at the cost of precision. This method is more effort to apply, requiring the data to be split into two discrete sets and processed adjacently. The two sets of perturbations are rejoined via their covariance, but the data splitting causes an SNR drop and thus a precision drop.

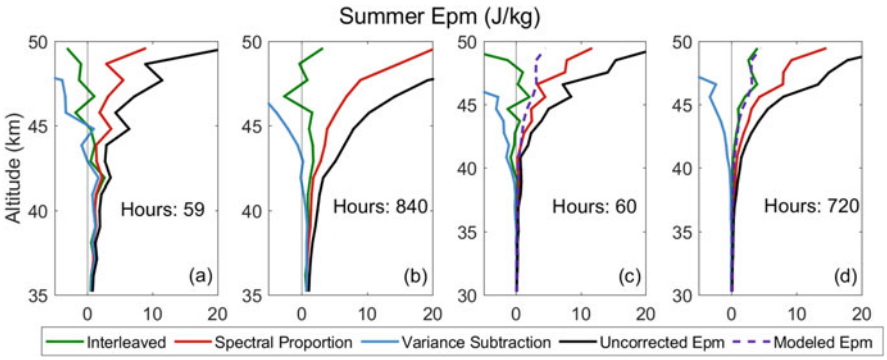


Fig. 74.1 Epm calculated from (**a**, **b**) small and large lidar data vs (**c**, **d**) small and large model data

74.2 Methodology

This McMurdo data uses temperature (T) for its r. Figure 74.1a, b show a comparison of each method applied to real lidar data taken over 10 years at the McMurdo Station [4]. This data was taken during the polar summer and thus represents a low SNR case, emphasizing the effects of the biases. E_{pm} is used to interpret wave strength and assess GW vertical development and is calculated by

$$E_{pm}(z) = \frac{1}{2}\left[\frac{g(z)}{N(z)}\right]^2 \cdot \frac{Var[r'(z)]}{r^2_{Bkg}(z)}, \tag{74.2}$$

where $N^2(z)$ is found by typical procedures [5]. Epm is used for this study due to its direct relation to variance making it optimal to demonstrate these methods. To understand the differences seen in Fig. 74.1, one must analyze their calculation.

74.2.1 Noise-Variance Subtraction (VS)

This method has long been the go-to for bias removal, being used for decades in atmospheric dynamics studies to calculate variance and flux properties. However, the need to advance accuracy and extend data usability has revealed issues with the simplicity of the approach. The noise-variance calculated by this method is

$$\mathrm{Var}_{\mathrm{VS}}[\Delta r(z)] = \overline{\Delta r(z,t)^2} = \frac{1}{k}\sum_{i=1}^{k}[\delta r(z,t_i)]^2, \tag{74.3}$$

and is incorporated into a corrected Epm by

$$E_{pm,VS}(z) = \frac{1}{2}\left[\frac{g(z)}{N(z)}\right]^2 \cdot \frac{\mathrm{Var}[r'_{\mathrm{Total}}(z)] - \mathrm{Var}_{\mathrm{VS}}[\Delta r(z)]}{r^2_{Bkg}}. \tag{74.4}$$

Expectedly, the noise-variance can become large under low SNR, and when it exceeds the variance of the wave perturbations, the method fails and results in negative variances. Figure 74.1 shows that the VS method actually begins to show a decreasing Epm before the values become negative; it fails gradually by an underestimation which increases with altitude. This makes the VS method somewhat dangerous as underestimated results may not be recognizable as such.

74.2.2 Spectral Proportion (SP) Method

This method, as mentioned prior, was developed to prevent negative trending under high-noise environments. This approach is more computationally expensive than the other two approaches, yet it is able to significantly reduce the effects of the noise bias. To implement the SP method, the time-altitude grid of data $r(z, t)$ is duplicated 1000 times. To each of these copies, normally distributed random noise is added with a standard deviation equal to the δr at that (z, t). Then, for each copy, a 1-D FFT is calculated for each altitude, and the spectra are averaged for that altitude over all 1000 runs. This yields a spectrum with a noise floor for each altitude. Various approaches can be used to calculate this noise floor, but the most reliable is to find the average of all minima at frequencies greater than 0.1 hr^{-1} while omitting the highest minima (to avoid minima above the noise floor). For each altitude, the proportion of wave energy occupying the total energy is calculated from the average spectra as

$$p(z) = \frac{\text{Area under curve} - \text{Area under noise floor}}{\text{Area under curve}}. \tag{74.5}$$

As the altitude increases (thus the SNR decreases), the noise floor rises and thus this proportion $p(z)$ decreases, and the $p(z)$ is used to calculate Epm by

$$E_{pm,SP}(z) = p(z) \cdot E_{pm,\mathrm{Total}}(z). \tag{74.6}$$

However, Fig. 74.1 shows disagreement between the methods under the high-noise higher altitudes. This is likely due to the nature by which the noise floor is determined. At high altitudes, the noise in the signal becomes strong and disrupts the averaged 1-D FFT, sporadically adding strong noise peaks to the spectra, complicating efforts to find the noise floor. If the noise-floor detection algorithm incorrectly identifies noise in the spectrum as a wave, it will underestimate $p(z)$ resulting in an under-corrected (overestimated) Epm. This could likely be corrected with a more robust noise floor detection algorithm, but the discrimination of a wave peak from a noise peak is very difficult. Possibility for overestimation aside, the SP method is generally effective at correcting for bias over a wide range of altitudes,

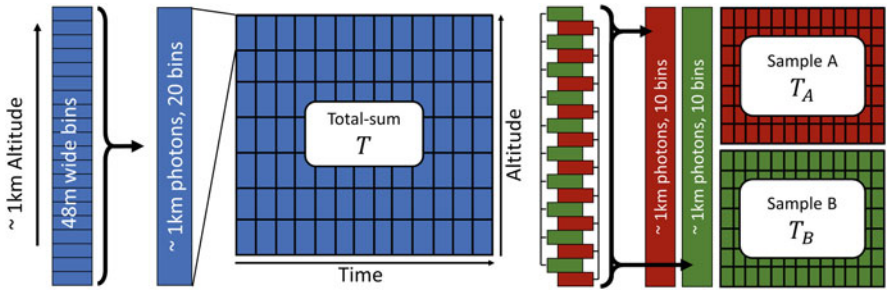


Fig. 74.2 Differences between traditional photon binning (left) and interleaved binning (right)

preventing negative values and agreeing with the interleaved method when used under the right conditions (discussed in Sect. 74.2.4). Figures detailing this method can be found in [1, 5].

74.2.3 Interleaved Method

This method begins before the photon counts are turned into atmospheric parameters, as opposed to the others which can be applied to the parameters themselves. The interleaved method relies on the fact that random noise perturbations (shot or instrument) are mean-zero and uncorrelated with both wave perturbations and other noise signals. To begin applying this method, the signals are split into two distinct samples, alternating in either time or altitude bins (see Fig. 74.2). Essentially, the decision to interleaved in time or altitude should be made with consideration to whichever allows the two samples to represent the most similar (z, t) space as possible, as this will improve accuracy (discussed in Sect. 74.2.4). Each of these samples will share no photon counts, and thus the random noise within will be entirely uncorrelated while the wave perturbations (as the photons are from the same spatiotemporal atmospheric parcel) should self-correlate extremely well. This method could also be done with two independent lidars placed adjacently, yet splitting the data into two samples via the interleaved approach only requires a single lidar. If done using two lidar systems, the wave perturbations could be guaranteed to be extremely well correlated (same spatiotemporal parcel) with no reduction in photon counts. The covariance of these samples is

$$\begin{aligned} &Cov\left[r'_{A,\text{Total}}\left(z_A\right), r'_{B,\text{Total}}\left(z_B\right)\right] \\ &= \overline{\left[r'_A\left(z_A,t\right)\cdot r'_B\left(z_B,t\right)\right]} + \overline{\left[r'_A\left(z_A,t\right)\cdot \Delta r_B\left(z_B,t\right)\right]} \\ &+ \overline{\left[r'_B\left(z_B,t\right)\cdot \Delta r_A\left(z_A,t\right)\right]} + \overline{\left[\Delta r_A\left(z_A,t\right)\cdot \Delta r_B\left(z_B,t\right)\right]} \end{aligned} \tag{74.7}$$

where the latter three terms will drop from the equation due to uncorrelation (with a sufficient sample size), leaving only wave-induced variance, processed into E_{pm} as

$$E_{pm,\mathrm{INT}} = \frac{1}{2}\left[\frac{g(z)}{N(z)}\right]^2 \cdot \frac{Cov\left(r'_{A,\mathrm{Total}}, r'_{B,\mathrm{Total}}\right)}{r_{Bkg}(z)^2}. \tag{74.8}$$

Departures of this covariance from an idealized wave-induced variance can be present as an overestimation of wave-variance caused by using too small of a sample size (as the latter three terms of Eq. 74.7 have not sufficiently approached zero) and an underestimation of wave variance (the first term in Eq. 74.7) due to uncorrelation in r' terms caused by not interleaving the samples finely enough. By interleaving finely and averaging over a sufficient sample size ("sufficient" being dependent on data SNR), the bias is statistically eliminated.

74.2.4 Uncertainty Analysis: Accuracy

To assess these methods, one must also consider their uncertainty. This is done by looking at the precision and accuracy of each method. Precision here is defined in two ways, the precision of the measurement due solely to noise in the data and precision of the data due to both noise and factoring in how well the data sample statistically represents the signal it is estimating. Gardner and Chu [3] and Jandreau and Chu [5] explain this statistical error in detail as the precision equations and values have been left out of this publication for brevity.

The accuracy of these methods can be assessed by comparing them to a forward modeled set of Epm measurements as shown in Fig. 74.1c, d. The forward model was created by simulating summer and winter photon counts with realistic noise in an atmosphere perturbed by waves of known parameters replicating those observed in the McMurdo data. These counts were processed such that a "true" Epm value could be calculated (the "modeled" profile in Fig. 74.1c, d). The result of each method is then compared to the "true" Epm in the simulated field. The VS method underestimates the Epm regardless of sample size, the SP overestimates but performs better with a small sample size, and INT approximates well but only with sufficient samples.

74.3 Conclusions

A researcher intending to implement these methods could utilize any of the three, yet the ultimate question is which one to use in each case. Looking at the performance of the variance subtraction method in Fig. 74.1, this method should only be used for data which is very confidently high SNR. In low altitudes, or in winter data (see [5]), this method performs decently well but is nearly always outperformed by the

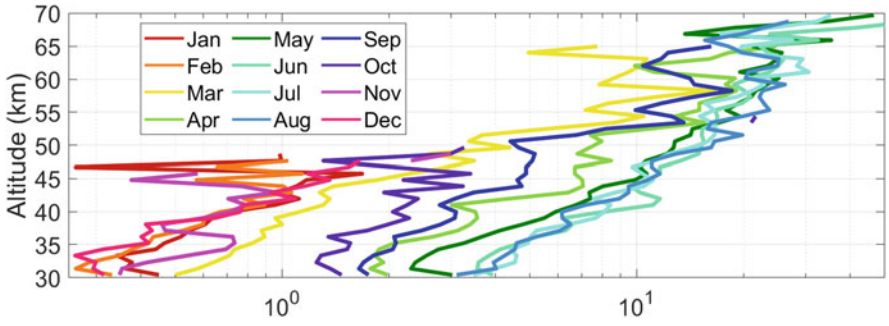


Fig. 74.3 Monthly average E_{pm} (J/kg) from 2011 to 2020 with their well-known seasonal asymmetry

other two. The only benefit to applying this method is that it is easy to implement and computationally cheap. The SP method on the other hand is effective into the mid-SNR range, providing reasonable bias removal in most cases with consistent results regardless of the size of data used. In the case that sufficient data is available, the interleaved method provides the most reliable bias removal. If a small set of data is processed however, the interleaved method can yield negative values (see Fig. 74.1). Even with a large sample size, low SNR data (upper Fig. 74.1b) can still yield negative values, so caution should be taken with applying all methods, as each has its advantages and drawbacks.

To demonstrate their performance, these methods were used to extend the McMurdo lidar's measurements to include year-round Epm calculation for the stratosphere and to reach higher into the mesosphere, shown by the interleaved method in Fig. 74.3.

References

1. Chu, X., et al.: Lidar observations of stratospheric gravity Waves from 2011 to 2015 at McMurdo (77.84°S, 166.69°E), Antarctica: 2 potential energy densities, lognormal distributions, and seasonal variations. J. Geophys. Res Atmos. **123**(15), 7910–7934 (2018)
2. Whiteway, J.A., Carswell, A.I.: Lidar observations of gravity wave activity in the upper stratosphere over Toronto. J. Geophys. Res. **100**(D7), 14113 (1995)
3. Gardner, C.S., Chu, X.: Eliminating photon noise biases in the computation of second-order statistics of Lidar temperature, wind, and species measurements. Appl. Opt. **59**(27), 8259–8271 (2020)
4. Chu, X., Yu, Z., et al.: Lidar observations of neutral Fe layers and fast gravity waves in the thermosphere (110-155 km) at McMurdo (77.8°S, 166.7°E), Antarctica. Geophys. Res. Lett. **38**, L23807 (2011)
5. Jandreau, J., Chu, X.: Comparison of three methodologies for removal of random-noise-induced biases from second-order statistical parameters of Lidar and radar measurements. Earth Space Sci. **9**, e2021EA002073 (2022)

Chapter 75
Extending the Useful Range of Fluorescence LIDAR Data by Applying the Layered Binning Technique

Gary W. S. Sutliff and Xinzhao Chu

Abstract Temperature and wind measurements in the mesosphere and lower thermosphere (MLT) can be obtained from resonance fluorescence LIDARs utilizing the principles of Doppler effects or Boltzmann distributions. The calculations for determining temperature and wind speed from photon counts are more sensitive to noise than simply determining density, so a more limited range is available for observations. The traditional approach for extending the observation range is to increase the bin size used for the calculations, by integrating over a larger altitude range, time range, or both. However, a larger bin size will limit the resolutions and small details will be missed. The layered binning technique is a data analysis method that extends the range of observation while keeping much of the fine detail. This technique is able to increase the range of observations by dynamically adjusting the binning in areas of low signal or high noise. Examples of using this technique have been able to extend the range of temperature and wind speed measurements by nearly 45%.

Keywords LIDAR · Temperature · Wind · Data analysis

75.1 Introduction

Resonance fluorescence LIDARs have become a common tool for measuring constituent concentrations, temperatures, wind velocities, and atmospheric fluxes in the upper atmosphere, particularly in the mesosphere and lower thermosphere (MLT) where the atmospheric metal layers form [1]. The temperature, wind speed, and flux measurements are made possible by using narrow-band lidar systems that are capable of distinguishing physical processes such as Doppler broadening and

G. W. S. Sutliff (✉) · X. Chu
Cooperative Institute for Research in Environmental Sciences and Department of Aerospace Engineering Sciences, University of Colorado Boulder, Boulder, CO, USA
e-mail: gary.sutliff@colorado.edu; xinzhao.chu@colorado.edu

© The Author(s), under exclusive license to Springer Nature Switzerland AG 2023

J. T. Sullivan et al. (eds.), *Proceedings of the 30th International Laser Radar Conference*, Springer Atmospheric Sciences,
https://doi.org/10.1007/978-3-031-37818-8_75

shift or Boltzmann distributions [2, 3]. However, calculations for temperatures and winds (as well as flux that depend on those) are more sensitive to noise than determining constituent densities directly from photon counts [4]. This sensitivity limits the range over which the temperatures and winds can be calculated to areas with high densities of the target constituents.

A standard approach for increasing the signal to noise ratio and extending the range for temperature and wind speed measurements is to increase the bin size used in the calculation by integrating over a larger time range, altitude range, or both. The reason for this can be demonstrated by looking at the temperature ratio used for calculating temperature [1], as shown in Eq. 75.1, where N_+ is the photon counts for the positive shifted laser return signal, ΔN_+ is the noise for the positive shifted signal, and N_- *and* N_a correspond to the negative shift and center frequency. As bin sizes get larger, the return signal will get larger while noise can be positive or negative. If a return signal is too small, the ratio could end up being a negative number which results in not being able to calculate the temperature:

$$R_T = \frac{(N_+ + \Delta N_+) + (N_- + \Delta N_-)}{(N_a + \Delta N_a)} \tag{75.1}$$

However, by using this approach, the extended range comes at the cost of having a lower resolution, which can hide finer features in the data set. Another common method is to use a default value for wind speed and temperature when they cannot be calculated; this is normally done at points where the data is just reaching the limit of the signal to noise ratio to fill in sporadic missing data points; this method tends to skew the data toward the chosen default values for the temperature and wind speed, which could be somewhat hidden when using a smoothing function on top of it. The layered binning technique is a solution that enables higher resolution in an extended data range without skewing the data toward default values.

75.2 Methodology

The core concept behind the layered binning technique is binning the data in multiple resolutions and then using the temperature and wind speed values calculated with the larger bins as the default values to replace bad data in the higher resolution bins. This technique is iterative with the temperature and wind speeds being calculated for the largest bin size first. For each consecutive layer of smaller bin sizes, the corresponding default value substitution takes place for any bin in which temperature or wind speed cannot be calculated. A graphical representation of this is shown in Fig. 75.1, where the white squares in the left figure represent bins with bad data and those same bins are shown in the right figure after the default value from the larger bin is substituted in. This is then repeated for each bin size iteration down to the smallest bins which allow for high resolution observations.

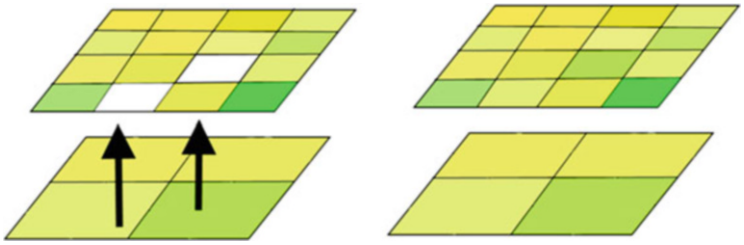


Fig. 75.1 (left) Representation of two binning layers with the larger inputting default values into the smaller bins. (right) Binning layers after substituting the values

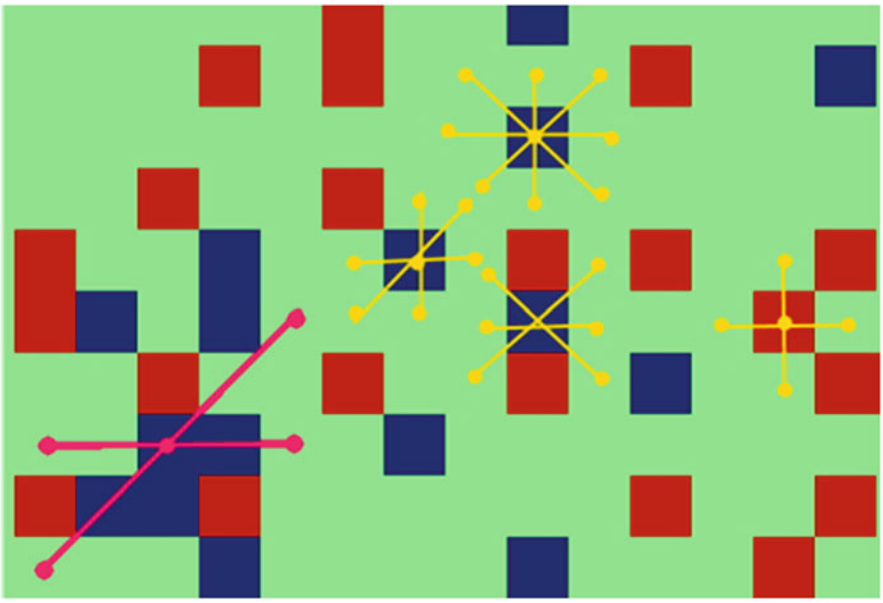


Fig. 75.2 Graphical representation of using interpolation for replacing bad data

Additionally, after each consecutive layer is generated, a second algorithm runs through the bins to find bins that have bad data but did not get a new default value due to the corresponding bins in the previous layer also having bad data. These bins then go through a limited interpolation, in which interpolation only takes place if the bin with bad data has a set of good data points on each side of it. Graphical representation of the interpolation is shown in Fig. 75.2, with green bins representing good temperature and wind data, red representing bad temperature data, and blue representing bad wind data. The yellow and pink lines in Fig. 75.2 represent sets of data points that are used for interpolation, which is generally done for bins directly adjacent as shown by the yellow lines but could also be extended out as shown by the pink lines. If more than one set of adjacent bins exist, they

are all used to find a more probable average. The averaging that takes place from interpolating bins also contributes to an apparent reduction in resolution in regions where many bins require interpolation since smaller features may be obscured.

The interpolation step is needed after each composite layer is generated, since as each time a higher resolution layer is added, there tends to be some bins in the higher resolution data that can be calculated that correspond with bad bins at the lower resolution layer. This could allow some of the lower resolution layers bad bins to appear to fill in throughout the iterative process.

The end result of this approach is higher resolution data layered on top of the lower resolution data, where at any point the highest resolution possible is used. However, a downside to this method is that as the measurements move further into the extended range, resolution will start to degrade.

75.3 Results

Progression through the layering algorithm can be seen by snapshots of multiple layers in Fig. 75.3. The figure at the top-left corner uses the largest binning (i.e., the lowest resolution) which are 7.68 km by 32 min. Figures of each consecutive layer, building off the previous generate layer, can be seen by following the images counterclockwise, with the bottom-left figure layering on bins of 1.92 km by 16 min, the bottom-right figure layering on bins of 480 m by 8 min, and the top-left figure layering on the highest resolution bins of 120 m by 4 min.

This method has been shown to significantly extend the useful range of analysis compared to temperature calculations that do not use layered binning. This can be seen by comparing the layered binning results with a maximum resolution of 120 m by 4 min (Fig. 75.4 (right)) with temperature calculations with a fixed resolution of 120 m by 4 min (Fig. 75.4 (left)). The layered binning provides results from 75 to 140 km, whereas the fixed resolution results only provide results from 75 to 120 km. This is an increase of nearly 45% in total range. The lower resolution as the layered binning figure (right) gets close to 140 km is evident, and some fine features may be lost as it approaches the altitude limit.

75.4 Conclusion

The layered binning technique appears to have significant potential by extending the observable range of LIDAR temperature and wind data in the MLT region of the atmosphere by nearly 45%. Further work to expand this technique to replace values when error calculations are above a set limit, rather than just when temperature and wind speed are not able to compute, would add additional usefulness but would cut back on the extension of the range. Additionally, work still needs to be done to verify the algorithms are indeed extending useful observations and not just

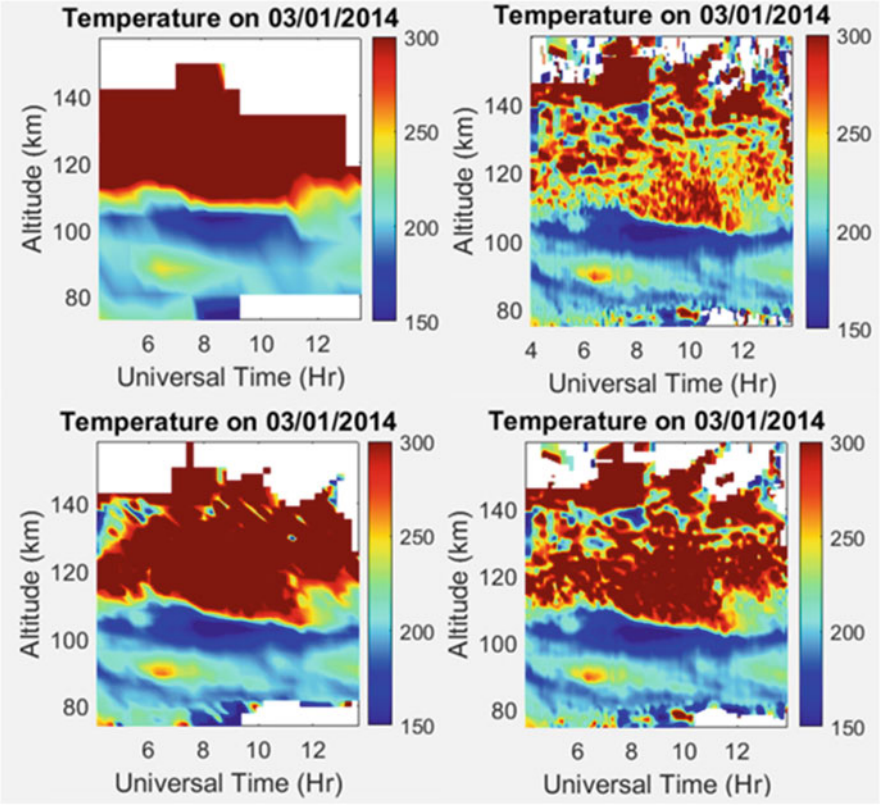


Fig. 75.3 Temperature data progressing through binning algorithm staring in top-left and moving counterclockwise

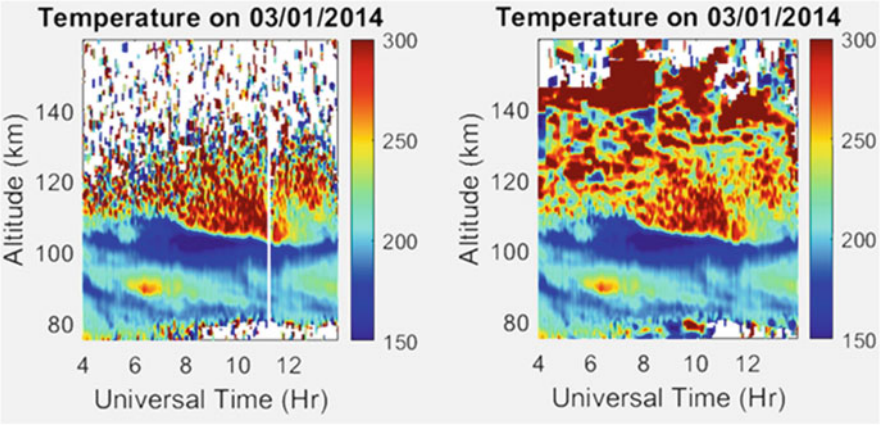


Fig. 75.4 (left) Temperature measurements without use of the layered binning technique. (Right) Same temperature data with using the layered binning technique.

amplifying noise. Wave features with coherent phase progression are indicators of real temperature and wind measurements, instead of noise. Comparing the wave parameters extracted from the extended temperature measurements with those from the Na density data would help such verifications.

References

1. Chu, X., Papen, G.: Chapter 5: Resonance fluorescence Lidar for measurements of the middle and upper atmosphere. In: Laser Remote Sensing. CRC Press, Boca Raton (2005)
2. She, C.Y., Latifi, H., Yu, J.R., Alvarez, R.J., Bills, R.E., Gardner, C.S.: Two-frequency Lidar technique for mesospheric Na temperature measurements. Geophys. Res. Lett. **17**(7), 929–932 (1990)
3. Chu, X., Pan, W., Papen, G., Gardner, C.S., Gelbwachs, J.: Fe Boltzmann temperature LIDAR: design, error analysis, and initial results at the North and South poles. Appl. Opt. **41**, 4400–4410 (2002)
4. Gardner, C.S., Chu, X.: Eliminating photon noise biases in the computation of second-order statistics of Lidar temperature, wind, and species measurements. Appl. Opt. **59**(27), 8259–8271 (2002)

Part VII
Measurement Techniques and Observations of Ocean Properties

Chapter 76
Interaction Between Sea Wave and Surface Atmosphere by Shallow Angle LED Lidar

Tatsuo Shiina, Kosuke Okubo, Nofel Lagrosas, and Alifu Xiafukaiti

Abstract Interaction between the sea surface and the lower atmosphere is important. Especially in the shore, such interaction becomes more fruitful but complex because the sea wave dynamics and wind will mix in the interaction. It is worthwhile to monitor such interaction for geophysics, marine science, and technologies for revetment and boat maneuver. In this study, we focused on the above interaction monitoring and its visualization. The LED-based mini-lidar is developed to visualize the interaction. To follow the high temporal and spatial dynamics in the shore, the LED lidar system has the high resolutions' performance of 0.2 s summation time and 0.15 m spatial intervals. We have been continued the field experiments in an inland sea (Tokyo bay) and oceans (Pacific ocean). The wave motions are confessedly different linking to the sea floor orientation, tide current, and weather. The LED lidar system set to the near horizontal direction at shallow angle. The interactions between the sea wave and the wind have been captured under the several weather conditions and observation locations. By the synchronized measurement with weather sensor, the sea wave dynamics are discussed with the wind profile.

Keywords LED lidar · Sea wave · Shallow angle · Interaction

76.1 Introduction

Interaction between the sea surface and the lower atmosphere is important not only for water circulation of the Earth but also for the transportation of minerals which includes sodium chloride, certain gases, and so on. Especially in the shore, such interaction becomes more fruitful but complex because the sea wave dynamics and wind will mix to the interaction. It is worthwhile to monitor such interaction for

T. Shiina (✉) · K. Okubo · N. Lagrosas · A. Xiafukaiti
Chiba University, Chiba, Japan
e-mail: shiina@faculty.chiba-u.jp; kobo0404the25th@chiba-u.jp; nofel@chiba-u.jp; xapkat_alip@chiba-u.jp

© The Author(s), under exclusive license to Springer Nature Switzerland AG 2023

J. T. Sullivan et al. (eds.), *Proceedings of the 30th International Laser Radar Conference*, Springer Atmospheric Sciences,
https://doi.org/10.1007/978-3-031-37818-8_76

geophysics, marine science, and technologies for revetment and boat maneuver. Up to now, the plural reports have been mentioned about the sea wave monitoring, while the above interaction between the sea wave dynamics and wind is not fully discussed [1–3].

In this study, we focused on the above interaction monitoring and its visualization. The LED-based mini-lidar is developed to visualize the interaction. The whole lidar system is compact and drive with DC buttery to operate it on shore. To follow the high temporal and spatial dynamics of sea wave in the shore, shallow angle observation is conducted with this LED mini-lidar. The interactions between the sea wave and the wind have been captured under the several weather conditions and observation locations. We discuss the sea wave echo analyses and its interactions under those weather conditions.

76.2 LED Mini-Lidar for Shallow Angle Sea Wave Measurement

The specification of the LED mini-lidar is summarized in Table 76.1. The lidar optics is biaxial type which specializes in short-range sea wave measurements. The transmitting LED power is improved to replace the LED pulse drive circuits from the multi-vibration circuits to the new circuits with Avalanche break-down effect of transistor. The optical output power is increased 15 W from <1 W, and pulse width is shortened from 10 ns to 5 ns. The receiver optics is the same with the former report [4–6], while the two detectors are set with orthogonal polarization as P and S.

The spectrum of the sea wave that we usually observe is from 0.1 to 1 Hz. To capture the characteristics of sea wave of 1 Hz, the measurements must be made repeatedly at least with the time period of less than 0.5 s. To follow its high temporal and spatial dynamics in the shore, the LED lidar system has the high resolutions'

Table 76.1 LED mini-lidar for wave observation

Transmitter	
LED pulse power	750 mW–> 15 W
Wavelength	385 nm
Beam diameter	50mmϕ
Beam divergence	10mrad
Repetition frequency	450 kHz–> 250 kHz
Receiver	
Telescope	Cassegrain
Diameter	127mmϕ
Field of view	<5mrad
Interference filter	$\lambda_0 = 385$ nm and $\Delta\lambda = 10$ nm
Detector	Photomultipliers for P/S



Fig. 76.1 Observation sites

performance of 0.2 s summation time and 0.15 m spatial intervals. It is accomplished by the originally developed high speed photon counter.

This lidar setup is good for the shallow angle measurement of 0–10° in depression angle. The transmitting beam has the larger divergence than the receiver's field of view, and they are overlapped from a few meters ahead to 300 m. The interaction between the sea wave dynamics and wind activities is monitored with this shallow angle lidar measurement.

The observation sites are located at an inland sea side (site 1: Kemigawa, Chiba, 35.6257° N, 140.0512° E) and Pacific ocean side (site 2: Sotokawa, Chiba, 35.6949° N, 140.8576° E) in Chiba, Japan, as shown in Fig. 76.1. In general, the inland sea has gentle and repetitive waves, while the ocean has rough waves. Each side sea wave is caused by tide, tide current, and wind activities.

76.3 Observations

Figure 76.2 shows the observation results of ocean waves at site 2, Sotokawa, on 27 December 2021. The wind direction was northwest. The depression angle was 10° at the shore. The path range was calculated with time of flight of lidar beam. The horizontal axis is time (JST) and the vertical axes are path range [m] on the left and wave speed [m/s] on the right. Color bar represents signal counts. The dispersed signals from the atmosphere are appeared at 4–7 m. The repetitive echoes at 9–17 m are sea wave echoes. Each wave echo has a slant line of right downward due to running to the shore. The pink colored marks represent the sign to exceed a certain threshold of wave echo counts to calculate the wave speed, that is, it is calculated with the slope of the wave echo length in its period. The white bars in the upper side of the graphs show the wind speeds. The same wave motions are captured on P and S polarization echoes, while the s-polarized echoes have more frequent signals than p-polarized echoes. Two wave echoes are observed in the period of 10–15 m. Their interval are 3 m. The strong wind brew at 20:36 caused those two wave combinations, and it is appeared as the inverse slant of right upward. This motion is

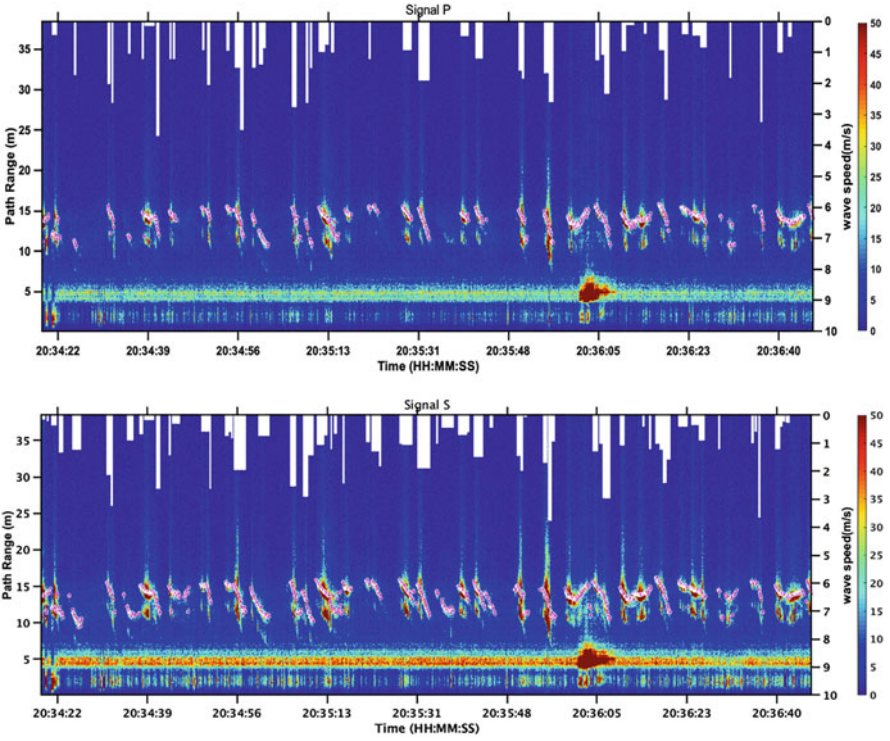


Fig. 76.2 Sea wave observation results at site 2: Sotokawa at 20:34–20:36 (JST) on 27 December 2021. Orthogonal polarizations of (**a**) P polarization and (**b**) S polarization

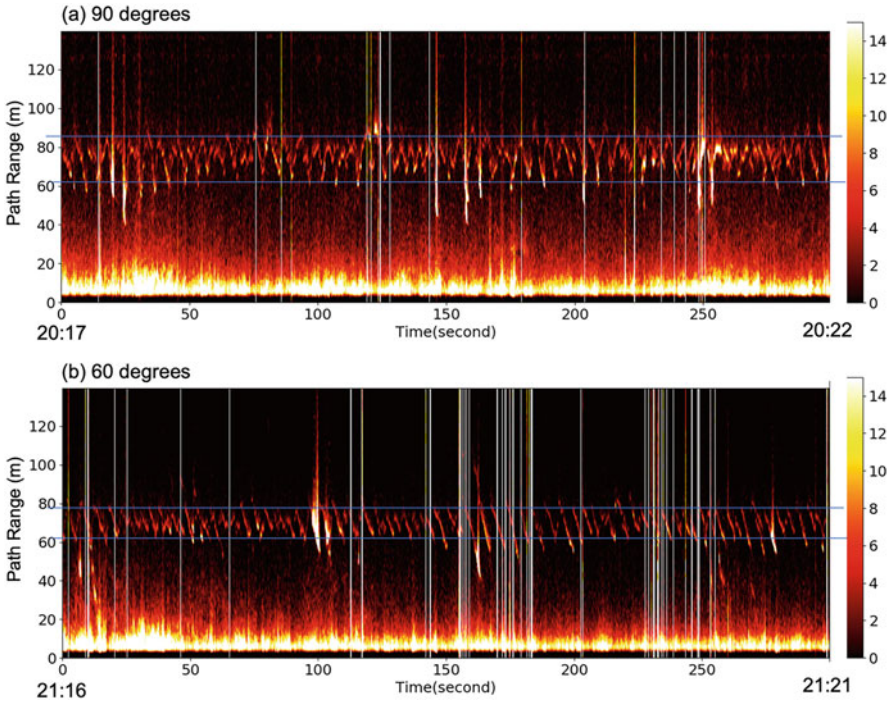


Fig. 76.3 Sea wave observation results at site 1: Kemigawa at 20:17–20:22 and 21:16–21:21 (JST) on 27 December 2021. Lidar sight directions of (**a**) perpendicular and (**b**) 60° against the wind direction

caused when the latter wave withdraw the former wave. The same motion is repeated twice on the following waves. The wind direction of northwest was contrary wind against the sea wave running direction.

Depolarization is discussed with these results. The average value of depolarization at 10–15 m is 0.933. The depression angle of 10° takes the incident angle of 80° to the sea surface. It is maximum difference between P and S polarizations in theory. We discuss them statistically and each wave motion.

Figure 76.3 shows the observation results of inland sea at Kemigawa in 11 December 2017. The observation position is an estuary. The day was strongly windy, and the sea wave was rough, too. The average wind was 7.18 m/s and its direction was southwest. The depression angle of the lidar setup was 3°. The running directions of wave and wind are perpendicular and 60° against the lidar sight direction. Figure 76.3a shows the orthogonal lidar setup against the wind direction. The periodic waves are observed. With this set-up, we can estimate the wave height with the depression angle, that is, the wave motion echoes are caused by the vibration of the wave at the fixed position on the wind direction. It is calculated as 1.0–1.3 m.

With the slant path observation at 60° in Fig. 76.3b, wave speed can be estimated. The wave echo vibration includes the wind direction vector, and it is calculated as 3.44–3.58 m/s.

76.4 Discussions

The shallow angle observation with LED mini-lidar can estimate the fundamental wave profile of wind speed, height, wavelength, period, and so on. Additional information is deduced with the long-term observation. The tide current is estimated by monitoring the sea surface level. FFT analysis is effective to catch wave dynamics. Not only the periodic motion of wave is monitored, but the ripple on the sea surface and mixed waves of plural directions are distinguished, too. The depolarization analysis reflects the wave front features against the incident angle of lidar transmitting beam. It also deduces the wave feature dynamics by following up its temporal change.

The shallow angle observation can enlarge the wave vibration, and its echo motions reflect their details. It frequently represents their ripples, while the periodic echoes in long-term observation indicates the marks interacted with temporal winds.

Figure 76.4 shows the wave speed variation due to the depression angle. As the depression angle increases in the shallow angle observation, the observed wave reaches to the lidar, that is, the wave reaches to the shore. The wave height increases because the sea depth is getting shallow. The variation of the wind speed in shallow angle observation reflects the sea depth profile in local sea area. Such information is useful for auto navigation of a vessel and leisure applications.

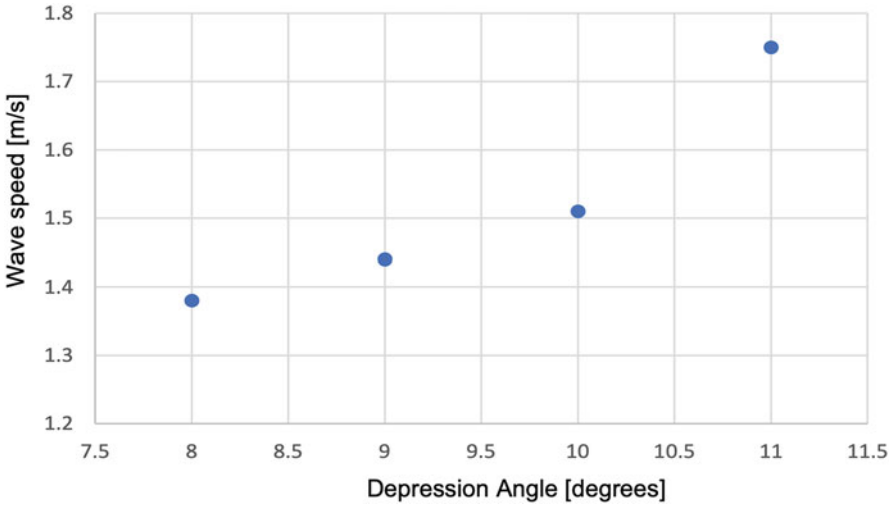


Fig. 76.4 Wave height variations in depression angle under the shallow angle observation with LED mini-lidar

76.5 Summary

In this study, we have been developed a LED-based mini-lidar to monitor sea wave fundamental profiles and to deduce additional information of wave dynamics interacted with winds. This time, wave motions are compared at the observation sites in an inland side and ocean side. Both can capture periodic wave motion reflected on the local wind profile.

In the former research, we have performed the visualization of the interaction between the wave motion and the surface atmosphere. Depending on the wind direction, the atmospheric echoes' flow synchronized with the wave motion, while the ripple marks were appeared on the wave echoes at a footprint of local wind activities.

On contrary, this report indicates the situation that strong wind causes the sea wave. Depending on the arrangement of lidar sight direction, wave profile is estimated. The relationship between the wave height and wind speed well coincides with the visual observation. The shallow angle measurement with the LED mini-lidar can monitor this relationship in local area. It is useful for marine leisure, fishing, and port management.

References

1. Belmont, M.R., Horwood, J.M.K., Thurley, R.W.F., Baker, J.: Shallow angle wave Profilig Lidar. J. Atmos. Ocean. Technol. **24**, 1150–1156 (2007)
2. Mikhalevich, V., Solntsev, M.: Laser methods for measuring the ocean surface-wave spectrum. EARSeL Adv. Remote Sens. **l**(2), 33–35 (1992)
3. Reineman, B.D., Lenain, L., Castel, D., Melville, W.K.: A portable airborne scanning Lidar system for ocean and coastal applications. Am. Meteorol. Soc. **26**, 2626–2641 (2009)
4. Shiina T., LED mini-lidar, 26th ILRC proceeding S1P-17, (2012)
5. Mori, Y., Shimada, S., Shiina, T., Baji, H., Takemoto, S.: Dynamic analysis of sea wave data measured by LED Lidar. SPIE Proc. **10006**, 100060G (2016)
6. Shiina T., and Mori Y., Shallow angle measurement of sea wave dynamics by LED mini-lidar, 28th ILRC proceedings 011_193, (2017)

Chapter 77
First Results of the COLOR (*C*DOM-Proxy Retrieval from ae*O*Lus *O*bse*R*vations) Project

D. Dionisi, S. Bucci, C. Cesarini, S. Colella, D. D'Alimonte, L. Di Ciolo, P. Di Girolamo, M. Di Paolantonio, N. Franco, G. Giuliano, G. Gostinicchi, T. Kajiyama, G. Liberti, E. Organelli, and R. Santoleri

Abstract During the last decade, new applications exploiting data from satellite-borne lidar measurements demonstrated that these sensors can give valuable information about ocean optical properties. Within this framework, COLOR (CDOM-proxy retrieval from aeOLus ObseRvations) is an ongoing (KO: 10/3/2021) 18-month feasibility study approved by ESA within the Aeolus+ Innovation program. COLOR objective is to evaluate and document the feasibility of deriving an in-water AEOLUS prototype product from the analysis of the ocean subsurface backscattered component of the 355 nm signal. In particular, COLOR project focuses on the AEOLUS potential retrieval of (1) diffuse attenuation coefficient for downwelling irradiance (Kd [m^{-1}]) and (2) subsurface hemispheric particulate backscatter coefficient (bbp [m^{-1}]).

The core activity of the project is the characterization of the signal from the AEOLUS ground bin. In principle, the ground bin backscattered radiation signal is generated by the interaction of the emitted laser pulse radiation with two media (atmosphere and ocean) and their interface. To characterize this ground bin, two

D. Dionisi (✉) · C. Cesarini · S. Colella · G. Giuliano · G. Liberti · E. Organelli · R. Santoleri
Institute of Marine Sciences, Italian National Research Council, Rome, Italy
e-mail: davide.dionisi@cnr.it

S. Bucci · L. Di Ciolo · G. Gostinicchi
Serco Italia S.p.A, Frascati, Italy

D. D'Alimonte · T. Kajiyama
AEQUORA, Lisbon, Portugal

P. Di Girolamo · N. Franco
School of Engineering, University of Basilicata, Potenza, Italy

M. Di Paolantonio
Institute of Marine Sciences, Italian National Research Council, Rome, Italy

School of Engineering, University of Basilicata, Potenza, Italy

© The Author(s), under exclusive license to Springer Nature Switzerland AG 2023

J. T. Sullivan et al. (eds.), *Proceedings of the 30th International Laser Radar Conference*, Springer Atmospheric Sciences,
https://doi.org/10.1007/978-3-031-37818-8_77

parallel and strongly interacting activities were developed: (a) radiative transfer numerical modelling and (b) AEOLUS data analysis.

The preliminary results about the abovementioned activities will be here presented.

Keywords AEOLUS · Ocean color · Satellite borne lidar

77.1 Introduction

The ESA Earth Explorer Wind Mission ADM-Aeolus (Atmospheric Dynamics Mission, ESA, 2008), successfully launched on 22 August 2018, has the aim to provide global observations of wind profiles, demonstrating the impact of wind profile data on operational weather forecasting and on climate research [1]. Within the Aeolus+ Innovation program, ESA has launched an Invitation To Tender (ITT, ESA AO/1- 9544/20/I/NS) to carry out studies aimed at exploring, developing, and validating innovative products and applications and exploiting the novel nature of Aeolus data.

Although Aeolus's mission primary objectives and subsequent instrumental and sampling characteristics are not ideal for monitoring ocean subsurface properties, the unprecedented type of measurements from this mission is expected to contain important and original information in terms of optical properties of the sensed ocean volume. As demonstrated by several studies in the last decades [2, 3], satellite-borne lidar measurements can give valuable information about ocean optical properties. Being the first HSRL (high spectral resolution lidar) launched in space, ALADIN (Atmospheric LAser Doppler Instrument) of ADM-Aeolus, gives an unprecedented new opportunity to investigate the information content of the 355 nm signal backscattered by the ocean subsurface components.

Based on the above considerations, COLOR (CDOM-proxy retrieval from aeOLus ObseRvations), a selected Aeolus+ Innovation ITT project, aims to evaluate and document the feasibility of deriving an in-water AEOLUS prototype product from the analysis of the ocean subsurface backscattered component of the 355 nm signal acquired by the ALADIN. An overview of the project and some preliminary results are presented.

77.2 COLOR Approach

COLOR project, which started on 10 March 2021, focuses on the AEOLUS potential retrieval of the ocean optical properties at 355 nm: diffuse attenuation coefficient for downwelling irradiance, K_d [m^{-1}], and subsurface hemispheric particulate backscatter coefficient, b_{bp} [m^{-1}]. In particular, being dominated by the absorption due to CDOM (chromophoric dissolved organic matter), K_d coefficient at

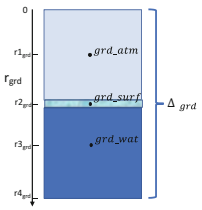


Fig. 77.1 Schematic geometry description of the AEOLUS ground bin

355 nm, K_d (355), can be used as a proxy to describe spatial and temporal variability of this variable, which contributes to regulating the Earth's climate.

To reach COLOR objectives, the work is organized in three phases: consolidation of the scientific requirements, implementation and assessment of AEOLUS COLOR prototype product, and scientific roadmap.

The core activity of the project is the characterization of the signal from the AEOLUS ground bin (Δr_{grd}). On average, the size of this acquisition bin is around 500 m with around 20% (i.e., 100 m) of the signal coming from the water subsurface. Thus, in principle, the Δr_{grd} backscattered radiation signal (B_{grd}) of the Mie AEOLUS channel is generated by the interaction of the emitted laser pulse radiation with two media (atmosphere and ocean, B_{atm} and B_{wat}, respectively) and their interface (B_{surf}, see Fig. 77.1):

$$S_X\,(\text{grd}) = M_X \left[\frac{A}{\left(r_{\text{atm}} + \frac{\Delta r_{\text{grd}}}{n}\right)^2} \right] B_{\text{grd}}\left(\pi, \Delta r_{\text{grd}}\right) T_A^2\,(r_{\text{atm}}) + S_{\text{bkd}},$$

where:

$$B_{\text{grd}}\left(\pi, \Delta r_{\text{grd}}\right) = \left(B_{\text{atm}} + B_{\text{surf}} + B_{\text{wat}}\right),$$

M is the total efficiency of the channel X, A is the area of the AEOLUS receiver, r_{atm} is the distance from the lidar to the surface, Δr_{grd} is the AEOLUS bin depth, n is the water refractive index, T_A is transmission through the atmosphere, and S_{bkd} is the background signal.

The backscattering component contribution due to the ocean subsurface can be written explicitly as follows:

$$B_{\text{wat}} = \int_0^{r_{\text{wat}}} \beta_{\text{wat}}\left(\pi, r'_{\text{wat}}\right) \exp\left[-2\int_0^{r'_{\text{wat}}} K_{\text{LID}}\left(r''_{\text{wat}}\right) dr''_{\text{wat}}\right] dr'_{\text{wat}},$$

where $\beta_{\text{wat}}(\pi, r'_{\text{wat}})$ is volume scattering coefficient at a scattering angle of π radians, which is the sum of the backscatter from water molecules and suspended particles (${\beta_{\text{wat}}}^{\text{M}}$ and ${\beta_{\text{wat}}}^{\text{P}}$, respectively) if $X =$ Mie or it is only equal to ${\beta_{\text{wat}}}^{\text{M}}$ if $X =$ Rayleigh, K_{LID} is the lidar attenuation coefficient in water.

To evaluate the feasibility of deriving an AEOLUS in-water product from the AEOLUS observations, COLOR proposes to develop a retrieval algorithm that is structured in three independent and consecutive phases:

1. Preprocessing analysis: Aimed to identify suitable measurements to be inverted.
2. Estimation of the in-water ground bin signal contribution: Aimed to remove contributions to the measured signal from variables other than the in-water ones.
3. Retrieval of in-water ground bin optical properties: Aimed to estimate the targeted in-water optical properties.

   Two parallel and strongly interacting activities are associated with each step of these phases:

   (a) Radiative transfer numerical modelling. This tool will be essential to simulate the relevant radiative processes expected to be responsible for the generation of AEOLUS surface bin signal.
   (b) AEOLUS data analysis. The objective of this activity will be to verify the information content of the AEOLUS ground bin signals and the assumptions for data product retrieval.

77.3 Results

First, a Monte Carlo-based radiative transfer numerical model was developed and validated to simulate AEOLUS signal propagation in ocean. In particular, numerical simulations were used to estimate (1) the fraction of radiant power backscattered by the sea surface as a function of the wind speed, (2) the fraction of radiant power back- transmitted from seawater to air at varying Chl-*a* values and different CDOM-added contributions, and (3) the fraction of back-transmitted radiant power specifically originated from the sea-bottom reflection.

As an example of RTMT simulation results, Fig. 77.2 shows the contribution of the water bin to the received signal, which is expressed as the back-transmitted radiant power ratio Ψ^{T} (i.e., the ratio of the total received radiant power over the emitted radiant power) as a function of Chl-a at varying CDOM contributions. Simulations are performed considering $Z_b = 500$ m for the sea bottom and $v_w = 6\ ms^{-1}$ for the wind speed. The reference Case-1 water corresponds to a CDOM factor $\alpha_{CDOM} = 1$. Optically complex waters where the CDOM contribution is n times that of Case-1 waters correspond to $\alpha_{CDOM} = n$ (a geometrical progression from 2 to 8 is considered). Results show a Ψ^{T} decrease as Chl-*a* and the α_{CDOM} factor increase. The results from these simulations identified "expected" conditions where the echoed lidar signal can be informative of optically active seawater constituents (e.g., $v_w < 8\ ms^{-1}$, Chl-a $> 0.1\ mg\ m^{-3}$ if $Z_b \approx 100$ m).

The second step was the design of an inversion algorithm to evaluate a potential AEOLUS ocean color product. This algorithm, which used only Mie channel

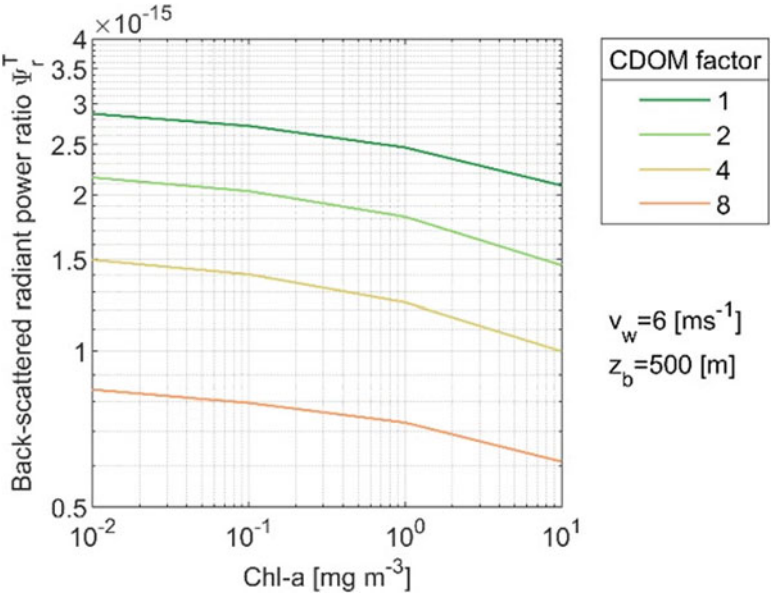


Fig. 77.2 Backscattered radiant power ratio Ψ^{T} for Chl-a = 0.01, 0.1, 1, and 10 mgm^{-3}. Different lines correspond to added CDOM for factors from 2 to 8 (the case labeled as 1 indicates Case-1 water conditions). The wind speed is $v_w = 6\ ms^{-1}$. The depth of the sea bottom is $Z_b = 500\ m$

observation, is capable to obtain analytically the term B_{wat} that includes all in-water contributions to the signal (backscattering and extinction from all components) from the range-corrected signals of bins 21, 22, and 23 under the following assumptions:

- The contributions to the measured signal in bin 23 from sea surface backscattering and from sea bottom reflection are negligible.
- Sea surface transmittance independent from the direction of propagation, that is, downward and upward.
- The difference between atmospheric backscattering contribution of bin 22 and 23 is negligible compared to the contribution of seawater in bin 23.
- Atmospheric backscattering dominated by molecular contribution both for the optical thickness and for the shape of the phase function.
- Homogeneity of the aerosol type in the marine atmospheric boundary layer (MABL) and known vertical distribution.

In order to have a very preliminary evaluation of the validity of the proposed model, the algorithm was applied to a set of AEOLUS data (i.e., from December 2019 to May 2021) extracted for the ocean test areas selected within COLOR project. Figure 77.3 depicts the probability density functions of the computed B_{wat}

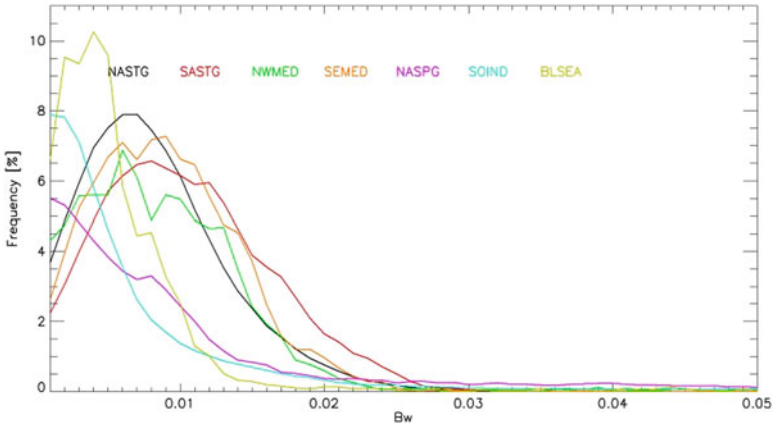


Fig. 77.3 Histogram plots for the Bwat derived using the developed AEOLUS ocean color algorithm for the Mie channel. The AEOLUS dataset from December 2019 to May 2021 have been used for the different test areas

for the different test areas. This figure seems to confirm the results obtained by the model: for oligotrophic regions, the values of B_{wat} are higher whereas for high absorption regions B_{wat} decreases. However, the negative values characterizing the optically complex waters highlight a possible limit of applicability of the algorithm only to low absorption waters. Further studies and assessment will be conducted in the last phase of COLOR project.

77.4 Summary and Conclusions

The COLOR project has the objective of evaluating the feasibility of deriving an in-water AEOLUS prototype product. COLOR core approach is the characterization of the AEOLUS ground bin signal coupling radiative transfer modeling and data analysis. The development of RTM to simulate AEOLUS signal propagation in ocean allowed to identify "expected" conditions where the lidar signal can be informative of optically active seawater constituents (e.g., vw < 8 ms^{-1}, Chl-a > 0.1 mg m-3 if Z_b ≈100 m). On the other hand, a potential AEOLUS ocean color inversion algorithm using only Mie channel was designed to compute analytically the term B_{wat} that includes both backscattering and extinction contributions to the signal from all in-water components. This algorithm, which needs to be validated and assessed, was applied to the AELOUS observations for a set of test areas. The very preliminary results seem to confirm the numerical simulations obtained by the developed RTM.

References

1. European Space Agency: ADM-Aeolus Science Report, ESA SP-1311, 2008
2. Behrenfeld, M., et al.: Global satellite-observed daily vertical migrations of ocean animals. Nature. **576**(7786), 7786 (2019). https://doi.org/10.1038/s41586-019-1796-9
3. Dionisi, D., et al.: Seasonal distributions of ocean particulate optical properties from spaceborne lidar measurements in Mediterranean and Black Sea. Remote Sens. Environ. **247**, 111889 (2020). https://doi.org/10.1016/j.rse.2020.111889

Chapter 78
Dual Wavelength Heterodyne LDA for Velocity and Size Distribution Measurements in Ocean Water Flows

Hongwei Zhang, Ziwang Li, Xiangcheng Chen, Jintao Liu, Kailin Zhang, Songhua Wu, Yan He, Weibiao Chen, and Junwu Tang

Abstract Air-sea coupling and energy circulation inside the ocean are the frontiers of ocean science and important directions of Earth's system science. Researchers have carried out extensive research on multi-scale dynamic characteristics and ecological environment parameter based on the development of advanced remote sensing technology. However, the lack of the noninvasive in situ detection technology for the high-resolution measurement of the marine micro-scale characteristics,

H. Zhang (✉)
Key Laboratory of Space Laser Communication and Detection Technology, Shanghai Institute of Optics and Fine Mechanics, Chinese Academy of Sciences, Shanghai, China

College of Marine Technology, Faculty of Information Science and Engineering, Ocean University of China, Qingdao, China

Laboratory for Regional Oceanography and Numerical Modeling, Pilot National Laboratory for Marine Science and Technology (Qingdao), Qingdao, China
e-mail: zhanghongwei8944@ouc.edu.cn

Z. Li · X. Chen · J. Liu · K. Zhang
College of Marine Technology, Faculty of Information Science and Engineering, Ocean University of China, Qingdao, China
e-mail: liziwang@stu.ouc.edu.cn

S. Wu
College of Marine Technology, Faculty of Information Science and Engineering, Ocean University of China, Qingdao, China

Laboratory for Regional Oceanography and Numerical Modeling, Pilot National Laboratory for Marine Science and Technology (Qingdao), Qingdao, China

Institute for Advanced Ocean Study, Ocean University of China, Qingdao, China

Y. He · W. Chen ·
Key Laboratory of Space Laser Communication and Detection Technology, Shanghai Institute of Optics and Fine Mechanics, Chinese Academy of Sciences, Shanghai, China

J. Tang
Laboratory for Regional Oceanography and Numerical Modeling, Pilot National Laboratory for Marine Science and Technology (Qingdao), Qingdao, China

© The Author(s), under exclusive license to Springer Nature Switzerland AG 2023

J. T. Sullivan et al. (eds.), *Proceedings of the 30th International Laser Radar Conference*, Springer Atmospheric Sciences,
https://doi.org/10.1007/978-3-031-37818-8_78

biological, physical, and chemical restricted the study of the microscale phenomenon and biological optics inside the ocean. The development of in situ detection techniques for microscale turbulence and particle size distribution in the ocean mixing layer would improve the understanding of the energy and matter transport inside the ocean. This article focuses on the great demand for the high-resolution in situ detection technology during the study of micro-scale turbulent flow structure and the size distribution measurement of micro-scale suspended particles. A laser Doppler current probe (LDCP) has been designed for the measurement of distributed two-component velocity with high spatial resolution. The sensor is an extension of the principle of laser Doppler anemometry (LDA). It is nonintrusive, highly accurate, and able to highly resolve the flow both in the time and spatial extensions. The LDCP has been proved to be effective tools to capture the micro-scale oceanic turbulence by carrying out field campaign at Yellow Sea. Algorithm to calculate the distribution of the suspended particles with small scale (1–10 μm) has developed, and it has been validated by the laboratory campaign.

Keywords Laser Doppler current probe · Size distribution · Ocean water flow

78.1 Introduction

Air-sea coupling and energy circulation inside the ocean are the frontiers of ocean science and important directions of Earth's system science. Ocean currents flow for great distances and together create the global conveyor belt, which plays a dominant role in determining the climate of many of the Earth's regions. More specifically, ocean currents influence the temperature of the regions and the transport of energy and mass through which they travel [1]. Ocean currents have significant impact on the physical processes, chemical processes, and biological processes inside the ocean. Generally, the physical properties of seawater are affected by the ocean current, which changes the temperature distribution, salinity distribution, and density distribution inside the ocean. High-precision measurements of ocean currents, especially at the boundary layer, are important for analyzing the micro-scale turbulence and sea-air interactions [2].

Researchers have carried out extensive research on multi-scale dynamic characteristics and ecological environment parameter based on the development of advanced remote sensing technology [3]. However, the lack of noninvasive, in situ technology that can make high resolution measurements of marine microscale characteristics has restricted our understanding of microscale phenomena and biological optics in the ocean [4]. The development of in situ detection techniques for microscale turbulence and particle size distribution in the ocean mixing layer would improve the understanding of the energy and matter transport inside the ocean. The most traditional method to characterize the particles (size, shape, morphology, and structure) is the scanning electronic microscopy technique by utilizing high spatial resolution images of the microscopic particles [5]. However,

the narrow sight view of the scope limited the number of small-scale particles which can be analyzed simultaneously. It is difficult to achieve the in situ observation for the tedious preparation of the samples to be placed under the microscope [6]. The Differential Electrical Mobility Analysis technique has been proved to be an effective tool to quantify the size distribution and concentration of the aerosol particles in the size range from 10 nm to 1000 nm [7]. Light extinction spectroscopy (LES) technique has been dedicated to assess the characterization of submicron particles. Nevertheless, what is clearly missing is the capability for these techniques to perform both in situ and real-time measurements [8]. The development of in-situ detection techniques for microscale turbulence and particle size distribution in the ocean mixing layer would improve the understanding of the energy and matter transport inside the ocean [9, 10].

The measurements of velocity gradients in shear flows play an important role in practical developments as well as in fundamental researches [11]. At present, the shear flow velocity profiles were often accomplished by using hot-wire anemometers, Pitot tubes, ultrasonic-based measurement technique, and ADCP (Acoustic Doppler Current Profiler) [12]. Nowadays, optical measurement techniques such as LDA (Laser Doppler Anemometer), PIV (Particle Image Velocimetry), PDA (Phase Doppler Anemometry), and SDV (Shadow Doppler Velocimetry) are becoming significant for studying fluid mechanics. Basing on the crossing of two coherent laser beams, Laser Doppler Anemometry are most common for flow measurements with features of nonintrusive and high accuracy.

The shortcomings of the existing current meter mainly concentrate on the low measurement resolution, small measurement range, large error, and the interference of flow field. A noncontact ocean current meter with high resolution and large measurement range are wanted to measure the ocean current at boundary layer. In this paper, characteristics of suspended particulate inside the ocean are studied. A laser Doppler current probe system with large measurement range is developed and applied to ocean current measurement.

This article focuses on the great demand for the high-resolution in situ detection technology during the study of micro-scale turbulent flow structure and the size distribution measurement of micro-scale suspended particles. A laser Doppler current probe (LDCP) has been designed for the measurement of distributed two-component velocity with high spatial resolution. The principle of laser Doppler anemometry and the experimental setup of LDCP system is described in Sect. 2. In Sect. 3, we investigate the results of LDCP system.

78.2 Laser Doppler Current Probe System

The LDCP system is a realization of the LDA principle for the velocity measurement of two-component flow field. Figure 78.1 illustrates the experimental setup of LDCP system. The laser configured to the LDCP system is a compact DPSS (diode-pumped solid-state) laser (Cobolt Calypso 04-01, Cobolt Inc., Sweden), which could

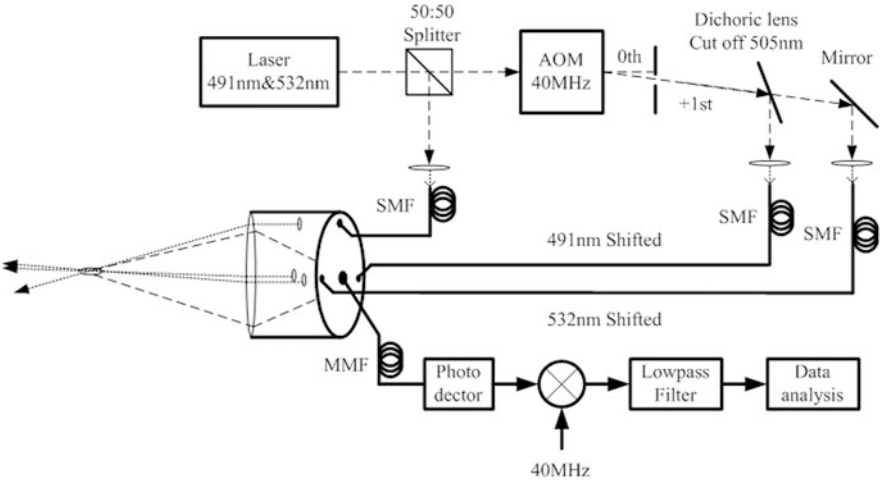


Fig. 78.1 Experimental setup of LDCP sensor

transmit laser beam at two wavelengths (491 nm and 532 nm) with 50 mW power at each wavelength. The laser beam was divided into two beams by a BS (beam separator): one beam was transmitted into profile sensor by single-mode fiber and the other beam passed through the AOM (from Gooch & Housego, England) with 40 MHz driver frequency. Only the +first diffraction orders of two wavelengths were used; all the other orders were blocked by beam stops. A dichroic mirror (cutoff 505 nm) was utilized to separate two different wavelengths laser from each other. The beams were then collimated into single-mode fiber by aspheric lenses and connected to the profile sensors. All the beams were brought to an intersection by a front lens with a 250 mm focal length. However, the distance of the measurement volume to the LDCP head can be changed by changing the front lens for different focal lengths.

In the transmitting system of the LDCP system, the front lens mentioned above also serves as the receiving unit. The most advantage of backward scattering system is the consistency of the LDCP system when it is placed mobile for various measurements. The light scattered by the particles passing through the measurement volume was transmitted to a photodetector by utilizing a multimode fiber.

78.3 Results and Discussion

78.3.1 Velocity Profile Measurements of Subsurface Current

Field observation of subsurface current has been carried out by configuring the LDCP system and traditional propeller current meter in a fixed cage (at about

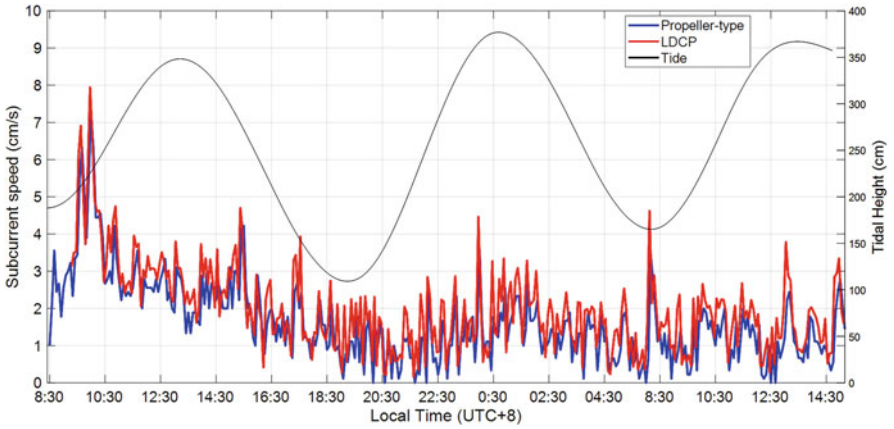


Fig. 78.2 Current speed measured by propeller-type current meter and LDCP system at about 1 m above the seafloor over time

1 m above the seafloor) for long-term observation. The subsurface current profiles obtained by the LDCP system and the propeller current meter are illustrated in Fig. 78.2; the red line represents the velocity measured by the LDCP system while the blue line depicts the results obtained by the traditional propeller-type current meter. The local tide information is presented by the black line. Here, measurements of different instruments show a similar trend; however, the LDCP system recorded higher speeds compared to the traditional propeller-type current meter.

The observation site is an appropriate site for the cooperative observation, as the small water level range and the tide. Here we directly compare results obtained by the LDCP system and the propeller-type current meter during the observation campaign (Fig. 78.3). The root-mean-square deviation between the speeds determined with both methods is 0.381 cm/s.

78.3.2 Size Measurement of the Micro-Scale Suspended Particles

The present work is based on the Lorenz–Mie theory to focus on the size distribution of the spherical and homogeneous suspended particles without multiple scattering. In the typical laser Doppler velocity technique, the scattering characteristics of micro-scale particles are mainly related to the diameter and are not related to the ratio of the scattered incident light and the spatial distribution of the scattered light. Thus, the particle size can be calculated by identifying this property. The methods for measuring particle size mainly include light absorption method based on total scattered light and light scattering method based on angular distribution of scattered light.

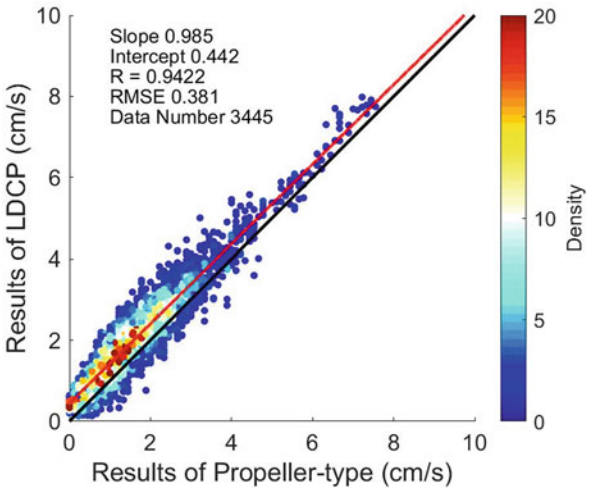


Fig. 78.3 Results obtained by the LDCP system and the propeller-type current meter during the cooperative observation campaign

The LDCP system measures the diameter of the particles based on the visibility of the Doppler signal fringe. The visibility of the Doppler signal can be expressed by the following formula:

$$\eta = \frac{\overline{I}_{\max} - \overline{I}_{\min}}{\overline{I}_{\max} + \overline{I}_{\min}} \tag{78.1}$$

where $\overline{I}_{\max}$ and $\overline{I}_{\min}$ are the maximum and minimum scattered light intensities of bright and dark fringes, respectively. It is important for this measurement to require uniform contrast of the fringes and to pass at or near the geometric center of the measurement volume. For the case of equal light intensity, the relationship between visibility and particle diameter and stripe spacing for a uniform sphere is as follows:

$$\eta \approx \frac{2J_1\left(2\pi r_p/d\right)}{2\pi r_p/d} \tag{78.2}$$

where J_1 is the first-order Bessel function, r_p is the particle diameter, and d is the internal fringe spacing of the measurement volume. Figure 78.4 is a plot of laser Doppler signal visibility versus tracer particle diameter and fringe spacing ratio. It can be seen from Fig. 78.4 that when the particle diameter is 1.62 times, 3.13 times, and 4.74 times the fringe interval, the visibility is zero. This characteristic is used by Farmer for glass spheres and shots with a known diameter between 15 μm and 120 μm [13]. In addition, the vibration of the visibility function cannot measure the particle diameter from a single value. The x-label of Fig. 78.4 represents the relationship between diameter r_p of particles and internal fringe spacing d of the measurement volume.

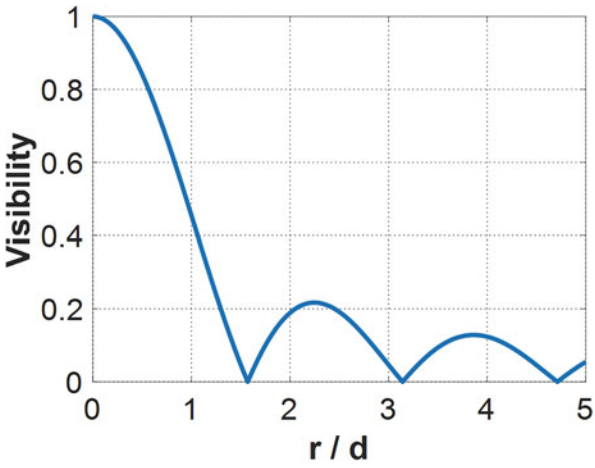


Fig. 78.4 Relationship between visibility and the particle size and range of fringes

Table 78.1 Categories of algae utilized in the laboratory observation campaign

No.	Categories	Size distribution
1	Chlorella	Single-celled green algae, spherical, oval, and diameter range: 3–8 μm
2	Halophila	Single-celled green algae, pear-shaped, oval, and diameter range: 3–14 μm
3	Diatom	Single-celled flagellate and diameter range: 3–20 μm
4	Flat algal	Single-celled green algae and diameter range: 9–24 μm

In order to verify the method of calculating the tracer particle diameter by using Doppler pulse signal visibility, chlorella, halophila, diatom, and flat algal were used as tracer particles in laboratory tests. The relevant characteristics are shown in Table 78.1.

Figure 78.5 shows the numerical distribution of the signal visibility of different algae on the first-order Bessel function using the Doppler pulsation signal visibility method in the experimental test. As can be seen from Fig. 78.5, the particle size distribution of chlorella is the smallest, about 3–5 μm; the particle size characteristics of salt algae and diatoms overlap greatly, and the particle size range is about 5–8 μm. The data has a lot of uncertainty. The Doppler pulsation signal of the spirulina shown in the figure has a visibility value between 0.18 and 0.42. When the signal visibility value is less than 0.23, the particle size corresponding to the visibility of the Doppler pulsation signal of the cyanobacteria cannot be accurately determined. When the signal visibility value is less than 0.23, the particle diameter may be between 7 and 9 μm and may be between 9 and 18 μm. There may be misjudgment in the process of automatic identification of the program, resulting in measurement error.

Generally, when it comes to measure the suspended particles with large scale such as cyanobacteria (the size of the suspended particles is larger than the fringe internals of the measurement volume), it is necessary to use a laser Doppler velocity signal in combination with a laser to excite the fluorescent signal or to combine

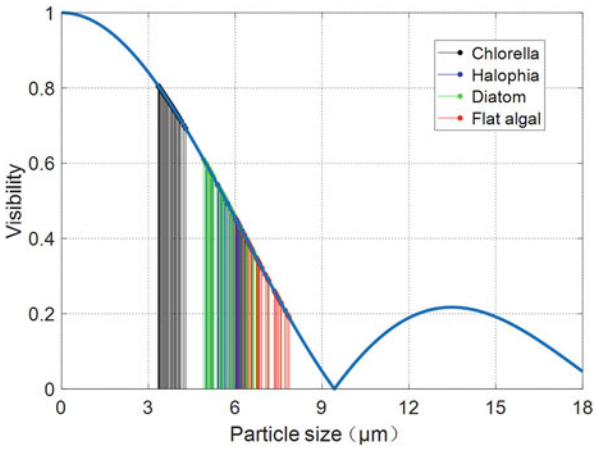


Fig. 78.5 Results of particle size observation campaign

the signal width information for suspension. Laser-induced fluorescence method is suitable for algae measurement with chlorophyll, and signal width information method is applied to inorganic particles or biochips that do not contain chlorophyll.

78.4 Conclusion

This article focuses on the great demand for the high-resolution in situ detection technology during the study of micro-scale turbulent flow structure and the size distribution measurement of micro-scale suspended particles. A LDCP system has been designed for the measurement of distributed two-component velocity with high spatial resolution. The sensor is an extension of the principle of LDA. It is nonintrusive, highly accurate, and able to highly resolve the flow both in the time and spatial extensions. The LDCP system has been proved to be an effective tool to capture the micro-scale oceanic turbulence by carrying out field campaign at Yellow Sea. Algorithm to calculate the distribution of the suspended particles with small scale (1–10 μm) has developed, and it has been validated by the laboratory campaign.

In terms of the large-scale suspended particles, size distribution measurement (10 μm–1 mm) can be obtained by combining laser-induced fluorescence and laser Doppler velocimetry. In this paper, the detection technology of small-scale tracer particles is explored by using Doppler pulse signal visibility method. In the subsequent research, the technology will be used to detect the particle size of large suspended particles.

References

1. Behrenfeld, M.J., Gaube, P., Della Penna, A.: Global satellite-observed daily vertical migrations of ocean animals. Nature. **576**, 257–261 (2019). https://doi.org/10.1038/s41586-019-1796-9
2. Boyd, P.W., Claustre, H., Levy, M., Siegel, D.A., Weber, T.: Multi-faceted particle pumps drive carbon sequestration in the ocean. Nature. **568**, 327–335 (2019). https://doi.org/10.1038/s41586-019-1098-2
3. Bellacicco, M., Volpe, G., Briggs, N., Brando, V., Pitarch, J., Landolfi, A., Colella, S., Marullo, S., Santoleri, R.: Global distribution of non-algal particles from ocean color data and implications for phytoplankton biomass detection. Geophys. Res. Lett. **45**, 7672–7682 (2018)
4. Xiao, J., Zhuang, Q., Law, B.E., Chen, J., Baldocchi, D.D., Cook, D.R., Oren, R., Richardson, A.D., Wharton, S., Ma, S.: A continuous measure of gross primary production for the conterminous United States derived from MODIS and AmeriFlux data. Remote Sens. Environ. **114**, 576–591 (2010)
5. Lee, H., Kwak, D.B., Kim, S.C., Pui, D.Y.: Characterization of colloidal nanoparticles in mixtures with polydisperse and multimodal size distributions using a particle tracking analysis and electrospray-scanning mobility particle sizer. Powder Technol. **355**, 18–25 (2019)
6. Park, J., Kwak, M., Song, N.W., Kim, J.: Effect of colloidal nanoparticle concentration on sizing analysis with an electrospray scanning mobility particle sizer. Appl. Nanosci. **10**, 329–336 (2020)
7. Guha, S., Li, M., Tarlov, M.J., Zachariah, M.R.: Electrospray–differential mobility analysis of bionanoparticles. Trends Biotechnol. **30**, 291–300 (2012)
8. Onofri, F., Barbosa, S., Touré, O., Woźniak, M., Grisolia, C.: Sizing highly-ordered buckyball-shaped aggregates of colloidal nanoparticles by light extinction spectroscopy. J. Quant. Spectrosc. Radiat. Transf. **126**, 160–168 (2013)
9. Giering, S.L.C., Cavan, E.L., Basedow, S.L., et al.: Sinking organic particles in the ocean—flux estimates from in situ optical devices. Front. Mar. Sci. **6**, 834 (2020)
10. Li, M.Z., He, Y.P., Liu, Y.D., et al.: Effect of interaction of particles with different sizes on particle kinetics in multi-size slurry transport by pipeline. Powder Technol. **338**, 915–930 (2018)
11. Andreas, V., Christian, B., Katsuaki, S., Lars, B., Jurgen, C.: Laser Doppler field sensor for high resolution flow velocity imaging without camera. Appl. Opt. **47**(27), 5028–5040 (2008)
12. Christoph, S., Humberto, C., Christoph, B.: Extended laser Doppler anemometer for near wall measurements. In: 15th International Symposium on Applications of Laser Techniques to Fluid Mechanics Lisbon, Portugal, 05–08 July (2010)
13. Farmer, W.: Visibility of large spheres observed with a laser velocimeter: a simple model. Appl. Opt. **19**, 3660–3667 (1980)

Part VIII
Space-Borne Lidar Missions, Instruments and Science

Chapter 79
Mitigation Strategy for the Impact of Low Energy Laser Pulses in CALIOP Calibration and Level 2 Retrievals

Jason Tackett, Robert Ryan, Mark Vaughan, Anne Garnier, Brian Getzewich, David Winker, and Charles Trepte

Abstract Since mid-2016, the frequency of low energy laser pulses emitted by the CALIPSO lidar has been slowly increasing due to pressure losses in the canister housing the laser. While originally confined primarily to the South Atlantic Anomaly (SAA) region, these low energy pulses now occur intermittently around the globe. Low energy pulses can cause calibration biases and degrade the science quality of level 2 retrievals. We describe a new low energy mitigation (LEM) algorithm that will be implemented incrementally in future versions of the CALIOP data processing to identify and reject affected profiles during calibration and feature detection. The LEM algorithm effectively eliminates low energy calibration biases, improves level 2 retrievals, and minimizes level 2 data loss.

Keywords CALIPSO · CALIOP · Laser energy

79.1 Introduction

The space-based lidar CALIOP was launched onboard the CALIPSO satellite in 2006 and since has provided a 16+-year record of vertically resolved aerosol and cloud measurements. The CALIOP transmitter is an Nd:YAG laser that is Q-switched and diode pumped, emitting at 532 and 1064 nm [1]. In mid-2016, the laser began experiencing intermittent low energy pulses due to pressure losses inside the laser canister that allow coronal arcing across the Q-switch. The low energy pulses primarily occur over the South Atlantic Anomaly (SAA) region (Fig. 79.1), where energetic particles increase the occurrence of coronal arcing. In recent years,

J. Tackett (✉) · M. Vaughan · B. Getzewich · D. Winker · C. Trepte
NASA Langley Research Center, Hampton, VA, USA
e-mail: jason.l.tackett@nasa.gov

R. Ryan · A. Garnier
Science Systems and Applications, Inc., Hampton, VA, USA

© The Author(s), under exclusive license to Springer Nature Switzerland AG 2023

J. T. Sullivan et al. (eds.), *Proceedings of the 30th International Laser Radar Conference*, Springer Atmospheric Sciences,
https://doi.org/10.1007/978-3-031-37818-8_79

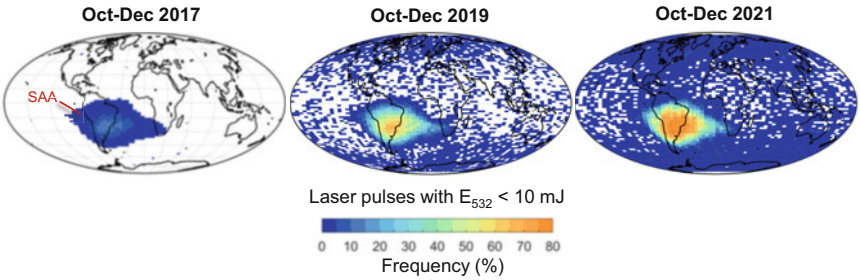


Fig. 79.1 Spatial distribution of low energy pulses. During October–December 2021, 37% of laser pulses in the SAA have low energy compared to 1% outside the SAA

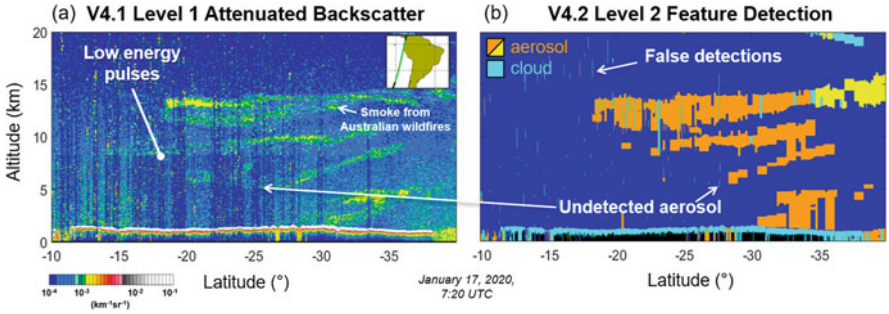


Fig. 79.2 (**a**) V4.1 532 nm attenuated backscatter and (**b**) V4.2 feature detection/classification for a CALIOP granule affected by low energy laser pulses near the SAA

low energy pulses have become more prevalent outside the SAA, albeit at lower frequencies. Low energy pulses primarily have 532 nm energies <10 mJ compared to nominal values of 90–100 mJ.

The most noticeable impacts on V4.1 level 1 and V4.2 level 2 data products are shown in Fig. 79.2 where optically thin aerosol is undetected and false feature detections occur at all altitudes in affected profiles. This example is an extreme case near the SAA, but false detections occur similarly outside the SAA at a lesser frequency. Whereas existing noise filters eliminate the influence of low energy pulses for the 532 nm night calibration, the 532 nm day and 1064 nm channels are both impacted at SAA latitudes. The goal of the CALIPSO project is to remove the low biases in level 1 calibration coefficients and rectify the science quality of level 2 retrievals affected by low energy pulses. This will be accomplished by a new low energy mitigation algorithm (LEM) that strategically rejects data affected by low energy pulses during the level 1 calibration and level 2 feature detection processes.

79.2 Low Energy Mitigation (LEM) Algorithm

The LEM algorithm balances two competing desires: maintain science quality similar to that of data with nominal laser energy and reject as little data as possible. To do this, LEM accounts for onboard averaging and level 2 averaging. This is important because these averaging processes extend the ill effects of low energy to neighboring profiles, even those with nominal energies. The fundamental resolution measured by the lidar receiver is 15 m vertical × 333 m horizontal [1]. The signal is averaged onboard the satellite prior to downlink to reduce transmitted data volume. The coarsest horizontal interval downlinked is a 5 km data "frame." Within a frame, five altitude regions are defined with different amounts of vertical and horizontal averaging, shown schematically in Fig. 79.3. We name the smaller averaging intervals within each altitude region as "subregions." Below 8.2 km, data are downlinked at 333 m "single-shot resolution."

The impact of a low energy pulse in any one of these subregions depends on how many single-shot samples are averaged together: one profile with low energy in region 4 may have a small impact on the five-shot average, but below 8.2 km where there is no horizontal averaging onboard, that low energy profile is surely unusable. To minimize data rejection while maintaining sufficient single sample SNR, LEM adopts a low energy threshold of $E_{532} < 10$ mJ and imposes the following constraints on individual profiles and subregions:

- Profiles with low energy are rejected in single-shot resolution regions 1 and 2.
- Subregions must contain at least two (out of three) profiles with good laser energy in region 3 and two (out of five) in region 4.
- *Some* un-rejected data must exist in each 1 km segment in regions 2 and 3 after applying the previous constraints to ensure a continuous profile.

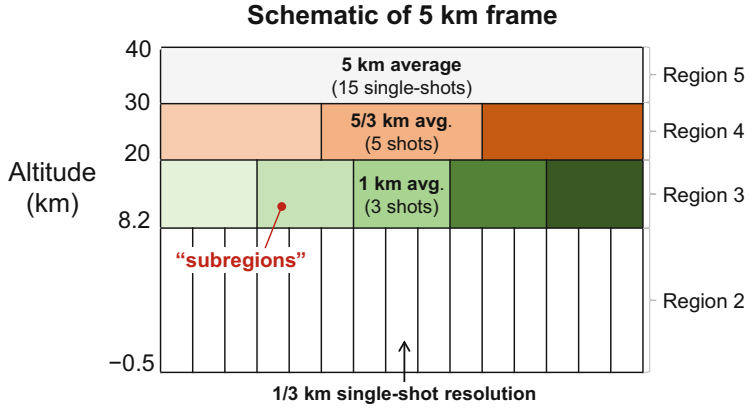


Fig. 79.3 Schematic of a 5 km frame showing how data is averaged onboard prior to downlink. For clarity, region 1 is not shown (−0.5 to −2 km)

It is important that enough valid profiles are included in the 5 km frame for features to be detected reliably in level 2. When too many profiles or subregions have been rejected, then the entire 5 km frame is also rejected. To enforce this requirement, the following additional constraints are implemented:

- At least 6 (out of 15) un-rejected profiles must exist in region 2.
- At least 3 (out of 5) un-rejected subregions must exist in region 3.
- At least 1 (out of 3) un-rejected subregion must exist in region 4.

The previous constraints ensure the data quality of 5 km frames used in 532 nm daytime calibration and for feature detection in level 2 processing. However, the level 2 feature detection algorithm also searches for weakly scattering features at 20 km and then 80 km resolution [2]. These resolutions were selected to approximately double the SNR for each subsequent average. Because the previous constraints will at times reject whole 5 km frames, LEM requires that at least 75% of the 5 km frames expected for a 20 km or 80 km average are not rejected. This allows the coarser resolutions to achieve at least ~86% of the expected SNR doubling or quadrupling. If fewer than 75% of 5 km frames are available, then feature detection is not invoked for the coarse resolution, and the contributing data are removed from subsequent coarser averages. Note that all minimum numbers and fractions given above are preliminary and subject to change.

79.3 LEM Application to Calibration

The current V4.1 calibration procedure for the 532 nm nighttime channel contains outlier rejection filters that successfully eliminate the influence of low energy pulses. However, additional filtering is necessary for the 532 nm daytime and 1064 nm channels. The 532 nm daytime calibration coefficients are calculated by comparing day and night clear-air scattering ratios matched by granule elapsed time at a high altitude where particulate loading is diurnally invariant [3]. The scattering ratios are based on 200 km horizontal averages that are further averaged across ±52 consecutive granules. Thus, low energy pulses within the 200 km segment in any of the 105 granules can affect the average. This effect is especially acute at SAA latitudes where multiple granules within the average pass through the SAA, causing the calibration bias in Fig. 79.4a and a substantial increase in its uncertainty. The LEM algorithm has been implemented for the 532 nm daytime calibration procedure in the V4.5 level 1 data release. It enforces subregion/frame acceptance criteria within each 200 km segment, thereby rejecting data affected by low energy. As a result, biases in the V4.1 532 nm day calibration at SAA latitudes are eliminated (Fig. 79.4a), and the calibration uncertainty is significantly reduced.

The LEM strategy for 1064 nm calibration is more aggressive. The 1064 nm calibration procedure scales 532 nm calibration coefficient based on “calibration quality” ice clouds, where the 1064 nm/532 nm ratio of signals is assumed to equal 1.01 [4]. The scale factors derived from these clouds are based on averages over

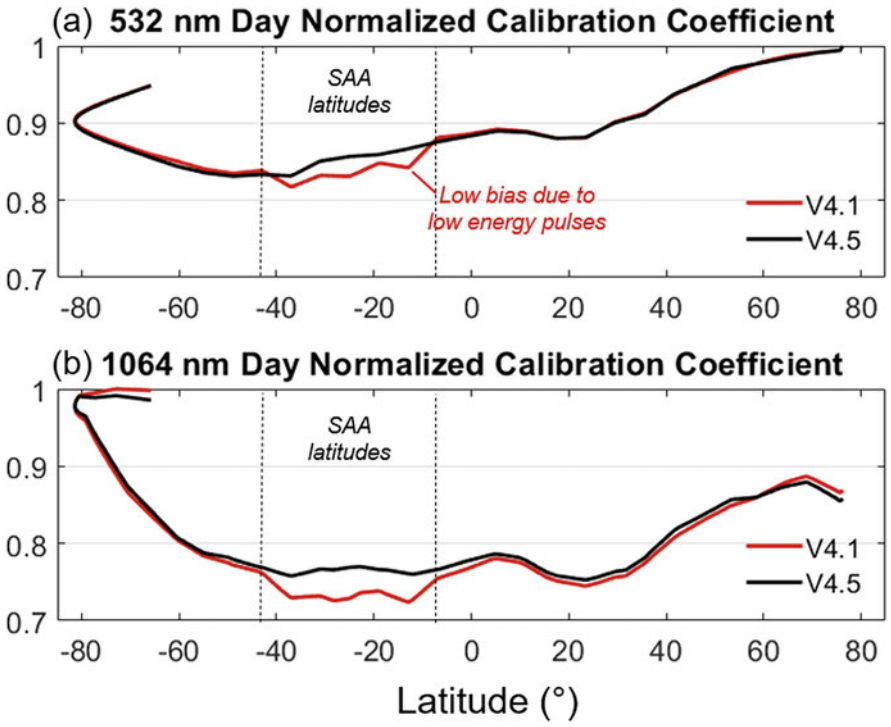


Fig. 79.4 November 2020 normalized calibration coefficients for V4.1 (red) and the low energy mitigated V4.5 (black) as a function of granule elapsed time converted to latitude

±52 consecutive granules, matched by granule elapsed time. Low energy pulses are not trapped by the quality filters in V4.1, which leads to biased scale factors and ultimately biased 1064 nm calibration coefficients, particularly at SAA latitudes. In V4.5, an additional quality filter is added: calibration quality clouds cannot contain any low energy pulses within their 5 km average. Adding this LEM filter effectively eliminates the 1064 nm calibration bias at SAA latitudes (Fig. 79.4b).

79.4 LEM Application to Level 2 Feature Detection

Following the release of V4.5, the LEM algorithm will be added to level 2 processing to reject segments of level 1 attenuated backscatter affected by low energy pulses prior to feature detection. Various quality control flags will be included in the level 2 products to document LEM operations, and special fill values will indicate where data has been rejected. Note that no data rejection will occur to the level 1 data products. Figure 79.5 shows the impact of LEM for the scene presented in Fig. 79.2. False detections are eliminated, rejected data are clearly

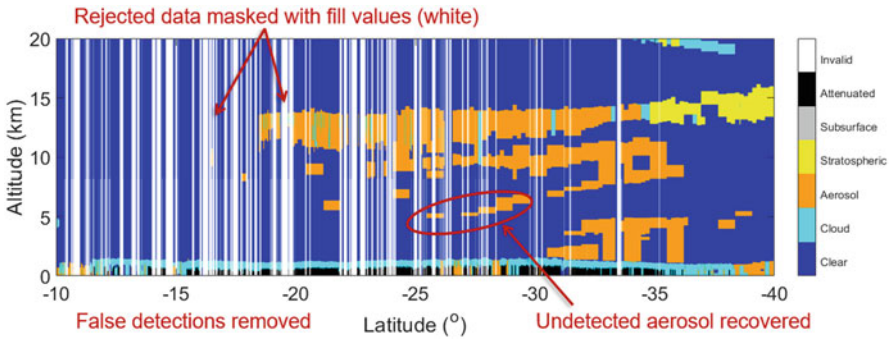


Fig. 79.5 Feature detection/classification for the same granule as Fig. 79.2, but with LEM applied

indicated with fill values, and previously undetected aerosol layers are now detected. The science quality of remaining data is markedly improved in this extremely complex example.

Based on preliminary assessments, LEM is expected to recover a substantial amount of level 2 data. Outside the SAA in late 2021, only 0.8% of 5 km frames are entirely rejected. The remaining 2.5% of frames containing low energy pulses meet LEM criteria and are recoverable; 96.7% of frames are unaffected low energy pulses. Inside the SAA, data recovery is more challenging given the greater number of low energy shots. During the same time period, 40% of frames are rejected and 29% are recoverable in the SAA; only 31% are unaffected.

79.5 Conclusion and Implementation Plan

The LEM algorithm is effective at removing biases in 532 nm day and 1064 nm calibration coefficients and improving the science quality of level 2 retrievals. By applying data rejection to small, targeted segments based on native averaging intervals, LEM minimizes data loss due to low energy pulses. The CALIPSO project will include LEM in the calibration procedures for the 2022 release of the V4.5 level 1 data product. The project plans to incorporate LEM into level 2 data processing in a post-V4.5 level 2 data release after 2022 to provide adequate time for validation.

References

1. Hunt, W.H., Winker, D.M., Vaughan, M.A., Powell, K.A., Lucker, P.L., Weimer, C.: CALIPSO Lidar description and performance assessment. J. Atmos. Ocean. Technol. **26**, 1214–1228 (2009)
2. Vaughan, M., Powell, K., Kuehn, R., Young, S., Winker, D., Hostetler, C., Hunt, W., Liu, Z., McGill, M., Getzewich, B.: Fully automated detection of cloud and aerosol layers in the CALIPSO Lidar measurements. J. Atmos. Ocean. Technol. **26**, 2034–2050 (2009)

3. Getzewich, B.J., Vaughan, M.A., Hunt, W.H., Avery, M.A., Tackett, J.L., Winker, D.M., Kar, J., Lee, K.-P., Toth, T.: CALIPSO Lidar calibration at 532-nm: version 4 daytime algorithm. Atmos. Meas. Tech. **11**, 6309–6326 (2018)
4. Vaughan, M., Garnier, A., Josset, D., Avery, M., Lee, K.-P., Liu, Z., Hunt, W., Pelon, J., Hu, Y., Burton, S., Hair, J., Tackett, J., Getzewich, B., Kar, J., Rodier, S.: CALIPSO Lidar calibration at 1064 nm: version 4 algorithm. Atmos. Meas. Tech. **12**, 51–82 (2019)

Chapter 80
Introducing the Cloud Aerosol Lidar for Global Scale Observations of the Ocean-Land-Atmosphere System: CALIGOLA

Paolo Di Girolamo, Alberto Cosentino, Francesco Longo, Noemi Franco, Davide Dionisi, Donato Summa, Simone Lolli, Enrico Suetta, Alessandro Perna, and Simona Zoffoli

Abstract CALIGOLA, while having a primary focus on atmospheric monitoring, presents also a strong potential in the characterization and study of the ocean-Earth-atmosphere system and the mutual interactions within it. Exploiting the three Nd:YAG laser emissions at 354.7, 532, and 1064 nm and the elastic (Rayleigh-Mie), depolarized, and Raman lidar echoes from atmospheric constituents, CALIGOLA will carry out 3λ profile measurements of the particle backscatter coefficient and depolarization ratio and 2λ profile measurements of the particle extinction coefficient from aerosols and clouds. These measurements will be used for the purpose of aerosol typing and for determining particle size and microphysical properties (Di Girolamo et al., Atmos Environ, 50: 66–78, 2012; J Geophys Res Atmos, 127:e2021JD036086, 2022). Furthermore, measurements of the elastic and depolarized backscattered echoes from the sea surface and the underlying layers will

P. Di Girolamo · N. Franco
Scuola di Ingegneria, Università della Basilicata, Potenza, Italy
e-mail: paolo.digirolamo@unibas.it

A. Cosentino · E. Suetta · A. Perna
Leonardo S.p.A, Pomezia (RM), Italy
e-mail: alberto.cosentino@leonardocompany.com

F. Longo · S. Zoffoli
Agenzia Spaziale Italiana, Rome, Italy
e-mail: francesco.longo@asi.it

D. Dionisi
ISMAR-CNR, Roma, Italy
e-mail: davide.dionisi@artov.ismar.cnr.it

D. Summa · S. Lolli (✉)
IMAA-CNR, Tito Scalo, Potenza, Italy
e-mail: donato.summa@imaa.cnr.it; simone.lolli@imaa.cnr.it

© The Author(s), under exclusive license to Springer Nature Switzerland AG 2023

J. T. Sullivan et al. (eds.), *Proceedings of the 30th International Laser Radar Conference*, Springer Atmospheric Sciences,
https://doi.org/10.1007/978-3-031-37818-8_80

be exploited to characterize optical properties of the marine surface (ocean color) and of the suspended particulate matter. Two specific measurement channels at 460 and 680 nm will be used to measure fluorescent scattering from marine chlorophyll and atmospheric aerosols for the characterization of the ocean primary production and for the purpose of aerosol typing, respectively. CALIGOLA will also allow accurate measurements of the small-scale variability of the Earth's surface elevation, primarily associated with variations in the terrain, vegetation, and forest canopy height. The space mission CALIGOLA is explicitly included in the ongoing ASI Three-Year Activity Plan (2021–2023), with a scheduled tentative launch window of 2026–2028.

Keywords Space Raman and fluorescence lidar · Aerosol typing · Size and microphysical properties · Ocean color and marine optical properties

80.1 Introduction

The Italian space industry, and specifically Leonardo S.p.A., has gained unique skills at international level in the development of space-qualified power laser sources for lidar Earth's observation applications (Aeolus, EarthCARE, [3]). Moreover, Leonardo S.p.A. and the Italian optical industry have a consolidated technical-scientific experience in the development of specific receiver subsystems for passive instruments and the payload thermo-mechanical structure that will be specialized for the CALIGOLA Mission. The Italian Space Agency (ASI) intends to benefit from these knowledges and skills to design and develop a lidar system for Earth's observation. The lidar is an active optical device developed after CO2 laser invention [4] that is widely used to monitor and investigate geometrical, microphysical, and optical properties of the atmosphere constituents [1, 2, 5, 6] thanks to its high spatial and temporal resolution. A Phase A study focusing on the technological feasibility of the laser source and receiver is ongoing, commissioned, and funded by ASI to Leonardo S.p.A. Scientific studies in support of the mission are also ongoing, with the University of Basilicata being the leading scientific institution.

By exploiting the three wavelengths emitted by a Nd: YAG laser source in the UV, VIS, and nIR and the polarized and depolarized elastic lidar (Rayleigh-Mie) and Raman echoes from atmospheric constituents, CALIGOLA will carry out vertical profile measurements of the particle backscatter coefficient at 354.7, 532, and 1064 nm, the extinction coefficient at 354.7 and 532 nm, and the depolarization ratio at 354.7, 532, and 1064 nm [7]. Furthermore, by exploiting the elastic polarized and depolarized backscatter echoes from the sea surface and the underlying water layers, CALIGOLA will measure the optical properties of the sea (ocean color) and the suspended particulate matter. This information is fundamental in the characterization of the seasonal and interannual dynamics of marine phytoplankton and in the study of its role in the marine biogeochemistry and in the global carbon cycle.

Two specific channels, and this represents an absolute novelty with respect to any previous space lidar mission, will measure fluorescence from atmospheric particles and marine chlorophyll to be used for the purpose of aerosol typing and the quantification of ocean primary production. It is to be underlined that numerous atmospheric aerosol types (biological particles, biomass fuels, sulfates, and dust) are fluorescent when excited with UV rays. Most part of the fluorescence spectrum is in the 400–700 nm interval [8]. This spectrum varies with the composition of the sounded aerosols, and consequently fluorescence measurements represent an effective tool for identifying aerosol typologies [9, 10]. Furthermore, since water is not fluorescent, fluorescence measurements from clouds allow obtaining information on aerosols inside clouds, at least on those located near the cloud base or top. CALIGOLA is therefore well suited to study of aerosol-cloud coexistence situations. CALIGOLA will also carry out accurate measurements of the small-scale variability of the Earth's surface elevation, associated with changes in the terrain, vegetation, and forest canopy.

The exploitation of subsystems already developed at national level for space applications, with a high TRL (TRL > 7), and the availability on the market of the few missing elements (i.e., receiver sensors such as photomultipliers for the UV) should allow developing the space lidar mission in a relatively short time (hopefully 4–6 years), ultimately leading to a mission with high scientific impact and timeliness. ASI is willing to pursue this mission in a coordinated way with one or more other European or extra-European space agencies, with a bilateral or multilateral contributed mission approach, and, in this regard, any interest from other Agencies is welcomed and desired.

For what concerns the timeliness of the mission, it is to be underlined that the ESA mission AEOLUS, launched in 2018, is providing unprecedented high-quality measurements of both wind and aerosol and clouds. AEOLUS hosts the high spectral resolution lidar ALADIN, with a primary focus on wind measurements and a secondary focus on particle backscatter/extinction measurements at 355 nm ($\beta_{355(z)}$ and $\alpha_{355(z)}$). However, although AEOLUS is demonstrating enormous longevity, it is unlikely that it will be still operational in the time frame 2026–2028.

The ESA mission EarthCARE, hosting the high spectral resolution lidar ATLID, will be launched in 2023 with a specific focus on the study of the relationship of clouds, aerosols, and radiation and the study of the role aerosols and clouds in reflecting incident solar radiation back into space and trapping infrared radiation emitted from Earth's surface. ATLID will provide single-wavelength (at 355 nm) particle backscatter/extinction/depolarization profile measurements ($\beta_{355(z)}$, $\alpha_{355(z)}$, and $\delta_{355(z)}$). EarthCARE has a design lifetime of 3 years, including a 6-month commissioning phase, and therefore its life cycle will likely partially superimpose with CALIGOLA. Furthermore, in 2030, NASA will launch the space mission "Aerosol-Cloud-Ecosystem" (ACE), hosting a lidar system operating at two wavelengths (532 and 1064 nm), both with depolarization measurement capability, but only one wavelength operated at high spectral resolution (532 nm), that is, $\beta_{532(z)}$, $\beta_{1064(z)}$, $\alpha_{532(z)}$, $\delta_{532(z)}$, and $\delta_{1064(z)}$.

Table 80.1 Power-aperture-efficiency product at the different wavelengths

	355	532	1064
Single pulse energy (mJ)	197	47	256
Repetiton rate (Hz)	51	51	51
Telescope aperture (m)	0.7	0.7	0.7
Laser Transmission & Beam expansion (%)	90	90	90
Telescope reflectivity (%)	92.5	85.5	91.5
Interference filters' CWL Tarsmission (%)	90	90	90
Quantum efficiency (%)	30	40	20
Power-aperture-efficiency (Wm^2)	0.869	0.256	0.745

With the aim of exploiting technological solutions and subsystems already developed at national level for space applications, with a high TRL (TRL > 7), the development of the laser source will benefit from the laser developments by Leonardo S.p.A. in the frame of the Aeolus follow-on activities (TXA-AFO). The laser source will be operated in un-seeded mode, with a repetition rate of 51 Hz and a single-pulse energy at 355, 532, and 1064 nm of ~200, ~50, and ~ 250 mJ, respectively. The laser will have an output full angle beam divergence smaller than 0.3 mrad, with a pointing jitter <0.02 mrad. The use of a × 10 beam expander will allow to get a final beam divergence of 30 μrad, which will be coupled with a receiver field of view of 40 μrad. The telescope development will benefit from previous developments by Officina Stellare or Media Lario, with a demonstrated capability to develop low-weight large aperture telescope with a primary mirror diameter of 0.5 m (max 0.7 m), based on the use of the Zerodur technology. The technical specifications considered in the simulations are illustrated in Table 80.1.

The expected performance of CALIGOLA has been assessed based on the application of an end-to-end lidar simulator [11, 12], which includes a forward module and a retrieval module. The forward module simulates the interaction mechanisms of the laser radiation with the atmospheric constituents and the behavior of all the devices present in the experimental system (telescope, optical reflecting and transmitting components, detectors), which ultimately allows generating synthetic lidar signals. The simulated signals are then fed into the retrieval module to obtain vertical profiles of multi-wavelength particle backscatter/extinction/depolarization profiles. The simulator finally provides statistical (RMS) and systematic (bias) uncertainties.

A possible platform is represented by the International Space Station (ISS), using two slots therein available from the European Space Agency. Alternative solutions are presently under consideration. The International Space Station has an orbiting height of 408 km, with an orbital velocity and period of 7.66 km/s and 92.68 min, respectively. The ISS is not located on a sun-synchronous polar orbit but on a mid-latitude orbit with an inclination of 51.6397. In case of deployment on the ISS, because of the lack of a sun-synchronicity, CALIGOLA will be not be able to revisit the same location on Earth at the same time daily. The simulations included in this paper refer to the orbital characteristics of the ISS.

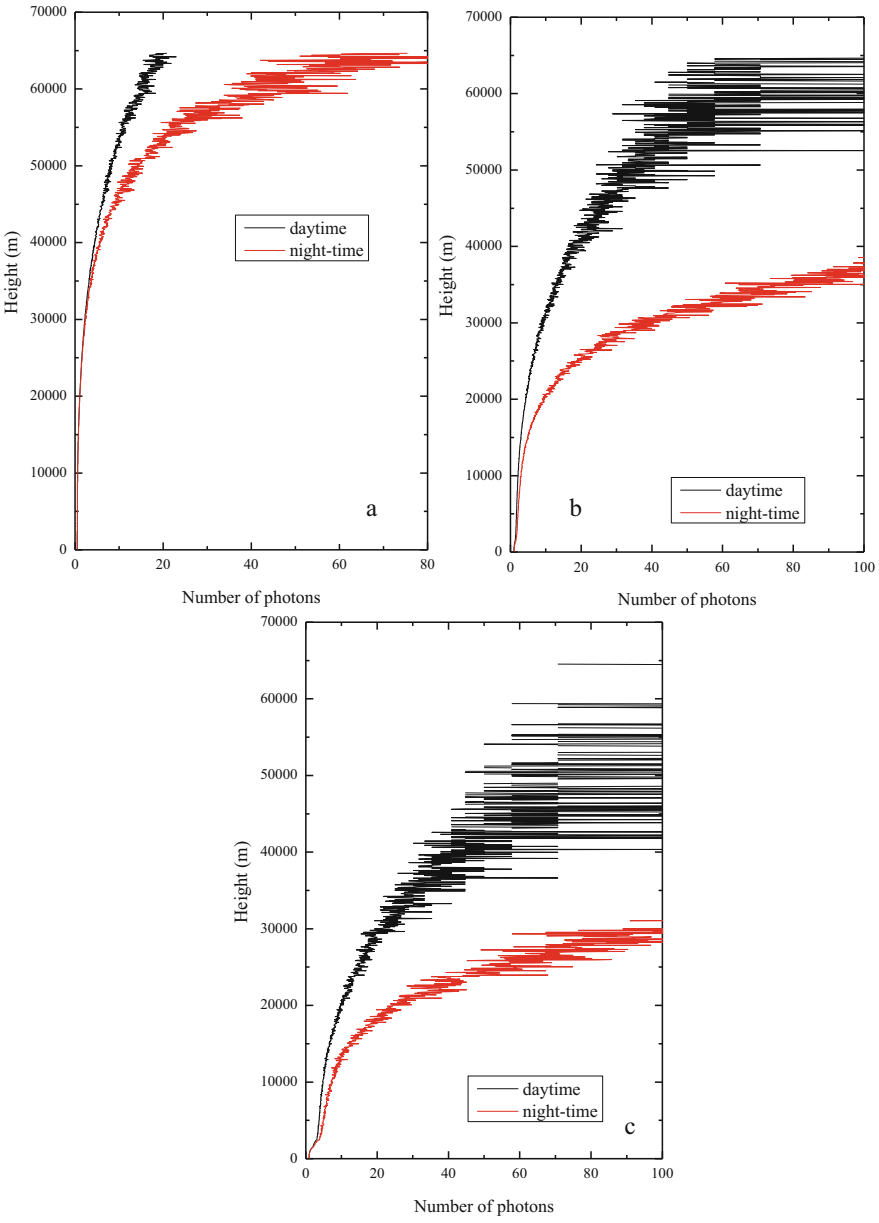


Fig. 80.1 Simulations of the statistical uncertainty affecting the elastic signals at 355 (panel **a**), 532 (panel **b**), and 1064 nm (panel **c**)

Figure 80.1 illustrates the simulations of the statistical uncertainty affecting the elastic signals at 355, 532, and 1064 nm. Results refer to clear sky conditions.

Simulations consider a horizontal resolution of 50 km, which corresponds to an averaging over 335 single-shot lidar echoes (with a pulse repetition rate of 50 Hz), and a vertical resolution of 200 m (dwell time = 1.33 usec). The ISS orbit is characterized by a β-angle varying in between ±75.1° during the year. In the simulations, a similar variability of the sun zenith angle (SZA) of the sub-satellite point was assumed.

References

1. Di Girolamo, P., Summa, D., Bhawar, R., Di Iorio, T., Cacciani, M., Veselovskii, I., Dubovik, O., Kolgotin, A.: Raman Lidar observations of a Saharan dust outbreak event: characterization of the dust optical properties and determination of particle size and microphysical parameters. Atmos. Environ. **50**, 66–78., ISSN: 1352-2310 (2012). https://doi.org/10.1016/j.atmosenv.2011.12.061
2. Di Girolamo, P., De Rosa, B., Summa, D., Franco, N., Veselovskii, I.: Measurements of aerosol size and microphysical properties: a comparison between Raman lidar and airborne sensors. J. Geophys. Res. Atmos. **127**, e2021JD036086 (2022). https://doi.org/10.1029/2021JD036086
3. Lolli, S., Delaval, A., Loth, C., Garnier, A., Flamant, P.H.: 0.355-micrometer direct detection wind lidar under testing during a field campaign in consideration of ESA's ADM-Aeolus mission. Atmospheric. Meas. Tech. **6**(12), 3349–3358 (2013)
4. Ciofini, M., Lapucci, A., Lolli, S.: Diffractive optical components for high power laser beam sampling. J. Opt. A Pure Appl. Opt. **5**(3), 186 (2003)
5. Lolli, S., Di Girolamo, P.: Principal component analysis approach to evaluate instrument performances in developing a cost-effective reliable instrument network for atmospheric measurements. J. Atmos. Ocean. Technol. **32**(9), 1642–1649 (2015)
6. Lolli, S., Sauvage, L., Loaec, S., Lardier, M.: EZ Lidar™: a new compact autonomous eye-safe scanning aerosol Lidar for extinction measurements and PBL height detection. Validation of the performances against other instruments and intercomparison campaigns. Optica pura y aplicada. **44**(1), 33–41 (2011)
7. Di Girolamo, P., Summa, D., Ferretti, R.: Multiparameter Raman Lidar measurements for the characterization of a dry stratospheric intrusion event. J. Atmos. Ocean. Technol. **26**, 1742–1762 (2009). https://doi.org/10.1175/2009JTECHA1253.1
8. Pan, Y.-L.: Detection and characterization of biological and other organic-carbon aerosol particles in atmosphere using fluorescence. J. Quant. Spectrosc. Radiat. Transf. **150**, 12–35 (2015)
9. Veselovskii, I., Hu, Q., Goloub, P., Podvin, T., Korenskiy, M., Pujol, O., Dubovik, O., Lopatin, A.: Combined use of Mie–Raman and fluorescence lidar observations for improving aerosol characterization: feasibility experiment. Atmos. Meas. Tech. **13**, 6691–6701 (2020). https://doi.org/10.5194/amt-13-6691-2020
10. Veselovskii, I., Hu, Q., Goloub, P., Podvin, T., Choël, M., Visez, N., Korenskiy, M.: Mie–Raman–fluorescence lidar observations of aerosols during pollen season in the north of France. Atmos. Meas. Tech. **14**, 4773–4786 (2021). https://doi.org/10.5194/amt-14-4773-2021
11. Di Girolamo, P., Behrendt, A., Wulfmeyer, V.: Spaceborne profiling of atmospheric temperature and particle extinction with pure rotational Raman Lidar and of relative humidity in combination with differential absorption Lidar: performance simulations. Appl. Opt. **45**, 2474–2494., ISSN: 0003-6935 (2006). https://doi.org/10.1364/AO.45.002474
12. Di Girolamo, P., Behrendt, A., Wulfmeyer, V.: Space-borne profiling of atmospheric thermodynamic variables with Raman lidar: performance simulations. Opt. Express. **26**(7), 8125–8161 (2018). https://doi.org/10.1364/OE.26.008125

Chapter 81
An Overview of the NASA Atmosphere Observing System Inclined Mission (AOS-I) and the Role of Backscatter Lidar

John E. Yorks, Scott Braun, Ed Nowottnick, Matt McGill, Courtney Schumacher, Jun Wang, Melanie Follette-Cook, James Campbell, and Michael Pavolonis

Abstract NASA has established the Earth System Observatory (ESO) to fulfill the science needs presented in the 2017 Earth Science Decadal Survey, and the Atmosphere Observing System (AOS) is a key component of ESO. The AOS mission will make measurements of aerosols, clouds, convection, and precipitation, which represents two of the designated observables in the decadal survey, to advance our understanding of the processes that drive cloud and precipitation properties (for low, high, convective, and frozen/mixed-phase clouds), convective vertical motion, air quality, aerosol redistribution, radiative transfer, and the relationships between these processes. AOS employs a two-orbit architecture (a polar orbit and an inclined orbit), thereby allowing AOS to cover a wide range of temporal and spatial scales and transforming our understanding of this critical part of the Earth's system. The

J. E. Yorks (✉) · S. Braun · E. Nowottnick · M. McGill
NASA Godard Space Flight Center, Greenbelt, MD, USA
e-mail: John.E.Yorks@nasa.gov

C. Schumacher
Department of Atmospheric Sciences, Texas A&M University, College Station, TX, USA

J. Wang
Department of Chemical and Biochemical Engineering, University of Iowa, Iowa City, IA, USA

M. Follette-Cook
NASA Godard Space Flight Center, Greenbelt, MD, USA

Morgan State University, Goddard Earth Sciences Technology and Research Center, Baltimore, MD, USA

J. Campbell
Naval Research Laboratory Monterrey, Monterey, CA, USA

M. Pavolonis
NOAA/NESDIS Center for Satellite Applications and Research, Springs, MD, USA

© The Author(s), under exclusive license to Springer Nature Switzerland AG 2023

J. T. Sullivan et al. (eds.), *Proceedings of the 30th International Laser Radar Conference*, Springer Atmospheric Sciences,
https://doi.org/10.1007/978-3-031-37818-8_81

inclined-orbit sensor suite (AOS-I, 55-degree inclination, 407 km altitude, notional launch in July 2028) includes a backscatter lidar called the Atmospheric Lidar Instrument for Clouds and Aerosol Transport (ALICAT), a Ku-band Doppler radar, and two microwave radiometers that provide short-time-differenced measurements. The goal of AOS-I is to determine the varying-time-of-day processes that control aerosol-convection-precipitation interactions, as well as the diurnal variability of convection, precipitation, high clouds, aerosol emissions, and air quality. This extended abstract provides (1) an overview of the AOS-I mission, (2) a description of the AOS-I science objectives, and (3) a preview of the critical role ALICAT plays in AOS-I science, applications, and synergy.

Keywords Clouds · Aerosols · Precipitation

81.1 Introduction

The Earth System Observatory (ESO) Atmosphere Observing System (AOS) was established by the NASA Science Mission Directorate Earth Science Division to fulfill the science recommendations of the 2017 Earth Science Decadal Survey for the Aerosols and Clouds, Convection and Precipitation (ACCP) designated observables [1]. The AOS Constellation Architecture is the result of a 2.5-year ACCP Architecture Study. The ACCP Architecture Study concluded in February 2021 and the mission was authorized to move into Pre-Phase A on May 23, 2021. Rather than treating these designated observables as two separate missions, the ACCP study recommended two missions with each focused on joint A and CCP science. Thus, the AOS architecture is composed of three components: (1) AOS-Inclined (or AOS-I) delivers information on diurnally varying processes associated with clouds, convection, precipitation, and aerosols from an inclined orbit (55-degree inclination, 407 km altitude), (2) AOS-Polar (AOS-P) provides improved understanding of the contributions of aerosol-cloud-precipitation interactions to global climate change uncertainty from a sun-synchronous orbit (450 km altitude and 1330 ascending node), and (3) a suborbital program formulated to provide in situ and remote-sensing measurements from surface-based and airborne instruments. This extended abstract will focus on the AOS-I science objectives and contributions from the backscatter lidar.

81.1.1 AOS-I Science and Applications

Convection and its associated rainfall/vertical motions have a strong diurnal cycle, especially over land in the tropics [2]. High clouds, especially tropical anvils that are generated from convective processes, also exhibit diurnal variability [3]. Aerosol emissions such as dust from deserts, smoke from fires, and black carbon from

Table 81.1 The AOS science objectives and key focus areas relevant to AOS-I

Science objective	Key science focuses
High clouds	Relationship between the horizontal extent and ice water path of convectively generated high clouds, convective vertical transport, and environmental factors
Convective storms	Relationship between vertical motion within convective storms and their (a) precipitation structures, (b) latent heating, (c) local thermodynamic environment, (d) ambient aerosol loading, and (e) diurnal variability
Air quality and aerosol attribution	Factors that relate air quality processes and diurnal variability of dust and smoke emissions, as well as the aerosol mixing layer height
Aerosol redistribution and processing	Wet removal and processing of aerosol by clouds and precipitation and impacts of vertical and long-range transport of aerosol

exhaust have strong vertical and diurnal variability that are critical to predicting transport and air quality [4]. Furthermore, processes such as isolated convection, mesoscale convective systems, air quality events, aerosol emissions, and small-scale aerosol removal and vertical transport occur at sub-daily timescales and small spatial scales (<300 km). While TRMM/GPM have observed the diurnal variability of convective precipitation, the processes that affect convective dynamics are complex and remain severely under observed around the globe, principally because these missions did not provide measurements of vertical motion. CALIPSO demonstrated an ability to detect and quantify thin high clouds [5] and optically thick aerosol layers such as dust [6] but did not sample at different times of the day. Given the hypotheses about the impact of aerosols on convective vertical motions [7], measurement of ambient aerosol profiles in the environment of convective clouds is of high interest.

The AOS-I project is designed to capture processes at sub-daily timescales, particularly diurnal variability related to objectives shown in Table 81.1 using a backscatter lidar to profile aerosols and thin high clouds, a contributed Ku-band wide-swath Doppler radar from the Japan Aerospace Exploration Agency (JAXA) to profile precipitation and convective vertical air motions, and a pair of passive microwave radiometers contributed by the National Centre for Space Studies (CNES) of France to study short-duration (on the order of 2 min) changes in ice water path and inferred vertical ice mass flux in convective storms and their associated high clouds. AOS-I, with a notional launch of mid-2028, provides early science that is critical given the future gap in radar/lidar capabilities. These collocated time-varying measurements will enable more accurate predictions of rain and severe weather, especially in the presence of aerosols, and improve our understanding of processes such as ice mass sedimentation rates that climate models are sensitive to but are not well constrained due to a lack of observations on a global scale [8]. The AOS-I backscatter lidar, called the Atmospheric Lidar Instrument for Clouds and Aerosol Transport (ALICAT), provides vertical structure of aerosols at different times of the day not sampled by AOS-P but critical to understanding

air quality processes and diurnal variability of aerosol emissions. Additionally, the AOS-I near real-time (<6-h latency) data provide key information to support decision making that will enable improved weather and air quality forecasting, disaster monitoring and models, and water resource management.

81.2 The ALICAT Instrument

ALICAT is a compact version of the Cloud-Aerosol Transport System (CATS) that operated on the International Space Station (ISS) for 33 months [9] capable of SmallSat implementation. ALICAT provides measurements of 532 and 1064 nm backscatter and depolarization by utilizing a high repetition rate and low pulse energy laser operating in conjunction with photon-counting detectors. This approach has been demonstrated with the CATS lidar on the ISS and over 20 years of use by the Cloud Physics Lidar (CPL) instrument on NASA aircraft [10]. The key to ALICAT's compact design is the reuse of crucial aspects of the CATS instrument or other space mission components (e.g., telescope, optical elements), coupled with significant new technologies (laser, electronics) designed specifically for SmallSat implementation, to provide a mature solution that meets AOS-I science objectives. Leveraging the CATS technology heritage and CATS/CALIPSO algorithm heritage enables ALICAT to provide the AOS mission with an affordable, low-risk standard backscatter lidar that advances current capabilities and performance. Primary instrument specifications are provided in Table 81.2. The ALICAT Level 1 data products include observable quantities such as total and perpendicular attenuated backscatter. These observables are required at fine resolutions to enable detection of small-scale aerosol plumes, and their accuracies are primarily a function of signal-to-noise ratio and calibration uncertainty. ALICAT's projected performance is provided in Table 81.2 based on simulations using the instrument specifications and the AOS-I orbit altitude. More information on the ALICAT measurement performance and simulations are provided in a 2022 ILRC extended abstract by Nowottnick et al. [11].

The AOS-I aerosol-related geophysical variables will be provided by ALICAT Level 2 data products. ALICAT will leverage strong algorithm heritage from CATS and CALIOP, as well as innovative ML techniques, to provide an aerosol-cloud vertical feature mask [12]. The primary required measurements are 532- and 1064-nm total and perpendicular attenuated backscatter with a 532-nm minimum detectable backscatter (MDB) of <8.0E-4 km^{-1} sr^{-1} at night and day to ensure accurate layer detection over all hours of the day. This MDB is based on CALIOP and CATS MDB for cirrus cloud between 10 and 12 km [9]. Table 81.2 shows expected MDB performance based on ALICAT instrument simulations. Volume depolarization ratio, especially at multiple wavelengths, is defined as the ratio of the parallel (total minus perpendicular) to perpendicular attenuated backscatter within detectable layers and is required for accurately discriminating between atmospheric features and determining aerosol type [13]. The aerosol extinction coefficient will be

Table 81.2 Traceability from AOS geophysical variables to ALICAT measurements and instrument projected performance. Numbers are still considered preliminary at this stage

Geophysical variables			Measurement		Instrument	
Geophysical variable	Requirements	Observables	Parameter	Projected performance	Parameter	Projected performance
Aerosol-cloud feature mask	**Range: 0.1–0.20 km Res: ≤350 m horizontal ≤60 m vertical**	Vertical profiles of attenuated total backscatter	Vertical resolution	30 m	Backscatter wavelengths	532 and 1064 nm
			Horizontal resolution	100 m	Lidar bin width	30 m
			532 nm SNR in aerosol layer (dust AOD = 0.3 over ocean)	20.7 (night) 11.0 (day)	Laser pulse repetition rate	4000 Hz
					Laser pulse energy	3 mJ (1064 nm) 2 mJ (532 nm)
Aerosol extinction (VIS, NIR)	**Unc: Maximum of 0.03 km^{-1}or 80% (VIS/NIR) Res: ≤5 km (10 km) horiz ≤60 m (120 m) vert**		1064 nm SNR in aerosol layer (dust AOD = 0.3 over ocean)	5.2 (night) 2.6 (day)	Telescope field-of-view (FOV)	85 mrad (532 nm) 115 mrad (1064 nm)
			532 nm min detectable backscatter at 5 km	4.1E-4 (night) 5.3E-4 (day)	Transmitted beam divergence	35 mrad (532 nm) 70 mrad (1064 nm)
			Calibration uncertainty	3–8% (532) 5–10% (1064)	Receiver efficiency	35.2% (532 nm) 27.6% (1064 nm)
			Calibration resolutions (SNR > 75)	750 km (hori) 2.5 km (vert.)	Detector quantum efficiency	60% (532 nm) 2% (1064 nm)
					Vertical data Collection range	37.5 km
Volume depolarization ratio (VIS, NIR)	**Range: 0.05–1.0 Unc: 100% (VIS/NIR) Res: ≤5 km (≤50 km) horiz, ≤60 m (≤500 m) vertical**	Vertical profiles of attenuated perpendicular backscatter	Polarization gain ratio uncertainty	3–5%	Depolarization wavelength	532 and 1064 nm
			Perpendicular attenuated backscatter SNR (dust AOD = 0.3 over ocean)	2.7/8.8 (532 nm, D/N) 1.0/2.6 (1064 nm, D/N)	Depolarization purity	~150:1

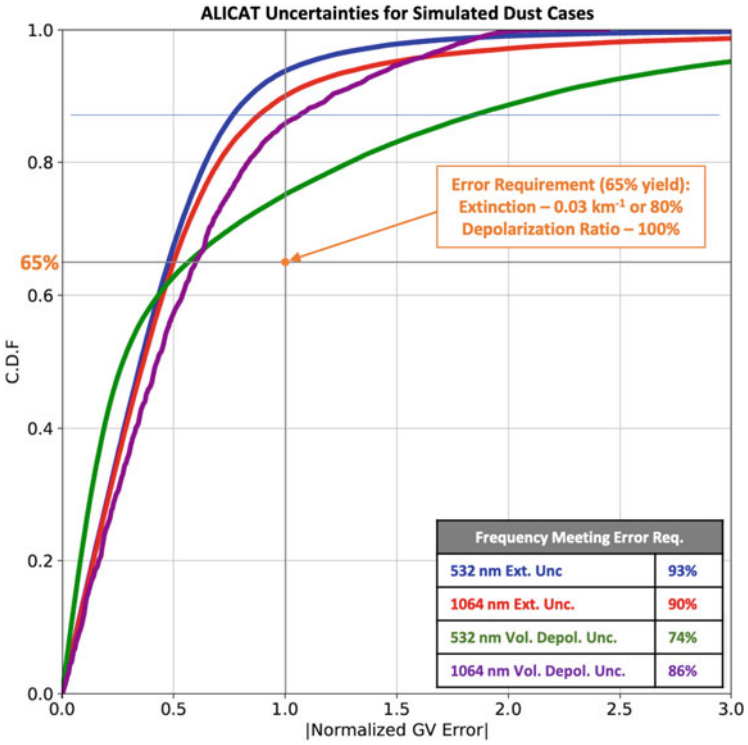


Fig. 81.1 A cumulative density function (CDF) for extinction uncertainty at 532 nm (blue) and 1064 nm (red) as well as volume depolarization ratio uncertainty at 532 nm (green) and 1064 nm (purple) show that ALICAT meets the corresponding normalized error requirements for clear sky dust cases. These clear sky dust cases include night (50%) and day (50%) conditions over ocean (60%) and desert (40%) with a solar zenith angle of 0.0 and layers between 0 and 2 km with AODs of 0.05–0.50. The extinction was estimated using the unconstrained (75%) and constrained (25%) retrievals described in Sect. 81.2.

estimated via unconstrained retrievals that assume a layer-average lidar ratio from a lookup table [5] or constrained retrieval using several methods, such as using passive aerosol optical depth (AOD) estimates or the signal loss method for lofted layers [14]. Preliminary ALICAT performance was simulated using realistic clear sky dust aerosol canonical cases and the GSFC lidar simulation model. These simulation results show that ALICAT meets the extinction and volume depolarization ratio requirements for these dust cases (Fig. 81.1).

81.3 ALICAT Contributions to AOS-I Science and Synergy

Backscatter lidars provide measurements of total attenuated backscatter, detection of aerosols (especially dust and smoke) and optically thin high clouds, and estimates of extinction and volume depolarization ratio vertical profiles. CALIOP has provided these measurements for over 15 years from a polar orbit. AOS-I extends and enhances these backscatter lidar measurements by (1) utilizing an inclined orbit to statistically sample diurnal variability of dust, smoke, and aerosol mixing layer height, (2) improving daytime SNR for better detection of aerosols, and (3) adding depolarization at two wavelengths for improved qualitative aerosol typing. These observations are critical to understanding the diurnal variability of aerosol emissions and air quality, as well as synergy with new geostationary weather and atmospheric composition satellites. These geostationary missions are designed to capture the diurnal variability of column properties (i.e., AOD) in the horizontal dimension but have limited information about the vertical distribution of aerosols and aerosol mixing heights.

AOS-I provides the first ever opportunity for synergy between varying-time-of-day Ku-band radar, microwave radiometer, and backscatter lidar data. These observations will enable the community to sample the diurnal cycle of convective storms by extending the GPM/TRMM record of precipitation profiles, while adding capabilities such as Doppler vertical motion, time-differenced radiometer measurements, and coincident aerosol profiles that will immensely improve our understanding of convective processes and the influence of aerosols on convection. These collocated datasets will also provide better 3-D precipitation estimates for aerosol wet removal and insights on aerosol vertical transport. Finally, AOS-I can improve our understanding of high clouds through these collocated datasets to better constrain cloud processes, such as ice mass sedimentation rate, in climate models.

References

1. National Academies of Sciences, Engineering, and Medicine: Thriving on our Changing Planet: a Decadal Strategy for Earth Observation from Space. The National Academies Press, Washington, DC (2018). https://doi.org/10.17226/24938
2. Nesbitt, S., co-authors: Storm morphology and rainfall characteristics of TRMM precipitation features. Mon. Weather Rev. **134**(10), 2702–2721 (2006)
3. Noel, V., co-authors: The diurnal cycle of cloud profiles over land and ocean between 51°S and 51°N, seen by the CATS spaceborne lidar from the International Space Station. Atmos. Chem. Phys. **18**, 9457–9473 (2018)
4. Lee, L., co-authors: Investigation of CATS aerosol products and application toward global diurnal variation of aerosols. Atmos. Chem. Phys. **19**, 12687–12707 (2019)
5. Hlavka, D.L., co-authors: Airborne validation of cirrus cloud properties derived from CALIPSO lidar measurements: optical properties. J. Geophys. Res. **117**, D09207 (2012)
6. Huang, J., co-authors: CALIPSO inferred most probable heights of global dust and smoke layers. J. Geophys. Res. Atmos. **120**, 5085–5100 (2015). https://doi.org/10.1002/2014JD022898

7. Khain, A., Rosenfeld, D., Pokrovsky, A.: Aerosol impact on the dynamics and microphysics of deep convective clouds. Q. J. R. Meteorol. Soc. **131**, 2639–2663 (2005). https://doi.org/10.1256/qj.04.62
8. Deng, M., Mace, G.G.: Cirrus cloud microphysical properties and air motion statistics using cloud radar Doppler moments: water content, particle size, and sedimentation relationships. Geophys. Res. Lett. **35**, L17808 (2008). https://doi.org/10.1029/2008GL035054
9. Yorks, J.E., co-authors: An overview of the CATS level 1 processing algorithms and data products. Geophys. Res. Lett. **43**, 4632–4639 (2016)
10. McGill, M.J., co-authors: Cloud physics Lidar: instrument description and initial measurement results. Appl. Opt. **41**, 3725–3734 (2002)
11. Nowottnick, E., co-authors: A Simulation capability developed for NASA GSFC's Spaceborne backscatter Lidars: overview and projected performance for the upcoming AOS mission. In: 30th International Laser Radar Conference (ILRC 26), June 2022 (2022)
12. Yorks, J.E., co-authors: Aerosol and cloud detection using machine learning algorithms and space-based Lidar data. Atmosphere. **2021**(12), 606 (2021)
13. Nowottnick, E., co-authors: Aerosol Detection from the cloud aerosol transport system on the international space station: algorithm overview and implications for diurnal sampling. Atmosphere. **13**(9), 1439 (2022)
14. Midzak, N., co-authors: Constrained retrievals of aerosol optical properties using combined Lidar and imager measurements during the FIREXAQ campaign. Front. Remote Sens. **3**, 818605 (2022). https://doi.org/10.3389/frsen.2022.818605

Chapter 82
Proposal for the Space-Borne Integrated Path Differential Absorption (IPDA) Lidar for Lower Tropospheric Water Vapor Observations

Makoto Abo, Chikao Nagasawa, Yasukuni Shibata, Osamu Uchino, Tetsu Sakai, Takashi Shibata, and Masaki Katsumata

Abstract Measurements of water vapor profiles are very important in the studies of atmospheric dynamics, clouds, aerosols, and radiation. Water vapor is the predominant greenhouse gas, and its vertical distributions are especially important in the global climate system. Water vapor data would lead to benefits in numerical weather predictions for localized heavy rainfall events and typhoon forecasting. We have proposed two-beam space-borne water vapor DIAL with the OPG/OPA transmitter using the absorption line of the 1300 nm band. An error simulation is performed assuming that the platform altitude is 250 km, the receiver diameter is 0.8 m, the laser energy is 20 mJ, and the repetition rate of the laser shot pair (on-off) is 500 Hz. It is shown that water vapor profile measurement relative error of less than 10% is possible between 0 and 2 km altitudes with spatial resolutions of 300 m vertically and 20 km horizontally in East Asia in summer.

M. Abo (✉) · C. Nagasawa · Y. Shibata
Tokyo Metropolitan University, Hino, Tokyo, Japan
e-mail: abo@tmu.ac.jp

O. Uchino
National Institute for Environmental Studies, Tsukuba, Ibaraki, Japan
e-mail: uchino.osamu@nies.go.jp

T. Sakai
Meteorological Research Institute, Tsukuba, Ibaraki, Japan
e-mail: tetsu@mri-jma.go.jp

T. Shibata
Nagoya University, Chikusa, Nagoya, Japan
e-mail: shibata_takashi@nagoya-u.jp

M. Katsumata
Japan Agency for Marine-Earth Science and Technology, Yokosuka, Kanagawa, Japan
e-mail: katsu@jamstec.go.jp

© The Author(s), under exclusive license to Springer Nature Switzerland AG 2023

J. T. Sullivan et al. (eds.), *Proceedings of the 30th International Laser Radar Conference*, Springer Atmospheric Sciences,
https://doi.org/10.1007/978-3-031-37818-8_82

Keywords DIAL · Water vapor · Numerical weather prediction

82.1 Introduction

In recent years, the occurrence of heavy rain due to the linear precipitation zone and the increase in the size of typhoons have become major social problems in terms of disaster prevention. The number of heavy rain disasters in Japan is increasing year by year, and measures for disaster prevention/mitigation and national resilience are urgent. Although these disasters can be mitigated by improving prediction accuracy, it has been pointed out that water vapor distribution information in the lower troposphere at sea is particularly important for prediction. The space-borne lidar can observe water vapor over the sea around Japan, and it is expected that the prediction accuracy will be improved by assimilating the data into the numerical weather prediction model.

Currently, water vapor observation is performed by radiosonde, terrestrial remote sensing, and satellite infrared/microwave sensor, but there are problems with spatial and temporal resolution. In addition, passive satellite observations have a wide horizontal coverage area, but their vertical resolution is insufficient. Accuracy, vertical resolution, and coverage are insufficient for quantitative evaluation of global water vapor circulation. The space-borne lidar provides global high-resolution and high-quality water vapor data, and since it has no bias error, it can also be used for calibration of passive remote sensing equipment and has a synergistic effect with surface observation by the satellite sensor.

82.2 Space-Borne Water Vapor DIAL

We have proposed a two-beam space-borne water vapor DIAL with the OPA (optical parametric amplifier) transmitter using the 1350 nm absorption band [1]. Figure 82.1 shows a block diagram of the proposed space-borne water vapor DIAL system, and Table 82.1 shows parameters of the space-borne water vapor DIAL. OPA system using QPM (quasi-phase matching) device is a one-path amplifier [2]. OPA is advantageous for space use because it has less restrictions than conventional phase-matching OPO (optical parametric oscillator). An error simulation is performed assuming that the platform altitude is 250 km (super-low altitude satellite), the receiver diameter is 0.8 m, the laser energy is 20 mJ, and the repetition rate of the laser shot pair (on-off) is 500 Hz. It has been shown that less than 10% water vapor profile measurement relative error is possible between 0.3 and 2 km altitudes with spatial resolutions of 300 m vertically and 20 km horizontally in East Asia in summer (Fig. 82.3).

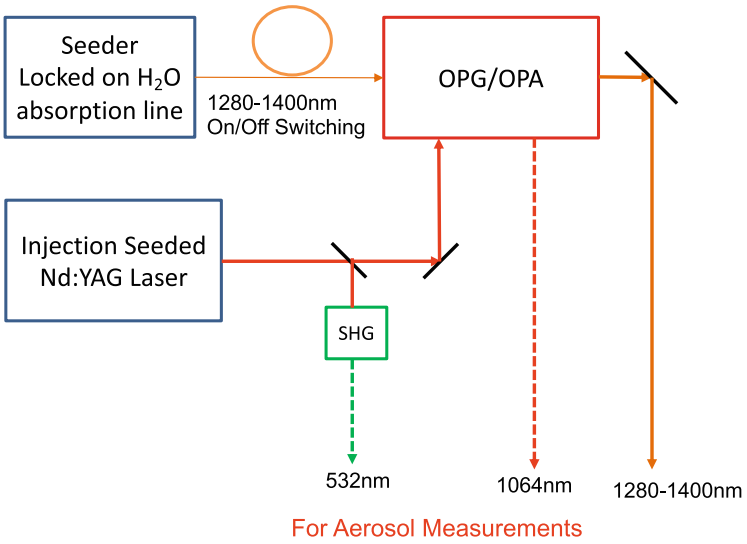


Fig. 82.1 Block diagram of the proposed space-borne water vapor DIAL system

Table 82.1 Parameters of the two-beam space-borne water vapor DIAL

Parameter	Value
Pulse energy	20 mJ(10 mJ for each beam)
Repetition rate	500 Hz (on/off pair)
Wavelength	1300 nm
Telescope aperture	0.8 m
Quantum efficiency	50% (APD)
Platform altitude	250 km
Ground track speed	7.8 km/s

82.3 IPDA DIAL

As well as the vertical water vapor distribution, measuring the amount of water vapor near the sea surface is important for forecasting heavy rainfall and estimating the flux between the ocean and the atmosphere. Therefore, without changing the specifications of the proposed DIAL mission, we investigated a possibility of DIAL observations of lower tropospheric and near surface water vapor using both signals of the atmospheric backscattering and the surface reflection by employing the integrated path differential absorption (IPDA) technique [3]. This technique uses the differential absorption of the signal reflected by the surface, which is stronger than the atmospheric backscattering signal (Fig. 82.2).

Figure 82.3 shows random error of water vapor density for the two-beam space-borne DIAL with vertical resolutions of 300 m/600 m and IPDA-DIAL. Horizontal resolution is 20 km and water vapor model is a mean summer profile over Japan. From the error simulation results, it is possible to observe the amount of water vapor

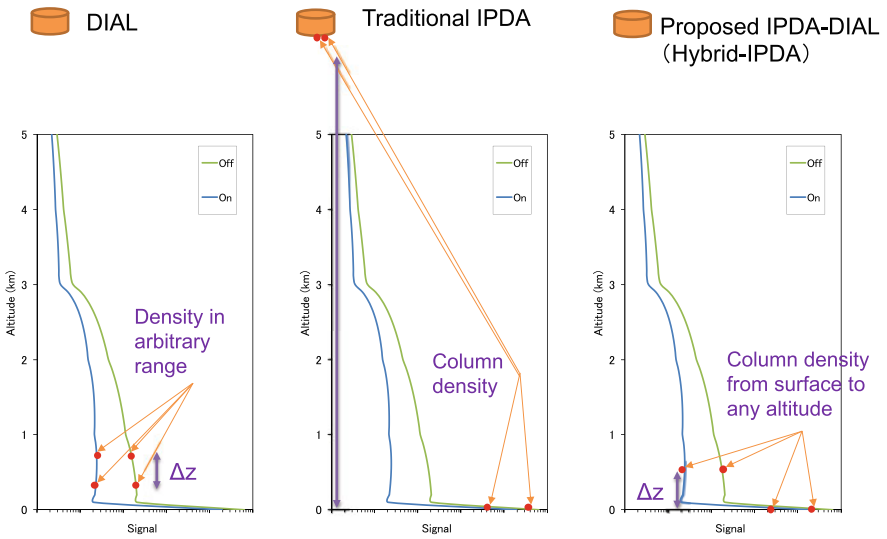


Fig. 82.2 Comparison of the space-borne DIAL, traditional IPDA, and proposed IPDA

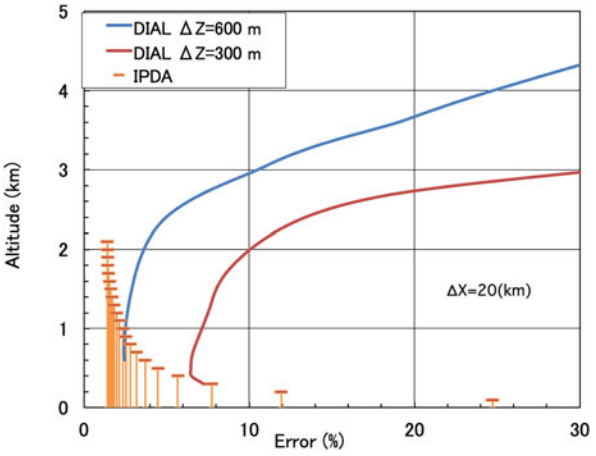


Fig. 82.3 Random error of water vapor density for the two-beam space-borne DIAL with vertical resolutions of 300 m/600 m and IPDA DIAL. Horizontal resolution is 20 km and water vapor model is a mean summer profile over Japan. The vertical bar in IPDA means that the statistical error is that of the column density in the range from surface to the marked altitude

from the surface to an altitude of 200 m with an error of 10% and from the surface to an altitude of 600 m with an error of 3%. This simulation assumes nighttime, but since the background light level is low in this wavelength range due to the absorption of water vapor, it is also advantageous for daytime observations.

82.4 Conclusion

It was found that the use of the IPDA DIAL method improves the measurement range and measurement accuracy in the low altitude region compared to the conventional space-borne DIAL. We will consider a small space-borne water vapor DIAL limited to measurement in the low altitude region, using the IPDA method.

References

1. Abo, M., Nagasawa, C., Shibata, Y., Uchino, O., Sakai, T., Shibata, T., Katsumata, M.: Proposal on the Spaceborne differential absorption Lidar for global water vapor profiling. J. Laser Radar Soc. Jpn. **1**(2), 72–78 (2020)
2. Shibata, Y., Nagasawa, C., Abo, M.: Development of 1.6 μm DIAL using an OPG/OPA transmitter for measuring atmospheric CO_2 concentration profiles. Appl. Opt. **56**, 1194–1201 (2017)
3. Abshire, J.B., Ramanathan, A., Riris, H., Mao, J., Allan, G.R., Hasselbrack, W.E., Weaver, C.J., Browell, E.V.: Airborne measurements of CO_2 column concentration and range using a pulsed direct-detection IPDA Lidar. Remote Sens. **6**, 443–469 (2014)

Chapter 83
Assimilation of Aerosol Observations from the Future Spaceborne Lidar Onboard the AOS Mission into the MOCAGE Chemistry: Transport Model

Flavien Cornut, Laaziz El Amraoui, Juan Cuesta, Roseline Schmisser, Jérôme Blanc, and Béatrice Josse

Abstract For the AOS (Atmosphere Observing System) mission, we analyze the contribution of the future 532 nm-HSR (high spectral resolution) spaceborne Lidar measurements implementing an Observing System Simulation Experiment (OSSE) based on the MOCAGE (*Modèle de Chimie Atmosphérique de Grande Echelle*) (Sič, Amélioration de la représentation des aérosols dans un modèle de chimie-transport: Modélisation et assimilation de données, 2014) Chemistry Transport Model (CTM). This first case study focuses on a Saharan dust event on March 2018 reaching Greece. Nature Run is extracted along the CALIOP (Cloud-Aerosol Lidar with Orthogonal Polarization) trajectory for a two-week period. Two simulations are computed, one with a standard "Klett" inversion (CALIOP-like) and an AOS lidar with HSR at 532 nm. The first results showed a better performance of the assimilation of AOS particulate backscatter products, both during intense and weak episodes. This ability to constrain extends over the entire domain in model space and allows improvements of a factor of ~1.5 and ~1.6 in terms of bias and RMSE compared to the assimilation of a CALIOP-like product on the description of desert dust AOD (AOD_DD) or vertical profiles.

Keywords Lidar · HSRL · AOS · OSSE · Data assimilation · aerosols

F. Cornut (✉) · L. El Amraoui · B. Josse
CNRM, Université de Toulouse, Météo-France, CNRS, Toulouse Cedex 1, France
e-mail: flavien.cornut@meteo.fr

J. Cuesta
Univ Paris Est Creteil and Université de Paris, CNRS, LISA, Créteil, France

R. Schmisser · J. Blanc
CNES, Toulouse Cedex 9, France

© The Author(s), under exclusive license to Springer Nature Switzerland AG 2023

J. T. Sullivan et al. (eds.), *Proceedings of the 30th International Laser Radar Conference*, Springer Atmospheric Sciences,
https://doi.org/10.1007/978-3-031-37818-8_83

83.1 Introduction

Monitoring aerosols and clouds with spaceborne lidars such as CALIOP (Cloud-Aerosol Lidar with Orthogonal Polarization) is essential for characterizing their vertical distributions. Lidar observations from CALIOP have improved the estimation of radiative forcing of aerosols and cloud feedbacks for more than 10 years, two of the main uncertainties for climate prediction [1]. However, the estimations of aerosol extinction profiles from backscatter lidars such as CALIOP rely on hypothesis of their optical properties (e.g., lidar ratio) and can therefore present large uncertainties. The Atmosphere Observing System (AOS) mission is an international collaborative program from NASA, CNES, JAXA, and CSA which aims to carry a new generation spaceborne lidar for better characterizing clouds and aerosols. The design of this lidar offers HSRL (high spectral resolution lidar) channel at 532 nm, thus avoiding the ambiguities in the estimations of aerosol extinction profiles. First results concerning the benefits of the AOS configuration to constrain MOCAGE are presented.

83.2 Method

83.2.1 OSSE

The OSSE (Observing System Simulation Experiment) approach is used in several domains to evaluate the added value of a future observing system in the global system [3]. A Nature Run (NR) that we consider as the reality and a Control Run (CR) trying to represent the same reality in a free model are simulated. Synthetic observations (SO) are computed from the NR with a lidar simulator called BLISS (Backscattering Lidar Signal Simulator) and assimilated in the CR. The Assimilation Run (AR) is then compared to the NR and the CR.

83.2.2 Nature Run and Control Runs

The NR is simulated by assimilating the aerosol optical depth (AOD) of MODIS (moderate resolution imaging spectroradiometer) at 550 nm in MOCAGE with the same method described in Sič et al. [4], using hourly 3D-FGAT variational method on a global domain at $1 \times 1°$ resolution. The period selected extends from 15 to 31 March 2018, corresponding to an important dust event reaching Greece around 22 and 23 of March, well documented in El Amraoui et al. [5]. Assimilation and statistics are realized over the domain, bounded by the coordinates $[-5, 65]$ latitudes N and $[-20, 40]$ longitudes E, including Europe and the Northern African Sahara. Table 83.1 summarizes the CR characteristics and their differences with the NR,

Table 83.1 Table of NR and CR characteristics

	Forecast	Assim	Repartition of emissions from level 1 (boundary layer) to seventh level						
NR	ERA-I	MODIS	52%	26%	13%	6%	3%	0%	0%
CR1	ERA-I	x	52%	26%	13%	6%	3%	0%	0%
CR2	ERA-I	x	91%	9%	0%	0%	0%	0%	0%
CR3	ERA-I	x	19%	17%	16%	14%	13%	11%	10%

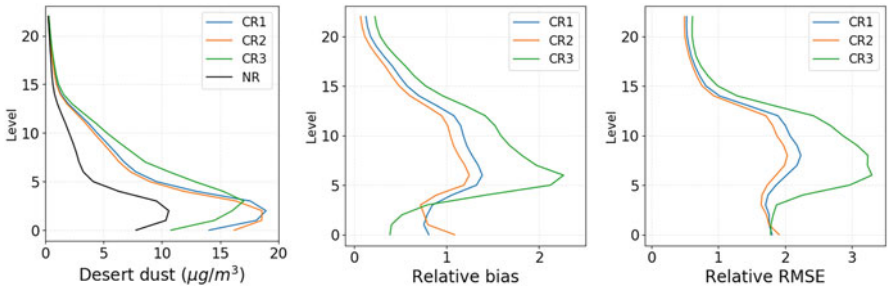


Fig. 83.1 DD concentration profiles in (μg/m^3) for CR$_i$ ($i = 1, 2, 3$) and associated relative bias and relative RMSE profiles (CR$_i$ vs NR). Averaged within the domain and time

constructed on the basis of the validated approach of Descheemaecker et al. [6]. CRs present large biases with respect to the NR, in terms of desert dust (DD) concentration and vertical distribution and thus in terms of AOD as well. CRs 1 and 2 are the closest ones while the impact of emitting homogeneously up to the seventh level induces much higher discrepancies in biases and variability (Fig. 83.1).

83.3 Synthetic Observations

83.3.1 BLISS Simulator

BLISS is an end-to-end backscattering lidar simulator developed by the CNES (Centre National d'Etudes Spatiales) in the context of MESCAL (Monitoring the Evolving State of Clouds and Aerosol Layers) phase 0 (pre-studies for AOS lidar definition) *[In the process of being validated]*. It takes as input geophysical (particular backscatter and extinction coefficient) and meteorological scene profiles, surface characteristics as well as optical properties of the instrument, and return as outputs the signal received by a backscattering spaceborne lidar from level 0 to level 2 retrieved products. It simulates HSRL with a given filter properties file or Klett lidar with a particular LR profile in input. BLISS is based on the lidar equations as presented in the Weitkamp [7]. We use for this study the software in its version 3.8.

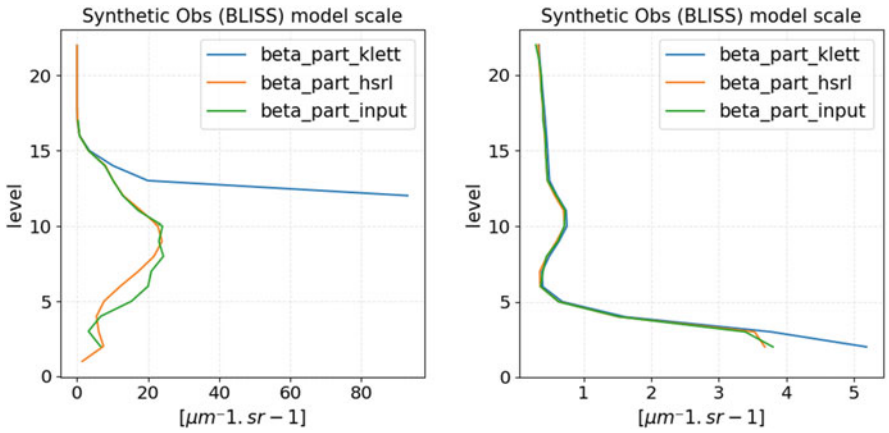


Fig. 83.2 Simulated β_{part} with Klett (blue) and HSRL (orange) inversion, input in green

83.3.2 Synthetic Observation Characterization

The Nature Run is extracted following a typical CALIOP trajectory with a resolution of one-point per grid of 1 × 1 (model resolution). Over the whole period, this represents about 4500 points (~300 per day). As we assimilate the SO in a 1 × 1 resolution model, horizontal resolution is fixed at 50 km, having a huge impact on the signal to noise ratio (SNR). Other parameters (instrumental, experimental, optical) are selected knowing typical lidar references and CALIOP architecture. Figure 83.2 shows two types of particular backscatter (β_{part}) SO, typical of an important plume of DD (left) and a relatively lower one (right). The divergence of the Klett inversion for the more dense column is a classic and well-documented limit of this algorithm, due to the difficulty of establishing the right assumptions in these extreme cases, where HSRL inversion provides a realistic restitution.

83.4 Results

83.4.1 Performances of the Assimilation

The performances of the assimilation are highly depending on the observed scene. Figures 83.3 and 83.4 illustrate two different scenes, one across a dense plume of DD (Fig. 83.3) and a second one avoiding it (Fig. 83.4). In the first case (divergence of Klett algorithm, cf. Sect. 83.3.2), the HSRL Assimilation Runs (ARsH) 1 and 2 manage to approximate the NR much more accurately than the Klett Assimilation Runs (ARsK); the relative biases go from 46% and 32% (ARsK 1, 2) to 1% and −4% (ARsH) against 76% and 52% for the CRs. Scores are calculated from

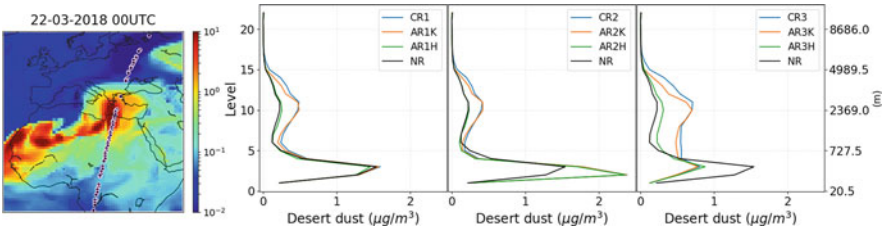


Fig. 83.3 (**a**) AOD (NR) on 22 March 2018 at 00UTC, the circles represent the satellite trajectory (**b–d**) DD concentration profiles for NR, CR_i, AR_iK, and AR_iH ($i = 1, 2, 3$) averaged along the trajectory

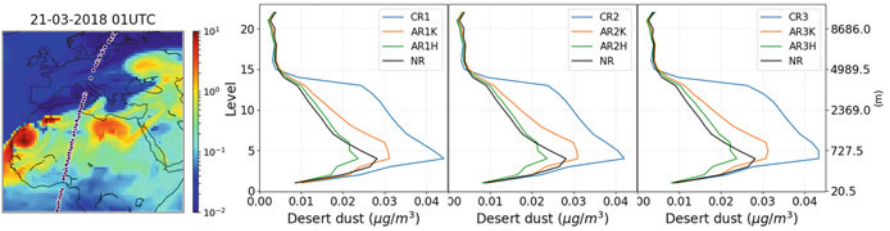


Fig. 83.4 Same legend as Fig. 83.3 but for 21 March 2018 at 01UTC

~1500 m to account for the capabilities of a lidar from space, biases, and RMSE given as a fraction of the NR. The variability is also significantly improved, from 138% and 112% (ARsK) to 44% and 38% (ARsH) compared to 238% and 178% for CRs. Run 3, with much larger deviations, shows the limits of OSSE since AR3H does not fit as closely to the NR as for the two previous runs.

In Fig. 83.4, the simulations, in accordance with Klett's theory, are not divergent, and the scene is rather qualitatively well represented in both cases. In this second case, the assimilation of a CALIOP-like product is much more efficient than in the previous case. The relative biases of the ARsK are 14%, 14%, and 17% against 54%, 51%, and 68% for the CRs. However, even in the case where the Klett inversion is more optimized than during an intense episode, the assimilation of the HSRL product shows a better approximation with the NR, with average biases of 0%, −1%, and 2%. The contribution is also significant for the variability, from 174%, 168%, and 200% (CRs) to 56%, 55%, and 59% (ARsK) down to 42%, 42%, and 44% (ArsH).

83.4.2 Improvement in the Model Space

The ability of an instrument to constrain a Chemical Transport Model (CTM) is then evaluated in the model space to quantify the propagation of information. Figure 83.5 represents the domain-wide and time-averaged DD concentration profiles. In the

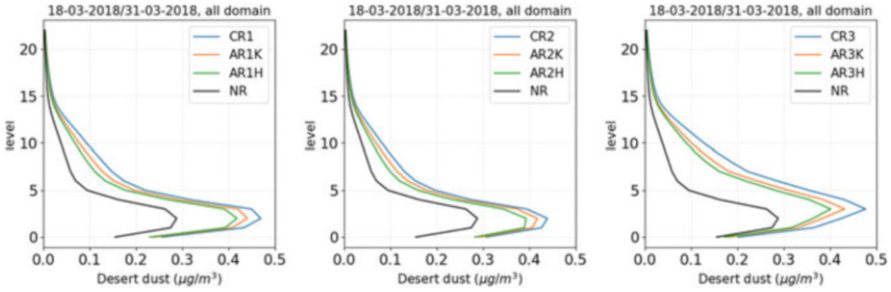


Fig. 83.5 Vertical profiles of DD ($\mu g/m^3$) for NR, CR_i, AR_iK, and AR_iH ($i = 1$ (**a**), 2 (**b**), 3(**c**))

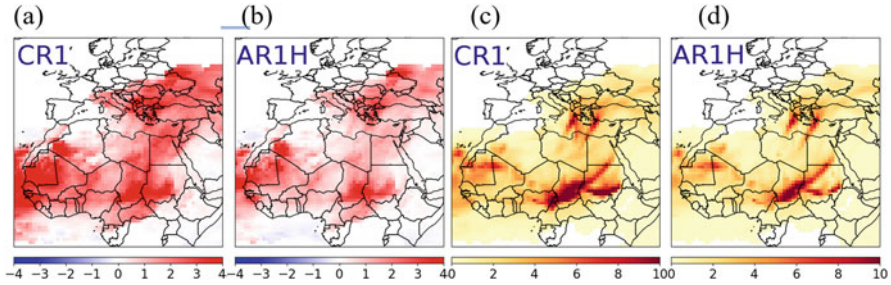


Fig. 83.6 Averaged (all days) AOD_DD biases (**a**, **b**) and RMSE (**c**, **d**) for CR1 and AR1H vs NR

model space, all levels can be studied since the propagation is done on the horizontal as well as on the vertical. Over the whole vertical, the constraint capacity of the models by lidars, whatever its technology, is significant; however, the benefits of the HSRL visible channel are by a factor of up to 2 compared to the assimilation of a CALIOP product over all levels. These benefits in terms of AOD_DD (AOD of Desert Dust) into bias reductions with NR compared to Control Runs of −44%, −38%, and − 59% for ARsK and − 66%, −59%, and − 81% for ARsH, over the entire domain. In terms of RMSE, these scores range from −35%, −28%, and − 53% (ARsK) to −58%, −51%, and − 78% (ARsH). The improvements in terms of bias are mainly concentrated on the strong emission areas and on the wide corridor between Central Africa and Eastern Europe. For the variability, the benefits are most important on the critical area between Chad and Egypt (e.g., CR1 and AR1H in Fig. 83.6).

83.5 Conclusions

The assimilation of HSRL products is more efficient than CALIOP-like products within an episode both with high and low aerosol concentrations in the observation. Even when the concentrations are rather low and the CALIOP-like products manage

to constrain the model significantly, the assimilation of future AOS products clearly shows the added value of the 532 nm HSRL channel in the case of an extreme desert dust episode. Despite the low horizontal resolution of lidar instruments, these products have a good capacity to constrain a CTM. AOS shows a large advantage over CALIOP by a factor from 1.32 to 1.5 for bias and from 1.47 to 1.82 for RMSE in terms of AOD_DD.

References

1. B. Sič, Amélioration de la représentation des aérosols dans un modèle de chimie-transport: Modélisation et assimilation de données, 2014
2. Winker, D., Pelon, J., Coakley Jr., J., Ackerman, S., Charlson, R., Colarco, P., Flamant, P., Fu, Q., Holf, R., Kittaka, C., et al.: The CALIPSO mission: a global 3D view of aerosols and clouds. Bull. Am. Meteorol. Soc. **91**(9), 1211–1229 (2010)
3. Timmermans, R.M., Schaap, M., Cuiltjes, P., Elbern, H., Siddans, R., Tjemkes, S., Vautard, R.: An observing system simulation experiment (OSSE) for aerosol optical depth from satellites. J. Atmos. Ocean. Technol. **26**, 2673–2682 (2009)
4. Sič, B., El Amraoui, L., Piacentini, A., Marécal, V., Emili, E., Cariolle, D., Prather, M., Attié, J.-L.: Aerosol data assimilation in the chemical transport model MOCAGE during the TRAQA/ChArMEx campaign: aerosol optical depth. Atmos. Meas. Tech. **9**, 5535–5554 (2016)
5. El Amraoui, L., Plu, M., Guidard, V., Cornut, F., Bacles, M.: A pre-operational system based on the assimilation of MODIS aerosol optical depth in the MOCAGE chemical transport model. Remote Sens. **14**(8), 2022 (1949)
6. Descheemaecker, M., Plu, M., Marécal, V., Claeyman, M., Olivier, F., Aoun, Y., Blanc, P., Wald, L., Guth, J., Sič, B., Vidot, J., Piacentini, A., Josse, B.: Monitoring aerosols over Europe: an assessment of the potential benefit of assimilating the VIS04 measurements from the futur MTG/FCI geostationary imager. Atmos. Meas. Tech. Discuss. **12**, 1251–1275 (2019)
7. Weitkamp, C.: Lidar-Range-Resolved Optical Remote Sensing of the Atmosphere Springer Series in Optical Sciences. Springer, New York (2005)

Chapter 84
Aerosol Optical Properties over Western Himalayas Region by Raman Lidar During the December 2019 Annular Solar Eclipse

Shishir Kumar Singh, S. R. Radhakrishnan, Rathore Jaswant, and Chhemendra Sharma

Abstract Solar eclipses represent the unique event to study the atmospheric response to the large scale and sharply variation of the incoming solar radiation. Because of the event's infrequency, only few studies have been conducted using Raman lidar to characterize this phenomenon (Kolev, Int J Remote Sens 26(16): 3567–3584, 2005). According to astronomical data, the eclipse in India started at about 8:00 IST and ended at 11:30 IST reaching the maximum eclipse coverage (44.7%) at about 9:30 IST. The aim of this paper is to document its effect in the troposphere through Raman lidar located at Palampur (India). This study reports the analysis of Raman lidar measurements taken during the December 26, 2019, annular solar eclipse. Raman lidar measurement at 355 nm has been performed at Palampur (latitude 32.1109° N and longitude 76.5363° E) in Western Himalayas, to investigate for the first time the impact of the annular solar eclipse on both the planetary boundary layer (PBL) height and the aerosol optical properties in entire aerosol column.

Keywords Solar eclipse · Raman lidar · Planetary boundary layer

84.1 Introduction

Solar eclipses represent the unique event to study the atmospheric responses to the large scale and sharp variability of the incoming solar energy. Solar eclipses can cause dynamical changes in the atmosphere, in addition to the evident reduction

S. K. Singh · S. R. Radhakrishnan (✉) · R. Jaswant · C. Sharma
Environmental Sciences and Biomedical Metrology Division, CSIR-National Physical Laboratory, New Delhi, India

Academy of Scientific and Innovative Research (AcSIR), Ghaziabad, Uttar Pradesh, India

© The Author(s), under exclusive license to Springer Nature Switzerland AG 2023

J. T. Sullivan et al. (eds.), *Proceedings of the 30th International Laser Radar Conference*, Springer Atmospheric Sciences,
https://doi.org/10.1007/978-3-031-37818-8_84

in incoming solar radiation [1]. Any change in radiative heating or cooling will be observed firstly in the planetary boundary layer (PBL) before reaching the open atmosphere. Because of the event's infrequency, only few studies have been conducted using Raman lidar to characterize this phenomenon [2].

According to Aplin et al. [3], lidar systems were initially used to study the atmospheric response to the solar eclipse of August 11, 1999 [3]. Satyanarayana et al. [4] examined the changes in aerosol extinction profiles obtained from lidar observations at the Trivandrum tropical station in India during the solar eclipse on August 11, 1999 [4].

Then, During August 11, 1999, solar eclipse in Sofia (Bulgaria), Kolev et al. [2] employed a lidar system to measure the mixing layer (ML) height time evolution (Bulgaria). They observed that the ML height began to decline shortly after the eclipse began, peaked near the eclipse full phase, and then increased again shortly after the eclipse ended [2]. Amiridis et al. [1] observed the evolution of the planetary boundary layer (PBL) over Greece during the total solar eclipse on March 29, 2006. Data showed that the solar eclipse caused a decrease in PBL height [1].

The aim of this work is to investigate the PBL height variation to the December 2019 solar eclipse through Raman lidar located at Palampur (India). This study reports the analysis of Raman lidar measurements taken during the annular solar eclipse on December 26, 2019. According to astronomical data, the eclipse in India started at about 8:00 IST (02:30 AM UTC) and ended at 11:30 IST (06:00 AM UTC), reaching the maximum eclipse coverage (44.7%) at about 9:30 IST (04:00 AM UTC).

84.2 Methodology

84.2.1 Study Site

A Raymetrics Raman Lidar system, LR111-D200, is installed at the National Physical Laboratory's remote monitoring station at the campus of CSIR-Institute of Himalayan Bioresource Technology (IHBT), Palampur, Himachal Pradesh, India, at an altitude of 1347 m above mean sea level to study the vertical profiles of physical and optical properties of aerosols and clouds. Palampur is located in the lower Himalayan region of Western Himalayas. Figure 84.1 shows the topographic map of Palampur. It is the first ground-based lidar facility in the Western Himalayan region of India.

84.2.2 Raman Lidar System

Raman lidar system is operated at 355 nm with Raman channel at 387 nm having a spatial resolution of 7.5 m. Before deriving optical properties from the raw lidar data, it has been temporally and spatially averaged. Other than this, the raw lidar

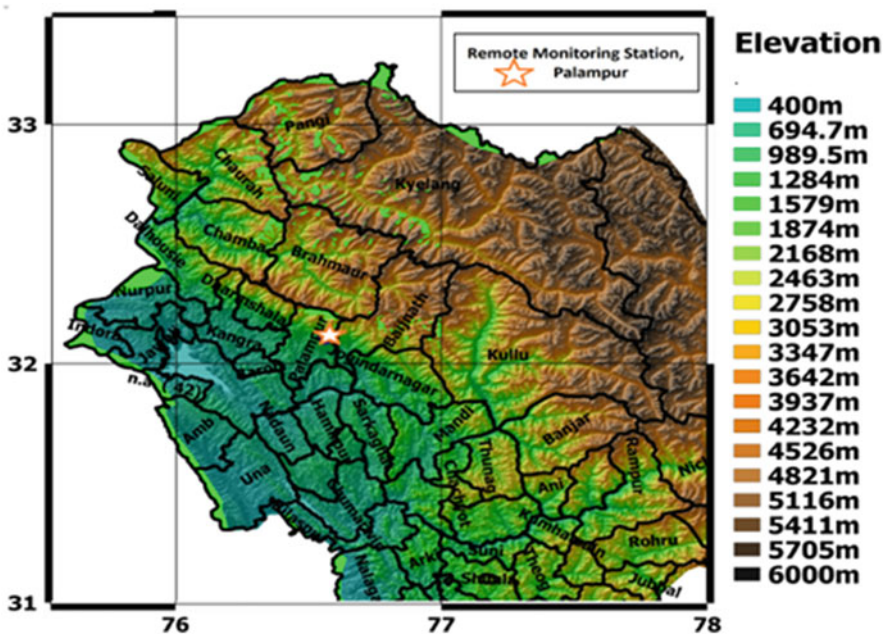


Fig. 84.1 Topographic map of Palampur

Table 84.1 Specifications of Raman lidar

Pulsed laser source	Nd:YAG (Quantel ULTRA100 series)
Wavelength	355 nm
Energy/pulse	32.8 mJ
Repetition rate	20 Hz
Laser beam divergence	<0.8 mrad
Telescope type	Cassegrain
Primary diameter	Nd:YAG (Quantel ULTRA100 series)
Secondary diameter	48 mm
Transmitter–receiver distance	212 mm
Field of view	2.3 mrad (adjustable from 0.5 to 3mrad)
Detectors	3 PMTs

data has been preprocessed with other corrections such as dead time correction of photon counting (PC) signal, background correction, bin shift correction, range correction, gluing, etc. by the software provided by manufacturer [5, 6]. The co-polarized and cross polarized Mie channels of the lidar system provide the linear depolarization ratio which is an indicator of the shape of the aerosol particle. The technical specifications of the Raman lidar system are given in Table 84.1.

84.3 Results

The Raman lidar data for December 26, 2019, has been used for the study. Figure 84.2 shows the mean profiles of the backscatter coefficient, linear depolarization ratio acquired between 8:00 AM and 12:20 PM IST (02:30 AM–06:50 AM UTC). During the eclipse, the main features of the signals are the presence of the aerosols in the PBL up to 1 km (approximated). The backscatter coefficient was found in the range from 4.81E-7 $m^{-1}sr^{-1}$ to 2.85E-6 $m^{-1}sr^{-1}$ in low altitude (up to 2 km). The linear volumetric depolarization ratio was in the range from 0.0103 to 0.115. The depolarization values were close to zero at the lower heights suggesting the dominance of spherical particles at the lower heights [1].

Figure 84.3 shows the temporal variation of extinction coefficient at 355 nm retrieved from the lidar measurements performed on December 26, 2019, to provide an overview of the aerosol loading and its vertical distribution up to 5 km AGL on the solar eclipse day. To trace the sources of pollutants, we have also plotted the HYSPLIT (Hybrid Single-Particle Lagrangian Integrated Trajectory) 3 days Back Trajectory for at two different levels, 500 m and 1000 m agl (above ground level). Results show that most of the aerosol loading was due to regional emissions at lower heights of the station. We can see the variation of boundary layer height

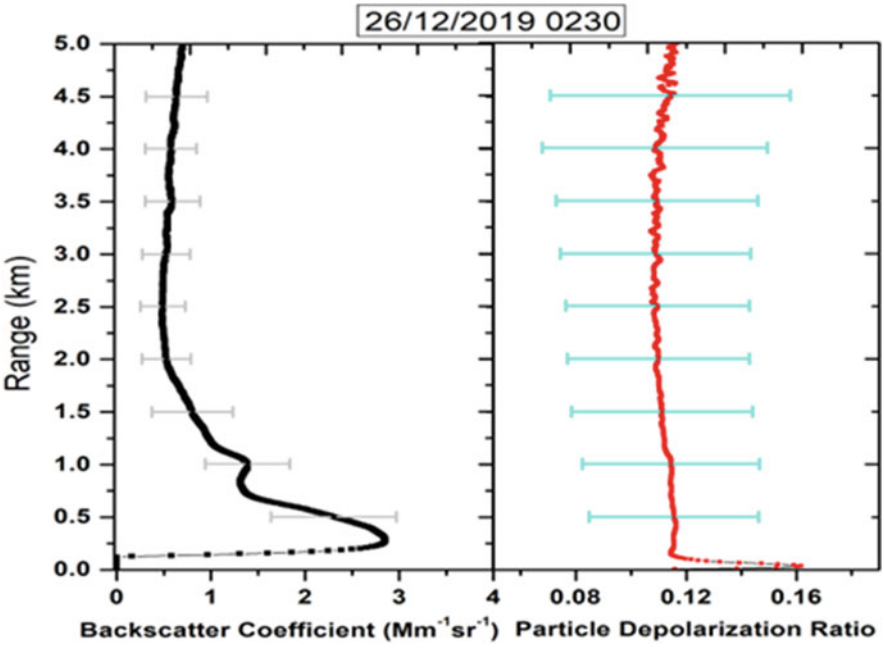


Fig. 84.2 Vertical profile of backscatter coefficient and particle depolarization ratio during solar eclipse

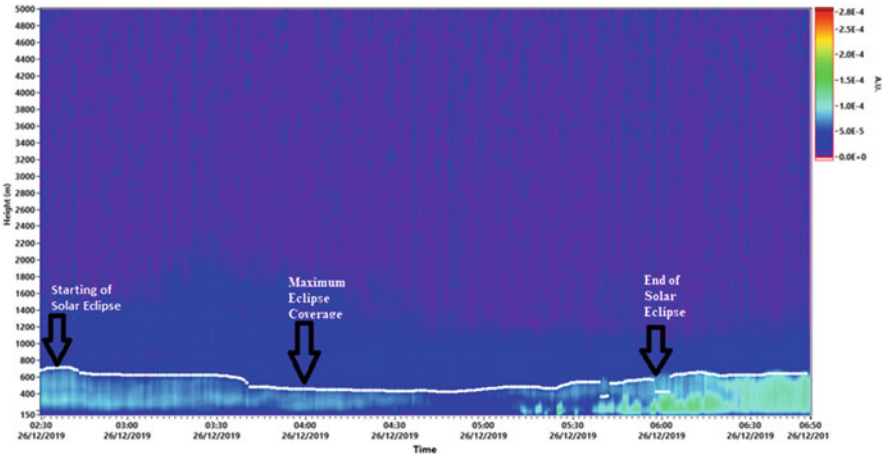


Fig. 84.3 Temporal variation of extinction coefficient and variation of planetary boundary layer for annular solar eclipse (time in UTC)

(532.3 ± 82.4 m) during the solar eclipse which was due to the decrease of the solar irradiance. The PBL is calculated using the gradient method as the height at which the lidar signal has the minimum gradient. The relation of solar eclipse with meteorological parameters will be added after further research. From the lidar data, it becomes clear that the influence of the eclipse has extended the change in the boundary layer height.

84.4 Conclusion

In conclusion, it becomes evident that the effect of the eclipse causes the variation in the boundary layer height. The results of this study must be taken as of general interest, as the solar eclipse is an important event, and we analyzed for the first time the impacts of solar eclipse on the aerosol optical properties and boundary layer height.

References

1. Amiridis, V., Melas, D., Balis, D.S., Papayannis, A., Founda, D., Katragkou, E., Giannakaki, E., Mamouri, R.E., Gerasopoulos, E., Zerefos, C.: Aerosol Lidar observations and model calculations of the planetary boundary layer evolution over Greece, during the march 2006 Total solar eclipse. Atmos. Chem. Phys. **7**, 6181–6189 (2007)
2. Kolev, N., Tatarov, B., Grigorieva, V., Donev, E., Simeonov, P., Umlensky, V., Kaprielov, B., Kolev, I.: Aerosol Lidar and in situ ozone observations of the planetary boundary layer over

Bulgaria during the solar eclipse of 11 August 1999. Int. J. Remote Sens. **26**(16), 3567–3584 (2005)
3. Aplin, K.L., Scott, C.J., Gray, S.L.: Atmospheric changes from solar eclipses. Philos. Trans. R. Soc. A. **374**, 20150217 (2016)
4. Satyanarayana, M., Veerabuthiran, S., Ramakrishna Rao, D., Presennakumar, B., Sreelatha, P., Appu, K.S.: Solar eclipse induced changes in aerosol extinction profiles: a case study of 11 Aug. 1999 solar eclipse using lidar at a tropical station Trivandrum. Indian J. Radio Space Phys. **31**, 82–87 (2002)
5. Jaswant, Radhakrishnan, S.R., Singh, S.K., Sharma, C., Shukla, D.K.: Initial assessment of lidar signal and the first result of a Raman lidar installed at a high-altitude station in India. Remote Sens. Appl. Soc. Environ. **18**, 100309 (2020). https://doi.org/10.1016/j.rsase.2020.100309
6. Singh, S.K., Radhakrishnan, S.R., Mishra, S.K., Shukla, D.K., Ranjan, A., Sharma, C.: Study of variation of aerosol optical properties over a high-altitude station in Indian Western Himalayan region, Palampur using Raman lidar system. J. Atmos. Chem. **79**, 1–23 (2022)

Chapter 85
The Clio HSRL Instrument Concept for the NASA AOS Mission

Chris Hostetler, Stephen Hall, Salvatore Scola, John Smith, Richard Hare, Amin Nehrir, Shane Seaman, Anthony Notari, Richard Ferrare, Sharon Burton, Kathleen Powell, Tyler Thorsen, Mark Vaughan, David Winker, Johnathan Hair, Robert Holz, Willem Marais, and Edwin Eloranta

Abstract The NASA Langley Research Center (LaRC) has designed the Clio High Spectral Resolution Lidar (HSRL) instrument concept for NASA's Atmosphere Observing System (AOS). The AOS mission is being developed by NASA in response to the National Academy of Sciences Decadal Survey for Earth Observations from Space and addresses two of five core science foci recommended through the Decadal Survey process: a focus on aerosol impacts on climate and air quality and a focus on global hydrological cycle and cloud-climate feedbacks. The AOS mission implementation, which follows the NASA Aerosol-Cloud-Convection-Precipitation (ACCP) Study recommendations, includes several instruments deployed in two orbital planes, one inclined and one polar. Clio is designed for deployment to the polar orbital plane along with a Doppler radar, microwave radiometer, polarimeter, long-wave IR imaging radiometer, and aerosol and water vapor limb sounders and contributes to both the aerosol and cloud science foci of the mission. Clio capabilities would provide major advances in aerosol and cloud measurements over those available from past spaceborne cloud/aerosol lidars in terms of accuracy, precision, sensitivity, and information content.

Keywords Aerosols · Clouds · Lidar · HSRL

C. Hostetler (✉) · S. Hall · S. Scola · J. Smith · R. Hare · A. Nehrir · S. Seaman · A. Notari · R. Ferrare · S. Burton · K. Powell · T. Thorsen · M. Vaughan · D. Winker · J. Hair
NASA Langley Research Center, Hampton, VA, USA
e-mail: chris.a.hostetler@nasa.gov

R. Holz · W. Marais · E. Eloranta
SSEC, UW Madison, Madison, WI, USA

© The Author(s), under exclusive license to Springer Nature Switzerland AG 2023

J. T. Sullivan et al. (eds.), *Proceedings of the 30th International Laser Radar Conference*, Springer Atmospheric Sciences,
https://doi.org/10.1007/978-3-031-37818-8_85

85.1 Measurement Objectives

The National Academy of Science's 2017 Decadal Survey for Earth Observation from Space recommended that NASA implement space missions to address five "Targeted Observables." Two of those observables, the Aerosols observable and Clouds, Convection, and Precipitation observable, were assessed in the context of a combined mission under the Aerosol-Cloud-Convection-Precipitation (ACCP) Study managed by the NASA Goddard Space Flight Center and staffed by subject matter experts from several NASA Centers and external institutions. The ACCP study team synthesized the Decadal Survey science recommendations into eight science objectives focusing on cloud-climate feedback, convection, and precipitation processes (including interactions with aerosols), aerosol impacts on air quality, and aerosol-related radiative effects (including aerosol direct and indirect radiative effects). To address these objectives, the study team recommended a mission architecture with 12 instruments deployed on satellites in 2 orbit planes: an inclined and a polar orbiting plane. The satellites recommended for the inclined orbit plane were to address AOS science objectives primarily related to convection and air quality, with a focus on capturing the diurnal aspects of processes. The satellites recommended for the polar orbiting plane were to address all AOS science objectives and employed more advanced instruments to better quantify aerosol and cloud microphysical as well as macrophysical properties that govern climate, convection, precipitation, and air quality processes. In 2021, the mission entered an official Pre-Phase A status under the name Atmosphere Observing System. The mission concept and instrument suite have evolved in Pre-Phase A to contain cost and risk, but the objectives remain the same. The Clio HSRL instrument is designed to fly on one of the two polar orbiting satellites along with a Doppler radar, microwave radiometer, polarimeter, and long-wave IR imaging radiometer. Clio (not an acronym) is named after the second eldest of the nine Greek muses in deference to CALIPSO's CALIOP lidar, which is pronounced like Calliope, the eldest of the muses.

To go beyond the science accomplished with CALIPSO, CloudSat, and the A-Train observations and address the climate science and air quality objectives set for the AOS polar segment, the AOS polar-orbit lidar must deliver higher accuracy, higher information content, and greater sensitivity than the CALIOP lidar. This drives the need for the HSRL technique at 532 nm on Clio. The HSRL technique overcomes errors associated with the often-uncertain retrieval assumption (i.e., the extinction-to-backscatter ratio) implicit in elastic backscatter lidar retrievals. Errors in this assumption accumulate as the retrieval proceeds downward through a profile and often lead to large biases in the planetary boundary layer, where much of the aerosol is located [1]. The HSRL technique [2] avoids the need for this assumption for retrieval of aerosol backscatter and, with the exception of regions of low aerosol loading, aerosol extinction profiles, thereby providing much higher accuracy for both profile products and aerosol optical depth. Combined with elastic backscatter lidar measurements at 1064 nm and depolarization measurements at

Table 85.1 Example of geophysical variables derived in whole or in part from Clio observations

Clio data products	Synergistic data products[a]
Aerosol cloud feature mask	Column and layer-resolved AOD
Particulate backscatter profiles	Column and layer-resolved fine mode AOD
Particulate extinction profiles	Column and layer-resolved absorption AOD
Particulate depolarization profiles	Column and layer-resolved aerosol effective radius
Aerosol optical depth (AOD)	Aerosol number concentration profile
Cloud optical depth	Cloud ice water path
Aerosol classification mask	Cloud liquid water path
Cloud phase	Cloud droplet number density
Mixed layer height	Cloud optical depth

[a]Synergistic products rely on combined retrievals using data from Clio and other AOS instruments, for example, the polarimeter, radar, microwave radiometer, and IR spectrometer

both wavelengths, Clio would provide a rich data set for aerosol classification [3], which is critical to source attribution. In addition to higher accuracy and information content, a driving requirement for AOS objectives concerning aerosol radiative effects includes greater sensitivity to diffuse, tenuous aerosols than has been enabled with CALIOP observations. This would be achieved with Clio by providing both higher SNR and advances in detectability inherent to the more direct HSRL measurement of aerosol backscatter. (See Sect. 85.3 for an example.)

Clio would provide several standalone aerosol and cloud geophysical variable data products, many of which are listed in Table 85.1. Also listed are data products that would be produced in synergistic retrievals employing data from Clio and other instruments. Standalone aerosol retrievals would be implemented via HSRL techniques, and synergistic aerosol retrievals would be implemented in combination with data from the polarimeter. Clio standalone cloud retrievals would be accomplished using a combination of elastic backscatter and HSRL techniques, and synergistic products would be implemented in combination with data from the radar, IR spectrometer, microwave radiometer, and polarimeter.

85.2 Clio Design Overview

A high-level block diagram of the Clio HSRL is shown in Fig. 85.1, and Table 85.2 provides a selective list of preliminary specifications. The elastic backscatter lidar technique is implemented at 1064 nm, and the HSRL technique is implemented at 532 nm. Both measurement channels are polarization-sensitive. Many aspects of the design are derived from the designs of LaRC's HSRL-2 airborne instrument and CALIOP.

The laser transmitter is an injection-seeded Nd:YAG laser that is similar in many ways to the pulsed laser on HSRL-2 but with a lower pulse repetition frequency and higher pulse energy. Fibertek, Inc. built the pulsed laser for HSRL-2 and developed

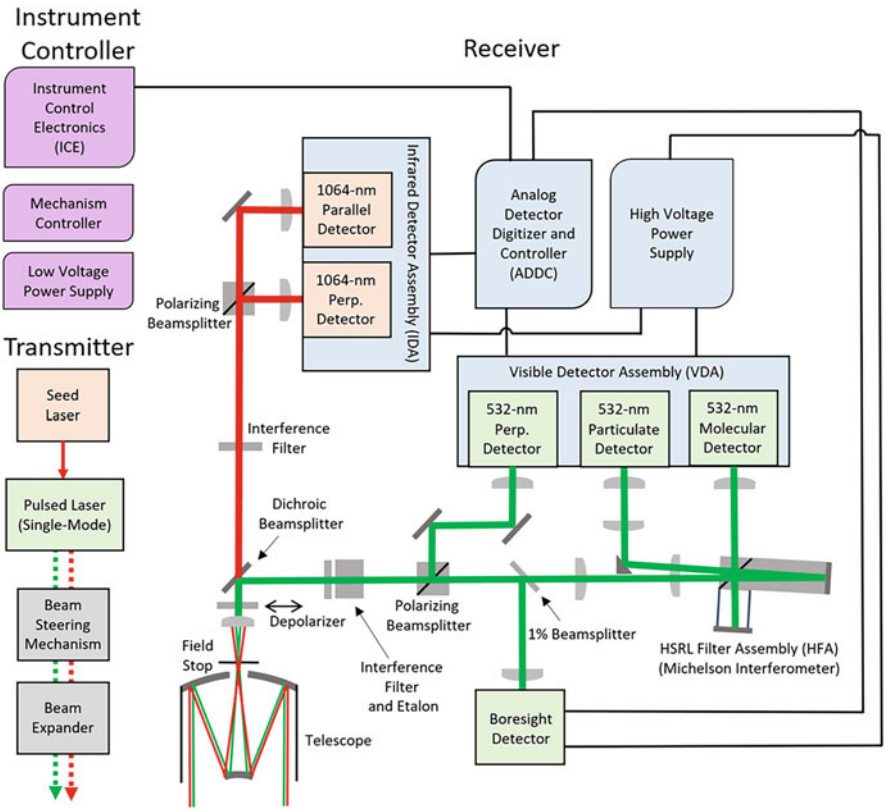


Fig. 85.1 Preliminary block diagram of the Clio HSRL instrument

Table 85.2 Preliminary subsystem parameters

Subsystem	Value
Laser energy	125 mJ at both 532 and 1064 nm
Laser rep-rate	70 shots/s (100 m between shots)
Telescope diameter	1 m
Field of view	208 μrad (~94 m footprint on Earth's surface similar to CALIOP)
Solar filtering	532 nm: etalon + IF filter; 1064 nm: IF filter
HSRL optical filter	Field-widened, off-axis Michelson
Detection	532 nm: PMTs; 1064 nm: APDs
Vertical sampling	532 nm: 5 m; 1064 nm: 10 m

a space variant of that laser in the mid-2010s under NASA technology funding. Fibertek is currently under contract to optimize their space variant design to meet Clio requirements.

The 532-nm HSRL receiver optical filter is based on the field-widened, off-axis Michelson interferometers that have been flown since 2012 on HSRL-2 to

implement the HSRL technique at 355 nm. LightMachinery Inc. developed the interferometer for HSRL-2 and is currently under contract to develop a space-qualified design to meet Clio requirements.

The detectors and detection electronics are based on both CALIOP and HSRL-2 detection subsystems. The concept for the 532-nm detectors is based on the photomultiplier tubes similar to those employed in HSRL-2, with analog-style readout based, in part, on the CALIOP design for which the detector output is electronically split to low-gain and high-gain digitizer channels to cover the large dynamic range required from space. The concept for the 1064-nm detectors is based upon the avalanche photodiodes similar to those flown on CALIOP and GEDI.

85.3 Expected Clio Performance

Clio's measurement performance has been estimated with a high-fidelity software simulator tool developed by LaRC co-author Powell. This tool was used extensively by the CALIPSO mission to assess CALIOP performance and was updated over the last several years to also simulate Clio and other HSRL design variants. Clio's performance has also been simulated independently by University of Wisconsin Madison co-author Marais, with good agreement with the LaRC simulator. Simulations have been conducted for both synthetic scenes and real-world scenes using high-SNR cloud/aerosol extinction and backscatter coefficients from ground and airborne HSRL instruments. Owing to the higher pulse repetition frequency, lower flight altitude (450 km vs 705 km), and other parameters, Clio's daytime SNRs are significantly higher than CALIOP's nighttime SNRs, and Clio's HSRL technique provides similar improvements in accuracy of derived aerosol extinction, backscatter, and depolarization profiles and in the detection of tenuous aerosol. An example simulated comparison with CALIOP is provided in Fig. 85.2. For this case, the truth scene that formed the basis of the Clio simulation was derived from data from LaRC's airborne HSRL-1 instrument (Fig. 85.2a). The data are from a coincident daytime under-flight of CALIOP over the Arctic Ocean on April 19, 2008, for which tenuous smoke and pollution aerosol from Asia occupied a significant fraction of the troposphere. Due to the high daytime background noise, it is difficult to see the aerosol features in the CALIOP Level-1 attenuated backscatter product (Fig. 85.2b), and the CALIOP V4.1 aerosol retrieval algorithms detected only the strongest aerosols in the scene (Fig. 85.2d). Figure 85.2c shows the aerosol backscatter retrieval from the simulated Clio HSRL signals, showing that Clio detects and quantifies aerosols that fall far below the CALIOP detection threshold, as recommended by [4] to reduce biases in lidar-derived estimates of aerosol direct radiative effect. AOS's objectives on aerosol indirect effect would also benefit from improved detectability and quantification of tenuous aerosol.

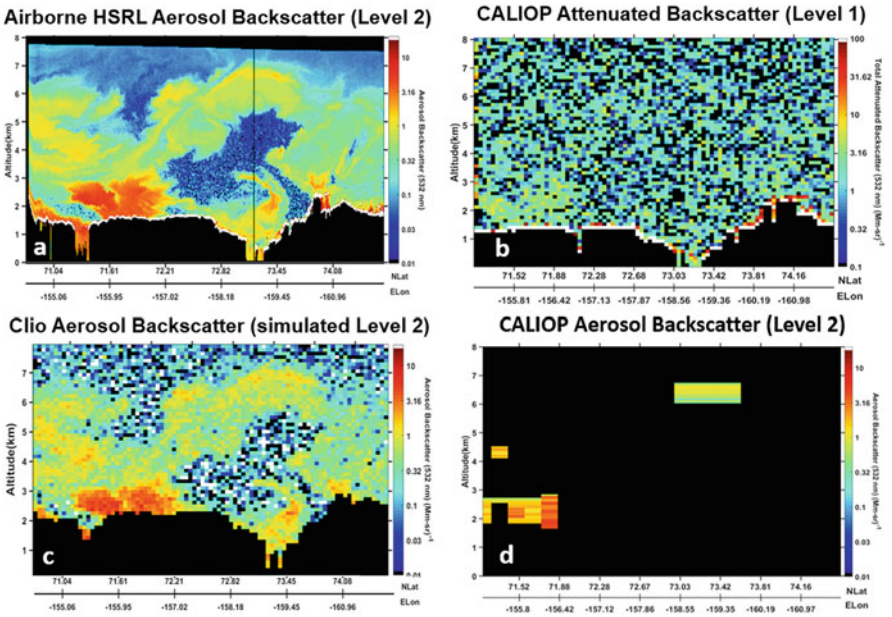


Fig. 85.2 (**a**) Aerosol backscatter retrieved from the LaRC airborne HSRL-1 instrument on a coincident under-flight of CALIPSO on April 19, 2008. (**b**) Level-1 attenuated backscatter product from CALIPSO for this scene averaged to 5 km horizontally and 120 m vertically. (**c**) Retrieved aerosol backscatter from simulated Clio HSRL measurements using airborne HSRL-1 under-flight data as input (same averaging as in (**b**)). (**d**) Level-2 aerosol backscatter product from the CALIOP V4.1 release for this scene (black color indicates regions where no aerosol was detected)

85.4 Path Forward

At the time of this writing, the AOS mission is in Pre-Phase A and launch of the polar-orbiting spacecraft is expected in late 2030. Mission-level and instrument-level requirement trade studies are underway and will continue through Phase A, which is due to begin in late 2022 or early 2023. The final selection of the AOS polar-orbit lidar instrument concept and specification of its requirements will be made by the end of Phase A. Presented here is a snapshot of a candidate lidar concept, the Clio HSRL, as it currently stands.

References

1. Young, S.A., Vaughan, M.A., Kuehn, R.E., Winker, D.M.: The retrieval of profiles of particulate extinction from Cloud–Aerosol Lidar and Infrared Pathfinder Satellite Observations (CALIPSO) data: uncertainty and error sensitivity analyses. J. Atmos. Ocean. Technol. **30**(3), 395–428 (2013)

2. Shipley, S.T., Tracy, D.H., Eloranta, E.W., Tauger, J.T., Sroga, J.T., Roesler, F.L., Weinman, J.A.: High spectral resolution lidar to measure optical scattering properties of atmospheric aerosols. 1: theory and instrumentation. Appl. Opt. **22**, 3716–3724 (1983)
3. Burton, S.P., Ferrare, R.A., Hostetler, C.A., Hair, J.W., Rogers, R.R., Obland, M.D., Butler, C.F., Cook, A.L., Harper, D.B., Froyd, K.D.: Aerosol classification using airborne High Spectral Resolution Lidar measurements – methodology and examples. Atmos. Meas. Tech. **5**, 73–98 (2012)
4. Thorsen, T.J., Ferrare, R.A., Hostetler, C.A., Vaughan, M.A., Fu, Q.: The impact of lidar detection sensitivity on assessing aerosol direct radiative effects. Geophys. Res. Lett. **44**, 9059–9067 (2017)

Chapter 86
Overview and Status of the Methane Remote Sensing Lidar Mission: MERLIN



Sabrina G. Arnold, Gerhard Ehret, Matthias Alpers, Caroline Bès, Philippe Bousquet, Cyril Crevoisier, Andreas Fix, Bruno Millet, and Martin Wirth

Abstract The Methane Remote Sensing Lidar Mission (MERLIN) aims at global observations of spatial and temporal gradients of atmospheric methane (CH_4) using spaceborne active measurements based on an integrated path differential absorption (IPDA) nadir-viewing lidar instrument. It is a joint French and German space mission which is currently in its phase D with a planned launch date in 2027. The main scientific goal of the mission is to provide the column-integrated dry-air mixing ratio of CH_4 (XCH_4) for all latitudes and for all seasons of the year with very small systematic errors. These precise spaceborne data will enable to significantly improve our knowledge of CH_4 sources especially in regions like the tropics and high latitudes where data is still sparse compared to other regions of the world.

Keywords Methane · Active remote sensing · Satellite

86.1 Introduction

Methane (CH_4) is known to be the second most important greenhouse gas after carbon dioxide (CO_2). On a 20-year timescale, the warming potential of CH_4 is

S. G. Arnold (✉) · G. Ehret · A. Fix · M. Wirth
DLR Institute of Atmospheric Physics, Oberpfaffenhofen, Germany
e-mail: sabrina.arnold@dlr.de

M. Alpers
DLR German Space Agency, Bonn, Germany

C. Bès · B. Millet
Centre National D'Etudes Spatiales, Toulouse, France

P. Bousquet
Laboratoire des Sciences du Climat et de l'Environnement, Gif sur Yvette, France

C. Crevoisier
Laboratoire de Météorologie Dynamique, Palaiseau, France

© The Author(s), under exclusive license to Springer Nature Switzerland AG 2023

J. T. Sullivan et al. (eds.), *Proceedings of the 30th International Laser Radar Conference*, Springer Atmospheric Sciences,
https://doi.org/10.1007/978-3-031-37818-8_86

even 84 times higher than that of CO_2. Therefore, reducing CH_4 emissions to slow down man-made climate change is of great urgency. Detailed observations of CH_4 also from space are critical to monitor and control the progress of these efforts.

The Methane Remote Sensing Lidar Mission (MERLIN) is a joint cooperation between Germany and France on developing and operating a satellite dedicated to monitor atmospheric CH_4 from space ([1, 2]). It will be the first space mission using active remote sensing for measuring atmospheric CH_4. The French space agency (CNES) is responsible for the satellite platform whereas the Germany space agency (DLR) is responsible for the payload. The satellite will be jointly operated, and the quality of the processed scientific mission data will be controlled by a French-German science expert group.

As an active mission, MERLIN has several advantages: Firstly, it is independent of sunlight which means MERLIN will deliver CH_4 column data with global coverage during all seasons with a relatively low bias. This is extremely important especially for the Arctic region which is likely to be especially affected by global warming due to climate change and where positive feedbacks such as melting permafrost occur. Furthermore, the light path is well known which minimizes the effects due to aerosol and thin cirrus scattering. The high spatial resolution with a small footprint of only about 150 m allows measurements in cloud holes. Analyzing signals backscattered from the cloud top instead of the ground, so-called cloud slicing, can deliver profile information. Another key advantage is the small systematic error which allows detection of the small large-scale gradients of atmospheric CH_4.

The MERLIN mission benefits from planned and realized other active space missions. Important heritage is provided in connection to the Earth Explorer missions Aeolus (ALADIN) and EarthCARE (ATLID) as well as by A-SCOPE (ESA mission for CO_2) and ASCENDS (NASA mission for CO_2). The technology of the MERLIN laser is a new development jointly performed by the Fraunhofer Institute for Laser Technology ILT and Airbus GmbH with technological support from DLR.

86.2 Methodology

The MERLIN payload consists of an integrated path differential absorption (IPDA) nadir-viewing lidar instrument. This method uses two laser pulses which have slightly different wavelengths (λ_{on} and λ_{off}). Those pulses are sent out by the instrument and scattered and reflected from the Earth's surface and cloud tops (see Fig. 86.1). The wavelength λ_{on} corresponds to the CH_4 absorption line manifold in the 1.64 μm near-infrared spectral region whereas only negligible absorption by CH_4 happens at the wavelength λ_{off}. Hence, the measurement at λ_{off} serves as a reference.

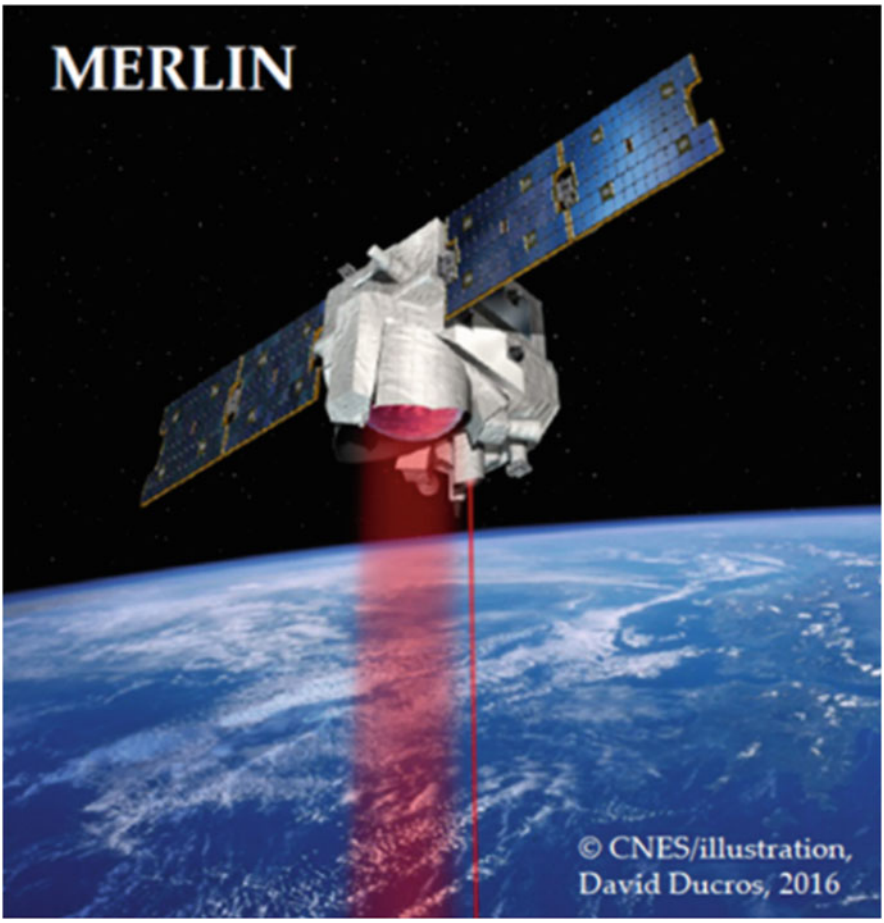


Fig. 86.1 Shown here is an artistic representation of the MERLIN satellite

With the light power $P_{\text{on/off}}$ and the emitted laser pulse energy $E_{\text{on/off}}$ at both frequencies, the differential atmospheric optical depth (DAOD) can be calculated [3]:

$$\text{DAOD} \equiv \frac{1}{2} \ln \frac{P_{\text{off}} \cdot E_{\text{on}}}{P_{\text{on}} \cdot E_{\text{off}}}$$

The DAOD can be converted into the column-integrated dry air mixing ratio of methane, XCH_4, which is the quantity of scientific interest:

$$XCH_4 = \frac{\text{DAOD}}{\int_0^{p_{\text{surf}}} \text{WF}(p) dp}$$

with

$$\mathrm{WF\,(p)} = \frac{\sigma_{\mathrm{on}}\,(p,T) - \sigma_{\mathrm{off}}\,(\mathrm{p,T})}{g\cdot\left(\mathrm{m_{dry-air}} + \mathrm{m_{H_2O}}\cdot \mathrm{q_{H_2O}}\right)}$$

as the weighting function. This function contains the methane absorption cross-sections for the online wavelength (σ_{on}) and for the offline wavelength (σ_{off}), dependent on pressure p and temperature T, g is the acceleration of gravity, $\mathrm{m_{dry\text{-}air}}$ is the average mass of a dry-air molecule, $\mathrm{m_{H2O}}$ is the mass of a water molecule, and $\mathrm{q_{H2O}}$ is the dry-air volume mixing ratio of water vapor.

The derived quantity XCH_4 can be used in inverse modeling to calculate CH_4 surface fluxes globally and down to a subcontinental scale.

Apart from the XCH_4 values which are also called the Level 2 product, the mission will also provide lower-level data, for example, the DAODs (Level 1b). Furthermore, secondary products or so-called spin-off data could be derived from MERLIN observations. Those products are cloud tops and vertical distribution, canopy height, and surface retro-reflectance.

Once launched, MERLIN will be in a sun synchronous polar low Earth orbit (LEO) with a height of approximately 500 km. The local time ascending node (LTAN) will be either 06:00 h or 18:00 h and MERLIN will have a repeat cycle of 28 days. With these orbit parameters, MERLIN will perform measurements around the whole globe with very good quality.

86.3 Status of the Mission

By now, the system definition is fully completed, and measurements on critical subsystems of the payload have been performed indicating that the mission will meet the defined requirements. Figure 86.2 shows the final version of the MERLIN satellite with all its technical components. Some details regarding the status of the mission are given in the next sections.

86.3.1 Schedule

After successfully completing the payload and the satellite critical design reviews, MERLIN is in phase D of its mission life cycle since mid-2021. Major upcoming milestones are the finalization of all receiver optic flight models (first quarter of 2023), the finalization of the laser flight model (second quarter of 2024), and the finalization of the IPDA payload (second quarter of 2026). The launch of MERLIN is anticipated to take place in 2027.

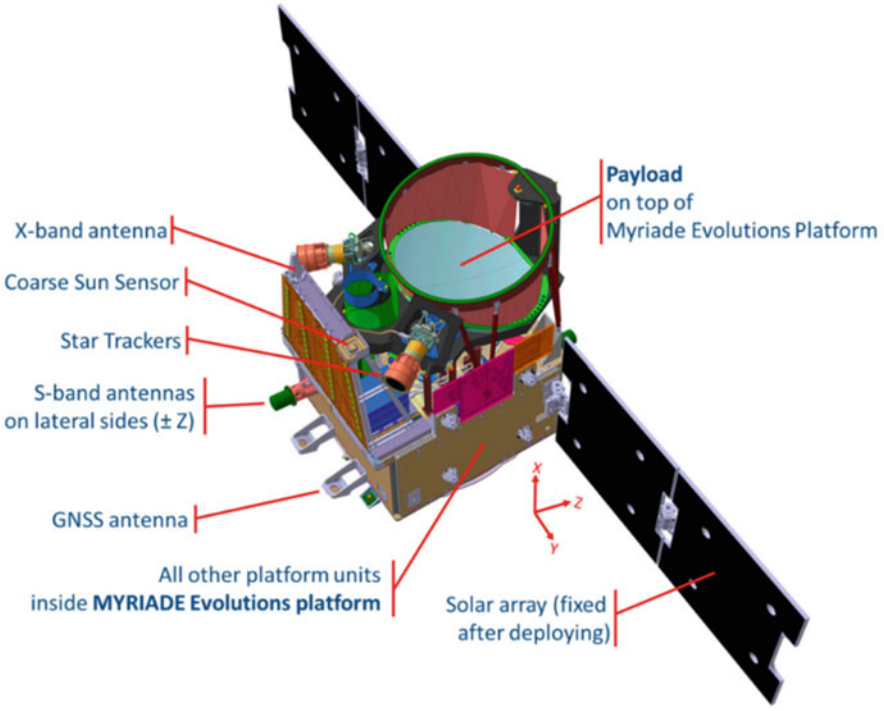


Fig. 86.2 MERLIN satellite with the IPDA lidar instrument from DLR attached on the MYRIADE evolution platform from CNES (Copyright Airbus Defence and Space)

86.3.2 Expected Performance

Different user requirements concerning the random and the systematic error have been defined for classifying the usefulness of MERLIN products when used in inverse modeling for retrieving CH_4 fluxes. The "threshold" requirement is the minimum requirement with values of 36 ppb for the random error and 3 ppb for the systematic error, respectively. Meeting the "breakthrough" requirement with values of 18 ppb for the random error and 2 ppb for the systematic error, respectively, results in a significant improvement to the current satellite observation system. This requirement is also regarded as the optimum from a cost-benefit point of view. Current performance estimations calculate a systematic error of 1.8 ppb, which is even less than the breakthrough requirement of 2.0 ppb.

It is shown that future MERLIN data will reduce the uncertainties regarding the CH_4 fluxes especially in the high latitudes [2]. In the boreal area, the expected uncertainty reduction when using MERLIN observations in inverse modeling instead of observations from the Greenhouse Gases Observing Satellite (GOSAT) is about 50%, which is significant for this climate sensitive region (see Fig. 86.3).

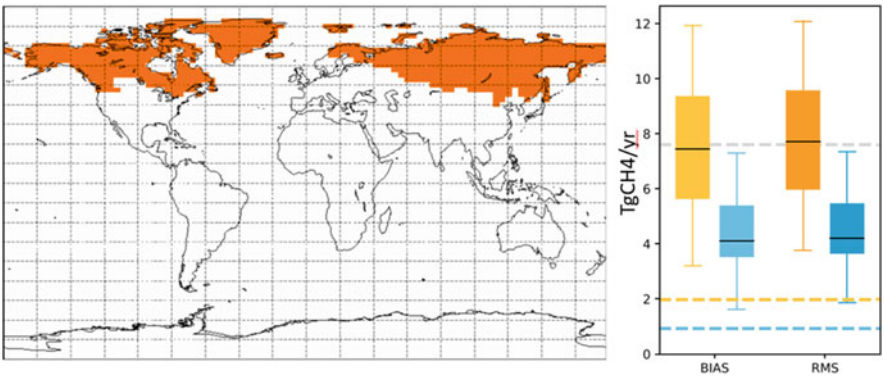


Fig. 86.3 Shown here is the uncertainty reduction for the boreal regions. In the left panel, the orange shaded areas indicate the boreal regions. In the right panel, the light and dark blue colors indicate the results for MERLIN whereas yellow and orange show the results for GOSAT. The dashed gray line indicates the prior, the dashed blue line is the mean MERLIN root means square (RMS), and the dashed yellow line denotes the mean GOSAT RMS

In order to improve the overall performance of MERLIN, strong efforts have been made to enhance the spectroscopic parameters in the spectral region of interest. A significant improvement could be achieved regarding the spectroscopic modeling of methane absorption in the band of the MERLIN online wavelength centered at 1645.552 nm [4]. The absorption spectroscopy of water vapor in this region around 1.64 μm could also be determined more precise [5]. In summary, this results in a more accurate determination of the weighting function.

86.4 Validation Efforts

Having a sophisticated validation strategy for the MERLIN observations is very important for achieving the goals of the mission. Ground-based networks, aircraft and balloon data, and other satellite data could be used for validating MERLIN data. Especially important are data from airborne campaigns because they provide CH_4 profiles which are very useful for validation efforts.

In order to prepare the validation of MERLIN, various campaigns such as the French initiative MAGIC (Monitoring of Atmospheric composition and Greenhouse gases through multi-Instruments Campaigns) and the Carbon Dioxide and Methane (CoMet) campaigns led by the DLR Institute for Atmospheric Physics have taken or will take place. CHARM-F (CO_2 and CH_4 Remote Monitoring-Flugzeug), an airborne demonstrator of MERLIN, has already measured weighted vertical columns of CH_4 (and CO_2) during CoMet 1.0 in 2018 on board the German HALO aircraft and during the MAGIC campaign in 2021 on board the French research aircraft ATR-42, respectively. This instrument will also be on board the HALO

aircraft during the CoMet 2.0 campaign in August and September 2022, focusing on the Canadian Arctic region. Together with complementary data from various other CH_4 sensors, the collected airborne lidar data during these campaigns are important not only for preparing the MERLIN validation. They also allow for mission support, such as algorithm development and improvement.

86.5 Summary and Outlook

The MERLIN mission aims to reduce uncertainties regarding the global methane budget. It will provide the first low-bias, global, spaceborne IPDA lidar data for atmospheric CH_4. Furthermore, the mission paves the way for future active remote sensing missions dedicated to monitoring greenhouse gases from space.

Acknowledgments The German MERLIN contribution is being granted by the German Federal Ministry of Economic Affairs and Climate Action under grant number 50EP1601.

References

1. Ehret, G., et al.: MERLIN: a French-German space Lidar Mission dedicated to atmospheric methane. Remote Sens. **9**, 1052 (2017)
2. Bousquet, P., et al.: Error budget of the methane remote Lidar mission and its impact on the uncertainties of the global methane budget. J. Geophys. Res. Atmos. **123** (2018). https://doi.org/10.1029/2018JD028907
3. Ehret, G., et al.: Space-borne remote sensing of CO_2, CH_4, and N_2O by integrated path differential absorption lidar: a sensitivity analysis. Appl. Phys. B. **90**, 593–608 (2008)
4. Vasilchenko, S., et al.: Accurate absorption spectroscopy of water vapor near 1.64 μm in support of the MEthane Remote LIdar missioN (MERLIN). J. Quant. Spectrosc. Radiat. Transf. **235**, 332–342 (2019)
5. Delahaye, T., et al.: Measurement and Modeling of air-broadened methane absorption in the MERLIN spectral region at low temperatures. J. Geophys. Res. Atmos. **124**, 3556–3564 (2019)

Chapter 87
A Simulation Capability Developed for NASA GSFC's Spaceborne Backscatter Lidars: Overview and Projected Performance for the Upcoming AOS Mission

Edward P. Nowottnick, John E. Yorks, Matthew J. McGill, Patrick A. Selmer, and Kenneth E. Christian

Abstract The Cloud-Aerosol Transport System (CATS) elastic backscatter lidar flew on the International Space Station (ISS) as a technology demonstration from 2015 to 2017. Ahead of the CATS launch, we developed a capability to simulate the projected performance of CATS for various simple, synthetic atmospheric scenes. The simulator served a critical role in the development and testing of CATS operational and near real-time algorithms prior to launch. Following CATS, we advanced our lidar simulator capability to simulate more complex scenes using inputs from global aerosol transport models and airborne/ground-based lidar observations to improve scene realism, complexity, and variability. This capability served a key role during the Earth Science Decadal Survey (ESDS) Aerosols, Clouds, Convection, and Precipitation (ACCP) study phase toward the development of the Atmospheric Lidar Instrument for Clouds and Aerosol Transport (ALICAT) elastic backscatter lidar planned to fly in the 55-degree inclined orbit of the upcoming Atmospheric Observing System (AOS) mission with an anticipated launch in 2028. Here, we present an overview of our lidar simulation capability, an overview of

E. P. Nowottnick (✉) · J. E. Yorks
NASA Goddard Space Flight Center, Greenbelt, MD, USA
e-mail: edward.p.nowottnick@nasa.gov; john.e.yorks@nasa.gov

M. J. McGill
The University of Iowa, Iowa City, IA, USA
e-mail: matthew-mcgill@uiowa.edu

P. A. Selmer
Science Systems and Applications Inc., Lanham, MD, USA
e-mail: patrick.a.selmer@nasa.gov

K. E. Christian
ESSIC, College Park, MD, USA
e-mail: kenneth.e.christian@nasa.gov

© The Author(s), under exclusive license to Springer Nature Switzerland AG 2023

J. T. Sullivan et al. (eds.), *Proceedings of the 30th International Laser Radar Conference*, Springer Atmospheric Sciences,
https://doi.org/10.1007/978-3-031-37818-8_87

the ALICAT instrument, and projected performance compared to CATS and AOS science requirements.

Keywords Aerosols · Clouds

87.1 Introduction

In February 2015, the Cloud-Aerosol Transport System (CATS) technology demonstration was launched for operations on the International Space Station (ISS). CATS was a high-repetition rate, low energy, elastic backscatter lidar that utilized photon-counting detectors that provided vertical measurements of attenuated backscatter and volume depolarization ratio primarily at 1064 nm for 33 months [1]. Prior to launch, we developed a capability to simulate CATS performance for simple scenes with under various viewing conditions and to serve as inputs for testing and development of preliminary CATS operational and near real-time algorithms that leveraged heritage algorithms from the airborne Cloud Physics Lidar (CPL) [2] and the spaceborne Cloud-Aerosol Lidar with Orthogonal Polarization (CALIOP) [3].

The NASA Atmospheric Observing System (AOS), part of the Earth System Observatory (ESO), has been designed in response to the 2017 Earth Science Decadal Survey (ESDS) call for Aerosols, Clouds, Convection, and Precipitation (ACCP) designated observables [4]. As part of the planned AOS architecture, an elastic backscatter lidar is planned to launch in 2028 in an inclined orbit with a 55-degree inclination at 407 km. This lidar, known as the Atmospheric Lidar Instrument for Clouds and Aerosol Transport (ALICAT), is a smaller, compact, and more capable version of CATS that will provide vertical measurements of attenuated backscatter and volume depolarization ratio at both 532 and 1064 nm. ALICAT will target the diurnal cycles of aerosol and cloud processes along with a Ku-band radar and 2 microwave radiometers that target convective processes in the AOS-inclined orbit.

During the ACCP's study phase, we improved upon our simulator capability to ingest months of global aerosol transport model scenes sampled along a satellite orbit and airborne/ground-based lidar observations as scene inputs to improve scene realism, complexity, and variability to assess ALICAT performance. In this extended abstract, we provide an overview of the simulator and assessment of performance compared to CATS and AOS science requirements.

87.2 ALICAT Overview

ALICAT is a compact, more capable version of CATS that can be implemented on SmallSats. Detailed ALICAT instrument performance specifications used in our performance simulations are provided in Yorks et al. [4]. The primary performance

differences between CATS and ALICAT are increased transmitted laser energy and improved aft optics for solar background rejection, all while in significantly smaller package. Additionally, while CATS primarily operated at 1064 nm only, improved cloud-aerosol discrimination and aerosol typing is expected from utilization of ALICAT total attenuated backscatter and volume depolarization ratio measurements at 532 and 1064 nm.

87.3 Simulator Description

Our simulator capability fundamentally simulates the number of photons detected with range from atmospheric (molecular and particulate), solar background, and dark count contributions. For brevity, Eq. 87.1 is a simplified version of the number of photons detected by the lidar system provided in more detail in [5]:

$$N(r) = \frac{C_{\text{bks}}}{r^2} \times \left(P_P\left(\pi, r\right) B_P(r)\right) + \left(P_M\left(\pi, r\right) B_M(r)\right) e^{-2\int_0^r \sigma(r\prime)dr\prime} + B_S + B_D \tag{87.1}$$

where N is the number of photons detected at range r, C_{bks} comprises of the instrument specification terms and overlap function for calibration, P_P and P_M are the particulate and molecular backscatter phase functions at 180°, B_P and B_M are the backscatter volume total scattering coefficients, B_S is the contribution for solar background, and B_D is the dark count contribution. Molecular contributions to the atmospheric term are simulated using either US standard atmosphere or global aerosol transport model atmospheric state variables as described in [6, 7]. Particulate contributions to the atmospheric term are determined from particulate backscatter and extinction profiles provided from either canonical cases, airborne or ground-based data, or global aerosol transport models. Contributions from solar background are a function of the wavelength-dependent solar constant, viewing conditions (i.e., solar zenith angle), surface type (i.e., surface reflectance), and instrument parameters such as bandpass filter width, telescope area, field of view, detector quantum efficiency, and optical transmission of the system. Viewing conditions that impact the solar background contribution can be prescribed directly or provided by a global aerosol transport model. Dark count contributions are provided by detector vendor. To include the impacts of detector noise, random Poisson noise is added to raw, simulated photon counts.

Level 1 products such as total attenuated backscatter and volume depolarization ratio are simulated and include systematic uncertainties such as calibration and polarization gain ratio uncertainty. Level 2 products such as particulate backscatter and extinction can be retrieved using several methods used by CATS, CALIPSO, and CPL and include unconstrained and several constrained retrieval approaches.

Our simulator is highly configurable and can readily simulate performance for various permutations of photon-counting elastic backscatter lidar systems by

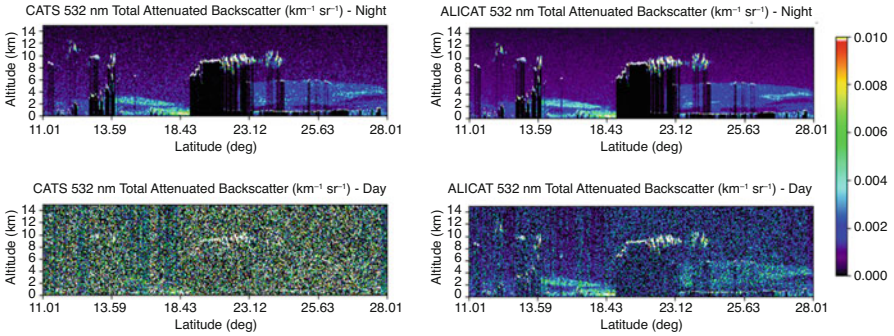


Fig. 87.1 Simulations of 532 nm nighttime (top) and daytime performance (bottom) for CATS (left) and ALICAT (right)

varying simulated spatial resolution of products, as well as instrument parameters such as transmitted laser energy, field of view, receiver aft optics, and detector quantum efficiency.

An example of the impact of instrument design on performance can be seen in Fig. 87.1, which compares 532 nm CATS and ALICAT spaceborne simulations of a dusty and cloudy scene observed by CPL for nighttime and daytime conditions. While small impacts can be observed between CATS and ALICAT night simulations, comparisons of daytime simulations of 532 nm total attenuated backscatter are drastic, owing to the significantly better signal-to-noise ratio (SNR) achieved in the ALICAT design.

87.4 Instrument Performance

87.4.1 Minimal Detectable Backscatter

One of the key geophysical variables provided by ALICAT for AOS is the vertical feature mask, which includes cloud-aerosol discrimination, as well as classification of cloud phase and aerosol type. Key driving measurement requirements for the vertical feature mask include 532 and 1064 nm total attenuated backscatter, the resolution of data products, and the minimal detectable backscatter (MDB) for feature detection. Simulations of a cirrus clouds with varying optical depths between 10 and 12 km show that the 532 nm MDB requirement (<8e-4 km^{-1} sr^{-1}) for feature detection is met during both daytime and nighttime conditions. The ALICAT MDB requirement is based on the nighttime CALIOP MDB at 5 km horizontal resolution provided in [1]. ALICAT meets the MDB requirement at 5 km and at finer resolutions, as low as 1–2 km during daytime and 100 m during nighttime (Fig. 87.2).

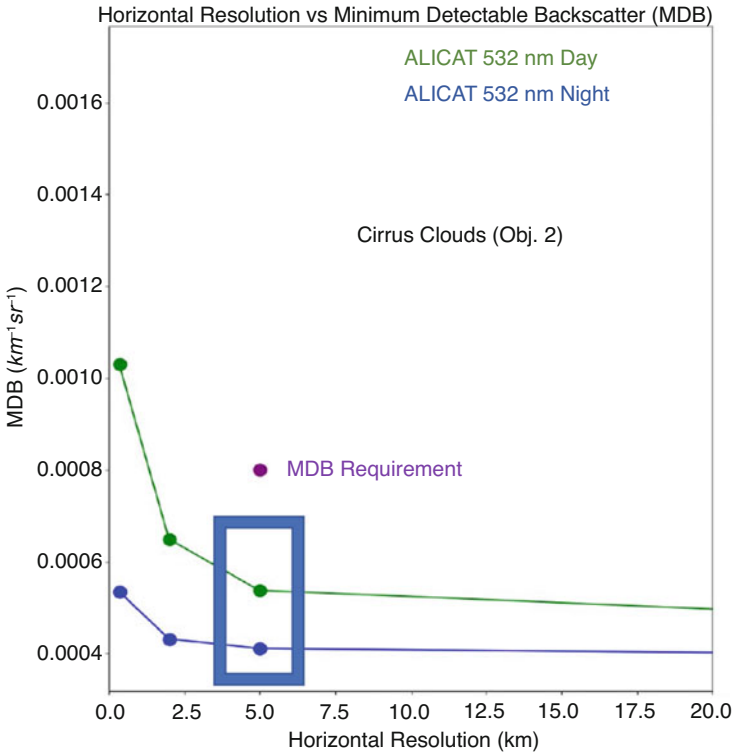


Fig. 87.2 Simulated ALICAT minimal detectable backscatter for a cirrus cloud as a function of horizontal resolution for nighttime and daytime conditions. Daytime conditions were simulated using a solar zenith angle of 0 degrees

87.4.2 Signal-to-Noise Ratio

Another key driving measurement requirement for ALICAT is sufficient SNR needed to meet aerosol extinction and volume depolarization ratio requirements for the AOS inclined mission as described in Yorks et al. [4]. Improved SNR from ALICAT compared to CATS is important for feature detection but also reduces random error in measurements of volume depolarization ratio and retrievals of particulate backscatter and extinction. Clear-sky simulations of various dust loadings over various surface types and day/night conditions were used to set SNR measurement requirements for ALICAT. Figure 87.3 shows an example of SNR for both 532 and 1064 nm for a 2 km thick dust layer over the ocean with AOD = 0.3 for nighttime and daytime conditions. The projected performance of ALICAT meets the SNR requirement with margin at both wavelengths.

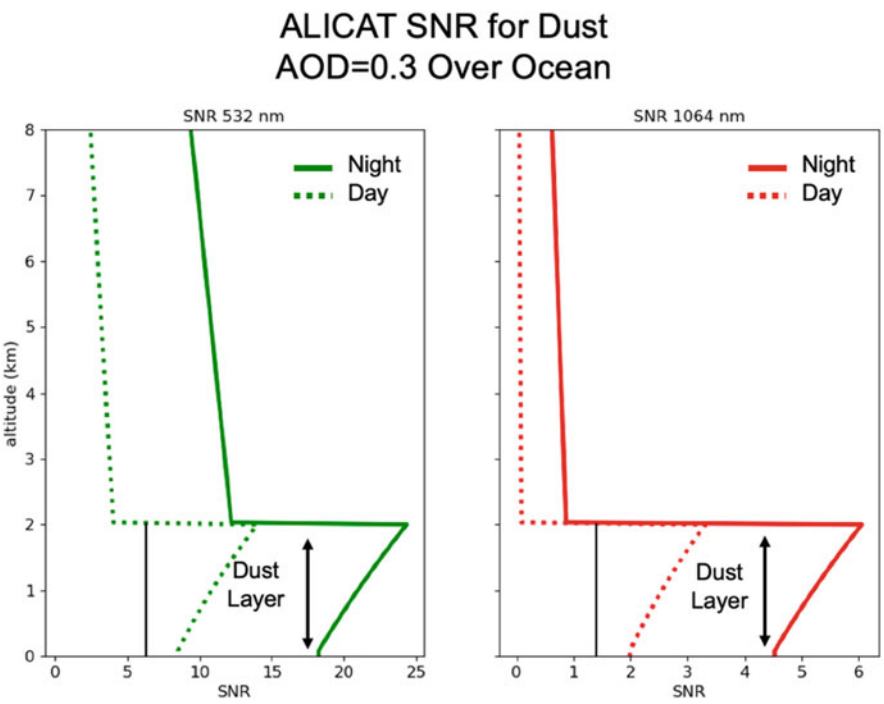


Fig. 87.3 Simulated ALICAT 532 nm (left) and 1064 (right) SNR for a dust layer over ocean during nighttime (solid) and daytime (dashed) conditions. Measurement requirement is indicated by the solid black line. Daytime conditions were simulated using a solar zenith angle of 0 degrees

87.5 Summary

In summary, we have provided an overview of our highly configurable spaceborne elastic backscatter lidar simulation capability that can use synthetic canonical cases, simulated scenes from global aerosol transport models, and real data acquired from ground-based and airborne platforms as inputs to simulate raw data, Level 1 products such as total attenuated backscatter and volume depolarization ratio, and Level 2 products such as particulate extinction. This capability was used to simulate projected performance and to determine measurement requirements for the ALICAT lidar that meet geophysical variable requirements for the AOS-inclined mission planned to launch in 2028.

References

1. Yorks, J.E., and co-authors: An overview of the CATS level 1 processing algorithms and data products. Geophys. Res. Lett. **43**(9), 4632–4639 (2016)

2. McGill, M.J., and co-authors: Cloud physics lidar: instrument description and initial measurement results. Appl. Opt. **41**, 3725–3734 (2002)
3. Winker, D.M., and co-authors: Overview of the CALIPSO mission and CALIOP data processing algorithms. J. Atmos. Ocean. Technol. **26**(11), 2310–2323 (2009)
4. Yorks, J.E., and co-authors: An overview of the NASA atmosphere observing system inclined mission (AOS-I) and the role of backscatter lidar. In: 30th International Laser Radar Conference (ILRC 26), 2022 (2022)
5. McGill, M.J.: Lidar–remote sensing. In: Encyclopedia of Optical Engineering, pp. 1103–1113. Marcel Dekker, New York (2003)
6. CATS. Algorithm Theoretical Basis Document. https://cats.gsfc.nasa.gov/media/docs/CATS_ATBD_BtWndO7.pdf
7. Collis, R.T.H., Russell, P.B.: Lidar measurement of particles and gases by elastic backscattering and differential absorption. In: Laser Monitoring of the Atmosphere, pp. 71–151. Springer, Berlin (1976)

Chapter 88
Aerosol Typing and Spaceborne Lidars: Potentials and Limitations

Athena Augusta Floutsi, Holger Baars, Moritz Haarig, and Ulla Wandinger

Abstract Lidars in space have advanced our knowledge in several research fields. With respect to aerosol and clouds, long-term observations have been acquired and intensively studied for more than 15 years starting with CALIPSO. Recently Aeolus was launched, and EarthCARE – another lidar-equipped mission – is scheduled for launch in 2024. The coexistence of these three (at the moment) different lidar-equipped missions in space cannot but point out their different capabilities, especially with respect to aerosol typing. The lidars onboard the aforementioned satellites operate at different wavelengths, target the observation of different atmospheric components (e.g., wind, aerosol), and, hence, often utilize different measuring techniques and principles (e.g., HSRL, circular vs. linear polarization). To overcome this issue, synergistic approaches between ground-based and spaceborne lidars should be utilized. In addition, the need for harmonization of the observations from those multiple satellites is more evident than ever, as it would provide new aerosol (and cloud) products with improved temporal coverage.

Keywords Aerosol typing · Lidars · Optical properties

88.1 Introduction

The history of lidars in space begins in 1994 with the LITE (Lidar In-space Technology Experiment) instrument inside the payload bay of the Space Shuttle Discovery [1, 2]. Within 9 days (STS-64 mission), LITE provided a pioneering dataset of the vertical structure of aerosol and clouds from the Earth's surface to the stratosphere and successfully served as a test bed for future spaceborne lidars.

The GLAS (Geoscience Laser Altimeter System) onboard ICESat (Ice, Cloud, and land Elevation Satellite) [3] was operational between 2002 and 2010. Even

A. A. Floutsi (✉) · H. Baars · M. Haarig · U. Wandinger
Leibniz Institute for Tropospheric Research, Leipzig, Germany
e-mail: floutsi@tropos.de; baars@tropos.de; haarig@tropos.de; wandinger@tropos.de

© The Author(s), under exclusive license to Springer Nature Switzerland AG 2023

J. T. Sullivan et al. (eds.), *Proceedings of the 30th International Laser Radar Conference*, Springer Atmospheric Sciences,
https://doi.org/10.1007/978-3-031-37818-8_88

though the main mission's goal was the monitoring and determination of the changes in polar ice-sheet volume, GLAS's 532-nm laser allowed the determination of the vertical distribution of clouds and aerosol [4].

The CALIOP (Cloud-Aerosol Lidar with Orthogonal Polarization) onboard NASA's (National Aeronautics and Space Administration) CALIPSO (Cloud-Aerosol Lidar and Infrared Pathfinder Satellite Observations) satellite is a direct descendant of LITE, and it was the first polarization lidar in space to provide global long-term atmospheric measurements [5]. Since 2006, CALIOP has measured vertical profiles of attenuated backscatter at visible (532 nm) and near-infrared (1064 nm) wavelengths, along with depolarization ratio in the visible channel. However, as an elastic-backscatter lidar, CALIOP is not able to perform direct extinction measurements. To enable the calculation of the extinction from the backscatter signals, the aerosol extinction-to-backscatter ratio (or lidar ratio) needs to be assumed.

In 2018, ESA (European Space Agency) launched the wind lidar mission Aeolus [6]. The satellite is equipped with a high-spectral-resolution lidar (HSRL), ALADIN (Atmospheric Laser Doppler Instrument). ALADIN acquires one-directional horizontal tropospheric and stratospheric wind profiles (mainly west-east), aiming to improve weather forecast, advance atmospheric dynamics research, and evaluate climate models [6, 7]. Apart from being the first Doppler lidar in space, ALADIN is also the first lidar in space able to measure extinction coefficients directly, and even though aerosol monitoring is not the main scope of Aeolus (due to the coarse resolution), aerosol and cloud optical properties are retrieved with ALADIN as spin-off products [7–9]. Recently, it was demonstrated that spin-off products such as the backscatter coefficient, the extinction coefficient, and the lidar ratio derived from ALADIN, even though preliminary (due to the ongoing algorithm improvements and quality assurance updates), agree very well with ground-based lidar measurements [10].

Together with CALIPSO and Aeolus, EarthCARE (Cloud, Aerosol and Radiation Explorer) will be the next satellite mission to be equipped with lidar. EarthCARE is a joint mission of ESA and JAXA (Japanese Aerospace Exploration Agency), scheduled for launch in 2023. EarthCARE's payload consists of four instruments: an ATmospheric LIDar (ATLID), a Cloud Profiling Radar (CPR), a Multi-Spectral Imager (MSI), and a Broad-Band Radiometer (BBR) [11]. ATLID is a 355-nm HSRL that will provide direct cloud and aerosol profile measurements of backscatter and extinction coefficients. Furthermore, ATLID can measure the depolarization ratio of the atmospheric particles [11, 12]. The primary goal of EarthCARE is radiative closure, which will be achieved in a synergistic approach from the two active and two passive instruments.

Apart from a successful technological achievement, lidars in space have been a significant scientific success as well. With respect to aerosol, lidars have advanced our understanding of the global aerosol distribution since they provide vertical profiles of aerosol and its microphysical and optical properties. All this information can help us assess the uncertainties induced to the climate system by the different aerosol effects. However, an accurate assessment requires detailed knowledge of the

aerosol type. In addition, aerosol typing is a key prerequisite for the improvement of the measurement retrievals, of existing models as well as for data assimilation purposes.

88.2 Aerosol Typing Schemes

88.2.1 The CALIPSO Aerosol Typing Scheme

CALIOP is an elastic backscatter lidar and, thus, not able to perform direct extinction measurements. The lidar ratio needs therefore to be assumed. Since the lidar ratio depends on the microphysical and chemical properties of the scattering particles present in the atmosphere, an aerosol typing scheme was developed for CALIPSO [13–15].

After a feature mask has been applied to the measurements, to identify regions of the same optical properties (i.e., features), the typing scheme categorizes the features into the aforementioned six aerosol types, which are desert dust, biomass burning, background (clean continental), polluted continental, polluted dust, and clean marine, by means of a decision tree. The decision tree takes into account the lidar-derived feature-integrated volume linear depolarization ratio and attenuated backscatter, feature height information, and external information such as geographical location, underlying surface type and season. Once an aerosol type has been selected from the decision tree, the corresponding lidar ratio (at 532 and 1064 nm) is assigned to the feature. Behind the aforementioned six aerosol types, there are aerosol models that are obtained from a multiyear AERONET cluster analysis [13] of the optical and physical properties of characteristic aerosol types [13] and, therefore, are representatives of the most frequently observed aerosol types at AERONET sites. In addition, every aerosol model has its own, predefined size distribution and microphysical properties (e.g., refractive indices).

88.2.2 The EarthCARE Aerosol Typing Scheme

The Hybrid End-To-End Aerosol Classification (HETEAC) model is an aerosol classification model that was developed for the EarthCARE mission [16]. The model serves as a common baseline for algorithm development and evaluation procedures within all EarthCARE development activities. Data synergy between the products of EarthCARE's ATLID, MSI, and BBR is further supported with HETEAC as consistency between their aerosol products is ensured. The approach is hybrid, meaning that the theoretical description of the aerosol microphysics is consistent with the aerosol optical properties obtained by observations, thus enabling radiative closure studies. In addition, the end-to-end model approach ensures a uniform

representation of the different aerosol types in terms of microphysical, optical, and radiative properties.

The first step in the HETEAC model development is the definition of the basic aerosol components. Based on an experimental basis [11] of optical properties from ground-based lidars at EarthCARE's wavelength (355 nm), four components were defined as representatives of the aerosol types observed in nature. These components comprise two fine modes, one strongly absorbing and one weakly absorbing, and two coarse modes, one with spherical particles and one with nonspherical particles. For each of these components, a mono-modal particle size distribution and a wavelength-dependent complex refractive index are assigned to obtain their microphysical description, based on ESA's Climate Change Initiative (CCI) project Aerosol_cci [17]. The mode radii and refractive indexes are obtained from AERONET and are considered typical for the aerosol components. To describe the scattering of the nonspherical particles, the spheroid model proposed by Gasteiger et al. [18] was chosen for HETEAC, mainly due to the degree of reproducibility of the observations (in terms of optical properties).

To account for aerosol mixtures of two or more modes, a multimodal representation is achieved by mixing rules. Each mode has specific scattering properties per unit particle volume, which are then used, in combination with the relative volume contribution of each mode, to derive the optical properties of the aerosol mixture. This procedure results in lookup tables (LUT) of the optical and radiative properties for the different mixing ratios between the aerosol modes at 355 nm. Even though HETEAC is optimized for the 355 nm wavelength, LUT have been constructed for other wavelengths as well. Once EarthCARE is in orbit, the LUT can be used in reverse to reveal the mixing ratio of the four different aerosol components from ATLID's measurements (at 355 nm only).

88.2.3 Aerosol Typing from Ground-Based Lidar Systems

The complexity and necessity of accurate aerosol typing have led to the development of many different approaches and methodologies. These methodology developments span from rather simple and straightforward threshold-based techniques to advanced Artificial Neural Network (ANN) algorithms [19].

With an emphasis on satellite missions and especially EarthCARE, ground-based remote-sensing measurements are essential for product and algorithm development and validation. To achieve this and with a specific focus on the aerosol classification and the radiative impact quantification, an aerosol typing methodology applicable to both ground-based and spaceborne lidar systems has been developed at the Leibniz Institute for Tropospheric Research (TROPOS) [20] and is briefly presented below.

The novel methodology for aerosol typing is based on the optimal estimation method (OEM) [21] and allows the identification of aerosol mixtures consisting of up to four different aerosol components from lidar measurements. Based on lidar-derived intensive (i.e., concentration-independent) parameters, that is, the lidar

ratio and the particle linear depolarization ratio (355 and 532 nm), the backscatter-related color ratio (532/1064 nm), and the extinction-related Ångström exponent (355/532 nm), the typing scheme allows the identification of up to four different aerosol components present in an aerosol mixture as well as the quantification of their contribution to the aerosol mixture in terms of relative volume. The four aerosol components considered in this typing scheme represent the most commonly observed aerosol particles in nature and are assumed to be physically separated from each other and, therefore, can create external mixtures. In particular, two components represent fine-mode particles, absorbing (FSA) and less absorbing (FSNA), and the remaining two aerosol components represent coarse-mode particles, spherical (CS) and nonspherical (CNS). These components can adequately represent the most frequently observed aerosol types in the atmosphere: smoke- and pollution-related aerosol and sea-salt and desert dust aerosol particles, respectively. Microphysical and optical properties of the predefined aerosol components are in accordance with HETEAC, thus permitting direct comparisons, algorithm harmonization, and further support to the validation activities for EarthCARE. The methodology is flexible, allowing thus its application to lidar systems with different configurations (e.g., single wavelength or multi-wavelength, Raman or elastic lidar).

88.3 Potential and Limitations

The aforementioned typing schemes have been developed for instruments with different capabilities, targeting different goals, and therefore have different strengths and limitations. For instance, several limitations in CALIPSO's classification scheme emerged after the release of new updated data versions. The most usually encountered issue was the aerosol layer misclassification, due to the surface-dependent decision tree of the typing scheme [22]. Algorithm changes (including new aerosol subtypes) and updates [15] led to a more accurate feature-type identification and aerosol-type classification, and thus, more reliable extinction retrievals, however, did not resolve the ambiguity regarding the aerosol type naming, which varies heavily in different aerosol studies and applications.

EarthCARE has a typing scheme specifically designed for ATLID that will also be utilized for radiative closure purposes. However, ATLID is a single wavelength (355 nm) HSRL, meaning that it has disadvantages compared to multi-wavelength lidars, especially concerning aerosol typing. In such cases, ground-based lidars and the flexible OEM-based aerosol typing scheme can provide additional information and combined to resolve the observed aerosol types.

Concerning aerosol typing, Aeolus has a drawback since it only detects the co-polar component of the emitted circular polarized light. This leads to the loss of signal in the case of polarizing particles such as mineral dust, volcanic ash, or ice crystals. Due to this signal loss, the backscatter coefficient is underestimated, while the particle-specific lidar ratio is overestimated. This effect imposes challenges to aerosol typing. At the moment, aerosol typing based on Aeolus observations can

only be achieved via a synergistic approach with ground-based lidars and with additional information (e.g., trajectory analysis, such as in [10]). A potential Aeolus follow-up mission would therefore benefit from enhanced polarization capabilities as well as from an aerosol typing scheme specifically designed for Aeolus.

During the presentation, a smoke event originating from the Californian wildfires of 2020 will be discussed in detail with respect to aerosol typing, to demonstrate how the different lidars observe smoke-related aerosol. The differences between the various available typing schemes will be also highlighted.

88.4 Conclusions

It becomes obvious that a common strategy for the harmonization of the products from the multiple spaceborne lidars should be established. This initiative should aim to meet the needs of the scientific community and to produce a new aerosol-typing product that will overcome commonly encountered issues such as the nomenclature and the availability of intensive optical properties in multiple wavelengths. This harmonized aerosol-typing dataset could be then used with higher confidence for modeling purposes and to improve the data assimilation procedures.

References

1. McCormick, M.P.: Scientific investigations planned for the Lidar In-Space Technology Experiment (LITE). Bull. Am. Meteorol. Soc. **74**(2), 205–214 (1993)
2. Winker, D.M.: An overview of LITE: NASA's lidar in-space technology experiment. Proc. IEEE. **84**(2), 164–180 (1996)
3. Schutz, B.E.: Overview of the ICESat mission. Geophys. Res. Lett. **32** (2005)
4. Spinhirne, J.D.: Cloud and aerosol measurements from GLAS: overview and initial results. Geophys. Res. Lett. **32** (2005)
5. Winker, D.M.: Overview of the CALIPSO mission and CALIOP data processing algorithms. J. Atmos. Ocean. Technol. **26**(11), 2310–2323 (2009)
6. Stoffelen, A.: ADM-Aeolus Doppler wind lidar observing system simulation experiment. Q. J. R. Meteorol. Soc. **132**, 1927–1947 (2006)
7. Straume, A.G.: ESA's space-based Doppler wind lidar Mission Aeolus – first wind and aerosol product assessment results. EPJ Web Conf. **237**, 01007 (2020)
8. Ansmann, A.: Particle backscatter and extinction profiling with the spaceborne high-spectral-resolution Doppler lidar ALADIN: methodology and simulations. Appl. Opt. **46**, 6606–6622 (2007)
9. Flamant, P.: ADM-Aeolus retrieval algorithms for aerosol and cloud products. Tellus A Dyn. Meteorol. Oceanogr. **60**(2), 273–286 (2008)
10. Baars, H.: Californian wildfire smoke over Europe: a first example of the aerosol observing capabilities of Aeolus compared to ground-based lidar. Geophys. Res. Lett. **48** (2021)
11. Illingworth, A.J.: The EarthCARE satellite: the next step forward in global measurements of clouds, aerosols, precipitation, and radiation. Bull. Am. Meteorol. Soc. **96**(8), 1311–1332 (2015)

12. do Carmo, J.P.: ATmospheric LIDar (ATLID): pre-launch testing and calibration of the European Space Agency instrument that will measure aerosols and thin clouds in the atmosphere. Atmos. **12**, 76 (2021)
13. Omar, A.H.: Development of global aerosol models using cluster analysis of Aerosol Robotic Network (AERONET) measurements. J. Geophys. Res. **110** (2005)
14. Omar, A.H.: The CALIPSO automated aerosol classification and lidar ratio selection algorithm. J. Atmos. Ocean. Technol. **26**(10), 1994–2014 (2009)
15. Kim, M.H.: The CALIPSO version 4 automated aerosol classification and lidar ratio selection algorithm. Atmos. Meas. Tech. **11**(11), 6107–6135 (2018)
16. Wandinger, U.: HETEAC: the Aerosol classification model for EarthCARE. In: EPJ Web of Conferences, vol. 119. EDP Sciences (2016)
17. Holzer-Popp, T.: Aerosol retrieval experiments in the ESA Aerosol_cci project. Atmos. Meas. Tech. **6**, 1919–1957 (2013)
18. Gasteiger, J.: Modelling lidar-relevant optical properties of complex mineral dust aerosols. Tellus B Chem. Phys. Meteorol. **63**(4), 725–741 (2011)
19. Nicolae, D.: A neural network aerosol-typing algorithm based on lidar data. Atmos. Chem. Phys. **18**, 14511–14537 (2018)
20. Floutsi, A.A.: Towards an automatic aerosol typing algorithm applicable for ground-based and spaceborne lidars. In: Living Planet Symposium (2019)
21. Rodgers, C.D.: Inverse Methods for Atmospheric Sounding. Oxford Series on Atmospheric, Oceanic and Planetary Physics. World Scientific Publishing Co. Pte. Ltd, Singapore (2000)
22. Kanitz, T.: Surface matters: limitations of CALIPSO V3 aerosol typing in coastal regions. Atmos. Meas. Tech. **7**, 2061–2072 (2014)

Chapter 89
Correcting CALIOP Polarization Gain Ratios for Diurnal Variations

Mark Vaughan, Sharon D. Rodier, Zhaoyan Liu, Anne Garnier, Kam-Pui Lee, Brian Getzewich, and Shan Zeng

Abstract Version 4.51 (V4.5) of the CALIPSO lidar level 1 (LL1) data products is targeted for public release in summer 2022. One of the most far-reaching changes implemented in this release is to the polarization gain ratio (PGR), which quantifies the gain between the 532 nm parallel and perpendicular channels in the CALIPSO receiver. The PGR is an essential calibration coefficient required for computing both the attenuated backscatter coefficients reported in the LL1 product and the volume depolarization ratios. Prior to V4.5, the PGR was assumed to be a slowly varying constant that remained invariant throughout both the day and night portions of any CALIPSO orbit. However, in response to recent discoveries, in V4.5 the PGR now varies diurnally. In this work, we describe the motivation for this change, briefly review the technique used to compute daytime PGR estimates, provide an overview of the V4.5 PGR implementation, and compare the V4.5 PGRs to those used in previous data releases.

Keywords CALIPSO · CALIOP · Depolarization · Calibration

89.1 Introduction and Problem Statement

The Cloud-Aerosol Lidar with Orthogonal Polarization (CALIOP), flying aboard the Cloud-Aerosol Lidar and Infrared Pathfinder Satellite Observations (CALIPSO) mission, measures 532 nm backscatter signals in polarization planes oriented parallel and perpendicular to the polarization plane of the transmitted laser light. The

M. Vaughan (✉) · Z. Liu · B. Getzewich
NASA-LaRC, Hampton, VA, USA
e-mail: mark.a.vaughan@nasa.gov; zhaoyan.liu@nasa.gov; brian.j.getzewich@nasa.gov

S. D. Rodier · A. Garnier · K.-P. Lee · S. Zeng
SSAI/NASA-LaRC, Hampton, VA, USA
e-mail: sharon.d.rodier@nasa.gov; anne.emilie.garnier@nasa.gov; kam-pui.a.lee@nasa.gov; shan.zeng@nasa.gov

© The Author(s), under exclusive license to Springer Nature Switzerland AG 2023

J. T. Sullivan et al. (eds.), *Proceedings of the 30th International Laser Radar Conference*, Springer Atmospheric Sciences,
https://doi.org/10.1007/978-3-031-37818-8_89

relative gain between these two receiver channels is quantified by the polarization gain ratio (PGR), which is a required parameter for calculating both the 532 nm total attenuated backscatter coefficients, $\beta'(r)$, and the 532 nm volume depolarization ratios, $\delta_v(r)$. The magnitude of the PGR is periodically assessed using an onboard calibration procedure in which a pseudo-depolarizer is inserted into the 532 nm optical path of the receiver. In this configuration, both the parallel and perpendicular channel detectors are illuminated by equal intensities of backscattered light, so that the PGR is readily calculated by dividing the mean backscattered signal in the perpendicular channel by the mean backscattered signal in the parallel channel [1].

For the first 10+ years of the CALIPSO mission, PGR calibrations were made during night orbit segments only, and the relative gain of the two receiver channels was assumed to remain diurnally invariant. However, also during this period, some unexpected day–night differences in $\delta_v(r)$ were reported for CALIOP measurements of cirrus clouds [2]. To investigate these disparities, in November 2016, the CALIPSO mission began conducting occasional "extended time" PGR measurements during which the pseudo-depolarizer was inserted into the optical path for continuous periods of 3–5 days. These very long dwell times are required to map the time-varying behavior of the PGR while simultaneously limiting random uncertainties in the daytime PGR estimates to levels commensurate with the existing nighttime record. Subsequent analyses of these extended time data show that the PGR systematically varies by ~6% from night to day, with day values being uniformly higher. As shown in Fig. 89.1, the PGR remains relatively constant throughout the night portion of an orbit, whereas day values are much more

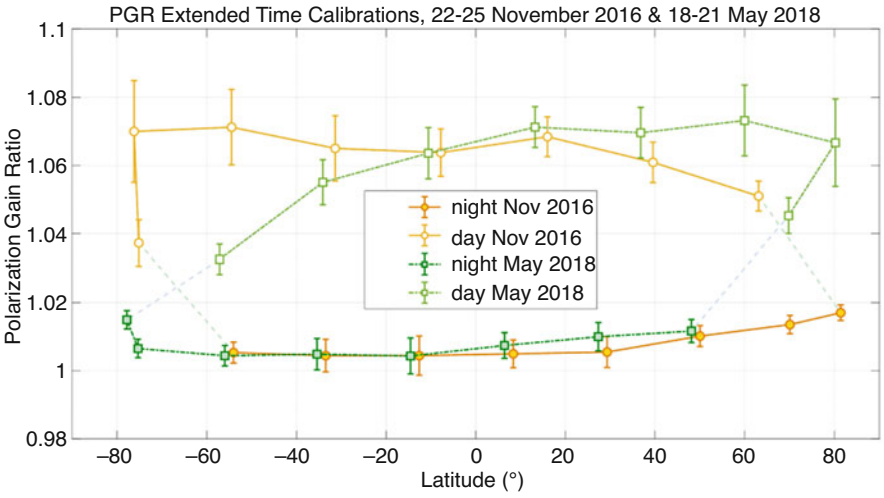


Fig. 89.1 Illustration of the intra-orbit variability of the CALIOP PGR determined during extended time PGR calibrations. Error bars represent three times the standard error of the mean. Temporal spacing between consecutive data points is ~347 s during the night and ~ 391 s during the day

changeable and only gradually converge to approximate stability. Daytime rates of change at the terminators are also seen to vary seasonally.

89.2 Near-Term Remediation

For better or worse, the diurnal variability in the PGR was not the only flaw recently uncovered in the CALIOP polarization calibration procedures. In this section, we provide an overview of all PGR-related changes made in anticipation of the upcoming CALIPSO lidar level 1 (LL1) version 4.51 (V4.5) data release.

89.2.1 Nighttime PGR Bias Correction

Prior to the first extended time PGR measurement, the CALIPSO team conducted an in-depth review of the PGR calibration software. One important but unanticipated outcome of this review was the discovery of a coding error that introduced a persistent high bias in the night PGR estimates. The consequences of eliminating this bug are illustrated in the mission-long PGR time histories presented in Fig. 89.2. The solid red line shows the erroneous nighttime calculation used both day and night for all CALIOP data releases prior V4.5. The solid blue line shows the corrected nighttime PGR estimates to be used in all future data releases. By some freakishly fortuitous coincidence, the erroneous V4.1 PGR estimates provide a reasonably close approximation to the newly developed daytime PGR estimates (shown in green) discussed in the following section.

89.2.2 Daytime PGR Estimates

Because the extended PGR measurements were not available for the first 10+ years of the mission, an alternative calibration method is required to characterize diurnal PGR changes. We do this using an approach pioneered by Liu et al. [3] which derives PGR estimates from daytime background measurements acquired above strongly scattering ice clouds. The solar background radiation measured above these clouds is largely unpolarized, due to multiple internal reflections within the ice crystals and the multiple scattering that occurs among these particles [4]. An estimate of the PGR can thus be derived using the ratio of CALIOP's polarization-sensitive background measurements.

Liu's method was originally developed using airborne measurements acquired at 1064 nm and has since been used for 1064 nm PGR calibration by the Cloud-Aerosol Transport System (CATS) lidar [5]. Adapting this scheme for use by CALIOP required additional considerations. While molecular scattering contribu-

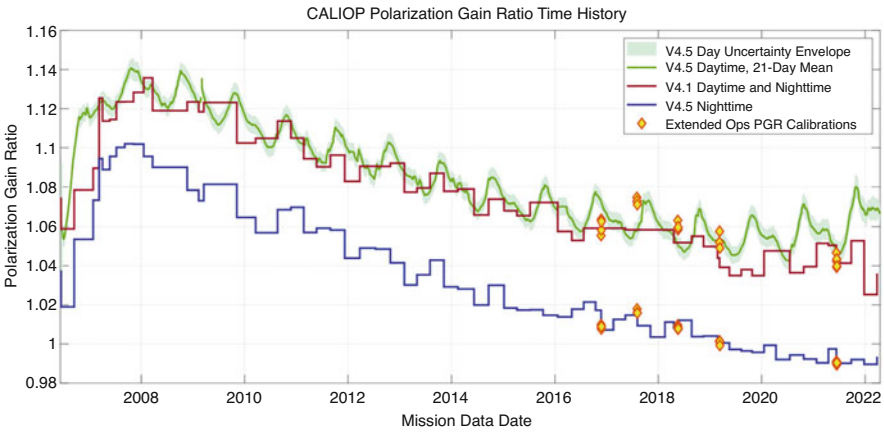


Fig. 89.2 Mission-to-date time histories of the CALIOP polarization gain ratio. Prior to the V4.5 data release, PGR calibrations were conducted during night orbit segments only. The solid red line shows the PGR estimates obtained from these measurements using the pre-V4.5 calibration software. The solid blue line shows PGR estimates obtained from these same measurements after correcting the software defect identified in Sect. 89.2.1. The solid green line shows daily mean daytime PGR estimates derived from background measurements above ice clouds using Liu's method (Sect. 89.2.2). The pale green region surrounding the daytime PGR estimates represents one standard deviation about the mean for each daily average. Yellow diamonds show daily mean PGR estimates obtained during all periodic extended time PGR calibration operations

tions to above cirrus background signals are negligible at 1064 nm, failing to account for the highly polarizing characteristics of molecular scattering at 532 nm can introduce PGR errors in the vicinity of ~3%. The CALIOP implementation of Liu's method accounts for molecular contributions to CALIOP's 532 nm background signals from above ice clouds via a lookup table created using a polarization-sensitive radiative transfer model [6].

Compensating for molecular scattering was not the only obstacle to be surmounted in implementing Liu's method. Surprisingly, identifying the appropriate measure of background also proved to be challenging. The CALIOP LL1 data product reports two measures of background intensity: background monitor readings and root-mean-square (RMS) baseline signal calculations. Unfortunately, neither parameter is suitable. As described in [7], CALIOP measures mean background signals for each laser pulse between altitudes of 112 km and 97 km above the Earth's surface. These quantities are then subtracted electronically from the output of the detectors and separately measured by a background monitor circuit. To use these background signals in the PGR calibration would require accurate scaling between the background monitor readings and the science channel digitizer outputs. Unfortunately, this scaling is uncertain and, due to component degradation and other (e.g., thermal) effects, also unlikely to remain constant. The RMS baseline parameter reports the standard deviation of the backscatter signals measured between 80 and 65 km. If CALIOP used photon counting rather than analog

detection, the square of the RMS baseline parameter should provide an accurate estimate of the mean signal in the baseline region. But this approach is obviated by the confounding effects introduced by the time-varying excess noise factors that characterize CALIOP's 532 nm photomultiplier detectors. While an independently derived noise scale factor (NSF) offers a potential solution [8], CALIOP's NSF estimates are derived from the same background measurements used in the PGR estimates and hence are not independent. After considerable testing and verification, a linear fitting of the output of Liu's method to daytime PGRs computed from the extended time measurements was found to be the most effective and reliable scaling between the available measures of background intensity and the required (but unavailable) science channel background measurements.

Figure 89.2 shows the CALIOP daytime daily mean PGR estimates derived using Liu's method (solid green line) and the daytime PGR estimates computed from all extended time measurements (yellow diamonds) to date. For Liu's method, individual PGR estimates are calculated from CALIOP's V4.2 level 2 5-km cloud layer products whenever the parallel channel RMS baseline exceeds an experimentally determined threshold of 1100 and the only layer detected in a profile is an opaque ice cloud with a top height higher than 6 km. Each data point represents an average taken over all samples acquired during a 24-h calendar day. The time series varies seasonally, with minima in July and maxima in October. The causes of this periodicity are not yet known.

89.2.3 Accommodating Day-to-Night and Night-to-Day Transitions

As seen in Fig. 89.1, the change between stable, near-constant night and day PGRs does not occur instantaneously. Based on an assessment of the five extended time PGR calibrations accumulated to date, the transition period between stable states lasts approximately 585 s. To characterize the variability of the PGR throughout an orbit, we use a piecewise linear approximation, as illustrated by the red dashed line in Fig. 89.3. The PGR is held constant during the night portions of any orbit, using the most recent PGR estimate obtained from CALIOP's standard nighttime-only PGR calibration operations. This is exactly the same procedure that has been used in all prior data releases. Daytime values are assigned by partitioning the daytime portion of the orbit into three segments. The first segment extends 585 s forward in time from the night-to-day terminator (at ~43.5 min in Fig. 89.3), and the third extends 585 s backward in time from the day-to-night terminator (at ~101.5 min in Fig. 89.3). The PGR is held constant throughout the second center segment at the Liu's method value calculated for the data acquisition date. PGRs in the first and third daytime segments are then linearly interpolated as a function of time between the Liu's method daytime constant PGR and the nighttime constant PGRs at the terminators.

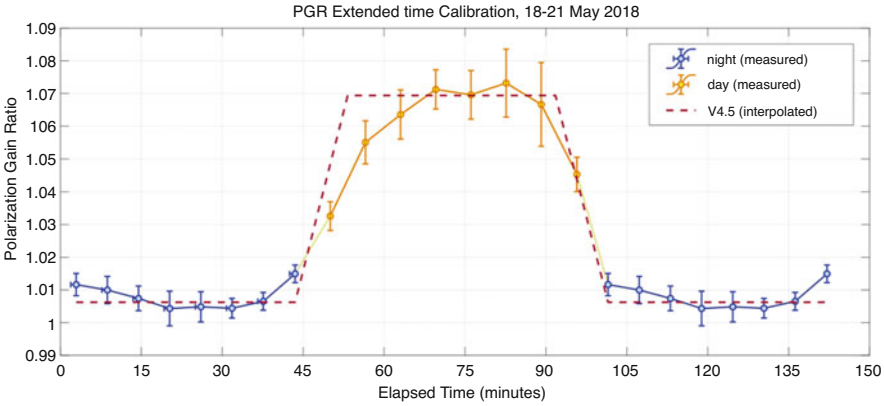


Fig. 89.3 Same May 2018 data as shown in Fig. 89.1 but plotted as a function of orbit elapsed time from the day-to-night terminator. The night data is replicated at the end of the day data to emphasize the periodicity of the diurnal changes in PGR. The dashed red line illustrates the piecewise linear approximation used to create the CALIOP V4.5 data products

89.3 Consequences for CALIPSO Lidar Level 1 Data Products

The expected changes in the CALIPSO V4.5 LL1 data as a result of changes in the PGR can be predicted by inspection of the relevant equations. Given $X_{\parallel}(r)$ and $X_{\perp}(r)$, representing background-subtracted, range-corrected, gain and energy normalized measurements in, respectively, CALIPSO's 532 nm parallel and perpendicular channels [1], the volume depolarization ratio is

$$\delta_v(r) = \frac{X_{\perp}(r)}{\mathrm{PGR} \times X_{\parallel}(r)}. \tag{89.1}$$

Since $X_{\parallel}(r)$ and $X_{\perp}(r)$ do not change between versions, the fractional change in δ_v from V4.1 to V4.5 is simply the V4.5 PGR divided by the V4.1 PGR. As seen in Fig. 89.2, daytime PGR changes are quite small; consequently, the changes in δ_v from V4.1 to V4.5 will be similarly small. For the attenuated backscatter coefficients,

$$\beta'(r) = {C_{\parallel}}^{-1} \left(X_{\parallel}(r) + {X_{\perp}(r)}\Big/{\mathrm{PGR}} \right) = {C_{\parallel}}^{-1} \left(1 + \delta_v(r)\right) X_{\parallel}(r) \tag{89.2}$$

where $C_{\parallel}$ is the parallel channel radiometric calibration coefficient [1]. Assuming $C_{\parallel}$ remains constant from V4.1 to V4.5, the relative change in β' from V4.1 to V4.5 is

$$\Delta\beta'(r) = \frac{1 + \delta_{\mathrm{V4.5}}(r)}{1 + \delta_{\mathrm{V4.1}}(r)} = \frac{(\mathrm{PGR}_{\mathrm{V4.1}}/\mathrm{PGR}_{\mathrm{V4.5}})\,\delta_{\mathrm{V4.1}}(r) + 1}{\delta_{\mathrm{V4.1}}(r) + 1}. \tag{89.3}$$

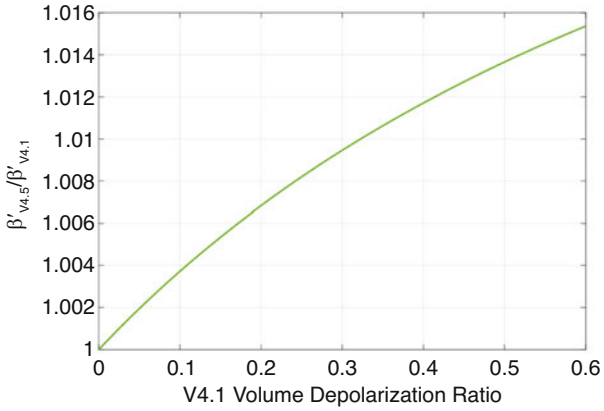


Fig. 89.4 Expected change in V4.5 β' relative to V4.1 β' as a function of δ_v in V4.1

For the 66 standard PGR calibrations acquired to date, the mean V4.1-to-V4.5 PGR ratio (i.e., the red line in Fig. 89.2 divided by the blue line) is 1.041. Figure 89.4 illustrates the expected change in β' from V4.1 to V4.5 for $0 \leq$ V4.1 $\delta_v \leq 0.6$. As seen in Fig. 89.2, day PGR changes from V4.1 to V4.5 are quite small. The changes in δ_v will be similarly small, except near the terminators where they will progressively transition to the night PGR ratio. How these changes will cascade into the CALIOP level 2 analysis is a fascinating topic that, sadly, lies well beyond the scope of this abstract.

References

1. Powell, K.A., et al.: CALIPSO lidar calibration algorithms: part I – nighttime 532 nm parallel channel and 532 nm perpendicular channel. J. Atmos. Ocean. Technol. **26**, 2015–2033 (2009)
2. Sassen, K., et al.: Ice cloud depolarization for nadir and off-nadir CALIPSO measurements. Geophys. Res. Lett. **39**, L20805 (2012)
3. Liu, Z., et al.: Validating lidar depolarization calibration using solar radiation scattered by ice clouds. IEEE Geosci. Remote Sens. Lett. **1**, 157–161 (2004)
4. Liou, K.N., et al.: Light scattering and radiative transfer in ice crystal clouds: applications to climate research. In: Mishchenko, K., Hovenier, J.W., Travis, L.D. (eds.) Light Scattering by Nonspherical Particles, pp. 417–449. Academic, San Diego (2000)
5. Yorks, J.E., et al.: An overview of the CATS level 1 processing algorithms and data products. Geophys. Res. Lett. **43**, 4632–4639 (2016)
6. Zhai, P., et al.: A vector radiative transfer model for coupled atmosphere and ocean systems with a rough interface. J. Quant. Spectrosc. Radiat. **111**, 1025–1040 (2010)
7. Hunt, W.H., et al.: CALIPSO lidar description and performance assessment. J. Atmos. Ocean. Technol. **26**, 1214–1228 (2009)
8. Liu, Z., et al.: Estimating random errors due to shot noise in backscatter lidar observations. Appl. Opt. **45**, 4437–4447 (2006)

Chapter 90
Performance Simulation of a Spaceborne Raman Lidar for ATLAS

Noemi Franco, Paolo Di Girolamo, Andreas Behrendt, Volker Wulfmeyer, Adolfo Comerón, Donato Summa, and David N. Whiteman

Abstract ATLAS, the Atmospheric Thermodynamic LidAr in Space, is a project aimed at developing the first spaceborne Raman Lidar capable to measure simultaneously water vapor mixing ratio and temperature profiles with high temporal and spatial resolution at global level. Within the project, proposed to the European Space Agency as a mission concept in the frame of "Earth Explorer-11 Mission Ideas," an end-to-end simulator has been developed to verify the technical and technological solutions of the different transmitting and receiving subsystems and to estimate the performance of ATLAS in different atmospheric conditions. The simulator consists of two separate modules that allow to calculate the roto-vibrational and pure rotational Raman signals. The simulated signals are then analyzed through consolidated techniques, in order to obtain retrieved profiles of water vapor mixing ratio and atmospheric temperature, together with their statistical and systematic uncertainties. As input data for the simulations, thermodynamic and optical parameters from the non-hydrostatic mesoscale model GEOS-5 Nature Run Ganymed Release were used. Data were extracted to simulate the performances

N. Franco (✉) · P. Di Girolamo
School of Engineering, University of Basilicata, Potenza, Italy
e-mail: noemi.franco@unibas.it

A. Behrendt · V. Wulfmeyer
Institut Fur Physik und Meteorologie, University of Hohenheim, Stuttgart, Germany
e-mail: volker.wulfmeyer@uni-hohenheim.de

A. Comerón
Universitat Politècnica de Catalunya, Barcelona, Spain
e-mail: comeron@tsc.upc.edu

D. Summa
School of Engineering, University of Basilicata, Potenza, Italy

IMAA-CNR, Tito Scalo, Potenza, Italy
e-mail: donato.summa@cnr.it

D. N. Whiteman
Howard University, Washington, DC, USA

© The Author(s), under exclusive license to Springer Nature Switzerland AG 2023

J. T. Sullivan et al. (eds.), *Proceedings of the 30th International Laser Radar Conference*, Springer Atmospheric Sciences,
https://doi.org/10.1007/978-3-031-37818-8_90

along several dawn-dusk orbits around the Earth for different days of the year, accurately chosen to consider different background conditions in dependence of the solar zenith angle variability. Both clear and cloudy sky conditions were considered, highlighting the capability of space lidars to obtain accurate measurements in variable atmospheric conditions.

Keywords Raman lidar · Spaceborne · End-to-end simulator

90.1 Introduction

Accurate measurements of water vapor mixing ratio and temperature profiles are crucial to improve our understanding of the climate system. The high variability of atmospheric temperature (T) and water vapor mixing ratio (WVMR) makes it essential to have measurements with both high temporal and spatial resolutions to resolve vertical gradients and inversions. Unfortunately, nowadays our observing capabilities still show a gap, since the actual techniques do not ensure a sufficient vertical resolution to retrieve vertical gradients, especially in the lower troposphere [1].

A global coverage of high temporal and spatial resolved measurements could strongly contribute in different research areas such as radiative transfer, land-atmosphere feedback, mesoscale circulation, and data assimilation [2].

Considering the deep impact of such observational progresses, the project ATLAS – Atmospheric Thermodynamics LidAr in Space – is aimed at the development of a spaceborne Raman lidar able to measure simultaneously atmospheric temperature and water vapor mixing ratio profiles. The project was proposed as a mission concept to the European Space Agency (ESA) in the frame of "Earth Explorer-11 Mission Ideas" call and is currently the subject of further studies within the project "As-Atlas," supported and funded by the Italian Space Agency (ASI).

In the recent past, an assessment of the specifications of the different lidar subsystems has been performed with an analytical simulation model for spaceborne Raman lidar systems [3, 4], demonstrating the capability of a Raman lidar to ensure accurate results in different standard atmospheric conditions (Mid Latitude Summer/Winter, Tropical, US Standard). Recently, a statistical analysis was conducted over a global model using a selection of the CALIPSO orbit, which confirmed the high-level performances of a spaceborne system [5].

90.2 The End-to-End Simulator

To assess the performances of ATLAS in a most realistic way, a numerical end-to-end simulator has now been developed. The simulator considers the behavior of all devices present in the experimental system (telescope, optical reflecting

and transmitting components, spectral selection devices, detectors, sampling units) which ultimately allows us to simulate the roto-vibrational and pure-rotational Raman signals measured by the spaceborne lidar through the application of a radiative transfer model in the forward module.

The simulated signals include a background contribution due to the solar radiation, which is calculated as the sum of the radiation scattered by the molecules and particles in the atmosphere, reflected by the Earth's surface and, eventually, by clouds. The background term is particularly important for the orbital simulations since it strongly depends on the geographic and atmospheric conditions. For this reason, instead of using a mean value, the background term is calculated for every observation using a numerical model that considers all contributing environmental factors, such as the solar zenith angle, the surface albedo, the cloud reflectivity, and their distribution, height, and optical thickness.

To estimate the background contribution, a numerical model was already proposed in [3]. Now this model has been improved considering an integration scheme for the light propagation that does not rely on a parallel plane approximation. This allows us to better evaluate the background contribution for solar zenith angles close to and larger than 90°. This is a crucial point for global simulations since the performance of spaceborne lidars on dawn-dusk orbit, characterized by solar zenith angles always close to 90°, is much higher than on polar orbits with daily overpasses at different local times, and such performance improvement can be properly assessed only if the abovementioned integration scheme for the light propagation is considered. The estimated variability of the peak signal-to-noise ratio as a function of the solar zenith angle for two different simulated signals is shown in Fig. 90.1.

The simulator can provide both clear and cloudy sky simulations, as shown in Fig. 90.2. Di Girolamo et al. [4] already demonstrated the capability of lidars to have a good accuracy also in the presence of cirrus clouds with an optical depth up to 0.3. On the other hand, it is also important to consider the shots between clouds that contribute advantageously to the measurement.

This is achieved in the cloud simulations using a weighted summation of signals with different cloud attenuation factors. These weights are calculated using a combinatorial procedure that takes into account the probability of encountering a cloud layer as a function of the cloud coverage fraction, that is, the portion of the integration length (50 km) covered by clouds. This computation is carried out altitude by altitude.

Finally, the simulated signals are perturbed using the Poisson statistics to simulate the statistical variability of the number of photons reaching the receiver. Additional statistical perturbations are considered to account for the statistical mechanisms associated with photon-electron multiplication.

In the retrieval module, the simulated signals are analyzed through consolidated lidar techniques to obtain profiles of atmospheric temperature and water vapor mixing ratio. As a preliminary step, a subtraction scheme is used to remove the background contribution, and a vertical average is applied to reduce the statistical fluctuations.

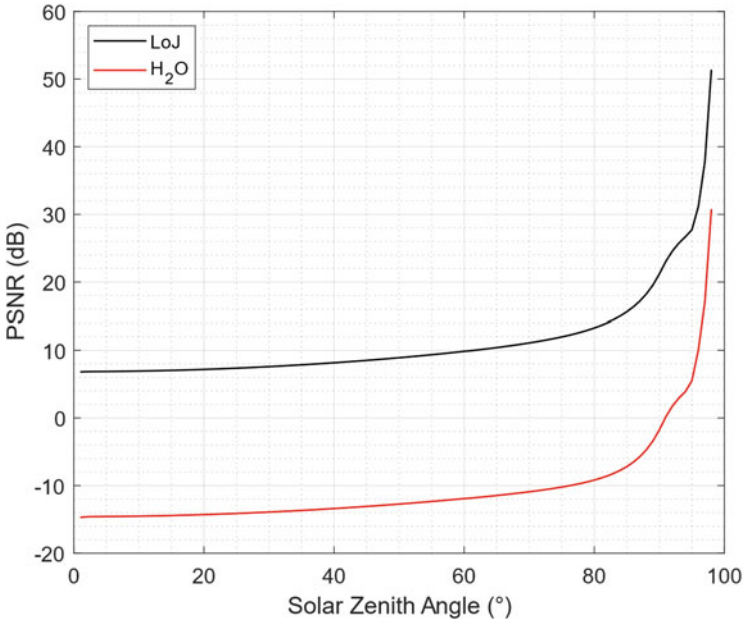


Fig. 90.1 Peak signal-to-noise ratio (dB) calculated as the ratio of simulated roto-vibrational water vapor Raman and low quantum number (LoJ) rotational and their respective atmospheric background for different solar zenith angles

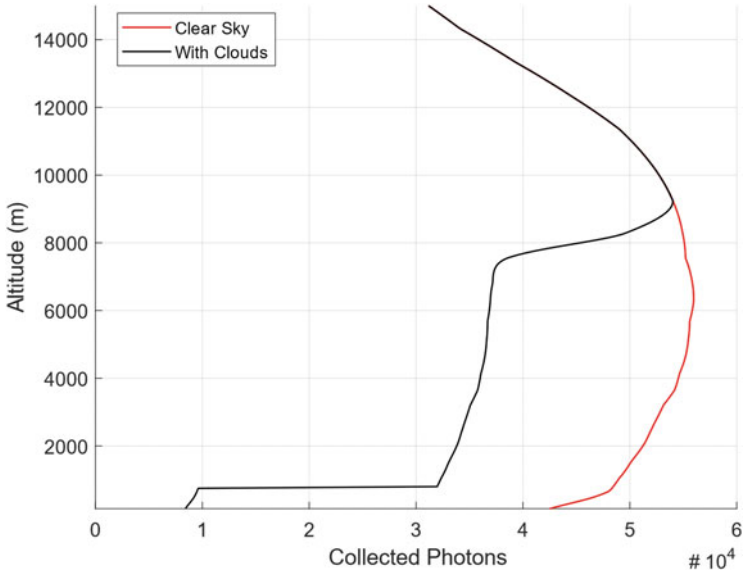


Fig. 90.2 Simulation of the same rotational signal in clear and cloudy conditions

The atmospheric temperature profile is obtained from the ratio of the high-to-low quantum number rotational Stokes and anti-Stokes Raman signals [6]. The water vapor mixing ratio profile is obtained from the ratio of the water vapor roto-vibrational Raman signal over a temperature-independent reference signal obtained as a weighted sum of the pure rotational Raman signals.

The statistical uncertainty is calculated by propagating the error; furthermore, the end-to-end scheme allows to also calculate the systematic error (bias) comparing the retrieved profiles with the original ones [7].

90.3 Simulation Results

Several simulations around the globe have been performed to estimate the performances of ATLAS. As input data for the simulations, thermodynamic and optical parameters from the non-hydrostatic mesoscale model GEOS-5 Nature Run Ganymed Release were used. The data were extracted to simulate the performance along several dawn-dusk orbits around the Earth for different days of the year, with the aim to evaluate different background conditions in dependence of the solar zenith angle. In a dawn-dusk orbit, the solar zenith angle oscillates in an interval centered at about 90°– corresponding to the passage on the equator – with a variability along the orbit that changes from ±3° (low background) to ±30° (high background). The results provided here are related to an intermediate variability of $90° \pm 15°$, corresponding to day 180 of the year, showing two full orbits around the globe from 6.00 to 9.00 UTC based on the GEOS-5 input data of 28 June 2009 (Fig. 90.3).

The simulations consider a satellite at an altitude of 450 km and have a vertical resolution of 200 m and a horizontal resolution of 50 km, corresponding to an integration time of 7.5 s. The technical specifications considered for the numerical simulations reflect the experimental setup of ATLAS and are listed in Table 90.1. The GEOS-5 dataset contains information about the vertical resolved cloud fraction and the in-cloud optical thickness for liquid and ice clouds; therefore, the simulations include the cloud contribution.

Table 90.1 Main specifications used for simulations

System configuration	Value
Nd:YAG laser tripled wavelength	354.7 nm
Single pulse energy	1 J
Pulse repetition frequency	200 Hz
Telescope diameter	2 m
Receiver FOV (HWHM)	12.5 μrad
Photomultiplier quantum efficiency	80%
Filter's peak transmission profile	80%

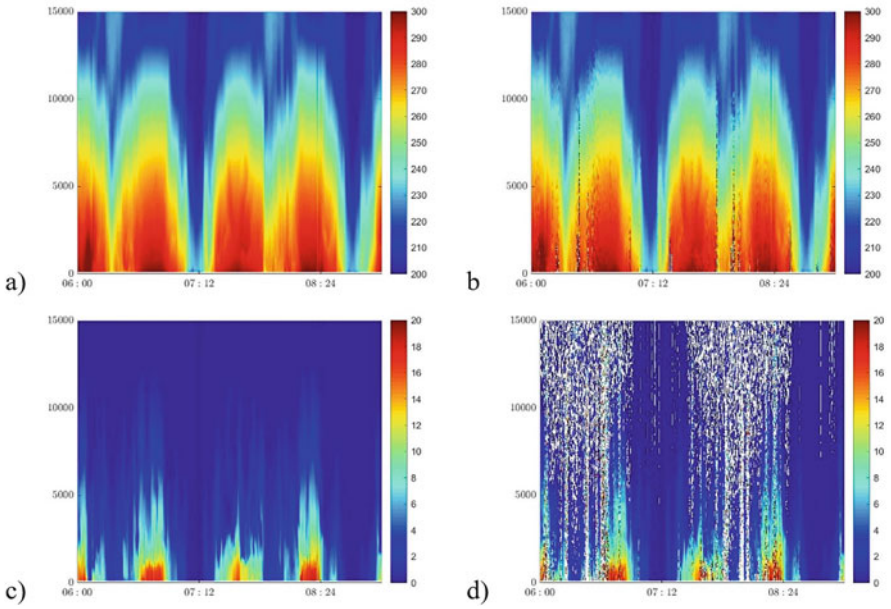


Fig. 90.3 Input (**a**) and retrieved (**b**) atmospheric temperature (°K) and input (**c**) and retrieved (**d**) water vapor mixing ratio (g/kg) profiles obtained through the simulations

The results show that the bias obtained comparing the input and retrieved temperature profiles is below 0.6 K, and the statistical uncertainty is less than 1–1.2 K up to 15 km along almost the entire orbit, except on those areas where the cloud cover is too thick. The austral hemisphere shows slightly better results, since the solar zenith angle reaches its maximum in this hemisphere, with a statistical uncertainty which drops down to 0.6 K.

The water vapor mixing ratio measurement shows a higher variability in terms of performance. In the tropical belt, the bias is below 5% and the percentage statistical uncertainty is below 10% up to 3 km, but they keep below, respectively, 15% and 30% up to 7 km. In the mid-latitudes, the uncertainty is below 30% up to 5 km and reaches 7 km with low background conditions, while the bias is 5–10%. The presence of clouds severely influences the performance that appears more degraded in the boreal hemisphere, where their effect is combined with higher background conditions.

The obtained results are compatible with the observational requirements to be fulfilled for applications in monitoring, verification, data assimilation, and process studies, for which the bias for temperature and water vapor mixing ratio should be less than 5% and 0.5 K, respectively, with a statistical uncertainty of 10% and 1 K [2].

These results appear to be encouraging and reinforce the idea to develop a spaceborne Raman lidar, confirming its measurement capabilities and paving the way for further research.

References

1. Gerard, É., Tan, D.G.H., Garand, L., Wulfmeyer, V., Ehret, G., Di Girolamo, P.: Major advances foreseen in humidity profiling from the water vapour lidar experiment in space (Wales). Bull. Am. Meteorol. Soc. **85**, 237–252 (2004). https://doi.org/10.1175/BAMS-85-2-237
2. Wulfmeyer, V., Hardesty, R.M., Turner, D.D., Behrendt, A., Cadeddu, M.P., Di Girolamo, P., Schlüssel, P., Van Baelen, J., Zus, F.: A review of the remote sensing of lower tropospheric thermodynamic profiles and its indispensable role for the understanding and the simulation of water and energy cycles. Rev. Geophys. **53**, 819–895 (2015). https://doi.org/10.1002/2014RG000476
3. Di Girolamo, P., Behrendt, A., Wulfmeyer, V.: Spaceborne profiling of atmospheric temperature and particle extinction with pure rotational Raman lidar and of relative humidity in combination with differential absorption lidar: performance simulations. Appl. Opt. AO. **45**, 2474–2494 (2006). https://doi.org/10.1364/AO.45.002474
4. Di Girolamo, P., Behrendt, A., Wulfmeyer, V.: Space-borne profiling of atmospheric thermodynamic variables with Raman lidar: performance simulations. Opt. Express OE. **26**, 8125–8161 (2018). https://doi.org/10.1364/OE.26.008125
5. Whiteman, D.N., Di Girolamo, P., Behrendt, A., Wulfmeyer, V., Franco, N.: Statistical analysis of simulated spaceborne thermodynamics lidar measurements in the planetary boundary layer. Front. Remote Sens. **0** (2022). https://doi.org/10.3389/frsen.2022.810032
6. Di Girolamo, P., Marchese, R., Whiteman, D., Demoz, B.: Rotational Raman lidar measurements of atmospheric temperature in the UV (2004). https://doi.org/10.1029/2003GL018342
7. Di Girolamo, P., Behrendt, A., Kiemle, C., Wulfmeyer, V., Bauer, H., Summa, D., Dörnbrack, A., Ehret, G.: Simulation of satellite water vapour lidar measurements: performance assessment under real atmospheric conditions. Remote Sens. Environ. **112**, 1552–1568 (2008). https://doi.org/10.1016/j.rse.2007.08.008

Chapter 91
Column Optical Depth (COD) Derived from CALIOP Ocean Surface Returns

Robert Ryan, Mark A. Vaughan, Sharon D. Rodier, Brian J. Getzewich, and David M. Winker

Abstract The Cloud Aerosol Lidar with Orthogonal Polarization (CALIOP) on board the Cloud Aerosol Lidar Infrared Pathfinder Satellite Observations (CALIPSO) satellite has been making near-global measurements of clouds and aerosols since mid-June 2006. Among the properties reported in CALIPSO data products are estimates of total column optical depth (COD) obtained by integrating the retrieved extinction coefficients of detected particulates (i.e. aerosols and clouds) from 36 km to the surface. However, due to algorithm detection limits and instrument sensitivities, particulates can go undetected when the particulate loading is especially diffuse or in regions where the signal is attenuated by overlying layers. Because extinction is not calculated where features are not detected, these undetected particulates can introduce low biases into the reported COD. Lidar ratio assumptions used in the extinction retrievals can also introduce errors. To minimize these biases, future releases of the CALIPSO lidar data products will implement an ocean-derived column optical depth (ODCOD) retrieval. The following paper briefly describes the algorithm, the current status of the algorithm development and verification efforts, and preliminary comparisons to collocated COD estimates derived using other retrieval schemes and obtained from other sensors.

Keywords CALIPSO · CALIOP · Optical depth

R. Ryan (✉) · S. D. Rodier
Science Systems and Applications, Inc., Hampton, VA, USA
e-mail: robert.a.ryan@nasa.gov; sharon.d.rodier@nasa.gov

M. A. Vaughan · B. J. Getzewich · D. M. Winker
NASA Langley Research Center, Hampton, VA, USA
e-mail: mark.a.vaughan@nasa.gov; brian.j.getzewich@nasa.gov; david.m.winker@nasa.gov

© The Author(s), under exclusive license to Springer Nature Switzerland AG 2023

J. T. Sullivan et al. (eds.), *Proceedings of the 30th International Laser Radar Conference*, Springer Atmospheric Sciences,
https://doi.org/10.1007/978-3-031-37818-8_91

91.1 Introduction

The Cloud Aerosol Lidar with Orthogonal Polarization (CALIOP) [1] lidar on board the Cloud Aerosol Lidar Infrared Pathfinder Satellite Observations (CALIPSO) [2] satellite has been taking global measurements of height-resolved profile information on the location, extent, and optical properties of clouds and aerosols since mid-June of 2006. CALIOP will detect the surface when the signal is not fully attenuated by clouds or aerosols, the magnitude of which can hold information about the atmospheric volume the signal passes through. The current CALIOP algorithms for estimating total column optical depth have both detection limits and instrument sensitivities which can cause a small but significant fraction of the column's particulates to remain undetected. This, in turn, underestimates the column optical depth.

This paper describes the new CALIOP ocean-derived column optical depth (ODCOD) algorithm developed from [3] for estimating total column effective optical depth (COD) from CALIOP's ocean surface lidar return. The COD retrieved by ODCOD is an *effective* optical depth estimate for all particulates in the entire column. These effective optical depths are not corrected for multiple scattering effects, and hence will be systematically lower than the single scattering COD estimates reported in cloudy columns in the current CALIOP level 2 data products. For columns containing only aerosols, for which no multiple scattering correction is applied in the extinction processing, the ODCOD estimates are expected to provide a valuable sanity check on the current COD estimates, which are obtained by integrating the retrieved extinction coefficients of detected particulates (i.e. aerosols and clouds) from 36 km to the surface. However, algorithm detection limits and instrument sensitivities can cause a small but significant fraction of the column's particulates to go undetected when the particulate loading is especially diffuse or in regions where the signal is attenuated by overlying layers. Because extinction coefficients are not calculated where features are not detected, these undetected particulates can introduce low biases into the reported COD. The lidar ratio assumptions typically used in the extinction retrieval represent a second important source of uncertainty in the existing COD estimates. The new ODCOD algorithm does not depend on the detection of clouds or aerosols, nor does it require any a priori estimates of lidar ratio. Instead, because ODCOD relies on surface backscatter, wind speed estimates, and an ocean scattering model, it delivers an independent estimate of effective COD.

91.2 Ocean Derived Column Optical Depth Technique

The system electronics of the CALIOP instrument pass the backscatter signal through a third-order low-pass Bessel filter. An important feature of this Bessel filter is that for an impulse like return signal (as occurs from a hard target or ocean

surface return), the time-height area of the impulse signal is preserved. The output of the filter is known as its impulse response function (IRF). The Bessel filter IRF broadens hard target returns in the time domain so that the input signal is spread over several CALIOP range bins. Onboard the spacecraft, the samples recorded are at 15 m range bins which equates to a 0.1 microsecond time delay between samples. CALIOP employs onboard averaging to reduce data storage and downlink size [1]. In the region around sea level, the lidar signal is averaged to 30 m range bins at 532 nm and 60 m range bins at 1064 nm. Even with the broadening effect of the IRF, the entire ocean return signal is contained in only 3–4 range bins at 532 nm and only 2 range bins at 1064 nm.

The difference in area between a measured return and an IRF modelled return is directly related to the amount of attenuation due to particulates in the atmospheric column above and provides a means to estimate the effective total two-way transmittance of the atmosphere from the ocean surface to the base of the CALIOP calibration region at 36 km. The area of the surface return is related to the effective total two-way transmittance (and thus COD) with Eq. (91.1):

$$T^2(z_s) = \frac{cA_{\mathrm{LPF}}}{2R_\lambda}, \tag{91.1}$$

where A_{LPF} is the area under the IRF, $T^2(z_s)$ is the effective total two-way transmittance at the ocean surface, R_λ is the ocean surface reflectance, and c is the speed of light. By dividing out the modelled molecular and ozone two-way transmission, the two-way transmission due to particulates alone can be found. R_λ can be estimated from empirical equations needing only the wind speed at 10 m above the ocean surface as an input [3].

The area under the IRF can be closely approximated using analytical best-fits of a hyperbolic tangent function for the rising part of the pulse and a Gaussian curve for the falling part. The only unknowns in finding the area from the modelled IRF are a scale factor α and the time delay x_s [3]. The time delay is found by iteratively adjusting the curve in the time domain until the ratio of the largest two points of the ocean surface return signal matches the ratio of the corresponding points on the IRF model curve. This procedure is shown in Fig. 91.1a. Then, the scale factor is found by iteratively adjusting the scale factor until the error is minimized between the points sampled on the IRF model curve at the same time delays as the downlinked samples as shown in Fig. 91.1b. Finally, to obtain the area under the IRF, the integral of the IRF is performed by integrating the functions of the two parts of the unscaled IRF model multiplied by the optimized scale factor.

ODCOD relies on CALIOP's surface detection algorithm for the location and vertical extent of surface returns at both wavelengths [4]. ODCOD performs best when the column particulate loading is relatively low and thus provides a stronger surface return. And because ODCOD is sensitive only to total column optical depth, it performs equally well for highly diffuse, weakly scattering layers (e.g. aged smoke) and highly concentrated, strongly scattering layers (e.g. cirrus clouds). This stands in contrast to the CALIPSO direct detection method, which performs

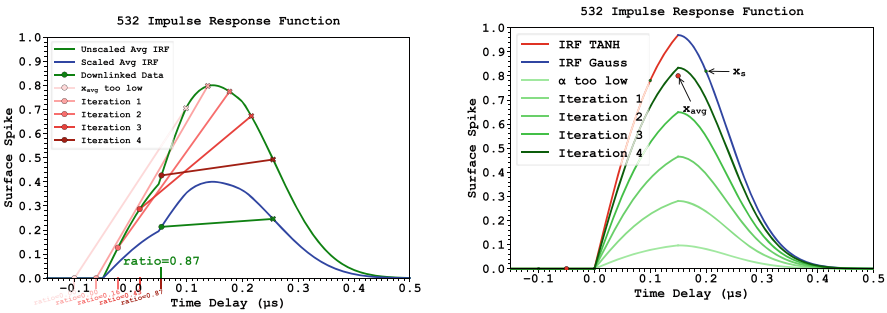


Fig. 91.1 Panel (**a**) shows a surface backscatter return on the y-axis and time delay in microseconds on the x-axis. This graphic shows how two sampled points (each joined by a bar) of the larger unscaled green curve can be iteratively repositioned along the time delay axis, until the matching ratio of the unknown "true" smaller blue curve sample points can be found. Panel (**b**) shows how, once the correct time delay is found, a modelled curve be iteratively scaled until two sampled points (shown as small green markers labelled x_s) which average to make the downlinked sample point (shown as the larger red markers labelled x_{avg}) match the measured data

substantially better for strongly scattering layers having backscatter magnitudes that show notable contrast relative to the ambient molecular backscatter [5].

91.3 Application to CALIPSO Algorithm

The ODCOD algorithm generates COD estimates over ocean at both single shot, 1 km, and 5 km resolutions wherever a qualifying surface return is detected. COD estimates are retrieved at both 532 nm and 1064 nm, but retrieval success rate tends to be less at 1064 nm due to the coarser vertical resolution. ODCOD attempts a retrieval based on a set of specific criteria. These include (1) no negative signal anomaly or surface saturation is detected, (2) the depolarization ratio indicates no sea ice in the surface return, (3) a reasonable time delay and scale factor can be solved, and (4) wind speeds are between 0 and 45 m/s. ODCOD is highly sensitive to wind speed and while the latter criteria is used for attempting a retrieval, we recommend that only wind speeds between 3 and 15 m/s be used when filtering for quality data.

CALIPSO ingests MERRA-2 [6] reanalysis data, including 10 m wind speeds, for use throughout the CALIPSO processing. While these 10 m wind speeds are found to be reasonably accurate high in the atmosphere, validation studies show that winds at 10 m above the ocean surface exhibit a low bias on the order of −0.5 m/s depending on latitude and season [7]. As illustrated in Fig. 91.2, the CALIPSO team has replicated these findings using wind speeds reported by AMSR-E and AMSR-2 [8]. Because an error of ~0.5 m/s low in wind speed translates into an ODCOD COD error of ~0.02 higher optical depths, the CALIPSO team is currently constructing a

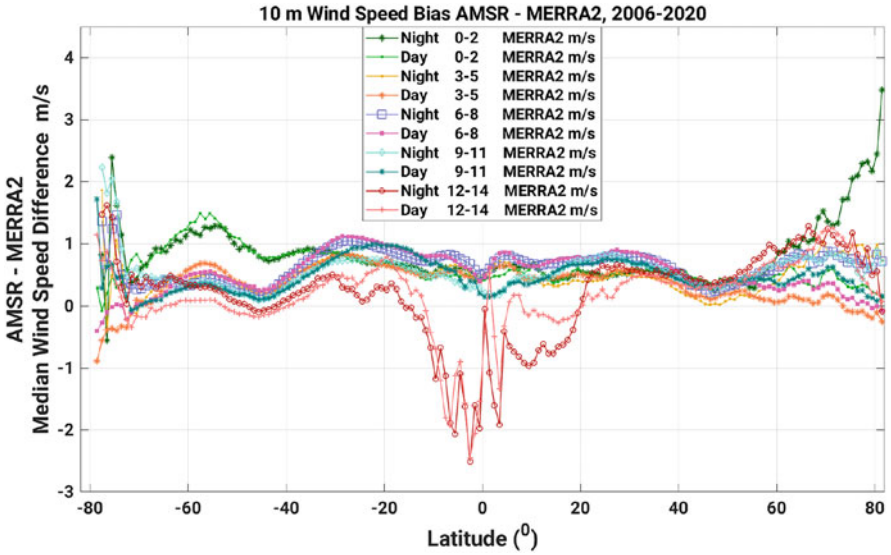


Fig. 91.2 Bias between 10 m wind speeds reported by MERRA 2 and AMSR-E/AMSR2, grouped by MERRA-2 wind speeds. MERRA-2 winds are seen to be low on the order of −0.5 m/s on average, with median differences ranging from over 2 m/s high to −3.5 m/s low with most of the biases being between −1 and 0 m/s

bias correction lookup table that will return AMSR-like wind speeds for MERRA-2 inputs.

91.4 Comparisons to Similar Datasets

We assess the performance of the ODCOD algorithm by comparing its outputs to two existing datasets. Figure 91.3a compares a beta version of the ODCOD 532 nm output with collocated MODIS 550 nm aerosol optical depths (AOD) [8]. The ODCOD dataset was created using AMSR-E wind speeds and only reports values in columns determined to be entirely cloud-free based on CALIPSO analyses. The vertical striping seen in Fig. 91.3a is an artifact of the different spatial resolutions of the two sensors. While ODCOD results are reported at single-shot resolution (333 m footprint spacing, 90 m footprint diameter), the pixel size for MODIS AOD product is 10 km × 10 km, so that multiple ODCOD values are located within a single MODIS pixel. The median difference between the two datasets is 0.0275, with MODIS being higher.

Figure 91.3b compares the ODCOD retrievals to perfectly collocated retrievals from the synergized optical depth of aerosols (SODA) method [9]. The SODA technique is similar to ODCOD, in that it uses CALIOP ocean surface returns to

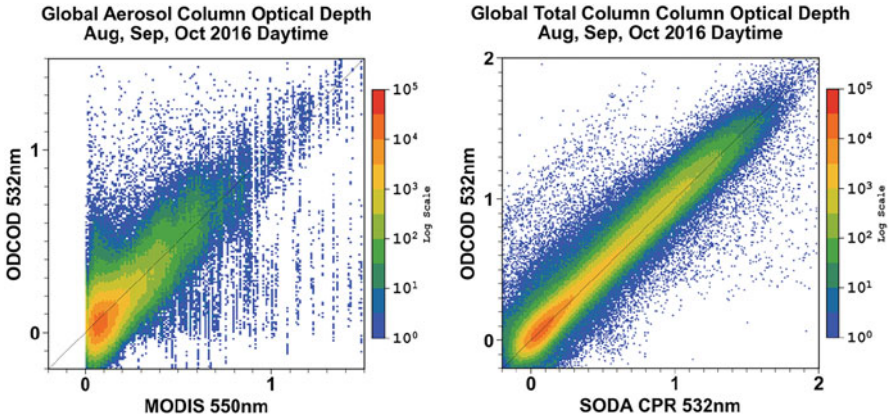


Fig. 91.3 Panel (**a**) compares aerosol optical depth retrieved by MODIS at 550 nm to ODCOD retrievals at 532 nm for daytime measurements acquired during the months of August, September, and October of 2016. Similarly, panel (**b**) compares SODA-CPR column optical depths retrieved at 532 nm to ODCOD 532 nm retrievals for daytime measurements of aerosols and thin clouds acquired during the months of August, September, and October of 2016

derive estimates of effective total column optical depths at both wavelengths. But in addition, SODA's synergistic retrievals also require collocated ocean surface returns from CloudSat's Cloud Profiling Radar. This highly innovative interdependence ultimately proved unfortunate, as a battery failure in April 2011 rendered CloudSat unable to operate during the nighttime portions of its orbit and hence the applicability of SODA algorithm described in [10] has since been limited to daytime retrieval opportunities only. Nevertheless, comparisons between ODCOD and SODA are hugely valuable in vicariously assessing the performance of ODCOD during those periods when the loss of CloudSat makes SODA unavailable. As seen in Fig. 91.3b, the agreement between ODCOD and SODA is quite good, with a median difference of 0.0085 optical depths SODA being higher. This comparison includes all columns for which CALIOP detected the ocean surface, so there are contributions from ice cloud and water clouds in addition to the ever-present aerosols. When the comparison is restricted to aerosols only, the median difference drops by an order of magnitude to 0.0008 with SODA higher.

91.5 Conclusion

ODCOD algorithm now delivers multi-resolution estimates of effective total column optical depths over global ocean surfaces. The derivation of these estimates is largely independent of the COD estimates reported in previous versions of the CALIOP data products, and hence can provide valuable insight into the correctness of several necessary assumptions made in the standard CALIOP extinction retrieval.

ODCOD shows good agreement with COD estimates derived using other sensors and other retrieval techniques and has the distinct advantage of delivering a continuous daytime and nighttime data record throughout the entire CALIPSO mission.

References

1. Hunt, W.H., Winker, D.M., Vaughan, M.A., Powell, K.A., Lucker, P.L., Weimer, C.: CALIPSO lidar description and performance assessment. J. Atmos. Ocean. Technol. **26**(7), 1214–1228 (2009)
2. Winker, D.M., Pelon, J., Coakley Jr., J.A., Ackerman, S.A., Charlson, R.J., Colarco, P.R., Flamant, P., Fu, Q., Hoff, R.M., Kittaka, C., Kubar, T.L., Le Treut, H., Mccormick, M.P., Mégie, G., Poole, L., Powell, K., Trepte, C., Vaughan, M.A., Wielicki, B.A.: The CALIPSO mission. Bull. Am. Meteorol. Soc. **91**(9), 1211–1230 (2010)
3. Venkata, S.L., Reagan, J.A.: Aerosol retrievals from CALIPSO lidar ocean surface returns. Remote Sens. **8**(12), 1006 (2016)
4. Vaughan, M., Lee, K.-P., Garnier, A., Getzewich, B.: Improvements to the CALIOP Surface Detection Algorithm, CALIPSO CloudSat Science Team Meeting, 1–3 March 2016, Newport News (2016)
5. Kacenelenbogen, M., Redemann, J., Vaughan, M.A., Omar, A.H., Russell, P.B., Burton, S., Rogers, R.R., Ferrare, R.A., Hostetler, C.A.: An evaluation of CALIOP/CALIPSO's aerosol-above-cloud (AAC) detection and retrieval capability over North America. J. Geophys. Res. **119**, 230–244 (2014)
6. Gelaro, R., and 30 coauthors: The modern-era retrospective analysis for research and applications, version 2 (MERRA-2). J. Clim. **30**(14), 5419–5454 (2017)
7. Carvalho, D.: An assessment of NASA's GMAO MERRA-2 reanalysis surface winds. J. Clim. **32**(23), 8261–8281 (2019)
8. Meissner, T., Wentz, F.J.: The emissivity of the ocean surface between 6 – 90 GHz over a large range of wind speeds and Earth incidence angles. IEEE TGRS. **50**(8), 3004–3026 (2012)
9. Remer, L.A., Kaufman, Y.J., Tanré, D., Mattoo, S., Chu, D.A., Martins, J.V., Li, R.-R., Ichoku, C., Levy, R.C., Kleidman, R.G., Eck, T.F., Vermote, E., Holben, B.N.: The MODIS aerosol algorithm, products, and validation. J. Atmos. Sci. **62**, 947–973 (2005)
10. Josset, D., Pelon, J., Protat, A., Flamant, C.: New approach to determine aerosol optical depth from combined CALIPSO and CloudSat Ocean surface echoes. Geophys. Res. Lett. **35**, L10805 (2008)

Chapter 92
Assessing Aeolus Aerosol Observational Capabilities for Data Assimilation in Air Quality and NWP Models

E. Proestakis, A. Benedetti, A. Dabas, V. Amiridis, E. Marinou, P. Paschou, A. Georgiou, A. Gkikas, A. Kampouri, A. Gialitaki, A. Tsekeri, W. McLean, and L. Steele

Abstract The EUMETSAT ADD-CROSS project aims to demonstrate the benefits of assimilating Aeolus L2A cloud and aerosol optical products for NWP, with and without possible expansions of the current instrument capabilities permitted by the new structural design envisaged for a future AEOLUS 2 mission. At the present, ALADIN transceiver enables the detection only of the returned co-polar component of the transmitted light. The use of a circularly polarized emission and the detection of the cross-polar component of the backscattered light are two potential options for the future. In order to assess their benefit, different experimental datasets (355 nm – w/wo cross-channel/linear and circular) to be used in the ECWWF's 4D-Var, have

E. Proestakis (✉) · V. Amiridis · E. Marinou · A. Gkikas · A. Tsekeri
IAASARS, National Observatory of Athens (NOA), Athens, Greece
e-mail: proestakis@noa.gr

A. Benedetti · W. McLean · L. Steele
European Centre for Medium-Range Weather Forecasts, Reading, UK

A. Dabas
CNRM, Université de Toulouse, Météo-France, CNRS, Toulouse, France

P. Paschou · A. Gialitaki
IAASARS, National Observatory of Athens (NOA), Athens, Greece

Laboratory of Atmospheric Physics, Physics Department, Aristotle University of Thessaloniki, Thessaloniki, Greece

A. Georgiou
IAASARS, National Observatory of Athens (NOA), Athens, Greece

Department of Informatics, Athens University of Economics and Business (AUEB), Athens, Greece

A. Kampouri
IAASARS, National Observatory of Athens (NOA), Athens, Greece

Department of Meteorology and Climatology, Aristotle University of Thessaloniki, Athens, Greece

© The Author(s), under exclusive license to Springer Nature Switzerland AG 2023

J. T. Sullivan et al. (eds.), *Proceedings of the 30th International Laser Radar Conference*, Springer Atmospheric Sciences,
https://doi.org/10.1007/978-3-031-37818-8_92

been produced based on CALIPSO profiles of particulate depolarization ratio and backscatter coefficient in the mid-visible. The specific objectives of ADD-CROSS are to (1) quantify the impact of the cross-channel on data assimilation in air quality and NWP models and (2) to quantify the impact of linear vs circular configuration in the absence of the cross-polar channel. The ADD-CROSS assimilation experiments will focus on the Western Sahara and the Tropical Atlantic Ocean in a 1-month time frame (September 2021 during which a major international campaign was carried out in the region, thus providing interesting independent data). Here, preliminary results of the under-development CALIPSO-based products to be used in the ECWWF's 4D-Var are presented.

Keywords Aeolus L2A · CALIPSO · NWP

92.1 Introduction

The European Organisation for the Exploitation of Meteorological Satellites (EUMETSAT) project entitled "Upgrading Aeolus aerosol observational capabilities towards improving air quality and NWP models" (ADD-CROSS) aims to demonstrate the benefits of assimilating Aeolus L2A optical products for NWP, taking into account possible expansions of the current instrument capabilities permitted by a new structural design envisaged for the AEOLUS 2 mission. The Aeolus-like datasets of optical products at 355 nm to be used in the ECWWF's 4D-Var is based on Cloud-Aerosol Lidar and Infrared Pathfinder Satellite Observation (CALIPSO) system Cloud-Aerosol Lidar with Orthogonal Polarization (CALIOP) [1] of the Level 2 (L2) aerosol optical products at 532 nm, for the Joint Aeolus Tropical Atlantic Campaign (JATAC) campaign – the ASKOS component (named after the Greek god of winds) defined experimental domain and for 09/2021. More specifically, the region of interest (RoI) includes the Western Sahara and the Tropical Atlantic Ocean (Fig. 92.1), taking advantage of the pronounced natural processes leading to the emission of large amounts of mineral particles and the subsequent transport of massive loads towards the maritime outflow regions. Besides the selection of RoI relies on the wealth of available observational dataset to be used for a complete and descriptive assessment analysis, thanks to the European Space Agency (ESA) JATAC-ASKOS Tropical Campaign conducted in Cape Verde (September 2021).

92.2 Methodology

The primary input datasets include CALIPSO CALIOP Version 4 (V4.21) Level 2 (L2) 5 km profiles of aerosol (APro) and clouds (CPro). More specifically, the key datasets include processing of particulate depolarization ratio (Fig. 92.2c) and total

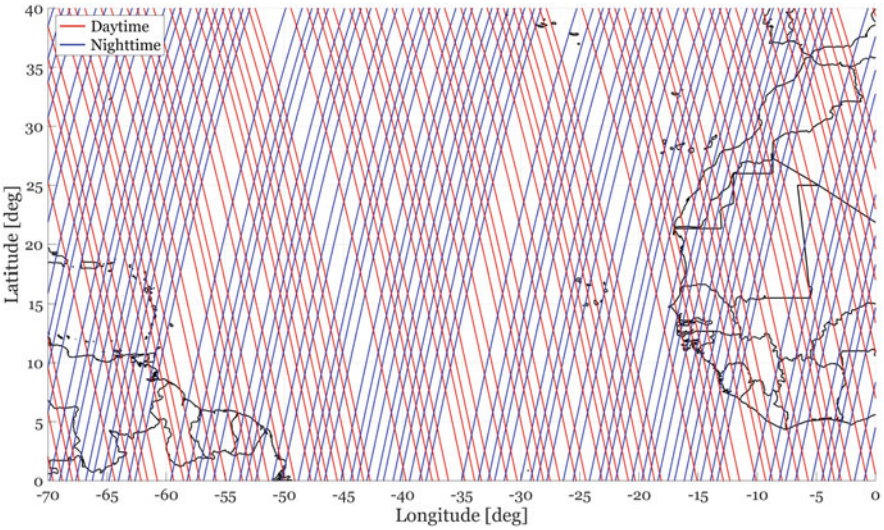


Fig. 92.1 The ADD-CROSS domain, encompassing the broader Western Sahara and Tropical Atlantic Ocean. The CALIPSO daytime and nighttime overpasses, during the ADD-CROSS period of interest of the ESA-JATAC-ASKOS Campaign in Cape Verde (September 2021), are shown in red and blue lines, respectively

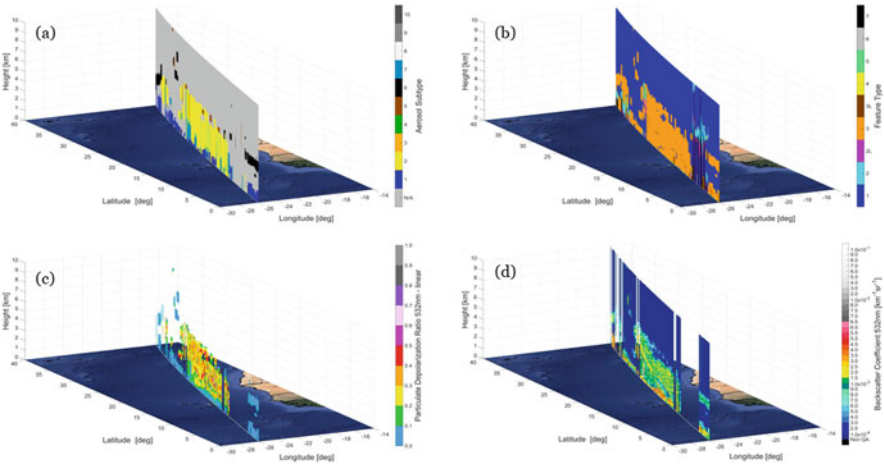


Fig. 92.2 Aerosol subtype (**a**), feature type (**b**), particulate depolarization ratio at 532 nm – linear (**c**), and total backscatter coefficient at 532 nm (**d**) for the CALIPSO orbit "2021-09-05T04-02-05ZN"

backscatter coefficient at 532 nm (Fig. 92.2d). The processing methodology, as a first step applies several quality assurance (QA) procedures [2]. Accordingly, the different intermediate steps applied towards establishing the Aeolus-like products (355 nm – w/wo cross-channel/linear and circular) follows the CALIPSO-based

subtype [3] classification (Fig. 92.2a) of the detected atmospheric layers identified and classified as aerosol (Fig. 92.2b).

With respect to the total backscatter coefficient spectral conversion factors between 532 nm and 355 nm, they are provided according to the ESA-LIVAS [4] project outputs. The aerosol-type-dependent backscatter-related Ångström exponents for the spectral conversions in the framework of LIVAS were established mainly based on EARLINET [5] (European Aerosol Research Lidar Network) ground-based multiwavelength measurements at 532 and 355 nm and based on Eq. 92.1.

$$\beta_{T,\ \lambda 2,\text{aer.sub.}} = \beta_{T,\lambda 1,\text{aer.sub.}} \left(\frac{\lambda_1}{\lambda_2}\right)^{\text{BAE}} \tag{92.1}$$

where $\lambda_1 = 532$ nm, $\lambda_2 = 355$ nm, and BAE is the LIVAS backscatter-related Ångström exponent per CALIPSO aerosol subtype. Moreover, particulate depolarization ratio 532-to-355 (linear) are provided according to Eq. 92.2.

$$\delta_{lin,355\text{nm}}(z) = K_d * \delta_{lin,532\text{nm}}(z) \tag{92.2}$$

where "K_d" are the literature-based aerosol-subtype-dependent particulate depolarization ratio spectral conversion factors.

The outputs, upon application of the 532-to-355 nm spectral conversion factors, provide the total backscatter coefficient at 355 nm and the particulate depolarization ratio at 355 nm – linear (Fig. 92.3).

Accordingly, the following steps provide 355 linear – to 355 circular conversion of particulate depolarization ratio and establishment of the co- and cross-backscatter coefficient components at 355 nm – circular. As a first step, the total backscatter coefficient, for emitted light of linear (''*lin*") or circular (''*cir*) polarization, is the sum of the backscatter light corresponding to the parallel ("∥") and cross ("⊥") components for linearly polarized light or the co-polar ("∥") and cross-polar ("⊥") components for circularly polarized light (Eq. 92.3).

$$\beta_{T,lin/cir}(z) = \beta_{\parallel,lin/cir}(z) + \beta_{\perp,lin/cir}(z) \tag{92.3}$$

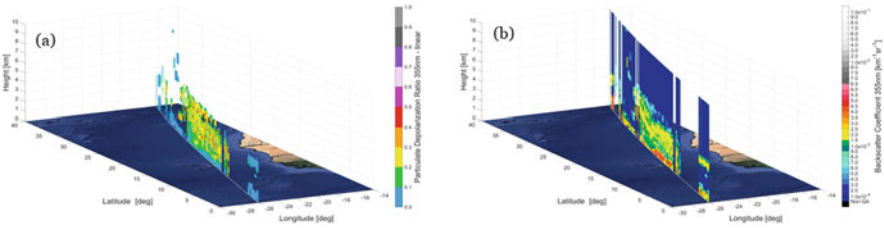


Fig. 92.3 Particulate depolarization ratio at 355 nm – linear (**a**) and total backscatter coefficient at 355 nm (**b**) for the CALIPSO orbit "2021-09-05T04-02-05ZN"

Accordingly, the formula provided in Eq. 92.4 relates to the linear depolarization ratio (∂_{lin}) and the circular depolarization ratio (∂_{cir}), in case of randomly oriented particles in the atmosphere and under single-scattering assumption [6, 7].

$$\delta_{cir}(z) = \frac{2\delta_{lin}(z)}{1 - \delta_{lin}(z)} \tag{92.4}$$

As a final step, the co-polar component can be computed based on Eq. 92.5.

$$\beta_{\parallel,lin/cir}(z) = \frac{\beta_{T,lin/cir}(z)}{1 + \delta_{lin/cir}(z)} \tag{92.5}$$

Based on Eqs. 92.3–92.5, and having as input the CALIPSO L2 APro 5 km V4.21 QA aerosol optical products, the total backscatter coefficient at 355 nm and the particulate depolarization ratio at 355 nm – circular are computed (Fig. 92.4).

92.3 Outcomes

The final outcome CALIPSO-based Aeolus-like dataset, towards facilitating DA, provides 355 nm – w/wo cross-channel – linear/circular products in Aeolus Basic Repeat Circle (BRC) of ~90 km horizontal resolution (#16 consecutive CALIPSO L2 5 km Pro), while with respect to vertical resolution, the original CALIPSO vertical resolution is maintained. More specifically, the following products are considered in Aeolus-like BRC:

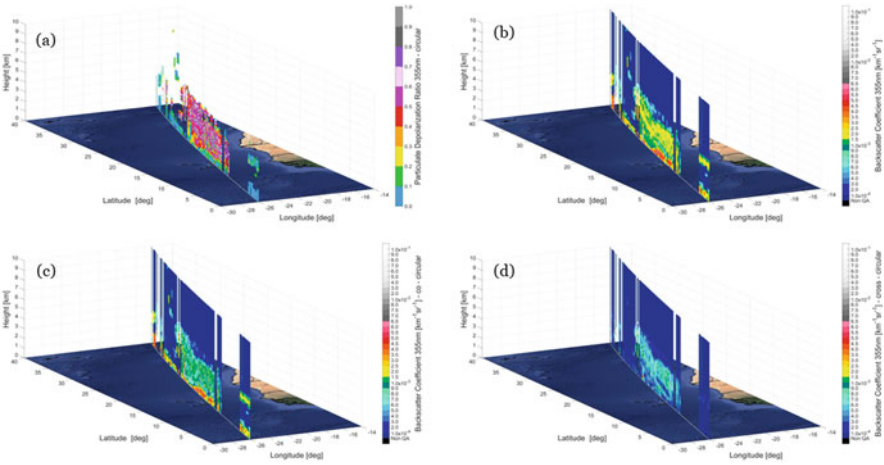


Fig. 92.4 Particulate depolarization ratio at 355 nm – circular (**a**), total backscatter coefficient at 355 nm (**b**), backscatter coefficient co- (**c**) and cross- (**d**) components for the CALIPSO orbit "2021-09-05T04-02-05ZN"

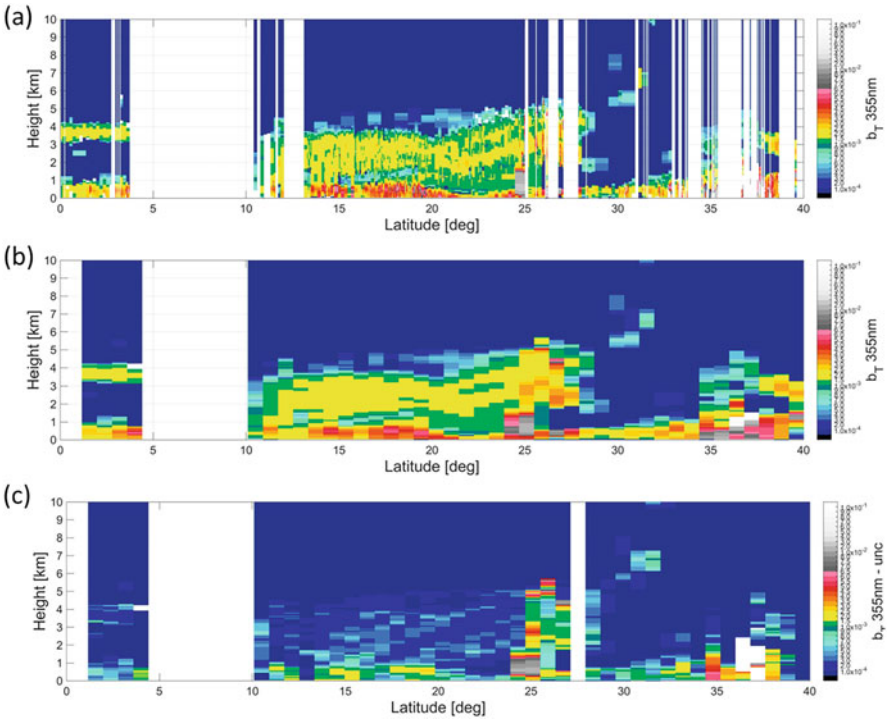


Fig. 92.5 "Backscatter coefficient 355 nm – co – circular" (**a**), "backscatter coefficient 355 nm – co – circular" in Aeolus BRC horizontal resolution (**b**), and "Backscatter Coefficient 355 nm – co – circular – unc" in Aeolus BRC horizontal resolution (**c**)

1. b_T – 355 nm and uncertainty
2. $b_{//}$ – 355 nm (circular) and uncertainty
3. $b_{\perp}$ – 355 nm (circular) and uncertainty
4. $b_{//}$ – 355 nm (linear) and uncertainty
5. $b_{\perp}$ – 355 nm (linear) and uncertainty

For the case of CALIPSO orbit "2021-09-05T04-02-05ZN", the total backscatter coefficient at 355 nm, including the co- and cross-components in assumed circular polarization scenario, including provision of uncertainties in terms of sqrt of the variance of the consecutive CALIPSO 5 km profiles in BRC, is provided (Fig. 92.5).

92.4 Future Steps

Future steps include the different experimental datasets (355 nm – w/wo cross-channel/linear and circular) to be used in the ECWWF's 4D-Var, to assess (1) the

impact of the cross-channel on data assimilation in air quality and NWP models and (2) the impact of linear vs circular configuration in the absence of the cross-polar channel. The assimilation experiment outputs, due to the extensive wealth of available observational data collected in the framework of the ESA-JATAC-ASKOS Tropical Campaign in Cape Verde, will be implemented for a complete and descriptive assessment analysis of the assimilation outputs.

References

1. Winker, D.M.: A global 3D view of aerosols and clouds. Bull. Amer. Meteorol. Soc. **91**, 1211–1230 (2010). https://doi.org/10.1175/2010BAMS3009.1
2. Tackett, J.L.: CALIPSO lidar level 3 aerosol profile product: version 3 algorithm design. Atmos. Meas. Tech. **11**, 4129–4152 (2018). https://doi.org/10.5194/amt-11-4129-2018
3. Kim, M.-H.: The CALIPSO version 4 automated aerosol classification and lidar ratio selection algorithm. Atmos. Meas. Tech. **11**(11), 6107–6135 (2018). https://doi.org/10.5194/amt-11-6107-2018
4. Amiridis, V.: LIVAS: a 3-D multi-wavelength aerosol/cloud database based on CALIPSO and EARLINET. Atmos. Chem. Phys. **15**, 7127–7153 (2015). https://doi.org/10.5194/acp-15-7127-2015
5. Pappalardo, G.: EARLINET: towards an advanced sustainable European aerosol lidar network. Atmos. Meas. Tech. **7**, 2389–2409 (2014). https://doi.org/10.5194/amt-7-2389-2014
6. Mishchenko, M.I., Hovenier, J.W.: Depolarization of light backscattered by randomly oriented nonspherical particles. Opt. Lett. **20**(12), 1356 (1995). https://doi.org/10.1364/OL.20.001356
7. Roy, G., Roy, N.: Relation between circular and linear depolarization ratios under multiple-scattering conditions. Appl. Opt. (2008). https://doi.org/10.1364/ao.47.006563

Chapter 93
High-Spectral-Resolution Lidars at the University of Wisconsin

Ilya Razenkov, Joseph Garcia, and Edwin Eloranta

Abstract Our group in the University of Wisconsin–Madison has developed several high-spectral-resolution lidars (HSRLs). The lidars we describe here use relatively high-power injection-seeded Nd:YAG lasers and iodine adsorption cells to separate Mie and Rayleigh scattered photons in the lidar returns. The instruments are eye safe for direct viewing and capable of continuous, remote operation with little maintenance. They have been deployed in numerous field campaigns in many locations around the globe. Over the years, these HSRL lidars had undergone multiple modifications improving the performance and adding new measurement capabilities such as extinction cross-section measurements, dual wavelength operation, and telescope elevation scanning. Here we provide a history of HSRL upgrades and a description of the latest upgrade.

Keywords High-spectral-resolution lidar · HSRL · University of Wisconsin

93.1 Introduction

The University of Wisconsin high-spectral-resolution lidars (HSRLs) are eye safe instruments capable of continuous, autonomous, low-maintenance operation in remote areas. In the past 20 years, our lidar group has constructed five instruments, four of which have undergone major upgrades. The instruments have been deployed in more than 25 different locations, including remote locations such as McMurdo station in Antarctica and Ellesmere Island, Nunavut in the Arctic along with airborne and shipborne deployments. This chapter provides a history of instrument upgrades and a description of the latest version under construction for the Department of Energy Atmospheric Radiation Measurement (ARM) program.

I. Razenkov (✉) · J. Garcia · E. Eloranta
University of Wisconsin-Madison, Madison, WI, USA
e-mail: razenkov@wisc.edu; joe.garcia@ssec.wisc.edu; eloranta@wisc.edu

© The Author(s), under exclusive license to Springer Nature Switzerland AG 2023

J. T. Sullivan et al. (eds.), *Proceedings of the 30th International Laser Radar Conference*, Springer Atmospheric Sciences,
https://doi.org/10.1007/978-3-031-37818-8_93

93.2 High-Spectral-Resolution Lidar Systems

HSRL systems have been under development at the University of Wisconsin since the 1970s [1–4]. The early instruments required the continuous presence of skilled personnel for instrument operation and maintenance.

A new generation of systems was introduced with the construction of the AHSRL in 2002 [5]. It was designed for continuous, autonomous operation in order to provide climate data on Arctic clouds and aerosols. The original AHSRL operated at a single 532 nm wavelength and a 4 kHz pulse repetition rate. It was equipped with 40 cm telescope and used high quantum efficiency APD photon counting detectors for its four channels: (1) cross polarized, (2) molecular, (3) high gain combined aerosol-molecular, and (4) low gain combined aerosol molecular. Over the years, the instrument underwent multiple upgrades including a dual-wavelength laser operating at 532 and 1064 nm and a combined aerosol-molecular channel at 1064 nm, along with wide-field-of-view molecular and combined aerosol-molecular channels operating at 532 nm. The wide field-of-view receiver was realized with a 7.5 cm refractive telescope viewing at 1 mrad field of view. The upgrade allowed for additional measurements of aerosol volume backscattering coefficient at 1064 nm and accurate extinction cross-section at 532 nm.

A lightweight, compact lidar instrument (GV-HSRL) for airborne deployment on the NSF-Gulfstream V aircraft was built for NCAR in 2010. The instrument received an all-carbon-fiber telescope frame and 40 cm lightweight telescope mirror. The instrument operates at 532 nm wavelength and is equipped with same channels as the original AHSRL. The instrument has not undergone the upgrades once it was certified for the aircraft use.

In 2012, we built the instrument (BagoHSRL) that became our testbed for the developments of new technologies most of which were later implemented in other HSRL's. The instrument was designed to have a lightweight carbon-fiber telescope mounted on the servo motor to enable telescope elevation scanning capability. The telescope can be mounted in two positions on the instrument: outside the instrument's shelter with 180 degrees scanning range and on the inside of the shelter to perform near horizon and near zenith scanning. The instrument originally operated at 532 nm had 4 channels same as the original AHSRL. Over time gained a 1064 nm output, and it currently has 9 receiver channels. This is the only HSRL instrument with an experimental atmospheric temperature measuring channel. It is implemented using a second pressure-broadened iodine absorption filter to observe the spectral width of the returned molecular signal [6].

Twin HSRLs for the Department of Energy Atmospheric Radiation Measurement program were built in 2011 [7]. They operated at 532 nm wavelength and were equipped with the same four channels as the original AHSRL. One of the instruments (NSHSRL) was deployed at the ARM measurement facilities in Barrow, AK from 2011 to 2019. It required only a few maintenance trips and had very small downtime over the 8-year deployment. An upgrade of this instrument was completed in 2020, see Fig. 93.1a. The laser was modified to operate at 532 and 1064 nm

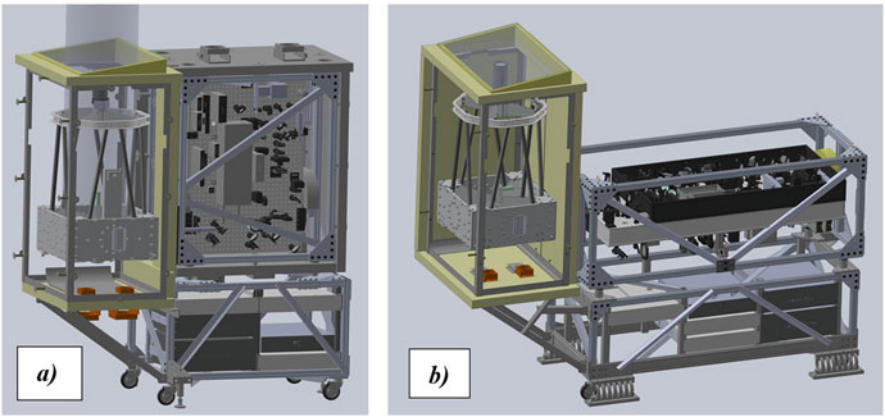


Fig. 93.1 CAD models with removed thermal panels: (**a**) NSHSRL model, (**b**) MF2HSRL model

wavelengths. Combined and molecular wide-field-of-view channels operating at 532 nm, with 1 mrad field-of-view, were added to the instrument using a 7.5 cm diameter refractive telescope. The NSHSRL also received two elastic scattering channels (co-pol and cross-pol) at 1064 nm. The telescope is mounted on a servo motor, and the instrument can scan near zenith angles to detect oriented ice crystals.

The second instrument (MF2HSRL) built in 2011 for DOE ARM program was part of its Mobile Facility 2 instrumentation. This instrument is currently undergoing modifications and is further described in this paper, see Fig. 93.1b. Table 93.1 shows the channels for HSRLs and years when the channels are first implemented.

All of the data acquired by the Department of Energy HSRL systems are available from: https://www.arm.gov/data. Data from UW, NCAR, and DOE systems can also be found at: http://hsrl.ssec.wisc.edu.

93.3 MF2 High-Spectral Resolution Lidar Design

The HSRL technique uses spectral information from the lidar returns, which requires a narrow high-spectral resolution laser (<100 MHz) and ~10 GHz laser frequency tuning capability. The transmitter is based on the diode pumped Nd:YAG laser from Photonics Industries. The laser emits two wavelengths 532 nm and 1064 nm and operates at 4 kHz pulse repetition rate. The single-mode diode (DFB) laser from QD-Lasers is used to injection seed the host laser cavity. The seed laser light is injected into the host laser cavity through a fast fiber-optic switch when the Q-switch is open. All the remaining time, the fiber-optic switch directs the seed laser light to a second output, where the 1064 nm light is frequency doubled for use for instrument calibration. The host laser cavity has a 90% output coupler and provides output for 1064 nm light. The 532 nm light generated by intracavity doubling crystal

Table 93.1 List of channels implemented in the HSRLs and year

Channel	AHSRL (U W)	GV-HSRL (NCAR)	BagoHSRL (U W)	NSHSRL (DOE)	MF2HSRL (DOE)
Molecular NFOV@532	2002/06	2008/06	2012/02	2011/03	2010/11
Combined high gain NFOV@532	2002/06	2008/06	2012/02	2011/03	2010/11
Combined low gain NFOV@532	2005/06	2008/06	2012/02	2011/03	2010/11
Cross-pol NFOV@532	2002/06	2008/06	2012/02	2011/03	2010/11
Temperature NFOV@532	–	–	2012/11	–	–
Molecular WFOV@532	2015/02	–	2014/04	2020/01	2022/07[a]
Combined WFOV@532	2018/10	–	2019/07	2020/01	2022/07[a]
Combined NFOV@1064	2015/02	–	2014/05	2020/01	2022/07[a]
Cross-pol NFOV@1064	2018/10	–	2018/02	2020/01	2022/07[a]
Molecular NFOV@1064	–	–	–	–	In progress

[a]Expected date, in progress

(KTP) escapes the cavity by means of the dichroic mirror. The 532 and 1064 nm beams are then recombined on the second dichroic mirror inside the laser head. This configuration provides output power ratio ~700 mW@532 nm:1400 mW@1064 nm and can be changed by using different output coupler. The interferometer-based cavity length controller (ICLC) tunes the host laser cavity to a resonant frequency of the seed laser. ICLC is also locking the laser output frequency to the iodine absorption line #1109 with accuracy of around ±15 MHz. The lidar transceiver parameters are summarized in Table 93.2. More details on transmitter and ICLC operation can be found in [8, 9].

In our MF2HSRL, the transmitter and the receiver are located on opposite sides of the breadboard. The breadboard is mounted to the frame with two ball joints and positioned horizontally in the operating state. It can be rotated 180 degrees inside the frame for maintenance. The part of the transmitter's optics, along with frequency control optics and interferometer, is on the bottom side of the breadboard, and the receiver is on the top. The laser is mounted under the breadboard using a kinematic mount. Figure 93.2 shows the complete optical diagram of the MF2HSRL. More details describing the optical design and transmitter of the BagoHSRL instrument with similar optical layout can be found in [9].

The MF2HSRL instrument will receive the molecular channel at 1064 nm implemented with a field-widened Michelson interferometer (FWMI). The FWMI

Table 93.2 MF2HSRL parameters

Transmitter		Receiver	
Laser photonics Ind.	DS10–532/1064	Scanning telescope	40 cm diameter
Transmitted power	200 mW@532 nm 600 mW@1064 nm	Narrow field of view	100 μrad
Laser spectral width	<50 MHz	Wide field of view	1 mrad
Spectral purity	<1:5000	Sky noise filter bandwidth 532 nm	7.5 GHz
Locking accuracy	30 MHz	Sky noise filter bandwidth 1064 nm	7 GHz
Pulse repetition rate	4 kHz	Iodine filter bandwidth (line 1109)	1.8 GHz
Telescope aperture	40 cm shared	Geiger-mode APD detectors	SPCM-AQRH-12
Transmitter div.	~2 μrad		

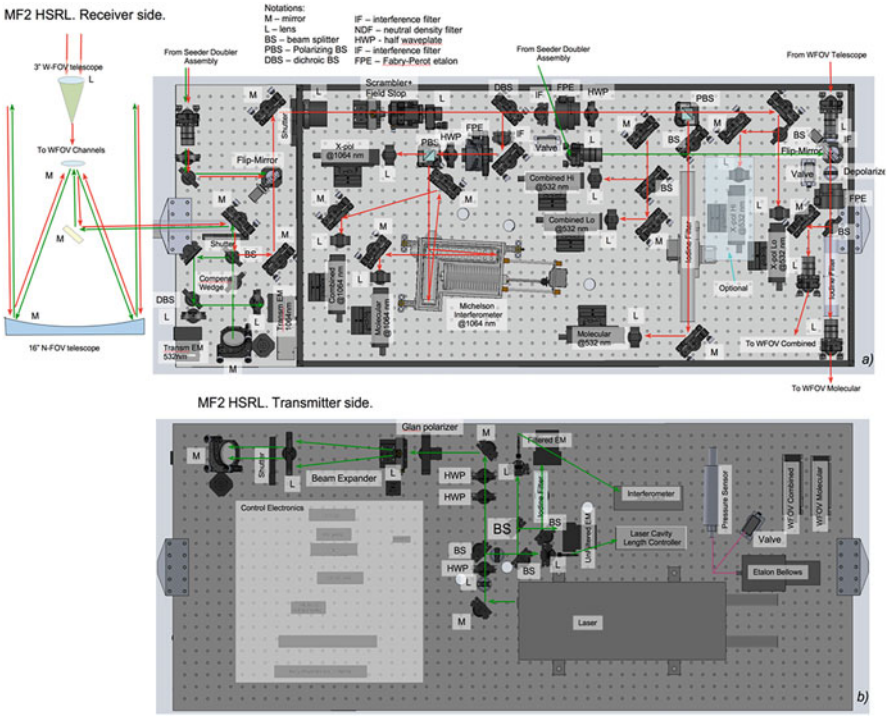


Fig. 93.2 Optical layout for MF2HSRL: (**a**) Receiver, top view of the breadboard, (**b**) transmitter, bottom view of the breadboard

will be formed with a solid glass arm and air arm. To reduce thermal sensitivity, the spacer material in the air arm is selected with CTE value to compensate for thermal change in the glass arm. The spectrometer will be tuned by pressure (air density). The proposed FSR is 1.5 GHz. The paper "Field-Widened Michelson Interferometer

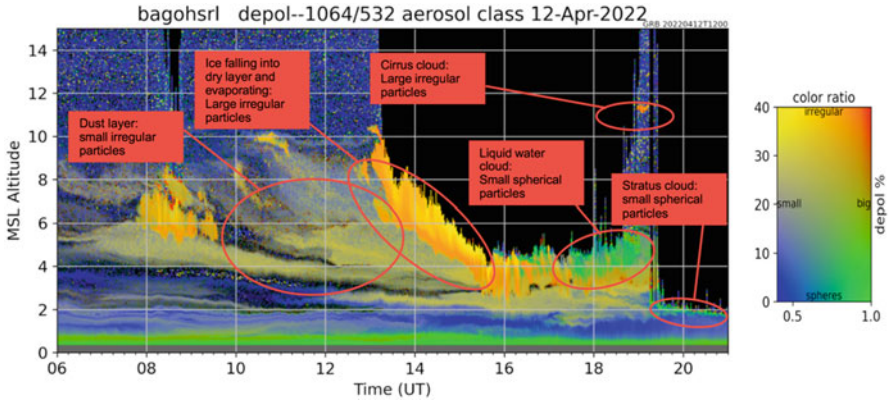


Fig. 93.3 Aerosol classification measured with BagoHSRL on April 12, 2022, from 6:00 to 21:00 UTC Madison, WI

as the Spectral Discriminator in a 1064 nm HSRL" by Zachary Buckholtz (see Proceedings for 30th ILRC) describes the design of the interferometer.

93.4 HSRL Data Example

An example of HSRL data demonstrates a capability of the dual-wavelength instrument to discriminate between different types of aerosols. An aerosol classification plot is shown in Fig. 93.3: range-time image of color ratio vs. depolarization. On April 12, 2022, the BagoHSRL instrument detected a dust layer, followed by snow precipitating and evaporating in the dry air below from 13:00 to 17:00 UTC; a liquid water cloud from 17:00 to 19:00 UTC with cirrus cloud at 12 km, and stratus cloud from 19:00 to 21:00 UTC. A mask is applied to the data with low signal-to-noise ratio.

References

1. Shipley, S.T., Tracy, D.H., Eloranta, E.W., Trauger, J.T., Sroga, J.T., Roesler, F.L., Weinman, J.A.: A high spectral resolution lidar to measure optical scattering properties of atmospheric aerosols: part 1: instrumentation and theory. Appl. Opt. **23**, 3716–3724 (1983)
2. Grund, C.J., Eloranta, E.W.: The University of Wisconsin high spectral resolution lidar. Opt. Eng. **30**, 6–12 (1991)
3. Piironen, P., Eloranta, E.W.: Demonstration of a high-spectral resolution lidar based on an iodine absorption filter. Opt. Lett. **19**, 234–236 (1994)
4. Eloranta, E.W.: High spectral resolution lidar. In: Weitkamp, K. (ed.) Lidar: Range-Resolved Optical Remote Sensing of the Atmosphere Springer Series in Optical Sciences. Springer, New York (2005)

5. Eloranta, E.W., Razenkov, I.A., Kuehn, R.E., Holz, R.E., Hedrick, J.P., Garcia, J.P.: A high spectral resolution lidar for operation in the Arctic. In: Atmospheric Radiation Measurement (ARM) Program Science Team Meeting, April 8–11. St Petersburg, FL (2002)
6. Razenkov, I.I., Eloranta, E.W., et al.: Advances in atmospheric temperature profile measurements using high spectral resolution lidar. In: Proceedings for 28th International Laser Radar Conference, June 25–30. Bucharest, Romania (2017)
7. Razenkov, I.A., Eloranta, E.W., Razenkov, I.I.: A high spectral resolution lidar for the department of energy. In: Proceedings for 25th International Laser Radar Conference, July 5–9. St. Petersburg, Russia (2010)
8. Lawson, M., Eloranta, E.: Dither cavity length controller with iodine locking. In: International Laser Radar Conference, 27th, ILRC 27, New York, NY, 5–10 July 2015. EPJ Web of Conferences (2016). https://doi.org/10.1051/epjconf/201611906003
9. Razenkov, I.I., Eloranta, E.W., et al.: High spectral resolution Lidar at the University of Wisconsin-Madison. In: Proceedings for 28th International Laser Radar Conference, June 25–30. Bucharest, Romania (2017)

Chapter 94
ATLID Algorithms Applied to ALADIN



David P. Donovan, Gerd-Jan van Zadelhoff, Ping Wang, and Lev Labzovskii

Abstract This chapter describes two novel algorithms for cloud and aerosol property retrievals that are being implemented in the ALADIN operational processor. These two algorithms are known as AEL-FM and AEL-PRO. AEL-FM provides a "feature-mask" based on ALADIN cross-talk corrected particulate ("Mie") and molecular ("Rayleigh") attenuated backscatter profiles. AEL-PRO, which uses AEL-PRO as an input (as well as the attenuated backscatter profiles), provides profiles of particulate backscatter and extinction. Both these algorithms are based on algorithms previously developed for application to the ATLID lidar onboard EarthCARE.

Keywords Space lidars · Clouds · Aerosols

94.1 Introduction

The Atmospheric Laser Doppler Instrument (ALADIN) is the world's first space-based Doppler wind lidar [1]. ALADIN operates at 355 nm and its main product is line-of-sight wind profiles. ALADIN directly detects the Doppler shift of the return signals using a variation of the High Spectral Resolution Lidar technique (HSRL), and two main detection channels are used, a "Mie" and a "Rayleigh" channel. ATLID (Atmospheric Lidar) is the lidar carried by the Earth Clouds and Aerosol Radiation Explorer (EarthCARE) mission. EarthCARE is a joint ESA-JAXA mission and will embark a cloud/aerosol lidar (ATLID) [2] as well as 3 other instruments. ATLID is a HSRL system, however, unlike ALADIN (which is

This work was supported by ESA.

D. P. Donovan (✉) · G.-J. van Zadelhoff · P. Wang · L. Labzovskii
Royal Netherlands Meteorological Institute, De Bilt, The Netherlands
e-mail: donovan@knmi.nl

© The Author(s), under exclusive license to Springer Nature Switzerland AG 2023

J. T. Sullivan et al. (eds.), *Proceedings of the 30th International Laser Radar Conference*, Springer Atmospheric Sciences,
https://doi.org/10.1007/978-3-031-37818-8_94

optimized for wind measurements), and ATLID is optimized exclusively for cloud and aerosol observations.

Both ALADIN and ATLID face similar challenges when it comes to the retrieval of aerosol and cloud properties. The most important challenge is the fact that the SNR ratios of the backscatter signals are low compared to, e.g., those associated with terrestrial lidars. The low SNR of the atmospheric signals creates difficulties when using standard HSRL inversion methods. Along-track averaging can increase the SNR, and however, the presence of clouds (and inhomogeneities in general) may lead to large biases in the retrievals.

Cloud and aerosol algorithms have been developed for ATLID that have focused on the challenge of making accurate retrievals of cloud and aerosol extinction and backscatter specifically addressing the low SNR nature of the lidar signals and the need for suitable binning of the data before averaging. Two of these algorithms are A-FM (ATLID feature mask) and A-PRO (ATLID profile processor). Based on these developments, AEL-FM and AEL-PRO have been developed for and are being applied to ALADIN observations.

94.2 Accurate Attenuated Backscatter profiles

Before describing AEL-FM and AEL-PRO, the generation of accurate corr-talk corrected attenuated backscatter (ATB) signals from ALADIN observations is discussed.

ALADIN has two main detection channels: the Rayleigh spectrometer (RSP)-based channel and the Mie spectrometer (MSP) channel. The RSP uses a dual Fabry–Pérot etalon spectrally centered on either side of the laser wavelength. With this channel, clear-air wind measurements are made. The relative amount of light detected in each channel is a function of the Doppler shift of the backscattered signal. The MSP provides actual spectra and is based on a Fizeau spectrometer. Using the spectra, in the presence of cloud/aerosol scatterers, the Doppler shift of the "Mie" peak can be determined.

For cloud and aerosol retrievals, it is necessary to be able to calculate the pure Ray and Mie attenuated backscatters. However, the MSP and RSP units both simultaneously detect substantial fractions of both the molecular Rayleigh and particulate backscatter, i.e., there is a substantial amount of cross-talk (CT) present. Correcting for this CT using the combination of the MSP and RSP signals is done as part of the standard L2a processing [3]. However, the results are affected by the Doppler shift of the return and the stability of the optical system as a whole.

As part of the AEL-FM and AEL-PRO development, an alternative means of producing CT corrected ATBs was developed. This method uses the MSP only and offers a simpler more robust correction procedure. With reference to Fig. 94.1, the method is based on dividing the spectrum into virtual "Mie" and "Rayleigh"

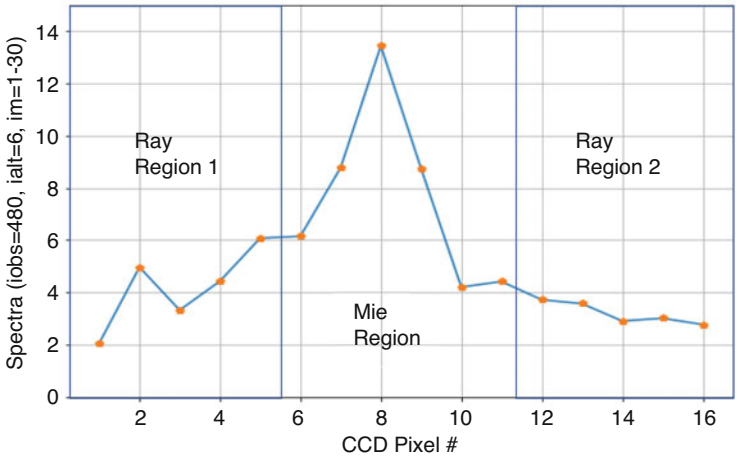


Fig. 94.1 Example spectrum from the MSP

regions. The CT coefficients are then calculated based on a model of the Fizeau spectrometer [4]. The 16 CCD column pixels cover a range of about 0.68 pm. The asymmetry of the return spectrum is a result of the non-uniform effective response of the MSP and is corrected for using a procedure that utilizes clear-air returns and the expected near-flatness of the Fizeau spectrometer response to the molecular backscatter spectrum on this scale.

The MSP-only method produces a set of CT coefficients that is more favorable (in terms of the SNR of the final CT corrected ATBs) than the set produced using the combined MSP+RSP system. In fact, the favorability of the MSP coefficients more than compensates for the lower number of counts used in the case of the Mie ATB and almost compensates in the case of the Ray ATB.

94.3 AEL-FM

AEL-FM provides an index that corresponds to the probability of a target being present and identifies clear-air as well as attenuated regions. The product is reported at the native resolution of the input ATBs (about 3 km horizontal resolution). The procedure combines a number of techniques including a hybrid median edge preserving filter (in order to identify "strong" returns) and iterative adaptive Gaussian smoothing (which is targeted toward weaker extended features). AEL-PRO is closely based on A-PRO which is described in more detail in [5] (Fig. 94.2).

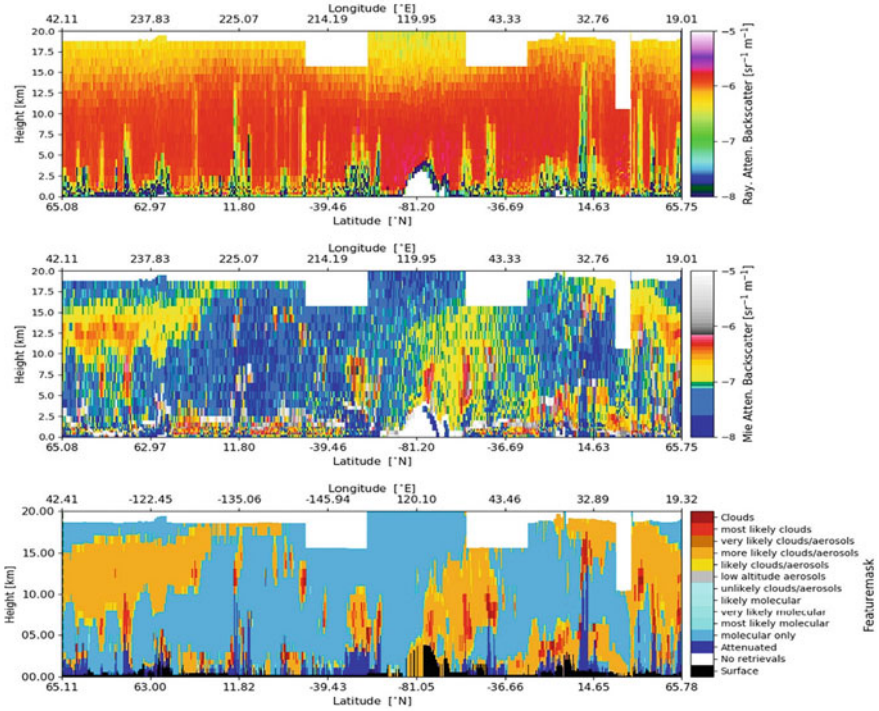


Fig. 94.2 Top: Rayleigh ATB over an orbit. Middle: corresponding Mie ATB. Bottom: corresponding AEL-FM product

94.4 AEL-PRO

AEL-PRO is based mainly on the EBD component of the A-PRO ATLID processor [5]. However, since ALADIN does not measure the depolarization ratio of the backscatter light, the classification aspects of AEL-PRO are very simplified with respect to A-PRO.

Like A-PRO, AEL-PRO uses a two-pass approach to cloud-screening and processing both strong features (e.g., clouds) and weak features (e.g., aerosols). Unlike A-PRO (which uses a somewhat conventional direct strategy to determining the "weak" feature extinction and backscatter fields), AEL-PRO uses the same optimal estimation forward model approach applied to both passes. Pass-1 of the algorithm is at a horizontal resolution of about 90 km, while the Pass-II is at the highest available resolution (about 3 km).

The cost function used in AEL-PRO is

$$\chi^2 = [(Y_i - y_i)]\left[C_{i,j}\right]^{-1}[(Y_i - y_i)]^t + \left[(X_{i_a} - x_{i_a})\right]\left[C_{a,i_a,j_a}\right]^{-1}\left[(X_{i_a} - x_{i,a})\right]^t, \tag{94.1}$$

where **y** is the observation-vector composed of the observed ATBs.

$$\mathbf{y} = \left(ATB_{Mie,1}, ATB_{Mie,2}.....ATB_{Mie,nz}, ATB_{Ray,1}.....ATB_{Ray,nz}\right). \quad (94.2)$$

x is the state vector

$$log(\alpha_1.....\alpha_{nz}, S_1....S_{nz}, Ra_1.....Ra_{nz}, C_{lid}), \quad (94.3)$$

where S is the lidar ratio, C_{lid} is the effective lidar calibration coefficient, and R_a is the effective particle size. $\mathbf{Y}(\mathbf{x})$ is the forward model, and $\mathbf{C}$ and $\mathbf{C_a}$ are the observation and a prior error correlation matrices. The particle sizes are used to account for multiple scattering effects, which for ALADIN, can be non-negligible for, e.g., ice cloud particles [6].

Example results of AEL-PRO applied to AEOLUS data when abundant smoke was present in the lower stratosphere are shown in Fig. 94.3. Looking at the profiles, it can be seen that the AEL-PRO results here are more consistent than the standard L2A product.

94.5 Validation

AEL-FM and AEL-PRO are being validated using different data sets. The work is still at an early stage, and however, ground-based Raman lidars are being used as well as CALIPSO and OMI observations.

94.5.1 Comparison with CALIPSO Observations

ALADIN and CALIPSO orbits do neither match in time nor in space. However, under conditions where extended "homogeneous" features are present (e.g., extended aerosol fields), orbit sections within a few 10s of kilometers and up to a few hours can yield useful comparisons. Such an example comparison between ALADIN and CALIPSO observations is shown in Fig. 94.4. Here, a good correspondence between the cloud and aerosol features between CALIPSO and ALADIN is present. Moreover, there is an impressive matching between the quantitative (Dust) aerosol extinction profiles retrieved via AEL-PRO and CALIPSO.

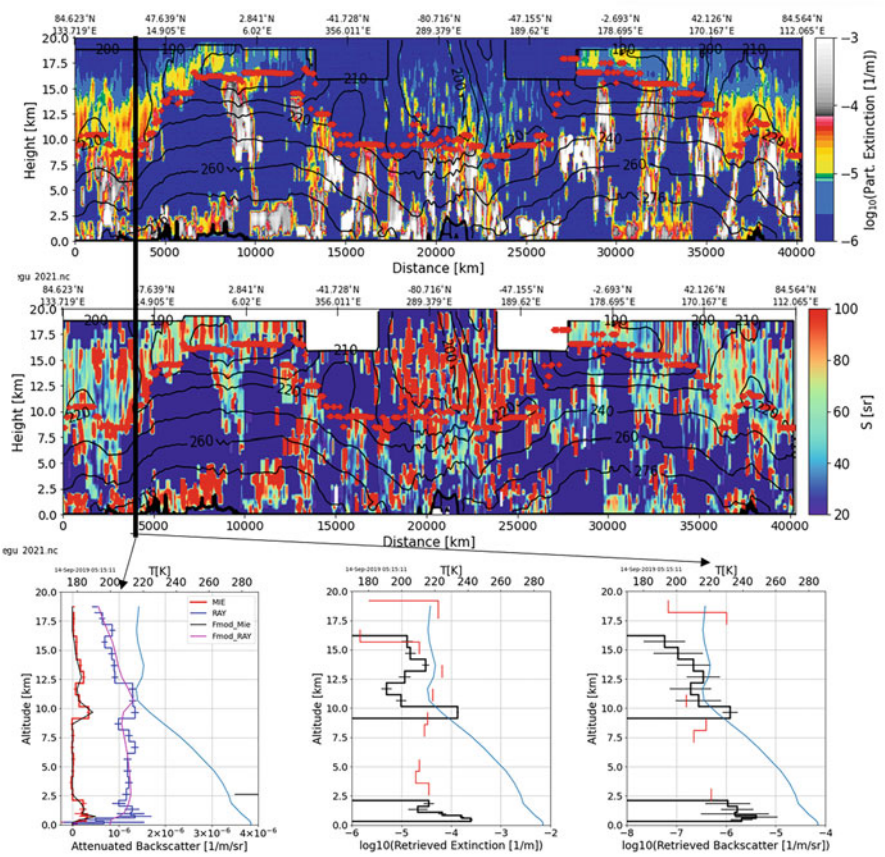


Fig. 94.3 Top: AEL-PRO retrieved extinction corresponding to the same data as shown in Fig. 94.1. The red dots denote the tropopause height. Middle: Corresponding retrieved lidar ratio. The Bottom-Panels show example profiles of the fitted and observed forward-modeled Mie and Ray ATBs as well as the retrieved particulate extinction and backscatter profiles. The thin-Red lines show the corresponding standard L2a SCA product

94.5.2 Comparisons with OMI AOT

In addition to CALIPSO, AOT measured at 354 nm using the OMI instrument onboard Aura [7] has been compared to AEL-PRO results. Example preliminary results are shown in Fig. 94.5, those the sample size is small a notable degree of correlation is present.

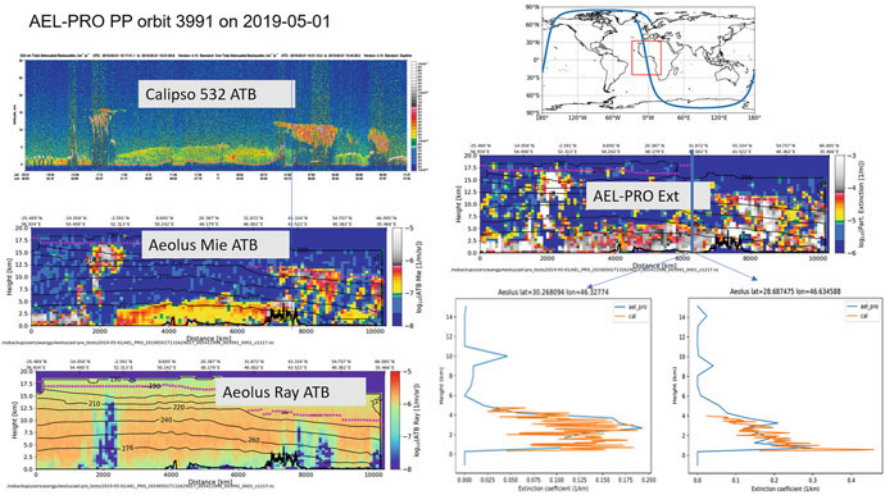


Fig. 94.4 CALIPSO and ALADIN ATBs and extinction retrieval within an orbit section within a few 10s of kilometers and 3.5 hrs on May 01, 2019

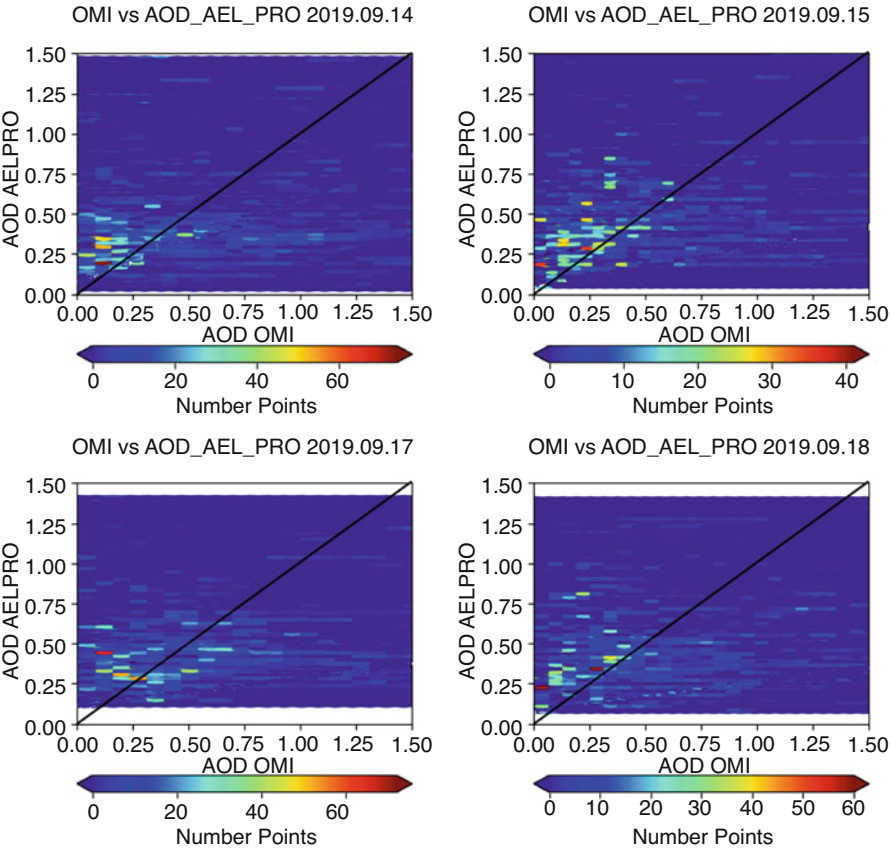


Fig. 94.5 AEL-PRO particulate optical thickness vs OMI UV AOT (over ocean) for a number of days in September 2019

94.6 Summary

At the time of this writing, AEL-FM and AEL-PRO are not yet fully implemented within the Aeolus operational processing chain. However, within the next months, they are planned to become operational.

The validation of the results is at an early stage but is accelerating due to the increasing amount of ground and aircraft-based lidar data available to the Aeolus Cal/Val efforts [8] as well as the use of CALIPSO and OMI observations.

Acknowledgments This work has been conducted under the ESA CARDINAL contract as well as the AEOLUS DISC project.

References

1. European Space Agency: ADM-Aeolus Science Report (2008), ESA SP-1311, 121 pp
2. Illingworth, A., et al.: The EarthCare satellite: The next step forward in global measurements of clouds, aerosols, precipitation and radiation. Bull. Am. Met. Soc. **96**, 1311–1332 (2014)
3. Flament, T., et al.: Aeolus L2A aerosol optical properties product: standard correct algorithm and Mie correct algorithm. Atmos. Meas. Tech. **14**, 7851–7871 (2021). https://doi.org/10.5194/amt-14-7851-2021
4. Novák, O., et al.: Fizeau interferometer system for fast high resolution studies of spectral line shapes. Rev. Sci. Instrum. **82**, 023105 (2011). https://doi.org/10.1063/1.3525102
5. Donovan, D.P, van Zadelhoff, G.-J., Williams, J.E., Wandinger, U., Haarig, M., Qu, Z.: Development of ATLID retrieval algorithms. EPJ Web of Conferences **237**, 01005 (2020). https://doi.org/10.1051/epjconf/202023701005
6. Donovan, D.P., Marseille, G.-J., Kloe, J., Stoffelen, A.: Aeolus L2 Activities at KNMI. EPJ Web of Conferences **237**, 01002 (2020). https://doi.org/10.1051/epjconf/202023701002
7. Torres, O., Ahn, C., Chen, Z.: Improvements to the OMI near-UV aerosol algorithm using A-train CALIOP and AIRS observations. Atmos. Meas. Tech. **6**, 3257–3270 (2013). https://doi.org/10.5194/amt-6-3257-2013
8. Joining forces for Aeolus. https://www.esa.int/Applications/Observing_the_Earth/FutureEO/Aeolus/Joining_forces_for_Aeolus. Last accessed 8th, May, 2022

Part IX
Synergistic Use of Multiple Instruments and Techniques, Networks and Campaigns

Chapter 95
Integrated Mobile System of Two-Wavelength Polarization Micro-pulse Lidar and Photometer for Aerosol Properties Retrievals: Comparisons with Reference Lidar

M. F. Sanchez Barrero, I. Popovici, P. Goloub, S. Victori, L. Proniewski, Q. Hu, T. Podvin, B. Holben, D. Giles, and A. LaRosa

Abstract The CIMEL CE376 micro-pulse lidar providing measurements at 532 and 808 nm and depolarization at 532 nm coupled with sun/moon photometers providing spectral aerosol optical depth (AOD) are integrated for synergetic mobile monitoring of aerosols properties. A first dataset of CE376 lidar-photometer performing on-road measurements was obtained during the FIREX-AQ (Fire Influence on Regional to Global Environments and Air Quality) field campaign deployed in summer 2019 over the Northwestern US. Despite the extreme environmental conditions limited the performance of instruments, we were able to investigate smoke optical properties close to the fire source. Backscatter, extinction profiles, column-integrated lidar ratio (LR) at 532 and 808 nm, in addition to volume

M. F. Sanchez Barrero (✉) · I. Popovici
CNRS, Laboratoire d'Optique Atmosphérique, Université de Lille, Lille, France
e-mail: mariafernanda.sanchezbarrero.etu@univ-lille.fr; m-sanchez@cimel.fr; ioanaelisabeta.popovici@univ-lille.fr; i-popovici@cimel.fr

P. Goloub · Q. Hu · T. Podvin
CNRS, Laboratoire d'Optique Atmosphérique, Université de Lille, Lille, France
e-mail: philippe.goloub@univ-lille.fr; qiaoyun.hu@univ-lille.fr; thierry.podvin@univ-lille.fr

S. Victori · L. Proniewski
CIMEL Electronique, Paris, France
e-mail: s-victori@cimel.fr; l-pronieswki@cimel.fr

B. Holben
Goddard Space Flight Center-NASA, Greenbelt, MD, USA
e-mail: brent.n.holben@nasa.gov

D. Giles · A. LaRosa
Goddard Space Flight Center-NASA, Greenbelt, MD, USA

Science Systems and Applications, Inc., Lanham, MD, USA
e-mail: david.m.giles@nasa.gov; anthony.d.larosa@nasa.gov

© The Author(s), under exclusive license to Springer Nature Switzerland AG 2023

J. T. Sullivan et al. (eds.), *Proceedings of the 30th International Laser Radar Conference*, Springer Atmospheric Sciences,
https://doi.org/10.1007/978-3-031-37818-8_95

linear depolarization ratio (VLDR) profiles at 532 nm, were obtained for a quality assured dataset. Since then, instrumental and algorithmic assessments took place at ATOLL (Atmospheric Observatory of liLLe) platform in Lille, France. METIS, an operational CE376 micro-pulse lidar, continuously performing and co-located with sun/moon photometers and with LILAS high-power multiwavelength lidar, part of EARLINET (European Aerosol Research LIdar NETwork), are considered for test and data validation prior other mobile campaign. Therefore, an event of Saharan dust transported to Lille in March–April 2021 is shown along with comparisons of aerosols retrievals from both METIS and LILAS lidars. Extinction profiles from both lidars are in good agreement, and absolute differences of 0.03 on the VLDR profiles are observed that are mainly related to differences in the optical design of the systems.

Keywords Aerosols · Variability · Lidar · Photometer · Synergy · Mobile measurements

95.1 Introduction

Environmental events such as volcanic eruptions, biomass burning, or desert dust storms inject high aerosols loads into the atmosphere, impacting the radiative balance from local to global scales, with repercussions on climate, human health, and economy. Hence, there is a need of continuous atmospheric monitoring, in addition to the existing interest of a better understanding on the microphysical properties of aerosols to quantify their impact. For these purposes, remote sensing techniques, in particular lidar and photometer, are widely used to assess the optical properties of aerosols suspended in the atmospheric column. The creation of networks like AERONET (AErosol RObotic NETwork) for the photometer and EARLINET for lidars permitted to cover several regions for monitoring local and transported aerosols. Nevertheless, measurements of the ground-based lidar and photometer are limited by their location with respect to the aerosols source and wind patterns. Therefore, the CIMEL CE376 micro-pulse lidar providing measurements at 532 nm and 808 nm and depolarization at 532 nm, coupled with sun/moon photometers providing spectral aerosol optical depth (AOD), were integrated for mobile monitoring of aerosols properties. Measurements of both remote sensing instruments on board mobile platforms offer the capability to study the spatiotemporal variability of aerosols in an extensive range of scenarios, reaching even remote areas.

A first database of collocated CIMEL CE376 lidar photometer on a mobile platform was obtained during the field campaign FIREX-AQ (Fire Influence on Regional to Global Environments and Air Quality) organized over the Northwestern US in summer 2019 [1]. The mobile systems made possible to follow the smoke plumes closer to their source. As a result, height-integrated aerosol optical properties were retrieved for a quality assured dataset. Since then, algorithmic and

instrumental assessment took place at ATOLL (ATmospheric Observatory of liLLe) platform operated by Laboratoire d'Optique Atmosphérique (LOA), University of Lille (50°36′41.2″N 3°08′26.5″E, 60 m a.s.l.) in the frame of AGORA-Lab LOA/CIMEL laboratory [2]. METIS, an operational CE376 lidar, continuously performing and co-located with photometers and with LILAS EARLINET lidar, are considered for test and data validation, prior to other mobile campaigns.

95.2 Mobile Observations During FIREX-AQ Campaign in 2019

During FIREX-AQ field campaign, the remote sensing instruments were installed in the mobile platform called DMU (dragon mobile unit) following the design of MAMS (mobile aerosol monitoring system) described in Popovici et al. [3]. The DMU performed measurements along the roads around the major fire sources as it is illustrated with the two 3D quicklooks in Fig. 95.1. Although the extreme conditions such as high temperatures, topography, and the presence of thick smoke plumes limited the performance of the instruments, we were able to investigate smoke optical properties close to the source. As a result, spectral AOD and Angstrom exponent (AE) spatial distributions were obtained from the photometer. Applying the AOD constrained Klett inversion method in BASIC code [4] on the lidar-photometer filtered dataset, extinction profiles and column-integrated lidar ratio (LR) were also derived. Volume linear depolarization ratio (VLDR) profiles at 532 nm provide qualitative information on the sphericity of aerosols thanks to the depolarization channels at 532 nm were also derived.

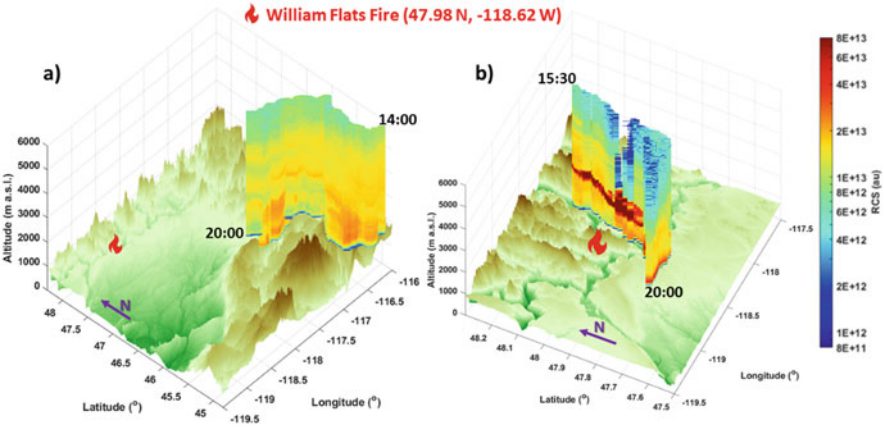


Fig. 95.1 3D Quicklooks of range corrected signal at 532 nm on top of the Digital Elevation Model (DEM SRTM at 30 m resolution) from the studied region during FIREX-AQ field campaign in summer 2019. Mobile observations during William Flats Fire on (**a**) August 4, 2019, and (**b**) August 5, 2019, from the CIMEL CE376 lidar embarked on DMU-1

Previous studies of fresh smoke transported 1 day away from the source reported LR of 60–85 sr for 532 nm [5–7] that are in agreement with the values observed for study cases during the campaign. The VLDR values at 532 nm that we observed were lower (0.02–0.04) in contrast to 0.04–0.06 reported in previous studies [6, 7].

95.3 Continuous Measurements at ATOLL Platform, Lille

Since the FIREX-AQ campaign, instrumental improvements were achieved, especially for the depolarization measurements on the METIS CIMEL CE376 lidar in operation in Lille. For aerosols retrievals, a modified AOD constrained lidar inversion algorithm has been adapted for simultaneous two-wavelength elastic lidar measurements. These algorithmic and instrumental assessments provided us a set of data convenient for validation using as reference LILAS lidar. Study cases are selected for comparisons of aerosol retrievals when both lidars are under similar operation conditions.

95.3.1 Study Case of Saharan Dust Transport

As an example of METIS data validation, we present an event of Saharan dust transported over Lille, France. In Fig. 95.2, we can see the intrusions of lofted dust layers between 1.5 km and 8 km a. s. l., with VLDR values varying from 0.15 up to 0.3. During the dust intrusion, seen on the RCS and VLDR quicklooks on April 1, the AOD values at 532 nm and 808 nm increase up to 1 and 0.9, respectively, and the AE (532/808) decreases from 1.5 to 0.2 confirming the strong presence of coarse mode aerosols.

During the night time of April 1, delimited with red dashed lines on Fig. 95.2, Raman and elastic profiles at 532 nm were measured with LILAS lidar. For intercomparisons of METIS and LILAS, we use averaged profiles between 20:00 and 22:00 UTC. Optical aerosols properties are retrieved with the 2-wavelength inversion for METIS and Raman inversion for LILAS. To constraint the inversions for METIS profiles, we used the AOD values at 2021-04-01 17:50 UTC and 2021-04-02 00:45 UTC. Hence, backscatter and extinction profiles at 532 nm and 808 nm for METIS and at 532 nm for LILAS were retrieved (Fig. 95.3a, b). VLDR and particle linear depolarization ratio (PLDR) at 532 nm for both lidars are also compared (Fig. 95.3c), as well as AE of 532–808 nm from METIS (Fig. 95.3e) are presented.

Backscatter and extinction coefficient profiles intercomparisons show good agreement between both lidars. The differences in extinction observed are related to the constant lidar ratio of 50 sr for METIS retrievals at 532 nm. From the profile of LR at 532 nm for LILAS (Fig. 95.3d), obtained with the Raman inversion, we can see that the first layer between 1.5 and 3 km a.s.l. is 50 sr on average, in contrast

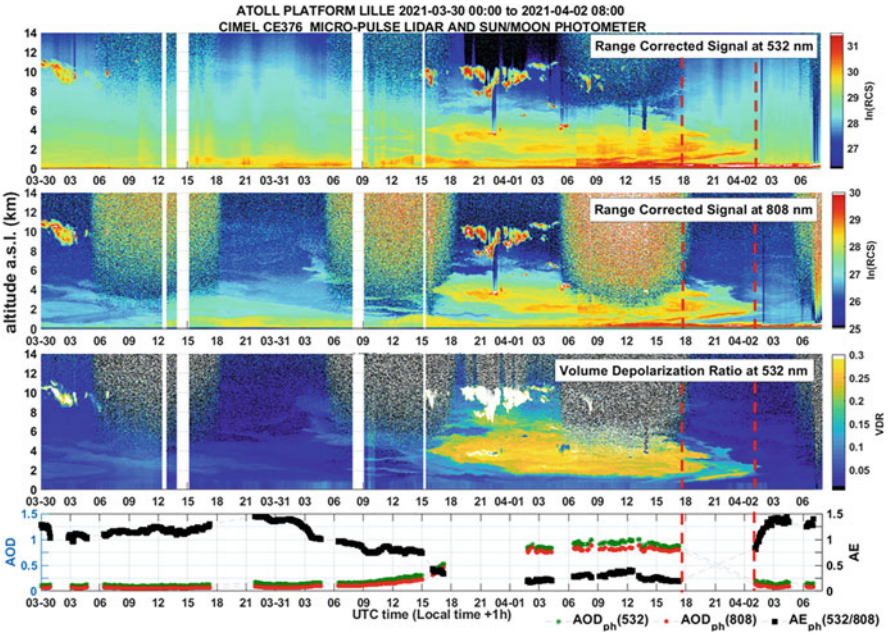


Fig. 95.2 Overview of synergetic measurements of METIS lidar and sun/moon photometers at ATOLL platform, Lille, France, during an event of Saharan dust transport from March 30 to April 2, 2021. From top to bottom: Quicklooks of the logarithm of RCS at 532 nm and 808 nm, quicklook of VLDR at 532 nm retrieved from METIS lidar, and time series of AOD at 532 nm and 808 nm with AE 532/808 derived from the sun/moon photometers. Red dashed lines indicate the time period considered for intercomparison

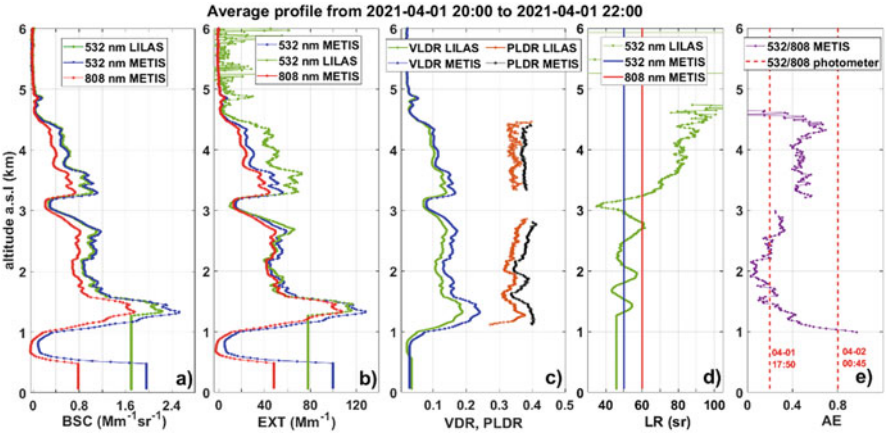


Fig. 95.3 LILAS-METIS intercomparisons of aerosols retrievals for the averaged measurements between 20:00 and 22:00 UTC on 2021-04-01. (**a**) Backscatter coefficient (BSC), (**b**) extinction coefficient (EXT), (**c**) VLDR and PLDR, (**d**) lidar ratio (LR), and (**e**) AE profiles

with 80 sr of the second layer between 3.3 and 4.7 km a.s.l. Thus, we see a better agreement in the lower layer than within the second layer. Absolutes differences of 0.03 on METIS VLDR profile with respect to LILAS are observed, which mainly come from differences on the optical design of the instruments. Nonetheless, both lidars show VLDR, PLDR values within the two layers comparable to those reported in previous works [8, 9] for dust transport. From the derived AE (532/808) profile, lower AE values for the first layer (on average 0.2) were observed compared to 0.47 at the second layer. So we get an indication that we are in the presence of two different air masses, which is also shown in the LR profile from LILAS lidar.

95.4 Conclusions and Perspectives

From the first mobile campaign involving a CIMEL CE376 lidar coupled with photometer, we were able to obtain height integrated optical properties of smoke aerosols at different ageing states, despite the harsh environmental conditions that limited the performance of the instruments. Also, a first assessment of lidar performances and limitations were achieved in the frame of the next CE376 version development.

The results of intercomparison between METIS and LILAS show good agreement when comparing backscatter and extinction profiles at 532 nm, despite the lower SNR (signal-to-noise ratio) on the micro-pulse lidar and the assumption on the lidar ratio for retrievals. VLDR profiles at 532 nm derived from METIS show absolute differences of 0.03 with respect to LILAS. These differences in VLDR profiles might be related to the optical elements in the reception modules of the lidars, requiring a better characterization, especially for the interference filters. For future campaigns of METIS-photometer embarked on mobile vectors, we are positive on obtaining valuable information on aerosols optical properties such as spectral extinction and depolarization in variable scenarios. Further work will include three main directions: (i) uncertainties' assessment, (ii) more elaborated joint retrieval combining spectral AOD and downward sky radiance from CE318T photometer and 2-wavelength CE376 lidar RCS, and (iii) application to data obtained during mobile observations campaigns.

References

1. FIREX-AQ White Paper 2019. Available at www.esrl.noaa.gov/csl/projects/firex-aq/whitepaper.pdf
2. AGORA-Lab Homepage: https://www.agora-lab.fr/
3. Popovici, I.E., Goloub, P., Podvin, T., Blarel, L., Loisil, R., Unga, F., et al.: Description and applications of a mobile system performing on-road aerosol remote sensing and in situ measurements. Atmos. Meas. Tech. **11**(8), 4671–4691 (2018)
4. Mortier, A.: Tendances et variabilités de l'aérosol atmosphérique à l'aide du couplage Lidar/Photomètre sur les sites de Lille et Dakar. Doctoral thesis, University of Lille 1 (2013)

5. Alados-Arboledas, L., Müller, D., Guerrero-Rascado, J.L., Navas-Guzmán, F., Pérez-Ramírez, D., Olmo, F.J.: Optical and microphysical properties of fresh biomass burning aerosol retrieved by Raman lidar, and star-and sun-photometry. Geophys. Res. Lett. **38**, 1 (2011)
6. Tesche, M., Ansmann, A., Müller, D., Althausen, D., Engelmann, R., Freudenthaler, V., Groß, S.: Vertically resolved separation of dust and smoke over Cape Verde using multiwavelength Raman and polarization lidars during Saharan Mineral Dust Experiment 2008. J. Geophys. Res. Atmos. **114**, D13 (2009)
7. Tesche, M., Gross, S., Ansmann, A., Mueller, D., Althausen, D., Freudenthaler, V., Esselborn, M.: Profiling of Saharan dust and biomass-burning smoke with multiwavelength polarization Raman lidar at Cape Verde. Tellus Ser. B Chem. Phys. Meteorol. **63**(4), 649–676 (2011)
8. Ansmann, A., Bösenberg, J., Chaikovsky, A., Comerón, A., Eckhardt, S., Eixmann, R., et al.: Long-range transport of Saharan dust to northern Europe: the 11–16 October 2001 outbreak observed with EARLINET. J. Geophys. Res. Atmos. **108**, D24 (2003)
9. Haarig, M., Ansmann, A., Engelmann, R., Baars, H., Toledano, C., Torres, B., et al.: First triple-wavelength lidar observations of depolarization and extinction-to-backscatter ratios of Saharan dust. Atmos. Chem. Phys. ***22***(1), 355–369 (2022)

Chapter 96
Regional Changes in the Dominant Aerosol Type Over Europe During the ACTRIS COVID-19 Campaign

K. A. Voudouri, D. Nicolae, L. Mona, G. D'Amico, N. Papagiannopoulos, E. Marinou, A. Kampouri, J. Vasilescu, C. Talianu, I. Stachlewska, R. Fortuna, M. Sicard, A. Rodriguez, S. Romano, M. R. Perrone, A. Floutsi, X. Shang, N. Siomos, A. Gialitaki, A. Tsekeri, D. Balis, and V. Amiridis

Abstract The coronavirus (COVID-19) spread around the world lead to the application of restrictions and strict stay-at-home mandates in the majority of the European countries, during the first quarter of 2020. An intensive observation campaign was organized during May 2020 by the European Aerosol Research

K. A. Voudouri (✉) · D. Balis
Laboratory of Atmospheric Physics, Aristotle University of Thessaloniki, Thessaloniki, Greece

D. Nicolae · J. Vasilescu · C. Talianu
National Institute of R&D for Optoelectronics (INOE2000), Magurele, Romania
e-mail: nnicol@inoe.ro; jeni@inoe.ro

L. Mona · G. D'Amico · N. Papagiannopoulos
Consiglio Nazionale delle Ricerche, Istituto di Metodologie per l'Analisi Ambientale, Potenza, Italy
e-mail: lucia.mona@imaa.cnr.it; giuseppe.damico@imaa.cnr.it

E. Marinou · A. Tsekeri · V. Amiridis
National Observatory of Athens ISAARS, Athens, Greece
e-mail: elmarinou@noa.gr; akampouri@noa.gr; togialitaki@noa.gr; atsekeri@noa.gr; vamoir@noa.gr

A. Kampouri
National Observatory of Athens ISAARS, Athens, Greece

Department of Meteorology and Climatology, Aristotle University of Thessaloniki, Thessaloniki, Greece
e-mail: akampouri@noa.gr

I. Stachlewska · R. Fortuna
Faculty of Physics, University of Warsaw, Warsaw, Poland
e-mail: iwona.stachlewska@igf.fuw.edu.pl; Rafal.Fortuna@fuw.edu.pl

© The Author(s), under exclusive license to Springer Nature Switzerland AG 2023

J. T. Sullivan et al. (eds.), *Proceedings of the 30th International Laser Radar Conference*, Springer Atmospheric Sciences,
https://doi.org/10.1007/978-3-031-37818-8_96

Lidar Network (EARLINET), part of ACTRIS (Aerosols, Clouds and Trace Gases Research Infrastructure), to investigate possible aerosol-type changes in the lower troposphere due to the decreased emissions during the COVID-19 lockdown and relaxation period. The current work is part of an extended study related to potential changes in the aerosol load over Europe. The dominant aerosol types are identified with NATALI aerosol classification scheme, applied upon the aerosol lidar-derived intensive products. The aerosol types within January–May 2020 are compared to the aerosol types from the reference period between 2015 and 2019.

Keywords EARLINET · Aerosol typing · Aerosol lidar-derived intensive properties · COVID-19 lockdown

96.1 Instrumentation and Methodology

The 21 participating EARLINET [1] stations (Fig. 96.1) performed measurements at least twice per day (minimum 2 h at noon, and minimum 2 h after sunset) from 1st of May till 31 of May during the COVID-19 campaign. These stations are located in regions where a complete or a partial lockdown was imposed; however in different time periods within 2020. In total, 693 measurements were performed (53%), out of the 1302 scheduled observations. In 27% of the cases, measurements could not be performed due to meteorological conditions (rain/very low clouds). Access to the laboratory and lack of personnel made the measurements impossible in 12% of the cases, whilst only 8% of the measurements could not be performed due to technical issues, or instrument setting and check-ups. For the purposes of the campaign, the

M. Sicard · A. Rodriguez
CommSensLab, Universitat Politècnica de Catalunya, Barcelona, Spain
e-mail: msicard@tsc.upc.edu; alejandro.rodriguez.gomez@upc.edu

S. Romano · M. R. Perrone
Mathematics and Physics Department, University of Salento, Lecce, Italy
e-mail: salvatore.romano@unisalento.it; maria.rita.perrone@le.infn.it

A. Floutsi
Leibniz Institute for Tropospheric Research, Leipzig, Germany
e-mail: floutsi@tropos.de

X. Shang
Finnish Meteorological Institute, Kuopio, Finland
e-mail: xiaoxia.shang@fmi.fi

N. Siomos
Meteorological Institute, Ludwig Maximilian Universität München, LMU, Munich, Germany
e-mail: Nikolaos.Siomos@physik.uni-muenchen.de

A. Gialitaki
Laboratory of Atmospheric Physics, Aristotle University of Thessaloniki, Thessaloniki, Greece

National Observatory of Athens ISAARS, Athens, Greece



Fig. 96.1 Lidar stations participating in the COVID-19 campaign, providing daily measurements of the aerosol profiles: (**a**) in yellow, stations measuring 2 times per day; (**b**) in red, stations providing quasi-continuous observations. In general, no measurements are performed during precipitation and presence of low clouds

measurements were submitted and processed with the Single Calculus Chain (SCC; [2]); the tool developed within EARLINET network, for the automatic analysis of aerosol lidar measurements. SCC delivers, in a fully automatic way, vertical profiles of the aerosol optical properties, starting from the raw data collected by the lidar systems.

In this work, the goal is the identification of the predominant aerosol type during the COVID-19 lockdown and relaxation period, from the combination of the mean-intensive optical parameters within an identified layer in the measured aerosol backscatter (β), extinction coefficient profiles (α), and linear particle depolarization ratio (δ). The intensive properties relevant to the typing study are the extinction-related Ångström exponent (AE), the backscatter-related Ångström exponent (BAE), the ratio of the backscatter coefficients profiles (color ratios – CRs), and the lidar ratio (LR). Nighttime retrievals (Level 2) of the aforementioned datasets served as input for the aerosol typing and characterization scheme of NATALI (Neural Network Aerosol Typing Algorithm Based on Lidar Data [3]). Depending on the nonavailability of the particle linear depolarization ratio from all stations during the reference period and the quality of the provided lidar profiles, the derived typing is made on a low resolution without depolarization ($3\beta + 2a$

configuration). In this low-resolution typing, the following six predominant aerosol types can be provided: continental, continental polluted, smoke, dust, maritime, and volcanic. In what follows, the continental polluted and smoke category were merged to a new category named as pollution. Pollution percentages are then compared with the other aerosol categories.

96.2 Results

In what follows, we separately investigate the polluted aerosols patterns (compared to the other aerosol percentages) in two atmospheric regions: the low troposphere (mainly affected by the human activity, the region between the full overlap and the 3 km; LT) and the free troposphere (layers above 3 km; FT). Figure 96.2 presents the difference of the identified polluted layers per month for whole Europe (January to May) for LT and FT. The aerosol types within January–May 2020 are compared with the aerosol types from the reference period between 2015 and 2019. This period is chosen as a reference one, due to the similar meteorological conditions and air mass sources affecting the stations within 2020.

The analysis denotes a pollution decrease in Europe both in March (start of the restrictions and strict stay-at-home mandates in the majority of the European

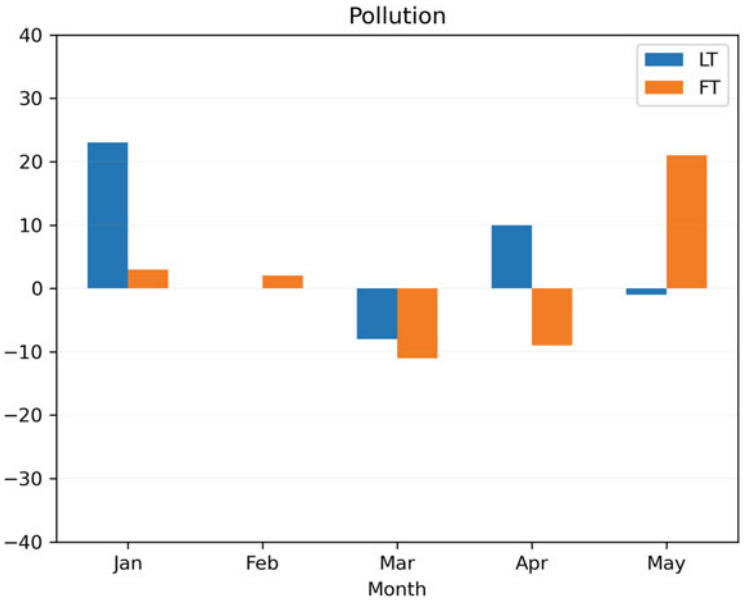


Fig. 96.2 Pollution (continental pollutes + smoke) differences (%) for Europe per month (January to May) for low troposphere (LT) and free troposphere (FT). The reference period is the EARLINET dataset between 2015 and 2019

Table 96.1 Clustering classification of the lidar stations participated in the COVID-19 campaign. Star indicates the stations that participated in the typing retrievals, with a 3b + 2a configuration. Detailed description of the lidar stations is available at EARLINET website

Station	Geographic cluster	Rural/urban environment
Athens*	Mediterranean	Urban
Barcelona*	Mediterranean	Urban
Belsk	East Europe	Urban
Bucharest*	East Europe	Pre-urban
Cabauw*	North Europe	Rural
Clermont-Ferrand	Central Europe	Pre-urban
Evora*	Mediterranean	Pre-urban
Granada*	Mediterranean	Urban
Kuopio*	North Europe	Rural
Lecce	Mediterranean	Pre-urban
Leipzig*	Central Europe	Urban
Lille	Central Europe	Rural
Limassol	Mediterranean	Urban
Hohenpeissenberg*	Central Europe	Rural
Palaiseau	Central Europe	Rural
Potenza*	Mediterranean	Rural
Roma-Tor Vergata	Mediterranean	Rural
Thessaloniki*	Mediterranean	Urban
Warsaw*	East Europe	Urban
Antikythera	Mediterranean	Rural
Belgrade	East Europe	Urban

countries) and May in the LT, while a significant increase is obvious in the FT, mainly attributed to the presence of biomass burning particles.

In what follows, the results are grouped and presented based on (i) predefined regional clusters (i.e., Central Europe, East Europe, North Europe, East Mediterranean, and West Mediterranean), (ii) the aerosol sources affecting each station (i.e., urban, pre- urban, and rural), and (iii) the aerosol layer height (LT and FT), so as to study the spatial variability of the pollution patterns and to strengthen our conclusions on the aerosol changes. Table 96.1 includes the lidar stations and the cluster classification.

96.2.1 Geographical Clustering

First, the pollution patterns are analyzed based on the following predefined regional clusters: (i) Central (CE) and North Europe (NE), (ii) East (EM) and West Mediterranean (WM), and (iii) East Europe (EE). Figure 96.3 (left) presents the results. The clustering analysis denotes a pollution decrease in the LT, starting from

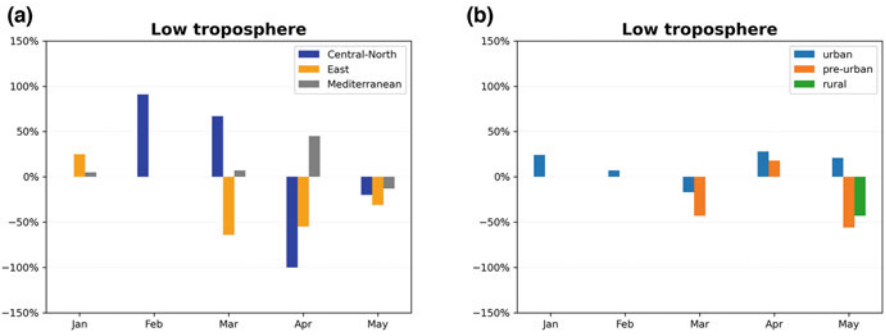


Fig. 96.3 (**a**) Pollution (continental pollutes + smoke) differences (%) for the three European regions (CE + NE, EE, WE + EM) per month and (**b**) pollution (continental pollution + smoke) differences (%) for the urban, rural, and pre-urban stations, per month, for the low troposphere

March, with the highest decrease for Central-North Europe (−100%). From the other hand, enhanced pollution contribution is marked in the Mediterranean region during April, with a percentage of 45%.

96.2.2 Urban and Rural Clustering

An additional analysis is presented, based on the station prevailing atmospheric conditions. The participated stations were clustered in the following three categories: urban, pre-urban, and rural. Figure 96.3 (right) shows the results. A general decreasing pattern is followed, during March and May, while a pollution increase is marked in April for the urban and pre-urban stations.

96.3 Conclusions

The EARLINET community demonstrated its near-real time capability and the coordinated activity during the COVID-19 lockdown and relaxation period, providing comprehensive information on the atmospheric structure. This work is the following work of a general work focused on the differences of the optical and intensive properties of EARLINET products between the climatologically period and 2020. Pollution differences (continental polluted + smoke layers) in Europe per month (January to May) for low and free troposphere shows a decrease in the low troposphere during May (starting from March), but a general increase (after March) in the high troposphere. The geographical clustering analysis also denotes a pollution decrease for all European cluster. Since the restrictive measures were imposed at different time periods within Europe, the effect of the lockdown has

manifested at different times in the different regions. The amplitude is also different in various regions, being related to the intensity of the activity that was affected by the lockdown. Thus, the interpretation of the overall aerosol scene should be made in correlation with meteorological conditions, past observations and models. Further discussion along with the climatological meteorological conditions and the air mass trajectory analysis is made.

Acknowledgments ACTRIS (www.actris.eu) has received funding from the European Union's Horizon 2020 research and innovation program under grant agreement numbers: 654109 (ACTRIS-2), 759530 (ACTRIS-PPP), 871115 (ACTRIS-IMP), and 824068 (ENVRI-FAIR). KAV acknowledges support of this work by the project "PANhellenic infrastructure for Atmospheric Composition and climatE change" (MIS 5021516), which is implemented under the Action "Reinforcement of the Research and Innovation Infrastructure," funded by the Operational Programme "Competitiveness, Entrepreneurship and Innovation" (NSRF 2014-2020) and co-financed by Greece and the European Union (European Regional Development Fund).

References

1. EARLINET homepage: https://www.earlinet.org/index.php?id=covid-19. Last accessed 13 May 2022
2. D'Amico, G., Amodeo, A., Baars, H., Binietoglou, I., Freudenthaler, V., Mattis, I., Wandinger, U., Pappalardo, G.: EARLINET single calculus chain – overview on methodology and strategy. Atmos. Meas. Tech. **8**, 4891–4916 (2015)
3. Nicolae, D., Vasilescu, J., Talianu, C., Binietoglou, I., Nicolae, V., Andrei, S., Antonescu, B.: A neural network aerosol-typing algorithm based on lidar data. Atmos. Chem. Phys. **18**, 14511–14537 (2018). https://doi.org/10.5194/acp-18-14511-2018

Chapter 97
The Role of Dry Layers and Cold Pools in the Activation of Mesoscale Convective Systems: A Characterization Study Based on the Combined Use of Raman Lidar and DIAL Measurements and MESO-NH Model Simulations

Paolo Di Girolamo, Marie-Noelle Bouin, Cyrille Flamant, Donato Summa, Benedetto De Rosa, and Noemi Franco

Abstract As part of the Cevennes-Vivarais site, the University of Basilicata Raman lidar system BASIL was deployed in Candillargues (Cévennes-Vivarais, Southern France Lat: 43°37′ N; Long: 04°04′ E; Elev: 1 m) and operated throughout the duration of HyMeX-SOP 1 (September–November 2012), providing high-resolution and accurate measurements, both in daytime and nighttime, of atmospheric temperature, water vapour mixing ratio and particle backscattering and extinction coefficient at three wavelengths.

Measurements carried out by BASIL on 28–29 September 2012 reveal a water vapour field characterized by a quite complex vertical structure. Reported measurements were run in the time interval between two consecutive heavy precipitation

P. Di Girolamo (✉) · N. Franco
Scuola di Ingegneria, Università della Basilicata, Potenza, Italia
e-mail: paolo.digirolamo@unibas.it

M.-N. Bouin
Météo-France/CNRM, Plouzané, France
e-mail: marie-noelle.bouin@meteo.fr

C. Flamant
LATMOS/IPSL, UPMC Univ. Paris 06 Sorbonne Universités, UVSQ, CNRS, Paris, France
e-mail: cyrille.flamant@latmos.ipsl.fr

D. Summa
IMAA-CNR, Tito Scalo, Potenza, Italia
e-mail: donato.summa@imaa.cnr.it

B. De Rosa
Scuola di Ingegneria, Università della Basilicata, Potenza, Italia

IMAA-CNR, Tito Scalo, Potenza, Italia

© The Author(s), under exclusive license to Springer Nature Switzerland AG 2023

J. T. Sullivan et al. (eds.), *Proceedings of the 30th International Laser Radar Conference*, Springer Atmospheric Sciences,
https://doi.org/10.1007/978-3-031-37818-8_97

events, from 15:30 UTC on 28 September to 03:30 UTC on 29 September 2012. Throughout most of this observation period, lidar measurements reveal the presence of four distinct humidity layers.

This research effort aims at assessing the origin and transport path of the different humidity filaments observed by BASIL on this day. In the research work, we also try to identify the presence of dry layers and cold pools and assess their role in the genesis of the mesoscale convective systems and the heavy precipitation events (HPEs) observed on 28–29 September 2012. Virtual potential temperature and equivalent potential temperature are considered as prognostic variables to identify cold pools, with the considered threshold value for virtual potential temperature and equivalent potential temperature being 23 °C and 52 °C, respectively. The study is based on the combined use of water vapour mixing ratio and temperature profile measurements from BASIL and water vapour mixing ratio profile measurements from the water vapour differential absorption lidar LEANDRE 2, supported by simulations from the mesoscale non-hydrostatic model MESO-NH.

Keywords Dry layers · Cold pools · Mesoscale convective systems · Raman lidar · MESO-NH

97.1 Introduction

Dry layers and cold pools play an important role in the genesis and evolution of mesoscale convective systems and heavy precipitation events (HPEs), especially in autumn in the Northwestern Mediterranean coasts [1]. Convection may be strongly forced by descending dry layers associated with the tropopause folding events and the consequent low-level moist convergence [2]. Very dry layers, with a water vapour mixing ratios less than ~2 g kg^{-1}, descending from the mid-troposphere down to the PBL top, have been found to play a major role in convective initiation and in the maintenance of back-building mesoscale convective systems [3]. The subsidence in the dry layer regions within the tropical troposphere may also suppress convection and lead to overall drying in these regions [4].

In addition to direct orographic forcing by the elevated terrain behind the coasts and the low-level moisture convergence at sea, the formation of a low-level cold pool is another important lifting mechanism favouring deep convection [5]. Cold pools are usually generated by rainfall evaporation in subsaturated air masses at an altitude of 1–2 km above surface level [6, 7].

Prognostic variables typically used to identify cold pools are the virtual potential temperature and the equivalent potential temperature [5]. Virtual potential temperature, directly related to the air masses density, is determined through the expression [6, 7]:

$$\theta_v(z) = T(z)\left(\frac{p_0}{p(z)}\right)^{R/cp}\left(1 - x_{H_2O}(z)\right)$$

with R and c_p being the dry air gas constant and specific heat, respectively, p_0 being the pressure at the surface level, and $p(z)$, $T(z)$ and $x_{\mathrm{H2O}}(z)$ being the pressure, temperature and water vapour mixing ratio at height z, respectively. Equivalent potential temperature, which characterizes the heat and moisture content of the inflow, is also considered as a proxy for cold pools and is given by the expression:

$$\theta_e(z) = T(z)\left(\frac{p_0}{p(z)}\right)^{R/cp} \exp\left(\frac{LW_s\left[T(z),\, p(z)\right]}{c_p T(z)}\right)$$

with L and w_s being the water condensation latent heat and the water vapour saturation mixing ratio, respectively. Threshold values for virtual/equivalent potential temperature are considered. Virtual potential temperature threshold value is taken equal to 23 °C ≈ 296 K, while equivalent potential temperature threshold value is taken equal to 52 °C ≈ 325 K.

97.2 Results

Measurements carried out by BASIL [8–16] in the time period 28–29 September 2012 reveal a water vapour field characterized by a quite complex vertical structure. Figure 97.1 illustrates the time evolution of the water vapour mixing ratio over the 12-h measurement period from 15:32 UTC on 28 September 2012 to 03:33 UTC on 29 September 2012. Throughout most of the observation period, lidar measurements reveal the presence of four distinct humid layers and two dry layers: a surface layer extending up to 0.4–0.8 km a.s.l., with x_{H2O} values up to 6 g kg^{-1}, a filamentary structure, first observed around 17:30 UTC, progressively descending from ~1 km down to ~0.5 km and having a variable vertical extent within the range 100–400 m, with x_{H2O} values up to 7 g kg^{-1}; two upper humid layers: one from ~1.3 to ~2.5 km, with values of x_{H2O} up to 7.5 g kg^{-1} and one located above up to approx. 4 km, with values of x_{H2O} not exceeding 6 g kg^{-1}. Based on the combined use of BASIL observations and MESO-NH & HYSPLIT back-trajectory analysis, we found that the humid air masses feeding the precipitation system originated in the North and Tropical Atlantic (4–5 days earlier) and in the tropical areas in Africa (10 days earlier). These humid air masses were transported in the lower troposphere for 3–4 days to finally subsidence upon reaching the Mediterranean basin 12–40 h before the HPEs.

Raman lidar measurements were run in the time interval between two consecutive heavy precipitation events. Consequently, the characterization of complex water vapour field structures and their genesis is also beneficial for a deeper comprehension of the two HPE events. Figure 97.2 illustrates the time evolution of the range corrected elastic signal at 1064 nm (RCS_{1064}) as measured by the Raman lidar BASIL over the same 12-h measurement period considered in Fig. 97.1. RCS_{1064} is a quantity providing information on the presence and the optical load of

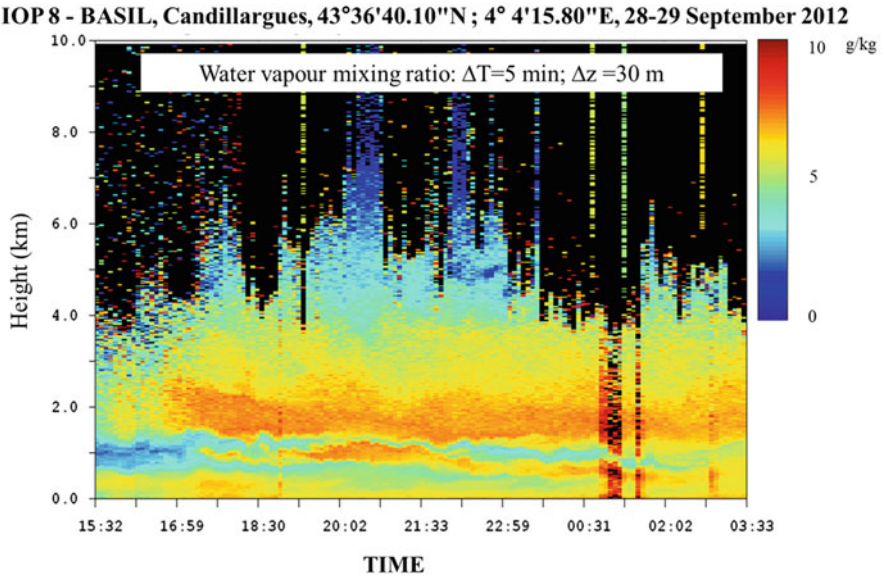


Fig. 97.1 Time evolution of the water vapour mixing ratio as measured by the Raman lidar BASIL over the 12-h measurement period from 15:32 UTC on 28 September 2012 to 03:33 UTC on 29 September 2012

aerosols, clouds and precipitations [9]. Stratiform clouds are present throughout the measurement period (red ellipses). Raman lidar measurements reveal the presence of very light precipitation events at ~16:00 UTC on 28 September 2012 and again in the time intervals 18:30–20:30 UTC and 00:30–03:30 UTC on 29 September 2012 (black ellipses). The figure above reveals the presence of Virga events, with most precipitating particles sublimating before reaching surface (complete sublimation observed only during the first event at 16:00 UTC).

Figure 97.3 illustrates the time evolution of atmospheric temperature as measured by the Raman lidar BASIL over the same 12-h measurement period considered in Figs. 97.1 and 97.2.

The temperature field is an important ingredient to determine the virtual potential temperature field. Figure 97.4 illustrates the time evolution of virtual potential temperature as measured by the Raman lidar BASIL over the same 12-h measurement period considered in Figs. 97.1, 97.2 and 97.3. Virtual potential temperature values smaller than the threshold value of 23 °C are observed for a 2-h interval during the night on 28–29 September 2012. We believe that this cold pool was generated by rainfall evaporation in sub-saturated air masses 1 km above surface level. We also believe that the formation of this low-level cold pool played an important role as lifting mechanism favouring the deep convection events taking place in the forthcoming hours.

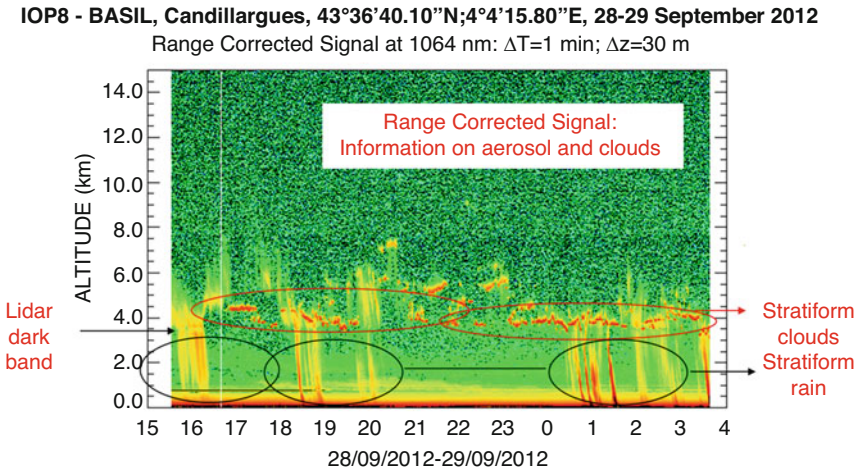


Fig. 97.2 Time evolution of the range corrected elastic signal at 1064 nm as measured by the Raman lidar BASIL over the 12-h measurement period from 15:32 UTC on 28 September 2012 to 03:33 UTC on 29 September 2012

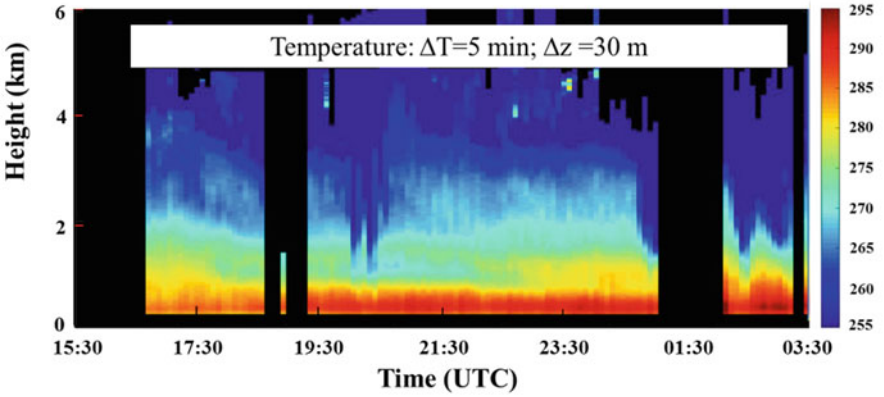


Fig. 97.3 Time evolution of atmospheric temperature as measured by the Raman lidar BASIL over the 12-h measurement period from 15:32 UTC on 28 September 2012 to 03:33 UTC on 29 September 2012

97.3 Conclusions

This research effort demonstrates the capability of water vapour and temperature Raman lidars to identify the presence of dry layers and cold pools and assess their role in the genesis of the mesoscale convective systems and the heavy precipitation events (HPEs).

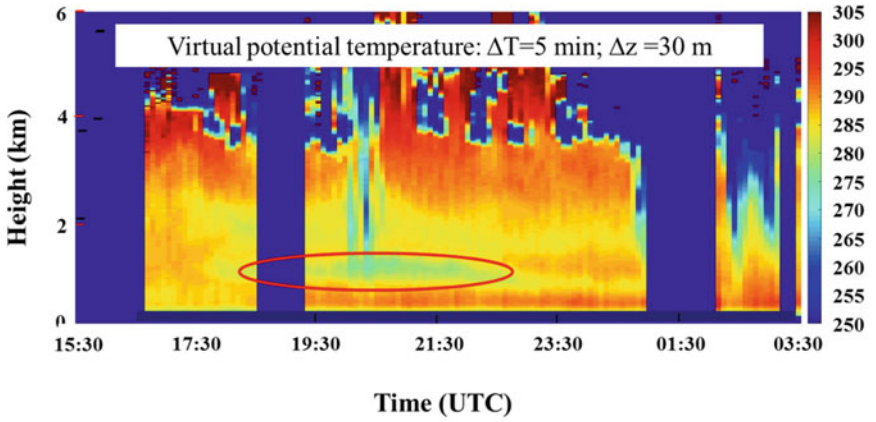


Fig. 97.4 Time evolution of virtual potential temperature as measured by the Raman lidar BASIL over the 12-h measurement period from 15:32 UTC on 28 September 2012 to 03:33 UTC on 29 September 2012

Acknowledgements This research has been supported by the Italian Ministry for Education, University and Research (grants STAC-UP and FISR2019-CONCERNING), and the Italian Space Agency (grants As-ATLAS and CALIGOLA).

References

1. Weckwerth, T.M., Bennett, L.J., Miller, L.J., Van Baelen, J., Di Girolamo, P., Blyth, A.M., Hertneky, T.J.: An observational and modeling study of the processes leading to deep, moist convection in complex terrain. Mon. Weather Rev. **142**, 2687–2708 (2014)
2. Russell, A., Vaughan, G., Norton, E., Ricketts, H., Morcrette, C., Hewison, T., Browning, K., Blyth, A.: Convection forced by a descending dry layer and low-level moist convergence. Tellus. **61A**, 250–263 (2009)
3. Lee, K.-O., Flamant, C., Ducrocq, V., Duffourg, F., Fourrié, N., Davolio, S.: Convective initiation and maintenance processes of two back-building mesoscale convective systems leading to heavy precipitation events in Southern Italy during HyMeX IOP 13. Q. J. R. Meteorol. Soc. **142**(700), 2623–2635 (2016)
4. Randel, W.J., Rivoire, L., Pan, L.L., Honomichl, S.B.: Dry layers in the tropical troposphere observed during CONTRAST and global behavior from GFS analyses. J. Geophys. Res. Atmos. **121**, 14,142–14,158 (2016). https://doi.org/10.1002/2016JD025841
5. Bouin, M.N., et al.: Processes leading to deep convection and sensitivity to sea-state representation during HyMeX IOP8 heavy precipitation event. Q. J. R. Meteorol. Soc. **143**(707), 2600–2615 (2017)
6. Ducrocq, V., Nuissier, O., Ricard, D.: A numerical study of three catastrophic precipitating events over Southern France. Part II: mesoscale triggering and stationarity factors. Q. J. R. Meteorol. Soc. **134**, 131–145 (2008). https://doi.org/10.1002/qj.199
7. Bresson, E., Ducrocq, V., Nuissier, O., Ricard, D., de Saint-Aubin, C.: Idealized numerical study of Southern France heavy precipitating events: identification of favouring ingredients. Q. J. R. Meteorol. Soc. **138**, 1751–1763 (2012)

8. Di Girolamo, P., Marchese, R., Whiteman, D.N., Demoz, B.B.: Rotational Raman lidar measurements of atmospheric temperature in the UV. Geophys. Res. Lett. **31**, L01106 (2004). https://doi.org/10.1029/2003GL018342
9. Di Girolamo, P., Summa, D., Ferretti, R.: Multiparameter Raman lidar measurements for the characterization of a dry stratospheric intrusion event. J. Atmos. Ocean. Technol. **26**, 1742–1762 (2009). https://doi.org/10.1175/2009JTECHA1253.1
10. Di Girolamo, P., Cacciani, M., Summa, D., Scoccione, A., De Rosa, B., Behrendt, A., Wulfmeyer, V.: Characterisation of boundary layer turbulent processes by the Raman lidar BASIL in the frame of HD(CP)2 Observational Prototype Experiment. Atmos. Chem. Phys. **17**, 745–767 (2017). https://doi.org/10.5194/acp-17-745-2017
11. Di Girolamo, P., Gagliardi, R.V., Pappalardo, G., Spinelli, N., Velotta, R., Berardi, V.: Two wavelength lidar analysis of stratospheric aerosol size distribution. J. Aerosol Sci. **26**, 989–1001., ISSN: 0021-8502 (1995). https://doi.org/10.1016/0021-8502(95)00025-8
12. Di Girolamo, P., Scoccione, A., Cacciani, M., Summa, D., De Rosa, B., Schween, J.H.: Clear-air lidar dark band. Atmos. Chem. Phys. **18**(7), 4885–4896 (2018)
13. Di Girolamo, P., De Rosa, B., Flamant, C., Summa, D., Bousquet, O., Chazette, P., Totems, J., Cacciani, M.: Water vapour mixing ratio and temperature inter-comparison results in framework of the hydrological cycle in the Mediterranean experiment – special observation period 1. Bull. Atmos. Ocean. Technol. **1**(2), 113–153 (2020). https://doi.org/10.1007/s42865-020-00008-3
14. Di Girolamo, P., De Rosa, B., Summa, D., Franco, N., Veselovskii, I.: Measurements of aerosol size and microphysical properties: a comparison between Raman lidar and airborne sensors. J. Geophys. Res. Atmos. **127**, e2021JD036086 (2022). https://doi.org/10.1029/2021JD036086
15. Di Girolamo, P., Summa, D., Bhawar, R., Di Iorio, T., Cacciani, M., Veselovskii, I., Dubovik, O., Kolgotin, A.: Raman lidar observations of a Saharan dust outbreak event: Characterization of the dust optical properties and determination of particle size and microphysical Parameters, Atmos. Environ. **50**, 66–78 (2012). https://doi.org/10.1016/j.atmosenv.2011.12.061
16. Di Girolamo, P., Flamant, C., Cacciani, M., Richard, E., Ducrocq, V., Summa, D., Stelitano, D., Fourrié, N., Saïd, F.: Observation of low-level wind reversals in the Gulf of Lion area and their impact on the water vapour variability, Q. J. R. Meteorol. Soc. **142** (Suppl 1): 153–172 (2016). https://doi.org/10.1002/qj.2767

Chapter 98
Advances in Characterizing Pollution Transport with Ground-Based and Airborne Profilers: Case Studies Within Houston, TX

John Sullivan, Johnathan Hair, Taylor Shingler, Richard Ferrare, Marta Fenn, Timothy Berkoff, Guillaume Gronoff, Maurice Roots, Trong Nyugen, Laurence Twigg, James Flynn, Travis Griggs, Paul Walter, Thomas Hanisco, Alexander Kotsakis, Ellsworth J. Welton, and Laura Judd

Abstract Recent advances in field observations relating to quantifying pollution transport from instrument suites operated by NASA and collaborating institutions occurred in September 2021 during TRACER-AQ (website: https://www-air.larc.nasa.gov/missions/tracer-aq/). This study in Houston TX was designed to measure air quality relevant constituents at high-spatial and temporal resolutions, which brought together many of these instrument profiling platforms. This paper will explore and highlight the remotely sensed (both active and passive) and in situ

J. Sullivan (✉) · T. Hanisco · A. Kotsakis · E. J. Welton
NASA Goddard Space Flight Center (GSFC), Greenbelt, MD, USA
e-mail: john.t.sullivan@nasa.gov

J. Hair · T. Shingler · R. Ferrare · M. Fenn · T. Berkoff · L. Judd
NASA Langley Research Center (LaRC), Hampton, VA, USA

G. Gronoff
NASA Langley Research Center (LaRC), Hampton, VA, USA

Science Systems and Applications, Lanham, MD, USA

M. Roots
University of Maryland, Baltimore County (UMBC), Baltimore, MD, USA

T. Nyugen · L. Twigg
NASA Goddard Space Flight Center (GSFC), Greenbelt, MD, USA

Science Systems and Applications, Lanham, MD, USA

J. Flynn · T. Griggs
University of Houston, Houston, TX, USA

P. Walter
St. Edward's University, Austin, TX, USA

© The Author(s), under exclusive license to Springer Nature Switzerland AG 2023

J. T. Sullivan et al. (eds.), *Proceedings of the 30th International Laser Radar Conference*, Springer Atmospheric Sciences,
https://doi.org/10.1007/978-3-031-37818-8_98

profiling capabilities of ground-based platforms such as ozone lidars, aerosol lidars, Pandora spectrometers, and balloons. Airborne profiles will also be emphasized to provide further regional context for the select case study date of September 9, 2021.

Keywords Lidar · Air quality · Ozonesonde

98.1 Introduction to TRACER-AQ

The TRacking Aerosol Convection ExpeRiment – Air Quality (TRACER-AQ) campaign is a field study co-sponsored by NASA and TCEQ (Texas Commission on Environmental Quality) with partners from DOE (Department of Energy) TRacking Aerosol Convection ExpeRiment and several academic institutions. This synergistic effort aimed to gain an updated understanding of the conceptual model of photochemistry and meteorological impact on ozone formation in the Houston region, provide observations for evaluating air quality models and satellite observations, and identify injustices due to air quality in relation to socioeconomic factors. The primary TRACER-AQ field observation period lasted from mid-August to late September 2021.

98.2 Profiling Platforms Used During TRACER-AQ

Individual profiling platforms are described below with an emphasis on highlighting a particularly poor air quality episode on September 9, 2021, suggesting long-range transport, local emission sources, and coastal meteorology all exacerbated pollution levels and poor air quality in the region.

98.2.1 HSRL-2/DIAL

To better understand pollution transport during TRACER-AQ, the NASA Gulfstream-V aircraft instrumented with GCAS (GEOCAPE Airborne Simulator, [1]) for making measurements of column NO_2 and HCHO as well as a lidar system HSRL-2 (high-spectral-resolution Lidar-2, [2]) to measure O_3 and aerosol vertical profiles over the course of 12 flight days. This work focuses on using the O_3 product from the HSRL-2 on September 9, 2021, during the third (*approx.* 19-22 UTC) raster pattern (Fig. 98.1, both panels). Figure 98.1 (left panel) is used to establish the spatial orientation of the aircraft flights and major landmarks/waypoints used in this work: University of Houston (UH), Liberty, La Porte, Galveston Bay, and the Gulf of Mexico.

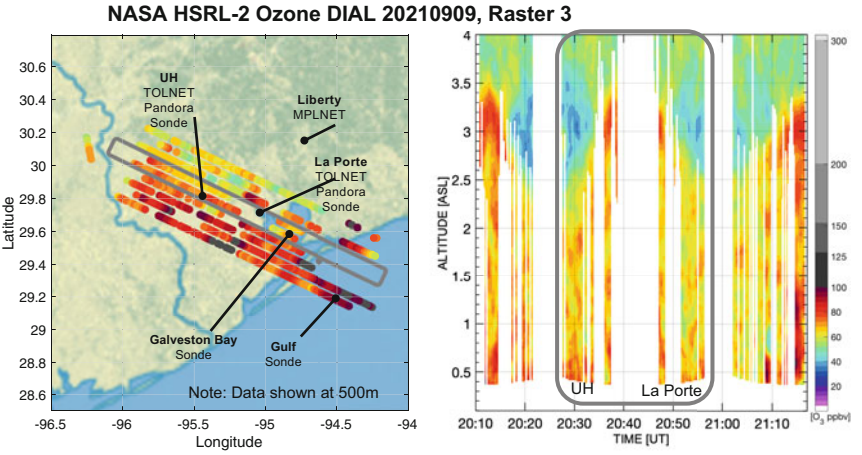


Fig. 98.1 NASA HSRL-2/DIAL O_3 observations from September 9, 2021, showing the O_3 mixing ratios at 500 m (left) for the Houston, TX domain and subset (right) showing the select overpasses

98.2.2 TOLNet and MPLNET

There continues to be a need for tropospheric O_3 and aerosol observations to better understand processes relevant to air quality and pollution transport. To address fundamental science and policy questions relating to O_3, ground-based remote sensing efforts from O_3 and aerosol lidar continue to be a high priority for the regulatory and scientific community. To ensure support of these efforts (especially with current and future geostationary satellites coming online) and to leverage the existing framework of knowledge within the larger atmospheric community, an interagency network initiated by NASA, NOAA, and EPA in 2011 began, known as the Tropospheric O_3 Lidar Network (TOLNet). Previous internetwork comparisons of TOLNet lidars describing accuracy and precision can be found in [3–5].

The NASA Micro-Pulse Lidar Network (MPLNET) [6] is a federated network of Micro-Pulse Lidar (MPL) systems designed to measure aerosol and cloud vertical structure and boundary layer heights. The data are collected continuously, day and night, over long time periods from sites around the world. Most MPLNET sites are co-located with sites in the NASA Aerosol Robotic Network (AERONET). MPLNET is also a contributing network to the World Meteorological Organization (WMO) Global Atmospheric Watch (GAW) Aerosol Lidar Observation Network, GALION.

The NASA LaRC LMOL ([7] UH, Fig. 98.2, top panel), NASA GSFC TOLNet ([8] La Porte, Fig. 98.2, middle panel), and NASA GSFC MPLNET (Liberty, Fig. 98.2, bottom panel) systems were deployed to TRACER-AQ to better quantify the temporal and vertical evolution of O_3 and aerosols. The MPLNET lidar was able to run continuously for the entire campaign, and the TOLNet lidars were

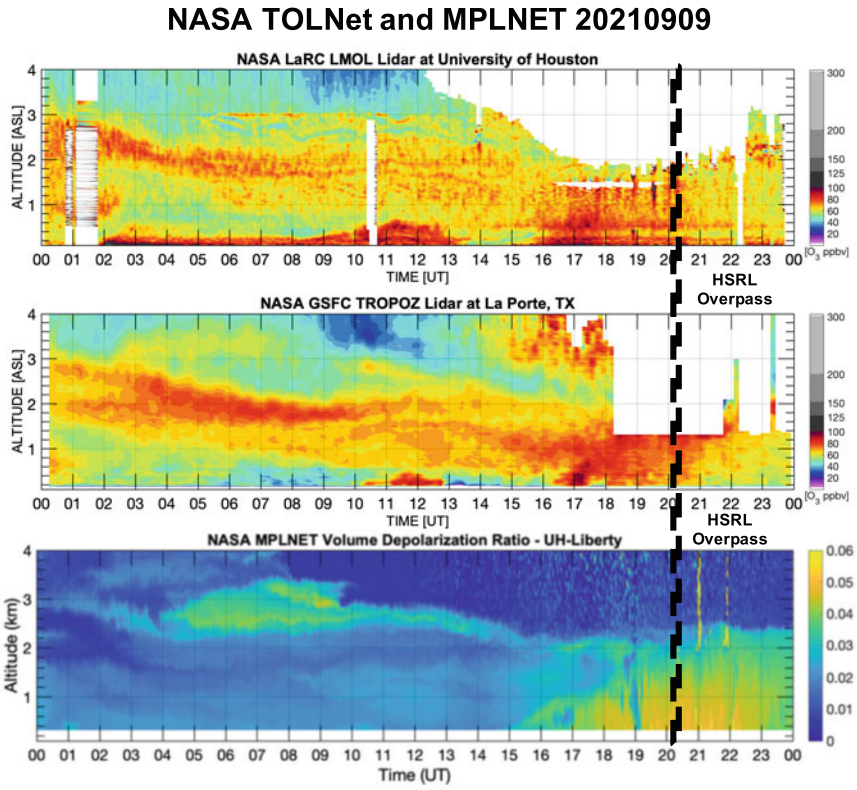


Fig. 98.2 The NASA LaRC LMOL (UH, top), NASA GSFC TOLNet (La Porte, middle), and NASA GSFC MPLNET (Liberty, bottom) systems on September 9, 2021

able to run continuously under certain episodes and to support flight days. This TOLNet/MPLNET hybrid approach at analyzing ozone/aerosol transport in the free troposphere has recently been described in [9].

98.2.3 Pandora Spectrometer

The NASA GSFC Pandora spectrometer system retrieves total-column trace-gas densities utilizing sun-/lunar-viewing and sky-scanning techniques. Validated, near-real-time data products include total-column O_3 and NO_2; however, experimental profiles of NO_2 (Figure 98.3) have also been recently developed using a MAX DOAS approach. Profiles of NO_2, a major ozone precursor, are needed in the profiling community to better understand the sources and transport of pollution events.

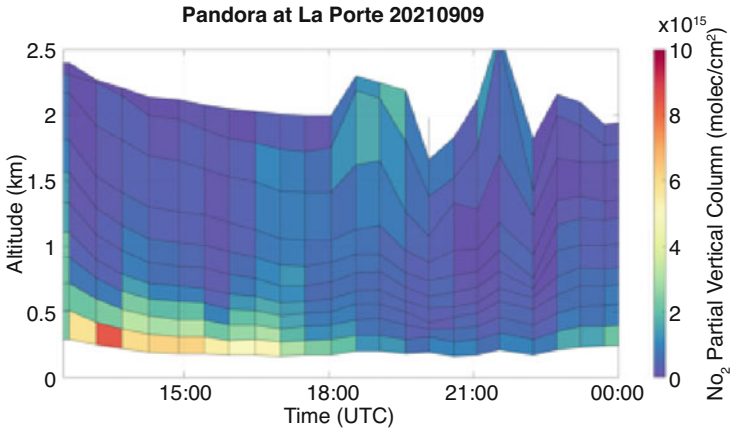


Fig. 98.3 Vertical profiles of NO_2 from the Pandora Spectrometer at La Porte on September 9, 2021

98.2.4 Ozonesondes

During the intensive measurement days of TRACER-AQ, O_3 sondes were deployed to measure profiles during peak pollution episodes in support of air quality forecast verification and aircraft-/ship-based observations. The measurements on September 9, 2021 (Fig. 98.3) show a set of synchronized (20 UTC ±/1 h) sonde launches at the Gulf of Mexico at 19 UTC, Galveston Bay at 20 UTC, UH at 20 UTC, and La Porte at 21 UTC. These times were selected to coincide with the aircraft overpass during raster 3, described in Fig 98.1. To generate these results, all O_3 sondes used processing algorithms with identical vertical resolution and temporal averaging in order to accurately identify processes linked to geophysical and chemical gradients (previously tested in other air quality campaigns, e.g., [10]).

98.3 Discussion

By the afternoon period, HSRL-2 O_3 observations indicate a spatial gradient in O_3 (Fig. 98.1, left panel) that is partially driven by a northerly flow throughout the continental region. This wind flow is corroborated with observations from the O_3 sondes (Fig. 98.4, right panel) and pushed urban emissions toward the southern portion of the Houston, TX region. The highest O_3 sonde sampled levels on this day were from the balloon released from the Gulf of Mexico, reaching nearly 130 ppbv (Fig. 98.4, left panel). However, this sonde was carried through an airmass approaching from the east/southeast and carried more moisture (>60% RH) within

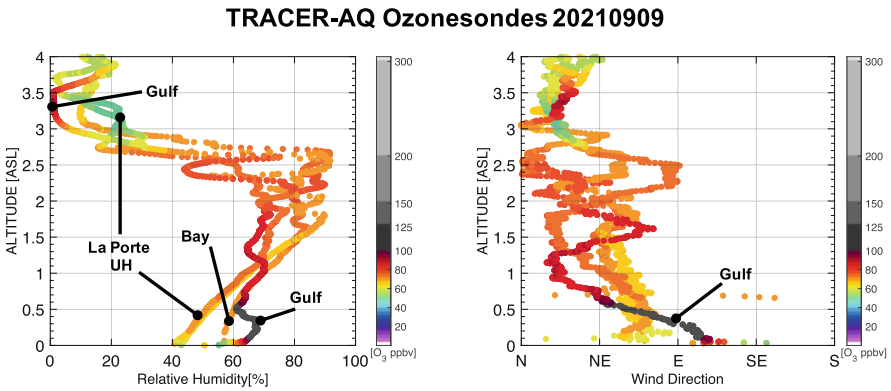


Fig. 98.4 Measurements of relative humidity (left) and wind direction (right) on September 9, 2021 (Fig. 98.3) show a set of synchronized O_3 sonde launches at Gulf of Mexico at 19 UTC, Galveston Bay at 20 UTC, UH at 20 UTC, and La Porte at 21 UTC (colored by O_3 mixing ratio)

several layers, as opposed to the other sondes during this period that were associated with predominantly northeasterly flow and quasi-adiabiatic temperature profiles.

As the convective boundary layer built up on September 9, ozone profiles from the HSRL-2 indicate a deep mixed layer to nearly 3.5 km. The profiles over UH and La Porte indicate the highest ozone values (80–85 ppbv) are observed at the top of the mixed layer, suggesting an additional source of O_3 beyond the photochemical production from surface sources that would likely stay in the first 500 m. This elevated layer was quantified in the 1–3 km region by TOLNet sites at UH and La Porte with an increased O_3 amount of 70–85 ppbv and with a distinctly elevated depolarization ratio (0.04–0.05) in the MPLNET observations at Liberty. This combination of high ozone laminae aloft, coupled with a capping of higher aerosol content, is indicative of long-range transport into the region. Furthermore, the ground-based lidars clearly indicated direct entrainment of these nocturnal O_3 and aerosol layers as the morning convective boundary layer begins to grow between 16 and 18 UT. Similarly, ozone lidars have been able to better understand nocturnal residual layers and their impact on the next day's chemical abundance with examples in [11–13]. We can return to the HSRL observations to more fully realize the vertical profile heterogeneity caused by the confluence of local pollution and long-range transported layers entraining across the domain.

The suite of observations presented in this work has helped to portray a more complete characterization of the overall O_3 pooling in the southern portion of the Houston, TX domain on September 9, 2021. Conceptually, observations indicate urban emissions were swept out over the water and were met with an eastward/southeastward air mass that acted as a blocking mechanism, fostering rapid O_3 production in the presence of low cloud cover and favorable photochemical conditions, which led to ozone levels above the 8-hr ozone standard at monitoring site southwest of Houston.

98.4 Conclusion

Using this synergistic suite of profiling observations, we have shown novel and unseen perspectives in the spatial and temporal distribution of the key photochemical species and atmospheric structure information, particularly with a focus on the temporal evolution of observations throughout the daytime in preparation for upcoming geostationary air quality observations.

References

1. Judd, L.M., Al-Saadi, J.A., Szykman, J.J., Valin, L.C., Janz, S.J., Kowalewski, M.G., Eskes, H.J., et al.: Evaluating Sentinel-5P TROPOMI tropospheric NO2 column densities with airborne and Pandora spectrometers near New York City and Long Island Sound. Atmos. Measur. Tech. **13**(11), 6113–6140 (2020)
2. Burton, S.P., Hostetler, C.A., Cook, A.L., Hair, J.W., Seaman, S.T., Scola, S., Harper, D.B., Smith, J.A., Fenn, M.A., Ferrare, R.A., Saide, P.E.: Calibration of a high spectral resolution lidar using a Michelson interferometer, with data examples from ORACLES. Appl. Opt. ***57***(21), 6061–6075 (2018)
3. Sullivan, J.T., McGee, T.J., DeYoung, R., Twigg, L.W., Sumnicht, G.K., Pliutau, D., Knepp, T., Carrion, W.: Results from the NASA GSFC and LaRC ozone lidar intercomparison: New mobile tools for atmospheric research. J. Atmos. Ocean. Technol. **32**(10), 1779–1795 (2015)
4. Leblanc, T., Brewer, M.A., Wang, P.S., Granados-Muñoz, M.J., Strawbridge, K.B., Travis, M., Firanski, B., et al.: Validation of the TOLNet lidars: the Southern California Ozone Observation Project (SCOOP). Atmos. Measur. Tech. **11**(11), 6137–6162 (2018)
5. Wang, L., Newchurch, M.J., Alvarez II, R.J., Berkoff, T.A., Brown, S.S., Carrion, W., De Young, R.J., et al.: Quantifying TOLNet ozone lidar accuracy during the 2014 DISCOVER-AQ and FRAPPÉ campaigns. Atmos. Measur. Tech. **10**(10), 3865–3876 (2017)
6. Welton, E.J., Stewart, S.A., Lewis, J.R., Belcher, L.R., Campbell, J.R., Lolli, S.: Status of the NASA Micro Pulse Lidar Network (MPLNET): overview of the network and future plans, new version 3 data products, and the polarized MPL. In: EPJ Web of Conferences, vol. 176, p. 09003. EDP Sciences (2018)
7. Gronoff, G., Robinson, J., Berkoff, T., Swap, R., Farris, B., Schroeder, J., Halliday, H.S., et al.: A method for quantifying near range point source induced O3 titration events using Co-located Lidar and Pandora measurements. Atmos. Environ. **204**, 43–52 (2019)
8. Sullivan, J.T., McGee, T.J., Sumnicht, G.K., Twigg, L.W., Hoff, R.M.: A mobile differential absorption lidar to measure sub-hourly fluctuation of tropospheric ozone profiles in the Baltimore–Washington, DC region. Atmos. Measur. Tech. **7**(10), 3529–3548 (2014)
9. Gronoff, G., Berkoff, T., Knowland, K.E., Lei, L., Shook, M., Fabbri, B., Carrion, W., Langford, A.O.: Case study of stratospheric intrusion above Hampton, Virginia: Lidar-observation and modeling analysis. Atmos. Environ. **259**, 118498 (2021)
10. Sullivan, J.T., Berkoff, T., Gronoff, G., Knepp, T., Pippin, M., Allen, D., Twigg, L., et al.: The ozone water–land environmental transition study: an innovative strategy for understanding Chesapeake Bay pollution events. Bull. Am. Meteorol. Soc. **100**(2), 291–306 (2019)
11. Dreessen, J., Sullivan, J., Delgado, R.: Observations and impacts of transported Canadian wildfire smoke on ozone and aerosol air quality in the Maryland region on June 9–12, 2015. J. Air Waste Manage. Assoc. **66**(9), 842–862 (2016)

12. Sullivan, J.T., Rabenhorst, S.D., Dreessen, J., McGee, T.J., Delgado, R., Twigg, L., Sumnicht, G.: Lidar observations revealing transport of O3 in the presence of a nocturnal low-level jet: regional implications for "next-day" pollution. Atmos. Environ. **158**, 160–171 (2017)
13. Kotsakis, A., Sullivan, J.T., Hanisco, T.F., Swap, R.J., Caicedo, V., Berkoff, T.A., Gronoff, G., et al.: Sensitivity of total column NO2 at a marine site within the Chesapeake Bay during OWLETS-2. Atmos. Environ. **277**, 119063 (2022)

Chapter 99
First Results of Inverted Aerosol Properties Through GRASP Algorithm, Using Polarized Data from the Multiwavelength Sun-Sky-Lunar Photometer in Barcelona, Spain

D. C. F. S. Oliveira, A. Rodriguéz-Gomez, A. Comerón, C. Muñoz-Porcar, O. Dubovik, A. Lopatin, M. E. Herrera, and M. Sicard

Abstract This work aims to assess some aerosol properties retrieved by GRASP algorithm whose inputs are degree of linear polarization (DOLP), radiances and aerosol optical depth (AOD) from new photometer at 7λ (level 1.5, version 3) and range-corrected signal (RCS) from lidar system at 3λ in the Universitat Politècnica de Catalunya (UPC). The volume size distribution (VSD), real/imaginary part of the refractive index (RRI and IRI) present accentuated under overestimations at shorter wavelengths in non-polarized configurations for a dust case while the polarized

D. C. F. S. Oliveira (✉) · A. Rodriguéz-Gomez · A. Comerón · C. Muñoz-Porcar
CommSensLab, Department of Signal Theory and Communications, Universitat Politècnica de Catalunya (UPC), Barcelona, Spain
e-mail: daniel.camilo.fortunato@upc.edu; alejandro.rodriguez.gomez@upc.edu; comeron@tsc.upc.edu; constantino.munoz@upc.edu; michael.sicard@upc.edu

O. Dubovik · A. Lopatin · M. E. Herrera
GRASP-SAS, Generalized Retrieval of Aerosol and Surface Properties, Bachy, France
e-mail: oleg.Dubovik@univ-lille.fr; anton.lopatin@grasp-sas.com; milagros.herrera@grasp-sas.com

M. Sicard
CommSensLab, Department of Signal Theory and Communications, Universitat Politècnica de Catalunya (UPC), Barcelona, Spain

Ciències i Tecnologies de l'Espai-Centre de Recerca de l'Aeronàutica i de l'Espai/Institut d'Estudis Espacials de Catalunya (CTE-CRAE/IEEC), Universitat Politècnica de Catalunya (UPC), Barcelona, Spain
e-mail: michael.sicard@upc.edu

© The Author(s), under exclusive license to Springer Nature Switzerland AG 2023

J. T. Sullivan et al. (eds.), *Proceedings of the 30th International Laser Radar Conference*, Springer Atmospheric Sciences,
https://doi.org/10.1007/978-3-031-37818-8_99

configurations improve the coarse mode of VSD and the underestimations in RRI. The vertical distribution of volume concentration (VC) and backscatter profiles identify an aerosol layer between 3 and 4 km in which there is presence of small particles according to fine VC profiles and backscatter profile at 355 nm. The polarized data demonstrated improvements in the retrieved properties by GRASP algorithm.

Keywords Polarization · Photometer · Lidar · GRASP

99.1 Introduction

In recent decades, studies involving optical and microphysical properties of aerosols retrieved from polarized data have increased due to the ability of modern instruments to measure light polarization effects related to the shape of particles [1], improving aerosol characterization [2, 3]. In addition, generalized retrieval of atmosphere and surface properties (GRASP) algorithm [4] is a powerful tool to retrieve aerosol properties, radiative forcing, reflectance and surface data through data synergy between photometer and lidar system. By this means, polarized data can be an input for this algorithm.

In virtue of this potential synergy, the goal of the current study is to assess the retrieved aerosol properties from GRASP algorithm using the polarized and non-polarized data from the new Sun-sky-lunar photometer. This work is structured as follows: the instruments, the data and the input configurations are presented in Sect. 99.2; the main results are shown and discussed in Sect. 99.3; lastly, Sect. 99.4 concludes and gives future perspectives on the initial steps of this pioneering study.

99.2 Material and Methods

99.2.1 Ground-Based Remote Sensing

The fundamental data for this study was from the new AERONET Sun-sky-lunar multispectral photometer (CE318-TP9) [5] and from an ACTRIS/EARLINET multi-wavelength lidar system ($3\beta + 2\alpha + 2\delta + 1$WV). Both instruments are placed at the UPC, Barcelona, Spain. The new photometer includes wavelengths from 340 to 1640 nm and also provides polarized data [2, 3, 6] at level 1.5 (cloud screening criterion) of the Version 3 [7]. The current lidar system [8] provides three elastic channels (355, 532, 1064 nm) that were processed by single calculus chain (SCC)

Table 99.1 Synergy configurations for daytime

Period	Notation	Inputs
Daytime	D0	R + AOD (4λ)
	PD0	R + AOD + DOLP (4λ)
	D1	R + AOD (7λ)
	PD1	R + AOD + DOLP (7λ)
	D2	R + AOD (4λ) +3 RCS
	D3	R + AOD (7λ) +3 RCS

R indicates radiances, D indicates the daytime measurements and P indicates the polarized

tool for the automatic analysis of lidar measurements [9] according to the GRASP algorithm requirements for the RCS.

99.2.2 Data Preparation

The case presented in this study is a dust event of 11 February 2022 (aerosol load = 0.40 and Ångstrom Exponent = 0.5). The DOLP and radiances were taken by the almucantar sky scan that were symmetrically checked and normalized. Additionally, the DOLP, which is provided by AERONET [6], is computed by the three Stokes elements (I, Q and U) by DOLP $= \sqrt{Q^2 + U^2}/I$, where Q and U express the magnitude and direction of linear polarization and I is the total reflectance calculated by the radiances observed in the photometer channels with a linear polarizer oriented at 0°, 120° and 240° (P_1, P_2 and P_3) [6] as follows:

$$\begin{bmatrix} I \\ Q \\ U \end{bmatrix} = \begin{bmatrix} \frac{2}{3}(P_1 + P_2 + P_3) \\ \frac{2}{3}(2P_1 - P_2 - P_3) \\ \frac{2}{\sqrt{3}}(P_3 - P_2) \end{bmatrix} \tag{99.1}$$

99.2.3 Data Synergy

The data synergy was inverted by GRASP algorithm with its inversion mode and single-pixel setting, in which AOD, radiances (R), DOLP and RCS are the inputs to retrieve some aerosol properties during daytime, e.g. VSD, RRI, IRI and VC. To retrieve these properties, some daytime configurations (D) were established, making this study a pioneer for some configurations, e.g. polarized Sun photometer (P) plus lidar system (3 RCS). Table 99.1 shows the configurations and their respective input data for this work.

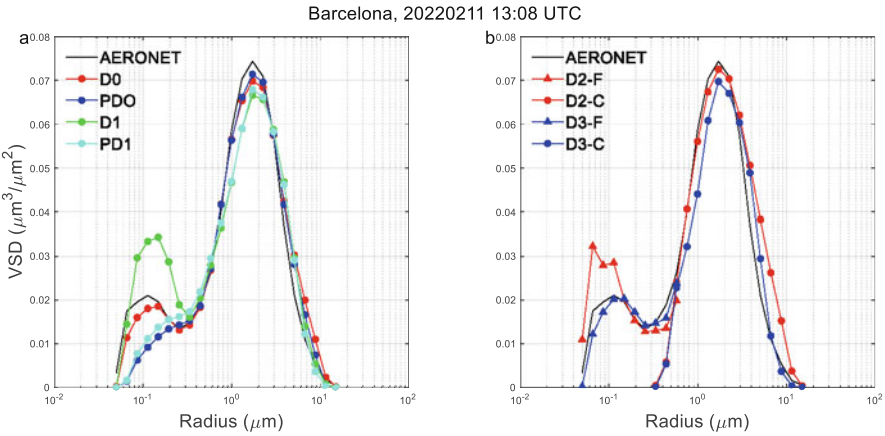


Fig. 99.1 Volume size distribution retrieved by AERONET in black line and GRASP algorithm in colorful lines on 11 February 2022. (**a**) Inversions with photometer (D0, PD0, D1 and PD1) and (**b**) inversions with photometer + UPC lidar system (D2 and D3). F is fine mode and C is coarse mode

99.3 Results and Discussion

99.3.1 D0, PD0, D1 and PD1 Configurations

Figures 99.1 and 99.2 show the retrieved aerosol columnar microphysical properties by GRASP algorithm with D0, PD0, D1, PD1, D2 and D3 configurations in comparison with AERONET inversions (VSD, IRI and RRI). Figure 99.1b displays the retrievals from D2 and D3 configurations, in which coarse mode is dominant (~0.07 $\mu m^3/\mu m^2$). D0 and D3 have a better agreement with the fine mode of the AERONET VSD, whereas D1 and D2 overestimate it in the fine mode, probably a consequence of the sensitivity of short wavelengths in these configurations. PD0 and PD1 slightly increase VSD in coarse mode compared to D0 and D1, whereas the fine mode is underestimated by them. These polarization changes were also observed by [2, 3] in China and Dakar (Senegal) for desert dust events, respectively. Noticeable shifts are visible in higher radii when D2 and D3 configurations are used. Some studies [10–12] observed a similar shift, and they attributed it to the influence of the lidar at scattering angles of 180° that contributes to the size distribution in the coarse mode for the configuration (D2) during dust events [10–12] in Minsk (Belarus), in Granada/Cerro Poyos (Spain) and in Finokalia (Greece), respectively.

At shorter wavelengths, the IRI from GRASP algorithm ranges from 0.005 to 0.012 and overestimates AERONET inversion for all configurations (in Fig. 99.2a) with sharp peaks at 500 nm (D1 and PD1) and at 870 nm (D0 and PD0). The differences between PD0 and D0 and PD1 and D1 are non-significant and can be disregarded [3]. Coarse mode in D2 and D3 overestimates the AERONET inversion at all wavelengths (Fig. 99.2b). Ref. [10] found a similar result for the coarse mode

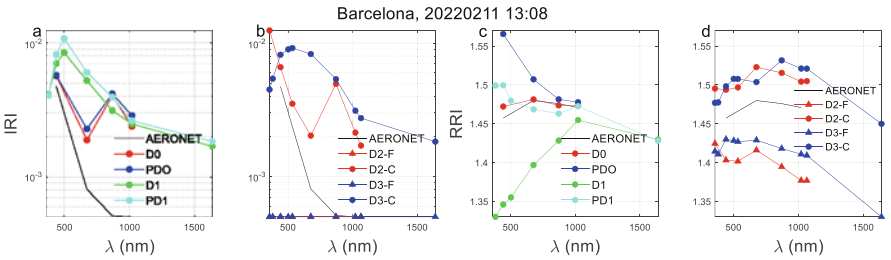


Fig. 99.2 Imaginary (**a**, **b**) and real (**c**, **d**) indexes on 11 February 2022. AERONET inversion is in black line and GRASP inversions are in colorful lines for photometer (D0, PD0, D1 and PD1) and photometer + UPC lidar system configurations (D2 and D3). F is fine mode and C is coarse mode

of the D2 configuration. However, the values of fine IRI remain almost constant, underestimating the IRI from AERONET. A rather low spectral dependence was observed by [11] as well in fine mode and D2 configuration. The RRI from GRASP varies from 1.33 to 1.57, with higher values at shorter wavelengths for D0, PDO and PD1 (Fig. 99.2c) and overestimating the AERONET inversion also at shorter wavelengths. This behaviour for PD0 is in accordance with [3] measured in Dakar, Senegal (2011–2012) during a dust event. Moreover, D1 underestimates the AERONET inversion at shorter wavelengths, but is corrected by PD1. Fine modes of D2 and D3 underestimate while the coarse modes overestimate the RRI from AERONET inversion. These last results agree with [10] for D2 configuration during dust events in Minsk, Belarus.

99.3.2 D2 and D3 Configurations

Figure 99.3a–e shows the VC profiles (a and b) followed by backscatter profiles calculated by GRASP outputs in comparison with SCC (c–e) in the range 0.2–6 km asl for a dust event on 11 February 2022. All profiles in the Fig. 99.3a–e identify an aerosol layer between 3 and 4 km even the fine mode of the VC (Fig. 99.3a), which means that there is a considerable presence of small aerosols within the identified layer. In Fig. 99.3a, the averages inside the layer are 0.28/0.37 $\mu m^3/cm^2$ (D2/D3). Profiles also show a considerable aerosol layer below 1 km (0.37/0.36 $\mu m^3/cm^2$ – average concentration). The coarse VC profiles show a good agreement between D2 and D3 (Fig. 99.3b) with maximum values of 0.33/0.36 $\mu m^3/cm^2$ (D2/D3). The aerosol backscatter profiles have better agreement to the SCC profiles at 1064 and 532 nm in the aerosol layer between 3 and 4 km (Fig. 99.3d, e). Furthermore, the aerosol backscatter profile at 355 nm also exhibits a layer below 1 km (Fig. 99.3c). Once again, the smaller particles contribution is evident in the GRASP retrievals. Meanwhile, D2 and D3 overestimate the SCC backscatter in the ultraviolet channel, and D2 and D3 underestimate the SCC profile in visible

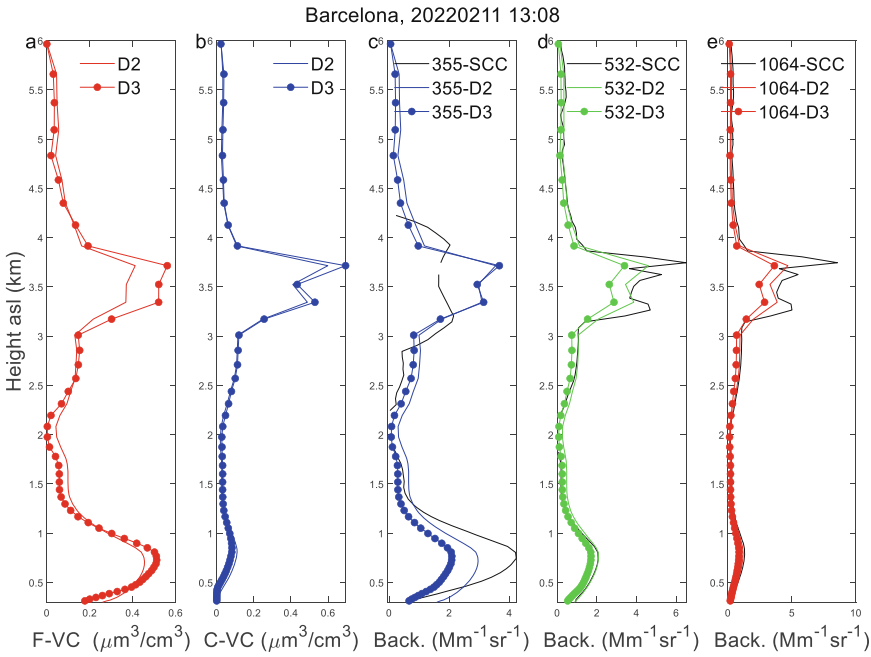


Fig. 99.3 The VC (**a**, **b**) and aerosol backscatter (**c**–**e**) profiles retrieved by GRASP algorithm for D2 and D3 configurations on 11 February 2022. SCC backscatter profiles are in black solid line (**c**–**e**) and GRASP profiles are in colourful lines. F and C indicate fine and coarse modes

and infrared channels (Fig. 99.3d, e). D3 has the lowest average value within the dust layer compared to the D2 at 532 nm (2.0 $Mm^{-1}sr^{-1}$/2.67 $Mm^{-1}sr^{-1}$) and D2 at 1064 nm (1.95 $Mm^{-1}sr^{-1}$/2.61 $Mm^{-1}sr^{-1}$), D3/D2, respectively. This underestimation caused by GRASP in the aerosol backscatter profiles was reported by [11, 12] at 532 nm and by [11] at 1064 nm within dust layers in Granada and Cerro Poyos, Spain [11] and in Finokalia, Greece [12].

99.4 Conclusions and Outlook

For the first time, GRASP algorithm has demonstrated its ability to perform different inversions based on the measurements from new multiwavelength Sun-sky-lunar photometer with polarization data in the new input configurations: R + AOD at 7λ (D1), R + AOD + DOLP at 7λ (PD1) and R + AOD at 7λ +3β (D3). The observations were performed in a dust event in Barcelona, Spain, on 11 February 2022. Using polarized data (PD0 and PD1) as GRASP input showed improvements on the coarse mode of the volume size distribution and the real part of refractive

index. The new photometer wavelengths (380, 500 and 1640 nm) and lidar system channels (355, 532 and 1064 nm) added to the basic configuration (D0) could explain the differences of the retrieved properties in the ultraviolet region which was related to the presence of small particles in this study, inside the layer between 3 and 4 km and below 1 km.

The future works will concern the evaluation of other aerosol properties like single scattering albedo, sphere fraction and others, with the configurations already presented (D0, PD0, D1, PD1, D2 and D3) and adding the DOLP in D2 and D3. Errors and residuals will be evaluated as well to reinforce the improvements by polarized data. Furthermore, new input configuration for GRASP algorithm can be introduced with UPC lidar system and Sun-sky-lunar photometer.

References

1. Emde, C., Buras, R., et al.: The impact of aerosols on polarized sky radiance: model development, validation, and applications. Atmos. Chem. Phys. **10**, 383–396 (2010)
2. Li, Z., Goloub, P., Dubovik, O., et al.: Improvements for ground-based remote sensing of atmospheric aerosol properties by additional polarimetric measurements. J. Quant. Spectrosc. Radiat. Transf. **110**, 1954–1961 (2009)
3. Fedarenka, A., Dubovik, O., et al.: Utilization of AERONET polarimetric measurements for improving retrieval of aerosol microphysics: GSFC, Beijing and Dakar data analysis. J. Quant. Spectrosc. Radiat. Transf. **179**, 72–97 (2016)
4. Dubovik, O., Herman, M., et al.: Statistically optimized inversion algorithm for enhanced retrieval of aerosol properties from spectral multi-angle polarimetric satellite observations. Atmos. Meas. Tech. **4**, 975–1018 (2011)
5. Barreto, Á., Cuevas, E., et al.: The new sun-sky-lunar Cimel CE318-T multiband photometer – a comprehensive performance evaluation. Atmos. Meas. Tech. **9**, 631–654 (2016)
6. Knobelspiesse, K., van Diedenhoven, B., et al.: Cloud thermodynamic phase detection with polarimetrically sensitive passive sky radiometers. Atmos. Meas. Tech. **8**, 1537–1554 (2015)
7. Giles, D.M., Sinyuk, A., et al.: Advancements in the Aerosol Robotic Network (AERONET) Version 3 database – automated near-real-time quality control algorithm with improved cloud screening for Sun photometer aerosol optical depth (AOD) measurements. Atmos. Meas. Tech. **12**, 169–209 (2019)
8. Zenteno-Hernández, J.A., Comerón, A., et al.: A comparative analysis of aerosol optical coefficients and their associated errors retrieved from pure-rotational and vibro-rotational Raman lidar signals. Sensors. **21**, 1277 (2021)
9. D'Amicol, G., Amodeo, A., et al.: EARLINET single calculus chain – overview on methodology and strategy. Atmos. Meas. Tech. **8**, 4891–4916 (2015)
10. Lopatin, A., Dubovik, O., et al.: Enhancement of aerosol characterization using synergy of lidar and sun-photometer coincident observations: the GARRLiC algorithm. Atmos. Meas. Tech. **6**, 2065–2088 (2013)
11. Benavent-Oltra, J.A., Román, R., et al.: Comparative assessment of GRASP algorithm for a dust event over Granada (Spain) during ChArMEx-ADRIMED 2013 campaign. Atmos. Meas. Tech. **10**, 4439–4457 (2017)
12. Konsta, D., Tsekeri, A., et al.: The potential of GRASP/GARRLiC retrievals for dust aerosol model evaluation: case study during the PreTECT Campaign. Remote Sens. **13**, 873 (2021)

Chapter 100
Radiative Budget in the Lower Tropical Stratosphere from the Combination of Balloon-Borne Lidar and Radiometric Measurements

François Ravetta, Thomas Lesigne, Vincent Mariage, Jérôme Bureau, Alain Hauchecorne, and Jacques Pelon

Abstract The atmospheric layer near the tropical tropopause (14–18.5 km), referred to as the Tropical Tropopause Layer (TTL), is a key region of the Earth's atmosphere and the gateway to the stratosphere. Along their ascent through the extremely cold TTL (<200 K), air parcels undergo ice formation and freeze-drying, which is ultimately responsible for the dryness of the stratosphere, of dramatic importance for stratospheric chemistry and the Earth's radiative balance. TTL ice clouds (cirrus) also directly affect the Earth's radiative budget. Combined lidar and radiometric measurements onboard stratospheric balloons make it possible to estimate their radiative forcing at a fine scale.

Keywords Balloon-borne lidar · Radiative budget · Lower stratosphere

100.1 Scientific Context and Balloon-Borne Payload

The Strateole-2 project is an international effort led by French scientists aiming at in situ and remote-sensing observations of the (Tropical Tropopause Layer) TTL using long-duration balloons (SPBs) developed by the French Space Agency (CNES). The balloons drift with the wind for several months at targeted altitudes, enabling quasi-Lagrangian measurements.

Using lidar observations, two goals of this project are to better understand the modulation of cirrus properties by gravity waves [1] and to better assess the forcing of the lower stratosphere by cirrus [2] During the first Strateole-2 scientific campaign, three nadir-looking backscatter lidars were flown in the lower

F. Ravetta (✉) · T. Lesigne · V. Mariage · J. Bureau · A. Hauchecorne · J. Pelon
LATMOS-CNRS, Sorbonne University, Paris, France
e-mail: francois.ravetta@latmos.ipsl.fr

© The Author(s), under exclusive license to Springer Nature Switzerland AG 2023

J. T. Sullivan et al. (eds.), *Proceedings of the 30th International Laser Radar Conference*, Springer Atmospheric Sciences,
https://doi.org/10.1007/978-3-031-37818-8_100

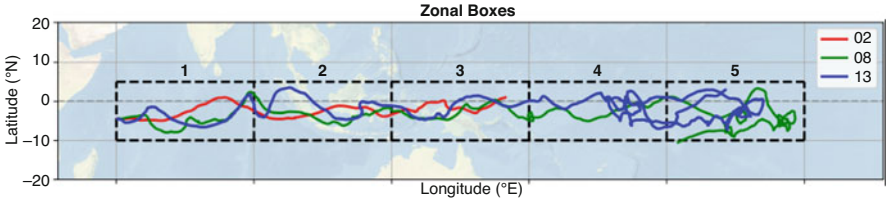


Fig. 100.1 Tracks (red, blue, and green lines) of the three Strateole2 flights with a BeCOOL lidar onboard

stratosphere. These three flights, from October 20, 2021 to January 25, 2022, correspond to 679 hours of night-time measurements (cf. Fig. 100.1).

The BeCOOL backscatter nadir-looking lidar [3] has a a vertical sampling of 15 meters, a temporal resolution of 1 minute, and a horizontal resolution ranging from 0. 1 to 1 km, depending on the speed of the balloon. Assuming thermal equilibrium of the balloon with the surrounding atmosphere [4], upward broadband long-wave radiation fluxes has also been estimated at night from the balloon gas temperature, with a temporal resolution of 5 minutes.

100.2 Balloon-Borne Lidar Observations

Figure 100.2 is a cross section of the range-correct backscattered signal of the lidar, using a logarithmic scale, from November 11, 2021 to January 10, 2022. The left side of this figure corresponds to a flight over the Indian Ocean and the Maritime Continent (Indonesia). A lot of clouds are observed (yellow areas), associated with convective activity over the Maritime Continent. In this case, the lidar is not able to see anymore the surface and the aerosol-rich marine boundary layer. The right side of the figure corresponds to the eastern part of the Equatorial Pacific ocean. Clear sky conditions or high cirrus prevail there.

The lidar signal is calibrated assuming clear sky conditions in the lower stratosphere (from 1 to 2 km away from the instrument), relying on the Rayleigh scattering computed from ERA5 meteorological profiles. When a cloud or an aerosol layer is detected, extinction profiles are retrieved using a classical Klett algorithm [5], with an a priori lidar ratio of 25 sr. A simple integration provides the optical depth of each layer. If a purely molecular signal is observed before and after the layer, the value of the lidar ratio is iteratively adjusted in order to have the computed optical depth matching the observations. When a cloud is optically thick, it is not possible to estimate the extinction profile and the cloud optical depth. This is mostly the case for convective clouds. In this case, only the altitude of the top of the cloud is monitored.

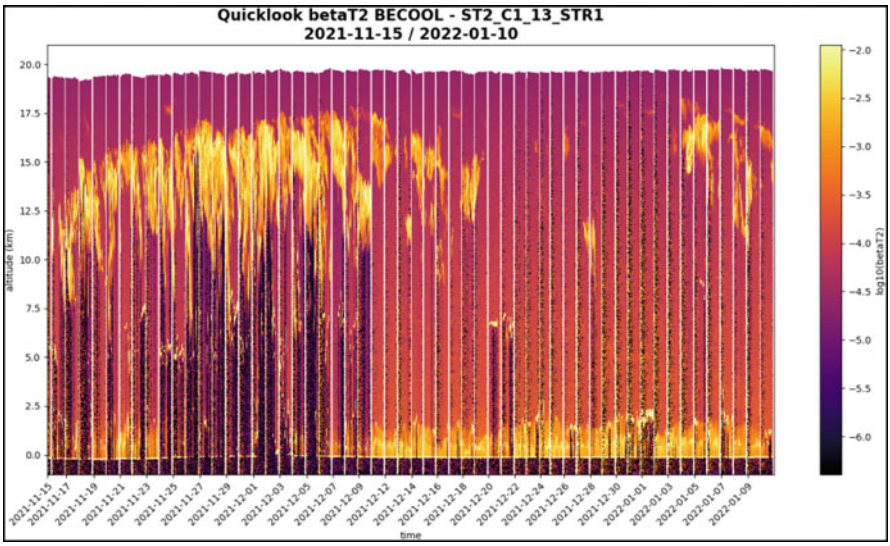


Fig. 100.2 Vertical cross section (altitude against time) of the range corrected backscattered lidar signal for the third Strateole2 flight with a BeCOOL lidar onboard

100.3 Discussion

Combining observations from the balloon-borne lidar and the temperature sensor makes it possible to discuss the variability of upward long-wave radiation against cloud optical thickness. As expected, the outgoing long-wave irradiance strongly depends on the scene observed. For clear sky conditions, upward thermal radiation is mostly due to the emission of the warm ocean surface. It is larger than the emission of the cold upper surface of an optically thick convective cloud. For optically thin clouds, measured thermal fluxes lie in between these two extreme cases (see Fig. 100.3).

Radiative transfer calculations have been done using the ARTDECO v1.2.0 package based on DISORT [6] with 8 streams and k-distributions to capture this variability using lidar observations as input parameters. The irradiances were integrated from 4 to 500 micrometers. To compute the gaseous absorption, we took into account H_2O, CO_2, and O_3. The vertical profiles of temperature, H_2O and O_3 were taken from ECMWF ERA5, 37 levels (date = 202110201723, long. = 60.63, lat. = −4.86), completed by AFGL1 (tropical) above 50 km. The CO_2 value was taken from ground measurements. Only one scattering particle type was considered (water ice). For its optical properties and size distribution, we used a modeled cirrus at 223 K (cir200 model from [7]). The extinction profile was taken from BeCOOL measurements (20211020 1723), scaled to match a desired total optical depth (from 10 to 0.001). Radiative forcing is computed by subtracting a clear sky modeled irradiance profile.

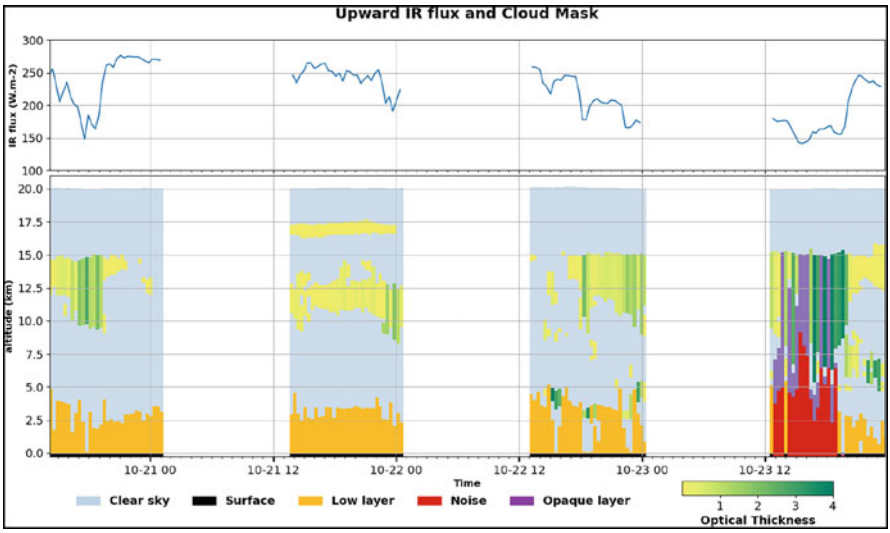


Fig. 100.3 Lower panel: vertical cross section (altitude against time) of the cloud optical thickness (color bar from yellow to green) for four nights. Clear sky is in gray. Purple and red colors correspond to convective clouds. Orange is used for the marine boundary layer and low-level clouds. Upper panel: long-wave upward irradiance (in W m^{-2}) derived from the temperature of the gas in the balloon (blue line) against time for the same four nights

Table 100.1 Estimate of the instantaneous radiative forcing due to a cirrus cloud

Cirrus optical depth	10	1	0.1	0.01	0.001
Radiative forcing (Wm^{-2})	−58	−29	−4.5	−0.48	−0.05

Results are shown in Table 100.1. Clouds being colder than the sea surface temperature, the larger the cloud optical thickness, and the higher the cloud, the larger the absolute value of the radiative forcing. Negative forcing corresponds here to a lower value of outgoing long-wave radiation, thus to a warming of the climate system. No albedo effect has to be considered as measurements are only available during the night.

100.4 Perspectives

The results presented here are only a first estimate of the radiative forcing of the cirrus in the TTL. This will be investigated in more detail, and the fine scale variability observed by the balloon-borne lidar will be addressed. Comparison with spaceborne lidar observations have also been investigated. It turns out that BeCOOL is able to capture subvisible clouds and aerosol layers not seen otherwise.

References

1. Kim, J.-E. et al.: Ubiquitous influence of waves on tropical high cirrus clouds. Geophys. Res. Lett. **43**(11), 5895–5901 (2016)
2. Vaillant de Guélis, T., et al.: Using space lidar observations to decompose longwave cloud radiative effect variations over the last decade. Geophys. Res. Lett. **44**(23), 11–994 (2017)
3. Ravetta, F., et al.: BeCOOL a balloon-borne microlidar system designed for cirrus and convective overshoot monitoring. In: 29th ILRC Conference (2020)
4. Hauchecorne, A., Pommereau, J.P.: Stratospheric radiometric measurements from constant-level balloons. J. Appl. Meteorol. **18**(11), 1385–1396 (1979)
5. Klett, J.: Lidar inversion with variable backscatter/extinction ratios. Appl. Opt. **24**(11), 1638–1643 (1985)
6. Stamnes, K., Tsay, S., Wiscombe, W., Jayaweera, K.: Numerically stable algorithm for discrete-ordinate-method radiative transfer in multiple scattering and emitting layered media. Appl. Opt. **2**(27), 2502–2509 (1988)
7. Hess, M., Koepke, P., Schult, I.: Optical properties of aerosols and clouds: the software package OPAC. Bull. Am. Meteorol. Soc. **79**, 831–844 (1998)

Chapter 101
Spatial Distribution Analysis of the TROPOMI Aerosol Layer Height: A Pixel-by-Pixel Comparison to EARLINET and CALIOP Observations

K. Michaildis, M.-E. Koukouli, D. S. Balis, M. de Graaf, and J. P. Veefkind

Abstract The aim of this study is to report on a detailed validation of the aerosol layer height (ALH) satellite product derived from the TROPOMI/S5P instrument, using as reference spatially and temporally colocated measurements from the well-established EARLINET lidars (Pappalardo G, et al. Atmos Meas Tech 7:2389–2409. https://doi.org/10.5194/amt-7-2389-2014, 2014) and CALIOP/CALIPSO observations (Winker DM, et al. Bull Am Meteor Soc 91:1211–1229. https://doi.org/1310.1175/2010BAMS3009.1, 2010) over the Mediterranean. The time period from 2018 to 2022 is selected for the validation analysis. The TROPOMI Level-2 ALH (Veefkind JP, et al. Remote Sens Environ 120:70–83. https://doi.org/10.1016/16j.rse.2011.09.027, 2012) is an operational product since 2019 focusing on the retrieval of vertically localized aerosol layers in the free troposphere (desert dust, biomass burning aerosol, and volcanic ash plumes) for cloud-free cases. Knowledge of the ALH is essential for understanding the impact of aerosols on the climate system. Lidar instruments are a good source for validating retrieved ALHs from passive satellite sensors since they provide aerosol profile information, such as the backscatter and extinction coefficients, at different wavelengths with a vertical resolution of a few meters. The comparison between TROPOMI and lidar plume heights shows that, on average, the TROPOMI aerosol layer heights are slightly lower, compared to CALIPSO (-0.75 ± 0.98km) and EARLINET (-1.02 ± 0.96km), which is likely due to the different measurement techniques and the TROPOMI product limitations.

K. Michaildis (✉) · M.-E. Koukouli · D. S. Balis
Laboratory of Atmospheric Physics, Aristotle University of Thessaloniki, Thessaloniki, Greece
e-mail: komichai@auth.gr; balis@auth.gr; mariliza@auth.gr

M. de Graaf · J. P. Veefkind
Royal Netherlands Meteorological Institute (KNMI), De Bilt, The Netherlands
e-mail: martin.de.graaf@knmi.nl; pepijn.veefkind@knmi.nl

© The Author(s), under exclusive license to Springer Nature Switzerland AG 2023

J. T. Sullivan et al. (eds.), *Proceedings of the 30th International Laser Radar Conference*, Springer Atmospheric Sciences,
https://doi.org/10.1007/978-3-031-37818-8_101

Keywords Aerosol layer height · TROPOMI · EARLINET · CALIPSO

101.1 Introduction

101.1.1 Scope of the Study

In this study, we use the aerosol layer height product derived by the TROPOMI/S5P in synergy with the EARLINET and CALIPSO lidar observations. The TROPOMI/S5P operational satellite height product focuses on the retrieval of vertically localized aerosol layers in the free troposphere (such as desert dust, biomass burning aerosol, and volcanic ash plumes). Lidar profiles from a space-born instrument, such as CALIPSO, and from a suite of ground-based lidars, such as the European EARLINET database, are an optimal way to validate retrieved ALHs from passive satellite sensors. The choice of using the Mediterranean as a study area arises from the fact that the majority of colocations among TROPOMI, EARLINET, and CALIOP are concentrated around this region. In addition, over land, the TROPOMI ALH product has decreased capabilities compared to over sea surfaces since, over bright surfaces, the retrieval algorithm becomes increasingly sensitive to errors in the surface albedo features.

101.2 Instrumentation and Data

101.2.1 TROPOMI S5P Data

TROPOMI is the single payload on the Sentinel-5P satellite that has a Sun-synchronous orbit with a local overpass time of around 1:30 pm and has near full-surface coverage on a daily basis [3]. The TROPOMI aerosol layer height (AER_LH) algorithm was developed by the Royal Netherlands Meteorological Institute (KNMI) and utilizes the absorption in the oxygen A band of the spectrum between 759 and 770 nm [4]. In case of bright surfaces and thin aerosol layers, the aerosol layer height is expected to be more robust over dark surfaces such as sea and oceans. In the current study, we use only TROPOMI retrievals over the water surfaces. A more detailed description of the TROPOMI aerosol layer height product can be found in [4].

101.2.2 Ground-Based Lidar Data (EARLINET)

The European Aerosol Research Lidar Network [1], established in 2000, provides an excellent opportunity to provide a large collection of quality-assured ground-based

data of the vertical distribution of the aerosol optical and geometrical properties over Europe. The main information stored in the files of the EARLINET database is the vertical distribution of aerosol backscatter and aerosol extinction coefficients together with their errors, mainly at one or more out of the following wavelengths: 355 nm, 532 nm, and 1064 nm. The database also includes volume and particle depolarization ratio profiles at 532 nm. The lidar stations belong to EARLINET is a suitable source for the long-term validation of satellite aerosol products, such as the TROPOMI aerosol layer height. The ability of the EARLINET data to successfully assess and validate space-borne ALH observations has already been demonstrated for the GOME2/MetOp aerosol height products [5]. The intercomparison showed that the GOME-2 AAH measurements provide a good estimation of the aerosol layer altitude sensed by the EARLINET ground-based lidars.

101.2.3 CALIOP/CALIPSO Data

Cloud-Aerosol Lidar with Orthogonal Polarization (CALIOP), onboard CALIPSO, provides information on the vertical distribution of aerosols and clouds as well as on their optical properties over the globe with unprecedented spatial resolution. CALIOP, the principal instrument on board the CALIPSO satellite, is a standard dual-wavelength (532 and 1064 nm) backscatter lidar, operating a polarization channel at 532 nm [2]. While CALIOP has excellent vertical resolution and could resolve the layer heights of multiple plumes in a single profile, its swath width is very narrow and has a 16-d global coverage. In this study, we use CALIPSO Level 2 (version 4.21) product includes the vertical location of layers, backscatter and extinction profiles, the discrimination of aerosol layers from clouds, and the classification of the aerosol layers in eight subtypes.

101.3 Validation Methodology and Results

101.3.1 Comparison of TROPOMI ALH Against EARLINET

The validation of S5P TROPOMI level 2 OFFL AER_LH data presented here is based on comparisons with ground-based lidar stations belonging to the EARLINET network. Lidar data from 7 stations were considered in this analysis covering period from May 2018 till March 2022. The geographical distribution of the selected EARLINET stations is depicted in Fig. 101.1. All participating stations (red circles) operate high-performance multiwavelength lidar systems. The location of the stations across the Mediterranean basin is an ideal test environment for TROPOMI ALH features due to their proximity to the Sahara Desert and Europe, with frequently observed events of mineral dust and smoke particles.

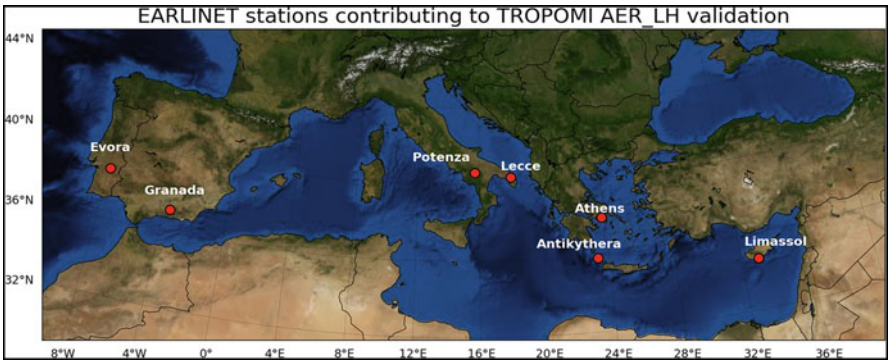


Fig. 101.1 Geographical distribution of EARLINET ground-based stations for which colocations with S5P L2 AER_LH data were used for the selected study period

TROPOMI observations colocated with the ground-based EARLINET measurements are found by selecting all filtered and averaged TROPOMI pixels within a radius of 150 km around each station and with a maximal time difference of 4 h. Pixels with an associated quality assurance value of less than 0.5 were excluded. Some of the known data quality issues are not covered by the quality flags, such as insensitivity to very high altitudes aerosol layers, treatment of multilayer clouds, treatment of ice clouds, snow/ice conditions, and Sun-glint effect. Those pixels where hence additionally removed. As input to the validation processing, we use the lidar backscatter coefficient profiles at 1064 nm (and/or 532 nm), analyzed by the single calculus chain (SCC) algorithm [5] for quality-assured measurements. For the layer height retrieval from the EARLINET products, we used a standard methodology in order to calculate the weighted backscatter height using the level-2 backscatter profiles 1064 nm (or 532 nm) according to the expression:

$$\mathrm{ALH_{bsc}} = \frac{\int_{z_i=1}^{z_i=n} z_i \cdot \beta_{aer,i}(z)dz}{\int_{z_i=1}^{z_i=n} \beta_{aer,i}(z)dz} \tag{101.1}$$

The $\mathrm{ALH_{bsc}}$ represents an effective ALH weighted by the aerosol backscatter signal at each altitude level and is consistent with ALH as defined in the TROPOMI algorithm. We applied Eq. (101.1), to all lidar backscatter profiles collocated to TROPOMI measurements. The results of the comparison between the TROPOMI and EARLINET-derived aerosol heights for 34 identified collocated cases are shown in Fig. 101.2 (left), which shows the scatterplot of TROPOMI ALH against EARLINET data. By defining a weighted height from EARLINET aerosol backscatter profile products ($\mathrm{ALH_{bsc}}$), the quantitative validation at pixels over the selected EARLINET stations illustrates that TROPOMI ALH is highly consistent with $\mathrm{ALH_{bsc}}$, with a high correlation coefficient $R = 0.89$ and mean bias -1.02 ± 0.96 km. The S5P TROPOMI ALH is systematically smaller than the

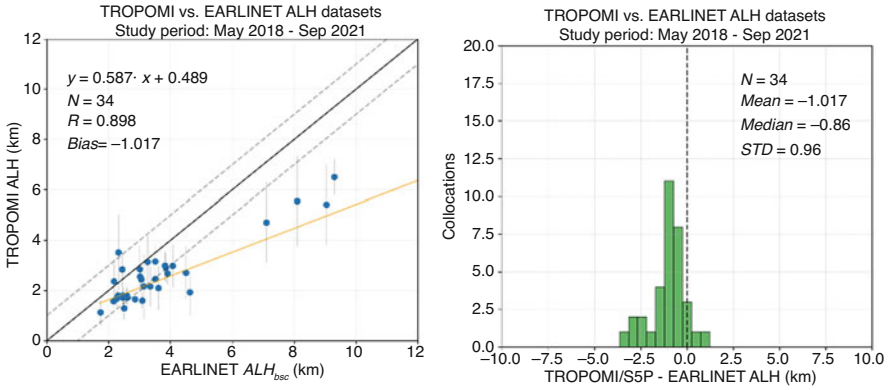


Fig. 101.2 (Left) Scatterplot of TROPOMI ALH versus EARLINET ALH calculated by aerosol backscatter profiles. Error bars of each scatter indicate standard deviations for ALH values of the collocated pixels. (Right) Distribution of the absolute differences

EARLINET results, as also seen in Fig. 101.2 (right), which shows the histogram of absolute difference. More detailed information about the methodology, the corresponding results, and limitations can be found in the work of [7].

101.3.2 Comparison of TROPOMI ALH Against CALIPSO

For the comparison between CALIOP and TROPOMI, only CALIOP plume heights over central-eastern Mediterranean are retained, filtered out were the ones categorized as dust plumes. A total of 8 coincident CALIOP lidar measurements for CALIPSO overpass over central-eastern Mediterranean for the time period between July 2018 and March 2022 are analyzed. Following the methodology described in [6] for the validation of the TROPOMI-retrieved ALH, we used CALIOP level 2 (version 4.21) aerosol extinction profiles at 5 km spatial resolution, retrieved from CALIOP observations of attenuated backscatter at 532 nm. The closest distances, within 2 h, between the CALIOP footprint of the CALIPSO overpass and the locations of the TROPOMI center pixels are selected, respectively, to create collocated datasets.

A pixel-by-pixel comparison of the CALIOP ALH and TROPOMI ALH for all the cases is presented in Fig. 101.3, left. During this comparison, every cloud-filtered and sun-glint-filtered TROPOMI pixel with ALH information colocated to a specific CALIOP level-2 aerosol extinction profile is used. Overall, for the ensemble of the eight selected cases, a low agreement (0.28) can be observed for TROPOMI-CALIOP retrievals with a slope and intercept of 0.33 and 2.45, respectively. Also, on the right illustrated the histogram of the absolute differences between the two datasets, with a mean and median residual values close to zero and typically within −0.8.

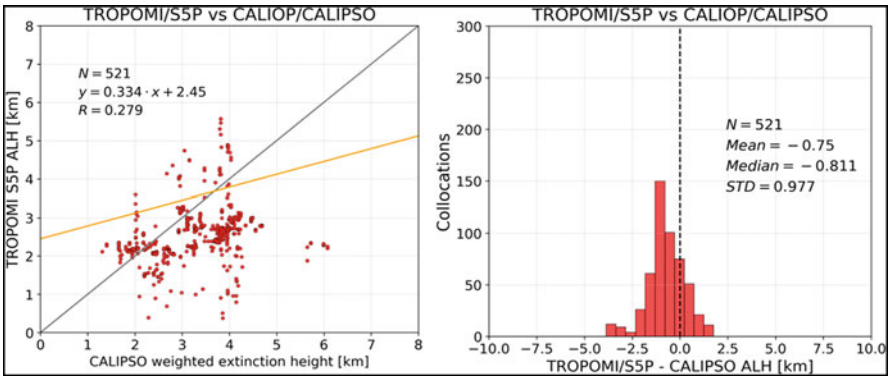


Fig. 101.3 (Left) Scatterplot and (right) distribution of absolute differences between TROPOMI and CALIOP for all collocated pairs

101.4 Conclusions

In this study, the TROPOMI ALH is compared for the first time with the EARLINET lidar database for the time period between 2018 and 2022. Moreover, the comparison of TROPOMI against CALIOP and EARLINET data is still limited to several case studies. Overall, the analysis of TROPOMI ALH observations against EARLINET in the Mediterranean area shows good correlation with ground-based, demonstrating the ability of the TROPOMI observations to properly capture the temporal variability of tropospheric aerosol plumes. The comparison shows that, on average, the TROPOMI aerosol layer heights are slightly lower but within ± 1 km, compared to EARLINET (-1.02 ± 0.96 km). In the future, other lidar stations that are part of the EARLINET network will be included in the comparison for further validation of the satellite products on continental scale. In the case of TROPOMI-CALIPSO comparison, a low agreement (0.28) was found, indicating the need for more investigation. A larger sample of collocations should be sought and also a selection of stricter spatiotemporal criteria should be taken into account. Considering the differences, mainly due to the different remote sensing technique, the temporal collocation, the satellite pixel size, and the point view of the lidar observations, these results are quite promising.

Acknowledgments We thank all Co-Principal Investigators and their staff for establishing and maintaining the EARLINET sites used in this investigation (https://www.earlinet.org). We also acknowledge the TROPOMI/S5P L2 data from Copernicus Services Data Hub https://s5phub.copernicus.eu) and the CALIOP Level 2 aerosol profile data from the NASA Langley Research Center Atmospheric Science Data Center (https://eosweb.larc.nasa.gov/project/calipso)

References

1. Pappalardo, G., et al.: EARLINET: towards an advanced sustainable European aerosol lidar network. Atmos. Meas. Tech. **7**, 2389–2409 (2014). https://doi.org/10.5194/amt-7-2389-2014
2. Winker, D.M., et al.: The CALIPSO mission: a global 3D view of aerosols and clouds. Bull. Am. Meteor. Soc. **91**, 1211–1229 (2010). https://doi.org/10.1175/2010BAMS3009.1
3. Veefkind, J.P., et al.: TROPOMI on the ESA Sentinel-5 Precursor: a GMES mission for global observations of the atmospheric composition for climate, air quality and ozone layer applications. Remote Sens. Environ. **120**, 70–83 (2012). https://doi.org/10.1016/j.rse.2011.09.027
4. Nanda, S., et al.: A first comparison of TROPOMI aerosol layer height (ALH) to CALIOP data. Atmos. Meas. Tech. **13**, 3043–3059 (2020). https://doi.org/10.5194/amt-13-3043-2020
5. Michailidis, K., et al.: First validation of GOME-2/MetOp absorbing aerosol height using EARLINET lidar observations. Atmos. Chem. Phys. **21**, 3193–3213 (2021). https://doi.org/10.5194/acp-21-3193-2021
6. D'Amico, G., et al.: EARLINET single calculus chain – overview on methodology and strategy. Atmos. Meas. Tech. **8**, 4891–4916 (2015). https://doi.org/10.5194/amt-8-4891-2015
7. Michailidis, K., et al.: Validation of the TROPOMI/S5P aerosol layer height using EARLINET lidars. Atmos. Chem. Phys. Discuss. [preprint] (2022). https://doi.org/10.5194/acp-2022-412, in review

Chapter 102
First Results from the Aeolus Reference Lidar eVe During the Tropical Campaign JATAC at Cabo Verde

P. Paschou, N. Siomos, E. Marinou, H. Baars, A. Gkikas, G. Georgoussis, D. Althausen, R. Engelmann, J. von Bismarck, T. Fehr, and V. Amiridis

Abstract The eVe lidar is a novel ground-based lidar system designed to provide ground reference measurements of aerosols and clouds optical properties facilitating the validation of the corresponding Aeolus products of aerosols and clouds. The lidar is implemented in a dual-laser/dual-telescope configuration that emits linearly

P. Paschou (✉)
Institute for Astronomy, Astrophysics, Space Applications and Remote Sensing, National Observatory of Athens, Athens, Greece
e-mail: pepaschou@noa.gr

Laboratory of Atmospheric Physics, Physics Department, Aristotle University of Thessaloniki, Thessaloniki, Greece

N. Siomos
Institute for Astronomy, Astrophysics, Space Applications and Remote Sensing, National Observatory of Athens, Athens, Greece

Laboratory of Atmospheric Physics, Physics Department, Aristotle University of Thessaloniki, Thessaloniki, Greece

Fakultät für Physik, Meteorologisches Institut, Ludwig-Maximilians-Universität, Munich, Germany

E. Marinou · A. Gkikas · V. Amiridis
Institute for Astronomy, Astrophysics, Space Applications and Remote Sensing, National Observatory of Athens, Athens, Greece

H. Baars · D. Althausen · R. Engelmann
Leibniz Institute for Tropospheric Research (TROPOS), Leipzig, Germany

G. Georgoussis
Raymetrics S.A., Athens, Greece

J. von Bismarck
European Space Agency (ESA/ESRIN), Frascati, Italy

T. Fehr
European Space Agency (ESA/ESTEC), Noordwijk, The Netherlands

© The Author(s), under exclusive license to Springer Nature Switzerland AG 2023

J. T. Sullivan et al. (eds.), *Proceedings of the 30th International Laser Radar Conference*, Springer Atmospheric Sciences,
https://doi.org/10.1007/978-3-031-37818-8_102

and circularly polarized light at 355 nm and detects the depolarization in the elastically backscattered lidar signals as well as the inelastically backscattered both from linear and circular emission. eVe mimics the observational geometry and configuration of Aeolus whereas is capable to operate as a traditional ground-based linear polarization lidar system. The lidar was deployed in the Joint Aeolus Tropical Atlantic Campaign (JATAC) for the validation of the Aeolus products. During JATAC operations, an unpreceded eVe dataset was acquired aiming to facilitate the Aeolus calibration and validation efforts. In addition, the good performance of the eVe lidar was validated against an EARLINET approved lidar system, the PollyXT that was also deployed for the JATAC operations.

Keywords eVe lidar · Aeolus reference lidar · JATAC

102.1 Introduction

The Aeolus mission [1, 2] is an atmospheric Earth Explorer Core mission of the European Space Agency (ESA). Aeolus is designed to provide profiles of the wind in the troposphere and the lower stratosphere [3] as well as the profiles of the particle (aerosols and clouds) optical properties such as the extinction coefficient, the backscatter coefficient, and the lidar ratio (Level 2A; [4]). The single payload onboard Aeolus is the Atmospheric Laser Doppler Instrument (ALADIN), a high spectral resolution lidar. ALADIN emits circularly polarized light at 355 nm while pointing at 35° from nadir [5] and detects only the co-polar component of the elastically backscattered light [4]. When depolarizing targets (e.g. dust, volcanic ash and ice crystals) are present in the atmosphere, the undetected cross-polar component of the backscattered light is non-negligible resulting in underestimation of the particle backscatter coefficient that Aeolus measures [6]. Focusing on the validation of the Aeolus particle optical properties (L2A) and the assessment of the Aeolus backscatter coefficient underestimation on depolarizing scenes, a dedicated ground-based lidar system (eVe lidar) was developed to be the European Space Agency's reference lidar system for the validation of the Aeolus aerosol product. This paper provides a brief description of the operation principle of the developed lidar and presents first results from the eVe measurements performed during the Joint Aeolus Tropical Atlantic Campaign (JATAC) at Cabo Verde on summer 2021.

102.2 The eVe Lidar

The eVe lidar is a combined linear/circular polarization lidar system with Raman capabilities that operates at 355 nm implementing a dual-laser/dual-telescope configuration that can point at multiple azimuth and off-zenith angles [7]. The emission unit consists of two lasers, one emitting linearly polarized light and the other circularly polarized light at 355 nm. In the receiver unit, two telescopes are used

to collect sequentially the backscattered light from the interleaved emission of the two lasers. The collected backscattered lidar signals are optically separated through two wavelength separation units (WSUs) and are recorded by five photomultipliers tubes (PMT) with a raw signal height resolution of 3.75 m. The WSU from telescope 1 (WSU1) utilizes a linear polarization analyzer with two polarization-sensitive channels for measuring the depolarization in the elastically backscattered signals from linear emission. A Raman channel is also deployed in WSU1 to detect the inelastically backscattered lidar signals from both linear and circular emission. The WSU from telescope 2 (WSU2) utilizes a circular polarization analyzer and two polarization-sensitive channels for measuring the depolarization in the elastically backscattered signals from circular emission. As such, the eVe lidar products are the profiles of the particle backscatter and extinction coefficients and the lidar ratio originated from both linear and circular emission, the volume and particle linear depolarization ratios, and the volume and particle circular depolarization ratios at 355 nm.

The dual-laser/dual-telescope configuration facilitates the performance of linear and circular depolarization measurements simultaneously and along with the system's capability to point at multiple azimuth/off-zenith angles, allows eVe to simultaneously reproduce the operation of the ALADIN lidar onboard Aeolus, i.e. circularly polarized emission at 35° off-nadir, as well as the operation of a traditional linear polarization lidar system, i.e. with linearly polarized emission and any pointing geometry.

102.3 The JATAC Campaign

The Joint Aeolus Tropical Atlantic Campaign (JATAC) was held at the remote islands of Cabo Verde during July and September 2021. The main aim of JATAC was to provide reference measurements of the wind profiles, and the aerosols and clouds optical properties for the validation of the Aeolus products by deploying airborne and ground-based instrumentation. ASKOS is the ground-based component of JATAC that was held in Mindelo on the island of Sao Vicente, Cabo Verde, where high quality of ground-based wind, aerosol, and cloud observations were collected from instruments such as the eVe lidar, a PollyXT lidar, a wind lidar, a cloud radar and a sun photometer (https://askos.space.noa.gr/) for the Aeolus calibration and validation (Cal/Val) efforts.

102.3.1 Lidar Intercomparison (eVe vs. Polly^{XT})

The collocated operation of the eVe and PollyXT lidars during ASKOS/JATAC comprised a great opportunity to perform an intercomparison study between the two lidars in order to cross-validate both systems and evaluate their performance. The

PollyXT lidar is an automated multiwavelength polarization-Raman-Water vapor lidar system [8] that has been recently set up in the aerosol and cloud remote sensing facility in Mindelo, Cabo Verde for long-term lidar observations on 24/7 basis. The PollyXT lidar emits linearly polarized light at 355, 532 and 1064 nm while pointing at 5° off-zenith and retrieves the profiles of the particle backscatter and extinction coefficients (355, 532 and 1064 nm), the lidar ratio (355, 532 and 1064 nm), the volume and particle linear depolarization ratios (355, 532 and 1064 nm), the Angstrom exponent (355/532 nm and 532/1064 nm) and the water vapour mixing ratio.

Since the PollyXT lidar performs polarization measurements using linearly polarized light, only the eVe products from the linear emission can be used for the lidar intercomparison on 16 September 2021 (Fig. 102.1). The averaged profiles from PollyXT (including both far-field and near-field channels) lidar have been retrieved within the timeframe from 20:00 to 20:19 UTC and the averaged profiles from eVe lidar have been retrieved a few minutes later within the timeframe from 20:16 to 20:54 UTC. Although the lidar products from each lidar has been derived using their corresponding processing software, the same window length (750 m) has been applied by each software for smoothing the lidar signals aiming to provide as homogeneous retrievals as possible. In addition, for the intercomparison purposes the eVe lidar measurements on 16 September 2021 were performed while pointing at 5° off-zenith in order to reproduce the operation of PollyXT lidar.

According to Fig. 102.1, below 1 km and inside the marine boundary layer, the backscatter coefficient ($\beta^{particle}$) reaches values up to 7.5 $Mm^{-1}sr^{-1}$, the extinction coefficient ($\alpha^{particle}$) values are up to 100 Mm^{-1} and the lidar ratio is approximately 20 sr. In addition, low values of the volume and particle linear depolarization ratios are observed (less than 0.02 and 0.05, respectively) for the suspended

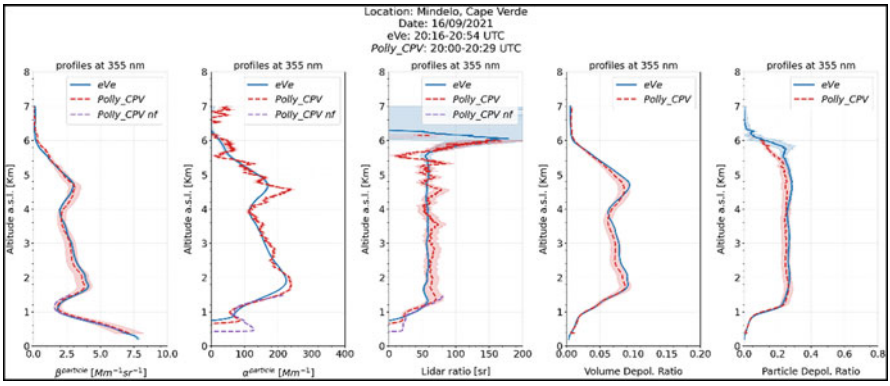


Fig. 102.1 Lidar products intercomparison between eVe (blue solid line) and PollyXT (red dashed line for the far-field retrieval; purple dashed line for the near-field retrieval) lidars from the collocated measurements on 16 September 2021. The common lidar products at 355 nm (from left to right) are the particle backscatter coefficient, the particle extinction coefficient, the lidar ratio, and the volume and particle linear depolarization ratios

marine aerosols. On top of the PBL, the dust layer extends up to 6 km where the backscatter coefficient ranges from 3 to 4 $Mm^{-1}sr^{-1}$, the extinction coefficient ranges from 100 to 220 Mm^{-1}, and the lidar ratio is approximately 50 sr. The volume linear depolarization ratio ranges from 0.06 to 0.09, while the particle linear depolarization ratio is approximately 0.25. A very good agreement between the eVe and PollyXT profiles for all lidar products is observed in Fig. 102.1, validating the good performance of both systems. The observed deviations in the particle extinction coefficient and the lidar ratio profiles are attributed to the nosier PollyXT signals compared to eVe.

102.3.2 Aeolus Evaluation Using eVe Measurements

In the context of the ASKOS/JATAC campaign, targeted measurements of the eVe lidar were performed every Friday evening when Aeolus is flying nearby the site. In July and September 2021, 8 collocated measurements between eVe and Aeolus were found and analyzed for the validation of the Aeolus L2A products. Targeted measurements of eVe (13 in total) were also performed in September during the overflights of the deployed aircrafts carrying in situ and remote sensing instrumentation.

The Aeolus overpass from site on Friday 10 September 2021 was selected to demonstrate the eVe lidar products as well as the Aeolus L2A products for the Aeolus validation studies (Fig. 102.2). During the Aeolus overpasses, eVe lidar was measuring with the Aeolus pointing geometry in order to reproduce Aeolus from ground. For the comparison with the Aeolus products, the eVe Aeolus-like backscatter and lidar ratio profiles (light blue; Fig. 102.2) have been calculated according to Paschou et al. [7] in order to harmonize the ground-based profiles with the corresponding Aeolus products taking into consideration the undetected cross-polar component from Aeolus.

According to the eVe profiles (Fig. 102.2) within the marine boundary layer (below 1 km), the backscatter coefficient reaches up to 10 $Mm^{-1}sr^{-1}$, the extinction coefficient values are up to 200 Mm^{-1}, and the mean lidar ratio is approximately 25 sr. Additionally, the volume and particle linear depolarization ratios are less than 0.02 and 0.04, respectively, indicating the presence of marine almost spherical particles. Regarding the volume and particle circular depolarization ratios, their values are less than 0.05 and 0.08, respectively. Above 1 km, dust particles are suspended in the atmosphere up to 6 km where the backscatter ranges from 0.6 to 3.2 $Mm^{-1}sr^{-1}$, the extinction coefficient ranges from 20 to 165 Mm^{-1}, and the mean lidar ratio is about 53 sr. The volume linear depolarization ratio ranges from 0.06 to 0.09, while the mean particle linear depolarization ratio is approximately 0.28. The volume circular depolarization ratio ranges from 0.06 to 0.09, while the mean particle circular depolarization ratio is approximately 0.76.

Moreover, at the altitude ranges where the dust layer resides (1–6 km), the calculated eVe Aeolus-like backscatter profile ranges from 0.4 to 2 $Mm^{-1}sr^{-1}$, and

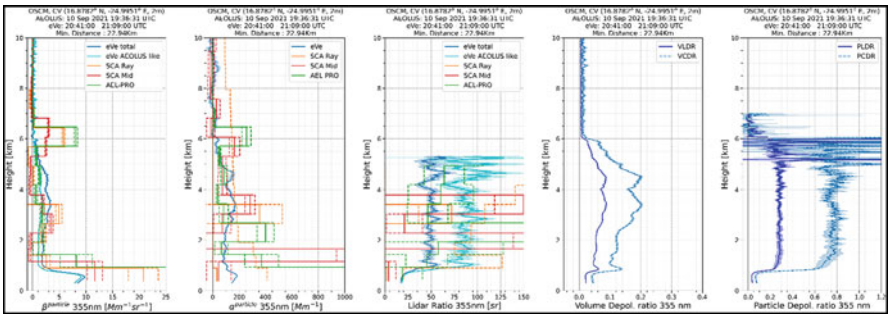


Fig. 102.2 The eVe lidar products of particle backscatter ($\beta^{particle}$) and extinction ($\alpha^{particle}$) coefficients, lidar ratio, volume depolarization ratio, and particle depolarization ratio from linear (dark blue) and circular (blue) emission along with the Aeolus-like profiles (light blue) from circular emission retrieved from the eVe measurement during the nearest Aeolus overpass from site on 10 September 2021. The Aeolus L2A profiles retrieved from the SCA (orange and red) and AEL-PRO (green) algorithms from Baseline 12 are also provided

it is underestimated with respect to the total backscatter profile by approximately 43%. Similarly, the eVe Aeolus-like lidar ratio is around 88 sr instead of the total lidar ratio of 53 sr, which results in an expected overestimation of approximately 77%. In the comparison with the Aeolus L2A profiles, the Aeolus backscatter from both algorithms is overestimated compared to the Aeolus-like backscatter from eVe below 1.5 km, with the SCA-mid bin profile (red) to be the less overestimated. Above 1.5 km, the Aeolus backscatter presents good agreement with the eVe Aeolus-like profile, but it is slightly underestimated at approximately 2 km and 4–5 km. The deviation between Aeolus and eVe Aeolus-like profile at 6 km is attributed to a cloud that is observed only from Aeolus, since the eVe profiles are originated from a measurement where the cloud contaminated signals have not been considered in the analysis. For the extinction profile, both Aeolus algorithms retrieve noisy profiles up to 4 km, but a good agreement with the eVe extinction profile is observed above 4 km except the cloud presence at 6 km only for Aeolus. The Aeolus lidar ratio profiles are too noisy to be compared against eVe.

102.4 Summary

The eVe lidar is the ground refence system for the Aeolus L2A products Cal/Val that was deployed in the JATAC. The acquired eVe dataset from JATAC has been used to validate the system's good performance against the PollyXT lidar and to provide first results on the validation of the Aeolus L2A products. Overall, the comparison between the eVe and the Aeolus L2A profiles indicates better agreement above 2 km for the Aeolus backscatter and extinction profiles with the extinction to be noisier and too noisy Aeolus lidar ratio retrievals. Nevertheless, the collocated eVe-Aeolus

dataset will be further enriched from the forthcoming ASKOS 2022 operations at Cabo Verde.

References

1. Stoffelen, A., Pailleux, J., Källén, E., Vaughan, J.M., Isaksen, L., Flamant, P., Wergen, W., Andersson, E., Schyberg, H., Culoma, A., Meynart, R., Endemann, M., Ingmann, P.: The atmospheric dynamics mission for global wind field measurement. Bull. Am. Meteorol. Soc. **86**(1), 73–88 (2005)
2. Reitebuch, O.: The spaceborne wind lidar mission ADM-Aeolus. In: Schumann, U. (ed.) Atmospheric Physics, Research Topics in Aerospace, pp. 815–827. Springer, Heidelberg (2012)
3. Tan, D.G.H., Andersson, E., De Kloe, J., Marseille, G.-J., Stoffelen, A., Poli, P., Denneulin, M.-L., Dabas, A., Huber, D., Reitebuch, O., Flamant, P., Le Rille, O., Nett, H.: The ADM-Aeolus wind retrieval algorithms. Tellus A Dyn. Meteorol. Oceanogr. **60**(2), 191–205 (2008)
4. Flament, T., Trapon, D., Lacour, A., Dabas, A., Ehlers, F., Huber, D.: Aeolus L2A aerosol optical properties product: standard correct algorithm and Mie correct algorithm. Atmos. Meas. Tech. **14**, 7851–7871 (2021)
5. Lolli, S., Delaval, A., Loth, C., Garnier, A., Flamant, P.H.: 0.355-micrometer direct detection wind lidar under testing during a field campaign in consideration of ESA's ADM-Aeolus mission. Atmos. Meas. Tech. **6**(12), 3349–3358 (2013)
6. Flamant, P., Dabas, A., Martinet, P., Lever, V., Flament, T., Trapon, D., Olivier, M., Cuesta, J., and Huber, D.: Aeolus L2A Algorithm Theoretical Baseline Document, Particle Optical Properties Product, Version 5.7. Available at: https://earth.esa.int/eogateway/catalog/aeolus-l2a-aerosol-cloud-optical-product (2021). Last accessed 25 May 2022
7. Paschou, P., Siomos, N., Tsekeri, A., Louridas, A., Georgoussis, G., Freudenthaler, V., Binietoglou, I., Tsaknakis, G., Tavernarakis, A., Evangelatos, C., von Bismarck, J., Kanitz, T., Meleti, C., Marinou, E., Amiridis, V.: The eVe reference polarisation lidar system for the calibration and validation of the Aeolus L2A product. Atmos. Meas. Tech. **15**, 2299–2323 (2022)
8. Engelmann, R., Kanitz, T., Baars, H., Heese, B., Althausen, D., Skupin, A., Wandinger, U., Komppula, M., Stachlewska, I.S., Amiridis, V., Marinou, E., Mattis, I., Linné, H., Ansmann, A.: The automated multiwavelength Raman polarization and water-vapor lidar PollyXT: the neXT generation. Atmos. Meas. Tech. **9**, 1767–1784 (2016)

Chapter 103
Analysis of a Mid-Atlantic Ozone Episode Using TOLNet and Pandora



Maurice Roots, Sergio Diaz, John T. Sullivan, Ruben Delgado, and Belay Demoz

Abstract A large effort has been made to establish ozone lidars across the mid-Atlantic region of the United States. By 2023, there will be 4 Tropospheric Ozone Lidar Network (TOLNet) sites across the mid-Atlantic region: Hampton, VA with Hampton University and NASA Langley Research Center (LMOL); Greenbelt, MD with NASA Goddard Space Flight Center (TROPOZ); and Manhattan, NY will have one at the City College of New York (CCNY). This novel venture will bring much-needed profiling of ozone to key areas in the region; however, its networked coverage will be sparse with sites being $\leq$200 miles apart. To extend the utility of both the TOLNet and Pandora networks, we have begun using their observational products to interpret boundary layer abundances to extract new science and understanding of pollution dynamics. We present a case study of this effort from a NAAQS ozone exceedance episode from May 19 to 21, 2021. High-resolution observations from active and passive remote sensors capture the evolution of this event. The ozone episode evolved from entrainment of a transported polluted air mass followed by recirculation in the region leading to a quick lofting by down-slope winds (as noted by ceilometer backscatter and vertically resolved wind profiles), which are situated in the plume for next-day entrainment. Collocated wind, aerosols, and ozone profiles in the Beltsville – Greenbelt, MD area indicated an air-mass change occurring near 14 LT May 20, 2021, marking the arrival of a well-mixed layer of ozone from the north. For this case, the Pandora total column ozone enhancement showed good agreement both temporally and quantitatively with TROPOZ 0–2 km integrated column (a TEMPO-like proxy). This shows the

M. Roots (✉) B. Demoz
University of Maryland, Baltimore County (UMBC), Baltimore, MD, USA

Joint Center for Earth Systems Technology (JCET) at UMBC, Baltimore, MD, USA

S. Diaz
University of Maryland, Baltimore County (UMBC), Baltimore, MD, USA

J. T. Sullivan · R. Delgado
NASA Goddard Space Flight Center (GSFC), Greenbelt, MD, USA
e-mail: mroots1@umbc.edu

© The Author(s), under exclusive license to Springer Nature Switzerland AG 2023

J. T. Sullivan et al. (eds.), *Proceedings of the 30th International Laser Radar Conference*, Springer Atmospheric Sciences,
https://doi.org/10.1007/978-3-031-37818-8_103

potential for future synergy in air quality event identification and characterization, especially in those that are driven by meteorological enhancement and transport. A byproduct of this work is an analysis of the seasonal variability of ozone in the mid-Atlantic domain using TOLNet, Pandora, sondes, and surface trace-gas monitors. This work aims to aid in the resolution of NASA decadal surface questions, support the upcoming TEMPO mission, and serves to demonstrate the usefulness of multi-instrument perspectives in the analysis of air quality event evolution and spatio-temporal variability. Further work will focus on the comparison of these datasets with NASA GEOS-CF and current satellite products.

Keywords Ozone · TOLNET · Pandora · Mid-Atlantic

103.1 Introduction

Ozone (O_3) is a naturally occurring oxidant gas. It is a secondary pollutant meaning it is not directly emitted and thus formed from photochemical reactions involving nitrogen oxides and volatile organic compounds (i.e., NOx and VOCs). Ozone continues to be a by-product of urbanization and is a substantial threat to human health and ecosystems. Previous studies have focused on summertime ozone where production is a result of increased emission of precursors and surface solar radiation. Local and synoptic meteorology are also important drivers for the transport of pollutants and the formation of air quality episodes. The mid-Atlantic region is known to have nocturnal low-level jets (NLLJs) and downslope winds (DSW), which can enhance and/or inhibit ozone production in the region [3]. Biomass burnings and interstate transport of precursors are also enhancement factors [1, 2]. These factors contribute to the difficulty in accurately modeling and managing tropospheric and surface ozone. However, incorporating the collocated multi-instrument perspective helps quantify the evolution and variability of ozone during events of meteorological enhancement and transport.

103.2 Data and Methods

Presented here is an analysis of a recent air ozone episode (May 19–21, 2021) that impacted the mid-Atlantic region with multiple exceedances of the National Ambient Air Quality Standards (NAAQS) for surface ozone concentrations. Interesting features of this episode include deviation from recent exceedance trends, the arrival of the well-mixed polluted air mass, and nocturnal ozone increases. The analysis incorporates multiple datasets of in situ and remote sensing measurements. Observations of ozone were taken in column abundance from Pandora spectrometers, with vertically resolved profiles from balloon-borne ozone-sondes and in high-temporal resolution from the NASA GSFC Tropospheric Ozone (TROPOZ) lidar,

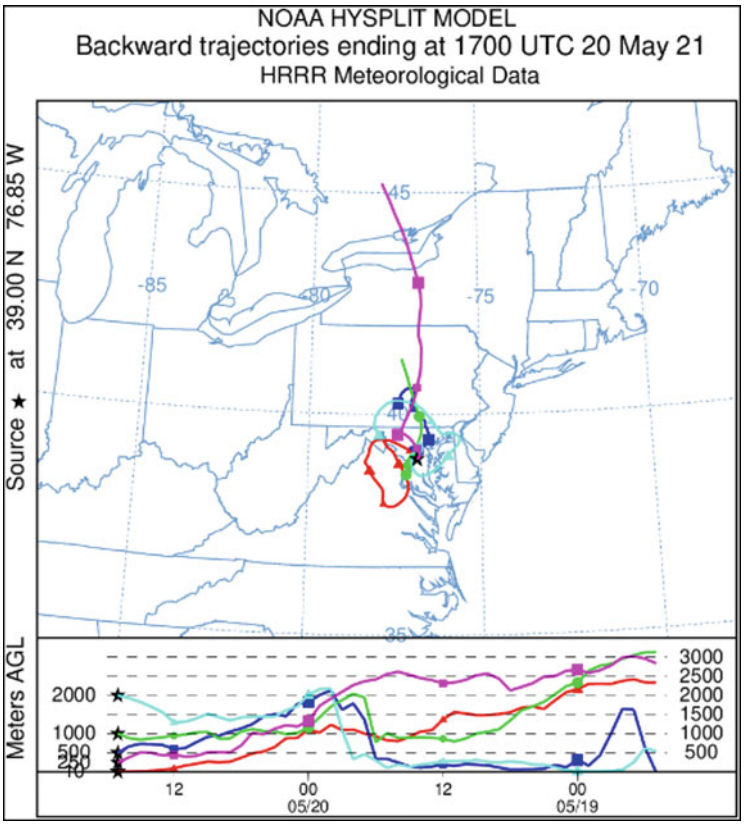


Fig. 103.1 HYSPLIT backtrajectory with mixing layer heigh inset initialized from NASA GSFC at 17 UTC. Shows recirculation and long-range transport

part of TOLNet. Profiles of aerosols and winds were taken by ceilometers (Unified Ceilometer Network, UCN) and MDE radar wind profilers (RWP), respectively. The focus of this work is on the Beltsville, MD – Greenbelt, MD area of which TROPOZ, RWP, Ceilometer, Pandora, Sonde, and MDE surface samplers are of near colocation (<10 km) (Fig. 103.1).

The TROPOZ system is a differential absorption lidar calibrated for detecting ozone concentrations [4]. The configuration of the TROPOZ system used for data collection in this study employs a 2-m CO_2 gas Raman cell pressurized to 0.41 MPa that is pumped with a 266 nm laser to output 287 and 299 nm as the second and third stokes shifts from stimulated Raman scattering. The collection optics use a 45 cm Newtonian telescope for the far field and a 10 cm telescope for the far field, which focus the return signal into photo multiplier tubes with interference filters (<1 nm resolution).

Surface ozone concentrations were observed in excess of 70 ppb for 4 days (May 18–22, 2021). Seven of the twenty Maryland surface monitoring sites recorded

exceedances of the 8-h NAAQS Ozone standard. Strong nocturnal increases in surface ozone were observed on the night of May 20, influenced by NLLJ turbulent downmixing [4]. HYSPLIT back-trajectory initialized from May 20 17 UTC shows recirculation of air in the Maryland-Virginia region accumulating from days prior. On May 20, the TROPOZ system, Ceilometer, Sonde profiles observed a well-mixed polluted boundary layer marked by the arrival of northeasterly winds observed at 12 UTC by RWP at Beltsville, MD (see Fig. 103.2).

The Pandora spectrometer has been validated to retrieve total column O_3 and NO_2 in agreement with satellite retrievals from the Ozone Monitoring Instrument (OMI). The Pandora delivers these column abundances at 5-min temporal resolution diurnally. TOLNet has been validated to deliver accurate vertical profiles of ozone at high vertical and temporal resolution ($\leq$20 m @ $\leq$10 min). By the fourth quarter of 2022 (Q4 2022), there will be 4 TOLNet sites across the Mid-Atlantic: Hampton, VA will have one at Hampton University and another at NASA Langley Research Center; Greenbelt, MD will have the NASA Goddard Space Flight Center (GSFC) Tropospheric Ozone Lidar (TROPOZ); and Manhattan, New York will have one at the City University of New York (CUNY), each $\leq$200 miles apart. To extend the utility of both TOLNet and Pandora networked observations, an effort has been created to convert the available TOLNet and Pandora observations into column abundances of ozone into a boundary layer product (as demonstrated in Fig. 103.3). The boundary layer ozone abundance is derived from removal of multi-year (2017–2021) mean and 0–2 km nocturnal sonde profile, and the residual in Pandora TCO is taken as boundary layer contribution in the absence of aloft layers (Fig. 103.4).

103.3 Results and Summary

Ozone episode May is out of the norm for this location. The episode evolved from entrainment of a transported polluted air mass then recirculation in the mid-Atlantic on May 19 and 20, 2021, followed by quick lofting by DSW (as shown by ceilometer and wind) resulting in next-day entrainment. The evolution of the PBL height from May 19–21 shows a clear relation to the 3-Stage Diurnal Boundary Model [3]. High-resolution observations from active and passive remote sensors captured the evolution of the ozone episode. Turbulent downburst from NLLJ is identified as causes of the nocturnal surface ozone increases, similarly to the event described by Sullivan et al. [5]. The Pandora total column ozone (TCO) data was filter by prescribed methods [6], reduced by synoptic trend and pre-event profile to then plot TCO enhancement in Fig. 103.4 from May 20, 2021. Which shows agreement with a subset of lidar-derived ozone (integrated from 0 to 2 km only) – a proxy for a TEMPO ozone product – thus encouraging potential for further usage in air quality episode characterization. A more in-depth analysis is required to identify what fraction of the Pandora TCO is background ozone, boundary layer ozone, and due to small-scale variability. This venture can be used to extract new science and understanding surrounding pollution transport throughout the troposphere. This

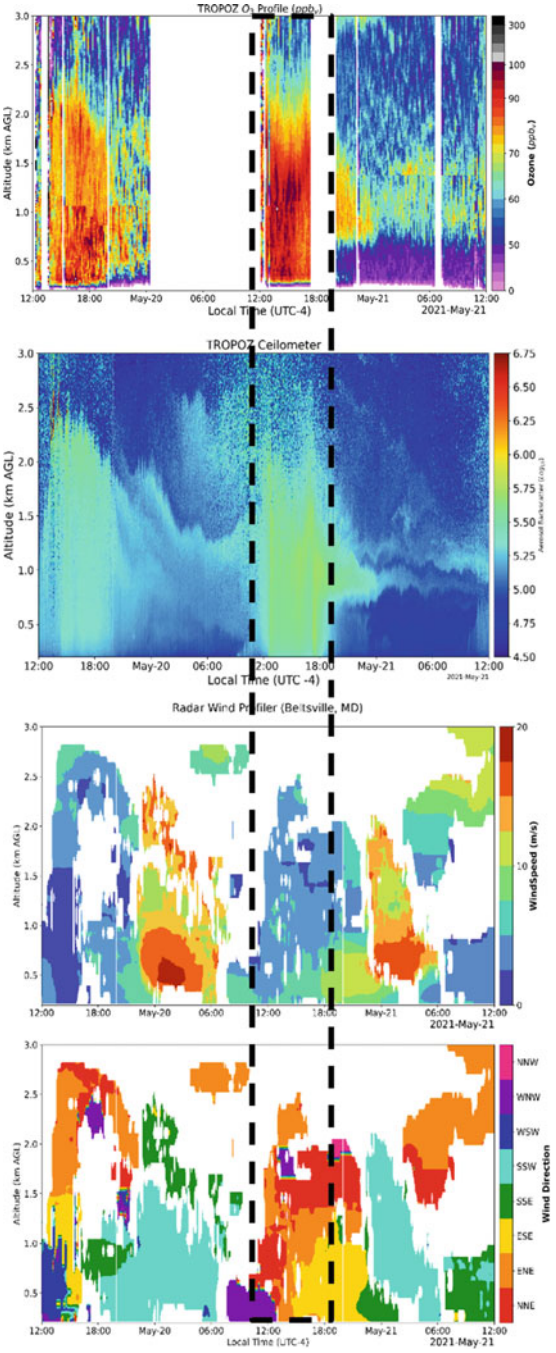


Fig. 103.2 May19–21, 2021 profiles during a polluted episode in MD (**a**) TOLNet observed ozone, (**b**) ceilometer aerosols backscatter, (**c**) and radar wind speed and direction

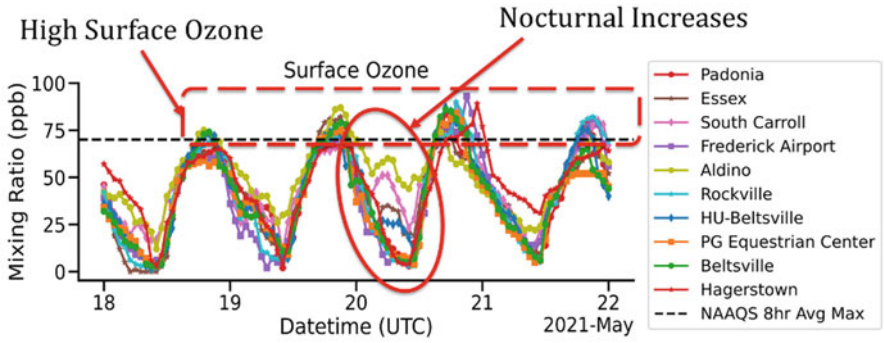


Fig. 103.3 Surface ozone concentrations recorded by select MDE site across Maryland. Note the strong nocturnal increases and lasting high surface ozone episode well above 70 ppbv

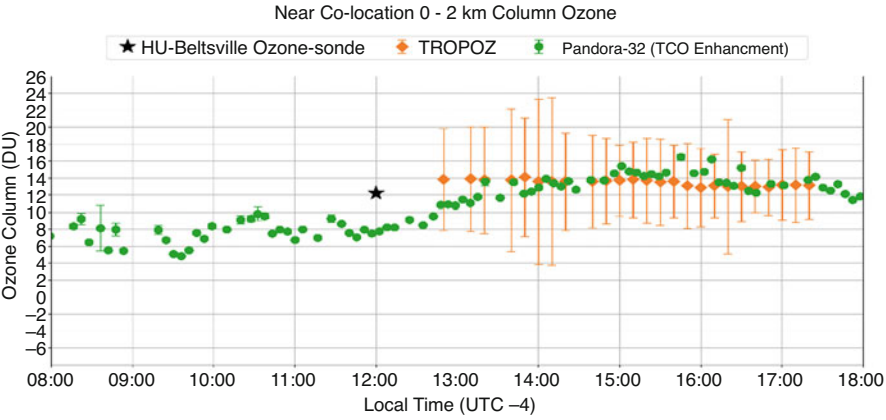


Fig. 103.4 Evolution of Ozone May 20 ozone episode from TOLNet lidar (TROPOZ), Pandora, and sonde. TCO enhancement derived from removal of multi-year (2017–2021) mean, and sonde 0–2 km nocturnal column (not shown)

work also serves to demonstrate the usefulness of multi-instrument perspectives in air quality event analysis and study of spatiotemporal variability.

Acknowledgments The authors would like to thank HU-Beltsville and the UMBC Lidar Group for their generous data contributions.

This material is based upon work supported by the US Department of Commerce, National Oceanic and Atmospheric Administration, Educational Partnership Program, under Agreement No. **#NA16SEC4810006**. The authors would like to thank Howard University National Center for Atmospheric Science and Meteorology (NCAS-M) program and NOAA Office of Education, Educational Partnership Program (NOAA EPP) for fellowship supporting Mr. Maurice Roots. Any opinions, findings, conclusions, or recommendations expressed in this publication are those of the authors and do not necessarily reflect the view of the US Department of Commerce, National Oceanic and Atmospheric Administration. The authors would also like to thank that GEM consortium and NASA GSFC for funding this project and coordinating this collaboration.

References

1. Dreessen, J., Sullivan, J., Delgado, R.: Observations and impacts of transported Canadian wildfire smoke on ozone and aerosol air quality in the Maryland region on June 9–12, 2015. J. Air Waste Manage. Assoc. **66**, 842–862 (2016). https://doi.org/10.1080/10962247.2016.1161674
2. Moghani, M., Archer, C.L., Mirzakhalili, A.: The importance of transport to ozone pollution in the U.S. Mid-Atlantic. Atmos. Environ. **191**, 420–431 (2018). https://doi.org/10.1016/j.atmosenv.2018.08.005
3. Rabenhorst, S., Whiteman, D.N., Zhang, D.-L., Demoz, B.: A case study of mid-Atlantic nocturnal boundary layer events during WAVES 2006. J. Appl. Meterol. Climatol. **53**, 2627–2648 (2014). https://doi.org/10.1175/JAMC-D-13-0350.1
4. Sullivan, J.T., McGee, T.J., Sumnicht, G.K., Twigg, L.W., Hoff, R.M.: A mobile differential absorption lidar to measure sub-hourly fluctuation of tropospheric ozone profiles in the Baltimore–Washington, D.C. region. Atmos. Meas. Tech. **7**, 3529–3548 (2014). https://doi.org/10.5194/amt-7-3529-2014
5. Sullivan, J.T., Rabenhorst, S.D., Dreessen, J., McGee, T.J., Delgado, R., Twigg, L., Sumnicht, G.: Lidar observations revealing transport of O3 in the presence of a nocturnal low-level jet: regional implications for "next-day" pollution. Atmos. Environ. **158**, 160–171 (2017). https://doi.org/10.1016/j.atmosenv.2017.03.039
6. Tzortziou, M., Herman, J. R., Cede, A., Abuhassan, N.: High precision, absolute total column ozone measurements from the Pandora spectrometer system: comparisons with data from a Brewer double monochromator and Aura OMI: Pandora Total Column Ozone Retrieval. J. Geophys. Res. **117** (2012). https://doi.org/10.1029/2012JD017814

Chapter 104
A Difference of the Depolarization Ratio Detected at Locally Generated Dust and Transported Asian Dust Over Japan with AD-Net

Atsushi Shimizu, Tomoaki Nishizawa, Yoshitaka Jin, and Nobuo Sugimoto

Abstract The depolarization ratio near the surface measured by lidars in AD-Net (Asian dust and aerosol lidar observation network) was utilized to distinguish the long-range transported Asian dust and locally generated dust over Japan. In February 2017, locally generated dusts were frequently observed in Tsukuba, and May 2017 was a typical month of Asian dust. Thus, two histograms of depolarization ratio constructed from observational data of these 2 months were compared, and a 0.4 (40%) was identified as a threshold of two kinds of mineral dust particles: locally generated (large) dust and long-range transported Asian dust. A climatological analysis of data obtained by four lidars in Japan revealed that the local dust events were not observed in other regions of Japan.

Keywords Asian dust · Local dust · Depolarization ratio

104.1 Introduction

The Asian dust, generated and upward lifted at Gobi desert and Taklamakan Desert, is transported eastward and deposited around the Pacific limb area. The environmental impact of Asian dust particles is various, including the health effects like a cause of respiratory diseases [3–6, 10]. Thus, a monitoring and forecasting of Asian dust is an important task for meteorological or environmental agencies in China, Korea, and Japan. The Asian particles reach at downstream countries mainly during March and May. To the contrary, locally generated dust in Japan prevails in Kanto area around Tokyo, the capital of Japan in early spring season accompanied

A. Shimizu (✉) · T. Nishizawa · Y. Jin · N. Sugimoto
National Institute for Environmental Studies, Tsukuba, Japan
e-mail: shimizua@nies.go.jp

© The Author(s), under exclusive license to Springer Nature Switzerland AG 2023

J. T. Sullivan et al. (eds.), *Proceedings of the 30th International Laser Radar Conference*, Springer Atmospheric Sciences,
https://doi.org/10.1007/978-3-031-37818-8_104

by a strong southerly wind after dry days. Such dust particles are not transported for long distance because their diameter is larger than Asian dust particles. However, its impact is not clarified yet because the objective detection criteria are not defined in the meteorological observations.

Here, the difference of depolarization ratio of the Asian dust and locally generated dust was investigated using AD-Net lidar, and the criteria to distinguish them by lidar observation results are proposed.

104.2 Lidar Observations in AD-Net

AD-Net [8] is a network of dual wavelength Mie-scattering lidars In Japan, Korea, China, and Mongolia to detect of both Asian dust and anthropogenic particles in near real time. The independent lidar in AD-Net equips a flashlamp-pumped Nd:YAG laser as a light source, a telescope with a diameter of 20 cm, two PMTs for visible with polarization, and an APD for IR detection. 16-bit AD converters are employed to record the signal intensity. 10-Hz pulses are emitted continuously for 5 minutes, and backscattered signals are accumulated. Then, the system rests for 10 minutes. Thus, every 15 minutes vertical profiles of backscatter intensities for 532 nm parallel and perpendicular components and 1064-nm total are recorded with 6-m vertical resolution. Fernald's inversion [1] with the assumption of fixed lidar ratio ($S_1 = 50\,sr$) was applied for clear profiles after vertical averaging to 30 m, and the obtained extinction coefficient of aerosols is divided into two components, dust extinction coefficient and spherical particle extinction coefficient based on the depolarization ratio [7].

104.3 Periods of Locally Generated Dust and Asian Dust

To identify the statistical difference of optical parameters of two kinds of dust, first, we determined two periods in which both dusts were dominant in the atmosphere over Tsukuba. Long-range transported Asian dust is significant during March and May around western Pacific limb (Korea/Japan). However, locally generated dust in Kanto area, Japan mainly occurs in earlier spring, February or March. The amount of rain is small in this period, and dried surface including crop fields before planting provides mineral particles into the atmosphere when the strong southerly wind (in Japanese, "Haru-Ichiban," which means the first significant wind in spring season) blows. In 2017, strong local dust occurs in 2, 7, and 8 February. A pollen counter (an optical particle counter that detects large particles with the diameter of 28–35 micrometers) operated at Tsukuba by the Ministry of Environment showed significant peaks on these days. However, such peaks are not a signature of actual floating pollen because the first date of pollen emission was confirmed on 16 February by a human-eye observation of deposition plates using a microscope [2].

Thus, larger particles observed on 2, 7, and 8 February were considered as mineral particles. There was no emission of Asian dust in source regions (Gobi desert), nor the dust report from meteorological observatories between the source region and Tsukuba. Thus, the mineral particles are considered as locally generated dust. The time–height variation of highly depolarized region from lidar signals also confirmed that. In May, long-range transported Asian dust is dominant in mineral dust particles because the local dust was not generated due to wet land surface including rice paddies filled by water in this season. In the following sections, February and May 2017 are treated as a local dust month and an Asian dust month.

104.4 Statistical Analysis of Optical Parameters

The probability densities of particulate depolarization ratio at 532 nm near the surface (altitude of 120 m) for February and May in Tsukuba are shown in Fig. 104.1a. Apparently, the larger values were confirmed in February where the locally generated dusts were dominant in Tsukuba. Contrarily, the values in May

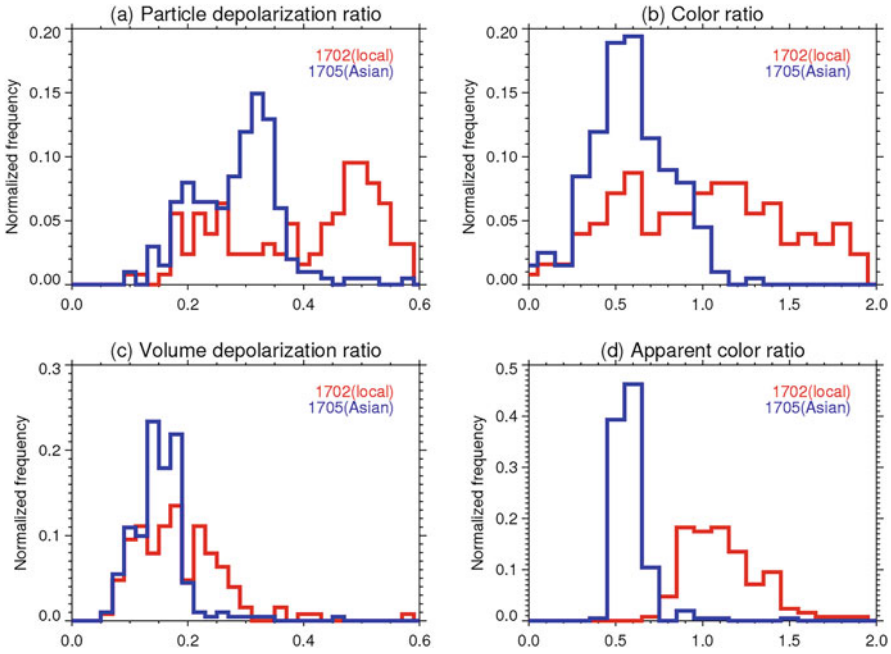


Fig. 104.1 Frequency distributions of optical parameters detected by a lidar in Tsukuba in February (red) and May (blue) at 120-m altitude. (**a**) particulate depolarization ratio, (**b**) color ratio (ratio between the backscatter coefficient at 1064 nm to that at 532 nm), (**c**) volume depolarization ratio, and (**d**) apparent color ratio (the ratio between the attenuated backscatter ratio at 1064 nm and that at 532 nm)

were smaller. Although apparent color ratio (Fig. 104.1d) shows a clear difference in 2 months, some fluctuated structures appeared in the time–height sections during dust periods. Thus, the particulate depolarization ratio is utilized in the following climatological analysis.

104.5 Climatology of Local Dust and Asian Dust

The frequency distribution of particulate depolarization ratio of spring season in Tsukuba in Kanto, Toyama in central Japan, Matsue in western Japan and Nagasaki in Kyushu during 2015–2019 was investigated. Figure 104.2 shows a strong site dependency that solely in Tsukuba the higher (greater than 0.5) depolarization ratio was detected in February and March. In other three sites, such higher depolarization ratio was not detected, and thus the occurrence of local dust was not so common at regions other than Kanto. Nagasaki observatory is located at the western part of Japan, and in analyzed period this region suffers from transboundary air pollution particles which have basically spherical shape. The frequent mixture of spherical

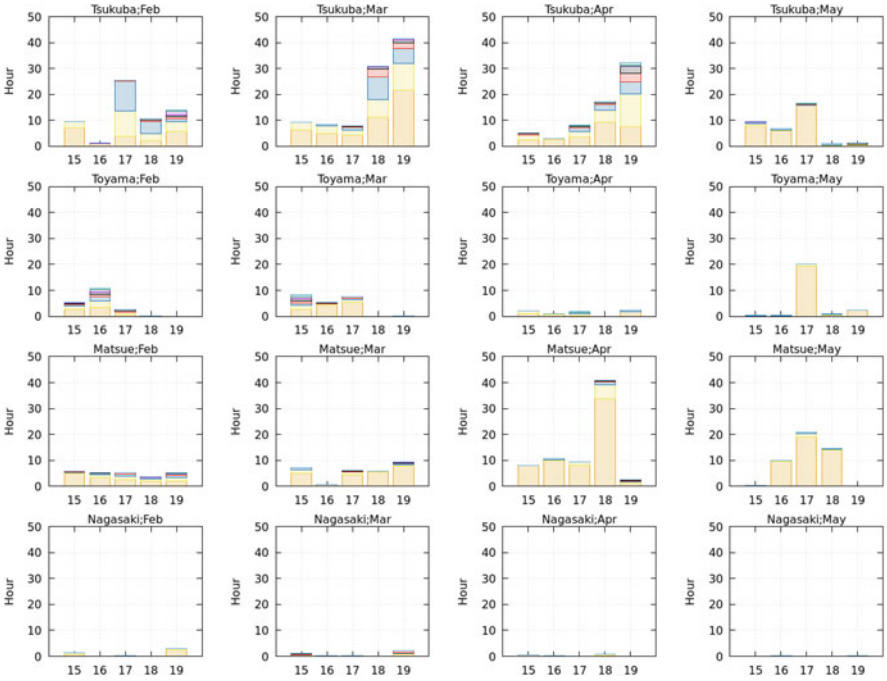


Fig. 104.2 Total hours in which highly depolarized particles were observed over Ad-Net lidars in February–May 2015–2019. Abscissa in each panel indicates years. Orange, ivory, and light blue areas correspond to the hours of 30–40$, 40–50%, and 50–60% depolarization ratios, respectively

pollution with Asian dust might cause some decrement of depolarization ratio in Nagasaki [9].

104.6 Concluding Remarks

The usability of particulate depolarization ratio for discrimination between locally generated dust and transported Asian dust was demonstrated using AD-Net data. If the difference of environmental impact of two kinds of dust was considered, AD-Net should provide additional information on the total dust extinction coefficient which just expresses the total amount of non-spherical particles.

Acknowledgments This work was supported by the Environment Research and Technology Development Fund (JPME20205001) of the Environmental Restoration and Conservation Agency provided by Ministry of the Environment of Japan.

References

1. Fernald, F.G.: Analysis of atmospheric lidar observations: some comments. Appl. Opt. **23**(5), 652–653 (1984)
2. Kafun-Joho-Kyokai: Map of Initial Date of Flying Cedar Pollen (2017). https://pollen-net.com/KAFUNMAP/kafunmap_2017.html (Accessed 2022.5.15, in Japanese)
3. Kanatani, K.T., Hamazaki, K., Inadera, H., Sugimoto, N., Shimizu, A., Noma, H., Onishi, K., Takahashi, Y., Itazawa, T., Egawa, M., Sato, K., Go, T., Ito, I., Kurozawa, Y., Konishi, I., Adachi, Y., Nakayama, T.: Effect of desert dust exposure on allergic symptoms; A natural experiment in Japan. Ann. Allergy Asthma Immunol. **116**(5), 425.e7–430.e7 (2016). https://doi.org/10.1016/j.anai.2016.02.002
4. Michikawa, T., Yamazaki, S., Shimizu, A., Nitta, H., Kato, K., Nishiwaki, Y., Morokuma, S.: Exposure to Asian dust within a few days of delivery is associated with placental abruption in Japan: a case-crossover study. BJOG Int. J. Obstet. Gynaecol. **127**(3), 335–342 (2020). https://doi.org/10.1111/1471-0528.15999. https://obgyn.onlinelibrary.wiley.com/doi/abs/10.1111/1471-0528.15999
5. Nakamura, T., Hashizume, M., Ueda, K., Shimizu, A., Takeuchi, A., Kubo, T., Hashimoto, K., Moriuchi, H., Odajima, H., Kitajima, T., Tashiro, K., Tomimasu, K., Nishiwaki, Y.: Asian dust and pediatric emergency department visits due to bronchial asthma and respiratory diseases in Nagasaki, Japan. J. Epidemiol. **26**(11), 593–601 (2016). https://doi.org/10.2188/jea.JE20150309
6. Nakamura, T., Nishiwaki, Y., Hashimoto, K., Takeuchi, A., Kitajima, T., Komori, K., Tashiro, K., Hasunuma, H., Ueda, K., Shimizu, A., Odajima, H., Moriuchi, H., Hashizume, M.: Association between Asian dust exposure and respiratory function in children with bronchial asthma in Nagasaki Prefecture, Japan. Environ. Health Prev. Med. **25**(1), 8 (2020). https://doi.org/10.1186/s12199-020-00846-9
7. Shimizu, A., Sugimoto, N., Matsui, I., Arao, K., Uno, I., Murayama, T., Kagawa, N., Aoki, K., Uchiyama, A., Yamazaki, A.: Continuous observations of Asian dust and other aerosols by polarization lidars in China and Japan during ACE-Asia. J. Geophys. Res. **109**(D19), D19S17 (2004). https://doi.org/10.1029/2002JD003253

8. Shimizu, A., Sugimoto, N., Nishizawa, T., Jin, Y., Batdorj, D.: Variations of dust extinction coefficient estimated by lidar observations over Japan, 2007–2016. Sci. Online Lett. Atmos. **13**, 205–208 (2017). https://doi.org/10.2151/sola.2017-037
9. Sugimoto, N., Nishizawa, T., Shimizu, A., Matsui, I., Kobayashi, H.: Detection of internally mixed Asian dust with air pollution aerosols using a polarization optical particle counter and a polarization-sensitive two-wavelength lidar. J. Quant. Spectrosc. Radiat. Transf. **150**, 107–113 (2015). https://doi.org/10.1016/j.jqsrt.2014.08.003. https://www.sciencedirect.com/science/article/pii/S0022407314003367
10. Ueda, K., Shimizu, A., Nitta, H., Inoue, K.: Long-range transported Asian Dust and emergency ambulance dispatches. Inhal. Toxicol. **24**(12), 858–867 (2012). https://doi.org/10.3109/08958378.2012.724729

Chapter 105
Identification of Mixed-Phase Clouds Using Combined CALIPSO Lidar and Imaging Infrared Radiometer Observations

Anne Garnier, Jacques Pelon, David Winker, Melody Avery, Mark Vaughan, and Yongxiang Hu

Abstract Using the so-called Hu diagram relating layer-integrated depolarization ratio (δ_v) and layer-integrated attenuated backscatter at 532 nm (γ'_{532}), the Cloud Aerosol Lidar and Infrared Pathfinder Satellite Observation (CALIPSO) lidar can effectively discriminate between liquid water clouds, clouds composed of randomly oriented ice (ROI) crystals, and ice clouds that contain some fraction of horizontally oriented ice (HOI) crystals. A recently proposed Hu diagram update splits the original water region into a more compact pure liquid regime and two mixed-phase regions. We propose an extended Hu diagram that additionally identifies mixed-phase clouds by incorporating perfectly colocated microphysical index (β_{eff}) and effective diameter (D_e) retrievals in the thermal infrared window obtained from the CALIPSO imaging infrared radiometer (IIR). First, using the β_{eff} index, we identify regions of the Hu diagram which are seemingly associated with mixed-phase clouds. Second, we characterize opaque water clouds in the updated Hu diagram. Water clouds with top temperatures lower than 238 K, when ice is expected in the upper portion of the cloud, fall distinctly into a proposed mixed-phase region. IIR D_e varies as expected with lidar ratio in the tighter liquid water region and is larger due to the presence of ice in the mixed-phase region. Finally, we show that the HOI class clusters into two main families of δ_v-γ'_{532} relationships, suggesting mixed-phase

A. Garnier (✉)
RSES/Analytical Mechanics Associates, Hampton, VA, USA
e-mail: anne.emilie.garnier@nasa.gov

J. Pelon
LATMOS, Sorbonne University, Paris, France
e-mail: jacques.pelon@latmos.ipsl.fr

D. Winker · M. Avery · M. Vaughan · Y. Hu
NASA Langley Research Center, Hampton, VA, USA
e-mail: david.m.winker@nasa.gov; melody.a.avery@nasa.gov; mark.a.vaughan@nasa.gov; yongxiang.hu-1@nasa.gov

© The Author(s), under exclusive license to Springer Nature Switzerland AG 2023

J. T. Sullivan et al. (eds.), *Proceedings of the 30th International Laser Radar Conference*, Springer Atmospheric Sciences,
https://doi.org/10.1007/978-3-031-37818-8_105

clouds with smaller D_e and pure ice clouds with larger D_e, which is confirmed by Monte Carlo simulations published in the literature.

Keywords CALIPSO · IIR · Cloud phase · Mixed-phase clouds · Remote sensing

105.1 Introduction

The radiative impact of clouds strongly depends on their thermodynamic phase. The partitioning between water and ice for the clouds detected by CALIPSO's Cloud Aerosol Lidar with Orthogonal Polarization (CALIOP) is determined based on the relationship between two quantities measured at 532 nm: the layer-integrated depolarization ratio (δ_v) and the layer-integrated attenuated backscatter (γ'_{532}). Using the so-called Hu diagram relating δ_v and γ'_{532}, which was established from Monte Carlo simulations, CALIPSO can effectively discriminate between liquid water clouds, clouds composed of randomly oriented ice (ROI) crystals, and ice clouds that contain some fraction of horizontally oriented ice (HOI) crystals [1]. The latter are characterized by contributions from specular reflections of laser light from (quasi) horizontally aligned crystal facets perpendicular to the laser beam that generate strongly enhanced backscatter coupled with reduced (to near zero) depolarization. HOIs were frequently observed at the beginning of the CALIPSO mission, when the platform was tilted at an angle of 0.3° off nadir, but they are only rarely seen since December 2007 when the tilt angle was changed to 3° off nadir. Recently, an updated Hu diagram was proposed by [2], who split the original water boundaries used in the CALIOP algorithm into a tighter region for liquid water clouds and two mixed-phase regions: ROI-mix and HOI-mix.

The CALIPSO imaging infrared radiometer (IIR) retrieves cloud effective emissivity in each of the three channels (8.65, 10.6, and 12.05 μm) and a subsequent microphysical index (β_{eff}) defined here as the ratio of the effective absorption optical thicknesses in the 12.05 μm and 10.6 μm channels. This index and a second one derived from channels 12.05 μm and 8.65 μm are used to retrieve an effective diameter (D_e) [3]. The β_{eff} index is very sensitive to small particles and, as shown in [1], it is unambiguously larger for water clouds composed of smaller droplets than for ice clouds often composed of larger crystals. In this chapter, we expand on [1] and examine IIR β_{eff} and D_e as a possible identifier of mixed-phase clouds in the original and updated Hu diagrams. The CALIOP layer-integrated attenuated color ratio (defined as $\gamma'_{1064}/\gamma'_{532}$) is also considered, because it has been shown to be sensitive to ice/water phase [4].

105.2 Results

The CALIOP and IIR data are from the colocated CALIOP version 4.20 level 2 5-km cloud layer products and IIR level 2 track products, respectively. Because IIR is a passive instrument, we select scenes with only one cloud in a CALIOP column. We require that γ'_{532} and δ_v have not been modified by the CALIOP cloud clearing algorithm, meaning that some clouds with top altitudes lower than 4 km are not included in this analysis.

105.2.1 IIR Retrievals in the Hu Phase Diagrams

We examine IIR retrieved properties in the Hu phase diagrams in candidate mixed-phase clouds; that is, water clouds with top temperatures (T_{top}) colder than 273 K and ROIs with base temperatures (T_{base}) warmer than 233 K, taken as the temperature threshold for homogeneous freezing. The results shown in Fig. 105.1 are for semi-transparent clouds that (a) do not fully attenuate the laser beam, thus ensuring accurate determination of cloud base; (b) are detected at night, when the CALIOP signal to noise ratio is the largest; and (c) occur over oceans to minimize IIR uncertainties. This assessment uses all 12 months of 2008, when the platform tilt angle is 3° and HOIs are rarely detected. The parameters shown in Fig. 105.1 vs. γ'_{532} and δ_v correspond to samples where IIR D_e retrievals are successful. Following [1], the red lines represent the limit between the ROI (above) and water (below) sectors, and the green lines represent the limit between the water (above) and HOI (below) sectors. The dashed lines are the new tighter boundaries for water clouds proposed by [2]. According to [2], the clouds between the upper dashed and black solid lines are ROI-mix and the few clouds between the lower dashed and black solid lines are HOI-mix.

As seen in Fig. 105.1a, the largest β_{eff} (>1.35) are in water clouds and lie mostly between the dashed lines. The largest color ratios (Fig. 105.1c) around 1.15–1.2 are in water clouds and match remarkably well the largest β_{eff}. The color ratios are prevailingly smaller than 1.05 in ROIs, where β_{eff} is smaller than 1.1. For both β_{eff} and the color ratio, we see a transition region for $\gamma'_{532} > \sim 0.03\ sr^{-1}$, which covers the ROI-mix region and part of the ROI sector, with intermediate β_{eff} values around 1.15–1.25 and intermediate color ratios around 1.05–1.12. Both β_{eff} and the color ratios suggest the presence of mixed-phase clouds in this intermediate region. IIR ε_{eff} (Fig. 105.1b) is related to visible cloud optical depth. Thus, the relationship between ε_{eff} and γ'_{532} varies with lidar ratio and multiple scattering contribution, which both differ in ROIs and in water clouds [5]. As seen in Fig. 105.1b, the ε_{eff} -γ'_{532} relationships vary continuously from the water to the ROI phase regimes, with a marked change for ε_{eff} >0.7 at the upper dashed line, which, again, is consistent with a phase change from liquid water to mixed-phase clouds (ROI-mix) as proposed by [2].

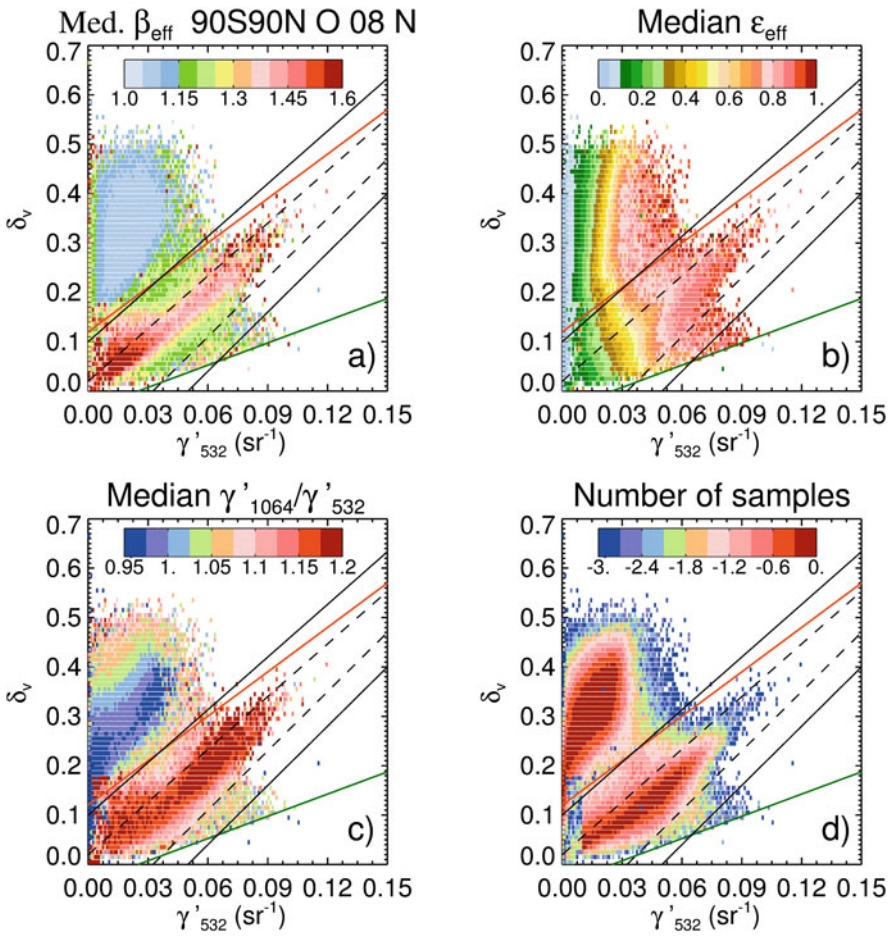


Fig. 105.1 Median IIR β_{eff} index (**a**), median IIR effective emissivity at 12.05 μm (**b**), median lidar color ratio (**c**), and normalized number of samples in logarithm scale (**d**) in nighttime semi-transparent ROIs with T_{base} >233 K and water clouds with T_{top} <273 K over oceans in 2008

105.2.2 Water Clouds

For a more representative analysis of water clouds with T_{top} <273 K, we now examine the opaque water clouds that fully attenuate the lidar laser beam, which represent about 90% of the daytime water clouds over ocean. Noting that a small fraction of these clouds has T_{top} <233 K, with therefore ice expected in the upper portion of the cloud, we examine the location of the water clouds in the updated Hu diagram as a function of T_{top}. Cloud location is expressed as the difference between cloud δ_v and the depolarization ratio ($\delta_{v_wat\text{-}mix}$) at the border between the water region and the ROI-mix region (upper dashed line), computed using γ'_{532} and the

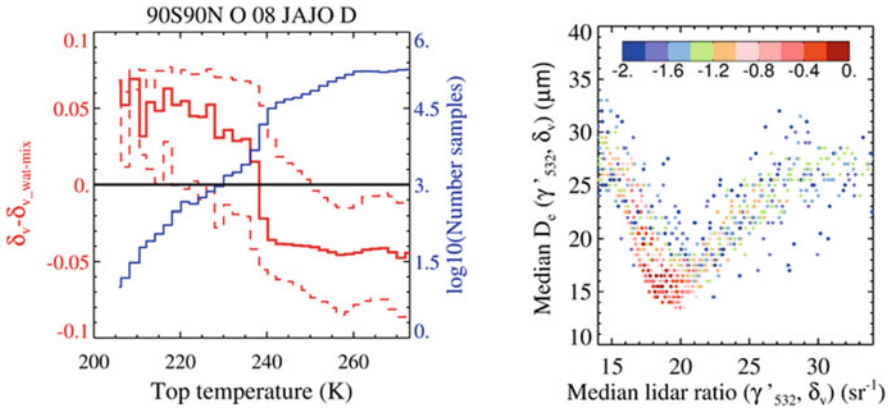


Fig. 105.2 (left) $\delta_v - \delta_{v_wat\text{-}mix}$ (left axis, solid red: median, dashed red: 10th and 90th percentiles) representing the position in the updated Hu diagram and number of samples (blue, right axis) vs. top temperature; (right) IIR D_e vs. lidar ratio colored by normalized number of samples in logarithm scale for daytime oceanic opaque water clouds with T_{top} <273 K in January, April, July, and October 2008

equation given in [2]. As seen in Fig. 105.2 (left), median ($\delta_v - \delta_{v_wat\text{-}mix}$) exhibits a marked change from positive values at T_{top} <238 K (i.e., clouds in the proposed ROI-mix region) to negative values (i.e., clouds in the tight water region) at T_{top} >238 K. In this example, less than 1% of the water clouds with T_{top} <273 K have T_{top} <238 K, but 8% of the water clouds are in the ROI-mix region. Figure 105.2 (right) shows IIR D_e (γ'_{532}, δ_v) vs. lidar ratio (γ'_{532}, δ_v), which, for opaque clouds, is retrieved from the CALIOP extinction algorithm [5], colored by the number of samples in each (γ'_{532}, δ_v) bin. The overall median lidar ratio is 18.6, in agreement with [5]. In the liquid water region, where lidar ratios are between ~14 and ~20 sr, IIR D_e decreases as lidar ratio increases, and reaches its minimum at ~20 sr, in agreement with [2]. IIR D_e increases with lidar ratio larger than 20 sr, which is found in clouds located in the ROI-mix region. This increase of D_e is explained by an increasing contribution of larger ice crystals, thereby confirming the presence of ice in the ROI-mix region proposed by [2].

105.2.3 HOI Clouds

Figure 105.3 shows IIR D_e and the number of samples in opaque ice clouds classified as HOIs in 2007 when the platform tilt angle was 0.3°. They lie in the water and HOI sectors (i.e., under the red line), and their layer centroid temperature is between 233 and 273 K [1], and therefore liquid droplets can be present. For reference, we also added opaque ROIs (above the red line) in the same range of centroid temperature as HOIs. All the clouds in Fig. 105.3 are north of 40° N over

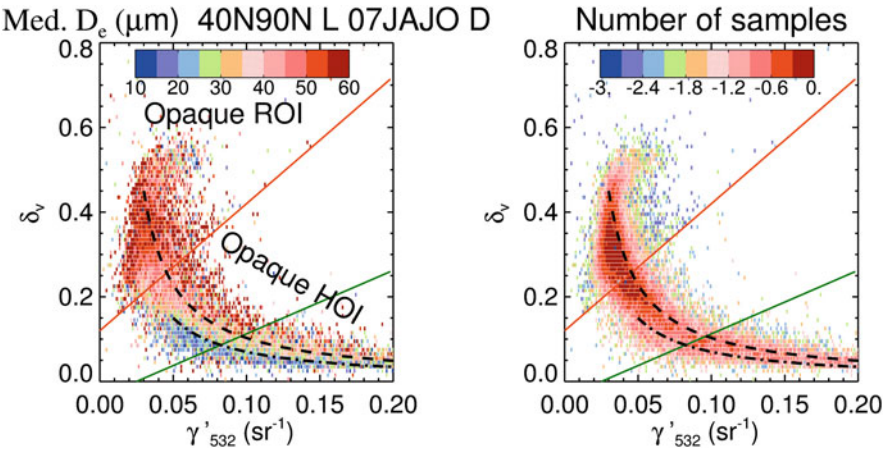


Fig. 105.3 Median IIR D_e (left) and normalized number of samples in logarithm scale (right) in opaque HOIs and ROIs of centroid temperature between 233 and 273 K over land north of 40° N in January, April, July, and October 2007

land, where HOIs are frequently detected in the Northern Hemisphere. Unlike in ROIs, small D_e values (<25 μm) are seen in the HOIs, which are located on an arc starting near the center of the water sector around $\gamma'_{532} = 0.05$ sr^{-1} and $\delta_v = 0.15$ and extending into the HOI sector. These small D_e values are due to large β_{eff} indices as seen in water clouds, which suggests the presence of small liquid droplets. Overplotted are δ_v-γ'_{532} relationships simulated by [6] for pure ice clouds (dashed) and mixed-phase clouds (dot-dashed) of optical depth equal to 4. The mathematical expression is

$$\gamma\prime_{532} = \frac{(\delta_v)_r \cdot (\gamma\prime_{532})_r}{1 + (\delta_v)_r} \cdot \left(1 + \frac{1}{\delta_v}\right), \tag{105.1}$$

where $(\gamma'_{532})_r$ and $(\delta_v)_r$ characterize the observations not impacted by HOIs. The pure ice relationship in Fig. 105.3 is obtained using $(\gamma'_{532})_r = 0.03$ and $(\delta_v)_r = 0.45$ determined from observations at 3° tilt angle, and the mixed-phase relationship is obtained using $(\gamma'_{532})_r = 0.05$ and $(\delta_v)_r = 0.15$. Note that the pure ice relationship is in close agreement with the function derived empirically by [7]. The simulations confirm that the HOI class clusters into two main families of δ_v-γ'_{532} relationships, with mixed-phase clouds where D_e is smaller and pure ice clouds where D_e is larger. Approximately 30% of the HOIs in Fig. 105.3 are identified as mixed-phase clouds, and their layer centroid temperature is (259 ± 5) K.

105.3 Concluding Remarks

Combined with perfectly colocated CALIOP observations, IIR retrievals in the Hu diagrams provide new insights into the identification of mixed-phase clouds. IIR β_{eff} and D_e are unambiguously different in the tight water and ROI-mix regions proposed by [2], and the differences are consistent with these phase differences. Initial analyses in semi-transparent clouds suggest that the color ratio could be used as an efficient indicator when IIR retrievals are not possible or not successful. A fraction (~30 %) of the clouds identified as HOI are actually mixed-phase clouds, which could be identified using δ_v-γ'_{532} relationships, as established by [6], when IIR retrievals are not available.

References

1. Avery, M.A., Ryan, R.A., Getzewich, B.J., Vaughan, M.A., Winker, D.M., Hu, Y., Garnier, A., Pelon, J., Verhappen, C.A.: CALIOP V4 cloud thermodynamic phase assignment and the impact of near-nadir viewing angles. Atmos. Meas. Tech. **13**, 4539–4563 (2020)
2. Mace, G.G., Benson, S., Hu, Y.: On the frequency of occurrence of the ice phase in supercooled Southern Ocean low clouds derived from CALIPSO and CloudSat. Geophys. Res. Lett. **47**, e2020GL087554 (2020)
3. Garnier, A., Pelon, J., Pascal, N., Vaughan, M.A., Dubuisson, P., Yang, P., Mitchell, D.L.: Version 4 CALIPSO Imaging Infrared Radiometer ice and liquid water cloud microphysical properties – Part I: the retrieval algorithms. Atmos. Meas. Tech. **14**, 3253–3276 (2021)
4. Vaughan, M., Garnier, A., Josset, D., Avery, M., Lee, K.-P., Liu, Z., Hunt, W., Pelon, J., Hu, Y., Burton, S., Hair, J., Tackett, J.L., Getzewich, B., Kar, J., Rodier, S.: CALIPSO lidar calibration at 1064 nm: version 4 algorithm. Atmos. Meas. Tech. **12**, 51–82 (2019)
5. Young, S.A., Vaughan, M.A., Garnier, A., Tackett, J.L., Lambeth, J.D., Powell, K.A.: Extinction and optical depth retrievals for CALIPSO's Version 4 data release. Atmos. Meas. Tech. **11**, 5701–5727 (2018)
6. Zhou, C., Yang, P., Dessler, A.E., Hu, Y., Baum, B.A.: Study of horizontally oriented ice crystals with CALIPSO observations and comparison with Monte Carlo radiative transfer simulations. J. Appl. Meteorol Climatol. **51**(7), 1426–1439 (2012)
7. Hu, Y., Vaughan, M., Liu, Z., Lin, B., Yang, P., Flittner, D., Hunt, B., Kuehn, R., Huang, J., Wu, D., Rodier, S., Powell, K., Trepte, C., Winker, D.: The depolarization-attenuated backscatter relation: CALIPSO lidar measurements vs. theory. Opt. Express. **15**, 5327–5332 (2007)

Chapter 106
Huntsville Mobile RO_3QET Launch

Shi Kuang, Mike Newchurch, Paula Tucker, Todd McKinney, Brendan Lee, Susan Alexander, and Casey Calamaio

Abstract We have developed a mobile observation platform, named the Rocket-city Ozone Quality Evaluation in the Troposphere (RO_3QET), for studying air quality and its health impacts. The integrated system consists of an O_3 differential absorption lidar with both vertical and scanning measurement capabilities for measuring O_3 and aerosol profiles, an ozonesonde station, surface O_3 monitors, an unmanned aerial vehicle, and an instrument for regular meteorological observations. Affiliated with the Tropospheric Ozone Lidar Network (TOLNet), this mobile system performs routine operations at its home station, the campus of the University of Alabama in Huntsville, and at field campaign deployments in remote sites. This short chapter reports the capabilities of this new platform and presents some experimental data.

Keywords Lidar · Tropospheric ozone · Aerosol mobile laboratory · Air quality

106.1 Introduction

Tropospheric O_3 is an air pollutant causing negative health impacts on the ground [1] and is also a critical short-lived greenhouse gas impacting climate by contributing to the Earth's global warming. Despite significant regulatory efforts and pollution-control programs developed over the past 20 years in the most densely populated regions of the globe, recent reports of continuing free-tropospheric O_3 increase [2] have triggered the need to enhance our tropospheric O_3 observation capabilities.

The Rocket-city Ozone Quality Evaluation in the Troposphere (RO_3QET) mobile laboratory of the University of Alabama in Huntsville (UAH) is a newly

S. Kuang (✉) · M. Newchurch · P. Tucker · T. McKinney · B. Lee · S. Alexander · C. Calamaio
University of Alabama in Huntsville, Huntsville, AL, USA
e-mail: kuang@nsstc.uah.edu; mike.newchurch@uah.edu; prt0002@uah.edu; tm0155@uah.edu; bjl0017@uah.edu; sa0010@uah.edu; casey.calamaio@uah.edu

© The Author(s), under exclusive license to Springer Nature Switzerland AG 2023

J. T. Sullivan et al. (eds.), *Proceedings of the 30th International Laser Radar Conference*, Springer Atmospheric Sciences,
https://doi.org/10.1007/978-3-031-37818-8_106

developed observation system integrating laser remote sensing, radiosondes, surface observations, and unmanned aerial vehicle (UAV) measurements for convenient deployment in a field campaign. The primary instrument is an O_3 lidar, which also provides routine observations to better understand physical processes driving the O_3 and aerosol budgets in various environmental conditions and to validate the tropospheric O_3 measurements of space-borne missions, such as TEMPO (Tropospheric Emissions: Monitoring of POllution; http://tempo.si.edu) and TROPOMI (TROPOspheric Monitoring Instrument, http://www.tropomi.eu/) [3]. The RO_3QET lidar plays a leading role in the North-American-based Tropospheric Ozone Lidar Network (TOLNet) and is also affiliated with the international Network for the Detection of Atmospheric Composition Change (NDACC).

106.2 Instruments

The instruments of RO_3QET are integrated into a customized, well-engineered container mounted on a Navistar International 4400 heavy-duty chassis, which has two independent 25 kW diesel generators for providing enough power for three lasers, all other instruments, and environmental control. Various laser, optical, and electronic components are mounted on a shock- and vibration-protected T-slotted framing truss.

The O_3 differential absorption lidar in RO_3QET was converted from a fixed-site, vertical lidar previously described by Kuang et al. [4, 5]. The transmitter currently comprises two Raman-shifted lasers at 289 and 299 nm pumped by two 30-Hz, 266-nm Nd:YAG lasers with hardware for a third 283-nm channel also in place. The receiving system for vertical profiling consists of three receivers with diameters of 2.5, 10, and 40 cm, respectively, to cover the measurement range from 0.1 km to about 7 km above ground level (AGL) with a 1-min integration time. A shorter integration time is preferred for mobile measurements because it corresponds to a shorter moving distance resulting in higher horizontal resolution. However, the short integration reduces the maximum measurable altitude due to lower signal-to-noise ratios (SNR). Narrow-band solar filters are employed in the 40-cm receiver to increase the SNR at high altitudes, while wide-band filters are employed in the other receivers. RO_3QET is planned for both vertical and scanning receiving systems. The two systems have different telescopes and, but, share the same transmitter. Switching between them is realized by program-controlled flip mirrors. Because the scanning receiving system is only partially finished, its description will be presented in a later paper.

Table 106.1 lists the major parameters for the RO_3QET instruments. A 2B Model 205 O_3 monitor and a WS700-UMB weather sensor have been installed on the roof of the RO_3QET vehicle for surface measurements. Another smaller-sized O_3 monitor, 2B Personal O_3 Monitor (POM), can be carried by a UAV or

Table 106.1 Specifications of the instruments in RO_3QET

Instrument	Model	Measured variable	Altitude (AGL)	Sampling time	Uncertainty
Lidar	N/A	O_3 number density	0.1–7 km	1 min	10%
		Aerosol backscatter	0.1–7 km	1 min	$5{\cdot}10^{-7}$ m^{-1} sr^{-1}
Ozonesonde	ENSCI 2Z	O_3 number density	0–35 km	~1 s	10%
Radiosonde	iMet	Temperature	0–35 km	1 s	0.5 °C
		Pressure			1 hPa
		Relative humidity			5%
		GPS height			30 m
O_3 monitor	2B 205 dual beam	O_3 mixing ratio	2 m	2 s	1 ppb or 2%
	2B POM	O_3 mixing ratio	On a truck, UAV, or aircraft	2 or 10 s	1.5 ppb or 2%
PM sensor	PlanTower PMS5003	PM concentration	On a truck, UAV, or aircraft	1 s	10%
Weather sensor	Lufft WS700-UMB	Temperature	2 m	1 s	0.5 °C
		Pressure			0.5 hPa
		Relative humidity			2%
		Wind direction			3°
		Wind speed			0.3 m/s or 3%
		Precipitation			20%
		Radiation			5%
GPS sensor	DIYmall VK-162	Latitude	2 m	1 s	5 m
		Longitude			5 m

small, manned aircraft for additional aerial observations. Ozonesonde is a reliable O_3 profiling technique under a variety of weather conditions and RO_3QET carries ozonesonde supplies prepared for launching at any time. Due to the low cost, multiple PlanTower PMS5003 particular matter (PM) sensors can be deployed to different platforms or different locations for intercomparison or studying aerosol horizontal gradients. Previous experiments (e.g., [6]) suggest that PMS5003 sensors exhibit good precision, but its measurement accuracy is highly variable with environmental factors such as humidity and temperature, so a post-correction is typically needed. A Global Positioning System (GPS) sensor has been tested to provide sufficiently accurate latitude and longitude tracking when the vehicle quickly moves.

106.3 Measurements

Figure 106.1 presents an example of RO_3QET measurements made on Alabama highways on April 27, 2022, with a moving speed of about 95 km/h. For a better visual effect, the vertical O_3 and aerosol profiles overlaid on the Google Earth Pro map show only the single trip of the measurements from 15:32 and 16:25 UTC, while the 2-dimensional curtains at the right lower corner show all the data. A 1-min integration time was chosen for the lidar signal detection to obtain a balance

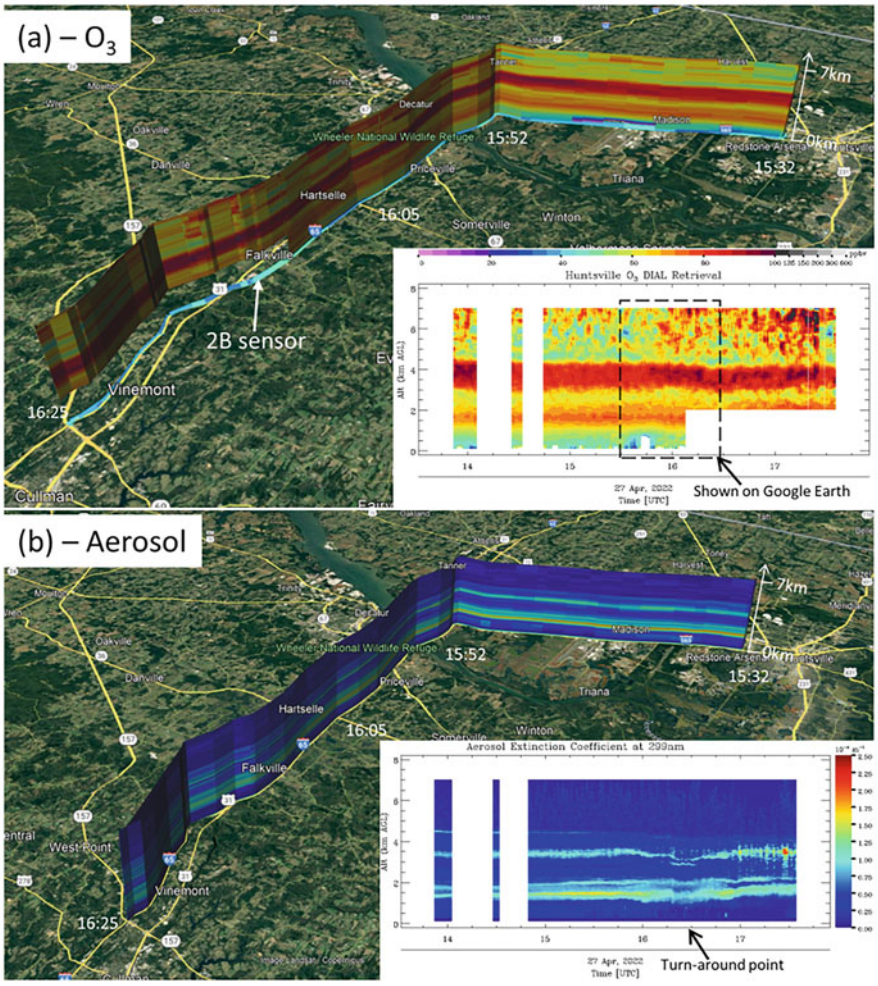


Fig. 106.1 (**a**) O_3 mixing ratios and (**b**) aerosol extinction coefficients measured by RO_3QET on the I-565 and I-65 highways in Alabama on April 27, 2022, showing smoke transported from New Mexico wildfires

between the horizontal resolution and O_3 measurement uncertainties. A 1-min running average was applied on the surface O_3 measured by 2B POM. An iterative computation algorithm is coupled to the ozone lidar retrieval for aerosol profile retrieval with uncertainties arising from assumed aerosol extinction-to-backscatter ratio (or lidar ratio), air density profile, ozone retrievals, and lidar signal detection noise [7]. The aerosol extinction curtain in Fig. 106.1 shows multiple smoke layers between 1 and 4.5 km associated with the New Mexico wildfires based on the analysis of modeling and satellite data. The symmetric aerosol structures with the vehicle turn-around time axis at 16:25 UTC suggest different geographic aerosol distribution (lower smoke altitude in the south) due to the smoke transport processes.

The UAH ceilometer data suggests a daily mixing layer height at about 1 km AGL at noon for this day. Enhanced free-troposphere O_3 associated with the smoke structures is shown by the lidar curtain compared to the PBL O_3 (~50 ppbv). The O_3 data below 2 km after 16:10 UTC is missed because of a movement of an optics element during driving causing misalignment of the absorption line (289 nm) with the 4″ receiver. Besides a higher requirement for vibration and shock protection during fast vehicle movement, we also learned in this experiment that stronger sunlight with the receivers exposed out of the laboratory increased measurement uncertainties for the channels with wideband filters. This may require replacement with narrowband filters or further reduction of the receiver field of view.

106.4 Summary

We have developed a mobile RO_3QET laboratory able to measure O_3 and aerosol profiles with lidar and balloon-borne instruments and in situ with UAVs and surface O_3 and meteorological observations. This system can make routine lidar observations at the host lidar station, measure at a remote site contributing to a field campaign, or measure O_3 and aerosol horizontal gradients while underway on roadways.

References

1. Anenberg, S.C., West, J.J., Fiore, A.M., Jaffe, D.A., Prather, M.J., Bergmann, D., et al.: Intercontinental impacts of ozone pollution on human mortality. Environ. Sci. Technol. **43**(17), 6482–6487 (2009)
2. Wilkins, J.L., de Foy, B., Thompson, A.M., Peterson, D.A., Hyer, E.J., Graves, C., et al.: Evaluation of stratospheric intrusions and biomass burning plumes on the vertical distribution of tropospheric ozone over the Midwestern United States. J. Geophys. Res. Atmos. **125**(18) (2020)
3. Mettig, N., Weber, M., Rozanov, A., Burrows, J.P., Veefkind, P., Smith, N., et al.: Combined UV and IR ozone profile retrieval from TROPOMI and CrIS measurements. Atmos. Measur. Tech. **15**(9), 2955–2978 (2021)

4. Kuang, S., Burris, J.F., Newchurch, M.J., Johnson, S., Long, S.: Differential absorption lidar to measure subhourly variation of tropospheric ozone profiles. IEEE Trans. Geosci. Remote Sens. **49**(1), 557–571 (2010)
5. Kuang, S., Newchurch, M.J., Burris, J., Liu, X.: Ground-based lidar for atmospheric boundary layer ozone measurements. Appl. Opt. **52**(15), 3557–3566 (2013)
6. Malings, C., Tanzer, R., Hauryliuk, A., Saha, P.K., Robinson, A.L., Presto, A.A., Subramanian, R.: Fine particle mass monitoring with low-cost sensors: corrections and long-term performance evaluation. Aerosol Sci. Technol. **54**(2), 160–174 (2020)
7. Kuang, S., Wang, B., Newchurch, M.J., Knupp, K., Tucker, P., Eloranta, E.W., et al.: Evaluation of UV aerosol retrievals from an ozone lidar. Atmos. Measur. Tech. **13**(10), 5277–5292 (2020)

Part X
Model Validation and Assimilation Using Lidar Data

Chapter 107
Retrieval of Aerosol Properties from Multiwavelength Raman Lidar Data Based on Maximum Likelihood Estimation

Yuyang Chang, Qiaoyun Hu, and Philippe Goloub

Abstract An algorithm based on the maximum likelihood estimation (MLE) to retrieve height-resolved aerosol microphysical properties from Mie-Raman lidar measurements is proposed. Compared to the linear inversion methods with regularization, this algorithm greatly reduces the number of individual solutions of the underdetermined lidar inverse system and adds flexibility in incorporating different types of measurements and a priori information. The algorithm is used to retrieve the particle size distribution (PSD), total volume concentration (V_t), effective radius (R_{eff}) and complex refractive index $m = n - ik$ by inverting '$3\beta + 2\alpha$' measurements and the retrieval accuracies with and without the influence of random measurement error are evaluated through numerical simulations. To further examine the performance of the algorithm, it is applied to several aerosol events detected by the Mie-Raman-polarization-fluorescence lidar, LILAS. We conclude that the $3\beta + 2\alpha$ could provide enough information on retrieving PSD, V_t, R_{eff} and the real part of m (n), but the retrieval of the imaginary part of m (k) relies more on a priori information. Moreover, it is also insufficient to calculate the retrieval uncertainty by error propagation.

Keywords Aerosol · Lidar observations · Maximum likelihood estimation

107.1 Introduction

The retrieval of height-resolved microphysical properties of tropospheric aerosol, such as particle size distribution (PSD) and complex refractive index m ($m = n - ik$), is of great interest in the field of aerosol remote sensing since the end of 1990s

Y. Chang (✉) · Q. Hu · P. Goloub
CNRS, UMR 8518-LOA-Laboratoire d'Optique Atmosphérique, Université de Lille, Lille, France
e-mail: yuyang.chang@univ-lille.fr; qiaoyun.hu@univ-lille.fr; philippe.goloub@univ-lille.fr

© The Author(s), under exclusive license to Springer Nature Switzerland AG 2023

J. T. Sullivan et al. (eds.), *Proceedings of the 30th International Laser Radar Conference*, Springer Atmospheric Sciences,
https://doi.org/10.1007/978-3-031-37818-8_107

when accurate extinction (α) and backscattering (β) coefficients were able to be provided by high-performance multiwavelength (MW) Mie-Raman lidars. Retrieval algorithms combining the inversion of Fredholm equations with regularization and the minimum discrepancy method were widely studied and applied to various scenarios in the past two decades. However, the inversion of Fredholm equations only gives a PSD (individual solution) defined in an inversion window $[r_{\min}, r_{\max}]$ and a grid point of m (n, k). Depending on the number of inversion windows and m grid points, thousands of individual solutions could be derived, and it is a challenging task to identify the qualified solutions (solution space) from all the individual solutions due to the underdetermination and ill-posedness of the lidar inverse problem. On the other hand, linear inversion often confronts negative solutions, which is actually incorrect for a PSD. Moreover, with the development of high-performance MW Mie-Raman-polarization-fluorescence lidars like LILAS [1], more sources of measurements are expected either to be directly inverted or to provide constraints to the solution, while it is not flexible enough for the traditional algorithms to take them into account. To this end, we propose a non-linear retrieval algorithm based on maximum likelihood estimation (MLE). Instead of inverting linear Fredholm equations at every m grid point, it simultaneously derives PSD and m by making non-linear fitting of the measurements, which greatly reduces the number of individual solutions and the complexity of identifying the solution space. On the other hand, by regarding a priori constraints as virtual measurements, the underdetermination and ill-posedness decrease to some extent. Besides, non-linear iteration ensures non-negative solutions by implementing logarithmic transformation.

107.2 Methodology

The measurement vectors and constraint vectors can be expressed as

$$\mathbf{y}_l = \mathbf{f}_l(\mathbf{x}) + \boldsymbol{\varepsilon}_l \tag{107.1}$$

where $\mathbf{f}_l(\bullet)$ is the forward model operating on the retrieval parameter vector $\mathbf{x}$ and $\boldsymbol{\varepsilon}$ is the error between the measured values and theoretical values. The subscript l varies from 1 to 3, representing the $3\beta + 2\alpha$ measurements ($l = 1$), smoothing constraints on the PSD ($l = 2$) and a priori information on m ($l = 3$), respectively. The basic idea of the MLE inversion model is to assume the error terms as independent Gaussian errors so that the maximum likelihood function (MLF) of $\mathbf{x}$ is constructed as

$$L(\mathbf{x}) = P(\boldsymbol{\varepsilon}, \mathbf{x}) = \prod_l \frac{1}{(2\pi)^{n/2}|\mathbf{C}_l|^{1/2}} \exp\left\{-\frac{1}{2}\left[\mathbf{y}_l - \mathbf{f}_l(\mathbf{x})\right]^T \mathbf{C}_l^{-1}\left[\mathbf{y}_l - \mathbf{f}_l(\mathbf{x})\right]\right\} \tag{107.2}$$

where $\mathbf{C}_l$ is the covariance matrix of $\boldsymbol{\varepsilon}_l$ and the superscript n is the dimension of $\boldsymbol{\varepsilon}_l$. The retrieval parameter vector can be derived by maximizing the MLF, which is equivalent to minimize the following cost function:

$$\chi^2 = \left[\mathbf{y}_l - \mathbf{f}_l(\mathbf{x})\right]^T \mathbf{C}_l^{-1} \left[\mathbf{y}_l - \mathbf{f}_l(\mathbf{x})\right] \tag{107.3}$$

The minimization procedure is realized by the Levenberg–Marquardt method with the stopping condition $\chi^2(\mathbf{x}^{(i)}) < p - q$ where p and q are the number of total general measurements and the number of retrieval parameters.

We use the spherical and spheroidal scattering model [2] to calculate the $3\beta + 2\alpha$ measurements. For the smoothing constraints on PSD, we limit its second-order difference to vary in a certain neighborhood of 0. The a priori information on m can be obtained from, for example, lidar aerosol typing or back trajectory analysis. To avoid negative solutions, we make the logarithmic transformation similar to [2]. By implementing these steps, the number of individual solutions is greatly reduced and only related to the number of inversion windows. Likewise, the identification of solution space is simple: we select the retrieved PSDs close to a log-normal distribution with small fitting errors and average them to obtain a final unique solution.

107.3 Numerical Simulations

To test the performance of the algorithm, synthetic $3\beta + 2\alpha$ measurements are simulated by aerosol models, which have different refractive indices and whose particle volume size distributions (VSD) conform to the multi-modal log-normal distribution but have different distribution parameters. The VSD can be expressed as

$$v(\ln r) = \frac{dV_t}{d\ln r} = \sum_{i=f,c} \frac{V_i}{\sqrt{2\pi}\sigma_{v,i}} \exp\left[-\frac{\left(\ln r - \ln r_{v,i}\right)^2}{2{\sigma_{v,i}}^2}\right] \tag{107.4}$$

where the subscript i indicates the fine mode ($i = \mathrm{f}$) or coarse mode ($i = \mathrm{c}$). In each mode, V_i represents the volume concentration, $\sigma_{v,i}$ the geometric standard deviation and $r_{v,i}$ the mode radius. We set up 4 types of PVSDs and 25 combinations of (n, k) for the test, which are listed in Table 107.1.

The algorithm is then applied to these synthetic measurements. Fig. 107.1 shows the retrieved VSDs and (n, k)'s for Type 1 and Type 3 when $n = 1.6$ and $k = 0.01$.

It can be seen that although the bimodal distribution of Type 3 is reflected in the averaged solution, the coarse mode shows larger dispersion with the alteration of the inversion window while the fine mode is more stable. The underestimation of both n and k is due to the choice of the a priori values: 1.5 for n and 0.005 for k.

Table 107.1 Aerosol models used for generating synthetic 3β + 2α measurements

VSD parameters	
Type 1	$V_f = 1$, $r_{Vf} = 0.2\ \mu m$, $\sigma_f = 0.4$
Type 2	$V_c = 1$, $r_{Vc} = 1.2\ \mu m$, $\sigma_c = 0.6$
Type 3	$V_f = 2/3$, $r_{Vf} = 0.2\ \mu m$, $\sigma_f = 0.4$, $V_c = 1/3$, $r_{Vc} = 2\ \mu m$, $\sigma_c = 0.6$
Type 4	$V_f = 1/6$, $r_{Vf} = 0.2\ \mu m$, $\sigma_f = 0.4$, $V_c = 5/6$, $r_{Vc} = 2\ \mu m$, $\sigma_c = 0.6$
Complex refractive index m	
n	1.4, 1.45, 1.5, 1.55, 1.6
k	0.001, 0.005, 0.01, 0.015, 0.02

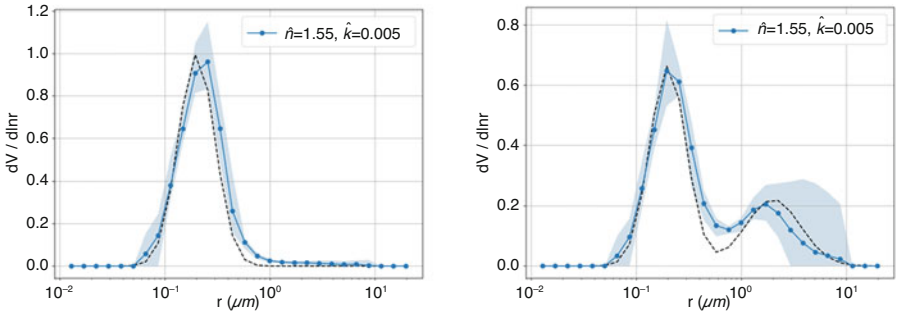


Fig. 107.1 Retrieved final VSDs (solid lines) and refractive indices (the legends) for Type 1 (left) and Type 2 (right) when $n = 1.6$, $k = 0.01$. The shaded areas show the upper and lower boundaries of the solution space. The true distributions are shown in dashed lines

Table 107.2 Third quartile of the retrieval differences of the volume concentration (V), effective radius (r_{eff}), real part (n) and imaginary part (k) of the refractive index for all the cases in Table 107.1

	V	r_{eff}	n	k
Type 1	13%	8%	0.030	49%
Type 2	24%	19%	0.031	43%
Type 3	18%	16%	0.034	55%
Type 4	23%	19%	0.042	55%

The differences of n are shown in absolute values while others are shown in percentage

It reveals that the 3β + 2α measurements are less sensitive to m than VSD in some regions and a priori information on m is important for improving retrieval results.

For each case of retrieval, we compared the difference between the true volume concentration (V), effective radius (r_{eff}) and those calculated from the retrieved VSD, and the difference between the true refractive index and the retrieved one. Table 107.2 shows the third quartile of the differences. We found that fine-mode predominated types (Type 1, Type 3) own better retrieval accuracies of V and r_{eff} than coarse-mode predominated types, while the monomodal types (Type 1, Type 2) have better retrieval accuracies of n and k. Cases with the lowest accuracies appear when $n = 1.4$, $k = 0.001$, where n and k are largely overestimated and have little difference with the a priori values.

Table 107.3 The same as Table 107.2 but under 10% (standard deviation) measurement noise

	V	r_{eff}	n	k
Type 1	26%	21%	0.04	51%
Type 2	24%	22%	0.04	52%
Type 3	25%	28%	0.04	52%
Type 4	35%	36%	0.05	65%

To evaluate the influence of random measurement error, the synthetic measurements were added with 10% (standard deviation) random noise and inverted for 100 times so that there were 10,000 retrievals in total. Similar to Table 107.2, the third quartile of the differences of V, r_{eff}, n and k under measurement noise are listed in Table 107.3. Compared with the results shown in Table 107.2, it can be seen that the aerosol type that provides the best accuracy (i.e., Type 1) when inverting the error-free data is most influenced by measurement error. On the other hand, the imaginary part is the least influenced parameter, proving the poor sensitivity of the measurements to this quantity.

We also explore the possibility of quantifying the influence of measurement error on an individual solution through error propagation. We found when measurements are distorted by less than 10%, the variations of V, r_{eff}, n and k for nearly 90% of the cases in Table 107.1 can be approximated by the first-order differential of the inversion model with accuracy better than 10%. However, when measurement uncertainty is 10%, the difference between the standard deviation estimated by error propagation and that derived from random experiments often exceeds 50%. One important reason is the alteration of the iteration number due to the influence of measurement error.

107.4 Application to Real Lidar Measurements

Here we show an example of applying our algorithm to a smoke event detected by LILAS (LIlle Lidar AtmosphereS), a MW Mie-Raman-polarization-fluorescence lidar developed by Laboratoire d'Optique Atmosphérique, to retrieve the microphysical properties of biomass burning aerosol. The measurements were made from 22:30 UTC 11 to 03:00 UTC 12 September 2020, at University of Lille and biomass burning aerosols from the California wildfire were characterized by lidar aerosol typing and back-trajectory [1]. The left panel of Fig. 107.2 shows the retrieved profiles of V_{t}, r_{eff}, n and k for the measurements, which are typical values for aged biomass burning aerosols whose particles grew and absorption decreases compared to freshly emitted smoke due to the aging effect [1]. The error bars are extracted from Table 107.3, Type 1. The right panel of Fig. 107.2 shows the retrieved VSDs at several distinct layers and the closest AERONET retrieval (L2.0) for comparison.

We also applied our algorithm to other cases, including a retrieval of urban aerosol during the pollen season in Lille and a Saharan dust event in Dakar. The latter was compared with the result retrieved by the regularization method [3], where

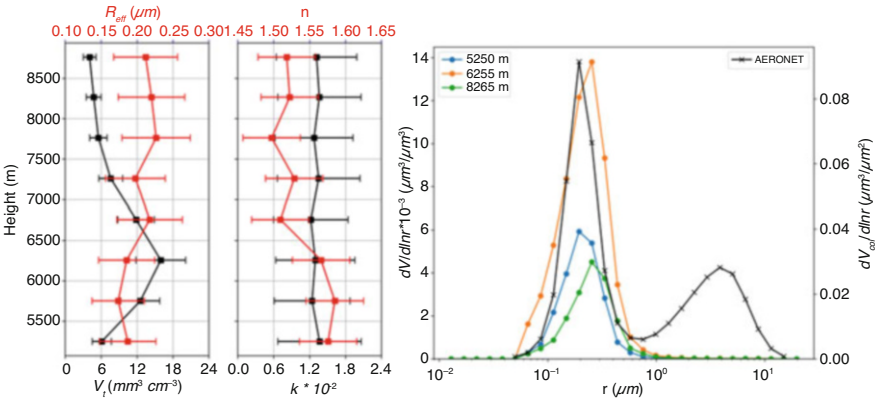


Fig. 107.2 Profiles of retrieved V_t, r_{eff}, n and k for LILAS measurements made during 22:30 UTC 11-03:00 UTC 12 September 2020, at University of Lille (left); retrieved VSDs at 5250 m, 6255 m, 8265 m, together with the AERONET (L2) retrieval on September 11 at 13:55 UTC

good consistency was derived. Furthermore, all the retrieved properties were in accordance with our knowledge of typical aerosol types and were able to reproduce the $3\beta + 2\alpha$ measurements with differences smaller than the expected measurement uncertainty (10%).

107.5 Conclusions

We developed an aerosol retrieval algorithm based on maximum likelihood estimation (MLE) to retrieve microphysical properties of tropospheric aerosol from lidar measurements. Compared with traditional retrieval algorithm based on regularization methods, this algorithm greatly reduces the number of individual solutions and the complexity of identifying solution space. Moreover, it is more flexible to incorporate different types of measurements and a priori information. At present, with this algorithm, we invert the $3\beta + 2\alpha$ lidar measurements to derive particle volume size distribution (VSD) and refractive index m ($m = n + ik$), and integral parameters like volume concentration (V) and effective radius (r_{eff}) are calculated from the retrieved VSD. We tested the algorithm with error-free synthetic measurements and synthetic measurements distorted by random noise with 10% standard deviation. The corresponding retrieval accuracies are summarized in Tables 107.2 and 107.3, respectively. We demonstrated the first-order approximation of the inversion model holds for estimating the variation of retrieval parameters of an individual solution when measurements are distorted by less than 10%. However, when measurement uncertainty is 10%, the information content is insufficient to estimate the retrieval uncertainty of an individual solution. Applications of the algorithm to typical aerosol observation scenarios received satisfying results that

are consistent with other literatures. In the very near future, the first version of the algorithm will be implemented into the AUSTRAL (AUtomated Server for the TReatment of Atmospheric Lidars) processing framework to more efficiently evaluate the code with real lidar data and finally implement automatic retrievals. In parallel, we plan to incorporate more lidar-measured quantities such as spectral depolarization and fluorescence measurements into the MLE algorithmic frame, either as directly invertible measurements or as extra constraints, to improve the retrieval performance and accuracy.

Acknowledgments The authors acknowledge the support of ESA/QA4EO program, CNRS-INSU National Observation Service PHOTONS-AERONET/EARLINET teams, and Lille University for the observation activity at LOA. The authors thank the GRASP team for providing the database of the particle scattering model.

References

1. Hu, Q., Goloub, P., Veselovskii, I., et al.: The characterization of long-range transported North American biomass burning plumes: what can a multi-wavelength Mie-Raman-polarization-fluorescence lidar provide? J. Atmos. Chem. Phys. **22**, 5399–5414 (2022). https://doi.org/10.5194/acp-22-5399-2022
2. Dubovik, O., Sinyuk, A., Lapyonok, T., et al.: Application of spheroid models to account for aerosol particle nonsphericity in remote sensing of desert dust. J. Geophys. Res. **111**, D11208 (2006). https://doi.org/10.1029/2005JD006619
3. Veselovskii, I., Goloub, P., Podvin, T., et al.: Retrieval of optical and physical properties of African dust from multiwavelength Raman lidar measurements during the SHADOW campaign in Senegal. J. Atmos. Chem. Phys. **16**, 7013–7028 (2016). https://doi.org/10.5194/acp-16-7013-2016

Chapter 108
Polarimetric Multiple Scattering LiDAR Model Based on Poisson Distribution

Grégoire Tremblay and Gilles Roy

Abstract Multiple scattering is always present in LiDAR measurements. It is a major cause of signal depolarization in water clouds. For a given probing wavelength, the LiDAR signal is a function of the aerosol size distribution, of the cloud range, of the cloud optical depth, and of the LiDAR Field of View. A relatively simple polarimetric multiple scattering model is presented. It uses Poisson statistics to determine the distribution of the photon's scattering order at a given optical depth and takes into account the aerosol's properties as well as the optical characteristics of the LiDAR. The results are compared with Monte Carlo simulations performed on three cloud types and on a moderate water fog. Good agreement is demonstrated for the total LiDAR signal and the depolarization parameter.

Keywords LiDAR · Scattering · Polarization · Modeling

108.1 LiDAR Poisson Distribution Model

The probability that a photon sustains k forward scattering is expressed by the Poisson distribution

$$Poisson(\gamma, k) = \frac{\gamma^k}{(k)!} exp(-\gamma), \tag{108.1}$$

where γ corresponds to the optical depth. Using the Equivalent Medium Theorem (EMT), we propose a Multiple Scattering LiDAR model (MS LiDAR model here-

G. Tremblay (✉)
RDDC Valcartier, Québec, QC, Canada
e-mail: gregoire.tremblay@DRDC-RDDC.gc.ca

G. Roy
Lidar Consultant, Shannon, QC, Canada

© The Author(s), under exclusive license to Springer Nature Switzerland AG 2023

J. T. Sullivan et al. (eds.), *Proceedings of the 30th International Laser Radar Conference*, Springer Atmospheric Sciences,
https://doi.org/10.1007/978-3-031-37818-8_108

after) that considers forward scattering events followed by a single backscattering toward the detector. The resulting modified Poisson distribution is written as

$$LiPoisson(\gamma, k) = exp(-\gamma)Poisson(\gamma, k) = \frac{\gamma^k}{(k)!}exp(-2\gamma). \tag{108.2}$$

The single scattering LiDAR equation corresponds to $k = 0$ and does not take forward scattering into consideration, just a single backscattering. The higher scattering orders (2, 3, 4, etc.) are obtained for $k = 1, 2, 3 \ldots$

The MS LiDAR model is built on a few premises. (1) The forward scattering phase functions can be modeled by summing two Gaussian curves: one for the forward scattering diffraction peak and one for a round lens geometrical scattering. (2) The backscattering depolarization parameter can be modeled as a function of the forward scattering diffraction peak. (3) The convolution of the forward scattering phase function can model higher forward scattering orders (FSOs). Higher scattering orders generated during propagation are assumed to originate from the optical axis. Forward scatterings do not depolarize the signal. (4) The multiply scattered photons returning to the receiver encountered only one backscattering event. (5) The extra path length produced by multiple scattering is negligible and produces no delay compared to the single scattering return.

Figure 108.1(left) provides the $LiPoisson(\gamma, k)$ distribution. $LiPoisson(\gamma, k)$ contains no information on the nature of the aerosol cloud or on the characteristics of the LiDAR. In order to obtain the LiDAR signal for the different scattering orders, the $LiPoisson(\gamma, k)$ distribution needs to be multiplied by a function, named in here the Backscattering Energy Fraction (BEF_k), that will take into account the aerosol's properties (as defined by the scattering phase function) for a given probing wavelength, the geometry of the LiDAR (mainly the FoV (θ)), and the cloud characteristics (range and optical depth). The LiDAR signal and its perpendicular polarization components for scattering order k are written as the

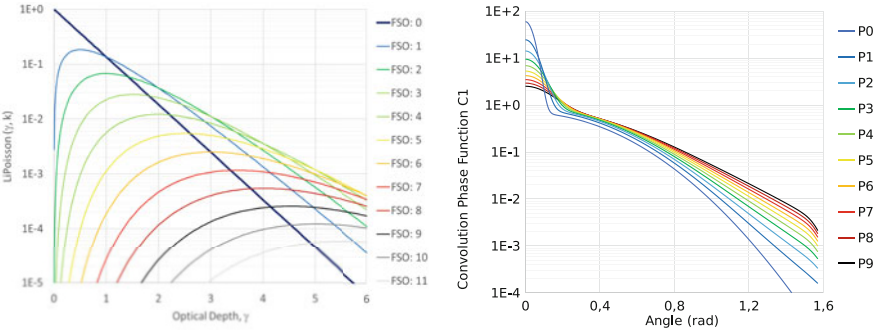


Fig. 108.1 Left: $LiPoisson(\gamma, k)$ scattering order distribution as a function of optical depth for Forward Scattering Orders (FSO) k ranging from 0 to 11. Right: initial phase function p_0 and phase functions of higher scattering orders obtained by convolution for the C1 cumulus water cloud

product of $LiPoisson(\gamma, k)$ with a range-dependent function, $P^*(R)$ and BEF_k. The LiDAR return for the forward scattering order k is

$$P_k(\theta, R_c) = P^*(R_c) \cdot LiPoisson(\gamma, k) \cdot BEF_k(). \tag{108.3}$$

Similarly, the perpendicular component of the LiDAR signal is written as

$$S_k(\theta, R_c) = P^*(R_c) \cdot LiPoisson(\gamma, k) \cdot BEFS_k(), \tag{108.4}$$

with $P^* = P_0^* \cdot \alpha(R_c) \cdot p_0(\lambda, \pi)$ and $P_0^* = P_0 \cdot A/R_c^2 \cdot c\tau/2 \cdot \eta \cdot O(R_c)$. In these expressions, P_0 is the laser pulse power in *watt*, A is the collecting area in m^2, R_c is the cloud base range in m, τ is the pulse duration in s, c is the speed of light in *m/s*, $p_0(\lambda, \pi)$ is the backscattering phase function at λ in sr^{-1}, and $\alpha(R)$ is the extinction coefficient in m^{-1}. $BEFS_k()$ is the backscattering energy fraction for the perpendicular polarization. Taking into account the EMT, the total LiDAR signal is the summation of all the scattering orders k multiplied by 2

$$P(\theta, R_c) = P(R_c) + 2\sum_{k=1}^{k=n} P_k(\theta, R_c), \tag{108.5}$$

where $P(R_c)$ is the single scattering LiDAR signal. Since single scattering occurs at 180°, none is expected in perpendicular polarization and it takes the form

$$S(\theta, R_c) = 2\sum_{k=1}^{k=n} S_k(\theta, R_c). \tag{108.6}$$

The measured depolarization parameter is the ratio of the perpendicular signal over the total signal

$$D = \frac{S(\theta, R_c)}{P(\theta, R_c)}. \tag{108.7}$$

We have $0 < BEF_k(\theta, R, p(r, \lambda)) < 1$, and a value of 1 means that all the backscattered light is collected by the LiDAR. The calculation of $BEF_k(\theta, R, p(r, \lambda))$ is done independently for the different forward scattering orders, k. It bears close resemblance to the calculation of the second-order scattering (one forward scattering followed by a backscattering) with three major differences. First, the higher order phase functions are obtained from convolutions of the aerosol scattering phase function; second, we use the ratio of the extinction over the optical depth, $\alpha(R)/\gamma(R_c)$, for normalization; and third, we use the normalized backscattering phase function, p_0^+ averaged over $\beta_b[165°–180°]$. Using β to define the scattering angle and starting with $k = 1$,

$$BEF_k(\theta, R_c, p(r, \lambda)) = 2\pi \int_{R_a}^{R_c} \int_0^{\theta} \frac{\alpha(R)}{\gamma(R_c)} p_{k-1}(\beta) sin(\beta) p_0^+ dR d\theta. \quad (108.8)$$

The relation between the scattering angle β and the LiDAR FoV θ is

$$\theta = \arctan \frac{(R_c - R)\tan(\beta)}{R_c}. \quad (108.9)$$

$p_{k-1}(\beta)$ is the scattering phase function of order $k-1$. It is obtained by calculating the convolution of the original phase function, $p_0(\beta)$, with the previously calculated phase function of forward scattering order $k-1$:

$$p_k(\beta) = p_{k-1}(\beta) \star p_0(\beta). \quad (108.10)$$

An example of convolution on cumulus water cloud is provided in Fig. 108.1(right).

In order to estimate the depolarization parameter, the MS perpendicular component, $S(\theta, R_c)$, needs to be evaluated. It is expressed as

$$S_k(\theta, R_c) = P_0^* \cdot LiPoisson(\gamma, k) \cdot BEFS_k() \cdot \alpha(R_c) \cdot p_0(\lambda, \pi), \quad (108.11)$$

where

$$BEFS_k(\theta, R_c, p(r, \lambda)) = 2\pi \int_{R_a}^{R_c} \int_0^{\theta} \frac{\alpha(R)}{\gamma(R_c)} p_{k-1}(\beta) sin(\beta) p_\perp^+(\beta_b) dR d\beta, \quad (108.12)$$

and where $p_\perp^+(\beta_b)$ is the perpendicular component of the backscattering phase function, and $\beta_b = \pi - \beta + \theta$. It is calculated using the definition of D_p (Eq. (108.7))

$$p_\perp^+(\beta_b) = D_p(\beta_b) \cdot p_0^+. \quad (108.13)$$

Please note that a full version of the model was published in Applied Optics [1].

108.2 Phase Functions and Depolarization Parameters

The forward Mie phase functions and the backscattering depolarization parameter are modeled as a function of the width of the diffraction peak, β_d. The forward scattering phase function is then written as the sum of two Gaussian curves as shown in Ref. [2]

$$p_0(r, \beta) = \frac{1}{2\pi\beta_d^2} exp\left(-\beta^2/\beta_d^2\right) + \frac{A_g}{2\pi\beta_g^2} exp\left(-\beta^2/\beta_g^2\right), \quad (108.14)$$

where $\beta_d = 0.585(\lambda/2r_e)$, *and* $\beta_g = 0.481$; $A_g = 0.89$. In these expressions, r_e is the effective radius of the aerosol λ is the wavelength, β_d is the width of the phase function diffraction peak, and β_g is the width of the geometrical optics component; units are in *radians*. The detailed development of the depolarization parameter model of $D(\beta, r_e)$ is in Ref. [2].

108.3 Results

The model is applied to calculate LiDAR signals from Cumulus (C1), Stratocumulus (SC), Nimbostratus (NS), and Moderate Water Fog (MWF) [3]. The water clouds are assumed characterized by a gamma size distribution with the parameters listed in Table 108.1. The gamma distribution is of the form

$$n(r) = \frac{b^a}{\Gamma(a)} r^{(a-1)} exp(-br), \tag{108.15}$$

where *n(r)* is the number of droplets of radius *r*, and *a* and *b* are coefficients, whose values are provided in Table 108.1. The other parameters in Table 108.1 are the effective radius r_e, the cloud base R_a, and the cloud top R_t. The extinction is equal to zero at R_a and linearly increases up to R_b until the optical depth equals 0.835 in the interval $[R_a\ R_b]$. The extinction is equal to α from R_b to R_t so that all the clouds have an extinction equal to 5.165 in $[R_b\ R_t]$. The LiDAR operates at 1064 nm, and the value of the averaged normalized backscattering phase function, p_0^+ is 0.77, 0.77, 0.67, and 0.82 for the C1, SC, NS, and MWF cloud types, respectively. Figure 108.2 shows the results for calculations done using a LiDAR FoVs of 1 mrad for all clouds plus 4 mrad for NS, 8 mrad for SC, and 12 mrad for C1 and MWF. The results are compared with Monte Carlo (MC) simulations [4]. The LiDAR signals and the depolarization parameters are plotted as a function of range for the various FoVs. The single scattering Poisson model result is in gray, the model results at various FoVs are in dashed lines, the MC results are in continuous lines, the total LiDAR signal with a 1 mrad FoV is in red, the total LiDAR signal at larger FoV is in blue, the D parameter at 1 mrad is in yellow, and the D parameter at larger FoV is in green. The optical depth (OD) is displayed in black dotted lines. The maximum number Forward Scattering Order (FSO) considered for a given FoV is indicated in the figure caption as FSO=XX.

Table 108.1 The cloud parameters

		b (μm^{-1})	r_e (μm)	R_a (m)	R_b (m)	R_t (m)	α (m^{-1})
C1	7	1.5	5.99	1000	1100	1409	0.0167
SC	3	0.75	6.62	1000	1045	1186	0.0367
NS	3	0.425	11.58	500	519	577	0.0889
MWF	7	3	3	250	431	993	0.0092

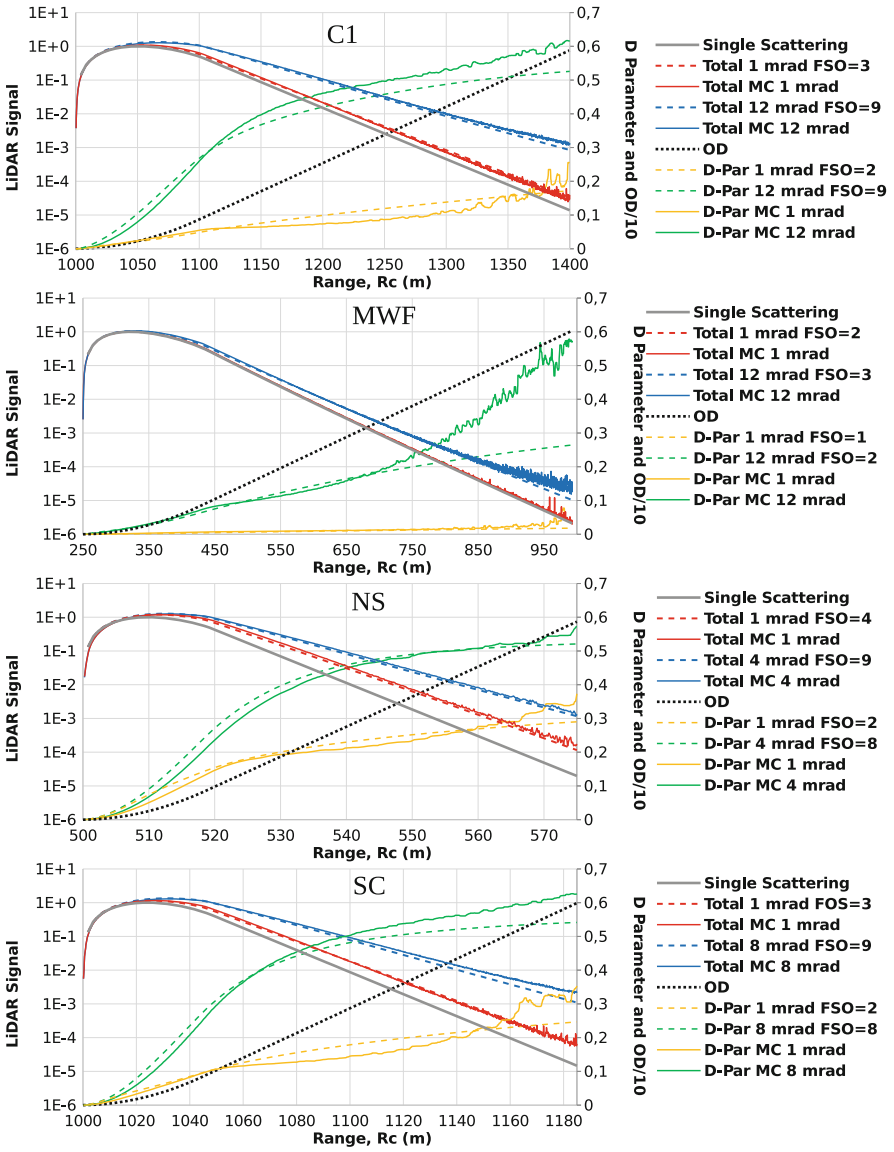


Fig. 108.2 Total LiDAR signals (Total) and depolarization parameters (D-Par) as a function of range for the different FoVs for three types of cloud and a moderate water fog

108.4 Conclusion

The MS LiDAR model based on Poisson statistics combined with the EMT and the specificities of the LiDAR shows good agreement with MC simulations for

various cloud types and FoVs. In its present form, the model assumes the transverse dimension of the receiver's FOV in the cloud is much less than the optical mean free path of photons in the cloud. This is usually the case for ground-based LiDAR but not appropriate for LiDAR measurements from space.

Acknowledgments We would like to thank Luc R. Bissonnette for reviewing the model.

References

1. Roy, G. Tremblay, G.: Polarimetric multiple scattering LiDAR model based on Poisson distribution. Appl. Opt. **61**, 5507–5516 (2022). https://doi.org/10.1364/AO.458566
2. Roy, G., Tremblay, G., Cao, X.: Scattering phase function depolarization parameter model and its application to water droplets sizing using Off-Axis LiDAR measurements at multiple angles. Appl. Opt. **57**(4), 969–977 (2018)
3. Hutt, D.L.: Investigation with Multiple Field of View LiDAR. Ph.D. Thesis Laval University, Québec (1995)
4. Tremblay, G., Roy, G.: High fidelity imaging algorithm for the Undique imaging monte Carlo simulator. EPJ Web of Conferences **119**, 06011 (2016)

Chapter 109
Assimilating Radar and Lidar Observations to Improve the Prediction of Bore Waves During the 2015 PECAN Field Campaign

Zhifeng Yang, David N. Whiteman, Xingchao Chen, Yunji Zhang, Belay Demoz, Jose D. Fuentes, Charles Ichoku, and Joseph L. Wilkins

Abstract The assimilation of radar reflectivity and radial velocity from the WSR-88D radar and lidar water vapor profile observations could improve the forecast of location and timing of bore associated with nocturnal convection. This study describes the assimilation of such data observed during the 2015 Plains Elevated Convection at Night (PECAN) field campaign. The model and data assimilation system employed is the Pennsylvania State University Weather Research and Forecasting model Ensemble Kalman Filter (PSU-WRF-EnKF) cycling data assimilation system. The lidars include the Atmospheric Lidar for Validation, Interagency Collaboration and Education (ALVICE), University of Wyoming King Air compact Raman lidar, Atmospheric Radiation Measurement (ARM) Raman lidar, and National Center for Atmospheric Research (NCAR) micropulse Differential Absorption Lidar (DIAL). The bore propagation was observed by both radar and ALVICE lidar in Kansas, on 14 July 2015, and a nocturnal convection initiated near the bore/density current. Without assimilating any observations, the WRF model didn't well simulate the location of the bore, even though it captured the bore structure quite well. The assimilation of WSR-88D radar observations improved the location and timing forecasts of the nocturnal convection and the associated bore.

Z. Yang (✉) · D. N. Whiteman · C. Ichoku · J. L. Wilkins
Howard University, Washington, DC, USA

X. Chen · Y. Zhang · J. D. Fuentes
Penn State University, State College, PA, USA
e-mail: xzc55@psu.edu; juf15@psu.edu; yuz31@psu.edu

B. Demoz
University of Maryland Baltimore County, Baltimore, MD, USA
e-mail: bdemoz@umbc.edu

Joint Center for Earth Systems Technology, Baltimore, MD, USA
e-mail: bdemoz@umbc.edu

© The Author(s), under exclusive license to Springer Nature Switzerland AG 2023

J. T. Sullivan et al. (eds.), *Proceedings of the 30th International Laser Radar Conference*, Springer Atmospheric Sciences,
https://doi.org/10.1007/978-3-031-37818-8_109

Keywords PECAN · EnKF · Radar · Lidar · Reflectivity · Radial Velocity · Water Vapor

109.1 Introduction

109.1.1 Bore

A bore is a wave disturbance that can occur in air and water and is often manifested as in surface observations as a pressure jump of up to 2 mb in a very short time (<5 min) and accompanied with atmospheric undulations (hence undular bore). Bore waves are generated by the movement of density current and its collision with a stable air mass often in the warm and moist sector of the atmosphere (Fig. 109.1a). The collision leads to the surface becoming colder than the upper layer air, which forms the more stable inversion layer (Fig. 109.1b) and hence a conduit for the wave to travel ahead of the frontal surface. Bore can be related to severe weather as they can initiate thunderstorms when interacting with mountains, which helps to initiate thunderstorms. This work is among the very few studies, if not the only, that assimilates radar and lidar profiles of a bore wave case from the Plains Elevated Convection at Night (PECAN) data sets.

To forecast bores accurately, Johnson et al. [11] suggested three main ingredients to resolve the evolution of the nocturnal boundary layer and low-level jet, and a correct forecast of the formation, location, temperature profile, and depth of the density current. First, it is the accurate forecast of the surrounding mesoscale environment of the bore, e.g., the Froude number of the undisturbed fluid, the depth of the obstacle, and the depth of the undisturbed stable fluid, which contribute to the bore amplitude. Second, it is the accurate forecast of the parent convection that generates the density current. This study satisfies this requirement by initializing with global analysis data and assimilating conventional and radar data. Third, it is

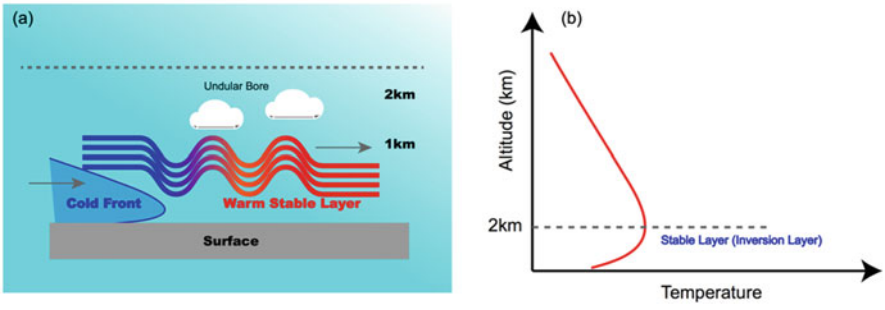


Fig. 109.1 (**a**) Schematic representation of the collision between cold front and warm stable layer in the atmosphere. (**b**) Atmospheric temperature vertical profile

the sufficiently fine model grid spacing to resolve the bore structure. The previous studies showed the grid spacing should be around 1–2 km to resolve the horizontal wavelength of bore.

109.1.2 Radar and Lidar Assimilation

The Weather Surveillance Doppler Radar (S-band Doppler weather radar, WSR-88D) radial velocity assimilation can improve and benefit tropical cyclone position and intensity, and its forecasts are superior to simulations without radar data assimilation [8], and the tornadic supercell thunderstorm [9]. Zhang et al. [9] evaluated the performance by assimilating radar reflectivity and radial velocity separately and jointly and found the improvements of clouds analysis by assimilating reflectivity alone or both reflectivity and radial velocity. However, the forecasts of the radar data assimilations, both separate and joint assimilations, failed to capture the initiation and evolution stages of storms.

To resolve the fine-scale processes within the planetary boundary layer (PBL), active remote-sensing lidar (e.g., Raman lidar) observations at high temporal and vertical resolutions are used for both temperature and water vapor profiles [7]. The high accuracy avoids the need for a challenging data bias correction. The high temporal resolution estimates the representativeness errors in the study region, which facilitates the research on the statistics of turbulent fluctuations, covariances, and fluxes, and the subgrid-scale variability. The lidar water vapor profiles assimilation improves the root mean square error (RMSE) when comparing against independent radiosonde water vapor observations [12].

109.1.3 Motivations and Novelty

PECAN focuses on improving the understanding and simulation of the processes that initiate and maintain convection and convective precipitation at night over the central portion of the Great Plains region of the United States. The motivation of this work is to improve the understanding and forecasting skill of nocturnal convection initiation by assimilating Doppler weather radars and ground-based remote sensing profilers that affect the forecasts of bore-related convection.

This study explores the impacts and benefits of ensemble-based assimilation on assimilating Doppler weather radar reflectivity and radial velocity, lidar water vapor vertical profile to capture bore waves. The novelty of this study is employing lidar water vapor assimilation and coupling with radar and Raman lidar assimilation. The objective is to better understand the strength and limitations of each observation type, by assimilating Doppler weather radar and Raman lidar separately and jointly.

109.2 Data Sets and Model Configuration

109.2.1 NEXRAD Radar and Raman Lidar Data

WSR-88D radar can detect precipitation and wind, and its data can be processed to map precipitation patterns and movement. The radar sites used in this study are shown as red dots in Fig. 109.2.

This study also utilizes water vapor vertical profile measurements from four lidars, i.e., ALVICE lidar, NCAR DIAL lidar, University of Wyoming King Air Compact Raman Lidar (CRL) lidar, and ARM Raman lidar. Figure 109.2 shows the lidar locations in blue squares. The flight paths of the University of Wyoming King Air are also indicated as color lines (Fig. 109.2). More detailed set up for PECAN and associated instrument and data is discussed in Geerts et al. [2].

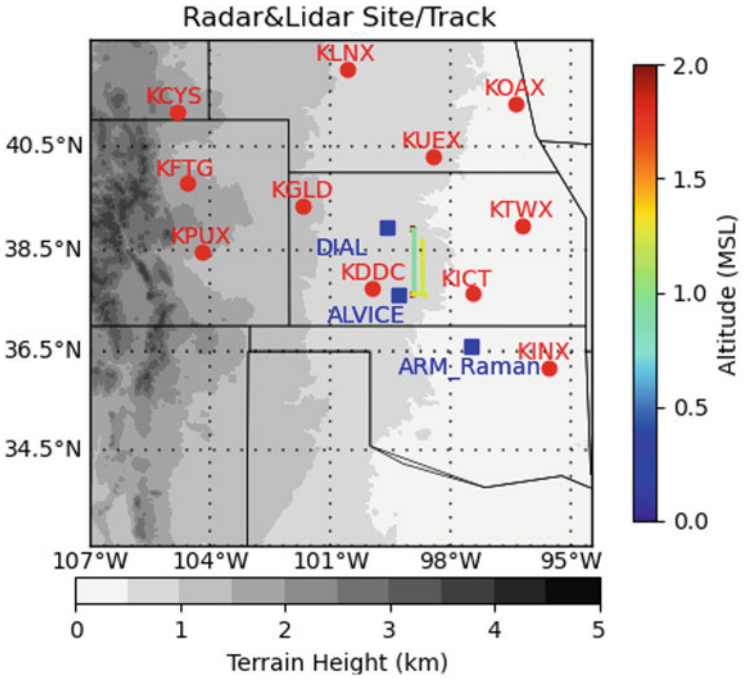


Fig. 109.2 Terrain height (kilometers above sea level, ASL) in the study domain (white-black contour), overlaid with the radar sites (red dots with site names), lidar sites (blue squares with lidar names), and University of Wyoming King Air flight paths (color-coded line shows the flight path height)

109.2.2 Study Domain and Model Configuration

The model domain includes Nebraska, Kansas, Colorado, Oklahoma, and north Texas (Fig. 109.2). To the west of the domain are the Rocky Mountains (3 km terrain height) and to the east are the central plains (0.5 km terrain height). The horizontal grid spacing is 3 km and 51 vertical levels are used. The highest model level is located at 50 hPa, and 19 vertical levels in the lowest 1 km above ground level (AGL) are designed to resolve the PBL.

The Advanced Research core of the Weather Research and Forecasting (WRF-ARW) model version 3.8.1 has been employed in this study. Physical parameterizations used are listed below. Physical parameterization schemes applied in the model include the six-species double-moment Thompson et al. [5] microphysics scheme, unified Noah land surface model, Monin–Obukhov–Janjic′ Eta scheme for surface layer parameterization, and Mellor–Yamada–Janjic′ TKE scheme for PBL processes. The longwave and shortwave radiation schemes are the Rapid Radiative Transfer Model for General Circulation Models (RRTMG) schemes. Simulated radar reflectivity is calculated using the built-in module of the Thompson et al. [5] microphysics scheme.

109.2.3 Data Assimilation System

The Pennsylvania State University Weather Research and Forecasting model Ensemble Kalman Filter (PSU-WRF-EnKF) cycling data assimilation system was developed by Meng and Zhang [3, 4] and Zhang et al. [8]. The EnKF method employed in this study is the serial EnKF with square root modification, called Ensemble Square Root Filter (EnSRF, [6]). To avoid filter divergence, the relax-to-prior-perturbation (RTPP) technique and Gaspari and Cohn [1] localization were used. The horizontal and vertical radii of influence (ROI) are 10 km and 10 model levels (Radar) and 100 km and 10 model levels (Lidar), respectively.

109.3 Experiment Design

The ensemble WRF model was initiated from 1800Z July 13, 2015 (Fig. 109.3). The first 20 members are the GEFS analyses at 18Z July 13, 2015. The rest 20 members are generated from the 6-hour GEFS forecast initialized from 12Z July 13, 2015. The first eight-hour model simulations are treated as spin-up and discarded (until 0200Z July 14, 2015). The conventional surface data assimilation is from 0200Z to 0600Z and assimilated every 20 min (equal to report interval of METAR stations). Other assimilated observations are the following. The radar data assimilation starts at 0200Z and lasts until 0600Z. The assimilation window is 5 min. The assimilated

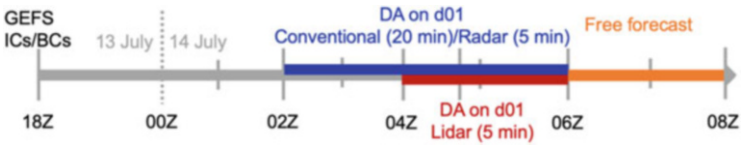


Fig. 109.3 Timeline of model spin-up, the data assimilation cycling, and ensemble free forecasts

Table 109.1 Designed experiments

Experiment	DA (Y or N)		Model performance
Spin-up: 18Z 13 July	Domain 01 (d01, 3 km)	Domain 02 (d02, 1 km)	d01: mesoscale meteorology d02: bore wave
Baseline	Y	N	C: temperature, wind, pressure
RAD	Y	N	C & R: reflectivity, radial velocity
LID	Y	N	C & L: water vapor mixing ratio
RADLID	Y	N	C, R & L

Y Yes, *N* No, *C* Conventional, *R* Radar, *L* Lidar

variables include radial velocity and reflectivity. The lidar assimilation starts from 0400Z to 0600Z. The free forecast is from 0600Z to 0800Z, which is used to evaluate the radar and lidar data assimilation performance.

The designed experiments are shown in Table 109.1. The baseline experiment is to test the performance only assimilating conventional meteorological observations (e.g., buoy, ship, and radiosonde). The RAD experiment is to verify the performance of assimilating both conventional meteorological observations and radar reflectivity and radial velocity. The LID experiment is to check the assimilating lidar water vapor mixing ratio observations. Finally, the RADLID experiment is to examine the performance of assimilating all the observation data.

109.4 Preliminary Results

Without assimilating radar data, the ensemble model simulation shows spurious clouds over Colorado (Fig. 109.4b, c), which is significantly stronger than the radar observed composite reflectivity (Fig. 109.4a). At 0500Z July 14, 2015, after 3-h assimilation of radar reflectivity and radial velocity (36 assimilation cycles), the model simulated composite reflectivity appears similar to the real radar observation (Fig. 109.4d, f), which means EnKF is successfully assimilating radar data into the WRF model. However, the radar assimilation didn't realistically capture the clouds over eastern Kansas. The possible reason is that all the ensemble members did not capture this short life-time cloud system (0000Z-0400Z July 14, 2015). After three hours of the assimilation, the spurious clouds occurred at the southern Colorado, primarily due to the fact that even the lowest radar scan at 0.58 elevation angle

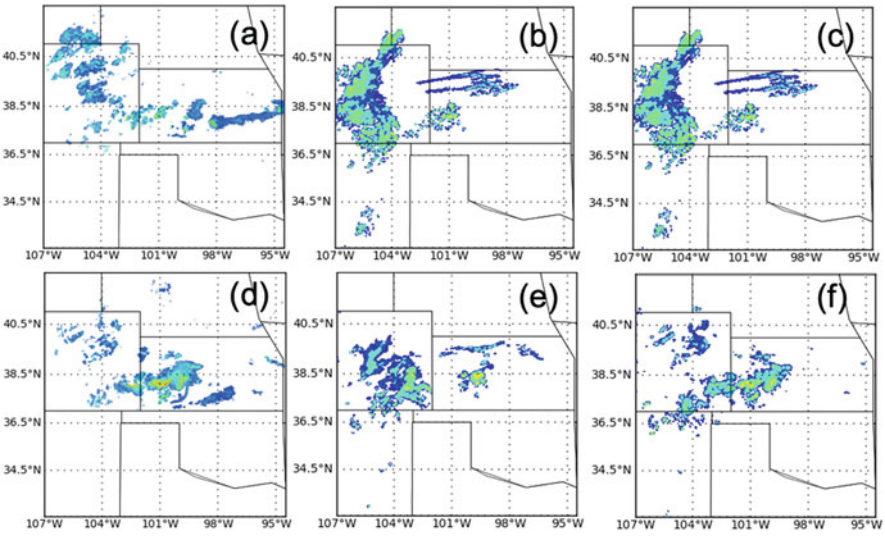


Fig. 109.4 Composite reflectivity from NEXRAD radar (first column), ensemble model simulation (second column), and radar assimilation (third column, RAD). The first to second rows are at 0200Z (**a**, **b**, **c**) and 0500Z (**d**, **e**, **f**) July 14, 2015, respectively

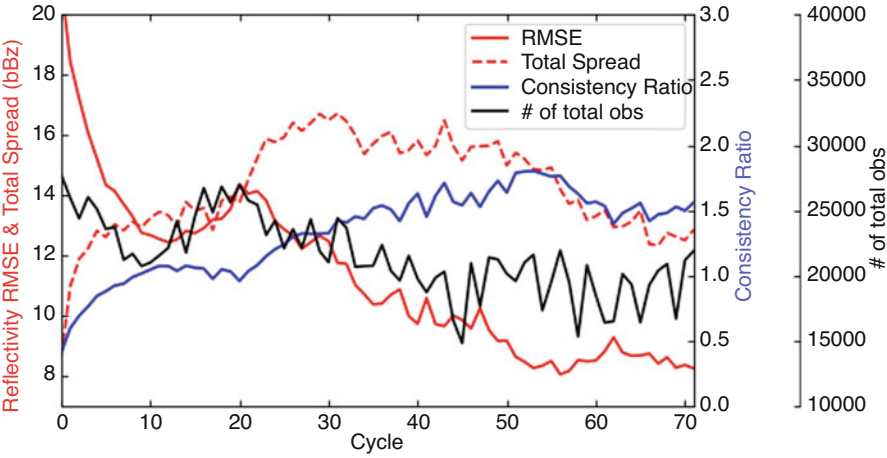


Fig. 109.5 Evolution of RMSE (solid red line), total spread (dashed red line), consistency ratio (solid blue line), and the number of total radar observations (solid black line) for reflectivity

can be 1–2 km above the surface in regions 100–200 km away from the radar site, and there are no radar observations available to remove the excessive amount of hydrometeors near the surface [9].

The diagnostics of radar assimilation performance can be quantified by the following statistical metrics, e.g., RMSE, total spread (defined as the square root of both model spread and observation spread), and consistency ratio [10]. Figure 109.5

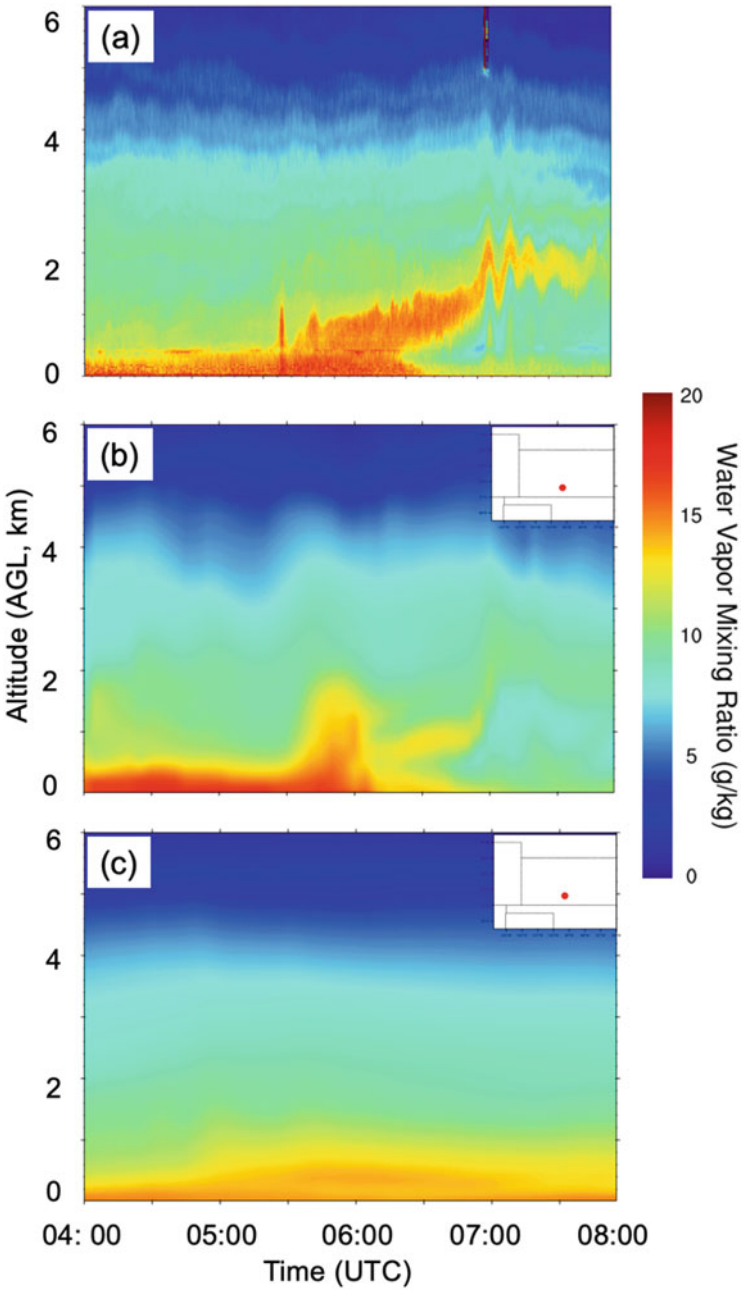


Fig. 109.6 Water vapor mixing ratio vertical profile time series from ALVICE lidar observation (**a**), model with radar assimilation (**b**), and model without radar assimilation (**c**). The inset map on the upper right shows the location of FP2. *UTC* Coordinated Universal Time

shows the evolution of these statistical metrics for reflectivity. The reflectivity RMSE decreases consistently from 20 dBZ at the first assimilation cycle to 8 dBZ at the last assimilation cycle (Fig. 109.5a), which means the model simulation is approaching the radar observed reflectivity. The total spread keeps around 10~16 dBZ. Consequently, the consistency ratio stays around 1.0~1.5 through the whole assimilation period. Meanwhile, the number of total radar observations is around 20000.

After assimilating radar data, the water vapor field is expected to better agree with the lidar observations. The ALVICE water vapor and model simulated water vapor vertical profiles from both with and without radar assimilation are presented in Fig. 109.6. ALVICE observed water vapor was 20 g kg^{-1}, which was concentrated below 1 km before it was lifted up at 0630Z. Bore wave occurred at 0700Z as a result of gravity and lifting force. The equilibrium height is 1.8 km, and wave amplitude is about 0.5 km (Fig. 109.6a). After assimilating ALVICE lidar water vapor profiles, air was lifted to 0.5 km. Wave pattern can be observed in Fig. 109.6b. The water vapor vertical profile time series from model simulation without radar observations assimilated shows the flat water vapor distribution below 1 km, with water vapor mixing ratio around 13 g kg^{-1} (Fig. 109.6c).

109.5 Conclusions

The assimilation of radar reflectivity and radial velocity helps model correct the location and structure of MCS and reduces the convection intensity. The statistical metrics indicates that reflectivity RMSE is reduced substantially from the beginning of radar assimilation to the end of radar assimilation, and its consistency ratio stays stable. Meanwhile, the assimilation of radar observations also corrects the water vapor vertical profile, when compared with the ALVICE lidar observed water vapor mixing ratio.

Acknowledgment The National Science Foundation supported this research (Award AGS 2000103). We would like to acknowledge high-performance computing support from Cheyenne (doi:10.5065/D6RX99HX) provided by NCAR's Computational and Information Systems Laboratory, sponsored by the National Science Foundation. B. Demoz, J. Fuentes, and C. Ichoku acknowledge support from the NOAA Educational Partnership Program with Minority Serving Institutions (NOAA/EPP/MSI) under Agreement no. NA16SEC4810006 (NCAS-M).

References

1. Gaspari, G., Cohn, S.E.: Construction of correlation functions in two and three dimensions. Q. J. R. Meteorol. Soc. **125**, 723–757 (1999). https://doi.org/10.1002/qj.49712555417
2. Geerts, B., Parsons, D., Ziegler, C.L., Weckwerth, T.M., Biggerstaff, M.I., Clark, R.D., Coniglio, M.C., Demoz, B.B., Ferrare, R.A., Gallus Jr., W.A., Haghi, K.: The 2015 plains elevated convection at night field project. Bull. Am. Meteorol. Soc. **98**(4), 767–786 (2017). https://doi.org/10.1175/BAMS-D-15-00257.1

3. Meng, Z., Zhang, F.: Tests of an ensemble Kalman filter for mesoscale and regional-scale data assimilation. Part III: comparison with 3DVAR in a real-data case study. Mon. Wea. Rev. **136**, 522–540 (2008a). https://doi.org/10.1175/2007MWR2106.1
4. Meng, Z., Zhang, F.: Tests of an ensemble Kalman filter for mesoscale and regional-scale data assimilation. Part IV: comparison with 3DVAR in a month-long experiment. Mon. Wea. Rev. **136**, 3671–3682 (2008b). https://doi.org/10.1175/2008MWR2270.1
5. Thompson, G., Field, P.R., Rasmussen, R.M., Hall, W.D.: Explicit forecasts of winter precipitation using an improved bulk microphysics scheme. Part II: implementation of a new snow parameterization. Mon. Wea. Rev. **136**, 5095–5115 (2008). https://doi.org/10.1175/2008MWR2387.1
6. Whitaker, J.S., Hamill, T.M.: Ensemble data assimilation without perturbed observations. Monthly weather review. **130**(7), 1913–1924 (2002). https://doi.org/10.1175/1520-0493(2002)130<1913:EDAWPO>2.0.CO;2
7. Whiteman, D.N., Demoz, B., Rush, K., Schwemmer, G., Gentry, B., Di Girolamo, P., Comer, J., Veselovskii, I., Evans, K., Melfi, S.H., Wang, Z.: Raman lidar measurements during the international H2O project. Part I: instrumentation and analysis techniques. J. Atmos. Ocean. Technol. **23**(2), 157–169 (2006). https://doi.org/10.1175/JTECH1838.1
8. Zhang, F., Weng, Y., Sippel, J.A., Meng, Z., Bishop, C.H.: Cloud-resolving hurricane initialization and prediction through assimilation of Doppler radar observations with an ensemble Kalman filter. Mon. Wea. Rev. **137**, 2105–2125 (2009). https://doi.org/10.1175/2009MWR2645.1
9. Zhang, Y., Stensrud, D.J., Zhang, F.: Simultaneous assimilation of radar and all-sky satellite infrared radiance observations for convection-allowing ensemble analysis and prediction of severe thunderstorms. Mon. Wea. Rev. **147**(12), 4389–4409 (2019). https://doi.org/10.1175/MWR-D-19-0163.1
10. He, J., Zhang, F., Chen, X., Bao, X., Chen, D., Kim, H. M., Yang, K.: Development and evaluation of an ensemble-based data assimilation system for regional reanalysis over the Tibetan Plateau and surrounding regions. J. Adv. Model. Earth Syst. **11**(8), 2503–2522 (2019). https://doi.org/10.1029/2019MS001665
11. Johnson, A., Wang, X., Haghi, K.R., Parsons, D.B.: Evaluation of forecasts of a convectively generated bore using an intensively observed case study from PECAN. Mon. Weather Rev. **146**(9), 3097–3122 (2018). https://doi.org/10.1175/MWR-D-18-0059.1
12. Thundathil, R., Schwitalla, T., Behrendt, A., Wulfmeyer, V.: Impact of assimilating lidar water vapour and temperature profiles with a hybrid ensemble transform Kalman filter: Three-dimensional variational analysis on the convection-permitting scale. Q. J. R. Meteorol. Soc. **147**(741), 4163–4185 (2021). https://doi.org/10.1002/qj.4173

Part XI
Joint CLRC-ILRC Session: Past, Present and Future Synergy of Heterodyne and Direct Detection Lidar Applications

Chapter 110
First Discovery of Regular Occurrence of Mid-Latitude Thermosphere-Ionosphere Na (TINa) Layers Observed with High-Sensitivity Na Doppler Lidar and New Data Processing Techniques over Boulder

Yingfei Chen and Xinzhao Chu

Abstract We report the first discovery of regular occurrence of mid-latitude thermosphere-ionosphere Na (TINa) layers (110–150 km) over Boulder (40.13°N, 105.24°W), Colorado. Detection of tenuous Na layers (~0.1–1 cm^{-3} from 150 to 130 km) was enabled by high-sensitivity Na Doppler lidar. A new data processing technique is applied to pave the way for the discovery, which is Na volume mixing ratio calculations. For the first time, TINa layers are observed occurring regularly in various months and years, descending from ~125 km after dusk and from ~150 km before dawn. About 7 years of lidar observations reveal Boulder TINa dawn layers with nearly 100% occurrence rate (160 out of 164 nights of observations). These layers provide a natural laboratory for studying the ion-neutral coupling and act as tracers for extending the profiling of neutral wind and temperature into the E to lower F regions. Such potentials offered by the TINa layers promote future advancement of lidar technologies for even higher detection sensitivities to enable new science endeavors.

Keywords High-sensitivity Na Doppler lidar · Thermosphere-ionosphere Na (TINa) layers · Volume mixing ratio calculations

Y. Chen (✉) · X. Chu
Cooperative Institute of Research in Environmental Sciences & Department of Aerospace Engineering Sciences, University of Colorado Boulder, Boulder, CO, USA
e-mail: Yingfei.Chen@colorado.edu; Xinzhao.Chu@colorado.edu

© The Author(s), under exclusive license to Springer Nature Switzerland AG 2023

J. T. Sullivan et al. (eds.), *Proceedings of the 30th International Laser Radar Conference*, Springer Atmospheric Sciences,
https://doi.org/10.1007/978-3-031-37818-8_110

110.1 Introduction

Thermosphere-ionosphere metal (TIMt) layers were discovered at McMurdo, Antarctica in 2011 by Chu et al. [1]. TIMt is an intriguing phenomenon because these layers provide a natural laboratory and tracer to study the complicated space-atmosphere interactions in the thermosphere and ionosphere in the upper atmosphere. TIMt layers have been observed in the neutral Fe (iron, TIFe), Na (sodium, TINa), and K (potassium, TIK) species in both the polar and tropical regions but quite rarely at midlatitudes until 2021 when regular occurrence of TINa layers was discovered with a high-sensitivity Na Doppler lidar at Boulder [2]. This paper will introduce why we could discover the TINa layers occurring regularly before dawn and after dusk every night for the first time in the world. The reported layers are tenuous, and their detection is enabled by a Na Doppler lidar developed at the University of Colorado Boulder, which possesses very high detection sensitivity. Moreover, to observe those layers clearly, a new data processing technique is applied, and this creative method also helps us to figure out the regular occurrence of TINa layers. Boulder TINa layer extends the ground-based lidar observations into the space, i.e., in the E to lower F regions (~100–200 km altitude) where measurements of the neutral atmosphere are scarce but plasma-neutral interactions are rich. These layers themselves also pose intriguing questions about the mechanisms of ion transport, as leading theories hypothesize that such neutral TINa layers are formed via the neutralization of converged $TINa^{+}$ ion layers.

110.2 Methodology

After more than 30 years of lidar observations at mid-latitudes, only intermittent occurrence of TINa layers in the 100–200 km was reported from a few observations until 2021. The first discovery of regularly occurring mid-latitude TINa layers was made over Boulder, Colorado [2]. For the first time, Na layers have been observed regularly descending from ~125 km after dusk and from ~150 km before dawn shown in Fig. 110.1 left column. Such regular occurring observations are challenging as they demand high detection sensitivity of lidars and creative data processing techniques. Only by combining the two can this decades-long problem be solved. We discuss both aspects here.

110.2.1 Why High Sensitivity Is a Must?

The TINa detection is difficult because such low density demands very high detection sensitivities (better than 0.1 cm^{-3}). Most Na lidars operated in the world

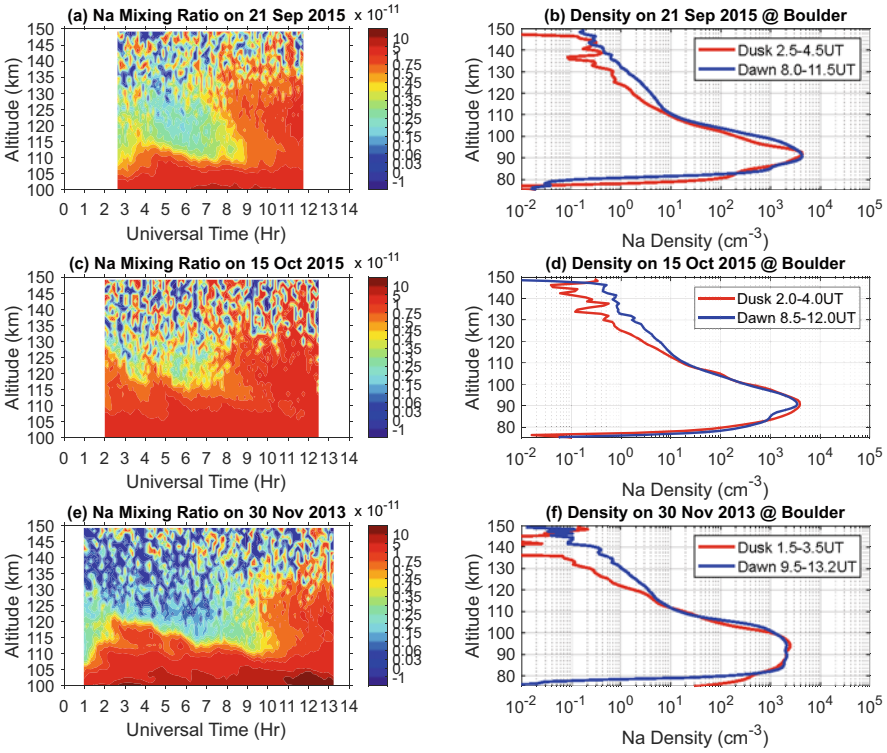


Fig. 110.1 Na Doppler lidar observations of thermosphere-ionosphere Na layers at Boulder over multiple nights. (left) Na volume mixing ratio plotted in uneven color scales. (right) Vertical profiles of Na density for dusk (red) and dawn (blue) layers at Boulder. The Na densities and mixing ratios were derived at resolutions of 7.5 min and 0.96 km

have detection limits above a few cm^{-3} and signal levels well below that achieved by the STAR lidar [3], so TINa signals would be buried in their background noise. Indeed, an earlier version of the STAR lidar, before it was upgraded to high sensitivity, could not detect TINa layers above 115 km [4]. Therefore, it is understandable why many years of lidar observations at midlatitudes did not discover such TINa layers until Chu, Chen et al. [2].

Hence, achieving such high sensitivity will be a very important factor to make TINa observations. Our observations were made at Table Mountain Observatory (40.13°N, 105.24°W), north Boulder with an advanced resonance-fluorescence lidar—the Student Training and Atmospheric Research (STAR) Na Doppler lidar. In order to enable the detection of tenuous Na layers, it uses an 81-cm diameter prime-focus Newtonian telescope with high-efficiency receiver architecture [3] and employs a narrowband laser transmitter tuned to the D2a line at 589 nm [5]. Laser transmitter was updated to improve Na signal levels by 20–50 times, to ~1000–2000 counts per laser shot in summer 2011, enabling high-sensitivity detection. Such

high-quality measurements of vertical winds and temperatures in the mesopause region were used in studies of high-to-medium frequency gravity waves [6].

Furthermore, after the upgrade, the Na density detection limit is better than 0.1 cm^{-3} as shown in Fig. 110.1 right column above 130 km. The uncertainty (precision) of Na density varies from ~0.1% at the mesospheric peak to ~2–10% in the thermosphere-ionosphere Na. However, with high-quality TINa data taken at the same time when high-quality measurements of vertical winds and temperatures were made [6], why were no TINa observations reported until much later? That is exactly another aspect of the combination we will discuss about, the remarkable data analysis techniques—volume mixing ratio calculations.

110.2.2 Why Mixing Ratio Calculation Is Important?

Using mixing ratio calculations to better quantify the TINa layers was first introduced in Chu et al. [7]. In that paper, Na and Fe volume mixing ratios were calculated by dividing the Na- and 372-nm Fe density profiles by the corresponding total atmospheric number densities at McMurdo provided by the MSISE00 model [8]. Then the Na volume mixing ratio contour clearly exhibits the TINa layer features of downward phase progression of gravity waves with periods ranging from ~24 min to many hours. By comparing the Fe and Na mixing ratio, striking differences between the two can be highlighted. The clear features of TINa cannot be observed using only density contour.

In this case, Na volume mixing ratio calculations are powerful data analysis techniques, which also paved the way for the first discovery of regularly occurring TINa layers. Similarly, dividing the Na density profiles with the corresponding total atmospheric number density profiles at Boulder provided by the MSISE00 model can give us Na volume mixing ratio as shown in the Eq. (110.1). Using such data processing techniques helps exhibit the TINa layer features more clearly—the signature of semidiurnal tidal waves with downward phase progression, which significantly increases the possibility of further studying those TINa layers' features after discovering them.

$$\text{Na volume mixing ratio} = \frac{\rho_{\text{Na}}}{\rho_{\text{atmosphere}}} \tag{110.1}$$

We select one night from November to illustrate in Fig. 110.2 the full range (80–150 km) of Na number densities, relative density perturbations, and volume mixing ratios. It is worth to point out that TINa layers were observed in various months and years in the nighttime E region (100–150 km). The relative Na density perturbations are computed by subtracting the nightly mean profile and then dividing by this mean profile. The Na volume mixing ratios are calculated by the method and equation shown above. Note that 7 UT corresponds to Boulder local midnight, and 1 and 13 UT correspond to dusk and dawn (6pm and 6am local time). The

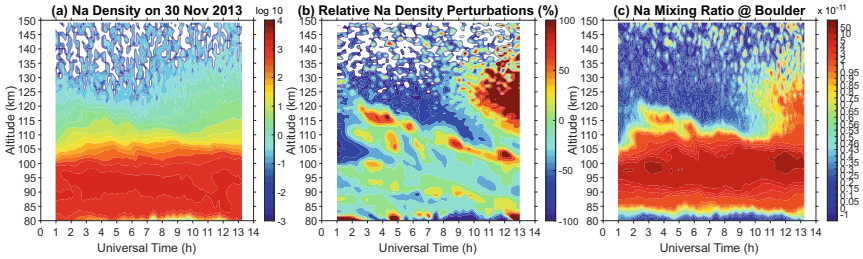


Fig. 110.2 The full range (80–150 km) contours of Na density, relative density perturbation, and volume mixing ratio observed on 30 November 2013 over Boulder, Colorado

most distinct feature is a TINa layer broad in time and altitude before dawn, which exhibits ascending features in the envelope of Na total density (Fig. 110.2a) from 10 to 13UT but descending features in the mixing ratio (Fig. 110.2c) from ~140 km around 10UT to ~110 km around 13UT. Such TINa layer occurs almost every night as long as the observations are long enough to cover the sunrise time. Another distinct feature is a concentrated descending TINa layer occurring at dusk, which starts to descend at 2 UT from ~120 km to ~105 km merging with the main layers. Between the dusk and dawn layers, a third layer near the local midnight occurs occasionally, it does not show up on most of the cases.

As shown in Fig. 110.2, the relative Na density perturbations (Fig. 110.2b) show layer features with downward phase progression much better than the Na density contour (Fig. 110.2a), while the Na volume-mixing-ratio contour makes two different layers much more clearly than the other two plots. This is why mixing ratio calculation is important for us to make the first discovery of regular occurrence of mid-latitude TINa layers over Boulder. The classification of dawn, dusk TINa layers based on the limited nights shown in Fig. 110.2 is consistent with a larger database consisting of 7 years (2011–2017) of measurements that are presented in the next section.

110.3 Results and Discussion

With the combination of lidar's high detection sensitivity and the Na volume mixing ratio calculations, occurrence study of both Boulder TINa dawn and dusk layers can be made. Seven years of lidar observations reveal Boulder TINa dawn layers with nearly 100% occurrence rate (160 out of 164 nights of observations), while observations also indicate that Boulder TINa dusk layers occur regularly for qualified observation nights, mainly during winter seasons (57 out of 78 nights of observations).

One-night lidar observation can be considered as a qualified night for dawn layer occurrence study if the observation lasts minimum 3 h including sunrise time.

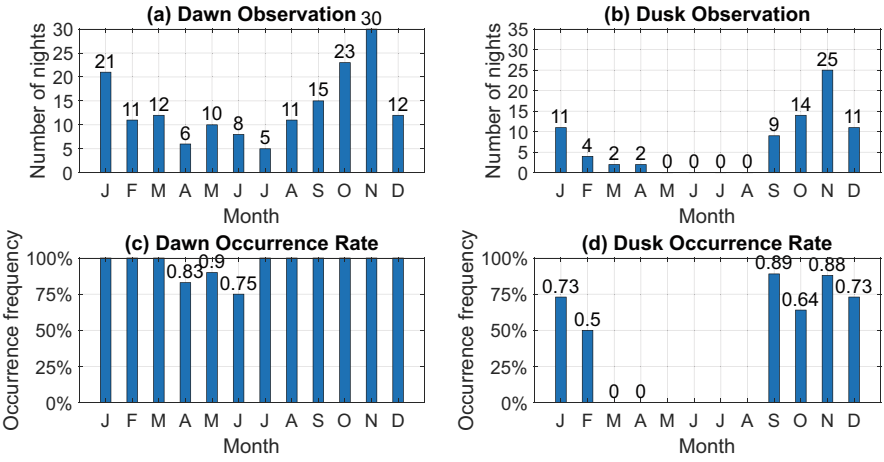


Fig. 110.3 Occurrence study of dawn and dusk layer cases for individual months from 2011 to 2017 at Boulder (40.13°N, 105.24°W), Colorado

Then two extra criteria for dawn layer occurrence: (1) Layers maximum altitude over 125km and (2) downward phase progression till the end of observation. Our statistical study for all dawn layers from 7 years (2011–2017) of lidar observations over Boulder shows that among the total 164 qualified nights of dawn layer observations, only 4 cases had no dawn layer occurrence that were during April to June. Therefore, the occurrence rate of Boulder dawn layer is 97.56%, almost 100% as shown in the Figure 110.3c. Now with the nearly 100% occurrence rate, the surprisingly regular occurrence of Boulder TINa dawn layers is decisively confirmed for the first time at midlatitudes.

Similarly, one-night lidar observation can be counted in statistical database for dusk layer occurrence study if the observation lasts minimum 3 h including 2 UT. Then criteria for dusk layer occurrence: (1) Layers maximum altitude over 115 km and (2) downward phase progression. There are totally 78 qualified nights of dusk layer observations, mostly in winter seasons (from September to February). During May–August, although lidar observations were made successfully, their durations of nighttime only observations were short with the lidar starting time later than 2 UT. In this case, most of our observations during May–August were excluded for dusk layer occurrence study. Although the occurrence rate of dusk layers (73%) is not close to 100%, it is still very high compared to other TINa observations at midlatitudes. In summary, TINa dusk layers can still be considered as regular occurrence based on much higher occurrence rate than other observations. It is worth to point out that the irregular occurring third layer between dusk and dawn layers sometimes can reach extremely high altitudes, even ~180 km. The total occurrence rate for this third midnight layer is much lower, only around 15%. Figures for such interesting midnight layer cases cannot be shown in this report due to the page limit.

110.4 Conclusions and Outlook

We report the first discovery of regular occurrence of mid-latitude thermosphere-ionosphere Na (TINa) layers over Boulder, Colorado. Detection of tenuous Na layers (~0.1–1 cm^{-3} from 150 to 130 km) was enabled by high-sensitivity Na Doppler lidar. A new data analysis technique is applied to pave the way for the discovery, which is the Na volume-mixing-ratio calculations. Boulder TINa layers are observed occurring regularly in various months and years, descending from ∼125 km after dusk and from ∼150 km before dawn every night. With occurrence study using 7 years of lidar data, the dawn layers at Boulder have been confirmed with regular occurrence for the first time in the world, while dusk layers can also be considered as regular occurrence.

In the future, ground-based observations need to extend to space observations where complicated space–atmosphere interactions are very important. In this case, lidars with high detection sensitivity enabled by large-aperture telescope, high-efficiency receiver architecture, and powerful transmitter will likely lead to the detection of tenuous TIMt layers globally. These layers provide a natural laboratory for studying the ion-neutral coupling and act as tracers for profiling the neutral wind and temperature in the E to F regions. Observing these metal layers also provides a unique way of monitoring vertical transport in the thermosphere and ionosphere.

References

1. Chu, X., Yu, Z., et al.: Lidar observations of neutral Fe layers and fast gravity waves in the thermosphere at McMurdo, Antarctica. Geophys. Res. Lett. **38**, L23807 (2011)
2. Chu, X., Chen, Y., et al.: Mid-latitude thermosphere-ionosphere Na layers observed with high-sensitivity Na Doppler lidar over Boulder. Geophys. Res. Lett. **48**(11), 1–10 (2021)
3. Smith, J.A., Chu, X.: High-efficiency receiver architecture for resonance-fluorescence and Doppler lidars. Appl. Opt. **54**(11), 3173–3184 (2015)
4. Huang, W., et al.: Simultaneous, common-volume lidar observations and theoretical studies of correlations among Fe/Na layers and temperatures in the mesosphere and lower thermosphere at Boulder Table Mountain. J. Geophys. Res. Atmos. **118**(15), 8748–8759 (2013)
5. Chu, X., Papen, G.: Resonance fluorescence lidar for measurements of the middle and upper atmosphere. In: Fujii, T., Fukuchi, T. (eds.) Laser Remote Sensing, pp. 179–432. CRC Press, Boca Raton (2005)
6. Lu, X., et al.: Statistical characterization of high-to-medium frequency mesoscale gravity waves by lidar-measured vertical winds and temperatures in the MLT. J. Atmos. Solar-Terrestrial Phys. **162**, 3–15 (2017)
7. Chu, X., et al.: First simultaneous lidar observations of thermosphere-ionosphere Fe and Na (TIFe and TINa) Layers at McMurdo (77.84°S, 166.67°E), Antarctica with concurrent measurements of aurora activity, enhanced ionization layers, and converging electric field. Geophys. Res. Lett. **47**(20) (2020)
8. Picone, J.M., et al.: NRLMSISE-00 empirical model of the atmosphere: Statistical comparisons and scientific issues. J. Geophys. Res. **107**(A12), 1468 (2002)

Part XII
50 Years of Lidar Observations: The Tip of the Laser Remote Sensing Iceberg?

Chapter 111
Field-Widened Michelson Interferometer as the Spectral Discriminator in a 1064-nm HSRL

Zachary Noel Buckholtz, Ilya Razenkov, and Edwin Eloranta

Abstract The performance of a model field-widened Michelson interferometer (FWMI) as the spectral discriminator for a 1064-nm high-spectral resolution lidar (HSRL) channel is presented. The technique of HSRL separates the Doppler-broadened molecular backscatter from the narrow Mie scattering from atmospheric aerosols using a fine-tuned narrowband filter or spectral discriminator. Our simulated FWMI consists of one glass arm and one air spaced arm with a composite metal spacer designed to make the interferometer thermally invariant. The FWMI is pressure tuned to the desired wavelength.

Keywords High spectral resolution lidar · Aerosols · Angstrom exponent

111.1 Introduction

Information on particle size distributions is a key necessity for reducing the uncertainty in climate models caused by clouds and aerosols. Attempts have been made to improve these measurements, and however these methods have important limitations. Sun photometers are able to provide information on particle size distributions, but they are not able to provide information on vertical structure. Existing lidar systems can provide high-resolution vertical measurements of aerosol optical properties of the whole aerosol population, but, because these systems operate at a single wavelength, they do not provide information about the aerosol distribution itself.

Here, we describe a model for a field-widened Michelson interferometer (FWMI) as the aerosol spectral discriminator for the 1064 nm channel of an existing Nd:YAG HSRL system [1] operating at 532 nm, allowing for HSRL measurements at two wavelengths. HSRL systems are used to measure the optical properties of clouds

Z. N. Buckholtz (✉) · I. Razenkov · E. Eloranta
University of Wisconsin—Madison, Madison, WI, USA
e-mail: buckholtz@wisc.edu

© The Author(s), under exclusive license to Springer Nature Switzerland AG 2023

J. T. Sullivan et al. (eds.), *Proceedings of the 30th International Laser Radar Conference*, Springer Atmospheric Sciences,
https://doi.org/10.1007/978-3-031-37818-8_111

and atmospheric aerosols with absolute calibration and high vertical resolution, useful for the study of air quality, cloud physics, and the direct and indirect aerosol effects. HSRL systems are often implemented using frequency-doubled Nd:YAG lasers. These systems have an HSRL channel at 532 nm, with an iodine vapor cell as the spectral discriminator, and a standard backscatter lidar channel at 1064 nm.

Recent studies have also explored the possibility of using an FWMI at 532 nm [2]. In addition, NASA has implemented an HSRL channel at 355 nm using an FWMI on their HSRL-2 [3]. The FWMI described here provides sufficient angular acceptance of the received signal without losses due to absorption in an atomic vapor cell. The robust measurements of aerosol optical properties at two wavelengths provided by this instrument would allow for measurement of the Angstrom exponent and therefore provide information on aerosol size distributions. In addition, the CALIOP instrument on NASA's CALIPSO satellite has a standard backscatter channel operating at 1064 nm. Having a ground-based HSRL system operating at 1064 nm would be useful for calibrating and validating data from CALIOP or future space-based missions, such as the upcoming AOS mission.

Our model FWMI consists of one fused silica arm and one air arm supported with a metal spacer, shown in Fig. 111.1. The air arm allows for pressure tuning of the FWMI. The metal spacer is made of a composite material which has a coefficient of thermal expansion (CTE) that has been tuned to make the optical path difference (OPD) thermally invariant. The OPD between the two arms is optimized so that the transmitted signal minimizes the aerosol backscatter signal while retaining much of the molecular backscatter signal. This transmitted channel would be used as the molecular channel, while the reflected channel would be used for the combined channel. We determine the specifications for a feasible FWMI and analyze the performance of the FWMI under various errors. Our model shows a performance of 20.8 dB attenuation of the aerosol signal leakage in the molecular channel.

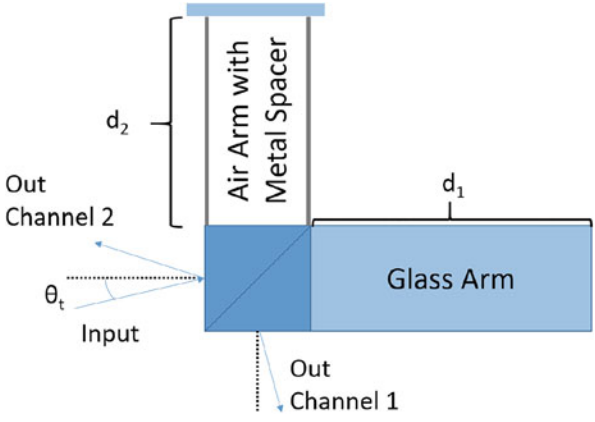


Fig. 111.1 Optical diagram of the FWMI. One arm is composed of glass and the other is composed of an air gap with metal spacers. The interferometer is operated at a slight tilt, θ_t, so that the output reflected back toward the input, referred to as channel 2, is usable as the combined channel. The channel 1 output will act as the HSRL molecular channel

111.2 Instrument

For our model, we assume that the intensities in each arm are equal. The transfer function for a Michelson interferometer is given by

$$T(\Delta\nu,\theta)=\frac{1}{2}\left(1+\cos\left(2\pi\left(\frac{\Delta\nu}{FSR(\theta)}+\frac{\nu_0\Delta OPD(\theta)}{c}\right)\right)\right), \tag{111.1}$$

where θ is the angle of incidence on the interferometer, $\Delta\nu$ is the detuning from the center frequency, $FSR(\theta)$ is the free spectral range which is determined by the optical path difference (OPD) between the two arms, and $\Delta OPD(\theta)$ represents any changes in the OPD. The center frequency, ν_0, is determined by setting $\Delta OPD=0$ and multiplying the FSR by a half-integer. By setting the center frequency, this way and setting the OPD and FSR so that the center frequency of the FWMI is equal to the frequency of the transmitted laser, we ensure that the transmission of the center frequency is near zero. This means that the transmission of the aerosol backscatter through channel 1 of the FWMI will be at a minimum, while the wings of the molecular backscatter are transmitted through the interferometer. These transmission properties make the FWMI channel 1 the HSRL molecular channel.

The OPD can be determined from the following equation:

$$OPD(\theta)=2\left(n_1d_1\sqrt{1-\frac{sin^2(\theta)}{n_1^2}}-n_2d_2\sqrt{1-\frac{sin^2(\theta)}{n_2^2}}\right), \tag{111.2}$$

where θ is the angle of incidence on the interferometer, n_i are the indices of refraction in the two arms, and d_i are the lengths of the arms.

The OPD is a function of the incident angle. To minimize the FWMI's sensitivity to tilt and divergence angle, we can expand Eq. (111.2) in theta and set the second-order term to zero (the first-order term is already zero). The angle derivative of Eq. (111.2) along with Eq. (111.2) itself can be used as a system of two equations to find the lengths of the two arms [2].

Since the arm lengths and indices are temperature-dependent, the OPD is also a function of temperature. In order to set the temperature tuning rate for the OPD, the air arm spacer can be made out of a composite material with the C.T.E. required to give the proper tuning rate. In order to set our temperature tuning rate, we take the temperature derivative of Eq. (111.2) and set it equal to the desired tuning rate, which in our case is zero. The temperature derivative of the glass index of refraction is found from the following equation:

$$\Delta n_g=\frac{n_g^2-1}{2n_g}\left(D_0\Delta T+D_1\Delta T^2+D_2\Delta T^3+\frac{E_0\Delta T+E_1\Delta T^2}{\lambda^2-\lambda_{tk}^2}\right), \tag{111.3}$$

Table 111.1 Specifications for simulated FWMI

FSR (GHz)	1.5	Air arm Spacer CTE (ppm/°C)	13.47
Glass Arm Length (mm)	131.571	Pressure Tuning (FSR/atm)	47.62
Air Arm Length (mm)	90.771	Tilt angle (°)	1.5
Glass index	1.449609	Wavefront error (λ)	0.01
Glass β (dn/dT, ppm/°)	7.933	Aperture (mm)	25

where n_g is the index of refraction at a reference temperature, ΔT is the deviation from the reference temperature, and λ is the wavelength in microns. The dispersion formula used to find n_g for the glass we used in our simulations is the Sellmeier 1 formula in [4]. The temperature and pressure dependence of the index of refraction of air is given by

$$n_{air} = 1 + \frac{\left(6432.8 + \frac{2949810\lambda^2}{146\lambda^2 - 1} + \frac{25540\lambda^2}{41\lambda^2 - 1}\right) 1.0 \times 10^{-8} P}{1 + 3.14785 \times 10^{-3}(T - 15)}, \tag{111.4}$$

where P is the pressure in atmospheres, T is the temperature in Celsius, and λ is the wavelength in microns. Since we have the arm lengths from the procedure described above along with the indices of refraction for glass and air, we then solve for the C.T.E. for the air arm. The results of these calculations are shown in Table 111.1.

111.3 Simulation Results

The parameters used to run our simulations can be found in Table 111.1. The glass composing the glass arm is a type of fused silica produced by Schott known as Lithosil [5]. The CTE of the metal spacer in the air arm was chosen so that the OPD was thermally invariant. Between the field widening and thermal invariance, our FWMI is robust against errors in the tilt or beam divergence angle and setpoint temperature. However, the FWMI is still sensitive to temperature gradients in the low thermal conductivity glass arm causing a mirror tilt. Given the CTE and dimensions for the glass arm, we find that keeping gradients across the width of the glass arm to below 0.04 °C keeps the FOM to within 1% of the maximum value [6]. Wavefront errors induced by surface imperfections were modeled following Cheng et al. [2].

The FSR was chosen in order to maximize the molecular transmission in the molecular channel, T_m, while minimizing the aerosol transmission in the same channel, T_a. As a figure of merit, we chose the ratio of these two quantities to evaluate the performance of our model instrument, T_m/T_a. A Gaussian line shape with a standard deviation of 35 MHZ was chosen for the aerosol backscatter spectrum, and the molecular backscatter spectrum is the Cabannes–Brillouin backscatter at a temperature of 300 K and a pressure of 1 atm. The results are shown in Fig. 111.2.

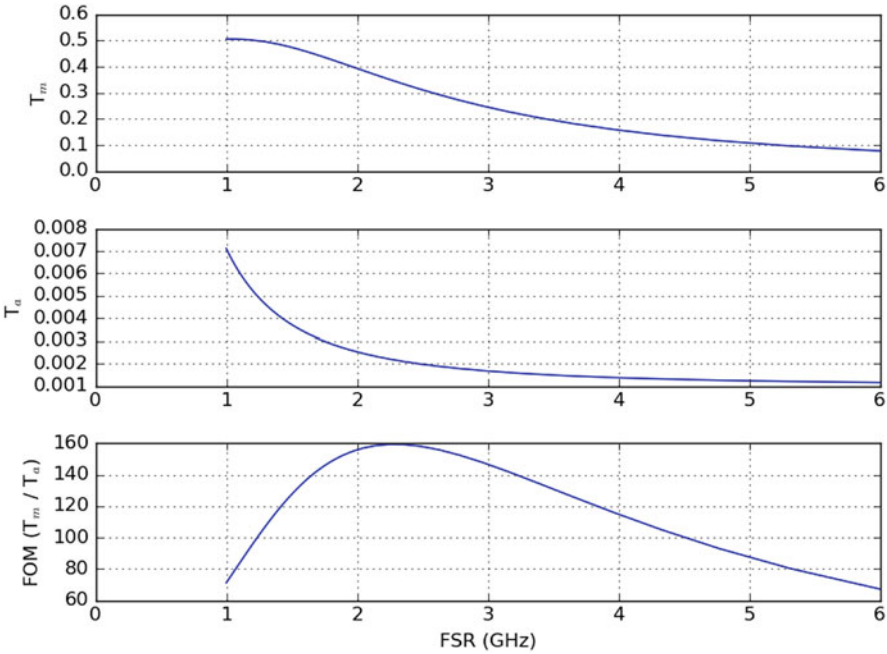


Fig. 111.2 Performance of the FWMI versus FSR. To choose an FSR, we must balance maximizing transmission of the molecular backscatter (top plot, T_m) in channel 1 (see Fig. 111.1) while minimizing the transmission of the aerosol backscatter (middle plot, T_a). The bottom plot shows our chosen figure of merit to evaluate the performance of the FWMI: T_m/T_a. With an FSR of 1.5 GHz, the FOM is about 120

An FSR of 1.5 GHz keeps T_m close to the maximum of 50%, while T_a is less than 1% of T_m. Our FOM shows a maximum because the wavefront error creates a floor for T_a. The wavefront error was taken to be 0.01λ for these simulations.

The performance of the FWMI depends on laser frequency lock error. In practice, the laser frequency will be set in order to keep the laser tuned to the iodine absorption feature at 532 nm. The FWMI will then be locked to the laser frequency via density tuning with pressure as a stand-in measurement for density (the FWMI will be sealed). Figure 111.3 shows the change in the FOM versus lock error, defined as the difference between the 532-nm iodine line and the frequency that is a half-integer multiple of the FSR. The figure also includes detuning limits for different tolerances of FOM variation. Since the FWMI is designed to be relatively insensitive to temperature and tilt angle, the main concern for controlling locking error is the air pressure within the air arm. Given the FWMI's pressure tuning rate, see Table 111.1, and the tolerances given in Fig. 111.3, pressure must be controlled down to 0.086 mbar in order to keep the FOM within 1% of its maximum value.

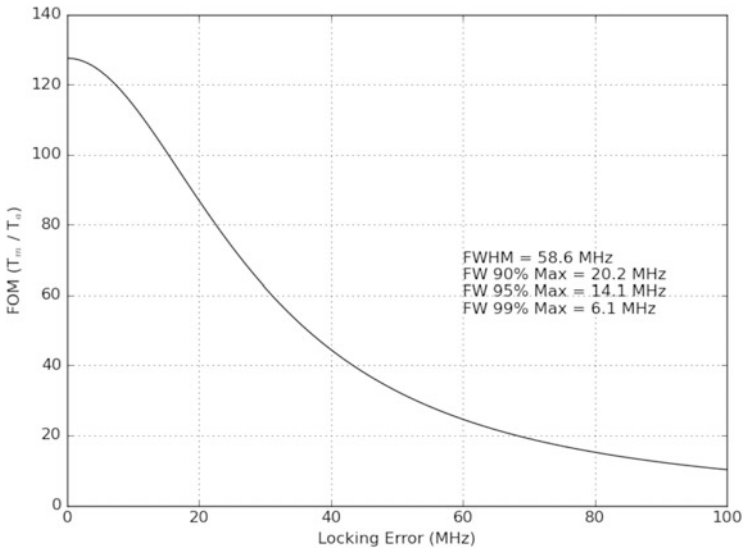


Fig. 111.3 Variation of the FOM versus locking error. Also shown are the limits on lock error for different tolerances on FOM variation. For example, to keep the FOM within 1% of the maximum, the lock error must be less than ±3.05 MHz

References

1. Razenkov, I.A., Garcia, J.P., Eloranta, E.W.: Development of high spectral resolution lidars at the University of Wisconsin. In: Proceedings for 30th International Laser Radar Conference, June 26–July 1, virtual (2022)
2. Cheng, Z., Liu, D., Luo, J., Yang, Y., Zhou, Y., Zhang, Y., Duan, L., Su, L., Yang, L., Shen, Y., Wang, K., Bai, J.: Field-widened Michelson interferometer for spectral discrimination in high-spectral-resolution lidar: theoretical framework. Opt. Express **23**(9), 12117–12134 (2015)
3. Burton, S.P., Hostetler, C.A., Cook, A.L., Hair, J.W., Seaman, S.T., Scola, S., Harper, D.B., Smith, J.A., Fenn, M.A., Ferrare, R.A., Saide, P.E., Chemyakin, E.V., Müller D.: Calibratoin of a high spectral resolution lidar using a Michelson interferometer, with data examples from ORACLES. Appl. Opt. **57**(21), 6061–6075 (2018)
4. ZEMAX®Optical Design Program User's Manual (ZEMAX Development Corporation, 2010)
5. Lithosil Datasheet. http://www.unitedlens.com/pdf/schott_optical_glass_cat.pdf. Last accessed 27 April 2022
6. Born, M., Wolf, E.: Principles of Optics. 5th edn. Pergamon Press, Oxford (1975)

Chapter 112
Long-Term Monitoring of the Stratosphere by Lidars in the Network for the Detection of Atmospheric Composition Change

Wolfgang Steinbrecht, Thierry Leblanc, Sophie Godin-Beekmann, Sergey M. Khaykin, Alain Hauchecorne, Philippe Keckhut, Richard Querel, Daan P. J. Swart, and Thomas J. McGee

Abstract Lidars are excellent tools for routine profile measurements of ozone, temperature, and aerosol in the stratosphere. Different from most other techniques, the lidar measurements are essentially self-calibrating. This inherently insures long-

The authors dedicate this contribution to the memory of Gérard Mégie and Stuart McDermid.

W. Steinbrecht (✉)
Deutscher Wetterdienst, Hohenpeissenberg, Germany
e-mail: wolfgang.steinbrecht@dwd.de

T. Leblanc
Jet Propulsion Laboratory, California Institute of Technology, Wrightwood, CA, USA
e-mail: thierry.leblanc@jpl.nasa.gov

S. Godin-Beekmann
LATMOS/IPSL, Sorbonne University, Paris, France
e-mail: sophie.godin-beekmann@latmos.ipsl.fr

S. M. Khaykin · A. Hauchecorne · P. Keckhut
LATMOS/IPSL, UVSQ University Paris-Saclay, Paris, France
e-mail: sergey.khaykin@latmos.ipsl.fr; alain.hauchecorne@latmos.ipsl.fr; philippe.keckhut@latmos.ipls.fr

R. Querel
NIWA, Lauder, New Zealand
e-mail: richard.querel@niwa.co.nz

D. P. J. Swart
RIVM, Bilthoven, The Netherlands
e-mail: daan.swart@rivm.nl

T. J. McGee
NASA Goddard Space Flight Center, Greenbelt, MD, USA
e-mail: thomas.j.mcgee@nasa.gov

© The Author(s), under exclusive license to Springer Nature Switzerland AG 2023

J. T. Sullivan et al. (eds.), *Proceedings of the 30th International Laser Radar Conference*, Springer Atmospheric Sciences,
https://doi.org/10.1007/978-3-031-37818-8_112

term stability and has made lidars a key component of the Network for the Detection of Atmospheric Composition Change (NDACC). Some NDACC lidar stations have provided measurement records covering almost 40 years and are expected to continue for many years. We present some milestones in the development of these lidars and show long-term atmospheric changes they have measured. The lidar data are also used as a reference for validation and for merging of (generally shorter) satellite records.

Keywords Ozone · Temperature · Aerosol

Early atmospheric applications of lidar include the detection of enhanced stratospheric aerosol after the 1963 Agung eruption [1], profile measurements of stratospheric ozone [2] after the 1974 discovery that anthropogenic chlorine could destroy ozone in the stratosphere, and lidar measurements of stratospheric and mesospheric temperature [3]. The discovery of the ozone hole in 1984 and subsequent international agreements for the protection of the ozone layer (Vienna Convention, 1985; Montreal Protocol, 1987) triggered a lot of interest in such measurements, and significant funding increases. To complement global satellite measurements with key instruments at ground-based stations [4], NASA initiated the international Network for the Detection of Stratospheric Change (NDSC), later renamed to Network for the Detection of Atmospheric Composition Change (NDACC) [5]. Figure 112.1 shows a map of lidar stations involved in NDACC, along with stations of the much more recent North American Tropospheric Ozone Lidar Network (TOLNET).

NDACC has played a key role in focusing lidar measurements taken at the individual stations and establishing network-wide standards and best practices through algorithm intercomparisons [6], specific multi-instrument campaigns [7, 8], more general network-wide assessments [9–11], and, last but not least, by standardizing uncertainty analysis [12].

Nearly continuous measurements of ozone and temperature in the upper stratosphere, starting in the late 1980s/early 1990s, are a major achievement of NDACC lidars. Figures 112.2 and 112.3 show the ozone and temperature long-term evolution measured by lidars and microwave radiometers at five NDACC stations and obtained by merging data from different satellite instruments or from stratospheric meteorological analyses. Altogether, the different data sets provide a consistent picture of ozone decline from the 1980s to the late 1990s, as well as evidence for a beginning ozone recovery since about 2000. Effectively, ozone follows the inverse of stratospheric chlorine loading (given by ESC, magenta line in Fig. 112.2). Superimposed are large fluctuations, e.g., due to the quasi-biennial oscillation (QBO) of atmospheric transports in the tropical stratosphere, and a small variation due to the 11-year cycle of solar activity. For temperature, the data show a long-term cooling of the stratosphere, caused by the ever-increasing CO_2 concentration in the atmosphere.

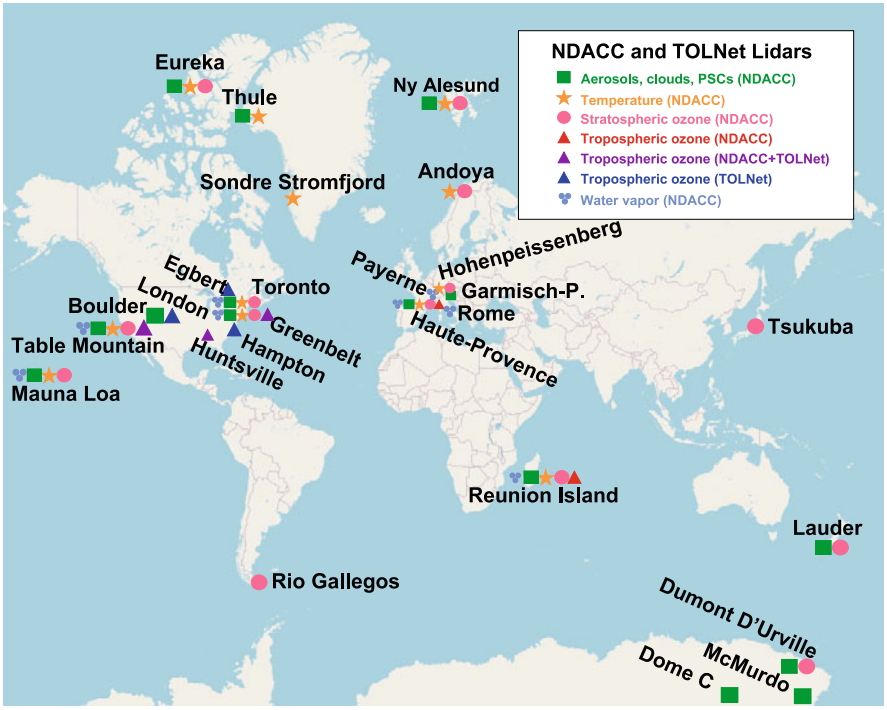


Fig. 112.1 Lidar stations in the worldwide Network for the Detection of Atmospheric Composition Change (NDACC) and in the North American Tropospheric Ozone Lidar Network (TOLNET). Symbols give the types of measurement taken. Not all stations are currently operational

Another parameter measured very well by lidar is stratospheric aerosol loading, which is enhanced by major explosive volcanic eruptions, and sometimes also by pyro-convection from the largest wild fires. Figure 112.4 shows the evolution of stratospheric aerosol at northern mid-latitudes as measured by NDACC lidars and satellite instruments. The largest aerosol loading was measured after the 1991 eruption of Mt. Pinatubo, followed by a long decay. Since 2005, enhanced transport from the Asion monsoon and a number of smaller volcanic eruptions enhanced stratospheric aerosol again, with the most recent injection in Fig. 112.4 coming from the Raikoke eruption in 2019. Most recently, lidars have observed stratospheric aerosol from the Australian wildfires of 2019–2020.

It is expected that NDACC lidars will continue these measurements and document the expected recovery of the ozone layer, as well as the continuing stratospheric cooling. More recent additions to NDACC's lidar capabilities are Raman lidar measurements of water vapor in the (lower) stratosphere and Doppler wind lidar measurements from the upper troposphere to the mesosphere.

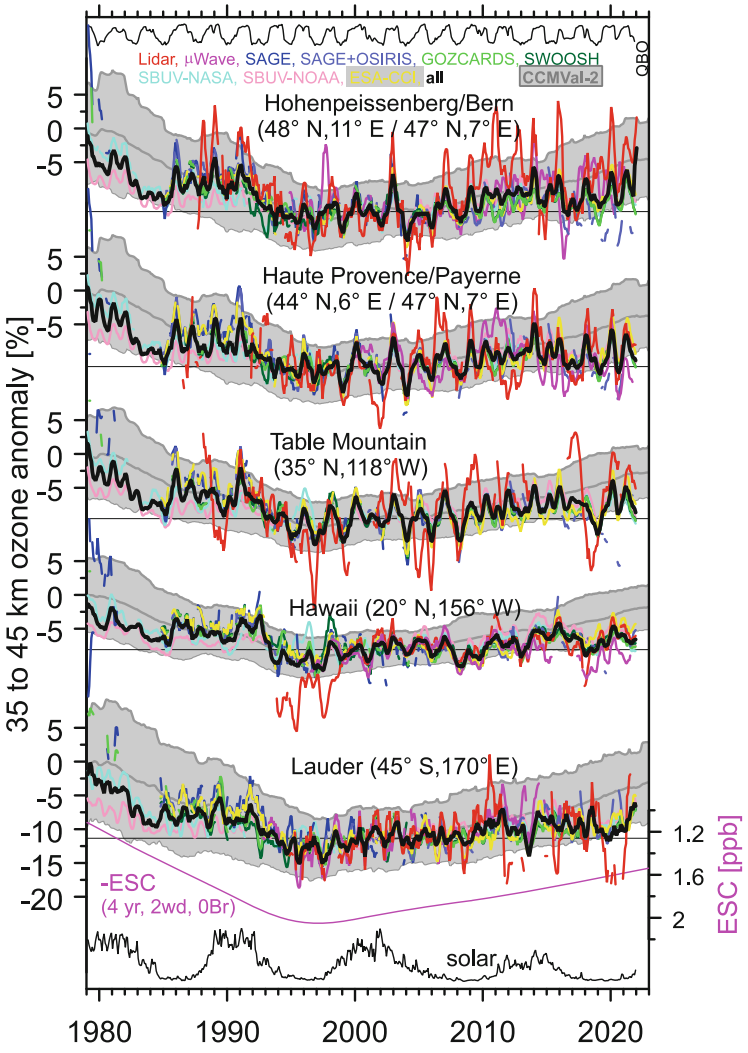


Fig. 112.2 Time series of ozone content in the upper stratosphere near 42 km altitude (2 hPa pressure) above NDACC stations. Red: measured by NDACC lidars and magenta: measured by NDACC microwave radiometers. Other colors: zonal means from different merged satellite data sets. Black: average over all available data. Gray shading in the background: Simulated range from the Chemistry Climate Model Validation 2 initiative. The black curves at the bottom and at the top give proxies for 11-year solar cycle and the quasi-biennial oscillation. The magenta curve at the bottom gives a proxy for ozone depletion (effective stratospheric chlorine). Adapted from [10]

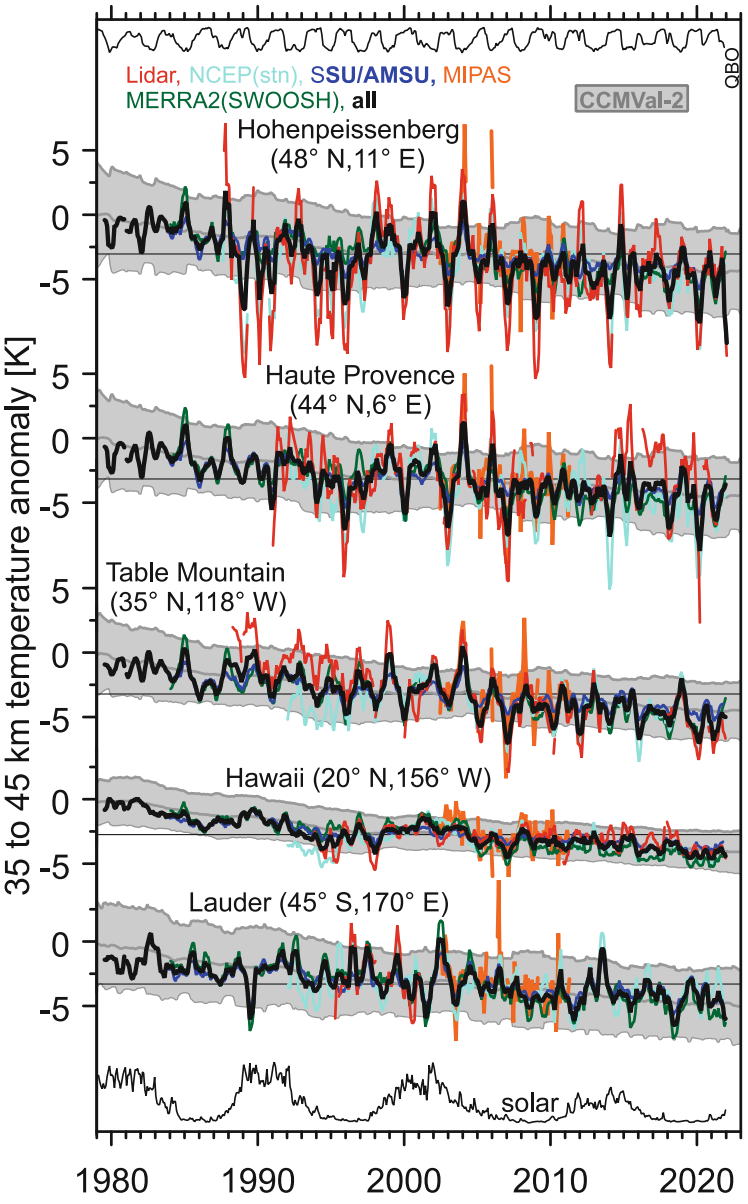


Fig. 112.3 The same as the previous figure, but for temperature in the upper stratosphere. Red: measured by NDACC lidars and cyan: from stratospheric meteorological analyses by the US National Center for Environmental Prediction. Other colors: zonal means from satellite data or MERRA2 meteorological analyses. Black: average over all available data. Gray shading in the background: simulated range from the Chemistry Climate Model Validation 2 initiative. Adapted from [10]

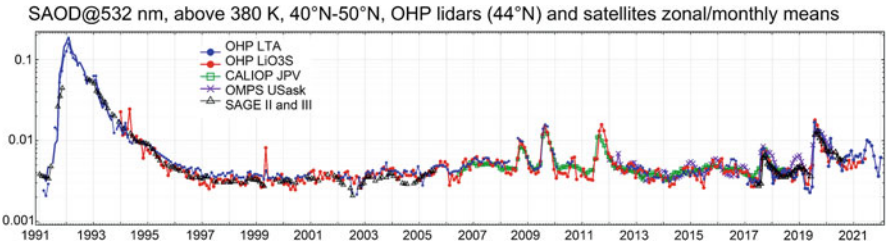


Fig. 112.4 Time series of stratospheric aerosol optical depth recorded by two lidars at the Observatoire de Haute-Provence NDACC station (blue and red dots), along with zonal means from the space-borne CALIOP lidar and the SAGE II, SAGE III, and OMPS satellite instruments. Note the logarithmic *y*-axis. Updated from [13]

Acknowledgments The authors dedicate this contribution to the memory of Gérard Mégie and Stuart McDermid. Both were excellent and visionary lidar scientists and key people in developing the Network for the Detection of Stratospheric Change (NDSC, renamed to NDACC in 2005). Unfortunately, Gérard and Stuart passed away much too early (in 2004 and 2021).

Part of this research was carried out at the Jet Propulsion Laboratory, California Institute of Technology, under a contract with the National Aeronautics and Space Administration (80NM0018D004).

References

1. Fiocco, G., Grams, G.: Observations of the aerosol layer at 20 km by optical radar. J. Atm. Sci. **21**(3), 323–324 (1964). https://doi.org/10.1175/1520-0469(1964)021<0323:OOTALA>2.0.CO;2
2. Mégie, G., et al.: Vertical profile of stratospheric ozone by lidar sounding from the ground. Nature **270**, 329–331 (1977). https://doi.org/10.1038/270329a0
3. Hauchecorne, A., Chanin, M.-L.: Density and temperature profiles obtained by lidar between 35 and 70 km. Geophys. Res. Lett. **7**(8), 565–568 (1980). https://doi.org/10.1029/GL007i008p00565
4. McDermid, I.S.: Ground-based lidar and atmospheric studies. Surv. Geophys. **9**(2), 107–122 (1987). https://doi.org/10.1007/BF01904118
5. De Maziere, M., et al.: The Network for the Detection of Atmospheric Composition Change (NDACC): History, status and perspectives. Atmos. Chem. Phys. **18**(7), 4935–4964 (2018). https://doi.org/10.5194/acp-18-4935-2018
6. Godin, S., et al.: Ozone differential absorption lidar algorithm intercomparison. Appl. Opt. **38**(30), 6225–6236 (1999). https://doi.org/10.1364/AO.38.006225
7. Margitan, J.J., et al.: Stratospheric ozone intercomparison campaign (STOIC) 1989: overview. J. Geophys. Res. **100**(D5), 9193–9208 (1995). https://doi.org/10.1029/95JD00509
8. Wing, R., et al.: Evaluation of the new DWD ozone and temperature lidar during the Hohenpeißenberg Ozone Profiling Study (HOPS) and comparison of results with previous NDACC campaigns. Atmos. Meas. Tech. **14**, 3773–3794 (2021). https://doi.org/10.5194/amt-14-3773-2021
9. Keckhut, P., et al.: Review of ozone and temperature lidar validations performed within the framework of the Network for the Detection of Stratospheric Change. J. Env. Monit. **6**(9), 721–733 (2004). https://doi.org/10.1039/B404256E

10. Steinbrecht, W., et al.: Ozone and temperature trends in the upper stratosphere at five stations of the Network for the Detection of Atmospheric Composition Change. Int. J. Remote Sens. **30**(15–16), 3875–3886 (2009). https://doi.org/10.1080/01431160902821841
11. Hubert, D., et al.: Ground-based assessment of the bias and long-term stability of 14 limb and occultation ozone profile data records. Atmos. Meas. Tech. **9**, 2497–2534 (2016). https://doi.org/10.5194/amt-9-2497-2016
12. Leblanc, T., et al.: Proposed standardized definitions for vertical resolution and uncertainty in the NDACC lidar ozone and temperature algorithms, 3 Parts. Atmos. Meas. Tech. **9**(8), 4029–4101 (2016). https://doi.org/10.5194/amt-9-4029-2016
13. Khaykin, S.M., et al.: Variability and evolution of the midlatitude stratospheric aerosol budget from 22 years of ground-based lidar and satellite observations. Atmos. Chem. Phys. **17**, 1829–1845 (2017). https://doi.org/10.5194/acp-17-1829-2017

Chapter 113
Stratospheric Aerosol: 45 Years of Lidar Measurements at Garmisch-Partenkirchen



Thomas Trickl, Hannes Vogelmann, Helmuth Giehl, Horst Jäger, and Matthias Perfahl

Abstract The long-term lidar measurement series of stratospheric aerosol started in 1976 has been continued in third generation with a new lidar system since 2017. This was just in time to cover a new period of elevated-aerosol events. The new system yields high-quality backscatter coefficients up to almost 50 km. This was important during the period 2020 to spring 2021 when a small amount of particles was observed at altitudes of up to 40 km, possibly originating from the tropical eruption of Ulawun in June 2019. Most of the aerosol spikes in the recent period of the time series are related to an unprecedented rise in strong biomass-burning injections into the stratosphere resulting in aerosol signatures in part up to more than 20 km. It is hard to ascribe this sudden rise in occurrence just to a slowly developing climate change.

Keywords Stratospheric aerosol · Lidar · Series

113.1 Introduction

The stratospheric aerosol layer has been studied because of its impact on radiation (e.g., [1–4]) and air chemistry, in particular ozone depletion [5–7]. The layer has been monitored since 1972 with balloon- and satellite-borne sensors as well as with lidar remoted sensing [8–11]. Due to its excellent vertical resolution, lidar became an important tool almost right from the beginning [12, 13]. A number of stratospheric aerosol sounding stations provided routine long-term measurements at different latitudes [9, 14–22] and were later in part adopted by the Network for the Detection of Atmospheric Composition Change (NDACC, formerly NDSC).

T. Trickl (✉) · H. Vogelmann · H. Giehl · H. Jäger · M. Perfahl
Karlsruher Institut für Technologie, IMK-IFU, Garmisch-Partenkirchen, Germany
e-mail: thomas@trickl.de; hannes.vogelmann@kit.edu

© The Author(s), under exclusive license to Springer Nature Switzerland AG 2023

J. T. Sullivan et al. (eds.), *Proceedings of the 30th International Laser Radar Conference*, Springer Atmospheric Sciences,
https://doi.org/10.1007/978-3-031-37818-8_113

In 1973, lidar sounding of aerosol started at IMK-IFU (Garmisch-Partenkirchen, Germany) with a ruby lidar (694.3 nm) purchased from Impulsphysik. In 1976, the activities were extended to the stratosphere, after adding a photon counter. Since 1991 Nd:YAG lasers have been used which has greatly improved the performance. The results until 2011 are described in Refs. [15, 17]. Between 2012 and 2015 the number of measurements gradually decreased due to frequent system failure, in particular data storage issues. Since 2017, the measurements have been continued at the nearby high-altitude station Schneefernerhaus (UFS, lidar laboratory: 2675 m a.s.l.), which extends our series to more than 45 years. Here, we give a brief overview of the new system and the results obtained. A full account of the work is given in Ref. [22].

113.2 System Description

The new lidar is integrated into the water-vapor differential-absorption lidar at the Schneefernerhaus high-altitude research station (UFS) at 2675 m a.s.l. [23]. It, thus, benefits from the already existing large (0.65-m-diameter) receiver and the existing optical set-up with separate near-field and far-field detection. The electronics have been optimized over the years and feature extreme linearity [24, 25]. We use Hamamatsu R7400U-03 photomultiplier tubes with custom-made sockets and high-speed discriminators (both from Romanski sensors), the latest version of Licel transient digitizers (20 MHz, 12 bits) with ground-free input stage and a FastComtec MCS6A 5 GHz photon counting system. Just a very small exponential decay of the analog signal must be corrected that is slightly higher at 532 nm than in the ultraviolet [24, 25] because of the larger signal-time area of the lidar return. The far-field return is spectrally filtered by a 0.25-nm interference filter (Materion Barr) that almost quantitatively suppresses the residual background during nighttime and allows for analog daytime measurements to more than 25 km.

Most importantly, a frequency-doubled injection-seeded Nd:YAG laser with 100 Hz repetition rate and 120 mJ pulse energy at 532.24 nm serves as the light source (Innolas, Spitlight DPSS 250). Due to accumulating the signals for 100,000 laser shots, a substantial increase in the signal-to-noise ratio was achieved. The performance at lower altitude is improved by analog data acquisition instead of photon counting. No noise-enhancing signal attenuation is needed in this way, and dead-time effects are avoided. The signal level is also strongly enhanced by the much higher altitude of the research station. Even at 25 km the signal is still enhanced by 50% with respect to the valley (730 m a.s.l.). Finally, at UFS, there is a higher number of clear-sky nights than at IFU in the valley. The disadvantage of difficult access to UFS with three cable cars is compensated by full remote control of the system via the internet.

There was also a change in the data-evaluation procedure. Until 2011, the backscatter coefficients had been retrieved with an interactive approach. The measurements afterwards were evaluated with a Klett program quality assured

within EARLINET (European Aerosol Research Network) and extended for the options needed for stratospheric sounding. This complex procedure is in detail described in Ref. [22]. The enhanced quality of the data achieved allows us to retrieve the aerosol backscatter coefficient to the end of the NCEP (National Centers for Environmental Prediction) reference densities around 55 km. The system will be further upgraded within the European infrastructure ACTRIS.

113.3 System Performance

In Fig. 113.1 we show the backscatter coefficients for the nighttime measurement on January 7, 2021. The three curves for far-field photon counting and near- and far-field analog detection agree well in the overlapping parts of their useful ranges. The values for photon counting are considerably less noisy at high altitudes but not around 12 km. This is due to the shot noise in the raw signal decreases with distance, which is not the case for the analog signal.

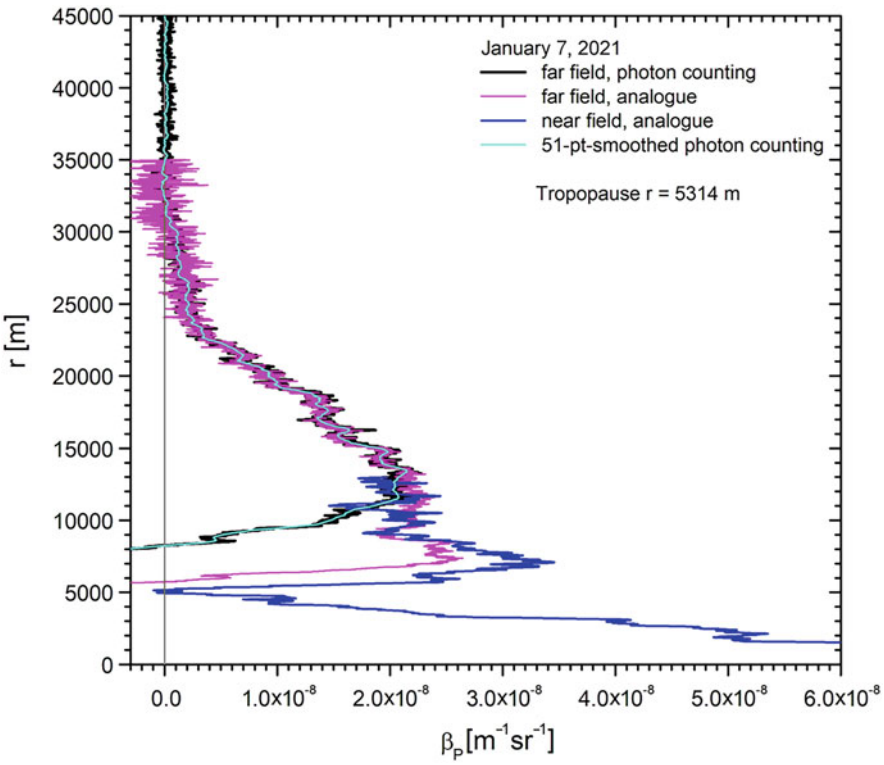


Fig. 113.1 532-nm particle backscatter coefficients for all three channels as a function of distance r (see legend inside the figure; bin width: 7.5 m). $r = 0$ corresponds to 2675 m a.s.l

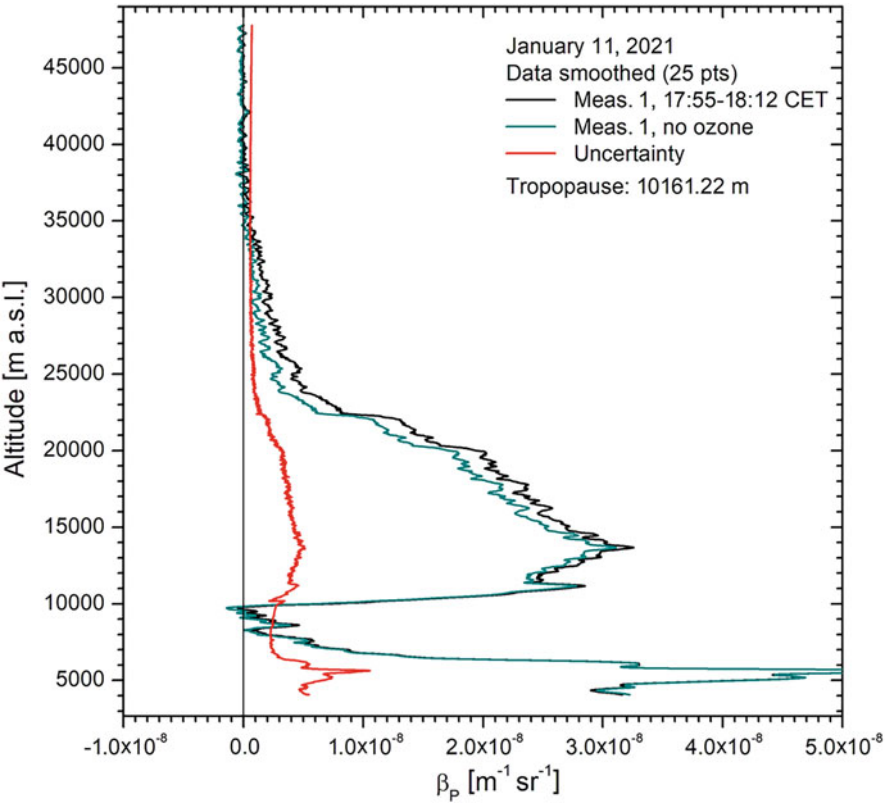


Fig. 113.2 532-nm particle backscatter coefficients with and without ozone correction. The profiles are smoothed with a ±12-bin siding arithmetic average for clearness

The aerosol layer clearly exceeds the typically reached 25–27 km a.s.l. normally observed. As can be seen from the averaged backscatter coefficients from the counting channel (cyan) a weak contribution extends to 34 km a.s.l. (distance $r = 31.2$ km). This contribution is tentatively ascribed to the tropical eruption of Ulawun on June 26, 2019. In 2020 this layer had been slightly more intense and reached 40 km (see Sect. 113.4).

Figure 113.2 shows the influence of the ozone correction which can by no means be neglected. As expected, it maximizes around 25 km a.s.l. We use climatological monthly averages from the nearby Hohenpeißenberg ozone soundings.

113.4 Observations and Conclusions

Figure 113.3 shows the latest update of the series of the integrated backscatter coefficient until February 2022. By tradition, the values are converted from 532.24 nm

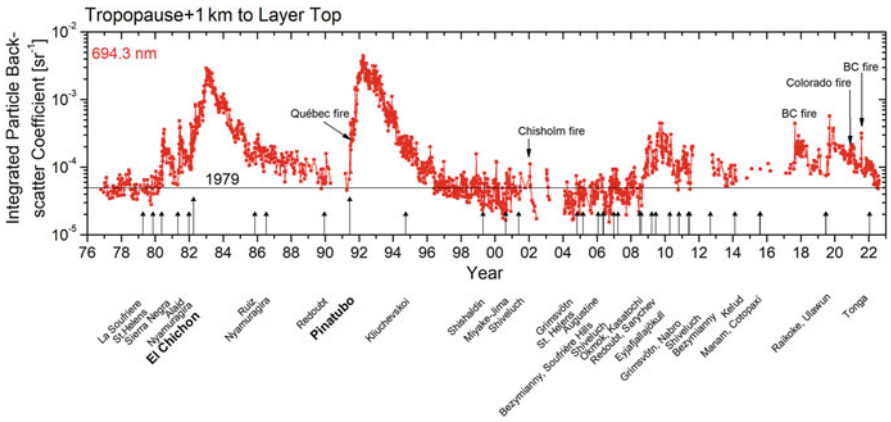


Fig. 113.3 694.3-nm integrated particle backscatter coefficients (1976–2022)

to the ruby-laser wavelength of 694.3 nm, by applying data from Ref. [26]. In 2014 and 2015 the number of the measurements that could be successfully stored in the computer strongly diminished due to the more and more unreliable performance of the data transfer.

The new system started operation just in time before the beginning of a series of spectacular particle injections into the stratosphere. Six pronounced peaks have been registered since 2017 that will be briefly explained below. More details will be given in a full-size publication [22].

These recent events were mostly attributed to giant pyro-cumulonimbus bursts, two over British Columbia [27], yielding the most pronounced loading of the stratosphere by biomass burning plumes above our site since the Québec plume on July 1, 1991. The plumes reached altitudes between 16 and 24 km. Despite an increase of mid-latitude biomass burning in a warmer and drier atmosphere [e.g., 16, 28] this sudden rise in occurrence and violence is difficult to understand.

Normally, the upper boundary of the aerosol layer in our observations is below 30 km. In summer 2019, the two volcanoes Raikoke (Kuril Islands) and Ulawun (New Guinea) strongly erupted. The Raikoke plume was observed with very short delay, whereas particles that we tentatively ascribe to the tropical eruption arrived half a year later, at altitudes in part even up to 40 km. This observation suggests northward transport in the Brewer-Dobson circulation [29]. It is interesting to note that no similarly pronounced contribution was registered after the Pinatubo eruption. The high-altitude layer gradually tapered off until April 2021.

The excellent performance of the new lidar system together with advances in transport modelling and the use of satellite data have led to a step forward in the understanding of the stratospheric aerosol distribution [28].

Acknowledgments The authors thank all the colleagues and funding agencies who supported the measurements over that many years. W. Steinbrecht kindly made available the Hohenpeißenberg ozone profiles. This work is now funded by the German Federal Ministry for Education and Research within the European research infrastructure ACTRIS.

References

1. Charlson, R.J., Langner, J., Rodhe, H., Leovy, C.B., Warren, S.G.: Perturbation of the northern hemisphere radiative balance by backscattering from anthropogenic sulfate aerosols. Tellus B. **43**, 152–163 (1991)
2. Hansen, J., Sato, M., Lacis, A., Ruedy, R.: The missing climate forcing. Philos. Trans. R. Soc. B. **352**, 231–240 (1997)
3. Robock, A.: Volcanic eruptions and climate. Rev. Geophys. **38**, 191–219 (2000)
4. Solomon, S., Daniel, J.S., Neely III, R.R., Vernier, J.-P., Dutton, E.G., Thomason, L.W.: The persistently variable "background" stratospheric aerosol layer and global climate change. Science. **333**, 866–870 (2011)
5. Jäger, H., Wege, K.: Stratospheric ozone depletion at northern midlatitudes after major volcanic eruptions. J. Atmos. Chem. **10**, 273–287 (1990)
6. Solomon, S., Portmann, R.W., Garcia, R., Thomason, L.W., Poole, L.R., McCormick, M.P.: The role of aerosol variations in anthropogenic ozone depletion at northern midlatitudes. J. Geophys. Res. **101**, 6713–6727 (1996)
7. Solomon, S.: Stratospheric ozone depletion: a review of concepts and history. Rev. Geophys. **37**, 275–316 (1999)
8. Deshler, T., Anderson-Sprecher, R., Jäger, H., Barnes, J., Hofmann, D.J., Clemesha, B., Simonich, D., Grainger, R.G., Godin-Beekmann, S.: Trends in the non-volcanic component of stratospheric aerosol over the period 1971–2004. J. Geophys. Res. **111**, D01201, 21 pp (2006). https://doi.org/10.1029/2005JD006089
9. Deshler, T.: A review of global stratospheric aerosol: measurements, importance, life cycle, and stratospheric aerosol. Atmos. Res. **90**, 223–232 (2008)
10. Kremser, S., Thomason, L.W., von Hobe, M., Hermann, M., Deshler, T., Timmreck, C., Toohey, M., Stenke, A., Schwarz, J.P., Weigel, R., Fueglistaler, S., Prata, F.J., Vernier, J.-P., Schlager, H., Barnes, J.E., Antuña-Marrero, J.-C., Fairlie, D., Palm, M., Mahieu, E., Notholt, J., Rex, M., Bingen, C., Vanhellemont, F., Bourassa, A., Plane, J.M.C., Klocke, D., Carn, S.A., Clarisse, L., Trickl, T., Neely, R., James, A.D., Rieger, L., Wilson, J.C., Meland, B.: Stratospheric aerosol – observations, processes, and impact on climate. Rev. Geophys. **54**, 278–335 (2016). https://doi.org/10.1002/2015RG000511
11. Bingen, C., Robert, C.E., Stebel, K., Brühl, C., Schallock, J., Vanhellemont, F., Mateshvili, N., Höpfner, M., Trickl, T., Barnes, J.E., Jumelet, J., Vernier, J.-P., Popp, J., de Leeuw, G., Pinnock, S.: Stratospheric aerosol data records for the climate change initiative: development, validation and application to chemistry-climate modelling. Remote Sens. Environ. **203**, 296–321 (2017)
12. McCormick, M.P., Swissler, T.J., Chu, W.P., Fuller, W.H.: Post-volcanic stratospheric aerosol decay as measured by lidar. J. Atmos. Sci. **35**, 1296–1303 (1978)
13. Simonich, D.M., Clemesha, B.R.: A history of aerosol measurements at São José dos Campos, Brazil (23 S, 46 W) from 1972 to 1995. In: Ansmann, A., Neuber, R., Rairoux, P., Wandinger, U. (eds.) Advances in Atmospheric Remote Sensing with Lidar, pp. 379–382. Springer, Berlin/Heidelberg/New York (1997)
14. Osborn, M.T., DeCoursey, R.J., Trepte, C.R., Winker, D.M., Woods, D.C.: Evolution of the Pinatubo volcanic cloud over Hampton, Virginia. Geophys. Res. Lett. **22**, 1101–1104 (1995)
15. Jäger, H.: Long-term record of lidar observations of the stratospheric aerosol layer at Garmisch-Partenkirchen. J. Geophys. Res. **110**, D08106, 9 pp (2005). https://doi.org/10.1029/2004JD005506

16. Trickl, T., Giehl, H., Jäger, H., Vogelmann, H.: 35 years of stratospheric aerosol measurements at Garmisch-Partenkirchen: from Fuego to Eyjafjallajökull, and beyond. Atmos. Chem. Phys. **13**, 5205–5225 (2013)
17. Zuev, V.V., Burlakov, V.D., Nevzorov, A.V., Pravdin, V.L., Savelieva, E.S., Gerasimov, V.V.: 30-year lidar observations of the stratospheric aerosol layer state over Tomsk (Western Siberia, Russia). Atmos. Chem. Phys. **17**, 3067–3081 (2017)
18. Khaykin, S.M., Godin-Beekmann, S., Hauchecorne, A., Pelon, J., Ravetta, F., Keckhut, P.: Stratospheric smoke with unprecedentedly high backscatter observed by lidars above Southern France. Geophys. Res. Lett. **45**, 1639–1646 (2018)
19. Zuev, V.V., Gerasimov, V.V., Nevzorov, A.V., Savelieva, E.S.: Lidar observations of pyrocumulonimbus smoke plumes in the UTLS over Tomsk (Western Siberia, Russia) from 2000 to 2017. Atmos. Chem. Phys. **19**, 3341–3356 (2019)
20. Khaykin, S., Legras, B., Bucci, S., Sellitto, P., Isaksen, L., Tence, F., Bekki, S., Bourassa, A., Rieger, L., Zawada, D., Jumelet, J., Godin-Beekmann, S.: The 2019–2020 Australian wildfires generated a persistent smoke-charged vortex rising up to 35 km altitude. Commun. Earth Environ. **1**, 22, 12 pp (2020). https://doi.org/10.1038/s43247-020-00022-5
21. Chouza, F., Leblanc, T., Barnes, J., Brewer, M., Wang, P., Koon, D.: Long-term (1999–2019) variability of stratospheric aerosol over Mauna Loa, Hawaii, as seen by two co-located lidars and satellite measurements. Atmos. Chem. Phys. **20**, 6821–6839 (2020)
22. Trickl, T., Vogelmann, M. D., Fromm, H., Jäger, H., Perfahl, M.: A new generation of the stratospheric aerosol lidar at Garmisch-Partenkirchen – 45 years of lidar vertical sounding. Atmos. Chem. Phys. (2023) (submitted)
23. Vogelmann, H., Trickl, T.: Wide-range sounding of free-tropospheric water vapor with a differential-absorption lidar (DIAL) at a high-altitude station. Appl. Opt. **47**, 2116–2132 (2008)
24. Trickl, T., Giehl, H., Neidl, F., Perfahl, M., Vogelmann, H.: Three decades of tropospheric ozone-lidar development at Garmisch-Partenkirchen, Germany. Atmos. Meas. Tech. **13**, 6357–6390 (2020)
25. Klanner, L., Höveler, K., Khordakova, D., Perfahl, M., Rolf, C., Trickl, T., Vogelmann, H.: A powerful lidar system capable of one-hour measurements of water vapour in the troposphere and the lower stratosphere as well as the temperature in the upper stratosphere and mesosphere. Atmos. Meas. Tech. **14**, 531–555 (2021)
26. Jäger, H., Deshler, T.: Lidar backscatter to extinction, mass and area conversions for stratospheric aerosols based on midlatitude balloonborne size distribution measurements. Geophys. Res. Lett. **29**(19), 4 pp (2002). https://doi.org/10.1029/2002GL015609
27. Baars, H., et al.: The unprecedented 2017–2018 stratospheric smoke event: decay phase and aerosol properties observed with the EARLINET. Atmos. Chem. Phys. **19**, 15183–15198 (2019)
28. Blunden, J., Boyer, T., Eds.: State of the climate in 2020. Bull. Am. Meteor. Soc. 102, Si–S475 (2020). https://doi.org/10.1175/2021BAMSStateoftheClimate.1
29. Trepte, C.R., Hitchman, M.H.: Tropical stratospheric circulation deduced from satellite aerosol data. Nature. **355**, 626–628 (1992)